Transactions of the ASME®

Transactions of the ASME, Journal of Heat Transfer (ISSN 0022-1481) is published quarterly (Feb., May, Aug., Nov.) for $155 per year by The American Society of Mechanical Engineers, 345 East 47th Street, New York, NY 10017. Second class postage paid at New York, NY and additional mailing offices. POSTMASTER: Send address changes to Transactions of the ASME, Journal of Heat Transfer, c/o THE AMERICAN SOCIETY OF MECHANICAL ENGINEERS, 22 Law Drive, Box 2300, Fairfield, NJ 07007-2300.
CHANGES OF ADDRESS must be received at Society headquarters seven weeks before they are to be effective. Please send old label and new address.
PRICES: To members, $29.00, annually; to nonmembers, $155.00. Add $15.00 for postage to countries outside the United States and Canada.
STATEMENT from By-Laws. The Society shall not be responsible for statements or opinions advanced in papers or . . . printed in its publications (B7.1, para. 3).

INDEXED by Applied Mechanics Reviews and Engineering Information, Inc.

Journal of Heat Transfer

Published Quarterly by The American Society of Mechanical Engineers

VOLUME 111 • NUMBER 4 • NOVEMBER 1989

ANNOUNCEMENTS

TECHNICAL PAPERS

(Contents continued)

TECHNICAL NOTES

(Contents continued on page 836)

(Contents continued)

On the Thermal Conductivity of Dispersed Ceramics

G. P. Peterson
Assistant Professor of Mechanical Engineering.
Mem. ASME

L. S. Fletcher
Dietz Professor of Mechanical Engineering.
Fellow ASME

Department of Mechanical Engineering,
Texas A&M University,
College Station, TX 77843

Because of high operating temperatures, advanced high-performance gas turbines will require the use of new types of material. Included among these materials will be dispersed ceramic composites capable of withstanding high temperatures and providing the required strength and wear characteristics. Presented here is a review of several analytical methods by which the effective thermal conductivity of these materials can be determined. In addition, the description and results of an experimental investigation designed to measure the effective thermal conductivity of four of these materials, tungsten carbide–cobalt, tungsten–copper, silicon nitride, and titanium diboride, are presented. Measurements were made over a temperature range of 300 K to 900 K in order to determine the mean effective thermal conductivity and the temperature dependence of this conductivity. The results of the experimental investigation are compared to the values obtained from several of the analytical methods presented and also with other data available in the literature.

Introduction

The high operating temperatures associated with advanced high-performance gas turbines will require the use of new types of composite materials (Viswanathan and Dolbec, 1987). These materials may include nonhomogeneous materials such as layered, fibrous, or dispersed materials, comprised of combinations of conductive and nonconductive constituents. Regardless of the type of composite material used, knowledge of the thermal properties is essential for determination of the material strength characteristics and for the successful development of the necessary technology base. For this reason, a review of the literature pertaining to thermal conductivity studies of composites was conducted. The results of this review indicated a lack of experimental data related to the effective thermal conductivity of dispersed composite materials. Hence an experimental investigation was conducted to determine the thermal conductivity of four fairly diverse advanced ceramic materials, which could be used in the development of advanced high performance gas turbine components. The effective thermal conductivity of these four materials, tungsten carbide–cobalt, tungsten–copper, silicon nitride (with a titanium carbide bonding agent), and titanium diboride were evaluated over a temperature range of 300 K to 900 K in order to determine the mean effective thermal conductivity and the temperature dependence of this conductivity. The results of this experimental investigation are compared to the values obtained from several of the analytical methods presented and to other data available in the literature.

Analysis

Composite materials can be classified into three broad categories, layered, fibrous, and dispersed. Thermal conductivity and contact conductance studies for layered composite materials (O'Callaghan et al., 1977; Veziroglu et al., 1979; Yovanovich et al., 1982; Hagen, 1987) and fibrous composites (Gorring and Churchill, 1961; Han and Cosner, 1981; Peterson and Fletcher, 1987; Mandell et al., 1987) have been performed previously and the resulting characteristics are reasonably well understood. In the case of metallic ceramics and other dispersed materials, however, only limited investigations have been conducted.

Several analytical investigations have been conducted including relationships based on direct measurement, semi-empirical relations, and approximate and theoretical techniques (Torquato, 1987). Among the analytical approximations that exist for determining the effective thermal conductivity of dispersed materials, the most well known are those of Rayleigh (1892) or Gorring and Churchill (1961). More recently, Dul'nev (1965), Beran (1968), Hale (1974), and Hashin (1983) have developed expressions that are all similar in that they require precise information about the individual constituents. An example of this type is the expression developed by Dul'nev for determining the effective thermal conductivity of dispersed systems with unidirectional conduction and one of the phases interconnected.

$$\frac{k_e}{k_1} = c^2 + \nu(1-c)^2 + \frac{2\nu c(1-c)}{1-c(1-\nu)} \tag{1}$$

where

$$c = \frac{x/(0.5-x)}{1+[x/(0.5-x)]} \tag{2}$$

$$\nu = k_1/k_2 \tag{3}$$

and x is found from

$$4x^3 - 3x^2 + \frac{1-\phi_2}{4} = 0 \tag{4}$$

This expression, which has no temperature constraints, yields two positive real values, the larger of which should be used.

Because of the difficulty involved in measuring all possible combinations of constituent thermal conductivities, k_1 and k_2, and volume fractions, ϕ_1 and ϕ_2, along with the microstructure properties, such as orientation, size, and connectivity of the individual constituents, which do not even appear in Dul'nev's expression, the most useful of the existing analytical techniques are those that establish upper and lower bounds. With these bounds the effective thermal conductivity can be determined using the known constitutive information. As additional information becomes available, these bounds can be tightened and will more closely approximate the actual values.

Torquato and Stell (1985) have presented a review of available bounding techniques for two-dimensional and three-dimensional composite media (i.e., $d=2$ and $d=3$), which could lead to a highly cost-effective means of optimally developing and manufacturing advanced composite materials. For three-dimensional materials such as those of interest here, several

Contributed by the Heat Transfer Division and presented at the ASME Winter Annual Meeting, Chicago, Illinois, November 29–December 2, 1988. Manuscript received by the Heat Transfer Division June 23, 1988. Keywords: Conduction, High-Temperature Phenomena, Measurement Techniques.

bounding techniques have been developed. The first of these was developed by Hashin and Shtrikman (1962) in which the bounds on k_e for three-dimensional ($d=3$) isotropic media were established as

$$k_L \leq k_e \leq k_U \tag{5}$$

where

$$\frac{k_L}{k_1} = \frac{1+(d-1)\phi_2\beta_{21}}{1-\phi_1\beta_{21}} \tag{6}$$

$$\frac{k_U}{k_2} = \frac{1+(d-1)\phi_1\beta_{12}}{1-\phi_1\beta_{12}} \tag{7}$$

and

$$\beta_{ij} = \frac{k_i - k_j}{k_i + (d-1)k_j} \qquad i \neq j \tag{8}$$

No temperature bounds were given and as can be seen, the effective thermal conductivity is only a function of the number and type of material (in this case two), the thermal conductivity ratio, the dimension d, and the volume fraction of the two materials, eliminating the need for microstructural information to be known. As defined by Brown (1955) these bounds serve as second-order bounds in that they are exact through second order in $(k_2 - k_1)$ (Torquato, 1987).

Expressions for higher order bounds also have been developed, but require information, such as the mean cluster sizes, in addition to the volume fractions. These expressions most commonly employ the principles of minimum potential and minimum complementary energy. Beran (1968) derived third-order bounds for three-dimensional isotropic systems using the first two terms of the perturbation expansion of the fields. Using a single threefold integral, Torquato and Stell (1985) and Milton (1981a) independently developed a method to represent the sixfold integrals of certain three-point correlation functions. Two dimensional analogs of the Berans bounds have been developed by Silnutzer (1972), while Milton (1982) expressed these terms of the volume fractions and a single threefold integral (Torquato, 1986).

As mentioned previously, all of the third-order bounds require an additional parameter ζ_2, which depends on the n-point probability functions S_1, S_2, and S_3. This three-point parameter, ζ_2, can be defined for two and three dimensions, respectively, as

$$\zeta_2 = 1 - \frac{4}{\pi\phi_1\phi_2}\int_0^\infty \frac{dr}{r}\int_0^\infty \frac{ds}{s}\int_0^\pi d\theta \cos(2\theta) x\left[S_3(r, s, \theta) - \frac{S_2(r)S_2(s)}{S_1}\right] \tag{9}$$

$$\zeta_2 = 1 - \frac{9}{2\phi_1\phi_2}\int_0^\infty \frac{dr}{r}\int_0^\infty \frac{ds}{s}\int_{-1}^1 d(\cos 2\theta)P_2(\cos\theta) x\left[S_3(r, s, \theta) - \frac{S_2(r)S_2(s)}{S_1}\right] \tag{10}$$

where P_2 is the second-order Legendre polynomial. This expression is based upon a probability function that depends upon the probability of a triangle, with two sides of length r and s and an included angle of θ, having all three verticies in a single component material when placed randomly in the dispersed ceramic (Torquato, 1987).

A series of fourth-order bounds, which compensate for the effects of inclusions on the temperature profile by an averaging process and the effects of local or microconduction for media without contact resistance, have been developed by Ben-Amoz (1976). This method utilizes a variational technique to generalize the heat conduction equation. The resulting Euler-Lagrange equation yields an expression that includes some of the effects of variations in the microstructure, which can be solved using Laplace transform techniques. The boundary conditions are somewhat complicated and require an additional surface boundary condition referred to as the "hyperflux" (the spatial derivative of the heat flux).

Baker-Jarvis and Inguva (1985) have extended this analysis and presented a new exact solution to the nonhomogeneous problem utilizing Green's function techniques. The resulting boundary conditions, the temperature and temperature gradient at the boundary surfaces, are simpler, more physically meaningful than those originally proposed by Ben-Amoz (1976). Finally, higher order bounds (i.e., nth-order bounds) have also been developed (Milton, 1981b), but will not be discussed here.

Experimental Investigation

Due to the technological importance of accurately knowing the effective thermal conductivity and other thermal properties of materials, a large body of experimental data is necessary. For this reason, an experimental investigation was conducted to determine the effective thermal conductivity of four advanced dispersed ceramic materials, tungsten carbide–cobalt, tungsten–copper, silicon nitride (with a titanium carbide bonding agent), and titanium diboride. The experimental facilities used in this investigation, along with the details of the facility construction, operation, and accuracy, have been reported previously by Duncan (1987). The experimental facility, shown in Fig. 1, consisted of a vertical column composed of a guard heater, a heat source, two Stainless Steel 304 test fixtures, the test specimen, a load cell and a heat sink. The fixtures and test specimens were arranged to form a cylindrical column with the test specimen sandwiched between the two stainless steel test fixtures. Each stainless steel fixture was held in one of two identical dual function heat source/heat sink fixtures. The heat source consisted of three 200-W cartridge heaters. These heaters were placed in a copper housing, which was connected to the fixture opposite the end in contact with the test specimen. A silicone heat sink compound was applied to the contacting surfaces of the housing and the fixture to enhance the thermal conductance between them. The heat sink consisted of a copper coil, in which an ethylene-glycol coolant was circulated,

Nomenclature

- c = dummy variable, defined by equation (2)
- d = dimensions considered
- k = conductivity
- P = second-order Legendre polynomial
- r = first side of the triangle used in the probability function
- S = probability function
- s = second side of the triangle used in the probability function
- x = dummy variable, defined by equation (4)
- β = parameter, defined by equation (8)
- ζ = artificial parameter, defined by equations (9) and (10)
- θ = included angle between sides r and s of a triangle
- ν = ratio of thermal conductivities of the primary materials
- ϕ = volume fraction

Subscripts

- 1 = primary material
- 2 = secondary material
- e = effective
- L = lower bound
- U = upper bound

Table 1 Properties of the test specimens

Property	(WC-Co)	(W-Cu)	(Si_3N_4-TiC)	(TiB_2)
Density ($kg/m^3 \times 10^{-3}$)	13.61	14.74	3.6-3.9[a]	4.52[a]
Thermal expansion ($K^{-1} \times 10^6$)	7.5[b]	3.7[c]	3.0[a]	7.8[a]
Vickers hardness ($kg/m^2 \times 10^{-6}$)	1765	238	2000[a]	3800
Young's modulus (kg/m^2)	—	—	3.3×10^{-2}	80
Specific heat (J/kg-K)[b]	2501	133.9	1256	1088
Chemical composition (percent)	WC 86.09	W 75.36	Si_3N_4 74.92	Ti 67.98
	C 13.04	Cu 24.61	TiC 23.9	B 31.25
	Ta <0.01	Si <0.01	Fe <0.01	C 0.37
	Nb <0.01	H_2 <0.01	Ca <0.01	N 0.12
		Ni <0.01	Al <0.01	O_2 0.48
		N_2 <0.01	Mn <0.01	Al <0.01
		P <0.01	Mg <0.01	Fe <0.01
			Zr <0.01	Mg <0.01
			Cr <0.01	P <0.01
				Si <0.01

[a] Obtained from the manufacturer.
[b] Touloukian (1972).
[c] Pure tungsten value.

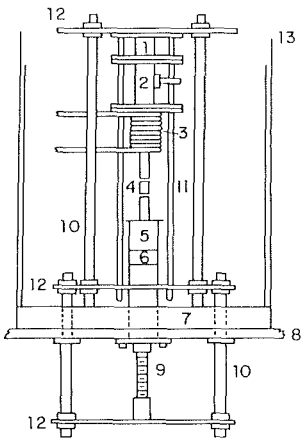

1 LOAD BELLOWS
2 LOAD CELL
3 HEAT SINK
4 TEST SPECIMENS
5 HEAT SOURCE
6 GUARD HEATER
7 FEEDTHROUGH RING
8 BASE PLATE
9 SCREW JACK
10 SUPPORT RODS
11 GUIDE RODS
12 SUPPORT PLATES
13 BELL JAR

Fig. 1 Experimental test apparatus

wrapped around the copper housing, and silver soldered to its surface. A passive radiation shield made of silver-teflon, a high emissivity/low absorptivity material, 11.43 cm in diameter, surrounded the test column to assure minimal radiation losses. A high-pressure pneumatic loading system was used to maintain a constant load on the test column. The load was applied by bleeding high-pressure nitrogen gas into the stainless steel bellows vessel located at the top of the column. A load cell coupled with a demodulator allowed the mechanical load to be monitored without disturbing the vacuum or the test specimen.

Test specimens 2.54 cm in diameter and 3.80 cm long were prepared from each of the four test materials. The samples were first turned and then ground to ensure that the contacting surfaces were flat. A fifth test specimen was prepared from an electrolytic iron reference material obtained from the National Bureau of Standards for use as a calibration standard. A series of nine Chromel-Alumel AWG-30 thermocouples was used to determine the temperature distribution in the test specimen and the two stainless steel fixtures. These thermocouples were placed in number 56 holes drilled to the centerline of the sample, packed in place with a silver-filled thermally conductive epoxy, and wrapped once around the outside surface to improve the measurement accuracy. Radial heat losses were monitored by thermocouples located on the surface of each test specimen.

Once the thermocouples had been installed and the fixtures assembled, the test specimen was placed in the experimental test facility and isolated from the surrounding atmosphere by a bell jar sealed with a silicone vacuum grease. The tests were conducted in a vacuum environment to eliminate the effects of any interstitial fluids on the thermal conductivity. A vacuum of 5×10^{-5} torr was maintained using an Acatel 2300 roughing pump in series with an NRC VHJ-6 oil diffusion pump. A 46 $\times$ 76 cm Pyrex bell jar was used to encase the thermal test facility, and four NRC model 531 thermocouple gages, in conjunction with two Bayard-Alpert ionization gage tubes and a controller, were used to monitor the vacuum quality.

Experimental Procedure

A total of five materials were tested, the four test materials, tungsten carbide-cobalt (WC-Co), tungsten-copper (W-Cu), silicon nitride (Si_3N_4), titanium diboride (TiB_2), and the NBS electrolytic iron reference material (ERM). The tungsten carbide-cobalt material tested was supplied by GTE Valentine Corporation and was approximately 87 percent tungsten carbide and 13 percent cobalt. It had an initial tungsten carbide grain size of between one and three microns. The tungsten-copper material was composed of approximately 75 percent tungsten and 25 percent copper. The silicon nitride material tested was developed by Sumitomo of Japan for use with standard electrodischarge machining techniques and utilized titanium carbide as the bonding material, making the composition approximately 75 percent silicon nitride and 25 percent titanium carbide. The titanium diboride sample was supplied by Union Carbide and was prepared by hot pressing a mixture, which prior to sintering was comprised of approximately 68 percent titanium and 32 percent boron to 95-98 percent of the theoretical density shown in Table 1. The precise chemical compositions of the samples along with several other physical and thermophysical properties of the four materials tested are shown in Table 1. Figures 2(*a*) through 2(*d*) illustrate the grain structure for each of the four materials tested. In Figs. 2(*a*), 2(*b*), and 2(*c*), the darker areas represent the cobalt, copper, and titanium carbide, respectively, while the lighter areas are the tungsten carbide, tungsten, and silicon nitride. As shown, with the exception of the titanium diboride, Fig. 2(*d*), all of the materials are truly dispersed, with individual particles of the minor constituent embedded in the major constituent.

The NBS electrolytic iron reference material was purchased

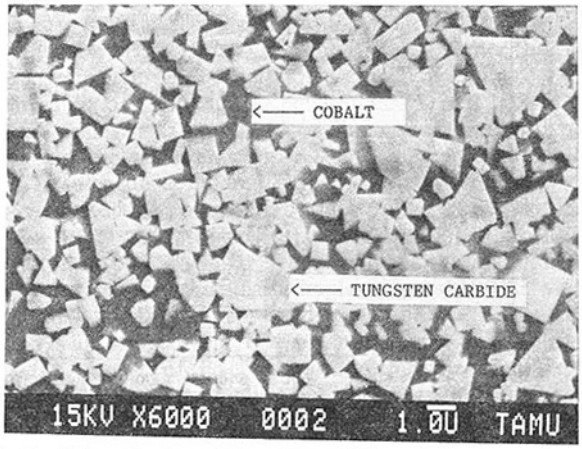

Fig. 2a Microstructure of tungsten carbide-cobalt test specimen

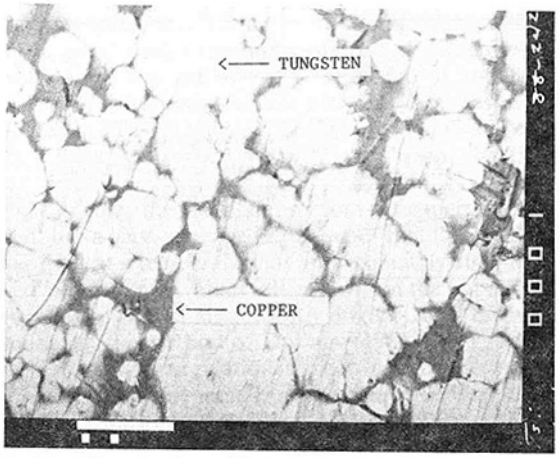

Fig. 2b Microstructure of tungsten-copper test specimen

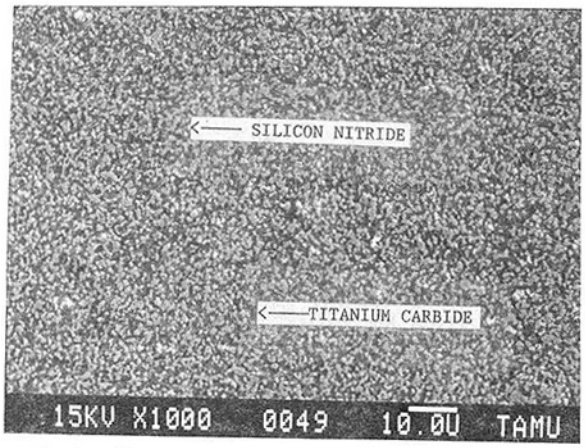

Fig. 2c Microstructure of silicon nitride test specimen

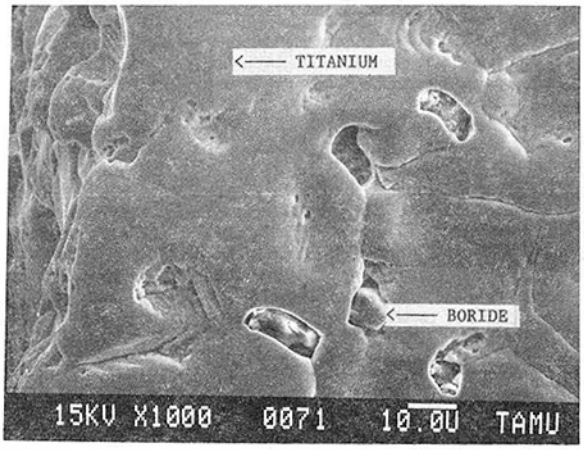

Fig. 2d Microstructure of titanium diboride test specimen

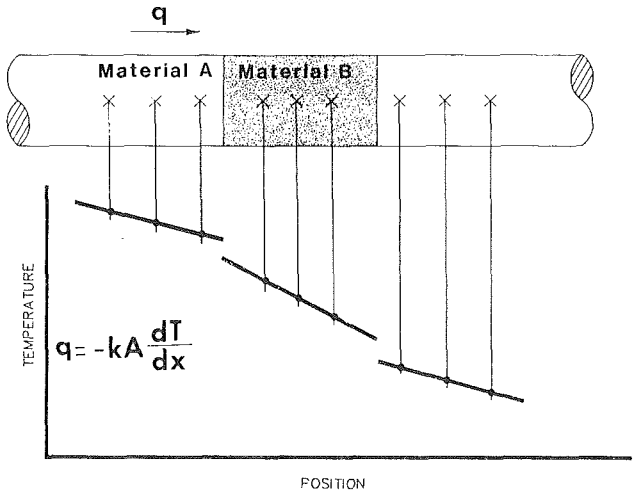

Fig. 3 Determination of the effective thermal conductivity

from the National Bureau of Standards in Boulder, CO. Prior to testing the four test specimens, the electrolytic iron reference material was placed into the test facility and the thermal conductivity was measured over a temperature range similar to that anticipated for the ceramic test specimens, in order to calibrate the stainless steel fixtures.

For each test, the specimen surfaces were wiped clean with acetone and coated with a thin layer of thermally conductive grease to improve the contact at the interfaces. The specimens then were inserted between the two test fixtures. The entire test column was visually aligned and a load was applied by pressurizing the bellows vessel to insure that the surfaces remained in contact. The radiation shields were then put in place, the test chamber evacuated, and the specimens allowed to outgas for 4–5 hours.

Tests were conducted over a mean specimen temperature range of from 300 to 900 K. The specimen mean temperature conditions were set by adjusting the heater voltages and the temperature of the coolant bath. Once steady state had been reached for each setting, the temperature distribution in the fixtures and test specimen was recorded. Steady state was assumed to have been reached when no individual thermocouple exhibited a temperature change of more than 0.2 K over a period of one hour.

As shown in Fig. 3, with the experimentally verified thermal conductivity of the stainless steel fixtures and the measured temperature distribution in the fixtures, the heat flux in both the upper and lower fixtures could be determined. Radiation losses were assumed to be negligible. Using the average of these two heat fluxes, which were typically within ±2 percent of each other, and the measured temperature distribution in the test specimen, the thermal conductivity of each specimen could be calculated. The experimental uncertainty associated with the measurement of the thermal conductivity was computed to be ±6.5 percent. Contributing factors to this uncertainty were uncertainties resulting from the temperature measuring system and with the technique used to compute the heat flux in the test fixtures.

Results and Discussion

The results of the calibration tests conducted on the electrolytic iron are shown in Fig. 4. As illustrated, the experi-

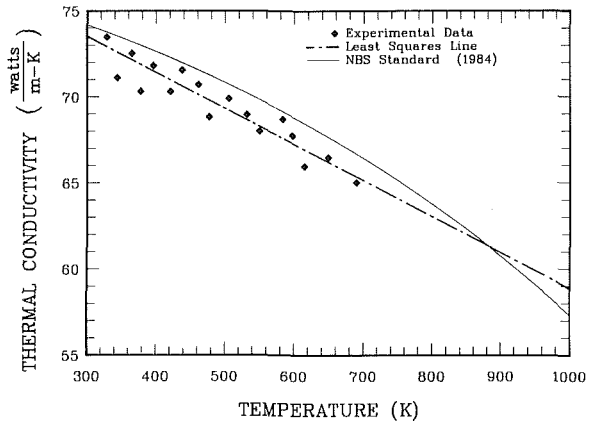

Fig. 4 Experimental results of the calibration tests on electrolytic iron

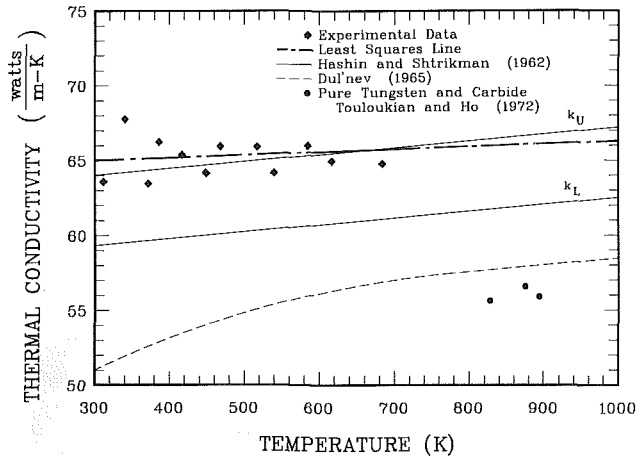

Fig. 5 Comparison of the measured thermal conductivity and other referenced values for tungsten carbide–cobalt

mental results are consistently lower than the values specified by the National Bureau of Standards. However, all of the data are within 4 percent of the NBS certified value. Because of this slight difference, a least-squares curve fit was used to adjust the thermal conductivity of the stainless steel fixtures used in the computation of the heat flux. The resulting temperature-dependent thermal conductivity for the stainless steel over the temperature range investigated here (300 K–900 K) was expressed as

$$k = 6.9337 + (2.4364 \times 10^{-2})T \qquad (11)$$

where the thermal conductivity k is in W/m-K and the temperature T is in degrees Kelvin. Use of this expression resulted in a better correlation between the NBS certified value and the measured value than that obtained using standard tabular data for the thermal conductivity of stainless steel. This adjusted thermal conductivity for the stainless steel fixtures was used for each of the four samples tested.

Figures 5 through 8 present the results of the experimental tests performed on the four materials evaluated, tungsten carbide–cobalt, tungsten–copper, silicon nitride, and titanium diboride, respectively, and compares these values with the values predicted by the analytical methods of Dul'nev (1965) and Hashin and Shtrikman (1962) using a three-dimensional approximation (i.e., $d = 3$). In the case of the tungsten carbide–cobalt (Fig. 5), the results of previous tests conducted on commercially pure tungsten carbide (Touloukian, 1967) are presented for comparative purposes. As illustrated, the thermal conductivity of the tungsten carbide–cobalt ceramic tested is approximately 20 percent higher than that of the pure tungsten

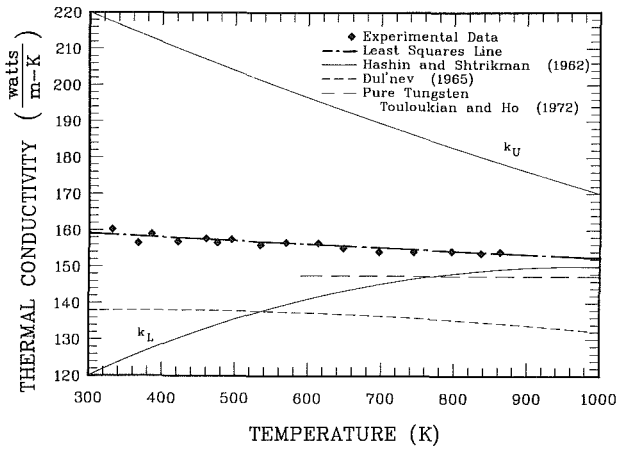

Fig. 6 Comparison of the measured thermal conductivity and other referenced values for tungsten–copper

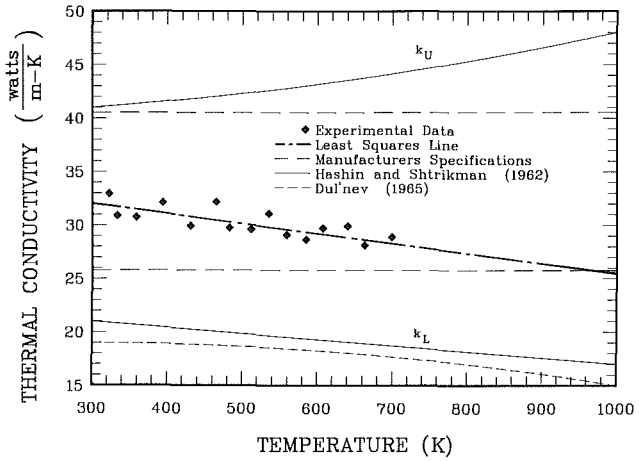

Fig. 7 Comparison of the measured thermal conductivity and other referenced values for silicon nitride with titanium boride

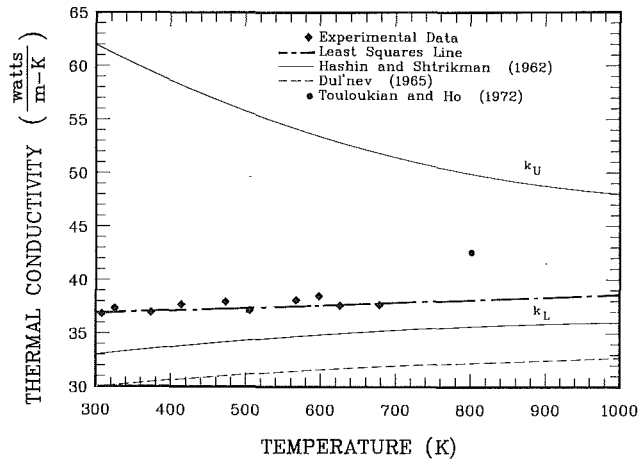

Fig. 8 Comparison of the measured thermal conductivity and other referenced values for titanium diboride

carbide. Not enough information is available in this temperature range to make any comparisons on the trend with respect to increased temperature. However, at higher temperatures the literature indicates a trend toward increased thermal conductivity with respect to increased temperature similar to that shown. Using temperature-dependent thermal conductivity values for the individual components, obtained from the literature, and the analytical methods of Dul'nev (1965) and Hashin and Shtrikman (1962), the predicted and measured

values were compared. As illustrated, the experimental values are slightly higher at low temperatures than the upper bound as predicted by equation (7) and significantly higher than the values predicted using the method developed by Dul'nev (1965) for the range of temperatures between 300 K and 1000 K.

Figure 6 illustrates the results of the experimental tests performed on the tungsten–copper test specimen. The experimental results are compared with the results from previous tests conducted on commercially pure tungsten (Touloukian and Ho, 1972). As illustrated, the results obtained in this investigation display a similar decrease in the thermal conductivity with respect to the mean sample temperature. As would be expected, the thermal conductivity of the tungsten–copper ceramic is higher than that of the commercially pure tungsten due to the presence of the copper. All of the experimental data are within the upper and lower bounds as predicted using the method of Hashin and Shtrikman (1962), and although the data are significantly higher than the values obtained using the Dul'nev (1965) model, the trend, decreasing with respect to temperature, is similar for the temperature range evaluated.

Figure 7 presents the results of the tests conducted on silicon nitride. As mentioned previously, the test specimen used in this investigation was provided by Sumitomo of Japan, and was developed specifically for use with EDM processes. The thermal conductivity range specified by the manufacturer was from 25.9 W/m-K to 41.86 W/m-K. As shown, the experimentally determined thermal conductivity falls within the bounds specified by the manufacturer for the temperature range evaluated, but a least-squares line indicates that it would reach the lower limit at a temperature of approximately 1000 K. The measured experimental values fall well within the upper bound and lower bounds and significantly higher than the values predicted using the method of Dul'nev (1965).

Figure 8 illustrates the relationship between the thermal conductivity and the mean sample temperature for titanium diboride. One additional reference point was found in the literature (Battelle, 1964). This value of 43.26 W/m-K lies outside of the temperature range tested, but is approximately 12 percent above the least-squares line. Although as illustrated in Fig. 2(*d*), the titanium diboride does not consist of two separate well-defined constituents as do the others, a comparison of the measured experimental values and the predicted values was performed. As illustrated, again, the experimental data are all within the predicted limits, but approximately 10 to 15 percent higher than the values predicted using the method developed by Dul'nev (1965).

Conclusions

The purpose of this experimental investigation was to provide additional thermal conductivity data for several candidate materials for use in advanced gas turbines. The results presented establish a baseline along with temperature-dependent trends within the temperature range of 300 K to 1000 K. Accumulation of data of this type will be helpful in the development and verification of analytical models designed to predict the thermal performance characteristics of these materials and in establishing the maximum operating temperature and rate at which heat can be dissipated within the individual components.

In comparing the analytical techniques developed by Hashin and Shtrikman (1962) and Dul'nev (1965), two trends are apparent. First, all of the experimental data obtained, with the exception of a portion of the tungsten carbide–cobalt, fall well within the upper and lower bounds defined by the method developed by Hashin and Shtrikman (1962), indicating that it accurately predicts these bounds. Second, the analytical model developed by Dul'nev (1965) significantly underpredicts the thermal conductivity in all cases tested, but does accurately predict the trend. It should be noted that the accuracy of the analytical predictions evaluated is strongly dependent on the individual constituent thermal conductivities.

Acknowledgments

The authors would like to express their thanks to the AGIE Corporation, Locarno, Switzerland, for providing partial support for this investigation.

References

Baker-Jarvis, J., and Inguva, R., 1985, "Heat Conduction in Heterogeneous Materials," ASME JOURNAL OF HEAT TRANSFER, Vol. 107, pp. 39–43.

Battelle Memorial Institute, 1964, *Refractory Ceramics for Aerospace—A Materials Selection Handbook*, The American Ceramics Society Inc., Columbus, OH.

Ben-Amoz, M., 1976, "Heat Conduction for Composite Materials," *ZAMP*, Vol. 27, pp. 335–345.

Beran, M. J., 1968, *Statistical Continuum Theories*, Wiley, New York.

Brown, W. F., 1955, "Solid Mixture Permittivities," *J. of Chem. Physics*, Vol. 23, pp. 1514–1517.

Dul'nev, G. N., 1965, "Heat Transfer Through Solid Disperse Systems," *Inzhenero-Fizicheskii Zhurnal*, Vol. 9, No. 3, pp. 339–404.

Duncan, A. B., 1987, "Effective Thermal Conductivity of Packed Beds of Spheres," M.S. Thesis, Mechanical Engineering Department, Texas A&M University, College Station, TX.

Gorring, R. L., and Churchill, S. W., 1961, "Thermal Conductivity of Heterogeneous Materials," *Chemical Engineering Progress*, Vol. 57, No. 7, pp. 53–59.

Hagen, K. D., 1987, "A Solution to Unsteady Conduction in Periodically Layered, Composite Media Using a Perturbation Method," ASME JOURNAL OF HEAT TRANSFER, Vol. 109, pp. 1021–1023.

Hale, D. K., 1974, "The Physical Properties of Composite Materials," *Journal of Material Science*, Vol. II, pp. 2105–2141.

Han, L. S., and Cosner, A. A., 1981, "Effective Thermal Conductivities of Fibrous Composites," ASME JOURNAL OF HEAT TRANSFER, Vol. 103, May, pp. 387–392.

Hashin, Z., 1983, "Analysis of Composite Materials," ASME *Journal of Applied Mechanics*, Vol. 50, pp. 481–505.

Hashin, Z., and Shtrikman, S., 1962, "A Variational Approach to the Theory of the Effective Magnetic Permeability of Multiphase Materials," *Journal of Applied Physics*, Vol. 33, pp. 1514–1517.

Mandell, J. F., Grande, D. H., and Jacobs, J., 1987, "Tensile Behavior of Glass/Ceramic Composite Materials at Elevated Temperatures," ASME *Journal of Engineering for Gas Turbines and Power*, Vol. 109, pp. 267–273.

Milton, G. W., 1981a, "Bounds on the Electromagnetic Elastic, and Other Properties of Two-Component Composites," *Phys. Rev. Letters*, Vol. 46, pp. 542–545.

Milton, G. W., 1981b, "Bounds on the Transport and Optical Properties of a Two-Component Composite Material," *Journal of Applied Physics*, Vol. 52, pp. 5294–5304.

Milton, G. W., 1982, "Bounds on the Elastic and Transport Properties of Two-Component Composites," *J. of the Mech. and Phys. of Solids*, Vol. 30, pp. 177–191.

NBS Standard, 1984, NBS Standard Reference Publication, NBSIR 84-3007.

O'Callaghan, P. W., Jones, A. M., and Probert, S. D., 1977, "Effect of Thermal Contact Resistance on the Performance of Transformer Lamination Stacks," *App. Energy*, Vol. 3, pp. 13–22.

Peterson, G. P., and Fletcher, L. S., 1987, "A Review of Thermal Conductivity in Composite Materials," 22nd AIAA Thermophysics Conference, Honolulu, HI, June 8–10, Paper No. AIAA-87-1586.

Rayleigh, L., 1892, "On the Influence of Obstacles Arranged in Rectangular Order Upon the Properties of a Medium," *Phil. Mag.*, Vol. 34, p. 481.

Silnutzer, N., 1972, "Effective Constraints of Statistically Homogeneous Materials," Ph.D. Thesis, University of Pennsylvania, Philadelphia, PA.

Torquato, S., 1987, "Bounds on the Thermal Conductivity of Disordered Heterogeneous Media," *Proc. of the 1987 ASME/JSME Thermal Engineering Joint Conference*, pp. 359–367.

Torquato, S., and Stell, G., 1985, "Bounds on the Effective Thermal Conductivity of a Dispersion of Fully Penetrable Spheres," *Letters in App. and Engr. Science*, Vol. 23, pp. 375–384.

Touloukian, Y. S., 1967, *Thermophysical Properties of High Temperature Solid Materials*, MacMillan, New York.

Touloukian, Y. S., and Ho, C. Y., 1972, *Thermophysical Properties of High Temperature Solid Materials*, TPRC Series IFI, Plenum Press, New York.

Veziroglu, T. N., Williams, A., Kakac, S., and Nayak, P., 1979, "Prediction and Measurement of the Thermal Conductance of Laminated Stacks," *Int. J. of Heat and Mass Trans.*, Vol. 22, No. 3, pp. 447–459.

Viswanathan, R., and Dolbec, A. C., "Life Assessment Technology for Combustion Turbine Blades," ASME *Journal of Engineering for Gas Turbines and Power*, Vol. 109, pp. 115–123.

Yovanovich, M. M., DeVaal, J., and Hegazy, A. H., 1982, "A Statistical Model to Predict Thermal Gap Conductance Between Conforming Rough Surfaces," AIAA Paper No. 82-0888.

Effective Thermal Conductivity Within Packed Beds of Spherical Particles

A. B. Duncan
Graduate Research Assistant,
Department of Aerospace and
Mechanical Engineering,
University of Notre Dame,
Notre Dame, IN 46556

G. P. Peterson
Associate Professor of Mechanical
Engineering.
Mem. ASME

L. S. Fletcher
Dietz Professor of Mechanical
Engineering.
Fellow ASME

Department of Mechanical Engineering,
Texas A&M University,
College Station, TX 77843

An investigation of the effective thermal conductivity of packed beds of spherical particles was conducted. Included is a brief review of related analytical and experimental investigations, along with a description of the results from an experimental program. Five beds of different materials were evaluated to determine the effective thermal conductivity as a function of the mechanical load on the bed, the conductivity of the bed material, and the interstitial gaseous environment surrounding the bed particles. The effective thermal conductivity of the packed beds were found to be dependent upon the thermal conductivity of the bed material and the axial load. The presence of an interstitial gas increased the effective thermal conductivity of the bed by a factor of two in almost all cases. The experimental results obtained for vacuum conditions were compared with two existing analytical models that assumed elastic deformation of the spheres. The analytical models slightly underpredicted the effective thermal conductivity for hard materials with low thermal conductivities below the elastic limit, and slightly overpredicted the effective thermal conductivity above the elastic limit for these materials. For soft materials with relatively high thermal conductivities, the analytical models overpredicted the effective thermal conductivity by as much as an order of magnitude.

Introduction

Packed beds of spherical particles are found in thermal insulation, chemical catalysts, heat exchangers, automotive catalytic converters, nuclear reactor fuel rods, and many other applications in which spherical components interface with each other and with flat, convex, or concave surfaces. A number of investigations have been conducted in order to analyze the thermal behavior of this geometric configuration. Heat transfer in packed beds results from a combination of conduction, radiation, and convection. The conduction contribution, which is usually the most significant, is dependent not only upon the thermal conductivity of the particle material and the surrounding gas, but also on the interfacial contact areas through which heat flows and the contact resistance occurring at these interfaces (Yovanovich, 1967). Radiation is largely temperature dependent and is most significant at high temperatures. A study by Chen and Churchill (1963) concluded that in beds of glass or aluminum oxide particles of cylindrical or irregular grains, the radiation effects are important only for temperatures above 1140 K. Wakao and Vortmeyer (1971) have shown that the convective contribution is principally dependent on the local fluid pressure and the packing density of the bed. This contribution generally will increase as the fluid pressure or void fraction increases.

The experimental program presented here was designed to evaluate the effect of the mechanical load and the thermal conductivity of both the spherical particle material and the surrounding gaseous environment, on the effective thermal conductivity of five randomly packed beds of different materials in three different gaseous environments.

Analytical Solutions

For a load F, a sphere and rigid isothermal plane are in contact over an area with radius a (Timoshenko and Goodier, 1946). The total displacement in the direction of load F can be expressed as

$$\omega(r) = \begin{cases} a^2(2-r^2/a^2)/2\rho & \text{if } r \le a \\ \dfrac{(a^2[(2-r^2/a^2)\ \arcsin\ a/r + (r^2/a^2-1)^{1/2}])}{\pi\rho} & \text{if } r > a \end{cases} \tag{1}$$

The dimensionless contact radius $\epsilon = a/\rho$ can be determined from classical elasticity theory as

$$\epsilon = (Pa/E)^{1/3} \tag{2}$$

Here P is the Hertzian contact stress and E represents the modulus of elasticity of the sphere material. Since only elastic deformations of the sphere are considered in this expression, it is possible to have an expression relating the maximum value of the dimensionless contact radius ϵ to the physical properties of the sphere (Timoshenko and Goodier, 1946).

Yovanovich (1973a) investigated the problem of heat conduction between single spheres in contact. A general analytical method, which defines conduction shape factors for systems bounded by two isothermal surfaces, was extended to the particular case of elastically deformed spheres that lie between two rigid planes. In this investigation, elastic theory was used to define the deflection of the sphere under loading and the contact area between the spheres and the rigid planes.

The mathematical solution to determine the temperature difference between two spheres in contact with isothermal contact areas A_1 and A_2 can be found as

$$T_1 - T_2 = \frac{Q}{2ka} - \frac{Q}{\pi ka}\int_0^\infty \left(\frac{2e-l\rho}{1+e_l^2\rho}\right) J_0(lr)\ \sin\ (la)\ \frac{dl}{l} \tag{3}$$

(Yovanovich, 1973a). Equation (3) then can be used to develop an expression for the thermal resistance

$$R_c = \frac{(T_1 - T_2)}{Q} = \frac{1}{2ka} - \ln\left(\frac{1}{\pi k\rho}\right) \tag{4}$$

where R_c represents the contact resistance to heat conduction between two surfaces. This can be expressed on a unit area basis in terms of ϵ as

Contributed by the Heat Transfer Division and presented at the ASME Winter Annual Meeting, Chicago, Illinois, November 28–December 2, 1988. Manuscript received by the Heat Transfer Division June 23, 1988. Keywords: Conduction, Packed and Fluidized Beds, Porous Media.

$$R_c = 0.885\ (1 - 0.443\epsilon)/k\epsilon \tag{5}$$

When the contact radius is small relative to the sphere radius, as is usually the case with elastic deformation, the contact resistance is due entirely to the constriction of heat flow lines and the total resistance becomes

$$R_c = 0.885/k\epsilon \tag{6}$$

General Bed of Spherical Particles

A separate category of expressions for predicting the effective thermal conductivity in a packed bed of spheres is to extend the analysis of a single sphere to that of the entire bed. Two general methods of predicting the apparent conductivity of porous substances exist (Yovanovich, 1973b):

(*i*) the method of generalized thermal conductivities, and
(*ii*) a method based upon the geometry of a typical element.

The first method postulates that the effective thermal conductivity is a function of the thermal conductivities of the solid and fluid in the voids, the volume concentrations of the solid and fluid, and the distribution of the two phases within the porous substance. In the second method, typical particle shape, size, and packing are assumed and the heat transfer through such an element is calculated.

The method, which is based on typical element geometry, a "unit cell" approach, lends itself well to analytical solution techniques since the physical relationships of all particles in the bed are consistent. In this review, two "generalized conductivity" solutions, three "unit cell geometry" solutions, and two numerical solutions based on unit cell geometry are presented and discussed.

General Conductivity Solutions

Gorring and Churchill (1961) discuss some of the simpler exact solutions that exist. These solutions assume that the two phases of the packed bed can be represented by series or parallel resistive circuits. These relationships have previously been shown significantly to under and overpredict the actual values for multiphase beds, respectively (Peterson and Fletcher, 1987).

Hadley (1986) presented the results of an analytical and experimental investigation, based on a general conductivity approach, which dealt with the effective thermal conductivity of packed metal powders. For a two-phase granular system, the effective thermal conductivity of a packed bed was found to be

$$k_{\text{eff}} = (k_f)\left\{\frac{(1-m)f_o + \dfrac{k_s}{k_f}\left(1-(1-m)f_o\right)}{1-(1-m)(1-f_o) + \dfrac{k_s}{k_f}(1-m)(1-f_o)}\right\} \tag{7}$$

Here $(1-m)$ is the solid volume fraction, and f_o is an empirical constant.

This analytical expression was developed for metal powders and used a technique developed by Batchelor (1972), which predicted the bulk properties of the two-phase mixture by assuming a very small void fraction. Although the expression shown in equation (7) compared quite well with the experimental results obtained by Batchelor (1977), it is inappropriate for use in the packed beds of this investigation due to the large void fractions encountered.

Kaganer (1966) developed a method by which the thermal resistance of a sphere with two contact areas could be determined. This analysis was further expanded to packed beds. The effective thermal conductivity (k_{eff}) of a granular material was given as

$$k_{\text{eff}} = Qh/A\Delta T \tag{8}$$

where Q is the heat flux through an individual particle, h is the height corresponding to the temperature difference ΔT, and A is the cross-sectional area in the bed corresponding to a single particle. Each sphere in the bed was assumed to be in contact with N other spheres and $N/3$ contacts of a sphere are associated with the direction of each of three mutually perpendicular axes. From this analysis, it was apparent that $N/6$ contacts would be associated with each of the two opposite directions along any one of the axes. Hence, contact in a single direction could be with only one space. The physical meaning is apparent in that the numerical value of the heat flux through one sphere in the direction of the temperature gradient can be represented as a function of Q_1, which is related to T_1, as

$$Q = |Q_1|N/6 \tag{9}$$

The bed area associated with one particle can be related to other bed parameters by the relation

$$m = 1 - (4\pi 2h^3/3hA) \tag{10}$$

Therefore

$$A = \frac{2\pi 2h^2}{3(1-m)} \tag{11}$$

Values of N, the number of spheres in contact with a given sphere, are known only for certain types of regular packing; however, an empirical relation for $m > 0.3$ is given as

Nomenclature

A = area
a = contact radius
E = modulus of elasticity
F = total load
f_o = empirical constant introduced in equation (7)
h = height of packed bed
k = thermal conductivity
l = length
m = volume fraction = $V_{\text{gas}}/V_{\text{solid}}$
N = number of spheres in contact with any sphere
N_t = number of spheres per unit length
N_a = number of spheres per unit area
P = Hertzian contact stress
P_1 = mean value of the compressive stress
Q = heat flow rate
r = coordinate axis
R = thermal resistance
S_p = empirical constant introduced in equation (18)
S_r = empirical constant introduced in equation (19)
S_j = empirical constant introduced in equation (19)
S_f = empirical constant introduced in equation (19)
T = temperature
V = volume
z = coordinate axis
ϵ = dimensionless contact radius = a/ρ
λ = density
ν = Poisson ratio
ρ = sphere radius
$\omega(r)$ = displacement of a sphere under a point load as a function of r

Subscripts

c = contact
eff = effective
s = solid
f = fluid
1 = sphere number one
2 = sphere number two

$$N = 11.6\ (1 - m) \tag{12}$$

When a load is applied to a bed of spheres, the contact area between spheres can be determined using the Hertz contact stress relation

$$a = [(3/8)(1 - \nu^2)\ P_1 \rho]^{1/3} \tag{13}$$

In this expression, ν represents the Poisson ratio, ρ is the sphere radius, and P is again the Hertzian stress. In equation (13), a mean value of the compressive stress P_1 is used. These relations were then used to find an expression for the Hertzian contact radius a as

$$a = 0.93\rho[(1 - \nu^2)(1 - m)^2 P/E]^{1/3} \tag{14}$$

where E is the modulus of elasticity of the sphere material. The rate of heat flow through one sphere can be combined with equation (3) to yield

$$k_{\text{eff}} = 3.12\ (1 - m)^{4/3}\ k_s[P/E]^{1/3} \tag{15}$$

Because this expression is based upon an elastic contact model, it would appear to be inappropriate for use in situations where the applied load results in plastic deformation of the spheres in the bed.

Unit Cell Solutions

Much work has been done in the investigation of packed beds of spheres using a unit cell model. Gorring and Churchill (1961) presented a model based on a cubic array of particles, which assumed point contacts in the direction of conduction and zero sideways conduction. In addition, they also evaluated a method that relied on the assumption of uniform packing and discussed solutions that utilized a generalized conductivity approach (Gorring and Churchill, 1972). In this second approach the effective thermal conductivity of a simple cubic array of joined, truncated spheres having circles having circles of contact radius a was given as

$$\frac{k_{\text{eff}}}{k_s} = \frac{\rho}{a} + \frac{1}{\pi} \ln \frac{2\rho}{a} \tag{16}$$

This method assumed that the fluid phase had zero conductivity, and the contact areas of the truncated spheres were assumed to be known. The latter assumption makes this method of limited use in randomly packed beds such as that considered in the present investigation.

Chan and Tien (1973) analytically derived both exact and approximate equations for solid, hollow, and coated spheres, and for packing situations involving different void fractions. Again, a Hertzian analysis was used to describe the contact areas shared by the spheres. The steady-state heat conduction equation was solved by the method of separation of variables for solid, hollow, and surface-coated microspheres. The conductance of the spherical bed was presented as

$$k_{ij} = \frac{N_a}{N_t} \frac{1}{R_{ij}} \tag{17}$$

where the first subscript refers to the type of sphere (hollow, solid, or coated), and the second subscript refers to the packing pattern (simple cubic, body-centered cubic, and face-centered cubic). Also, R represents the constriction resistance of a single particle, and N_t and N_a are the number of particles per unit length and unit area, respectively. An expression for the effective thermal conductivity of a packed bed of solid spheres was developed as

$$k_{\text{eff}} = S_p k_s[(1 - \nu^2)P/E]^{1/3} \tag{18}$$

where S_p is a constant depending on the packing pattern of the bed of spheres.

$$S_p = \frac{1.56}{S_r S_j} \left(\frac{N_a}{N_t}\right) \left(\frac{0.75 S_f r_o}{N_a}\right)^{1/3} \tag{19}$$

Again, a is the contact radius, S_r is a constant based on the value of a/ρ, and S_j, S_f, S_p, S_n, N_t, and N_a are constant parameters for different packing patterns. Values provided for use in beds of randomly packed spheres are provided by the authors. This closed-form analytical solution agreed well with the experimental data of Cunnington and Tien (1972) obtained for solid microspheres of low thermal conductivity (approximately 5×10^{-4} W/mK).

Tien and Nayak (1975) have used the analytical expression developed by Chan and Tien (1973) to express the thermal conductivity of lunar soils. The expression for solid conductance to a depth z in the bed of soil is

$$k_{\text{eff}} = k_s B \left[\frac{(1 - \nu^2)\lambda_s V_s z}{ED^3}\right]^{1/3} \tag{20}$$

where λ_s and V_s are, respectively, the density and volume of a particle, B is a constant that depends on the packing pattern, and D is the particle diameter. Tien and Nayak also state in their discussion that, based upon the experimental results obtained, statistically random packed powder beds have an average solid fraction ranging from 56 to 65 percent.

Numerical Solutions

Wakao and Vortmeyer (1971) derived a theoretical relationship between the effective thermal conductivity of a bed with cubic packing, and the gas pressure within the bed. They defined a unit cell as a cylinder of height equal to the sphere radius and a radius equal to 1.05 times the sphere radius. A relaxation method was applied to calculate the steady-state temperature distribution of the cell. Effective conductivities were calculated for the following conditions:

(*i*) conduction with point contact;
(*ii*) conduction with point contact and radiation;
(*iii*) conduction and radiation with finite contact areas.

Analytical results were found to agree quite well with the available experimental data used in their investigation.

Kato and Wakao (1969) used a relaxation method to solve the combined conduction and radiation heat transfer equation for regularly packed beds of spheres. The basic problem was to solve the heat transfer equation for a defined unit cell with the appropriate applied boundary conditions. Each unit cell was further divided into elements and the solid and gas conduction in the cell were represented by a network of rods. The numerical results obtained again agreed well with the available experimental data.

In summary, it is apparent that although several analytical models exist that are capable of predicting the effective thermal conductivity of packed beds of spherical particles, almost all of these models are limited to spheres in a vacuum environment. In addition, most of the available experimental data are for microspheres with very low thermal conductivities.

Experimental Investigation

In order to determine the validity of the different analytical techniques for a wide range of materials, an experimental investigation was conducted on randomly packed beds, comprised of spherical particles of uniform size and one material. Five packed beds were tested, one each with 2.38-mm-dia spheres of Aluminum 2017, yellow brass, Stainless Steel 316, zirconium oxide, and lead-free glass. For the three metallic materials, the size distribution was ±1 percent while for the lead-free glass and the zirconium oxide, the size distribution was ±5 percent. All of the particles were spherical in shape with smooth ground surfaces in the case of the metals and smooth fired surfaces in the case of the zirconium oxide and lead-free glass particles. Table 1 lists the materials tested along with the mechanical properties as specified by the manufacturer.

Table 1 Summary of sphere materials and properties

Material	Yield Strength (MPa)	Poisson's Ratio	Conductivity (W/mK)	Modulus of Elasticity (GPa)
Aluminum 2017	275	0.33	165	71
Yellow Brass	310	0.32	137	106
Stainless Steel 316	290	0.29	15.54	207
Zirconium Oxide	103	0.27	1.38	137
Lead Free Glass	55	0.21	1.21	76

Experimental Facility

The experimental investigation was conducted using an experimental facility designed to measure the contact resistance of various interfacial materials. It consisted of a vertical column composed of a heat source, two Stainless Steel 304 test fixtures, the test bed specimen, a load cell, and a heat sink. The fixtures and test bed specimens were arranged so that a cylindrical column of spherical particles was sandwiched between the two stainless steel test fixtures. The test bed particles were contained within a stainless steel tube lined with an insulating material to reduce the heat transferred through the sleeve. The top stainless steel insert was placed in a copper fixture containing three 200-W heaters. The other stainless steel insert was placed in a similar copper fixture that had a copper coil, in which a water coolant was circulated, wrapped around, and silver soldered to its surface. These two fixtures functioned as the heat source and sink, respectively. A silicon heat sink compound was applied between the fixture and the stainless steel inserts to enhance the thermal conductance. A passive radiation shield consisting of a reflective cylindrical surface 114.3 mm in diameter surrounded the test specimen to reduce radiation losses.

In order to vary the load applied to the test specimen, a high-pressure gas loading system was used. The load was applied by bleeding high-pressure nitrogen gas into a stainless steel bellows vessel located at the top of the column shown in Fig. 1. A load cell coupled with a demodulator allowed the mechanical load to be monitored without disturbing the vacuum or the test specimen. The load cell and its instrumentation were calibrated from 0 to 8674 N prior to the experimental test program with a proving ring and a series of tests were conducted to insure that the sleeve did not affect the loading mechanism or instrumentation.

A series of nine thermocouples were used to determine the average heat flux in the top and bottom inserts and the temperature distribution in the packed bed of spheres. In each of the stainless steel inserts, three Chromel-Alumel AWG-30 thermocouples were used, while in the packed bed of spheres, three Chromel-Alumel AWG-24 thermocouples were used. The smaller gage size was chosen for the inserts to reduce any disturbance to the heat flux pattern. In order to obtain thermocouple beads the same size as those of the spherical particles, larger AWG-24 thermocouple wire was selected. Use of this wire resulted in a thermocouple bead approximately the same diameter as the spheres in the packed bed. Temperature data were obtained using an automated data acquisition system interfaced with a microcomputer. This provided a means by which the temperature distribution of the test specimen could be determined. The experimental uncertainty associated with this temperature measurement system along with the resulting error in the computation of the heat flux of the test specimen was found to be ± 12 percent using the method of Kline and McClintock (1953).

Once assembled, the loading system, inserts, and test specimen were placed in a bell jar, which could be evacuated. The required vacuum was provided by a primary roughing pump and an oil diffusion pump.

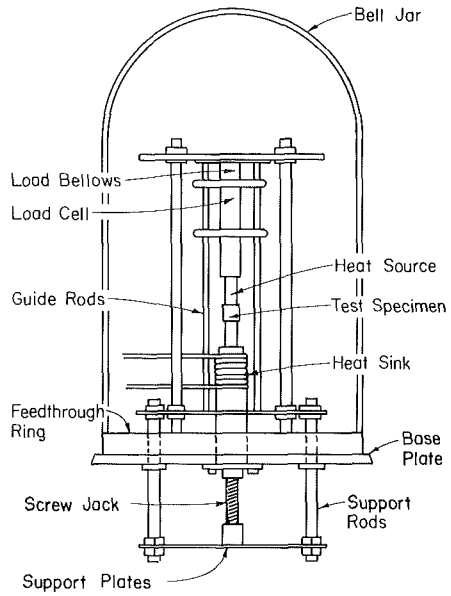

Fig. 1 Experimental test facility

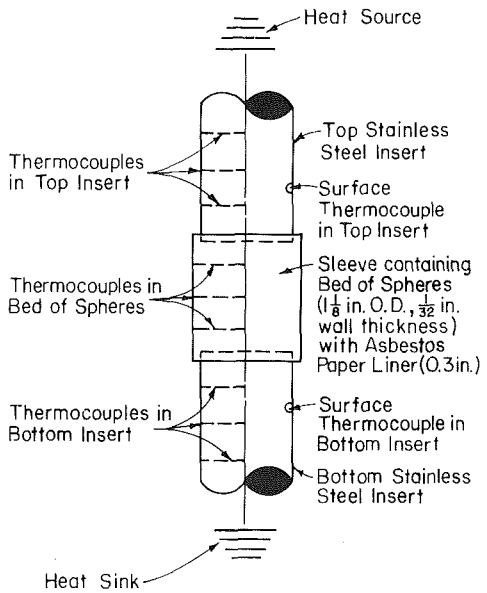

Fig. 2 Packed bed test specimens

The test specimen, shown in Fig. 2, consisted of a randomly packed bed of spheres contained in a 25.4-mm-dia, 57.2-mm-long metallic sleeve. Placed in each end of the sleeve was a 63.5-mm-long insert made of AISI-304 stainless steel. These cylinders were drilled to the centerline with a number 56 drill for thermocouple placement. The sleeve containing the packed bed of spheres was fabricated from stainless steel and had a liner of asbestos paper 0.76 mm thick to reduce conduction from one insert to the other through the sleeve. The AWG-24 thermocouples used to determine the temperatures of the bed passed through three 2.38 mm holes drilled in the sleeve and were located along the centerline of the bed.

The locations of thermocouples in the packed bed were determined through the use of a neutron radiograph. Because the element gadolinium is highly visible in neutron radiography, it was sprinkled on the thermocouple wires and held in place under shrink wrap to enhance the visibility of the thermocouples in the bed.

Experimental Procedure

The packed bed test specimens were placed in the test facility and the thermocouples were connected in order to monitor the temperatures. The vertical test column was isolated from the surrounding atmosphere by the bell jar and sealed with a silicone vacuum grease.

Steady-state temperature data, which defined the temperature distribution in the test specimen, were used to determine the effective thermal conductivity of the packed bed of spheres. Data were taken at various loads over an apparent bed pressure of 0 to 1.2 MPa. Steady-state temperature data were taken at intermediate loads in three different gaseous environments. In this manner, the effect of the interstitial gas on the effective thermal conductivity of the packed bed could be observed. Two gaseous environments were investigated, argon and nitrogen, both at atmospheric pressure, and at a vacuum of less than 10^{-3} torr. The experimental procedure was designed to maintain a constant mechanical load, while measuring the effective thermal conductivity, in each of the two different gaseous environments.

Initially, the test chamber was evacuated and the heat flux adjusted until the steady-state average temperature of the packed bed of spheres was 338 ± 2 K. A steady-state condition was assumed to have been reached when no individual thermocouple exhibited a temperature change of more than 0.5 K over a period of one hour. An initial reading was taken and the bell jar was then evacuated and backfilled to atmospheric pressure with nitrogen gas. After approximately eight hours, the steady state temperatures of the bed were again recorded. The test chamber was again evacuated, backfilled with argon, and data recorded once steady state had been reached.

The temperature data obtained in the experimental program were used to determine the effective thermal conductivity of the packed beds assuming one-dimensional heat conduction. Since the thermal conductivity of the stainless steel inserts had been determined using a standard NBS reference material, the value of the heat flux through each insert could be computed using these values and the measured temperature data. The heat flux values determined for the two stainless steel inserts differed by less than 3 percent due to small radial losses; hence, the average of the measured heat fluxes, in the two fixtures was assumed to be the amount transferred through the packed bed of spheres. This average heat flux, along with the measured temperature distribution within the packed beds, was used to calculate the effective thermal conductivity of each of the five different beds using equation (8).

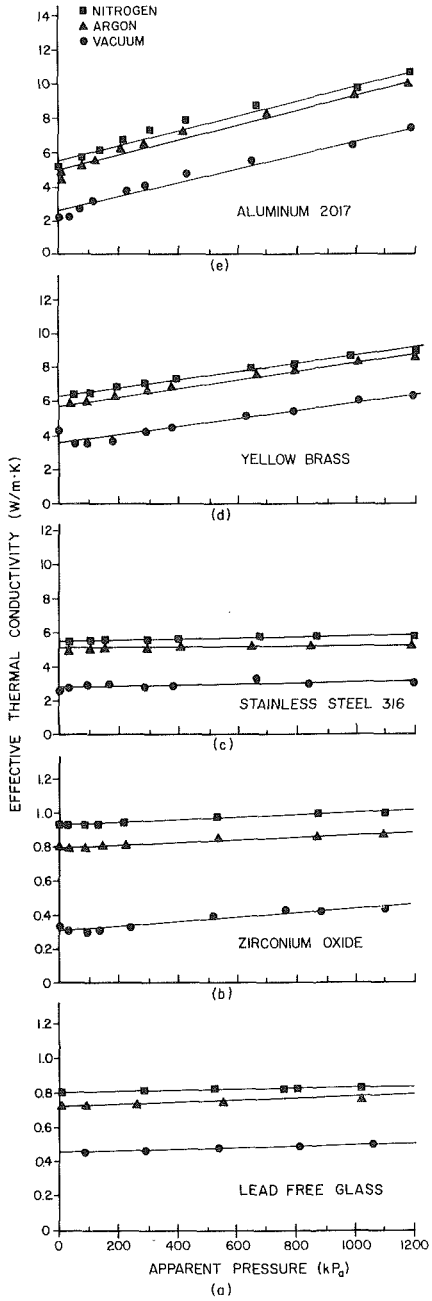

Fig. 3 Effective thermal conductivity as a function of apparent bed pressure for nitrogen, argon, and vacuum environments for the five packed beds

Results and Discussion

Figures 3(*a*) through 3(*e*) show the experimentally obtained thermal conductivities for the five types of packed beds tested, lead-free glass, zirconium oxide, Stainless Steel 316, yellow brass, and Aluminum 2017, as a function of the apparent bed pressure. As shown, each packed bed exhibited the highest thermal conductivity in the nitrogen environment. Because the thermal conductivity of argon is slightly lower than that of nitrogen, the effective thermal conductivities in the argon environment were also lower. In each case the smallest thermal conductivities were obtained in the vacuum environment.

The experimental data clearly reveal the significance of the gas environment on the effective thermal conductivity. Although the thermal conductivity of the gas was much lower than that of the spherical materials, the gaseous contribution had a dramatic effect on the effective thermal conductivity of the packed bed, increasing the effective thermal conductivity by a factor of two in most cases. This would appear to be reasonable since the gaseous area through which heat is conducted is much greater than the spherical contacts, which for a free-standing bed is a series of point contacts. Because of this small contact area, the constriction to heat flow was so large that the flow of heat through the gas represents a significant percentage of the overall heat transferred in the packed bed. Figures 3(*a*) through 3(*e*) also indicate that the increases in conductivity of the nitrogen and argon environments are constant over the entire load range evaluated.

Because the mechanical loads used in this investigation were sufficient to result in plastic deformation and all of expressions presented previously were developed for elastically deforming spheres, the analytical solutions found in the literature were considered inappropriate at high apparent pressures. It is appropriate, however, to compare several of these analytical predictions with the data observed during "no load" or "light load" conditions, and to compare the trends of these predictions as they depart from the intended load

Table 2 Parallel and series conductivity predictions

	Stainless Steel 316	Cartridge Brass	Aluminum 2017-T4	Zirconium Oxide	Lead Free Glass
SERIES					
Argon	0.29	0.49	0.51	0.056	0.048
Nitrogen	0.22	0.61	0.72	0.077	0.067
PARALLEL					
Argon	9.33	82.21	99.00	0.836	0.734
Nitrogen	9.34	82.22	99.02	0.839	0.737

regime with the data observed during very light or near elastic loading.

The experimental values obtained for the effective conductivities of the packed beds were compared with four of the analytical expressions reviewed in the literature, the simple expressions presented by Gorring and Churchill (1961) and the analytical predictions of Kagner (1966) and Chan and Tien (1973). Because the analytical expression developed by Tien and Nayak (1975) is an extension of the Chan and Tien (1973) model and yields very similar results, no comparison was made. Also, since the numerical codes were unavailable, no comparison was made with the models of developed by Wakao and Vortmeyer (1971) or Kato and Wakao (1969).

The simple expressions presented by Gorring and Churchill (1961) (i.e., the series and parallel combinations of the individual conductivities of each phase) were compared with the experimental values obtained for the "free-standing," zero load beds of spheres. Table 2 presents the results of this comparison for beds of free-standing spheres in a gaseous environment. A void fraction value of 0.4 was used for the randomly packed spheres. The series approximation yields values that are comparatively low. With the exception of the beds of zirconium oxide and glass, which have thermal conductivities much closer to that of the gases used, the parallel combination yields values that are several orders of magnitude higher than those measured. The large deviation of these predictions from the experimental results would indicate that these expressions are invalid for this type of prediction, a conclusion supported by the work of Peterson and Fletcher (1987).

As stated previously, the experimentally obtained thermal conductivity values in vacuum were also compared with the analytical predictions of Kagner (1966) and Chan and Tien (1973). The Kaganer expression, equation (15), requires the volume fraction m, which is empirically derived and provided by the author. For the Chan and Tien expression, equation (18), all the necessary empirical parameters were provided by the authors. Both of these expressions were based on elastic theory and did not consider the contribution of an interstitial gas on the overall effective thermal conductivity.

Figures 4(a) through 4(e) illustrate the results of these comparisons. The elastic limit is indicated for each packed bed by a vertical line, with the modeling predictions beyond this limit indicated by a dashed line. A best fit curve was drawn through the experimental data using a least-squares fit for each bed. As shown, a majority of the experimental data obtained in this investigation lies well beyond the elastic limit.

Several trends are apparent when these five graphs are compared. First, for the hard materials with low thermal conductivities, lead-free glass, zirconium oxide, and Stainless Steel 316, the analytical models underpredicted the effective thermal conductivity below the elastic limit, but overpredicted the effective thermal conductivity above the elastic limit. Although the range of mechanical loads evaluated in the present experiment produced stresses in excess of those for which the analytical models were designed, it appears that as the apparent stress approaches zero the analytical and experimental values begin to reach reasonably similar values. This would

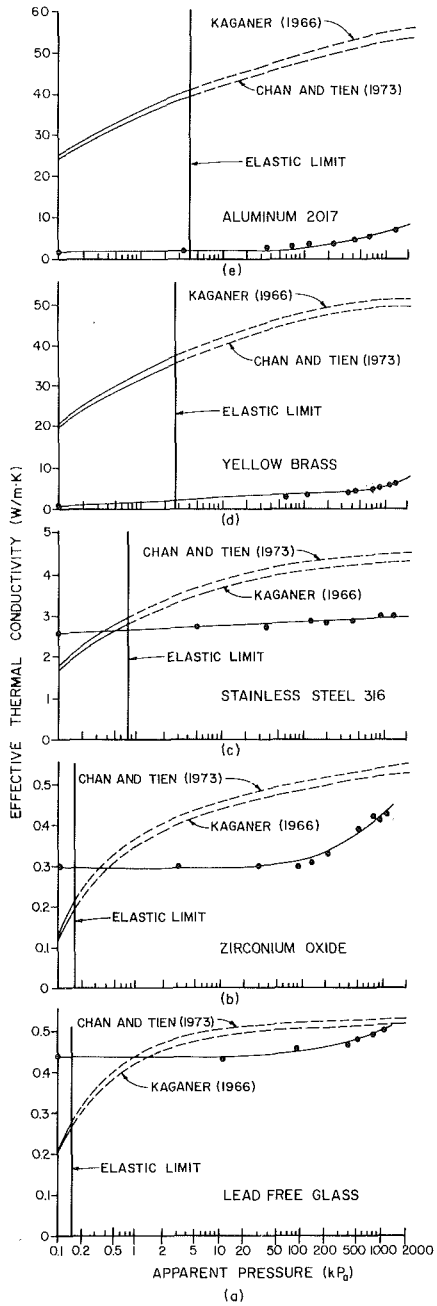

Fig. 4 Comparison of analytical predictions and experimental results for the five packed beds

support the validity of the analytical solutions in their intended region of use.

Second, for the soft materials with relatively high thermal conductivities, yellow brass and Aluminum 2017, the analytical models overpredicted the effective thermal conductivity by as much as an order of magnitude. Third, although the analytical solutions predict similar values, the analytical predictions of Chan and Tien (1973) are slightly above those of Kaganer (1966) for the hard materials, while for the soft materials they are reversed.

In previous studies involving the effective thermal conductivity of solid and hollow glass spheres and ceramic spheres, with and without thin metallic coatings, the analytical results of both Chan and Tien (1973) and Kaganer (1966) were found to compare quite well with experimental data (Cunnington and Tien, 1972). However in those studies, the materials tested were all hard materials with relatively low thermal conductivities when compared to the yellow brass and Aluminum

2017 spheres used in this investigation. Because the analytical results compare quite favorably with the experimental results obtained in this investigation for the stainless steel, zirconium oxide and glass spheres, it appears that these analytical models should not be used for packed beds comprised of soft materials with high thermal conductivities.

Conclusions

As expected, clear relationships between the mechanical load and the effective thermal conductivity, and between the bed material and the effective thermal conductivity, were observed. In addition, and perhaps more importantly, the effective thermal conductivity of the packed beds were found to be strongly dependent upon the presence and the thermal conductivity of interstitial gases. The gaseous contribution was found to have a consistent and predictable effect on the effective conductivity of the packed beds, with the effective thermal conductivity increasing by a factor of two at low loads in almost all cases where gas was present. Examination of the effect of variations in the porosity of the bed and the effect of variations in the gas temperatures may provide better insight into this gas conductivity contribution.

The series and parallel resistance analysis techniques presented appear to be inappropriate for use in predicting the effective conductivity of the packed beds of spheres used in this investigation, because of the wide range of effective conductivities obtained. Although the analytical predictions of Chan and Tien (1973) and Kaganer (1966) yield accurate results for packed beds of materials with very low thermal conductivities in the elastic deformation region, the accuracy of these two methods appears to decrease significantly as the thermal conductivity of the sphere material increases or when the load is such that plastic deformation occurs.

References

Batchelor, G. K., 1972, "Sedimentation in a Dilute Dispersion of Spheres," *Journal of Fluid Mechanics*, Vol. 52, No. 2, pp. 245–268.

Chan, C. K., and Tien, C. L., 1973, "Conductance of Packed Spheres in a Vacuum," ASME JOURNAL OF HEAT TRANSFER, Vol. 95, pp. 302–308.

Chen, J. C., and Churchill, S. W., 1963, "Radiant Heat Transfer in Packed Beds," *AIChE Journal*, Vol. 9, No. 1, pp. 35–41.

Cunnington, G. R., and Tien, C. L., 1972, "Heat Transfer in Microsphere Cryogenic Insulation," *Proceedings of the Cryogenic Engineering Conference*, Boulder, CO, Aug. 10–12.

Gorring, R. L., and Churchill, S. W., 1961, "Thermal Conductivity of Heterogeneous Materials," *Chemical Engineering Progress*, Vol. 57, No. 7, pp. 53–59.

Hadley, G. R., 1986, "Thermal Conductivity of Packed Metal Powders," *International Journal of Heat and Mass Transfer*, Vol. 29, No. 6, pp. 909–920.

Kaganer, M. G., 1966, "Contact Heat Transfer in Granular Material Under Vacuum," *Journal of Engineering Physics*, Vol. 11, No. 1, pp. 30–36.

Kato, K., and Wakao, N., 1969, "Effective Thermal Conductivity of Packed Beds," *Journal of Chemical Engineering of Japan*, Vol. 2, No. 1, pp. 24–33.

Kline, S. J., and McClintock, 1953, "Describing Uncertainties in Single-Sample Experiments," *Mechanical Engineering*, Vol. 75, No. 3, pp. 3–8.

Peterson, G. P., and Fletcher, L. S., 1987, "Effective Thermal Conductivity of Sintered Heat Pipe Wicks," *Journal of Thermophysics and Heat Transfer*, Vol. 1, No. 4, pp. 343–347.

Tien, C. L., and Nayak, A. L., 1975, "Analytical Models for Lunar Soil Thermal Conductivity," presented at the AIAA Tenth Thermophysics Conference, Denver, CO, May 27–29.

Timoshenko, S. P., and Goodier, J. N., 1946, *Theory of Elasticity*, McGraw-Hill, St. Louis, MO.

Wakao, N., and Vortmeyer, D., 1971, "Pressure Dependency of Effective Thermal Conductivity of Packed Beds," *Chemical Engineering Science*, Vol. 26, pp. 1753–1765.

Yovanovich, M. M., 1967, "Thermal Contact Resistance Across Elastically Deformed Spheres," *Journal of Spacecraft and Rockets*, Vol. 4, pp. 119–122.

Yovanovich, M. M., 1973a, "A General Expression for Predicting Conduction Shape Factors," presented at the AIAA 11th Aerospace Sciences Meeting, Washington, DC, Jan. 10–12, Paper No. 73-121.

Yovanovich, M. M., 1973b, "Apparent Conductivity of Glass Microspheres From Atmospheric Pressure to Vacuum," presented at the ASME-AIChE Heat Transfer Conference, Atlanta, GA, Aug. 5–8, ASME Paper No. 73-HT-43.

Design of Cooling Towers by the Effectiveness-NTU Method

H. Jaber

R. L. Webb

Department of Mechanical Engineering,
The Pennsylvania State University,
University Park, PA 16802

This paper develops the effectiveness-NTU design method for cooling towers. The definitions for effectiveness and NTU are totally consistent with the fundamental definitions used in heat exchanger design. Sample calculations are presented for counter and crossflow cooling towers. Using the proper definitions, a person competent in heat exchanger design can easily use the same basic method to design a cooling tower of counter, cross, or parallel flow configuration. The problems associated with the curvature of the saturated air enthalpy line are also treated. A "one-increment" design ignores the effect of this curvature. Increased precision can be obtained by dividing the cooling range into two or more increments. The standard effectiveness-NTU method is then used for each of the increments. Calculations are presented to define the error associated with different numbers of increments. This defines the number of increments required to attain a desired degree of precision. The authors also summarize the LMED method introduced by Berman, and show that this is totally consistent with the effectiveness-NTU method. Hence, using proper and consistent terms, heat exchanger designers are shown how to use either the standard LMED or effectiveness-NTU design methods to design cooling towers.

Introduction

Berman (1961) described how the "log-mean enthalpy method" (LMED) may be applied to cooling tower design. He also developed a correction factor to account for the curvature of the saturated air enthalpy curve. In their 1940 publication, London et al. introduced definitions of ϵ and NTU to use in plotting cooling tower test data. However, these definitions are not generally consistent with the basic defintions used today in heat exchanger design. They developed empirical curve fits of their ϵ-NTU curves for design purposes. Moffatt (1966) is apparently the first to derive the ϵ-NTU equation for a cooling tower (counterflow). As will be shown later, his definitions do not agree with the basic definitions of ϵ and NTU for certain combinations of water and air flow rate. Others have used their ϵ and/or NTU definitions for graphic representation of test data. Other than Moffatt (1966), no authors have attempted to employ these definitions actually to design a cooling tower.

The F-LMTD and ϵ-NTU methods have long been used for design of heat exchangers. It is desirable to apply the basic concepts of the F-LMTD and ϵ-NTU methods to the design of evaporative heat exchangers (cooling towers and evaporative fluid coolers or condensers). The objective of this paper is to show how the ϵ-NTU method may be applied to cooling tower design. The present development will observe the precise concept definitions used in the ϵ-NTU method for heat exchangers and be applicable to all cooling tower operating conditions.

Traditional cooling tower design methods typically use a method and nomenclature that are unlike the traditional F-LMTD and ϵ-NTU heat exchanger design methods. Hence, heat exchanger designers cannot successfully translate their design methodology to cooling tower design. A key benefit of the present development is that heat exchanger designers will clearly understand how to apply their understanding of heat exchanger design to cooling towers.

Simultaneous heat and mass transfer processes occur in cooling towers. Hence, the design equations must account for both energy transfer processes. The complexity of the design equations may be simplified using the moist air enthalpy potential proposed by Merkel (1926). The enthalpy potential method is approximate, and combines the driving potential of the heat and mass transfer processes into a single enthalpy driving potential. The driving potential is the enthalpy difference of the moist air at the water film–air interface and the bulk air stream. Webb (1988) presents a critical discussion of precise and approximate design methods. Attempts to apply the F-LMED or ϵ-NTU methods to cooling tower design must use the enthalpy driving potential. Thus, the "log-mean enthalpy difference" (LMED) corresponds to the "log-mean temperature difference" (LMTD) of heat exchanger design. One problem associated with use of the F-LMED or ϵ-NTU methods for cooling tower design is that the slope of the saturated air enthalpy curve (i_s) versus temperature is a curved line. So, use of the F-LMED method will involve errors associated with approximating this curve with a straight line. Berman (1961) rigorously applied the F-LMED method to cooling towers, and defined a correction factor (δ) to correct for the curvature of the i_s versus T curve. The correction factor essentially provides a two-increment design ($N=2$). The derivation of this correction factor is presented in the Appendix.

Traditional cooling tower design methods typically use an incremental method, which approximates the i_s versus T curve into N segments, where N may be in the range of 4 or more. Each segment is a straight line approximation to the i_s versus T curve. The simplest application of the F-LMED or ϵ-NTU methods to cooling tower design would use one segment ($N = 1$). It will be shown that one may use $N > 1$ if increased accuracy is desired.

Application of the ϵ-NTU method to cooling tower design requires physical and algebraic definition of the effectiveness (ϵ) and the "number of transfer units" (NTU). A number of attempts have been made to define ϵ and NTU for cooling tower design. However, virtually all of these definitions are flawed, in the sense that they are inconsistent with the corresponding basic definitions used for heat exchanger design. Baker (1984) and the *ASHVE Guide* (1941) have defined ϵ and NTU strictly for convenience, and they have not attempted to apply these definitions to the actual ϵ-NTU design method. Baker (1984) essentially dismissed his definition as being of "no value." The ϵ-NTU design method for heat exchangers involves use of the "capacity rate ratio" ($C_R = C_{\min}/C_{\max}$).

Contributed by the Heat Transfer Division and presented at the ASME Winter Annual Meeting, Boston, Massachusetts, December 13–18, 1987. Manuscript received by the Heat Transfer Division April 6, 1988; revision received November 15, 1988. Paper No. 87-WA/CRTD-2. Keywords: Heat Exchangers, Mass Transfer.

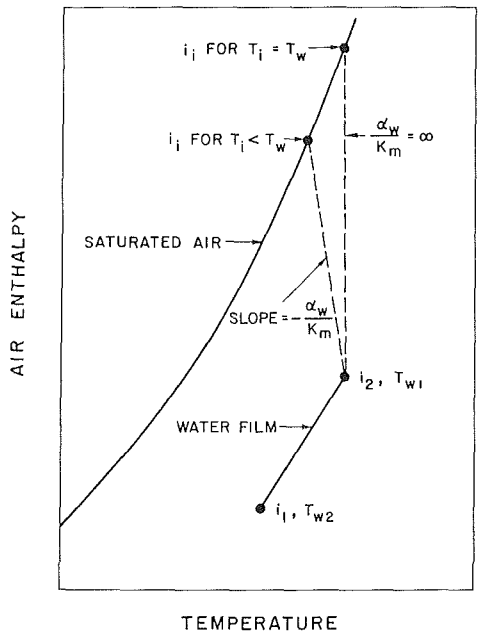

Fig. 1 Water operating line on enthalpy-temperature diagram

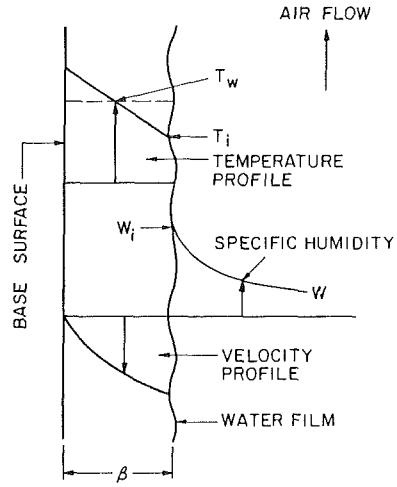

Fig. 2 Gravity-drained water film with temperature, velocity, and humidity ratio profiles

Whillier (1976) defined a term "tower capacity factor," which was intended to correspond to the capacity rate ratio used in heat exchanger design. His definition was not consistent with the definition of C_R. Nor did he attempt to establish an algebraic relationship for ϵ-NTU. Moffatt (1966) was apparently the first to attempt to establish an algebraic ϵ-NTU relationship. As will be shown later, his method works if the water is the minimum capacity rate fluid, but fails if it is not. Except for Moffatt's work, the rash of NTU definitions reported in the literature have contributed little but a myriad of conflicting definitions.

The Driving Potential

As presented by Webb (1988) the driving potential is

$$dq = [\alpha_a \mathrm{Le}^{2/3}(T_i - T) + h_{gi}K_m(W_i - W)]dA \quad (1)$$

The first term accounts for the single-phase heat transfer from the water-air interface to the air, and the second term is the water evaporated at the interface. Webb (1988) shows that equation (1) may be approximated as the enthalpy driving potential, given by

$$dq = K_m(i_i - i)dA \quad (2)$$

The present ϵ-NTU formulation uses $(i_i - i)$ as the driving potential. This potential corresponds to $(T_H - T_C)$ used in heat exchanger design.

Figure 1 shows a plot of air enthalpy versus water temperature for a counterflow cooling tower. The curved line is the enthalpy of saturated air (i_s) and the straight line is the "water operating line." The driving pontential $(i_i - i)$ is illustrated by the dashed lines. Typically, one assumes that the water-air interface temperature is equal to the local mixed water temperature, which is an approximation. Actually, the interface temperature is less than the local mixed water temperature. The water film-air process at the interface is illustrated in Fig. 2. The dashed line in Fig. 1 of slope $-\alpha_w/K_m$ defines the interface temperature. Since the water film heat transfer coef-

Nomenclature

A = heat transfer area, m^2
A = approach = $T_{w2} - T_{wb}$, °C
a = heat and mass transfer area per unit volume, m^2/m^3
c_p = fluid specific heat, kJ/kg-°C
C_R = capacity rate ratio = $m_{\min}/m_{\max}$
C = fluid capacity rate = mc_p, kJ/s-°C
d = differential element
E = error defined as $(1 - \mathrm{NTU}_r/\mathrm{NTU}) \times 100$, percent
f' = slope of saturated air enthalpy versus temperature curve = di_i/dT, kJ/kg-°C
h = enthalpy of water, kJ/kg
i = enthalpy of moist air at bulk condition, kJ/kg
i_i = enthalpy of moist air at interface condition: i_{i1} at water inlet, i_{i2} at water outlet, i_{iav} at average temperature of increment, kJ/kg
ΔI = enthalpy difference between air at interface and local bulk air, $\Delta I_1 = i_{i2} - i_1$, $\Delta I_2 = i_{i1} - i_2$, ΔI_m defined by equation (3) (or (5))
K_m = mass transfer coefficient, kg/m^2-s
Le = Lewis number of moist air
m = fluid mass flow rate, kg/s
m_w^+ = water side capacity rate, kg/s
N = number of increments
NTU = number of transfer units, as defined by equation (16)
q = heat exchange, kW
R = cooling range = $T_{w1} - T_{w2}$, °C
T = temperature, °C
U = overall heat transfer coefficient, kW/m^2K
V = cooling tower packing volume, m^3
W = humidity ratio = kg of steam/kg of dry air
z = packing depth (in air flow direction), m
α = heat transfer coefficient, kW/m^2-s
β = water film thickness, m
δ = enthalpy correction factor, kJ/kg
ϵ = thermal effectiveness = $q_{\mathrm{act}}/q_{\max}$

Subscripts

1 = air or water inlet conditions
2 = air or water outlet conditions
a = air
act = actual heat transfer
av = average
C = cold fluid
f = liquid water
g = saturated water vapor
H = hot fluid
i = at air-water interface
m = moist air
s = saturated air
w = water
wb = wet bulb

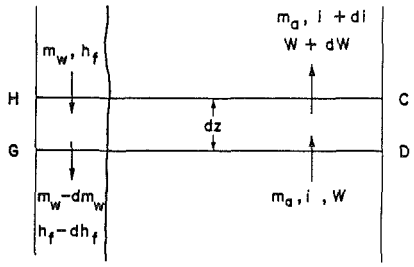

Fig. 3 Control volume illustrating the heat and mass transfer processes at the air-water interface

ficient is unknown, one typically assumes the path of the $\alpha_w/K_m = \infty$ line, which is the vertical dashed line. The assumption $\alpha_w/K_m = \infty$ will be employed in the present analysis. However, this assumption is not necessary for the ϵ-NTU equations to be developed.

F-LMED Formulation

Assuming a linear variation of i_s versus T, one may define the log-mean enthalpy difference (LMED) for the cooling tower process illustrated in Fig. 1 as

$$\Delta I_m = \frac{\Delta I_2 - \Delta I_1}{\ln (\Delta I_2/\Delta I_1)} \tag{3}$$

where $\Delta I_1 = i_{i2} - i_1$ and $\Delta I_2 = i_{i1} - i_2$.

The F-LMTD method of heat exchanger design uses the UA value of the heat exchanger. The corresponding value for cooling tower design is $K_m A$. As seen in Fig. 1, the i_s versus T curve is not a straight line. Hence, equation (3) introduces an approximation. Berman (1961) developed an analytical based correction factor to correct for the nonlinearity of the i_s versus T curve, which is derived in the Appendix. The correction factor δ is given by

$$\delta = (i_{i1} + i_{i2} - 2i_{iav})/4 \tag{4}$$

Note that the enthalpy correction factor is independent of T_{wb}, A (approach), and m_w/m_a. It is a function of the cooling range only. Figure 4 presents the enthalpy correction factor versus the exit water temperature (T_{w2}) for different values of the cooling range.

Introducing equation (4) in equation (3) gives the corrected LMED

$$\Delta I_m = \frac{\Delta I_2 - \Delta I_1}{\ln [(\Delta I_2 - \delta)/(\Delta I_1 - \delta)]} \tag{5}$$

UA and LMTD are used in heat exchanger design; the corresponding definitions for cooling tower design are $K_m A$ and LMED. The flow configuration correction factor (F) used in heat exchanger design applies equally well to cooling tower design.

Effectiveness-NTU Method

Figure 3 shows a control volume on a differential element of the cooling tower. Equation (1) is the transport equation for the energy transfer from water to air. An energy balance on the water film and the air, over the length dz, gives

$$dq = m_w c_{pw} dT_w = m_a di \tag{6}$$

The ϵ-NTU derivation is performed for a counterflow cooling tower, using the terminology defined in Fig. 1. The derivation essentially parallels that for a counterflow heat exchanger. It is necessary to express dq in equation (1) in terms of the air enthalpy. The slope of the i_s versus T curve is defined as

$$f' = di_i/dT_w \tag{7}$$

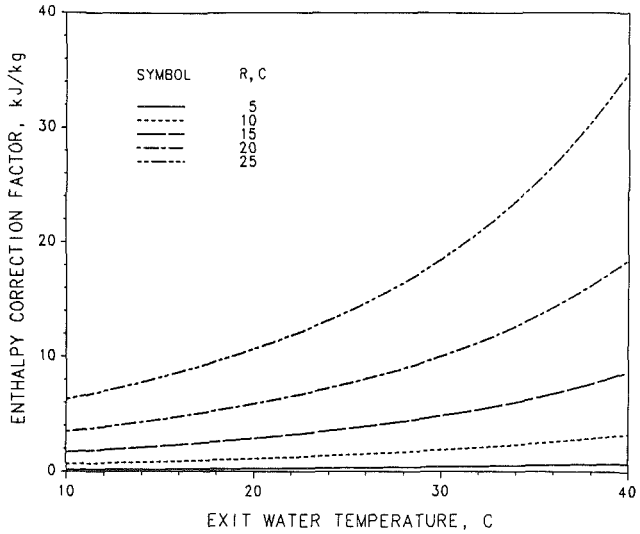

Fig. 4 Enthalpy correction factor δ versus the exit water temperature T_{w2} for different cooling ranges R

Substitution of dT_w from equation (7) into equation (6) and solving for di_i gives

$$dq = (m_w c_{pw}/f')di_i \tag{8}$$

Using $di = dq/m_a$ from equation (6) and equation (8) one may write $di_i - di = d(i_i - i)$ as

$$d(i_i - i) = dq[(f'/m_w c_{pw}) - 1/m_a] \tag{9}$$

When one solves equation (9) for dq and substitutes the result into equation (2), the result is

$$\frac{d(i_i - i)}{(i_i - i)} = K_m[(f'/m_w c_{pw}) - 1/m_a]dA \tag{10}$$

The corresponding equation that occurs in the ϵ-NTU development for a heat exchanger with $C_H = C_{\min}$ is

$$\frac{d(T_H - T_C)}{(T_H - T_C)} = U[1/m_H c_{pH} - 1/m_C c_{pC}]dA \tag{11}$$

Notice that equation (10) contains the term m_a, as compared to the "capacity rate" $m_C c_{pC}$ in equation (11). By analogy with equation (11), we will define m_a as the air capacity rate for a cooling tower, and the water capacity rate as

$$m_w^+ = m_w c_{pw}/f' \tag{12}$$

Consistent with heat exchanger design terminology, we will define

$$C_R = m_{\min}/m_{\max} \tag{13}$$

There are two possible cases: $m_w^+ < m_a$ and $m_w^+ > m_a$.

Case 1: $m_w^+ < m_a$. After substituting $m_w^+ = m_{\min}$ and $m_a = m_{\max}$ in equation (10) one obtains

$$\frac{d(i_i - i)}{(i_i - i)} = \frac{K_m dA}{m_{\min}}(1 - C_R) \tag{14}$$

Equation (14) corresponds to the heat exchanger ϵ-NTU equation

$$\frac{d(T_H - T_C)}{(T_H - T_C)} = \frac{UdA}{C_{\min}}(1 - C_R) \tag{15}$$

In heat exchanger design, the term $UA/C_{\min}$ is defined as the "number of transfer units," NTU. The analogous definition for the NTU of a cooling tower is

$$\text{NTU} = \frac{K_m A}{m_{\min}} \tag{16}$$

Previous works on cooling towers, in which NTU was defined, have not observed the precise definition of equation (16). Some authors (London et al., 1940; Moffatt, 1966; Zivi and Brand, 1956) have defined K_mA/m_a as the "NTU of the air," while others (Kelly, 1976; Keyes, 1972; Majumdar and Singhal, 1983; Baker and Shryock, 1961) have defined K_mA/m_w as "the NTU of the water." The authors assert that equation (16) is the only correct and consistent definition.

Next, it is necessary to define the heat exchange "effectiveness" ϵ. This will be defined identically to that used for heat exchanger design

$$\epsilon = q_{act}/q_{max} \tag{17}$$

where

$$q_{max} = m_{min}(i_{i1} - i_1) \tag{18}$$

Referring to Fig. 1 and integrating equation (14) between the entering and leaving air states, i_1 and i_2, respectively, gives

$$\frac{i_{i2} - i_1}{i_{i1} - i_2} = \exp[-\text{NTU}(1 - C_R)] \tag{19}$$

It can be shown that

$$\frac{i_{i2} - i_1}{i_{i1} - i_2} = \frac{\epsilon - 1}{\epsilon C_R - 1} \tag{20}$$

Equating equations (19) and (20) gives the final ϵ-NTU equation for the counterflow cooling tower

$$\epsilon = \frac{1 - \exp[-\text{NTU}(1 - C_R)]}{1 - C_R \exp[-\text{NTU}(1 - C_R)]} \tag{21}$$

Equation (21) is identical to the ϵ-NTU expresssion for a counterflow heat exchanger.

For case 1 where $m_{min} = m_w^+$, if the exit water temperature is assumed to be equal to the air entering wet bulb temperature, then one can write q_{max} as $m_w^+ (T_{w1} - T_{wb})$. Under such conditions one can show that the effectiveness can be expressed as

$$\epsilon = \frac{T_{w1} - T_{w2}}{T_{w1} - T_{wb}} = \frac{R}{R + A} \tag{22}$$

Case 2: $m_a < m_w^+$. For this case, $m_a = m_{min}$ and $m_w^+ = m_{max}$. Substitution of these expressions into equation (10) gives equation (14). Continuing as for Case 1 leads to equation (21).

For Case 2, one cannot write the effectiveness in terms of temperatures, as was done in equation (22) for Case 1. For Case 2, one may express the effectiveness by

$$\epsilon = \frac{m_w c_{pw}(T_{w1} - T_{w2})}{m_{min}(i_{i1} - \delta - i_1)} \tag{23}$$

Discussion of the ϵ-NTU Design Method

Using the definitions for effectiveness and NTU described above, the resulting ϵ-NTU equations for a counterflow cooling tower have been shown to be identical to those for heat exchanger design. It may also be shown that the ϵ-NTU equations for crossflow heat exchangers are also applicable to crossflow cooling towers. Use of the unmixed/unmixed ϵ-NTU equation is recommended. Similarly, a parallel flow cooling tower would be designed using the ϵ-NTU equation for a parallel flow heat exchanger.

The definition for effectiveness satisfies the thermodynamic definition, $\epsilon = q_{act}/q_{max}$, and the NTU must be defined as K_mA/m_{min}. The myriad of definitions in the cooling tower literature for effectiveness and NTU are generally inconsistent with those used here.

The heat exchanger designer should have no difficulty in understanding cooling tower analysis, since precisely the same basic definitions for effectiveness and NTU are used, and the same algebraic equation for the ϵ-NTU relationship applies. A one-increment design ($N = 1$) may be performed very quickly.

The ϵ-NTU (or the F-LMED) method is subject to approximations involved in linearizing the i_s versus T curve as a straight line. However, the desired accuracy can be obtained by breaking the design down into N increments. Traditional cooling tower design methods typically use an incremental method. One may use the correction factor (δ) given by equation (4) for the ϵ-NTU method, which essentially gives a two-increment design. To do this, one redefines i_{i1} and i_{i2} as $(i_{i1} - \delta)$ and $(i_{i2} - \delta)$, respectively. Hence, the definition of ϵ is rewritten as

$$\epsilon = \frac{m_w c_{pw}(T_{w1} - T_{w2})}{m_{min}(i_{i1} - \delta - i_1)} \tag{24}$$

A typical problem that often arises in cooling tower design is the determination of the NTU when T_{wb}, R, A, and m_a/m_w are given. The traditional method of solution is to use the curves given in publications by Kelly (1976) and The Cooling Tower Institute (1967). These curves are based on use of the Merkel method, and were generated for a wide range of practical operating conditions. The Cooling Tower Institute curves (1976) were generated using the Tchebychev integration method with three increments ($N = 3$). One may very simply use the ϵ-NTU graphs (or equations) for the particular flow configuration desired (counter, cross, or parallel flow), with three increments, to design for any of the operating conditions. A simple procedure for a one-increment design using the enthalpy correction factor is outlined below:

1 Calculate the slope of the saturation line, $f' = \Delta i_i/R$.
2 Calculate $m_w^+ = m_w c_{pw}/f'$ and compare to m_a to determine $C_R = m_{min}/m_{max}$.
3 Find $\Delta i = (m_w/m_a)c_{pw}R$.
4 Calculate the effectiveness $\epsilon = (m_a \Delta i) / [m_{min}(i_{i1} - \delta - i_1)]$.
5 Read (or calculate) the ϵ-NTU from chart (or equation).

One should note that, for two or more increments, it is possible for the minimum capacity rate fluid to change over the length of the water temperature range. This is because of the change of slope of the i_s versus T curve (see equation (12)). If this happens, one merely redefines C_R and m_{min} for the increment.

Illustration of the ϵ-NTU Design Method

This section presents numerical results for counterflow cooling towers using the ϵ-NTU method. The calculations presented here are performed for a range of practical operating conditions, as a function of number of increments (N) between 1 and 10. By varying the number of increments, one may estimate the number of increments required to attain a particular desired degree of accuracy. All calculations were performed assuming $\alpha_w/K_m = \infty$ and neglecting the effect of evaporation on the air enthalpy leaving the increment. However, the first assumption has no bearing on use or applicability of the ϵ-NTU method.

Calculations were performed for the following operating conditions listed in Table 1. The number of increments was varied between 1 and 10. The value calculated is the NTU required to perform the cooling duty corresponding to the operating conditions listed in Table 1. The calculated results are presented in Figs. 5–8 in the form of Error (E) = $(1 - \text{NTU}_r/\text{NTU}) \times 100$ percent versus the number of increments (N), where NTU_r is the "precise" NTU. NTU_r is calculated using the traditional design method of integrating equation (25) using Simpson's rule with 10 increments.

$$\frac{K_mA}{m_a} = \sum_{i=1}^{N} \frac{\Delta i}{i_i - i} \tag{25}$$

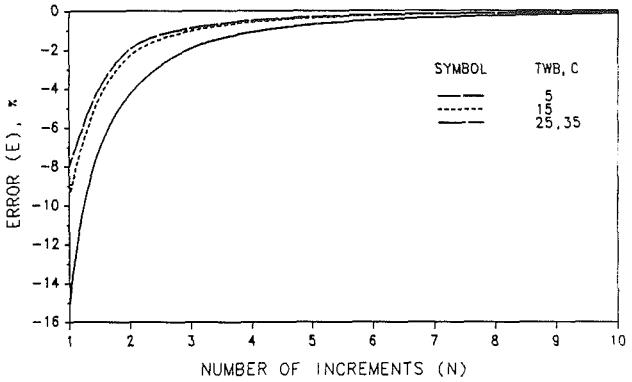

Fig. 5 Error E versus the number of increments N for m_w/m_a = 1.0, R = 12°C, A = 8°C

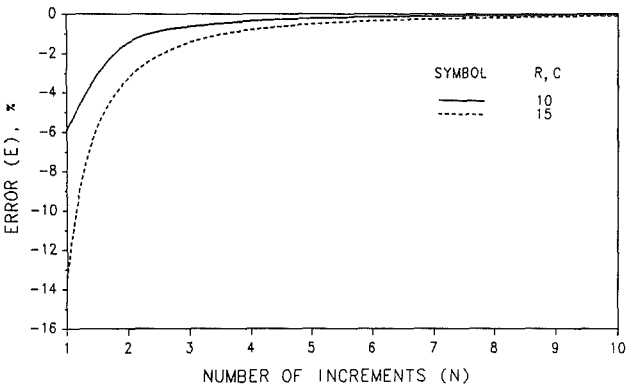

Fig. 6 Error E versus the number of increments N for m_w/m_a = 1.0, T_{wb} = 20 °C, A = 8°C

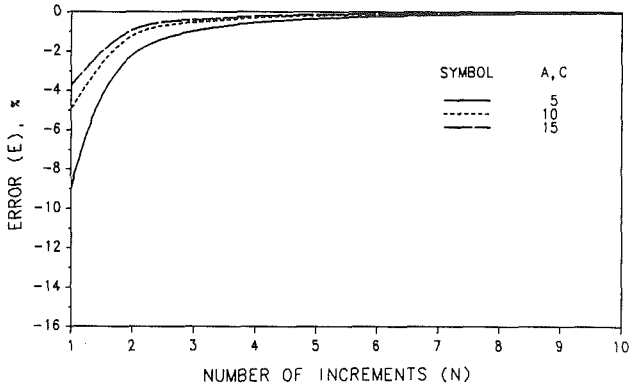

Fig. 7 Error E versus the number of increments N for m_w/m_a = 1.0, R = 10°C, T_{wb} = 20 °C

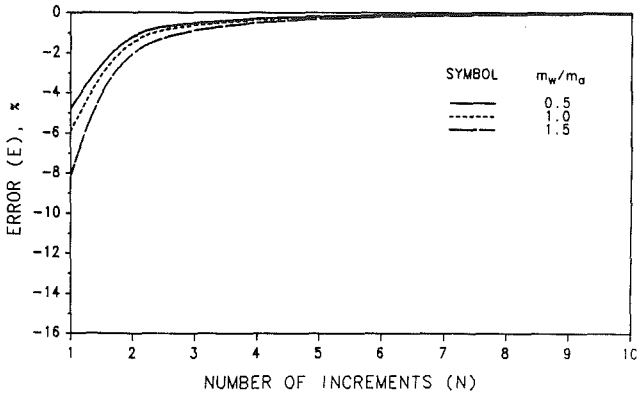

Fig. 8 Error E versus the number of increments N for T_{wb} = 20°C, R = 10°C, A = 8°C

Figures 5–8 show that the ϵ-NTU method underpredicts the NTU. Table 2 gives the minimum required number of increments to achieve a design, within 2 percent of the 10-increment Simpson integration reference. Table 3 shows the effect of the correction factor on the accuracy of a one-increment design. For the range of parameters considered in Table 1, a one-increment design with an enthalpy correction factor will produce less than 3 percent error. The tower characteristic was also calculated using the Tchebychev integration technique. This method gave approximately 1 percent error with respect to the Simpson reference for the range of operating conditions listed in Table 1. A similar result can be achieved using the ϵ-NTU method with three increments.

Examples of Sizing and Rating Calculations

A sizing problem determines the NTU (size of the tower) for given air and water conditions. A rating calculation determines the leaving water temperature for given air and water inlet conditions and the tower characteristic.

Counterflow Sizing Calculation. The following example presents a one-increment sizing calculation for a counterflow cooling tower. The same procedure would be used per increment for a multi-increment design. Both the ϵ-NTU and LMED methods will be illustrated.

Consider the following operating conditions: Water enters at a temperature of 35°C and is cooled to 30°C. The corresponding saturation enthalpies are i_{s1} = 129.54 kJ/kg and i_{s2} = 99.96 kJ/kg. The air entering is 25°C (wet bulb) with an enthalpy of i_1 = 76.6 kJ/kg. The mass flow rate ratio is m_w/m_a = 1.0. The average water temperature is T_{wav} = (30 + 35)/2 = 32.5°C and the corresponding saturation enthalpy is i_{sav} = 113.92 kJ/kg. The enthalpy correction factor is calculated using equation (4) giving a value of 0.414 kJ/kg.

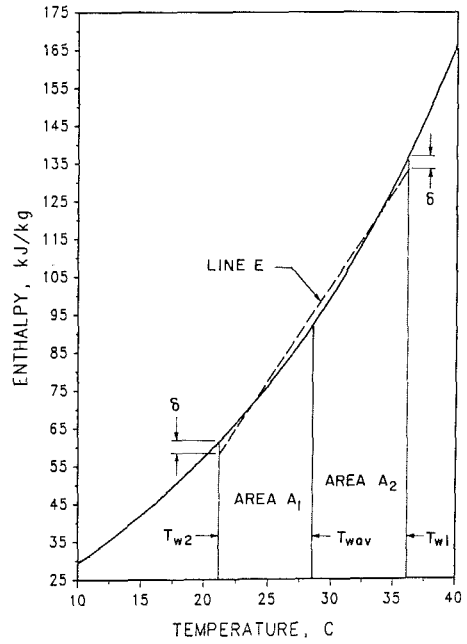

Fig. 9 Graphic representation of the enthalpy correction factor δ

The air enthalpy change is found from the energy balance, equation (6): $\Delta i = (m_w/m_a)c_{pw}R$ = 20.93 kJ/kg; the air exit enthalpy is i_2 = 97.53 kJ/kg.

1 The LMED Method.

$$\Delta I_1 = i_{s2} - i_1 = 99.96 - 76.6 = 23.36 \text{ kJ/kg}$$

$$\Delta I_2 = i_{s1} - i_2 = 129.54 - 96.54 = 33.09 \text{ kJ/kg}$$

Table 1 Operating conditions for calculations

T_{wb}, °C	A, °C	R, °C	m_w/m_a	Figure
5-35	8	12	1.0	5
20	8	10, 20	1.0	6
20	5-15	10	1.0	7
20	8	20	0.5-1.5	8

Table 2 Number of increments necessary to achieve a design within 2 percent of the 10-increment Simpson integration, without using the enthalpy correction factor δ

T_{wb}, °C	A, °C	R, °C	m_w/m_a, °C	N	Figure
5-35	8	12	1.0	3	5
20	8	10-20	1.0	3	6
20	5-15	10	1.0	2	7
20	8	10	0.5-1.5	2	8

Table 3 Effect of the enthalpy correction factor (δ) on a one-increment design using the ϵ-NTU method

T_{wb}, °C	A, °C	R, °C	m_w/m_a	Error, percent	Figure
5-35	8	12	1.0	<3	5
20	8	10-20	1.0	<3	6
20	5-15	10	1.0	<2	7
20	8	10	0.5-1.5	<3	8

Using equation (5), $\Delta I_m = 27.56$ kJ/kg and hence $K_mA/m_w = 0.76$.

2 *The ϵ-NTU Method.* Applying equation (7) we get:

$$f' = (129.54 - 99.96)/5 = 5.916 \text{ kJ/kg-°C}$$

If $m_wc_{pw}/m_a < f'$, then $m_w^+ < m_a$ (Case 1). The terms ϵ, C_R, and NTU are calculated using equations (17), (18), (13), and (16), respectively

$$\epsilon = [m_a(i_2 - i_1)]/[m_{\min}(i_{s1} - \delta - i_1)] = 0.555$$

$$C_R = m_{\min}/m_{\max} = 0.708$$

$$\text{NTU} = K_mA/m_{\min} = 1.051 \text{ or } K_mA/m_w = 0.74$$

The small difference in numerical values obtained by both methods is due to round-off errors.

Counterflow Rating Calculation. Assume that the given is $K_mA/m_w = 1.87$ and $m_w/m_a = 1.0$. The air and water inlet conditions are $T_{w1} = 35$°C and $T_{wb} = 20$°C, respectively. The corresponding air and water enthalpies are 129.54 kJ/kg and 57.544 kJ/kg (the correct exit water temperature is 25°C; however, for the sake of illustration it will be assumed that this fact is not known). An exit water temperature is assumed, say $T_{w2} = 29$°C, and hence a mean water temperature is calculated as $T_{wav} = (35+29)/2 = 32$°C. The exit and mean water enthalpies are then $i_{s2} = 94.851$ kJ/kg and $i_{sav} = 110.95$ kJ/kg, respectively. The following steps are carried out exactly as in a sizing problem:

$$\delta = (i_{s1} + i_{s2} - 2i_{sav})/4 = 0.623 \text{ kJ/kg}$$

$$f' = (i_{s1} - i_{s2})/(T_{w1} - T_{w2}) = 5.782 \text{ kJ/kg-°C}$$

$$\Delta i = m_wc_{pw}\Delta T_w/m_a = 25.121 \text{ kJ/kg}$$

If $m_wc_{pw}/m_a < f'$, then $m_w^+ < m_a$ (Case 1). Hence

$$C_r = M_{\min}/m_{\max} = m_w^+/m_a = m_wc_{pw}/f'm_a = 0.724$$

$$\epsilon = (m_a\Delta i)/[m_w^+(i_{s1} - \delta - i_1)] = 0.486$$

At the calculated values of C_R and ϵ, one obtains NTU = $K_mA/m_{\min} = 0.84$ and $K_mA/m_w = 0.608$, as compared to the given value of 1.87. One may continue the iterative calculation using a bi-section method until the calculated tower characteristic agrees with the given value.

The counterflow rating calculations may be performed without iterations using the following procedure:

1 Specify the leaving water temperature.
2 Set several ΔT_w increments and calculate the K_mA/m_a required for each increment. Sum the K_mA/m_a values for each increment.
3 When the calculations for the last increment yields $\Sigma K_mA/m_a$ greater than the given value, decrease the ΔT_w for the last increment and continue until $\Sigma K_mA/m_a$ equals the given value.

Crossflow Sizing Calculation. The operating conditions are considered to be the same as those in the counterflow sizing example. All the parameters are calculated the same way and have the same numerical values as before, except for the value of the NTU, which depends on the crossflow ϵ-NTU relation used. It is recommended to use the unmixed/unmixed relation. The NTU is found from tables given in the Kays and London book (1984) to be 1.169 and the tower characteristic as $K_mA/m_a = 0.827$.

Comparison With Moffatt's Analysis

The one-increment ϵ-NTU design method developed by Moffatt (1966) provides results in agreement with the present Case 1 ($m_{\min} = m_w^+$). Moffatt defined effectiveness as $R/(R+A)$, which agrees with equation (22). His NTU was defined as K_mA/m_a. Moffatt's analysis will not give the correct answer if ($m_{\min} = m_a$).

Conclusions

1 The analysis presented herein shows how the ϵ-NTU theory of heat exchanger design may be applied to cooling towers. The effectiveness and NTU are defined by equations (17) and (16), respectively. The effectiveness and NTU definitions are in precise agreement with those used for heat exchanger design, and are applicable to all cooling tower operating conditions.

2 One-increment sizing calculations may be quickly performed for any flow configuration. The calculations are improved by using multi-increments and/or the enthalpy correction factor.

3 The influence of the four independent variables, R, A, T_{wb}, and m_w/m_a on the accuracy of the ϵ-NTU method is evaluated as a function of the number of increments used. The ranges of the parameters considered is given in Table 1. The calculations show that:

(*a*) The NTU is underpredicted when the ϵ-NTU method is used. For $R < 20$°C and $T_{wb} > 15$°C, the underprediction is 4-8 percent for a one-increment design, and less than 3 percent for a two-increment design. The underprediction is highest for low wet bulb temperatures and high cooling ranges.

(*b*) Use of the enthalpy correction factor reduces the error associated with a lower number of increments. Moreover, a one-increment design with this correction factor is equivalent to a two-increment design without the correction.

4 Using the methods outlined herein, a person competent in the ϵ-NTU (or the F-LMTD) method of heat exchanger design can use the same procedure to design cooling towers of any flow configuration.

5 Using the ϵ-NTU curve for the appropriate flow configuration, one may quickly calculate the required NTU for specified operating conditions. This negates the need for the extensive sets of curves given by Kelly (1976) and the Cooling Tower Institute (1967).

References

ASHVE, 1941, *ASHVE Heating, Ventilation, Airconditioning Guide*, 19th ed., Chap. 26, pp. 522–523.

Baker, D. R., and Shryock, H. A., 1961, "A Comprehensive Approach to the Analysis of Cooling Tower Performance," ASME JOURNAL OF HEAT TRANSFER, Vol. 83, pp. 339–350.

Baker, D., 1984, *Cooling Tower Performance*, Chemical Publishing Co., New York, Chap. 6, p. 101.

Berman, L. D., 1961, in: *Evaporative Cooling of Circulating Water*, 2nd ed., Henryck Sawistowski, ed., Pergamon Press, New York, Chap. 2, pp. 94–99; translated from Russian by R. Hardbottle.

Cooling Tower Institute, 1967, *Cooling Tower Institute Performance Curves*, The Cooling Tower Institute, Houston, TX.

Kays, W. M., and London, A. L., 1984, in: *Compact Heat Exchangers*, 3rd ed., McGraw-Hill, New York, Chap. 2, p. 51.

Kelly, N. W., 1976, *Kelly's Handbook of Crossflow Cooling Tower Performance*, Neil W. Kelly & Associates, Kansas City, MO.

Keyes, R. E., 1972, "Methods of Calculation for Natural Draft Cooling Towers," presented at the 13th National Heat Transfer Conference, Denver, CO, Aug. 6–9.

London, A. L., Mason, W. F., and Boelter, L. M. K., 1940, "Performance Characteristics of a Mechanically Induced Draft, Counterflow, Packed Cooling Tower," *Trans. ASME*, Vol. 62, pp. 41–50.

Majumdar, A. K., Singhal, A. K., and Spalding, D. B., 1983, "Numerical Modeling of Wet Cooling Towers—Part 1: Mathematical and Physical Models," ASME JOURNAL OF HEAT TRANSFER, Vol. 105, pp. 728–735.

Merkel, F., 1926, "Verdunstungskuhlung," *VDI Zeitschrift deutscher Ingenieure*, Vol. 70, pp. 123–128.

Moffatt, R. J., 1966, "The Periodic Flow Cooling Tower: A Design Analysis," Technical Report No. 62, Dept. Mechanical Engineering, Stanford University, CA.

Webb, R. L., 1988, "A Critical Review of Cooling Tower Design Methods," in: *Heat Transfer Equipment Design*, R. K. Shah, E. C. Subbarao, and R. A. Mashelkar, eds., Hemisphere Pub. Corp., Washington, DC, pp. 547–558.

Whillier, A., 1976, "A Fresh Look at the Performance of Cooling Towers," *ASHRAE Trans.*, Vol. 82, pp. 269–282.

Zivi, S. M., and Brand, B. B., 1956, "Analysis of the Cross-Flow Cooling Tower," *Refrigeration Engineering*, Vol. 64, No. 8, pp. 31–34.

APPENDIX

The derivation of the enthalpy correction factor is given below with reference to Fig. 9. The saturation line is divided into two straight line segments resulting in two trapezoids whose areas are A_1 and A_2, respectively; hence

$$A_1 = (i_{i1} + i_{iav})\,(T_{wav} - T_{w2})/2 \tag{26}$$

$$A_2 = (i_{i1} + i_{iav})\,(T_{w1} - T_{wav})/2 \tag{27}$$

T_{wav} is the average water temperature, $T_{wav} = (T_{w1} + T_{w2})/2$. Line E is drawn such that the area under it is equal to $A_1 + A_2$. Denoting this area by A, we have

$$A = [(i_{i2} - \delta) + (i_{i1} - \delta)]\,(T_{w1} - T_{w2})/2 \tag{28}$$

where δ is a correction factor. Setting $A = A_1 + A_2$ and using the definition of T_{wav}, the final desired result is

$$\delta = (i_{i1} + i_{i2} - 2i_{iav})/4 \tag{29}$$

Performance Characteristics of a Concentric Annular Heat Pipe: Part I—Experimental Prediction and Analysis of the Capillary Limit

A. Faghri
Professor.

S. Thomas
Graduate Research Assistant.

Mechanical Systems Engineering,
Wright State University,
Dayton, OH 45435

This paper describes the design, testing, and theoretical capillary limit prediction of a new heat pipe configuration, which is the concentric annular heat pipe. The concentric annular heat pipe is made of two concentric pipes of unequal diameters that create an annular vapor space. With this arrangement, capillary wicks can be placed on both the inside of the outer pipe and the outside of the inner pipe. This design significantly increases the heat capacity per unit length compared to conventional heat pipes, since the cross-sectional area of the wick as well as the surface area for heating and cooling are increased. The heat pipe was tested for the temperature distribution in the three sections of the heat pipe under various tilt angles and heating loads through the inner and outer pipes in the evaporator section. A simple analysis for the prediction of the capillary limitation of the concentric annular heat pipe is presented.

Introduction

Since the invention of the heat pipe by Grover et al. (1964) 25 years ago, much study has been done in the areas of heat pipe operation, factors limiting heat pipe performance, heat pipe applications, and design modifications for the improvement of the performance of heat pipes.

Because of the simplicity of design and ease of manufacture and maintenance, heat pipes have found applications in a wide variety of areas (Dunn and Reay, 1982; Chi, 1976) including energy conversion systems, cooling of nuclear reactors, cooling of electronic equipment, and high-performance space applications. The performance of a heat pipe often is critical and is judged in part by the amount of heat a unit length of the heat pipe can transport.

The need for an increase in the performance has led to intensive studies into the performance limitations of heat pipes and has spawned new designs ranging from complex chamber configurations to sophisticated composite capillary wick structures (Oshima, 1984). The new design proposed here is as simple as the original heat pipe design, and at the same time is expected to increase the heat transport capacity significantly.

The concentric annular heat pipe, as shown in Fig. 1, consists of two concentric pipes of unequal diameters attached by means of end caps, which create an annular vapor space between the two pipes. Wick structures are placed on both the inner surface of the outer pipe and the outer surface of the inner pipe. The space inside the inner pipe is open to the surroundings. An increase in performance is expected as a result of the increase in surface area exposed for the transfer of heat into and out of the pipe, and the increase in the cross-sectional area of the wick inside the pipe.

A significant limitation in any heat pipe design is that imposed by the performance of the wick. A specific capillary force is available in the heat pipe based on the type of wick used and the cross-sectional area of wick material available to transport liquid back to the evaporator section. As the heat rate into the pipe increases, the evaporation rate of fluid in the evaporator section also increases, which places a greater demand on the wick structure to pump the condensed liquid in the condenser section to the evaporator section. When the wick can no longer supply liquid to the evaporator section at a rate equal to the rate of evaporation occurring in that section, the capillary limit for that heat pipe has been reached. The result is that the liquid in the wick does not completely wet the evaporator section due to the liquid evaporating prematurely, which is called evaporator section dryout. The temperature of the evaporator section then increases dramatically to dangerous levels, until it is no longer safe to operate the heat pipe. By placing wick material on both internal walls of the concentric annular heat pipe, nearly twice as much wick cross-sectional area is available to pump condensate. Hence the capillary limit of the new heat pipe is expected to be significantly increased.

The exposed surface area available for heat input and output is important to the performance of heat pipes. Conventional heat pipe designs are limited in exposed surface area to that area on the outside of the pipe; thus radial heat flux occurs only through that surface. The annular heat pipe utilizes the exposed surface of the outer and inner pipes to increase the total radial heat flux. It is expected that this increase in exposed surface area per unit length of pipe will result in a large increase in the heat transport capacity of the pipe.

Several advantages of the concentric annular heat pipe are

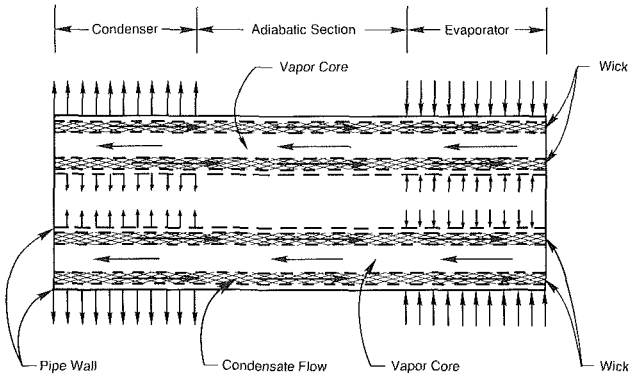

Fig. 1 Concentric annular heat pipe

Contributed by the Heat Transfer Division and presented at the National Heat Transfer Conference, Houston, Texas, July 1988. Manuscript received by the Heat Transfer Division May 4, 1988. Keywords: Heat Pipes and Thermosyphons.

apparent. First, the heat transport per unit length of this design will be more than that of the original heat pipe design. In many applications space is at a premium, so any increase in the heat transport for a given pipe size is significant. Second, since this design, like the original heat pipe design, is not specific to any working fluid, wick structure, or container material, many of the existing methods used to create high-capacity heat pipes can be used in conjunction with the concentric annular design. Certainly for high-power performance one can utilize any high-performance composite capillary wick structure. Finally, the annular heat pipe will be as easy to manufacture as a standard heat pipe, requiring no expensive tooling or other treatment. By this simple change in heat pipe design a large increase in performance with a minimum amount of sophistication has been achieved, making heat pipes more economical to build and use. A way that the concentric annular heat pipe could be used deals with applications that require exceptionally long heat pipes. Presently, when a very long heat pipe is needed the manufacturer builds several smaller heat pipes and ties these pipes together side-by-side and insulates where they are joined. This method is used because of the limitation of the capillary wick over long distances. Instead of tying the pipes together side-by-side where the area of contact between the pipes is minimal, a concentric annular heat pipe could be used to join the two pipes by sliding the end of each pipe into the inner pipe of the annular heat pipe. This method would increase the area of contact significantly, which would increase the heat transfer capability of the extended heat pipe.

Analysis of the Capillary Limitation of the Concentric Annular Heat Pipe

In this section a simple analysis for predicting the capillary heat transport limitation of the concentric annular heat pipe will be presented. This is done to show the improvement of the heat transport capability of the new design over a conventional heat pipe with the same outer dimensions. This comparison is valid because the same assumptions were made for the prediction of the capillary limit of the conventional heat pipe.

Consider an annular heat pipe as shown in Fig. 1 when operating under steady-state conditions. The sum of the pressure changes in the closed-cycle system may be described by the following mathematical relation:

$$2[P_v(z_{\text{ref}})-P_v(z)]+[P_v(z)-P_{L,I}(z)]+[P_v(z)-P_{L,O}(z)] \quad (1)$$
$$+[P_{L,I}(z)-P_{L,I}(z_{\text{ref}})]+[P_{L,I}(z_{\text{ref}})-P_v(z_{\text{ref}})]$$
$$+[P_{L,O}(z_{\text{ref}})-P_v(z_{\text{ref}})]+[P_{L,O}(z)-P_{L,O}(z_{\text{ref}})]=0$$

Introducing into the above equation the capillary pressure P_C, defined as the pressure at the vapor side of the liquid interface minus that of the liquid side, results in

$$P_{C,I}(z)+P_{C,O}(z)=P_{C,I}(z_{\text{ref}})+P_{C,O}(z_{\text{ref}})+2\Delta P_v(z-z_{\text{ref}}) \quad (2)$$
$$+\Delta P_{L,I}(z_{\text{ref}}-z)+\Delta P_{L,O}(z_{\text{ref}}-z)$$

where in general the notation $\Delta P(z-z_{\text{ref}})$ means that ΔP is evaluated over the distance $(z-z_{\text{ref}})$.

Assuming that the z_{ref} is such that it is located at $z_{\min}$ where the capillary pressure is minimum and equal to zero results in the following equation:

$$P_{C,I}(z)+P_{C,O}(z)=2\Delta P_v(z-z_{\min})+\Delta P_{L,I}(z_{\min}-z) \quad (3)$$
$$+\Delta P_{L,O}(z_{\min}-z)$$

In conventional heat pipes, there exists a maximum capillary pressure that can be developed for a liquid-wick pair. However, for the concentric annular heat pipe there exist two different maximum capillary pressure forces for the inner and outer tubes. If a heat pipe is to operate continuously without drying out the wick, the required capillary pressure for each wall should not exceed the maximum possible capillary pressure. The magnitude of the capillary pressure may be determined by balancing the forces at the liquid-vapor interface. This requires that the maximum capillary pressure for each wall should be:

$$P_{C,\max,I}=\frac{2\sigma}{r_{c,I}} \quad (4)$$

$$P_{C,\max,O}=\frac{2\sigma}{r_{c,O}}$$

where r_c is the effective capillary radius of the wick pores at the liquid-vapor interface. For axially grooved wicks, r_c is equal to the groove width as shown by Chi (1976).

Upon the assumption of laminar flow and incompressible fluid, and neglecting the inertia terms and the shear stress at the vapor-liquid interface in the conservation of momentum equation, one can get the following force balances for the liquid flow in the inner and outer wall grooves:

$$\frac{dP_{L,I}}{dz}=\frac{-4\tau_{L,I}}{D_{h,L,I}}\pm\rho_L g\sin\theta \quad (5)$$

$$\frac{dP_{L,O}}{dz}=\frac{-4\tau_{L,O}}{D_{h,L,O}}\pm\rho_L g\sin\theta \quad (6)$$

where τ_L is the viscous stress at the liquid-solid interface and $D_{h,L}$ is the hydraulic diameter for the wick and is equal to $4\,W\,\delta/(W+2\,\delta)$ for open rectangular grooves where δ is the groove depth and W is the groove width.

Equations (5) and (6) can be represented in terms of the local axial heat flux Q_I and Q_O for the inner and outer walls, respectively

Nomenclature

A = cross-sectional area
D = diameter
f = coefficient of friction
g = gravitational acceleration
h_{fg} = heat of vaporization
K = wick permeability
L = heat pipe length
$\dot{m}$ = mass flow rate
P = pressure
ΔP = pressure difference
Q = axial heat flux
r_c = effective capillary radius
Re = Reynolds number
t = wall thickness
ΔT = temperature difference
w = velocity
W = groove width
z = axial distance along the heat pipe
δ = groove depth
ϵ = porosity
θ = inclination angle
μ = viscosity
ν = kinematic viscosity
ρ = density
σ = surface tension
τ = shear stress

Subscripts

av = average
C = capillary
ea = evaporator and adiabatic
h = hydraulic
I = inner wall
L = liquid phase
max = maximum
min = minimum
O = outer wall
ref = reference
v = vapor phase
W = wick

$$\frac{dP_{L,I}}{dz} = -F_{L,I}Q_I \pm \rho_L g \sin\theta \tag{5a}$$

$$\frac{dP_{L,O}}{dz} = -F_{L,O}Q_O \pm \rho_L g \sin\theta \tag{6a}$$

The F functions are defined in the following way:

$$F_{L,I} = \frac{\nu_L}{K_I A_{W,I} h_{fg}} \tag{7}$$

$$F_{L,O} = \frac{\nu_L}{K_O A_{W,O} h_{fg}} \tag{8}$$

where K is the wick permeability, A_w the wick cross-sectional area, ϵ the porosity, f the friction coefficient, and Re_L the wick-liquid Reynolds number. These properties are defined by the following relationships:

$$\mathrm{Re}_{L,I} = \frac{D_{h,L,I} w_{L,I}}{\nu_L} \qquad \mathrm{Re}_{L,O} = \frac{D_{h,L,O} w_{L,O}}{\nu_L}$$

$$f_{L,I} = \frac{\tau_{L,I}}{\rho_L \dfrac{w_{L,I}^2}{2}} \qquad f_{L,O} = \frac{\tau_{L,O}}{\rho_L \dfrac{w_{L,O}^2}{2}} \tag{9}$$

$$Q_I = w_{L,I}\epsilon_I A_{W,I}\rho_L h_{fg} \qquad Q_O = w_{L,O}\epsilon_O A_{W,O}\rho_L h_{fg}$$

$$K_I = \frac{\epsilon_I D_{h,L,I}^2}{2(f_{L,I}\mathrm{Re}_{L,I})} \qquad K_O = \frac{\epsilon_O D_{h,L,O}^2}{2(f_{L,O}\mathrm{Re}_{L,O})}$$

The total local axial heat flux Q is the sum of the inner wall local axial heat flux Q_I and the outer wall local axial heat flux Q_O. Laminar incompressible fully developed fluid flow analysis in open rectangular passages shows that $f\cdot\mathrm{Re}$ is only a function of the geometry and dimensions of the wick. Therefore Q_I and Q_O are the only variables in equations (5*a*) and (6*a*) that change with axial distance along the heat pipe. The value of $f\cdot\mathrm{Re}$ needed for the evaluation of F can be obtained from Chi (1976) for the family of rectangular tubes as well as flow between concentric cylinders.

The problem of calculating the vapor pressure drop in the annulus is complicated in the evaporating and condensing regions by the radial vapor flow due to evaporation and condensation. It is convenient to neglect this effect of blowing and suction on the vapor pressure drop to obtain a closed-form solution. For a more accurate prediction one should use an analysis that includes the effect of blowing and suction on the vapor pressure drop as given by Faghri (1986) and Faghri and Parvani (1988). Upon the application of the conservation of axial momentum to the vapor flow between the concentric pipes, one obtains the following relationship provided that the flow is laminar:

$$A_v \frac{dP_v}{dz} = -\tau_{v,I}(\pi D_I) - \tau_{v,O}(\pi D_O) - A_v \frac{d\rho_v w_v^2}{dz} + (\dot{m}_I + \dot{m}_O) w_v \tag{10}$$

Since the mass flux of the vapor is related to the axial heat flux at the same z ($Q = \rho_v w_v A_v h_{fg}$), equation (10) can be presented in the following form when the last term on the right-hand side of the above equation is neglected:

$$\frac{dP_v}{dz} = -F_{v,av}Q - E_v \frac{dQ^2}{dz} \tag{11}$$

where

$$F_{v,av} = \frac{2(f_{v,av}\mathrm{Re}_v)\nu_v}{A_v D_{h,v}^2 h_{fg}}$$

$$f_{v,av} = \frac{\tau_{v,av}}{\rho_v w_v^2/2} = \frac{D_O\tau_{v,O} + D_I\tau_{v,I}}{(D_O + D_I)\rho_v w_v^2/2}$$

$$\mathrm{Re}_v = \frac{\rho_v w_v D_{h,v}}{\mu_v}$$

$$D_{h,v} = D_O - D_I$$

$$E_v = \frac{1}{A_v^2 \rho_v h_{fg}^2}$$

Substituting $\Delta P_L(z - z_{\min})$ and $\Delta P_v(z - z_{\min})$ from equations (5*a*), (6*a*), and (11) into equation (3) and neglecting the effect of gravity results in the following equation:

$$2\sigma\left(\frac{1}{r_{c,I}} + \frac{1}{r_{c,O}}\right) = 2F_{v,av}\int_0^L Q dz + \int_0^L (F_{L,I}Q_I + F_{L,O}Q_O) dz$$

The above relation simplifies, if one assumes that the geometry and dimensions of the grooves of the inner pipe are the same as the outer pipe, as well as the same heat input to the inner and outer walls, i.e., $F_{L,I} = F_{L,O} = F_{L,av}$ and $Q_I = Q_O = Q/2$.

$$\int_0^L Q dz = \frac{2\sigma\left(\dfrac{1}{r_{c,I}} + \dfrac{1}{r_{c,O}}\right)}{2F_{v,av} + F_{L,av}}$$

The maximum heat transport for a conventional heat pipe is given by the following equation:

$$\int_0^L Q dz = \frac{2\sigma/r_c}{F_L + F_v}$$

A comparison of the maximum heat transport capillary limit of the axially grooved concentric annular heat pipe proposed for experiment to a conventional heat pipe with the same outer diameter using the above analysis shows an increase of 80 percent using water as the working fluid at 100°C with the dimensions of the pipes and grooves as specified in Tables 1 and 2. The experimental prediction of the capillary limit indicated the same relative increase for this new design over the conventional heat pipe.

Experimental Apparatus and Procedure

Because the major objective of this project is to compare the performance of the concentric annular heat pipe to the performance of a conventional heat pipe of the same size, it was decided that two pipes should be built: a conventional heat pipe and a concentric annular heat pipe (see Tables 1 and 2, respectively). The pipes are of equal length and have the same external diameters. This allows a comparison of the performance per unit size. The two pipes are made of the same material and utilize the same working fluid. In order to observe the capillary pressure effect, the two pipes employ the same wick structure, although the concentric annular heat pipe has approximately twice the wick volume. With this criterion, it is hoped that a valid comparision can be made.

Summaries of the design parameters for the annular and the conventional heat pipe are given in Tables 1 and 2, respectively. It was decided that the wick structure to be used in the heat pipe would be axial grooves, which eliminated the need for a complicated wick installation procedure (Fig. 2).

The outer copper pipe to be used in the two heat pipes was commercially available, 973 mm in length and o.d. = 50 mm with 120 0.5 mm × 0.5 mm axial grooves extruded on the inner

Table 1 Design summary of the concentric annular heat pipe

Materials			
Outer pipe	Copper		
Inner pipe	Copper		
End caps	Copper		
Working Fluid	Water		
Dimensions			
Total Length	973 mm	Outer pipe	Inner pipe
Evaporator Length	300 mm	OD 50 mm	29.7 mm
Adiabatic Length	473 mm	ID 46.6 mm	25.4 mm
Condenser Length	200 mm	Tw 1.7 mm	2.15 mm
Grooves			
		Outer pipe	Inner pipe
Number		120	97
Width		0.5 mm	0.5 mm
Depth		0.5 mm	0.5 mm
Total groove volume	54.25 cc		
Fluid Inventory			
Quality	Distilled water		
Quantity	68 cc filled at 21°C		

Table 2 Design summary of conventional pipe

Materials		
Outer pipe	Copper	
End caps	Copper	
Working Fluid	Water	
Dimensions		
Total Length	973 mm	
Evaporator Length	300 mm	OD 50 mm
Adiabatic Length	473 mm	ID 46.6 mm
Condenser Length	200 mm	Tw 1.7 mm
Grooves		
Number	120	
Width	0.5 mm	
Depth	0.5 mm	
Total groove volume	30 cc	
Fluid Inventory		
Quality	Distilled water	
Quantity	41 cc filled at 21°C	

Table 3 Heater assembly design specifications

Dimensions	Inner Assembly	Outer Assembly
Length	300 mm	300 mm
OD	25.4 mm	---
ID	---	50.4 mm
Surface Area	15959.3 mm^2	32142.3 mm^2
Heating Element		
Length	2.24 m	2.38 m
Diameter	2.36 mm	4.77 mm
Voltage	220 v	220 v
Max. Power	1200 w	4800 w
Assembly Base		
Material	Aremcolox 502-600	
Length	300 mm	
OD	19.05 mm	
Thermocouples		
NBS Type	T (30 gauge)	T (28 gauge)
# of thermocouples	7	7

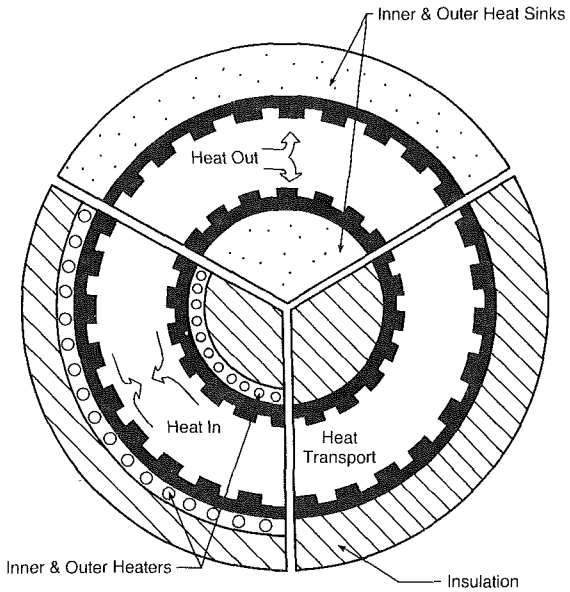

Fig. 2 Concentric annular heat pipe design concept

wall. The inner pipe for the annular heat pipe was machined from a copper tube with i.d. = 25.4 mm and o.d. = 29.7 mm. Ninety-seven 0.5 mm × 0.5 mm axial grooves were cut on the outer wall over the length of the pipe using a vertical milling machine with a precision saw cutter. The ends of each pipe were machined so that the end caps fit snugly into them.

All of the parts were carefully fabricated, cleaned, and deoxidized using the standard procedures suggested by Chi (1976), and the end caps were TIG welded to the tubes in an inert argon gas environment. A bellows-type valve was attached to the fill tube of the heat pipe to facilitate sealing, purging, and charging of the fluid inventory inside the heat pipe. A thermocouple probe was inserted through the condenser end cap a distance of 75 mm into the vapor core to measure the vapor temperature.

The heat pipes were processed in a specially built heat pipe filling station. The conventional and concentric annular heat pipes were evacuated to a vacuum on the order of 10^{-5} torr, and filled with 41 and 68 cc of degassed, distilled water at 21°C, respectively.

Heat was input to the concentric annular heat pipe by two heaters (see Table 3). The inner heater assembly was designed to slide into the inner pipe (i.d. = 25.4 mm) in the evaporator end of the concentric annular heat pipe. It consisted of a 2.24-m-long, 1200 W heater rod coiled around a core of insulating material 300 mm in length. This heater assembly was covered with thermally conductive cement so that its outer

diameter was o.d. = 25.2 mm. This allowed the completed inner heater assembly to slide into the inner pipe of the concentric annular heat pipe. Seven thermocouples were mounted on the outer surface of the heater assembly to measure the temperature of the inner wall of the heat pipe in the evaporator section.

The outer heater for the concentric annular heat pipe was a 4800-W heater rod of length 2.38 m and diameter 4.77 mm. The heater rod was tightly wrapped around the evaporator in a uniform spiral arrangement and was held in place with Sauereisen electric heater cement. This prevented the heater rod from expanding away from the heat pipe when the heater was operating. Seven thermocouples were mounted between the heater coils on the pipe wall to monitor the outer evaporator temperature. Each heater assembly was powered by its own 220-V variable a-c transformer, allowing the heat input to be varied from zero to the maximum wattage. The power input was monitored by a voltmeter and an ammeter connected to each variac and was checked with precision wattmeters.

The wall temperature of the adiabatic section of the concentric annular heat pipe was measured by thermocouples mounted on both the inner and outer walls. Seven thermocouples were mounted on a rod of insulating material (Aremcolox 502-600) of o.d. = 25.2 mm that was inserted into the inner pipe in the adiabatic section. Seven thermocouples were mounted directly onto the outer walls of the concentric annular heat pipe. A thermocouple was also mounted on each end cap of the heat pipe.

The condenser section of the concentric annular heat pipe has two heat sinks (see Table 4). The inner heat sink fits inside the inner pipe of the heat pipe. The outer heat sink fits over the outer pipe of the heat pipe. The inner heat sink (o.d. = 25.4 mm) has two end caps. One cap has two holes—one inlet and one outlet—and the other cap is solid. An inner baffle runs the length of the heat sink and has a hole in it at the end where the solid end cap is. This forces the coolant to travel the entire length of the heat sink, which ensures even cooling. The length of the inner heat sink is the length of the condenser section plus the length of each end cap. The total length is 219 mm. T-fittings were placed at the inlet and outlet of the inner heat sink to allow for the installation of thermocouples in the coolant stream with which the mixed-mean inlet and outlet temperatures were measured. Four axial grooves were cut on the outside of the inner heat sink to accommodate eight thermocouples, which were placed at regular intervals along the length of the heat sink. This allowed for the measurement of the temperature distribution on the inside of the inner pipe. These grooves are cut 6.35 mm wide × 1.59 mm deep and run the length of the heat sink.

The outer heat sink for the concentric annular heat pipe was 1/4 in. o.d. soft copper tubing, which was tightly wrapped around the condenser section and held in place with clamps at each end. The coils of tubing were wrapped around the pipe such that the coils were side-by-side. T-fittings were placed at the inlet and outlet of the outer heat sink to measure the inlet and outlet temperatures of the cooling water.

The outer heater for the conventional heat pipe was two heater rods of length 2.24 m and diameter 2.36 mm. Each heater rod was tightly wrapped around one-half of the length

Table 4 Heat sink design specifications

Dimensions	Inner Sink	Outer Sink
Length	219 mm	200 mm
OD	25.4 mm	63.5 mm
ID	---	50.4 mm
Surface Area	17475 mm^2	31667 mm^2
Material		
Outer pipe	Copper (tw = 1.27 mm)	1/4 in OD Copper tubing
Baffle	Copper	---
Working fluid	Water	Water
Thermocouples		
NBS Type	T (30 gauge)	
# of thermocouples	8	
Flow Meter		
Max. flow rate	906 ml/min.	1812 ml/min.
Min. flow rate	24 ml/min.	48 ml/min.
Fluid	Water	Water

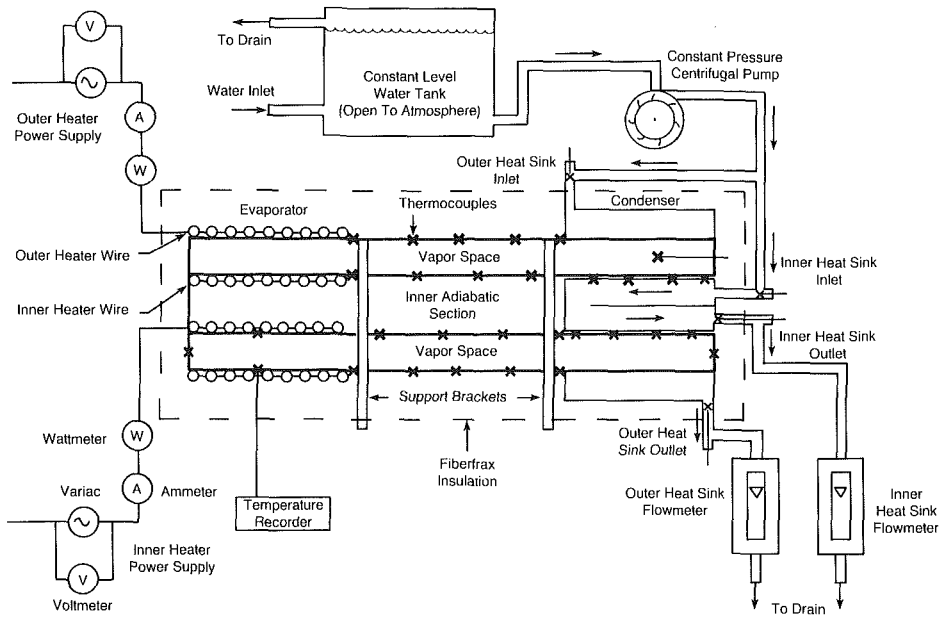

Fig. 3 Experimental setup

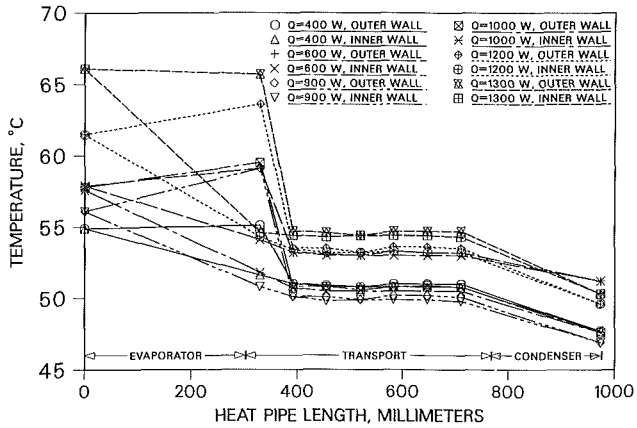

Fig. 4 Axial temperature profile for the concentric annular heat pipe

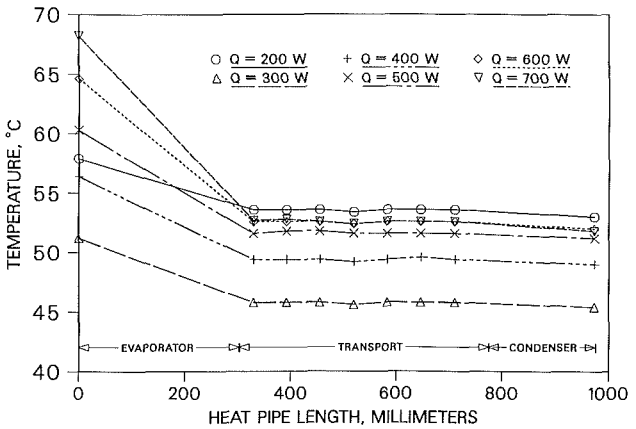

Fig. 5 Axial temperature profile for the conventional heat pipe

of the evaporator section with an even spiral pitch. The heaters were covered with electric heater cement and seven thermocouples were mounted between the coils on the pipe wall. When the conventional heat pipe was tested, the heat input through each heater was the same to ensure uniform heating.

The adiabatic section and the condenser section of the conventional heat pipe were identical with respect to the thermocouple instrumentation and the the heat sink as the outer adiabatic section and the outer condenser section of the annular heat pipe.

A schematic of the test setup is shown in Fig. 3. The heat pipes were mounted on a test stand with the required heater and heat sink assemblies installed complete with thermocouples. The thermocouples were attached to a monitoring device and variable area flow meters were installed at the outlet of the heat sinks to measure cooling water flow rates. Cooling water was supplied to the heat sinks by a centrifugal pump connected to a constant head reservoir in order to maintain constant pressure and therefore a steady coolant flow.

The entire length of the heat pipe assembly was insulated with 6 in. of "Fiberfrax" insulation material. The heat pipe was made parallel to the base of the test setup and the base was then mounted on leveling jacks. Using these jacks the heat pipe could be adjusted to any tilt angle desired.

Tests were performed to establish the maximum heat transport capacity of the heat pipe before wick dryout at negative (adverse) and zero tilt angles. The operating (adiabatic) temperature was held at $50°C \pm 5°C$ for all of the tests to ensure repeatability of the results. A thermocouple probe was used to compare the vapor temperature to adiabatic wall temperatures to confirm the absence of noncondensible gases in the condenser end of the heat pipe. Energy balances between the heat input by the heaters and the heat removed by the heat sinks were monitored, and flow rates through the heat sinks were maintained to ensure an energy balance of at least 90 percent. The criterion used to establish the maximum heat transport capacity was steady-state operating conditions with no evaporator dryout. Evaporator dryout was defined as that point when the temperature difference between the adiabatic section and the evaporator end cap was greater than 12°C. Type T thermocouples were used, which can be read with an uncertainty of $\pm 1/4$ percent. A standard error analysis technique was applied for the calculation of the heat rate Q, which yielded an uncertainty of ± 6 percent.

Results

Information was gathered from several test runs on each heat pipe and the data were combined to observe the overall performance of the concentric annular heat pipe with an emphasis on an increase in the heat transport capacity as compared to the conventional heat pipe. Figures 4 and 5 show the axial temperature profiles of the two pipes up to the maximum stable heat transport capacity. These graphs show that the concentric annular heat pipe performed nearly 82 percent better than the conventional heat pipe, showing a maximum stable operating limit of 1300 W as compared to 700 W for the conventional heat pipe.

The axial temperature profiles of the concentric annular heat pipe are shown in Fig. 4. In this graph, each power setting has the same line texture but the inner temperature profile has a different data point symbol than the outer temperature profile. For example, the first test is for a total heat input of 400 W. The inner temperature distribution for this setting is denoted by a solid line with triangles marking data points. The outer temperature profile for this same setting is shown by a solid line with octagons marking data points. Figure 4 shows clearly that the temperatures of the inner and outer adiabatic sections were isothermal and within 1°C of each other for all of the power settings.

The heat input in the inner wall evaporator is smaller than the outer wall evaporator due to smaller heater capacity in the inner wall in comparison to the outer heater in the present experiment as well as the possibility of boiling due to the smaller surface area. Upon combining the results of Figs. 4 and 8, one can see how the heat is distributed between the inner and outer walls.

Figure 5 shows the temperature distributions of the conventional heat pipe under various heat loads. The adiabatic temperatures for this pipe at all of the settings were also isothermal to within 1°C.

Adverse tilt tests were performed on the concentric annular heat pipe at tilt angles from -1 deg to 0 deg and the results are shown in Fig. 6. An adverse tilt is when the evaporator section is above the condenser section, which forces the condensate to be pumped uphill by the wick structure. Positive (favorable) tilt angle tests were not performed on the concentric annular heat pipe because the heater temperature in the inner evaporator section exceeded the maximum temperature recommended by the manufacturer of the thermocouples that were used in the inner heater section at powers above 1300 W. Figure 6 demonstrates that the maximum input power increases as the evaporator section is lowered with respect to the condenser section of the concentric annular heat pipe.

The heat transport rate versus the tilt angle for the conventional heat pipe is shown in Fig. 7. The maximum stable heat rate for the conventional heat pipe at 0 deg tilt was 700 W. This heat pipe displayed the same behavior in the tilt test as the concentric annular heat pipe.

The condenser heat output through the inner and outer pipe

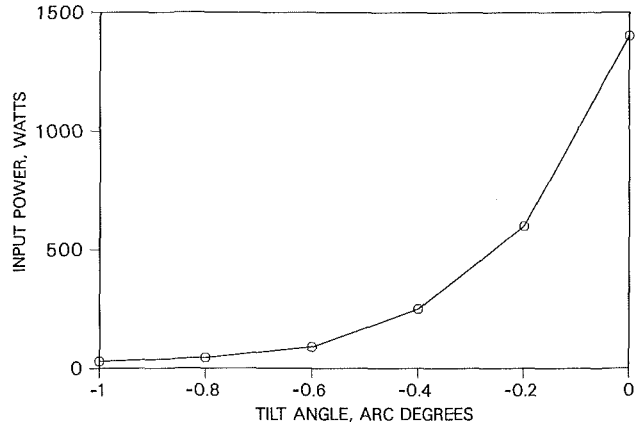

Fig. 6 Maximum input power versus tilt angle for the concentric annular heat pipe

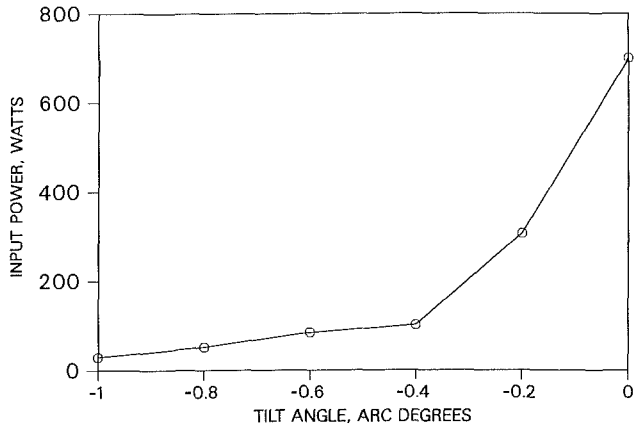

Fig. 7 Maximum input power versus tilt angle for the conventional heat pipe

walls versus the evaporator heat input through each pipe wall is presented in Fig. 8. This graph shows that the heat input through the inner pipe wall in the evaporator section is significantly smaller than the heat extracted from the inner pipe in the condenser section at all of the power settings. Likewise, the heat input through the outer pipe in the evaporator is greater than the heat taken away by the outer condenser. This means that all of the working fluid that condenses onto the inner pipe wall in the condenser section does not reach the inner evaporator section. This phenomenon is the result of communication of the working fluid between the inner and outer pipes. A meniscus is formed in the condenser section where the inner pipe and the end cap are joined, which allows part of the working fluid that condenses onto the inner pipe to drain down to the outer pipe. In future investigations this phenomenon should be prevented by proper wick and end cap design. This will increase the amount of heat that can be transferred by the inner pipe.

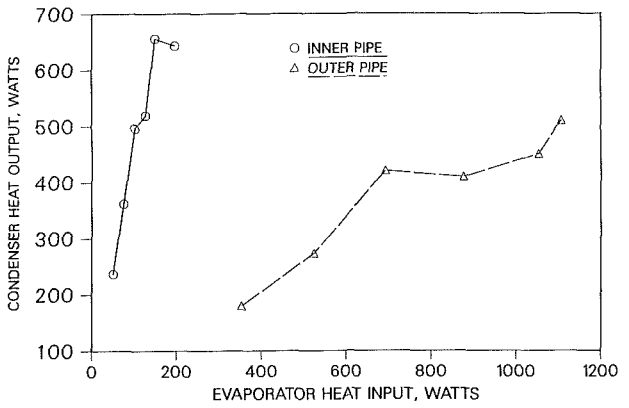

Fig. 8 Evaporator and condenser performance for the concentric annular heat pipe

Conclusions

A new heat pipe design called the concentric annular heat pipe has been developed and a 1-m-long copper–water prototype was fabricated and tested successfully. The design is simple to manufacture and can be used with any existing high-performance wick structure. This design shows a significant increase in the heat capacity per unit length compared to conventional heat pipes with the same outer diameter. The potential of the application of the new design in the heat exchange industry would be significant compared to conventional heat pipes due to size, geometry, and heat capacity performance. Furthermore, temperature uniformity in the inner and outer walls makes this device an ideal simplified temperature control device for furnace applications.

Acknowledgments

Funding for this work was provided by the Thermal Energy Group of the Aero Propulsion Laboratory of the U.S. Air Force under contract No. F-33615-81-C-2012. The authors are indebted to Dr. E. T. Mahefkey and Dr. J. E. Beam for their technical assistance during the project.

References

Chi, S. W., 1976, *Heat Pipe Theory and Practice*, Hemisphere Publishing Corporation, New York.

Dunn, P. D., and Reay, D. A., 1982, *Heat Pipes*, 3rd ed., Pergamon Press, New York.

Faghri, A., 1986, "Vapor Flow Analysis in a Double-Walled Concentric Heat Pipe," *Numerical Heat Transfer*, Vol. 10, pp. 583–595.

Faghri, A., and Parvani, S., 1988, "Numerical Analysis of Laminar Flow in a Double-Walled Annular Heat Pipe," *Journal of Thermophysics and Heat Transfer*, Vol. 2, No. 2, pp. 165–171.

Grover, G. M., Cotter, T. P., and Erikson, G. F., 1964, "Structures of Very High Thermal Conductance," *Journal of Applied Phys.*, Vol. 35, No. 6, pp. 1990–1991.

Oshima, K., 1984, *Research and Development of Heat Pipe Technology*, Japan Technology and Economics Center, Inc., Tokyo.

Performance Characteristics of a Concentric Annular Heat Pipe: Part II—Vapor Flow Analysis

A. Faghri
Professor,
Mechanical Systems Engineering,
Wright State University,
Dayton, OH 45435

The solutions of the equations of fluid motion for compressible and incompressible flow in a concentric annular heat pipe have been analyzed. In addition, a similarity solution is presented that can predict the pressure losses in all the segments of the concentric annular heat pipe as well as conventional heat pipes. A theoretical analysis to predict the sonic limit for this new heat pipe is also presented.

Introduction

The analysis of heat pipes can be classified into the solutions of three fluid mechanics problems: (1) the pressure loss associated with the vapor flow in the evaporator, adiabatic, and condenser sections, (2) the pressure loss due to the liquid flow return path in the wick, and (3) the interaction between the liquid and vapor flows. The analysis for the last two problems is basically similar for different heat pipe structures but the dynamics of vapor flow is more complex due to the geometry and boundary specifications for nonconventional heat pipes. This is especially true for the performance analysis of the concentric annular heat pipe, which is shown in Fig. 1. In determining the heat capacity transmitted through this heat pipe, it is necessary to know the pressure losses in the separate segments of the heat pipe. The compressible vapor flow analysis is also needed for the sonic limit.

Many investigators have examined the problem of vapor flow in porous pipes and conventional heat pipes using numerical and analytical methods. The analysis of these theoretical and experimental investigations shows that approximate solutions of the Navier-Stokes equations using similarity analysis over the length of the condenser region for conventional heat pipes is valid for radial Reynolds numbers ranging from $0 < \mathrm{Re} < 2.3$ and $\mathrm{Re} > 9.1$ (Yuan and Findelstein, 1955; Bankston and Smith, 1973). In contrast to the condenser section, similarity solutions have been found to exist for all values of the radial Reynolds number in the evaporator section. Numerical solutions of the complete governing equations of motion for conventional heat pipes were also considered by Bankston and Smith (1973), Tien and Rohani (1974), and Busse and Prenger (1984). However, there is a disagreement among the investigators (Tien and Rohani, 1974; Busse and Prenger, 1984) on the validity of the usage of the parabolic version of the equations of motion to predict the vapor pressure drop in conventional heat pipes.

Faghri (1986) analyzed the two-dimensional, steady, and incompressible flow of vapor in a concentric annular heat pipe. The parabolic presentation of the governing equations of motion was used for the solution of the vapor flow in the evaporator, adiabatic, and condenser segments of the heat pipe. The solutions for the evaporator, adiabatic, and condenser sections were obtained independently of each other. This was possible by assuming a zero inlet axial velocity at the evaporator inlet and a fully developed profile at the inlet of the adiabatic and condenser sections. Due to these assumptions, an implicit marching finite-difference method was possible. Numerical solutions of the complete Navier-Stokes equations were also presented by Faghri and Parvani (1988) in order to allow for all of the features of laminar flow, especially in the condenser section in a problem that was clearly of the elliptic type.

This paper is a summary of the methods used for the calculation of the pressure drops in the different heat pipe segments and a theoretical investigation of the characteristics of the concentric annular heat pipe at low, moderate, and high-temperature applications. Because of the limitations of the previous studies for incompressible flow, a one-dimensional analysis of compressible vapor flowing within the evaporator and adiabatic sections of a concentric annular heat pipe, including the effect of friction, is also given for the calculation of the sonic limit. Practical and accurate equations for the calculation of the pressure losses are given that can be applied to concentric annular heat pipes as well as conventional heat pipes.

Compressible Flow: One-Dimensional Analysis

The parameters limiting heat transport in conventional heat pipes are capillary limitations, sonic effects, entrainment, and boiling limitations. The type of limitation restricting the heat transport capability is determined by the temperature range under consideration, the working fluid, the wick structure, and the dimensions of the heat pipe. It is believed that the sonic limitation is not greatly influenced by any aspect of the wick structure except the vapor core size. Therefore, the choking phenomena should be of primary interest in the concentric annular heat pipe due to the fact that the vapor velocity becomes large and significant compared to the vapor sonic velocity. There have been many different vapor models proposed to analyze the gas dynamics choking phenomena in conventional heat pipes. Theoretical and experimental treatments of the sonic limitation have been made in the early stages of heat pipe development by Levy (1968, 1971), Kemme (1969), and Deverall et al. (1970). In this type of analysis the inertial forces and the compressibility effects are the most important phe-

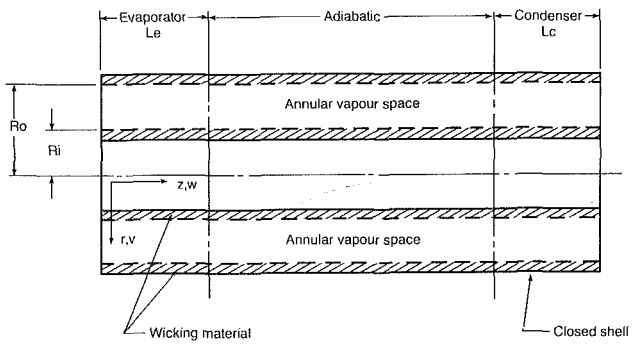

Fig. 1 Concentric annular heat pipe and coordinate system

Contributed by the Heat Transfer Division and presented at the National Heat Transfer Conference, Houston, Texas, July 1988. Manuscript received by the Heat Transfer Division May 4, 1988. Keywords: Heat Pipes and Thermosyphons.

nomena. The most recent prediction of the choking phenomenon in conventional heat pipes was done by Busse and Prenger (1984). They used the boundary layer approximation including the compressibility effects and predicted the choking phenomenon as a function of the radial Reynolds number. The analysis made here for concentric annular heat pipes is similar to those made by Levy (1968, 1971).

The analogy between the axial flow of vapor in the evaporator and the flow of a gas through a converging-diverging nozzle is well documented for conventional heat pipes. Similar to the analysis of conventional heat pipes, the flow in the vapor portion of the evaporator section of the concentric annular heat pipe can be thought of as annular flow between porous walls with mass injection at the walls. The following assumptions are made for the one-dimensional analysis of compressible vapor flow in the evaporator and adiabatic sections of the concentric annular heat pipe:

1 Frictional effects do not consider the effect of mass transfer.
2 The radial mass flow rate through the walls is uniform.
3 The radial distributions of the vapor temperature and pressure are neglected.

The principal of the conservation of mass, momentum, and energy as applied to a differential control volume element of length dz in the annulus requires

$$A_v \frac{d}{dz}(\rho w) = \dot{m}_{I,E} + \dot{m}_{O,E} \tag{1}$$

$$\frac{dP}{dz} = -\frac{d(\rho w^2)}{dz} - \frac{4\bar{\tau}_w}{D_h} \tag{2}$$

$$\frac{d(h+w^2/2)}{dz} = -\frac{\dot{m}_{O,E}}{\dot{M}}\left(\frac{w^2}{2} - \frac{V_{O,E}^2}{2} + h - h_g\right) - \frac{\dot{m}_{I,E}}{\dot{M}}\left(\frac{w^2}{2} - \frac{V_{I,E}^2}{2} + h - h_g\right) \tag{3}$$

At this stage it is necessary to introduce some specific information on the vapor equation of state due to the compressibility flow analysis. Two different models have been used in the analysis of conventional heat pipes. These are the perfect gas and the equilibrium two-phase models. The equilibrium two-phase model is more realistic and therefore it has been used for the present analysis. The temperature and pressure are related by the Clausius-Clapeyron equation $dP/P = (h_{fg}/R)(dT/T^2)$ and the specific volume v' and enthalpy h are expressed in terms of the vapor quality x, the specific volume of saturated liquid and vapor, the enthalpy of the saturated liquid, and the latent heat of vaporization as done in the standard analysis of two-phase models. Upon using v_g' as approximated by RT/P and assuming that the specific volume of saturated liquid and liquid heat are constant quantities, the following relation is obtained for the axial pressure gradient:

$$\frac{dP}{dz} = \frac{\dfrac{w^2}{v'z}\left[2h_{fg} + \dfrac{(v_g'-v_f')}{v'}\left[w^2 - z\left\{\dfrac{\dot{m}_{O,E}}{\dot{M}}\left(\dfrac{w^2}{2} - \dfrac{V_{O,E}^2}{2} + h - h_g\right) + \dfrac{\dot{m}_{I,E}}{\dot{M}}\left(\dfrac{w^2}{2} - \dfrac{V_{I,E}^2}{2} + h - h_g\right)\right\}\right]\right] + F}{\left[-\left(h_{fg} + \dfrac{(v_g'-v_f')}{v'}w^2\right) + \dfrac{xw^2v_g'}{Pv'^2}\left(1 - \dfrac{RT}{h_{fg}}\right)h_{fg} + \dfrac{C_{pf}T^2w^2(v_g'-v_f')R}{h_{fg}Pv'^2}\right]} \tag{4a}$$

where $F = \dfrac{4\bar{\tau}_w}{D_h}\left(h_{fg} + \dfrac{w^2(v_g'-v_f')}{v'}\right)$.

The axial quality and velocity gradients are

$$\frac{dx}{dz} = \frac{\left[-1 + \left(1 - \dfrac{RT}{h_{fg}}\right)\dfrac{xw^2v_g'}{Pv'^2}\right]\dfrac{dP}{dz} - \dfrac{2w^2}{zv'} - \dfrac{4\bar{\tau}_w}{D_h}}{\left(\dfrac{v_g'-v_f'}{v'^2}\right)w^2} \tag{5a}$$

and

$$\frac{dw}{dz} = \frac{w}{z} + \frac{wxv_g'}{v'P}\left(\frac{RT}{h_{fg}} - 1\right)\frac{dP}{dz} + w\left(\frac{v_g'-v_f'}{v'}\right)\frac{dx}{dz} \tag{6a}$$

For both the inner and outer walls, the mass injection rates were taken to be uniform over the length of the evaporator section and are related to the axial mass flow rate $\dot{M}$ and the inner and outer local heat rate per unit length of the evaporator by the following relations:

$$\dot{M} = (\dot{m}_{I,E} + \dot{m}_{O,E})z \tag{7}$$

Nomenclature

A' = constant used in equation (26) = $(1-K^2)/\ln 1/K$
A_v = cross-sectional area of the vapor flow passage
B = constant used in defining C = $(1-K^4)/(1-K^2)$
C = constant used in equation (26) = $4(|\mathrm{Re}_{I,E}| + |\mathrm{Re}_{O,E}|)/(B-A')(1-K^2)$
C' = constant used in equation (28) = $4(|\mathrm{Re}_{I,C}| + |\mathrm{Re}_{O,C}|)/(B-A')(1-K^2)$
C_{pf} = constant pressure specific heat of liquid
dz = increment in the z direction
D' = constant used in equation (28) = $2/(B-A')$
D_h = hydraulic diameter
DI = inner pipe diameter
DO = outer pipe diameter
f = friction factor
h = enthalpy of vapor
h_{fg} = enthalpy of evaporation
h_g = enthalpy of saturated vapor
K = ratio of the inner radius to the outer radius
K' = ratio of specific heats of vapor
LA = length of the adiabatic section
LC = length of the condenser section
LE = length of the evaporator section
LT = total length of the heat pipe
$\dot{m}$ = mass injection rate per unit length of evaporator
$\dot{M}$ = axial mass flow rate
M = vapor Mach number
P = vapor pressure
P^+ = normalized pressure = $(P-P_e)/\rho(w_{A,m})^2$
Q = heat transfer rate per unit length of evaporator
Q_s = sonic heat rate
r = radial coordinate
R = gas constant
R^+ = normalized radial distance = r/RO
RI = inner pipe radius
RO = outer pipe radius
Re = radial Reynolds number
$\mathrm{Re}_{I,E}$ = inner wall radial Re in evaporator = $(RI)(V_{I,E})/\nu$
$\mathrm{Re}_{I,C}$ = inner wall radial Re in condenser = $(RI)(V_{I,C})/\nu$
$\mathrm{Re}_{O,E}$ = outer wall radial Re in evaporator = $(RO)(V_{O,E})/\nu$

$$Q_{O,E} = \dot{m}_{O,E}\left(h_{fg} + \frac{V_{O,E}^2}{2}\right) \tag{8}$$

$$Q_{I,E} = \dot{m}_{I,E}\left(h_{fg} + \frac{V_{I,E}^2}{2}\right) \tag{9}$$

The radial velocities at the inner and outer walls are calculated in terms of the inner and outer local heat rate per unit length by the following relations, since the second term in equations (8) and (9) is small compared to the first term in the right-hand side of the same equations:

$$V_{O,E} = \frac{Q_{O,E}}{\pi\, DO\, \rho_g\, h_{fg}} \tag{10}$$

$$V_{I,E} = \frac{Q_{I,E}}{\pi\, DI\, \rho_g\, h_{fg}} \tag{11}$$

The relation

$$f = \frac{\bar{\tau}_w}{\rho\, w^2/2} = \frac{C_1}{\mathrm{Re}_z} \tag{12}$$

was used to calculate the laminar shear stress in the evaporator and adiabatic segments, where the constant C_1 is obtained from Kays and Crawford (1980) in terms of K. The above equation neglects the effect of mass transfer on the friction coefficient. It has already been well documented that blowing reduces the friction coefficient and therefore the actual prediction of the numerical results should be expected to lie between the numerical results for no friction and the results with friction. Equations (4*a*)–(6*a*) reduce to the governing equations for conventional heat pipes if $Q_{I,E} = \dot{m}_{I,E} = V_{I,E} = 0$ and represent frictionless flow if $\bar{\tau}_w = 0$.

Expressions similar to equations (4*a*), (5*a*), and (6*a*) will be obtained for the adiabatic section. These relations for the adiabatic section cannot be obtained from the evaporator results using $\dot{m}_{I,E} = \dot{m}_{O,E} = 0$, because the inlet condition to the adiabatic section is different from that to the evaporator section and one is not able to use equation (7) for the adiabatic section. These relations for the axial pressure, quality, and velocity gradients for the adiabatic section are

$$\frac{dP}{dz} = \frac{\left(\frac{w^2(\nu_g' - \nu_f')}{\nu'} + h_{fg}\right)\frac{4\bar{\tau}_w}{D_h}}{\left[-\left(h_{fg} + \frac{(\nu_g' - \nu_f')}{\nu'}w^2\right) + \frac{xw^2\nu_g'}{P\nu'^2}\left(1 - \frac{RT}{h_{fg}}\right)h_{fg} + \frac{C_{pf}T^2w^2(\nu_g' - \nu_f')R}{h_{fg}P\nu'^2}\right]} \tag{4b}$$

$$\frac{dx}{dz} = \frac{\left[-1 + \left(1 - \frac{RT}{h_{fg}}\right)\frac{xw^2\nu_g'}{P\nu'^2}\right]\frac{dP}{dz} - \frac{4\bar{\tau}_w}{D_h}}{\left(\frac{\nu_g' - \nu_f'}{\nu'^2}\right)w^2} \tag{5b}$$

and

$$\frac{dw}{dz} = \frac{wx\nu_g'}{\nu' P}\left(\frac{RT}{h_{fg}} - 1\right)\frac{dP}{dz} + w\left(\frac{\nu_g' - \nu_f'}{\nu'}\right)\frac{dx}{dz} \tag{6b}$$

Equations (4*b*)–(6*b*) form a system of three simultaneous first-order ordinary differential equations that can be solved for P, x, and w as functions of z provided that $Q_{I,E}$ and $Q_{O,E}$ are specified. It should be noted that the temperature and pressure are related through the Clausius–Clapeyron equation. These equations are solved by digital computer using the Runge–Kutta integration scheme. In the upstream end of the evaporator for the initial conditions, the incompressible assumption was made to obtain the following linear relation for the velocity at the initial step:

$$w_i = \frac{4(V_{I,E}\, DI + V_{O,E}\, DO)}{DO^2 - DI^2}\, z_i \tag{13}$$

All of the calculations are started at the upstream end of the evaporator where the fluid is assumed to be saturated vapor ($x = 1$) at the operating temperature of 773 K. In order to obtain the sonic limit, a certain $Q_{I,E}$ and $Q_{O,E}$ were assumed and then increased step by step in an iteration process. The process was continued until the Mach number, $M = (w/\sqrt{K'RT})$, reached unity at the exit of the adiabatic section when considering the friction or reached unity at the exit of the evaporator section when friction is neglected. The thermophysical properties of sodium were obtained by Vargaftik (1975).

The calculations were made for three different cases for the same sodium heat pipe with outer and inner diameters of 0.0444 m and 0.0294 m, respectively, and with evaporator and adiabatic section lengths of 0.08 m and 0.04 m, respectively. The three cases are: (1) neglecting the effect of friction and no

Nomenclature (cont.)

$\mathrm{Re}_{O,C}$ = outer wall radial Re in condenser = $(RO)(V_{O,C})/\nu$
Re_z = axial Reynolds number
T = temperature
v = radial component of the vapor velocity
v^* = dimensionless radial velocity = $v\, RO/\nu$
$V_{I,E}$ = blowing velocity at inner wall in evaporator
$V_{I,C}$ = suction velocity at inner wall in condenser
$V_{O,E}$ = blowing velocity at outer wall in evaporator
$V_{O,C}$ = suction velocity at outer wall in condenser
$V_{I,w}$ = radial velocity at inner wall
$V_{O,w}$ = radial velocity at outer wall
w = axial component of vapor velocity
$w_{A,m}$ = mean axial velocity in adiabatic section
$w_{z,m}$ = local mean axial velocity
$w_{z,m}^*$ = dimensionless local mean axial velocity = $w_{z,m}/w_{A,m}$
W^+ = normalized axial velocity = $w/w_{z,m}$
w^* = dimensionless axial velocity = $w/w_{A,m}$
x = vapor quality
z = axial coordinate
z^* = dimensionless axial coordinate = $z\nu/(w_{A,m})(RO^2)$
μ = fluid absolute viscosity
ν = kinematic viscosity
ν' = specific volume of vapor
ν_f' = specific volume of saturated liquid
ν_g' = specific volume of saturated vapor
ρ = fluid density
ρ_g = density of saturated vapor
$\bar{\tau}$ = mean shear stress

Subscripts

A = adiabatic section
C = condenser section
e = entrance of evaporator section
E = evaporator section
I = inner wall
i = initial step
O = outer wall
m = mixed-mean
w = at the wall
z = at any z location

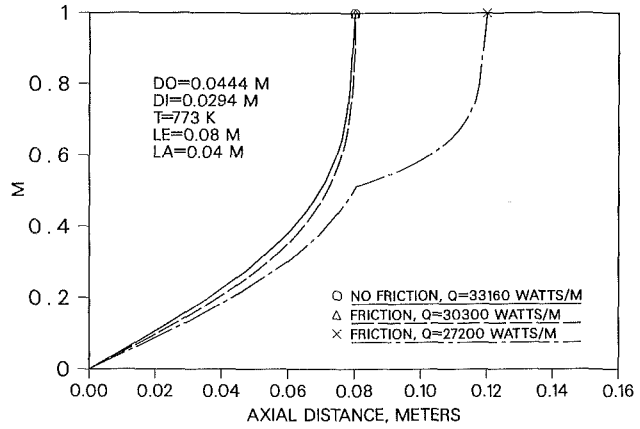

Fig. 2 Mach number variation along the concentric annular heat pipe under symmetric heating at the occurrence of the sonic limit

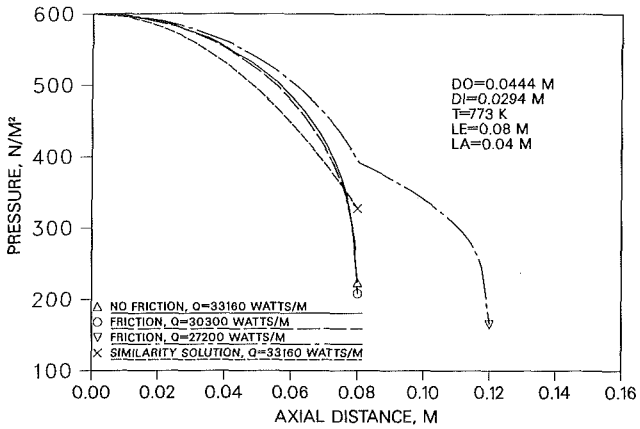

Fig. 3 Pressure variation along the concentric annular heat pipe under symmetric heating at the occurrence of the sonic limit

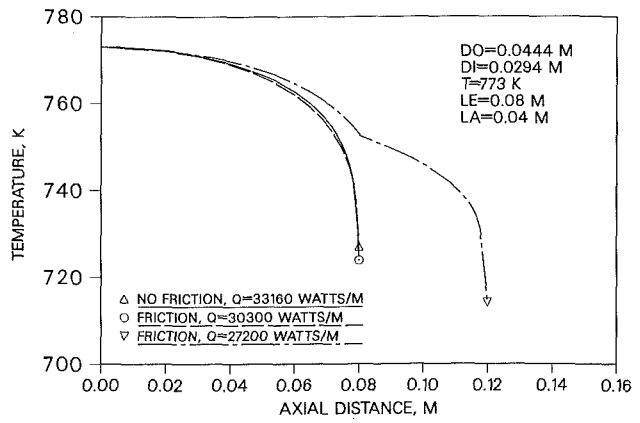

Fig. 4 Temperature variation along the concentric annular heat pipe under symmetric heating at the occurrence of the sonic limit

adiabatic section, (2) including the effect of friction and no adiabatic section, (3) including the effect of friction and having an adiabatic section. Figures 2–4 are graphs of the axial variation of the Mach number M, the static pressure P, and the temperature T, respectively, along the concentric annular heat pipe under a symmetric heating load when the sonic limit occurs. The infinite downstream gradients of M, P, and T are another indication of the gas dynamics choking phenomenon predicted by the above analysis. When considering the effect of friction, the value of the critical sonic heat rate Q_s = 15,150 W/m is smaller than the case neglecting friction (Q_s = 16,580 W/m) by about 10 percent for this particular heat pipe and operating conditions. If there is an adiabatic section, the result will become even smaller (Q_s = 13600 W/m) and the sonic limit will occur at the exit of the adiabatic section.

Using the simple perfect gas model, the following equation can be obtained for the sonic limit heat flux calculation for the annular heat pipe:

$$Q_s = \frac{\rho\sqrt{K'RT}\, h_{fg} \frac{\pi}{4}(DO^2 - DI^2)}{\sqrt{2(K+1)}} \tag{14}$$

where equation (14) is reduced to the equation given by Levy (1968) for $DI = 0$. The above equation underpredicts the actual numerical result presented in Figs. 2–4 for the case, which includes the effect of friction by 1/2 percent for the given operating conditions. Similar agreements were observed under asymmetric heating loads ($Q_{I,E} = 1/3\ Q_{O,E}$) with the same total heat load.

Incompressible Flow: Two-Dimensional Analysis

The physical problem under consideration is a right circular cylindrical annular cavity as shown in Fig. 1. It is assumed that the vapor flow in all the segments of the concentric annular heat pipe—evaporator, adiabatic, and condenser sections—is operating under laminar, incompressible, steady conditions and the properties of the fluid are constant. The uniform radial inflow and outflow boundary conditions are modeling evaporation and condensation. Since the annulus is closed at both ends, it is required that the fluid that enters into the evaporator segment flow out through the condenser section. The differential equations associated with this axisymmetric problem are the continuity and the momentum equations as given below in cylindrical coordinates

$$\frac{\partial}{\partial z}(\rho w) + \frac{1}{r}\frac{\partial}{\partial r}(\rho r v) = 0 \tag{15}$$

$$w\frac{\partial}{\partial z}(\rho w) + v\frac{\partial}{\partial r}(\rho w) = -\frac{\partial P}{\partial z} + \mu\left[\left\{\frac{\partial^2 w}{\partial z^2}\right\} + \frac{1}{r}\frac{\partial w}{\partial r} + \frac{\partial^2 w}{\partial r^2}\right] \tag{16}$$

$$w\frac{\partial}{\partial z}(\rho v) + v\frac{\partial}{\partial r}(\rho v) = -\frac{\partial P}{\partial r} + \mu\left[\left\{\frac{\partial^2 v}{\partial z^2}\right\} + \frac{1}{r}\frac{\partial v}{\partial r} + \frac{\partial^2 v}{\partial r^2}\right] \tag{17}$$

It should be noted that in equations (16) and (17) the terms in braces are associated with axial diffusion terms. These terms are neglected when the parabolic version is considered but are accounted for in the elliptic case.

The boundary conditions are defined as follows:

$$\begin{aligned} w(0, r) &= v(0, r) = 0 \\ w(LT, r) &= v(LT, r) = 0 \\ w(z, RI) &= w(z, RO) = 0 \\ v(z, RI) &= V_{I,w}(z) \\ v(z, RO) &= V_{O,w}(z) \\ P\left(0, \frac{RI+RO}{2}\right) &= 0 \end{aligned} \tag{18}$$

The radial blowing and suction velocities at the inner and outer walls are taken to be uniform over the heating or cooling sections and are related to the local heat rate per unit length by the following relations:

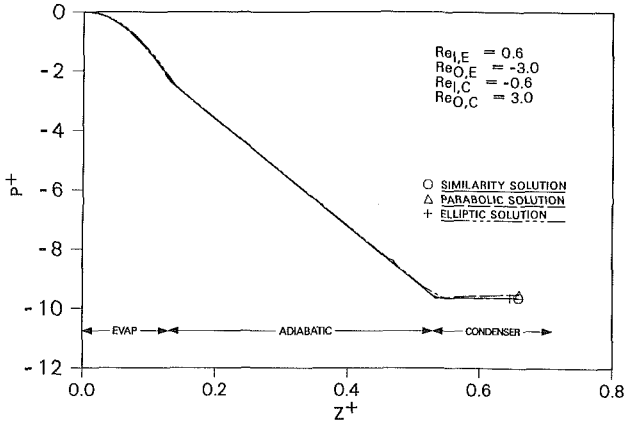

Fig. 5 Comparison of elliptic, parabolic, and similarity analyses of the normalized pressure distribution along the concentric annular heat pipe for K = 0.2 and low radial Reynolds numbers

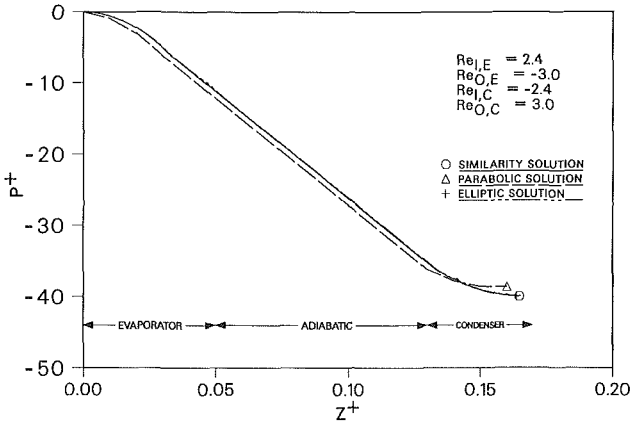

Fig. 6 Comparison of the elliptic, parabolic, and similarity analyses of the normalized pressure distribution along the concentric annular heat pipe for K = 0.8 for moderate radial Reynolds numbers

$$V_{O,E} = \frac{Q_{O,E}}{\pi DO\rho h_{fg}}$$

$$V_{I,E} = \frac{Q_{I,E}}{\pi DI\rho h_{fg}}$$

$$V_{O,C} = \frac{Q_{O,C}}{\pi DO\rho h_{fg}}$$

$$V_{I,C} = \frac{Q_{I,C}}{\pi DI\rho h_{fg}}$$

The parabolic and elliptic presentations of the governing equations of fluid motion for steady two-dimensional laminar flow in a concentric annular heat pipe with various distributions of heating and cooling loads have been analyzed numerically. The results show that the flow reverses in long condenser segments or at very high condensation rates and the parabolic presentation provides a sufficiently accurate picture of the vapor pressure variations at both low and high evaporation and condensation rates.

In order to investigate the accuracy and reliability of the numerical results obtained from the boundary layer analysis (Faghri, 1986) with those obtained by the elliptic presentation of the governing equations, a comparison was made for two radius ratio K values. Faghri (1986) employed the boundary layer approximation and analyzed the vapor flow in the evaporator and condenser sections independently. The elliptic analysis is accomplished by solving the vapor flow in the concentric annular heat pipe as one domain all along the heat pipe. The grid spacing in the present work was systematically varied and the results for different grid sizes were compared to the extrapolated results of an infinitesimal grid spacing. A mesh with 40 cells in the radial direction and 80 cells in the axial direction was used for all the results reported in this paper.

Figure 5 presents the normalized pressure distribution P^+ along the heat pipe for the case with K = 0.2. The evaporator radial Reynolds numbers at the inner and outer walls are 0.6 and −3.0, respectively. The condenser radial Reynolds number at the inner wall is −0.6, while the radial Reynolds number at the outer wall is 3.0. The pressure drop results obtained from using the elliptic version of the governing equations are within 1 percent of those obtained by the boundary layer approximation.

Figure 6 presents the normalized pressure distribution P^+ for the case with K = 0.8 and the radial Reynolds numbers at the inner wall in both the evaporator and condenser sections equal to 2.4. The radial Reynolds number at the outer wall in both the evaporator and condenser is set at 3.0. This case shows a deviation of 7 percent between the elliptic and parabolic presentations of the governing equations.

Figure 7 presents the normalized pressure variation for the case with K = 0.65 and the evaporator and condenser radial Reynolds numbers of 1000 for both walls. The flow reversed for this particular case in the condenser section due to the very high condenser radial Reynolds numbers.

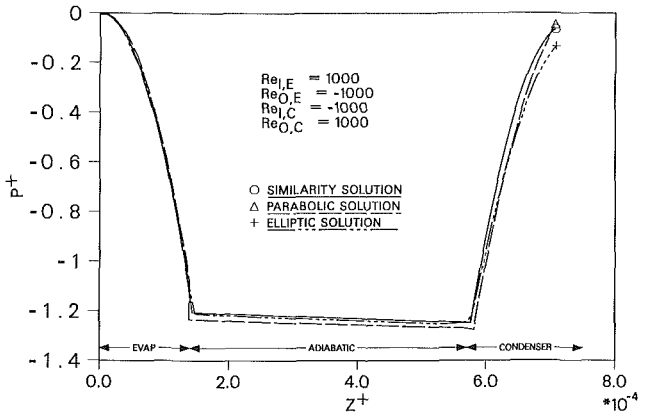

Fig. 7 Comparison of the elliptic, parabolic, and similarity analyses of the normalized pressure distribution along the concentric annular heat pipe for K = 0.65 and high radial Reynolds numbers

Incompressible Flow: Similarity Analysis

From the study by Faghri and Parvani (1988), one can generalize that the vapor flow in an annular heat pipe becomes fully developed in a very short distance from the evaporator end cap and this similar profile repeats itself in the adiabatic and condenser sections for low as well as moderate radial Reynolds numbers. This entry distance is not of significance in many practical applications. The criterion for a fully developed flow is that the normalized axial velocity $W^+ = w/w_{z,m}$ is invariant along the pipe. One very interesting feature of the numerical results given by Faghri and Parvani (1988) was that W^+ was similar for various radial Reynolds numbers including the case with zero inner and outer radial Reynolds numbers. The fully developed normalized velocity profile for annular flow for zero blowing velocity can be easily obtained analytically

$$W^+ = \frac{w}{w_{z,m}} = \frac{w^*}{w^*_{z,m}} = \frac{2\left[1 - R^{+2} + \left\{\frac{1-K^2}{\ln 1/K}\right\}\ln(R^+)\right]}{\left[\frac{1-K^4}{1-K^2} - \frac{1-K^2}{\ln 1/K}\right]} \quad (19)$$

The dimensionless local mean axial velocity $w^*_{z,m}$ can be obtained by making a mass balance in the evaporator section of the heat pipe

$$w^*_{z,m} = \frac{2(\mathrm{Re}_{I,E} + |\mathrm{Re}_{O,E}|)z^*}{1-K^2} \tag{20}$$

According to the numerical results, equation (19) also approximately presents the normalized velocity W^+ for all radial Reynolds numbers and K values in the fully developed region.

Assuming that the fluid is incompressible, the normal radial velocity along the length of the pipe walls is constant, and the pressure along the radius of the pipe is constant, the system of equations in dimensionless form describing the vapor flow is reduced to the following form:

$$w^* \frac{\partial w^*}{\partial z^*} + v^* \frac{\partial w^*}{\partial R^+} = -\frac{\partial P^+}{\partial z^*} + \frac{1}{R^+}\frac{\partial}{\partial R^+}\left(R^+ \frac{\partial w^*}{\partial R^+}\right) \tag{21}$$

$$R^+ \frac{\partial w^*}{\partial z^*} + \frac{\partial (v^* R^+)}{\partial R^+} = 0 \tag{22}$$

The boundary conditions appropriate for the evaporator section are as follows:

$$\begin{aligned} v^*(R^+, 0) &= w^*(R^+, 0) = 0 \\ w^*(K, z^*) &= w^*(1, z^*) = 0 \\ v^*(K, z^*) &= \frac{RO\ V_{I,E}}{\nu} = \frac{\mathrm{Re}_{I,E}}{K} \\ v^*(1, z^*) &= \frac{RO\ V_{O,E}}{\nu} = \mathrm{Re}_{O,E} \end{aligned} \tag{23}$$

The system of equations of (21) and (22) is reduced to the following equation by elimination of the radial velocity in the evaporation section:

$$w^* \frac{\partial w^*}{\partial z^*} + \left[\frac{\mathrm{Re}_{I,E}}{R^+} - \frac{1}{R^+}\int_K^{R^+} R^+ \frac{\partial w^*}{\partial z^*} dR^+\right]\frac{\partial w^*}{\partial R^+} = -\frac{\partial P^+}{\partial z^*} + \frac{1}{R^+}\frac{\partial}{\partial R^+}\left(R^+ \frac{\partial w^*}{\partial R^+}\right) \tag{24}$$

The pressure drop is obtained by substituting expression (19) into the following integral equation:

$$\int_K^1 w^* \frac{\partial w^*}{\partial z^*} R^+ dR^+ - \int_K^1 \left[\frac{\partial w^*}{\partial R^+}\int_K^{R^+}\left(R^+ \frac{\partial w^*}{\partial z^*}\right) dR^+\right] dR^+ = -\frac{\partial P^+}{\partial z^*}\left(\frac{1}{2} - \frac{K^2}{2}\right) + \left(R^+ \frac{\partial w^*}{\partial R^+}\right)\Bigg|_K^1 \tag{25}$$

The pressure drop along the evaporator section of the concentric annular heat pipe is calculated using the following expression:

$$P_E^+ = \frac{2}{K^2-1}\left[Cz^{*2}(1-K^2) + \frac{C^2 z^{*2}}{2}\left\{\frac{1}{3} - \frac{3}{4}A' + \frac{A'^2}{2} - K^2 + K^4 - 2A'K^2 \ln K + A'K^2 - \frac{K^6}{3} + A'K^4 \ln K - \frac{A'K^4}{4} - A'^2K^2(\ln K)^2 + A'^2K^2 \ln K - \frac{A'^2K^2}{2}\right\}\right] \tag{26}$$

A similar analysis can be made for the pressure drop in the condenser section by using the appropriate form for $w^*_{z,m}$ in equation (19). The following expression for $w^*_{z,m}$ is obtained by a mass balance in the condenser zone:

$$w^*_{z,m} = 1 - \frac{2(|\mathrm{Re}_{I,C}| + \mathrm{Re}_{O,C})z^*}{(1-K^2)} \tag{27}$$

The pressure drop in the condenser segment using the parabolic profile is given by

$$P_C^+ = 4[(K^2 - 1 + C' \cdot E)/(K^2-1)][(C'z^{*2}/2) - D'z^*] \tag{28}$$

where E is

$$E = \left\{\frac{1}{6} - \frac{3A'}{8} + \frac{A'^2}{4} - \frac{K^2}{2} + \frac{K^4}{2} - \frac{K^6}{6} - A'K^2 \ln K + \frac{A'K^2}{2} + \frac{(A'K^4 \ln K)}{2} - \frac{A'K^4}{8} - \frac{A'^2K^2(\ln K)^2}{2} + \frac{A'^2K^2 \ln K}{2} - \frac{A'^2K^2}{4}\right\} \tag{29}$$

It should be noted that equation (28) can be used to predict the pressure loss in the adiabatic segment by assuming $\mathrm{Re}_{I,C} = \mathrm{Re}_{O,C} = 0$

$$P_A^+ = -4D'z^* \tag{30}$$

Figures 3, 5, 6, and 7 also demonstrate the normalized pressure distribution using the similarity analysis. The excellent agreement between the similarity analysis and the solution of the elliptic version of the governing equations indicates that the axial velocity profile becomes fully developed in a short distance and stays parabolic all along the length of the heat pipe for both cases. The flow did not reverse for the first two cases because the condenser zone is short and the radial Reynolds numbers are small. There is a region where the flow reverses in the condenser for case 3 because the radial Reynolds numbers are high (Faghri and Parvani, 1988). This demonstrates that the similarity results surprisingly predict the pressure variation when the flow reverses as well. Furthermore, when $K = \mathrm{Re}_{I,E} = \mathrm{Re}_{I,C} = 0$, the above equations reduce to the following forms for conventional heat pipes:

$$P_E^+ = -8|\mathrm{Re}_{O,E}|\, z^{*2} - \frac{16}{3}\mathrm{Re}_{O,E}^2 z^{*2} \tag{31}$$

$$P_A^+ = -8z^* \tag{32}$$

$$P_C^+ = 8\left(1 - \frac{2}{3}|\mathrm{Re}_{O,C}|\right)(|\mathrm{Re}_{O,C}|z^{*2} - z^*) \tag{33}$$

The above equations are in agreement with similar relations developed for conventional heat pipes (Busse, 1968).

Conclusions

The results of the investigation warrant the following conclusions:

1 Equation (14) can be used to predict the sonic limit for the concentric annular heat pipe under symmetric and asymmetric heating loads.

2 Accurate estimates of the pressure loss in the evaporator section for compressible and incompressible vapor flows may be made by using equation (26).

3 An accurate prediction of the pressure loss can be made all along the concentric annular heat pipe by using the parabolic version of the equations of motion and solving for the pressure drops in the different segments of the heat pipe independently of each other. This can be done by assuming that the inlet axial velocity in the evaporator zone is zero and the axial velocity has a parabolic inlet profile for the adiabatic and condenser sections.

4 The hydrodynamic entry lengths for the evaporator, adiabatic, and condenser sections are very short and can be neglected in many practical applications. This justifies the usage of a similarity velocity profile along the length of the concentric annuluar heat pipe.

5 Accurate estimates of the pressure losses may be made by using equations (26), (28), and (30) for the evaporator, condenser, and adiabatic segments of the concentric annular heat pipe.

Acknowledgments

Funding for this work was provided by the Thermal Energy Group of the Aero Propulsion Laboratory of the U.S. Air Force under contract No. F-33615-81-C-2012. The author is indebted to Dr. E. T. Mahefkey and Dr. J. E. Beam for their technical assistance during this project.

References

Bankston, C. A., and Smith, H. J., 1973, "Vapor Flow in Cylindrical Heat Pipes," ASME JOURNAL OF HEAT TRANSFER, Vol. 95, pp. 371–376.

Busse, C. A., and Prenger, F. C., 1984, "Numerical Analysis of the Vapor Flow in Cylindrical Heat Pipes," in: *Research Development of Heat Pipe Technology*, Vol. I, pp. 214–219.

Busse, C. A., 1968, "Pressure Drop in the Vapor Phase of Long Heat Pipes," presented at the Thermionic Conversion Specialists Conference, Palo Alto, CA.

Deverall, J. E., Kemme, J. E., and Florschuetz, L. W., 1970, "Sonic Limitations and Start-Up Problems of Heat Pipes," Los Alamos Scientific Laboratory Rept. No. LA-4578.

Faghri, A., 1986, "Vapor Flow Analysis in a Double-Walled Concentric Heat Pipe," *Numerical Heat Transfer*, Vol. 10, No. 6, pp. 583–595.

Faghri, A., and Parvani, S., 1988, "Numerical Analysis of Laminar Flow in a Double-Walled Annular Heat Pipe," *Journal of Thermophysics and Heat Transfer*, Vol. 2, No. 2, pp. 165–171.

Kays, W. M., and Crawford, M., 1980, *Convective Heat and Mass Transfer*, McGraw-Hill, New York.

Kemme, J. E., 1969, "Ultimate Heat Pipe Performance," *IEEE Transaction on Electronic Devices*, Vol. ED-16, pp. 717–723.

Levy, E. K., 1968, "Theoretical Investigation of Heat Pipes Operating at Low Vapor Pressure," ASME *Journal of Engineering for Industry*, Vol. 90, No. 4, pp. 547–552.

Levy, E. K., 1971, "Effect of Friction on the Sonic Velocity Limit of Sodium Heat Pipes," presented at the AIAA 6th Thermophysics Conference, Tullhomer, TN.

Tien, C. L., and Rohani, A. R., 1974, "Analysis of the Effects of Vapor Pressure Drop on Heat Pipe Performance," *Int. Journal of Heat and Mass Transfer*, Vol. 17, pp. 61–67.

Vargaftik, N. B., 1975, *Handbook of Physical Properties of Liquids and Gases*, Hemisphere Publishing Corporation, Washington, DC.

Yuan, S. W., and Findelstein, A. B., 1955, "Laminar Flow With Injection and Suction Through a Porous Wall," *Proceedings of the Heat Transfer and Fluid Mechanics Institute*, Los Angeles, CA.

Proposed Method for Measuring Local Heat Transfer Coefficients of Isothermal Surfaces

T. Kumada
Department of Nuclear Engineering,
Faculty of Engineering,
Hokkaido University,
Sapporo 060, Japan

A method has been proposed for measuring local heat transfer coefficients. The method uses the change of a wet surface temperature by radiation heating and can be applied to isothermal conditions and with large variations of the local heat transfer coefficients along the surface of a body. The present method is based on the heat balance equation, which expresses a simple relationship between humidity and wet-bulb temperatures. An experiment was devised to measure the local heat transfer coefficient along a flat plate. The results confirmed the effectiveness of the present method to measure local and overall heat and mass transfer coefficients with reasonable accuracy.

Introduction

It is generally difficult to measure local heat and mass transfer coefficients accurately for isothermal conditions, particularly when there is a large variation along a surface. This problem is further complicated if the surface is curved or has a complex geometry.

For the condition of constant heat flux along surfaces, a method for measuring the local heat transfer coefficient along a plate has been used by Ota and Kon (1974). In this method, a thin foil of metal is attached to the plate and heated electrically. The heat transfer coefficient is calculated by dividing the net convection heat transfer rate by the temperature difference between the wall and the main stream. For a gas stream, convective heat transfer usually prevails under the nearly isothermal condition of the wall. For this case, complex equipment and procedures are needed to measure the local heat transfer coefficient with reasonable accuracy.

In a previous paper (Kumada et al., 1986), it was clarified that the heat and mass transfer coefficients over the surface can be determined with reasonable accuracy using the mean evaporation rate of water from a flat wet plate and the difference between the mean surface temperature over the plate and the wet-bulb temperature. This method can be applied in order to determine the local coefficients of heat and mass transfer, if the local evaporation rate can be exactly measured. Since it is generally difficult to measure the local evaporation rate, this method cannot be applied directly to measure heat and mass transfer coefficients.

The present method was developed to measure conveniently and easily local heat and mass transfer coefficients by measuring the radiation heat flux and the variation of the temperature of a wetted surface. In this method, the surface of a body is covered with a thin, smooth, silk cloth and wet with liquid, e.g., water or methanol. The body is set in an air stream and its surface temperature is measured by traversing a thin sheathed thermocouple beneath the wet cloth covering the surface of the body after it reaches steady state close to the wet-bulb temperature. Then, the surface temperature is measured again after it receives radiant heat flux from halogen lamps and reaches a new steady state. The local heat and mass transfer coefficients are then calculated from heat and mass balance equations. The present paper describes a theory that derives the local heat and mass transfer coefficients from the measured temperature as well as an experiment for measuring the local heat and mass transfer coefficients of a flat plate.

Contributed by the Heat Transfer Division for publication in the JOURNAL OF HEAT TRANSFER. Manuscript received by the Heat Transfer Division September 29, 1987. Keywords: Evaporation, Forced Convection, Measurement Techniques.

Principle of Measurement

Heat Transfer Coefficient. When fluid flows over a phase boundary, the fluid in immediate contact with the fixed surface can properly be said to be stagnant. The fact that resistances to heat and mass transfer are confined largely to a region quite close to the phase boundary suggests the idea of a thin stagnant film adjacent to a surface. If this thin layer is stagnant, the transport must be by molecular diffusion. The picture then is that of a stagnant film through which transport is solely by molecular diffusion. For the case of a low evaporation rate, this stagnant film model can be applied to the present measurement. The temperature of a free surface of a liquid or a surface covered with the smooth cloth wetted with water or methanol in a steady-state condition is determined to make a balance between the heat input to the surface and the heat flux brought about by vapor diffusion. The convective heat flux q_c is expressed by the stagnant film model for the case of small blowing factor c_w by evaporation, as described by Sherwood et al. (1975),

$$q_c = h_H (T_\infty - T_w) \frac{c_w}{e^{c_w} - 1} \tag{1}$$

where $c_w = \dot{m} c_{pv} \delta_H / \lambda = \dot{m} c_{pv} / h_H$ (Bedingfield and Drew, 1950) and $c_w/(e^{c_w}-1)$ appearing in equation (1) is often called the Ackermann correction for mass transfer. The evaporation rate, $\dot{m}$ is expressed by vapor diffusion in the stagnant film

$$\dot{m} = \beta_w h_D \left(\frac{PM_v}{RT_f}\right) \ln \left(\frac{1 - Y_\infty}{1 - Y_w}\right) \tag{2}$$

where β_w is a correction factor by Bedingfield and Drew (1950), approximately expressed as follows:

$$\beta_w = 1 - \frac{1}{2}\left(\frac{M_v - M_g}{\bar{M}} - \frac{1}{1 - Y_w}\right)(Y_w - Y_\infty) \tag{3}$$

and $\bar{M}$ is average molecular weight. If the blowing factor is not small enough to neglect, then it can be easily calculated by substituting equation (2) into $c_w = \dot{m} c_{pv}/h_H$ and using the analogy between heat and mass transfer such as Colburn's relationship for turbulent flow (Kumada, 1985, p. 238). The temperature of an evaporating surface is usually lower than that of the surroundings, and the surface receives radiative heat transfer from the surroundings and conductive heat transfer from its bottom and side walls. The vaporation rate $\dot{m}$ occurs by the total heat input q_t into the wet surface, which is expressed as follows:

$$q_t = q_c + q_s = \dot{m} L_w \tag{4}$$

where q_s is the radiative and conductive heat input from the surroundings, except for convective heat and additional

radiative heat flux q_r into the evaporation surface. To obtain the relation between heat and mass transfer, equation (4) is transformed by substituting equations (1) and (2) as follows:

$$Ch_H(T_\infty - T_w)\frac{c_w}{e^{c_w}-1} = L_w\beta_w h_D\left(\frac{PM_v}{RT_f}\right)\ln\left(\frac{1-Y_\infty}{1-Y_w}\right) \tag{5}$$

where

$$C = 1 + [q_s/h_H(T_\infty - T_w)](e^{c_w}-1)/c_w \tag{6}$$

When $q_s = 0$, then $C = 1$, and equation (5) reduces to the following:

$$h_H(T_\infty - T_{wB})\frac{c_{wB}}{e^{c_{wB}}-1} = L_{wB}\beta_{wB}h_D\left(\frac{PM_v}{RT_f}\right)\ln\left(\frac{1-Y_\infty}{1-Y_{wB}}\right) \tag{7}$$

The temperature T_f in equations (5) and (7) is defined as a film temperature. The difference between T_w and T_{wB} is small; therefore, T_f in these equations is taken to be the same. The unknown parameter C is determined by taking the ratio of equations (5) and (7)

$$C = [1 + 0.5(c_w - c_{wB})]\left(\frac{L_w}{L_{wB}}\right)\left(\frac{\beta_w}{\beta_{wB}}\right)\left(\frac{T_\infty - T_{wB}}{T_\infty - T_w}\right) \times \ln\left(\frac{1-Y_\infty}{1-Y_w}\right)\Big/\ln\left(\frac{1-Y_\infty}{1-Y_{wB}}\right) \tag{8}$$

where $c \ll 1$ and $c/(e^c - 1)$ is approximated to be $1 - 0.5c$. The differences in L_w, L_{wB}, and β_w, β_{wB} are small and equal, respectively, and $0.5\,(c_w - c_{wB})$ can be neglected. Equation (8) is reduced to the following simple form:

$$C = \left(\frac{T_\infty - T_{wB}}{T_\infty - T_w}\right)\left(\frac{Y_w - Y_\infty}{Y_{wB} - Y_\infty}\right) \tag{9}$$

If this wet surface receives an additional radiation flux q_r, the equation corresponding to equation (8) can be obtained as follows:

$$C' = [1 + 0.5(c'_w - c_{wB})]\left(\frac{L'_w}{L_{wB}}\right)\left(\frac{\beta'_w}{\beta_{wB}}\right)\left(\frac{T_\infty - T_{wB}}{T_\infty - T'_w}\right) \times \ln\left(\frac{1-Y_\infty}{1-Y'_w}\right)\Big/\ln\left(\frac{1-Y_\infty}{1-Y_w}\right) \tag{10}$$

where

$$C' = 1 + (q'_s + q_r)/\{h_H \cdot (T_\infty - T'_w)c'_w/(e^{c'_w} - 1)\} \tag{11}$$

q'_s is not equal to q_s because the surface temperature increases from T_w to T'_w with q_r. q'_s and q_s are expressed as the summation of radiative and conductive heat inputs from the surroundings

$$q'_s = q'_{r\infty} + q'_{\text{con}} \tag{12}$$

$$q_s = q_{r\infty} + q_{\text{con}} \tag{13}$$

where $q'_{r\infty}$, $q_{r\infty}$ are the net radiative heats and q'_{con}, q_{con} are the conductive heats to the wet surface coming from the surroundings with and without q_r, respectively. $q_{r\infty}$ can be expressed as

$$q_{r\infty} = \sigma\epsilon_w(T_\infty^4 - T_w^4) \tag{14}$$

where ϵ_w is the emissivity of the wet surface and σ is the Boltzmann constant. When T_∞, $T_w >> T_\infty - T_w$, $q_{r\infty}$ can be approximated to be

$$q_{r\infty} = 4\sigma\epsilon_w T_\infty^3(T_\infty - T_w) \tag{15}$$

$q'_{r\infty}$ is similarly expressed as

$$q'_{r\infty} = 4\sigma\epsilon_w T_\infty^3(T_\infty - T'_w) \tag{16}$$

The conductive heats q_{con}, q'_{con} to the wet surface through the test body are also nearly proportional to the temperature difference $T_\infty - T_w$ and $T_\infty - T'_w$, respectively. Then, the following equation can be easily obtained:

$$q'_s = q_s\frac{T_\infty - T'_w}{T_\infty - T_w} \tag{17}$$

If q'_s and q_s are cancelled from equations (6) and (11), then h_H can be expressed as

Nomenclature

a = thermal diffusivity, m^2/h
A, B = constants defined by equation (35)
c = blowing factor
c_p = specific heat, kW·s/kgK
C = correction factor defined by equation (6)
l = length of a plate, m
h_H = local heat transfer coefficient at $\dot{m} \to 0$, $kW/m^2 \cdot K$
h_D = local mass transfer coefficient at $\dot{m} \to 0$, m/s
H = half-thickness of a plate, m
L = latent heat, kW·s/kg
$\dot{m}$ = evaporation rate, $kg/(m^2 \cdot s)$
M = molecular weight, kg
P = total pressure, kg/m
q_c = convection heat flux into a wet surface, kW/m^2
q_r = radiation heat flux into a wet surface, kW/m^2
q_s = erroneous heat input on a wet surface, kW/m^2
q_t = total heat input on a wet surface, kW/m^2
R = universal gas constant, kW·s/kg·K
s = height of step, m
T = temperature, K
u = velocity along a surface, m/s
x = distance from the leading edge of evaporation surface, m
y = distance in direction perpendicular to a surface, m
Y = mole fraction of vapor
β = correction factor of Bedingfield and Drew (1950)
δ_H = thickness of thermal conduction at $\dot{m} \to 0$, m
λ = thermal conductivity, kW/(m·K)
ν = dynamic viscosity, m^2/s

Subscripts and Superscripts

e = measured value
f = film temperature
g = noncondensing gas
t = true value
v = vapor
w = for the case of $q_s \neq 0$
wB = for the case of $q_s = 0$
∞ = mainstream
$'$ = with radiation heating
$*$ = with blowing
$-$ = mean value

Dimensionless quantities

Le = Lewis number = a/D
Nu = Nusselt number = $h_H l/\lambda$
Nu_x = Nusselt number = $h_H x/\lambda$
Pr = Prandtl number = ν/a
Re = Reynolds number = ul/ν
Re_H = Reynolds number = uH/ν
Re_x = Reynolds number = ux/ν
Sh = Sherwood number = $h_D l/D$
Sh_x = Sherwood number = $h_D x/D$

$$h_H = q_r/\{(T_\infty - T'_w) \times (C'-1)(1-0.5c'_w) - (T_\infty - T_w)(C-1)(1-0.5c_w)\} \quad (18)$$

where $c/(e^c-1)$ is approximated to be $1-0.5c$. If the radiation heat flux q_r is small enough and the evaporation rate $\dot{m}$ is also small, the blowing factors c_w and c'_w can be neglected as compared to unity, and h_H can be expressed approximately as follows:

$$h_H = \frac{q_r}{(T_\infty - T'_w)(C'-1) - (T_\infty - T_w)(C-1)} \quad (19)$$

From equation (1) the heat transfer coefficients with the blowing of c_w can be expressed as

$$h^*_H = h_H \frac{c'_w}{e^{c'_w}-1} \quad (20)$$

Mass Transfer Coefficient. The evaporation rates $\dot{m}$ and $\dot{m}'$ can be expressed using the heat transfer coefficient h_H, respectively,

$$\dot{m} = \frac{C h_H (T_\infty - T_w) c_w}{L_w (e^{c_w}-1)} \quad (21)$$

$$\dot{m}' = \frac{C' h_H (T_\infty - T'_w) c'_w}{L'_w (e^{c'_w}-1)} \quad (22)$$

Combining equations (21) and (22), h_H can be eliminated as follows:

$$\dot{m}' = \dot{m}\left(\frac{C'}{C}\right)\left(\frac{T_\infty - T'_w}{T_\infty - T_w}\right)\left(\frac{c'_w}{c_w}\right)\left(\frac{e^{c_w}-1}{e^{c'_w}-1}\right) \quad (23)$$

where $L_w = L'_w$, because the difference between T_w and T'_w is small. The difference $\Delta q_s = q_s - q'_s$ can be expressed using equations (1), (4), (17), and (21) as follows:

$$\Delta q_s = \left(\frac{C-1}{C}\right)\dot{m} L_w \left(\frac{T'_w - T_w}{T_\infty - T_w}\right) \quad (24)$$

The difference of convective heat $\Delta q_c = q_c - q'_c$ $(= \dot{m}L_w/C - \dot{m}L_w/C')$ is expressed by combining equations (21) and (22) to yield the following equation:

$$\Delta q_c = \frac{\dot{m} L_w}{C}\left\{1 - \left(\frac{T_\infty - T'_w}{T_\infty - T_w}\right)\left(\frac{c'_w}{c_w}\right)\left(\frac{e^{c_w}-1}{e^{c'_w}-1}\right)\right\}. \quad (25)$$

The mass fluxes $\dot{m}$ and $\dot{m}'$ are expressed as follows:

$$\dot{m} L_w = q_c + q_s \quad (26)$$

$$\dot{m}' L_w = q'_c + q'_s + q_r. \quad (27)$$

The relation among $\dot{m}$, $\dot{m}'$, and q_r is expressed by the difference between equations (26) and (27) as follows:

$$(\dot{m}' - \dot{m}) L_w = (q_r + q'_c + q'_s) - (q_c + q_s) = q_r - \Delta q_c - \Delta q_s \quad (28)$$

By substituting equations (23), (24), and (25) into equation (28) and arranging the equation, $\dot{m}$ is expressed as follows:

$$\dot{m} = (q_r/L_w)/\left\{\left(\frac{C'}{C}\right)\left(\frac{T_\infty - T'_w}{T_\infty - T_w}\right)\left(\frac{c'_w}{c_w}\right)\left(\frac{e^{c_w}-1}{e^{c'_w}-1}\right) - 1 + \frac{1}{C} - \frac{1}{C}\left(\frac{T_\infty - T'_w}{T_\infty - T_w}\right)\left(\frac{c'_w}{c_w}\right)\left(\frac{e^{c_w}-1}{e^{c'_w}-1}\right) + \left(\frac{C-1}{C}\right)\left(\frac{T'_w - T_w}{T_\infty - T_w}\right)\right\} \quad (29)$$

If the blowing parameters c_w and c'_w are small enough to neglect, equation (29) reduces to the following simple form:

$$\dot{m} = (q_r/L_w)/\left\{\left(\frac{C'-C}{C}\right)\left(\frac{T_\infty - T'_w}{T_\infty - T_w}\right)\right\} \quad (30)$$

The mass transfer coefficient h^*_D is generally expressed as follows:

$$h^*_D = \frac{\dot{m}}{Y_w - Y}\left(\frac{RT_f}{PM_v}\right) \quad (31)$$

where h^*_D is the mass transfer coefficient with blowing. The evaporation rate $\dot{m}$ is also expressed using the stagnant film model as follows:

$$\dot{m} = \beta_w h_D \left(\frac{PM_v}{RT_f}\right)\ln\left(\frac{1-Y_\infty}{1-Y_w}\right) \quad (32)$$

By substituting equation (32) into equation (31), the relation between h_D and h^*_D can be obtained

$$h_D = \frac{Y_{BM}}{\beta_w} h^*_D \quad (33)$$

where $Y_{BM} = (Y_w - Y_\infty)/\ln[(1-Y_\infty)/(1-Y_w)]$, and h^*_D is the mass transfer coefficient for the blowing parameter c_w and is determined by equation (31).

Error Evaluation

The quantities T_∞, $T_w(Y_w)$, $T'_w(Y'_w)$, Y_∞, and q_r must be measured precisely to determine the local heat and mass transfer coefficients h_H and h_D by equations (19) and (33). If Y_∞ is determined from the wet-bulb temperature, measurements of T_∞, T_w, T'_w, and q_r are necessary to determine the transfer coefficients h_H and h_D. If the true values of these quantities are denoted by adding a subscript t and the experimental errors δT_∞, δT_w, etc., then

$$T_\infty = T_{\infty t} + \delta T_\infty, \qquad T_{wB} = T_{wBt} + \delta T_{wB}$$
$$T_w = T_{wt} + \delta T_w, \qquad T'_w = T'_{wt} + \delta T'_w \quad (34)$$

For simplicity, the mole fraction Y of the vapor is expressed by

$$Y = A\exp\left(-\frac{B}{T}\right) \quad (35)$$

For water vapor/air the deviation between the vapor pressure table and the values predicted by equation (35) are within 0.3 percent if $A = 1.8333 \times 10^6$, $B = 5324$ in the range of room temperature, and $T_w = 283.15 \sim 303.15$ K. The blowing effect for water vapor/air can be neglected because the main purpose of the present discussion is to estimate the errors in h_H and h_D. By substituting equation (34) into equation (9) and approximating T_{wt} and δT_w to be T_{wBt} and $\delta T'_w$, respectively, the following relation between C and the measured temperatures can be obtained:

$$C = C_t\left[1 - \frac{\delta T_w - \delta T_\infty}{T_{\infty t} - T_{wt}} - \frac{(Y_{wB} - Y_{\infty t})(\delta T_{wB} - \delta T_\infty)}{(Y_{wt} - Y_{\infty t})(T_{\infty t} - T_{wt})} + \frac{B}{T^2_{wt}(Y_{wt} - Y_{\infty t})}(Y_{wt}\delta T_w - Y_{wB}\delta T_{wB})\right] \quad (36)$$

where

$$C_t = \{(T_{\infty t} - T_{wt})/(T_{\infty t} - T_{wBt})\} \times \{(Y_{wt} - Y_{\infty t})/(Y_{wBt} - Y_{\infty t})\} \quad (37)$$

Each term, including the temperatures in the brackets [ ], is as small as $\delta T/(T_{\infty t} - T_{wt})$ as compared with unity. We can measure each temperature to be within the error of 0.1 K; then each error of these terms is within 0.01. In this case the error in C is estimated to be within a few percent. δT_∞ is included in the second and third terms in the brackets [ ], but these terms cancel out, because the difference in Y_{wB} and Y_{wt} is small. The correction factors C and C' are contained in equations (19) and (30) for the forms of $C'-C$, C'/C; therefore it can be easily understood that the order of errors in h_H and h_D is the same order as in C and C'.

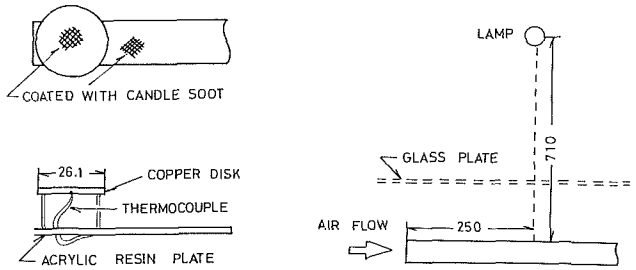

Fig. 1(a) Apparatus for measuring radiation flux; (b) experimental setup for measuring local heat transfer coefficient

In order to determine the heat transfer coefficient exactly, it is generally necessary to correct for the radiative heat exchange between the heated wall and the surroundings. In this method, this correction is unnecessary because the ratio of the total heat flux to the convective heat flux C can be calculated.

Experimental

There are two ways to heat a wet surface: one is to heat wires or meshes submerged in the wet surface electrically, and the other is to heat the wet surface with incident radiation. The advantage of the former is that it allows determination of heat flux based on the consumption of electricity, although it is still difficult to measure the temperature of the wet surface accurately. On the other hand, for radiation heating it is necessary to determine the radiant heat absorbed in the wet surface. In the present paper, the method of radiation heating was adapted to measure the transfer coefficients h_H and h_D.

Measurement of Heat Flux of Incident Radiation. Figure 1(*a*) shows the apparatus for measuring the radiation flux from the lamp to each position on the wet surface. Figure 1(*b*) shows the experimental setup for measuring the local heat transfer coefficient of a plate. The copper disk is set at the same level as the wet surface of a test plate in the duct and is heated by the heat flux of incident radiation through the glass plate. The received heat flux q_r on the wet surface is calculated from the rate of temperature rise of the disk and the assumption that the emissivities of the surfaces coated with soot of the copper disk and the wet surface are 0.96 and 0.93, respectively. The distribution of heat flux on the wet surface need not be kept uniform, but the surface should be heated so as to guarantee a more uniform temperature distribution.

Experimental Setup. The arrangement of the test section is shown in Fig. 2. The left side of the test section is connected to the exit of a wind tunnel. The test plate is placed in the center of the duct, which is made of acrylic resin, except for the glass plate in front of the halogen lamp. The radiation incident from the lamp goes through the glass plate and heats the wet surface of the test plate.

The uniformity of the mean velocity over the cross section of the duct, except for the region close to the walls, is within 3 percent. The test plate is made of acrylic resin sheets 0.5 and 2 mm in thickness, and its size is $20 \times 120 \times 370$ mm. The details of the test plate are shown in Fig. 2. The tungsten wire in the halogen bulb was heated to 2100 K. The light beam from the lamp contains the light wave band of absorption coefficient a_ν (cm^{-1}) < 10. The light beam passing through the wet surface causes a temperature gradient in the normal direction of the surface and an error in the temperature measurements. To prevent the light beam from passing through the wet surface, the surface of the plate is painted black and covered with two layers of thin smooth black silk cloth. The cloth is wetted by water from a container on the top of the plate by capillary forces. The heat conduction from the rear side of the water pan also causes a temperature gradient in the normal direction of the surface. Careful consideration of the plate design was made in order to maintain a good adiabatic condition of the rear side of the wet surface.

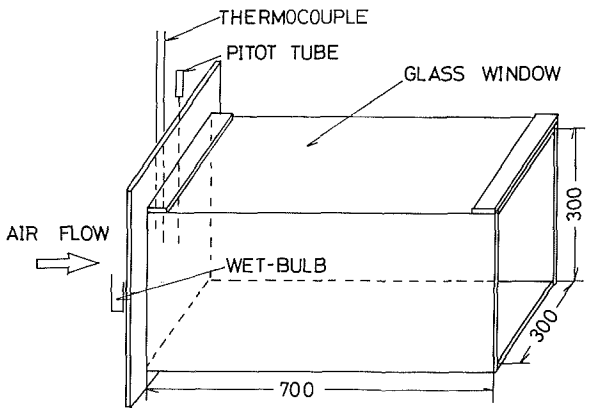

Fig. 2 Test section

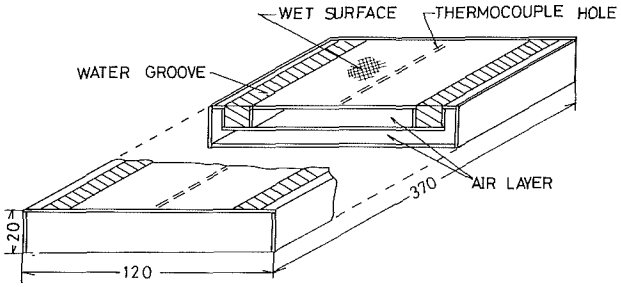

Fig. 3 Details of a evaporation test plate

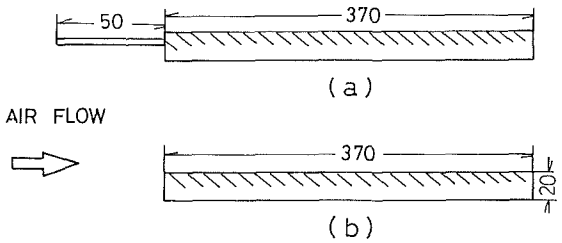

Fig. 4 Attachments installed in the front of a wet plate

Measurement of Surface Temperature. In order to measure the temperature of the wet surface, a thin groove was made on the rear side of an acrylic resin plate and covered with a sheet of acrylic resin plate 0.5 mm thick. The size of the groove was 1.0 mm wide and 0.5 mm high. A thermocouple sheathed by stainless steel (its outer diameter was 0.25 mm) was used to measure the distribution of surface temperature. To minimize the error of temperature measurements by conduction along the thermocouple sheath, the groove was oiled with machine oil to keep good thermal contact between the thermocouple and the wall of the groove. The temperature profiles along the groove were measured by moving the thermocouple in the goove.

Figure 4 shows two arrangements used to measure the local heat transfer coefficient. In this figure, the wetted surface is shown by oblique lines. Figure 4(*a*) shows an apparatus similar to that used by the Kumada et al. (1986) for measurements of mean heat transfer coefficients. Figure 4(*b*) shows an apparatus similar to that used by Ota and Kon (1974) for constant heat flux conditions.

In order to measure the transfer coefficients, the surface

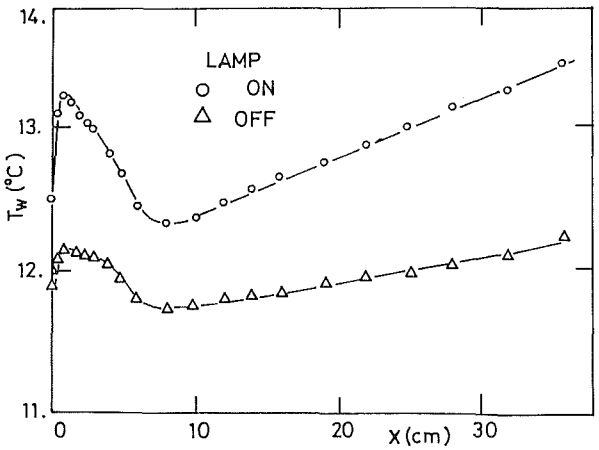

Fig. 5 Temperature distribution along the surface of a plate

cloth is wetted with distilled water and the side grooves of the water pan are filled with distilled water. During the measurements, the water level is kept constant by supplying distilled water from a water container. Thermal equilibrium was achieved 20 min after the halogen lamp switch was turned on. Then, the thermocouple was moved along the thin groove and the temperatures of each position was measured. As shown in Fig. 5, the points of measurement are dense in the region of large variations of transfer coefficients and widely spaced in the remaining region. The same measurements were repeated after the lamp switches were turned off and thermal equilibrium of the water pan was achieved once again.

Results

Heat Flux of Radiation q_r. The heat flux distribution of radiation q_r is maximum just under the lamp and 10 percent lower than the maximum value at the edge of the water pan. As the transfer coefficients h_H and h_D are determined based on conservation of heat and mass, and the value of q_r at each point along the wet surface of the plate, complete uniformity of q_r is not necessary. It is desirable to heat the surface strongly in the presence of large transfer coefficients to achieve nearly isothermal conditions along the plate.

Temperature Distribution Along the Wet Surface. Figure 5 shows the temperature distribution along the surface of the plate for the lamp turned on and off. The temperature variation along the surface when the lamp is on is caused mainly by the radiative heat flux. Since the surface is heated with a nearly constant radiative heat flux, the temperature of the surface is relatively low at positions where the transfer coefficients are high. The temperature when the lamp is off also varies along the surface, because the radiative heat exchange between the surroundings and the surface is almost constant along the surface. The difference of the surface temperature for the lamp turned on and off is almost inversely proportional to the transfer coefficients.

Corroboration of the Method. Kumada et al. (1985) and Kumada (1986) conducted experiments for the purpose of measuring the mean heat transfer coefficient from surfaces wetted with liquid into a heated turbulent air stream. In these experiments the mean heat transfer coefficient was determined by measuring the weight of liquid evaporation from the surfaces using the geometry of the liquid pan shown in Fig. 4(*a*). In this method the mean Nusselt number is expressed as

$$\overline{\mathrm{Nu}} = \frac{\dot{\bar{m}}_D L_w l}{\bar{C}\lambda(T_\infty - \bar{T}_w)} \frac{e^{\bar{c}_w} - 1}{\bar{c}_w} \tag{38}$$

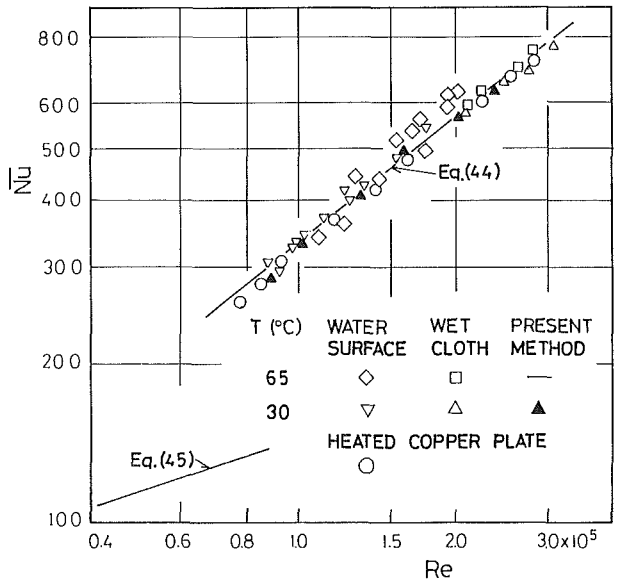

Fig. 6 Comparison among mean Nusselt numbers

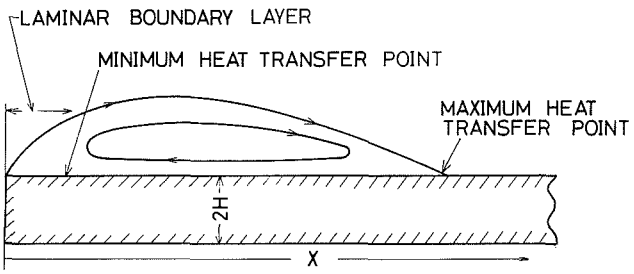

Fig. 7 Flow configuration and coordinate system

Based on the local values of $\dot{m}$, $T_\infty - T_w$, C, and c_w, the mean values of these parameters are approximately expressed as follows:

$$\dot{\bar{m}} = \frac{1}{l}\int_0^l \frac{Ch_H(T_\infty - T_w)c_w}{L_w(e^{c_w} - 1)}\,dx \tag{39}$$

$$T_\infty - \bar{T}_w = \frac{1}{l}\int_0^l (T_\infty - T_w)dx \tag{40}$$

$$\bar{C} = [1 + 0.5(\bar{c}_w - c_{wB})]\left(\frac{L_w}{L_{wB}}\right)\left(\frac{\beta_w}{\beta_{wB}}\right)\left(\frac{T_\infty - T_{wB}}{T_\infty - \bar{T}_w}\right) \tag{41}$$

$$\bar{c}_w = \dot{\bar{m}} c_{pv}\bar{\delta}_H/\lambda \tag{42}$$

where $\bar{\delta}_H = (1/l)\int_0^l(\lambda/h_H)dx$. The mean Nusselt number for the present method can be obtained by substituting mean values of $\dot{\bar{m}}$, $T_\infty - \bar{T}_w$, $\bar{C}$, and $\bar{c}_w$ into equation (38). Figure 6 shows a comparison between the mean Nusselt numbers calculated from equation (38) and the data of Kumada et al. (1968) by the weight method. The present mean Nusselt number is in excellent agreement with the values found by the weight method and the values predicted by equation (43)

$$\overline{\mathrm{Nu}} = 0.037\mathrm{Re}^{0.8}\mathrm{Pr}^{0.33} \tag{43}$$

This shows that it is possible to measure the local heat transfer coefficient accurately by the present method.

Local Heat Transfer Coefficient of Blunt Plate. Ota and Kon (1974) measured velocity profiles in the boundary layer along a blunt plate and gave the flow configuration shown in Fig. 7. The flow separates at the leading edge and reattaches on the plate surface and subsequently redevelops in the

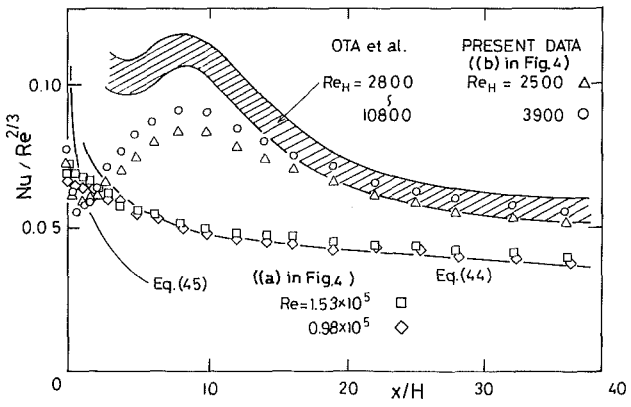

Fig. 8 Local heat transfer coefficients

downstream direction. They also measured local heat transfer coefficients along the blunt plate under the condition of constant heat flux by directly heating a thin metal film on the plate in the range of Reynolds number $Re = 2800 \sim 10{,}800$. The heat transfer coefficient is always maximum at $x/H = 8$ and this position is confirmed to be the reattachment point with the tuft. Distributions of heat transfer coefficient are shown by the upper cross-hatched band in the form of $Nu/Re^{2/3}$ for various Reynolds numbers in Fig. 8. The value of $Nu/Re^{2/3}$ is independent of the Reynolds number with some scatters and is a function of only the distance from the leading edge. To compare these results with the present method, the heat and mass transfer coefficients were measured using a plate similar to that measured by Ota and Kon (1974), as shown in Fig. 4(*b*). The theoretical Nusselt numbers for the plate with a sharp leading edge heated over its entire length are also shown in Fig. 8

$$\text{for turbulent flow} \quad Nu_x = 0.0296\ Pr\ Re_x^{0.8} \tag{44}$$

$$\text{for laminar flow} \quad Nu_x = 0.332\ Pr^{1/3}\ Re_x^{0.5} \tag{45}$$

The value of $Nu/Re^{2/3}$ with the present method sharply decreases near the leading edge, increases in the region of $x/H > 1$, reaches the maximum value near the reattachment point of the boundary layer ($x/H \doteqdot 8$), and decreases in the region $x/H > 8$. In the region $x/H < 15$, the present values of $Nu/Re^{2/3}$ are considerably smaller than those of Ota and Kon. The minimum value of $Nu/Re^{2/3}$ is estimated to occur at about $x/H = 1$ and to be about the same as that predicted by equation (45) for laminar flow from the laminar flow pattern near the leading edge of the blunt plate shown in Fig. 7. The minimum value of $Nu/Re^{2/3}$ by Ota and Kon (1974), however, occurs at about $x/H = 5$ and is much larger than that predicted with equation (45). This difference seems to come from differences of thermal conditions and heat conduction in the plates. The heat convection from the front surface of the plate used by Ota and Kon (1974) contributes to the heat transfer coefficient in the upstream region of the plate. The shift of the minimum point of h_H to the right comes from the heat conduction within the plate and the thin stainless steel sheet (0.05 mm thick and 100 mm wide).

The local heat transfer were also measured for the case of $Re = 0.98 \times 10^5$ using the plate shown in Fig. 4(*a*). The results are illustrated in Fig. 8: The Nusselt number is smaller near the leading edge of the plate, and larger in the downstream region, than the values given by equation (44).

Conclusions

The methods measuring local heat transfer coefficient by heating a thin metal, which was adapted by Ota and Kon, are not always reliable. Therefore, a new method was proposed to measure more easily the local heat transfer coefficients of a nearly isothermal surface of a body. In this method, the variations of surface temperature after and before radiation heating were measured, and the local heat transfer coefficients of a blunt plate were measured using the known heat flux of radiation on the measured surface. The overall results revealed the method to be useful for measuring the local heat transfer coefficients under isothermal conditions even when there was a large change of the coefficient along a surface.

Acknowledgments

The author would like to acknowledge the helpful advice of Prof. R. Ishiguro and the assistance of Messrs. W. Nosaka and K. Minami. This work was supported in part by a Grant-in-Aid for Scientific Research from the Ministry of Education, Science, and Culture of Japan.

References

Bedingfield, C. H., and Drew, T. B., 1950, "Analogy Between Heat Transfer—A Psychrometric Study," *Ind. Eng. Chem.*, Vol. 42, pp. 1164-1173.

Boelter, L. M. K., Gordon, H. S., and Griffin, J. K., 1946, "Free Evaporation Into Air of Water From a Free Horizontal Quiet Surface," *Ind. Eng. Chem.*, Vol. 38, pp. 596-167.

Kumada, T., 1985, *Handbook of Heat and Mass Transfer, Vol. 1: Heat Transfer Operations*, N. P. Cherimisinoff, ed., Chap. 7, pp. 231-259.

Kumada, T., Hirota, T., Tamura, N., and Ishiguro, R., 1986, "Heat and Mass Transfer With Liquid Evaporation Into a Turbulent Air Stream," ASME JOURNAL OF HEAT TRANSFER, Vol. 108, pp. 4-8.

Ota, T., and Kon, N., 1974, "Heat Transfer in the Separated and Reattached Flow on a Blunt Flat Plate," ASME JOURNAL OF HEAT TRANSFER, Vol. 96, pp. 459-462.

Sherwood, T. K., Pigford, R. L., and Wilke, C. R., 1975, *Mass Transfer*, McGraw-Hill Kogakusha, Ltd., p. 257.

J. W. Baughn[1]
Professor.
Mem. ASME

C. A. Dingus
Research Assistant.
Assoc. Mem. ASME

M. A. Hoffman
Professor.
Mem. ASME

University of California,
Davis, CA 95616

B. E. Launder
Professor,
University of Manchester,
Faculty of Technology,
Manchester, United Kingdom
Fellow ASME

Turbulent Heat Transport in a Circular Duct With a Narrow Strip Heat Flux Boundary Condition

Experiments and computations have been performed for turbulent air flow in a circular duct in which uniform heating is applied over a 60 deg arc of the circumference. The results are compared to those for both a uniform heat flux around the full circumference of the duct and for a uniform heat flux around half the circumference. The flow was hydrodynamically fully developed at the start of heating and there were negligible buoyancy effects. Both the experimental results and the computations show that the local heat transfer coefficients for the narrow strip (60 deg wide) are less than the values for uniform heating around the full circumference but greater than the values for uniform heating around half the circumference (180 deg). This rather surprising result is a consequence of the temperature distribution in the fluid and the definition of the local heat transfer coefficient, which is based on the bulk temperature.

Introduction

Heat transfer to turbulent flow in a circular duct is commonly encountered in heat exchangers and many other applications. As a result there are numerous studies of the heat transfer characteristics of such flows, both experimental and computational. The majority of these studies are for thermal boundary conditions that are uniform around the full circumference of the duct. In many practical cases this is adequate since either the heat transfer on the outside of the duct is distributed sufficiently uniformly around the full circumference or conduction in the duct wall is sufficiently strong to produce nearly uniform boundary conditions over the entire inside circumference. However, there are important applications where the imposed external heat flux and the wall conduction are such that the thermal boundary conditions for the turbulent flow on the inside surface of the duct are highly nonuniform. Under these conditions, the local heat transfer coefficients in the region of high heat flux are lower than those that occur with boundary conditions that are uniform around the full inside circumference. This rather surprising result has been shown in previous studies, both experimental and computational. It is quite important since it means that thermal design engineers who use the common values of heat transfer coefficients for uniform boundary conditions will underestimate the local wall temperatures even if they use the local heat flux in their computations. This could result in early failure of equipment.

Previous heat transfer experiments with nonuniform circumferential boundary conditions that have used air ($Pr = 0.7$) include those by Black and Sparrow (1967), Knowles and Sparrow (1979), and Baughn et al. (1978, 1984). Those using water ($Pr = 3.5$–11.5) include Chan et al. (1975) and Schmidt and Sparrow (1978). The boundary conditions of Black and Sparrow (1967) were nearly sinusoidal while those of the other studies were half heating. Theoretical studies include an early laminar flow study by Reynolds (1960), and turbulent flow studies by Reynolds (1965), Gartner et al. (1974), Chieng and Launder (1979), and Baughn et al. (1984).

In our previous work (Baughn et al., 1984) a top-half heating boundary condition with turbulent air flow ($Re = 47{,}400$) was used to try to assess the adequacy of a nonisotropic thermal diffusivity model for representing turbulent diffusion processes in pipe flow with strongly nonuniform circumferential heating. Although the nonisotropic model gave consistently better agreement with the data, the differences between the nonisotropic and isotropic predictions were small, the Nusselt number being modified by only a few percent. The authors felt that perhaps a more severe nonuniformity in the boundary condition would increase both the effects of the nonuniformity on the local Nusselt number and the importance of including a nonisotropic diffusivity in the computations. Since the most severely nonuniform boundary condition to date had been half heating, we decided to rebuild and improve the previous apparatus and to use it to study the thermal development when uniform heating was applied only to a narrow axial strip 60 deg wide. We had previously observed a 20 percent reduction in the fully developed local heat transfer coefficient near the center of a 180 deg wide strip (i.e., half heating). Our expectation was that the more severe nonuniformity of a narrow 60 deg strip would cause a further decrease in the heat transfer coefficient with a correspondingly greater dependence of the predicted behavior on the anisotropy of the thermal diffusivity. As shown in this paper neither of these expectations was borne out.

Description of Experiment

The apparatus used in these experiments was an improved version of the one used for our earlier work (Baughn et al., 1984), rebuilt as described by Dingus (1986). The rebuilding was necessary to conform to new electrical safety standards and the improvements were primarily in the calibration of the thermocouples, the data acquisition, and the data reduction program. Although the original apparatus is described in the earlier work, a brief description is included here for completeness.

A basic diagram of the experimental apparatus is shown in Fig. 1. The duct consists of a series of straight circular acrylic tubes, which are connected with flanges and aligned with a laser. Each individual tube is 1.83 m long and has an i.d. of 9.5 cm with a 0.32 cm wall thickness. There are six tubes, three

[1]Note: Authors are listed in alphabetical order.

Contributed by the Heat Transfer Division for publication in the JOURNAL OF HEAT TRANSFER. Manuscript received by the Heat Transfer Division November 23, 1987; revision received December 21, 1988. Keywords: Forced Convection, Turbulence.

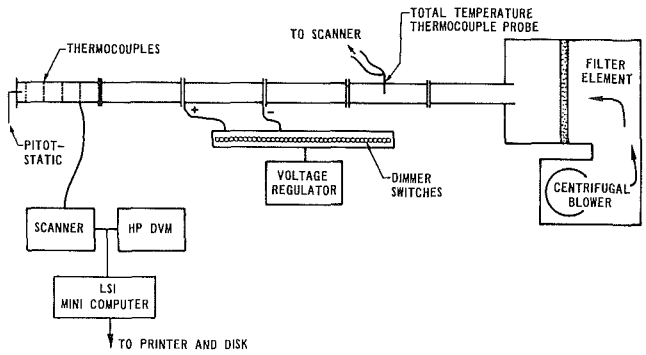

Fig. 1 Diagram of the experimental apparatus

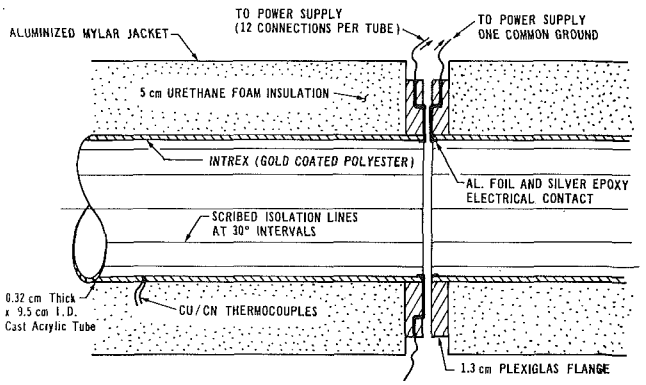

Fig. 2 Cross section of a portion of the heated tube showing the electrical connections at the flange between two tube sections

of which contain heaters and three of which are used upstream of the heated region for hydrodynamic development. The minimum hydrodynamic development length used was 58 diameters (i.e., three unheated tubes upstream) although in some runs it was longer, since in some runs there were one or two upstream tubes with heaters that were not heated (as described below). Previous measurements with this apparatus have shown that this does indeed lead to hydrodynamically fully developed flow. The flow rate was measured with an ASME orifice meter and the air temperature was measured with a thermocouple, which was calibrated against a standard platinum resistance thermometer using an HP 3052 data acquisition system and a calibration and measurement algorithm (Dingus, 1986).

The acrylic tubes in the heated sections have a gold-coated polyester sheet glued on the inside as shown in Fig. 2. The gold coating is electrically heated to provide a uniform inner-wall heat-flux boundary condition (conduction in the wall has been shown to be very small). The local wall temperature is measured and used with the local air bulk temperature to determine the local heat transfer coefficient. This experimental technique is described in greater detail by Baughn et al. (1985). In the apparatus used for these experiments the temperature is measured with type T thermocouples (40 gage or 0.13 mm diameter), mounted on the back of the gold-coated polyester sheet. Previous work has shown that the thermocouple lead wire conduction effects are negligible in this arrangement. The thermocouple leads were passed through holes in the acrylic tubes to the data acquisition system. In more recent experiments using the electrically heated coating technique, the authors map the coated surface temperature distribution with liquid crystals as described by Baughn et al. (1986).

The outside of the acrylic tubes is covered with a 5-cm-thick urethane foam cylinder and then wrapped with aluminized mylar for further insulation. A two-dimensional conduction analysis of the composite (polyester sheet, acrylic tube, and foam) has demonstrated that the conduction in the duct walls is very low and that the thermocouples on the polyester sheet correctly measure the inside surface temperature. Only a small (usually less than 4 percent) correction to the surface heat flux for the wall conduction was necessary. As described in the discussion of the data reduction below, another small correction has been made to the surface heat flux for radiation exchange between the heated gold coating and the unheated portion of the inner wall of the duct to give the convective heat flux to the air flow. This radiation correction was approximately 4 percent for the narrow strip heating (60 deg) case and approximately 3 percent for the half heating (180 deg) case.

The gold coating on the inside surface had scribed electrical isolation lines at 30 deg circumferential intervals; these were made with a sharp razor before gluing the sheets to the inside surface of the tubes. The strip of 60 deg width, which was electrically heated, consisted of the top two 30 deg wide strips as shown in Fig. 3. The heating power to each strip was controlled by individual dimmer switches that were connected to the ends of each strip with copper electrodes. Since there were two heated strips on each of three heated tubes, a total of six dimmer switches were used. The rms voltage applied to each strip by its individual dimmer switch was adjusted during the experiment to obtain the same heat flux for each strip (accounting for slightly different areas and resistances for each strip).

Although up to three different tubes were heated, only the master tube was instrumented with thermocouples. The thermocouples were located at four axial locations on this master tube. The position of this master tube relative to the other

Nomenclature

A = strip area
C = constant
c_p = specific heat
D = inside diameter
f_2 = correction factor for local heating
h = heat transfer coefficient
k = thermal conductivity
L = total length of heating
m = mass flow rate
Nu = Nusselt number
$\mathrm{Nu}_{fd,\,fc}$ = fully developed Nusselt number with full circumferential heating
P = pressure
Pe_t = turbulent Peclet number = Re Pr_t
Pr_t = turbulent Prandtl number
Pr_{t_∞} = turbulent Prandtl number far from wall
q_{cd} = conductive heat flux
q_{cv} = convective heat flux
q_e = electrical heating per unit area
q_R = radiative heat flux
R = strip resistance
r = radial coordinate
r_O = wall inside radius
Re = Reynolds number based on D
T_B = local bulk temperature
T_w = local wall temperature
U = axial average velocity
u_θ = tangential velocity
u_r = radial velocity
V = strip voltage
y = coordinate from wall
y^+ = dimensionless distance from wall
z = axial coordinate
Γ_t = turbulent diffusivity
$\Gamma_{t,r}$ = radial turbulent diffusivity
$\Gamma_{t,\theta}$ = tangential turbulent diffusivity
θ = angular coordinate
ν = air kinematic viscosity
ν_t = turbulent kinematic viscosity
ρ = air density

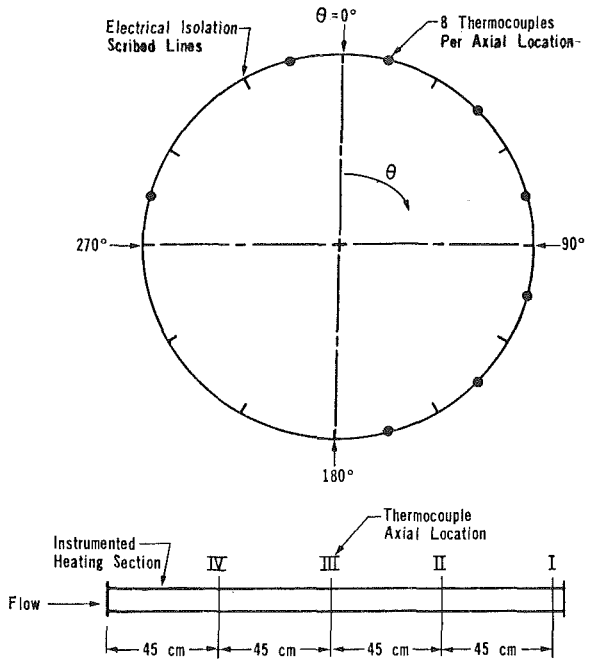

Fig. 3 Thermocouple positions of the heated tube and locations of the electrical isolation lines

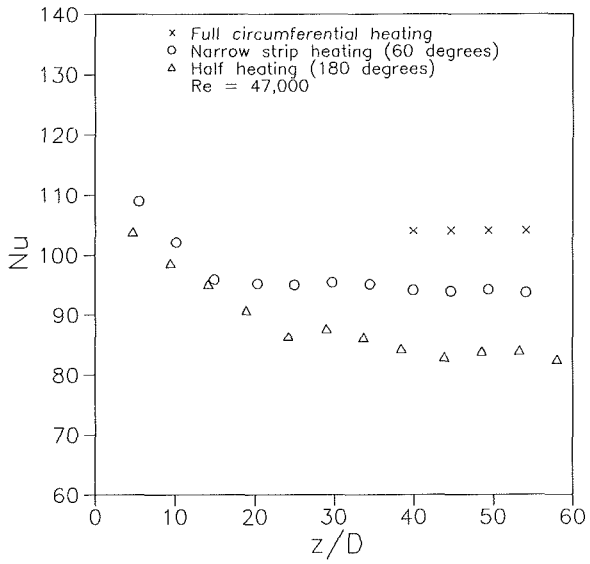

Fig. 4 Experimental results for the axial variation of the Nusselt number (strip results are 15 deg from the center of the strip)

tube. The position of this master tube relative to the other heated tubes was fixed at the exit of the assembly. Runs were made with only this tube heated to obtain the first four axial (z/D) data points, then with this tube and the adjoining (upstream) tube heated to obtain the next four axial data points, and finally with all three tubes (both of the two upstream tubes and the master tube) heated to obtain the last four axial data points. The thermocouples used in this study to determine the local heat transfer coefficients were actually mounted at $+15$ deg and -15 deg from the top as shown in Fig. 3. Top heating was used in all runs in order to avoid the possibility of buoyant secondary flows. In the present experiments, the flux Richardson number R_f was below 10^{-3}, ensuring negligible buoyant effects on the turbulent mixing.

The desired results in these experiments were the local heat transfer coefficients h (and the local Nusselt numbers, $\mathrm{Nu} = hD/k$) at various axial positions for a known turbulent Reynolds number. The local heat transfer coefficient was determined from the following equation:

$$h(\theta,z) = \frac{q_{cv}(\theta,z)}{T_w(\theta,z) - T_B(z)} \tag{1}$$

where $q_{cv}(\theta, v)$ is the local convective heat flux, $T_w(\theta, z)$ is the local wall temperature, and $T_B(z)$ is the local axial air bulk temperature. The local convective heat flux is given by

$$q_{cv}(\theta,z) = f_2(\theta,z)q_e(\theta,z) - q_{cd}(\theta,z) - q_R(\theta,z) \tag{2}$$

where $q_e(\theta, z)$ is the average electrical heating rate per unit area of a given strip (i.e., $V^2/(RA)$), $f_2(\theta, z)$ is a correction factor that accounts for the small local variations in the heating of the gold coating caused by variations in the coating thickness or strip width, $q_{cd}(\theta, z)$ is the local conduction heat transfer, and $q_R(\theta, z)$ is the local radiation heat transfer of the surface.

The average electrical heating rate is determined by measuring the rms voltage on each strip and correcting for the very slight temperature dependence of the coating resistance using the temperature coefficient of resistance as described by Baughn et al. (1984, 1985). The correction factor $f_2(\theta, z)$ is determined by an "in-situ" technique (described by Baughn et al., 1984), which assumes that the local heat transfer coefficient is the same at all locations for thermally fully developed flow and uniform heating around the full circumference. The full range of values for the $f_2(\theta, z)$ correction factor was 0.95 to 1.06, but typical values were in the range of 0.97 to 1.03. The radiation correction was determined using the measured temperature distribution and doing a detailed radiation enclosure analysis.

The bulk temperature (assuming incompressible flow with constant properties) was calculated from

$$T_B(z) = T_B(0) + \frac{1}{mc_p}\int_0^z [q_e(\theta, z) - q_{cd}(\theta, z)]dA \tag{3}$$

where m is the mass flow rate, and $T_B(0)$ is the bulk temperature at the inlet of the heated tube. Radiation losses from the heated strip have no effect on the bulk temperature since they are absorbed by the adjoining wall inside the ducts (except very near the exit where no data are used).

A thorough and complete uncertainty analysis (using standard techniques and assuming 20:1 odds) is given by Dingus (1986). The total uncertainty in the Reynolds number was found to be 1.2 percent. The uncertainty in the Nusselt number was 3.3 percent. The largest contributor to the uncertainty was the surface emissivity, which was 0.4 ± -0.1 (Jalili, 1988). The uncertainty in position is estimated at 1.0 mm, which is approximately $0.01D$ axially or 1.2 deg circumferentially.

It should be noted that although the uncertainty in the local Nusselt number is 3.3 percent, the relative values of Nusselt number for uniform half heating and strip heating can be compared with a lower uncertainty than this suggests since most of the uncertainty is caused by systematic errors and would be nearly the same for all three sets of measurements.

Experimental Results

Slight variations in the Reynolds number from run to run were handled by assuming that the Nusselt number is proportional to $\mathrm{Re}^{0.8}$, and then adjusting the measured Nusselt numbers at the measured Reynolds number to a reference Reynolds number of 47,000 for the full data set and presenting the results for this Reynolds number as shown in Fig. 4.

The fully circumferential heating data (360 deg) in Fig. 4 were taken only for thermally fully developed flow. Since these data were used to determine the correction factor $f_2(\theta, z)$, there is no axial variation in their values (i.e., in determining the correction factor, it was assumed that the heat transfer

coefficient was constant for the fully developed full circumferential heating case).

The half-heating results shown in Fig. 4 were obtained by using the earlier data of Baughn et al. (1984) newly reduced using our improved data reduction program. The narrow strip heating results were obtained as described above using the same data reduction program as that for the uniform and half heating data.

As can be readily seen in Fig. 4, the Nusselt numbers for the narrow strip (60 deg) heating case at thermally fully developed conditions fall between those for half heating (180 deg) and full circumferential (360 deg) heating. This was quite surprising to the authors and resulted in considerable examination of the experimental procedure and data reduction. After convincing ourselves that the experimental results were reliable we decided to perform some computations to see whether our speculations on the cause of these unexpected results were reasonable.

Computational Explorations

The same simple forward-marching, finite-volume solver has been adopted as used by Baughn et al. (1984) and Chieng and Launder (1979). The flow field is fully developed and axisymmetric and is obtained from a numerical solution of the axial momentum equation for fully developed pipe flow

$$0 = -\frac{1}{\rho}\frac{dP}{dz} + \frac{1}{r}\frac{d}{dr}\left[(\nu + \nu_t)\, r \frac{dU}{dr}\right] \tag{4}$$

subject to boundary conditions $dU/dr = 0$ at $r = 0$ and $U = 0$ at the pipe surface $r = r_O$. The streamwise pressure gradient dP/dx is prescribed and, following the recommendation of Kays and Crawford (1980), the turbulent viscosity is obtained from one of the following expressions:

$$\nu_t = (0.41)^2 y^2 (1 - \exp(-y^+/26))^2 \left|\frac{dU}{dr}\right| \tag{5}$$

$$\nu_t = \nu\left[\frac{0.41 y^+}{6}\right][1 + (r/r_o)][1 + 2(r/r_o)^2] \tag{6}$$

Equation (5) was employed near the wall but was replaced by equation (6) where equation (6) gives a smaller value of ν_t. The velocity field was solved for 50 nonuniformly spaced radial nodes and stored for use in computing the evolution of the three-dimensional thermal field. In making those computations the radial thermal diffusivity was obtained from

$$\Gamma_t = \nu_t / \mathrm{Pr}_t \tag{7}$$

where the turbulent Prandtl number is given by the following function of the Peclet number:

$$\mathrm{Pr}_t(r) = \frac{1}{\dfrac{1}{2\mathrm{Pr}_{t_\infty}} + \dfrac{C\mathrm{Pe}_t}{\sqrt{\mathrm{Pr}_{t_\infty}}} - (C\mathrm{Pe}_t)^2\left[1 - \exp\left(-\dfrac{1}{C\mathrm{Pe}_t\sqrt{\mathrm{Pr}_{t_\infty}}}\right)\right]} \tag{8}$$

where

$$\mathrm{Pe}_t = (\nu_t/\nu),\ \mathrm{Pr}_{t_\infty} = 0.86,\ C = 0.2$$

Equation (8) is also taken from Kays and Crawford (1980); it may be regarded as a correlation of the experimental data for fully developed, uniformly heated pipe flow with axisymmetric heating. It should be applicable here for a circumferentially varying heat flux in those regions where the heat flux is primarily radial. This is the case near the center of the heated strip ($\theta = 0^0$) where the main attention is directed here. Finally

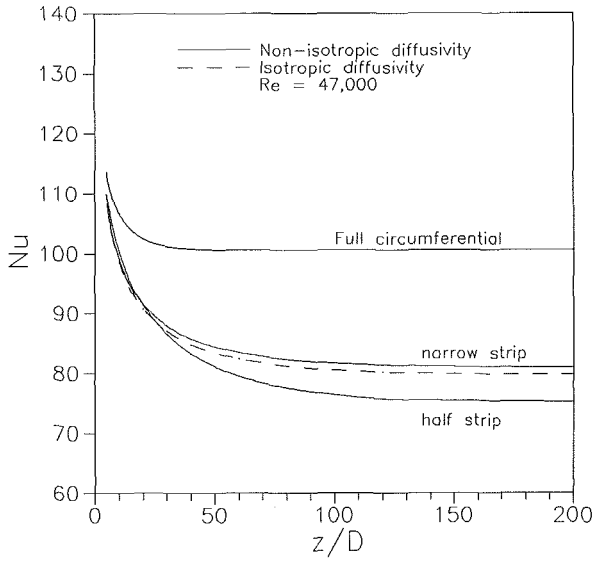

Fig. 5 Computational results for the axial variation of the Nusselt number (strip results are 15 deg from the center of the strip)

the tangential diffusivity is assumed to be related to the radial diffusivity by

$$\Gamma_{t,\theta} = \Gamma_{t,r}\overline{u_\theta^2}/\overline{u_r^2} \tag{9}$$

The mean square velocity fluctuations in the radial and circumferential directions are supplied numerically from a fit to the measurements of Laufer (1954). There is a significant body of evidence in support of equation (9) (e.g., Baughn et al., 1984, and Chieng and Launder, 1979). The above prescription for the radial and tangential diffusivities was used in the numerical solutions of the energy equation

$$U\frac{\partial T}{\partial z} = \frac{1}{r}\frac{\partial}{\partial r}\left[(\Gamma + \Gamma_{t,r})r\frac{\partial T}{\partial r}\right] + \frac{1}{r}\frac{\partial}{\partial \theta}\left[\frac{1}{r}(\Gamma + \Gamma_{t,\theta})\frac{\partial T}{\partial \theta}\right] \tag{10}$$

Baughn et al. (1984) employed only 26 circumferential nodes. In view of the steeper temperature gradients that were expected for top-half and for strip heating all the computations were made on a 50×50 grid with typically 500 forward steps. The Nusselt numbers for the 50×50 grid were found to be within 2 percent of the eariler 26×26 grid runs for the uniform circumferential heating case. Thus we are grid independent for this case. For the 60 deg wide strip heating case, we found a difference of 6.2 percent in the Nusselt number at 0 deg between 50×50 grid and the earlier 26×26 grid. Thus it is expected that the numerical uncertainty in Nusselt number with the 50×50 grid used here is well within 2 percent at 0 deg. The computations required approximately one half hour per run on a VAX 750.

Figure 5 shows, for the three cases considered, the development of the computed Nusselt number downstream from the start of heating along a line 15 deg removed from the point of symmetry to correspond with the location of the thermocouples (these results were computed for a Reynolds number of 44,800 and adjusted to the same Reynolds numbers as the experimental results, i.e., 47,000, using $\mathrm{Re}^{0.8}$ as noted above). Several interesting results emerge. First we note that the fully developed value of Nu for the 60 deg wide heated strip case is higher than for half heating in agreement with the measurements shown in Fig. 4. Moreover, the asymptotic level is reached (for practical purposes) at a larger z/D for half heating, a feature that is again in accord with Fig. 4 (the experimental results) but that runs counter to intuition; i.e., the

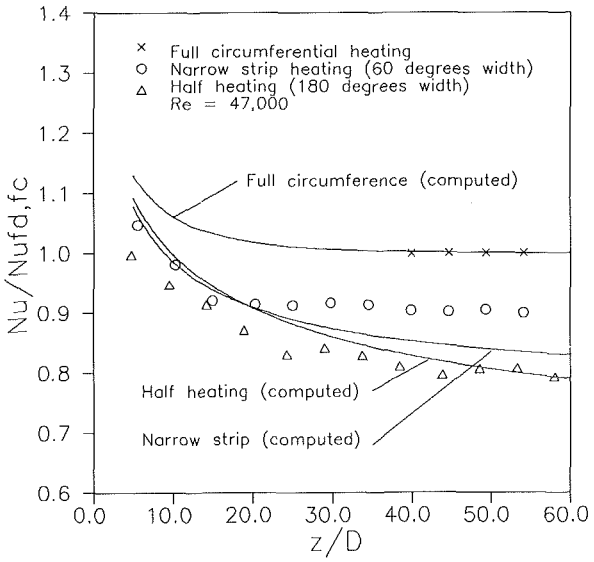

Fig. 6 Comparison of measured and computed normalized Nusselt number (strip results at 15 deg from the center of the strip)

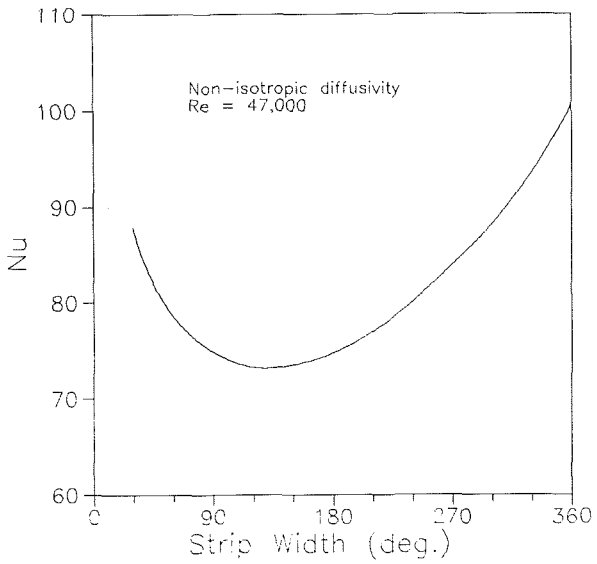

Fig. 7 Effect of the strip width on the Nusselt number at the center of the strip

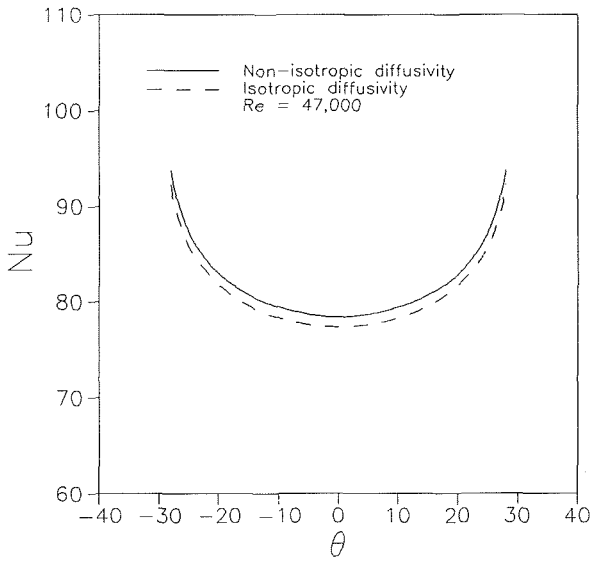

Fig. 8 Distribution of the Nusselt number around a narrow strip for fully developed flow (z/D = 200)

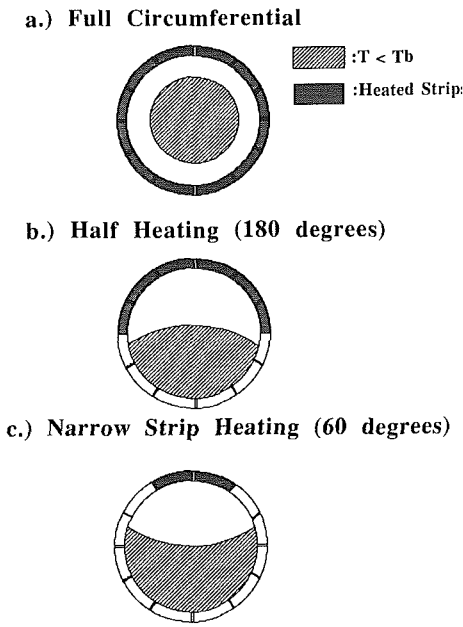

Fig. 9 Computed bulk temperature isotherms for different strip widths

60 deg wide strip results are not an extrapolation of the other two cases. Thirdly, the computed level of Nu for the 60 deg strip is lower than the experiments indicate. This can be seen in Fig. 6 where the experimental results and the computed results are each normalized to the fully developed Nusselt number for full circumferential heating. The difference between the computed and measured values is most evident for the 60 deg strip heated case. Part of this difference could be a result of some of the experimental uncertainties, such as the radiation correction (which is largest for this case). Nevertheless, the difference seems to lie outside the uncertainty of the data. A further interesting feature of the computations is that use of equation (9) in place on an isotropic diffusivity raises the predicted fully developed value of Nu by only 1.5 as shown in Fig. 5.

In view of the initially surprising increase in Nusselt number when the heated strip width was reduced from 180 deg to 60 deg, computations were also made for other strip widths. The resultant dependence of Nu on the angular width of the heated strip, for the fully developed limit, is shown in Fig. 7. Values of the Nusselt number are given at the center of the heated section. It can be seen that a minimum level of Nu occurs for a strip width of about 130 deg.

The distribution of the local Nusselt number across the narrow 60 deg strip is shown in Fig. 8. This shows that the local Nusselt number does vary considerably across the width of the strip. It may also explain some of the discrepancy in the computed and measured values since a small position error in the measurements could cause a larger than expected uncertainty.

From the experimental and computational results reported above, it is clear that the dependence of Nusselt number on the width of the heated strip is markedly different according to whether the strip is narrow (<130 deg) or wide (>130 deg). The underlying reason for this different behavior may be inferred from the bulk temperature isotherms shown in Fig. 9. Note that the region of the duct flow cross section that is above the bulk temperature is smaller for the narrow strip heating (60 deg) case than for the half heating (180 deg) case. These calculations are for the *same* heat flux and the *same* bulk temperature. We might expect then that the wall

temperature of the narrow strip would be lower (i.e., the cooler bulk temperature being closer to the heated region) than that of the half heating. From equation (1) it can be seen that this lower wall temperature (for a fixed heat flux and bulk temperature) would correspond to a higher heat transfer coefficient and Nusselt number. This behavior is actually a consequence of defining the local heat transfer coefficient in terms of the bulk temperature. This effect is similar to the surprising behavior (even including negative heat transfer coefficients) found by Reynolds (1960) for the laminar case.

Conclusions

This paper has helped clarify the effects of turbulent heat diffusion processes in pipes where heating is applied over only a portion of the circumference. The paradoxical experimental result that Nusselt numbers are lower for half heating (180 deg) than for either full circumferential heating (360 deg) or narrow strip heating (60 deg) has been confirmed by our numerical studies. Although initially surprising, the result becomes more understandable when the temperature distribution within the fluid is considered.

References

Baughn, J. W., Hoffman, M. A., Launder, B. E. and Samaraweera, D. S. A., 1978, "Three-Dimensional Turbulent Heat Transport in Pipe Flow: Experimental and Model Validation," ASME Paper No. 78-WA/HT-15.

Baughn, J. W., Hoffman, M. A., Launder, B. E., and Takahashi, R. K., 1984, "Turbulent Heat Transport in Circular Ducts With Circumferentially Varying Heat Flux," ASME JOURNAL OF HEAT TRANSFER, Vol. 106, pp. 64–70.

Baughn, J. W., Takahashi, R. K., Hoffman, M. A., and McKillop, A. A., 1985, "Local Heat Transfer Measurements Using an Electrically Heated Thin Gold-Coated Plastic Sheet," ASME JOURNAL OF HEAT TRANSFER, Vol. 107, pp. 953–959.

Baughn, J. W., Hoffman, M. A., and Makel, D. B., 1986, "Improvements in a New Technique for Measuring Local Heat Transfer Coefficients," *Review of Scientific Instruments*, Vol. 57, No. 4, pp. 650–654.

Black, A. W., and Sparrow, E. M., 1967, "Experiments on Turbulent Heat Transfer in a Tube With Circumferentially Varying Thermal Boundary Conditions," ASME JOURNAL OF HEAT TRANSFER, Vol. 89, pp. 258–268.

Chan, A. L., Baughn, J. W., and Hoffman, M. A., 1975, "Nonuniform Circumferential Heat Flux Experiments in a Circular Tube," ASME Paper No. 75-WA/HT-52.

Chieng, C. C., and Launder, B. E., 1979, "On the Calculation of Turbulent Heat Transport in Flow Through an Asymmetrically Heated Pipe," *Numerical Heat Transfer*, Vol. 2, pp. 359–371.

Dingus, C., 1986, "Turbulent Heat Transport in a Circular Duct With Narrow Strip Heating Along the Top," M.S. Thesis, University of California, Davis, CA.

Gartner, D., Johanssen, K., and Ramm, H., 1974, "Turbulent Heat Transfer in a Circular Tube With Circumferentially Varying Thermal Conditions," *International Journal of Heat and Mass Transfer*, Vol. 17, pp. 1003–1013.

Jalili, V., 1988, "Emissivity Measurements using 'Intrex G'," Diploma of Technical Science Dissertation, University of Manchester Institute of Science and Technology, United Kingdom.

Kays, W. M., and Crawford, M. E., 1980, *Convective Heat and Mass Transfer*, 2nd ed., McGraw-Hill, New York.

Knowles, G. R., and Sparrow, E. M., 1979, "Local and Average Heat Transfer Characteristics for Turbulent Airflow in an Asymmetrically Heated Tube," ASME JOURNAL OF HEAT TRANSFER, Vol. 101, pp. 635–641.

Laufer, J., 1954, "The Structure of Turbulence in Fully Developed Flow," NACA Report 1174.

Reynolds, W. C., 1960, "Heat Transfer to Fully Developed Laminar Flow in a Circular Tube With Arbitrary Circumferential Heat Flux," *Trans. ASME*, Vol. 82, No. 2, p. 108.

Reynolds, W. C., 1963, "Turbulent Heat Transfer in a Circular Tube With Variable Circumferential Heat Flux," *Int. J. Heat Mass Transfer*, Vol. 6, pp. 445–454.

Schmidt, R. R., and Sparrow, E. M., 1978, "Turbulent Flow of Water in a Tube With Circumferentially Nonuniform Heating, With and Without Buoyancy," ASME JOURNAL OF HEAT TRANSFER, Vol. 100, pp. 403–409.

J. W. Baughn
Professor.
Mem. ASME

M. A. Hoffman
Professor.
Mem. ASME

Department of Mechanical Engineering,
University of California, Davis,
Davis, CA 95616

B. E. Launder
Professor,
Department of Mechanical Engineering,
University of Manchester Institute
of Science and Technology,
Manchester M60 1QD, United Kingdom
Fellow ASME

Daehee Lee
Assistant Professor,
Department of Mechanical Engineering,
California State University, Sacramento,
Sacramento, CA 95819
Mem. ASME

C. Yap
Assistant Professor,
Department of Mechanical and
Production Engineering,
National University of Singapore,
Singapore 0511

Heat Transfer, Temperature, and Velocity Measurements Downstream of an Abrupt Expansion in a Circular Tube at a Uniform Wall Temperature

Detailed heat transfer, temperature, and velocity data are reported for the turbulent flow downstream of an abrupt increase in tube diameter (2.5:1) in which the downstream tube is maintained at a uniform elevated temperature. The heat transfer experiments cover downstream Reynolds numbers ranging from 4300 to 44,500, the flow being fully developed at the exit of the small tube (i.e., the abrupt expansion step). Maximum local heat transfer coefficients are proportional to the upstream Reynolds number to the power 2/3 with the location of the maximum moving upstream slightly as the Reynolds number is increased. Heat transfer data at a Reynolds number of 17,300 are supplemented by velocity and temperature profiles, which are especially informative. They bring out clearly that the viscous sublayer, despite the thinning that is believed to occur in the vicinity of the reattachment point, still provides the major resistance to heat transfer. The correct prediction of the Nusselt–Reynolds number relation in reattaching flows is thus crucially dependent on the variation of turbulent diffusivity in the "buffer" region of the flow.

Introduction

The application of computational fluid dynamics to industrial problems in convective heat transfer has stimulated the need for detailed and accurate measurements of convective heat transfer coefficients in recirculating flows supported by corresponding data for the temperature and velocity fields. Only by providing such detailed coverage can one properly assess whether a turbulent flow solver is actually providing a correct simulation of the flow; for example, a reasonably correct prediction of the heat transfer coefficient for a particular flow field could result from compensating errors in the computed turbulent diffusivities in different regions. When later applied to a slightly different flow the same turbulent flow solver could provide incorrect heat transfer coefficients.

The present paper contributes to such a data base. The geometry considered is that of the abrupt pipe expansion in a circular tube, a configuration that, besides being of direct industrial importance, is a simple geometry to handle computationally and allows precise unambiguous entry conditions to be achieved. Our earlier abrupt expansion data (Baughn et al., 1984, 1987a), in common with other investigations over the past thirty years (Ede et al., 1956; Krall and Sparrow, 1966; Zemanick and Dougall, 1970), employed a (nominally) uniform wall heat flux boundary condition. The present experiment has been designed to provide a uniform wall temperature. This was done both to discover what effect this change brings to the Nusselt number distribution and to provide an independent check on the existence of the distinct minimum value of heat transfer coefficient reported in Baughn et al. (1984) at about one step height downstream of the abrupt expanion step. Measurements of the surface heat flux (and corresponding heat transfer coefficient) are supplemented by detailed interior temperature distributions and, in the nonrecirculation region of the flow, by mean velocity profiles. These experiments complement the recent velocity, temperature, and heat flux measurements of Vogel and Eaton (1985), who examined the flow over a backward-facing step with a downstream surface at a uniform wall heat flux.

Experimental Apparatus

A general diagram of the apparatus used in the experiments is shown in Fig. 1. Filtered ambient air, delivered by a blower,

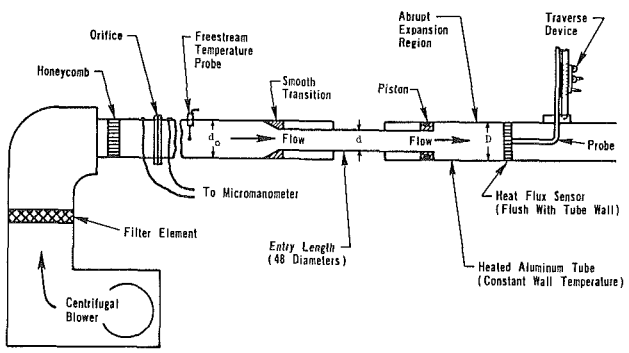

Fig. 1 Diagram of the apparatus for the velocity and temperature measurements downstream of an axisymmetric abrupt expansion

Contraibuted by the Heat Transfer Division for publication in the JOURNAL OF HEAT TRANSFER. Manuscript received by the Heat Transfer Division March 31, 1988. Keywords: Forced Convection, Measurement Techniques, Turbulence.

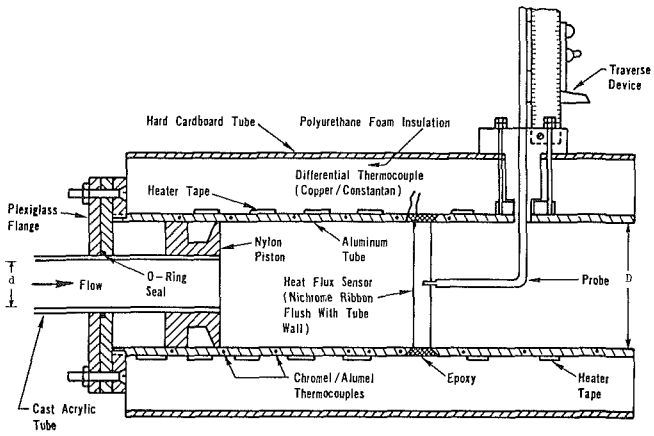

Fig. 2 Cross-sectional diagram showing the details of the abrupt expansion region and setup of the traverse mechanism for velocity and temperature measurements

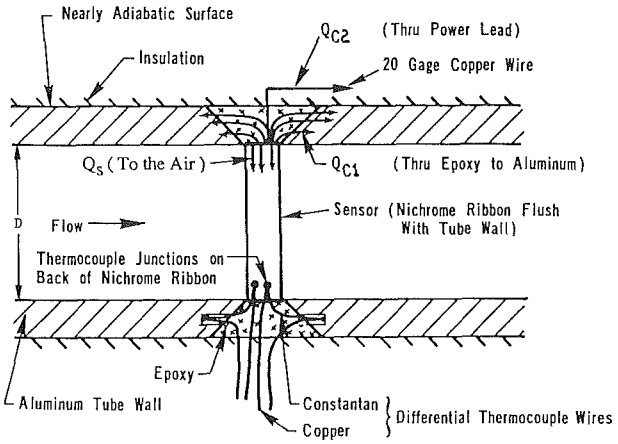

Fig. 3 Cross-sectional diagram of the heat flux sensor

first entered a cast acrylic tube of 6.35 cm i.d. (defined as d_0), which contained flow straighteners (honeycomb), and flow rate and free-stream temperature sensors. The flow then entered a long smooth acrylic tube of 3.81 cm i.d. (defined as d), which led to an abrupt expansion into a heated aluminum tube of 9.53 cm i.d. (defined as D).

The cast acrylic tube (6.35 cm i.d.) contained an ASME orifice plate flow meter with a thermocouple located 108 cm (17 diameters) downstream from the orifice plate. A smaller tube (3.81 cm i.d.) led directly into the abrupt expansion and was 48 diameters in length to ensure a nearly fully developed velocity profile just before the abrupt expansion step. The abrupt expansion into the heated section was formed by a movable nylon piston, thereby allowing it to be placed in any position relative to a heat flux gage in the heated aluminum tube. A detailed drawing is shown in Fig. 2.

The heated aluminum tube of 9.53 cm i.d. had a total length of 152 cm (16 diameters) and a wall thickness of 0.64 cm and was heated with electrical heating elements wrapped on the outside. The thick walls and high thermal conductivity provided a uniform wall temperature boundary condition. Eighteen chromel-alumel 30 gage (0.025 cm) thermocouples were positioned along the tube to measure the tube outer wall temperature and to check uniformity.

The heated section itself was completely covered with 5.1-cm-thick polyurethane foam to reduce heat losses to a negligible level. Using a finite element code for two-dimensional conduction analysis, the calculated axial and circumferential wall temperature distribution verified that the inner wall should be constant to within ±0.2°C. Later measurements confirmed this nearly uniform wall temperature.

Located flush with the tube inner wall (114 cm downstream from the upstream end) of the heated aluminum tube was a specially designed sensor, shown in Fig. 3, for the measurement of the local time-average heat flux from a surface at a uniform temperature (Baughn et al., 1987b). The main element in this sensor was an electrically heated nickel/chromium ribbon (0.14 cm thick, 0.32 cm wide). This ribbon was surrounded with epoxy, which effectively insulated it thermally and electrically from the aluminum tube walls on both sides. Eight copper-constantan differential thermocouples (0.008 cm diameter) were mounted 90 deg apart and on both sides of the ribbon to make differential temperature measurements between the ribbon and the tube wall, as well as to check the

Nomenclature

A_s = ribbon (sensor) surface area, m^2
C_e = thermal conductance between the ribbon and the aluminum tube, W/K
c_p = specific heat, J/kg K
d = upstream tube diameter, m
D = heated (downstream) tube diameter, m
EMF = electromotive force, mV
h = heat transfer coefficient, W/m^2 K
H = step height $\equiv (D-d)/2$
i.d. = tube inside diameter
k_a = thermal conductivity of air, W/m K
m = mass flow rate, kg/s
Nu = Nusselt number
Nu_{DB} = fully developed Nusselt number based on Dittus-Boelter's correlation
P_e = ribbon electric power, W
Q_c = conduction heat loss rate, W
Q_s = ribbon (sensor) surface heat transfer rate, W
q_s'' = ribbon (sensor) surface heat flux, W/m^2
Re_d = Reynolds number based on upstream diameter d
Re_D = Reynolds number based on downstream diameter D
$Re_{d,max}$ = upstream Reynolds number based on maximum centerline velocity
R_s = ribbon (sensor resistance, Ω
T_b = fluid bulk temperature, °C
T_{in} = air temperature upstream of the expansion, °C
T_s = ribbon (sensor) temperature, °C
T_w = wall (aluminum) temperature, °C
U = mean velocity in x direction, m/s
u = fluctuating velocity in x direction, m/s
u' = rms of the axial turbulent velocity fluctuation, m/s
U_{max} = maximum (centerline) velocity, m/s
$U_{0(max)}$ = maximum (centerline) velocity at the abrupt expansion, m/s
V_s = ribbon (sensor) voltage, V
x = axial position downstream of an abrupt expansion step, m
y = radial position measured from the tube wall, m

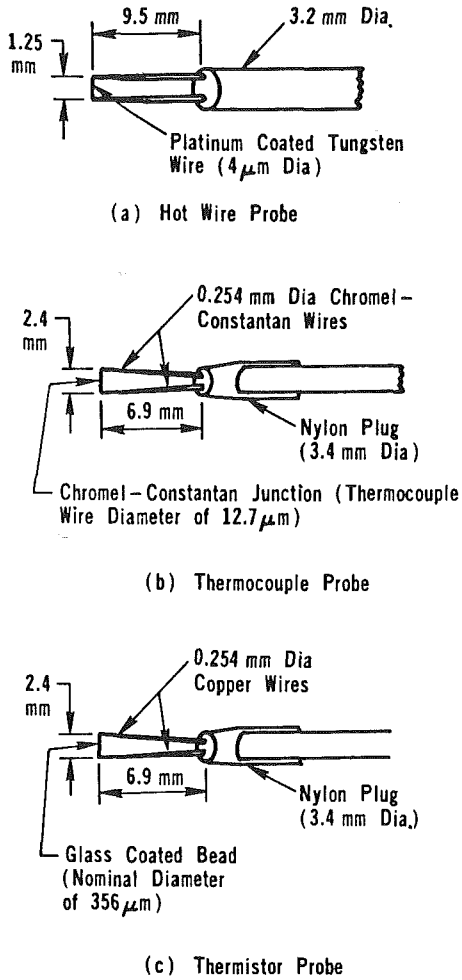

Fig. 4 Sketches of the three temperature probes employed

symmetry of the heat transfer. One side of the welded copper-constantan junction was electrically welded to the ribbon and the other side was inserted into a hole on the adjacent inclined tube wall as shown in Fig. 3.

To heat the ribbon, solid copper wires (0.081 cm) were spot-welded to both ends of the ribbon, through which the power was supplied. Uncertainty analyses by Lee (1987) and Baughn et al. (1987b) showed that the heat flux sensor has an uncertainty of ±1.9 percent for a typical experimental convective heat flux of 874 W/m^2. The detailed design, operation, and applications of this heat flux gage are also given by Lee (1987) and Baughn et al. (1987b).

Located 8.7 cm downstream from the heat flux gage was a traverse mechanism for the probes that were used in the temperature and velocity profile measurements. Several different types of probe were used as shown in Fig. 4. For the mean velocity measurements, a single hot-wire probe was used along with a TSI-1050 anemometer system. For the temperature measurements, three different probes were used: a hot-wire probe with a 4 μm diameter (operated in the constant-current mode), a fine chromel-constantan thermocouple probe with a wire diameter of 12.7 μm, and a miniature thermistor probe with a nominal diameter of 356 μm.

Each probe was mounted in a traverse mechanism, as shown in Figs. 1 and 2, and inserted in the flow with the probe tip positioned at the same axial location as the heat flux gage. The traverse mechanism was mounted on top of the aluminum tube so that the probe could be traversed across the vertical diameter at the measurement section downstream of the abrupt expansion. The radial position of each probe was measured to an accuracy of 0.05 mm using a vernier caliper on the traverse mechanism.

Prior to measurements, the hot-wire probe was calibrated over the range of $0.8 < U < 3.8$ m/s and $4.1 < U < 35.6$ m/s. The two ranges of velocity provided a greater accuracy in the calibration curve over a broad range. The scatter in the calibration data was within ±1.4 percent for the lower range and ±0.67 percent for the higher velocity range.

Experimental Procedure

In order to verify that the inlet velocity profile in the smaller upstream tube (with 3.81 cm i.d.) was fully developed turbulent flow, the piston was moved until the hot-wire probe was positioned inside the smaller tube about 2.86 cm upstream of the abrupt expansion step. The mean velocity distribution, $U(r)$, and the streamwise rms component of the turbulence intensity,

$$u' \equiv \sqrt{u^2}$$

were then measured as the hot-wire probe was traversed from bottom to top across the full diameter of tube to check the flow symmetry.

The mean velocity measurements downstream of the axisymmetric abrupt expansion were started at 22 step heights downstream from the expansion step, where the traverses were made across the full diameter of the tube. After the first set of measurements was completed, the piston was moved downstream (i.e., toward the probe) by increments of a few step heights and the procedure was repeated until the probe was within 0.25 step heights of the piston.

A typical data run for the heat flux and mean temperature measurements would begin by turning on the blower and the aluminum tube heaters with the nylon piston positioned 22 step heights upstream from the heat flux gage. During the 2-h period normally allowed to reach steady state, the cylinder heaters were periodically adjusted to obtain a difference between the wall temperature and the inlet air temperature, $(T_w - T_{in})$, of about 10°C and to obtain a constant and uniform tube wall temperature within ±0.2°C (by monitoring temperature variations with the data acquisition system). The 10°C temperature difference was chosen to be high enough to result in low uncertainties in the Nusselt number while being low enough to result in negligible air property variations.

Once steady state had been obtained, the voltage into the ribbon was increased or decreased according to the differential thermocouple EMF readings until near null readings were obtained on all eight differential thermocouples. Under this condition heat transfer between the ribbon and the adjacent aluminum tube walls was negligible (within the determined uncertainty) and the electrical power into the ribbon was essentially equal to the heat rate out of the ribbon surface to the air flow (except for very small conduction heat losses discussed in the data reduction section).

After the heat flux measurement at one axial position, the mean fluid temperature was then measured with the piston located at the same position, and traverses were made across the full diameter of the tube. These measurements were made for a downstream Reynolds number, Re_D, of 17,300, which was only slightly different from the Reynolds number at which the other measurements were made. Separate runs were made for the temperature measurements using each of the three different probes (shown in Fig. 4): the hot-wire probe (operated in a constant current mode), the thermistor probe, and the chromel-constantan thermocouple probe.

Since the free-stream temperature generally increased slightly during the time that the blower was running, it was recorded

before and after each run. The free-stream temperature used in the data reduction was taken to be average of these two readings. The difference between the two free-stream temperature measurements was normally less than 0.05°C. The tube wall temperature T_w was taken to be the average of the measurements by the two sets of three thermocouples, which were located 90 deg apart, 0.5 D upstream and downstream from the heat flux sensor.

After the initial test for the heat flux and temperature measurements at 22 step heights was completed, the piston was moved downstream by increments of two step heights and the procedure was repeated until the piston was within 0.25 step heights upstream from the heat flux gage. Each set of measurements was taken 50 to 60 min after the piston was moved to allow steady state to be re-established.

Data Reduction

The heat losses from the nickel/chrominum ribbon of the heat flux gage are shown in Fig. 3. Following the approach adopted by both Kraabel et al. (1980) and Baughn et al. (1987b), we note that for the ribbon:

Electical power = Convection heat transfer rate + Conduction in leads and epoxy

$$P_e = Q_s + Q_{c1} + Q_{c2} \quad (1)$$

Expressing each of these terms as a function of the measurands, they become, respectively,

$$P_e = V_s^2/R_s \quad (2)$$

where V_s is the voltage across the sensor (i.e., ribbon) and R_s is the ribbon resistance. The very low temperature coefficient of the Ni/Cr alloy ($8 \times 10^{-5}\ K^{-1}$) makes it possible to consider the ribbon resistance constant (i.e., to neglect its temperature dependence). No lead wire heating is included since the voltage was measured with a separate set of leads welded to the ends of the ribbon (a "four-wire" method)

$$Q_s = h(x)A_s(T_s(x) - T_b(x)) \quad (3)$$

where $h(x)$ is the local heat transfer coefficient at axial position x of the sensor from the upstream piston, A_s is the ribbon surface area, $T_s(x)$ and $T_b(x)$ are, respectively, the ribbon temperature and bulk temperature of air flow at the ribbon location x from the upstream piston.

$$Q_{c1} + Q_{c2} = C_e(T_s(x) - T_w(x)) \quad (4)$$

where C_e is the overall thermal conductance between the ribbon and the aluminum walls and $T_w(x)$ is the local temperature of the aluminum tube wall adjacent to the heat flux gage. The value for C_e was determined experimentally by inserting foam insulation into the tube (thereby insulating the surface of the ribbon) and applying a voltage to the ribbon.

Combining equations (1) through (4), we obtain an expression for the energy balance of the ribbon

$$V_s^2/R_s = h(x)A_s(T_s(x) - T_b(x)) + C_e(T_s(x) - T_w(x)) \quad (5)$$

Equation (5) is needed for the uncertainty analysis. However, when the ribbon power is adjusted to give a null reading for the differential thermocouples, the heat transfer between the ribbon and tube wall goes to zero. Under this condition, the temperature difference between the ribbon and the tube wall approaches zero and the energy balance can be put in terms of the local Nusselt number

$$\mathrm{Nu}(x) = h(x)D/k_a = (V_s^2/R_s)D/[A_s(T_s(x) - T_b(x))k_a] \quad (6)$$

where k_a is the thermal conductivity of air. To find the local bulk temperature, it is necessary to integrate from the abrupt expansion step to the local position, i.e.,

$$T_b(x) = T_i(t) + \int_0^x \left(\frac{q_s''(x)\pi D}{\dot{m}\, c_p}\right) dx \quad (7)$$

where $T_i(t)$ is the inlet bulk temperature at the time when the local heat flux data at axial position x were obtained, and $q_s''(x)$ is the local heat flux given by Q_s/A_s.

The uncertainty in the Nusselt number, estimated with odds of 20:1 and using the methods of Kline and McClintock (1953), is ±2.8 percent for a convective heat flux of approximately 874 W/m^2. Details on the method of estimating the uncertainties and the contributions of individual measurands are given by Baughn et al. (1987b) and Lee (1987).

Discussion of Results

Heat transfer measurements downstream of an axisymmetric abrupt expansion were made with a small diameter to large diameter ratio of 0.4 over the Reynolds numbers range of 4300 to 44,500 (based on downstream diameter). These were reported by Baughn et al. (1986). Velocity and temperature measurements were also made for the same diameter ratio over the Reynolds numbers range of 4100 to 17,400. These were reported by Baughn et al. (1987c).

The development of the streamwise mean velocity profile at eight different locations downstream of the abrupt expansion is shown in Fig. 5. The downstream centerline velocity normalized by the centerline velocity in the smaller upstream tube just at the step is also shown in Fig. 6 (which can be used to convert the results of Fig. 5 to actual velocities). The decay of this centerline velocity as it approaches the fully developed value downstream is clearly seen in Fig. 6. The shear layer starting from the expansion lip grows rapidly before reattaching to the wall at approximately 9 step heights downstream. (The single hot wire is unable to resolve flow direction or backflow and so for the first stations the data are clipped where it is felt they cease to be meaningful). The downstream flow recovery is evident in Fig. 5. By 22 step heights downstream the mean velocity is essentially uniform for radii up to about 80 percent of the tube radius. Profiles at other Reynolds number are given by Lee (1987), but as their form is very similar to those of Fig. 5, they are not shown.

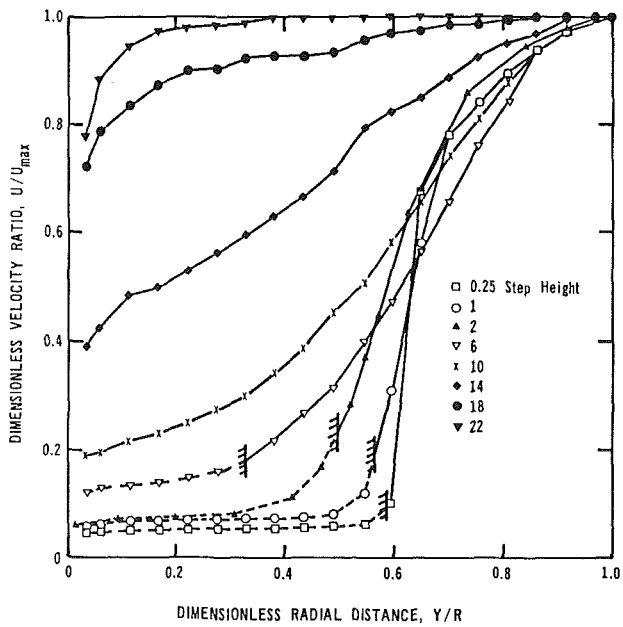

Fig. 5 Mean velocity profiles in the abrupt expansion region for $Re_D = 17{,}400$ and $d/D = 0.4$. The vertical bars indicate the approximate position of the edge of the recirculation region.

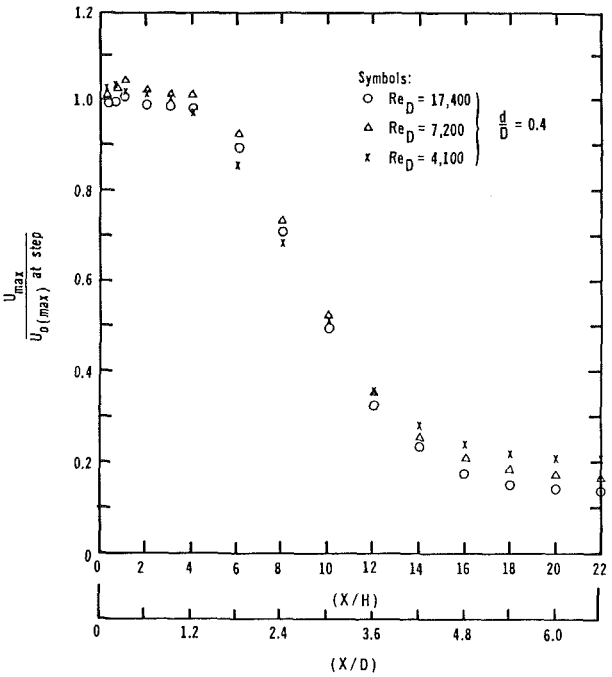

Fig. 6 Axial distribution of the maximum (centerline) velocity in the abrupt expansion region divided by the maximum (centerline) velocity at the abrupt expansion step

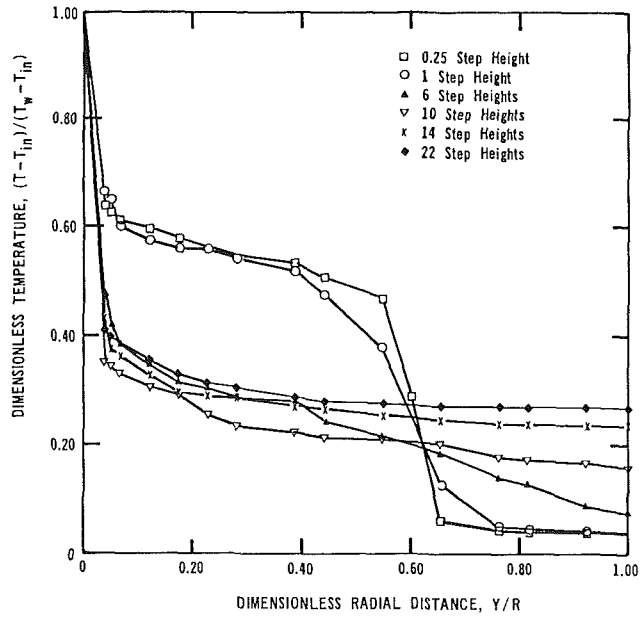

Fig. 7 Mean temperature profiles in the abrupt expansion region measured by the thermocouple probe (Re_D = 17,300, d/D = 0.4)

There is a weak Reynolds number effect on the data of Fig. 6 with the rate of decay of U_{max} increasing as the Reynolds number is raised. This behavior is generally in accord with a relative shift in the surface heat transfer data with Reynolds number on which we comment below. The more rapid decay in the centerline velocity at higher Reynolds number is apparently associated with a faster initial growth of the mixing layer immediately following the discharge from the smaller tube.

The mean temperature profiles in the large tube were taken only at $Re_D = 17{,}300$. There was generally very close agreement among the values obtained by the three different temperature sensing probes although, on the whole, the agreement between the thermocouple and thermistor values was slightly better than with the hot wire. For this reason only the mean temperature profiles measured by the fire wire thermocouple probe are presented in Fig. 7. The first two profiles show clearly the growth of the thermal mixing layer immediately after the step. A noticeable feature is the quite different shapes of the temperature profile at $x/H = 6$ and 10 from the corresponding velocity profiles in Fig. 5. Vigorous turbulent mixing in the separated region produces a situation in which the great majority of the temperature drop between the wall and the centerline occurs within a thin annulus extending from the wall a distance of only some 5 percent of the tube radius. It follows that the surface heat transfer rates will be dominated by the turbulent mixing processes taking place in this near-wall layer.

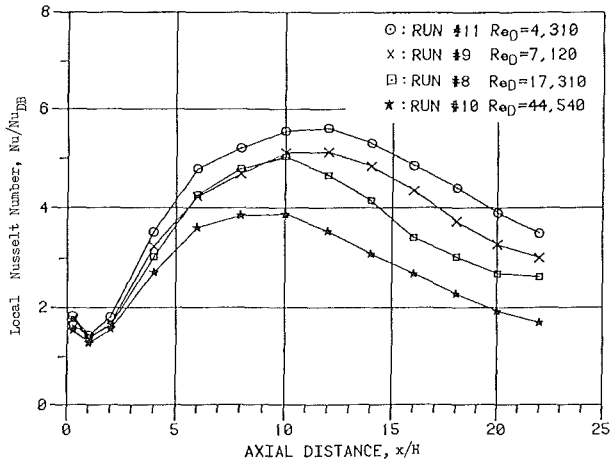

Fig. 8 Distribution of local Nusselt number in the axisymmetric abrupt expansion for $d/D = 0.4$

The local wall heat fluxes have been obtained at four values of Re_D covering a decade of Reynolds numbers. In Fig. 8, following the practice introduced by Zemanick and Dougall (1970), the local Nusselt numbers are normalized by those given by the Dittus-Boelter correlation for the heat transfer coefficient in fully developed pipe flow and the distance downstream is normalized by the step height $H\,[\equiv (D-d)/2]$.

The peak values of the Nusselt number range from 5.6 times this fully developed value at the smallest Re_D to 3.9 times at the highest Re_D, which indicates a maximum value of Nusselt number proportional to the Reynolds number to the power 2/3, a commonly found exponent in separated flows. Indeed, as shown in Fig. 9, the present data are well correlated by the expression

$$Nu_{max} = 0.2\ Re_d^{2/3} \qquad (Pr = 0.7)$$

which was also found to fit our earlier data with a uniform heat flux boundary condition for several different values of d/D (Baughn et al., 1984).

There is an indication from Fig. 8 that the location of the maximum Nusselt number shifts progressively upstream from approximately $12(\pm 1)$ to approximately $9(\pm 1)$ step heights from the expansion step as the Reynolds number is raised (at least over the range of Re_D from 4300 to 44,500 investigated in the present experiment). This trend is consistent with the more rapid decay of streamwise centerline velocity noted above since the more rapid the decay the shorter the recirculation region. Flow visualization experiments using tufts showed that the position of the average reattachment point (or region) has approximately the same dependency on Reynolds number as the position of the maximum heat transfer. The position of the average reattachment position decreased from about 12 to about 9 step heights downstream of the abrupt expansion as the Reynolds number increased from 4100 to 17,400 (Lee,

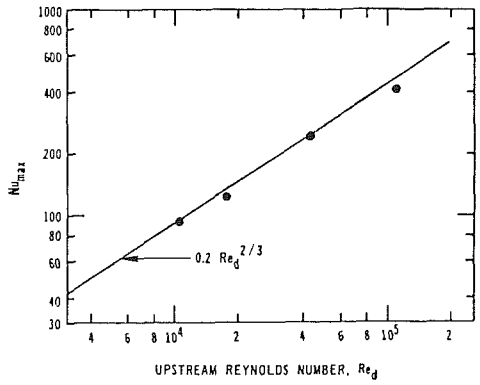

Fig. 9 Effect of upstream Reynolds number on the maximum Nusselt number for an axisymmetric abrupt expansion experiment with $d/D = 0.4$

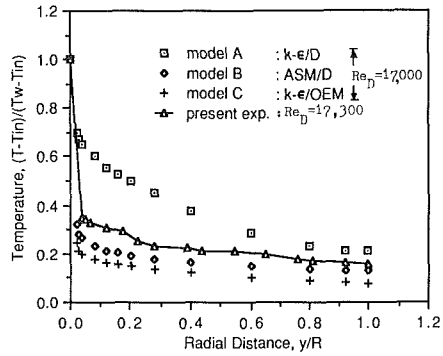

Fig. 11(A) Predicted temperature profiles (Yap, 1987): k-ϵ/D: k-ϵmodel with damping; ASM/D: algebraic stress model with damping; k-ϵ/OEM: k-ϵ/one equation model ($x/H = 10$)

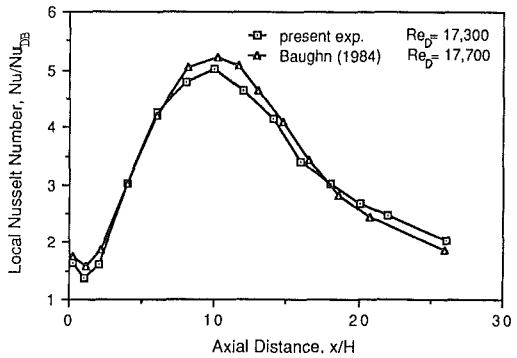

Fig. 10 Comparison of the present results with Baughn (1984)

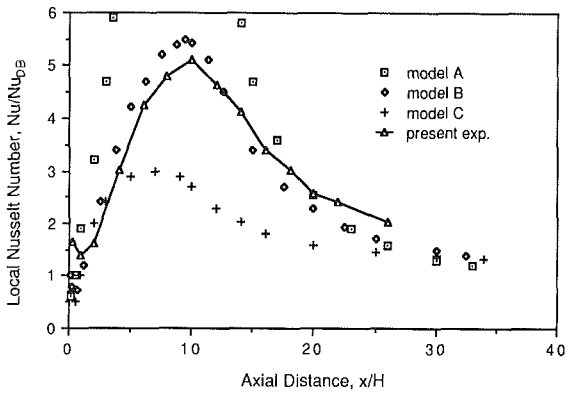

Fig. 11(B) Predicted Nusselt number distributions (Yap, 1987)

1987). Vogel and Eaton (1985) have convincingly shown that for the flow over a backward-facing step the peak Nusselt number essentially coincides with the reattachment point and, in view of the close similarity in the flows, it is reasonable to assume that the same is true in the axisymmetric abrupt expansion also.

The minimum in Nusselt number at $x/H \cong 1.0$ first reported by Baughn et al. (1984) is also clearly evident in the present data (see Fig. 8). Indeed, we see from Fig. 10 that the Nusselt number distribution along the tube is very similar for the uniform wall heat flux and uniform wall temperature boundary conditions. The slight differences may be partly due to experimental uncertainty, but are also a consequence of the difference in the thermal boundary condition (uniform wall temperature in this case and uniform wall heat flux for Baughn et al. (1984)), especially at $x/H \cong 1.0$ where the minimum Nusselt number is consistently lower for the uniform wall temperature case.

Finally to emphasize the need for temperature profiles as well as surface heat fluxes in assessing a computational scheme, Figs. 11(A) and 11(B) compare the present experiments with the finite difference computations of Yap (1987) employing three different models of turbulent transport. The details of these computations are reported by Yap (1987) and are beyond the scope of the present paper. Here we wish to note simply that Model B would be judged highly successful from considering only the Nusselt number distribution. The availability of the experimental temperature profiles however enables us to conclude that while the overall "thermal resistance" given by this model is about correct at any position, the radial variation of the effective conductivity must be significantly in error.

Conclusions

1 We have obtained good quality heat transfer data in the region downstream of an axisymmetric abrupt expansion for a uniform wall temperature boundary condition with relatively low uncertainties in the results using a heat flux sensor for the direct measurement of the heat flux to the fluid. We have also obtained mean velocity and temperature data using various probes, as well as flow visualization data using tufts downstream of the abrupt expansion.

2 For an upstream-to-downstream diameter ratio of 0.4, the location of the peak Nusselt number progressively shifts upstream from 12 to 9 step heights from the expansion step as the downstream Reynolds number is raised from 4300 to 44,500. This trend is consistent with the more rapid decay of the streamwise centerline velocity at higher Reynolds number, which is associated with a faster initial growth of the mixing layer, since the more rapid the decay the shorter the recirculation region. This upstream movement of the maximum Nusselt number is accompanied by a decrease in its magnitude from 5.6 to 3.9 times greater than the corresponding fully developed tube flow values for the range of Re_D investigated.

3 Flow visualization experiments using tufts show that the position of the average reattachment point has approximately the same dependency on Reynolds number as the position of the maximum Nusselt number.

4 The magnitude of the maximum Nusselt number shows a strong dependence on the Reynolds number. Over the present range of Reynolds numbers, and for an expansion ratio of 0.4, the maximum Nusselt number is well correlated by $0.2\ Re_d^{2/3}$, which was also found to fit the results for a uniform wall heat flux boundary condition. (It should be

noted that prior to the present study, however, many experiments for air flow had implied a Reynolds number exponent of nearly 0.8, apparently due to conduction losses in the tube walls.)

5 The experimental results show that a minimum Nusselt number occurs at about 1 step height from the abrupt expansion step, with an increase of the heat transfer rate as the upsteam corner region is approached, indicating the possible existence of a secondary recirculation in the upstream corner near the step of the abrupt expansion. The magnitudes of the minimum Nusselt number are up to about 1.4 times greater than the fully developed pipe flow values.

6 For the two different thermal wall boundary conditions (i.e., uniform wall heat flux and uniform wall temperature) the heat transfer characteristics (magnitude and position of the minimum and maximum Nusselt numbers) in the recirculation and reattachment regions downstream of the abrupt expansion are in good agreement with each other.

7 The temperature profiles show that due to a vigorous turbulent mixing in the recirculation region the great majority of the temperature drop between the wall and the centerline occurs within a thin annulus extending from the wall a distance of only 5 percent of the tube radius. This suggests that the heat transport is dominated by the turbulent mixing processes taking place in the near-wall layer.

Acknowledgments

The authors gratefully acknowledge the support of the National Science Foundation for this research under Grant No. MEA-8103657. The program manager was Dr. Win Aung. Authors are listed in alphabetical order.

References

Baughn, J. W., Hoffman, M. A., Launder, B. E., and Takahashi, R. K., 1984, "Local Heat Transfer Downstream of an Abrupt Expansion in a Circular Channel With Constant Wall Heat Flux," ASME JOURNAL OF HEAT TRANSFER, Vol. 106, pp. 789–796.

Baughn, J. W., Hoffman, M. A., and Lee, Daehee, 1986, "Heat Transfer Measurements Downstream of an Abrupt Expansion in a Circular Duct With a Constant Wall Temperature," presented at the ASME Winter Annual Meeting, Anaheim, CA, Paper No. 86-WA/HT-100.

Baughn, J. W., Hoffman, M. A., Takahashi, R. K., and Lee, Daehee, 1987a, "Heat Transfer Downstream of an Expansion in the Transition Reynolds Number Regime," ASME JOURNAL OF HEAT TRANSFER, Vol. 109, pp. 43–48.

Baughn, J. W., Hoffman, M. A., and Lee, Daehee, 1987b, "An Instrument for the Measurement of the Heat Flux Distribution along a Contour of a Surface at Uniform Temperature," 24th AIChE/ASME National Heat Transfer Conference, Pittsburgh, PA, HTD-Vol. 71, pp. 11–17.

Baughn, J. W., Hoffman, M. A., Lee, Daehee, and Yap, C., 1987c, "Turbulent Velocity and Temperature Profiles Downstream of an Abrupt Expansion in a Circular Duct With a Constant Wall Temperature," *Proceedings of the ASME/JSME Thermal Engineering Joint Conference*, Honolulu, HI, Vol. 1, pp. 449–454.

Ede, A. J., Hislop, C. I., and Morris, R., 1956, "Effect on the Local Heat Transfer Coefficient in a Pipe of an Abrupt Distribution of the Fluid Flow: Abrupt Convergence and Divergence of Diameter Ratio 2:1," *Proc. Inst. of Mech. Engrs.*, London, Vol. 170, No. 38, pp. 1113–1126.

Kline, S. J., and McKlintock, F. A., 1953, "Describing Uncertainties in Single Sample Experiments," *Mechanical Engineering*, Vol. 75, No. 1, pp. 3–8.

Kraabel, J. S., Baughn, J. W., and McKillop, A. A., 1980, "An Instrument for the Measurement of Heat Flux From a Surface With Uniform Temperature," ASME JOURNAL OF HEAT TRANSFER, Vol. 102, pp. 576–578.

Krall, K. M., and Sparrow, E. M., 1961, "Turbulent Heat Transfer in the Separated, Reattached and Redevelopment Regions of a Circular Tube," ASME JOURNAL OF HEAT TRANSFER, Vol. 83, pp. 131–136.

Laufer, J., 1954, "The Structure of Turbulence in Fully Developed Pipe Flow," NACA Tech Report No. 1174.

Lee, Daehee, 1984, "Measurement of the Turbulent Heat Transport Downstream of an Abrupt Expansion in a Circular Duct With a Constant Wall Temperature," M.S. Thesis, University of California, Davis.

Lee, Daehee, 1987, "Turbulent Heat Transfer and Fluid Flow Measurements Downstream of Abrupt Expansions and in a Cavity of a Circular Tube at a Uniform Wall Temperature," Ph.D. Dissertation, University of California, Davis.

Vogel, J. C., and Eaton, J. K., 1985, "Combined Heat Transfer and Fluid Dynamics Measurements Downstream of a Backward-Facing Step," ASME JOURNAL OF HEAT TRANSFER, Vol. 107, pp. 922–929.

Yap, C., 1987, "Turbulent Heat and Momentum Transfer in Recirculating and Impinging Flows," Ph.D. Dissertation, The University of Manchester, Faculty of Technology, England.

Zemanick, P. P., and Dougall, R. S., 1970, "Local Heat Transfer Downstream of Abrupt Circular Channel Expansion," ASME JOURNAL OF HEAT TRANSFER, Vol. 92, pp. 53–60.

J. W. Baughn
Professor,
Department of Mechanical Engineering,
University of California,
Davis, CA 95616
Mem. ASME

P. T. Ireland
St. Anne's College and Department of
Engineering Science,
Oxford University,
Oxford, United Kingdom OX26HS
Fellow ASME

T. V. Jones
Professor,
St. Catherine's College and Department of
Engineering Science,
Oxford University,
Oxford, United Kingdom OX26HS

N. Saniei
Lecturer,
Department of Mechanical Engineering,
University of California,
Davis, CA 95616

A Comparison of the Transient and Heated-Coating Methods for the Measurement of Local Heat Transfer Coefficients on a Pin Fin

Measurements of the local heat transfer coefficients on a pin fin (i.e., a short cylinder in crossflow) in a duct have been made using two methods, both of which employ liquid crystals to map an isotherm on the surface. The transient method uses the liquid crystal to determine the transient response of the surface temperature to a change in the fluid temperature. The local heat transfer coefficient is determined from the surface response time and the thermal properties of the substrate. The heated-coating method uses an electrically heated coating (vacuum-deposited gold in this case) to provide a uniform heat flux, while the liquid crystal is used to locate an isotherm on the surface. The two methods compare well, especially the value obtained near the center stagnation point of the pin fin where the difference in the thermal boundary condition of the two methods has little effect. They are close but differ somewhat in other regions.

Introduction

The measurement of local heat transfer coefficients for complex geometries with their correspondingly complex flows is important in many applications. For example, in gas turbines local heat transfer coefficients are needed for designing blade coolant passages, and in electronic and computer packages local heat transfer coefficients are needed to design cooling systems to prevent chip overheating. Measurements of the local heat transfer coefficient provide both needed design data and a check on computational models for the prediction of heat transfer for such complex flows.

Two experimental techniques that have been used for the global measurement of local heat transfer coefficients over a surface are the transient method (Ireland and Jones, 1985) and the heated-coating method (Baughn et al., 1985). Other techniques for local measurements include the heat flux sensor method (Baughn et al., 1987), which uses a sensor at selected positions, and the naphthalene method (Sparrow et al., 1984), which makes global measurements of mass transfer that are then related to heat transfer by analogy. Direct comparisons of different methods under identical flow conditions are important. A recent comparison of the transient method and the heated-coating method for heat transfer to the curved wall of a wind tunnel by Jones and Hippensteele (1987) has shown that these two methods produce consistent results for similar flows, although there were large differences in the measurements due to their differing thermal boundary conditions.

This paper deals with a comparison of the transient and the heated-coating methods for the case of flow around a pin fin in a duct where a centerline stagnation point exists. At the stagnation point the heat transfer coefficient should be independent of the thermal boundary condition. Significant improvements in these two methods have recently been made by adapting liquid crystals for the surface temperature measurement. For example, Ireland and Jones (1986) have used the transient method with a chiral nematic (thermochromic) liquid crystal on the surface of a plastic (Perspex) substrate. These were also the methods used by Jones and Hippensteele (1987). Baughn et al. (1986a) have used the heated-coating method by applying the same liquid crystal directly on the surface of an ultrathin (vacuum-deposited) electrically heated gold coating.

An apparatus that was previously used for a study of pin fin heat transfer using the transient method (see Ireland and Jones, 1986) was selected for the present comparison for several reasons: it provides an interesting and important complex flow; a full set of transient data existed; and a heated-coating pin fin could be easily substituted in the existing apparatus for the transient method pin fin previously used. Flow around a pin fin (or pedestal, i.e., a short cylinder mounted across a duct with flow in the duct) is a complex three-dimensional flow with flow separation and vortices. It is a geometry of interest in such areas as internal blade cooling in gas turbines and electronic cooling systems.

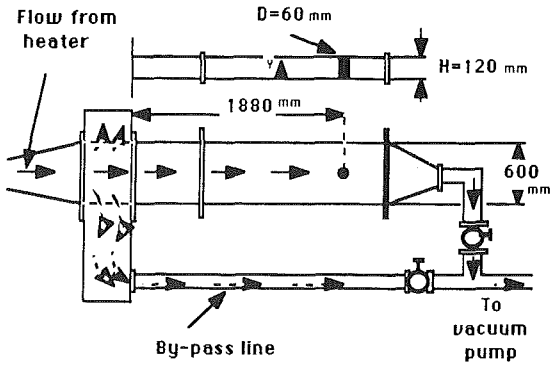

Fig. 1 Diagram of the apparatus

Contributed by the Heat Transfer Division and presented at the 33rd International Gas Turbine and Aeroengine Congress and Exhibition, Amsterdam, The Netherlands, June 6–9, 1988. Manuscript received by the Heat Transfer Division March 31, 1988; revision received January 23, 1989. Paper No. 88-GT-180. Keywords: Finned Surfaces, Flow Separation, Measurement Techniques.

Experimental Apparatus

A basic diagram of the duct used in this study is shown in Fig. 1. The duct was 0.6 m wide and 0.12 m high. Diagrams of the pin fin design for the transient method and for the heated-coating method are shown in Figs. 2(*a*) and 2(*b*), respectively. The pin fin diameter was 6.0 cm, which corresponds to an L/D of 2.0. It was mounted 1.88 m downstream of a bypass section giving an upstream development length of approximately 16 duct heights. Upstream of the bypass section there were heater and diffuser sections.

When used with the transient method the flow is initially stabilized in the bypass line with no flow in the test duct. In this case the heaters are used to raise the flow air temperature to 60–70°C, while the apparatus remains at ambient temperature. The test is begun by simultaneously closing the bypass valve and opening the in-line valve. Details on the experimental procedure for the transient method with this apparatus are given by Ireland (1987).

When used with the heated-coating method, the flow is unheated and is stabilized directly in the main duct containing the pin fin. The flow rate was adjusted so that the pin fin Reynolds number based on the pin diameter and the center velocity was 18,000 since a complete set of data using the transient method was available at this Reynolds number. The air velocity distribution was measured just upstream of the pin fin with a pitot tube and the air temperature distribution was measured near the same location with a calibrated thermocouple.

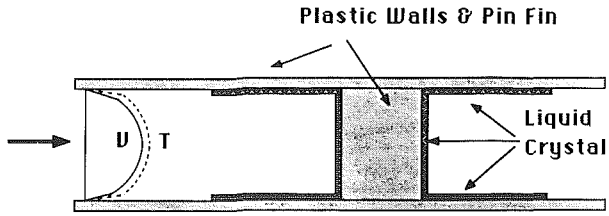

Fig. 2(*a*) Diagram of transient method

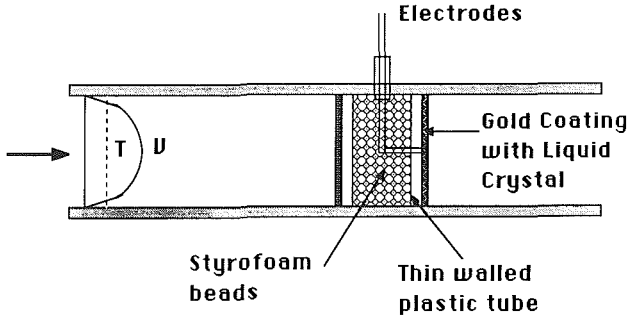

Fig. 2(*b*) Diagram of heated-coating method

Transient Method

The transient method has a long history and a complete review is beyond the scope of this paper. It was used for many years at high temperatures in shock tunnels for the measurement of heat flux (Schultz and Jones, 1973). In these applications the surface was usually a ceramic and the surface temperature was measured with a film resistance thermometer (usually platinum). Although some early external thermal paint measurements are reviewed by Schultz and Jones (1973) and Jones (1977), the use of the transient technique at lower temperatures for internal flows has been developed more recently. Clifford et al. (1983) first used phase change paints on acrylic (Perspex) models to study heat transfer within gas turbine blade cooling passages. More recently Ireland and Jones (1985, 1986) have used liquid crystals on the surface as the temperature sensor. The technique can be used for very complex geometries including curved ducts (Metzger and Larson, 1986) and complex gas turbine blade cooling passages (Clifford et al., 1983; Saabas et al., 1987).

The basic principles and the data reduction for this method are described by Ireland and Jones (1985, 1986) and Ireland (1987) so only a brief review is given here. The transient method uses the surface temperature transient in response to a fluid temperature change as a measure of the surface heat flux and the corresponding heat transfer coefficient. For example, if a step change in the fluid temperature is induced, the surface temperature for a semi-infinite body with one-dimensional heat transfer is given by

$$(T_w - T_i)/(T_a - T_i) = 1 - e^{\gamma^2}\,\mathrm{erfc}(\gamma)$$
$$\gamma = h\sqrt{t}\,/\,\sqrt{\rho c k_w} \tag{1}$$

When the surface has a low thermal diffusivity (e.g., plastic), this one-dimensional assumption is often a good approximation, since the surface temperature response is limited to a thin layer near the surface and lateral conduction can be shown to be small (Dunne, 1983). In the present work, although the inlet fluid temperature is very close to a step change, the actual air temperature transient is measured and used in the data reduction. Although both thermal paints and melting point coatings (see Clifford et al., 1983, and Metzger et al., 1986, respectively) and liquid crystals (Ireland and Jones, 1986) have been used for the surface temperature measurement, liquid crystals have been found to be particularly suitable since their response is repeatable and their color play can be easily recorded with a video system (Ireland and Jones, 1986). In the present study the pin fin and duct walls are Perspex and the liquid crystal is silk-screen printed on the inside surface duct walls and on the pin fin (see Fig. 2*a*).

The video recording provides the time and location of the color play on the surface. In the present study the initial surface temperature is near 20°C, the flow temperaure is approximately 70°C, and three liquid crystals were used simultaneously in a single coating. The crystal color band

Nomenclature

A = area of gold coating
c = specific heat of substrate
D = diameter of pin fin
f = gold coating nonuniformity factor
$\mathrm{F_g}$ = Frössling number = $\mathrm{Nu}/\sqrt{\mathrm{Re}}$
h = heat transfer coefficient
H = pin fin and pedestal height
I = gold coating current
k_w = thermal conductivity of substrate
Nu = local Nusselt number based on D
q_c = convective heat flux
q_L = heat flux loss due to conduction
Re = Reynolds number based on D and U_{cL}
t = time
T_a = air temperature
T_i = initial wall temperature
T_{Lc} = liquid crystal temperature
T_w = wall surface temperature at time t
U = velocity at position y
U_{cL} = centerline velocity
V = voltage across gold coating
y = distance from duct wall
z = distance from pin centerline
ϵ = emissivity of liquid crystal surface
θ = angle around pin fin or cylinder as measured from the front
ρ = density of plastic substrate
σ = Stefan-Boltzmann constant

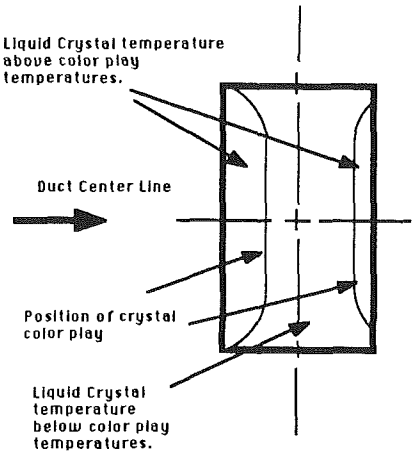

Fig. 3 Sketch of the pin fin from video frame showing location of the liquid crystal color play for the transient method (viewed from the side, $\theta = 90$ deg)

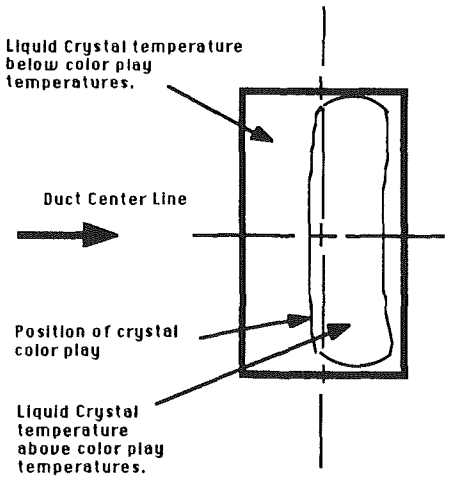

Fig. 4 Sketch of the pin fin from a 35 mm photograph showing location of the liquid crystal color play for the heated-coating method (viewed from the side, $\theta = 90$ deg)

(e.g., the range of temperature over which the colors occur) was approximately 1°C and occurred at temperatures of 31, 35, and 41.2°C. Figure 3 shows the location of the liquid crystal colors at a particular time as sketched from a video frame. The line of constant color on this sketch would represent an isotherm and is a line of constant heat transfer coefficient.

The uncertainty in the measurement of the heat transfer coefficient with the transient method has been estimated for these results using standard uncertainty methods (Kline and McKlintock, 1953), with odds of 20:1. The individual contributions of each measurand to the total uncertainty are given in Table 1. The total uncertainty is estimated as 7.2 percent. The uncertainty in the Reynolds number was estimated to be approximately 1 percent, which is much lower than that of the heat transfer coefficient, so the total uncertainty in the Frössling number is essentially the same as that of the Nusselt number (and the heat transfer coefficient). The uncertainty in the position around the pin fin is estimated to be ±5° on the front and rear and ±2° on the side and the uncertainty in the position along the pin fin (z) is estimated to be ±1.0 mm.

Heated-Coating Method

The heated-coating method also has a long history and again space does not allow a complete review here. It has recently been described by Baughn et al. (1985, 1986a), so only a brief description is included here. In the heated-coating

Table 1 Uncertainty analysis: contribution of individual measurands

x_i	Value	δx_i	$\frac{\delta x_i}{\mathrm{Nu}_i}\frac{\partial \mathrm{Nu}\times 100}{\partial x_i}$
A. Transient Method			
t	12 s	0.1	0.8
ρck	569	29	5.0
$T_{Lc}-T_a$	14 K	0.5	3.6
T_i-T_a	41.5 K	0.3	0.7
			Nu uncertainty = 7.2 percent
B. Heated-Coating Method			
I	0.86 A	0.01	1.2
V	7.6 V	0.1	1.3
A	0.0226 m^2	0.00045	2.0
f	1.0	0.02	2.0
ϵ	0.5	0.1	2.4
$T_{Lc}-T_a$	10.2 K	0.15	1.0
T_a	31.6°C	0.2	2.0
			Nu uncertainty = 4.7 percent

method a very thin conductive coating (vacuum-deposited gold in this case) on the surface of a plastic substrate (a thin polyester sheet mounted to a plastic tube in this case) is electrically heated. Conduction in the plastic substrate is generally quite small (less than 1 percent of the surface heating) so that the surface boundary condition is very close to a uniform heat flux. An early example of this is the copper coating used in a flat duct by Hatton and Woolley (1972). Several methods for measuring the surface temperature have been used including thermocouples (Baughn et al., 1985) and the resistance of the coating itself (Oker and Merte, 1981). In recent developments Hippensteele et al. (1983, 1985, 1987), Simonich and Moffat (1982), and Baughn et al. (1986a) have used liquid crystals to map the surface isotherms. Since the heat flux can be adjusted by changing the electrical voltage on the electrodes, the surface temperatures can be increased or decreased. When this is done an isotherm on the surface corresponds to a line of constant heat transfer coefficient. The local heat transfer coefficient at the position of the color play is then given by

$$h = q_c/(T_{Lc}-T_a) \tag{2}$$

where q_c is given by

$$q_c = fIV/A - \epsilon\sigma(T_{Lc}^4 - T_a^4) - q_L \tag{3}$$

and f is the ratio of the local electrical heating to the average heating and accounts for nonuniformity in the coating. The radiation correction assumes the surrounding walls have a large area and are at the ambient temperature.

In the present study, a narrow band liquid crystal with a color play of 0.7°C at approximately 42°C is used. The ambient temperature was approximately 25°C. The position of the color play is moved on the surface by adjusting the electrical heating. A typical photograph showing the color distribution for a particular power setting is shown in Fig. 4. A line of constant color represents both an isotherm and a line of constant heat transfer coefficient, the value being given by equation (2).

The uncertainty in the measurement of the heat transfer coefficient has been estimated for these measurements at 4.7 percent. The individual contributions of the measurands are shown in Table 1.

Since at these low values of the heat transfer coefficient the thermal radiation correction can be as high as 3–7 percent, the uncertainty caused by the emissivity may be significant. Measurements of the emissivity were made by inserting the pin fin in a vacuum chamber. For the thin silk-screened liquid crystal coating used here the emissivity was found to be 0.5 with an uncertainty of 0.1. A thicker brushed-on coating of liquid crystal had an emissivity of 0.9. As shown in Table 1, the uncertainty in emissivity is the largest contributor to the total uncertainty. Another important source of uncertainty is f

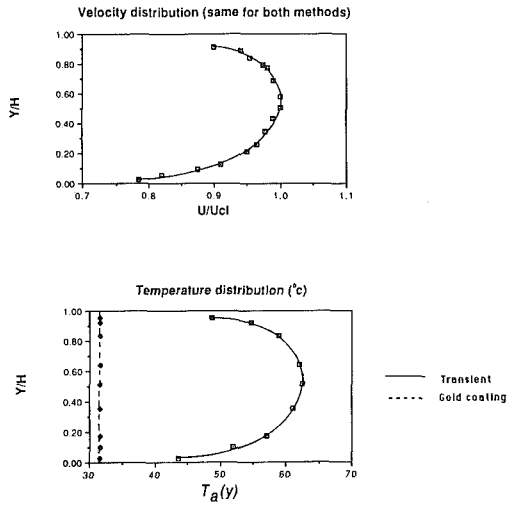

Fig. 5 Typical velocity and temperature distribution upstream of the pin fin

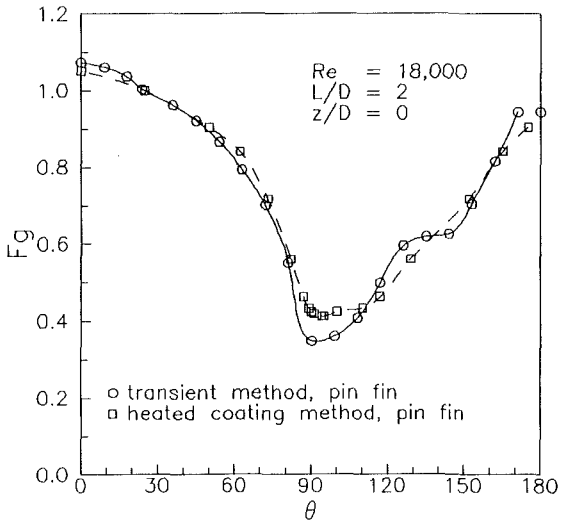

Fig. 6 Comparison of transient and heated-coating methods for a pin fin at the centerline (Z/D = 0)

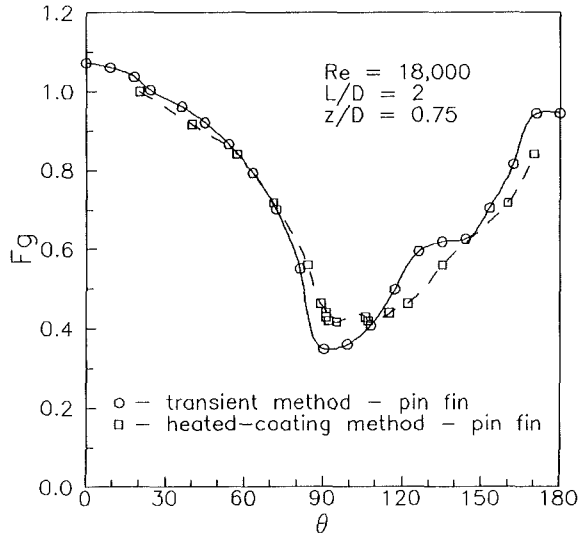

Fig. 7 Comparison of transient and heated-coating methods for a pin fin at Z/D = 0.75

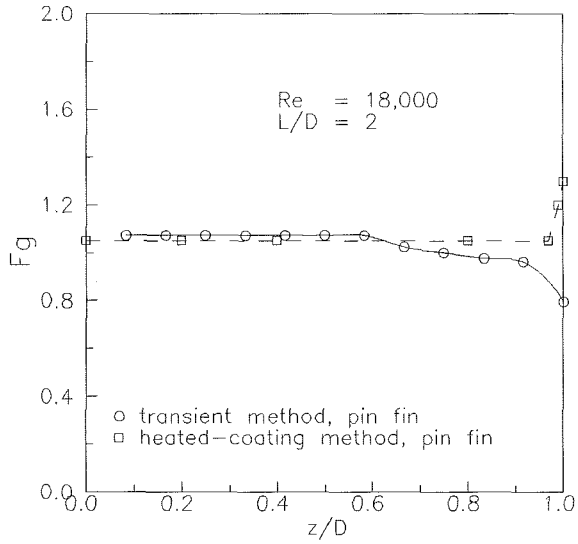

Fig. 8 Comparison of transient and heated-coating methods along the leading edge of the pin fin

(the nonuniformity in the coating). For a small carefully selected sheet such as used here the nonuniformity may be as low as 2 percent as given here. In general, it may be much higher (up to 6 percent).

The uncertainty in the Reynolds number is estimated at 1 percent, which contributes little to the total uncertainty in the Frössling number. The uncertainty in position is the same as that for the transient method.

Results

The velocity and temperature profiles upstream of the pin fin are shown in Figs. 5(*a*) and 5(*b*), respectively. Although the velocity profiles are the same, the upstream air temperature distributions are quite different. The air has been heated for the transient method and has a distribution across the channel, while it is at ambient temperature and is uniform for the heated-coating method. The distribution for the transient method is caused by the heat transfer to the upstream duct walls, while in the heated-coating method the walls are at ambient temperature (the same as the air) and act as adiabatic boundary condition. Only the pin fin surface is heated for the heated-coating method results reported here.

The heat transfer coefficient distribution around the pin (given in terms of the Frössling number based on the centerline velocity, pin fin diameter, and centerline temperature) is shown in Fig. 6 for the centerline ($z/D = 0.0$) and in Fig. 7 for a position farther out along the pin fin ($z/D = 0.75$). In both methods and for both of these distributions the heat transfer coefficient is based on the centerline air temperature measured just upstream of the pin fin. The Reynolds number is based on the centerline velocity near the same position.

For the centerline position ($z/D = 0.0$) the results from both methods are very similar and agree well within the estimated uncertainties at the stagnation point. Farther out on the pin fin ($z/D = 0.75$) the heat transfer coefficients over the front of the pin fin for the heated-coating methods are higher than those for the transient method. This is a consequence of the difference in the temperature distribution across the duct for the transient method and heated-coating method. The heat transfer coefficients are based on the centerline air temperature and the wall boundary conditions are different in both cases. As a result, as we approach the duct wall, the two methods diverge. This is shown in Fig. 8 where the Frössling number distribution along the leading edge of the pin fin is compared.

In order to understand these results, it is helpful to recall the effect of wall thermal boundary condition on the heat transfer coefficient distribution around an infinite cylinder (Papell, 1981). The stagnation line values for the infinite cylinder should be independent of the thermal boundary conditions. However, the distribution of the heat transfer coefficient around the cylinder is quite different for different boundary conditions. A cylinder with uniform heat flux boundary condition has a higher heat transfer coefficient on the front and in the region of separation than one with a uniform temperature. At the rear of the cylinder the heat transfer coefficient for the uniform temperature boundary condition increases rapidly and becomes greater than that for the uniform heat flux.

The heated-coating method provides a uniform heat flux boundary condition and the transient method approximates a uniform wall temperature boundary condition. The results shown in Figs. 6 and 7 are consistent with these boundary condition effects.

Conclusions

Heat transfer results for the transient and heated-coating methods have been compared for a pin fin in a duct and found to compare well in absolute value in the stagnation region. Differences observed away from the stagnation point are consistent with the effect of the different thermal boundary conditions imposed by the two methods. This comparison increases the confidence in both of these powerful methods. The transient method (which approximates a uniform temperature boundary condition) is very useful for handling very complex geometries. The heated-coating method (which provides a uniform heat flux boundary condition) is restricted to geometries with curvature in one direction, but provides relatively low uncertainty absolute results, which are useful for comparison to computational results.

Acknowledgments

The authors gratefully acknowledge the support of the University of California UERG program, the S.E.R.C., the Ministry of Defence (procurement executive) and Rolls Royce Ltd., and kind permission of Rolls Royce to publish the work. The technical support of Mr. P. Timms is also gratefully acknowledged. The authors are listed in alphabetical order.

References

Baughn, J. W., Takahashi, R. K., Hoffman, M. A., and McKillop, A A., 1985, "Local Heat Transfer Coefficient Measurements Using an Electrically Heated Thin Gold-Coated Sheet," ASME JOURNAL OF HEAT TRANSFER, Vol. 107, pp. 953–959.

Baughn, J. W., Hoffman, M. A., and Makel, D. B., 1986a, "Improvements in a New Technique for Measuring Local Heat Transfer Coefficients," *Review of Scientific Instruments*, Vol. 57, pp. 650–654.

Baugh, J. W., Elderkin, A. A., and McKillop, A. A., 1986b, "Heat Transfer From a Single Cylinder, Cylinders in Tandem, and Cylinders in the Entrance Region of a Tube Bank With a Uniform Heat Flux," ASME JOURNAL OF HEAT TRANSFER, Vol. 108, pp. 386–391.

Baughn, J. W., Iacovides, H., Jackson, D. C., and Launder, 1987, "Local Heat Transfer Measurements in Turbulent Flow Around a 180-Deg Pipe Bend," ASME JOURNAL OF HEAT TRANSFER, Vol. 109, pp. 43–48.

Clifford, R. J., Jones, T. V., and Dunne, S. T., 1983, "Techniques for Obtaining Detailed Heat Transfer Coefficient Measurements Within Gas Turbine Blade and Vane Cooling Passages," ASME Paper 83-GT-58.

Dunne, S. T., 1983, "A Study of Flow and Heat Transfer in Gas Turbine Cooling Passages," D. Phil. Thesis, Oxford University, Oxford, United Kingdom.

Hatton, A. P., and Wooley, N. H., 1972, "Heat Transfer in Two-Dimensional Turbulent Confined Flows," *Proceedings of the Institute of Mechanical Engineers*, Vol. 186, pp. 625–633.

Hippensteele, S. A., Russell, L. M., and Stepka, F. S., 1983, "Evaluation of a Method for Heat Transfer Measurements and Thermal Visualization Using a Composite of a Heater Element and Liquid Crystals," ASME JOURNAL OF HEAT TRANSFER, Vol. 105, pp. 184–189.

Hippensteele, S. A., Russell, L. M., and Torres, F. J., 1985, "Local Heat Transfer Measurements on a Large-Scale Model Turbine Blade Airfoil Using a Composite of a Heater Element and Liquid Crystals," ASME *Journal of Engineering for Gas Turbines and Power*, Vol. 107, pp. 953–960.

Hippensteele, S. A., Russell, L. M., and Torres, F. J., 1987, "Use of a Liquid Crystal and Heater Element Composite for Quantitative, High-Resolution Heat-Transfer Coefficients on a Turbine Airfoil Including Turbulence and Surface-Roughness Effects," NASA TM 87355.

Ireland, P. T., and Jones, T. V., 1985, "The Measurement of Local Heat Transfer Coefficients in Blade Cooling Geometries," *AGARD Conference Proceedings No. 390*, Paper No. 28.

Ireland, P. T., and Jones, T. V., 1986, "Detailed Measurements of Heat Transfer on and Around a Pedestal in Fully Developed Passage Flow," *Proceedings of the International Heat Transfer Conference*, Vol. 3, pp. 975–980.

Ireland, P. T., 1987, "Internal Cooling of Turbine Blades," D. Phil. Thesis, Oxford University, Oxford, United Kingdom.

Jones, T. V., 1977, "Heat Transfer, Skin Friction, Total Temperature and Concentration Measurements," *Measurements of Unsteady Fluid Dynamic Phenomena*, B. E. Richards, ed., McGraw-Hill, New York, pp. 63–102.

Jones, T. V., and Hippensteele, S. A., 1987, "High-Resolution Heat-Transfer-Coefficient-maps Applicable to Compound Surfaces Using Liquid Crystals in Transient Wind Tunnels," *24th ASME/AIChE National Heat Transfer Conference*, ASME HTD-Vol. 71.

Kline, S. J., and McKlintock, F. A., 1953, "Describing Uncertainties in Single Sample Experiments," *Mechanical Engineering*, Vol. 75.

Metzger, D. E., and Larson, E. E., 1986, "Use of Melting Point Surface Coatings for Local Convective Heat Transfer Measurements in Rectangular Channel Flows with 90-deg Turns," ASME JOURNAL OF HEAT TRANSFER, Vol. 108, pp. 48–54.

Oker, E., and Merte, H., Jr., 1981, "Semi-transparent Gold Film as Simultaneous Surface Heater and Resistance Thermometer for Nucleate Boiling Studies," ASME JOURNAL OF HEAT TRANSFER, Vol. 103, pp. 65–68.

Papell, S. S., 1981, "Influence of Thermal Boundary Conditions on Heat Transfer from a Cylinder in Crossflow," NASA Technical Paper 1894.

Saabas, H. J., Arora, S. C., and Messeh, W. Abdel, 1987, "Application of the Transient Test Technique to Measure Local Heat Transfer Coefficients Associated With Augmented Airfoil Cooling Passages," ASME Paper No. 87-GT-212.

Schultz, D. L., and Jones, T. V., 1973, "Heat Transfer Measurements in Short Duration Hypersonic Facilities," Agardograph No. 165.

Simonich, J. C., and Moffat, R. J., 1982, "A New Technique for the Measurement of Heat Transfer Coefficient," *Review of Scientific Instruments*, Vol. 53, pp. 678–683.

Sparow, E. M., Stahl, T. J., and Traub, P., 1984, "Heat Transfer Adjacent to the the Attached End of a Cylinder in Crossflow," *International Journal of Heat and Mass Transfer*, Vol. 27, pp. 233–242.

Turbulent Forced Convection Inside a Parallel-Plate Channel With Periodic Variation of Inlet Temperature

W. S. Kim

M. N. Özişik

Mechanical and Aerospace Engineering Department,
North Carolina State University,
Raleigh, NC 27695-7910

The analysis of heat transfer in turbulent forced convection subject to a periodically varying inlet temperature leads to a nonclassical Sturm–Liouville type eigenvalue problem for which no known solution is available. In this work a new methodology is developed to alleviate the need for the solution of a complex eigenvalue problem in the analysis of turbulent forced convection inside a parallel-plate channel with a periodicially varying inlet temperature and a uniform constant wall temperature. In this approach, the problem is transformed to the solution of a system of coupled ordinary differential equations in the complex domain, which could readily be solved. For the cases considered it is demonstrated that the solutions obtained from the decoupled system, referred to as the lowest-order solution, produce sufficiently accurate results. The variation of the amplitudes and phase lag of both fluid bulk temperature and the wall heat flux along the channel is investigated and a simple approximate analytic formula is developed for determining the variation of the phase lag for the bulk temperature along the channel.

Introduction

There are many engineering applications of forced convection inside ducts in which the inlet temperature of the fluid is subjected to periodic variation. The solution of heat transfer problems of this type usually leads to the solution of complex eigenvalue problems for which no known solutions are available. The principal difficulty in the analysis of such problems has been the finding of a solution for the resulting complex eigenvalue problem.

Sparrow and de Farias (1968) investigated the transient slug flow in a parallel-plate channel wherein the thermal conditions at the wall were determined by the dynamics of the problem. The fluid inlet temperature was assumed to vary periodically in a sinusoidal manner with an arbitrary frequency, thereby facilitating a Fourier series synthesis to accommodate other periodic variations. Kakaç (1975) considered the general problem of the decay of time-varying inlet temperature along the duct, but numerical results could not be presented for the formal solutions because the associated complex eigenvalue problem could not be solved. Kakaç and Yener (1973, 1979) obtained formal solutions of the energy equation of transient forced convection for the decay of a periodically varying inlet temperature for fully developed turbulent flow between two parallel plates; but as the resulting complex eigenvalue problem could not be solved, they resorted to an experimental technique based on a frequency response approach. Only the first eigenquantities could be determined and the phase lag analysis was limited to lower values of the Reynolds number because the phase differences could not be easily determined as the Reynolds number increased. More recently, Cotta and Özişik (1986) studied analytically the laminar forced convection with periodic variations of inlet temperature. They used a variation of the generalized integral transform technique advanced by Özişik and Murray (1974) in order to circumvent the need to solve the complex eigenvalue problem. In this work, we employ the methodology used by Cotta and Özişik (1986) to solve the forced convection in fully developed turbulent flow between two parallel plates subjected to a periodic variations of inlet temperature.

Contributed by the Heat Transfer Division for publication in the JOURNAL OF HEAT TRANSFER. Manuscript received by the Heat Transfer Division May 9, 1988; revision received December 20, 1988. Keywords: Forced Convection.

Analysis

We consider transient heat transfer to the incompressible fully developed turbulent flow in the thermal entrance region of a smooth, parallel-plate channel subjected to periodically varying inlet temperature. We assume initial transients have passed and a quasi-steady-state condition is established. Axial conduction, viscous dissipation, free convection, and wall conjugation effects are neglected.

The mathematical formulation of the problem includes the energy equation given in the form

$$\frac{\partial T(x, y, t)}{\partial t} + u(y)\frac{\partial T(x, y, t)}{\partial x} = \frac{\partial}{\partial y}\left[(\alpha+\epsilon_h)\frac{\partial T(x, y, t)}{\partial y}\right] \quad \text{in } 0<y<b,\ x>0,\ t>0 \tag{1a}$$

and the boundary conditions taken, respectively, as

$$T(0, y, t) = T_o + \Delta T_o e^{i\omega t}, \qquad 0\le y\le b, \qquad t>0 \tag{1b}$$

$$\left.\frac{\partial T(x, y, t)}{\partial y}\right|_{y=0} = 0, \qquad x>0, \qquad t>0 \tag{1c}$$

$$T(x, b, t) = T_o, \qquad x>0, \qquad t>0 \tag{1d}$$

The problem is expressed in the dimensionless form as

$$\frac{\partial \theta(\xi, \eta, \tau)}{\partial \tau} + w(\eta)\frac{\partial \theta(\xi, \eta, \tau)}{\partial \xi} = \frac{\partial}{\partial \eta}\left[\epsilon(\eta)\frac{\partial \theta(\xi, \eta, \tau)}{\partial \eta}\right] \quad \text{in } 0<\eta<1,\ \xi>0,\ \tau>0 \tag{2a}$$

$$\theta(0, \eta, \tau) = e^{i\Omega\tau}, \qquad 0\le\eta\le 1, \qquad \tau>0 \tag{2b}$$

$$\left.\frac{\partial \theta(\xi, \eta, \tau)}{\partial \eta}\right|_{\eta=0} = 0, \qquad \xi>0, \qquad \tau>0 \tag{2c}$$

$$\theta(\xi, 1, \tau)=0, \qquad \xi>0, \qquad \tau>0 \tag{2d}$$

Since only the periodic response is of interest, we seek a solution in the form

$$\theta(\xi, \eta, \tau)=\tilde{\theta}(\xi,\eta)e^{i\Omega\tau} \tag{3}$$

which results in the following problem for the function $\tilde{\theta}(\xi, \eta)$

$$w(\eta)\frac{\partial\tilde{\theta}(\xi, \eta)}{\partial\xi}=\frac{\partial}{\partial\eta}\left[\epsilon(\eta)\frac{\partial\tilde{\theta}(\xi, \eta)}{\partial\eta}\right]-i\Omega\tilde{\theta}(\xi, \eta) \tag{4a}$$

$$\tilde{\theta}(0, \eta)=1 \tag{4b}$$

$$\left.\frac{\partial\tilde{\theta}(\xi, \eta)}{\partial\eta}\right|_{\eta=0}=0 \tag{4c}$$

$$\tilde{\theta}(\xi, 1)=0 \tag{4d}$$

where the models used for turbulent velocity distribution and eddy diffusivity are given in the Appendix A.

This problem can be formally solved by the classical integral transform technique (Mikhailov and Özişik, 1984) or the separation of variables; however, the complete numerical solution would require the evaluation of the eigenvalues, eigenfunctions, and the normalization integral of the corresponding complex nonclassical Sturm–Liouville system, for which no known solution is available. To alleviate this difficulty we follow an approach similar to that described by Özişik and Murray (1974) and consider an alternative eigenvalue problem to construct the integral transform pair needed for the transformation of the system (4). This eigenvalue problem is obtained from the natural eigenvalue problem for the original complex system (4) by omitting the complex part.

$$\frac{d}{d\eta}\left[\epsilon(\eta)\frac{d\psi(\mu_k, \eta)}{d\eta}\right]+\mu_k^2 w(\eta)\psi(\mu_k, \eta)=0 \text{ in } 0<\eta<1 \tag{5a}$$

$$\left.\frac{d\psi(\mu_k, \eta)}{d\eta}\right|_{\eta=0}=0 \tag{5b}$$

$$\psi(\mu_k, 1)=0 \tag{5c}$$

and by utilizing the eigenfunctions of this system, we define the following integral transform pair:

Inversion:

$$\tilde{\theta}(\xi, \eta)=\sum_{k=1}^{\infty}\frac{1}{N_k^{1/2}}\psi(\mu_k, \eta)\bar{\tilde{\theta}}_k(\xi) \tag{6a}$$

Transform:

$$\bar{\tilde{\theta}}_k(\xi)=\int_0^1 w(\eta)\frac{\psi(\mu_k, \eta)}{N_k^{1/2}}\tilde{\theta}(\xi, \eta)d\eta \tag{6b}$$

where the normalization integral is given by

$$N_k=\int_0^1 w(\eta)[\psi(\mu_k, \eta)]^2 d\eta \tag{7}$$

We now proceed to the solution of system (4). Equation (4*a*) is operated on by the operator

$$\int_0^1\frac{\psi(\mu_k, \eta)}{N_k^{1/2}}d\eta$$

and the eigenvalue problem (5), the boundary conditions (4*c*, *d*) are utilized to obtain

$$\frac{d\bar{\tilde{\theta}}_k}{d\xi}+\mu_k^2\bar{\tilde{\theta}}_k(\xi)+i\Omega\sum_{j=1}^{\infty}a_{kj}^*\bar{\tilde{\theta}}_j(\xi)=0 \tag{8a}$$

with the transformed inlet condition given by

$$\bar{\tilde{\theta}}_k(0)=\bar{f}_k=\int_0^1 w(\eta)\frac{\psi(\mu_k, \eta)}{N_k^{1/2}}d\eta$$

$$=\frac{1}{N_k^{1/2}}\left\{-\frac{1}{\mu_k^2}\frac{d\psi(\mu_k, 1)}{d\eta}\right\} \tag{8b}$$

where

$$a_{kj}^*=a_{jk}^*=\frac{1}{(N_k N_j)^{1/2}}\int_0^1\psi(\mu_k, \eta)\psi(\mu_j, \eta)d\eta \tag{8c}$$

System (8) forms a set of infinite, coupled, first-order, linear differential equations, which can be replaced by a finite number of coupled equations if a sufficiently large number of terms are considered in the summation appearing in equation (8*a*). Therefore, taking a sufficiently large number of equations, N, the system (8) can be expressed in matrix form as

$$\{X'(\xi)\}+[A]\{X(\xi)\}=0 \tag{9a}$$

subject to the initial condition

$$\{X(0)\}=\{f\} \tag{9b}$$

Nomenclature

[A] = coefficient matrix in system (9)
a_{kj} = elements of coefficients matrix [A], equation (9*e*)
a_{kj}^* = defined by equation (8*c*)
b = half the spacing between the parallel plates
{C} = vector of constants, equation (13*a*)
De = equivalent diameter = $4b$
{f} = transformed initial condition vector defined by equation (9*d*)
$\bar{f}_k$ = defined by equation (8*b*)
f_m = friction factor
i = $\sqrt{-1}$
N = order of matrix [A]
N_k = normalization integral defined by equation (7)
Pr = Prandtl number = ν/α
Re = Reynolds number = $u_m\, De/\nu$
R^+ = parameter defined in Appendix A = $(\mathrm{Re}/4)\sqrt{f_m/8}$
$T(x, y, t)$ = fluid temperature distribution
T_o = mean temperature of inlet oscillations
ΔT_o = amplitude of inlet oscillations
t = time variable
u_m = fluid bulk mean velocity = $1/b\int_0^b u dy$
$u(y)$ = streamwise fluid velocity
u^+ = dimensionless velocity = $u/u_m\sqrt{f_m/8}$
{v} = eigenvectors of matrix [A]
$w(\eta)$ = dimensionless velocity = u/u_m
{X(ξ)} = vector defined by equation (9*c*)
x = axial coordinate
y = transverse coordinate
y^+ = dimensionless distance from wall
α = thermal diffusivity of fluid

where the prime denotes differentiation with respect to ξ. The vectors $\{X(\xi)\}$ and $\{f\}$ are defined by

$$\{X(\xi)\} = \{\bar{\tilde{\theta}}_1(\xi), \bar{\tilde{\theta}}_2(\xi), \ldots, \bar{\tilde{\theta}}_N(\xi)\}^T \tag{9c}$$

$$\{f\} = \{\bar{f}_1, \bar{f}_2, \ldots, \bar{f}_N\}^T \tag{9d}$$

and the elements (a_{kj}) of the matrix [A] are given by

$$(a_{kj}) = (\delta_{kj}\mu_k^2 + i\Omega a_{kj}^*), \qquad k, j = 1, 2, \ldots, N \tag{9e}$$

where a_{kj}^* is defined by equation (8c) and δ_{kj} is the Kronecker delta

$$\delta_{kj} = \begin{cases} 0 & k \neq j \\ 1 & k = j \end{cases} \tag{9f}$$

The matrix [A] is complex, full, and nonhermitian. To solve system (9), we first assume that the matrix [A] has a full set of N linearly independent eigenvectors and then seek solutions of the form

$$\{X(\xi)\} = \{V\}e^{-\lambda\xi} \tag{10}$$

where the scalar λ and the constant vector $\{V\}$ are yet to be determined. Introducing equation (10) into equation (9a), we obtain the following system of homogeneous algebraic equations:

$$([A] - \lambda[I])\{V\} = 0 \tag{11}$$

where [I] is the $N \times N$ identity matrix. Equation (11) corresponds to the problem of finding eigenvalues and respective eigenvectors of the complex matrix [A].

Let $\{X^{(1)}\}, \{X^{(2)}\}, \ldots, \{X^{(N)}\}$ form a fundamental set of solutions for equation (9a); then the solution of the initial value problem (9) can be written as a linear combination of these fundamental solutions in the form

$$\{X(\xi)\} = c_1\{X^{(1)}(\xi)\} + \ldots + c_N\{X^{(N)}(\xi)\} \tag{12a}$$

or

$$\{X(\xi)\} = c_1\{V^{(1)}\}e^{-\lambda_1\xi} + \ldots + c_N\{V^{(N)}\}e^{-\lambda_N\xi} \tag{12b}$$

The system of equations (12b) can be written more compactly in the form

$$\{X(\xi)\} = [\Psi(\xi)]\{C\} \tag{12c}$$

where $[\Psi(\xi)]$ is the fundamental matrix of the system (8), which is defined by

$$\begin{bmatrix} v_1^{(1)}e^{-\lambda_1\xi} & \ldots & v_1^{(N)}e^{-\lambda_N\xi} \\ \cdot & \cdot\ \cdot\ \cdot & \cdot \\ \cdot & \cdot\ \cdot\ \cdot & \cdot \\ \cdot & \cdot\ \cdot\ \cdot & \cdot \\ v_N^{(1)}e^{-\lambda_1\xi} & \ldots & v_N^{(N)}e^{-\lambda_N\xi} \end{bmatrix}$$

To determine the unknown integration constants $\{C\}$, we constrain the solution given by equation (12c) to satisfy the initial condition (9b) and obtain the following linear system of algebraic equations:

$$[\Psi(0)]\{C\} = \{f\} \tag{13a}$$

This result establishes the constant $c_1, c_2, \ldots, c_N$ where

$$[\Psi(0)] = [v_k^{(j)}], \qquad k, j = 1, 2, \ldots, N \tag{13b}$$

and $v_k^{(j)}$ are the elements of the matrix $[\Psi(0)]$.

The complex equations (11) and (13) have been numerically solved, respectively, by using the subroutine DEVCCG (IMSL Library, 1987), which computes all of the eigenvalues and eigenvectors of a complex matrix and the subroutine DLFICG (IMSL Library, 1987), which solves a system of linear algebraic equations having a complex general coefficient matrix. Knowing the eigenvalues, eigenvectors and the coefficients $\{C\}$, the function $\{X(\xi)\}$, which represents the transformed temperature distribution $\bar{\tilde{\theta}}_k(\xi)$, can be determined. When $\bar{\tilde{\theta}}_k(\xi)$ is known, the function $\tilde{\theta}(\xi, \eta)$ is obtained by the inversion formula (6a). Noting that the dimensionless temperature $\theta(\xi, \eta, \tau)$ is related to the function $\tilde{\theta}(\xi, \eta)$ by equation (3), the dimensionless wall heat flux q_w is evaluated from its definition

$$q_w = -\left.\frac{\partial\theta(\xi, \eta, \tau)}{\partial\eta}\right|_{\eta=1} = -\left.\frac{\partial\tilde{\theta}(\xi, \eta)}{\partial\eta}\right|_{\eta=1} e^{i\Omega\tau} \tag{14a}$$

where

$$-\left.\frac{\partial\tilde{\theta}(\xi, \eta)}{\partial\eta}\right|_{\eta=1} = -\sum_{k=1}^{\infty}\frac{1}{N_k^{1/2}}\psi'(\mu_k, 1)\bar{\tilde{\theta}}_k(\xi) \tag{14b}$$

The fluid average temperature is determined from its definition

Nomenclature (cont.)

$\epsilon(\eta)$ = dimensionless total diffusivity $= 1 + \frac{\epsilon_h}{\alpha}$

ϵ_h = eddy diffusivity for heat

ϵ_m = eddy diffusivity for momentum

η = dimensionless transverse variable $= y/b$

$\theta(\xi, \eta, \tau)$ = dimensionless temperature profile $= [T(x, y, t) - T_o]/\Delta T_o$

$\bar{\theta}(\xi, \eta)$ = separated dimensionless temperature distribution

$\tilde{\theta}_{av}(\xi)$ = separated fluid bulk temperature

λ = eigenvalues of matrix [A]

μ_k = eigenvalues of eigenvalue problem (5)

ν = kinematic viscosity of fluid

ξ = dimensionless axial variable $= \frac{16x/De}{\mathrm{Re\ Pr}}$

τ = dimensionless time $= \alpha t/b^2$

$\Psi(\xi)$ = fundamental matrix of system (12)

$\psi(\mu, \eta)$ = eigenfunctions of eigenvalue problem (5)

Ω = dimensionless frequency of inlet oscillations $= \omega b^2/\alpha$

ω = frequency of inlet oscillations

Subscripts

j = column index in system (9e)

k = row index in system (9e) and order of eigenvalue

L = lowest-order solution

Superscripts

~ = separation symbol defined by equation (3)

- = integral transform with respect to η

+ = as in u^+, y^+, R^+ (Appendix A)

′ = indicating derivatives

$$\theta_{av}(\xi, \tau) = \int_0^1 w(\eta)\theta(\xi, \eta, \tau)d\eta$$

$$= e^{i\Omega\tau}\int_0^1 w(\eta)\tilde{\theta}(\xi, \eta)d\eta$$

$$\equiv e^{i\Omega\tau}\tilde{\theta}_{av}(\xi) \tag{15a}$$

where

$$\tilde{\theta}_{av}(\xi) = \sum_{k=1}^{\infty} \bar{f}_k \bar{\tilde{\theta}}_k(\xi) \tag{15b}$$

Considering only N terms in the summation of the solution for $\bar{\tilde{\theta}}_k(\xi)$, i.e., $k=1$ to N, yields

$$\bar{\tilde{\theta}}_1(\xi) \cong c_1\, v_1^{(1)} e^{-\lambda_1 \xi} + \ldots + c_N\, v_1^{(N)} e^{-\lambda_N \xi}$$

$$\vdots \tag{16}$$

$$\bar{\tilde{\theta}}_N(\xi) \cong c_1\, v_N^{(1)} e^{-\lambda_1 \xi} + \ldots + c_N v_N^{(N)} e^{-\lambda_N \xi}$$

Since equations (14) and (15) define complex quantities, the final solutions for the temperature gradient at the wall and the average temperature can be conveniently expressed in polar coordinates, respectively, as

$$-\left.\frac{\partial\theta(\xi, \eta, \tau)}{\partial\eta}\right|_{\eta=1} = A_h(\xi)\exp\{i[\Omega\tau + \phi_h(\xi)]\} \tag{17}$$

$$\theta_{av}(\xi, \tau) = A_b(\xi)\exp\{i[\Omega\tau + \phi_b(\xi)]\} \tag{18}$$

where A and ϕ are, respectively, amplitudes and phase lags of oscillations with respect to the inlet condition. They can be evaluated by considering the real and imaginary parts of equations (14) and (15).

Lowest-Order Solution

So far we transformed the solution of the original complex problem to the solution of an infinite number of coupled first-order complex ordinary differential equations. We define the lowest-order solution for this problem as the one that is developed by using the results obtained from the decoupled form of system (8). Clearly, if the coefficient matrix of the system of equations (8) were a diagonal matrix, the system would be decoupled.

Our examination of the coefficient matrix reveals that for all values of Ω and Reynolds number considered in the present study, the diagonal element are dominant with respect to non-diagonal elements. This matter will be discussed further in the Results section. This fact suggests a straightforward approach for obtaining an approximate solution for the problem, by setting $j=k$ in the summation in equation (8a). The resulting decoupled system, representing the lowest-order analysis, is given by

$$\frac{d\bar{\tilde{\theta}}_{L,k}(\xi)}{d\xi} + (\mu_k^2 + i\Omega a_{kk}^*)\bar{\tilde{\theta}}_{L,k}(\xi) = 0 \tag{19a}$$

$$\bar{\tilde{\theta}}_{L,k}(0) = \bar{f}_k, \qquad k = 1, 2, \ldots \tag{19b}$$

which has the solution

$$\bar{\tilde{\theta}}_{L,k}(\xi) = \bar{f}_k e^{-\mu_k^2 \xi}\exp(-i\Omega a_{kk}^* \xi) \tag{20}$$

The inversion of this result by the inversion formula (6a) gives the lowest-order solution as

$$\tilde{\theta}_L(\xi, \eta) = \sum_{k=1}^{\infty} \frac{1}{N_k^{1/2}} \bar{f}_k\, \psi(\mu_k, \eta) e^{-\mu_k^2 \xi}\exp(-i\Omega a_{kk}^* \xi) \tag{21}$$

The lowest-order solution for $\partial\tilde{\theta}_L(\xi, \eta)/\partial\eta\,|_{\eta=1}$, needed in the definition of the wall heat flux q_w, is determined by introducing equation (20) into equation (14b) to give

$$-\left.\frac{\partial\tilde{\theta}_L(\xi, \eta)}{\partial\eta}\right|_{\eta=1}$$

$$= -\sum_{k=1}^{\infty} \frac{1}{N_k^{1/2}} \bar{f}_k \psi'(\mu_k, 1) e^{-\mu_k^2 \xi}\exp(-i\Omega a_{kk}^* \xi) \tag{22}$$

Similarly, $\tilde{\theta}_{L,av}(\xi)$, needed for the determination of average temperature $\theta_{av}(\xi, \tau)$, equation (15a), is determined as

$$\tilde{\theta}_{L,av}(\xi) = \sum_{k=1}^{\infty} (\bar{f}_k)^2 e^{-\mu_k^2 \xi}\exp(-i\Omega a_{kk}^* \xi) \tag{23}$$

Again, the dimensionless wall heat flux and the average temperature from the lowest-order solution can be conveniently expressed in polar coordinates as

$$-\left.\frac{\partial\theta_L(\xi, \eta, \tau)}{\partial\eta}\right|_{\eta=1} = A_{L,h}(\xi)\exp\{i[\Omega\tau + \phi_{L,h}(\xi)]\} \tag{24}$$

$$\theta_{L,av}(\xi,\tau) = A_{L,b}(\xi)\exp\{i\Omega\tau + \phi_{L,b}(\xi)]\} \tag{25}$$

where $A_{L,h}$, $A_{L,b}$, and $\phi_{L,h}$, $\phi_{L,b}$, are, respectively, amplitudes and phase lag of oscillations for heat flux and average temperature with respect to the inlet condition for the lowest-order solution.

Results and Discussion

We now present the variations of the amplitude and the phase lag for the dimensionless bulk temperature along the channel.

For computational purposes, we consider a set of Reynolds numbers $\mathrm{Re} = 1\times10^4$, 5×10^4, 1×10^5, 5×10^5, and 1×10^6 and the dimensionless frequency of inlet oscillations $\Omega = 0.1$, 0.5, 1, and 2 for $\mathrm{Pr} = 0.7$.

The algebraic eigenvalue problem (11) and the linear system of algebraic equations (13a) are solved by using subroutines from the IMSL Library (1987) and the functions $\bar{\tilde{\theta}}_k(\xi)$ are obtained in the form of equation (16). Once $\bar{\tilde{\theta}}_k(\xi)$ is obtained, the variations of the dimensionless wall heat flux and the fluid bulk temperature can be determined.

For an accuracy of four significant digits in the calculation of amplitude and phase lag for the average temperature, the number of terms $N \leq 50$ was more than sufficient everywhere in the region. For most cases the convergence would be achieved with 10 to 15 terms, and in regions sufficiently away from the inlet only few terms were needed.

The lowest-order analysis given by equation (21) provides an explicit approximate solution, which is useful for fast numerical evaluations in most practical applications. The reason for the lowest-order solution to yield accurate results is the fact that diagonal elements of the matrix [A] for all the cases considered here were dominant. The validity of this concept is apparent from the data presented in Table 1, which show that eigenvalues λ_k and the diagonal elements a_{kk} of the matrix [A] are identical up to six significant figures for all Reynolds number and Ω except $\mathrm{Re} = 1\times10^4$ and 5×10^4 with $k=1$. For these two cases, the agreement for the real parts was to four significant digits. Since the problems of diagonalizing a matrix and solving a system of linear first-order differential equations are mathematically equivalent, the comparison of eigenvalues and diagonal elements justifies the decoupling procedure to obtain the lowest-order solutions.

Figure 1 shows the variations of the amplitude of the dimensionless bulk temperature along the channel at various values of Reynolds numbers for $\mathrm{Pr} = 0.7$. As expected the amplitude

Table 1 Comparison of three eigenvalues λ_k and diagonal elements a_{kk} for $k = 1$, 3, and 5 of the coefficient matrix [A] for different values of dimensionless frequency Ω and Reynolds number for Pr = 0.7

Re	Ω	k	k = 1 Real	k = 1 Imaginary	k = 3 Real	k = 3 Imaginary	k = 5 Real	k = 5 Imaginary
1×10^4	0.5	λ_k	(0.854613E+01,	0.460493E+00)	(0.467826E+03,	0.514634E+00)	(0.158082E+04,	0.611067E+00)
		a_{kk}	(0.854611E+01,	0.460493E+00)	(0.467826E+03,	0.514634E+00)	(0.158082E+04,	0.611067E+00)
	2	λ_k	(0.854646E+01,	0.184197E+01)	(0.467826E+03,	0.205853E+01)	(0.158082E+04,	0.244427E+01)
		a_{kk}	(0.854611E+01,	0.184197E+01)	(0.467826E+03,	0.205853E+01)	(0.158082E+04,	0.244427E+01)
5×10^4	0.5	λ_k	(0.269718E+02,	0.477661E+00)	(0.155657E+04,	0.523315E+00)	(0.551516E+04,	0.530379E+00)
		a_{kk}	(0.269718E+02,	0.477661E+00)	(0.155657E+04,	0.523315E+00)	(0.551516E+04,	0.530379E+00)
	2	λ_k	(0.269718E+02,	0.191064E+01)	(0.155657E+04,	0.209326E+01)	(0.551516E+04,	0.212151E+01)
		a_{kk}	(0.269718E+02,	0.191064E+01)	(0.155657E+04,	0.209326E+01)	(0.551516E+04,	0.212151E+01)
1×10^5	0.5	λ_k	(0.460558E+02,	0.481477E+00)	(0.278357E+04,	0.524957E+00)	(0.982067E+04,	0.530195E+00)
		a_{kk}	(0.460558E+02,	0.481477E+00)	(0.278357E+04,	0.524957E+00)	(0.982067E+04,	0.530195E+00)
	2	λ_k	0.460558E+02,	0.192591E+01)	(0.278357E+04,	0.209983E+01)	(0.982067E+04,	0.212078E+01)
		a_{kk}	0.460558E+02,	0.192591E+01)	(0.278357E+04,	0.209983E+01)	(0.982067E+04,	0.212078E+01)
5×10^5	0.5	λ_k	(0.167298E+03,	0.486891E+00)	(0.113484E+05,	0.525249E+00)	(0.399229E+05,	0.530354E+00)
		a_{kk}	(0.167298E+03,	0.486891E+00)	(0.113484E+05,	0.525249E+00)	(0.399299E+05,	0.530354E+00)
	2	λ_k	(0.167298E+03,	0.194756E+01)	(0.113484E+05,	0.210099E+01)	(0.399299E+05,	0.212142E+01)
		a_{kk}	(0.167298E+03,	0.194756E+01)	(0.113484E+05,	0.210099E+01)	(0.399229E+05,	0.212142E+01)
1×10^6	0.5	λ_k	(0.295852E+03,	0.488430E+00)	(0.210800E+05,	0.524576E+00)	(0.742165E+05,	0.529544E+00)
		a_{kk}	(0.295852E+03,	0.488430E+00)	(0.210800E+05,	0.524576E+00)	(0.742165E+05,	0.529544E+00)
	2	λ_k	(0.295852E+03,	0.195372E+01)	(0.210800E+05,	0.209830E+01)	(0.742165E+05,	0.212078E+01)
		a_{kk}	(0.295852E+03,	0.195372E+01)	(0.210800E+05,	0.209830E+01)	(0.742165E+05,	0.212078E+01)

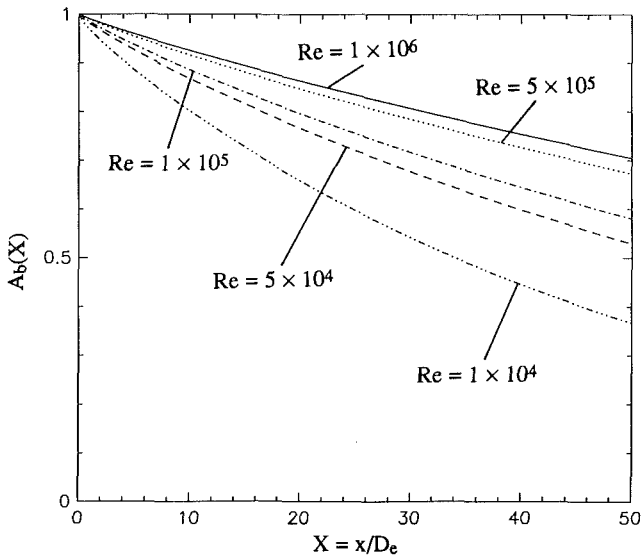

Fig. 1 Variation of the amplitude of the dimensionless bulk temperature along the channel at various values of Reynolds numbers for Pr = 0.7

decays faster along the channel as the Reynolds number decreases.

Figure 2 and 3 presents the variations of the phase lag of the dimensionless bulk temperature along the channel at various values of dimensionless frequency of inlet oscillations, Ω, for $\mathrm{Re} = 1 \times 10^4$ and $\mathrm{Re} = 1 \times 10^5$, respectively. These results show that phase lag increases as Ω increases. For a given Reynolds number, if the increase in Ω is interpreted as a decreasing value of the thermal diffusivity of the fluid α, the fluid heat capacity is regarded as a factor controlling the fluid temperature variation. That is, the thermal storage in the fluid decays the information sensed at each axial location downstream with respect to the inlet disturbances carried by the thermal wave.

Figures 4 and 5 show the variations of the phase lag of the dimensionless bulk temperature along the channel at the various values of Reynolds number for $\Omega = 0.5$ and 2, respectively. For a given Ω, if the increase of the Reynolds number is interpreted as a increasing value of the fluid velocity, the fluid with higher Reynolds number transfers more rapidly the information of the inlet disturbances carried by the thermal wave than the one with lower Reynolds number. So, phase lag decreases as Reynolds number increases as shown in Figs. 4 and 5.

We also compared the lowest-order and the complete solutions for all cases considered here. As expected from Table 1, there was little difference betwen them as far as the graphic presentation is concerned and, therefore, were not presented.

Based on the cases studied here, it seems that the phase lag varies linearly with the dimensionless axial distance x/De along the channel. Therefore we developed an approximate formula for the variation of the phase lag of the bulk temperature given by

$$-\phi_b\left(\frac{x}{De}\right) = 10\,\frac{\mathrm{Pr}\cdot\Omega}{\mathrm{Re}}\,\frac{x}{De} \quad \text{for } 10^4 \le \mathrm{Re} \le 10^6,\ \mathrm{Pr} = 0.7 \quad (26)$$

which can predict phase lag with maximum error 4.27 percent compared to the results obtained from the present analysis.

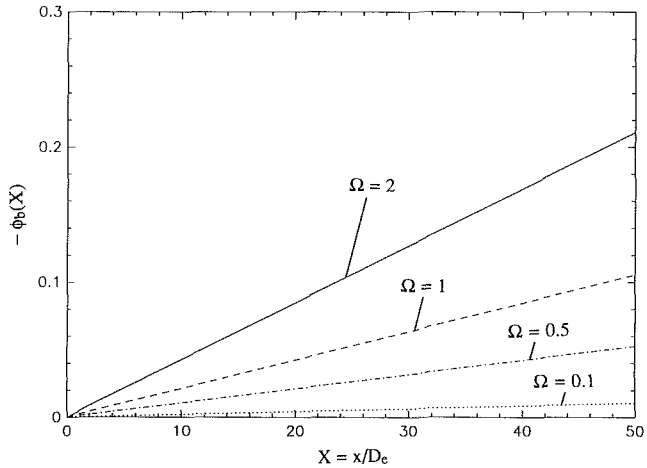

Fig. 2 Variation of the phase lag of the dimensionless bulk temperature along the channel at various values of Ω for $Re = 1 \times 10^4$, Pr = 0.7

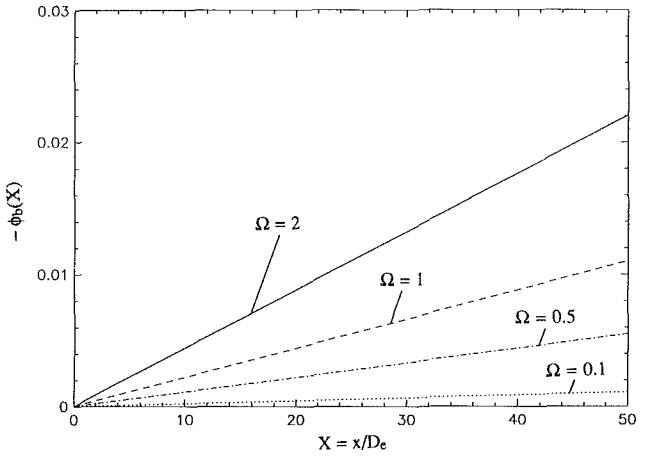

Fig. 3 Variation of the phase lag of the dimensionless bulk temperature along the channel at various values of Ω for $Re = 1 \times 10^5$, Pr = 0.7

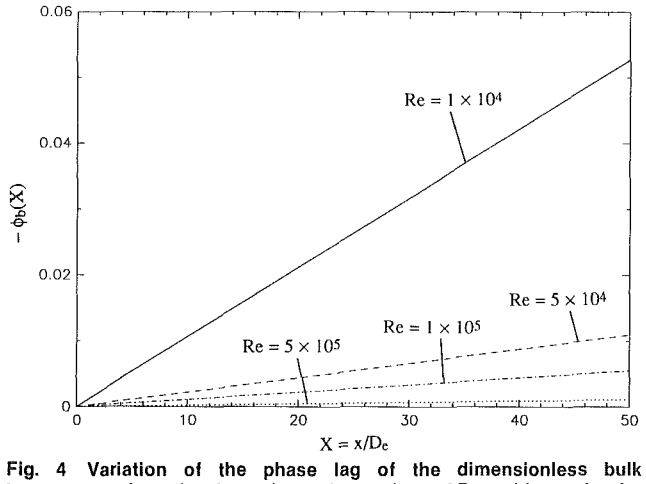

Fig. 4 Variation of the phase lag of the dimensionless bulk temperature along the channel at various values of Reynolds number for Ω = 0.5.

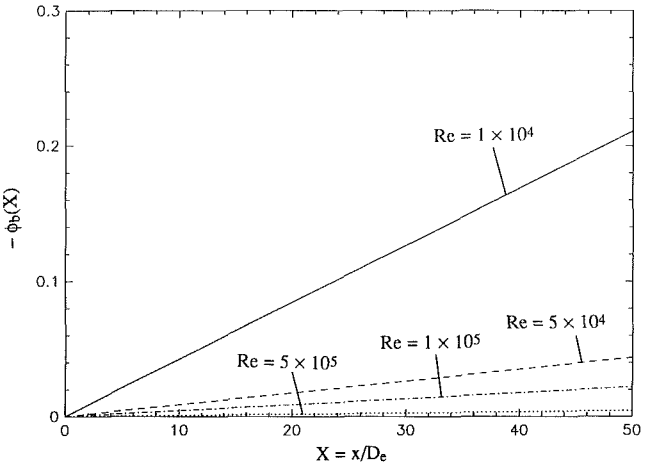

Fig. 5 Variation of the phase lag of the dimensionless bulk temperature along the channel at various values of Reynolds number for Ω = 2.0

Conclusion

A methodology is presented for solving turbulent forced convection inside a parallel-plate channel with a periodically varying inlet temperature and a uniform constant wall temperature. The lowest-order analysis provides a sufficiently accurate explicit approximate solution useful for fast numerical evaluations. Based on the results of the cases studied here, a simple analytic expression is developed for determining the variations of phase lag for bulk temperature along the channel.

References

Boyce, W. E., and DiPrima, R. C., 1977, *Elementary Differential Equations*, 3rd ed., Wiley, New York.

Cotta, R. M., and Özişik, M. N., 1986, "Laminar Forced Convection Inside Ducts With Periodic Variation of Inlet Temperature," *Int. J. Heat Mass Transfer*, Vol. 29, pp. 1495–1501.

IMSL Library, 1987, Edition 10, GNB Building, 7500 Ballaire Blvd., Houston, TX 77036.

Kakaç, S., 1975, "A General Analytical Solution to the Equation of Transient Forced Convection With Fully Developed Flow," *Int. J. Heat Mass Transfer*, Vol. 18, pp. 1449–1453.

Kakaç, S., and Yener, Y., 1973, "Exact Solution of the Transient Forced Convection Energy Equation for Timewise Variation of Inlet Temperature," *Int. J. Heat Mass Transfer*, Vol. 16, pp. 2205–2214.

Kakaç, S., and Yener, Y., 1979, "Frequency Response Analysis of Transient Turbulent Forced Convection for Timewise Variation of Inlet Temperature," in: *Turbulent Forced Convection in Channels and Bundles*, S. Kakaç and D. B. Spalding, eds., Vol. 2, pp. 865–880, Hemisphere, New York.

Kays, W. M., and Crawford, M. E., 1980, *Convective Heat and Mass Transfer*, McGraw-Hill, New York.

Larson, R. I., and Yerazunis, S., 1973, "Mass Transfer in Turbulent Flow," *Int. J. Heat Mass Transfer*, Vol. 16, pp. 121–128.

Mikhailov, M. D., and Özisik, M. N., 1984, *Unified Analysis and Solutions of Heat and Mass Diffusion*, Wiley, New York.

Mikhailov, M. D., and Vulchanov, N. L., 1983, "A Computational Procedure for Sturm–Liouville Problems," *J. Comp. Phys.*, Vol. 50, pp. 323–336.

Özisik, M. N., and Murray, R. L., 1974, "On the Solution of Linear Diffusion Problems With Variable Boundary Condition Parameters," ASME Journal of Heat Transfer, Vol. 96, pp. 48–51.

Reichardt, H., 1951, "Vollstandige Darstellung der turbulenten Geschwindigkeits-verteilung in glatten Leitungen," *Z. Angew. Math. Mech.*, Vol. 31, pp. 208–219.

Spalding, D. B., 1961, "Heat Transfer to a Turbulent Stream From a Surface With a Step-Wise Discontinuity in Wall Temperature," *Conf. Intern. Developments in Heat Transfer*, ASME, Boulder, CO, Part II, pp. 439–446.

Spalding, D. B., 1961, "A Single Formula for the 'Law of the Wall'," ASME *Journal of Applied Mechanics*, Vol. 28, pp. 455–457.

Sparrow, E. M., and de Farias, F. N., 1968, "Unsteady Heat Transfer in Ducts With Time-Varying Inlet Temperature and Participating Walls," *Int. J. Heat Mass Transfer*, Vol. 11, pp. 837–853.

von Karman, T., 1939, "The Analogy Between Fluid Friction and Heat Transfer," *Trans. ASME*, Vol. 61, pp. 705–710.

APPENDIX A

The three-layer turbulent velocity distribution is taken as laminar sublayer (Spalding, 1961; von Karman, 1939):

$$u^+ = y^+ \text{ for } 0 \le y^+ < 5$$

buffer layer (Spalding, 1961; von Karman, 1939):

$$u^+ = -3.05 + 5 \ln y^+ \text{ for } 5 \le y^+ < 30$$

turbulent core (Reichardt, 1951; Kays and Crawford, 1980):

$$u^+ = 5.5 + 2.5 \ln\left[y^+ \frac{1.5(1+\eta)}{1+2\eta^2}\right] \text{ for } y^+ > 30$$

The momentum eddy diffusivity is taken as (Spalding, 1961)

$$\frac{\epsilon_m}{\nu} = \frac{k}{E}\left[e^{ku^+} - 1 - ku^+ - \frac{(ku^+)^2}{2!} - \frac{(ku^+)^3}{3!}\right] \text{ for } y^+ < 40$$

where $k = 0.407$ and $E = 10$, and (Reichardt, 1951)

$$\frac{\epsilon_m}{\nu} = \frac{kR^+}{6}(1-\eta^2)(1+2\eta^2) \text{ for } y^+ \ge 40$$

where

$$k = 0.4,\ R^+ = \frac{\mathrm{Re}}{4}\sqrt{\frac{f_m}{8}},\ y^+ = (1-\eta)R^+,$$

$$u^+ = \frac{u}{u_m\sqrt{f_m/8}},\ \text{and}\ \eta = y/b$$

The turbulent Prandtl number $\mathrm{Pr}_t\ (= \epsilon_m/\epsilon_h)$ is taken as (Larson and Yerazunis, 1973)

$$\mathrm{Pr}_t = 0.86 \quad \text{for} \quad \mathrm{Pr} = 0.7$$

where ϵ_h is the eddy diffusivity for heat.

APPENDIX B

Determination of Friction Factor f_m

The relation between Reynolds number $\mathrm{Re} = u_m De/\nu$ and R^+ is given by

$$\frac{\mathrm{Re}}{4} = \int_0^{R^+} u^+ \, dy^+ \tag{1}$$

which can be transformed as

$$\sqrt{\frac{f_m}{8}}\int_0^1 u^+(\eta)\, d\eta = 1 \tag{2}$$

For a given Reynolds number, equation (2) provides a transcendental equation for the determination of f_m.

D. A. Zumbrunnen[1]

F. P. Incropera

R. Viskanta

Heat Transfer Laboratory,
School of Mechanical Engineering,
Purdue University,
West Lafayette, IN 47907

Convective Heat Transfer Distributions on a Plate Cooled by Planar Water Jets

Convective heat transfer distributions have been measured for planar water jets impinging on a plate. The cooling effectiveness of two nozzles, each with a different discharge width, is compared for a range of impingement velocities. Measurements were made under transient conditions, and results are presented both during and after the period for boundary layer growth on an initially dry plate. Heat transfer correlations and discussions of pertinent parametric effects are provided.

Introduction

Impinging jets are used in many industrial processes. For example, paper and textiles are often dried by jets of air (Martin, 1977). Liquid jets are employed to cool steel strips and plates (Kohring, 1985) and can be used to remove heat from electronic circuitry (Ma and Bergles, 1983). A drawback to circular jets is that nonuniform cooling occurs between arrays of jets, due to their radial symmetry. Nonuniform cooling is especially undesirable for steel strip, since regions of reduced strength due to recrystallization and grain growth can arise where cooling is deficient (Adcock, 1962; Morgan et al., 1965; Kohring, 1985). However, planar jets, sometimes referred to as "slot jets" or "wall jets," can span the entire surface and thereby provide more uniform cooling.

A possible configuration for cooling electronic packages is depicted in Fig. 1. A single planar jet impinges on a flat, thermally conductive substrate. The chips are placed at locations of enhanced cooling, as indicated by a typical distribution of the convection heat transfer coefficient beneath the jet. Since the peaks in heat transfer coefficient adjacent to the stagnation line are due to transitions to a turbulent boundary layer, their locations could be controlled by placing boundary layer trips on the substrate. The convective heat transfer distribution might also be made more uniform by placing additional trips on the substrate. Several similar substrates could be joined to form a closed surface or stacked with each substrate cooled by a separate nozzle. A single nozzle could provide the equivalent cooling of three or possibly more nozzles, reducing flow interference between adjacent nozzles.

In jet impingement, a stagnation zone is formed where the velocity component u_∞ at the edge of the velocity boundary layer is related to the distance x_j by

$$u_\infty = Cx_j \tag{1}$$

where C is a constant (Schlichting, 1979). Beyond the stagnation zone, du_∞/dx_j approaches zero and u_∞ approaches the jet impingement velocity. If the discharge velocity of the jet is uniform, fluid acceleration is nearly completed at about two jet widths from the stagnation line. A theoretical expression for the heat transfer coefficient at the stagnation point for two-dimensional laminar flows (Evans, 1968) is

$$h_0 = 0.57\, k\left(\frac{C}{\nu}\right)^{1/2} \mathrm{Pr}^n \tag{2}$$

where n is a constant dependent on Pr ($n \simeq 0.38$ for $1 < \mathrm{Pr} < 5$) and the velocity gradient C is related to the nozzle width. With decreasing width, C increases, since fluid is accelerated away from the stagnation line over shorter distances.

The favorable pressure gradient in the stagnation zone tends to laminarize turbulent flows (Schlichting, 1979). Hence, laminar stagnation flow solutions are sometimes applied to turbulent jets. In actuality, however, turbulence enters outer reaches of the boundary layer, and laminar solutions such as equation (2) often underpredict actual heat transfer rates. Studies of flows past spheres and cylinders have clarified how turbulence can affect heat transfer in a stagnation region. Kuethe et al. (1959) performed turbulence measurements for cylindrical bodies with hemispherical ends in a low-turbulence wind tunnel with airflow parallel to the cylinder axis. They found that fluctuating velocity components just beyond the boundary layer in the stagnation region were considerably larger than in the free stream. The phenomenon was attributed to "the stretching of vortex filaments in the diverging flow near

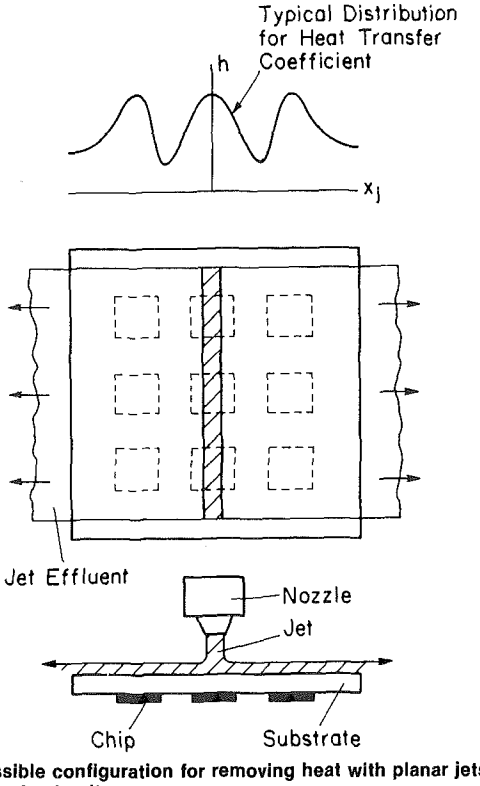

Fig. 1 Possible configuration for removing heat with planar jets from microelectronic circuitry

[1]Current address: Department of Mechanical Engineering, Clemson University, Clemson, SC 29634.

Contributed by the Heat Transfer Division for publication in the JOURNAL OF HEAT TRANSFER. Manuscript received by the Heat Transfer Division September 23, 1988. Keywords: Forced Convection, Jets, Transient and Unsteady Heat Transfer.

the stagnation point," an effect that is now commonly known as vorticity amplification.

Flow visualization studies were performed by Sadeh and Brauer (1980) for the stagnation region of a cylinder in cross flow. Smoke was injected into an air stream and turbulence was controlled with a grid comprised of regularly spaced cylindrical bars. The results revealed "a coherent vortex flow substructure near the stagnation zone," in which "pairs of counterrotating vortex tubes of equal size were distributed with their axes parallel to the streamlines near the cylinder's surface." The tubes resided just beyond the boundary layer and single eddies were intermittently swept into the flow around the cylinder, penetrating the boundary layer. These observations with cylinders are useful in understanding the stagnation zone beneath a planar jet. In an impinging jet, however, eddies have different scales and orientations, and the stagnation zone is therefore likely to have a vortex flow substructure that is less organized than that observed by Sadeh and Bauer (1980).

Gardon and Akfirat (1965) studied convective heat transfer distributions on flat plates cooled by air jets. Secondary peaks adjacent to the stagnation point were observed for both planar and circular jets. The secondary peaks were attributed to a transition to turbulent flow in the boundary layer owing to the decrease in the stabilizing effect of the favorable pressure gradient away from the stagnation point. Heat transfer coefficients near the stagnation point were greater at larger separation distances between the jet and impingement surface, even though momentum transfer to the surrounding air served to reduce the air velocity along the stagnation streamline. This effect was attributed to increased small-scale turbulence in the incident air stream arising from the degradation of the initial jet by the surrounding air. Metzger et al. (1974) cautioned against using correlations based on gas jets to predict heat transfer for liquid jets, even when the effect of Prandtl number is included. They cited significant errors due to large differences in Prandtl number and the fact that momentum transfer to the surrounding medium is reduced since liquid jets are frequently submerged in a much lower density fluid like a gas.

Heat transfer distributions for liquid planar jets have been considered in relatively few experimental studies. McMurray et al. (1966) experimentally determined local heat transfer coefficients for a planar water jet ($w = 0.64$ cm) impinging on an electrically heated nickel–chromium strip. Measurements were performed for impingement velocities ranging from 9.2 to 18.3 m/s ($69{,}000 \lesssim \mathrm{Re}_{w_c} \lesssim 137{,}000$). Secondary peaks in the heat transfer coefficient were found adjacent to the peak occurring at the stagnation line and were attributed to transitions to turbulent flow. The following correlation was proposed for the impingement zone:

$$\mathrm{Nu}_{x_j}\,\mathrm{Pr}^{-1/3} = K[\mathrm{Re}_{x_j}\,(u_\infty/v_{jc})]^{1/2} \tag{3}$$

where u_∞/v_{jc} was found from potential flow theory and K was an empirical constant. Good agreement with experimental data was found with $K = 0.75$, yielding heat transfer coefficients near the stagnation line larger than theoretical values given by equation (2) with $n = 0.38$ and $\mathrm{Pr} = 5$ by a factor of 1.43.

Miyasaka and Inada (1980) examined the effect of impingement velocity beneath a planar water jet ($w = 1$ cm) issuing from a convergent nozzle. Impingement velocities from 1.1 to 15.3 m/s ($10{,}500 \lesssim \mathrm{Re}_{w_c} \lesssim 157{,}000$) were considered. Temperature and pressure measurements were made at several locations to determine the local heat transfer and flow velocity beyond the boundary layer. The heat transfer coefficients measured near the stagnation region were found to be larger by a factor of 1.8 than those predicted from equation (2). In a related study (Inada et al., 1981), similar experiments were performed at a much smaller Reynolds number ($\mathrm{Re}_{w_c} = 940$) and experimental heat transfer results agreed with theoretical predictions.

In this study, impingement velocities and jet widths are considered that are typical of industrial planar jet systems. Water is used since many industrial processes utilize liquid jets and since most prior work has involved air jets. The cooling effectiveness of two nozzles, each with a different discharge width, is compared. A downward discharging orientation is

Nomenclature

A_N = flow area at nozzle opening
c = specific heat of plate
C = velocity gradient, equation (1)
$\bar{C}$ = dimensionless velocity gradient $= w_c\,C/v_{jc}$
D = plate thickness
g = acceleration due to gravity
h = heat transfer coefficient
H = separation distance between nozzle opening and plate, equation (4)
k = thermal conductivity
L = plate length
Nu_{x_j} = Nusselt number $= hx_j/k$
Nu_{w_c} = jet Nusselt number $= hw_c/k$
P = static pressure
$\bar{P}$ = dimensionless pressure $= (P-P_\infty)/(\rho v_{jc}^2/2)$
Pr = Prandtl number evaluated at $T_f = \mu c_p/k$
q = heat flux
Q = volumetric flow rate to nozzle
Re_j = Reynolds number $= v_{jc}w_c/\nu\,(T_\infty)$
Re_{w_c} = jet Reynolds number $= v_{jc}w_c/\nu(T_f)$
Re_{x_j} = Reynolds number $= v_{jc}x_j/\nu(T_f)$
t = time
T = temperature
T_f = local film temperature $= (T_p(\bar{x}) + T_\infty)/2$
$T_{f,av}(\bar{x})$ = $(T_{p,av}(\bar{x}) + T_\infty)/2$
T_p = local surface temperature of plate
$T_{p,av}(\bar{x})$ = $\int_0^{\bar{x}} T_p(x)\,dx/\bar{x}$
T_{pi} = initial temperature of plate
u_∞ = x component of velocity beyond velocity boundary layer
$\bar{u}_\infty$ = velocity ratio $= u_\infty/v_{jc}$
v_j = nozzle discharge velocity, equation (6)
v_{jc} = jet impingement velocity, equation (4)
w = nozzle width
w_c = jet width, equation (5)
x_j = horizontal distance from stagnation line, Fig. 4
x_p = horizontal distance from plate midpoint, Fig. 4
$\bar{x}$ = dimensionless position $= x_j/w_c$
y_p = vertical distance from plate midpoint, Fig. 4
θ = dimensionless surface temperature of plate $= (T_p - T_\infty)/(T_{pi} - T_\infty)$
μ = dynamic viscosity
ν = kinematic viscosity $= \mu/\rho$
ρ = mass density

Subscripts

0 = pertaining to stagnation line, $\bar{x} = 0$
av = average value
c = value corrected for gravitational acceleration and thinning
i = initial value
p = plate
∞ = liquid free stream

Superscripts

c = critical value for onset to turbulent boundary layer

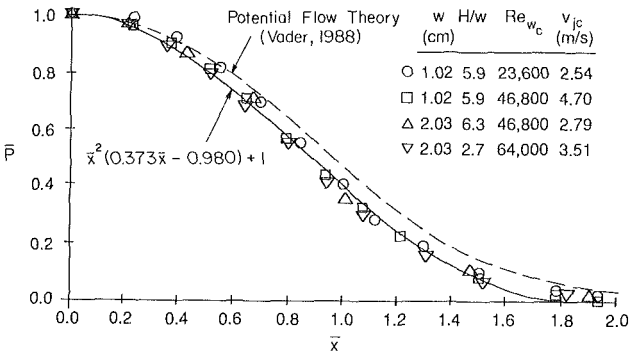

Fig. 2 Measured pressure distribution for the nozzles used in the experiments

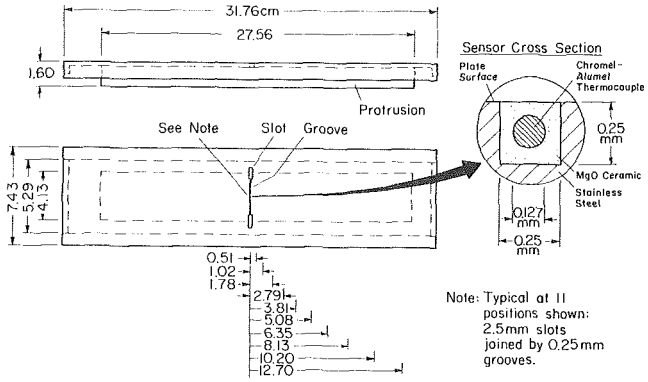

Fig. 3 Positions and details of temperature sensors attached to the surface of the plate

used to facilitate corrections to jet velocities and widths due to gravity. Measurements of local heat transfer coefficients are made under transient conditions as a test specimen is cooled and are presented both during and after the period for boundary layer growth on an initially dry plate. Unlike previous studies, which have often employed thin electrical strip heaters, the transient temperature distributions of a comparatively thick impingement plate are representative of many stationary cooled surfaces where significant conjugate heat transfer occurs. Heat transfer correlations and discussions of pertinent parametric effects are provided.

Experimental Apparatus and Methods

Two nozzles with unique slot widths were fabricated. One nozzle had a 1.02-cm opening and the other had a 2.03-cm opening. Each nozzle consisted of a convergent zone and a transition section, which straightened the flow prior to discharge. The water temperature was measured with a thermocouple installed just above the nozzle inlets. Demineralized water from a vented tank was supplied to the nozzles with a centrifugal pump. Flow rate was measured with a turbine meter and regulated by a throttling valve. Water in the tank was maintained at temperatures as high as 60°C by an electrical immersion heater.

Corrections to the jet discharge velocity and width were made to account for thinning due to gravitational acceleration. In accordance with mass and momentum conservation for a two-dimensional jet, the following relationships were used:

$$v_{jc} = \sqrt{v_j^2 + 2gH} \tag{4}$$

$$w_c = v_j w / v_{jc} \tag{5}$$

where

$$v_j = Q/A_N \tag{6}$$

Local heat transfer coefficients for jet impingement cooling depend on the static pressure distribution on the impingement surface (Schlichting, 1979). The static pressure distribution for each nozzle was measured with a water manometer connected to a small sensing port drilled through a plastic plate. Measured pressure distributions were identical for the two nozzles and are given in Fig. 2. Impingement velocities at the stagnation line based on stagnation pressure were about 4 percent greater than corresponding values of v_{jc} found with equations (4) and (6). The theoretical pressure distribution for a planar jet with uniform discharge velocity (Fig. 2) therefore differs slightly from the measured distribution (Scholtz and Trass, 1970; Sparrow and Lee, 1975).

The test cell was that part of the apparatus onto which the planar jet impinged and which contained instrumentation needed to make heat transfer measurements. It consisted of a plate and a carriage. The carriage supported the plate and accommodated thermocouple wires. The jet impinged on the top side of the plate, which was flat and smooth. The bottom side had a rectangular protrusion, which extended into the carriage, and a continuous lip at the edges to prevent water infiltration. A gap between the protrusion and the interior of the carriage was provided for insulation. The test cell was heated in an electric furnace and transferred along a track to the test area beneath the nozzle. The plate and carriage were fabricated completely from AISI type 304 stainless steel to prevent differential thermal expansion and to maintain water purity.

The temperature of the plate surface was measured using surface-mounted sensors. The plate and a cross-sectional view of a typical surface temperature sensor are shown in Fig. 3. Each sensor was made from 0.127-mm chromel-alumel wire (AISI type K) and a ceramic adhesive. The surface temperature sensors were bonded by the ceramic adhesive to the plate in shallow spanwise grooves. The grooves terminated at slots where connections were made to heavier lead wires. Thermocouple junctions were aligned with the longitudinal centerline of the plate to take advantage of the symmetry of the dividing jet. The junctions were formed from a pancakelike weld. Excess weld material was carefully removed, yielding a cylindrical junction with a diameter no larger than that of the thermocouple wire. The lead wires passed through vertical holes at the end of the slot, into insulated gaps adjacent to the plate protrusion, and out of the carriage for connection to the data acquisition system.

To begin each experiment, the test cell was placed in the furnace and heated to a prescribed temperature. It was then transferred along a track and the plate midpoint was aligned beneath the midpoint of the nozzle. An insulated enclosure was moved into position around the test cell, and the water supply system was adjusted to provide the desired flow rate. Data acquisition was initiated and the insulated enclosure was removed to expose the test cell to the jet abruptly. Initial plate temperatures of 88°C to 205°C were selected and water temperature was controlled from 21°C to 60°C. In experiments where the initial plate temperature exceeded the saturation temperature (100°C), surface temperatures quickly decreased (in less than 200 ms) to temperatures below the saturation temperature.

The 11 surface temperature sensors in Fig. 3 were scanned sequentially, beginning with the sensor located at the plate's midpoint. Readings were completed within 9 ms and the scans were repeated 200 ms after the beginning of the preceding scan. Scanning was performed for 12 s, giving 60 scans containing 11 readings. The scans provided the plate surface temperature distribution at a time t_s ($0 \le t_s \le 12$ s), which was evaluated according to $t_s = (s_i - 1)\Delta t_d$, where s_i was the scan number (e.g., 1, 2, 3, . . . , 60) and $\Delta t_d = 200$ ms. Scanning was terminated at 12 s since the temperature difference between the plate surface and the water became too small ($\lesssim 8$°C) for accurate measurements of the local heat transfer coefficients.

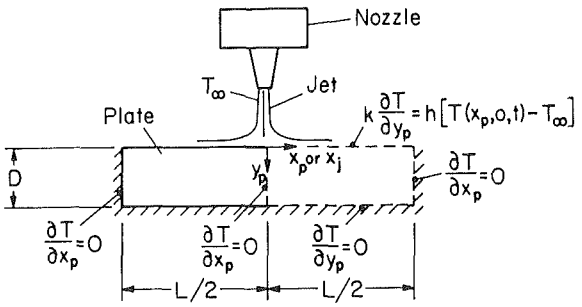

Fig. 4 Representation of thermal model used in data reduction

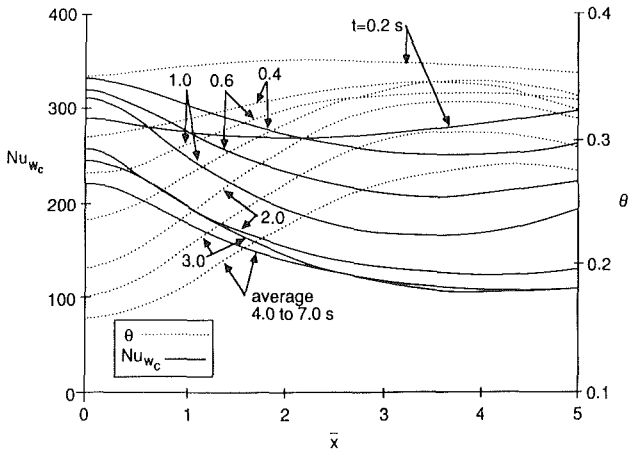

Fig. 5 Local Nusselt numbers and dimensionless surface temperatures at times after cooling was initiated with the wide nozzle (w = 2.03 cm) for H = 5.6 cm, Re_j = 16,100, T_{pl} = 205°C, T_∞ = 21.9°C, and v_j = 0.76 m/s

In the thermal model used for data reduction, the plate was idealized as a rectangular region enclosed by the broken lines in Fig. 4. With the temperature at the surface known from measurements, the plate temperature distribution was found from a solution to the two-dimensional energy equation

$$\rho c \frac{\partial T}{\partial t} = \frac{\partial}{\partial x_p}\left[k \frac{\partial T}{\partial x_p}\right] + \frac{\partial}{\partial y_p}\left[k \frac{\partial T}{\partial y_p}\right] \tag{7}$$

The discretized version of equation (7) and appropriate boundary conditions (Fig. 4) were formulated with temperature-dependent properties in accordance with the implicit methods described by Patankar (1980). The corresponding system of finite difference equations was solved using the line-by-line method with the tridiagonal matrix algorithm. Local heat transfer coefficients along the plate were calculated with the numerical models and the surface temperature measurements. Nodal temperatures for $y_p = 0$ were found for each time step from a least-squares fit to the surface temperature data using a fifth-order polynomial. The time step in the numerical model was equal to the sampling period during data acquisition (Δt_d = 200 ms). The positions of the surface temperature sensors in Fig. 3 and the sampling period were carefully selected by reducing surface temperature data generated by a simulation model of the anticipated experimental conditions (Zumbrunnen, 1988). Experimental uncertainties are tabulated in the Appendix.

Results and Discussion

Boundary Layer Growth Period. Convective heat transfer distributions during the boundary layer growth period on the initially dry plate are shown in Fig. 5. Surface temperatures are given in terms of the dimensionless variable θ, which is representative of the thermal energy transferred to the liquid from the plate. Results are given only for $\bar{x} \geq 0$ since the flow and heat transfer are symmetric about the stagnation line ($\bar{x} = 0$). For $t \leq 0.6$ s, during which time thermal and velocity boundary layers thicken, local Nusselt numbers are larger than those at later times and their distributions are more uniform. Eventually, local Nusselt numbers fluctuate randomly about an average distribution. Fluctuations are attributed principally to errors associated with the rapid sampling rate used to measure the surface temperatures. Time-averaged heat transfer and surface temperature distributions are presented in the subsequent figures and were used to correlate experimental results. Averaging over 15 time steps was found to be optimal, since a greater number did not affect the average appreciably ($\leq$ 1 percent) and since results eventually became less accurate as the temperature difference between the plate and water decreased. Averages were performed for 3 s $\leq t \leq$ 6 s for w = 1.02 cm and for 4 s $\leq t \leq$ 7 s for w = 2.03 cm.

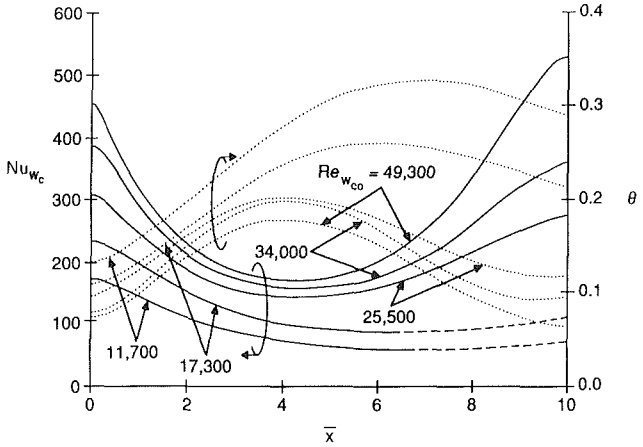

Fig. 6 The effect of impingement velocity on local Nusselt numbers with the narrow nozzle (w = 1.02 cm) in terms of Reynolds number for H = 5.6 cm and T_∞ = 21°C with $Re_{w_{c0}}$ = 49,300: T_{pl} = 88°C, v_j = 4.52 m/s; $Re_{w_{c0}}$ = 34,000: T_{pl} = 93°C, v_j = 3.07 m/s; $Re_{w_{c0}}$ = 25,500: T_{pl} = 95°C, v_j = 2.27 m/s; $Re_{w_{c0}}$ = 17,300: T_{pl} = 90°C, v_j = 1.53 m/s; $Re_{w_{c0}}$ = 11,700: T_{pl} = 97°C, v_j = 1.01 m/s

Effect of Impingement Velocity. The effect of impingement velocity on local Nusselt numbers is shown in Fig. 6 for w = 1.02 cm. Dimensionless surface temperatures are also shown for completeness. Results correspond to the period following boundary layer growth. At the stagnation line, Nusselt numbers increase with increasing impingement velocity, and the behavior is consistent with equations (1) and (2), which yield

$$Nu_{w_{c0}} = 0.57\,(\bar{C} Re_{w_{c0}})^{1/2} Pr^n \tag{8}$$

The dimensionless velocity gradient $\bar{C}$ is a constant dependent only on physical characteristics of the impinging jet such as separation distance H (Miyazaki and Silberman, 1972) and uniformity in jet discharge velocity (Sparrow and Lee, 1975). For the jets of this study, $\bar{C}$ = 0.99, as determined from the measured pressure distribution of Fig. 2 and Euler's equation (Schlichting, 1979) for inviscid flow

$$\frac{d(\bar{u}_\infty^2)}{d\bar{x}} = -\frac{d\bar{P}}{d\bar{x}} \tag{9}$$

In Fig. 6, the higher Nusselt numbers at the larger Reynolds numbers decline more rapidly with increasing $\bar{x}$. This occurs since the dimensionless flow acceleration distance from the stagnation line in terms of $\bar{x}$ depends on $\bar{P}(\bar{x})$ (Fig. 2) according to equation (9), and not on the impingement velocity v_{jc}. The dashed portions of the curves for $Re_{w_{c0}}$ = 11,700 and $Re_{w_{c0}}$ = 17,300 correspond to regions for which plate flow

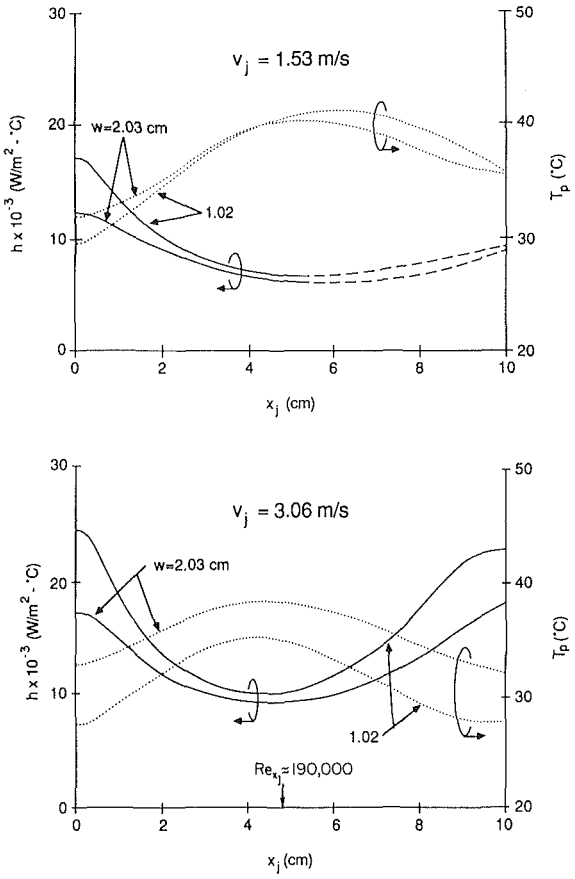

Fig. 7 Effect of jet width on heat transfer coefficients for H = 5.6 cm, T_{pl} = 90°C, and T_∞ = 21°C

conditions were influenced by reduced flow zones near the nozzle sidewalls. At larger Reynolds numbers, the reduced flow zones were thinner and had little influence on plate conditions. Transitions to a turbulent boundary layer occur on the plate for $Re_{w_{c0}} > 17{,}300$, causing increases in Nu_{w_c} for $\bar{x} \gtrsim 5$. Peak values for Nu_{w_c} beyond the transition points arise near the far edge of the plate and increase with increasing Reynolds number. Significantly, these peak values exceed those at the stagnation point for $Re_{w_{c0}} \geq 34{,}000$.

An estimate was made of the critical Reynolds number, $Re^c_{x_j} = v_{jc}x^c_j/\nu$, corresponding to the onset of a turbulent boundary layer. The critical distance from the stagnation line (x^c_j) was taken to be the distance where the minimum Nusselt number occurred. Results at low impingement velocities affected by the flow distortion on the plate (Fig. 6) were not utilized. The average value for $Re^c_{x_j}$ was 190,000 based on 17 experiments for both nozzles (w = 1.02 cm and w = 2.03 cm). The standard deviation was 35,000, giving an expected standard deviation in the average value of 8500 ($35{,}000/\sqrt{17}$). Average values for each nozzle were identical, suggesting that the onset location is not influenced by the free surface of the jet, since the nozzle widths differed by a factor of two.

Effect of Jet Width. The effect of jet width is most readily illustrated in terms of the spatial distribution of the local heat transfer coefficient h (Fig. 7). With $Nu_{w_{c0}} \propto Re^{1/2}_{w_{c0}}$ from equation (8), the ratio of heat transfer coefficients at $x_j = 0$ for two jets of different width but identical impingement velocity and kinematic viscosity is simply $h_{01}/h_{02} = (w_{c2}/w_{c1})^{0.5}$, where w_{c1} and w_{c2} are the corrected jet widths (equation (5)). The results of Fig. 7 are in fair agreement with this relationship, although a smaller exponent is suggested by the experiments. In fact, subsequent correlations for w = 1.02 cm give $Nu_{w_{c0}} \propto Re^{0.608}_{w_{c0}}$, which yields $h \propto w_c^{-0.392}$. The larger Reynolds number exponent is a consequence of vorticity amplification, which enhances heat transfer near the stagnation line (Sutera et al., 1963).

In Fig. 7 with v_j = 1.53 m/s, heat transfer coefficients are nearly equal for $x_j \gtrsim 3$, suggesting that the influence of jet width is largely confined to the impingement zone. The dashed portions of the curves again indicate the area on the plate where flow conditions are influenced by nozzle wall effects. Transitions to turbulent boundary layers are evident for v_j = 3.06 m/s at $x_j \approx 5$ cm. For $Re_{x_j} \gtrsim 190{,}000$, the heat transfer coefficient for w = 1.02 cm increases more rapidly, even though flow velocities are identical for both curves. This result may be due to a greater interaction between the free surface and developing turbulence in the boundary layer, owing to the reduced water layer height on the plate for the narrow nozzle. For example, observed waviness in the free surface of the water could enhance turbulence in the boundary layer.

Correlations. If the Prandtl number Pr is included, theoretical heat transfer distributions may generally be expressed as

$$Nu_{w_c}Re^{-m}_{w_c}Pr^{-n} = g(\bar{x}) \tag{10}$$

where $g(\bar{x})$ is an $\bar{x}$-dependent function and m and n are constants (Inada et al., 1981). Thermophysical properties are evaluated at the local film temperature T_f. Equation (10) reduces to equation (8) at $\bar{x} = 0$, where $g(\bar{x}) = 0.57\bar{C}^{1/2}$ and m = 1/2. Donaldson et al. (1971) assigned an exponent of m = 0.8 to an analogous expression for circular air jets, since the value is commonly associated with a turbulent boundary layer (Schlichting, 1979). In this study, the onset of turbulence in the boundary layer occurred several jet widths from the stagnation line where $Re_{x_j} \approx 190{,}000$. Therefore, a value of 0.8 is inappropriate for $Re_{x_j} \lesssim 190{,}000$. Although equation (8) suggests that m = 0.5 for laminar flow, experimental values of $Nu_{w_{c0}}$ were compared to theoretical values given by equation (8) and were found to be larger by factors ranging from 1.6 to 1.9. Such increases are attributed to vorticity amplification in the stagnation zone and possibly due to small instabilities associated with the transition to a turbulent boundary layer (White, 1974) beyond the stagnation zone. Thus, the Reynolds number exponent m depends on the interplay of vorticity amplification, turbulence, and the stabilizing influence of the favorable pressure gradient in the accelerating flow near the stagnation line. Since the boundary layer is therefore neither laminar nor fully turbulent, it may be surmised that $0.5 < m < 0.8$. This premise is supported by the range of Reynolds number exponents ($0.5 \leq m \leq 0.8$) in the correlations reviewed by Downs and James (1987).

With thermophysical properties determined at the film temperature T_{f0}, experimental values of $Nu_{w_{c0}}$, Pr_0, and $Re_{w_{c0}}$ were used in a least-squares analysis to find optimal stagnation line values for m and $g(0)$ in equation (10). The Prandtl number exponent n could not be precisely determined from the data, since the experimental uncertainty was comparable to the influence of Prandtl number over the range $3.0 \lesssim Pr_0 \lesssim 6.0$. Consequently, a Prandtl number exponent of 0.4 was selected that is consistent with the values reported in the review by Downs and James (1987) where $0.33 \leq n \leq 0.42$, and that reflects a dependence of vorticity amplification on Prandtl number (Sutera et al., 1963).

Local heat transfer distributions for v_j = 1.54 m/s and w = 2.03 cm are given in Fig. 8 over the experimental Prandtl number range. Differences in $Re_{w_{c0}}$ are due to the temperature

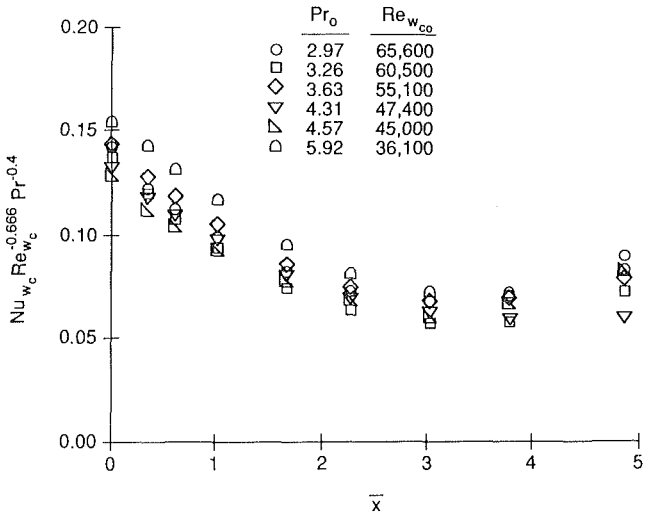

Fig. 8 Comparison of local heat transfer distributions obtained for different Prandtl numbers with w = 2.03 cm and v_j = 1.54 m/s

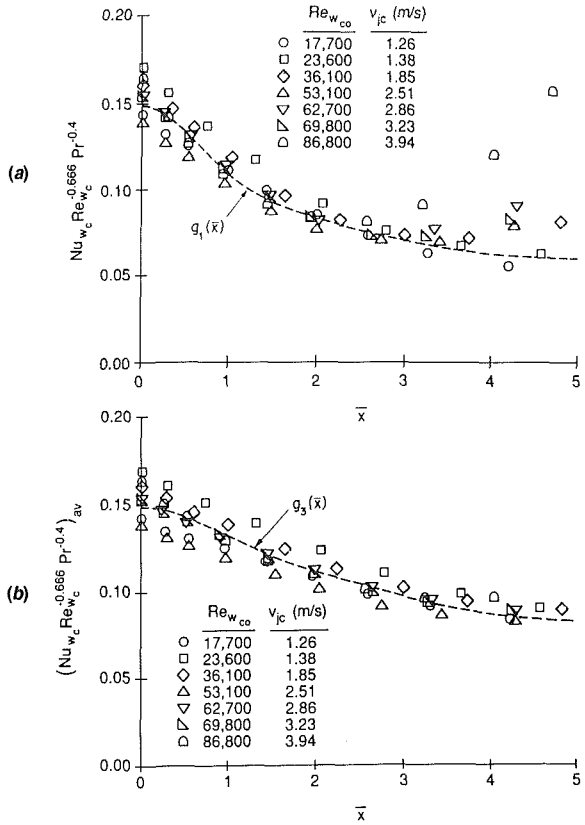

Fig. 9 Heat transfer distributions at different Reynolds numbers with Pr$_0$ = 5.7 ± 0.3 and w = 2.03 cm: (*a*) local, and (*b*) average

dependence of the kinematic viscosity of water. The scatter in the results is consistent with the experimental uncertainty, and the results may thereby be correlated with equation (10) over the experimental Prandtl number range. While the results of Fig. 8 pertain to a single impingement velocity, those of Fig. 9(*a*) correspond to different velocities. Results for $\bar{x} \gtrsim 3.5$ and $Re_{w_{c0}} \gtrsim 53{,}100$ deviate from the distribution due to transitions to turbulence. A polynomial fit to the combined results of Figs. 8 and 9(*a*) (w = 2.03 cm), excluding those affected by the transition, is indicated in Fig. 9(*a*) and is given by

$$Nu_{w_c} Re_{w_c}^{-0.666} Pr^{-0.4} = g_1(\bar{x}) \qquad (11a)$$

where

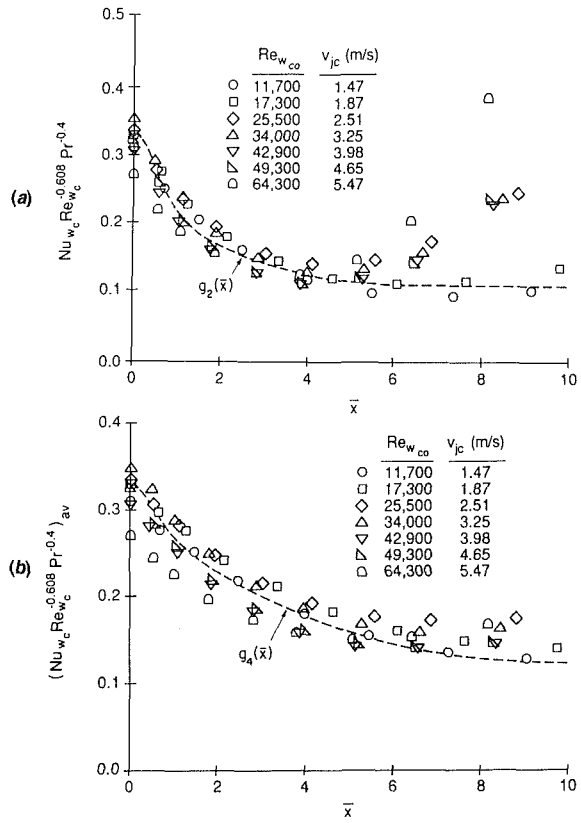

Fig. 10 Heat transfer distributions at different Reynolds numbers with Pr$_0$ = 6.2 ± 0.2 and w = 1.02 cm: (*a*) local, and (*b*) average

$$g_1(\bar{x})|_{0\le\bar{x}\le1.5} = 0.149 - \bar{x}^2(0.01303\bar{x}^2 - 0.06517\bar{x} + 0.09333) \qquad (11b)$$

$$g_1(\bar{x})|_{1.5\le\bar{x}\le5} = 0.1208 + \bar{x}(0.00233\bar{x} - 0.02383) \qquad (11c)$$

Equation (11) is applicable for $Re_{x_j} < 190{,}000$ and $0 \le \bar{x} \le 5$ and is accurate to within 3 percent of the average of the combined results shown in Figs. 8 and 9(*a*).

Experimental heat transfer distributions for w = 1.02 cm are given in Fig. 10(*a*). Deviations from the distribution are evident at higher Reynolds numbers for $\bar{x} \gtrsim 5$, since transitions to turbulent flow occur. Relative to Fig. 9(*a*), transition occurs at lower values of $Re_{w_{c0}}$, since flow velocities are higher with the narrow nozzle. Transition occurs in a relatively small region ($4 \lesssim \bar{x} \lesssim 6$) since the plate temperatures are lower at higher impingement velocities and the change in Re_{x_j} is offset by the increased water viscosity. The polynomial fit to the average of these results (to within 3.7 percent) for $Re_{x_j} \le 190{,}000$ and $0 \le \bar{x} \le 10$ is given by

$$Nu_{w_c} Re_{w_c}^{-0.608} Pr^{-0.4} = g_2(\bar{x}) \qquad (12a)$$

where

$$g_2(\bar{x})|_{0\le\bar{x}\le1.5} = 0.330 - \bar{x}^2(0.1356\bar{x}^2 - 0.4373\bar{x} + 0.4168) \qquad (12b)$$

$$g_2(\bar{x})|_{1.5\le\bar{x}\le6.0} = 0.2437 + \bar{x}(0.004148\bar{x} - 0.04733) \qquad (12c)$$

$$g_2(\bar{x})|_{6.0\le\bar{x}\le10.0} = 0.109 \qquad (12d)$$

For Re_{w_c} = 17,000, values for $Nu_{w_c} Pr^{-0.4}$ given by equations (11) and (12) differ by about 18 percent for $\bar{x}$ = 0 and by about 7 percent for $\bar{x}$ = 4. These differences decrease at higher Reynolds numbers, and for Re_{w_c} = 60,000, the differences are 14 and 0.2 percent at $\bar{x}$ = 0 and $\bar{x}$ = 4, respectively. In all cases, values of $Nu_{w_c} Pr^{-0.4}$ are greater for the narrow nozzle. Better agreement occurs away from the stagnation line, where

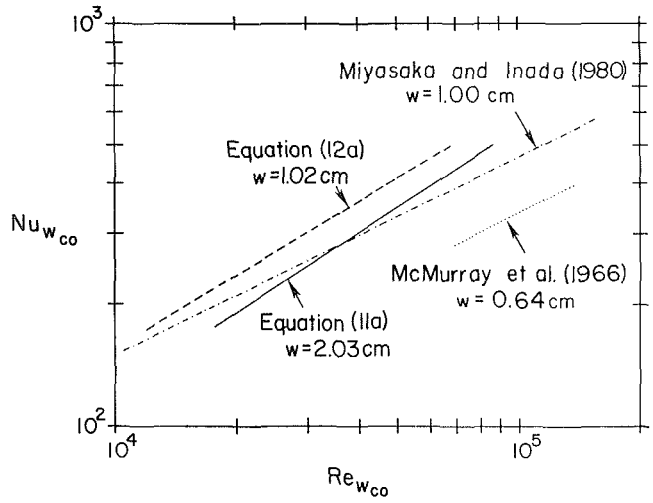

Fig. 11 Comparison of heat transfer correlations for $Pr_0 = 4.0$ and $\bar{x} = 0$

the effect of vorticity amplification is reduced. The smaller differences at $\bar{x} = 4$ are consistent with the discussion pertaining to Fig. 7.

In engineering applications, local heat transfer rates are frequently not required and predictions of overall or "average" heat transfer rates over a specified region are more useful. Experimental results have therefore been used to develop correlations for average heat transfer coefficients occurring over a specified distance from the stagnation line. The average heat transfer coefficient over a dimensionless distance $\bar{x}$ from the stagnation line was calculated from

$$h_{av}(\bar{x}) = \frac{\int_0^{\bar{x}} h(x)[T_p(x) - T_\infty]dx}{\int_0^{\bar{x}} [T_p(x) - T_\infty]dx} \tag{13}$$

and the corresponding average Nusselt number is $(Nu_{w_c})_{av} = h_{av}w_c/k$. Thermophysical properties required by the correlations were evaluated at an average film temperature $T_{f,av}$ over the distance $\bar{x}$ (see Nomenclature). The resulting distributions are given in Figs. 9(*b*) and 10(*b*). A polynomial fit for $w = 2.03$ cm and $\bar{x} \leq 5$ is given to within 2 percent of the average for the combined results of Figs. 8 and 9(*a*) by

$$(Nu_{w_c}Re_{w_c}^{-0.666}\,Pr^{-0.4})_{av} = g_3(\bar{x}) \tag{14a}$$

where

$$g_3(\bar{x})|_{0\leq\bar{x}\leq2.5} = 0.149 - \bar{x}^2(0.002631\bar{x}^2 - 0.01637\bar{x} + 0.03153) \tag{14b}$$

$$g_3(\bar{x})|_{2.5\leq\bar{x}\leq5} = 0.1775 + \bar{x}(0.004\bar{x} - 0.0390) \tag{14c}$$

For $w = 1.02$ cm and $\bar{x} \leq 10$, the polynomial fit to within 2.5 percent of the averaged results is

$$(Nu_{w_c}Re_{w_c}^{-0.608}\,Pr^{-0.4})_{av} = g_4(\bar{x}) \tag{15a}$$

where

$$g_4(\bar{x})|_{0\leq\bar{x}\leq2.0} = 0.330 - \bar{x}^2(0.02544\bar{x}^2 - 0.1118\bar{x} + 0.1474) \tag{15b}$$

$$g_4(\bar{x})|_{2.0\leq\bar{x}\leq10.0} = 0.2953 + \bar{x}(0.002067\bar{x} - 0.0378) \tag{15c}$$

It is important to note that equations (14) and (15) apply to positions on only one side of the jet. Values for $(Nu_{w_c})_{av}$ given by equations (14) and (15) with $Re_{w_c} = 17{,}000$ differ by about 18 percent for $\bar{x} = 0$ and by about 14 percent for $\bar{x} = 4$. For $Re_{w_c} = 60{,}000$, values differ by about 14 percent for $\bar{x} = 0$ and by about 7 percent for $\bar{x} = 4$.

Nusselt numbers measured near the stagnation line are larger than theoretical values given by equation (8) by factors ranging from 1.6 to 1.9. These factors are similar to values of 1.5 to 2.0 measured by Donaldson et al. (1971) for circular air jets and to the factor of 1.8 measured by Miyasaka and Inada (1980) for planar water jets. As previously mentioned, experimental values are greater due to turbulence in the jets.

A comparison of heat transfer correlations pertaining to planar water jets is given in Fig. 11. Results of this study are in good agreement with those presented by Miyasaka and Inada (1980). Differences are attributed to individual jet characteristics such as turbulence level and velocity uniformity.

Concluding Remarks

A transient cooling technique was used to infer local Nusselt number distributions for planar water jets impinging on a heated plate. Measurements were made for jet widths of 1.02 and 2.03 cm and for jet velocities between 1.26 and 5.92 m/s. Following an initial interval of approximately 1 s, during which time velocity and thermal boundary layers were established, a nearly steady Nusselt number distribution was achieved. For moderate to large jet velocities, the distributions were influenced by a pronounced transition to turbulence, which corresponded to $Re_{x_j} \approx 1.9 \times 10^5$. Upstream of the transition location, data for local and average Nusselt numbers were correlated by expressions of the form $Nu_{w_c} = Re_{w_c}^m\,Pr^{0.4}\,g(\bar{x})$. Although separate correlations were developed for each of the nozzle widths, differences prior to the transition point are small (< 18 percent) and decrease with increasing distance from the stagnation line. For a fixed velocity, heat transfer coefficients in the stagnation zone are larger for the narrow jet, since fluid acceleration occurs over a shorter distance. Hence, in addition to providing enhanced cooling, narrow jets are more efficient in removing heat per unit of expended fluid. At the stagnation line, experimental results exceed laminar flow predictions by factors ranging from 1.6 to 1.9. The discrepancy is attributed to turbulence in the jet and vorticity amplification in the stagnation zone. Although not considered in this study, opportunities for additional heat transfer enhancement may be associated with placing vortex generators on the plate. In addition to stimulating enhancement due vorticity amplification, the generators would induce early transition to turbulence.

Acknowledgments

This research was supported by the National Science Foundation of the United States under grant No. CPE-8414613.

References

Adcock, J. N., 1962, "The Laminar Jet System for Cooling Hot Steel Strip," *Journal of the Iron and Steel Institute*, Vol. 200, pp. 909–913.

Donaldson, C. Dup., Snedeker, R., and Margolis, D., 1971, "A Study of Free Jet Impingement. Part 2. Free Jet Turbulent Structure and Impingement Heat Transfer," *Journal of Fluid Mechanics*, Vol. 45, pp. 477–512.

Downs, S. J., and James, E. H., 1987, "Jet Impingement Heat Transfer—A Literature Survey," ASME Paper No. 87-HT-35.

Evans, H. L., 1962, "Mass Transfer Through Laminar Boundary Layers," *International Journal of Heat and Mass Transfer*, Vol. 5, pp. 35–57.

Gardon, R., and Akfirat, J. C., 1965, "The Role of Turbulence in Determining the Heat Transfer Characteristics of Impinging Jets," *International Journal of Heat and Mass Transfer*, Vol. 8, pp. 1261–1272.

Hatta, N., Kokado, J., Hirohiko, T., Harada, J., and Hiraku, K., 1984, "Predictable Modeling for Cooling Process of a Hot Plate by a Laminar Water Bar," *Archiv fur Eisenhuttenwesen*, Vol. 55, pp. 143–148.

Inada, S., Miyasaka, Y., and Izumi, R., 1981, "A Study of the Laminar Flow Heat Transfer Between a Two-Dimensional Water Jet and a Flat Surface With Constant Heat Flux," *Bulletin of the JSME*, Vol. 24, pp. 1803–1810.

Kohring, F. C., 1985, "Waterwall Water-Cooling Systems," *Iron and Steel Engineer*, June, pp. 30–36.

Kuethe, A. M., Willmarth, W. W., and Crocker, G. H., 1959, "Stagnation Point Fluctuations on a Body of Revolution," *The Physics of Fluids*, Vol. 2, pp. 714–716.

Ma, C. F., and Bergles, A. E., 1983, "Boiling Jet Impingement Cooling of Simulated Microelectronic Chips," in: *Heat Transfer in Electronic Equipment*, ASME, New York, pp. 5–12.

Martin, H., 1977, "Heat and Mass Transfer Between Impinging Gas Jets and Solid Surfaces," in: *Advances in Heat Transfer*, Academic Press, New York, Vol. 13, pp. 1–60.

McMurray, D. C., Myers, P. S., and Uyehara, O. A., 1966, "Influence of Impinging Jet Variables on Local Heat Transfer Coefficients Along a Flat Surface With Constant Heat Flux," in: *Proceedings 3rd International Heat Transfer Conference*, AIChE, New York, Vol. II, pp. 292–299.

Metzger, D. E., Cummings, K. N., and Ruby, W. A., 1974, "Effects of Prandtl Number on Heat Transfer Characteristics of Impinging Liquid Jets," *Proceedings, 5th International Heat Transfer Conference*, Japan Society of Mechanical Engineers and Society of Chemical Engineers, Tokyo, Vol. II, pp. 20–24.

Miyasaka, Y., and Inada, S., 1980, "The Effect of Pure Forced Convection on the Boiling Heat Transfer Between a Two-Dimensional Subcooled Water Jet and a Heated Surface," *Journal of Chemical Engineering of Japan*, Vol. 13, pp. 22–28.

Miyazaki, H., and Silberman, E., 1972, "Flow and Heat Transfer on a Flat Plate Normal to a Two-Dimensional Laminar Jet Issuing From a Nozzle of Finite Height," *International Journal of Heat and Mass Transfer*, Vol. 15, pp. 2097–2107.

Moffat, R. J., 1988, "Describing the Uncertainties in Experimental Results," *Experimental Thermal and Fluid Science*, Vol. 1, pp. 3–17.

Morgan, T. E., Dancy, T. E., and Korchynsky, M., 1965, "Improved Steels Through Hot Strip Mill Controlled Cooling," *Journal of Metals*, Vol. 17, pp. 829–831.

Patankar, S. V., 1980, *Numerical Heat Transfer and Fluid Flow*, McGraw-Hill, New York.

Sadeh, W., and Brauer, H., 1980, "A Visual Investigation of Turbulence in Stagnation Flow about a Circular Cylinder," *Journal of Fluid Mechanics*, Vol. 99, pp. 53–64.

Schlichting, H., 1979, *Boundary Layer Theory*, 7th ed., McGraw-Hill, New York.

Scholtz, M. T., and Trass, O., 1970, "Mass Transfer in a Nonuniform Impinging Jet," *American Institute of Chemical Engineering Journal*, Vol. 16, pp. 82–96.

Sparrow, E. M., and Lee, L., 1975, "Analysis of Flow Field and Impingement Heat/Mass Transfer Due to a Nonuniform Slot Jet," ASME Paper No. 75-HT-UU.

Sutera, S. P., Maeder, P. F., and Kestin, J., 1963, "On the Sensitivity of Heat Transfer in the Stagnation Point Boundary Layer to Free Stream Vorticity," *Journal of Fluid Mechanics*, Vol. 16, pp. 497–520.

Vader, D. T., 1988, "Convective and Boiling Heat Transfer from a Heated Surface to an Impinging, Planar Jet of Water," Ph.D. Thesis, Purdue University, West Lafayette, IN.

White, F. M., 1974, *Viscous Fluid Flow*, McGraw-Hill, New York, pp. 426–441.

Zumbrunnen, D. A., 1988, "A Study of Heat Transfer from Stationary and Moving Plates Cooled by Planar Jets of Water," Ph.D. Thesis, Purdue University, West Lafayette, IN.

APPENDIX

Experimental Uncertainty

Uncertainties in the experimental results were estimated according to the method of sequential perturbation (Moffat, 1988) and are tabulated in Table 1. Larger uncertainties are associated with higher Reynolds numbers and local heat transfer coefficients, since the temperature difference between the plate surface and liquid was smaller.

Table 1 Estimated uncertainties (percent) in the local heat transfer coefficients and Nusselt numbers

w = 1.02 cm				w = 2.03 cm			
	$Re_{w_{c0}}$				$Re_{w_{c0}}$		
$\bar{x}$	11,700	34,000	64,300	$\bar{x}$	17,700	53,100	86,800
0	11.6	14.6	17.4	0	11.0	11.7	12.2
4	10.2	11.2	12.9	2	10.4	10.7	10.9
10	10.0	14.2	25.1	5	9.9	10.9	12.9

Measurements of the Thermal Characteristics of Heated Turbulent Jets in Crossflow

S. A. Sherif
Department of Mechanical Engineering,
University of Miami,
Coral Gables, FL 33124
Mem. ASME

R. H. Pletcher
Department of Mechanical Engineering,
Iowa State University,
Ames, IA 50011
Fellow ASME

An experimental investigation of the thermal characteristics of heated turbulent jets discharging into a cross-flowing stream in a water channel is reported. Hot water was injected vertically upward from a circular pipe located near the channel bottom to simulate the heated jet. Fiber-film probes along with appropriate anemometers and bridges were operated in the constant-current mode as cold films to measure both mean and fluctuating temperatures. Profiles of mean and rms temperatures are presented for heated turbulent jets at velocity ratios of 1, 4, and 7 and for jet discharge temperatures approximately 28 to 42°C higher than the free-stream temperature. Measurements were carried out in the jet and its wake both in and outside the jet plane of symmetry.

Introduction

The terms jet and plume are sometimes used interchangeably. Generally, however, in a jet, the kinetic energy and momentum are large at discharge, having been imparted to the flow by a pressure drop through an orifice, nozzle, or tube. A plume is a free shear flow in which the primary source of kinetic energy and momentum flux arises through body forces. Forced plumes and buoyant jets are flows whose motion is in transition from a jet to a plume (Rodi, 1982).

Jets may be heated, cooled, or isothermal relative to the ambient fluid. The jet densimeteric Froude number at the discharge, defined as $\mathrm{Fr} = U_j/(gD|\Delta\rho/\rho_\infty|)^{1/2}$, is a measure of the relative importance of momentum forces and buoyancy forces. A positively buoyant jet (or simply a buoyant jet) is a jet whose fluid is less dense than the ambient fluid. This is usually the case in a heated jet. A negatively buoyant jet (or a sinking jet) is a jet whose fluid is denser than the ambient fluid. This is usually the case in a cooled jet. Positive or negative buoyancy can also be generated by changing the composition of the ambient or jet fluids; e.g., by adding salt to the jet fluid (Cavola and Davis, 1983; Ayoub, 1971; Fan, 1967). There are instances, however, where there are temperature or concentration differences between the jet and ambient fluids and yet the jet is classified as purely momentum. In these cases the jet discharge velocity is so high that momentum forces dominate over the buoyancy forces. That is, they are characterized by large Froude numbers (usually > 10).

Because of the practical significance of jets discharging into crossflowing streams, numerous theoretical and experimental investigations have been carried out. Experimental investigations have been reported by Bryant and Cowdrey (1955), Slawson and Csanady (1967), Hewett et al. (1971), and Bringfelt (1968). Callaghan and co-workers (1948, 1949, 1951), Ruggeri and Callaghan (1950), and Ruggeri (1952), in a series of investigations using a wind tunnel, studied the penetration and general correlations of temperature profiles downstream of air jets discharged at various angles to an air stream. Campbell and Schetz (1971, 1972, 1977) studied the behavior of thermal effluents discharged into waterways by a single jet injection mechanism. They determined the trajectory and growth for a range of discharge velocities and temperatures. Ramsey (1969) and Ramsey and Goldstein (1970) introduced a heated jet at angles of 90 and 35 deg to the mainstream flow direction using a low-velocity, low-turbulence wind tunnel. They reported visualization studies using tufts of yarn and a carbon dioxide–water fog. Temperature profiles in the interaction region were presented for blowing rates (defined as the ratio of mass flux of injected gas to mass flux of free stream) from 0.1 to 2.0 for normal injection and at blowing rates of 1.0 and 2.0 for 35-deg injection. Kamotani and Greber (1972) presented longitudinal and transverse distributions of velocity, temperature, and turbulence intensity. Their detailed measurements and smoke photographs of the flow indicated that the jet structure is dominated by a vortex wake, which forms behind the jet. The experiments also indicated that the components of crossflow normal and parallel to the jet trajectory independently control the entrainment rate. Andreopoulos (1983) presented results for mean temperature in a nonbuoyant heated jet issuing perpendicularly into a cold air stream for velocity ratios of 0.25, 0.5, 1, and 2, and velocity–temperature fluctuation statistics at a velocity ratio of 0.5. The mean temperature profiles at the jet exit were found to be considerably nonuniform at low velocity ratios, indicating an early mixing between the cold and hot fluids. He reported that the extra rate of strain due to streamline curvature and the longitudinal and normal temperature gradients affect the rate of generation of temperature fluctuations and turbulent heat fluxes. He observed that there are regions of the flow where the streamlines are unstably curved, but the generation of temperature fluctuations is damped. Andreopoulos also observed that the eddy diffusivity is well-behaved across the flow only at downstream positions where the turbulent Prandtl number has rather high values close to the wall and reaches values around 0.9 away from the wall. Other related work includes that of Chu and Goldberg (1974), Chu (1979), Kim (1985), Wright (1977), Andreopoulos and Rodi (1984), Andreopoulos (1985), Sykes et al. (1986), Claus (1985), and Harloff and Lytle (1988).

Although the measurements reported in the literature on heated jets or plumes in crossflow seem to be numerous, few studies went beyond investigating the jet trajectory and spread. Measurements dealing with the mean temperature field are generally fewer than those on the velocity field. With the exception of the work by Andreopoulos (1983), Ramaprian and Haniu (1983) (two-dimensional jets), and more recently Wark

Contributed by the Heat Transfer Division and presented at the Joint AIAA/ASME Thermophysics and Heat Transfer Conference, Boston, Massachusetts, June 2-4, 1986. Manuscript received by the Heat Transfer Division June 7, 1988. Paper No. 86-HT-34. Keywords: Jets, Plumes, Turbulence.

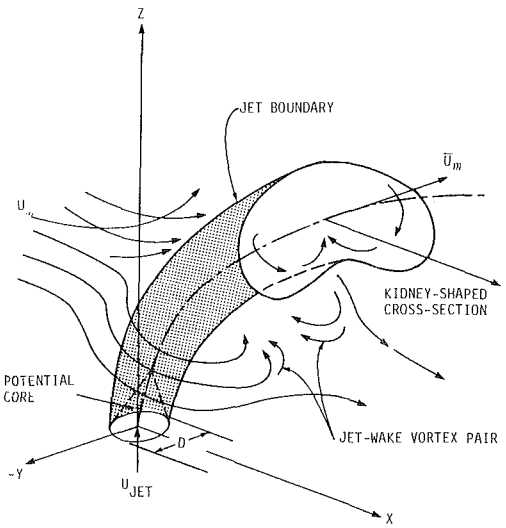

Fig. 1 The round turbulent jet in a crossflow

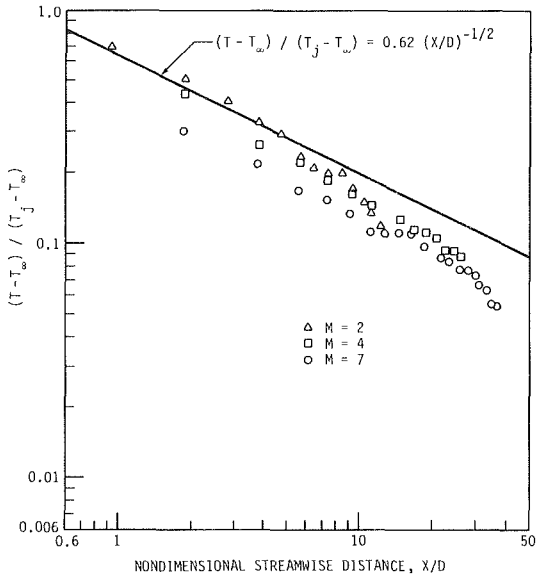

Fig. 2 Decay of centerline temperature excess ratio

and Foss (1988), there is no work known to the authors that reported measurements on the root mean square temperature fluctuations. The measurements reported by Andreopoulos (1983), however, are restricted to low velocity ratios (less than 2.0).

At the beginning of the research program on which this paper partly reports, it was felt that there was a need to provide extensive and reliable data on the velocity, temperature, and turbulence structure of the jet in crossflow. This should help guide the development, improvement, and testing of better prediction methods based on advanced and more sophisticated turbulence models. The data should also be helpful in terms of increasing understanding of the complex interaction mechanism between the turbulent jet and the crossflow. This flow is generally characterized by distortions in the jet cross section, flow separation and reversal, and strong and rapid temperature fluctuations. Rodi (1982) reports that the effect of buoyancy forces and buoyancy-generated turbulence on the interaction mechanism between the jet and the cross stream is still far from being understood (see Fig. 1). One of the objectives of the research program on which this paper is partly based was to contribute to increasing that understanding.

Experimental Techniques

The measurements were carried out in the 0.61 m × 1.067 m semiclosed circuit water channel at Iowa State University. The test section was formed by an aluminum plate, 12.7 mm thick, 0.457 m wide, and 1.829 m long with a rounded (1:2 ellipse) leading edge and a trailing edge flap. The plate was positioned 152 mm above the bottom of the channel. The plate length was chosen taking into account the range of jet trajectories for different jet inlet conditions. The plate width was chosen so as not to interfere with the turbulent boundary layers already developed on the channel sides. Two false sidewalls having a thickness of 8.73 mm, a height of 0.965 m, and the same plate length of 1.829 m were installed on both sides of the plate to promote two dimensionality for the flow and to serve as supporting members for the plate. Hot water was injected vertically upward from the plate through a circular pipe of 13.84 mm inside diameter. The thickness of the boundary layers developing on the false walls has been kept to a minimum by providing streamlined leading edges to the false walls. The flap provided at the plate trailing edge was adjusted so as to minimize the elliptic effects in the flow field and ensure that the flow approached the plate at a zero angle of incidence.

A DISA constant current anemometer was used in conjunction with a DISA 55R11 fiber-film probe for mean and fluctuating temperature measurements. The constant current anemometer was comprised of a DISA 55M01 main unit, a DISA 55M05 power pack, and a DISA 55M20 temperature bridge. A constant probe current of 2.5 mA was used for all runs. This relatively high value of the probe current was chosen because of the desire to increase probe sensitivity to temperature fluctuations. The velocity dependence was checked and was found to be negligible at this value of the probe sensor current. The DISA 55R11 probe was calibrated for temperature measurements using a Haake A81 constant temperature bath with a resolution of 0.056°C and a calibrated copper-constantan thermocouple attached to the fiber-film probe support. The water bath was placed inside the channel to permit the probe to be lowered and immersed in the bath water. The water

Nomenclature

A = temperature calibration constant
B = temperature calibration constant
D = jet diameter at discharge
$E, \bar{E}$ = instantaneous and time-averaged constant current anemometer voltage
e = a-c component of the constant current anemometer output voltage
M = velocity ratio = U_j/U_∞
$T, \bar{T}$ = instantaneous and time-averaged temperature
t' = fluctuating temperature
T_j = jet discharge temperature
T_∞ = free-stream temperature
U_j = jet discharge velocity
U_∞ = free-stream velocity
X = streamwise distance measured from center of jet discharge pipe
Y = transverse (spanwise) distance measured from center of jet discharge pipe
Z = vertical distance measured from jet injection platform

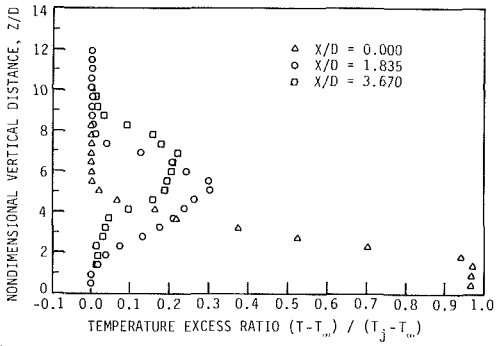

Fig. 3(*a*) Mean temperature profiles for heated jets, $M = 7$, $Y/D = 0$, Fr = 63.688, Re = 62,377

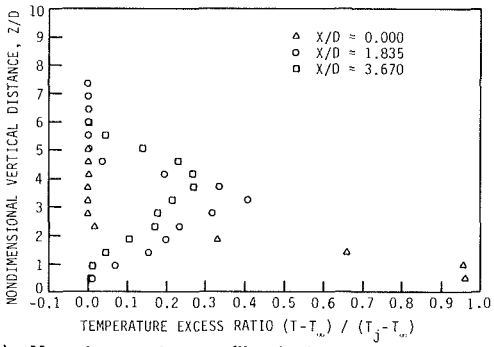

Fig. 4(*a*) Mean temperature profiles for heated jets, $M = 4$, $Y/D = 0$

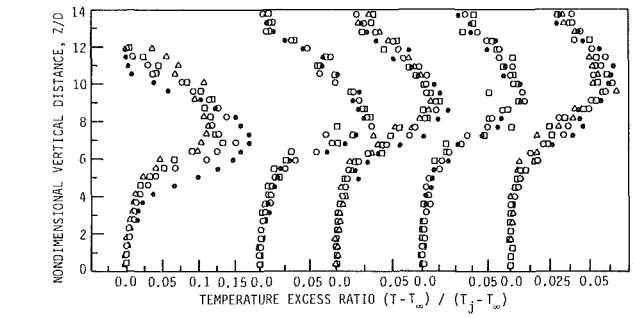

Fig. 3(*b*) Mean temperature profiles for heated jets, $M = 7$, $Y/D = 0$, Fr = 63.688, Re = 62,377

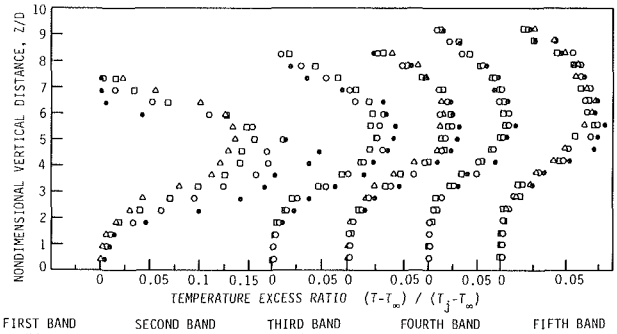

Fig. 4(*b*) Mean temperature profiles for heated jets, $M = 4$, $Y/D = 0$, Fr = 35.973, Re = 36,263

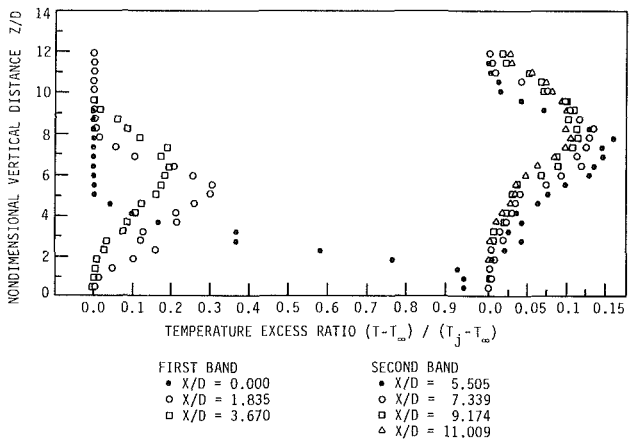

Fig. 3(*c*) Mean temperature profiles for heated jets, $M = 7$, $Y/D = 0.462$, Fr = 63.688, Re = 62,377

temperature was initially set at 10°C and the output voltage of the constant current anemometer and the water temperature were recorded. The temperature was gradually increased (by increments of 1.1°C) and at each setting, both the anemometer output voltage and the bath temperature were recorded and stored. The calibration run was considered completed after the acquisition of 20 calibration points. A linear relationship always resulted between the anemometer output voltage and the bath temperature, which was represented by the following equation:

$$\bar{E} = A + B\,\bar{T} \tag{1}$$

where A and B are constants determined by a least-square curve-fit of the calibration data. Correlation coefficients of 0.999998 or better were always obtained using this procedure. The overall uncertainty in the temperature measurement was less than 2 percent.

The root mean square temperature fluctuation, on the other hand, was measured using the a-c component of the anemometer output voltage. This is based on the assumption that the instantaneous value of the anemometer voltage behaves, rigorously, in the same manner as the d-c component. After some manipulation the following equation for the mean square fluctuations can obtained:

$$\overline{e^2} = B^2\,\overline{t'^2} \tag{2}$$

The overall uncertainty in the measurement of the root mean square temperature fluctuation is less than 12 percent.

Results and Discussion

Mean Temperature. The jet centerline temperature was measured for a number of velocity ratio/Froude number combinations. The temperature excess ratio, defined as $(T - T_\infty)/(T_j - T_\infty)$, is plotted against the nondimensional downstream distance X/D in Fig. 2.

As can be observed, the choice of the excess temperature ratio to normalize the centerline temperature makes the data appear similar. For heated jets, Andreopoulos (1983) noted that for $0.25 \le M \le 2$ and $X/D \le 10$, the maximum (centerline) temperature is proportional to $(X/D)^{-1/2}$. He observed, for example, at $M = 2$ that his data and those of Ramsey and Goldstein (1970) fell on the $0.62\,(X/D)^{-1/2}$ curve. These observations are confirmed by the $M = 2$ data shown in Fig. 2 up to a downstream distance of $X/D = 5$, but the above correlation is not valid for $X/D > 5$.

The mean temperature profiles are presented in terms of the nondimensional temperature excess ratio, $(T - T_\infty)/(T_j - T_\infty)$, for a velocity ratio of 7 both in and outside the jet plane of symmetry and for velocity ratios of 4 and 1 in the plane of symmetry only. The free-stream velocity was 0.35 m/s for all

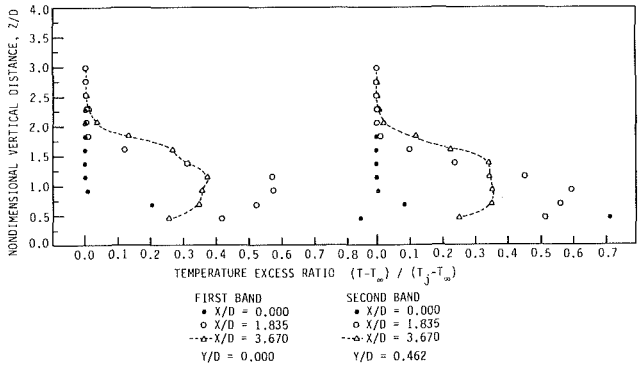

Fig. 5 Mean temperature profiles for heated jets, M = 1, Fr = 9.222, Re = 8822

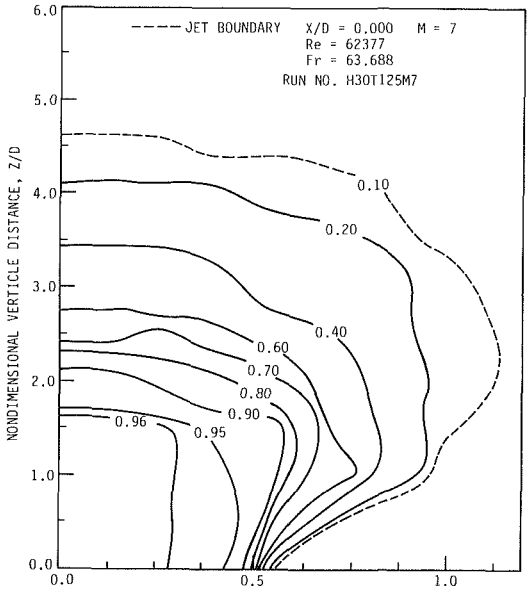

Fig. 6(*a*) Contour plots of $(T - T_\infty)/(T_j - T_\infty)$, M = 7, X/D = 0

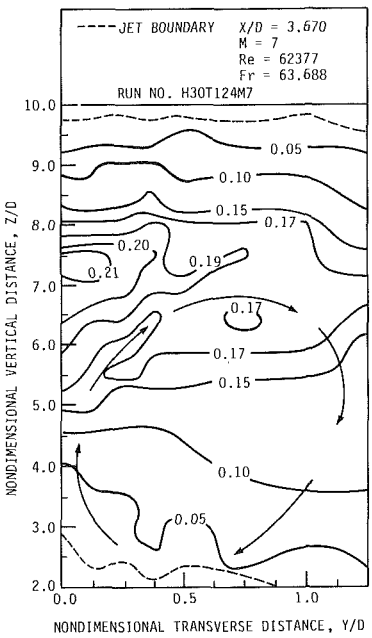

Fig. 6(*b*) Contour plots of $(T - T_\infty)/(T_j - T_\infty)$, M = 7, X/D = 3.670

three velocity ratios. For the largest velocity ratio, M = 7, the jet and free-stream temperatures were 52°C and 18.5°C, respectively, resulting in a Froude number of 63.69 and a Reynolds number of 62,377 at the jet discharge. The same discharge and free-stream temperatures were used for the intermediate velocity ratio, M = 4, resulting in Froude and Reynolds numbers at the jet discharge of 35.97 and 36,263, respectively. For the smallest velocity ratio, M = 1, discharge and free-stream temperatures of 50°C and 17°C, respectively, were used, resulting in Froude and Reynolds numbers at the jet discharge of 9.22 and 8822, respectively. Results of the largest velocity ratio (M = 7) case are presented in Fig. 3, while those of the intermediate velocity ratio (M = 4) are presented in Fig. 4. For the smallest velocity ratio (M = 1) case, the results are given in Fig. 5. It should be noted that the horizontal scale is not the same for all profiles shown in these figures.

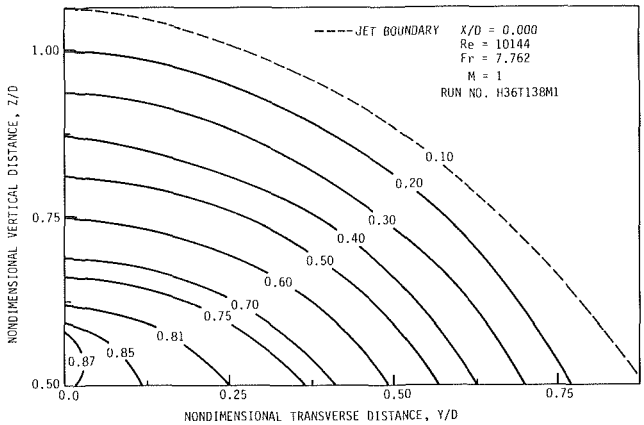

Fig. 7(*a*) Contour plots of $(T - T_\infty)/(T_j - T_\infty)$, M = 1, X/D = 0

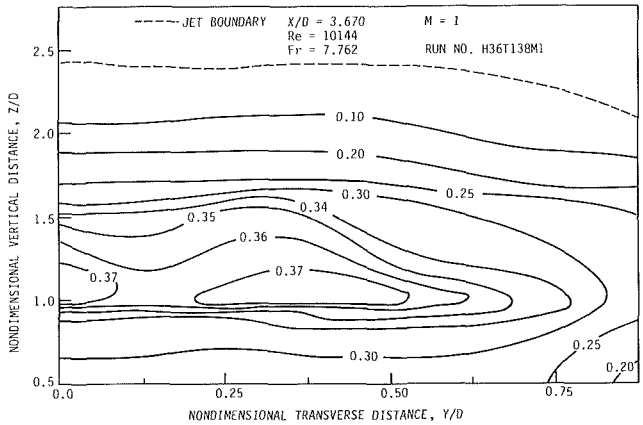

Fig. 7(*b*) Contour plots of $(T - T_\infty)/(T_j - T_\infty)$, M = 1, X/D = 3.670

For M = 7 and M = 4, traverses as far downstream as X/D = 36.697 jet diameters are presented in the jet plane of symmetry. For M = 1, traverses as far downstream as X/D = 3.67 are presented. Outside the plane of symmetry, traverses as far as X/D = 11.009 are presented at a lateral position of Y/D = 0.462 for M = 7. The same is true for M = 1 except that the traverses are presented up to X/D = 3.67. Additional measurements can be found in Sherif (1985).

Comparing temperature profiles at the three velocity ratios considered reveals interesting information on the flow character, especially in the jet wake. Examination of the temperature values for M = 1 near the wall indicates that the temperature excess ratio is not zero. This means that the fluid adjacent to the wall is apparently not free stream as is the case for higher velocity ratios. This means that, for smaller velocity ratios, the jet interacts with the wall at small values of X/D where the value of the temperature excess ratio is relatively high, while, for larger velocity ratios, that interaction takes place at much larger values of X/D where the temperature

excess ratio has a much smaller value. In other words, for smaller velocity ratios, the wall temperature can be significantly affected by the temperature of the jet fluid, while that is unlikely to happen for larger velocity ratios. The former case is in effect that which occurs in discrete film cooling (e.g., of gas turbine blades) except that the velocity ratio here is slightly higher than that normally used for film cooling.

Further examination of the temperature profiles for all three velocity ratios both in and outside the plane of symmetry indicates that the location and magnitude of the maximum temperature remain virtually unchanged up to $Y/D = 0.462$. The data indicate that the location of the maximum temperature relative to the wall is an increasing function of the velocitiy ratio. The data also reveal that the value of the temperature excess ratio is a decreasing function of the velocity ratio. The maximum value of the temperature excess ratio at a downstream position of $X/D = 3.67$ is approximately 0.22 for $M = 7$ compared with 0.26 for $M = 4$ and 0.37 for $M = 1$. This simply means that the initial mixing region is shorter for larger velocity ratios. The effect of the jet can still be seen as far downstream as $X/D = 36.697$. This can be seen by examining the values of the temperature excess ratio at this downstream position (0.063 for $M = 7$ and 0.074 for $M = 4$).

The effect of the lateral spreading of the jet can best be understood by examining the contour plots of the temperature excess ratio, $(T - T_\infty)/(T_j - T_\infty)$, at different downstream positions for velocity ratios of 7 and 1. For $M = 7$, contour plots at downstream positions of $X/D = 0$ and 3.67 are presented in Fig. 6 while similar plots are given in Fig. 7 for $M = 1$.

Squire (1950) defined the jet edge as the boundary on which the velocity is 10 percent of the centerline value. A similar definition is adopted here employing the centerline temperature excess ratio in place of the centerline velocity. This resulted in the dashed lines shown in Fig. 6 for $M = 7$ and Fig. 7 for $M = 1$. The jet growth with increasing downstream distance can be easily seen for both velocity ratios. These figures also indicate that jet spread is an increasing function of the velocity ratio. This observation was confirmed by the flow visualization study, the results of which have been presented in Sherif (1985). This observation is also consistent with a similar trend observed for jets in coflowing ambients (Madni, 1975).

Further examination of the contour plots reveals information on the structure of the cross section of the jet and its wake including the vortex region. For example, at $M = 7$ just above the jet discharge plane ($X/D = 0$), the constant temperature lines indicate smooth spreading in both the transverse and vertical directions. Farther downstream a developing vortex pair in the wake causes the cross section to look like a horseshoe (Sherif, 1985). At $X/D = 3.67$ (Fig. 6(*b*)), the jet cross section is distorted even further and looks more like a kidney. Chan and Kennedy (1972) report that the vortex pair in the wake induces, in turn, another pair of weaker vortices, with the same sense, in the jet itself. Platten and Keffer (1968) argue that these vortices account for a large portion of the entrainment of the free-stream fluid into the jet, which causes it to expand and diffuse much more rapidly than the free jet. These observations seem to be supported by the results of the present study, in general, and the constant temperature contours in particular. Farther downstream, the wake vortex pattern seems to weaken, as evidenced by flatter contour lines in the wake region (Sherif, 1985).

For $M = 1$, a more gradual diffusion of the temperature field is observed in the jet than at the larger velocity ratios. This can be seen from the more widely spaced and uniform nature of the isotherms as shown in Fig. 7(*a*). This trend prevails only near the jet periphery when M is higher than unity. Farther downstream, the kidney-shaped cross section is seen to exist as early as $X/D = 1.835$ (Sherif, 1985). The jet wake

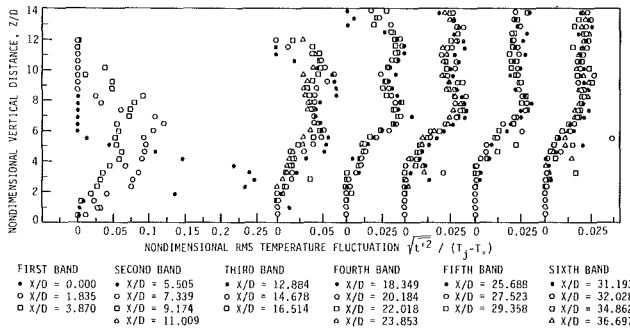

Fig. 8 Root mean square temperature fluctuation profiles for heated jets, $M = 7$, $Y/D = 0$, Fr = 63.688, Re = 62,377

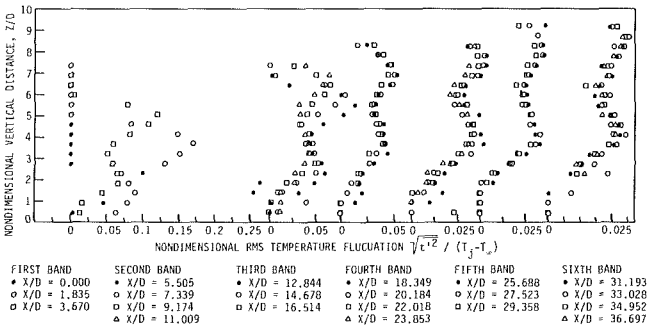

Fig. 9 Root mean square temperature fluctuation profiles for heated jets, $M = 4$, $Y/D = 0$, Fr = 35.973, Re = 36,263

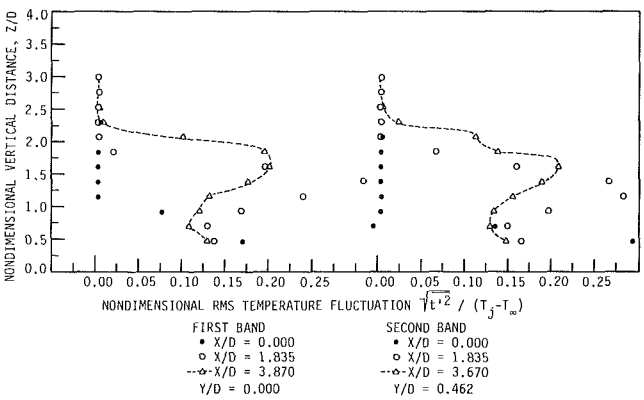

Fig. 10 Root mean square temperature fluctuation profiles for heated jets, $M = 1$, Fr = 9.222, Re = 8822

region, however, is a very narrow one and the vortical pattern is not easily distinguishable. This latter observation is consistent with previous observations made regarding the existence of a high-temperature region between the jet and the wall, which means (as explained earlier) that the fluid adjacent to the wall is not entirely free stream.

Further examination of the constant temperature contours indicates that the temperature gradient is larger above the jet centerline than in the wake. This is evidence of the asymmetry usually associated with the jet discharging to a crossflow. The extent of this asymmetry increases if the jet and the wake regions are considered as the domain of interest. In the jet core, however, the axisymmetric assumption was shown to be a useful approximation (Hwang and Pletcher, 1978) for prediction purposes.

Fluctuating Temperature. Fluctuating temperature profiles are presented in the plane of symmetry in terms of the dimensionless quantity, $\sqrt{t'^2}/(T_j - T_\infty)$, for the same downstream position and velocity ratios for which the mean temperature profiles were presented. These are shown in Fig. 8 for $M = 7$, Fig. 9 for $M = 4$, and Fig. 10 for $M = 1$.

Examination of the temperature fluctuation profiles above the jet discharge ($X/D = 0$), for the three velocity ratios considered, reveals that the fluctuations in temperature increase with decreasing velocity ratios. For example, $\sqrt{\overline{t'^2}}$ reaches a peak value of 25 percent of $(T_j - T_\infty)$ for $M = 7$ (Fig. 8) compared with 27 percent for $M = 4$ (Fig. 9) and 32 percent for $M = 1$ (Fig. 10). The locations of these peaks correspond to the locations of the maximum mean temperature gradient ($Z/D = 2.75$ for $M = 7$, 1.8 for $M = 4$, and 0.7 for $M = 1$). Farther downstream, the temperature fluctuations decrease. At $X/D = 3.67$, for example, the maximum value of the fluctuations is 8 percent of $(T_j - T_\infty)$ for $M = 7$ compared with 12 percent for $M = 4$, and 20 percent for $M = 1$. These maxima still, however, occur at the locations of maximum mean temperature gradient ($Z/D = 8.25$, 5.2, and 1.55, respectively).

Farther downstream, a characteristic shape with two local maxima and one minimum emerges (the minimum near the wall is discounted because of boundary effects). Careful examination of the locations of minimum fluctuations in temperature indicates that they correspond closely to the locations where the nondimensional mean temperature is maximum. At a downstream position corresponding to $X/D = 16.514$, for example, the minimum $\sqrt{\overline{t'^2}}$ occurs at $Z/D = 8.6$ for $M = 7$ (Fig. 8) and 5.2 for $M = 4$ (Fig. 9). These values compare with 8 and 4.85 for the corresponding locations of the maximum mean temperature (Figs. 3(*b*) and 4(*b*)). At the farthest downstream position, $X/D = 36.697$, the minimum fluctuations occur at $Z/D = 9$ for $M = 7$ (Fig. 8) and 6.3 for $M = 4$ (Fig. 9), compared with 9.9 and 6 for the corresponding locations of the maximum mean temperature (Figs. 3(*b*) and 4(*b*)). This simply means that the temperature fluctuations are at their minimum level (in the jet field) on or very close to the jet centerline. This is primarily because of the low level of entrainment and turbulent mixing (thus creating a thermally stable region) in the jet core.

The two maxima observed in the $\sqrt{\overline{t'^2}}$ profiles, as explained earlier, correspond closely to the locations of maximum temperature gradient. At a downstream position of $X/D = 12.844$, the two maxima take place at $Z/D = 6.8$ and 10.9 for $M = 7$ (Fig. 8) and $Z/D = 3.2$ and 6.8 for $M = 4$ (Fig. 9). It is not difficult to see that these locations correspond very closely to the regions of maximum gradients in the mean temperature (Fig. 3(*b*) for $M = 7$ and 4(*b*) for $M = 4$). The same trend is seen to remain at the farthest downstream position, $X/D = 36.697$. For $M = 1$, on the other hand, one of the two local maxima occurs very close to the wall. At a downstream position of $X/D = 3.67$ (Fig. 10), for example, this takes place at $Z/D = 0.46$. Examination of Fig. 5 indicates the existence of a large mean temperature gradient at approximately the same Z/D position.

Further examination of the temperature fluctuation profiles indicates that the larger peak consistently occurs above the jet centerline and not in the wake. This is expected since it was shown, using the constant temperature contours, that the region above the jet centerline possesses a larger temperature gradient than that in the wake, thus contributing to the generation of $\sqrt{\overline{t'^2}}$.

Data on the temperature fluctuations outside the jet plane of symmetry are reported extensively in Sherif (1985). In the region $0 < Y/D < 0.462$, for example, the temperature fluctuation profiles have, more or less, the same shape. At larger lateral distances, the $\sqrt{\overline{t'^2}}$ profiles start to deviate gradually from those at the centerplane. More nonuniformities are generally observed in the neighborhood of the jet side boundaries where large temperature gradients, and consequently large temperature fluctuations, exist. These gradients are further enhanced by the existence of the two counterrotating vortices in the jet wake, as confirmed by the contour plots presented earlier in this section.

Conclusions

The measurements give a reasonably detailed picture of the mean and fluctuating temperature fields of a heated turbulent jet discharging into a cold water stream in crossflow. The initial mixing region was shown to be shorter for larger velocity ratios. The data for $M = 2$ confirm the findings of Andreopoulos (1983) that the centerline temperature excess ratio is proportional to $(X/D)^{-1/2}$ for $0.25 \leq M \leq 2$ and $X/D \leq 5$. The data also show that the jet lateral and vertical spread is smoother for smaller velocity ratios as evidenced by fewer distortions in the constant temperature contours. This was shown to be consistent with a similar finding by Ramsey and Goldstein (1970).

The downstream development of both the jet and its wake has been documented for velocity ratios of 1 and 7 up to a downstream location of $X/D = 3.67$. The change of the jet cross section (at the jet discharge) to horseshoelike immediately downstream of the jet discharge to kidneylike farther downstream was best observed through changes in the constant temperature contours at a number of downstream locations for the velocity ratios mentioned above. The existence of the double vortex structure in the downstream portion of the jet was confirmed and was shown consistently to occur in the jet wake for larger velocity ratios (greater than one). For smaller velocity ratios, a weaker vortex pattern was identified.

A double peak pattern seems to develop for the profiles of the temperature fluctuations. One peak usually occurs in the wake, while a larger peak occurs above the jet centerline in a region of a higher temperature gradient. This was shown by Sherif (1985) to be the behavior of other turbulence quantities such as the turbulence intensity, turbulent velocity fluctuations, and the turbulent kinetic energy.

The wall temperature is more likely to be influenced by the jet temperature in the low velocity ratio jet. Furthermore, in the low velocity ratio case, the wake was shown not to be as pronounced and, thus, the mixing process should not be expected to be as good as that observed for higher velocity ratios.

Acknowledgments

This material is based on work supported by the National Science Foundation under grants ENG-7812901 and MEA-8211713. Support from the Graduate College and the Department of Mechanical Engineering at Iowa State University is also gratefully acknowledged.

References

Andreopoulos, J., 1983, "Heat Transfer Measurements in a Heated Jet-Pipe Flow Issuing Into a Cold Cross-Stream," *Physics of Fluids*, Vol. 26, pp. 3201–3210.

Andreopoulos, J., and Rodi, W., 1984, "Experimental Investigation of Jets in a Cross-Flow," *J. Fluid Mechanics*, Vol. 138, pp. 93–127.

Andreopoulos, J., 1985, "On the Structure of Jets in a Crossflow," *J. Fluid Mechanics*, Vol. 157, p. 163.

Ayoub, G. M., 1971, "Dispersion of Buoyant Jets in a Flowing Ambient Fluid," Ph.D. Thesis, Department of Civil Engineering, University of London, United Kingdom.

Bringfelt, B., 1968, "Plume Rise Measurements at Industrial Chimneys," *Atmospheric Environment*, Vol. 2, pp. 575–598.

Bryant, L. W., and Cowdrey, C. F., 1955, "Effects of Velocity and Temperature of Discharge on the Shape of Smoke Plumes From a Funnel or Chimney: Experiments in a Wind Tunnel," *Proceedings, The Institute of Mechanical Engineers*, Vol. 169, pp. 371–384.

Callaghan, E. E., and Ruggeri, R. S., 1948, "Investigation of the Penetration of an Air Jet Directed Perpendicularly to an Air Stream," NACA TN No. 1615.

Callaghan, E. E., and Bowden, D. T., 1949, "Investigation of Flow Coefficients of Circular, Square, and Elliptical Orifices at High Pressure Ratios," NACA TN No. 1947.

Callaghan, E. E., and Ruggeri, R. S., 1951, "A General Correlation of Tem-

perature Profiles Downstream of a Heated-Air Jet Directed Perpendicularly to an Air Stream," NACA TN No. 2466.

Campbell, J. F., and Schetz, J. A., 1971, "Penetration and Mixing of Heated Jets in a Waterway With Application to the Thermal Pollution Problem," AIAA Paper No. 71-524.

Campbell, J. F., and Schetz, J. A., 1972, "Flow Properties of Submerged Heated Effluents in a Waterway," AIAA Paper No. 72-79.

Campbell, J. F., and Schetz, J. A., 1977, "Analysis of the Injection of a Heated, Turbulent Jet Into a Moving Mainstream, With Emphasis on a Thermal Discharge in a Waterway," Report No. VPI-E-72-24, Virginia Polytechnic Institute and State University, Blacksburg, VA.

Cavola, R. G., and Davis, L. R., 1983, "An Experimental Investigation of Negatively Buoyant Jets Discharged Into a Cross Flow," ASME Paper No. 83-WA/HT-105.

Chan, T., and Kennedy, J. F., 1972, "Turbulent Nonbuoyant or Buoyant Jets Discharged Into Flowing or Quiescent Fluids," Report No. 140, Iowa Institute of Hydraulic Research, The University of Iowa, Iowa City, IA.

Chu, V. H., and Goldberg, M. B., 1974, "Buoyant Forced-Plume in Cross Flow," *J. Hyd. Div.*, HY9, ASCE, Sept., pp. 1203–1214.

Chu, V. H., 1979, "L.N. Fan's Data on Buoyant Jets in Crossflow," *J. Hyd. Div.*, HY5, ASCE, May, pp. 612–617.

Claus, R. W., 1985, "Numerical Calculation of Subsonic Jets in Crossflow With Reduced Numerical Diffusion," NASA TM 87003.

Fan, L. N., 1967, "Turbulent Buoyant Jets Into Stratified and Flowing Ambient Fluids," Report No. KHR-15, W. M. Keck Laboratory, California Institute of Technology, Pasadena, CA.

Harloff, G. J., and Lytle, J. K., 1988, "Three-Dimensional Viscous Flow Computations of a Circular Jet in Subsonic and Supersonic Cross Flow," *Proceedings First National Fluid Dynamics Congress*, Part 2, AIAA, Washington, DC, pp. 1159–1165.

Hewett, T. A., Fay, J. A., and Hoult, D. P., 1971, "Laboratory Experiments of Smokestack Plumes in a Stable Atmosphere," *Atmospheric Environment*, Vol. 5, pp. 767–789.

Hwang, S. S., and Pletcher, R. H., 1978, "Prediction of Turbulent Jets and Plumes in Flowing Ambients," Technical Report HTL-15, Department of Mechanical Engineering, Iowa State University, Ames, IA.

Kamotani, Y., and Greber, I., 1972, "Experiments on a Turbulent Jet in a Cross Flow," *AIAA Journal*, Vol. 10, No. 11, pp. 1425–1429.

Kim, J. H., 1985, "An Analytical Mixing Model for Buoyant Jet Injected Into Pipe Flow," ASME JOURNAL OF HEAT TRANSFER, Vol. 107, pp. 630–635.

Madni, I. K., 1975, "A Finite Difference Analysis of Turbulent, Axisymmetric, Buoyant Jets and Plumes," Ph.D. Thesis, Iowa State University, Ames, IA.

Platten, J. L., and Keffer, J. F., 1968, "Entrainment in Deflected Axisymmetric Jets at Various Angles to the Stream," UTME-T-6808, Mechanical Engineering Department, University of Toronto, Canada.

Ramaprian, B. R., and Haniu, J., 1983, "Turbulence Measurements in Plane Jets and Plumes in Crossflow," IIHR Report No. 266, Institute of Hydraulic Research, The University of Iowa, Iowa City, IA.

Ramsey, J. W., 1969, "The Interaction of a Heated Air Jet With a Deflecting Flow," Ph.D. Thesis, University of Minnesota, Minneapolis, MN.

Ramsey, J. W., and Goldstein, R. J., 1970, "Interaction of a Heated Jet With a Deflecting Stream," NASA CR-72613.

Rodi, W., 1982, *Turbulent Buoyant Jets and Plumes*, Pergamon Press, New York.

Ruggeri, R. S., and Callaghan, E. E., 1950, "Penetration of Air Jets Issuing From Circular, Square, and Elliptical Orifices Directed Perpendicularly to an Air Stream," NACA TN No. 2019.

Ruggeri, R. S., 1952, "General Correlation of Temperature Profiles Downstream of a Heated Air Jet Directed at Various Angles to an Air Stream," NACA TN No. 2855.

Sherif, S. A., 1985, "Measurements of the Flow and Thermal Characteristics of Turbulent Jets in Cross Flow," Ph.D. Thesis, Iowa State University, Ames, IA.

Slawson, P. R., and Csanady, G. T., 1967, "On the Mean Path of Buoyant, Bent-Over Chimney Plumes," *J. Fluid Mechanics*, Vol. 28, pp. 311–322.

Squire, H. B., 1950, "Jet Flow and Its Effects on Aircrafts," *Aircraft Engineering*, Vol. 22, p. 62.

Sykes, R. I., Lewellen, W. S., and Parker, S. F., 1986, "On the Vorticity Dynamics of a Turbulent Jet in a Crossflow," *J. Fluid Mechanics*, Vol. 168, pp. 393–413.

Wark, C. E., and Foss, J. F., 1988, "Thermal Measurements for Jets in Disturbed and Undisturbed Crosswind Conditions," *AIAA Journal*, Vol. 26, No. 8, pp. 901–902.

Wright, S. J., 1977, "Mean Behavior of Buoyant Jets in Cross Flow," *J. Hyd. Div.*, HY5, ASCE, May, pp. 499–513.

An Experimental Investigation of Natural Convection From an Isothermal Horizontal Plate

A. M. Clausing
Professor.
Mem. ASME

J. J. Berton[1]

Department of Mechanical and Industrial Engineering,
University of Illinois at Urbana-Champaign,
Urbana, IL 61801

An investigation of natural convection from a heated, upward-facing, square, horizontal plate to a surrounding gas medium is described in this paper. The results of the experimental investigation provide an improved correlation for the natural convection regime by accounting for variable property effects and extend the applicable Rayleigh number (Ra) range of the correlation over previous research. The large Rayleigh number regime is emphasized. The value of the Richardson number (Ri) at which combined convection influences become important is also determined. The ratio of the plate wall temperature T_w to the ambient temperature T_∞ is incorporated into the Nusselt number correlation in order to account for variable property influences. A cryogenic heat transfer tunnel, with test section temperatures that are varied between 80 K and 310 K, is used to help deduce the influences of the relevant parameters. The ranges of the dimensionless parameters investigated are $2 \times 10^8 < Ra < 2 \times 10^{11}$ and $1 < T_w/T_\infty < 3.1$.

Introduction

When the ratio of the absolute temperature of a heated object to the absolute ambient temperature, T_w/T_∞, is appreciably greater than unity, the thermophysical properties of the fluid within the thermal boundary layer vary markedly. Most analytical and experimental research performed during the past few decades has ignored all property variations except the basic density differences that generate the buoyancy force. This approach, which will be referred to as the constant-property case, is valid as long as T_w/T_∞ is near unity. Many applications exist, however, where T_w/T_∞ is much greater than unity. In these applications, the reference temperature that is chosen to evaluate the properties in constant-property correlations can strongly influence the values of the dimensionless parameters and the predicted rate of heat transfer.

The results of previous experimental work using the constant-property assumption differ greatly. While all researchers arrive at the same Rayleigh number exponent, their correlations differ by as much as 25 percent (see, for example, Bosworth, 1952; Hassan and Mohammed, 1970). Analytical solutions to the horizontal plate problem (see, for example, Rotem and Claassen, 1969; Pera and Gebhart, 1973) do not account for the effects of turbulence within the boundary layer and consequently are only applicable to low Rayleigh number, laminar flow.

The results reported in this study appreciably extend the horizontal plate correlation. Specifically, data are given for Rayleigh numbers more than six times greater than those reported by Fishenden and Saunders (1950), and up to 2000 times greater than those given by other researchers (see: Hassan and Mohamed, 1970; Fujii and Imura, 1972; Lloyd and Moran, 1974; Al-Arabi and El-Riedy, 1976). Also, all of the data in the literature are for T_w/T_∞ near unity, whereas in this study the range $1 < T_w/T_\infty < 3.1$ is investigated. The accuracy of the resulting correlation is greatly enhanced by deducing the influence of this additional parameter.

A matter of concern for researchers performing natural convection experiments is the influence of extraneous drafts or currents on their measurements. Experimenters go to great lengths to ensure that drafts do not adversely affect the results. In this study, the Richardson number, Ri, at which inertial influences become significant is resolved.

One reason for the absence of data in these important regimes is the difficulty of generating large Rayleigh numbers. Another problem is obtaining large values of T_w/T_∞ without masking the results by radiative heat transfer. For these reasons, a variable ambient temperature cryogenic facility, which was constructed at the University of Illinois at Urbana-Champaign (UIUC), is used in the investigation.

Experimental Apparatus and Procedure

The UIUC facility is a variable ambient temperature tunnel that can operate with test section temperatures between 80 K and 310 K. By reducing the temperature of the working fluid, dramatic changes occur in the thermophysical properties of the gas and large increases in the Rayleigh number can be realized. In order to achieve large Rayleigh numbers, previous investigators had to heat their models to temperatures far above 300 K. For example, Fishenden and Saunders (1950) used surface temperatures above 800 K. This necessitates the separation of the convective component of heat transfer from a large radiative component. In contrast, the radiative heat transfer in a high Rayleigh number test at cryogenic temperatures is typically less than one percent of the total heat transfer. The variable T_∞ feature of the UIUC facility also enables one to cover large ranges of the relevant dimensionless groups such as T_w/T_∞, Re, Ra, and Ri without changing models. Other advantages of the use of a cryogenic environment are described by Clausing (1982).

The UIUC cryogenic facility, which was extensively modified during the past three years in order to improve the quality of its flow field and its cooling characteristics, is illustrated in Fig. 1. The tunnel has a rectangular test section with a height of 1.2 m and a width of 0.6 m. It is a variable-speed, recirculating tunnel with a maximum test section velocity of 6 m/s. The test section temperature T_∞ is reduced for the cryogenic tests by the vaporization of liquid nitrogen in a newly installed, cascading, finned tube heat exchanger located just downstream of two 0.5-m-dia cast aluminum fans. The tunnel is carefully sealed and insulated with 0.4 m of urethane insulation. This insulation system, in combination with the thermal mass that

[1]Current address: Research Engineer, NASA Lewis Research Center, Cleveland, OH 44135.

Contributed by the Heat Transfer Division for publication in the JOURNAL OF HEAT TRANSFER. Manuscript received by the Heat Transfer Division March 31, 1988. Keywords: Cryogenics, Mixed Convection, Natural Convection.

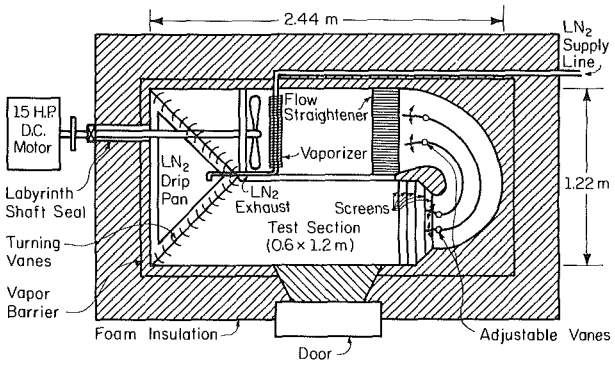

Fig. 1 Cross-sectional top view of cryogenic facility

lies inside the insulating envelope, results in a negligible variation of T_∞ during a test. Gaseous nitrogen is used as the working fluid in cryogenic tests, and air is used in experiments that are conducted with $T_\infty > 290$ K. A combination of four tuned vanes and a series of five screens (see Fig. 1) is used to obtain a flow field throughout the test section with a velocity uniformity of 1.5 percent and a turbulence intensity of 1.7 percent.

In order to generate larger Rayleigh numbers, the square plate is represented by an L by $L/2$ plate where $L = 0.6$ m (see Fig. 2). That is, the vertical line of symmetry that bisects the plate is replaced by a vertical adiabatic wall. The comparison of natural convection tests conducted with and without an additional vertical wall that bisects the $L/2 \times L$ plate shows that the extra viscous shear induced by a wall of symmetry has a negligible influence on the heat transfer from the plate. The $L/2 \times L$ model is divided into four thermally isolated calorimeters of equal mass and area in order to resolve areas of different convective heat transfer rates (see Fig. 2). Each calorimeter is 0.3 m × 0.15 m × 7.9 mm and weighs 0.98 kg. The calorimeters are highly polished, 6061-T6 aluminum plates. They are individually heated by thin foil resistance heaters of negligible thermal mass, which are mounted on the back sides. Directly underneath the model and the heaters is a 25-mm board of urethane insulation, a heated copper guard, and a second 25-mm board of insulation. The guard is maintained at the same temperature as the calorimeters to eliminate conductive heat flow in that direction. The model is instrumented with eighteen 30-gage copper-constantan, special-accuracy thermocouples. Automatic ice point references were used to hold the thermocouple reference junctions at 0°C (±0.02°C). The temperature distribution in the test section of the tunnel is determined with a grid of six identical thermocouples.

In a typical test, the four calorimeters are heated to an isothermal initial condition. The heaters are then turned off, and the flow, if desired, is initiated. The data acquisition system scans the 24 channels continuously at a rate of 12 channels

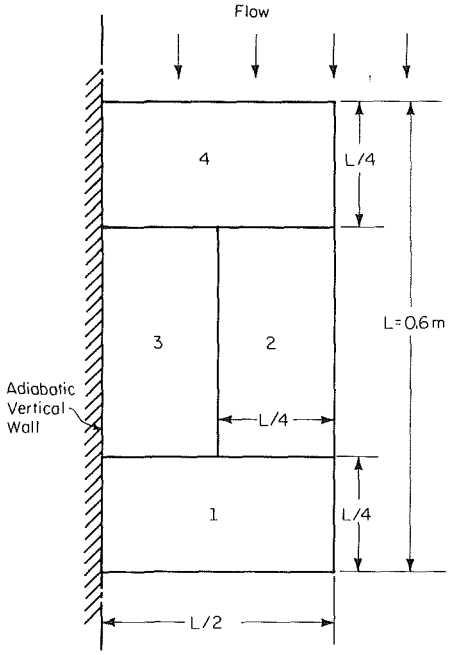

Fig. 2 Sketch of model illustrating calorimeter arrangement

per second, records the converted thermocouple readings in the memory of a microcomputer, averages the temperature readings of each of the four plates as well as other ensembles of interest, and graphically displays the specified temperatures and/or average temperatures. At the end of a test, the data are written on a diskette and subsequently are uploaded to a mainframe computer for further processing and plotting.

The rate of convective heat transfer from each plate is determined at a time after quasi-steady conditions are reached but before the thermal gradients within the plate become significant. The rate of heat transfer is determined from the rate of change of the internal energy of the respective calorimeter; that is, the convective heat transfer coefficient is determined from the energy balance

$$h = \frac{\dfrac{-mc_p}{A}\dfrac{dT_w}{dt} - \sigma\epsilon\,(T_w^4 - T_\infty^4)}{(T_w - T_\infty)} \tag{1}$$

where m is the mass of the calorimeter, c_p its specific heat, A is the heat transfer area, ϵ is the emissivity for polished aluminum, and σ is the Stefan–Boltzmann constant. The heat transfer surface is assumed to be gray, and the surroundings are assumed to be isothermal and black. The variations of both c_p and ϵ with calorimeter temperature are taken into account. The time derivative of the calorimeter temperature is determined with a central difference quotient. The average heat

Nomenclature

A = area, m²
c_p = specific heat, J/kg-K
f = defined by equation (4)
g = acceleration of gravity, m/s², or defined by equation (4)
h = heat transfer coefficient, W/m²-K
k = thermal conductivity, W/m-K
L = characteristic length, m
m = mass, kg
t = time, s
T = temperature, K
T^* = $(T - T_\infty)/(T_o - T_\infty)$
V = free-stream velocity, m/s
α = thermal diffusivity, m²/s
β = volume coefficient of expansion, K⁻¹
ϵ = emissivity
μ = dynamic viscosity, kg/m-s
ν = kinematic viscosity, m²/s
ρ = density, kg/m³
σ = Stefan–Boltzmann constant, W/m²-K⁴
Gr = Grashof number = $g\beta\Delta TL^3/\nu^2$
Nu = Nusselt number = hL/k
Pr = Prandtl number = ν/α
Ra = Rayleigh number = GrPr
Re = Reynolds number = VL/ν
Ri = Richardson number = Gr/Re^2

Subscripts

f = based on film temperature
o = initial condition
r = reference temperature
w = wall condition
∞ = tunnel ambient condition

Superscripts

$*$ = dimensionless quantity

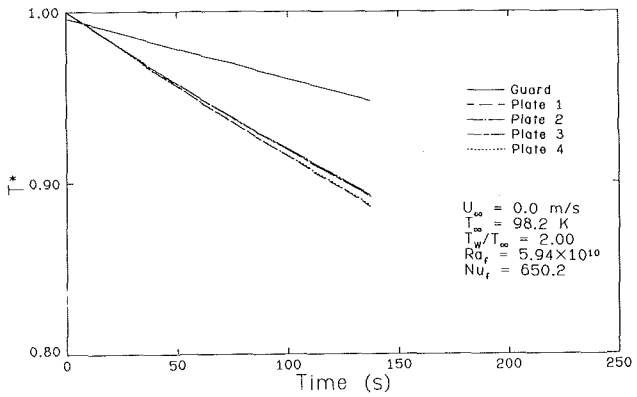

Fig. 3 Dimensionless calorimeter temperatures for a typical test

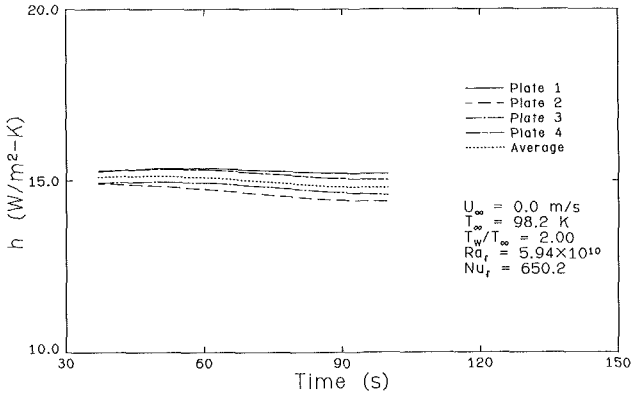

Fig. 4 Individual heat transfer coefficients for a typical test

transfer coefficient over the entire plate is determined by averaging the individual coefficients of the four identical plates.

Figures 3 and 4 show typical results for a 150 s, natural convection test with a Rayleigh number of 5.94×10^{10}, an ambient temperature of 98.2 K, and a temperature ratio T_w/T_∞ of 2.00. The smoothness of the temperature versus time and the h versus time curves attests to the accuracy of the experiment.

A Fluke Model 2240B automatic datalogger, in conjunction with a Texas Instruments Portable Professional Computer, is used for data collection. The datalogger measures the thermocouple potentials to within 0.1 μV. After considering the disturbing influences of the imperfect ice reference units, the voltage-to-temperature conversion error, and the datalogger accuracy, the temperature measurements are assigned a relative uncertainty of 0.05 K. Following an examination of the thermophysical property data of air, nitrogen, and aluminum, 2 percent uncertainties are assigned to the specific heat, density, viscosity, and conductivity data. An 8 percent uncertainty is assigned to the emissivity data. Uncertainties in the measurements of the characteristic length, heat transfer area, model mass, time, and the ambient temperature (due to the small but inevitable temperature stratification at cryogenic temperatures) are judged to be 0.001 m, 0.001 m^2, 0.001 kg, 0.5 s, and 2 K, respectively. The results of an uncertainty analysis show that the uncertainties in the heat transfer coefficients and Rayleigh numbers are 2 percent and the uncertainty in the Nusselt numbers is 3 percent. Further details of the experimental procedure can be found from Berton (1986).

Similitude Considerations

The set of dimensionless groups that influence natural and combined convection is deduced by an examination of the governing equations. The simplifying assumptions are (*i*) a steady flow of a Newtonian fluid, (*ii*) a perfect gas, (*iii*) negligible viscous dissipation and work done by compression, (*iv*) the dependent variables c_p/c_{pr}, ν/ν_r, and k/k_r are general functions of the dimensionless temperature ratio T/T_r, (*v*) isothermal gaseous surroundings at T_∞, and (*vi*) an isothermal surface at T_w. The Boussinesq approximation is not used. The dimensional analysis with these assumptions shows that the average Nusselt number for natural convection is dependent on

$$\mathrm{Nu} = f_1(\mathrm{Ra}, \mathrm{Pr}, T_w/T_\infty) \tag{2}$$

For combined convection, one obtains

$$\mathrm{Nu} = f_2(\mathrm{Ra}, \mathrm{Pr}, \mathrm{Ri}, T_w/T_\infty) \tag{3}$$

The determination of the function f_2 is not addressed in this paper; however, the limiting Richardson number at which combined convection influences become negligible is determined. The Prandtl number influence is also not resolved; thus, the results are only applicable to gases with a Pr of approximately 0.7. Experience has shown that for values of T_w/T_∞ near unity, the form of equations (2) and (3) is valid for both laminar and turbulent natural convection.

Table 1 Constants in variable property correlation, f_r (see equation (6))

Reference Temperature	a_1	a_2	a_3
Wall	0.433	0.626	−0.0581
Film	0.823	0.179	−0.0011
Ambient	1.212	−0.254	0.0405

The influence of variable properties is taken into account in equations (2) and (3) with the parameter T_w/T_∞. This contrasts with commonly used procedures—the reference temperature method and the property ratio method. Following the procedure used by Clausing (1983), the form of the correlation in the natural convection limit is assumed to be

$$\mathrm{Nu}_r = g(\mathrm{Ra}_r) \cdot f_r(\mathrm{Ra}_r, T_w/T_\infty) \tag{4}$$

where $g(\mathrm{Ra}_r)$ is defined as the constant-property correlation, that is, $f_r(\mathrm{Ra}_r, 1) = 1$. Although equation (4) is similar to the property ratio method, the stringent constraint of having to account for variable property influences with a function of a single property ratio is removed. The function f is, of course, a function of the reference temperature T_r, which is used in the evaluation of Nu and Ra; hence, the subscript r is employed. In this paper, the function f is evaluated for three reference temperatures: T_w, $T_f \equiv (T_w + T_\infty)/2$, and T_∞.

Results

An examination of the natural convection data from this investigation showed that

$$\mathrm{Nu} \propto \mathrm{Ra}^{1/3}, \quad 2 \times 10^8 < \mathrm{Ra} < 2 \times 10^{11} \tag{5}$$

over the specified Ra range of the data, if T_w/T_∞ were near unity. The data in this Rayleigh number range also showed that f is a strong function of only T_w/T_∞. Hence, it was assumed that the variable property influence could be accurately represented by a second-degree polynomial in T_w/T_∞. A least-squares, second-degree fit of the experimental data with the constraints $f(1) = 1$ and $\mathrm{Nu} \propto \mathrm{Ra}^{1/3}$ gives

$$\mathrm{Nu}_r = 0.140\ \mathrm{Ra}_r^{1/3}\ \{a_1 + a_2(T_w/T_\infty) + a_3(T_w/T_\infty)^2\} \tag{6}$$

where the constants a_i are given in Table 1 for the three different reference temperatures: T_w, T_f, and T_∞. The three variable property correlations and the corresponding experimental data are graphically illustrated in Fig. 5. The coefficient of 0.140 in the constant-property correlation, $g(\mathrm{Ra})$, agrees with the coefficient reported by Fishenden and Saunders (1950), who used the same Rayleigh number exponent. They used elevated pressures in order to obtain large Rayleigh numbers.

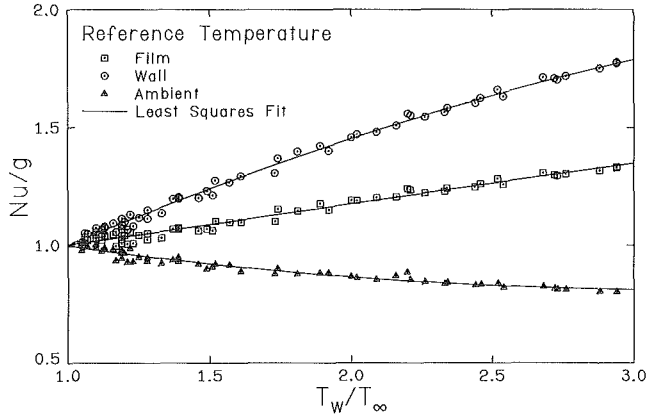

Fig. 5 Variable property correlation, natural convection data

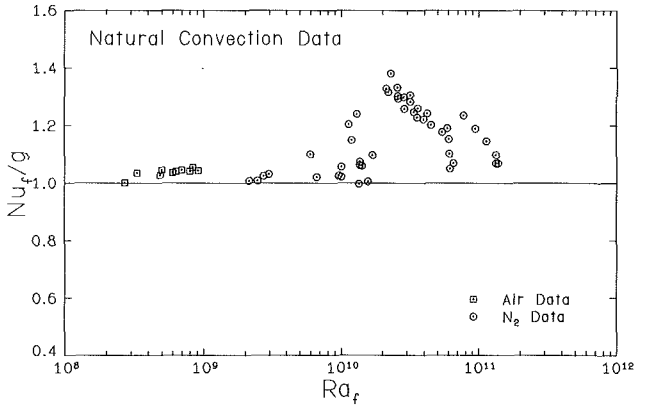

Fig. 6 Degree of correlation, including influence of only Ra

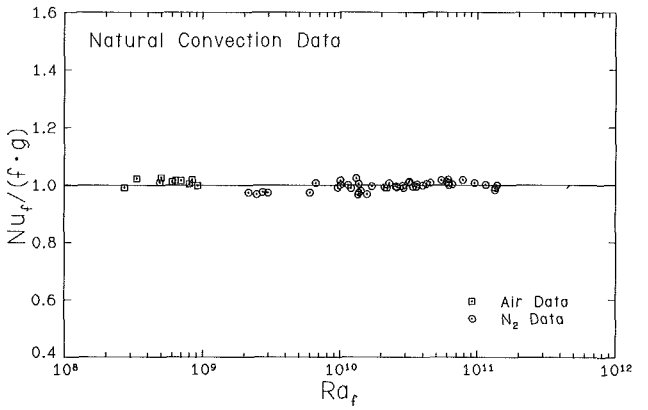

Fig. 7 Comparison between natural convection data and proposed correlation

The choice of reference temperature has, by definition, no influence on the constant-property correlation $g(\mathrm{Ra})$. The choice of reference temperature does, however, have a significant influence on $f(T_w/T_\infty)$, which can be seen in Fig. 5. The function f is greater than unity if the wall or film temperature is used as the reference temperature, whereas it is less than unity if the properties are based on the ambient temperature. This result contrasts with the correlations from a similar experiment, natural convection from an isothermal vertical surface, which were reported by Clausing (1983). For the case of a vertical plate, the function f is greater than unity regardless of the reference temperature used. The variable property influence is also significantly greater in the case of the vertical plate. In the present study, the function f is remarkably linear, which is evident from the relatively small values of the coefficient a_3. This is again in contrast with the marked curvature of f for the case of the vertical plate (Clausing, 1983). The linear nature of the function f suggests the use of the reference temperature method of compensating for variable properties. In this method, a reference temperature at which all properties are evaluated is chosen such that the function $g(\mathrm{Ra})$ achieves the maximum degree of correlation. If the reference temperature is chosen to be

$$T_r = T_w - 0.83(T_w - T_\infty), \qquad 1 \le T_w/T_\infty \le 3 \tag{7}$$

then the value of $f(T_w/T_\infty)$ is found to be unity and no property corrections are necessary for the range of temperature ratios investigated. Although the reference temperature method is widely used, it should be stressed that for other geometries, particularly in the case of vertical plates, the technique is not successful.

The agreement between Correlation (6) and the experimental data is illustrated in Figs. 6 and 7. Figure 6 shows the degree of correlation obtained with the constant-property correlation. This figure is a plot of the Nu_f divided by the function $g(\mathrm{Ra}_f)$ versus Ra_f. The inability of the constant-property correlation to predict the experimental results is evident. Deviations as large as 40 percent are present. Figure 7, a graph of $\mathrm{Nu}_f/(g \cdot f_f)$ versus Ra_f, clearly shows excellent agreement between the 56 data points and Correlation (6). The maximum deviation of any data point is only 3.3 percent.

The combined convection regime near the natural convection limit was also investigated in order to determine the Richardson number at which combined convection influences become significant. The data showed that in order for the free-stream velocity to increase the convective heat transfer by more than one percent, the Richardson number Ri_f must be less than 87. The increase is less than 5 percent if $\mathrm{Ri}_f > 33$. The influences of the 1.7 percent free-stream turbulence intensity and the distortion in the flow field, due to the finite model thickness and the presence of the vertical adiabatic wall, were estimated to be too large to delineate the functional relationship between the Nusselt number and the Richardson number accurately. Hence, these data are not presented in this paper (see Berton, 1986, for further information).

Conclusions

The following conclusions are drawn from the results of this investigation:

1 The variable property influence can be accounted for with a function of only T_w/T_∞ over the Rayleigh number range $2 \times 10^8 < \mathrm{Ra} < 2 \times 10^{11}$. The results for natural convection from a vertical plate (Clausing, 1983), gave: $f_f(\mathrm{Ra}, T_w/T_\infty) = 1$ in the laminar region, f_f equal to a function of both Ra and T_w/T_∞ in the transitional regime, and f_f equal to a function of only T_w/T_∞ in the turbulent regime. f_f reached values as high as 2 at $T_w/T_\infty = 2$ in the turbulent regime. The dependency of f_f on only T_w/T_∞ in this investigation indicates that all data lie in the turbulent domain. This is substantiated by the turbulent data reported by Fishenden and Saunders (1950), Fujii and Imura (1972), Lloyd and Moran (1974), and Al-Arabi and El-Riedy (1976).

2 The Nusselt number in the turbulent regime is strongly affected by property variations. Correlations proposed in the literature, such as the Fishenden and Saunders correlation, equation (3), are acceptable only if T_w/T_∞ is near unity. For example, the Nusselt number at $T_w/T_\infty = 3.0$ is 35 percent greater than the value predicted by the Fishenden and Saunders constant-property correlation.

3 Due to the linear nature of $f(T_w/T_\infty)$, a reference temperature can be selected that forces this function to be unity for the entire range of temperature ratios investigated. This reference temperature is $T_r = T_w - 0.83(T_w - T_\infty)$.

4 The combined convection data indicate that small to moderate drafts, such as doors opening or people moving about, can have an effect on the rate of heat transfer in "free"

convection. Further evidence of combined convection influences is the great effort taken by some investigators of natural convection phenomena to eliminate such influences in their experiments (see discussions given by Clausing, 1983).

Acknowledgments

The authors gratefully acknowledge the financial support of the National Science Foundation in sponsoring this research.

References

Al-Arabi, M., and El-Riedy, M. K., 1976, "Natural Convection Heat Transfer From Isothermal Horizontal Plates of Different Shapes," *International Journal of Heat and Mass Transfer*, Vol. 19, pp. 1399–1404.

Berton, J. J., 1986, "An Experimental Investigation of Natural and Combined Convection From an Isothermal Horizontal Plate," M.S. Thesis, University of Illinois, Urbana, IL.

Bosworth, R. L. C., 1952, *Heat Transfer Phenomena*, Wiley, New York, pp. 102–104.

Clausing, A. M., 1982, "Advantages of a Cryogenic Environment for Experimental Investigations of Convective Heat Transfer," *International Journal of Heat and Mass Transfer*, Vol. 25, pp. 1255–1257.

Clausing, A. M., 1983, "Natural Convection Correlations for Vertical Surfaces Including Influences of Variable Properties," ASME JOURNAL OF HEAT TRANSFER, Vol. 105, pp. 138–143.

Fishenden, M., and Saunders, O. A., 1950, *An Introduction to Heat Transfer*, Oxford University Press, London, pp. 95–99.

Fujii, T., and Imura, H., 1972, "Natural Convection Heat Transfer From a Plate With Arbitrary Inclination," *International Journal of Heat and Mass Transfer*, Vol. 15, pp. 755–767.

Hassan, K. E., and Mohamed, S. A., 1970, "Natural Convection From Isothermal Flat Surfaces," *International Journal Heat and Mass Transfer*, Vol. 13, pp. 1873–1886.

Lloyd, J. R., and Moran, W. R., 1974, "Natural Convection Adjacent to Horizontal Surfaces of Various Planforms," ASME JOURNAL OF HEAT TRANSFER, Vol. 96, pp. 443–447.

Pera, L., and Gebhart, B., 1973, "Natural Convection Boundary Layer Flow Over Horizontal and Slightly Inclined Surfaces," *International Journal of Heat and Mass Transfer*, Vol. 16, pp. 1131–1146.

Rotem, L., and Claassen, L., 1969, "Natural Convection Above Unconfined Horizontal Surfaces," *Journal of Fluid Mechanics*, Vol. 39, Part 1, pp. 173–192.

Natural Convection in Vertical Annuli: A Numerical Study for Constant Heat Flux on the Inner Wall

J. A. Khan

R. Kumar

Department of Mechanical Engineering,
Clemson University,
Clemson, SC 29631

A numerical investigation has been conducted to evaluate the effects of diameter ratio and aspect ratio in natural convection of gases within vertical annuli. The inner cylinder is maintained at uniform heat flux and the outer cylinder at constant temperature. The horizontal top and bottom walls are insulated. Detailed results of heat transfer rate, temperature, and velocity fields have been obtained for $1 \leq \kappa \leq 15$, $1 \leq A \leq 10$, *and* $100 < Ra_L^* < 10^7$. *The inner wall temperature is a function of diameter ratio and aspect ratio. The heat transfer results have been compared with those for isothermal heating, and have been found to be higher. The inner diameter is seen to be the appropriate length scale for high Rayleigh number flows and/or high radius ratios, and the radius ratio effect on heat transfer is seen to be insignificant for radius ratios greater than 10. The heat transfer results based on the inner diameter are in very good agreement with published experimental results, although these experiments were conducted for very high aspect ratio. Heat transfer correlations are provided.*

Introduction

Natural convection in enclosures is a subject that has been extensively treated in the literature. The effect of natural convection in a vertical annulus is significant in engineering problems. This heat transfer problem finds application in safety aspects of gas-cooled reactors and in furnace design. The present work deals with the heat transfer results in a vertical annulus with the inner wall maintained at constant heat flux, a cooled outer wall, and insulated top and bottom plates. In the special case of constant heat flux on the inner cylinder, very few studies exist in the literature. One of the earlier works in this geometry was done by Sheriff (1966) who provided experimental heat transfer data for diameter ratios close to unity. His experimental work considered natural convection in a vertical annulus with the same thermal boundary conditions given in the present study. His correlation for average Nusselt number is

$$\mathrm{Nu} = 0.25\ \mathrm{Ra}^{0.3} A^{-0.25} \tag{1}$$

where $10^5 \leq \mathrm{Ra} \leq 10^8$.

Sheriff (1966) considered three diameter ratios, $\kappa = 1.23$, 1.1, and 1.03 with aspect ratios of $A = 38$, 76, and 228, respectively. In equation (1), the effect of diameter ratio is absent and this is due to the short range of diameter ratios considered. Keyhani et al. (1983) made heat transfer measurements in a vertical annulus with the inner wall maintained at constant heat flux and the outer wall at constant temperature. They performed the experiments for a diameter ratio significantly higher than unity ($\kappa = 4.33$) and an aspect ratio of $A = 27.6$, and $10^3 < \mathrm{Ra}_L < 2.3 \times 10^6$. Based on their data, they presented the correlation for $\kappa = 4.33$ and $A = 27.6$

$$\mathrm{Nu} = 0.163\ \mathrm{Ra}^{0.322} \tag{2}$$

for $6.6 \times 10^3 \leq \mathrm{Ra} \leq 2.3 \times 10^6$.

For the vertical annulus with both walls at constant temperature, numerical and experimental data are available in the literature. The numerical values for Nusselt number was first given by de Vahl Davis and Thomas (1969) and the parametric studies were further extended by Thomas and de Vahl Davis (1970). The majority of the results were obtained for Pr = 1 and $1 \leq \kappa \leq 4$. Their correlation based on their numerical data included the diameter ratio effect and was given in the boundary layer regime as

$$\mathrm{Nu} = 0.286\ \mathrm{Ra}^{0.256}\ \mathrm{Pr}^{0.006}\ A^{-0.238}\ \kappa^{0.442} \tag{3}$$

Prasad and Kulacki (1985) obtained temperature data and heat transfer results experimentally using water, heptane, and ethylene glycol for $\kappa = 5.338$, $A = 0.5$, 1.0, and 1.5, and $8 \times 10^6 \leq \mathrm{Ra} \leq 3 \times 10^{10}$. The correlation given by Thomas and de Vahl Davis (1970) in equation (3) was seen to overpredict the experimental results of Prasad and Kulacki (1985). Kalam and Kumar (1987) obtained numerical results for various combinations of diameter ratios and aspect ratios in the vertical annulus and found that their Nusselt numbers were in good agreement with those of Thomas and de Vahl Davis (1970) for specific cases. However, the results of Kalam and Kumar also suggested that the correlation equation (3) overpredicted the heat transfer results, indicating that the dependence of the relevant parameters was not well established by the heat transfer correlation.

Assuming that the Nusselt number dependence on diameter ratio and aspect ratio would be the same as given in the correlation equation (3), Kayhani et al. (1983) obtained heat transfer correlation using equation (2)

$$\mathrm{Nu} = 0.188\ \mathrm{Ra}^{0.332}\ A^{-0.238}\ \kappa^{0.442} \tag{4}$$

in the boundary layer regime. Bhushan et al. (1983) extended the work of Keyhani et al. (1983) for two other combinations of aspect and diameter ratios, $A = 52.82$, $\kappa = 2.77$ and $A = 38.38$, $\kappa = 8.28$. The Nusselt numbers obtained from equation (4) overpredicted the experimental results by 16 to 18 percent. Landis and Yanowitz (1966) studied transient and steady free convection in a long vertical rectangular cell with constant heat flux on one of the vertical walls. Air, water, and silicone oil were used for $900 < \mathrm{Ra} < 2 \times 10^6$. They obtained temperature

Contributed by the Heat Transfer Division for publication in the JOURNAL OF HEAT TRANSFER. Manuscript received by the Heat Transfer Division December 23, 1987. Keywords: Enclosure Flows, Natural Convection, Numerical Methods.

and velocity profiles and also provided a correlation for Nusselt number

$$\mathrm{Nu} = 0.123\ \mathrm{Ra}^{0.279} \tag{5}$$

for $A = 20$ and $2 \times 10^3 \le \mathrm{Ra} \le 1.5 \times 10^6$. Lee et al. (1982) determined the structure of multicellular natural convection within tall, vertical, isothermal cylinders and rectangular cavities. The numerically predicted flow patterns consisted of cells that drifted upward at a speed that was in agreement with results from the linear theory of hydrodynamic stability, as well as with experimental measurements.

Thus, it is seen that most of the results obtained in the literature for a vertical annulus with a constant heat flux boundary condition on the inner wall have been reported only for very high aspect ratios and limited diameter ratios. This paper presents the results of a numerical study in the same geometry with the same boundary conditions for $1 \le A \le 10$, $1 \le \kappa \le 15$, and modified Rayleigh number of $100 < \mathrm{Ra}_L^* < 10^7$.

Mathematical Formulation

The governing equations fror a steady, laminar flow with negligible viscous dissipation and no heat generation, may be written as follows:

Continuity: $$\nabla \cdot \mathbf{V} = 0 \tag{6}$$

Momentum: $$\rho(\mathbf{V}\cdot\nabla)\mathbf{V} = -\nabla p + \mathbf{F} - \mu\nabla\times(\nabla\times\mathbf{V}) \tag{7}$$

Energy: $$\rho c_p(\mathbf{V}\cdot\nabla)T = k(\nabla\cdot\nabla)T \tag{8}$$

$\mathbf{F}$ is the body force given by

$$\mathbf{F} = \rho\mathbf{g}$$

Using the annular width L, the annulus is bound by the nondimensional radii $R_i = r_i/L$ on the inner cylinder and $R_o = r_o/L$ at the outer cylinder. In the vertical direction, Z varies from 0 to A $(= z_{\max}/L)$. The inner wall is at a constant heat flux q, and the outer wall at a constant temperature T_o.

The dimensionless quantities are

$$V_R = \frac{V_R' L}{\alpha};\quad V_z = \frac{V_z' L}{\alpha}$$

$$R = \frac{r}{L};\quad \tau = \frac{T - T_o}{\left(\frac{qL}{k}\right)} \tag{9}$$

$$\mathrm{Ra}_L^* = \frac{\beta g\left(\frac{qL}{k}\right)L^3}{\alpha\nu};\quad \kappa = \frac{r_o}{r_i};\quad A = \frac{z_{\max}}{L}$$

The Navier-Stokes equations are recast as vorticity-stream function equations. The following equations relate velocity $\mathbf{V}$ to vorticity ζ and vector potential ξ

$$\mathbf{V} = \nabla\times\xi$$
$$\zeta = \nabla\times\mathbf{V} \tag{10}$$

The axial component of ξ in two-dimensional flows is the stream function and henceforth will be denoted by ψ. ζ_θ is the azimuthal component of vorticity, hereinafter called ζ.

Using the nondimensional parameters, the final set of equations to be solved is (for a Boussinesq fluid):

$$\frac{\partial^2\psi}{\partial z^2} + \frac{\partial^2\psi}{\partial R^2} + \frac{1}{R}\frac{\partial\psi}{\partial R} - \frac{\psi}{R^2} = -\zeta \tag{11}$$

$$\frac{\partial}{\partial z}(V_z\zeta) + \frac{\partial}{\partial R}(V_R\zeta) = -\mathrm{Ra}_L^*\mathrm{Pr}\frac{\partial\tau}{\partial R} + \mathrm{Pr}\left\{\frac{\partial^2\zeta}{\partial z^2} + \frac{\partial^2\zeta}{\partial R^2} + \frac{1}{R}\frac{\partial\zeta}{\partial R} - \frac{\zeta}{R^2}\right\} \tag{12}$$

$$\left(V_R\frac{\partial\tau}{\partial R} + V_z\frac{\partial\tau}{\partial z}\right) = \left(\frac{\partial^2\tau}{\partial R^2} + \frac{1}{R}\frac{\partial\tau}{\partial z} + \frac{\partial^2\tau}{\partial z^2}\right) \tag{13}$$

The boundary conditions for the problem can be written using no-slip conditions for velocity, constant heat flux on the inner

Nomenclature

A = aspect ratio
C_p = specific heat
$\mathbf{F}$ = body force
g = gravitational acceleration
$\bar{h}$ = average heat transfer coefficient on the inner wall
k = thermal conductivity of the fluid
L = gap width $= r_o - r_i$
Nu_L = Nusselt number $= \frac{\bar{h}L}{k}$
Nu_{d_i} = Nusselt number $= \frac{\bar{h}d_i}{k}$
P = pressure
Pr = Prandtl number $= \frac{\nu}{\alpha}$
q = constant heat flux applied on the inner wall
r = radial coordinate
R = dimensionless radial coordinate $= \frac{r}{L}$
Ra_L^* = Rayleigh number $= \frac{\beta g\left(\frac{qL}{k}\right)L^3}{\alpha\nu}$
Ra, Ra_L = Rayleigh number $= \frac{\beta g(\Delta T)L^3}{\alpha\nu}$
Ra_{d_i} = Rayleigh number $= \frac{\beta g(\Delta T)d_i^3}{\alpha\nu}$
T = dimensional temperature
V_R = nondimensional radial velocity $= \frac{V_R' L}{\alpha}$
V_z = nondimensional vertical velocity $= \frac{V_z' L}{\alpha}$
V = velocity vector
V_R' = dimensional radial velocity
V_z' = dimensional vertical velocity
z = vertical coordinate
α = thermal diffusivity
α_ζ, α_ζ = parameters in the false-transient terms of vorticity and energy equations
β = coefficient of volumetric expansion
ΔT = temperature difference across the annulus; $(T_i - T_o)$ for isothermal heating, and $(T_{m,i} - T_o)$ for constant flux heating
ζ = vorticity
κ = radius ratio $= r_o/r_i$
ξ = vector potential
ρ = density
τ = dimensionless temperature $= \frac{(T - T_o)}{\left(\frac{qL}{k}\right)}$
ψ = stream function

Subscripts

CR = critical
C = conduction
d_i = based on inner diameter
i = inner wall
L = based on gap width
m = mean value on the inner wall
max = maximum value
min = minimum value
o = outer wall

cylinder, constant temperature on the outer cylinder, and insulated condition on the horizontal walls, as shown in Table 1.

Table 1 Boundary conditions

	$R=R_i$	$R=R_o$	$Z=0$	$Z=A$
τ	$\frac{\partial\tau}{\partial R}=-1$	$\tau=0$	$\frac{\partial\tau}{\partial z}=0$	$\frac{\partial\tau}{\partial z}=0$
ζ	$-\frac{\partial^2\psi}{\partial R^2}$	$-\frac{\partial^2\psi}{\partial R^2}$	$-\frac{\partial^2\psi}{\partial z^2}$	$-\frac{\partial^2\psi}{\partial z^2}$
ψ	0	0	0	0

Numerical Procedure

Equations (12) and (13) were made parabolic by the addition of false transient terms, $\frac{\mathrm{Pr}}{\alpha_\zeta}\frac{\partial\zeta}{\partial t}$ and $\frac{1}{\alpha_\tau}\frac{\partial\tau}{\partial t}$, to the left sides of vorticity and energy equations, respectively. These equations were solved by the Alternating Direction Implicit (ADI) method, and the stream function equation was solved by the successive overrelaxation (SOR) method. The factors α_ζ and α_τ were to be specified. Suitable choices of these parameters controlled the computational efficiency and stability of the solution. The most efficient choices for α_ζ and α_τ were 0.05 and 1, respectively. At high Rayleigh numbers, α_ζ was reduced to 0.015 and α_τ to 0.05; these choices were arrived at by trial and error. The selection of Δt depended upon the grid. It was chosen as 0.004 for uniform grid and 0.0012 for the nonuniform grid for most cases. The first and second derivatives in space were approximated by central differences and the time derivatives by the first-order difference. Derivatives at the boundaries were approximated by a three-point forward or backward differencing.

The choice of the diameter ratio κ, the aspect ratio A, and the Rayleigh number Ra, mainly determines the type of mesh

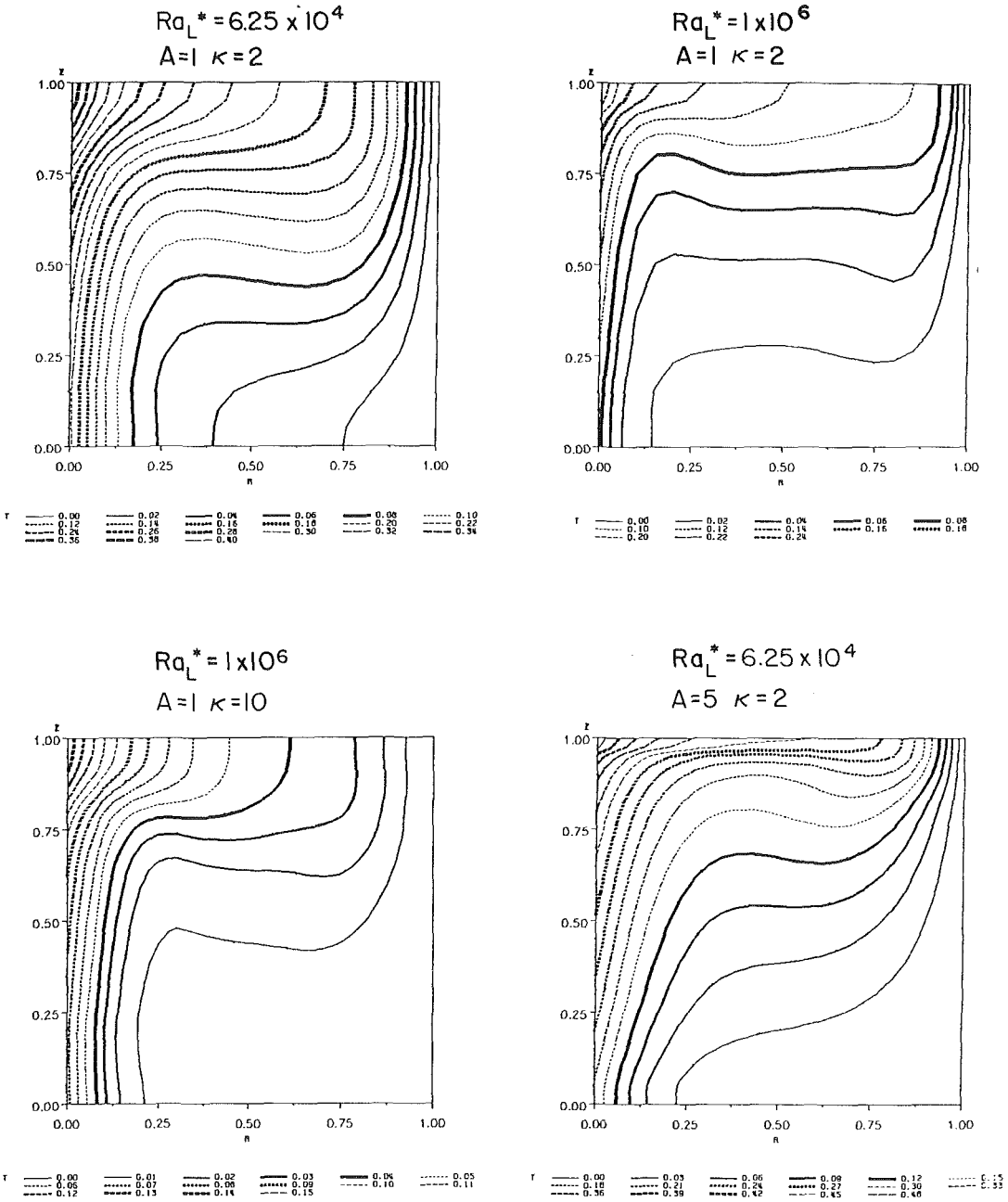

Fig. 1 Effect of diameter and aspect ratios on the isotherms

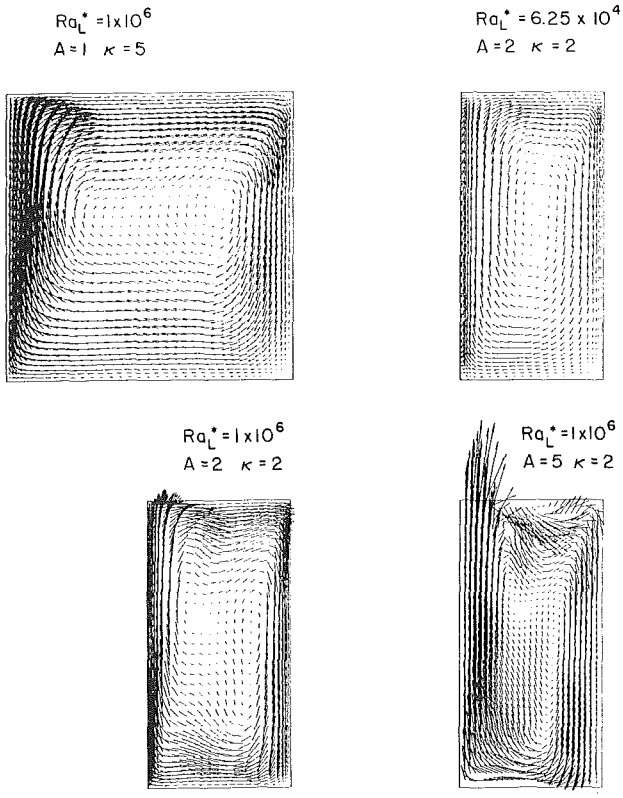

Fig. 2 Velocity field for various diameter and aspect ratios

to be used. The uniform and semi-uniform meshes employed in the present study are: $R \times z$: 21 × 21, 26 × 26, 27 × 41, 41 × 41. Grid independence of results was checked and ensured. In general, for $A = 1$ and high κ, a 41 × 41 grid was used. Validation studies were performed by generating heat transfer results for an isothermal boundary condition on the inner cylinder and comparing with the published data of de Vahl Davis and Thomas (1969) and Thomas and de Vahl Davis (1970). More details of this comparison are given by Kalam and Kumar (1987). Uniform meshes have been used for Rayleigh numbers less than 2×10^4 in some cases and less than 5×10^4 in other cases; semi-uniform meshes have been used for higher Rayleigh numbers. The semi-uniform grid was closely spaced near the walls, with the ratio of adjacent grid spacing maintained below 1.5, and uniformly spaced in the core of the annulus. The following criterion was used for checking convergence at each point:

$$|\phi_{new} - \phi_{old}| / |\phi_{new}|_{max} \leq \Gamma \tag{14}$$

where ϕ was the primary variable being tested and Γ was a prespecified constant, usually set at 10^{-4}. The agreement between the energy input at the inner cylinder and the energy output at the outer cylinder was also used to check the validity of the numerical scheme. The convergence parameter Γ was frequently reduced from 10^{-4} to 10^{-5} to maintain the energy balance within 2 percent.

Results and Discussion

Natural convection of gases with a Prandtl number of 0.7 is studied in a vertical annulus with the inner wall maintained at the constant heat flux and the outer wall at constant temperature. The important parameters, such as diameter ratio, aspect ratio, and Rayleigh number, have been varied, and heat transfer and fluid flow results have been obtained. The cases under consideration are $1 \leq A \leq 10$, $1 \leq \kappa \leq 15$, and $100 \leq Ra_L^* \leq 10^7$. Isotherms and velocity fields are presented. The numerical results for isothermal wall heating have been compared with the experimental results elsewhere (Kalam and Kumar, 1987) and they have been compared with isoflux heating in this paper. Heat transfer correlations are also given.

Temperature and Velocity Fields. Isotherms and velocity fields are given in Figs. 1 and 2 to illustrate the effects of diameter ratio, aspect ratio, and Rayleigh number using a few representative cases. The inference from these plots and other plots at various κ and Ra_L^* is as follows. When the inner wall is heated, the thermals rise, encounter the top adiabatic wall, travel radially outward toward the cold wall, and recirculate. The center of rotation is almost in the middle of the annulus. With the increase in heat flux, Ra_L^* increases, the velocity of the fluid increases. The isotherms suggest that the heat transfer rate would increase as the diameter ratio is increased. This is consistent with our Nusselt number results for different κ, which will be discussed later. Also, for higher κ, the center of rotation moves closer to the cold wall.

For the same diameter ratio, as the aspect ratio is increased (Fig. 1*d*), the thermals spread away from the inner cylinder. For convenience, the height of the cylinder is scaled down for plotting purposes. The center of rotation moves toward the top adiabatic wall. Since some of the hot fluid returns to the middle of the cavity (Fig. 2*d*), the heat transfer rate for the same Rayleigh number will actually diminish as the aspect ratio is increased.

The local temperature values along the inner wall are plotted as a function of diameter ratio and aspect ratio in Fig. 3 for $Ra_L^* = 5 \times 10^4$, the maximum temperature occurs at the top corner of the inner cylinder, and the minimum occurs at the bottom corner. This behavior is seen for all Ra_L^* and κ. As the diameter ratio is increased, the temperature profile appears to be smoother and flatter, almost like the profile for an isothermal cylinder. Table 2 shows that for a given Ra_L^* and A, as κ is increased, the normalized maximum temperature (with respect to mean temperature) decreases, and the minimum temperature increases. The Rayleigh number and aspect ratio effects seem to be that as these parameters are increased, the maximum and the minimum normalized temperatures increase and decrease, respectively. These effects are quantified further in Fig. 4 where Nu_{max} and Nu_{min} versus Ra_L^* curves are given as functions of A and κ. It is clear that $Nu_{max}\left(=\frac{1}{\tau_{min}}\right)$ increases with κ; however, the rate of increase decreases at higher Ra_L^* (Fig. 4*a*). A similar effect is seen for the aspect ratio as well, in Fig. 4(*b*).

The Nu_{min} versus Ra_L^* plots indicate that the maximum temperature (i.e., $1/Nu_{min}$) increases with Ra_L^* before starting to fall again. This increase is conspicuous for small diameter ratios (Fig. 4*c*) and high aspect ratios (Fig. 4*d*). It is also interesting to note that the Rayleigh number at which the relative maximum occurs increases as the aspect ratio is increased.

Heat Transfer Results. If a mean temperature $T_{m,i}$ is determined on the inner wall, the heat transfer coefficient is given by the equation

$$\bar{h}(T_{m,i} - T_o) = q \tag{15}$$

from which an average Nusselt number may be defined as

$$Nu_L = \frac{1}{\tau_m} \tag{16}$$

where τ_m is the nondimensionalized mean temperature on the inner wall. The heat transfer results are presented in terms of Nu_L versus Ra_L^* for various diameter ratios and two aspect ratios in Figs. 5(*a*) and 5(*b*). $\kappa = 1$ represents a rectangular cavity. In order to obtain the heat transfer results for a cavity, the equations that were written in polar coordinates may be

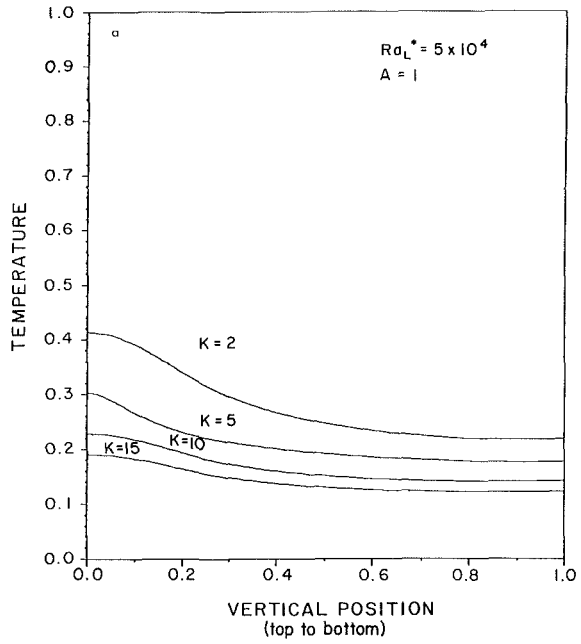

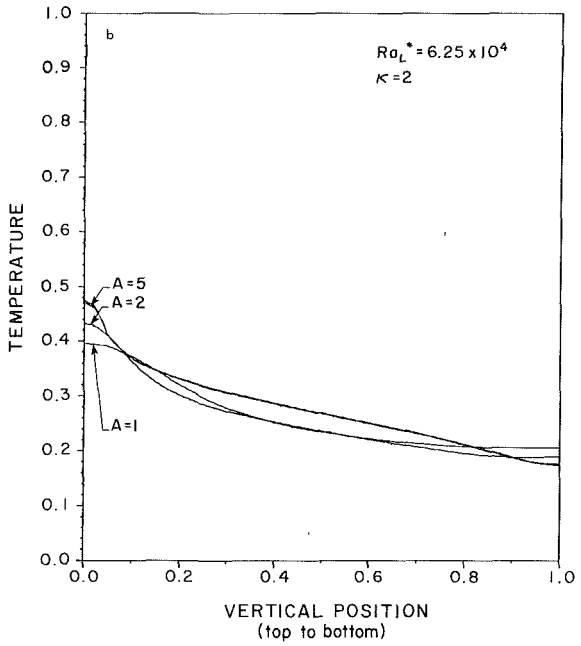

Fig. 3 Local nondimensional temperature on the inner wall: (*a*) diameter ratio effect, (*b*) aspect ratio effect

easily reformulated in Cartesian coordinates by replacing $\frac{1}{R^2}$ and $\frac{1}{R}$ by 1 in the terms in which they appear. At low modified Rayleigh numbers, the heat transfer rate is due to conduction, and the calculated Nusselt numbers were within 1 percent of the theoretical values obtained from

$$\mathrm{Nu}_C = \frac{\kappa - 1}{\ln \kappa} \tag{17}$$

The critical Rayleigh number Ra_{CR} at which conduction flow regime ceases has been calculated based on the criterion $\mathrm{Nu}_L/\mathrm{Nu}_C = 1.1$, as suggested by Thomas and de Vahl Davis (1970). As the diameter ratio increases for both $A = 1$ and $A = 5$, the conduction flow regime extends to higher Ra_L^* values. The heat transfer curves take the form $\mathrm{Nu}_L = C\ \mathrm{Ra}_L^{*n}$. All the curves tend to converge at high Ra_L^*. This is particularly true

Table 2 Maximum temperature normalized by mean temperature on the inner wall

Ra_L^*	A	κ	$\tau_{max}/\tau_{m,i}$	$\tau_{min}/\tau_{m,i}$
		2	1.475	0.791
5×10^4	1	5	1.442	0.856
		10	1.416	0.881
		15	1.377	0.891
10^6		2	1.943	0.682
	1	5	1.769	0.830
		10	1.762	0.881
		15	1.603	0.863
6.25×10^4	1		1.535	0.798
	2	2	1.686	0.745
	5		1.688	0.624

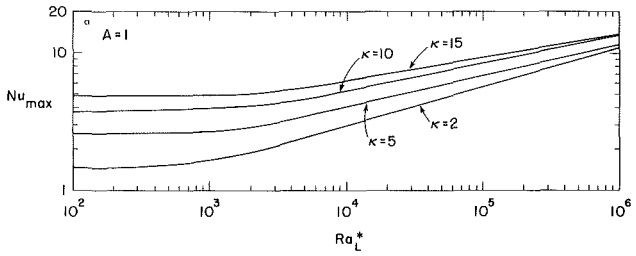

Fig. 4(*a*) Nu_{max} versus Ra_L^*, diameter ratio effect

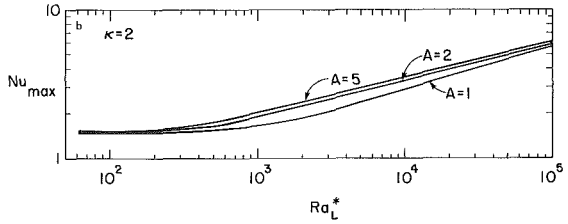

Fig. 4(*b*) Nu_{max} versus Ra_L^*, aspect ratio effect

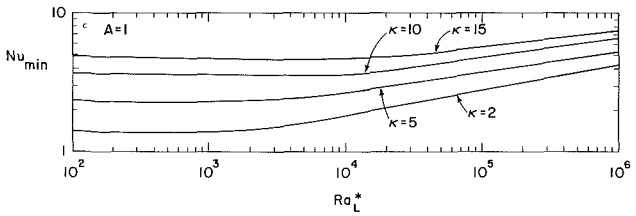

Fig. 4(*c*) Nu_{min} versus Ra_L^*, diameter ratio effect

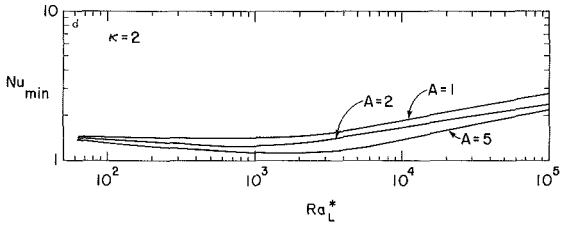

Fig. 4(*d*) Nu_{min} versus Ra_L^*, aspect ratio effect

Fig. 4 Maximum and minimum Nu versus Ra_L^*

for $\kappa = 10$ and 15, at which there is a difference of less than 8 percent in heat transfer results for $\mathrm{Ra}_L^* > 5 \times 10^5$. From Fig. 5(*b*), it seems that when the aspect ratio is increased from $A = 1$ to $A = 5$, the extent of the conduction flow regime is not altered. However, as seen in Fig. 6, for $\kappa = 2$, when A is increased from 5 to 10, the conduction regime extends to high Ra_L^* values. Results have been obtained (not shown here) for $\kappa = 2$ and $A = 2$ to confirm that the transition from conduction to convection flow regime occurs at the same Ra_L^* for $\kappa = 2$

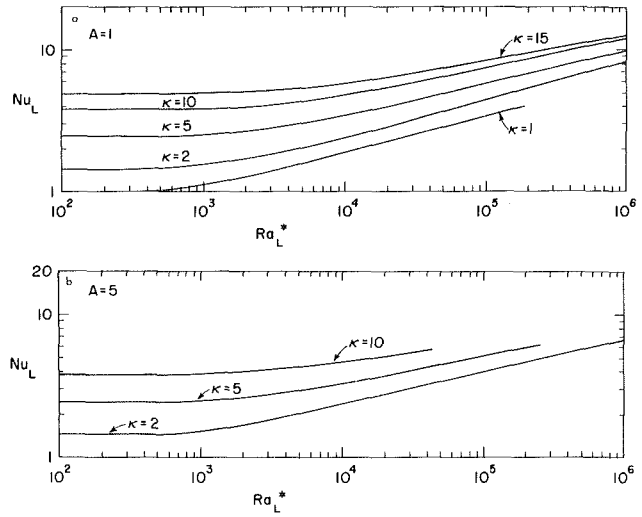

Fig. 5 Heat transfer results: Nu_L versus Ra_L^*, diameter ratio effect for (*a*) $A = 1$; (*b*) $A = 5$

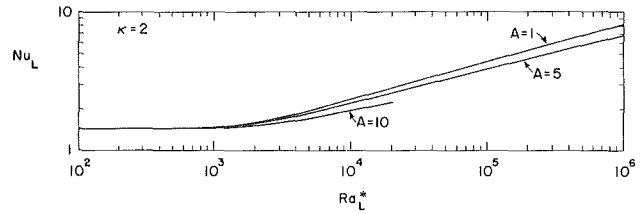

Fig. 6 Heat transfer results: Nu_L versus Ra_L^*, aspect ratio effect, $\kappa = 2$

as A is increased from 1 to 5. However, as the aspect ratio is increased to 10 (Fig. 6), the conduction regime is seen to be extended. Also, as the aspect ratio is increased from 1 to 10, the heat transfer rate decreases. The heat transfer curves diverge for various A at high Ra_L^*, unlike those that show the diameter ratio effect.

Comparison of Isothermal and Heat Flux Boundary Conditions. If the difference between the mean temperature on the heat flux wall and the temperature on the outer wall is considered equal to the imposed temperature difference in the corresponding isothermal case, i.e.,

$$T_{m,i} - T_o = T_i - T_o \tag{18}$$

then the heat transfer results of both boundary conditions may be compared. It may be derived from the above condition that the Rayleigh number Ra_L based on the temperature difference $(T_{m,i} - T_o)$ is given by

$$Ra_L = \frac{Ra_L^*}{Nu_L} \tag{19}$$

The heat transfer results are plotted in terms of Nu_L versus Ra_L to show the effects of κ and A in Figs. 7(*a*) and 7(*b*). The heat transfer rates are the same for both types of heating in the conduction regime. However, the conduction flow regime is smaller for all κ for isoflux heating due to the early takeoff of Nusselt number curves. So, the heat transfer rates are consistently higher for isoflux heating compared to the isothermal case. The difference increases with increase in Ra_L, and decreases with κ. For example, at $Ra_L = 10^5$, a difference of 15 percent in Nu_L is noted for $\kappa = 2$, which decreases to 9 percent for $\kappa = 15$. From Fig. 7(*b*), it is once again seen that the transition occurs at around the same Ra_L when A is increased from 1 to 5 for $\kappa = 2$; however, when A is further increased to 10, a delay in the flow regime is seen to exist. Also, the Nusselt numbers are the same for both boundary conditions at least up to $Ra_L = 5000$. Results were not obtained for $A = 10$ beyond $Ra_L = 5000$.

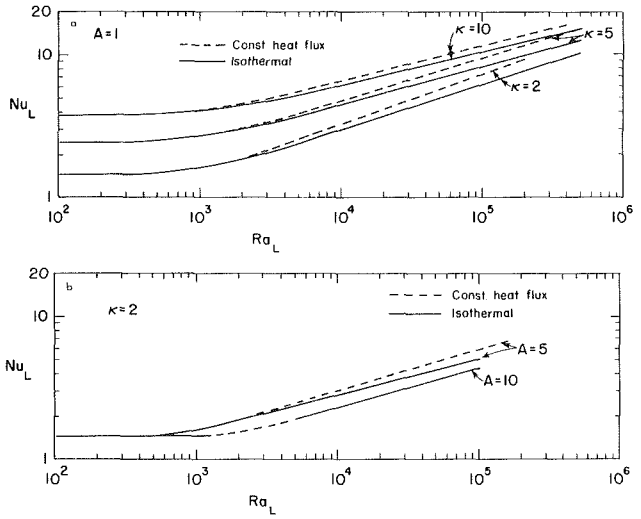

Fig. 7 Comparison of isoflux and isothermal boundary conditions: Nu_L *versus* Ra_L *for* (*a*) $A = 1$, *diameter ratio effect;* (*b*) $\kappa = 2$, *aspect ratio* effect

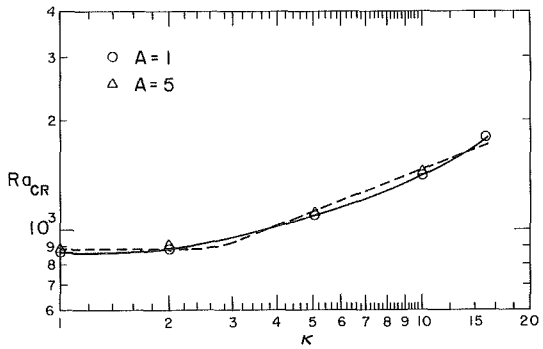

Fig. 8 Prediciton of transition to flow regime, critical Rayleigh number, Ra_{CR} versus κ

The solid curve in Fig. 8 represents the critical Rayleigh number for various κ and aspect ratios of 1 and 5. As shown earlier in Fig. 7(*b*), Ra_{CR} does not change significantly for $1 \leq A \leq 5$. Another interesting feature is that Ra_{CR} has a constant value of 860 (±3 percent) for $\kappa = 1$ and 2, and increases with κ from there on. The dotted line in Fig. 8 gives the approximate representation of Ra_{CR} versus κ. Based on the Ra_{CR} values for $\kappa = 5$, 10, and 15, it is reasonable to arrive at an equation of the form

$$Ra_{CR} = C\kappa^m \tag{20}$$

for $\kappa > 2$ and $1 \leq A \leq 5$.

Comparison of Results With Experiments. Keyhani et al. (1983) presented a correlation based on their data for $A = 27.6$ and $\kappa = 4.33$, given by equation (2), and modified it to account for the effects of diameter ratio and aspect ratio, as given by equation (4). Although the κ and A dependence appearing in equation (4) was presented for isothermal cylinders by Thomas and de Vahl Davis (1970), Kalam and Kumar (1987) and Prasad and Kulacki (1985) have shown that the correlation equation (4) overpredicts the heat transfer results. Interestingly enough, Fig. 7 shows that the isoflux boundary condition predicts a higher heat transfer rate compared to the isothermal problem, and hence the κ and A dependence of equation (4) is expected to correlate the data better.

The heat transfer data given thus far suggest that for large diameter ratios ($\kappa \geq 10$), even for low aspect ratios such as $A = 1$, the annulus behaves as a single cylinder in an infinite domain. In such a situation, the inner diameter d_i should be the length scale instead of the gap length L, and is expected

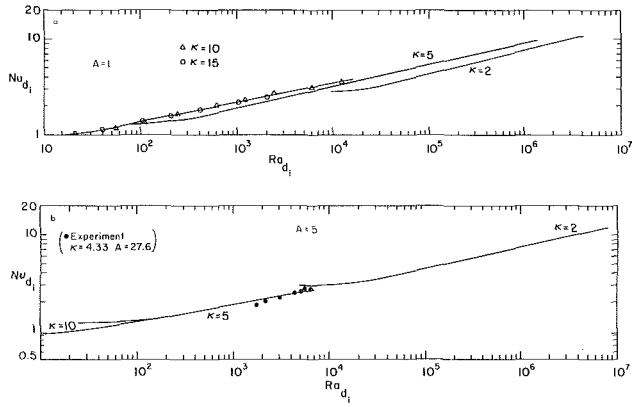

Fig. 9 Comparison of heat transfer results with the experimental data of Keyhani et al. (1983), Nu_{d_i} versus Ra_{d_i} for *a*) $A = 1$; (*b*) $A = 5$

to collapse the data better. The plots of Nu_{d_i} versus Ra_{d_i} are given for $A = 1$ and 5 in Figs. 9(*a*) and 9(*b*). In Fig. 9(*a*), the effect of κ is shown. For $\kappa = 10$ and 15, Nu_{d_i} values are nearly the same at Ra_{d_i}. It is clear that for high κ, d_i is the length scale and gives more information about the heat transfer than when plotted as Nu_L versus Ra_L. Also, at high Ra_{d_i}, i.e., $Ra_{d_i} = 2 \times 10^4$, $\kappa = 5$, 10, and 15 give the same Nu_{d_i}. Thus, at high Ra_{d_i}, even $\kappa = 5$ is seen to give the single-cylinder solution. As the aspect ratio is increased, as shown in Fig. 9(*b*), it is interesting to see that the Nu_{d_i} results for $\kappa = 2$, 5, and 10 fall nearly on the same line. Seven experimental points from Keyhani et al. (1983) for $\kappa = 4.33$ and $A = 27.6$ are plotted in the range of the numerical data obtained for $\kappa = 5$. The numerical and experimental data differ by less than 8 percent. It may be reasonable to infer that for $\kappa > 5$ and $A > 5$, if the inner diameter is taken as the length scale, the aspect ratio dependence is negligible for high Rayleigh numbers.

Heat Transfer Correlations. For a given aspect ratio and Rayleigh number, if Nu versus κ is plotted on a log-log graph, the slope is seen to be large for small κ and small for high κ (i.e., between $\kappa = 5$ and 10) before the curve levels off. This behavior suggests that the diameter ratio dependence on Nusselt number had to be carefully examined. The constant exponent of κ for heat transfer correlation as given in equation (3) by Thomas and de Vahl Davis does not correlate the data well. Based on the numerical data presented here for $1 \leq \kappa \leq 15$ and $1 \leq A \leq 10$, the following correlation based on modified Rayleigh number is obtained in the boundary layer regime:

$$Nu_L = 0.239\ Ra_L^{*0.225} \kappa^{\frac{0.303}{\kappa} + 0.316} A^{-0.05} \tag{21}$$

In terms of Rayleigh number Ra_L, the above equation may be written as

$$Nu_L = 0.158\ Ra_L^{0.29} \kappa^{\frac{0.303}{\kappa} + 0.316} A^{-0.05} \tag{22}$$

The correlation given above has an exponent of κ, which is a function of κ. This exponent decreases with increasing κ as was observed earlier, thus fitting the data better. The standard deviation error between the correlation and the numerical data was 4.6 percent. The present correlation was compared with the correlation given in equation (2) by Keyhani et al. (1983) for $\kappa = 4.33$ and $A = 27.6$. In the lower end of the boundary layer regime, the difference between the two results was as high as 17 percent; however, the difference continued to drop at high Ra_L to as low as 3.9 percent for $Ra_L = 10^6$. A simpler correlation may be obtained for $\kappa > 5$ and $A > 5$ using d_i as the length scale as follows:

$$Nu_{d_i} = 0.455\ Ra_{d_i}^{0.202} \tag{23}$$

Conclusions

Numerical results have been obtained for natural convection of gases in a vertical annulus with the inner cylinder maintained at constant heat flux. The outer cylinder is isothermal and the top and the bottom plates are insulated. Heat transfer and fluid flow results have been presented in terms of Nusselt numbers, local and maximum temperature on the inner wall, isotherms, and velocity field in the annulus. Several combinations of parameters in the range of $1 \leq A \leq 10$, $1 \leq \kappa \leq 15$, and $100 < Ra_L^* < 10^7$ have been considered.

The inner cylinder temperature is a strong function of κ and A. For a given Ra_L^*, the ratio of the peak temperature to the mean temperature decreases with diameter ratio but the aspect ratio has the opposite effect.

The heat transfer rate is higher for a constant heat flux boundary compared to an isothermal boundary when the temperature difference is the same. The percentage difference decreases as κ increases. No such observation could be made of the aspect ratio effect.

For a given κ, the transition from conduction to flow regime occurs at about the same Ra_L for $1 \leq A \leq 5$. This critical Rayleigh number is seen to be constant ($Ra_{CR} = 880$) for $k \leq 2$; however, it varies linearly with κ on a logarithmic scale, for $\kappa > 2$.

The present numerical results were correlated to include aspect ratio and diameter ratio dependence. This correlation equation compared well with the correlation equation (2) provided by Keyhani et al. (1983) based on their experimental results for $\kappa = 4.33$ and $A = 27.6$ for high Rayleigh numbers.

For large diameter ratios, d_i is seen to be the appropriate length scale, and the plots of Nu_{d_i} versus Ra_{d_i} showed that the numerical data for $\kappa = 10$ and 15 merge into one curve for $A = 1$. It is also seen that at high Ra_{d_i}, the heat transfer rate for $\kappa = 5$ also reaches an asymptotic limit. For higher aspect ratios ($A = 5$), the experimental data of Keyhani et al. (1983) plotted on the Nu_{d_i} versus Ra_{d_i} curve are in very good agreement with the present data for $\kappa = 5$ and $A = 5$. This seems to suggest that if d_i is used as the length scale for $\kappa \geq 5$ and $A \geq 5$, the aspect ratio effect on the heat transfer rate may not be significant.

References

Bhushan, R., Keyhani, M., Christensen, R. N., and Kulacki, R. A., 1983, "Correlation Equations for Free Convection in a Vertical Annulus With Constant Heat Flux on the Inner Wall," ASME JOURNAL OF HEAT TRANSFER, Vol. 105, pp. 910–912.

de Vahl Davis, G., and Thomas, R. W., 1969, "Natural Convection Between Concentric Vertical Cylinders," *High Speed Computing in Fluid Dynamics, Physics of Fluids*, Supplement II, pp. 198–207.

Kalam, M. A., and Kumar, R., 1987, "Numerical Study of Laminar Natural Convection in Vertical Annulus," *Proc. 5th In. Conf. on Numerical Methods in Thermal Problems*," Montreal, Canada.

Keyhani, M., Kulacki, F. A., and Christensen, R. N., 1983, "Free Convection in a Vertical Annulus With Constant Heat Flux on the Inner Wall," ASME JOURNAL OF HEAT TRANSFER, Vol. 105, pp. 454–459.

Landis, F., and Yanowitz, H., 1966, "Transient Natural Convection in a Narrow Vertical Cell," *Proc. 3rd. Int. Heat Transfer Conf.*, Chicago, IL, Vol. 2, pp. 139–151.

Lee, Y., Korpela, S. A., and Horne, R. N., 1982, "Structure of Multicellular Natural Convection in a Tall Vertical Annulus," *Proc. 7th Int. Heat Transfer Conf.*, Munich, Federal Republic of Germany, Vol. 2, pp. 221–226.

Prasad, V., and Kulacki, F. A., 1985, "Free Convection Heat Transfer in a Liquid-Filled Annulus," ASME JOURNAL OF HEAT TRANSFER, Vol. 107, pp. 596–602.

Sheriff, N., 1966, "Experimental Investigation of Natural Convection in Single and Multiple Vertical Annuli With High Pressure Carbon Dioxide," *Proc. 3rd Int. Heat Transfer Conf.*, Chicago, IL, Vol. 2, pp. 132–138.

Thomas, R. W., and de Vahl Davis, G., 1970, "Natural Convection in Annular and Rectangular Cavities—A Numerical Study," *Proc. 4th Int. Heat Transfer Conf.*, Paris, France, Vol. 4, Paper No. N.C. 2.4.

Natural Convection in a Cylindrical Porous Enclosure With Internal Heat Generation

V. Prasad
Mem. ASME

A. Chui

Department of Mechanical Engineering,
Columbia University,
New York, NY 10027

A numerical study is performed on natural convection inside a cylindrical enclosure filled with a volumetrically heated, saturated porous medium for the case when the vertical wall is isothermal and the horizontal walls are either adiabatic or isothermally cooled. When the horizontal walls are insulated, the flow in the cavity is unicellular and the temperature field in upper layers is highly stratified. However, if the top wall is cooled, there may exist a multicellular flow and an unstable thermal stratification in the upper region of the cylinder. Under the influence of weak convection, the maximum temperature in the cavity can be considerably higher than that predicted for pure conduction. The local heat flux on the bounding walls is generally a strong function of the Rayleigh number, the aspect ratio, and the wall boundary conditions. The heat removal on the cold upper surface decreases with the aspect ratio, thereby increasing the Nusselt number on the vertical wall. The effect of Rayleigh number is, however, not straightforward. Several correlations are presented for the maximum cavity temperature and the overall Nusselt number.

Introduction

Convective heat transfer in volumetrically heated porous layers is of fundamental importance to a number of technological applications, such as nuclear reactor safety, storage of agricultural products, fermentation processes in food industries, chemical packed-bed reactors, and is also of interest in environmental sciences, geophysics, and astrophysics. This has lead many investigators to study buoyancy-induced flow and heat transfer in heat-generating porous media.

Much of the work on this topic has been concerned with horizontal porous layers. Only recently, the authors have started investigating the natural convection due to internal heat generation in other types of porous configurations. Notable among them are the work of Haajizadeh et al. (1984), Prasad (1985, 1987), and Blythe et al. (1985) on vertical cavities, Vasseur et al. (1984) on horizontal annuli, and Stewart and Dona (1985, 1988) on a vertical cylinder.

Stewart and Dona (1985, 1988) considered the free convection in a finite vertical cylinder filled with a heat-generating porous medium. They first studied the low Rayleigh number flow and reported that the heat transfer was conduction dominated for Ra $\leq$ 0.2. Their recent work for a cylinder with isothermal surfaces showed that the isotherms were compressed near the top and side of the cylinder as the Rayleigh number was increased. They also observed secondary cells near the top edge of the centerline for Ra $> 1.75 \times 10^3$, in addition to the primary recirculating flows. The study was conducted for a cylinder height-to-diameter ratio of unity and Rayleigh numbers up to 2500.

The purpose of the present work is to study the natural convection in a vertical cylinder filled with a volumetrically heated, saturated porous medium for wide range of parameters; $1 \leq A \leq 20$ and Ra $\leq 10^4$. The effects of wall boundary conditions on the temperature and flow fields are examined for three different cases: (*i*) isothermally cooled vertical wall and adiabatic horizontal walls, (*ii*) the top and side walls isothermally cooled and the bottom adiabatic, and (*iii*) all walls isothermal.

Contributed by the Heat Transfer Division and presented at the ASME Winter Annual Meeting, Boston, Massachusetts, December 1987. Manuscript received by the Heat Transfer Division July 13, 1987. Keywords: Geophysical Heat Transfer, Natural Convection, Porous Media.

Formulation and Numerical Method

The physical system under consideration is as shown in Fig. 1. It is assumed that the porous matrix is isotropic, homogeneous, and saturated with an incompressible fluid. The thermophysical properties of the fluid and solid matrix are constant except for the fluid density variation in the body force term. Also, the heat is generated by a uniformly distributed energy source, which induces the buoyant flow in the porous layer and thereby provides a driving mechanism for natural convection within the cylinder.

In the present study, the vertical wall of the cylinder has been considered as isothermally cooled at T_c while the horizontal walls are either adiabatic or cooled at a constant temperature T_c. Hence, three different situations are considered for the numerical computation. These three cases are: (*i*) both top and bottom walls adiabatic, (*ii*) insulated bottom and cooled top, and (*iii*) both top and bottom isothermally cooled.

The governing equations for axisymmetric, steady flow through Darcy porous medium are:

$$\frac{\partial}{\partial r}(ru') + \frac{\partial}{\partial z}(rv') = 0 \tag{1}$$

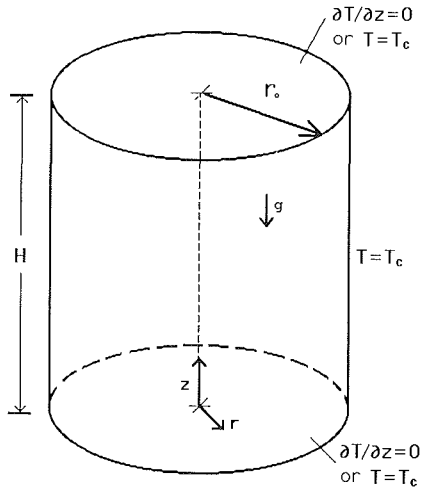

Fig. 1 Geometric configuration, coordinate system, and the boundary conditions

$$\frac{1}{\rho}\frac{\partial p}{\partial r}+\frac{\nu}{K}u'=0 \tag{2}$$

$$\frac{1}{\rho}\frac{\partial p}{\partial z}+\frac{\nu}{K}v'+g=0 \tag{3}$$

$$u'\frac{\partial T}{\partial r}+v'\frac{\partial T}{\partial z}=\alpha\left[\frac{1}{r}\frac{\partial}{\partial r}\left(r\frac{\partial T}{\partial r}\right)+\frac{\partial^2 T}{\partial z^2}\right]+\frac{S}{\rho c} \tag{4}$$

These equations can be nondimensionalized by defining the dimensionless variables as $R=r/r_o$, $Z=z/H$, $u=u'/(\alpha/r_o)$, $v=v'/(\alpha H/r_o^2)$, and $\theta=(T-T_c)/(Sr_o^2/2k)$. Further, by eliminating the pressure term from the momentum equations by cross-differentiation and employing the Boussinesq approximation, the governing equations (1)–(4) can be rewritten in the stream function–temperature form as

$$A^2\frac{\partial}{\partial R}\left[\frac{1}{R}\frac{\partial\psi}{\partial R}\right]+\frac{\partial}{\partial Z}\left[\frac{1}{R}\frac{\partial\psi}{\partial Z}\right]=\mathrm{Ra}\,A\frac{\partial\theta}{\partial R} \tag{6}$$

$$\frac{\partial\psi}{\partial R}\frac{\partial\theta}{\partial Z}-\frac{\partial\psi}{\partial Z}\frac{\partial\theta}{\partial R}=\frac{\partial}{\partial R}\left(R\frac{\partial\theta}{\partial R}\right)+\frac{1}{A^2}\frac{\partial}{\partial z}\left(R\frac{\partial\theta}{\partial Z}\right)+2R \tag{7}$$

As a result of symmetry about the axis of the cylinder, $r=0$, we need to solve equations (6) and (7) only in the half cylinder $0\le r\le r_o$ and $0\le z\le H$, referred to as the "half cavity." Here, it is assumed that the fluid velocity and the heat flow normal to the centerline are zero. The streamline and isotherm patterns show that this assumption is certainly valid in the stable convection regime. However, in the oscillatory convection state, it may be necessary to carry out the computations in the entire cylinder.

The relevant hydrodynamic and thermal boundary conditions are

$$R=0,\ \psi=0,\ \partial\theta/\partial R=0; \tag{8a}$$

$$R=1,\ \psi=0,\ \theta=0; \tag{8b}$$

$$Z=0,\ \psi=0,\ \partial\theta/\partial Z=0\ \text{(cases I and II)};\ \theta=0\ \text{(case III)} \tag{8c}$$

$$Z=1,\ \psi=0,\ \partial\theta/\partial Z=0\ \text{(case I)};\ \theta=0\ \text{(cases II and III)} \tag{8d}$$

It should be noted that the present formulation does not consider the inertia and viscous diffusion effects, which may be significant under certain circumstances. The recent studies on non-Darcy effects, however, indicate that the Darcy flow model may be valid for a wide range of Rayleigh number when Darcy number $\mathrm{Da}<10^{-6}$ and $\mathrm{Pr}>1$. The values of Da and Pr together with the fluid Grashof number will then determine the upper limit of Ra for the validity of Darcy formulation. For example, in the case of a differentially heated cavity, the Darcy solution is valid for the modified Rayleigh number ($=2$ Ra/Nu) as high as 5000 for $\mathrm{Da}=10^{-6}$, which is much larger than the upper limit of Ra considered in the present calculation.

Finite-difference equations are derived from equations (6) and (7) by integration over finite area elements following a procedure outlined by Gosman et al. (1969). The discretization in this scheme is equivalent to central differences for all terms except the convective term in the energy equation, for which the second upwind differencing has been employed. The successive substitution formulas derived in this way satisfy the convergence criterion and are quite stable for many circumstances.

To solve the system of algebraic equations thus obtained, a SOR point iterative scheme is used that makes use of the new values as soon as they are available. Generally, the temperature is overrelaxed and/or the stream function is underrelaxed. The solution technique is well described in the literature and has been widely used for recirculating flows. The applicability of the method and its accuracy in predicting convective flows in annular and rectangular enclosures have already been discussed elsewhere (Prasad, 1983, 1985).

Several trial runs were made to select a proper grid field.

Nomenclature

A = aspect ratio $=H/r_o$
c = specific heat of fluid at constant pressure, J/kg-K
D = diameter of the cylinder, m
Da = Darcy number $=K/r_o^2$
g = acceleration due to gravity, m/s^2
H = height of the cylinder, m
h = local heat transfer coefficient, W/m^{2}K
$\bar{h}$ = average heat transfer coefficient on the cold wall, W/m^{2}K
K = permeability of saturated porous medium, m^2
k = effective thermal conductivity of porous medium, W/m-K
$\overline{\mathrm{Nu}}$ = overall Nusselt number based on cylinder radius $=\bar{h}r_o/k$
p = pressure, Pa
$\bar{q}$ = dimensionless local heat flux on vertical wall $=2q_L/Sr_o=-\partial\theta/\partial R$ $(R=1)$
q_L = local heat flux on the cold wall, W/m^2
R = dimensionless distance in radial direction $=r/r_o$
r = radial coordinate, m
r_o = radius of the cylinder, m
Ra = Rayleigh number based on cylinder radius $=g\beta KSr_o^3/2k\nu\alpha$
Ra_H = Rayleigh number based on height $=g\beta KSr_o^2H/2k\nu\alpha$
S = volumetric heat generation, W/m^3
T = temperature, K
u' = fluid velocity in r direction, m/s
u = dimensionless velocity in r direction $=u'/(\alpha/r_o)$
v' = fluid velocity in z direction, m/s
v = dimensionless velocity in z direction $=v'/(\alpha H/r_o^2)$
z = axial coordinate, m
Z = dimensionless distance in axial direction $=z/H$
α = thermal diffusivity $=k/\rho c$, m^2/s
β = isobaric coefficient of thermal expansion of fluid, K^{-1}
η = heat rejected on a cold wall as the fraction of the energy generated in the cylinder
θ = dimensionless temperature $=(T-T_c)/(Sr_o^2/2k)$
ν = kinematic viscosity, m^2/s
ρ = density of fluid, kg/m^3
σ = standard deviation
ψ = stream function

Subscripts

ad = adiabatic walls
b = bottom wall
c = cooled wall
cond = conduction
H = based on the cylinder height H
m = based on mean temperature on the line of symmetry
max = maximum
o = line of symmetry ($r=0$)
s = side wall
t = top wall

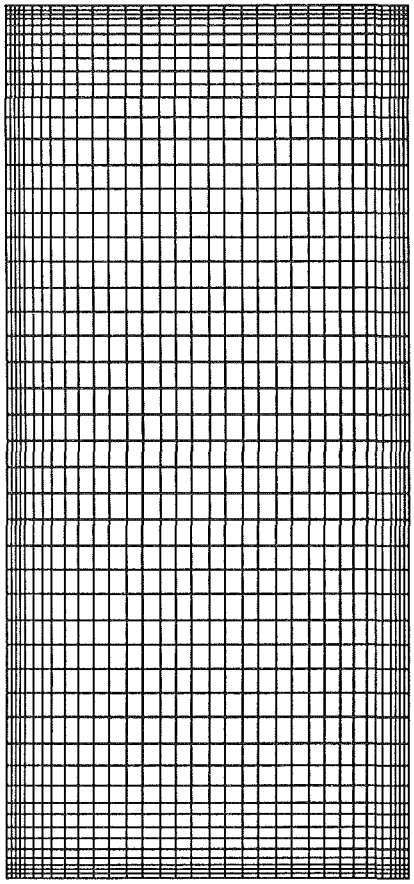

Fig. 2 A representative nonuniform grid field

Since the flow structure changes substantially with the Rayleigh number, the aspect ratio, and the wall boundary conditions, and is highly complex in some situations, a large number of nodes are required to obtain reasonably accurate results. Hence, the grid fields used for the present computations generally vary from 41×51 to 41×61 nodes, with uniform grids for $\mathrm{Ra} < 10^3$ and nonuniform grids for higher Rayleigh numbers. (Figure 2 presents one such nonuniform grid field.) However, the multicellular flows at high Rayleigh numbers (cases II and III) indicate that the varying grid fields may not be suitable for those computations. Calculations for several cases of high Rayleigh number have thus been repeated with uniform grid fields of 51×101 to 81×81 to check the accuracy of predicted temperature and flow fields.

The computations have been restricted to Rayleigh numbers up to 10^4 primarily because (*a*) the steady-state formulation has been used here, and the solutions exhibit multicellular flows that may fluctuate at high values of Ra, (*b*) the numerical instability is always a severe problem at large Rayleigh numbers, and (*c*) the formulation does not account for the viscous diffusion and inertia effects, which are generally significant at high Rayleigh numbers.

Based on the trial solutions for various combinations of Ra and A, a convergence criterion of 0.01 percent or lesser change in both θ and ψ at all nodes in the domain has been selected to test the convergence of the iterative scheme. To further check the accuracy of the numerical results, an overall energy balance has been used for the system that compares the heat generated within the cylinder with that removed on the cold wall(s). Generally, the energy closure is achieved within 1 percent. However, for very low and high Rayleigh numbers, a variation up to 4 percent has been accepted to keep the computational cost low. The trial runs for various combinations of Ra, A, and wall boundary conditions have indicated that the

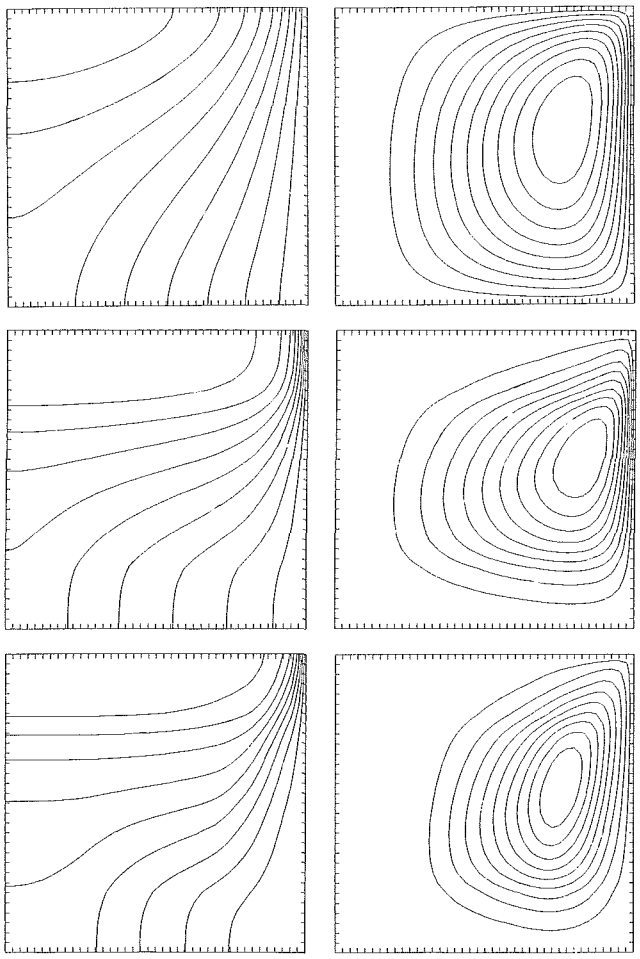

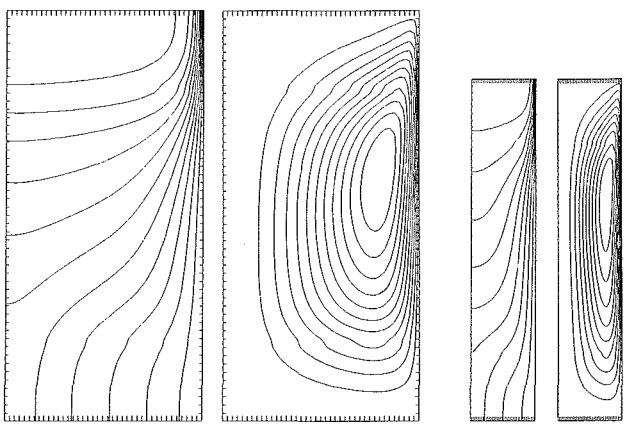

Fig. 3 Isotherms and streamlines for Case I, adiabatic top and bottom walls: (*a*) $\mathrm{Ra} = 10^2$, $A = 1$ ($\Delta\theta = 0.399$, $\Delta\psi = 0.148$), (*b*) $\mathrm{Ra} = 10^3$, $A = 1$ ($\Delta\theta = 0.018$, $\Delta\psi = 0.508$), (*c*) $\mathrm{Ra} = 10^4$, $A = 1$ ($\Delta\theta = 0.078$, $\Delta\psi = 1.483$), (*d*) $\mathrm{Ra} = 10^3$, $A = 2$($\Delta\theta = 0.018$, $\Delta\psi = 0.316$), and (*b*) $\mathrm{Ra} = 10^3$, $A = 5$ ($\Delta\theta = 0.028$, $\Delta\psi = 0.242$)

reported values of ψ, θ, and $\overline{\mathrm{Nu}}$ are within 3 percent of the asymptotic values. Further details of the computational scheme are omitted here for brevity and may be found in earlier publications of the first author (Prasad, 1983, 1985).

Results and Discussion

A cylinder with isothermally cooled vertical wall and adiabatic horizontal walls (Case I) has been considered as the base case for the present work. Hence, the numerical results for this boundary condition have been obtained for a wide

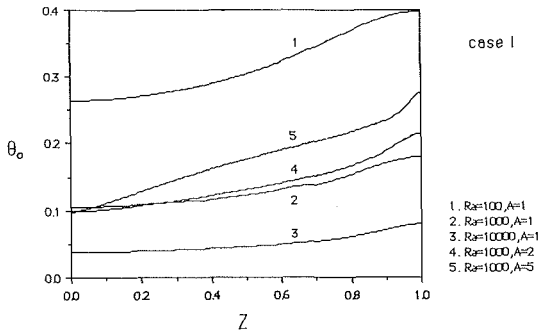

Fig. 4 Centerline temperature distribution for the adiabatic horizontal walls (case I): (1) Ra = 100, $A = 1$; (2) Ra = 1000, $A = 1$; (3) Ra = 10,000, $A = 1$; (4) Ra = 1000, $A = 2$; (5) Ra = 1000, $A = 5$

range of parameters, $1 \leq A \leq 20$ and $\mathrm{Ra} \leq 10^4$. The effects of variation in horizontal wall boundary condition are then studied for a few specific values of Rayleigh number.

Adiabatic Horizontal Walls

Velocity and Temperature Fields. Flow patterns and temperature fields for selected values of Ra and A are presented in Fig. 3. For pure conduction, the isotherms are vertical and dense near the side wall; $\theta_{\mathrm{cond}} = 0.5\,(1-R^2)$. As the Rayleigh number increases, a recirculatory motion is set up because of the buoyancy effects. The flow consists of an asymmetric single cell filling the entire half-cavity (Fig. 3*a*) and rotating slowly in the clockwise direction (counterclockwise in the left half of the cylindrical cavity). This asymmetric nature of the convective cells at low Rayleigh numbers is caused by the imposed thermal boundary conditions and is further strengthed by the curvature effects. It may be noted that the recirculating flows in a rectangular half-cavity at low Rayleigh numbers are not as asymmetric as observed here (Haajizadeh et al., 1984; Prasad, 1985).

When the heat generation rate (or Ra) is increased, the streamlines move closer to the vertical wall, indicating higher vertical velocities in the side wall region and low velocities in the core (Fig. 3*b* and *c*). Although the velocity field remains unicellular at all Rayleigh numbers, the boundary layer effects on the side wall are strengthened by an increase in the buoyancy forces. Also, the flow strength in the core, particularly in the upper and lower portions of the cylinder, does not increase as much as in the wall region. The domain where the upward velocity is positive thus extends with the Rayleigh number, and thereby reduces the region for downward flow.

As is expected, the temperature field is also strongly affected by the increase in buoyancy forces. At low Rayleigh numbers, $\mathrm{Ra} < 10$, the isotherms exhibit minimal distortion from the pure conduction solution, indicating that the conduction is still the dominant mode of energy transport (Fig. 3*a*).

However, as the Rayleigh number increases, the buoyant flow begins to influence the isotherm pattern. This perturbation in the conduction temperature field first takes place at the center of the top surface and gradually propagates toward the bottom region in the core, and also toward the top edge of the side wall in the upper region (Figs. 3*b* and *c*). This is primarily because the upward buoyant flow in the core transports energy from the lower portion of the cylinder to the upper layers. No heat removal on the top surface then results in a stably stratified convective field in the upper region. The extent of this thermally stratified region continually increases with the Rayleigh number.

However, for a fixed Ra, the intensity and extent of the thermal stratification reduces with an increase in the aspect ratio (Fig. 3*b*, 3*d*, and 3*e*). As a result, the vertical velocity increases in the core producing stronger boundary layer effects on the wall at high aspect ratios.

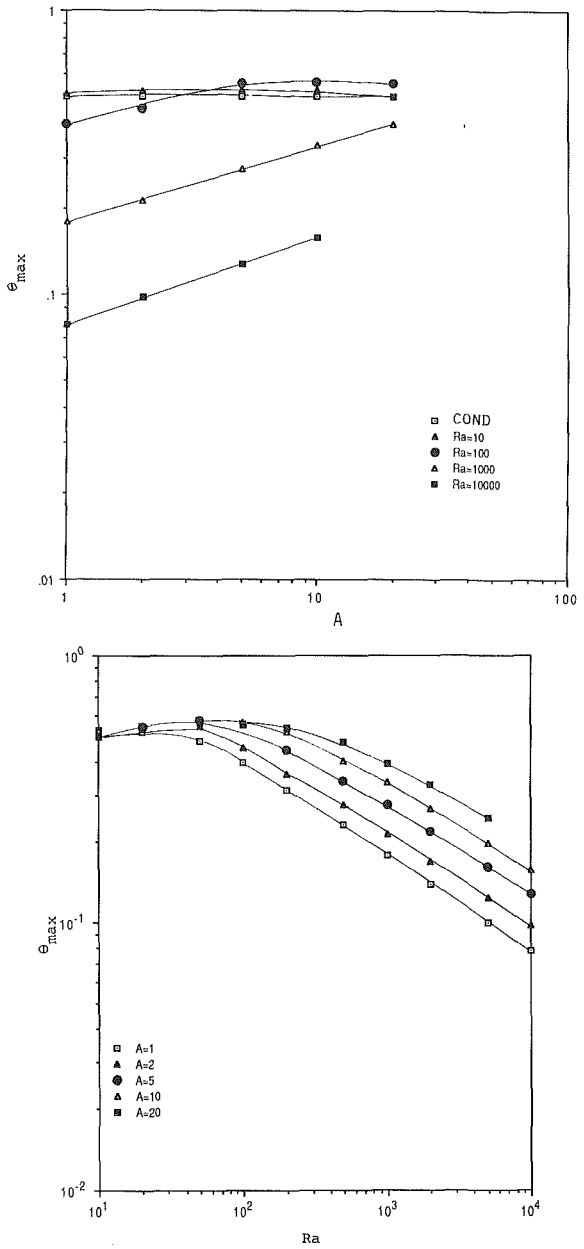

Fig. 5 Variation in maximum cylinder temperature for the adiabatic horizontal walls

Centerline Temperature Distribution. Figure 4 presents the temperature distribution on the centerline of the cylinder. As the Rayleigh number increases, the dimensionless temperature θ_o is observed to decrease from its conduction value of 0.5 everywhere except in a small distance from the top edge (to be discussed later). This decrease in θ_o is larger in the lower portion owing to the higher velocities of returning cold fluid, which is heated gradually during its rise in the central part of the cylinder.

Although the dimensionless temperature θ_o is found to decrease with an increase in the buoyancy forces, it does not mean that the actual temperature has dropped. Since the Rayleigh number is directly proportional to the heat generation rate S, and the dimensionless temperature θ is indirectly proportional to S, the temperature distribution in Fig. 4 should be carefully inspected to derive any conclusion. In general, the dimensional temperature $(T_o - T_c)$ increases with Ra or S, the rate of increase being higher at low Rayleigh numbers.

Table 1 Coefficient C_1 and exponent m for θ_{max} correlation (equation (10))

A	C	m	$\sigma \times 10^4$	Ra≥
1	2.081	0.356	2.25	100
2	2.146	0.334	2.39	100
5	2.490	0.321	2.73	200
10	2.708	0.306	4.64	200
20	3.024	0.295	3.94	500

Table 2 Coefficient C_2 and exponent n for θ_{max} correlation (equation (11))

Ra	C	n	$\sigma \times 10^5$
$5x10^2$	0.234	0.237	0.83
10^3	0.180	0.266	7.81
$2x10^3$	0.138	0.288	0.67
$5x10^3$	0.098	0.301	3.38
10^4	0.079	0.306	2.03

Table 3 Coefficient C_3 and exponent r for equation (15)

A	C	r	$\sigma \times 10^3$	Ra ≥
1	0.492	0.400	0.26	100
2	0.536	0.377	0.85	100
5	0.431	0.377	0.43	200
10	0.386	0.362	0.74	200

Table 4 Maximum cylinder temperature and its location for $A = 1$, 5, and 20; the mean Nusselt number for Case I is also reported

		θ_{max}			Location for θ_{max}		$\overline{Nu}$
A	Ra	I	II	III	II	III	I
1	0	0.500	0.482	0.233	0,0	0,0.50	2.000
	10^2	0.398	0.285	0.192	0,0.56	0,0.60	3.155
	10^3	0.180	0.134	0.116	0,0.73	0,0.73	7.639
	10^4	0.078	0.059	0.054	0,0.89	0.54,0.84	19.841
5	0	0.500	0.500	0.500	0,0.03	0,0.50	2.000
	10^2	0.556	0.475	0.449	0,0.90	0,0.90	2.513
	10^3	0.277	0.241	0.237	0,0.94	0.05,0.94	5.695
	10^4	0.128	0.098	0.103	0.85,0.97	0.58,0.98	14.006
20	0	0.500	0.500	0.500	0,0.26	0,0.26	2.000
	10^2	0.554	0.506	0.506	0,0.97	0,0.97	2.120
	10^3	0.396	0.368	0.367	0.05,0.98	0.05,0.98	3.686
	10^4	0.197	0.183	0.183	0.012,0.99	0.01,0.99	8.584

Figure 4 further shows that the centerline temperature θ_o at a location Z increases with the aspect ratio. Also, the taller the cylindrical cavity, the larger is the temperature gradient $\partial\theta_o/\partial Z$ at any height Z. This does not imply that the dimensional temperature gradient $\partial T/\partial z$ increases with A. Indeed, for a cylinder of fixed radius r_o, $\partial T/\partial z$ decreases as the height of the cylinder is increased, which is evident from Fig. 4 and the expression

$$\frac{\partial T}{\partial z} = \frac{Sr_o}{2k} \frac{1}{A} \frac{\partial \theta}{\partial Z} \tag{9}$$

Maximum Temperature. As can be expected, the temperature is always maximum at the center of the upper surface. When Ra → 0 (conduction), θ_{max} is independent of aspect ratio and is equal to 0.5. An increase in Rayleigh number beyond zero, however, enhances the maximum temperature in the cylinder. Figure 5(*a*) shows this for $0 < \text{Ra} \leq 10$, $1 \leq A < 20$ and $\text{Ra} < 100$, $A > 2$. For a given aspect ratio, the maximum temperature θ_{max} thus increases with Ra to a peak value and then starts decreasing. This increase in θ_{max} beyond its pure conduction value is characteristic of the conduction flow regime, and is primarily because the fluid reaching the upper surface in the central region is unable to transport energy effectively since the velocities are low in that region (Haajizadeh et al., 1984; Prasad, 1985; Vasseur et al., 1984).

In Fig. 5(*a*), θ_{max} for $\text{Ra} = 10$ is observed to decrease with an increase in the aspect ratio, and attains its conduction value at $A = 20$, indicating that $\text{Ra} = 10$ is not large enough to initiate a recirculatory flow at this aspect ratio. Indeed, an interesting behavior is exhibited by the curve for $\text{Ra} = 100$, which shows that θ_{max} increases with A and attains a peak value (>0.5) at $A \simeq 10$, beyond which it starts decreasing. The variation in θ_{max} with Ra and A as demonstrated in Figs. 5(*a*) and 5(*b*) clearly implies that the taller the cylindrical cavity, the higher is the Rayleigh number required for the recirculating flow to start and the longer (in terms of Ra) the conduction flow regime persists. Once the flow approaches the asymptotic flow regime, θ_{max} starts decreasing with an increase in Rayleigh number. Finally, in the boundary layer regime, the $\ln(\theta_{max})$-versus-$\ln(\text{Ra})$ curve attains a slope close to $-1/3$. This seems to be a universal slope for the boundary layer free convection in an enclosure filled with a heat-generating, Darcy porous medium (Vasseur et al., 1984; Haajizadeh et al., 1984; Prasad, 1985).

In the boundary layer regime, the maximum temperature may be correlated as

$$\theta_{max} = C_1 \ \text{Ra}^{-m}, \text{ for fixed } A \tag{10}$$

where C_1 and m are given in Table 1 for various values of A. In general, the exponent m decreases as the aspect ratio of the cylinder is increased, the variation being largest at low aspect ratios. A similar variation in slope m has been reported for the rectangular cavity (Prasad, 1985).

Figure 5(*a*) further shows that it is possible to correlate the maximum temperature with the aspect ratio

$$\theta_{max} = C_2 \ A^n, \text{ for fixed Ra} \tag{11}$$

The values of C_2 and n are reported in Table 2 for $\text{Ra} > 500$. A generalized correlation for the tall cylinder may also be obtained as

$$\theta_{max} = 1.604 \ \text{Ra}^{-0.321} \ A^{0.279}, \ \text{Ra} \geq 500 \text{ and } A \geq 2. \tag{12}$$

which predicts maximum temperature within 5 percent of the numerical data.

Overall Heat Transfer. For the problem considered here, there is no well-defined characteristic temperature difference to express the heat transfer coefficient. However, one can define an overall Nusselt number based on either the maximum temperature in the cylinder or the mean temperature on the centerline. When the heat transfer coefficient is defined in terms of $(T_{max} - T_c)$, the overall Nussel number is obtained as

$$\overline{\text{Nu}}_{max} = \bar{h} r_o / k = 1/\theta_{max} \tag{13}$$

which can be easily obtained from Fig. 5 and equations (10)–(12).

In a similar way, the average Nusselt number based on the mean temperature difference $(T_m - T_c)$ can be expressed as

$$\overline{\text{Nu}} = 1/\theta_m \tag{14}$$

which is presented in Fig. 6 and Table 4. In the conduction regime, $\overline{\text{Nu}} \to 2$ for all values of A. An increase in Rayleigh number is always associated with an increase in Nu. However,

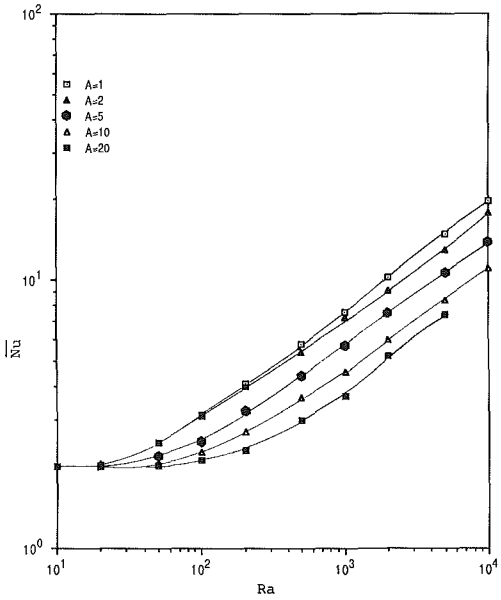

Fig. 6 Overall Nusselt number as a function of Rayleigh number and aspect ratio

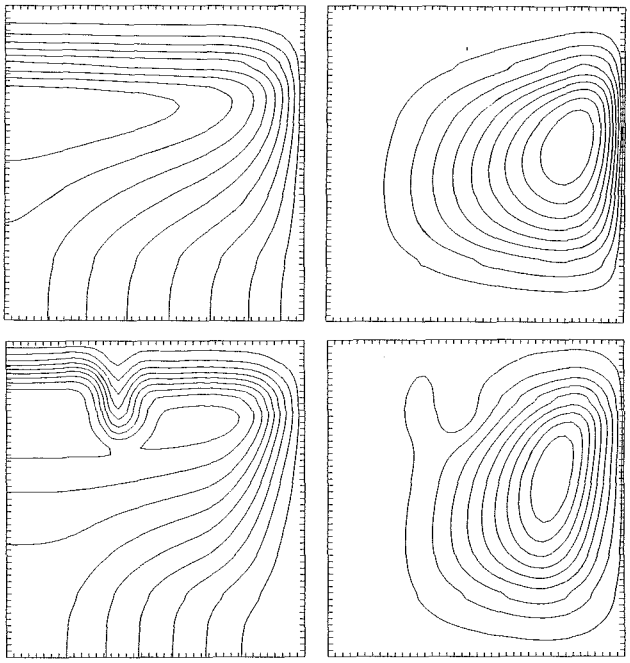

the taller the cylinder, the lower the average heat transfer coefficient. Figure 6 further shows that when the Rayleigh number is high, the Nusselt number curve for a fixed A is almost a straight line, a characteristic of the boundary layer heat transfer on the cold wall.

In the boundary layer regime, the overall Nusselt number may thus be correlated as

$$\overline{\mathrm{Nu}} = C_3\ \mathrm{Ra}^r, \text{ for a fixed } A \qquad (15)$$

The values of C_3 and r are presented in Table 3 for $A < 20$. A correlation for $A = 20$ could not be obtained because the Nusselt number for this aspect ratio does not show a straight line behavior for the range of Ra considered here (Fig. 6). It is interesting to note that the value of r in the present case is very close (within 1 percent) to that reported for a vertical cavity (Prasad, 1985). However, the difference in C_3 is significant, the present values being up to 35 percent lower than that obtained by Prasad.

Cold Horizontal Wall(s)

Temperature and Flow Fields. Typical isotherms and streamlines presented in Figs. 7 and 8 show that the temperature and velocity fields are significantly modified by changing the horizontal wall(s) boundary condition from adiabatic to cold. When the top wall is cold, it provides an additional surface for the removal of heat, thereby drastically changing the temperature field in the upper layers (Fig. 7). Hence, the temperature does not increase monotonically with Z as in the case of adiabatic horizontal surfaces (case I). Indeed, the temperature decreases with height in the upper layers, while in the lower region, it increases with Z. This results in an unstable thermal stratification in the upper portion of the cylinder and produces maximum temperature at $Z < 1$.

Since the fluid approaching the top portion of the side wall has already rejected a significant fraction of energy on the top surface, the boundary layer effects on the side wall are weaker in the present case as compared to that observed in case I (Figs. 3 and 7). Moreover, an unstable stratification in the upper layers causes a Bénard convection-type condition, which at high Rayleigh numbers results in a multicellular flow in the half cavity. This is evident from the streamlines for Ra - 10^4 and $A = 1$ (Fig. 7*b*). The temperature and flow fields at large Ra are therefore highly complex. An increase in aspect ratio

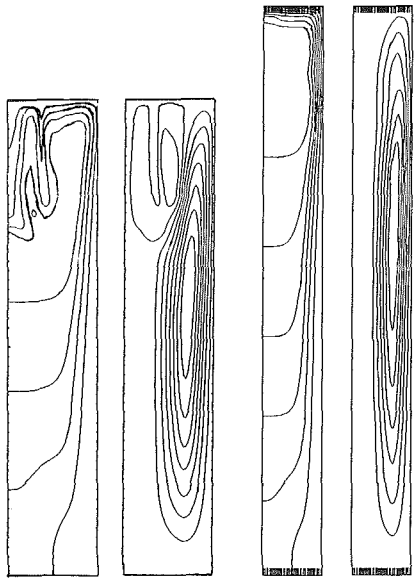

Fig. 7 Isotherms and streamlines for cold top and side walls (case II); (*a*) Ra = 10^3, $A = 1$ ($\Delta\theta = 0.014$, $\Delta\psi = 0.503$); (*b*) Ra = 10^4, $A = 1$ ($\Delta\theta = 0.060$, $\Delta\psi = 1.586$); (*c*) Ra = 10^4, $A = 5$ ($\Delta\theta = 0.020$, $\Delta\psi = 0.970$); (*d*) Ra = 10^4, $A = 10$ ($\Delta\theta = 0.02$, $\Delta\psi = 0.081$)

further complicates the isotherm and streamline patterns (Fig. 7*c*). In the case of $A = 1$, the temperature field exhibits only one inverted thermal plume while there exists an additional (upward) plume at $A = 5$ (Figs. 7*b* and 7*c*). This produces a U-shaped secondary cell at $A = 5$.

It is, however, interesting to note that the secondary flow disappears when the cavity becomes very tall (Fig. 7*d*). This is primarily because the heat removed at the top surface is much less than that rejected on the side wall and the buoyant flow is much stronger to allow any kind of thermal plume to be developed. Also, the inversely stratified convective field extends to a very small portion of the cylindrical cavity.

When the bottom wall is cooled (case III), the flow field further weakens and a stably stratified temperature field is produced in the bottom portion of the cylinder (Fig. 8). At high Rayleigh numbers, the flow again becomes multicellular as in

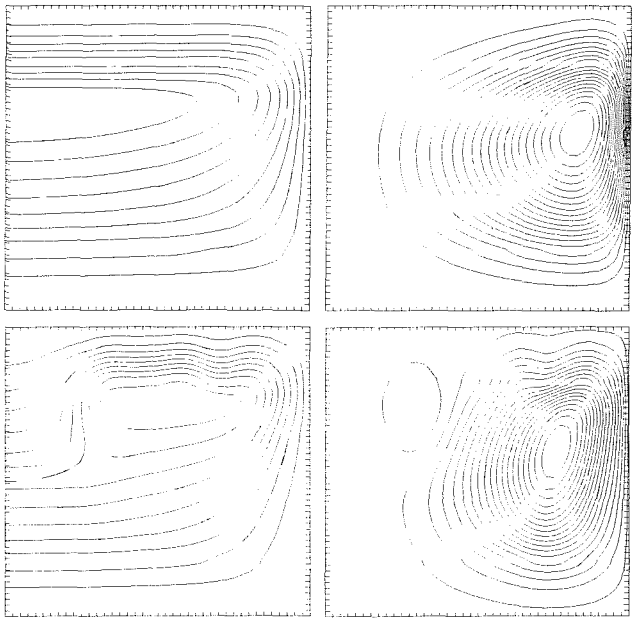

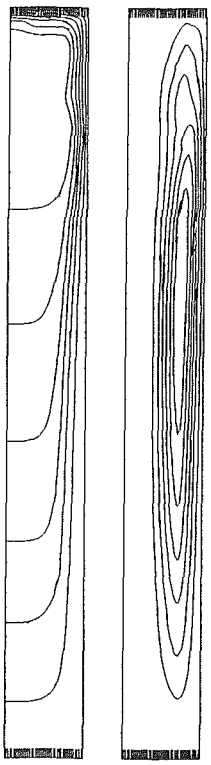

Fig. 8 Isotherms and streamlines for all walls cold (case III): (*a*) Ra = 10^3, $A = 1$ ($\Delta\theta = 0.012$, $\Delta\psi = 0.213$); (*b*) Ra = 10^4, $A = 1$ ($\Delta\theta = 0.054$, $\Delta\psi = 0.613$); and (c) Ra = 10^4, $A = 10$ ($\Delta\theta = 0.020$, $\Delta\psi = 0.796$)

case II. However, the secondary cell does not exist at high aspect ratios when both the horizontal walls are cold.

Multicellular flow has also been demonstrated by the solutions obtained by Stewart and Dona (1987) for a cylindrical cavity of $A = 2$ (case II.) The occurrence of secondary flows in cylinders filled with volumetrically heated fluids is fairly well documented (Lambha et al., 1978; Gartling, 1982). However, it is interesting to note that no such secondary cells are observed in the absence of curvature effects (Prasad, 1987).

It should be noted that at high Rayleigh numbers, the solutions for cases II and III exhibited an oscillating behavior and failed to converge to the desired iterative accuracy, which may be attributed to the phenomenon commonly referred to as the fluctuating Bénard convection. This interesting phenomenon could not be further explored because of the steady-state formulation used in the present study. Also, the viscous diffusion and inertia effects can significantly influence the multicellular flow behavior as shown recently by Kladias and Prasad (1988) for a horizontal porous layer heated from below.

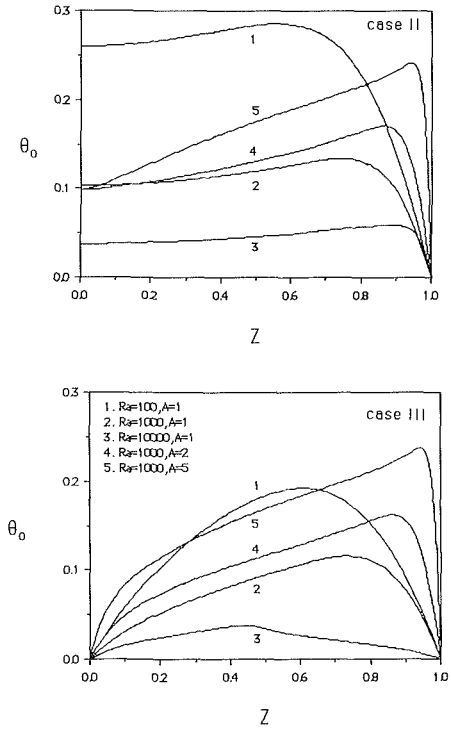

Fig. 9 Centerline temperature distribution for (*a*) case II, and (*b*) case III

Centerline Temperature Distribution. When the bottom wall is adiabaric (case II), the conduction temperature field requires that the temperature be maximum at the center of the bottom surface. The centerline temperature then nonlinearly decreases from this maximum value to zero at $Z = 1$. However, in the convection regime, the temperature at the center of the bottom surface decreases as the buoyant flow is strengthened. Hence, θ_o for Ra > 0 does not increase monotonically with Z (Fig. 9*a*). Indeed, it increases with Z in the lower portion of the cylinder, and reaches a maximum at some point on the centerline, beyond which it starts decreasing. The higher the Rayleigh number, the closer is the location for θ_{max} to the top surface. Since the fraction of energy removed on the upper surface decreases with an increase in A, the location for $\theta_{o,max}$ is found to be very close to $Z = 1$ at higher aspect ratios.

The temperature profile changes further if the bottom wall is also cooled (case III). The conduction temperature field now shows a peak at $Z = 0.5$, and θ_o decreases from this peak value to zero as Z is increased or decreased. However, in the convection regime, the temperature in the lower portion of the cylinder decreases with the Rayleigh number while that in the upper layers increases with Ra (Fig. 9*b*). The location for θ_{max} thus moves up with Ra as observed for case II. The effect of aspect ratio is also very similar in both the cases II and III.

Maximum Temperature. The variation in maximum temperature θ_{max} with Ra and A is reported in Figs. 10(*a*) and 10(*b*) for cases II and III, respectively. As is evident from the isotherms (Figs. 7 and 8), θ_{max} may not necessarily lie on the

centerline, particularly at high Rayleigh numbers and low aspect ratios. For example, when Ra = 10^4 and $A = 5$, θ_{max} exists at (0.85, 0.97) and (0.58, 0.94) for cases II and III, respectively (Table 4).

For case II, the conduction values of θ_{max} is slightly lower than 0.5 for $A = 1$. However, $\theta_{max,cond}$ increases to 0.5 at $A = 2$ and is independent of aspect ratio thereafter (Fig. 10*a*). This value of $\theta_{max,cond}$ is identical to that obtained for case I. When all the wall of cylinder are cold (case III), $\theta_{max,cond}$ is quite low at $A = 1$. Nevertheless, it increases asymptotically with the aspect ratio to 0.5 (Fig. 10*b*). Figures 10(*a*) and 10(*b*) further indicate that the stronger the buoyancy effects, the lower the maximum temperature in the cavity. As observed for case I, the slope for the θ_{max} curve is almost a constant in the boundary layer regime. A comparison between Figs. 5 and 10 reveals that θ_{max} is largest for case I when both the horizontal walls are insulated, and is lowest for case III when all the walls are cooled (also see Table 4). It is also evident from these results that the effect of bottom wall boundary condition on θ_{max} is minimal.

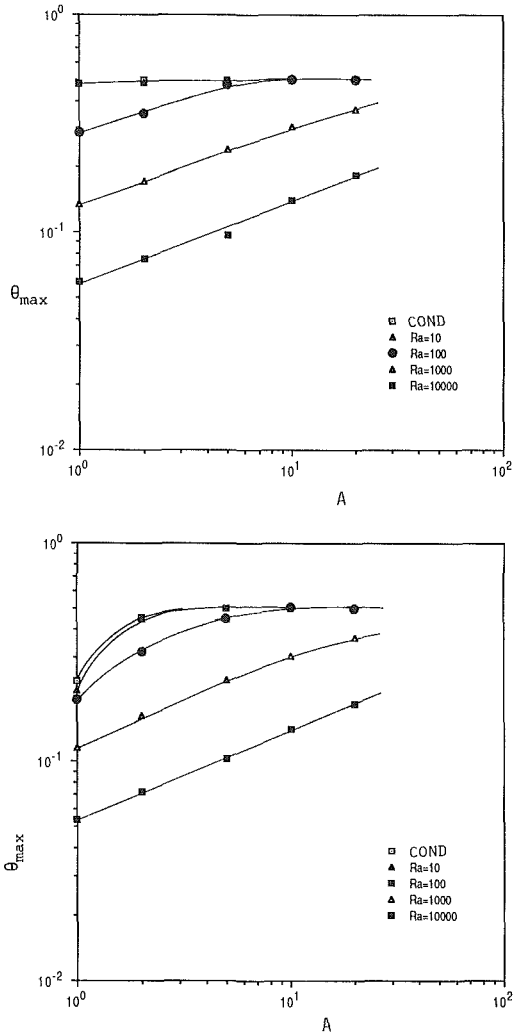

Fig. 10 Maximum temperature for (*a*) case II, and (*b*) case III

Heat Transfer Results. The local heat flux $\bar{q}$ is presented in Fig. 11 for all the cold walls. On the vertical wall, the heat flux increases with Z and attains a maximum value at a point close to the top edge, beyond which it starts decreasing. It may be recalled that in the case of adiabatic horizontal walls (case I), $\bar{q}$ is maximum at the top edge (1, 1).

Figure 11 further shows that the heat flux distribution changes significantly with the horizontal wall boundary condition(s), particularly when the flow is multicellular and the thermal plume is in existence. The $\bar{q}$ distribution for Ra = 10^4 is quite interesting, and exhibits the large-scale influence of the unstable stratification in the top wall region. This variation in top surface heat flux gets further complicated with an increase in the height of the cylinder (Fig. 7). However, when the aspect ratio is very large, $\bar{q}$ decreases monotonically from the center to the edge of the top wall. For case III, the $\bar{q}$ distribution on the bottom surface is rather straight foward, almost uniform heat removal except for a small portion near the edge. This is a characteristic of the stable thermal stratification in the lower portion of the cylinder (Fig. 8).

Finally, the fraction of total energy removed on each wall η is presented in Figs. 12 and 13 for cases II and III, respectively. For both of these cases, the heat removal on the vertical wall η_s increases asymptotically with the aspect ratio. However, the effect of Rayleigh number is not straightforward. If the buoyancy forces are not so strong as to complicate the flow structure and the isotherm patterns in the upper region, η_s decreases as the Rayleigh number is increased. This is at least true for Ra $\leq 10^3$ (Figs. 12*a* and 13*a*). There exists a critical Rayleigh number as a function of aspect ratio and the bottom wall boundary condition, beyond which η_s increases with Ra.

The heat rejection on top wall varies accordingly (Figs. 12*b* and 13*b*). Whenever the fraction of generated energy removed on the side wall η_s increases with Ra, η_t is observed to decrease, and vice versa. However, the effect on heat removal at the bottom surface (case III) is independent of these variations; η_b decreases monotonically with Ra and A (Fig. 13*c*). The higher the aspect ratio and/or the Rayleigh number, the smaller the fraction of energy rejected at the bottom surface. It is thus evident that the effect of the upper surface boundary condition is generally quite significant, while the bottom wall

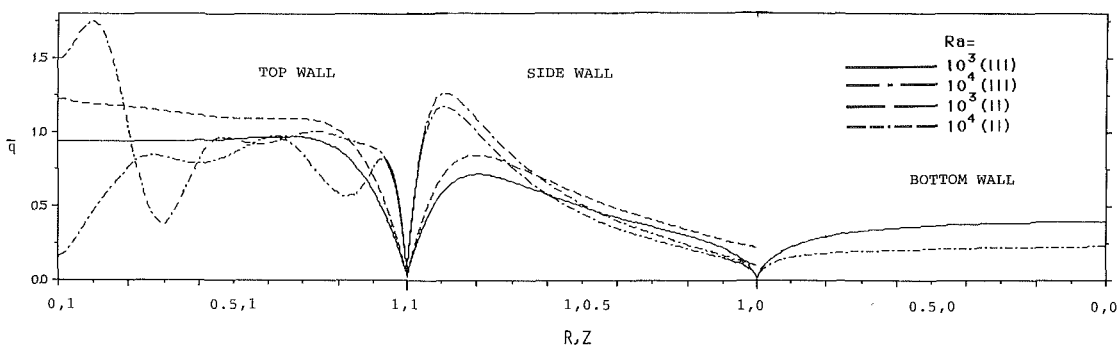

Fig. 11 Normalized local heat flux for cold walls: (*a*) case II, and (*b*) case III

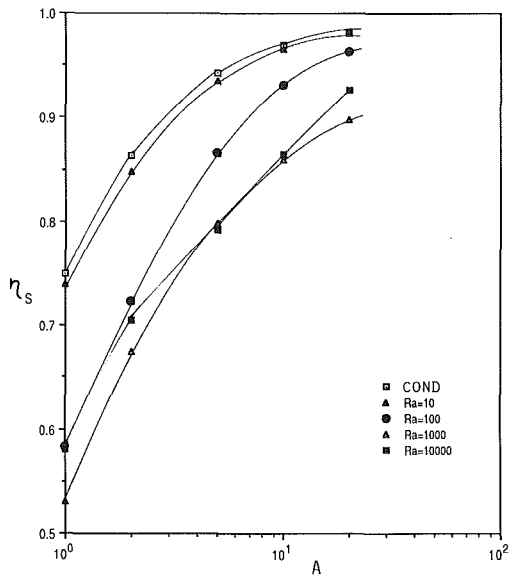

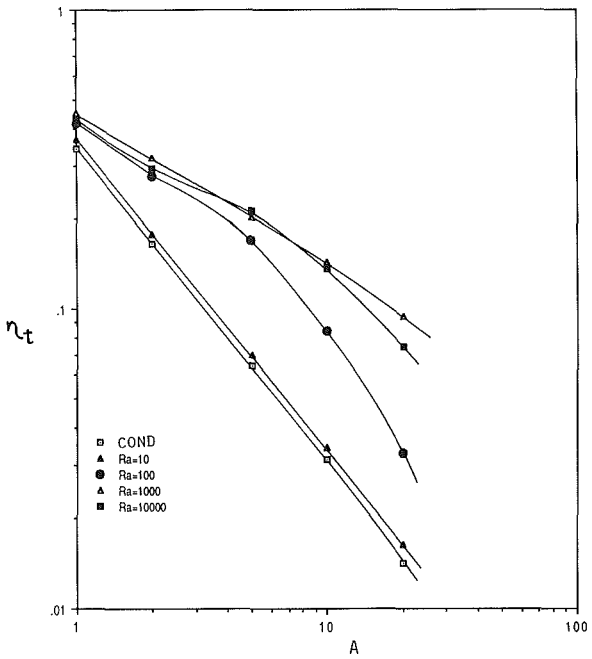

Fig. 12 Fraction of energy rejected on various walls when the top and side walls are cooled (case II)

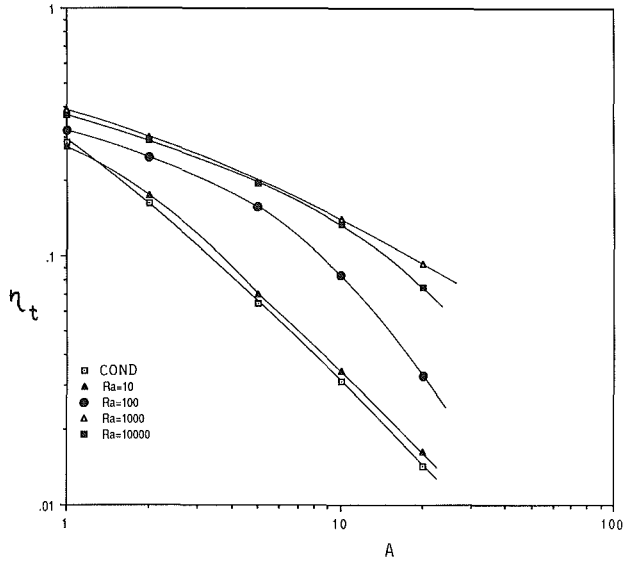

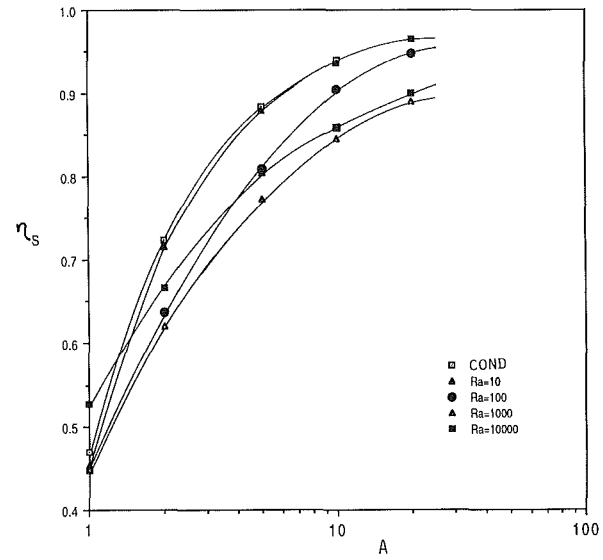

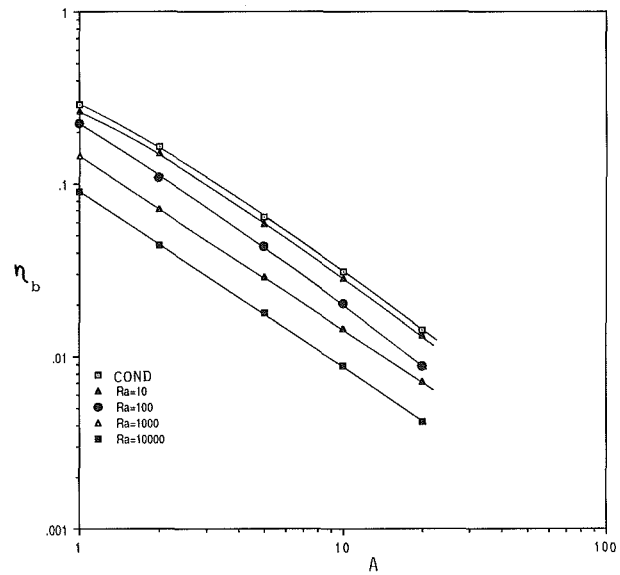

Fig. 13 Fraction of energy rejected on various walls when they are all cooled (case III)

boundary condition has little influence on the flow field and the heat transfer rate.

Conclusion

Natural convection in a cylindrical cavity filled with a volumetrically heated porous medium has been numerically investigated for the case when the vertical walls are cooled at a constant temperature and the horizontal walls are either adiabatic or isothermally cooled. The results obtained for a wide range of Rayleigh number and aspect ratio indicate that the flow in the half-cavity is unicellular, and the temperature field in the upper layers is stably stratified, provided the top and bottom walls are insulated. When the top surface is cooled to provide an additional access to heat removal, the flow for certain combinations of Ra and A becomes multicellular. A highly unstable thermal stratification is then produced in the top wall region with the possibility of inverted thermal plume. On the contrary, the variation in the bottom surface boundary

condition has little influence on the flow field and the thermal stratification in the upper region. However, it produces a stably stratified temperature field in the lower portion of the cylinder.

The dimensional temperature at any location in the cylindrical cavity increases with the Rayleigh number. The maximum temperature for the case when the horizontal walls are adiabatic occurs at the center of the top surface. In the boundary layer regime, the slope of the ln (θ_{max})-versus-ln (Ra) curve is almost a constant and is close to $-1/3$; θ_{max} at high Rayleigh numbers shows similar linear variation with the aspect ratio. Several correlations (equations (10)–(12)) are thus presented for the maximum cavity temperature.

The maximum temperature θ_{max}, however, decreases significantly with the change in the horizontal wall boundary condition from adiabatic to isothermally cooled. The lower the aspect ratio and/or the Rayleigh number, the larger the variation in θ_{max}, and the farther away its location from the upper surface. It is also possible that θ_{max} may occur at a location away from the centerline.

The local heat flux on the cold wall(s) is a strong function of the boundary condition at the horizontal walls besides Ra and A. A highly interesting $\bar{q}$ profile, with more than one peak, is obtained for the top surface at high Rayleigh numbers. In general, the fraction of energy removed on the top surface decreases with the aspect ratio while that on the side wall increases with A. However, the effect of Rayleigh number on heat removal at various walls is not straightforward. There exists a critical Rayleigh number as a function of aspect ratio for which the heat rejection on the top surface is maximum and that on the side wall is minimum. The effect of bottom wall boundary condition is generally minimal in the convection regime.

Reference

Blythe, P. A., Daniels, P. G., and Simpkins, P. G., 1985, "Convection in a Fluid-Saturated Porous Medium Due to Internal Heat Generation," *International Communications in Heat and Mass Transfer*, Vol. 12, pp. 493–504.

Gartling, D. K., 1982, "A Finite Element Analysis of Volumetrically Heated Fluids in an Axisymmetric Enclosure," *Finite Elements in Fluids*, R. H. Gallagher et al., eds., Vol. 4, pp. 233–249.

Gosman, A. D., Pun, W. M., Runchal, A. K., Spalding, D. B., and Wolfshtein, M., 1969, *Heat and Mass Transfer in Recirculating Flows*, Academic Press, New York.

Haajizadeh, M., Ozguc, A. F., and Tien, C. L., 1984, "Natural Convection in a Vertical Porous Enclosure With Internal Heat Generation," *International Journal of Heat and Mass Transfer*, Vol. 27, pp. 1893–1902.

Lambha, N. K., Korpela, S. A., and Kulacki, F. A., 1979, "Thermal Convection in a Cylindrical Cavity With Uniform Volumetric Energy Generation," *Heat Transfer 1978,* Proceedings, 6th International Heat Transfer Conference, Toronto, Hemisphere, Washington, DC, Vol. 2, pp. 311–316.

Kladias, N., and Prasad, V., 1988, "Non-Darcy, Oscillating Convection in Horizontal Porous Layers Heated From Below," *Proceedings, 1st National Fluid Dynamics Congress*, Cincinnati, Part 3, pp. 1757–1764; AIAA, Washington, DC

Prasad, V., 1983, "Natural Convection in Porous Media – An Experimental and Numerical Study for Vertical Annular and Rectangular Enclosures," Ph.D. Dissertation, University of Delaware.

Prasad, V., 1985, "Thermal Convection of a Heat Generation Porous Medium in a Rectangular Cavity," *Heat Transfer in Porous Media and Particulate Flows*, ASME HTD-Vol. 46, pp. 209–216.

Prasad, V., 1987, "Thermal Convection in a Rectangular Cavity Filled With a Heat Generating, Darcy Porous Medium," ASME JOURNAL OF HEAT TRANSFER, Vol. 109, pp. 697–703.

Stewart, W. E., Jr., and Dona, C. L. G., 1986, "Low Rayleigh Number Flow in a Heat Generating Porous Media," *International Communications in Heat and Mass Transfer*, Vol. 13, pp. 281–294.

Stewart, W. E., Jr., and Dona, C. L. G., 1988, "Free Convection in a Heat Generating Porous Medium in a Finite Vertical Cylinder," ASME JOURNAL OF HEAT TRANSFER, Vol. 110, pp. 517–520.

Vasseur, P., Hung Nguyen, T., Robillard, L., and Tong Thi, V. K., 1984, "Natural Convection Between Horizontal Concentric Cylinders Filled With a Porous Layer With Internal Heat Generation," *International Journal of Heat and Mass Transfer*, Vol. 27, pp. 337–349.

Natural Convection in Horizontal Porous Layers: Effects of Darcy and Prandtl Numbers

N. Kladias[1]

V. Prasad
Mem. ASME

Department of Mechanical Engineering,
Columbia University,
New York, NY 10027

Natural convection in horizontal porous layers heated from below is studied by employing a formulation based on the Brinkman-Forchheimer-extended Darcy equation of motion. The numerical solutions show that the convective flow is initiated at lower fluid Rayleigh number Ra_f than that predicted by the linear stability analysis for the Darcy flow model. The effect is considerable, particularly at a Darcy number Da greater than 10^{-4}. On the other hand, an increase in the thermal conductivity of solid particles has a stabilizing effect. Also, the Rayleigh number Ra_f required for the onset of convection increases as the fluid Prandtl number is decreased. In the stable convection regime, the heat transfer rate increases with the Rayleigh number, the Prandtl number, the Darcy number, and the ratio of the solid and fluid thermal conductivities. However, there exists an asymptotic convection regime where the porous media solutions are independent of the permeability of the porous matrix or Darcy number. In this regime, the temperature and flow fields are very similar to those obtained for a fluid layer heated from below. Indeed, the Nusselt numbers for a porous medium with $k_f = k_s$ match with the fluid results. The effect of Prandtl number is observed to be significant for $Pr_f < 10$, and is strengthened with an increase in Ra_f, Da, and k_s/k_f. An interesting effect, that a porous medium can transport more energy than the saturating fluid alone, is also revealed.

1 Introduction

Natural convection in a horizontal porous layer is one of the fundamental problems concerning heat transfer in porous media and has been studied extensively (Combarnous and Bories, 1975; Cheng, 1978). The early works on the convective instability of a porous layer heated from below, so-called Benard convection in a porous medium, are from Horton and Rogers (1945) and Lapwood (1948), who predicted a critical Rayleigh number, $Ra_c^* = 4\pi^2$, for the onset of convection. Most of the theoretical works that followed these initial studies are based on the Darcy model for flow through porous media.

Experimental studies dealing with the horizontal porous layer problem are rather limited. However, the experimental data for various media showed a large-scale variation in the heat transfer results as a function of the solid-fluid combination and the grain size (Cheng, 1978). It is widely realized that a proper understanding of inertia, viscous diffusion, and wall-channeling effects, and hydrodynamic and thermal dispersion is of paramount importance to an accurate modeling of energy transport in porous media.

Forchheimer (1901) was the first to suggest a second-order nonlinear relationship between the filtration velocity and the pressure gradient to account for the inertia effects

$$dp/dx = aq + bq^2 \qquad (a,\ b = \text{const}) \tag{1}$$

As a result of various theoretical and experimental investigations, a large number of nonlinear equations of motion appeared thereafter in the literature. Most of these models are heuristic in nature and attempt to fit the experimental data without any physical basis. The majority are of the form of equation (1) with the only exception being that the coefficients a, b may be functions of ϵ, ν, d, etc. (Bear, 1972). Generally, these coefficients may be treated as constants if the porous medium can be considered as isotropic and homogeneous. Later, Choudhary et al. (1976) introduced the generalized form of Forchheimer's equation of motion.

The effects of an impermeable boundary on flow in a porous medium originate from the momentum diffusion caused by the wall frictional resistance, which is in addition to the bulk frictional drag induced by the solid matrix as characterized by Darcy law. Brinkman (1947) presented the following equation to account for the the boundary drag:

$$\frac{\partial p}{\partial x} + \mu' \frac{\partial^2 q}{\partial x^2} - \frac{\mu}{K} q = 0 \tag{2}$$

This also allows us to satisfy the "no-slip" conditions on the walls. Tam (1969) put Brinkman's approach in a better theoretical perspective.

In recent years, several attempts have been made to examine the non-Darcy effects on free convection in porous media. However, most of these studies consider geometric configurations other than a horizontal porous layer, and will not be reviewed here for brevity.

Rudraiah and co-workers (1980, 1984) were probably the first to consider the Darcy-Brinkman model to study Benard convection in a porous layer. For the Darcy number $Da \to \infty$, they recovered the Malkus and Veronis (1958) fluid results while for $Da \to 0$ (lower than 10^{-5}), the Darcy solution was obtained. They observed that the critical modified Rayleigh number for the onset of convection increases as Da increases. It was also reported that for small values of Da ($\leq 10^{-4}$) the convective heat transport is almost independent of the Prandtl number. Nield (1983), however, argued that the Brinkman equation is not justified to account for the no-slip boundary condition because of the limitations on this model. He observed that Rudraiah's analysis predicts a proper value of $Ra_{f,c}$ for the fluid, but fails to provide a correct value for the Darcy porous medium.

Somerton (1983) argued in favor of a strong Prandtl number effect based on the facts that the problem is analogous

[1] Present address: Webster Research Center, Xerox Corporation, North Tarrytown, NY 10951.

Contributed by the Heat Transfer Division and presented at the National Heat Transfer Conference, Houston, Texas, August 1988. Manuscript received by the Heat Transfer Division April 20, 1988. Keywords: Enclosure Flows, Natural Convection, Porous Media.

to the Benard convection in fluid layers and the contribution of the inertia term is governed by Pr*. In a recent work, Georgiadis and Catton (1986) used a mixed finite difference–Galerkin scheme to solve a non-Darcian model, which accounts for inertial and boundary effects in an infinite horizontal porous layer. They have attributed the divergence in heat transfer results primarily to inertia effects, characterized by Fs/Pr*. Their Nusselt number predictions agree with the measured values of Combarnous and Bories (1975) only qualitatively, to show that the Nusselt number decreases with increasing Fs/Pr*. Better agreement has been obtained with the experimental data of Jonsson and Catton (1987) who also presented correlations of the form $\overline{\mathrm{Nu}} = \mathrm{Ra}^{*m}\,(\mathrm{Fs/Pr}^*)^{-n}$ for two ranges of Fs/Pr*. These experimental results showed a significant influence of Prandtl number for Fs/Pr* > 10.

In a recent study, the present authors have examined the viscous diffusion and inertia effects in a horizontal porous layer (Kladias and Prasad, 1987). Computations were carried out in two phases. In the first part, the numerical results were obtained for the Brinkman-extended Darcy equation of motion, the governing parameters being modified Rayleigh and Darcy numbers. In the second part, solutions were presented for the Forchheimer-extended Darcy equation, the governing parameters in this case being the modified Rayleigh number and the ratio of Forchheimer and Prandtl numbers, Fs/Pr*. The numerical results indicate that the temperature and flow fields, and consequently, the heat transfer rates are significantly affected by the variation in Darcy, Forchheimer, and Prandtl numbers. The convective effects are reduced and the flow approaches the conduction regime with an increase in Da or Fs/Pr* for a fixed Ra*. The higher the values of Ra*, Da, or Fs/Pr*, the stronger are the effects. Also, the critical modified Rayleigh number for the onset of convection increases with the Darcy number.

The purpose of the present work is to consider the complete equation of motion, and examine the significance of both the Forchheimer and the Brinkman modifications on the predictions of buoyancy-induced flow and heat transfer in horizontal porous layers heated from below. This work will show that it is more appropriate to consider the fluid flow parameters and the porous matrix structure parameters separately. Also, the numerical solutions demonstrate the existence of a Darcy number-independent asymptotic convection regime where the porous media solutions for $k_f = k_s$ match the fluid results. It will also be shown that the Prandtl number and conductivity ratio effects may be significant under certain circumstances. Indeed, the critical Rayleigh number for the onset of convection is a strong function of Da, Pr_f, and λ.

Mathematical Formulation

Governing Equations. Consider a two-dimensional horizontal porous layer heated from below at a constant temperature and isothermally cooled at the top surface; the side walls are adiabatic. The rectangular cavity thus defined is supposed to reproduce a particular thermoconvective roll in a porous layer of infinite extent. In the porous medium of nondeformable solid matrix, the saturating fluid is considered to be a normal Boussinesq fluid, the thermophysical properties of solid and fluid are assumed to be constant, and the viscous dissipation is negligible. Furthermore, the solid particles and the fluid are assumed to be in local thermodynamic equilibrium.

The conservation equations for mass, momentum, and

Nomenclature

A = aspect ratio $= D/H$
b = porous matrix structure property associated with the Forchheimer velocity-square term, m
c = isobaric specific heat, J/kg-K
d = characteristic particle dimension, m
D = width of porous layer, m
Da = Darcy number $= K/H^2$
Fs = Forchheimer number $= b/H$
$\vec{g}$ = body force vector, m/s^2
g = acceleration due to gravity, m/s^2
H = height of porous layer, m
k = thermal conductivity, W/m-K
k_m = effective thermal conductivity of fluid-saturated porous medium, W/m-K
K = permeability of porous medium, m^2
m = number of cells in a cavity of aspect ratio A, equation (21)
Nu = local Nusselt number, equation (24)
$\overline{\mathrm{Nu}}$ = overall Nusselt number, equation (23)
n = mode of convection, equation (21)
p = pressure, Pa
Pr* = modified Prandtl number $= \nu/\alpha_m$
Pr_f = fluid Prandtl number $= \nu/\alpha_f$
q = one-dimensional filtration velocity, m/s
Ra_f = fluid Rayleigh number $= g\beta H^3 \Delta T/\nu\alpha_f$
Ra = Rayleigh number $= g\beta H^3 \Delta T/\nu\alpha_m$
Ra* = modified Rayleigh number $= g\beta K H \Delta T/\nu\alpha_m$
S = specific heat ratio $= (\rho c)_m/(\rho c)_f$
t' = time, s
t = dimensionless time $= t/(H^2/\alpha_m)$
T = temperature, K
ΔT = temperature difference between bottom and top surfaces $= T_h - T_c$, K
u = dimensionless velocity in x direction
v = dimensionless velocity in y direction
$\mathbf{V}$ = filtration velocity vector, m/s
$\underline{V}$ = dimensionless velocity vector $= \mathbf{V}/(\alpha_m/H)$
x, y = Cartesian coordinates, m
X = dimensionless distance in x direction $= x/H$
Y = dimensionless distance in y direction $= y/H$
α = thermal diffusivity $= k/\rho c$, m^2/s
α_m = thermal diffusivity of porous medium $= k_m/(\rho c)_f$, m^2/s
α_w = wave number, m/A
β = isobaric coefficient of thermal expansion of fluid, 1/K
ϵ = porosity
ζ = dimensionless vorticity
θ = dimensionless temperature $= (T - T_c)/\Delta T$
Λ = viscosity ratio $= \mu'/\mu$
λ = conductivity ratio $= k_f/k_m$
μ = dynamic viscosity of fluid, kg/m-s
μ' = apparent viscosity for Brinkman's viscous drag term, kg/m-s
ν = kinematic viscosity of fluid, m^2/s
ρ = density, kg/m^3
σ = amplification factor in equation (21)
ψ = dimensionless stream function

Subscripts

c = cooled surface
f = fluid
h = heated surface
m = fluid-saturated porous medium
s = solid
w = wall

energy based on the Brinkman-Forchheimer-extended Darcy flow model are:

Continuity:

$$\nabla \cdot \mathbf{V} = 0 \tag{3}$$

Momentum:

$$\frac{\rho_f}{\epsilon}\frac{\partial \mathbf{V}}{\partial t'} + \frac{\rho_f}{\epsilon^2}(\mathbf{V}\cdot\nabla)\mathbf{V} = -\nabla p + \rho_f \mathbf{g} - \frac{\mu}{K}\mathbf{V}$$

$$-\rho_f \frac{b}{K}|\mathbf{V}|\mathbf{V} + \mu'\nabla^2\mathbf{V} \tag{4}$$

Energy:

$$(\rho c)_m \frac{\partial T}{\partial t'} + (\rho c)_f \mathbf{V}\cdot\nabla T = k_m \nabla^2 T \tag{5}$$

Dimensional Analysis. To reduce the above set of equations to their dimensionless form, the following scales are employed: length: H, temperature: ΔT, velocity: α_m/H, and time: H^2/α_m. These dimensionless equations may then be transformed into the stream function-vorticity-temperature equations in the usual way:

$$\nabla^2\psi = \zeta \tag{6}$$

$$\frac{Da}{\lambda \mathrm{Pr}_f}\left\{\frac{1}{\epsilon}\frac{\partial \zeta}{\partial t} + \frac{1}{\epsilon^2}\left(u\frac{\partial \zeta}{\partial X} + v\frac{\partial \zeta}{\partial Y}\right)\right\}$$

$$= \lambda\,\mathrm{Ra}_f\,\mathrm{Da}\frac{\partial \theta}{\partial X} - \zeta - \frac{\mathrm{Fs}}{\lambda \mathrm{Pr}_f}|\mathbf{V}|\zeta - \frac{\mathrm{Fs}}{\lambda \mathrm{Pr}_f}\left\{v\frac{\partial |\mathbf{V}|}{\partial X} - u\frac{\partial |\mathbf{V}|}{\partial Y}\right\} + \Lambda\,\mathrm{Da}\left\{\frac{\partial^2 \zeta}{\partial X^2} + \frac{\partial^2 \zeta}{\partial Y^2}\right\} \tag{7}$$

$$S\frac{\partial \theta}{\partial t} + u\frac{\partial \theta}{\partial X} + v\frac{\partial \theta}{\partial Y} = \frac{\partial^2 \theta}{\partial X^2} + \frac{\partial^2 \theta}{\partial Y^2} \tag{8}$$

The relevant hydrodynamic and thermal boundary conditions are

$$u = v = \psi = 0 \text{ on all boundaries,} \tag{9}$$

$$\theta = 1,\ Y = 0;\ \theta = 0,\ Y = 1;\ \text{and } \partial\theta/\partial X = 0,\ X = 0 \text{ and } A. \tag{10}$$

The vorticity boundary conditions are derived from zero tangential velocity conditions, and will be discussed later.

Evidently, the steady-state free convection in saturated porous media is governed by

$$\text{Fluid Rayleigh number } \mathrm{Ra}_f = g\beta H^3 \Delta T/\nu\alpha_f \tag{11}$$

$$\text{Fluid Prandtl number } \mathrm{Pr}_f = \nu/\alpha_f \tag{12}$$

$$\text{Darcy number Da} = K/H^2 \tag{13}$$

$$\text{Forchheimer number Fs} = b/H \tag{14}$$

$$\text{Conductivity ratio } \lambda = k_f/k_m \tag{15}$$

$$\text{Viscosity ratio } \Lambda = \mu'/\mu \tag{16}$$

and porosity ϵ. Three of these parameters, porosity ϵ, Darcy number Da, and Forchheimer number Fs, are the porous matrix scaling parameters, while the Rayleigh and Prandtl numbers, Ra_f and Pr_f, depend on only the fluid properties. The conductivity ratio λ and viscosity ratio Λ, on the other hand, depend on both the solid and fluid properties. A justification of the present dimensional analysis and the significance of these parameters has been reported recently by the present authors (Prasad et al., 1988; Kladias and Prasad, 1988).

For the Ergun model employed in the present study, the Darcy and Forchheimer numbers can be obtained as

$$\mathrm{Da} = \frac{\epsilon^3}{150(1-\epsilon)^2}\left(\frac{d}{H}\right)^2 \tag{17}$$

$$\mathrm{Fs} = \frac{1.75}{150(1-\epsilon)}\left(\frac{d}{H}\right) \tag{18}$$

which yield

$$\mathrm{Fs} = C(\epsilon)\mathrm{Da}^{0.5} \tag{19}$$

It is uncertain what one should use for the apparent viscosity, μ' in equation (4); the fluid viscosity μ, or a viscosity that accounts for the concentration of the particles as Einstein's correction does for dilute suspensions. Lundgren (1972) attempted to resolve this issue by extending a statistical formulation and adapting it to the problem of a fixed bed of spheres. He concluded that the viscosity ratio μ'/μ rises slightly above 1 as the porosity ϵ decreases from unity, attains a maximum at $\epsilon = 0.8$, and decreases rapidly when $\epsilon < 0.7$, its value being close to zero for $\epsilon = 0.6$. A large variation thus exists between the Einstein and Lundgren predictions for μ'/μ and that obtained from $\mu'/\mu = 1/\epsilon$ when $\epsilon < 0.7$. It is not clear which of these correlations is more accurate for low values of ϵ.

Numerical Method

In the present numerical scheme, all spatial derivatives in equations (6)-(8) are approximated by the central differences, whereas a forward difference discretization is used for the time derivative. An alternating direction implicit (ADI) procedure is used to perform the time integration for the vorticity and temperature equations (7) and (8). The stream function equation (6), on the other hand, is solved by the Gauss-Seidel SOR iterative scheme at each time step. The scheme is formally first-order accurate, and is unconditionally stable for the linear case. However, the steady-state solutions are second-order accurate.

It is well established that the convection terms cause difficulties in achieving a stable solution. For the present problem, this is particularly true at high velocities since the contribution of convective terms in equations (7) and (8) is then increased. This difficulty has been overcome to some extent by employing very small time steps of the order of 10^{-3}-10^{-5}, which made it possible to obtain discretizations for high values of Ra_f, Da, Fs, and low Prandtl numbers.

It should be further noted that there are various ways in which the Forchheimer term in equation (4) can be treated to obtain a discretized vorticity equation. One approach, as employed in the present scheme, is to split this term in two parts as shown in equation (7), and use the first part together with the implicit terms and the rest as a linearized source. Alternatively, the entire Forchheimer term in equation (4) can be considered as a source. A detailed discussion on the treatment of this term in a numerical scheme and its effect on the final solution has been presented by Prasad and Tuntomo (1987).

Another important aspect of the present scheme is the boundary conditions for vorticity since the wall vorticity is an extremely important evaluation. At no-slip boundaries, ζ is obtained from the no-slip conditions. Jensen's as well as Wood's higher-order representations have been found to generate unstable solutions at low Darcy numbers (Lauriat and Prasad, 1986) due to the nature of porous media velocity profiles, which display peaks very close to the wall at low values of Da. Hence, the Thom first-order form has been used for the present computations, which yields:

$$\zeta_w = \frac{2\psi_{w+1}}{(\Delta n)^2} \tag{20}$$

where Δn is the grid size normal to the wall.

As is typical of the present problem, an initial perturbation in the temperature field is required to drive the solution in the convective state. An initial temperature distribution of the sinusoidal form

$$\theta = 1 - Y + \sigma \cos(\pi m X) \sin(\pi n Y) \tag{21}$$

is introduced that produces a unicellular convective flow in a square cavity in the stable convection regime. In the present study, both the number of cells m in a cavity of aspect ratio A and the mode of convection n have been taken as unity following Caltagirone (1975) and Schubert and Straus (1979). The criterion used for the iterative convergence of the stream function at each time step or the steady-state solution for the vorticity and temperature is

$$\max_{i,j} \left\{ \left| \frac{\phi_{i,j}^{\text{new}} - \phi_{i,j}^{\text{old}}}{\phi_{i,j}^{\text{new}}} \right| \right\} < r \tag{22}$$

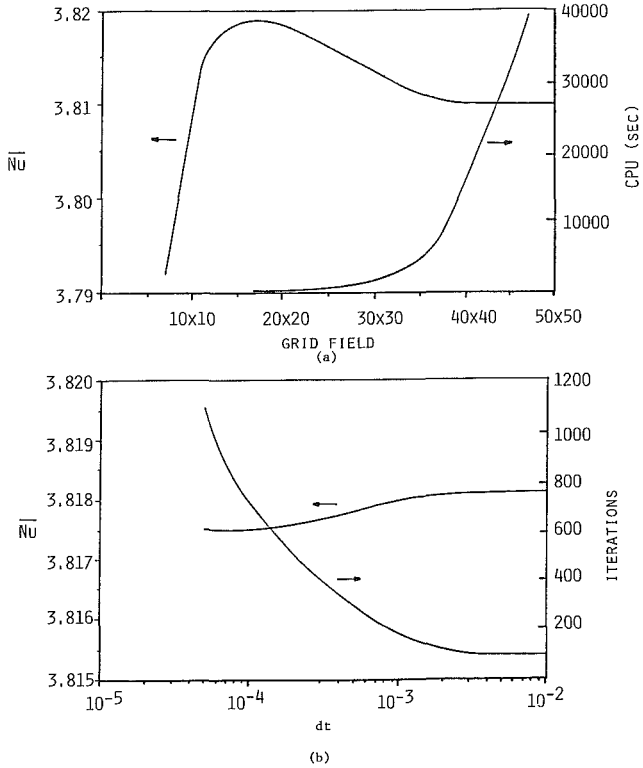

Fig. 1 Effect of (a) grid size, and (b) time step on the Nusselt number, the number of iterations, and the CPU time ($Ra^* = 200$, $Da = 10^{-6}$)

where ϕ may be ζ, ψ, or θ. The solution is assumed to have reached steady state when r at all nodes in the computational domain between two time steps is less than 10^{-4} for both ζ and θ. The value of r used for χ is 10^{-3}.

To select the proper mesh size for the present computations, results were obtained for various values of Ra* and Da. The dependence of the average Nusselt number on the grid size is presented in Fig. 1(*a*) for one of the trial cases, Ra* = 200, Da = 10^{-6} ($\Delta t = 0.01$) together with the CPU time on DEC 20 machines. A 31×31 uniform grid field yields a Nusselt number as 3.818 and $\psi_{\max}$ as 8.913, which vary by only 0.13 and 0.32 percent, respectively, from the values obtained by Caltagirone (1975) with a 48×48 grid field. A complete comparison between the present values and those reported by Caltagirone (1975) and Schubert and Straus (1979) for the Darcy flow model is presented in Table 1 where the largest variation is seen to be 0.55 percent.

A comparison between the present solutions and those reported by Georgiadis and Catton (1986) for the Darcy-Brinkman-Forchheimer model is presented in Table 2, where the largest variation is seen to be 3.7 percent. The comparison is made for three solid-fluid combinations for which the above authors compared their numerical results with the experimental data of Jonsson and Catton (1987). For modified Rayleigh numbers less than 200 we have used the "left" wavenumbers (denoted by a superscript L in Table 2), which have been shown by Georgiadis and Catton (1986) to provide the best agreement with the experimental data. The only exception is glass-oil, where their closure criterion produced only "right" wavenumbers, which have been used in our comparison. It should be noted that the "left" and "right" wavenumbers are the values of α_w lying to the left and right, respectively, of the peak of the Nusselt-versus-wave numbers plot for given Ra*, and have been selected based on the maximum entropy production criterion (see Georgiadis and Catton, 1986, for further details).

The effect of the time increment on the Nusselt number as well as the number of time steps to achieve steady state are reported in Fig. 1(*b*) (31×31 grid field). In general, a 31×31 grid field provides the best compromise between the accuracy, convergence, and economy for the case of a square cavity. To have an additional check on the accuracy of the results, an overall energy balance is used for the system. For this, the

Table 1 Overall Nusselt numbers for a square cell (Darcy flow model) compared with published results

Ra*	50	100	200	250	300
Present	1.443	2.659	3.818	4.197	4.535
Caltagirone (1975)	1.450	2.651	3.813	4.199	4.523
Schubert and Straus (1979)		2.651	3.808		4.510

Table 2 Overall Nusselt numbers for Darcy-Brinkman-Forchheimer model compared with the results of Georgiadis and Catton (1986)

Solid-fluid	Pr*	$Da \times 10^5$	$Fs \times 10^3$	Wavenumber $\pi m/A$	Ra*	Georgiadis and Catton (1986)	Nusselt number present
Glass-water	4.5	0.9247	1.851	3^L	100	2.571	2.624
		0.5201	1.041	2.90^L	150	3.357	3.315
		0.5201	1.205	6.75^R	225	4.351	4.275
		0.5201	1.205	7.20^R	275	4.928	4.830
Glass-oil	236	1.130	1.760	5^R	150	3.450	3.379
		1.130	1.760	6.55^R	250	4.700	4.526
Steel-water	0.58	1.194	1.634	3^L	100	2.450	2.466
		1.194	1.634	2.90^L	150	3.071	3.008
		0.568	1.133	2.71^L	200	3.642	3.620
		0.568	1.133	7.20^R	275	4.800	4.700

L = left; R = right wavenumbers taken from Georgiadis and Catton (1986).

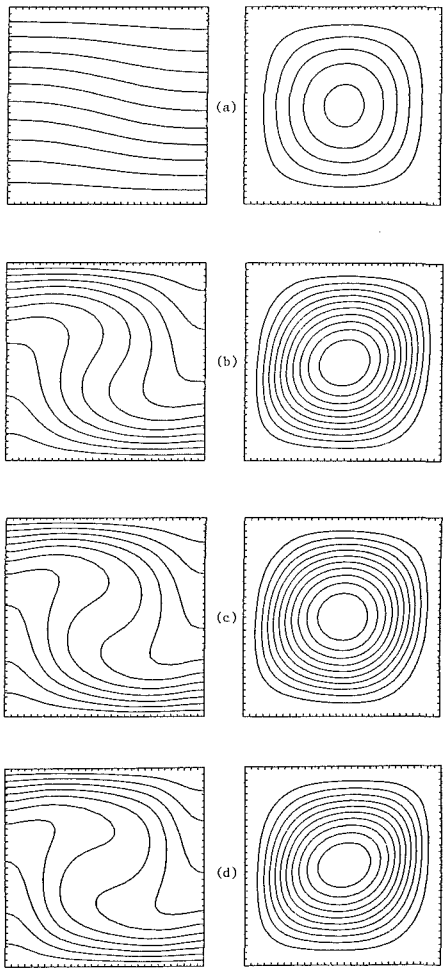

Fig. 2 Isotherms ($\Delta\theta = 0.091$) and streamlines for $Ra_f = 5 \times 10^4$, $Pr_f = 1$: (*a*) $Da = 10^{-3}$ ($\Delta\psi = 0.064$), (*b*) $Da = 10^{-2}$ ($\Delta\psi = 0.566$), (*c*) $Da = 10^{-1}$ ($\Delta\psi = 0.820$), and (*d*) fluid ($\Delta\psi = 0.990$)

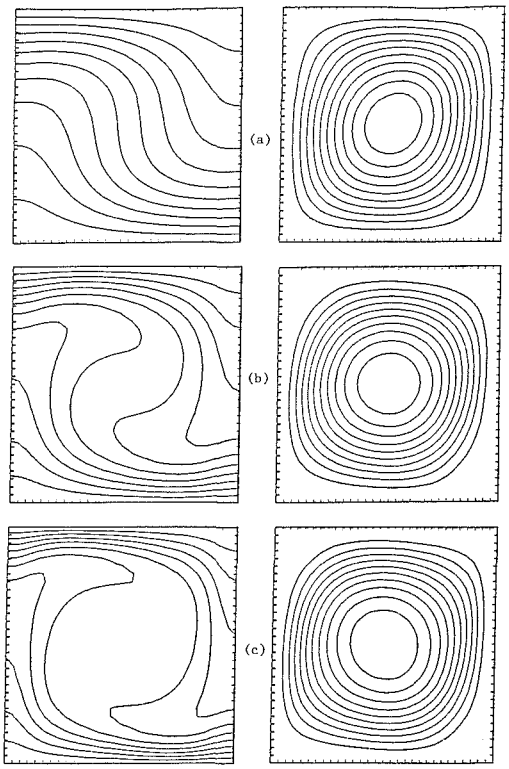

Fig. 3 Isotherms ($\Delta\theta = 0.091$) and streamlines for $Ra_f = 10^5$, $Pr_f = 1$; (*a*) $Da = 10^{-3}$ ($\Delta\psi = 0.328$), (*b*) $Da = 10^{-1}$ ($\Delta\psi = 1.158$), and (*c*) fluid ($\Delta\psi = 2.370$)

fractional difference of energy input at $Y = 0$ and heat rejected at $Y = 1$ is obtained, which has always been less than 0.01 percent.

The average Nusselt number at any Y location is obtained as:

$$\overline{\mathrm{Nu}} = (1/A)\int_0^A \mathrm{Nu}(X, Y)dX \tag{23}$$

where the local Nusselt number

$$\mathrm{Nu} = v\theta - \partial\theta/\partial Y. \tag{24}$$

Further details on the present numerical scheme are presented by Kladias (1988).

Results and Discussion

The computations have been carried out for the Brinkman-Forchheimer-extended Darcy formulation by employing the Ergun model, which assumes the Darcy and Forchheimer numbers as defined by equations (17) and (18), respectively. A typical value of the porosity of a randomly packed sphere bed, $\epsilon = 0.4$, is used for the numerical solutions reported here. This fixes the constant C in equation (19) as 0.55, the viscosity ratio $\Lambda = 2.5$. Also, all the calculations are performed for a square cell, $A = 1$. Therefore, the varying parameters in the present study are fluid Rayleigh and Prandtl numbers, the Darcy number for the porous matrix, and the conductivity ratio, i.e., $Ra_f\, Pr_f$, Da, and λ. The heat transfer results are presented here in graphic form, as a continuous function of Ra_f. For the tabulated values of Ra_f and other parameters at which the calculations were carried out, the reader is referred to Kladias (1989).

Effect of Darcy Number. To understand properly the effect of the porous matrix scaling parameter Da, the computations have been carried out for various values of Ra_f and Da, for $Pr_f = 1$ and $\lambda = 1$. The isotherms and streamlines for $Da = 10^{-3}$–10^{-1} and corresponding values of Fs according to equation (19) are presented in Figs. 2 and 3 for $Ra_f = 5 \times 10^4$ and 10^5, respectively, together with the fluid solutions. The effect of an increase in Darcy number appears to be very similar at all fluid Rayleigh numbers. The recirculating flow is increased and the thermal stratification in the upper and lower regions is strengthened with an increase in Darcy number. For $Ra_f = 5 \times 10^4$, ψ_{max} increases from 0.487 at $Da = 10^{-3}$ to 6.222 at $Da = 10^{-2}$. Also, the temperature gradients near the top left and bottom right corners become sharper. Evidently, for a given system the flow intensity and thermal activity increase with the Darcy number since the permeability of the porous matrix has increased, thereby reducing the resistance to flow.

Figures 4(*a*) and 4(*b*) further show the change in vertical velocity at mid-height, $Y = 0.5$ and the horizontal velocity at $X = 0.5$, respectively, for $Ra_f = 5 \times 10^4$. Since $Ra^* = 50$ ($Ra_f = 5 \times 10^4$ and $Da = 10^{-3}$) is slightly greater than $Ra_c^* = 4\pi^2$ for the onset of convection in the case of Darcy flow, the convective flow seems to have just been established. At higher Darcy numbers, the velocity peaks are observed to be quite away from the wall, a phenomenon that cannot be predicted by the Darcy or Darcy-Forchheimer flow models. Interestingly, the location of peak velocity moves away from the wall with an increase in Da, and the wall vorticity diffuses in the whole cavity. Although the velocity distribution changes significantly with the increase in Da from 10^{-2} to 10^{-1}, the variation in the temperature distribution is minimal. This is also evident from the isotherms in Figs. 2 and 3.

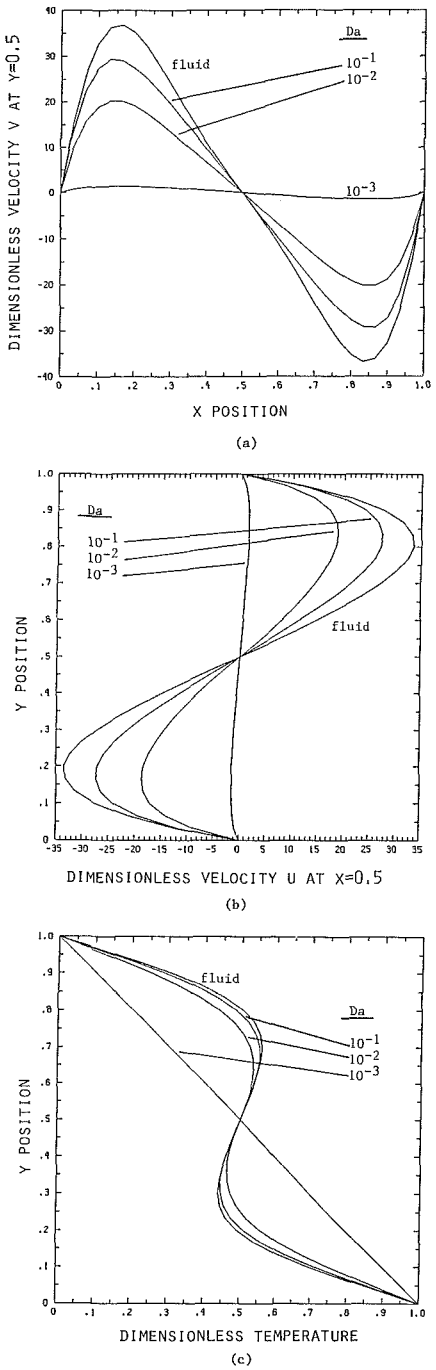

Fig. 4 Effect of Darcy number on velocity and temperature distributions: (a) vertical velocity at midheight, (b) horizontal velocity at midplane, and (c) temperature at midheight

An interesting aspect that is revealed from a closer observation of Figs. 2–4 is that as the Darcy number increases from 10^{-2} to 10^{-1}, an asymptotic convection regime is reached. The variations in the temperature and flow fields in this regime are minimal. Moreover, the streamline and isotherm patterns for $Da = 10^{-1}$ are very close to those for the fluid at the same Rayleigh numbers (compare Figs. 2*c* with 2*d*, and 3*b*, with 3*c*). The velocity and temperature distributions in Figs. 4(*a–c*) show similar asymptotic behavior and closeness to the fluid solutions.

The local heat transfer rates on the heated wall for $Ra_f = 5 \times 10^4$ and $Da = 10^{-3}$–10^{-1} as well as the fluid results are presented in Fig. 5. Nu is minimum at $X = 0$ and increases with X to a peak value. However, in a region close to the other side wall, the local heat transfer decreases with an increase in X.

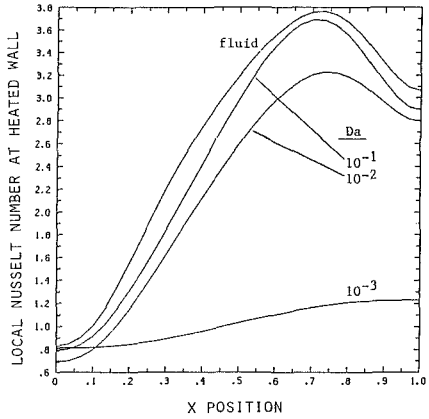

Fig. 5 Local Nusselt number on the bottom surface

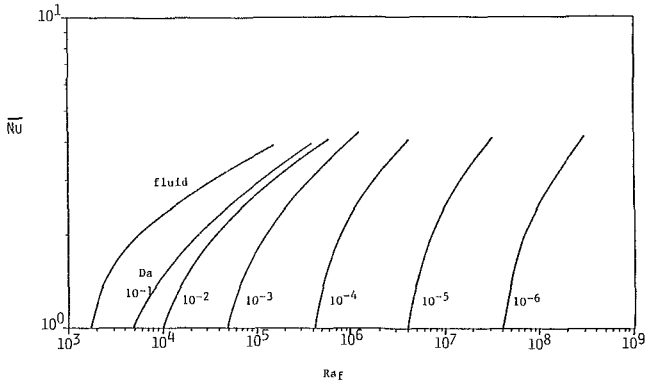

Fig. 6 Effect of Darcy number on heat transfer rate in the stable convection regime

Again, the values of Nu for $Da = 10^{-1}$ are very close to that for the fluid layer. Here, it should be noted that the Darcy number of the order of 10^{-3} corresponds to a porous layer of $d/H \simeq 1$ and 0.4 while $Da \sim 0(10^{-1})$ corresponds to layers of $d/H \simeq 1$ and $\epsilon \simeq 0.9$. Therefore, the solutions for $Da > 10^{-2}$ are more for an academic exercise. However, these results help in clearly showing the effect of Darcy number.

The overall Nusselt number is presented in Fig. 6 as a function of Ra_f and Da together with the fluid solutions. It should be noted that the fluid Nusselt numbers obtained by employing the present numerical scheme are within 4 percent of the values reported by McDonough and Catton (1983). Figure 6 clearly shows that $\overline{Nu}$ increases with both the fluid Rayleigh number and the Darcy number. For a densely packed medium (low permeability, $Da < 10^{-4}$) the Nusselt number curves are almost parallel. In this range, the contribution of the inertia and viscous diffusion terms are negligible, and the Darcy flow model can be acceptable. However, the range of validity for the Darcy model will decrease with an increase in the fluid Rayleigh number. It should be noted that the numerical solutions reported in Fig. 6 do not exceed $Ra_f/Ra_{f,c} = 9$ for $Da < 10^{-4}$. Since fluctuations are observed beyond a critical Rayleigh number, $Ra_f = 380/Da$, the effects of Ra_f and Da change sharply. Oscillatory, non-Darcy convection has been examined in detail in a separate paper by the present authors (Kladias and Prasad, 1988). Here, we will restrict our discussion to only the stable convection regime.

The Nusselt number curves for $Da > 10^{-4}$ are observed to have different slopes, and are nonparallel (Fig. 6). Clearly, the effect of Darcy number decreases with an increase in Da beyond 10^{-4}, i.e., in the asymptotic convection regime. The overall heat transfer rates at high Darcy and Rayleigh numbers are then very close to those obtained for the fluid; the variation between Nu for $Da = 10^{-1}$ and fluid is about 20 percent at

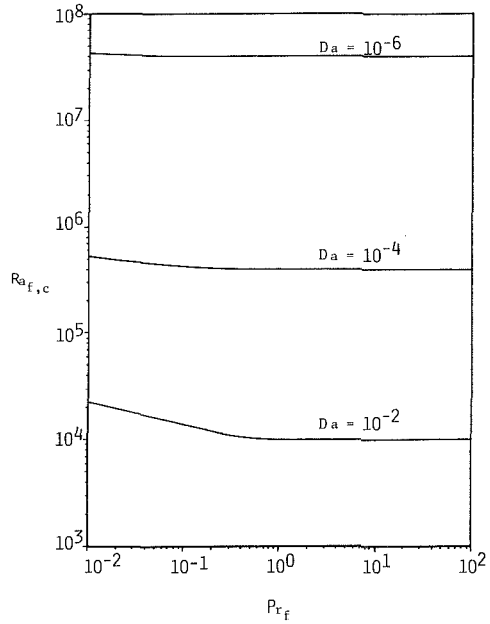

Fig. 7 Critical Rayleigh number for the onset of convection

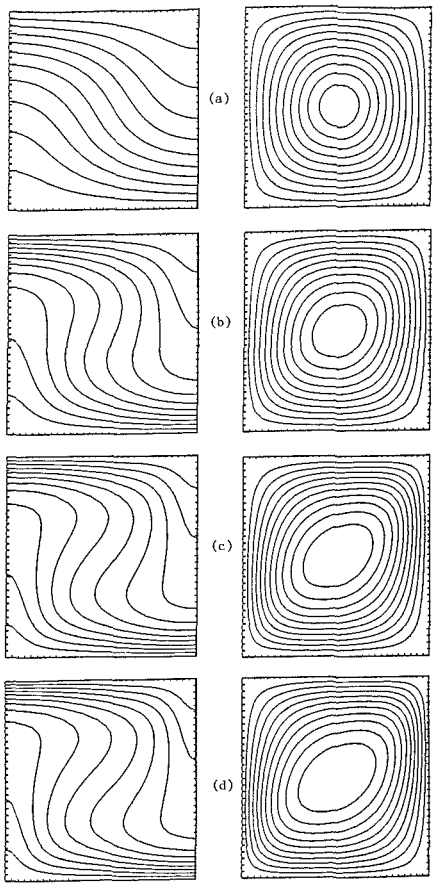

Fig. 8 Isotherms ($\Delta\theta = 0.091$) and streamlines for $Ra_f = 2 \times 10^6$, $Da = 10^{-6}$ for (*a*) $Pr_f = 0.01$ ($\Delta\psi = 0.215$), (*b*) $Pr_f = 0.1$ ($\Delta\psi = 0.533$), (*c*) $Pr_f = 1$ ($\Delta\psi = 0.722$), and (*d*) $Pr_f = 100$ ($\Delta\psi = 0.808$)

$Ra_f = 10^5$. Similar asymptotic trends can be observed in the experimental data of Buretta and Berman (1976) for a horizontal cavity, of Seki et al. (1978) for a vertical cavity, and of Prasad et al. (1985) for a vertical annulus.

The effect of Darcy number on the onset of convection is also demonstrated in Fig. 6. As expected, the Nusselt number approaches its conduction value of unity when $Ra_f = 4 \times 10^7$ for $Da = 10^{-6}$($Ra^* = 40$). However, the critical modified Rayleigh number Ra^* for the onset of convection increases with Da, as also predicted by the Darcy-Brinkman solutions (Prasad et al., 1988; Rudraiah, 1984; Rudraiah et al., 1980). Figure 7 presents $Ra_{f,c}$ as a function of Darcy and Prandtl numbers.

Effect of Prandtl Number. To examine the effects of fluid Prandtl number, the numerical solutions have been obtained for $Pr_f = 10^{-2}$, 10^{-1}, 1, 10, 10^2, and 10^3 with $Da = 10^{-6}$, 10^{-4}, and 10^{-2}. These values of Pr_f have been selected to represent the low (liquid metal), moderate, and high (heavy oils) Prandtl number regimes while the values of Darcy number characterize the densely packed, moderate, and highly permeable porous matrix. Also, $Da = 10^{-2}$ may belong, under certain conditions, to the asymptotic convection regime.

The isotherms and streamlines for $Pr_f = 0.01$, 0.1, 1, and 100 are presented in Figs. 8(*a–d*) for $Ra_f = 2 \times 10^6$ and $Da = 10^{-4}$. These plots indicate that the flow rate increases with the fluid Prandtl number, and an asymptotic regime is reached where, in analogy with the Benard convection in fluid layers, the temperature and flow fields are insensitive to a further increase in Pr_f. Indeed, in Fig. 8(*a*) a slow flow is observed for $Pr_f = 0.01$, and the axis of the cell is close to the vertical middle plane. But with an increase in Prandtl number, the recirculatory flow becomes stronger, and the axis of the cell moves toward the left diagonal of the cavity. The value of ψ_{max} is changed from 2.37 at $Pr_f = 0.01$ to 8.4 at $Pr_f > 10$. The isotherm patterns change accordingly. The temperature gradients near the top left and bottom right corners become sharper with an increase in Pr_f. The transport of energy due to crossflow is thus increased.

It is important to note that the prediction of the above modifications in temperature and flow fields with Pr_f has been possible because of the inclusion of inertia terms in the equation of motion (4). Since the influence of these terms diminishes with an increase in the Prandtl number, the solutions indicate an asymptotic behavior toward Darcy–Brinkman solutions. Although the plots presented in Fig. 8 are for fixed values of Ra_f and Da, it is easy to visualize that a similar trend will be demonstrated at all Rayleigh and Darcy numbers.

Significant changes in the velocity and temperature fields with Pr_f are further shown in Fig. 9 where the vertical velocity profile at midheight and the temperature distribution at midplane are presented for $Pr_f = 10^{-2}$–10^3. It is evident that the velocity increases substantially with an increase in fluid Prandtl number for $Pr_f < 10$. However, the effect may be reversed in the core if the Rayleigh and/or the Darcy number is high (Fig. 9*a*). The vertical velocity v is observed to increase sharply a small distance from the wall, but the peak shifts towards the core as Pr_f increases. On the other hand, the effect of Prandtl number on the flow and temperature distribution is negligible at $Pr_f > 10$. Here, it should be noted that a similar asymptotic trend has been observed by Somerton (1983), and Jonsson and Catton (1987) for a horizontal porous layer, and has also been reported for a fluid layer.

The overall Nusselt number is presented in Figs. 10(*a–c*) as a function of Ra_f and Da. $\overline{Nu}$ increases with the fluid Prandtl number at all values of Ra_f and Da under the conditions that the flow is in the convective state, $Ra_f > Ra_{f,c}$, and the Prandtl number is not high, to yield a Pr_f-independent solution ($Pr_f < 10$ for the present range of Ra_f and Da). Figure 10 further shows that the effect of Pr_f is more pronounced at higher Rayleigh and/or Darcy numbers. Also, the Darcy and Darcy–Brinkman solutions plotted in this figure indicate that the contribution of inertia term increases significantly with a reduction in Pr_f. Hence, if the inertia effects are not accounted for, there may be significant errors in predictions, particularly at low values of Pr_f. The above variation in

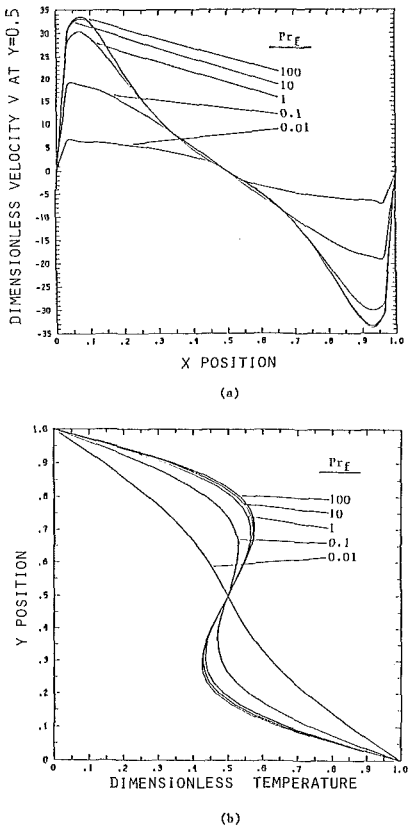

Fig. 9 Effect of Prandtl number on (*a*) vertical velocity and (*b*) temperature distribution at midheight for $Ra_f = 2 \times 10^6$, $Da = 10^{-4}$

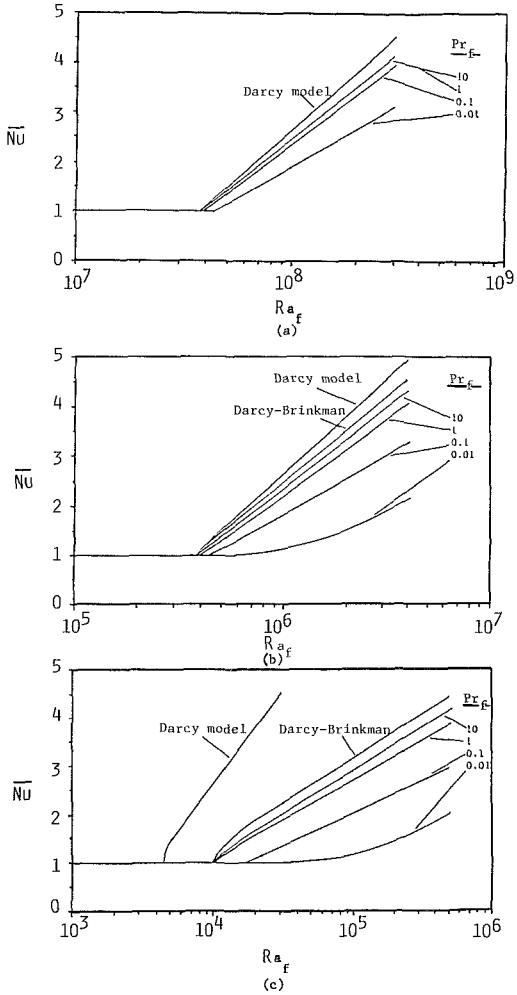

Fig. 10 Effect of Prandtl number on heat transfer rate: (*a*) $Da = 10^{-6}$, (*b*) $Da = 10^{-4}$, and (*c*) $Da = 10^{-2}$

Nusselt number with Pr_f is in agreement with the conclusion made by Somerton (1983), and Jonsson and Catton (1987). However, their correlations need to be modified to include the boundary effects through the inclusion of Darcy number.

Another interesting aspect of the effect of fluid Prandtl number on the heat transfer rate in connection with Da is revealed by a closer look at Figs. 7 and 10(*a–c*). At low Darcy numbers, $Da \leq 10^{-6}$, Pr_f has a negligible effect on the critical Rayleigh number for the onset of convection. This agrees with the conclusion made by Georgiadis and Catton (1986). However, at higher values of Da, the onset may be delayed if the Prandtl number is low. For example, $Ra_{f,c}$ is equal to 5×10^5 when $Da = 10^{-4}$ and $Pr_f = 0.01$, which corresponds to $Ra^* = 50$. Indeed, a combination of low Pr_f and high Da significantly delays the initiation of convective flow; $Ra_{f,c} > 10^4$ ($Ra_c^* > 100$) for $Pr_f \leq 0.1$, $Da = 10^{-2}$ (Fig. 10*c*). Clearly, whenever the Darcy number is increased beyond 10^{-6} and Prandtl number decreases below 10, the effect of Pr_f must be considered.

The above effect of Prandtl number on the critical Rayleigh number for the onset of convection in a porous layer heated from below agrees qualitatively with the effect of Pr_f in the case of a fluid layer (Verhoeven, 1964; Samuels and Churchill, 1967; Chao et al., 1982; Bertin and Ozoe, 1986). As noted by Samuels and Churchill (1981), this is primarily due to significant contributions of the nonlinear convective term at low Prandtl numbers. They, indeed, have argued that the linear stability analysis is not valid for $Pr_f < 1$. In the case of porous media, this issue did not arise earlier since the stability analysis has been generally performed on the Darcy flow model, which is linear. However, when the non-Darcy flow is considered, the solution becomes Prandtl number dependent due to the inclusion of Forchheimer's inertia term, whose contribution at low Pr_f is of the same order as that of the Brinkman viscous diffusion term. In fact, a linear stability analysis for the Darcy-Brinkman flow model would not be valid at high Darcy numbers and low Prandtl numbers.

If an effort is made to obtain the critical Rayleigh number for the onset of convection as a function of Pr_f, by extrapolating the computed values to the conduction state ($Nu = 1$) by plotting ($Nu - 1$) against ($1/Ra_f$), a correlation may be obtained as

$$(\overline{Nu} - 1) = B \ln(Ra_{f,c}/Ra_f), \qquad \text{for a fixed Da} \qquad (25)$$

where B is a function of Pr_f. It should be noted that this equation is not in a linear form as presented by Malkus and Veronis (1958) and employed by others (Bertin and Ozoe, 1986).

The critical Rayleigh numbers obtained from equation (25) may then be employed to develop a correlation for $Ra_{f,c}$ in terms of Prandtl number

$$Ra_{f,c} = R \exp(C_1/Pr_f), \qquad \text{for a fixed Da} \qquad (26)$$

where R is the value of $Ra_{f,c}$ for $Pr_f \to \infty$, and C_1 is a constant. The values of R and C_1 are presented in Table 3 for $Da = 10^{-6}$ and 10^{-4}. It is evident from this table that the predicted values of critical Rayleigh number are very close to the extrapolated $Ra_{f,c}$ from the numerical data.

It is now possible to use equation (26) to obtain a Nusselt number correlation in terms of Ra_f and Pr_f

$$\overline{Nu} = 1 - C_2 [C_1/Pr_f + \ln(R/Ra_f)], \qquad \text{for a fixed Da} \qquad (27)$$

where C_2 is a function of Pr_f, and is listed in Table 3. Equation (27) generally predicts the mean Nusselt number within 1.5 percent of the computed values reported in Figs. 10(*a*) and 10(*b*) for $Da = 10^{-6}$ and 10^{-4}, respectively. The difference

Table 3 Values of empirical constants for equations (26) and (27); also a comparison between extrapolated and predicted values of $Ra_{f,c}$

Da	Pr_f	R	C_1	C_2	Critical Rayleigh number, equation (26)	from extrapolation
10^{-6}	1000	38,470,769	0.80×10^{-3}	1.5514	38,470,798	38,461,538
	10			1.5452	38,473,695	38,461,538
	1			1.5432	38,500,040	38,535,646
	0.1			1.4535	38,764,478	38,759,690
	0.01			1.0875	41,510,857	41,511,000
10^{-4}	1000	398,929.37	0.13×10^{-3}	1.3999	398,929.9	390,930.4
	10			1.3997	398,980.9	390,930.4
	1			1.3297	399,445.1	395,569.6
	0.1			1.0239	404,116.2	437,062.9
	0.01			0.5263	453,940.2	450,450.5

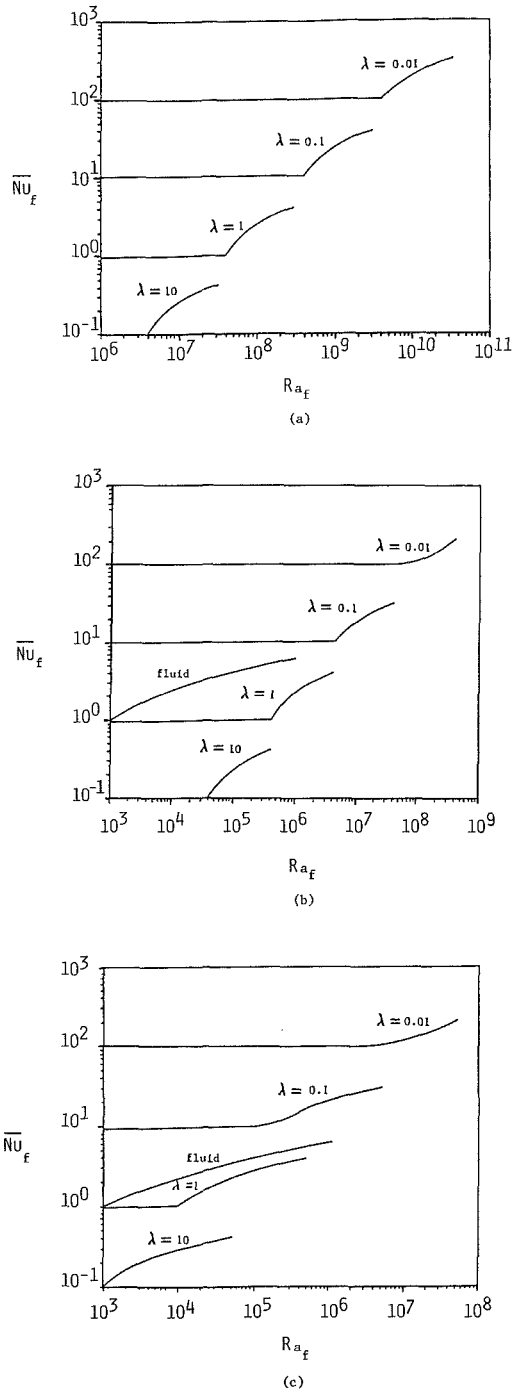

Fig. 11 Variation in heat transfer rate with conductivity ratio, for (a) $Da = 10^{-6}$, (b), $Da = 10^{-4}$, and (c) $Da = 10^{-2}$

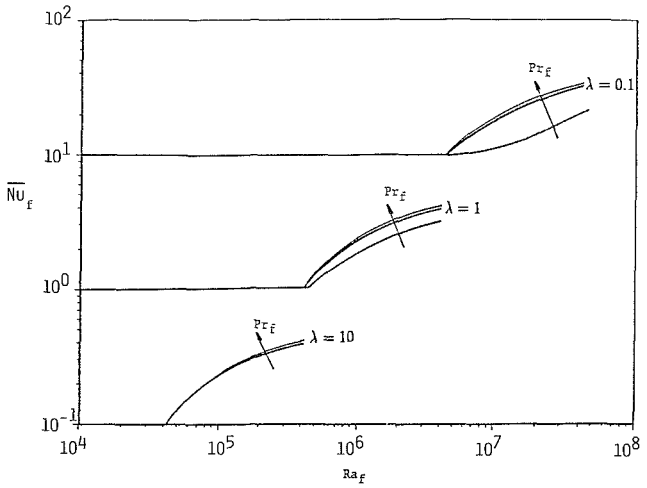

Fig. 12 Combined effects of conductivity ratio and fluid Prandtl number on the heat transfer rate

between the predictions and numerical data, however, increases up to 4 percent as $Ra_f \rightarrow Ra_{f,c}$.

Effect of Thermal Conductivity. To present the effect of thermal conductivity ratio, $\lambda = k_f/k_m$, on the convective heat transfer, Nusselt numbers of $Da = 10^{-6}$, 10^{-4}, and 10^{-2}, and $Pr_f = 1$ are reported in Figs. 11(*a*), 11(*b*), and 11(*c*), respectively. As can be observed, the heat transfer rate for fixed values of Ra_f and Da always increases with an increase in the thermal conductivity of solid particles k_s, and therefore, with a reduction in the conductivity ratio λ. It is possible that a porous medium of low conductivity ratio can transport more energy even in the conduction mode than the saturating fluid alone in the convection regime. This behavior has also been shown by the Darcy-Brinkman solutions (Prasad et al., 1988). However, the contribution of the inertia term becomes significant at low conductivity ratios, and the nature of the curve changes, as demonstrated by the curves for $\lambda = 0.01$ in Fig. 11(*b*) and for $\lambda = 0.1$ and 0.01 in Fig. 11(*c*).

Figure 11(*c*) further shows that the porous media Nusselt numbers are closer to the fluid solutions at high Rayleigh numbers, a phenomenon observed earlier at high values of Da. Also, the lower the conductivity ratio, the higher is the Rayleigh number required for the onset of convection. This is primarily because the high-conductivity solid particles have a stabilizing effect on the convective instability.

The effect of variation in both the conductivity ratio and the fluid Prandtl number is demonstrated in Fig. 12. As can be seen, the lower the thermal conductivity of solid matrix or the higher the conductivity ratio λ, the weaker is the dependence on Prandtl number. Although the aforementioned effects of λ can be qualitatively observed from the Darcy solutions, a

more reasonable dependence is predicted by the Darcy–Brinkman–Forchheimmer flow model since λ can greatly enhance or reduce the contribution of inertia terms.

Conclusion

A higher-order formulation based on the Brinkman–Forchheimer extended Darcy equation of motion shows that the free convection in porous media is governed by the fluid parameters, the Rayleigh and Prandtl numbers; the porous matrix structure parameters, the porosity, Darcy, and Forchheimer numbers; and the combined parameters, the conductivity, viscosity, and specific heat ratios.

Numerical results are obtained for stable, unicellular, steady-state convection in horizontal porous layers heated from below for $A=1$, $\epsilon=0.4$, $\mathrm{Fs}=0.55\mathrm{Da}^{0.5}$ (Ergun model) and $\Lambda=1/\epsilon$ by employing a finite-difference scheme based on an ADI procedure, which is second-order accurate under steady-state.

The critical Rayleigh number for the onset of convection decreases from a value predicted by the Darcy flow model, $\mathrm{Ra}_{f,c}=4\pi^2/\lambda\mathrm{Da}$, as the Darcy number and/or the conductivity ratio is increased, whereas the Prandtl number has an opposite effect. The effect of Darcy number is observed to be significant for $\mathrm{Da}>10^{-4}$. The heat transfer results indicate the existence of an asymptotic convection regime where the Nusselt number is almost independent of the permeability of the porous matrix or the Darcy number. In this convective state, the porous media results match with the fluid solutions provided the thermal conductivities of solid particles and fluid are identical.

The effect of Prandtl number is quite significant at low values of Pr_f, and is observed to diminish as Pr_f increases beyond unity. For the present range of parameters, the solution is almost independent of Prandtl number dependence for $\mathrm{Pr}_f>10$. However, the higher the Rayleigh number, the Darcy number, and/or the conductivity ratio, the stronger is the Prandtl number dependence.

The numerical solutions also show interesting effects of the conductivity ratio. Namely, it is possible that a porous medium can transport significantly larger amounts of energy compared to the fluid alone. The conditions required for this are that the porous matrix be highly permeable and the thermal conductivity of solid particles be higher than that for the fluid, $k_s>k_f$. An increase in Rayleigh number and a reduction in Prandtl number further strengthens this effect.

Acknowledgments

The present research was conducted under support (Grant No. CBT-85-04100) from the National Science Foundation.

References

Bear, J., 1972, *Dynamics of Fluids in Porous Media*, Elsevier, New York.

Bertin, H., and Ozoe, H., 1986, "Numerical Study of Two-Dimensional Natural Convection in a Horizontal Fluid Layer Heated From Below by Finite Element Method: Influence of Prandtl Number," *International Journal of Heat and Mass Transfer*, Vol. 29, pp. 439–450.

Brinkman, H. C., 1947, "A Calculation of the Viscous Force Exerted by a Flowing Fluid on a Dense Swarm of Particles," *Applied Science Research*, Vol. A1, pp. 27–34.

Buretta, R. J., and Berman, A. S., 1976, "Convective Heat Transfer in a Liquid Saturated Porous Layer," ASME *Journal of Applied Mechanics*, Vol. 43, pp. 249–253.

Caltagirone, J. P., 1975, "Thermoconvective Instabilities in a Horizontal Porous Layer," *Journal of Fluid Mechanics*, Vol. 27, pp. 269–287.

Chao, P., Churchill, S. W., and Ozoe, H., 1982, "The Dependence of the Critical Rayleigh Number on the Prandtl Number," *Convective Transport and Instability Phenomena*, J. Zierep and H. Oertel, Jr., eds., pp. 55–70.

Cheng, P., 1978, "Heat Transfer in Geothermal Systems," *Advances in Heat Transfer*, Vol. 14, pp. 1–105.

Choudhary, M., Propster, M., and Szekely, J., 1976, "On the Importance of the Inertial Terms in the Modeling of Flow Maldistribution in Packed Beds," *AIChE Journal*, Vol. 22, p. 600.

Combarnous, M. A., and Bories, S. A., 1975, "Hydrothermal Convection in Saturated Porous Media," *Advances in Hydrosciences*, Vol. 10, pp. 231–307.

Forchheimer, F., 1901, "Wasservevegung durch Boden," *Z. Ver. Deutsch. Ing.*, Vol. 45, pp. 1782–1788.

Georgiadis, J. G., and Catton, I., 1986, "Prandtl Number Effect on Benard Convection in Porous Media," ASME JOURNAL OF HEAT TRANSFER, Vol. 108, pp. 284–290.

Horton, C. W., and Rogers, F. T., 1945, "Convection Currents in a Porous Medium," *Journal of Applied Physics*, Vol. 16, p. 367.

Jonsson, T., and Catton, I., 1987, "Prandtl Number Dependence of Natural Convection in Porous Media," ASME JOURNAL OF HEAT TRANSFER, Vol. 109, pp. 371–377.

Kladias, N., 1988, "Non-Darcy Free Convection in Horizontal Porous Layers," Doctoral Dissertation, Columbia University, NY.

Kladias, N., and Prasad, V., 1987, "Numerical Study for Inertia and Viscous Diffusion Effects on Benard Convection in Porous Media," *Proceedings of the Fifth International Conference on Numerical Methods in Thermal Problems*, pp. 797–810.

Kladias, N., and Prasad, V., 1988, "Non-Darcy Oscillatory Convection in Horizontal Porous Layers Heated From Below," *Proceedings of the First National Fluid Dynamics Congress*, AIAA, Vol. 3, pp. 1757–1764.

Lapwood, E. R., 1948, "Convection of a Fluid in a Porous Medium," *Proceedings of the Cambridge Philosophical Society*, Vol. 44, pp. 508–521.

Lauriat, G., and Prasad, V., 1986, "Natural Convection in a Vertical Porous Cavity: A Numerical Study for the Brinkman-Extended Darcy Formulation," ASME JOURNAL OF HEAT TRANSFER, Vol. 109, pp. 688–696.

Lundgren, T. S., 1972, "Slow Flow Through Stationary Random Beds and Suspension of Spheres," *Journal of Fluid Mechanics*, Vol. 51, pp. 273–299.

Malkus, W. V. R., and Veronis, G., 1958, "Finite Amplitude Cellular Convection," *Journal of Fluid Mechanics*, Vol. 4, pp. 225–260.

McDonough, J. M., and Catton, I., 1982, "Accuracy of the Mean Field Approximation and the Physical Effect of Prandtl Number in Benard Convection," *The Physics of Fluids*, Vol. 25, pp. 1502–1505.

Nield, D. A., 1983, "The Boundary Correction for the Rayleigh-Darcy Problem: Limitation of the Brinkman Equation," *Journal of Fluid Mechanics*, Vol. 128, pp. 37–46.

Prasad, V., Lauriat, G., and Kladias, N., 1988, "Reexamination of Darcy–Brinkman Solutions for Free Convection in Porous Media," *Proceedings of the 25th National Heat Transfer Conference*, Vol. 1, ASME HTD-Vol. 96, pp. 567–579.

Prasad, V., and Tuntomo, A., 1987, "Inertial Effects on Natural Convection in a Vertical Porous Cavity," *Numerical Heat Transfer*, Vol. 11, pp. 295–320.

Prasad, V., Kulacki, F. A., and Keyhani, M., 1985, "Natural Convection in Porous Media," *Journal of Fluid Mechanics*, Vol. 150, pp. 89–119.

Rudraiah, N., 1984, "Non-linear Convection in a Porous Medium With Convective Acceleration and Viscous Force," *The Arabian Journal for Science and Engineering*, Vol. 9, pp. 153–167.

Rudraiah, N., Veerappa, B., and Rao, S. B., 1980, "Effects of Nonuniform Thermal Gradient and Adiabatic Boundaries on Convection in Porous Media," ASME JOURNAL OF HEAT TRANSFER, Vol. 102, pp. 254–260.

Samuels, M. R., and Churchill, S. W., 1967, "Stability of a Fluid in a Rectangular Region Heated From Below," *AIChE Journal*, Vol. 13, pp. 77–85.

Schubert, G., and Straus, J. M., 1979, "Three Dimensional and Multicellular Steady and Unsteady Convection in Fluid Saturated Porous Media at High Rayleigh Numbers," *Journal of Fluid Mechanics*, Vol. 94, pp. 25–38.

Seki, N., Fukusako, S., and Inaba, H., 1978, "Heat Transfer in a Confined Rectangular Cavity Packed With Porous Media," *International Journal of Heat and Mass Transfer*, Vol. 21, pp. 985–989.

Somerton, C. W., 1983, "The Prandtl Number Effect in Porous Layer Convection," *Applied Science Research*, Vol. 40, pp. 333–344.

Tam, C. K. W., 1969, "The Drag on a Cloud of Spherical Particles in Low Reynolds Number Flow," *Journal of Fluid Mechanics*, Vol. 38, pp. 537–546.

Verhoeven, J. D., 1964, "Experimental Study of Thermal Convection in a Vertical Cylinder of Mercury Heated From Below," *The Physics of Fluids*, Vol. 12, pp. 1733–1740.

Mixed Convection Plume—Application of Superposition

C. Y. Wang
Michigan State University,
East Lansing, MI 48824
Mem. ASME

By comparing with the exact similarity solution for the mixed convection plume of the point source, the limitation of the Oseen boundary layer solution is established. Superposition principles are given and applied to the cases of the vertical and the horizontal finite heated wire. Three-dimensional thermal and velocity fields are determined.

Introduction

The axisymmetric vertical plume from a hot point source is one of the basic problems in free convection. Closed-form boundary layer similarity solutions for Prandtl numbers 1 and 2 were first obtained by Yih (1951). The similarity equations were integrated numerically for various Prandtl numbers by Fujii (1963). Reviews of related literature may be found in Jaluria (1980) and Gebhart et al. (1988). The similarity equations for the axisymmetric plume also admit solutions for mixed convection, a property not shared by the two-dimensional plume. The problem of an additional external uniform flow in the direction of the plume is exactly the same as a falling point source. To the author's knowledge, the mixed convection case was first studied by Crane (1977), who used perturbations to find the flow due to a weak heat source. Numerical integration for arbitrary source strength was first performed by Appalaswamy and Jaluria (1980). Variations of the same problem were published by Afzal (1983), Riley and Drake (1983), Rao et al. (1985), and Afzal (1985).

No literature covers the case of several interacting heat sources, or when the heat source has a shape other than a point. This is due to the fact that tedious numerical methods are necessary to integrate the governing partial differential equations, which are nonlinear and three dimensional. The present paper investigates the possibility of an easier method, i.e., using superposition of point source solutions to obtain the combined plume of distributed sources.

A necessary condition for superposition is that both the governing equations and the boundary conditions are linear and homogeneous. For the plume in still air, these equations are basically nonlinear and superposition does not seem to be possible. For mixed convection, however, linearization may be possible through the Oseen approximation. In what follows we shall determine the limitations of Oseen linearization and apply the superposition method to the case of the heated wire of finite length. This is important in, for example, hot-wire anemometry. We assume the wire is infinitesimally thin such that the momentum deficiency due to viscous drag is negligible compared to that due to thermal convection.

Exact Similarity Solution for Falling Point Source

For a point source at the origin, the boundary layer equations under the standard Boussinesq assumption are

$$(ru)_x + (rv)_r = 0 \tag{1}$$

$$uu_x + vu_r = \nu(ru_r)_r/r + \tilde{g}\beta(T - T_\infty) \tag{2}$$

$$uT_x + vT_r = \nu(rT_r)_r/(r\mathrm{Pr}) \tag{3}$$

Here (x, r) are the axial and radial coordinates and (u, v) are the corresponding velocity components, ν is the kinematic viscosity, $\tilde{g}$ is gravitational acceleration, β is the thermal coefficient of expansion, T is the temperature, and Pr is the Prandtl number. Of course, the boundary layer solution is not valid near $x = 0$, where the solution would be singular. The boundary conditions are that at infinity, the velocity and temperature approach U_∞ and T_∞,

$$r \to \infty, \quad u \to U_\infty, \quad T \to T_\infty \tag{4}$$

and that velocities and temperature are smooth and symmetric about the axis $r = 0$. The total heat flux Q is also conserved:

$$Q = 2\pi\rho C_p \int_0^\infty (T - T_\infty) urdr \tag{5}$$

where ρ is the density and C_p is the specific heat. Using the transformation

$$\psi = \nu x f(\zeta), \quad T - T_\infty = \frac{Q}{2\pi\rho C_p \nu x} g(\zeta) \tag{6}$$

$$\zeta \equiv \frac{U_\infty r^2}{4\nu x} \tag{7}$$

The similarity equations are

$$(\zeta f'')' + \frac{1}{2} ff'' + \alpha g = 0 \tag{8}$$

$$(\zeta g')' + \frac{\mathrm{Pr}}{2} (fg)' = 0 \tag{9}$$

$$\int_0^\infty gf' d\zeta = 1 \tag{10}$$

where α is a nondimensional number signifying the relative importance of heat source Q.

$$\alpha \equiv \frac{\tilde{g}\beta Q}{\pi\rho C_p \nu U_\infty^2} \sim (\text{Grashof number})/(\text{Reynolds number})^2 \tag{11}$$

In the case when forced and free convections are opposite in direction, $\tilde{g}$ and α are negative. The boundary conditions are

$$f'(\infty) = 2, \quad g(\infty) = 0 \tag{12}$$

$$f(0) = 0, \quad f'(0), g'(0) \text{ bounded} \tag{13}$$

Using equation (12), equation (9) reduces to

$$\zeta g' + \frac{\mathrm{Pr}}{2} fg = 0 \tag{14}$$

The easiest way to integrate the similarity equations numerically is as follows. Let

$$\zeta = A\xi, \quad f(\zeta) = F(\xi), \quad g(\zeta) = G(\xi)/(A^2\alpha) \tag{15}$$

Equations (8), (13), and (14) become

$$(\xi F'')' + \frac{1}{2} FF'' + G = 0 \tag{16}$$

Contributed by the Heat Transfer Division for publication in the JOURNAL OF HEAT TRANSFER. Manuscript received by the Heat Transfer Division June 13, 1988. Keywords: Mixed Convection, Plumes, Wakes.

$$\xi G' + \frac{\mathrm{Pr}}{2} FG = 0 \tag{17}$$

$$F(0) = 0 \tag{18}$$

Since the equations are singular on the axis, we expand the dependent variables about $\xi = 0$:

$$F = a_1 \xi + a_2 \xi^2 + a_3 \xi^3 + 0(\xi^4) \tag{19}$$

$$G = b_0 + b_1 \xi + 0(\xi^2) \tag{20}$$

Substitution into equations (16) and (17) and equating powers of ξ yield

$$F''(0) = -G(0) \tag{21}$$

$$G'(0) = -\frac{\mathrm{Pr}}{2} F'(0) G(0) \tag{22}$$

$$F'''(0) = \frac{1}{4} (\mathrm{Pr} + 1) F'(0) G(0) \tag{23}$$

Thus there are only two independent initial values $F'(0)$ and $G(0)$. For a given Pr, the problem is governed by only one parameter α and we can prescribe one of the initial values without loss of generality, say $G(0) = \pm 1$ (same sign as $\tilde{g}$ or α). Equation (10) gives

$$\int_0^\infty GF' d\xi = \alpha A^2 \tag{24}$$

We define K as the normalized total heat through a circle of radius r

$$\frac{dK}{ds} \equiv GF' \qquad K(0) = 0 \tag{25}$$

Thus

$$K(\infty) = \alpha A^2 \tag{26}$$

For given Pr and $G(0) = \pm 1$, pick any $F'(0)$ and integrate equations (16)–(18), (21)–(23), and (25) as an initial value problem using the fifth-order Runge-Kutta-Fehlberg algorithm. The singularity at $\xi = 0$ is avoided since all necessary derivatives at zero are determined beforehand. An asymptotic analysis on equations (16) and (17) shows that as G approaches zero, F' approaches constant exponentially for large ξ. The integration terminates at ξ^* when $K(\xi)$ approaches a constant within an error of 10^{-6}. A step size of $\Delta\xi = 0.05$ is found to be sufficient. Then

$$\alpha = \frac{4K(\xi^*)}{[F'(\xi^*)]^2} \tag{27}$$

$$g(0) = \frac{G(0)}{K(\xi^*)}, \qquad f'(0) = \frac{2F'(0)}{F'(\xi^*)} \tag{28}$$

Figures 1 and 2 show the results for $\mathrm{Pr} = 0.7$ (air) and $\mathrm{Pr} = 7$ (water).

The Oseen Approximation

The Oseen approximation partially takes into account the inertial terms. Let

$$u \equiv U_\infty + u_1 \tag{29}$$

Using both Oseen and boundary layer simplifications the governing equations are

$$U_\infty \frac{\partial u_1}{\partial x} = \frac{\nu}{r} \frac{\partial}{\partial r}\left(r \frac{\partial u_1}{\partial r}\right) + \tilde{g}\beta(T - T_\infty) \tag{30}$$

$$U_\infty \frac{\partial T}{\partial x} = \frac{\nu}{\mathrm{Pr}\, r} \frac{\partial}{\partial r}\left(r \frac{\partial T}{\partial r}\right) \tag{31}$$

For the point source the boundary conditions are

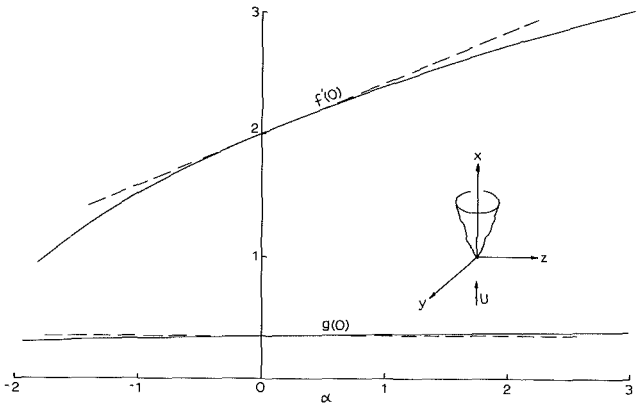

Fig. 1 Heat source in vertical stream; values of normalized maximum temperature difference g(0) and normalized maximum velocity excess f'(0) as function of heat strength parameter α: ——— exact solution ····· Oseen boundary layer solution, equations (43) and (44), Pr = 0.7

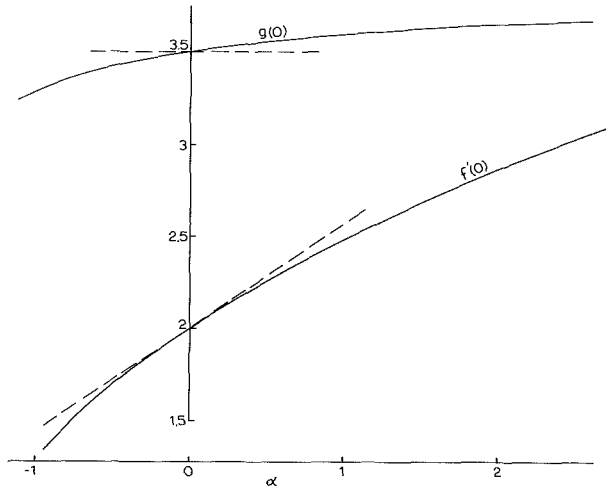

Fig. 2 Same legend as Fig. 1; Pr = 7

$$Q = 2\pi\rho C_p \int_0^\infty U_\infty (T - T_\infty) r dr \tag{32}$$

$$r \to \infty, \quad u_1 \to 0, \quad T \to T_\infty; \quad r = 0, \quad \frac{\partial u_1}{\partial r} = 0, \quad \frac{\partial T}{\partial r} = 0 \tag{33}$$

We use a similar transform

$$u_1 = \frac{\alpha U_\infty}{2} f_1'(\zeta), \qquad T - T_\infty = \frac{Q}{2\pi\rho C_p \nu x} g_1(\zeta) \tag{34}$$

The governing equations become

$$(\zeta f_1'')' + \zeta f_1'' + \alpha g_1 = 0 \tag{35}$$

$$g_1' + \mathrm{Pr}\, g_1 = 0 \tag{36}$$

$$\int_0^\infty g_1 d\zeta = \frac{1}{2} \tag{37}$$

$$f_1(0) = 0, \quad f_1'(\infty) = 0, \quad g_1(\infty) = 0 \tag{38}$$

The solution is

$$g_1(\zeta) = \frac{\mathrm{Pr}}{2} e^{-\mathrm{Pr}\zeta} \tag{39}$$

$$f_1(\zeta) = \frac{\mathrm{Pr}}{2(\mathrm{Pr} - 1)} \{\zeta[E_1(\zeta) - E_1(\mathrm{Pr}\zeta)] + \frac{1}{\mathrm{Pr}} (e^{-\mathrm{Pr}\zeta} - 1) - (e^{-\zeta} - 1)\} \qquad \mathrm{Pr} \neq 1 \tag{40}$$

$$f_1 = \frac{1}{2}(1 - e^{-\zeta}) \qquad \Pr = 1 \tag{41}$$

where E_1 is the exponential integral

$$E_1(\zeta) \equiv \int_\zeta^\infty \frac{e^{-t}}{t}\, dt \tag{42}$$

Thus

$$\frac{2\pi\rho C_p \nu x (T_{\max} - T_\infty)}{Q} = g(0) = g_1(0) = \frac{\Pr}{2} \tag{43}$$

$$\frac{2u_{\max}}{U_\infty} = f'(0)) = 2 + f_1'(0) = 2 + \frac{\alpha \Pr}{2(\Pr - 1)} \ln \Pr \qquad \Pr \neq 1 \tag{44}$$

$$f'(0) = 2 + \frac{\alpha}{2} \qquad \Pr = 1 \tag{45}$$

where $T_{\max}$ and $u_{\max}$ are the maximum temperature and velocity at a given x. We see in Figs. 1 and 2 that the Oseen solution compares well with the exact solution. In terms of the maximum velocity the two solutions differ by less than 5 percent if $-0.4 < \alpha < 0.6$ at $\Pr = 7$, and the range can be extended to $-1.2 < \alpha < 2.2$ at $\Pr = 0.7$. The maximum temperature difference of the Oseen solution is accurate to 5 percent for $-0.4 < \alpha < 1.6$ at $\Pr = 7$ and $-0.9 < \alpha < 1.7$ at $\Pr = 0.7$. The range of validity of α for the Oseen solution (within 5 percent error) as a function of other Prandtl numbers is shown in Fig. 3. We see the Oseen solution is not limited to only small α (weak heat input). In many cases, especially at small Pr, the upper limit of admissible α can be quite large. Note that the Oseen solution is the first two terms (and no more) of the Crane's (1977) asymptotic solution.

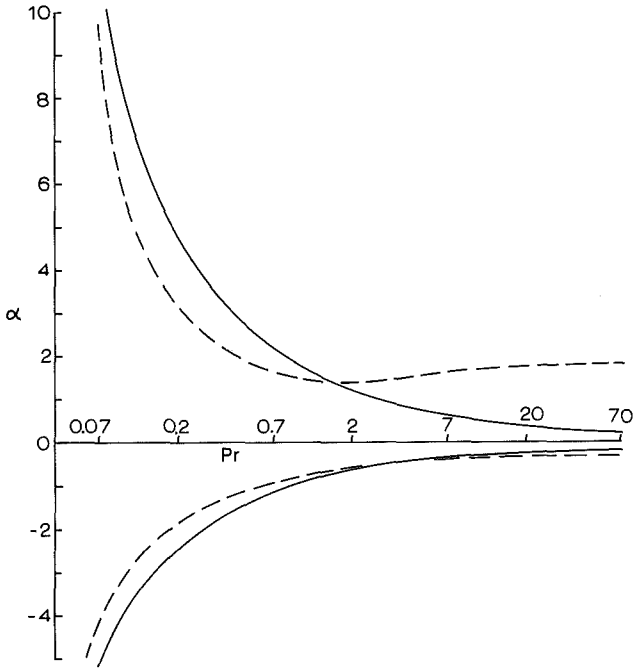

Fig. 3 Heat source in vertical stream; limits of α as a function of Prandtl number for less than 5 percent error using Oseen boundary layer approximation: ——— $f'(0)$, ····· $g(0)$

Superposition

What is important is that equations (30)–(33) are linear and homogeneous in u_1 and $(T - T_\infty)$. Thus it is possible to superpose solutions.

For N discrete heat sources Q_i at X_i, Y_i, Z_i, we let

$$\alpha_i = \frac{\tilde{g}\beta Q_i}{\pi\rho C_p \nu U_\infty^2}, \quad \zeta_i = \frac{U_\infty[(y - Y_i)^2 + (z - Z_i)^2]}{4\nu(x - X_i)} \tag{46}$$

Then the combined temperature distribution is

$$T = T_\infty + \sum_{\substack{i=1 \\ x > X_i}}^{N} \frac{Q_i}{2\pi\rho C_p \nu (x - X_i)}\, g_1(\zeta_i) \tag{47}$$

The combined flow field is

$$u = U_\infty \left[1 + \frac{1}{2} \sum_{\substack{i=1 \\ x > X_i}}^{N} \alpha_i f_1'(\zeta_i)\right] \tag{48}$$

provided the total α_i is within the range of α over which the Oseen approximation is valid.

For a continuous distribution of heat along a space curve $X(s)$, $Y(s)$, $Z(s)$ with s as arc length, let $q(X, Y, Z)$ be the heat flux per length of curve, and

$$\zeta = \frac{U_\infty[(y - Y)^2 + (z - Z)^2]}{4\nu(x - X)} \tag{49}$$

Then

$$T = T_\infty + \frac{1}{2\pi\rho C_p \nu} \int_\Gamma \frac{q g_1(\zeta)}{x - X}\, ds \tag{50}$$

$$u = U_\infty \left[1 + \frac{\tilde{g}\beta}{2\pi\rho C_p \nu U_\infty^2} \int_\Gamma q \frac{df_1}{d\zeta}(\zeta) ds\right] \tag{51}$$

where Γ is along the segments of the curve where $x > X(s)$.

Mixed Convection Plume of a Heated Vertical Wire

Let the wire be uniformly heated located on the x axis between $0 \le X \le L$. Define normalized temperature difference τ and velocity difference u. For $x \le L$ the curve Γ is from zero to x. Equations (39) and (50) give

$$\tau \equiv \frac{2\pi\rho C_p \nu (T - T_\infty)}{q} = \int_0^x \frac{g_1(\zeta)}{x - X}\, dX = \frac{\Pr}{2} E_1(\Pr \zeta_0) \tag{52}$$

where

$$\zeta = \frac{U_\infty r^2}{4\nu(x - X)}, \quad \zeta_0 \equiv \frac{U_\infty r^2}{4\nu x}; \quad \zeta_1 \equiv \frac{U_\infty r^2}{4\nu(x - L)} \tag{53}$$

Using equations (40) and (51) and integrating by parts give

$$u \equiv \frac{2\pi\rho C_p \nu U_\infty (u - U_\infty)}{\tilde{g}\beta q L} = \frac{1}{L} \int_0^x \frac{df_1}{d\zeta}\, dX$$

$$= \frac{\Pr}{2(\Pr - 1)L} \int_{\zeta_0}^\infty (e^{-\zeta} - e^{\Pr\zeta}) \frac{X}{\zeta}\, d\zeta$$

$$= \frac{\Pr x}{2(\Pr - 1)L} [e^{-\Pr\zeta_0} - e^{-\zeta_0} + (1 + \zeta_0)E_1(\zeta_0) - (1 + \Pr\zeta_0)E_1(\Pr\zeta_0)] \tag{54}$$

For $\Pr = 1$ equation (54) is replaced by

$$u = \frac{x}{2L} [e^{-\zeta_0} - \zeta_0 E_1(\zeta_0)] \tag{55}$$

When $x > L$ the curve Γ is from zero to L. We find

$$\tau = \int_0^L \frac{g_1(\zeta)}{x - X}\, dX = \frac{\Pr}{2} [E_1(\Pr\zeta_0) - E_1(\Pr\zeta_1)] \tag{56}$$

$$u = \frac{\Pr}{2(\Pr - 1)} \left\{\frac{x}{L} [(1 + \zeta_0)E_1(\zeta_0) - (1 + \Pr\zeta_0)E_1(\Pr\zeta_0) - (1 + \zeta_0)E_1(\zeta_1) + (1 + \Pr\zeta_0)E_1(\Pr\zeta_1) - e^{-\zeta_0} + e^{-\Pr\zeta_0} + e^{-\zeta_1} - e^{-\Pr\zeta_1}] + E_1(\zeta_1) - E_1(\Pr\zeta_1) - e^{-\zeta_1} + e^{-\Pr\zeta_1}\right\} \qquad \Pr \neq 1 \tag{57}$$

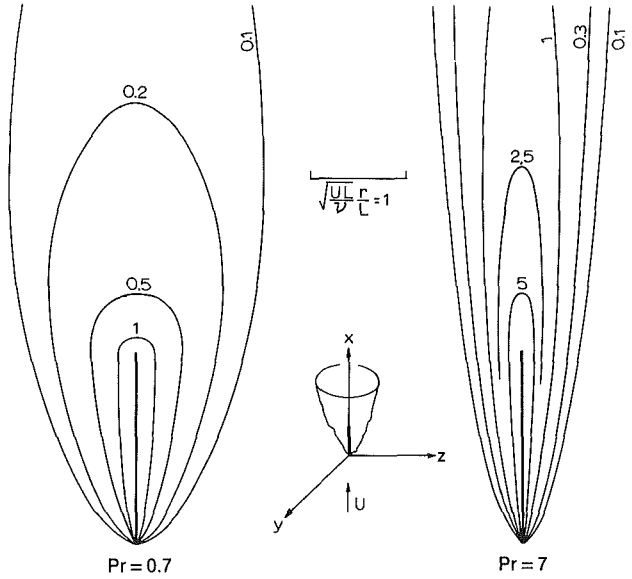

Fig. 4 Isotherms τ for the heated vertical wire in vertical stream; note horizontal scale

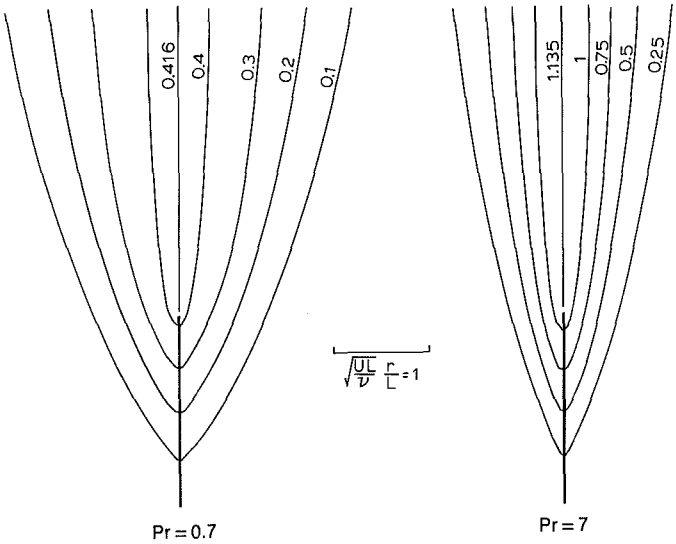

Fig. 5 Constant vertical velocity curves u for the heated vertical wire

$$u=\frac{x}{2L}\left\{e^{-\zeta_0}-\left(1-\frac{L}{x}\right)e^{-\zeta_1}+\zeta_0[E_1(\zeta_1)-E_1(\zeta_0)]\right\}$$
$$\mathrm{Pr}=1 \tag{58}$$

Figure 4 shows the isotherms τ, which are axially symmetric about the x axis. Both forced and natural convection are toward the positive x axis. Notice that the radial scale is multiplied by the square root of the length-based Reynolds number. Thus when the forced flow increases the thermal boundary layer thickness decreases. The thickness also decreases with increased Prandtl number.

Due to the parabolic nature of the governing equations, a point at a given location x is affected only by the points less than x. The temperature on the wire is infinite because of the finite heat flux with zero surface area. If a small wire radius is allowed the temperature would be high but constant. For large x one can show the far wake approaches that of a point source with strength qL.

Figure 5 shows the excess vertical velocity lines u induced by natural convection. On the axis the excess velocity increases linearly from zero at $x=0$ to a value of $\mathrm{Pr}(\ln \mathrm{Pr})/2(\mathrm{Pr}-1)$ at $x=L$ and stays constant thereafter for $x\geq L$. As the width of the velocity boundary layer increases more fluid will be entrained. It is better to plot the lines of constant u instead of the streamlines since the latter are almost parallel.

Mixed Convection Plume of a Heated Horizontal Wire

Let the wire be uniformly heated, on the z axis between $0\leq Z\leq L$. Equation (50) gives the normalized temperature difference

$$\tau=\frac{1}{x}\int_0^L g_1(\zeta)dZ=\frac{1}{2}\sqrt{\frac{\pi \mathrm{Pr}\nu}{U_\infty x}}\exp\left(-\frac{\mathrm{Pr}U_\infty y^2}{4\nu x}\right)\varphi(\mathrm{Pr},x,z) \tag{59}$$

where

$$\zeta=\frac{U_\infty}{4\nu x}[y^2+(Z-z)^2] \tag{60}$$

and

$$\varphi(\mathrm{Pr},x,z)\equiv\sqrt{\frac{U_\infty \mathrm{Pr}}{\pi\nu x}}\int_0^L \exp\left[\frac{-\mathrm{Pr}U_\infty(Z-z)^2}{4\nu x}\right]dZ$$
$$=\begin{cases}\mathrm{erf}(\sqrt{\mathrm{Pr}}\lambda_1)-\mathrm{erf}(\sqrt{\mathrm{Pr}}\lambda_0) & z<0\\ \mathrm{erf}(\sqrt{\mathrm{Pr}}\lambda_1)+\mathrm{erf}(\sqrt{\mathrm{Pr}}\,|\lambda_0|) & 0<z<L\\ \mathrm{erf}(\sqrt{\mathrm{Pr}}\,|\lambda_0|)+\mathrm{erf}(\sqrt{\mathrm{Pr}}\,|\lambda_1|) & z>L\end{cases} \tag{61}$$

Here

$$\lambda_0\equiv -z\sqrt{\frac{U_\infty}{4\nu x}},\quad \lambda_1\equiv (L-z)\sqrt{\frac{U_\infty}{4\nu x}} \tag{62}$$

and erf is the error function. For $\mathrm{Pr}\neq 1$ the normalized velocity difference is

$$u=\frac{1}{L}\int_0^L \frac{df_1}{d\zeta}dZ=\frac{\mathrm{Pr}}{2(\mathrm{Pr}-1)}\left[E_1(\zeta_1)-E_1(\mathrm{Pr}\zeta_1)+\frac{1}{L}\int_{\zeta_0}^{\zeta_1}\frac{Z}{\zeta}(e^{-\zeta}-e^{-\mathrm{Pr}\zeta})d\zeta\right] \tag{63}$$

where

$$\zeta_0\equiv\frac{U_\infty(y^2+z^2)}{4\nu x},\quad \zeta_1\equiv\frac{U_\infty[y^2+(L-z)^2]}{4\nu x} \tag{64}$$

Unfortunately the last integral cannot be integrated analytically in the general case. Restricting to the plane of $y=0$ gives

$$u=\frac{\mathrm{Pr}}{2(\mathrm{Pr}-1)}\left\{E_1(\lambda_1^2)-E_1(\mathrm{Pr}\lambda_1^2)+\frac{2}{L}\sqrt{\frac{\pi\nu x}{U_\infty}}\left[\varphi(1,x,z)-\frac{1}{\sqrt{\mathrm{Pr}}}\varphi(\mathrm{Pr},x,z)\right]+\frac{z}{L}[E_1(\lambda_0^2)-E_1(\mathrm{Pr}\lambda_0^2)-E_1(\lambda_1^2)+E_1(\mathrm{Pr}\lambda_1^2)]\right\} \tag{65}$$

For $\mathrm{Pr}=1$ we have

$$u=\frac{1}{2L}\sqrt{\frac{\pi\nu x}{U_\infty}}\exp\left(-\frac{U_\infty}{4\nu x}y^2\right)\varphi(1,x,z) \tag{66}$$

Figure 6 shows lines of constant $(\tau U_\infty L/\nu)$ for $\mathrm{Pr}=0.7$ and $\mathrm{Pr}=7$. One unit of vertical scale is one unit of $U_\infty L^2/4\nu$. Thus as U_∞ increases, isotherms decrease in value and lengthen in the vertical direction. Again, as $x\to\infty$, the thermal wake approaches that of a concentrated point source of same total strength. The excess velocity u is plotted in Fig. 7. In contrast

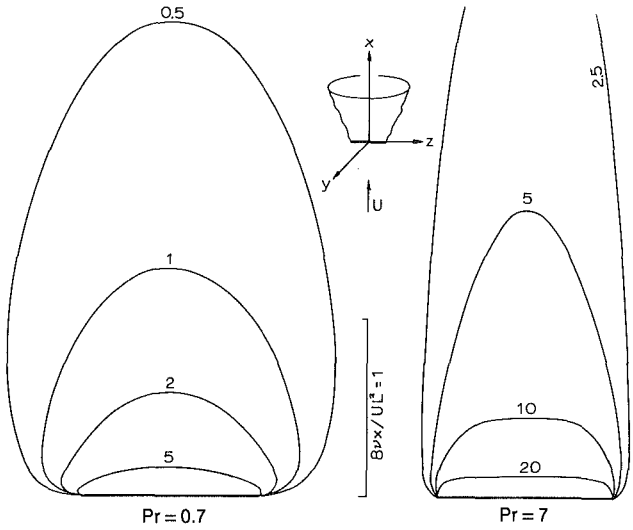

Fig. 6 Isotherms ($\tau U_\infty L/\nu$) for the heated horizontal wire in the vertical stream; note vertical scale

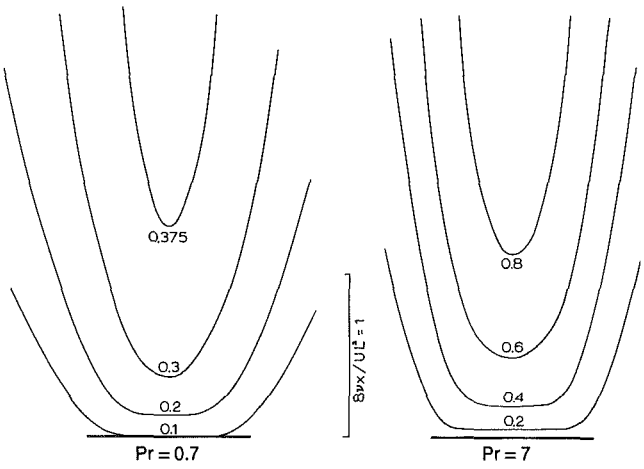

Fig. 7 Constant velocity curves u for the heated horizontal wire

to the vertical wire, the velocity excess on the centerline gradually increases from zero and approaches the constant $\Pr(\ln \Pr)/2(\Pr - 1)$ at large distances. The temperature field and the flow field are very much three dimensional.

Discussion

For the two-dimensional infinite line source, Wesseling (1975) found that the Oseen approximation is not uniformly valid, i.e., fails at large distances. This is probably due to the infinite heat input of the ideal problem, somewhat similar to the infinite drag force in the Stokes paradox. The present paper is based on the point source solution, which has finite heat input. Thus the difficulties of the two-dimensional case do not occur.

As mentioned in the introduction, we assumed the momentum deficiency due to viscous drag is negligible compared to that due to thermal convection. This assumption can always be satisfied for heated wires of small enough diameter. For a wire of radius b perpendicular to uniform flow, our results would not be valid in the thin velocity boundary layer on the surface and the near wake, which is at most several diameters downstream. However, these dynamic effects diminish to zero as the radius b approaches zero. For the far wake it can be shown (Rosenhead, 1963) the velocity deficiency due to drag is proportional to $(b/x)\exp(-\zeta)$, which is infinitesimal compared to the constant velocity deficiency due to thermal effects. As for a wire parallel to the stream, the maximum boundary layer thickness due to no slip is proportional to $(L/|\ln b|)^{1/2}$, which again tends to zero as $b \to 0$ (Glauert and Lighthill, 1955). The far wake effect is even less than that of the wire perpendicular to the stream, since the drag created is much lower.

Unfortunately, experimental verification of the temperature or velocity fields of a mixed convection plume do not seem to exist. Most experiments are concerned with the total heat transfer (e.g., Gebhart and Pera, 1970; Morgan, 1975), which is the determination of Q. It is hoped that the present paper would encourage some experimental measurements, especially inside the mixed convection plume.

Conclusions

Using the Oseen boundary layer approximation, we have solved the mixed convection plume of thin finite heated wires such as those used in hot-wire anemometry. The method can be applied to other three-dimensional shapes. Of importance is Fig. 3, which gives the range of validity of the parameter α such that the superposition method is applicable.

References

Afzal, N., 1983, "Mixed Convection in an Axisymmetric Buoyant Plume," *International Journal of Heat and Mass Transfer*, Vol. 26, pp. 381–388.

Afzal, N., 1985, "Mixed Convection Plume Above a Point Heat Source in a Vertical Stream," *International Journal of Heat and Mass Transfer*, Vol. 28, pp. 2043–2047.

Appalaswamy, A. V., and Jaluria, Y., 1980, "Axisymmetric Plume Flow in a Vertical Uniform Free Stream," ASME *Journal of Applied Mechanics*, Vol. 47, pp. 667–669.

Crane, L. J., 1977, "The Round Plume Due to a Falling Point Source of Heat," *Journal of Applied Mathematics and Physics (ZAMP)*, Vol. 28, pp. 599–606.

Fujii, T., 1963, "Theory of the Steady Laminar Natural Convection Above a Horizontal Line Heat Source and a Point Heat Source," *International Journal of Heat and Mass Transfer*, Vol. 6, pp. 597–606.

Gebhart, B., Jaluria, Y., Mahajan, R. L., and Sammakia, B., 1988, *Buoyancy-Induced Flows and Transport*, Hemisphere, New York, Chap. 4.

Gebhart, B., and Pera, L., 1970, "Mixed Convection From Long Horizontal Cylinders," *Journal of Fluid Mechanics*, Vol. 45, pp. 49–64.

Glauert, M. B., and Lighthill, M. J., 1955, "The Axisymmetric Boundary Layer on a Long Thin Cylinder," *Proceedings of Royal Society of London*, Vol. A230, pp. 188–203.

Jaluria, Y., 1980, *Natural Convection Heat and Mass Transfer*, Pergamon, Oxford, United Kingdom, Chap. 4.

Morgan, V. T., 1975, "The Overall Convective Heat Transfer From Smooth Cylinders," *Advances in Heat Transfer*, Vol. 11, pp. 199–264.

Rao, K. V., Armaly, B. F., and Chen, T. S., 1985, "Mixed Convection Plumes Arising From a Thermal Point Source," ASME JOURNAL OF HEAT TRANSFER, Vol. 107, pp. 720–722.

Riley, D. S., and Drake, D. G., 1983, "Mixed Convection in an Axisymmetric Buoyant Plume," *Quarterly Journal of Mechanics and Applied Mathematics*, Vol. 36, pp. 43–54.

Rosenhead, L., 1963, *Laminar Boundary Layers*, Clarendon, Oxford, United Kingdom, p. 456.

Wesseling, P., 1975, "An Asymptotic Solution for Slightly Buoyant Laminar Plumes," *Journal of Fluid Mechanics*, Vol. 70, pp. 81–87.

Yih, C. S., 1951, "Free Convection Due to a Point Source of Heat," *Proceedings, 1st U.S. Congress of Applied Mechanics*, pp. 941–947.

Wind Tunnel Experiments on Cooling Tower Plumes: Part 1—In Uniform Crossflow

J. Andreopoulos[1]
Department of Mechanical Engineering,
The City College,
City University of New York,
New York, NY 10031

Measurements of velocity and temperature field and flow visualization results are reported for an ideal case of a cooling-tower plume in the presence of a uniform crossflow for various velocity ratios, densimetric Froude numbers, and Reynolds numbers. Coherent structures in the form of jetlike, wakelike, or mushroom-type vortices have been observed. The type of structure depends primarily on the velocity ratio. As the Reynolds number increases, turbulent structures appear, which have vorticity of the same sign as the partner vortices in the low Reynolds number case. The measurements showed that there is a strong interaction between the bending plume or jet and the wake of the cooling tower, which is basically responsible for the downwash effect. The latter is generally quite strong at low velocity ratios and high Reynolds numbers. High turbulence intensities are produced in the wake of the tower for a distance of 6 to 8 diameters. The plume is diluted faster as the velocity ratio increases and buoyancy decreases. In the wake region of the stack dilution increases with increased buoyancy.

1 Introduction

Cooling-tower systems of large power plants release their heat into the atmosphere either in the form of sensible heat or as a combination of latent and sensible heat. The amount of heat released over a small area can be very large. Thus, there is legitimate concern about the effect of such heat disposal on natural atmospheric processes and about its ecological impact. The most satisfactory method to assess the atmospheric effects of heat release is direct measurement. However, there are great difficulties in obtaining reliable field data. The major difficulty is that the atmospheric conditions change very quickly over the time the experiment is running, i.e., the initial and boundary conditions change rather irregularly. Therefore, it is now generally recognized that laboratory modeling of cooling-tower installations is an effective means of resolving questions related to plume behavior.

There is a great number of experimental studies on cooling-tower plumes in the literature, which reflects the importance in engineering application and atmospheric pollution. Such studies are described by Jain and Kennedy (1980), Mery et al. (1980), Violet (1977), and Slawson and Csanady (1971). In these studies an effort has been made fully or partly to simulate the phenomena as they occur in nature. These phenomena are rather complicated and include: (1) turbulence production, mixing, and transport, (2) buoyancy effects, (3) two phases, i.e., air and water, (4) the influence of the cross-stream atmospheric boundary layer. Policastro et al. (1980) compiled field measurements to evaluate the performance of mathematical models. Their study shows that the available measurements, which included visible plume outline, trajectory, and dilution, were not sufficient for a fair comparison with the existing models and calculation methods.

Few of the abovementioned studies, however, include reliable measurements of turbulence quantities throughout the flow. The aim, therefore, of the current experimental program is to increase the physical understanding of the flow. In addition, the present study has been motivated by the less than completely satisfactory predictive capability of current plume numerical or theoretical models. The absence of turbulence measurements, which are important to complete the picture, considerably hampers the development of calculation methods, since a realistic modeling of the turbulent stresses and heat or mass fluxes requires an understanding of the turbulence processes, especially in the present complex situation of plumes discharged into the atmosphere with the presence of a crossflow. Therefore, an additional aim to that of physical understanding of the flow is to obtain reliable turbulence data throughout the flowfield, which can be used for testing and improving calculation methods.

Along these lines a single-phase experiment has been considered here under neutral atmospheric conditions. A further simplification concerning the model has been made: The plume was issuing into the crossflow from a cylinder stack having a certain height H and diameter D (see Fig. 1), which is not the situation of a natural-draft cooling tower. In this paper, the experimental results are reported for the case of a uniform crossflow while in the accompanying paper by Andreopoulos (hereafter mentioned as paper 2) the results are reported for the nonuniform crossflow case.

In both cases the following effects have been studied:

(*i*) The effects of Reynolds number
(*ii*) The effects of velocity ratio
(*iii*) The effects of the densimetric Froude number.

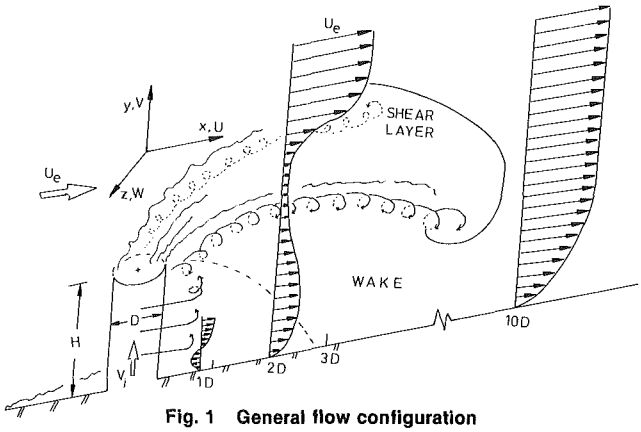

Fig. 1 General flow configuration

[1]Formerly at the Sonderforschungsbereich 80 of the University of Karlsruhe, Federal Republic of Germany.

Contributed by the Heat Transfer Division for publication in the JOURNAL OF HEAT TRANSFER. Manuscript received by the Heat Transfer Division March 11, 1988. Keywords: Flow Visualization, Plumes, Turbulence.

Each of the above parameters was varied while the other two remained constant. The study of the Reynolds number effects shows many important dynamic features in common with isothermal jets, while the study of the velocity ratio R indicated a considerable difference between low and high R plumes. The study of the densimetric Froude number effects was necessary to show how some important characteristics of the plume, like downwash, liftoff, spreading rate, etc., are affected by the stack densimetric Froude number.

The experimental program included a flow visualization study and mean and fluctuating velocity and temperature measurements with multiwire probes and thermocouples.

2 General Flow Configuration

The present flow is quite complicated in nature since it includes interaction of the jet flow, which is developing inside the pipe under circumferentially varying pressure gradient, with the free stream and the wake of the cylinder where the back pressure causes significant streamline curvature. A simplified picture of the jet as conceived from the present investigation, and previous work like that of Mousa et al. (1977), is shown in Fig. 1. The present flow is similar to the jet in the crossflow studies of Foss (1980), Keffer and Baines (1963), Crabb et al. (1981), Komotani and Greber (1972), Ramsey and Goldstein (1971), and Andreopoulos and Rodi (1984). The difference is that in these studies the jet was issuing from a circular outlet on a wall into a cross stream along the wall, while in the case of plumes the jet is issuing from a circular pipe that penetrates the cross stream by a height H.

The jet coming out of the pipe is bent by the cross stream while the latter is deflected by the jet in the normal and lateral direction. An important characteristic of the flow is that the shear layer emanating from the upstream edge of the cylinder is considerably thicker than that emanating from the downstream edge of the cylinder (lee side). The reason is that the former layer grows under the influence of an adverse pressure gradient while the latter is affected by a favorable pressure gradient. In fact, the annular boundary layer in the pipe has nonuniform thickness around the pipe circumference, which is a result of the continuously varying pressure gradient around the exit. Similar behavior has been found by Foss (1980) and Andreopoulos (1982) in the jet in a crossflow case, which can be considered as a limit of the present flow if $H = 0$. In these studies the exits of velocity profiles were found to be considerably distorted. Another similar feature between that flow and the present one is the existence of a pair of bound vortices with a "skew-induced" or pressure-driven secondary flow (Prandtl's first kind), which is due to the initially existing pipe flow vorticity, which is stretched and reoriented to give contributions in the longitudinal direction. The secondary motion induced by these vortices is responsible for the kidney shape of the bent-over jet and decays in the downstream direction under the action of the turbulent stresses.

There is, however, an important difference between the jet in a crossflow and the present one, namely that of the cylinder wake, which is responsible for the so-called "downwash" effect of the plume. This wake of the low aspect ratio cylinder and the bent-over jet interact strongly in a mutual way. There is also a wakelike region due to obstruction of the crossflow by the jet itself that is present in both cases and that seems to interact strongly with the wake of the solid body and to be more predominant than the wake of the cylinder.

There is also a reverse flow region in the wake, which is shown approximately in Fig. 1 as depicted from the flow visualization experiment and from tuft studies. In this region occasionally reverse flow can be expected, but it is not a closed recirculation zone where the instantaneous velocity vector always has a reverse direction. Therefore, it does not preclude certain careful use of the hot wire.

The ground level concentration of stack effluent downwind from a cooling tower is, for obvious reasons, of great importance. It depends on the strength of the downwash effect, which is the capture of stack effluent by the eddies on the lee side of the stack, and on the plume attachment or impingement on the ground. It turns out that the latter depends primarily on the velocity ratio and/or on the Reynolds number of the oncoming crossflow and secondarily on the jet densimetric Froude number. The downwash effect is a result of the flow separation behind the tower, which induces a sufficient under-pressure to bend the plume further downward. This drastically influences the location and the spreading of the plume even in the far field. Slawson et al. (1978) indicated that the far field trajectory can be shifted downward by up to 50 percent by downwash effects. In the near field this separation region causes increased mixing and increased entrainment of ambient fluid, which then entrains the plume. Generally, the flow picture in the wake of the tower is very complicated. Apart from the recirculation on the vertical plane, there is also a recirculation on the horizontal plane, which is caused by the shear layers separated from the external surface of the tower. These shear layers have the plume above them and they interact strongly with it. The present investigation shows that the wake of the plume is stronger than the wake of the tower and therefore, it is expected that some parts of the shear layers may be sucked into the wake of the plume and then entrain the plume.

At higher velocity ratios, neither downwash nor plume ground attachment is expected and the ground level concentrations of stack effluent should, therefore, be practically zero everywhere. At moderate velocity ratios, only downwash and no ground attachment is anticipated. At low velocity ratios, both downwash and plume attachment on the ground are expected.

3 Experimental Setup and Data Reduction

The measurements were made in the closed-circuit wind tunnel at the Sonderforschungsbereich 80, University of Karls-

Nomenclature

D = cooling tower inner diameter
Fr = densimetric Froude number = $V_j/(gD\,\Delta\rho/\rho_e)^{1/2}$
g = gravitational acceleration
H = cooling tower height above ground
R = velocity ratio = V_j/U_e
Re = Reynolds number = $U_e D/\nu$
$1/2\overline{q^2}$ = turbulent kinetic energy = $1/2\,(\overline{u^2} + \overline{v^2} + \overline{w^2})$
T = temperature
$\bar{U}, \bar{V}, \bar{W}$ = mean velocity components in x, y, z directions
u, v, w = velocity fluctuations about mean value
x, y, z = system of coordinates
β = volumetric expansion coefficient
Ω = vorticity vector

Subscripts

e = values at free stream of crossflow
j = values inside cooling tower

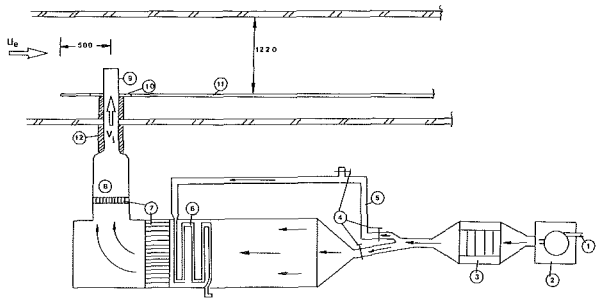

Fig. 2 Experimental arrangement: (1) flow valve; (2) two-stage compressor; (3) resistor box; (4) flow rate control valves; (5) bypass pipe; (6) heat exchanger; (7) flow straighteners; (8) settling chamber; (9) cylindrical cooling tower model; (10) turntable; (11) flat plate; (12) thermal insulation

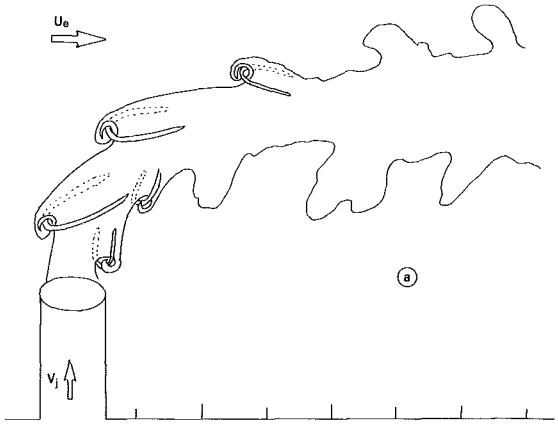

Fig. 3 Flow sketches for $R = 2.8$, Re = 2400, Fr = ∞

ruhe, which has an octagonally shaped working section 6 m long and 1.5 m in diameter, with an adjustable roof set to give zero pressure gradient. The experimental setup is illustrated in Fig. 2. A 6-m-long flat plate was installed 0.28 m above the tunnel floor. The size of the model was determined through a procedure described in Appendix A and selected to be 80 mm in internal diameter. This gave a geometric scale between the full size tower and the model of the order of 1:1000.

The jet/plume flow was supplied by the two-stage compressor 2 as shown in Fig. 2. The air flow leaving the compressor was heated in the box 3 by means of electrical resistors of total installed power of 19 kW. The resistors were controlled through automatic relays by the air flow valve 1 positioned at the compressor inlet. If the flow rate was extremely low, the resistors were automatically switched off to protect the installation from burning. To achieve high buoyancy forces, however, extremely high temperature and very low speeds were required. This was made possible by bypassing part of the flow to the heat exchanger 6 through the pipe 5. The valves 4 were used to control the flow rate in the model while the compressor was supplying air at the maximum rate. The whole heated-air supply was thermally insulated. A honeycomb 7 was used at two positions as flow straighteners. The last part of the model was made of brass pipe 2.5 mm thick and it was rotatable. Two models were used and their dimensions are shown in Table 1, together with the flow parameters. A total of five experiments have been carried out with different velocity ratios R, Reynolds numbers Re, and Froude numbers Fr. These experiments are intended to show the influence of the abovementioned parameters on the hydrodynamic field. Although the range of these parameters is rather limited, the results indicate that it is large enough to demonstrate significant changes in the flow structure.

Mean velocities and turbulence measurements were made with Constant Temperature Anemometers (CTA), DISA type 55M01, and home-made subminiature triple hot-wire probes with 5-μm wires. An effort has been made to keep the dimensions as small as possible. The probe consists of three single probes that have been constructed from ceramic tubes and stainless steel prongs.

Mean temperature and fluctuations were measured with a 1-μm "cold wire" mounted on probes clamped to the side of the triple-wire probe. The multiwire probe has a spatial resolution of 1.8 mm. The cold wire was operated by a Constant Current Anemometer (CCA), DISA type 55M01, with a temperature bridge. The heating current was not more than 0.15 mA and the temperature sensitivity was at least two orders of magnitude greater than the velocity sensitivity in all cases. The material of the wire was P1 + 10 percent Rd and its resistivity coefficient was measured to be between 0.00169 and 0.00170°C^{-1}. A typical value of the temperature sensitivity of a wire with $R = 70.52$ ohm at 20°C was 80 mV/°C. The noise level of the anemometer was of the order of 40 mV, which represents a temperature resolution no less than 0.5°C. Bearing in mind that the total initial temperature difference was roughly 110°C, this value of temperature resolution is very satisfactory. End-conduction effects were considered to be negligible because the length l over the diameter d of the wire was larger than 1000 (see Smits et al., 1978, and Lecordier et al., 1982). As a bonus the uncompensated frequency response of the anemometer increased to about 1.2 kHz and therefore, no further compensation was applied.

The four signals were digitized and stored on magnetic tapes for later data reductions. Thus, the instantaneous three velocity components *and* temperature were available simultaneously. The characteristic frequency of the large eddies was of the order of V_j/D, i.e., between 15 and 125 Hz, while the upper frequency limit is set by the spatial resolution of the probe, which was of the order of 1 to 2 kHz. Estimates of the viscous scales of the flow based on the dissipation rate of the turbulent kinetic energy, which was obtained by difference from the corresponding transport equation, indicated that the Kolmogorov length scale and passage time were of the order of 0.3 mm and 6 ms respectively. The Batchelor scale or temperature microscale is of the same order as the Kolmogorov length scale since the Prandtl number for air is close to 1.

All calibrations, which include velocity calibration, pitch and yaw calibration of the triple wire, and temperature calibration of the cold wire have been performed "in situ" and "on line" with the HP-1000 computer. It is, therefore, expected that gain problems are not present here.

The results include profiles of mean velocity and temperature, turbulent kinetic energy, shear stresses, and velocity-temperature correlations.

Finally, a flow visualization experiment has been carried out. The plume was visualized by introducing a fog of paraffin-oil droplets into the plenum chamber through a row of holes on a tube spanning the chamber width. The overpressure was small enough to ensure laminar flow. The photographic records were obtained with a cine-camera BOLEX model H-16 reflex with a rate of 46 frames per second. Negative prints have been also obtained from the cine-film and some of them are presented in Figs. 4 and 5.

Only a selection of the measured profiles and the flow visualization pictures will be presented here; further details are available in the departmental reports by Andreopoulos (1986a, 1986b).

4 Results

4.1 Instantaneous Structure. The flow visualization indicated the existence of coherent structures in the present flow for the first time. The type of structures depends primarily on the velocity ratio R.

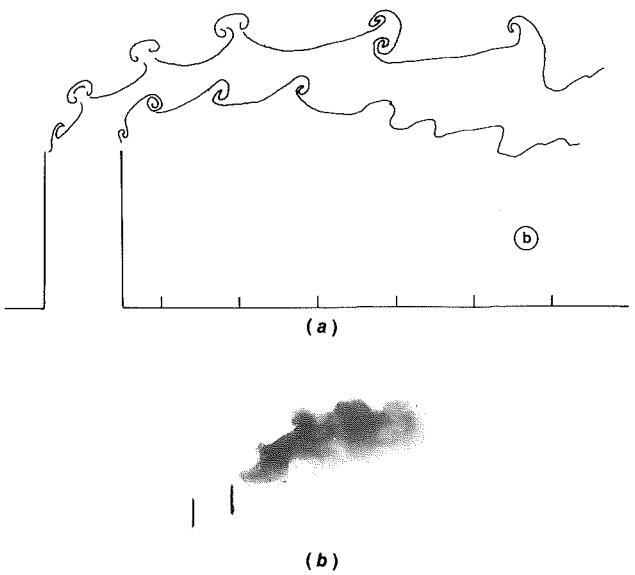

Fig. 4 (*a*) Flow sketch for the $R = 1$ case; (*b*) flow visualization of the $R = 1$, Re = 66,000, and Fr = ∞ experiment

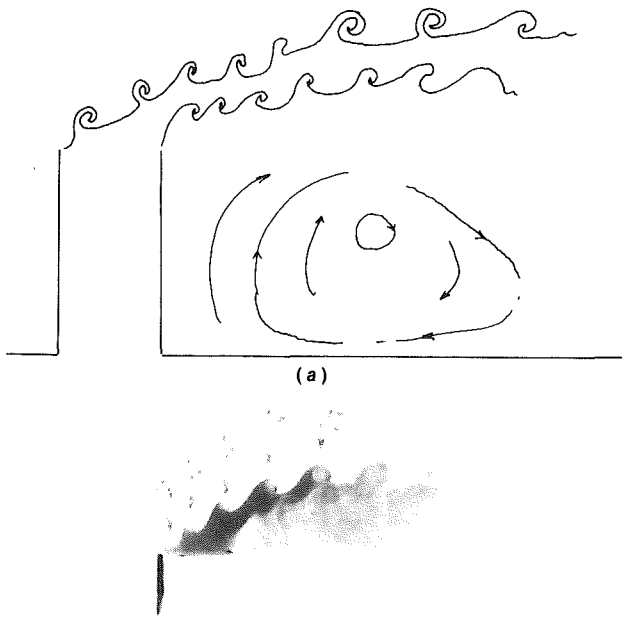

Fig. 5 (*a*) Flow sketch for the $R < 1$ case; (*b*) flow visualization of the $R = 0.2$, Re = 5800, and Fr = ∞ experiment

Figure 3 shows the observed flow structure for the case of $R \simeq 2.8$. The shear layers coming out of the pipe roll up at two different locations, i.e., at the upwind side and at the lee side of the pipe. If Ω_z is the vorticity of these rollings on the x-y plane, then Ω_z is positive in the vortices at the upwind side of the jet and negative in the vortices at the lee side of the jet. Although the vorticity of these rollings has the same sign as the vorticity of the layer inside the pipe, they do not belong to the same vortical ring, but they belong to two different vortices that are open at their legs, similar to those observed by Perry and Lim (1978) in their neutral buoyant jet and by Andreopoulos (1985) in the case of a jet in a crossflow. These vortices have jetlike structures and are a result of an instability phenomenon. The existing vorticity of the boundary layer inside the pipe plays a significant role in the formation of the vortices observed in these experiments. This vorticity is of the order V/δ where δ is the boundary layer thickness and V is a typical velocity just outside the boundary layer. Both V and δ were not uniformly distributed across the pipe exit. The boundary layer thickness δ was much smaller in the lee side of the pipe than in the upstream side while the opposite is true for the velocity V. Since the vorticity is proportional to δ^{-1} it may be expected that the existing vorticity in the pipe is greater in the lee side of the jet than in the upwind.

It is observed that the vortices at the upwind side of the jet are formed with the same frequency as the vortices on the lee side of the jet but with a considerable phase lag. The vortices on the lee side of the jet disappear very quickly while the others on the upwind side of the pipe persist much longer before they break down to turbulence. There are two reasons for this behavior: First, the streamlines in the wake region just behind the jet converge toward the plane of symmetry, resulting in a strongly negative gradient $\partial \bar{W}/\partial z$, which compresses the vortex lines and thus reduces the vorticity of the vortex; second, an important reason for weakening this vorticity is the strong turbulence in the wake of the cylinder and in the wake of the jet. Both effects contribute to the disappearance of the vortices on the lee side of the jet.

As the velocity ratio R is reduced, the flow structure changes significantly. Figures 4(*a*) and 4(*b*) show the instantaneous flow structure for $R = 1$. One striking feature of this flow is the appearance of mushroom-type vortices that are very regular. These vortices seem to be a result of superposition of vorticity shed from the inner surface of the pipe (i.e., originating from the shear layer inside the pipe) and vorticity of opposite sign, which exists in the crossflow shear layer separated from the outer surface of the pipe.

In this experiment wakelike vortices appear first on the upwind side of the pipe. These structures carry negative vorticity, i.e., opposite to that of the pipe flow. As they travel downstream another vortex is formed right behind them so that both appear to be on a mushroom-type vortical structure, which travels downstream.

At lower velocity ratios R, the flow pattern changed drastically. Figures 5(*a*) and 5(*b*) show a sketch and a flow visualization picture of the flow with $R = 0.2$. A row of wakelike vortices is formed in the upwind side of the pipe.

A row of jet-type vortices was also observed in the lower side of the jet. Pairing took place between two of them in the same row as well as between one of the lower row and one of the upper row of vortices.

As the Reynolds number increases (with R kept constant) the basic structure of the flow remain the same, but there is a considerable jitter among them.

Smoke was also observed to recirculate intermittently in the near-wake zone, for the small velocity ratio cases. The position of the center of this recirculation zone, which is not a closed recirculation zone, in the longitudinal direction depends strongly on the Reynolds number Re, while its position from the wall is a function of the velocity ratio. As the Reynolds number increases the center is formed closer to the pipe, while as the velocity ratio decreases it moves upward.

4.2 Time-Averaged Structure.

4.2.1 Mean Velocities. Figures 6(*a*) to 6(*c*) show the mean velocity vectors on the plane of symmetry $z/D = 0$ (where $W = 0$) for three of the five experiments shown in Table 1 at various downstream stations. The present flow is dominated by the mutual interaction of two low-pressure fields: the wake behind the bending-over jet and the wake of the cylinder. Their relative strength determines the general flow picture. There are two characteristic features that affect these two pressure fields and that ought to be mentioned: The higher the plume or the jet that penetrates the cross stream, the lower the pressure in the wake of the jet. This behavior has been verified in the jet-in-a-crossflow study of Andreopoulos (1982) where the wall static pressure has been measured for various velocity ratios.

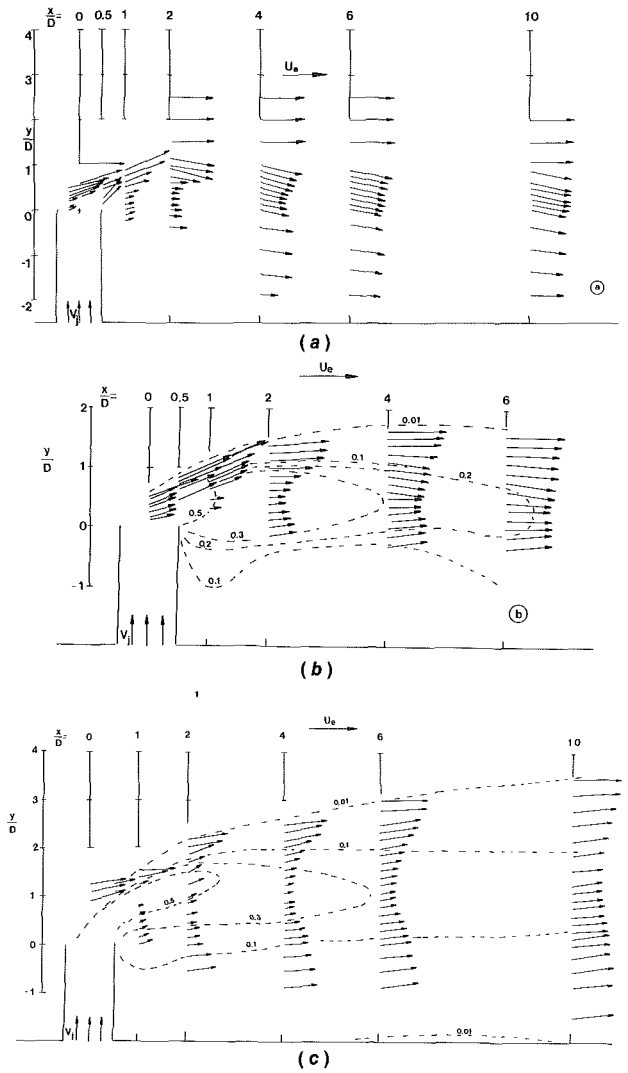

Fig. 6 (*a*) Mean velocity vectors on the plane of symmetry for the UFH1 experiment; (*b*) mean velocity vectors on the plane of symmetry for the UFH2 experiment; (*c*) mean velocity vectors on the plane of symmetry for the UFH4 experiment. Dotted lines: isotherms.

Similar arguments can be invoked for cylinders in a cross stream: the higher the aspect ratio of the cylinder, the stronger the low pressure in the wake.

Figure 6(*a*) gives the mean velocity vectors for the UHF1 experiment, which represents the highest Reynolds number case studied in the present investigation. The most important characteristic of this case is the downwash inclination of all velocity vectors downstream of the $x/D = 2$ location. This is not surprising since the bending over of the jet is considerably helped by the strong negative pressure in the near wake of the cylinder. It seems that, in this case, the wake of the cylinder dominates the flow behavior in the near field since it is stronger than the wake of the bending-over jet. As the Reynolds number decreases, the situation remains qualitatively the same but with large quantitative differences. This is shown in Fig. 6(*b*) where the mean velocity vectors are plotted for the UFH2 experiment, which has rather small buoyancy effects and the same velocity ratio as the UFH1 experiment but with considerably smaller Reynolds number. From Fig. 6(*b*) it is obvious that the vectors start to have a downwash inclination at $x/D = 4$ roughly, a distance larger than that of the flow of Fig. 6(*a*). This is in accordance with the general rule that indicates that length scales are reduced with increasing Reynolds number.

It seems that in the case of the UFH1 experiment the underpressure or rather the pressure coefficient in the wake of the cylinder is much lower than in the case of the UFH2 experiment for two reasons: first, because the aspect ratio of the cylinder is 25 percent higher in the UFH1 case than in the UFH2 experiment, and second, because the Reynolds number is higher. As a result of these two reasons, the bending over of the jet is faster in the UFH1 experiment than in the UFH2 experiment. In the latter experiment, the underpressure in the wake of the cylinder is weaker and seems that the low pressure in the wake of the bending over jet dominates the flow behavior. Apart from their low pressure, both wakes are characterized by strong acceleration of the flow in this region, which causes the fluid to rush to "fill" the wake. Thus, any nonzero inclination of the mean velocity vectors can be attributed to "filling" the wake effects and/or to low pressure effects. A few examples of these effects can be mentioned here: the upward motion at $x/D = 1$ in the wake of the cylinder in the UFH1 experiment (Fig. 6*a*) and at almost all downstream stations in the UFH2 experiment (Fig. 6*b*), is caused by the crossflow "filling" the wake of the bending over jet itself. The wake of the cylinder requires also "filling" by the cross flow. This is evident in the downstream profiles of Fig. 6(*a*) where the velocity vectors below the height of the exit plane increase with downstream distance.

Figure 6(*c*) shows the mean velocity vectors of the UFH4 experiment, which has a considerable amount of buoyancy forces. The Reynolds number and the velocity ratio R are roughly the same as those of the UFH2 experiment. Consequently, Fig. 6(*c*) should be directly compared to Fig. 6(*b*). There are two striking features in Fig. 6(*c*): One is the deeper penetration of the buoyant jet in the cross stream, which results in smaller velocities than the partner nonbuoyant flow (UFH2 experiment) because the jet is spread into larger regions in the y direction. The second feature is that almost all the velocity vectors are inclined upward even in regions close to the ground, where everything has been lifted off due to the low pressure in the wake of the jet and to the flow "filling" the wake of the jet as the conservation of the mass flow requires.

It seems that the wake of the jet is much stronger than the wake of the cylinder because the plume penetrates into the crossflow deeper, and therefore dominates the flow. Another reason for the upwash inclination of the velocity vectors is the secondary flow induced by the "bound" vortex is stronger when the plume penetrates the cross flow deeper.

The present measurements and the flow visualization did not show any recirculating fluid in the wake of the jet having a counterclockwise rotation. However, such a recirculation has been found in the experiments of Violet (1979) as well as in the calculations of Demuren and Rodi (1984) for $R = 1.7$ only. This ties up with the previously mentioned observation of the present study that the wake effects of the plume or jet become much stronger when the jet or plume penetrates the cross stream deeper, as is the case with high velocity ratio or strong buoyancy. At lower velocity ratios the calculations show characteristics similar to those observed in the present experimental investigation.

4.2.2 Mean Temperatures. Mean temperature is probably one of the most reliable quantities to measure even in regions of high turbulence intensities, such as the wake region behind the cylinder, because temperature is a scalar quantity and because temperature probes are more or less insensitive to flow direction. The latter may be important for an intrusive method of measuring temperature since such a probe can affect the flow field, which in turn alters the thermal field. To ensure that such effects are negligible, the probe has been yawed and pitched quite a few times without any significant change in mean temperature.

Figures 7(*a*) and 7(*b*) show some contours of isotherms plotted from the mean temperature measurements of the UFH2,

UFH3, UFH4, and UFH5 experiments. The isotherms correspond to values of the measured excess temperature $T - T_e$ normalized by the initial temperature difference $T_j - T_e$. Figure 7(*a*) shows the results of the UFH2 and UFH4 experiments with $R = 0.5$ and Fig. 7(*b*) contains the isotherms of the UFH3 and UFH5 experiments with $R = 0.2$. These results indicate that the plume is diluted faster as the velocity ratio increases and the Froude number increases (buoyancy decreases). In the wake region, however, dilution is high with higher buoyancy.

There is also evidence from these figures that the downwash effect is larger in Fig. 7(*b*). This indicates that this effect is stronger at low velocity ratios and high Froude numbers. In Fig. 7(*b*) Violet's (1977) results are plotted for comparison with the present results of the same velocity ratio R. His results, however, have been obtained at Fr = 0.8. Therefore, it is expected that his plume should have penetrated more into the cross stream than the present plume, with Fr = 3.3. However, this is not the case. There are several reasons for this disagreement. The first reason is that their boundary layer developed by the cross stream over the flat plate was very thick, of the order of $1H$. This could cause a faster spreading of the lower part of the plume. The second reason is that his model had an aspect ratio $H/D = 1.64$, which is smaller than the present one of 2, a fact that causes weaker low pressure in the wake of the cylinder. The third reason is the difference in Reynolds number. Their Reynolds number was 40,000 while the present one was only 15,500. In fact, the present experiment UFH1 showed that the higher the Reynolds number the stronger the downwash effect, i.e., the bending over of the jet takes place more quickly as the Reynolds number increases. The last reason is the internal inconsistencies of their data. Their concentrations obtained at low Reynolds numbers and at large streamwise distances are about 10 percent lower than those measured at high Reynolds numbers. It appears, therefore, that the disagreement between the present results and those of Violet (1977) is due to a combination of the above effects.

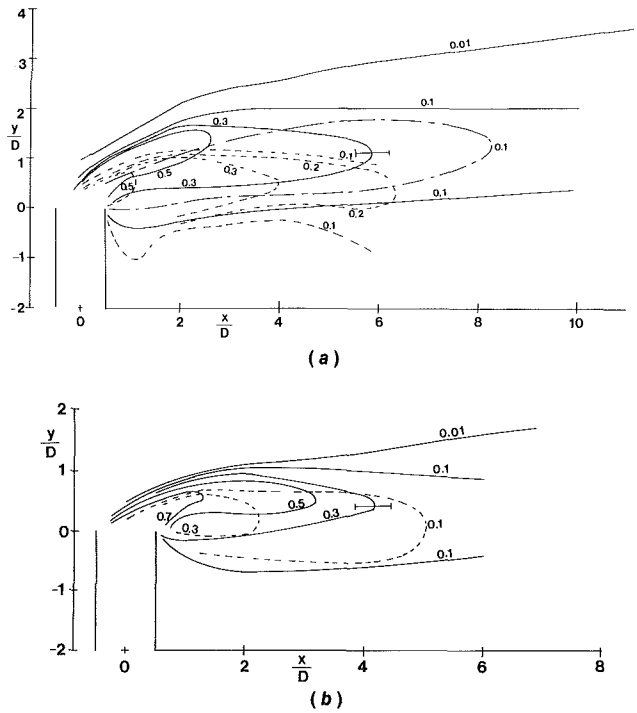

Fig. 7 (*a*) **Contours of isotherms at** $z/D = 0$: ——, **UFH2 experiment;** ·····, **UFH4 experiment;** —·—, **Violet (1977) experiment;** (*b*) **contours of isotherms at** $z/D = 0$: ——, **UFH3 experiment;** ·····, **UFH5 experiment**

The present results indicate that dilution of the plume is strongly affected by the velocity ratio R and buoyancy. Dilution is defined as the inverse of the normalized excess temperature. The downstream extent of the isotherms and the area they confine indicate the ability of the plume to dilute its initial concentration of smoke or other species. A comparison between the UFH2 and UFH4 data indicates that dilution decreases with increased buoyancy. The same conclusion can be reached by looking at the isotherms. They clearly indicate that increased buoyancy reduces the dilution of the plume, except in the region of the wake of the cylinder, where the data show that the plume dilution is increased by buoyancy. This result is in contrast to the observed behavior in vertical buoyant jets (see Chen and Rodi, 1980). It can be attributed to the interaction of the bent-over plume or jet with its wake and the wake of the cylindrical stack. Both wakes are regions of high turbulence intensities that affect the heat transfer in the lower extent of the plume or jet by changing the lateral/normal diffusion and the entrainment rate. This interaction is strong when the penetration of the jet or plume into the cross stream is small. Therefore it is not surprising that dilution increases with decreasing buoyancy for small velocity ratios. As the velocity ratio increases the flow penetrates more into the cross stream and the jet-wake interaction is weaker than in the cases of small R. Thus a change in the abovementioned dependency of the dilution on buoyancy may be expected.

4.2.3 Turbulent Kinetic Energy. The most characteristic turbulent quantity is the turbulent kinetic energy $1/2\,\overline{q^2}$, which is plotted in Figs. 8(*a*) to 8(*c*) for three of the experimental cases shown in Table 1.

The experimental results of the UFH1 experiment are shown in Fig. 8(*a*). The first two profiles look like the distribution of $\overline{q^2}$ in a pure shear layer. However, the distribution of $\overline{q^2}$ is governed by an interaction of different mechanisms of production through various mean velocity gradients, notably $\partial\bar{U}/\partial y$, $\partial\bar{V}/\partial x$, $\partial\bar{W}/\partial z$, $\partial\bar{U}/\partial z$, and by mean and turbulent transport from the upstream pipe flow. It appears, however, that in the region above the exit the production due to the mean velocity gradient $\partial\bar{U}/\partial y$ is the dominant process because $\overline{q^2}$ has a maximum around the position of maximum $\partial\bar{U}/\partial y$.

At the downstream stations $x/D = 1$ and 2 a second peak in $\overline{q^2}$ starts to develop inside the wake of the cylinder, which grows up very quickly at further downstream positions. Between the two peaks, there is a region of lower turbulence kinetic energy, which corresponds to the minimum of the mean velocity distribution in the wake of the plume. However, this region seems to disappear at the next station $x/D = 4$, where

Table 1 Flow parameters for the hot-wire measurements

Experiment	H, mm	D, mm	$\frac{H}{D}$	U_e, m/s	V_j, m/s	$R = \frac{V_j}{U_e}$	$\mathrm{Re} = \frac{U_e D}{\nu} \times 10^5$	T_e, °C	T_j, °C	$\mathrm{Fr} = \frac{V_j}{\sqrt{gD\,\Delta T/T_j}}$
UFH1	200	80	2.5	21	10.5	0.5	1.11	20	20	∞
UFH2	160	80	2.0	2.58	1.29	0.5	0.135	20	28.55	8.681
UFH3	160	80	2.0	6.48	1.29	0.2	0.339	20.2	29.1	8.624
UFH4	160	80	2.0	2.96	1.48	0.5	0.15	19.7	121.0	3.295
UFH5	160	80	2.0	7.50	1.5	0.2	0.332	20.0	132.0	3.22

the outer peak is hardly distinguishable, while at $x/D = 6$ it has completely disappeared. Since the turbulent kinetic energy produced in the wake seems to be twice as much as that produced in the shear layer a great part of the wake turbulence is expected to diffuse outward in the normal direction.

At $x/D = 1$ one more peak is evident at about $y/D \simeq 0$, followed by a change of sign in $\overline{uv}$ (not shown here). This may be attributed to the shear layer emanating at the downstream edge of the cylinder where the shear stress is positive. The turbulent kinetic energy reaches a maximum at $x/D = 4$ in the wake region and then it starts to decay continuously. Profiles of $\overline{q^2}$ at $z/D = -0.5$ are also shown in Fig. 8(*a*). At $x/D = 2$, two peaks are distinct. The first one, in the shear layer region, is associated with the velocity gradient $\partial\bar{U}/\partial y$, while the second takes place in a region where $\partial\bar{U}/\partial y$ is very small. In general, the $\overline{q^2}$ profiles off the plane of symmetry at $x/D = 2$ are much larger than those at the plane of symmetry $z/D = 0$. In fact the second maximum in the wake region is about 70 percent larger than that at $z/D = 0$. These high values of q^2 in the region of the cylinder wake are due to the high velocity gradient $\partial\bar{U}/\partial z$ and the $\overline{uw}$ correlation. The term $\overline{uw}\ \partial\bar{U}/\partial z$ is zero on the plane of symmetry and out of this plane can reach values up to $10^{-2}\ U_e^3/D$. It seems, therefore, plausible that this large production is transported by diffusion toward the plane of symmetry and then upward toward the wake of the jet or directly upward.

Similar features indicate the profiles of $\overline{q^2}$ of the UFH2 experiment shown in Fig. 8(*b*), although measurements inside the wake region of the cylinder have not been extended. The peak on the shear layer side is slightly larger in magnitude than that of the UFH1 experiment, which may be attributed to Reynolds number effects. A minimum can be also observed in the region of the wake of the plume, which does not persist more than $2D$ downstream. It seems that this minimum is a result of small production by $\partial\bar{U}/\partial y$ and increased destruction by $\partial\bar{U}/\partial z$, which is positive but with $\overline{u^2} > \overline{v^2}$. At the same time, the streamline convergence on the zox plane associated with the $\partial\bar{W}/\partial z$ gradient suppresses turbulent production too.

Farther downstream $\partial\bar{W}/\partial z$ becomes weaker while $\partial\bar{U}/\partial x$ is still significant. It therefore seems plausible that the main reason for the disappearance of this low $\overline{q^2}$ region is an excessive diffusion of turbulent kinetic energy coming out from the wake of the cylinder.

For the UFH4 experiment with significant buoyancy the $\overline{q^2}$ profiles are shown in Fig. 8(*c*). As in the case of the mean velocities, the $\overline{q^2}$ profiles do not vary much with longitudinal distance. The double peak behavior of the $\overline{q^2}$ profiles, which seems to persist more than $6D$ in the downstream direction, is associated with the $\partial\bar{U}/\partial y$ and $\partial\bar{U}/\partial z$ gradients. The peak in the wake of the cylinder is slightly larger than the same peak in the UFH1 experiment behavior, which is due to Reynolds number effects.

The effects of buoyancy on $\overline{q^2}$ can be characterized as direct and indirect. A direct effect on the turbulent kinetic energy production is the extra term of production due to buoyancy, namely $\beta g\overline{v\vartheta}$, which represents an exchange between $\overline{q^2}$ and potential energy. The increase of length scale and spreading indirectly affect turbulence production, since they alter first the velocity gradients, which in turn affect the production of $\overline{q^2}$ by shear. This seems to be the reason why the peak on the outer shear layer in the UFH4 experiment is considerably smaller than the peak in the UFH2 experiment. Buoyancy decreases the $\partial\bar{U}/\partial y$ gradient, which turns out to be the major contributor to the turbulent kinetic energy production despite the fact that the situation in this part of the plume in terms of stratification is unstable, and therefore, direct effects of buoyancy should be important because $\partial\bar{T}/\partial y < 0$.

A detailed discussion of the behavior of all the terms appearing in the transport equation of turbulent kinetic energy

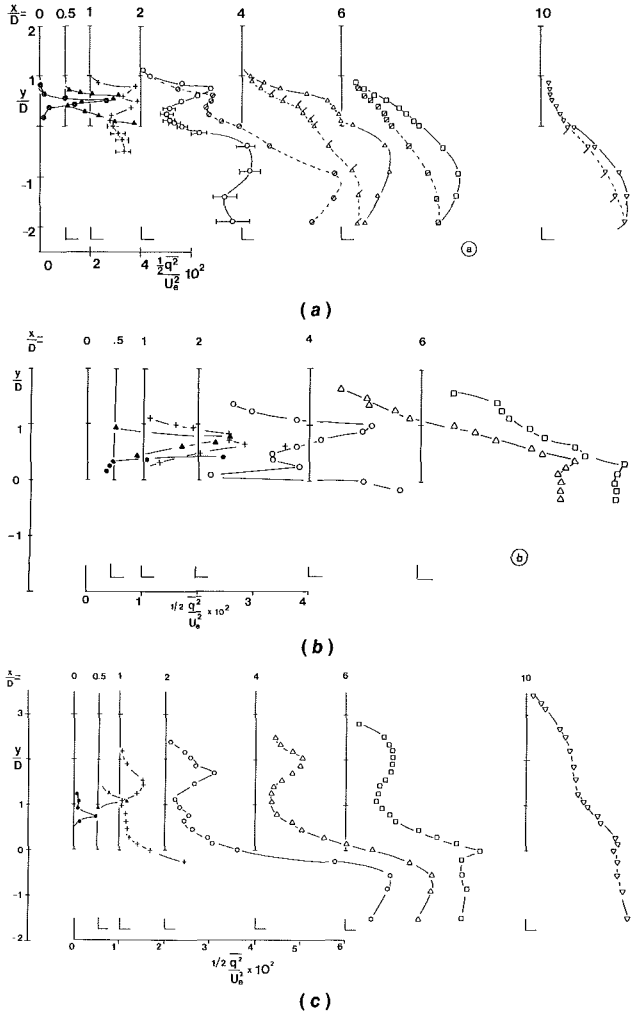

Fig. 8 (*a*) Turbulent kinetic energy profiles for the UFH1 experiment; symbols: •, $x/D = 0$; ▲, $x/D = 0.5$; +, $x/D = 1$; ○, $x/D = 2$; Δ, $x/D = 4$; □, $x/D = 6$; ▽, $x/D = 10$; solid line through symbols: $z/D = 0$; dotted line through symbols: $z/D = 0.5$ (flagged symbols); (*b*) turbulent kinetic energy profiles for the UFH2 experiment (symbols as in Fig. 8*a*); (*c*) turbulent kinetic energy profiles for the UFH4 experiment (symbols as in Fig. 8*a*)

that have been estimated from the present measurements is given in the reports by Andreopoulos (1986a, 1986b).

5 Conclusions

The present detailed measurements and flow visualization studies on the behavior of jets or plumes issuing into a cold cross stream through a cylindrical protrusion establish and document the flow dependence on the velocity ratio R, the Froude number Fr, and the Reynolds number Re. Coherent structures in the form of vortices have been observed in the present flow without any externally imposed excitation and classified, for the first time, according to the velocity ratio. In flows with $R > 1$ jetlike vortices appear in the upstream side of the cylindrical stack and remain well organized for the distance of a few diameters before breakdown to turbulence. For $R < 1$ wakelike vortices are formed, and for $R \simeq 1$ heterostrophic vortices in the form of a mushroom are present. While this describes the structure of the flow in the outer edge of the bending-over jet, jetlike vortices are formed in the lower edge of the jet, which break down to turbulence very soon due to the turbulence in the wake of the stack or the jet and to the vortex-line compression.

As the Reynolds number increases beyond the value of 6000, turbulent structures appear, which carry vorticity of the same sign as the partner vortices in the low Reynolds number case

of the same velocity ratio. The vorticity in these structures and/or vortices is attributed to a reorientation stretching or diffusion of the original pipe flow vorticity and also to vorticity of the shear layer separated from the outer surface of the cylindrical stack. Finally, pairing seems to be the mechanism for growing of the vortical structures or vortices.

The measurements showed that there is a strong interaction between the bending-over jet, its wake, and the wake of the cylinder. The low pressure in these wakes induces a lateral inward motion and also a downwash of the bent-over plume or jet. The latter, known as the downwash effect, is quite strong at low velocity ratios and high Reynolds numbers.

For all velocity ratios a shear layer with significant gradients of the streamwise velocity forms above the wake. As one proceeds downstream, the wake is "filled up" by the inward motion and the velocity gradients in the shear-layer and wake regions become smaller. High turbulent kinetic energy is produced in the wake of the cylinder, which is diffused toward the plane of symmetry and upward. This is due to high values of the lateral gradient of the longitudinal mean velocity component. Buoyancy production has a stabilizing effect in the wake region of the cylinder and it has a destabilizing effect, i.e., enhances turbulence production, at $y/D > 0$. The indirect effects of buoyancy are also large: The mean temperature and velocity profiles are dramatically changed by buoyancy. The spreading rate increases with buoyancy and the plume is diluted faster as the velocity ratio and buoyancy decrease. In the tower wake, increased buoyancy increases plume dilution.

Acknowledgments

The financial support of the Deutsche Forschungsgemeinschaft is gratefully acknowledged.

References

Andreopoulos, J., 1986a, "Wind Tunnel Experiments on Cooling Tower Plumes. Part I," Report No. SFB 210/E/18, University of Karlsruhe, Federal Republic of Germany.

Andreopoulos, J., 1986b, "Wind Tunnel Experiments on Cooling Tower Plumes. Part II," Report No. SFB/E/19, University of Karlsruhe, Federal Republic of Germany.

Andreopoulos, J., 1985, "On the Structure of Jets in a Cross-Flow," *J. Fluid Mech.*, Vol. 157, pp. 167–197.

Andreopoulos, J., 1982, "Measurements in a Jet-Pipe Flow Issuing Perpendicularly Into a Cross Stream," ASME *J. Fluid Engrg.*, Vol. 104, pp. 493–499.

Andreopoulos, J., and Rodi, W., 1984, "Experimental Investigation of Jets in a Crossflow," *J. Fluid Mech.*, Vol. 138, pp. 93–127.

Chen, C. J., and Rodi, W., 1980, *Vertical Turbulent Buoyant Jets*, Pergamon Press, New York.

Crabb, D., Durao, D. F. G., and Whitelaw, J. H., 1981, "A Round Jet Normal to a Cross Flow," ASME *J. Fluids Engrg.*, Vol. 103, pp. 142–152.

Demuren, A. O., and Rodi, W., 1984, "Three Dimensional Numerical Calculations of Flow and Plume Spreading Past Cooling Towers," 4th IAHR Cooling Tower Workshop, Interlaken, Oct. 1–5.

Jain, S., and Kennedy, J. F., 1980, "Physical Modeling of Cooling Tower Plumes," I.A.H.R. Cooling Tower Workshop, Sept. 21–25.

Foss, J., 1980, "Interaction Region Phenomena for the Jet in a Cross-Flow Problem," Rept. SFB 80/E/161, University of Karlsruhe, Federal Republic of Germany.

Keffer, J. F., and Baines, W. D., 1963, "The Round Turbulent Jet in a Cross Wind," *J. Fluid Mech.*, Vol. 15, pp. 481–496.

Komotani, Y., and Greber, I., 1972, "Experiments of Turbulent Jet in a Cross Flow," *AIAA J.*, Vol. 10, pp. 1425–1429.

Lecordier, J. C., Paranthoen, P., and Petit, C., 1982, "The Effect of the Thermal Prong-Wire Interaction on the Response of a Cold Wire in Gaseous Flows," *J. Fluid Mech.*, Vol. 124, pp. 457–473.

Maskell, E. C., 1965, "A Theory on the Blockage Effects of Bluff Bodies and Stalled Wings in a Closed Wind Tunnel," ARC R@M 3400.

Mery, P., Caneill, J. Y., Hodin, A., and Saab, A., 1980, "Dry Cooling Towers, Thermodynamic and Microphysical Impact of a 1000 MW Source Released in the Atmosphere," I.A.H.R. Cooling Tower Workshop, Sept. 21–25.

Morrison, G. L., 1974, "Effects of Fluid Property Variations on the Response of Hot-Wire Anemometers," *J. Physics E: Sci. Instrum.*, Vol. 7, pp. 434–436.

Moussa, Z. M., Trischka, J. W., and Eskinazi, S., 1977, "The Near Field in the Mixing of a Round Jet With a Cross Stream," *J. Fluid Mech.*, Vol. 80, pp. 49–80.

Perry, A. E., and Lim, T. T., 1978, "Coherent Structures in Coflowing Jets and Wakes," *J. Fluid Mech.*, Vol. 88, pp. 451–463.

Perry, A. E., Lim, T. T., and Chong, M. S., 1979, "Critical Point Theory and Its Application to Coherent Structures and the Vortex Shedding Process," Rept. FM-11, University of Melbourne, Australia.

Policastro, A. J., Carhart, R. A., Ziemer, S. E., and Haake, K., 1980, "Evaluation of Mathematical Models for Characterizing Plume Behavior From Cooling Towers," NUREG/CR-1581, Vol. 1, RB, R6.

Rae, W. H., and Pope, A., 1984, *Low Speed Wind Tunnel Testing*, Wiley, New York.

Ramsey, J. W., and Goldstein, R. J., 1971, "Interaction of a Heated Jet With a Deflecting Stream," ASME JOURNAL OF HEAT TRANSFER, Vol. 93, pp. 365–372.

Slawson, P. R., Coleman, J. H., and Frey, J. W., 1978, "Natural Draft Cooling Tower Plume Behavior at Paradise Steam Plant," Tennessee Valley Authority, Chattanooga, TN.

Slawson, P. R., and Csanady, G. T., 1971, "The Effect of Atmospheric Conditions on Plume Rise," *J. Fluid Mech.*, Vol. 47, pp. 33–49.

Smits, A. J., Perry, A. E., and Hoffman, P. H., 1978, "The Response to Temperature Fluctuations of a Constant-Current Hot-Wire Anemometer," *J. Physics E: Sci. Instrum.*, Vol. 11, pp. 909–914.

Viollet, L., 1977, "Etude de Jets dans des Courants Traversiers et dans des Millieux Stratifies," Report Electricite de France, Chatou, France.

Vrettos, N., 1984, "Experimentelle Untersuchung der Ausbreitung von Kuhlturmschwaden in Windkamal," Diplomarbeit, Institut fur Hydromechanik, University of Karlsruhe, Federal Republic of Germany.

APPENDIX

The size of the model was determined by considering the following requirements for the flow: First, a Reynolds number of the order of 10^4 should be achieved; second, a low densimetric Froude number flow should also be accomplished; third, the velocity ratio should be in the range $0.2 \leq R \leq 0.5$; fourth, distortion of the near and far field of the flow due to blockage should be minimal. In addition to these requirements a restriction on the maximum temperature difference had to be applied for safety reasons: $\Delta T = T_j - T_e = 110°C$ and therefore $\Delta T/T_j = 0.848$ for $T_e = 20°C$. The variation of Fr^2 with the pipe diameter D is shown in Fig. A1 for various values of U_e. On each of these lines the minimum value of D that corresponds to $Re = 10^4$ is marked. Blockage effects were calculated according to Maskell's theory (1965) given by Rae and Pope (1984): $\Delta V/V = 0.25\, A_m/A_w$ where ΔV is the velocity increment due to blockage, V is the velocity, A_m is the model frontal area, and A_w is the wind tunnel cross-sectional area. Since investigation of the far-field development was also part of this program, it was decided that velocity increment beyond the range of 0.2 percent of the free-stream velocity, which in fact is the level of free-stream turbulence in the tunnel, was not acceptable. For $H = 2D$, $A_m = 2D^2$ and $A_w = 1.44\ m^2$. Figure A1 indicates a typical variation of the parameters involved in the design of the present facility.

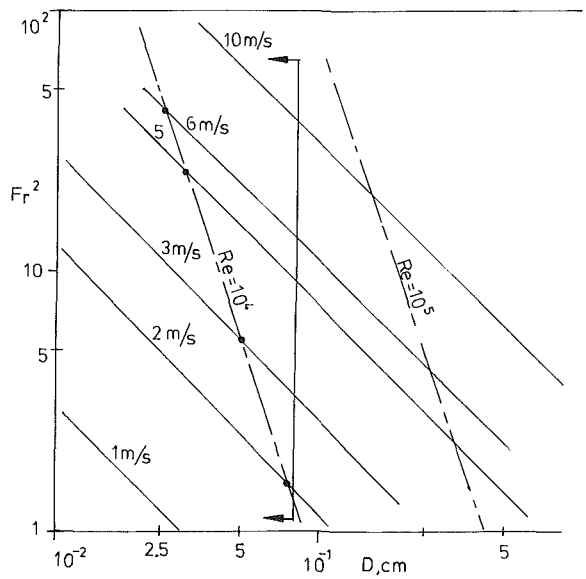

Fig. A1 Typical variation of Fr^2 versus D for $R = 0.5$ and $DT/T_j = 0.848$

Wind Tunnel Experiments on Cooling Tower Plumes: Part 2—In a Nonuniform Crossflow of Boundary Layer Type

J. Andreopoulos[1]
Department of Mechanical Engineering,
The City College,
City University of New York,
New York, NY 10031

The basic characteristics of plumes issuing into a boundary layer-type crossflow are reported. The flow can be considered as an interaction between two vorticity fields with different length scales and turbulence intensities. The large eddies of the oncoming boundary layer are responsible for the observed sudden changes in the plume direction. The type of structure emanating from the tower depends on the instantaneous velocity ratio. Mean velocities and normal velocity gradients are smaller than those in the case of uniform crossflow and therefore, the measured turbulence intensities are lower too. The cross-stream turbulence brings high-momentum fluid into the wake region and the velocity defect decays very rapidly. Dilution of the plumes takes place faster in the presence of external turbulence than in the case with uniform crossflow. The spreading rate is increased dramatically by the external turbulence, which causes different effects on the hydrodynamic and thermal fields.

1 Introduction

This paper is one of a series on cooling tower plumes and reports on a continuation of the work described in the accompanying paper by Andreopoulos (1989) (hereafter referred to as paper 1). In this work the case of a plume issuing in a boundary layer type crossflow has been studied in detail. The same experimental facilities have been used here as in the work described in paper 1. In this experiment, an artificially thickened boundary layer has been generated, while in the case of paper 1 the boundary layer developed over the flat plate was very thin and had no direct effect on the plume behavior. A general introduction to the work is given in paper 1, where the effects of the Reynolds number, velocity ratio, and densimetric Froude number on the plume development inside a uniform flow are described. In the present case, the plume is interacting with a nonuniform crossflow. One way to view this interaction is by considering the notion that the plume "feels" the crossflow as "free-stream" turbulence where this free-stream turbulence is not isotropic. It is known (Hancock, 1980; Castro, 1984) that free-stream turbulence significantly affects a boundary layer flow. However, in the case of a jet or shear layer in the presence of a coflowing stream with nearly isotropic free-stream turbulence, the changes are much stronger (Symes, 1979; Pui and Gartshore, 1979; Wygnanski et al., 1979). In the present work, the term "external turbulence" will be used to describe the nonisotropic turbulence of the crossflow instead of the term free-stream turbulence. This emphasizes the situation of the crossflow with nonuniform mean velocity profile and nonuniform turbulence stress profiles (Fig. 1). The present flow simulates in a certain way the real situation in nature and therefore, it is believed that the results may be directly applied to practical cases.

2 Experimental Setup and Measurement Techniques

The experimental facilities used here were the same as in paper 1. The cooling tower model, however, has been moved in the downstream direction to a position about 3 m from the leading edge of the flat plate.

The boundary layer was artificially thickened by using vortex generators/spires, surface-roughness elements, and boundary layer fences following the design procedure suggested by Irwin (1981). In designing these devices, special care has been made to match the requirements from the simulation point of view with those imposed by the wind tunnel. The thickness of the boundary layer, for example, should not exceed one half of the tunnel height, which was 1.5 m in the present case, and should be larger than one third of the height. Nagib et al. (1976) found that this is a comfortable operating range, which provides acceptable model scaling without inducing excessive streamwise pressure gradient due to boundary layer displacement. Since the boundary layer thickness is proportional to the height of the spires the latter has been chosen to be 500 mm. Details of the boundary layer generating system are shown in Fig. 2. Four spires were uniformly spaced in the tunnel with two cross-bars to provide the necessary deceleration of the flow. Without these bars the flow is similar to that of a wall jet. Roughness elements of the form shown in Fig. 2 generated the required turbulence intensities. The shape, the dimensions, and the locations of the bars and the roughness elements were determined by trial and error. The shear flow in the near wake of the spires had a thickness slightly less than the height h of the spires, but after a longitudinal distance of

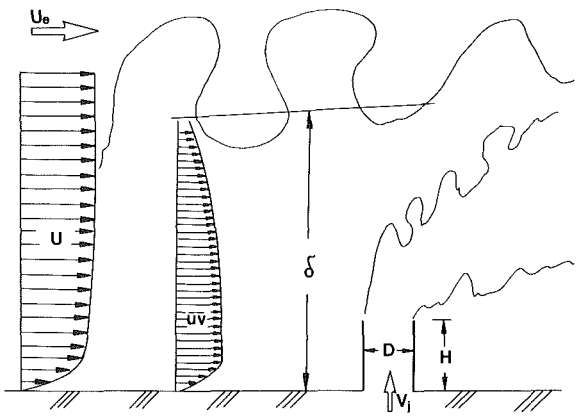

Fig. 1 Flow configuration

[1] Formerly at the Sonderforschungsbereich 80 of the University of Karlsruhe, Federal Republic of Germany.

Contributed by the Heat Transfer Division for publication in the JOURNAL OF HEAT TRANSFER. Manuscript received by the Heat Transfer Division March 11, 1988. Keywords: Flow Visualization, Plumes, Turbulence.

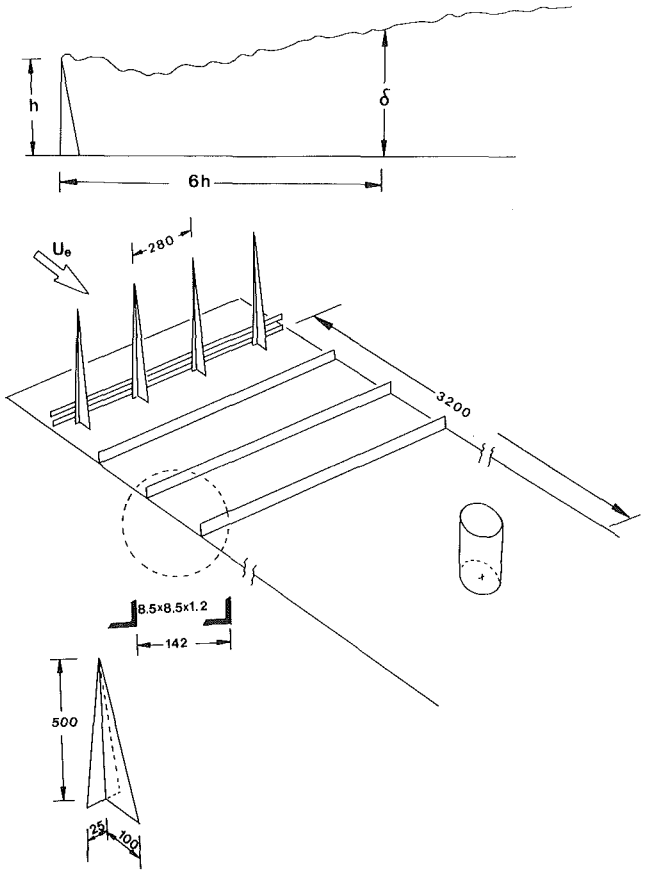

Fig. 2 Wind tunnel arrangement to artificially thicken the boundary layer; all dimensions in mm

$5h$, a self-preserving boundary layer flow was located at a distance $6h$ from the spires.

According to Ligrani et. al. (1983), the thickening device may be required to produce properties representative of normal behavior up to some specified level of information. The first four levels of information are considered to be wall quantities, mean velocity profiles, Reynolds stress component profiles, and spectra. A sample of these quantities is plotted in Fig. 3. It is seen in Fig. 3(*a*) that the mean velocities follow the logarithmic law of the wall with a velocity shift $\Delta U/u_\tau = 12.8$, for the lower Reynolds number case with $\mathrm{Re} = 0.9 \times 10^5$. Two experiments have been carried out with two different free-stream velocities $U = 3$ m/s and 7 m/s, which corresponds to $\mathrm{Re} = U_e\ \delta/\nu = 0.9 \times 10^5$ and 1.9×10^5, respectively. The Reynolds stress $\overline{u^2}$ and $\overline{uv}$ are plotted in Figs. 3(*b*) and 3(*c*). They closely follow Klebanoff's (1955) classical profiles. It is also clear that the region close to the wall is not adequately simulated. However, this seems unavoidable since the real bursting process of a normal boundary layer cannot be simulated either. It is also worthwhile to mention that the shear stress and turbulence intensities are not appreciably constant. As is mentioned by Hunt and Fernholz (1975), there is no theoretical reason and no meterological evidence for the constant-stress distributions found in other artificially thickened boundary layers over rough surfaces. It appears that all the present data collapse to a single curve when they are normalized by one velocity scale (u_τ) and one length scale (δ). This implies that turbulence quantities are self-preserving and therefore, the boundary layer may be considered to be at equilibrium. The spectra shown in Fig. 3(*d*) do not show any peaks in the lower frequency domain while they indicate quite clearly the $-5/3$ slope of the frequency domain of the inertial subrange. Although the spectra do not show any phase information, it is believed that the scale of the energetic eddies compares with the scales in the atmosphere.

A higher level of information has also been considered. The intermittency has been computed and found to be the same as that of naturally grown boundary layers. It is plotted in Fig. 3(*e*) and compared with the error function and the results of Murlis et al. (1982). We are aware of the fact that a full simulation of the atmospheric boundary layer is impossible. The turning, for example, of the wind direction in the so-called Ekman layer, which affects the ground level, is not modeled. On the other hand, we modeled the intermittency in the outer layer without knowing the intermittency in the atmospheric boundary layer. However, the present experimental arrangement constitutes a case with well-defined boundary conditions and controlled flow parameters. It can, therefore, provide important information on the physical structure of the flow and at the same time yield useful data for testing and improving calculation methods.

There is one more point concerning the scaling of the boundary layer that should be mentioned. The modeling law, which is the usual "law of the wall," is independent of the boundary layer thickness. This statement requires that the ratio H/z_o between the natural situation and the modeling situation should be the same, where H is the height of the cooling tower and z_o is the so-called roughness or meteorological parameter defined as $z_o = \nu/u_\tau \exp(-k(A - \Delta U/u))$, where k is the von Kármán constant ($k = 0.41$) and A is the additive constant in the smooth boundary layer law of the wall ($A = 5$). In the present case, $z_o = 2.2$ mm resulting in a ratio $H/z_o = 72.8$. The question is how thick the boundary layer thickness should be to achieve independence of H/δ. There is a possibility that this is valid only in the log-law region, i.e., for $y/\delta < 0.2$, which makes it very difficult to model high buildings with reasonable scale. For the case of a fence Raju et al. (1976) have shown that inner law scaling is valid up to $H/\delta = 1$, but the experiments of Castro and Robins (1977) have revealed a more complex situation. However, recently Sakomoto et al. (1982) have shown that "inner law" scaling is valid up to $H/\delta \cong 1$ for rough wall boundary layers. In the present situation the boundary layer, just upstream of the model, had a thickness of $\delta = 420$ mm and a skin friction $C_f = 0.0075$.

The hot-wire instrumentation and measurement techniques were the same as in paper 1. The flow parameter settings are shown in Table 1. Two major experiments have been carried out at one velocity ratio: one at low and another one at high densimetric Froude number. Apart from these two experiments in which the hydrodynamic and the thermal fields were mainly measured, four additional experiments have been made to measure the mean temperature field at two different velocity ratios. The flow parameter settings for this particular experiment are shown in Table 2.

The results include measurements of mean-velocity and temperature profiles, normal and shear stresses, turbulent kinetic energy and turbulent heat fluxes. A selection only of the obtained results will be presented and discussed here. A more detailed description can be found in the report by Andreopoulos (1986). They have been nondimensionalized by U_e and D. This does not imply that these are the proper scaling quantities.

The experimental uncertainty in this work as well as in the work of paper 1 was estimated to be about 6 percent for mean temperature, 9 percent for mean velocities, 13 percent for turbulent kinetic energy, and about 17 percent for the $\overline{uv}$ stresses and turbulent heat fluxes.

3 Results

3.1 Flow Visualization. The results of the flow visualization in paper 1 indicated a very strong dependence of the flow

Table 1 Flow parameters for the hot-wire measurements

Experiment	H mm	D mm	$\frac{H}{D}$	U_e, m/s	V_j, m/s	$R=\frac{V_j}{U_e}$	$\mathrm{Re}=\frac{U_e D}{\nu}$	T_e, °C	T_j, °C	Fr
NUFH1	150	80	2	2.6	1.30	0.5	0.136×10^5	16.1	31.5	6.75
NUFH2	160	80	2	3.05	1.50	0.5	0.159×10^5	19.9	147	3.13

Table 2 Flow parameters for the mean temperature measurements

Experiment	H mm	D mm	$\frac{H}{D}$	U_e, m/s	V_j, m/s	$R=\frac{V_j}{U_e}$	$\mathrm{Re}=\frac{U_e D}{\nu}$	T_e, °C	T_j, °C	Fr
NUFT1	160	80	2	3.04	1.52	0.5	0.159×10^5	19	143	3.14
NUFT2	160	80	2	7.61	1.52	0.2	0.398×10^5	16.7	144	3.11
NUFT3	160	80	2	6.45	1.29	0.2	0.337×10^5	17.5	30	6.91
NUFT4	160	80	2	2.6	1.30	0.5	0.136×10^5	17.3	31.4	6.82

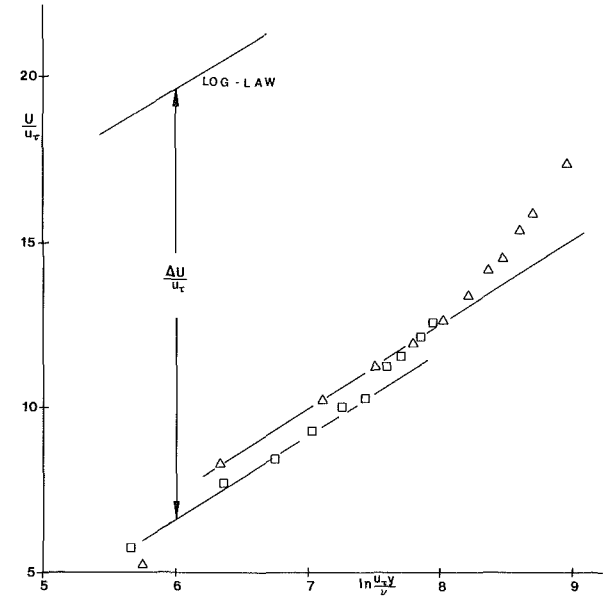

Fig. 3(*a*) Artificially thickened boundary layer; logarithmic mean velocity profiles: □, $\mathrm{Re}=U_e\delta/\nu=0.9\times10^5$; △, $\mathrm{Re}=1.9\times10^5$.

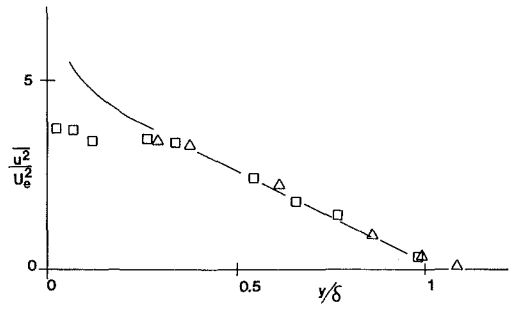

Fig. 3(*b*) Artificially thickened boundary layer, u^2-turbulence intensity; symbols as in Fig. 3(*a*); solid line, Klebanoff (1955)

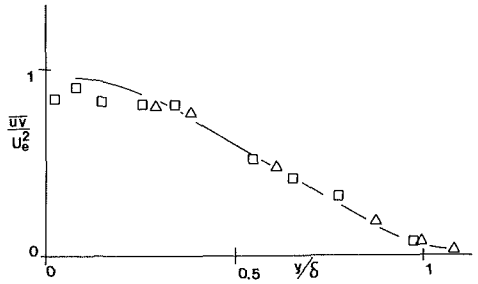

Fig. 3(*c*) Artificially thickened boundary layer, *uv* shear stress; symbols as in Figs. 3(*a*) and 3(*b*)

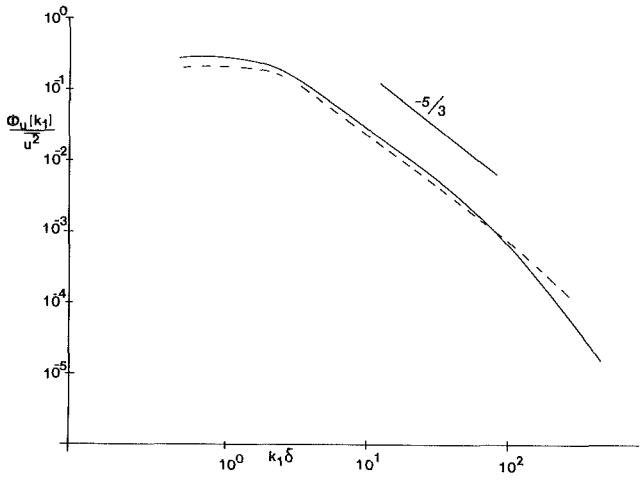

Fig. 3(*d*) Artificially thickened boundary layer; *u* spectra: ——, $y/\delta=0.544$, $\mathrm{Re}=0.9\times10^5$; ----, $y/\delta=0.848$, $\mathrm{Re}=1.97\times10^5$, $K=\omega/U$

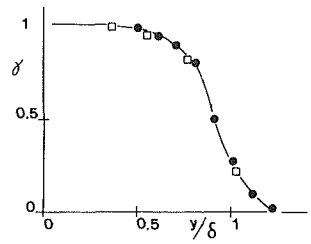

***Fig. 3(e)* Artificially thickened boundary layer; intermittency profile: □, $\mathrm{Re}=0.9\times10^5$; solid line, error function; •, Murlis et al. (1982)**

on velocity ratio, Reynolds number, and Froude number. The present case will be better understood if the jet or plume behavior is explained in terms of the salient features established in paper 1 that in any way are expected to occur also here. In general the effects of external turbulence can be determined through: (1) changes in the effective velocity ratio by altering the magnitude and the direction of the cross-stream velocity at $y=H$; (2) changes in the wake of the cylindrical stack and in the wake of the jet/plume as a follow-up result of the previous effect; (3) interaction of the jet structures or turbulent eddies with a turbulence field of different length scale and intensity.

It was shown in paper 1 that the type of structure emanating from the stack depends strongly on the velocity ratio R. Extrapolating this finding to the present case, it can be claimed that the type of structure to appear at the stack exit depends on the value of the instantaneous velocity ratio $R(t)=V_j/U(H)$, where $U(H)$ is the instantaneous cross-

stream velocity at $y=H$. This velocity varies about the mean $\bar{U}$ by, say, three times the root mean square (rms) value of the fluctuations if their distribution is Gaussian. Therefore, the instantaneous velocity ratio effectively can vary as $R_{\text{eff}} = V_j/\bar{U}(1.\pm 3.\sigma)$ where σ is the turbulence intensity. If $R_u = V_j/\bar{U}$ is the ratio in the case of a "uniform" cross stream then $R_{\text{eff}} \cong R_u(1.\pm 3.\sigma)$ is a "turbulence-augmented" effective velocity ratio.

The turbulence intensity σ at $y=H$ can be between 15 and 20 percent, which indicates that the effective velocity ratio may change by 60 percent. The implication, therefore, of a highly varying effective velocity ratio R is the appearance of almost all types of vortical structures in the cases of low nominal velocity ratios. Wakelike vortices and jetlike vortices are both present at the same time before they break down to turbulence very quickly.

The organized vortical structures of the jet flow observed in the low and high Reynolds number experiments were rapidly swept away by the cross-stream turbulence as soon as a large eddy of the oncoming boundary layer was passing the area above the exit of the stack. This behavior is not a surprise in view of the large length scale of the eddies of the boundary layer in comparison to those of the eddies of the pipe. A typical size of the boundary layer eddies is δ while the eddies of the pipe are typically of the order of D. In the present experiment, δ is roughly five times greater than D, and therefore, the large eddies of the boundary layer clearly dominate the interaction and generally the bulk flow development. It is the passage of the large eddies that causes the sudden change in the direction of the plume flow and results in large diffusion of it.

The present investigation showed that the organized vortical structures are rapidly affected by the external turbulence. This result indicates a different behavior from that of a shear layer (see Wygnanski et al, 1979) where the large scale structure is very little affected by free-stream turbulence of low or moderate intensity. The behavior of the present flow is a result of its highly violent interaction with the external turbulence, which is large in intensity and length scale.

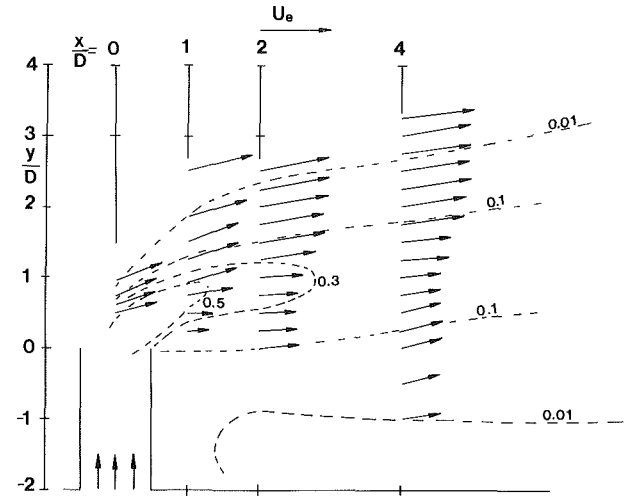

Fig. 4(a) Mean velocity vectors on the plane of symmetry for the NUFH1 experiment; dotted lines: isotherms.

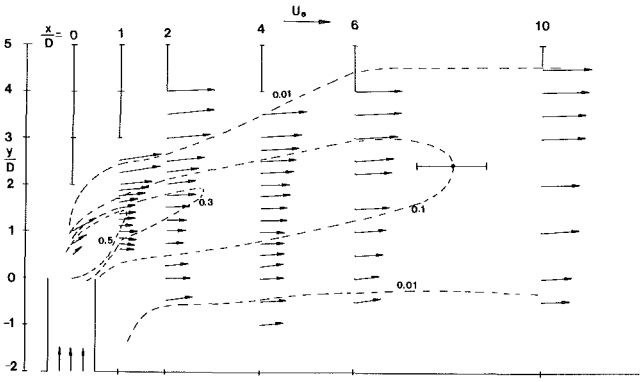

Fig. 4(b) Mean velocity vectors on the plane of symmetry for the NUFH2 experiment, dotted lines: isotherms

3.2 Measurements.

3.2.1 Mean Velocities. A selection only of the measured mean-velocity profiles at various downstream positions will be presented here for the two experiments shown in Table 1. The first experiment NUFH1 has been conducted at rather high Froude number where buoyancy effects are small, while the NUFH2 experiment involves some considerable buoyancy effects. Their flow-parameter settings correspond to the UFH2 and UFH4 experiments described in paper 1.

Figures 4(*a*) and 4(*b*) show the mean velocity vectors on the plane of symmetry for the two experiments NUFH1 and NUFH2, respectively. On the same figures some contours of isotherms are also plotted. They correspond to values of the normalized excess temperature $T-T_e/T_j-T_e$, and they indicate the extent of the thermal field.

A direct comparison of the present mean velocity vectors with those of the uniform crossflow experiments reveals three important characteristics: First, the magnitude of the velocity vectors is larger in the nonuniform crossflow experiments than in the uniform flow case; second, the velocity gradients seem to be smaller in the present case than those in the former case; third, the upper extent of the plume inside the nonuniform crossflow, as it has been depicted from the isotherms, is much higher than that of the uniform crossflow case, while the lower extent is more or less the same. This characteristic, which basically shows a higher spreading rate in the present case than that in the case of uniform crossflow, can be explained firstly in terms of an increased entrainment rate, which is known to be high in flows with external turbulence and second in terms of the velocity magnitude inside the plume of the present flow. Therefore, the conservation of mass suggests an increased "cross section" of the plume in the presence of external turbulence.

It is known that free-stream turbulence tends to reduce any velocity defect in wakes (Symes, 1979) and therefore, the increased magnitude of the velocity vectors in the wake of the plume or in the plume itself is not a surprise because external turbulence brings more high momentum fluid from the outside flow into the wake region. In other words the wake is being "filled" very fast in the presence of free-stream turbulence. However, the velocity vectors in the wake of the cylindrical stack (i.e., $y/H<0$) seem to be smaller in the present case of nonuniform crossflow than in the case of uniform flow described in paper 1. Under the abovementioned rule, one should expect the opposite to occur; the rule still applies to the present case but now the wake velocities should be compared with velocities upstream of the stack that are much smaller than U_e, rather than the external free-stream velocity U_e. The reader is reminded that the variation of mean velocities with y in the undisturbed boundary layer upstream of the cylinder is much stronger in the region below the stack exit than in the region above it.

3.2.2 Mean Temperatures. Contours of isotherms for the NUFH1 and NUFH2 cases have already been shown in Figs. 4(*a*) and 4(*b*) together with the mean velocity vectors at the plane of symmetry. These figures demonstrate a large diffusion of the initially released heat and momentum at the stack exit by the external turbulence. Despite the similarity

between heat and momentum transfer, the onset of buoyancy and external turbulence, as will be discussed later, may have different effects on the temperature and velocity fields. A comparison of the mean temperature profiles of the present case with those of paper 1 for the same conditions shows a striking feature: The gradients in the y direction are much smaller in the case of nonuniform crossflow than in the case of uniform crossflow. This implies that temperature fluctuations and turbulent heat fluxes will be smaller in the present case than in the case of paper 1. However, the opposite is true for the $\partial T/\partial x$ longitudinal gradient, which has large values in the vicinity of the stack, in the present experiment. As a result of this, the decay rate of the maximum excess temperature is almost twice as much as that of the uniform crossflow case. This is shown in Fig. 5(*a*) where the maximum temperature T_{max} of each profile has been plotted against longitudinal distance x for the NUFT1, NUFT4, UFH4, and UFH2 experiments. The initial decay rate of the T_{max} is much higher in the case of nonuniform crossflow than in the uniform crossflow for a distance of $2D$, then both become the same for $2<x/D<4$, and finally that of the uniform crossflow becomes slightly higher than that of the nonuniform cross-flow.

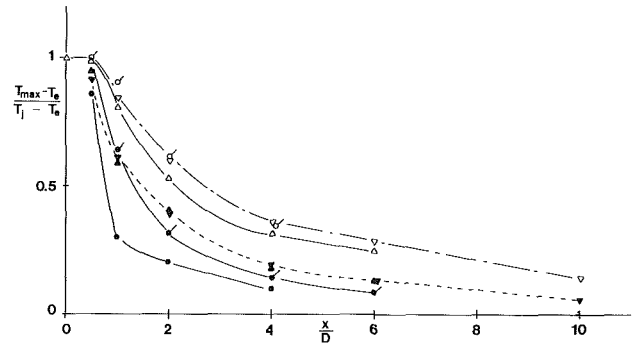

Fig. 5(*a*) Maximum temperature decay on the plane of symmetry; symbols: ◁, NUFT2 ($R=0.2$, Fr = 3.11); •, NUFT3 ($R=0.2$, Fr = 6.91); ▽, NUFT1 ($R=0.5$, Fr = 3.14); △, NUFT4 ($R=0.5$, Fr = 6.82); ◁, UFH5 ($R=0.2$, Fr = 3.22); ▽, UFH4 ($R=0.5$, Fr = 3.295); △, UFH2 ($R=0.5$, Fr = 8.681)

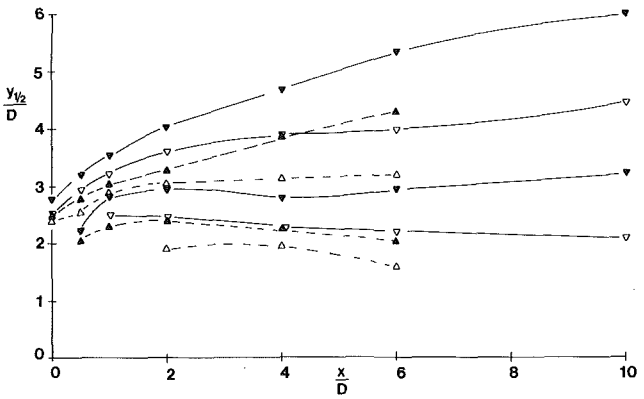

Fig. 5(*b*) Upper and lower extent of the plume based on half-width of temperature profiles (symbols as in Fig. 5*a*)

The variation of T_{max} with x is also indicative of the dilution of the plume. The reader is reminder that dilution is defined as the inverse of the normalized temperature $T-T_e/T_j-T_e$. The upper plot in Fig. 5(*a*) demonstrates that the dilution of the plume in the far field for the nonuniform crossflow becomes almost twice that of the uniform crossflow for the same velocity ratio $R = 0.5$. There is no clear effect of buoyancy on dilution for the case of the NUFT1 and NUFT4 experiments. However, temperature distribution at different positions indicates that dilution increases with increased Froude number. This is again demonstrated in Fig. 5(*a*) where T_{max} is plotted against x for the NUFT2 and NUFT3 experiments with the same velocity ratio $R=0.2$; dilution is much faster in the case of low buoyancy. This is not true in the region of the cylinder wake, where dilution seems to increase with increased buoyancy. These findings agree with the conclusions of paper 1, but there is a behavior in the present case of nonuniform crossflow that is in contrast to the results of paper 1. The present results indicate that dilution decreases as the velocity ratio increases. This is also shown in Fig. 5(*a*), where T_{max} is higher in the NUFT4 experiment ($R=0.5$) than in the NUFT3 experiment ($R=0.2$). This clearly demonstrates some of the strong effects of the external turbulence on the plume dilution.

Figure 5(*b*) shows the position of the "half width" $y_{1/2}$ of the jet, which indicates the upper and lower extent of the heated jet. It is defined as the position where the excess temperature becomes half of its maximum value. Only results for $R=0.5$ are plotted together with the results of the uniform crossflow experiment. It is obvious that the half width $y_{1/2}$ is higher with external turbulence and increased buoyancy. It is also interesting to see that the spreading rate in the upper edge is different from that in the lower edge. The spreading rates of the upper and the lower edge of the plumes for the experiments shown in Fig. 5(*b*) are given in Table 3 as they have been calculated from these data. Only the spreading rates of the far field are tabulated, since they seem to have reached a sort of constant value.

A comparison between the spreading rates of the plumes of the UFH2 and UFH4 experiments, as deduced from the temperature field, shows the following characteristics: First, buoyancy increases the spreading rate of the upper edge of the plume by 60 percent; second, the spreading rate of the lower edge is negative and is decreased (absolutely) by buoyancy by about the same amount of 60 percent; third, there is always a difference between the spreading rates of the upper and lower edges. The reason for this behavior is the turbulence in the wake of the cylinder, which acts as an external turbulence for the lower part of the plume. In the light of the present results, external turbulence increases the spreading rate and therefore, it might be expected that the lower edge experiences a higher spreading rate than the upper edge. In fact, this rule is confirmed in the UFH2 experiment where the lower extent of the plume is greater (absolutely) than the upper extent. In the UFH4 experiment, however, this rule is not obvious. The

Table 3 Spreading rate of the temperature and velocity fields for the $R = 0.5$ experiments; uncertainties of the order of 12 percent

Temperature Field				Velocity Field		
		$dy_{1/2}/dx$			$dy_{1/2}/dx$	
Experiment	Fr	Upper edge	Lower edge	Upper edge	Lower edge	External Turbulence
UFH2	8.68	+0.043	−0.105	+0.036	+0.031	−
UFH4	3.29	+0.069	−0.043	+0.0787	+0.478	−
NUFT1	3.14	+0.305	+0.064	(NUFH2)0.36(+20%)	+.30(±25%)	Yes
NUFT4	6.82	+0.249	−0.087	(NUFH1)0.195(±20%)	+.16(±25%)	Yes

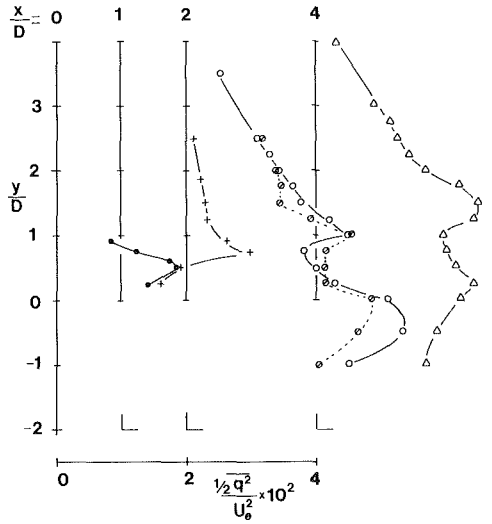

Fig. 6(a) Turbulent kinetic energy profiles for the NUFH1 experiments; symbols: •, $x/D = 0.0$; ▲, $x/D = 0.5$; +, $x/D = 1.0$; ○, $x/D = 2.0$; △, $x/D = 4.0$; □, $x/D = 6.0$; ▽, $x/D10.0$; flagged symbols: at $z/D = 0.5$

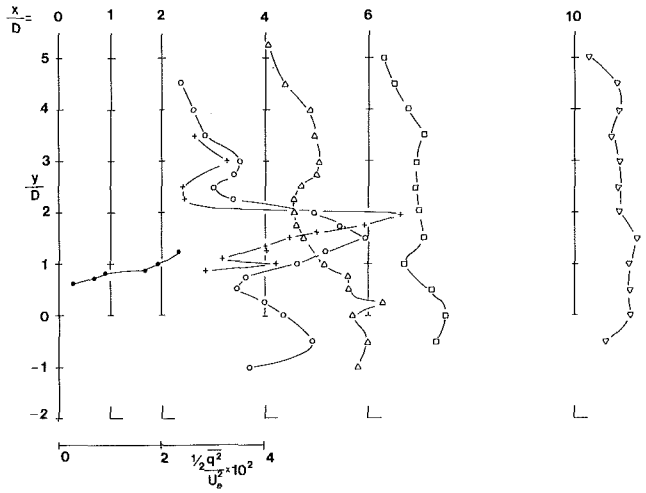

Fig. 6(b) Turbulent kinetic energy profiles for the NUFH2 experiments (symbols as in Fig. 6a)

results are masked by buoyancy, which causes additional effects, like a deeper penetration of the plume into the crossflow, which results in a weaker interaction of the bent-over plume with the wake of the cylindrical stack.

A comparison between the UFH2 and NUFT4 experiments demonstrates further the validity of the abovementioned rule: The spreading rate of the upper part of the plume of the NUFT4 experiment is about five times greater than that of the UFH2 experiment. The effect, however, of the external turbulence on the spreading rate of the lower edge is much smaller. In fact, it has been slightly reduced (absolutely). This reduction, which is just over the uncertainties involved in calculating the spreading rates, may be attributed to the differences in length scales or turbulence intensities between the turbulence in the wake and the external turbulence. Most probably an increased length scale of the external turbulence can cause a reduction in the spreading rate.

The onset of buoyancy on the plumes in the nonuniform crossflow case results in a further increase of the spreading rates. A comparison between the NUFT4 and NUFT1 experiments shows: first, a 23 percent increase of the spreading rate of the upper part of the plume; second, a spectacular change of sign of the lower part, which corresponds to about a 170 percent change. Since the Froude numbers between the NUFT1 and UFH4 experiments are roughly the same, a comparison of the spreading rates of these experiments also demonstrates some strong effects due to the external turbulence.

Another interesting characteristic is that the rate of spreading of the momentum field is the same, in sign and magnitude, in the upper and the lower part of the plume, as shown in Table 3, where the spreading rates deduced from the velocity field have also been tabulated. Rodi (1975), in a review of the available experimental data, concludes that the spreading rate of a round jet in still air, as deduced from the velocity field, is 0.086 and that of a plane shear layer 0.11. If the round jet issues into a coflowing parallel stream, with velocity 46 percent of that of the jet, then the spreading rate drops dramatically to 0.0349. The present date of the UFH2 experiment indicate a spreading rate of 0.036 for the upper edge of the jet, a value close to that suggested by Rodi and a positive spreading rate 0.031 for the lower edge; a negative value could be expected if the present flow behavior were closely similar to that of a round jet in a coflowing stream. The spreading rates of the upper edge of the velocity field compare very favorably with those deduced from the thermal field while those of the lower edge are opposite in sign. This spectacular difference in the speading rates between the thermal and momentum field in the lower part of the plume is most probably caused by the "wake turbulence," which may respond to heat in a quite different way than it does to momentum. There is evidence provided by Chevray and Tutu (1978) that suggests that the small eddies are more efficient in transporting heat than the large eddies, while the latter are more efficient in transporting momentum than the former. Similar effects of preferential transport of heat have been observed in boundary layer flows. Simonich and Bradshaw (1978) have demonstrated that for a 1 percent increase in free-stream turbulence intensity the skin friction increases by 4 percent and the Stanton number by 6 percent. Therefore, the difference in the spreading rates of the velocity and temperature fields under the presence of external turbulence is not surprising.

3.2.3 Turbulent Kinetic Energy. Figures 6(*a*) and 6(*b*) show the profiles of turbulence kinetic energy for the two experiments NUFH1 and NUFH2, respectively. The first two profiles of Fig. 6(*a*), although not complete, indicate a peak of $\overline{q^2}$ in the shear layer region of the bending-over jet, which is further developing at $x/D = 2$ and 4. At these stations a second peak is formed in the wake of the cylinder. The region between the two peaks seems to disappear very quickly, most probably due to a gradient diffusion type of turbulent transport.

In general, the values of $\overline{q^2}$ in the present case of a nonuniform crossflow are considerably smaller than those obtained in the case of a unform crossflow with the same velocity ratio R and the same Froude number. This is not surprising because the mean velocity gradient, as well as the lateral gradient $\partial \bar{U}/\partial z$, is small. The profiles of $\overline{q^2}$ at $z/D = -0.5$ for $x/D = 2$ shown in Fig. 6(*a*) indicate a similar development with a double peak and large diffusion of turbulence kinetic energy from the wake region of the stack toward the wake region at the jet.

A comparison of the present data at $x/D = 2$ and 6 with those of the UFH2 experiment of paper 1 shows that the peak values of $\overline{q^2}$ in the shear layer region and in the region of the wake of the cylinder are smaller in the case of nonuniform crossflow. It appears that the external turbulence reduces the normal velocity gradients in the far field.

The profiles of $\overline{q^2}$ of the NUFH2 experiment indicate some similar features. At $x/D = 2$, however, three peaks are present in the $\overline{q^2}$ profile. The lower is formed inside the wake of the cylinder while the middle is due to the high values of $\partial \bar{U}/\partial y$ in

the shear layer region of the plume. The third one also corresponds to a high value of $\partial U/\partial y$ since the mean U-velocity profile has a third local maximum/minimum point close to the outer edge of the plume. This local overshoot of the mean velocity above the neighboring values is evident at $x/D=1$ also and it has been found by Andreopoulos and Rodi (1984) in the cases of jets in a crossflow too. At stations farther downstream the kinetic energy generated in the shear layer or in the wake of the shear layer or in the wake of the cylinder diffuses toward the wake of the plume. The level of the peak values becomes smaller and smaller and at $x/D=10$ it seems that diffusion has evened out the $\overline{q^2}$ profile over most of the region between the wall and the outer edge of the plume.

A comparison between the $\overline{q^2}$ profiles in the region of the wake of the cylinder of the NUFH1 and NUFH2 experiments shows that the peak values are formed roughly at the same position $y/D=0.5$, while their level differs slightly, with that of the NUFH1 being higher. Similar behavior has been observed in the uniform crossflow experiments. It seems that buoyancy indirectly affects the wake region and $\overline{q^2}$ is smaller in the strongly buoyant cases than in the nonbuoyant cases with the same velocity ratio. This behavior may be due to the reduced spreading rate of the lower edge of the plume (see Table 3) or to the fact that the buoyant plume penetrates the cross stream deeper than the nonbuoyant jet with the same velocity ratio does. In any event, this suggests that the interaction between the wake of the cylinder and the plume itself becomes weaker with increased buoyancy.

4 Conclusions

A detailed study has been undertaken in order to establish the basic features of plumes or jets issuing in a nonuniform, boundary layer type crossflow. The present flow can be considered as an interaction between vorticity fields of different length scales and turbulence intensities. The results show some strong effects of the nonuniform cross stream on the plume development. The major conclusions of the present work can be summarized as follows: The large eddies of the oncoming boundary layer cause sudden changes in the direction of the plume flow and result in a fast diffusion of the plume. The concept of a turbulence-augmented velocity ratio has been found useful in explaining some of the bulk characteristics of the flow in terms of the features of a plume issuing in a uniform crossflow described in paper 1. Normal velocity and temperature gradients are smaller in the present case than in the case of paper 1. The wake region of the plume and of the cylindrical stack is "filled" very fast under the presence of free-stream turbulence since the latter brings high momentum fluid into this region. As a result of this mechanism the mean U-velocity profiles become monotonic within a very short distance from the stack exit. Dilution of the plumes takes place faster in the case of external turbulence than in the case of uniform crossflow. External turbulence inverses the effect of velocity ratio on the plume dilution under constant Froude number from that found in paper 1. Dilution decreases as the velocity ratio increases. The speading rate is increased substantially by the external turbulence. However, the speading rate of the momentum field is affected by external turbulence differently from that of the thermal field. This indicates that the two fields have quite different response to external turbulence. The level of the peak values of the turbulent kinetic energy and the $\overline{uv}$ stress (not shown here) is smaller in the present case than in the case of uniform crossflow. Both $\overline{q^2}$ and $\overline{uv}$ in the far field are mainly produced by the $\partial\bar{U}/\partial y$ velocity gradient while the other velocity gradient involved in the transport equations of $\overline{q^2}$ or $\overline{uv}$ are significant in the near field. Turbulent heat fluxes and temperature fluctuations are basically dominated by the temperature gradients $\partial T/\partial y$ and $\partial T/\partial x$.

The present results as well as those of paper 1 indicate that the near wake of the cylindrical stack plays an important part in the "downwash" phenomenon. The work described here has not aimed at investigating the characteristics of the reverse flow immediately behind the stack, and therefore, some important questions related to the behavior of the near wake have not been answered.

Acknowledgments

The research in these papers was sponsored by the Deutsche Forschungsgemeinschaft via the Sonderforschungsbereich 80. The author would like to acknowledge useful discussions with Professors J. F. Foss and W. Rodi and the technical assistance of Mr. D. Bierwirth. The data reduction was carried out on the UNIVAC 1108 computer of the University of Karlsruhe.

References

Andreopoulos, J., 1989, "Wind Tunnel Experiments on Cooling Tower Plumes: Part 1 – In Uniform Crossflow," ASME JOURNAL OF HEAT TRANSFER, Vol. 111, this issue.

Andreopoulos, J., 1986, "Wind Tunnel Experiments on Cooling Tower Plumes. Part 2: In Non-uniform Crossflow of Boundary Layer Type," Report SFB210/E/19, University of Karlsruhe, Federal Republic of Germany.

Andreopoulos, J., and Rodi, W., 1984, "Experimental Investigation of Jets in a Crossflow," *J. Fluid Mech.*, Vol. 138, pp. 33–127.

Castro, I. P., 1984, "Effects of Free-Stream Turbulence on Low Reynolds Number Boundary Layers," ASME *J. of Fluids Engineering*, Vol. 106, pp. 298–306.

Castro, I. P., and Robins, A. G., 1977, "The Flow Around a Surface-Mounted Cube in Uniform Turbulence Streams," *J. Fluid Mech.*, Vol. 79(2), pp. 307–335.

Chevray, R., and Tutu, N. K., 1978, "Intermittency and Preferential Transport of Heat in a Round Jet," *J. Fluid Mech.*, Vol. 38, pp. 133–160.

Counihan, J., 1969, "An Improved Method of Simulating an Atmospheric Boundary Layer in a Wind Tunnel," *Atmospheric Environment*, Vol. 3, pp. 197–214.

Hancock, P. E., 1980, "The Effects of Free-Stream Turbulence on Turbulent Boundary Layers," Ph.D. Thesis, Imperial College, United Kingdom.

Hunt, J. C. R., and Fernholz, H. 1975, "Wind Tunnel Simulation of the Atmospheric Boundary Layer: A Report on Euromech 50," *J. Fluid Mech.*, Vol. 70, pp. 543–559.

Irwin, H.P.A.H., 1981, "The Design of Spires for Wind Simulation," *J. Wind Engineering and Industrial Aerodynamics*, Vol. 7, pp. 361–366.

Klebanoff, P. S., 1955, "Characteristics of Turbulence in a Boundary Layer With Zero Pressure Gradient," NACA Rep. No. 1247.

Ligrani, P. M., Moffat, R. J., and Kays, W. M. 1983, "Artifically Thickened Turbulent Boundary Layers for Studying Heat Transfer and Skin Friction of Rough Surfaces," ASME *J. Fluids Engineering*, Vol. 105, pp. 146–153.

Murlis, J., Tsai, H. M., and Bradshaw, P., 1982, "The Structure of Turbulent Boundary Layers on Low Reynolds Numbers," *J. Fluid. Mech.*, Vol. 122, pp. 13–55.

Nagib, H. M., Morkovin, M. V., Yung, J. T., and Tan-Atichat, J., 1976, "On Modelling of Atmospheric Surface Layers by the Counter-Jet Technique," *AIAA J.*, Vol. 14(2), pp. 105–190.

Pui, N. K., and Gartshore, I. S., 1979, "Measurements of the Growth Rate and Structure in Plane Turbulent Mixing Layer," *J. Fluid Mech.*, Vol. 91, pp. 110–130.

Raju, R. K. G., Loeser, J., and Plate, E. J., 1976, "Velocity Profiles and Fence Drag for a Turbulent Boundary Layer Along Smooth and Rough Flat Plates," *J. Fluid Mech.*, Vol. 76 (2), pp. 383–393.

Sakamoto, H., Moriya, M., Taniguchi, S., and Arie, M., 1982, "The Form Drag of Three-Dimensional Bluff Bodies Immersed in Turbulent Boundary Layers," ASME *J. Fluids Eng.*, Vol. 104, pp. 326–334.

Simonich, J. C., and Bradshaw, P., 1978, "Effect of Free-Stream Turbulence on Heat Transfer Through a Turbulent Boundary Layer," ASME JOURNAL OF HEAT TRANSFER, Vol. 100, pp. 671–677.

Symes, C. R., 1979, "Freie Scherstromungen in Turbulenter Grundstromung," Dr-Ing. Thesis, University of Karlsruhe, Federal Republic of Germany.

Wygnanski, I., Oster, D., Fiedler, H., and Dziomba, B., 1979, "On the Perseverance of a Quasi-Two-Dimensional Eddy Structure in a Turbulent Mixing Layer," *J. Fluid Mech.*, Vol. 93, pp. 325–335.

Mixed Convective Low Flow Pressure Drop in Vertical Rod Assemblies: I—Predictive Model and Design Correlation

K. Y. Suh[1]

N. E. Todreas

W. M. Rohsenow

Departments of Nuclear and Mechanical Engineering,
Massachusetts Institute of Technology,
Cambridge, MA 02139

A predictive theory has been developed for rod bundle frictional pressure drop characteristics under laminar and transitional mixed convection conditions on the basis of the intraassembly and intrasubchannel flow redistributions due to buoyancy for a wide spectrum of radial power profiles and for the geometric arrangements of practical design interest. Both the individual subchannel correlations and overall bundle design correlations have been formulated as multipliers applied to the isothermal friction factors at the same Reynolds numbers. Standard and modified subchannel friction factors have been obtained to be used with spatial-average and bulk-mean densities, respectively. A correlating procedure has been proposed to assess the effects of interacting subchannel flows, developing mixed convective flow, wire wrapping, power skew, rod number, and transition from laminar flow. In contrast to forced convection behavior, a strong rod number effect is present under mixed convection conditions in bundle geometries. The results of this study are of design importance in natural circulation conditions because the mixed convection frictional pressure losses exceed the corresponding isothermal values at the same Reynolds numbers.

Introduction

This paper presents a predictive method for assessing pressure losses in single bundles of hexagonal arrangement under heated upward liquid flow (i.e., aiding flow) conditions in the laminar and transition mixed convection regimes. Both bare and wire-wrapped rod arrays are treated. Under the mixed convection condition the power-to-flow ratio increases to the point where both global and local flow redistributions due to buoyancy significantly affect the flow velocity and temperature fields within rod assemblies and subchannels. Although there have been a fair number of theoretical and experimental studies on the thermal characteristics of isolated bundles in mixed convection conditions, experimental pressure drop data are limited (Mawatari et al., 1982; Okada et al., 1985), and a comprehensive predictive theory for pressure loss is nonexistent.

The results of this study are of design importance because the resulting mixed convection friction losses are larger than those predicted for isothermal flows under the same Reynolds (Re) number conditions. These pressure loss correlations are applicable to the range of natural circulation flows in which buoyancy effects are of significance. The correlations, while validated with water experiments as reported in the companion paper (Suh et al., 1989), can be applied to liquid metal reactor (LMR) conditions using a bounding assumption for the Prandtl (Pr) number effect on the vertical mixed convective flow development.

Designers typically need two types of pressure loss correlation: first, individual subchannel correlations, which can be used with a lumped parameter subchannel analysis code for accurate analyses; second, an overall bundle design correlation for parametric analysis that is relatively simple and easy to use. In this work both types of correlation are developed, and in the companion paper the predictive theory is verified with existing literature data and a series of new experiments conducted as part of this study. The subchannel correlations, however, are subchannel axial-averaged formulations. Local axial formulations including buoyancy effects that could be utilized in distributed parameter analysis approaches (Ninokata et al., 1987) do not yet exist but could be developed based on the approaches presented in this paper.

Phenomenological Models

Relevant Physical Phenomena. Two distinct mechanisms are operative under the mixed convection regime in rod bundle geometries. One is a local intrasubchannel buoyancy effect associated with enhanced shear stress generation on the heated walls within a subchannel. The other is a global intraassembly buoyancy effect related to the bundle buoyant flow redistribution from the inlet isothermal profile. The flow redistribution is especially pronounced in bundles with radial power gradients. The liquid entering the heated bundle with uniform inlet radial velocity experiences a radial temperature difference due to the power skew. This causes a crossflow that increases the hot side velocity, and hence reduces the radial temperature differential. This decreased temperature differential will yield a reduction in bundle buoyancy force, and consequently a decrease in the hot side velocity. At a location sufficiently downstream, the radial velocity profile will effectively match the power profile for an adiabatic bundle (Huang, 1987).

The two phenomena are illustrated in Fig. 1 for the radially uniform power condition. Under inlet isothermal conditions, the fluid mass flux is greater in the edge versus the interior subchannels (Cheng and Todreas, 1986) of the bundle. Global bundle-wide buoyancy entrains the flow into the hotter interior subchannels. Simultaneously, the inlet isothermal parabolic velocity profile inside a subchannel is distorted into a double-humped mixed convective flow profile due to heat transferred from the diabatic rod surface.

In our model the local distortion of the velocity profile will

[1]Current affiliation: Fauske & Associates, Inc., Burr Ridge, IL 60521.

Contributed by the Heat Transfer Division and presented at the ASME Winter Annual Meeting, Boston, Massachusetts, December 13–18, 1987. Manuscript received by the Heat Transfer Division May 16, 1988; revision received January 18, 1989. Keywords: Mixed Convection.

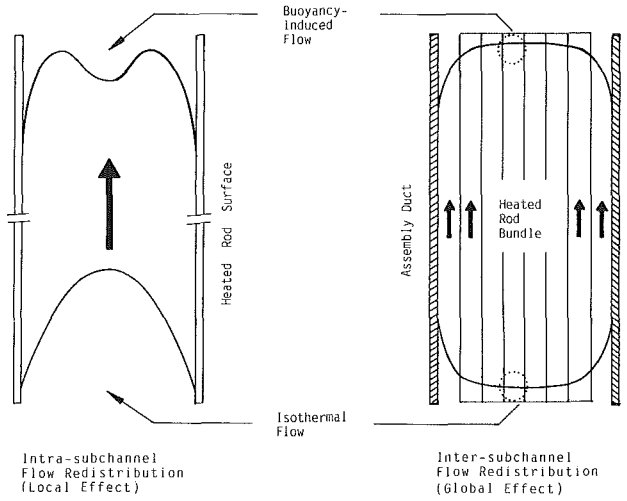

Fig. 1 Buoyancy-induced flow redistribution in bundle geometries

be accounted for by isolated subchannel mixed convection friction multipliers. The global flow redistribution will be accounted for by bundle mixed convection friction multipliers, which include the effect of developing bundle buoyancy between interacting subchannels. The relative importance of the two mechanisms has been found to depend primarily on the axial distance from the heated inlet, L_h/D_e, and to a lesser extent on the buoyancy to inertia force ratio, $\mathrm{Gr}_q/\mathrm{Re}$, and the number of rods inside the bundle (Suh, 1986).

Modeling Approach. The desired results are laminar friction pressure loss correlations in the form of friction factor–Reynolds number products for the bundle and individual subchannels, i.e., $(f\mathrm{Re})_i$, where $i = b$, 1, 2, and 3 for bundle, interior, edge, and corner subchannels, respectively. An effective approach for expressing these mixed convection $(f\mathrm{Re})_i$ products is in terms of multipliers, which are applied to existing isothermal products, $(f_0\mathrm{Re})_i$, for the same array geometries, i.e.,

$$(f\mathrm{Re})_b = \phi_t (f_0\mathrm{Re})_b \tag{1}$$

for bundles, where the total bundle multiplier ϕ_t incorporates the local subchannel and global bundle behavior and

$$(f\mathrm{Re})_i = \varphi_i (f_0\mathrm{Re})_i \qquad i = 1, 2, 3 \tag{2}$$

for subchannels.

The total bundle multiplier thus takes into account the global flow redistribution phenomenon, which is strongly dependent on the radial power distribution as well as the subchannel effect of local velocity profile distortion. Additionally, both types of multiplier account for buoyancy-affected flow development. The key variable upon which these multipliers depend in common is the ratio $\mathrm{Gr}_q/\mathrm{Re}$. All individual correlations are reduced to polynomial expressions of this dimensionless parameter. The effect of fluid Pr number on the development of subchannel and bundle flows is also treated. The isothermal friction factor–Reynolds number products for the geometries of interest are available from the correlations of Cheng and Todreas (1986).

An important facet of our correlations is the delineation of their limits of applicability. In particular, the transition from laminar flow marks this limit. It has long been known (Brown, 1960) that in circular tubes under mixed convection conditions not only do the laminar friction factors change from isothermal values but also turbulence develops at much lower Re numbers than in isothermal flows. The Re number for transi-

Nomenclature

A = axial average flow area
A_r = projected area of wire in a subchannel
c_p = specific heat of fluid at constant pressure
C_k = bundle buoyancy multiplier regression coefficients
D = rod diameter
D_e = equivalent hydraulic diameter
D_w = wire diameter
f = Darcy–Weisbach friction factor $= 2D_e\Delta p/\rho u^2 L$
F = ratio of gravity pressure gradient correction to friction pressure gradient
g = gravitational acceleration
G_k = bundle global multiplier regression coefficients
Gr_q = Grashof number $= \rho^2 g\beta q'' D_e^4/k\mu^2$
Gr_{qD} = Grashof number based on rod diameter $= (D/D_e)^4\mathrm{Gr}_q$
$\mathrm{Gr}_{\Delta T}$ = $\rho^2 g\beta\Delta T D_e^3/\mu^2$
H = wire lead length
k = thermal conductivity of fluid
l_k = subchannel buoyancy multiplier regression coefficients
L_h = axial heated length of rod
L_k = bundle local multiplier regression coefficients
$\dot{m}$ = mass flow rate
N = number of subchannels in a bundle
N_r = number of rods in a bundle
Δp = pressure drop
P = rod pitch
P_h = heated perimeter
P_w = wetted perimeter
Pr = Prandtl number $= \mu c_p/k$
$\dot{q}$ = heat rate
q'' = heat flux
Re = Reynolds number $= \rho u D_e/\mu$
S_k = bundle skew multiplier regression coefficients
T_k = bundle total multiplier regression coefficients
u = axial flow velocity
W_d = wire drag constant
W_s = wire sweeping constant
X = flow split parameter
z = axial coordinate
β = volumetric expansion coefficient of fluid
θ = angle the wire makes with respect to z axis
μ = dynamic viscosity of fluid
ρ = mass density of fluid
φ = subchannel friction factor multiplier
ϕ = bundle friction factor multiplier

Subscripts

0 = isothermal
b = bundle
ct = circular tube
g = global
i = b, 1, 2, or 3 for bundle, interior, edge, or corner subchannel, respectively
in = inlet
l = local
L = laminar or transition from laminar regime
n = subchannel index
out = outlet
s = skew
t = total
tr = transitional
T = turbulent or transition to turbulent regime

Superscripts

I = uniform power profile
IV = diametral power skew profile
dev = developing
f = frictional
mc = mixed convective
ww = wire-wrapped
$'$ = equivalent bare (without considering wire)
$\bar{}$ = mean average

tion to buoyancy-induced turbulence depends primarily on the Gr_q/Re parameter. If Gr_q/Re increases with temperature, as for water and liquid metals, turbulence is induced near heated surfaces even though the bulk flow is laminar. Rod bundle geometries exhibit different, more complicated phenomena of transition from laminar flow both in the forced convection regime (Cheng and Todreas, 1986) and in the mixed convection regime (Wang et al., 1981).

The transition phenomenon is complicated (Gebhart and Mahajan, 1982) and not readily amenable to engineering correlation. Here, for simplicity, it is postulated that transition occurs when the wall shear stress in heated upflow equals the critical wall shear stress under the corresponding isothermal flow condition. These wall shear stresses are proportional to $f\mathrm{Re}^2$ and $f_0\mathrm{Re}^2$, respectively. The resulting equation for the critical Re number for transition in heated upflow, Re_L, reduces to

$$\mathrm{Re}_L = \mathrm{Re}_{0L}\frac{(f_0\mathrm{Re})}{(f\mathrm{Re})} \tag{3}$$

Physically, high $f\mathrm{Re}$ is associated with large Gr_q/Re, and thus enhanced wall shear stress. To match the isothermal critical wall shear stress under mixed convection conditions, the Re_L number has to be lowered for higher $f\mathrm{Re}$. In equation (3), the isothermal $(f_0\mathrm{Re})$ factors and the critical Re_{0L} numbers can be evaluated using the Cheng-Todreas (1986) correlations. The mixed convection $(f\mathrm{Re})$ factors can be calculated using the correlations of this study. Hence the critical Re number in mixed convective flow can be determined as a function of the Gr_q/Re parameter and the geometry, i.e., subchannel versus bundle, fuel versus blanket type LMR assembly, and bare versus wire-wrapped rod. Experimental data are presented that confirm the validity of this model in the companion paper.

Subchannel Friction Factor Model and Correlation

Method of Representation. The multiplier φ_i, as defined by equation (2), will be developed first for wire-wrapped subchannels and then for bare subchannels. Cheng and Todreas (1986) have formulated the isothermal laminar flow wire-wrapped subchannel friction factors, $(f_0\mathrm{Re})_i$, in terms of geometric factors and empirical constants. Their formulation casts the interior subchannel friction factor, $(f_0\mathrm{Re})_1$, as the sum of the friction loss caused by the heated rod surface and the drag loss caused by the wire. For an edge region where a swirl flow is observed due to wire, they proposed that the edge and corner subchannel friction factors, $(f_0\mathrm{Re})_2$ and $(f_0\mathrm{Re})_3$, are solely due to the friction loss associated wth the swirl velocity on the heated surface; i.e., the form drag loss due to wire is negligible.

The resultant formulae were expressed as

$$(f_0\mathrm{Re})_1 = (f_0\mathrm{Re})_1'[(P_{w1}'/P_{w1}) + \varphi_1^{ww}] \tag{4}$$

$$(f_0\mathrm{Re})_2 = (f_0\mathrm{Re})_2'[1 + \varphi_2^{ww}] \tag{5}$$

$$(f_0\mathrm{Re})_3 = (f_0\mathrm{Re})_3'[1 + \varphi_3^{ww}] \tag{6}$$

where the wire correction parameters are defined as

$$\varphi_1^{ww} = [W_d/(f_0\mathrm{Re})_1'](3A_{r1}/A_1')(D_{e1}/H)(D_{e1}/D_w) \tag{7}$$

$$\varphi_2^{ww} = W_s(A_{r2}/A_2')\tan^2\theta \tag{8}$$

$$\varphi_3^{ww} = W_s(A_{r3}/A_3')\tan^2\theta \tag{9}$$

The complexity inherent in formulating the multiplier φ_i arises because the terms of equations (4), (5), and (6) comprising the products $(f_0\mathrm{Re})_i$ are not all equally affected by buoyancy. Our correlation is based on the proposal that buoyancy effects are significant only with regard to the friction terms associated with the vertical velocity components over the heated rod surface in the direction of the buoyant force. Hence by our hypothesis the following terms are unaffected by the buoyant force $\varphi_1^{ww}(f_0\mathrm{Re})_1'$, which represents the wire drag loss in the interior subchannel, and $\varphi_2^{ww}(f_0\mathrm{Re}_2)'$ and $\varphi_3^{ww}(f_0\mathrm{Re}_3)'$, which denote the additional friction loss resulting from the change in velocity from the axial to the swirl direction due to the wire in the edge and corner subchannels, respectively.

The developing buoyancy effect on the friction terms is then proposed to be accounted for by applying the parameter $[1 + (\varphi_i^{mc} - 1)\varphi_i^{\mathrm{dev}}]$. Note that this parameter approaches φ_i^{mc} in the limit of fully developed mixed convective flow, i.e., $\varphi_i^{\mathrm{dev}} = 1$. Of course the two new multipliers, φ_i^{mc} and φ_i^{dev}, must be formulated and their development will be presented in the next section. On the basis of this modeling approach the developing laminar mixed convection wire-wrapped subchannel friction factors can finally be expressed as

$$(f\mathrm{Re})_1 = (f_0\mathrm{Re})_1'\{(P_{w1}'/P_{w1})[1 + (\varphi_1^{mc} - 1)\varphi_1^{\mathrm{dev}}] + \varphi_1^{ww}\} \tag{10}$$

$$(f\mathrm{Re})_2 = (f_0\mathrm{Re})_2'\{[1 + (\varphi_2^{mc} - 1)\varphi_2^{\mathrm{dev}}] + \varphi_2^{ww}\} \tag{11}$$

$$(f\mathrm{Re})_3 = (f_0\mathrm{Re})_3'\{[1 + (\varphi_2^{mc} - 1)\varphi_3^{\mathrm{dev}}] + \varphi_3^{ww}\} \tag{12}$$

The local mixed convection multiplier for the edge subchannel has been utilized in equation (12) because the corner subchannel is of minor importance in bundle geometries and thus has not been separately treated. Equations (10) to (12) reduce to the corresponding isothermal bare subchannel friction factors in the limit, i.e., $P_{w1} = P_{w1}'$, $\varphi_i^{ww} = 0$, and $\varphi_i^{mc} = 1$. The wire-wrapped subchannel friction factor multipliers are then determined from equation (2) by application of equations (4) to (6), and (10) to (12), as

$$\varphi_1 = \frac{(f\mathrm{Re})_1}{(f_0\mathrm{Re})_1} = \frac{(P_{w1}'/P_{w1})[1 + (\varphi_1^{mc} - 1)\varphi_1^{\mathrm{dev}}] + \varphi_1^{ww}}{(P_{w1}'/P_{w1}) + \varphi_1^{ww}} \tag{13a}$$

$$\varphi_2 = \frac{(f\mathrm{Re})_2}{(f_0\mathrm{Re})_2} = \frac{[1 + (\varphi_2^{mc} - 1)\varphi_2^{\mathrm{dev}}] + \varphi_2^{ww}}{1 + \varphi_2^{ww}} \tag{14a}$$

$$\varphi_3 = \frac{(f\mathrm{Re})_3}{(f_0\mathrm{Re})_3} = \frac{[1 + (\varphi_2^{mc} - 1)\varphi_3^{\mathrm{dev}}] + \varphi_3^{ww}}{1 + \varphi_3^{ww}} \tag{15a}$$

The application of the buoyancy parameter to only the heated rod vertical friction component, which leads to the complex multipliers of equations (13*a*) to (15*a*), is appropriate if the wire drag and wire swirl contributions to the frictional loss are substantial ($\gtrsim$ 10 percent). The magnitude of these contributions depends primarily on bundle geometry, i.e., P/D and H/D, and flow regime. The wire effects are considerable in blanket assemblies (due to small wire wrap leads) and in turbulent flows, as Table 1 illustrates. However, for a typical wire-wrapped fuel assembly with $P/D = 1.25$ and $H/D = 35$, wire drag accounts for only 0.1 percent (interior subchannel) and wire swirl only 4 percent (edge subchannel)

Table 1 Effect of wire drag and wire swirl correction parameters on the subchannel multipliers φ_i of equations (13*a*)–(15*a*)

$\frac{\varphi_i - \varphi_i(\mathrm{with}\,\varphi_i^{ww}=0)}{\varphi_i}\times 100$	$P/D=1.07$ Laminar	$H/D=8$ Turbulent	$P/D=1.21$ Laminar	$H/D=47$ Turbulent	$P/D=1.25$ Laminar	$H/D=35$ Turbulent
Interior subchannel	1	114	0.04	10	0.1	23
Edge subchannel	16	53	2	7	4	14
Corner subchannel	41	136	4	14	8	25

and 8 percent (corner subchannel) of the total frictional loss in laminar flow conditions. For this case $\varphi_i^{ww} \cong 0$ and the φ_i's of equations (13*a*) to (15*a*) reduce to

$$\varphi_i = 1 + (\varphi_i^{mc} - 1)\varphi_i^{\text{dev}} \qquad (13b\text{–}15b)$$

The corresponding subchannel friction multipliers for bare subchannels are

$$\varphi_i' = \frac{(f\text{Re})_i'}{(f_0\text{Re})_i'} = 1 + (\varphi_i'^{\,mc} - 1)\varphi_i'^{\,\text{dev}} \qquad (13c\text{–}15c)$$

where $\varphi_i'^{\,mc}$ represents the mixed convection effect in bare subchannels, which differs from that applicable to wire-wrapped subchannels, i.e., φ_i^{mc}. Analogously the developing effect factor $\varphi_i'^{\,\text{dev}}$ differs from φ_i^{dev}.

Correlation of Subchannel Multipliers. Our task is to identify and develop the relevant buoyancy multipliers and laminar-transition criteria for bare and wire-wrapped subchannels, i.e., $\varphi_i'^{\,mc}$, $\varphi_i'^{\,\text{dev}}$, and Re_{iL}' as well as φ_i^{mc}, φ_i^{dev}, and Re_{iL}.

Fully Developed Bare Rod Mixed Convection: $\varphi_i'^{\,mc}$. Shear is locally enhanced at the heated wall. The effect of the unheated duct wall should also be assessed in the edge region. The standard and modified friction factors directly applicable to bare interior and edge subchannels were presented as the buoyancy multipliers (which are functions of the Gr_{qD}/Re parameter and the P/D ratio) times the isothermal values (Suh, 1986; Iannello et al., 1988). The modified friction factor is defined for use in applications where only bulk-mean temperatures are available, as is the case for lumped parameter analyses and most one-dimensional experiments. The standard friction factor should be utilized when the spatial-average temperatures are known. The Re number is based on the equivalent hydraulic diameter of the channel. However, the Gr_{qD} number is based on the rod diameter D, instead of equivalent diameter D_e, because the buoyancy effect is related to the heated perimeter and not to the hydraulic diameter of the flow channel.

Consequently, the standard and modified friction factor ratios are here defined as local subchannel buoyancy multipliers, which can be correlated as

$$\varphi_i'^{\,mc} = \frac{(f\text{Re})_i'}{(f_0\text{Re})_i'} = \exp\left(\sum_{k=0}^{4} l_k [\ln(1 + \text{Gr}_{qD}/\text{Re})]^k\right)_i \qquad (16)$$

or

$$\varphi_i'^{\,mc} = (1 + F_i)\frac{(f\text{Re})_i'}{(f_0\text{Re})_i'} = \exp\left(\sum_{k=0}^{4} l_k [\ln(1 + \text{Gr}_{qD}/\text{Re})]^k\right)_i \qquad (17)$$

where the correction parameter F_i was introduced to allow the use of the bulk-mean density to compute the gravity term of the momentum equation in lumped parameter analysis codes.

The modified friction factors are employed in this work in testing the predictive theory against the experimental data. The regression coefficients l_k are listed in Table 2. The coefficients were obtained by a least-squares error fitting technique, and a fitting error less than 5 percent results when the Gr_{qD}/Re parameter is less than the maximum value specified in the table.

Fully Developed Wire-Wrapped Mixed Convection: φ_i^{mc}. Since the buoyancy-affected flow phenomena in a wire-wrapped rod assembly are complicated, we propose a model that includes the most important physical effects by geometric factors. First, note that the local intrasubchannel buoyancy affects the fluid velocity profile and in turn the shear stress at the fluid–solid interface. Also observe that the heated rod outside surface (and not the wire-wrapped surface) is associated with the change in friction by virtue of buoyancy force in wire-wrapped rod assemblies.

The presence of the wire wrap is considered to affect the locally enhanced shear stress in two ways: (1) reduced flow area for buoyancy development, which is equivalent to an effective decrease in the rod pitch-to-diameter ratio P/D, and (2) increased wetted perimeter P_w relative to the heated perimeter P_h, as compared to the corresponding bare rod subchannel of the same P/D ratio. It is proposed to take into account the reduction of the flow area by applying the wire-wrapped to bare subchannel flow area ratio, A_i/A_i', to the bare multiplier itself, equation (16) or (17). The introduction of the wetted perimeter of the wire wrap is accounted for by replacing the corresponding bare rod diameter D by $(P_h/P_w)D$ in the Gr_{qD} number. The general ratio $(P_h/P_w)_i$ can be expressed as P_{w1}'/P_{w1} for a wire-wrapped bundle since (1) the applicable heated to wetted perimeter ratios for the subchannels are equal, i.e.,

$$P_{h2}/P_{w2} = P_{h3}/P_{w3} = P_{h1}/P_{w1}$$

and (2) for the interior subchannel geometry

$$P_{h1}/P_{w1} = P_{w1}'/P_{w1}$$

The wire-wrapped subchannel buoyancy multiplier is obtained by generalizing equation (16) or (17) to include the factors noted above as

$$\varphi_i^{mc} = 1 + (A_i/A_i')\left(\exp\left[\sum_{k=0}^{4} l_k \{\ln[1 + (P_{w1}'/P_{w1})^4(\text{Gr}_{qD}/\text{Re})]\}^k\right]_i - 1\right) \qquad (18)$$

Developing Buoyancy: φ_i^{dev} and $\varphi_i'^{\,\text{dev}}$. Now consider the effects of developing flow on the friction factor change caused by buoyancy. So far, the only available literature correlation

Table 2 Regression coefficients for subchannel multipliers of equations (16), (17), and (18) for hexagonal array geometry

Type	P/D	Subchannel	l_0	l_1	l_2	l_3	l_4	$(\text{Gr}_{qD}/\text{Re})_{\max}$
Standard	1.25	Interior	−3.411E−02	5.445E−02	−1.756E−02	1.173E−03	1.039E−04	5E+04
		Edge	−8.471E−02	1.708E−01	−8.263E−02	1.039E−02	−3.002E−04	5E+04
	1.08	Interior	−6.032E−02	9.659E−02	−3.390E−02	3.703E−03	−8.078E−05	1E+05
		Edge	−4.005E−01	7.417E−01	−2.581E−01	2.984E−02	−1.064E−03	1E+05
Modified	1.25	Interior	6.317E−02	−1.287E−01	6.712E−02	−1.275E−02	8.092E−04	5E+04
		Edge	−4.296E−01	7.987E−01	−3.518E−01	4.395E−02	−1.529E−03	5E+04
	1.08	Interior	−1.326E−03	−1.664E−02	1.848E−02	−4.585E−03	3.188E−04	1E+05
		Edge	−1.574E+00	2.868E+00	−9.510E−01	1.034E−01	−3.558E−03	1E+05

for a z/D effect is that due to Bishop et al. (1980) for a circular tube for the range $z/D > 5$

$$\varphi_{ct}^{\text{dev}} = [1 + 0.36(50D/z)^3]^{-1} \tag{19}$$

Rod bundle geometries introduce additional complexities in velocity profiles due to the azimuthal asymmetry of the subchannel shape. Even further complexity arises from the presence of wire-wrap spacers. Therefore equation (19) is transformed by replacing the tube diameter by a hydraulic diameter defined in terms of the heated perimeter rather than wetted perimeter

$$\varphi_i^{\text{dev}} = \{1 + 0.36[50(4A_i/P_{hi})/z]^3\}^{-1} \tag{20a}$$

for $z(P_{hi}/4A_i) > 5$, whereas

$$\varphi_i'^{\text{dev}}{}_i = \{1 + 0.36[50(4A_i'/P_{hi})/z]^3\}^{-1} \tag{20b}$$

for $z(P_{hi}/4A_i') > 5$.

Also the axial length over which the temperature and velocity profiles develop is highly dependent on the Pr number. The smaller the Pr number as in liquid metals, the sooner the flow field enters the fully developed region where the buoyancy-affected velocity profile remains invariant. The effect of the Pr number on the friction factor results has been evaluated using bounding assumptions and it has been found acceptable to express φ_i^{dev} and $\varphi_i'^{\text{dev}}$ as in equations (20*a*) and (20*b*). Since this evaluation is in terms of bundle multipliers it is presented in the Engineering Correlations and Sample Calculation section.

Thus, the first desired correlations, subchannel pressure loss multipliers φ_i, defined by equation (2), for use in lumped parameter codes have been obtained for wire-wrapped and bare subchannels, respectively, as

Wire-wrapped:

$$\varphi_i \equiv \frac{(f\text{Re})_i}{(f_0\text{Re})_i} = \text{equations (13}a\text{) through (15}a\text{)}$$

$$= \text{Function}\,(\varphi_i^{mc}, \varphi_i^{\text{dev}}, \varphi_i^{ww})$$

where

φ_i^{mc} = equation (18) with l_k given in Table 2 for both standard and modified friction factors

φ_i^{dev} = equation (20*a*)

φ_i^{ww} = equations (7) through (9)

Bare:

$$\varphi_i' = \frac{(f\text{Re})_i'}{(f_0\text{Re})_i'} = \text{equations (13}c\text{) through (15}c\text{)}$$

$$= \text{Function}\,(\varphi_i'^{mc}, \varphi_i'^{\text{dev}})$$

where

$\varphi_i'^{mc}$ = equations (16) and (17) with l_k given in Table 2 for both standard and modified friction factors

$\varphi_i'^{\text{dev}}$ = equation (20*b*)

Laminar-Transition Criteria. According to equation (3) the critical Re number for transition from laminar flow in bare subchannels for fully developed conditions can be calculated using equation (16) or (17) as

$$\text{Re}_{iL}' = \text{Re}_{0iL}'/\varphi_i'^{mc}$$

$$= \text{Re}_{0iL}' \exp\left(\sum_{k=0}^{4} (-l_k)[\ln(1 + \text{Gr}_{qD}/\text{Re})]^k\right)_i \tag{21}$$

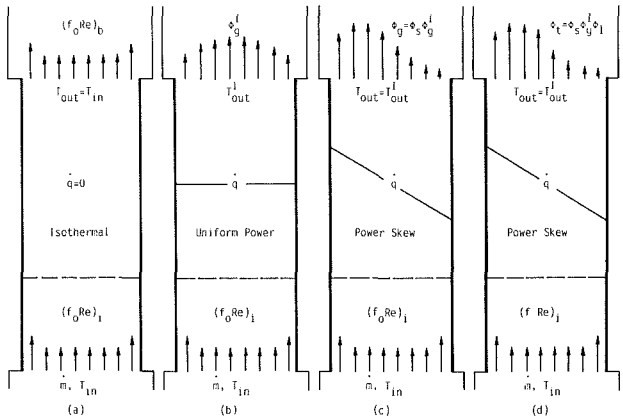

Fig. 2 Correlating procedure for bundle friction factor multipliers

For developing flow in bare subchannels, the critical laminar-transition Re number can analogously be evaluated using equations (13*c*)–(15*c*) as

$$\text{Re}_{iL}' = \text{Re}_{0iL}'/\varphi_i' \tag{22}$$

The subchannel multipliers, $\varphi_i'^{mc}$ and φ_i', for fully developed and developing flows, respectively, take on two separate values depending on whether the standard or the modified mixed convection friction factor is chosen.

Likewise, for developing flow in wire-wrapped subchannels, the critical laminar-transition Re number can be determined using equations (13*a*)–(15*a*) or (13*b*)–(15*b*) as

$$\text{Re}_{iL} = \text{Re}_{0iL}/\varphi_i \tag{23}$$

Equation (23) reduces to equation (21) in the limit of bare subchannel fully developed flow. The isothermal critical Re_{0iL}' and Re_{0iL} numbers can readily be determined from the Cheng–Todreas (1986) correlation.

Bundle Pressure Drop Model and Correlation

Correlation of Bundle Multipliers. The mixed convection bundle friction factor under a radial power skew condition is formulated by applying the global and local effects in terms of bundle buoyancy multipliers successively to the corresponding isothermal value, viz.

$$(f\text{Re})_b = \phi_t (f_0\text{Re})_b \tag{1}$$

where

$$\phi_t = \phi_g \phi_l \tag{24}$$

with the subscripts b, t, g, and l denoting bundle, total, global, and local, respectively.

This correlating procedure is illustrated in Fig. 2. In step (*a*) the isothermal bundle friction factor $(f_0\text{Re})_b$ is determined using the forced convection subchannel friction factors $(f_0\text{Re})_i$ and flow split parameters X_i for a given bundle total mass flow rate $\dot{m}_b$ and no heat input. In step (*b*) the uniform global buoyancy multiplier ϕ_g^I is evaluated as the ratio of globally increased bundle friction factor to the corresponding isothermal value at the same Re_b number. In this evaluation use is made of the forced convection subchannel friction factors $(f_0\text{Re})_i$, the flow split parameters affected by the global buoyancy force X_n^I for the same mass flow rate $\dot{m}_b$ and a bundle total heat rate $\dot{q}_b$. In step (*c*) the power skew global buoyancy multiplier ϕ_g, defined analogously to ϕ_g^I, is calculated and the skew multiplier is derived as the ratio $\phi_s = \phi_g/\phi_g^I$, utilizing the forced convection subchannel friction factors $(f_0\text{Re})_i$, the flow split parameters influenced by the global buoyancy X_n for the same mass flow rate $\dot{m}_b$, and the same heat rate $\dot{q}_b$, but in a radially nonuniform condition. Finally, in step (*d*) the power skew total buoyancy multiplier ϕ_t is determined as the ratio of

totally increased bundle friction factor to the corresponding isothermal value at the same Re_b number, and the local buoyancy multiplier is derived as the ratio $\phi_l = \phi_t/\phi_g$, using the complete set of mixed convection subchannel friction factors $(f\mathrm{Re})_i$, the flow split parameters influenced by the global buoyancy X_n for the same mass flow rate $\dot{m}_b$, and the same heat rate $\dot{q}_b$ as in the radially nonuniform condition. Utilization of the mixed convection friction factors has been found to yield slightly different flow splits in the heated bundle from those predicted using the forced convection friction factors. The differences however have been found to be minimal. Further, ϕ_l has been found to be essentially independent of the radial power profile, i.e.,

$$\phi_l \approx \phi_l^I \tag{25}$$

The correlating procedure utilizes a subchannel analysis code to calculate bundle pressure drops for steps (*a*) through (*d*). The input parameters and boundary conditions for each step have been fully specified. The subchannel analysis code must be capable of accounting for transverse flows between subchannels. In this work the ENERGY-IV code (Cheng and Todreas, 1986) was used to assess the global bundle-wide interacting subchannel flow redistribution effect under mixed convection conditions. The buoyancy multipliers can then be evaluated as mixed convection to forced convection friction factor–Reynolds number products at the same mass flow rate and inlet temperature utilizing the following relations.

The total buoyancy multiplier can be written as

$$\phi_t \equiv \frac{(f\mathrm{Re})_b}{(f_0\mathrm{Re})_b} = \frac{\Delta p_b^f}{\Delta p_{0b}^f}\,\frac{\bar{\rho}_b}{\rho_{in}}\,\frac{\mu_{in}}{\bar{\mu}_b} = \frac{\Delta p_b^f}{\Delta p_{0b}^f}\,\frac{u_{in}}{u_b}\,\frac{\mathrm{Re}_b}{\mathrm{Re}_{in}} \tag{26}$$

The global buoyancy multiplier is similarly evaluated as

$$\phi_g \equiv \frac{(f\mathrm{Re})_{bg}}{(f_0\mathrm{Re})_b} = \frac{\Delta p_{bg}^f}{\Delta p_{0b}^f}\,\frac{\bar{\rho}_b}{\rho_{in}}\,\frac{\mu_{in}}{\bar{\mu}_b} = \frac{\Delta p_{bg}^f}{\Delta p_{0b}^f}\,\frac{u_{in}}{u_b}\,\frac{\mathrm{Re}_b}{\mathrm{Re}_{in}} \tag{27}$$

It then follows from equations (24), (25), (26), and (27) that the local buoyancy multiplier equals

$$\phi_l \equiv \frac{\phi_t}{\phi_g} = \frac{(f\mathrm{Re})_b}{(f\mathrm{Re})_{bg}} = \frac{\Delta p_b^f}{\Delta p_{bg}^f} \approx \frac{\Delta p_b^{fI}}{\Delta p_{bg}^{fI}} \tag{28}$$

The skew multiplier can be calculated from equation (27) as

$$\phi_s = \frac{\phi_g}{\phi_g^I} = \frac{\Delta p_{bg}^f}{\Delta p_{bg}^{fI}} \tag{29}$$

The pressure drop components of equations (26) through (29) are obtained from subchannel analysis. The relationship between these components and the subchannel parameters, particularly the subchannel multipliers, can be displayed as follows.

The bundle frictional pressure drop component can be expressed in terms of subchannel variables as

$$\Delta p_b^f = (\bar{\rho}_n - \Sigma\bar{\rho}_n/N)gL_h \pm \frac{\dot{m}_b\bar{\mu}_n(f_0\mathrm{Re})_n}{2D_{en}^2(\Sigma A_n)(\Sigma\bar{\rho}_n/N)}\int_0^{L_h}\varphi_n X_n dz \tag{30}$$

where the summation is over N subchannels, the subchannel friction factor multipliers are given by equations (13*a*), (14*a*), and (15*a*), and X_n is the flow split parameter defined as

$$X_n = u_n/u_b \tag{31}$$

which is a function of heated bundle axial position z. Note that the positive sign is for upflow, and the negative sign for downflow in equation (30).

The global frictional pressure drop component can be expressed from equation (30), taking φ_n equal to unity for the global component, as

$$\Delta p_{bg}^f = (\bar{\rho}_n - \Sigma\bar{\rho}_n/N)gL_h \pm \frac{\dot{m}_b\bar{\mu}_n(f_0\mathrm{Re})_n}{2D_{en}^2(\Sigma A_n)(\Sigma\bar{\rho}_n/N)}\int_0^{L_h}X_n dz \tag{32}$$

where the laminar forced convection friction constant $(f_0\mathrm{Re})_n$ has been employed, thereby artificially excluding the local buoyancy effects within the subchannels.

The isothermal bundle frictional pressure drop can also be written in terms of subchannel parameters by simplifying equation (30), noting that $\bar{\rho}_n = \Sigma\bar{\rho}_n/N$, $\varphi_n = 1$, and X_n is constant along the axis, i.e.,

$$\Delta p_{0b}^f = \pm\frac{\dot{m}_b\mu_{in}(f_0\mathrm{Re})_n X_n L_h}{2D_{en}^2(\Sigma A_n)\rho_{in}} \tag{33}$$

where the coolant physical properties have been evaluated at the bundle inlet and are invariant along the whole bundle.

Equations (26) through (29), along with equations (30), (32), and (33), furnish the functional relationship between the subchannel multipliers φ, and the bundle multipliers ϕ. The computational results for the bundle multipliers can be correlated as polynomials of the following form by a least-squares fitting procedure:

$$\phi = \exp\left\{\sum_{k=0}^{4} C_k\,[\ln(1+\mathrm{Gr}_q/\mathrm{Re})]^k\right\}_b \tag{34}$$

where C_k are regression coefficients.

Application of the Predictive Model. The bundle mixed convective pressure drop model just developed is next applied to the MIT 19 rod bare ($P/D = 1.25$) and wire-wrapped ($P/D = 1.25$, $H/D = 35$) hexagonal array bundle geometries to investigate buoyant flow characteristics, utilizing the modified mixed convection subchannel friction factors. Some of the major bundle dimensions are rod diameter = 18.9 mm (0.746 in.), wire diameter = 4.67 mm (0.184 in.), inner flat-to-flat distance = 110 mm (4.33 in.), and heated length = 1626 mm (64 in.) with axially linear power profile.

Developing Buoyancy. It has been found that the bundle heated length L_h has a significant bearing on the global and local buoyancy effects in rod bundles. This is in contrast to the isothermal condition in bundles where the friction factor becomes essentially constant over the bundle length once the flow has fully developed. For isothermal laminar flow the typical entry length is $L/D_e \approx 0.08\mathrm{Re}$.

The bundle buoyancy multipliers ϕ_t, ϕ_g, and ϕ_l can be calculated as functions of the L_h/D_e ratio. The results are plotted in Fig. 3 where the local buoyancy multiplier is the difference between the total and global multipliers. Observe that (1) the three buoyancy multipliers monotonically increase with heated length, and (2) in a shorter bundle (or equivalently in the inlet region of a longer bundle) the global buoyancy is predominant over the local effect, whereas in a longer bundle the local buoyancy becomes comparable to the global buoyancy.

Figure 4 illustrates the functional relationships between the three buoyancy multipliers for bundles of different heated length under uniform power conditions. For both the bare and wire-wrapped bundles, the global buoyancy multiplier experiences an inflection around $L_h/D_e = 30$ and then attains a constant moderate slope from $L_h/D_e = 40$ onward. The local and total buoyancy multipliers increase monotonically along the heated length considered. They do, however, tend to asymptotes around $L_h/D_e = 120$ for the bare bundle, and 150 for the wire-wrapped bundle.

Wire Wrapping. The effect of wire wrapping on the bundle buoyancy multipliers was evaluated by Suh (1986). For aiding flow the total multipliers are essentially the same over

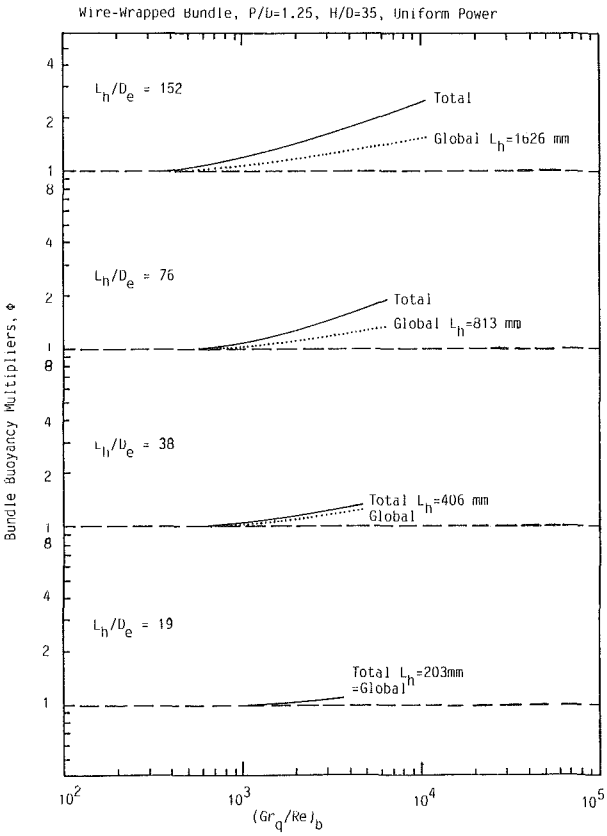

Fig. 3 Heated length effect on bundle friction factor multipliers

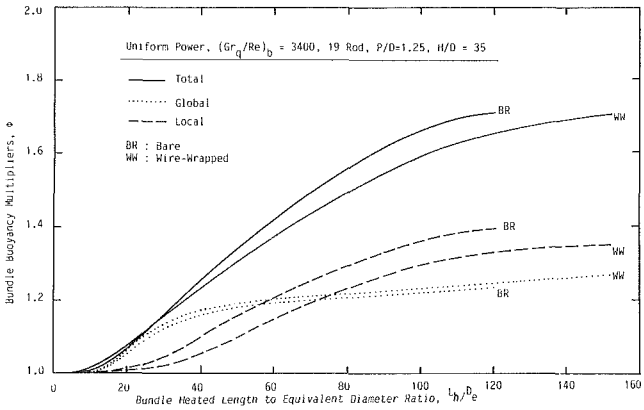

Fig. 4 Developing buoyancy bundle friction factor multipliers

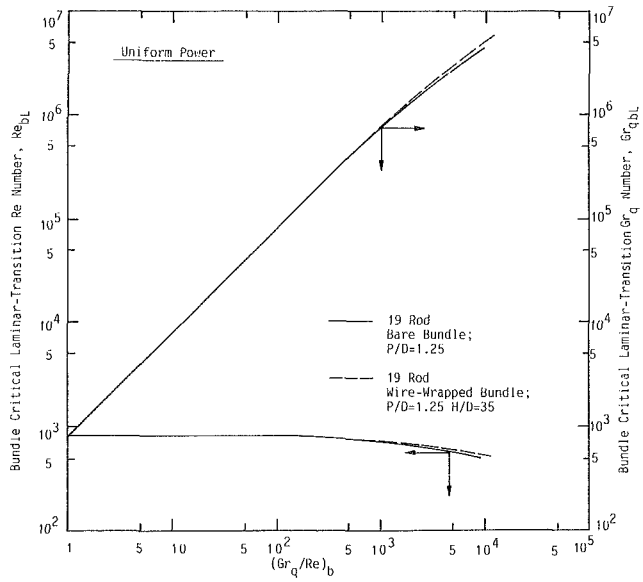

Fig. 5 Critical laminar-transition numbers affected by bundle local buoyancy

the Gr_q/Re parameter range considered for the MIT 19 rod bare and wire-wrapped bundles. However, the components comprising the total multiplier are not equal. Specifically the global multiplier is greater but the local multiplier is smaller in the wire-wrapped bundle than in the bare bundle. The larger global effect in the wire-wrapped bundle is due to greater flow redistribution among the subchannels across the heated section than in the bare bundle. On the other hand, the local intrasubchannel shear stress increase is reduced by the presence of wires, since the heated perimeter is less than the wetted perimeter and the flow area available for buoyancy effect development is reduced. These computational results have been confirmed experimentally (Suh, 1986).

Transition From Laminar Regime. It is assumed that for bundles where both the global and local buoyancy effects are operating only the local component is associated with the transition from the laminar regime in analogy with the subchannel criterion. Thus the critical bundle laminar-transition Re number Re_{bL} can be determined from equations (3) and (34) with $C_k = L_k$ for the local multiplier as

$$Re_{bL} = Re_{0bL}/\phi_l = Re_{0bL}\exp\left(\sum_{k=0}^{4}(-L_k)[\ln(1+Gr_q/Re)]^k\right)_b \tag{35}$$

where the isothermal Re_{0bL} number is calculated with the Cheng-Todreas (1986) correlation.

Given the $(Gr_q/Re)_b$ parameter, equation (35) can be used to determine the Re_{bL} number, which in turn gives the corresponding Gr_{qbL} number. The local bundle multiplier is essentially the same for all the power distributions. Thus the Re_{bL} and Gr_{qbL} numbers are considered to be independent of the power profile. Typical uniform power results are presented in Fig. 5 for the MIT 19 rod bare and wire-wrapped bundle geometries. As expected, the Gr_{qbL} number is an increasing function, while the Re_{bL} number is a decreasing function of the $(Gr_q/Re)_b$ parameter.

It is experimentally demonstrated in the companion paper that the local buoyancy diminishes and only the global buoyancy remains in effect as the transition proceeds from the laminar regime. The predictive multiplier for the transition regime is therefore based only on the global buoyancy effect.

Engineering Correlations and Sample Calculation

Bundle Friction Factor Equations. Since the bundle arrays considered are currently utilized for LMR applications, the determination of the Pr number effect on mixed convection frictional characteristics is of importance. The major concern is associated with the development of mixed convective velocity profiles. Since no developing flow correlations are available in the literature for liquid metals in mixed convection, we bounded the effect of enhancing the development of the mixed convection flow by reducing the regression coefficient of equation (20*a*) from 0.36 to 0.036. As a result, the bounding φ_i^{dev} equals 0.965 at $z(P_{hi}/4A_i) = 50$ whereas φ_i^{dev} due to equation (20*a*) is 0.735. The same values were chosen for the bare bundle equation (20*b*). The heated bundle total laminar buoyancy multipliers were calculated for the MIT 19-rod bare

Table 3 Regression coefficients for bundle multipliers of equation (34) for LMR fuel assembly ($P/D = 1.25$, $H/D = 50$, $L_h = 914$ mm = 36 in.)

N_r	C_k	$k=0$	$k=1$	$k=2$	$k=3$	$k=4$	$(\mathrm{Gr}_q/\mathrm{Re})_{\max}$
	G_k^I	−2.914E−01	5.561E−01	−2.163E−01	3.038E−02	−1.386E−03	3700
19	T_k^I	−1.645E−01	3.159E−01	−1.241E−01	1.572E−02	−5.107E−04	3700
	G_k^{IV}	−7.661E−02	1.537E−01	−6.954E−02	1.081E−02	−4.830E−04	4200
	G_k^I	3.701E−01	−6.823E−01	2.336E−01	−2.909E−02	1.283E−03	9400
37	T_k^I	7.003E−01	−1.298E+00	4.547E−01	−5.972E−02	2.829E−03	9400
	G_k^{IV}	5.804E−01	−1.080E+00	3.838E−01	−4.972E−02	2.255E−03	3000
	G_k^I	1.202E+00	−2.213E+00	7.543E−01	−9.408E−02	4.066E−03	5400
61	T_k^I	3.952E−01	−7.467E−01	2.815E−01	−4.014E−02	2.098E−03	3600
	G_k^{IV}	2.796E−01	−5.302E−01	2.014E−01	−2.768E−02	1.361E−03	3200
	G_k^I	1.652E−01	−3.104E−01	1.142E−01	−1.518E−02	7.484E−04	1800
91	T_k^I	1.803E−01	−3.501E−01	1.451E−01	−2.297E−02	1.370E−03	1400
	G_k^{IV}	−1.482E+00	2.720E+00	−8.997E−01	8.820E−02	−1.013E−03	1200

Table 4 Regression coefficients for bundle multipliers of equation (34) for LMR blanket assembly ($P/D = 1.08$, $H/D = 8$, $L_h = 1626$ mm = 64 in.)

N_r	C_k	$k=0$	$k=1$	$k=2$	$k=3$	$k=4$	$(\mathrm{Gr}_q/\mathrm{Re})_{\max}$
	G_k^I	−8.624E−03	2.488E−02	−2.154E−02	5.202E−03	−1.623E−04	1155
19	T_k^I	5.461E−01	−9.906E−01	3.151E−01	−3.363E−02	1.511E−03	1170
	G_k^{IV}	1.452E−01	−2.886E−01	1.274E−01	−2.041E−02	1.358E−03	1424
	G_k^I	1.780E−01	−3.624E−01	1.710E−01	−2.805E−02	1.730E−03	1137
37	T_k^I	6.157E−01	−1.176E+00	4.575E−01	−6.386E−02	3.503E−03	1138
	G_k^{IV}	1.312E−01	−2.623E−01	1.153E−01	−1.464E−02	7.175E−04	307
	G_k^I	−3.689E−03	1.444E−02	−1.972E−02	1.045E−02	−1.031E−03	145
61	T_k^I	1.734E−03	−1.875E−02	3.101E−02	−1.248E−02	2.108E−03	146
	G_k^{IV}	−6.969E−03	6.602E−03	6.670E−03	−3.145E−03	1.028E−03	60

and wire-wrapped bundles using the mixed convection friction factors with the above two developing multipliers. The results show that $\phi_l' = 1.395$ with equation (20*b*) versus $\phi_l' = 1.468$ with the bounding curve at $\mathrm{Gr}_q/\mathrm{Re} = 1800$ in the bare bundle, while $\phi_t = 1.374$ with equation (20*a*) versus $\phi_t = 1.426$ with the bounding curve at $\mathrm{Gr}_q/\mathrm{Re} = 1700$ in the wire-wrapped bundle. Considering the limitations associated with equation (19) (i.e., developed for $\mathrm{Pr} = 6$ and $\mathrm{Gr}_q/\mathrm{Re} = 465$ in circular tubes), the 5 percent increase for the bare bundle and the 4 percent increase for the wire-wrapped bundle of the bundle multipliers for the bounding case are tolerable uncertainties. Thus equations (20*a*) and (20*b*) with the regression coefficient of 0.36 are retained for LMR applications.

The regression coefficients for the correlating equation (34) are presented in Tables 3 and 4 for typical LMR fuel and blanket assemblies, respectively, for the uniform power global (G_k^I), uniform power total (T_k^I), and diametral skew global (G_k^{IV}) buoyancy multipliers. Only the most practical diametral power skew is considered, specifically a maximum-to-minimum rod power ratio of 1.5. The local multiplier coefficient can be determined from $L_k = T_k - G_k \approx T_k^I - G_k^I$, and the skew multiplier coefficient from $S_k = G_k - G_k^I$. The total multiplier is proposed as the laminar mixed convection multiplier, and the global multiplier as the transition multiplier. These multipliers are to be applied to the corresponding isothermal friction factors at the same Re number.

Figure 6 demonstrates the considerable effect of rod number on the bundle mixed convection friction factors. The bundle friction factors increase with bundle size in mixed convection, whereas they are practically independent thereof in forced convection. Further, the skew multipliers are fairly constant for the fuel assembly geometry while they increase with bundle size for the blanket assembly. This is in contrast to the forced convection regime where the rod number effect was found to be negligible (Cheng and Todreas, 1986).

Validation of the Correlating Equations. The engineering correlations developed in this work are validated against the water test data in the companion paper spanning the following parameter ranges in the MIT 19-rod bundles. The laminar flow test conditions varied as

	Wire-wrapped	Bare
Maximum-to-minimum power ratio	1 - 26	1 - 1.7
Maximum-to-average power ratio	1 - 2.55	1 - 1.28
Bundle inlet Re number	160- 350	150- 350
Bundle average Re number	164- 589	180- 570
Bundle average $\mathrm{Gr}_q/\mathrm{Re}$ number	6 -14,773	11 -18,500
Bundle average $\mathrm{Gr}_{\Delta T}/\mathrm{Re}$ number	1 - 5458	2 - 2840

The uniform power transition flow test conditions varied as

	Wire-wrapped	Bare
Bundle inlet Re number	800 -1153	600-1100
Bundle average Re number	1031-1379	600-1240
Bundle average $\mathrm{Gr}_q/\mathrm{Re}$ number	1558-2834	120-4940
Bundle average $\mathrm{Gr}_{\Delta T}/\mathrm{Re}$ number	78 - 212	6 - 340

The predictive model has been found satisfactorily to describe the mixed convective low flow friction loss characteristics in rod bundle geometries.

Design Procedure. Suppose that one wants to determine the bundle frictional pressure drop in a 19-rod wire-wrapped bundle with $P/D = 1.25$, $H/D = 50$, $L_h = 1626$ mm (64 in.), and $D_e = 10.72$ mm (0.422 in.) operating under the following conditions:

$$\mathrm{Gr}_{qb} = 1.64\mathrm{E}6 \qquad \mathrm{Re}_b = 470 \qquad (\mathrm{Gr}_q/\mathrm{Re})_b = 3489$$

1.5:1 diametral power skew (Type IV maximum-to-minimum rod power ratio)

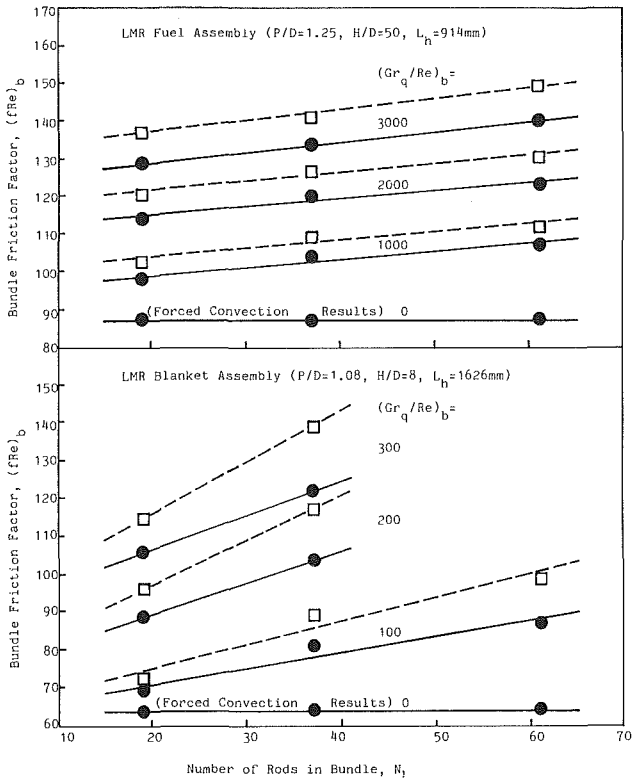

Fig. 6 Calculated bundle friction factors:—best fit lines for uniform power results (•) and— —best fit lines for 1.5:1 diametral power skew results (□)

First, confirm whether the flow regime is laminar. The laminar-transition Re_{bL} number is given by equation (35) as

$$\mathrm{Re}_{bL} = \mathrm{Re}_{0bL}/\phi_l = 798/1.348 = 592$$

where $\mathrm{Re}_{0bL} = 798$ from the Cheng-Todreas correlation and $\phi_l = 1.348$ from the following calculation. It is thus confirmed that the bulk flow is in the laminar regime (i.e., $\mathrm{Re}_b = 470 < \mathrm{Re}_{bL} = 592$). Note also that the bundle buoyancy-to-inertia parameter is within the range specified in Table 3 (i.e., $(\mathrm{Gr}_q/\mathrm{Re})_b = 3489 < (\mathrm{Gr}_q/\mathrm{Re})_{\max} = 3700$).

Now evaluate the bundle buoyancy multipliers. All multipliers are functions of $x = \ln(1 + \mathrm{Gr}_q/\mathrm{Re})$. Evaluating x yields $x = \ln(1 + 3489) = 8.158$.

From Table 3 the following bundle buoyancy multipliers are obtained per equation (34):

$$\phi_g^{IV} = \exp[-(7.661\mathrm{E}-2) + (1.537\mathrm{E}-1)x$$
$$-(6.954\mathrm{E}-2)x^2 + (1.081\mathrm{E}-2)x^3 - (4.830\mathrm{E}-4)x^4] = 1.322,$$
$$\phi_g^I = \exp[-(2.914\mathrm{E}-1) + (5.561\mathrm{E}-1)x$$
$$-(2.163\mathrm{E}-1)x^2 + (3.038\mathrm{E}-2)x^3 - (1.386\mathrm{E}-3)x^4] = 1.228,$$
$$\phi_t^I = \exp[-(1.645\mathrm{E}-1) + (3.159\mathrm{E}-1)x$$
$$-(1.241\mathrm{E}-1)x^2 + (1.572\mathrm{E}-2)x^3 - (5.107\mathrm{E}-4)x^4] = 1.532.$$

Thus $\phi_l^{IV} \approx \phi_l^I = \phi_t^I/\phi_g^I = 1.532/1.228 = 1.248$ and $\phi_s^{IV} = \phi_g^{IV}/\phi_g^I = 1.322/1.228 = 1.077$. Note that these multipliers are for $L_h = 914$ mm (36 in.) from Table 3.

One now needs to evaluate the effect of heated length. For $D_e = 10.72$ mm (0.422 in.), reading from the *WW* curves in Fig. 4 gives

$$\phi_t^I(L_h = 1626\ \mathrm{mm})/\phi_t^I(L_h = 914\ \mathrm{mm})$$
$$= \phi_t^I(L_h/D_e = 152)/\phi_t^I(L_h/D_e = 85) = 1.710/1.525 = 1.121,$$
$$\phi_g^I(L_h/D_e = 152)/\phi_g^I(L_h/D_e = 85) = 1.265/1.220 = 1.037,$$
$$\phi_l^I(L_h/D_e = 152)/\phi_l^I(L_h/D_e = 85) = 1.350/1.250 = 1.080.$$

No heated length multiplier is applied to the skew multiplier since this effect has already been accounted for in the uniform global multiplier. One then finds that for $L_h/D_e = 152$,

$$\phi_l^I = (1.248) \times (1.080) = 1.348,$$
$$\phi_g^I = (1.228) \times (1.037) = 1.273,$$
$$\phi_s^{IV} = 1.077.$$

The isothermal laminar bundle friction factor is $(f_0\mathrm{Re})_b = 87.68$ according to the Cheng-Todreas correlation. From equation (1) the desired parameter $(f\mathrm{Re})_b$ can finally be determined as

$$(f\mathrm{Re})_b = \phi_t(f_0\mathrm{Re})_b = \phi_s^{IV}\phi_g^I\phi_l^I(f_0\mathrm{Re})_b$$
$$= (1.077)(1.273)(1.348)(87.68) = (1.848)(87.68) = 162.0.$$

Observe that the frictional pressure drop could have been underestimated by as much as 46 percent if the isothermal bundle friction factor correlation had been adopted.

If the Re_b number is increased with $(\mathrm{Gr}_q/\mathrm{Re})_b$ fixed at 3489, the transition from laminar flow will be initiated from the exit of the heated bundle. As the Re_b number is further increased, this transition will progress downward and reach the inlet at the isothermal transition Re_b number of 798. Then only the global effect is significant so that

$$f = \phi_g^{IV} f_0 = \phi_s^{IV}\phi_g^I f_0 = (1.077)(1.273)f_0 = 1.371 f_0$$

at the same Re_b number.

In the intermediate Re_b number range, as transition proceeds downward through the bundle, the buoyancy multiplier reduces monotonically from the laminar to the transition value. No precise prediction method is available for this region. As a first approximation, it is suggested that a smoothed curve be used, which follows a gradual transition from the laminar to the transition correlations.

Conclusions

1 Phenomenological models have been proposed for the flow redistribution mechanisms and flow regime effects. The global and local buoyancy effects have been found to be operating and to have a significant bearing on the mixed convection frictional pressure loss characteristics.

2 A method of representation has been developed for laminar mixed convection subchannel friction factors along with the applicable laminar-transition criteria. The approach is to apply subchannel multipliers, which are functions of the effects of mixed convection, wire wrapping, and buoyancy development, to the corresponding isothermal bare subchannel values.

3 A systematic approach has been presented for predicting frictional pressure losses in a bundle. Account is taken of the effects of interacting and developing buoyancy flows, radial power skew, transition from laminar flow, and rod number using a subchannel analysis code with applicable subchannel friction factors. The mixed convection bundle design correlations are presented as the products of corresponding isothermal friction factors and buoyancy multipliers for the global and local effects.

4 Bundle design correlations have been presented for the laminar and transition flow frictional pressure drop calculation in typical LMR fuel and blanket wire-wrapped rod assemblies along with laminar-transition criteria. The total buoyancy multiplier is proposed as the laminar mixed convection regime multiplier. The global buoyancy multiplier is proposed as the transition regime multiplier. Contrasted to forced convection behavior, a strong rod number effect is present in mixed convection conditions.

5 A sample calculation has been given to demonstrate the proposed design procedure for evaluating the bundle friction pressure drops in laminar and transitional mixed convection

conditions. The result is of design importance because the mixed convection frictional pressure losses exceed the corresponding isothermal values at the same Re numbers.

Acknowledgments

The authors gratefully acknowledge the financial support provided for this work by the Power Reactor and Nuclear Fuel Development Corporation (PNC), Japan.

References

Bishop, A. A., Willis, J. M., and Markley, R. A., 1980, "Effects of Buoyancy on Laminar Vertical Upward Flow Friction Factors in Cylindrical Tubes," *Nuclear Engineering and Design*, Vol. 62, pp. 365–369.

Brown, W. G., 1960, "The Superposition of Forced and Free Convection at Low Flow Rates in a Vertical Tube," *VDI-Forschungsheft*, Vol. 480 (in German).

Cheng, S.-K., and Todreas, N. E., 1986, "Hydrodynamic Models and Correlations for Bare and Wire-Wrapped Hexagonal Rod Bundles—Bundle Friction Factors, Subchannel Friction Factors and Mixing Parameters," *Nuclear Engineering and Design*, Vol. 92, pp. 227–251.

Gebhart, B., and Mahajan, R. L., 1982, "Instability and Transition in Buoyancy-Induced Flows," *Advances in Applied Mechanics*, Vol. 22, pp. 231–315.

Huang, T.-T., 1987, "Flow Recirculation in Liquid Metal Reactor Rod Bundles," Sc.D. Thesis, Massachusetts Institute of Technology, Department of Nuclear Engineering, Cambridge, MA.

Iannello, V., Suh, K. Y., and Todreas, N. E., 1988, "Mixed Convection Friction Factors and Nusselt Numbers in Vertical Annular and Subchannel Geometries," *International Journal of Heat and Mass Transfer*, Vol. 31, pp. 2175–2189.

Mawatari, K., Namekawa, F., Handa, N., Kasahara, F., and Ishida, Y., 1982, "Natural Circulation Decay Heat Removal Experiments and Analysis in an LMFBR Fuel Assembly," *Proceedings, International Topical Meeting on LMFBR Safety and Related Design and Operating Aspects*, Lyon, France.

Ninokata, H., Efthimiadis, A., and Todreas, N. E., 1987, "Distributed Resistance Modeling of Wire-Wrapped Rod Bundles," *Nuclear Engineering and Design*, Vol. 104, pp. 93–102.

Okada, T., Efthimiadis, A., Iannello, V., and Todreas, N. E., 1985, "Mixed Convection Pressure Drop in Vertical Rod Bundles," *Proceedings, 3rd International Topical Meeting on Reactor Thermal Hydraulics*, Vol. 2, Paper No. 16. C.

Suh, K. Y., 1986, "Mixed Convective Low Flow in Vertical Rod Assemblies," Ph.D. Thesis, Massachusetts Institute of Technology, Department of Nuclear Engineering, Cambridge, MA.

Suh, K. Y., Todreas, N. E., and Rohsenow, W. M., 1989, "Mixed Convective Low Flow Pressure Drop in Vertical Rod Assemblies: II—Experimental Validation," ASME JOURNAL OF HEAT TRANSFER, Vol. 111, this issue.

Wang, S.-F., Todreas, N. E., and Rohsenow, W. M., 1981, "Subchannel Friction Factors for Bare Rod Arrays Under Mixed Convection Conditions," in: *Decay Heat Removal and Natural Convection in Fast Breeder Reactors*, Hemisphere Publishing Corp., Washington, DC, pp. 95–109.

K. Y. Suh[1]

N. E. Todreas

W. M. Rohsenow

Departments of Nuclear and Mechanical Engineering,
Massachusetts Institute of Technology,
Cambridge, MA 02139

Mixed Convective Low Flow Pressure Drop in Vertical Rod Assemblies: II—Experimental Validation

An experimental study has been conducted to validate the predictive models and correlations for laminar and transition flow frictional pressure loss in vertical rod bundles under mixed convection conditions. An experimental procedure has been developed to measure low differential pressures under mixed convection conditions in 19 heated rod bare and wire-wrapped assemblies. The proposed model has been found successfully to predict the effects of wire wrapping, power skew, transition from laminar regime, developing and interacting flow redistributions, and rod number on the friction loss characteristics in bundle geometries over the bundle average Gr_q/Re number range of 6 to 18,500.

Introduction

In this work the predictive models and correlations (Fig. 1) for the single bundle frictional pressure drop characteristics under natural circulation conditions proposed in the companion paper (Suh et al., 1989) are validated against the water test results available in the literature (Mawatari et al., 1982; Okada et al., 1985), and by a series of new experiments using water spanning a variety of transverse power distributions and geometric characteristics. The objective of our experiments was to assess the effects of wire wrapping, power skew, transition from laminar regime, and developing and interacting global and local flow redistributions on mixed convection pressure drop characteristics in hexagonal array rod bundles under heated upflow conditions. The correlations, while validated with water experiments, can be applied to liquid metal reactor (LMR) conditions using a bounding assumption for the Prandtl (Pr) number effect on the mixed convection flow development.

A procedure has been developed to measure low-magnitude differential pressures under mixed convection conditions. The experimental method improves upon our previous one (Okada et al., 1985) with respect to instrument drift correction and test section outlet temperature evaluation (Suh, 1986).

Comparison between the predicted and measured results demonstrates that the proposed method of correlation is capable of describing the various mixed convective low flow characteristics in rod bundles. The modified subchannel mixed convection friction factors that are compatible with the bulk-mean properties of coolants were utilized in the ENERGY-IV Code (Cheng and Todreas, 1986). The bulk-mean densities were consistently employed in evaluating the buoyancy terms in both calculations and experiments.

Experimental Apparatus and Measurement

Test Assemblies and Hydraulic Loop. Two heated 19-rod hexagonal array assemblies were built to measure frictional pressure drop using static pressure probes. One was a bare rod fuel geometry array ($P/D = 1.25$) and the other was a wire-wrapped fuel geometry array ($P/D = 1.25$, $H/D = 35$). Some of the major dimensions are rod diameter = 18.9 mm (0.746 in.), wire diameter = 4.67 mm (0.184 in.), inner flat-to-flat distance = 110 mm (4.33 in.) and heated length = 1626 mm (64 in.) with axially linear power profile. The assemblies were thermally insulated using fiberglass layers.

The hydraulic test loop shown in Fig. 2 was used to provide degassed water. Two parallel flow meters, with capacities of 1.240×10^{-4} m^3/s and 3.117×10^{-4} m^3/s, were used to measure the inlet flow rate. During mixed convection tests, the

Bundle Friction Factor Correlation

$(fRe)_b = \Phi_t\ (f_oRe)_b$

where $\Phi_t = \Phi_g\ \Phi_l$ and $\Phi_g = \Phi_s\ \Phi_g^I$

Rod Bundle Buoyancy Multipliers

$\Phi_t \triangleq (fRe)_b/(f_oRe)_b \sim \Delta p_b^f / \Delta p_{ob}^f$

$\Phi_g \triangleq (fRe)_{bg}/(f_oRe)_b \sim \Delta p_{bg}^f / \Delta p_{ob}^f$

$\Phi_l \triangleq \Phi_t / \Phi_g = \Delta p_b^f / \Delta p_{bg}^f \simeq \Delta p_b^{fI} / \Delta p_{bg}^{fI}$

$\Phi_s \triangleq \Phi_g / \Phi_g^I = \Delta p_{bg}^f / \Delta p_{bg}^{fI}$

Subchannel Friction Factor Correlation

$(fRe)_i = \varphi_i\ (f_oRe)_i$ $\qquad i=1,2$ and 3

where φ_i = Function $(\varphi_i^{mc}, \varphi_i^{ww}, \varphi_i^{dev})$

Fig. 1 Method of bundle friction factor correlation

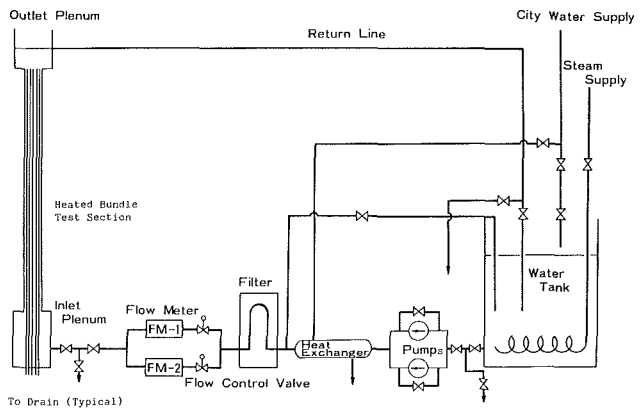

Fig. 2 Schematic of hydraulic test loop

[1]Current affiliation: Fauske & Associates, Inc., Burr Ridge, IL 60521.

Contributed by the Heat Transfer Division and presented at the ASME Winter Annual Meeting, Boston, Massachusetts, December 13-18, 1987. Manuscript received by the Heat Transfer Division May 16, 1988; revision received January 18, 1989. Keywords: Mixed Convection.

test section outlet heated water was discharged to drain to minimize drift or fluctuation in the inlet temperature of water drawn from the supply tank.

Differential Pressure Measurement. The differential pressure was measured by a Barocel electronic manometer with a high-precision pressure transducer. The signal was fed to TSI integrating voltmeter to obtain the time-averaged differential pressure. Investigations at low Re numbers required measurement of small differential pressures in the range of 0.001 to 1 torr.

The differential pressure measurement system is shown schematically in Fig. 3. Static pressure taps 1 and 2 were located in the hexcan at 152 mm and 1524 mm, respectively, downstream from the start of the heated length. The distance between the taps corresponded approximately to two wire wrap lead lengths of the MIT 19-rod wire-wrapped bundle. The same locations were adopted for the 19-rod bare bundle. The taps were positioned so as to detect the global buoyancy effect fully and to reduce the swirl flow effect. The manometer tubing was made of 0.635-mm tygon tube. The manometer was thermally insulated to minimize instrumentation drift caused by changes in the ambient temperature.

In order to evaluate the bundle friction factor from the measured pressure drop, the manometer reading (Δp_M) must be adjusted to allow for the difference between the densities of the fluid in the test section ($\bar{\rho}$) and the fluid in the manometer tubing (ρ_M) utilizing the relationship

$$\Delta p_b^f = \Delta p_M \pm (\rho_M - \bar{\rho}) g L \tag{1}$$

The plus sign in equation (1) is for upflow and the minus sign for downflow. The effect of this buoyancy term becomes pronounced in low Re number flow tests when very small differential pressures are to be measured and when the temperature differences between the test section and manometer tubing become significant. In these cases it is particularly important to ensure that this density term is accurately estimated.

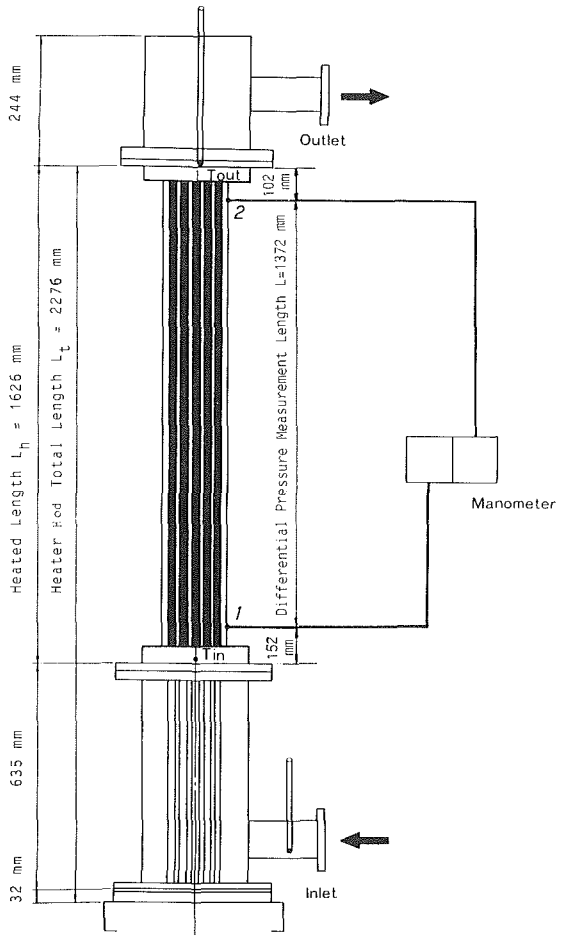

Fig. 3 Test bundle configurations and differential pressure measurement system

Nomenclature

c_p = specific heat of fluid at constant pressure
D = rod diameter
D_e = equivalent hydraulic diameter
D_w = wire diameter
f = Darcy–Weisbach friction factor $= 2D_e\Delta p/\rho u^2 L$
g = gravitational acceleration
Gr_q = Grashof number $= \rho^2 g\beta q'' D_e^4/k\mu^2$
Gr_{qD} = Grashof number based on rod diameter $= (D/D_e)^4 \mathrm{Gr}_q$
$\mathrm{Gr}_{\Delta T}$ = Grashof number based on axial bulk temperature rise $= \rho^2 g\beta\Delta T D_e^3/\mu^2$
H = wire lead length
k = thermal conductivity of fluid
L = pressure drop measurement length
L_h = axial heated length of rod
L_t = total length of rod
$\dot{m}$ = mass flow rate
Δp = pressure drop
P = rod pitch
$\dot{q}$ = heat rate
q'' = heat flux
Re = Reynolds number $= \rho u D_e/\mu$
T = temperature
ΔT = bulk fluid axial temperature rise
u = axial flow velocity
β = volumetric expansion coefficient of fluid
μ = dynamic viscosity of fluid
ρ = mass density of fluid
φ = subchannel friction factor multiplier
ϕ = bundle friction factor multiplier
Ψ = bundle intermittency factor

Subscripts

0 = isothermal
b = bundle
g = global
i = b, 1, 2, or 3 for bundle, interior, edge, or corner subchannel, respectively
in = inlet
l = local
L = laminar or transition from laminar regime
M = manometer
out = outlet
s = skew
t = total
tr = transitional
T = turbulent or transition to turbulent regime

Superscripts

I = uniform power profile
II = interior high, edge low power profile
III = interior low, edge high power profile
IV = diametral power skew profile
dev = developing
f = frictional
mc = mixed convective
ww = wire-wrapped
$'$ = equivalent bare (without considering wire)
$\bar{\ }$ = mean average

The manometer fluid density was evaluated as follows. The test loop was filled with degassed water, which was kept overnight to achieve an isothermal condition in the test section (at T_{in}) and in the manometer tubing (at T_M). At this point, however, the manometer reading was not zero since the two temperatures, T_{in} and T_M, still typically differed. Consequently the manometer was shifted to zero to respond as if $\rho_M = \rho_{in}$. During the mixed convection measurements the inlet temperature T_{in} was kept constant by employing a once-through mode loop operation, and the manometer temperature T_M was maintained constant by adopting long horizontal sections for the tubing. The zero setting procedure preceded each differential pressure measurement.

The test section fluid density was evaluated at the arithmetic mean bulk temperature between taps 1 and 2 as

$$\bar{\rho} = \frac{\rho_1 + \rho_2}{2} \tag{2}$$

where ρ_1 and ρ_2 correspond to the densities at temperatures

$$T_j = T_{in} + \frac{\dot{q}_b}{\dot{m}_b c_p} \frac{L_{hj}}{L_h}; \qquad j = 1, 2 \tag{3}$$

The mixed convection pressure drop measurement procedure is detailed by Suh (1986) for the heated upflow condition.

Selection of Transverse Power Profiles

In the companion paper (Suh et al., 1989) a predictive pressure drop model was developed to account for the two dominant phenomena: the local intrasubchannel buoyancy and the global intra-assembly buoyancy. This experimental work tests the capability of the proposed model to predict the total buoyancy effect due to various radial power profiles as well as the effects of wire wrapping, transition, and developing buoyancy. In particular, calculations were first performed for the four types of power distribution with an adiabatic boundary condition at the duct wall:

Type I. All 19 rods uniformly heated.
Type II. Interior 7 rods with high power; edge 12 rods with low power.
Type III. Interior 7 rods with low power; edge 12 rods with high power.
Type IV. Diametral power skew.

The Type I uniform power condition serves as the limiting case of decreasing peak-to-average power ratio. The mixed convection flow split at the heated section outlet was checked against the forced convection inlet flow split as calculated from the Cheng-Todreas (1986) correlation to determine the global flow redistribution for this Type I power profile. For Type II the objective was to increase the buoyancy-driven flow rates in the central zone at various power-to-flow combinations so that the global bundle-wide flow redistribution was readily differentiated from the inlet isothermal forced convection flow profile. The result was anticipated to be an appreciable increase in the global effect. Type III runs were executed to determine whether it is possible to decrease the global redistribution effect even below the effect for uniform power condition by preferentially heating the edge rods, thereby minimizing the change in the global flow distribution over the heated bundle. The purpose of Type IV runs was to estimate the bundle pressure drops with a realistic reactor power gradient.

Figure 4 presents the calculated flow distributions at the inlet and outlet of the heated bundle with these various radial power distributions. The typical bundle Re number was 550 and the bundle Gr_q/Re number was 4500 for all calculations. The results were obtained using the modified subchannel mixed convection friction factors in the ENERGY-IV code.

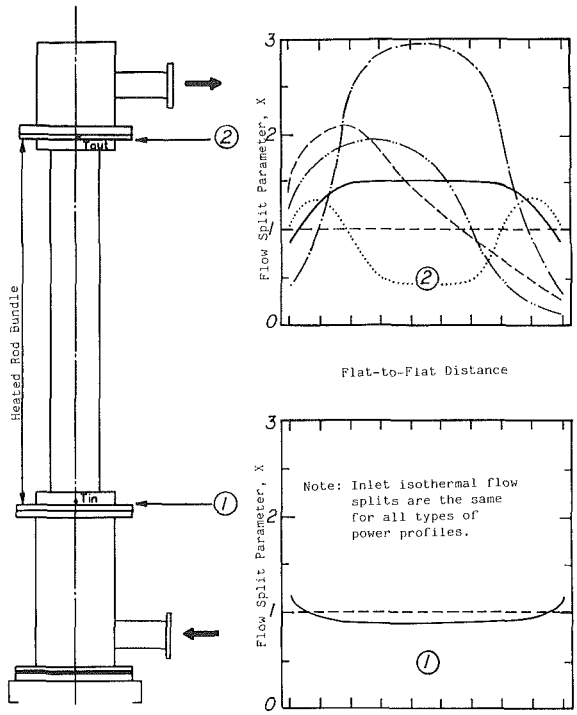

Fig. 4 Calculated global flow redistributions for uniform (———), interior high/edge low (—.—), interior low/edge high (.....), gradual diametral skew (— — —), and step diametral skew (—..—) power conditions

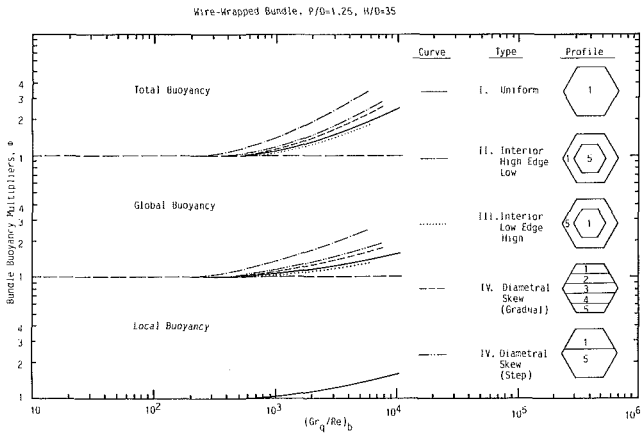

Fig. 5 Prediction of bundle friction factor multipliers for various power profiles

For the uniform power profile the global buoyancy effect gives rise to an increased flow in the central region of the bundle. When high power is applied to the interior seven rods in the Type II profile, the flow concentrates significantly in the central region. Highly heated edge rods in the Type III profile help maintain the high flow rate in the peripheral region, thereby yielding a minor change from the inlet isothermal flow profile. Buoyancy-induced flow is dominant in the hotter region of the bundle in the Type IV profiles as well.

Figure 5 summarizes the calculated bundle buoyancy friction factor-Reynolds number product multiplier ϕ, for the above power profiles. It is found that the Type II (interior high; edge low) profile results in the greatest global multiplier and hence the largest friction factor for a given bundle Gr_q/Re and Re number. The Type IV (diametral skew) results lie below the Type II curves with the step skew results slightly above the gradual gradient results for the same maximum-to-

minimum power ratio of 5:1. The uniform power curve lies below the Type IV curves. Interestingly enough, the Type III results are slightly lower than for uniform power because the velocity profile changes minimally from the inlet forced convection flow profile. Comparison among the three multipliers reveals that these differences can mainly be attributed to the global buoyancy effect. The most noticeable global flow redistribution takes place in Type II, with the ensuing increase in frictional pressure drop. Moreover the least amount of flow redistribution evidenced in Type III results in the least enhanced pressure drop. Of the two diametral power skews, the step change case is associated with a greater extent of global flow redistribution into the hotter side and hence a higher pressure drop than the gradual gradient. Figure 5 also shows that the local effect is essentially the same for all the power profiles. This is in accord with physical reasoning since the same subchannel mixed convection friction factors have been applied in the code calculations to simulate the local buoyancy effect.

These four power profiles were tested using the MIT 19-rod bare and wire-wrapped bundles over a wide range of maximum-to-minimum power ratios as described in the next section.

Experimental Validation and Interpretation

Data Base. Frictional pressure drops were measured for the following bundle average isothermal room temperature and heated mixed convection upflow conditions. In the 19-rod bare bundle tests the Re number ranged from 30 to 790 under isothermal conditions, which is less than the critical Re number for transition from an isothermal laminar flow of 798 according to the Cheng-Todreas (1986) correlation. For the laminar mixed convection tests the Re number ranged from 180 to 570, the Gr_q number from 3.27×10^3 to 1.06×10^7, and the Gr_q/Re parameter from 11 to 1.85×10^4 (corresponding to the $Gr_{\Delta T}/Re$ parameter from 2 to 2.84×10^3). For the transition mixed convection tests the Re number ranged from 600 to 1240, and the Gr_q/Re parameter from 120 to 4940 (corresponding to the $Gr_{\Delta T}/Re$ parameter from 6 to 340). In the 19-rod wire-wrapped bundle tests the Re number was varied from 30 to 720, while the isothermal transition Re number is again 798. For the mixed convection tests the Re number ranged from 160 to 590, the Gr_q number from 1.80×10^3 to 5.32×10^6, and the Gr_q/Re parameter from 6 to 1.48×10^4 (corresponding to the $Gr_{\Delta T}/Re$ parameter from 1 to 5.46×10^3).

The isothermal laminar friction factor data were correlated as

$$(f_0 Re)'_b = 92.06 \pm 9.15 \tag{4}$$

for the 19-rod bare bundle compared to the Cheng-Todreas correlation value of 95.26 ± 13.34. The experimental correlation for the isothermal laminar friction factor data was

$$(f_0 Re)_b = 83.13 \pm 7.79 \tag{5}$$

for the 19-rod wire-wrapped bundle compared to the Cheng-Todreas correlation value of 88.42 ± 12.38. For the transition flow regime, again the Cheng-Todreas isothermal correlation was utilized:

$$f_{btr} = f_{bL}(1 - \Psi)^{1/3} + f_{bT}\Psi^{1/3} \tag{6}$$

where

$$\Psi \equiv \frac{\log_{10} Re_b - \log_{10} Re_{bL}}{\log_{10} Re_{bT} - \log_{10} Re_{bL}} \tag{7}$$

The bundle buoyancy multipliers were obtained by dividing the experimental mixed convection friction factors by the corresponding isothermal frictional factors at the same bundle Re numbers (see Fig. 1). The thermophysical properties of water were evaluated at the bulk-mean temperature between the two pressure taps. The mixed convection experimental conditions for the bare and wire-wrapped bundles are summarized respectively in Tables 1 and 2.

Uncertainty analyses were performed for the isothermal and mixed convection tests (Suh, 1986). For the range of measurements (0.001 to 0.999 torr) the repeatability of the manometer measurement was estimated to be on the order of ± 1.0 percent. This was based on the scatter of repeated isothermal pressure drop measurements under the same flow rates including the resolution of the flowmeters utilized. In the mixed convection condition the gravity term introduced a more significant uncertainty than that associated with the manometer reading due to the fluctuations in the test section inlet and bulk-mean temperatures and the manometer tube temperature during the experiment. For a typical mixed convection run with Re_b = 450 and $(Gr_q/Re)_b$ = 2200, the total uncertainty for differential pressure measurements was estimated to be within ± 25 percent.

Table 1 Summary of test conditions for bare bundle

Flow regime	Laminar		Transition
Power profile	Uniform	Diametral gradual skew	Uniform
Inlet temperature, °C	19.3–24.3	19.2–24.3	15.8–33.4
Inlet flow rate, m^3/s	6.04×10^{-5} 1.26×10^{-4}	8.59×10^{-5} -1.24×10^{-4}	2.10×10^{-4} -2.95×10^{-4}
Inlet velocity, m/s	0.0122–0.0255	0.0181–0.0250	0.0424–0.0596
Average rod power, W	3.2–1348	23.3–1100	115–1503
Maximum-to-average rod power ratio	1:1	1.28:1	1:1
Outlet temperature, °C	20.7–77.2	30–70	18.4–49.4
Re	180–570	350–570	600–1240
Gr_q/Re	11–18500	85–11000	120–4940
$Gr_{\Delta T}/Re$	2–2840	11–1500	6–340

Table 2 Summary of test conditions for wire-wrapped bundle

Laminar flow	Type I	Type II	Type III	Type IV gradual skew	Type IV step change
Power profile	Uniform	*Interior high* edge low	*Interior low/0* edge high	Diametral skew	Diametral skew
Inlet temperature, °C	24.0–31.0	25.7–35.7	26.6–31.1	26.6–32.3	27.8–30.0
Inlet flow rate, m^3/s	6.04×10^{-5} -1.25×10^{-4}	7.06×10^{-5} -1.25×10^{-4}	1.13×10^{-4} -1.25×10^{-4}	8.06×10^{-5} -1.26×10^{-4}	1.22×10^{-4} 1.25×10^{-4}
Inlet velocity, m/s	0.0126–0.0261	0.0147–0.0261	0.0235–0.0261	0.0168–0.0263	0.0255–0.0261
Average rod power, W	3.2–1605	10.4–1288	25.9–1217	23.3–1530	17.7–1109
Maximum-to-average rod power ratio	1:1	1.310–2.547:1	1.125–1.583:1	1.280–2.374:1	1.550:1
Outlet temperature, °C	24.3–94.8	29.4–83.1	27.5–80.2	28.6–86.5	28.5–70.4
Re	164–541	306–589	312–507	293–578	328–513
Gr_q/Re	6–14773	25–9844	58–9184	60–11,414	42–6392
$Gr_{\Delta T}/Re$	1–5458	4–2599	10–1849	11–2133	7–1151

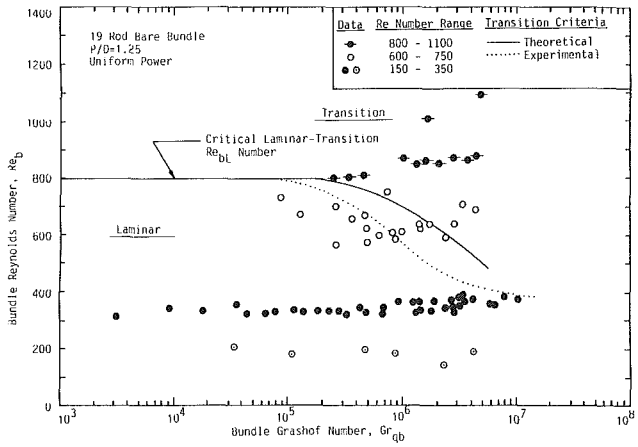

Fig. 6 Summary of bare bundle uniform power data with laminar-transition criteria

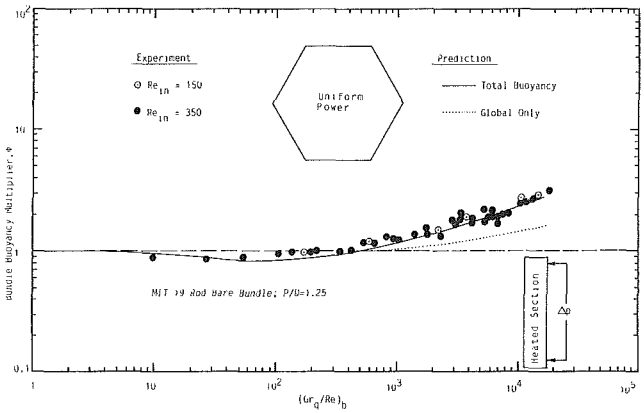

Fig. 7 Bare bundle uniform power laminar data with correlation curves

Results and Discussion

Bare Rod Bundle. Figure 6 summarizes the uniform power mixed convection data all taken in the MIT 19-rod bare bundle. No comparable data bases exist in the open literature for the hexagonal array bare rod bundles. The theoretical transition criterion (the solid curve) was established using the transition bundle Re_L and Gr_{qL} numbers determined by the method described in the companion paper. The experimental criterion (the dotted curve) is based on the observed magnitude of differential pressure fluctuations. On a time scale of 1 s, the data points above the experimental curve exhibited fluctuations greater than 0.01 torr, whereas those below the dotted curve exhibited very stable behavior with fluctuations less than 0.001 torr. The onset of sizable (± 0.01 torr) fluctuations in differential pressure was distinct. Note that the data at inlet Re between 150 (⊙) and 350 (●) lie below the criterion while the data at inlet Re between 800 and 1100 (●) lie above the criterion. The midrange data at inlet Re between 600 and 750 (○) are scattered across the criterion.

The laminar flow data are next plotted in terms of the total bundle buoyancy multiplier versus the bundle (Gr_q/Re) parameter in Fig. 7. First observe that the experimental data for the inlet Re numbers between 150 and 350 fall within a single data band. Second, the bundle buoyancy multiplier calculated with the modified mixed convection friction factors coupled with the developing multiplier satisfactorily predicts the data bank.

Figure 8 demonstrates that for the mild Type IV diametral power skew, the global bundle multiplier is comparable to that applicable to the uniform power case.

The transition region data are presented in Fig. 9 along with the laminar-transition data. The transition data with the inlet Re numbers between 800 and 1100 are found to follow the global bundle multiplier curve. The laminar-transition data with the inlet Re numbers between 600 and 750 are observed to follow the total bundle multiplier curve for laminar flow and then to experience a gradual transition onto the global bundle multiplier curve over a wide range of the Gr_q/Re parameter between 10^3 and 10^4. Therefore the gradual transition from the laminar flow behavior reflects the fact that the locally operating buoyant force diminishes relative to the globally occurring buoyant force. The global bundle multiplier has been calculated under the laminar flow condition (i.e., Re_b less than Re_{bL}) and is essentially the same as the one calculated under the transition regime where the Re number is between 800 and 1100.

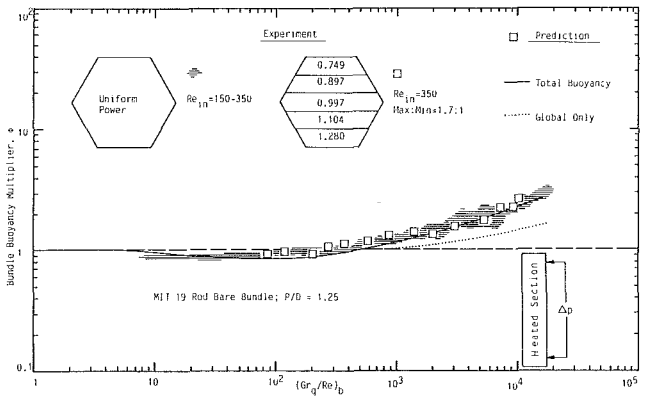

Fig. 8 Bare bundle Type IV gradual diametral power skew laminar data with correlation curves and uniform power data band

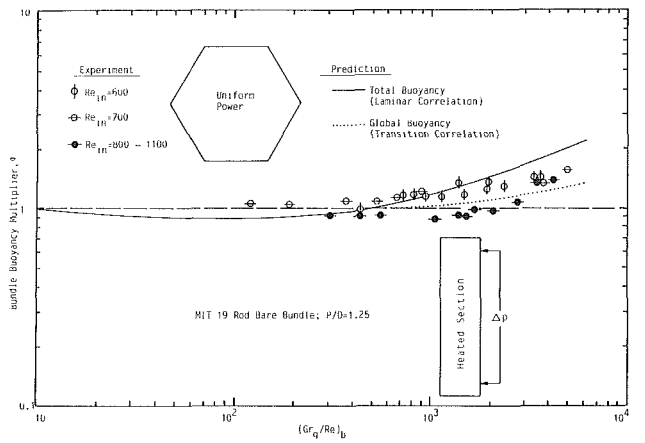

Fig. 9 Bare bundle uniform power transition data with correlation curves

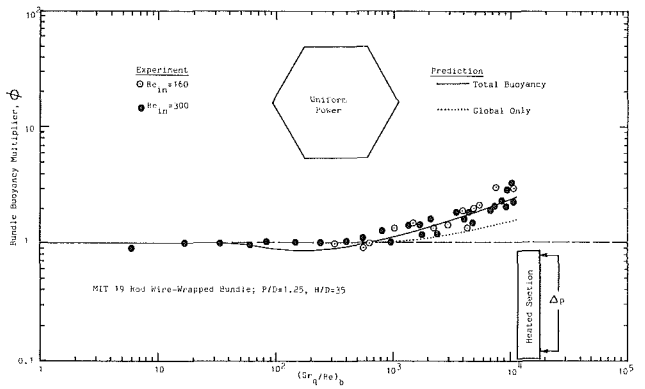

Fig. 10 Wire-wrapped bundle uniform power laminar data with correlation curves

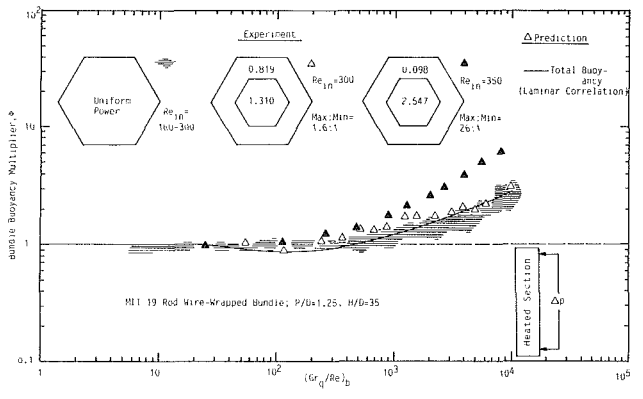

Fig. 11 Wire-wrapped bundle Type II interior high/edge low power skew laminar data with correlation curve and uniform power data band

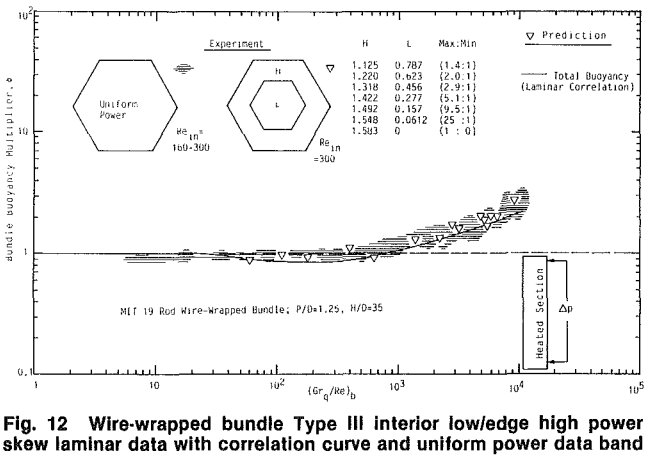

Fig. 12 Wire-wrapped bundle Type III interior low/edge high power skew laminar data with correlation curve and uniform power data band

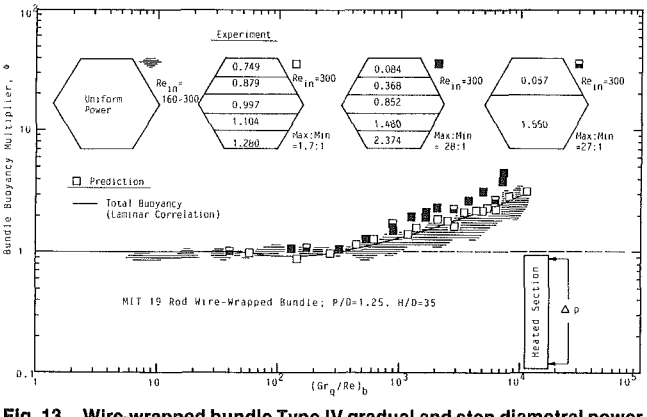

Fig. 13 Wire-wrapped bundle Type IV gradual and step diametral power skew laminar data with correlation curve and uniform power data band

Wire-Wrapped Rod Bundles. The laminar flow uniform power data are presented in Fig. 10. As was the case with the bare rod bundle, the experimental data for inlet Re numbers between 160 and 300 collapse onto a single data band. The data are satisfactorily predicted by the total bundle buoyancy multiplier calculated with the wire-wrapped subchannel modified mixed convection friction factors.

Figure 11 compares mild and severe Type II power skew data with uniform power data. The effect of radial power skew is apparent. The mild power skew (1.6:1) data are slightly above the uniform power data band and well predicted by the total bundle buoyancy multiplier curve. The high power skew (26:1) data are well above the uniform power data band. A prediction for this extreme case was not obtainable because the large crossflow created by this power skew led to numerical instabilities in the ENERGY-IV code.

The power skew Type III data at various skew ratios interestingly enough fall within the uniform power data bank in good agreement with the prediction curve, as demonstrated in Fig. 12. This test demonstrates the effect of minimizing the change from the inlet isothermal flow distribution by preferentially heating the edge rods.

Figure 13 provides the experimental data for Type IV diametral power skews representging a typical reactor power gradient. It is noted that the data for the 28:1 gradual skew and step change collapse onto the same data bank. The data for the moderate diametral skew (1.7:1) lie between the most severe skew data and the uniform power data. The moderate

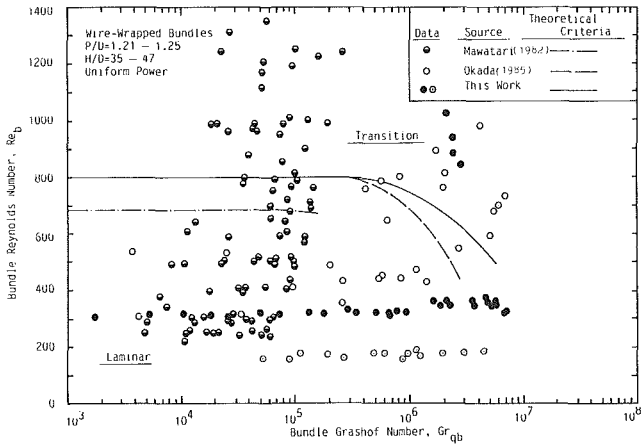

Fig. 14 Summary of wire-wrapped bundle uniform power data with laminar-transition criteria

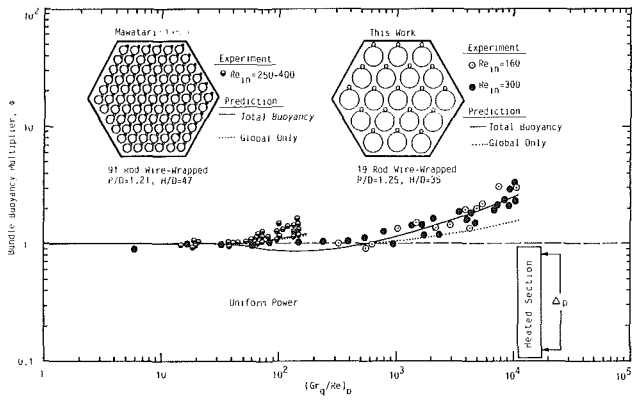

Fig. 15 Toshiba and MIT wire-wrapped bundles uniform power laminar data with correlation curves

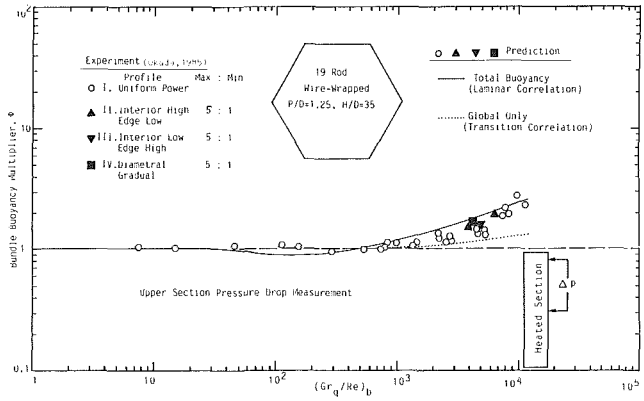

Fig. 16 Wire-wrapped bundle upper section data with correlation curves

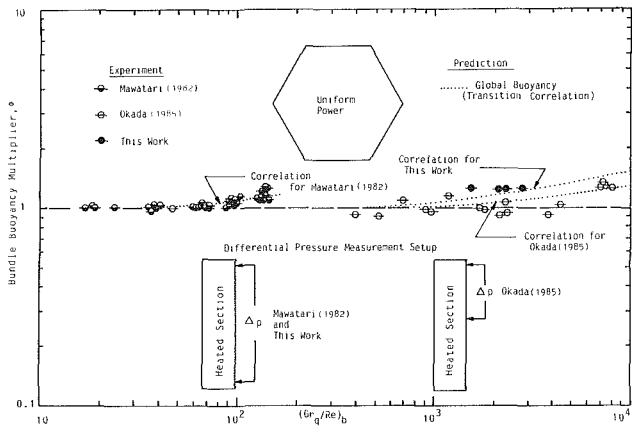

Fig. 17 Wire-wrapped bundle uniform power transition data with correlation curves

1.7:1 skew experimental results are well predicted by the correlation. Again, the solution for the extreme 28:1 power skew was not obtainable due to numerical instabilities in the ENERGY-IV code.

Figure 14 is a collection of the existing literature data from two sources together with the MIT data for both the laminar and transition regimes under the uniform power condition. The theoretical laminar-transition criteria are drawn for the three data groups. The onset of considerable (i.e., greater than 0.01 torr on a time scale of 1 s) fluctuations in differential pressure was apparent for the four transition flow data of this study. Unfortunately, however, an experimentally based criterion for the MIT wire-wrapped bundle was not obtained during our transition flow testing.

The laminar flow data of this work and those of Mawatari et al. (1982) are plotted in Fig. 15. Although the data are from two seemingly similar bundles (i.e., $P/D = 1.25$ versus 1.21, and $H/D = 35$ versus 47) the two data banks exhibit a considerable difference in behavior due to the difference in the bundle equivalent diameter D_{eb} resulting from the large difference in bundle rod number (19 in the MIT bundle versus 91 in the Mawatari bundle). However, the proposed correlation method includes this effect and yields total buoyancy prediction curves, which correctly represent each data band. This separation is on the order of 10^2, which is the same order of magnitude of $[(D_{eb})_{MIT}/(D_{eb})_{Mawatari}]^4 = 124$, which is incorporated in the bundle Gr_q number for the same order of the bundle Re number. Also, the difference in the heated lengths, i.e., 930 mm for the the Mawatari and 1626 mm for the MIT bundles, results in different relative importance of the two buoyancy effects. For the shorter Mawatari bundle the local effect is minimal, whereas for the longer MIT bundle the global and local effects are comparable according to the predicting correlations. Therefore a strong rod number effect exists in mixed convection (Suh et al., 1989), whereas it is negligible in forced convection conditions (Cheng and Todreas, 1986). Thus one of the significant capabilities of the proposed model has been demonstrated, i.e., it can adequately differentiate the effects of the equivalent diameter, heated length and rod number observed between bundles of similar P/D and H/D ratios.

Figure 16 demonstrates that the four power skew and the uniform power data of Okada et al. (1985) measured in the same 19-rod wire-wrapped bundle but over the downstream section merge on the bundle multiplier-$(Gr_q/Re)_b$ representation. As shown in the companion paper, the global flow redistribution occurs largely in the upstream section of heated rod assemblies. Thus the skew effect would only be appreciable in this region and discernible only if differential pressures were measured over the upstream section of the heated bundle. The collapse of the various power skew and uniform power data conforms to the prediction. Observe however that the data lie between the laminar total buoyancy and the global buoyancy prediction curves due to the transition from laminar conditions occurring at the high Re number (700–1100) flows adopted in the Okada et al. experiment.

All transition flow data are collected in Fig. 17 along with the corresponding prediction curves for the global effects. The transition data of Mawatari et al. (1982) are well predicted by the corresponding global prediction curve. They lie below the laminar data bank of Fig. 15. The transition data of Okada et al. (1985) are shown to scatter about the global curve for the

downstream section of the MIT 19-rod wire-wrapped bundle. On the other hand, since the data in our work were taken over the total heated length, our transition data lie about the increased global curve based on the total heated length.

Because of the limited data available, a quantitative description of the gradual transition behavior from the laminar condition can hardly be made. Although a gradually occurring transition over a wide range of $(Gr_q/Re)_b$ numbers is also expected for the wire-wrapped bundle, confirming experimentation needs to be undertaken with the Re numbers between the mixed convection and forced convection critical values, i.e., Re_{bL} and Re_{obL}.

One final point to note in Figs. 7 to 13, 15, and 16 is that the total laminar buoyancy multipliers initially decrease for the bundle $(Gr_q/Re)_b$ parameter between 10 and 500. This behavior is due to the modified edge subchannel mixed convection friction factors, which decrease in the early stage of buoyancy development (Suh, 1986). Therefore utilization of the forced convection friction factors may be conservative over the initial mixed convection regime.

Conclusions

1 An experimental procedure has been developed to measure low-magnitude differential pressures (0.001 to 1 torr) under mixed convection conditions within ± 25 percent total uncertainty. Special measures were taken to reduce the uncertainties in instrument drift correction and outlet temperature estimation.

2 It is demonstrated that the local buoyancy diminishes and only the global buoyancy remains in effect as the transition proceeds from the laminar regime. The transition has been observed to be inlet Reynolds number dependent, taking place very gradually over $10^3 < (Gr_q/Re)_b < 3 \times 10^3$ in the MIT 19-rod bare bundle for inlet Reynolds number of 600 to 700. A similar transition behavior is expected for wire-wrapped rod bundles.

3 The predictive model has been found successfully to describe the effects of wire wrapping, power skew, transition from laminar regime, developing and interacting global and local flow redistributions, and rod number on the mixed convective low flow friction pressure loss characteristics in rod bundle geometries. The correlations, while validated with water experiments, can be applied to LMR conditions on the basis of a bounding assumption for the Pr number effect on the mixed convective flow development. The laminar flow uniform and skewed power test conditions varied as

	Wire-wrapped	*Bare*
Bundle average Re number	164–589	180–570
Bundle average Gr_q/Re number	6–14,773	11–18,500

The transition flow uniform power test conditions ranged as

	Wire-wrapped	*Bare*
Bundle average Re number	1031–1379	600–1240
Bundle average Gr_q/Re number	1558–2834	120–4940

Acknowledgments

The authors gratefully acknowledge the financial support provided for this work by the Power Reactor and Nuclear Fuel Development Corporation (PNC), Japan.

References

Cheng, S.-K., and Todreas, N. E., 1986, "Hydrodynamic Models and Correlations for Bare and Wire-Wrapped Hexagonal Rod Bundles – Bundle Friction Factors, Subchannel Friction Factors and Mixing Parameters," *Nuclear Engineering and Design*, Vol. 92, pp. 227–251.

Mawatari, K., Namekawa, F., Handa, N., Kasahara, F., and Ishida, Y., 1982, "Natural Circulation Decay Heat Removal Experiments and Analysis in an LMFBR Fuel Assmebly," *Proceedings, International Topical Meeting on LMFBR Safety and Related Design and Operating Aspects*, Lyon, France.

Okada, T., Efthimiadis, A., Iannello, V., and Todreas, N. E., 1985, "Mixed Convection Pressure Drop in Vertical Rod Bundles," *Proceedings, 3rd International Topical Meeting on Reactor Thermal Hydraulics,* Vol. 2, Paper No. 16.C.

Suh, K. Y., 1986, "Mixed Convective Low Flow in Vertical Rod Assemblies," Ph.D. Thesis, Massachusetts Institute of Technology, Department of Nuclear Engineering, Cambridge, MA.

Suh, K. Y., Todreas, N. E., and Rohsenow, W. M., 1989, "Mixed Convective Low Flow Pressure Drop in Vertical Rod Assemblies: I – Predictive Model and Design Correlation," ASME JOURNAL OF HEAT TRANSFER, Vol. 111, this issue.

Mixed Convection Along a Wavy Surface

S. Ghosh Moulic

L. S. Yao

Department of Mechanical and Aerospace Engineering,
Arizona State University,
Tempe, AZ 85287-6106

The results of a study of mixed-convection flow along a wavy surface are presented. The forced-convection component of the heat transfer contains two harmonics. The amplitude of the first harmonic is proportional to the amplitude of the wavy surface; the second harmonic is proportional to the square of this amplitude. Thus, for a slightly wavy surface, only the influence of the first harmonic can be detected. The natural-convection component is a second harmonic, with a frequency twice that of the wavy surface. Since natural convection has a cumulative effect, the second harmonic eventually becomes the dominant component far downstream from the leading edge where forced convection is the dominant heat transfer mode. The results also demonstrate that the total mixed-convection heat flux along a wavy surface is smaller than that of a flat surface.

1 Introduction

The prediction of heat transfer from irregular surfaces is a topic of fundamental importance. Irregularities in manufacturing frequently occur in practice. Surfaces are sometimes intentionally roughened to enhance heat transfer. Surfaces with intentionally placed roughness elements are encountered in several heat transfer devices. Some examples are flat-plate solar collectors and flat-plate condensers in refrigerators. The presence of roughness elements disturbs the flow past a flat surface and alters the heat transfer rate.

Using a transformation method, Yao (1983) studied the natural-convection heat transfer from isothermal vertical wavy surfaces, as an idealized roughened surface. He obtained numerical results for a sinusoidal surface. His results show that the local heat transfer rate varies periodically along the wavy surface, with a frequency equal to twice the frequency of the surface.

Bhavnani (1987) carried out an experimental investigation of the natural-convection heat transfer characteristics of sinusoidal wavy surfaces, maintained at a constant temperature, using a Mach–Zehnder interferometer. His results differ from those of Yao (1983) in the amplitude and frequency of the local heat transfer rate. Bhavnani's data indicate that the period of the local heat transfer coefficient is about the same as that of the wavy surface, while the amplitude is higher than that predicted by Yao.

A close observation of the data of Bhavnani and Bergles (1989) reveals a mixture of two harmonics, the first of which has a frequency equal to that of the wavy surface, and an amplitude that is higher than the amplitude predicted by Yao (1983). As demonstrated in this paper, these are typical characteristics for mixed convection along a wavy surface, which differ from those for natural convection (Yao, 1983). This implies that the experiment may be influenced by the presence of an induced forced flow. Such a flow is commonly induced by a heated object in a room with cool walls. This induced flow acts as a forced convection to the heated wavy surface in their experiment. The present investigation was carried out to find the effect of a forced flow on free convection along a vertical wavy surface in order to verify this conjecture.

The analysis requires a knowledge of the inviscid flow along the wavy surface. For the sinusoidal surface considered by Yao (1983), the inviscid velocity is infinite at the leading edge, and the actual flow presumably separates there. To simplify the problem, a symmetric body with wavy surfaces, facing a uniform stream aligned with its vertical axis of symmetry, has been considered (Fig. 1). For this ideal angle of attack, the inviscid flow remains attached to the surface at the leading edge, although the pressure gradient predicted by potential-flow theory is infinite at the leading edge. The forced flow along the wavy surface cannot be computed by classical boundary-layer methods as the flow is subject to separation. In this investigation only cases in which the buoyancy forces are strong enough to prevent flow separation are considered.

For a vertical flat plate, the governing parameter for mixed convection is $(\mathrm{Gr}/\mathrm{Re}^2)_x = x/[u_\infty^2/(\gamma g(T_w - T_\infty))]$ for fluids with Pr of order one (Yao, 1987). Forced convection exists as a limit when $(\mathrm{Gr}/\mathrm{Re}^2)_x$ goes to zero, which occurs at the leading edge, and the free-convection limit can be reached when the value of the parameter $(\mathrm{Gr}/\mathrm{Re}^2)_x$ is large. The length scale $u_\infty^2/\gamma_g(T_w - T_\infty)$ represents the axial distance where the free-convection effect becomes as important as the forced-convection effect. This distance becomes shorter for a larger overheating (or a larger Gr), and longer for a higher speed flow (or a larger Re). For wavy surfaces, there are two additional length scales: the amplitude a and the wavelength λ of the wavy surface. The solution in this case depends on x/λ, a/λ, and $\mathrm{Gr}/\mathrm{Re}^2$.

The results of this investigation show that when

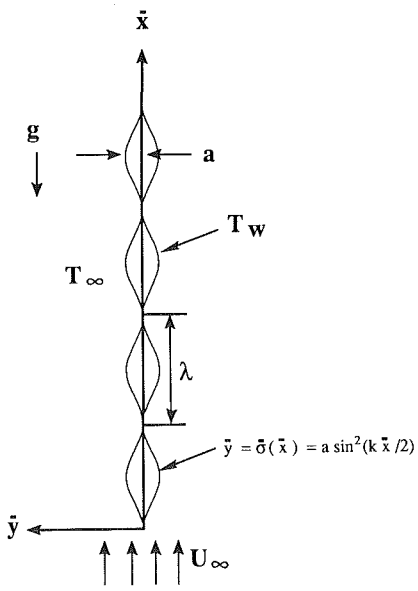

Fig. 1 Physical model and coordinates

Contributed by the Heat Transfer Division for publication in the JOURNAL OF HEAT TRANSFER. Manuscript received by the Heat Transfer Division September 23, 1988. Keywords: Finned Surfaces, Mixed Convection.

$Gr/Re^2 \sim 0(1)$ the local mixed-convection heat transfer rate consists of a mixture of two harmonics. The first harmonic, due to forced flow, has a frequency equal to that of the wavy surface. The second harmonic is dominant at large values of Gr/Re^2 and a/λ. The amplitude and frequency of the local mixed-convection heat transfer rate, for $Gr/Re^2 = 1$ and $a/\lambda = 0.2$, agree qualitatively with the experimental results of Bhavnani and Bergles (1989). This indicates that the experimental data are influenced by the circulation of air near the apparatus. However, a quantitative comparison cannot be made since the geometry considered in this investigation is different from that used by Bhavnani.

The inviscid solution obtained in this study is valid for small values of the amplitude-wavelength ratio a/λ only. For larger values of a/λ, the inviscid equations have to be solved numerically. No such restriction is imposed on the boundary layer equations. However, for large a/λ, classical boundary layer methods are inadequate, and a viscous-inviscid interaction model must be employed.

2 Analysis

The physical model considered is a plane, semi-infinite symmetric body with wavy surfaces, having a cusped leading edge. The axis of symmetry is aligned with the oncoming uniform stream. The geometry and coordinate system are illustrated in Fig. 1. The wavy surfaces are described by $y = \pm\sigma(x) = \pm a\sigma_1(kx)$, where a is the amplitude of the wavy surface, and k is the wave number. The mathematical formulation outlined below is valid for any function $\sigma(x)$ for which $\sigma(0) = \sigma'(0) = 0$. Later, a numerical solution is provided for the surface $\sigma = (a/2)(1 - \cos kx)$. The temperature of the wavy surfaces is held at a constant value T_w, which is higher than the ambient temperature T_∞. The flow is considered to be steady, laminar, and two-dimensional, and the Boussinesq approximation is employed.

The equations describing the flow are the continuity equation, the Navier-Stokes equations, and the energy equation. Using Prandtl's transposition theorem, as extended by Yao (1988), these equations may be written in dimensionless form as

$$\frac{\partial u}{\partial x} + \frac{\partial w}{\partial z} = 0 \tag{1a}$$

$$u\frac{\partial u}{\partial x} + w\frac{\partial u}{\partial z} = -\frac{\partial p}{\partial x} + F'\frac{\partial p}{\partial z} + \frac{1}{\mathrm{Re}}Lu + \frac{\mathrm{Gr}}{\mathrm{Re}^2}\theta \tag{1b}$$

$$u\frac{\partial w}{\partial x} + w\frac{\partial w}{\partial z} + F''u^2 = -(1+F'^2)\frac{\partial p}{\partial z} + F'\frac{\partial p}{\partial x} - \frac{\mathrm{Gr}}{\mathrm{Re}^2}F'\theta + \frac{1}{\mathrm{Re}}\left[Lw + 2F''\left(\frac{\partial u}{\partial x} - F'\frac{\partial u}{\partial z}\right) + F'''u\right] \tag{1c}$$

$$u\frac{\partial \theta}{\partial x} + w\frac{\partial \theta}{\partial z} = \frac{1}{\mathrm{Re\ Pr}}L\theta \tag{1d}$$

where

$$z = y - F(x) \tag{1e}$$

is a new transverse coordinate, measured from the surface $y = F(x)$;

$$L = \frac{\partial^2}{\partial x^2} + (1+F'^2)\frac{\partial^2}{\partial z^2} - 2F'\frac{\partial^2}{\partial x \partial z} - F''\frac{\partial}{\partial z} \tag{1f}$$

is the Laplacian operator in (x, z) coordinates;

$$w = v - F'(x)u \tag{1g}$$

is a quantity arising from the transformation; and the dimensionless variables are defined by

$$x = k\bar{x}, \quad y = k\bar{y}, \quad \sigma(x) = k\bar{\sigma}(\bar{x}) = \alpha\sigma_1(x) \tag{2a}$$

$$u = \bar{u}/u_\infty, \quad v = \bar{v}/u_\infty, \quad p = \bar{p}/(\rho\bar{u}_\infty^2) \tag{2b}$$

$$\theta = \frac{T - T_\infty}{T_w - T_\infty}, \quad \mathrm{Gr} = \gamma g(T_w - T_\infty)l^3/\nu^2, \quad \mathrm{Re} = u_\infty l/\nu \tag{2c}$$

$$\mathrm{Pr} = \mu c_p/\kappa, \quad \alpha = k\,a = 2\pi\,a/\lambda, \quad l = 1/k, \quad k = 2\pi/\lambda, \tag{2d}$$

where λ is the wavelength of the wavy surface and u_∞ is the velocity of the uniform stream approaching the body.

The transformation (1e) maps the surface $y = F(x)$ onto the surface $z = 0$. The function $F(x)$ is taken to be

$$F(x) = \sigma(x)\,H(x) \tag{2e}$$

where $H(x)$ is the unit step function

$$H(x) = \begin{cases} 1, & x > 0 \\ 0, & x < 0 \end{cases} \tag{2f}$$

This simplifies the boundary conditions, which have to be applied along the surface $y = 0$, $x < 0$ and $y = \sigma(x)$, $x > 0$.

2.1 Inviscid Flow. The inviscid flow equations are ob-

Nomenclature

a = amplitude of wavy surface
c_p = specific heat
g = gravitational acceleration
Gr = Grashof number $= g\gamma(T_w - T_\infty)\,l^3/\nu^2$
h = heat transfer coefficient
k = wave number $= 2\pi/\lambda$
l = characteristic length $= 1/k$
Nu = Nusselt number
p = pressure
Pr = Prandtl number = 1
q = heat flux
Re = Reynolds number
s = distance along the surface, measured from the leading edge
T = temperature
u = x component of velocity
u_w = x component of the velocity of the inviscid flow, evaluated at the surface
v = y component of velocity
w = transformed velocity
x = axial (Cartesian) coordinate
y = transverse (Cartesian) coordinate
z = transformed transverse coordinate, measured from the wavy surface
α = dimensionless amplitude
β = pressure gradient parameter
γ = thermal expansivity
θ = dimensionless temperature
κ = thermal conductivity
λ = wavelength of wavy surface
μ = dynamic viscosity
ν = kinematic viscosity
ρ = density
σ = surface geometry function
ψ = stream function

Superscripts

$^-$ = dimensional quantities
$'$ = derivative with respect to x
$^\sim$ = quantities associated with the boundary layer

Subscripts

m = mean value
w = surface
x = local value
∞ = free stream

tained by taking the limit $\mathrm{Re}\to\infty$, but $\mathrm{Gr}/\mathrm{Re}^2$ held finite, in equations (1). Since conduction outside the boundary layer is a higher order effect, the lowest-order outer inviscid flow is isothermal. For small α, the inviscid flow is given by (for details, see Ghosh Moulic, 1988)

$$\psi = z + \alpha\left[\sigma_1(x)H(x) - \frac{1}{\pi}\int_0^\infty \sigma_1(t)\,\frac{z}{(x-t)^2+z^2}\,dt\right] + 0(\alpha^2) \tag{3a}$$

where ψ is a stream function defined by

$$u = \frac{\partial\psi}{\partial z}, \qquad w = -\frac{\partial\psi}{\partial x} \tag{3b}$$

The x component of the inviscid velocity at the surface $y=\sigma(x)$ is given by

$$u_w(x) = 1 + \alpha\left[\frac{1}{\pi}\int_0^\infty \frac{\sigma_1'(t)}{x-t}\,dt\right] + 0(\alpha^2) \tag{3c}$$

2.2 Boundary Layer. The scales for the boundary layer are well known. The thickness of the boundary layer is $O(\mathrm{Re}^{-1/2})$. Accordingly, a stretched transverse coordinate is defined by

$$\tilde{z} = \mathrm{Re}^{1/2} z \tag{4a}$$

and the following inner variables are introduced:

$$u = \tilde{u}_1(x, \tilde{z}) \tag{4b}$$

$$w = \mathrm{Re}^{-1/2}\tilde{w}_1(x, \tilde{z}) \tag{4c}$$

$$\theta = \tilde{\theta}_1(x, \tilde{z}) \tag{4d}$$

$$p = \tilde{p}(x, \tilde{z}) \tag{4e}$$

Substitution of equations (4*a–e*) into equations (1*a–d*) yields the boundary layer equations.

The inviscid solution has a singularity at the leading edge. At $x=0$, du_w/dx is infinite. This singularity may be removed by the following transformation:

$$\eta = \tilde{z}\left(\frac{u_w}{2x}\right)^{1/2} \tag{5a}$$

$$\tilde{u}_1 = u_w(x)\tilde{u}(x, \eta) \tag{5b}$$

$$\tilde{w}_1 = \left(\frac{u_w}{2x}\right)^{1/2}\tilde{w}(x, \eta) \tag{5c}$$

$$\tilde{\theta}_1 = \tilde{\theta}(x, \eta) \tag{5d}$$

The boundary layer equations in (x, η) coordinates are

$$2x\frac{\partial\tilde{u}}{\partial x} + \frac{\partial\tilde{W}}{\partial\eta} + (\beta+1)\tilde{u} = 0 \tag{6a}$$

$$2x\tilde{u}\frac{\partial\tilde{u}}{\partial x} + \tilde{W}\frac{\partial\tilde{u}}{\partial\eta} + \left(2\beta + 2x\frac{\sigma'\sigma''}{1+\sigma'^2}\right)(\tilde{u}^2-1) = (1+\sigma'^2)\frac{\partial^2\tilde{u}}{\partial\eta^2} + \frac{\mathrm{Gr}}{(u_w\mathrm{Re})^2}\frac{2x\tilde{\theta}}{1+\sigma'^2} \tag{6b}$$

$$2x\tilde{u}\frac{\partial\tilde{\theta}}{\partial x} + \tilde{W}\frac{\partial\tilde{\theta}}{\partial\eta} = \frac{1+\sigma'^2}{\mathrm{Pr}}\frac{\partial^2\tilde{\theta}}{\partial\eta^2} \tag{6c}$$

where

$$\beta = \frac{x}{u_w}\frac{du_w}{dx} \tag{6d}$$

$$\tilde{W} = \tilde{w} - \eta\tilde{u} \tag{6e}$$

The boundary conditions are:

(*i*) On the wavy surface ($\eta=0$):

$$\tilde{u} = \tilde{W} = 0, \quad \tilde{\theta} = 1 \tag{6f}$$

(*ii*) Matching with the inviscid flow ($\eta\to\infty$):

$$\tilde{u}\to 1, \quad \tilde{\theta}\to 0 \tag{6g}$$

Although du_w/dx, and hence $(\partial\tilde{u}_1/\partial x)$ (x, ∞), is infinite at $x=0$, $\partial\tilde{u}/\partial x$ remains bounded at $x=0$. The transformation introduces du_w/dx in the equations, but it occurs in combination with x in the pressure gradient parameter β, which is bounded as $x\to 0$. The x derivatives disappear when x is set equal to zero in equations (6*a–c*). Therefore, the initial conditions can be obtained by setting $x=0$ in equations (6*a–c*) and solving the resulting system of equations. This is equivalent to using the Blasius solution as the starting profile. The transformation also removes most of the variation of the boundary layer thickness with x.

A finite difference solution of equations (6) was obtained by marching from $x=0$. Derivatives with respect to x were approximated by backward differences, while derivatives with respect to η were approximated by central differences. Since equations (6) are nonlinear and coupled, the solution at each x station was obtained iteratively. The iterations were continued until the absolute difference between the results of two successive iterations became less than 10^{-4}. After several trials, the grid size in the η direction was set at 0.01. A variable step Δx was used in the x direction. The choice of Δx was determined by insisting that the difference in the local heat transfer rate at the wall between two integrations from x to $x+\Delta x$ in first one and then two steps was everywhere less than 10^{-4}. The step size was doubled when this difference became less than 10^{-6} and halved when this difference became greater than 10^{-4}. In this way, a reasonable overall accuracy in the solution was achieved without using large amounts of computer time. Near the leading edge, a step size $\Delta x = 0.0015$ was required to obtain an accuracy of 10^{-4}. The step size was slowly increased to a maximum value of 0.05 in regions of favorable pressure gradient. In regions with adverse pressure gradient, Δx had to be reduced to 0.025. The numerical results presented are believed to be accurate to the third decimal point, and are much better than one tenth of one percent.

3 Results and Discussion

Numerical results have been obtained for the surface described by $\sigma_1 = (1/2)(1-\cos x)$ for amplitude-wavelength ratios of 0.1 and 0.2. Details of the inviscid surface velocity and pressure gradient and the local and average Nusselt numbers are presented for $\mathrm{Pr}=1$.

The potential-flow solution for the x component of velocity at the surface $y=(1/2)(1-\cos x)$ is

$$u_w(x) = 1 + \alpha\left[\frac{1}{2\pi}\int_0^\infty \frac{e^{-\rho x}}{1+\rho^2}\,d\rho - \frac{1}{2}\cos x\right] \tag{7}$$

The pressure gradient used in the boundary layer computations is given by

$$\frac{dp}{dx} = -\left[(1+\sigma'^2)u_w\frac{du_w}{dx} + \sigma'\sigma''u_w^2\right] \tag{8}$$

Equations (7) and (8) have been plotted in Figs. 2 and 3, respectively. Figure 2 shows that the flow accelerates along the rising portions of the surface (from trough to crest) where the slope σ' is positive, and decelerates along the portion of the surface from crest to trough, where the slope σ' is negative. Thus, u_w varies periodically along the surface with a frequency equal to that of the wavy surface. The pressure gradient distribution (Fig. 3) shows a mixture of two harmonics. The first harmonic has a frequency equal to that of the wavy surface. The pressure gradient is negative (favorable) in regions where the inviscid flow accelerates, and positive (adverse) in regions where the flow decelerates. The maximum and minimum values of the pressure gradient occur at the points of inflection of the wavy surface. At the leading edge $x=0$, the

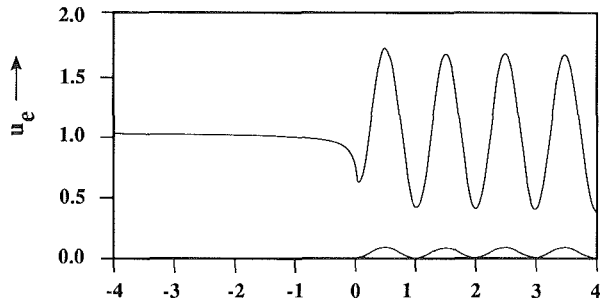

Fig. 2 Inviscid surface-velocity distribution

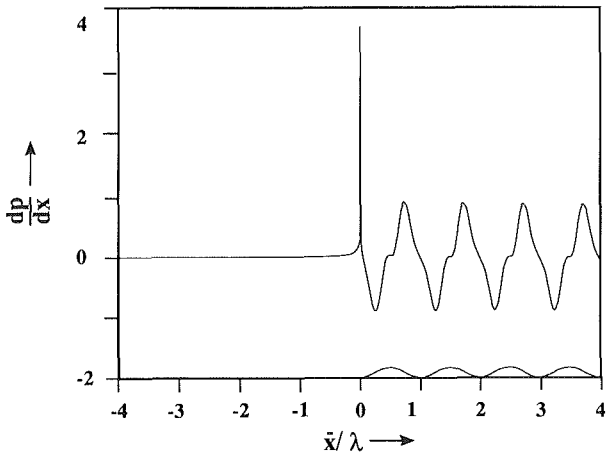

Fig. 3 Axial distribution of *dp/dx*

pressure gradient predicted by potential flow theory is infinite. This is because of the sudden change in curvature at $x=0$.

Figures 4–7 show the variation of the local Nusselt number, defined as

$$\mathrm{Nu}_x = \frac{h_x \bar{x}}{\kappa} = \frac{q\, l\, x}{\kappa(T_w - T_\infty)} \tag{9a}$$

Results for the limiting case of a flat plate ($a/\lambda \to 0$) have been included in Figs. 4–6 for comparison. A semi-infinite flat plate has no characteristic length scale, and for a given Prandtl number, $\mathrm{Nu}_x\,(2/\mathrm{Re}_x)^{1/2}$ for mixed convection along a flat plate is a function of a single parameter $(\mathrm{Gr}/\mathrm{Re}^2)_x$ (Yao, 1987). For the wavy surface considered in this analysis, there are two natural length scales: the amplitude a and the wavelength λ of the wavy surface. The reference length used in the analysis is proportional to λ. Thus, for a given Prandtl number, the problem is characterized by three parameters: x/λ, a/λ, and $\mathrm{Gr}/\mathrm{Re}^2$.

The axial distribution of $\mathrm{Nu}_x\,(2/\mathrm{Re}_x)^{1/2}$, given by

$$\mathrm{Nu}_x(2/\mathrm{Re}_x)^{1/2} = -[(1+\sigma'^2)u_w]^{1/2}\left(\frac{\partial\theta}{\partial\eta}\right)_{\eta=0} \tag{9b}$$

is plotted in Fig. 4(*a*), for $\mathrm{Gr}/\mathrm{Re}^2 = 1$, $\mathrm{Pr} = 1$, and $a/\lambda = 0$, 0.1, and 0.2. For forced convection along a flat plate, $\mathrm{Nu}_x\,(2/\mathrm{Re}_x)^{1/2}$ is a constant that depends only on the Prandtl number. In a mixed-convection boundary layer, forced convection dominates over natural convection near the leading edge. Thus, the curve for the flat plate starts with a value of 0.4696 at the leading edge, which corresponds to the value of $\mathrm{Nu}_x\,(2/\mathrm{Re}_x)^{1/2}$ for forced convection along a flat plate with $\mathrm{Pr} = 1$. For the wavy surface, the value of $\mathrm{Nu}_x\,(2/\mathrm{Re}_x)^{1/2}$ near the leading edge is slightly lower than that of the corresponding flat plate solution. This is due to reduced free-stream velocities near the leading edge (Fig. 2), as a result of which heat is convected away from the surface at a slower rate. The quantity $\mathrm{Nu}_x\,(2/\mathrm{Re}_x)^{1/2}$ increases monotonically with x, for the flat plate, as buoyancy forces come into play. The curves for the wavy surfaces show a periodic variation, with a mean value that increases monotonically with x, as the free convection effect is cumulative.

The curve for $a/\lambda = 0.1$ shows a frequency equal to the frequency of the wavy surface. The peaks of the local heat transfer rate occur near the peaks of the wavy surface, where the inviscid free-stream velocity is maximum, but are shifted slightly upstream of the crests of the wavy surface due to the nonlinear convection effect.

The curve for $a/\lambda = 0.2$ shows the presence of two harmonics, the first having a frequency equal to that of the wavy surface. This may be explained by referring to the boundary layer equations (6). The quantities σ', σ'', u_w, and du_w/dx have a frequency equal to that of the wavy surface, while the quantities σ'^2 and $\sigma'\sigma''$ have a frequency equal to twice that of the wavy surface. Thus, the pressure gradient parameter β, which involves u_w and its derivative, gives rise to the first harmonic, while the centrifugal, buoyancy, and diffusion terms, which involve σ'^2 and $\sigma'\sigma''$, give rise to the second harmonic. Since the amplitudes of the terms giving rise to the second harmonic are proportional to the square of the amplitude–wavelength ratio, the second harmonic becomes prominent at large values of a/λ. Thus, the second harmonic can be seen clearly in the curve for $a/\lambda = 0.2$ although it cannot be observed in the curve for $a/\lambda = 0.1$.

For $\mathrm{Gr}/\mathrm{Re}^2 = 10$ and 100, the presence of the second harmonic can be detected in the curve for $a/\lambda = 0.1$ (Figs. 5*a* and 6*a*). This is because the buoyancy term in equation (6*b*), which is one of the terms having a frequency equal to twice that of the wavy surface, is proportional to $\mathrm{Gr}/\mathrm{Re}^2$. Thus, the second harmonic becomes prominent at large values of $\mathrm{Gr}/\mathrm{Re}^2$.

The periodic nature of the local heat transfer rate is seen more clearly in Figs. 4(*b*), 5(*b*), and 6(*b*), in which the axial distribution of $\mathrm{Nu}_x\,(4/\mathrm{Gr}_x)^{1/4}$ is plotted. The variation of $\mathrm{Nu}_x\,(4/\mathrm{Gr}_x)^{1/4}$ with x for the flat plate may be explained as follows. The local heat transfer rate h_x varies as $x^{-1/4}$ for free convection along a flat plate, and as $x^{-1/2}$ for forced convection along a flat plate. Thus, the quantity $h_x x^{1/4}$, or equivalently, its dimensionless form $\mathrm{Nu}_x\mathrm{Gr}_x^{-1/4}$ is a constant for free convection along a flat plate, and varies as $x^{-1/4}$ for forced convection along a flat plate. In a mixed convection boundary layer, forced convection is the dominant mode of heat transfer near the leading edge, while farther downstream, free convection is the dominant mode of heat transfer. Hence, the curve of $\mathrm{Nu}_x(4/\mathrm{Gr}_x)^{1/4}$ versus x for the flat plate varies as $x^{-1/4}$ near $x=0$, and approaches the free convection limit, 0.5761 (for $\mathrm{Pr} = 1$) asymptotically, far downstream of the leading edge. The curves for the wavy surfaces $a/\lambda = 0.1$ and 0.2 exhibit the same periodic behavior as in Figs. 4(*a*), 5(*a*), and 6(*a*). However, the mean of the variation of $\mathrm{Nu}_x\,(4/\mathrm{Gr}_x)^{1/4}$ with x is very nearly constant, except near the leading edge, where $\mathrm{Nu}_x\,(4/\mathrm{Gr}_x)^{1/4} \sim x^{-1/4}$. The curves are thus "flattened" and the periodicity of the local heat transfer rate is clearly brought out.

Figure 7(*a*) shows the axial distribution of $\mathrm{Nu}_x\,(4/\mathrm{Gr}_x)^{1/4}$ for the wavy surface with $a/\lambda = 0.1$ for three values of the parameter $\mathrm{Gr}/\mathrm{Re}^2$. The free-convection limit is also plotted for comparison. The curve for $\mathrm{Gr}/\mathrm{Re}^2 = 1$ shows a frequency equal to the frequency of the wavy surface. The crests and troughs of the local heat transfer rate are shifted slightly upstream of the crests and troughs of the wavy surface. It is seen that as the value of the parameter $\mathrm{Gr}/\mathrm{Re}^2$ increases, the amplitude of the oscillations of $\mathrm{Nu}_x\,(4/\mathrm{Gr}_x)^{1/4}$ decreases, and the mixed-convection heat transfer rate approaches the free convection limit, which has a frequency equal to twice the frequency of the wavy surface (Yao, 1983). The results indicate that the local Nusselt number distribution consists of two harmonics. The numerical results show that the second harmonic is due to natural convection. The first harmonic is the leading-

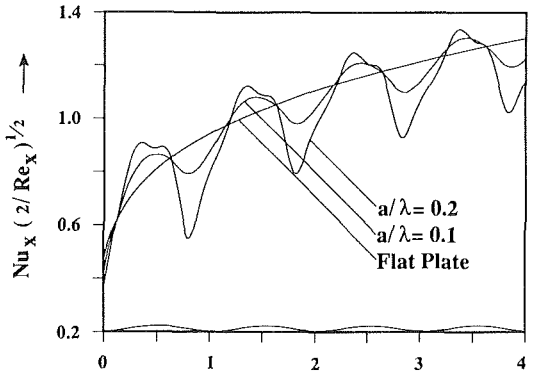

Fig. 4(*a*) Axial distribution of $Nu_x\ (2/Re_x)^{1/2}$ for $Gr/Re^2 = 1$

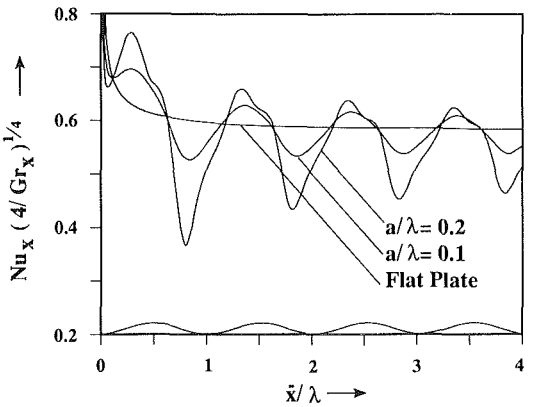

Fig. 4(*b*) Axial distribution of $Nu_x\ (4/Gr_x)^{1/4}$ for $Gr/Re^2 = 1$

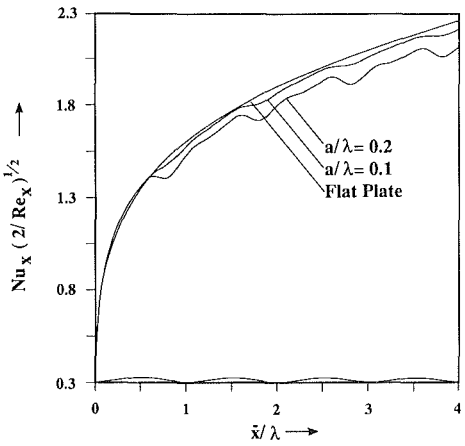

Fig. 5(*a*) Axial distribution of $Nu_x\ (2/Re_x)^{1/2}$ for $Gr/Re^2 = 10$

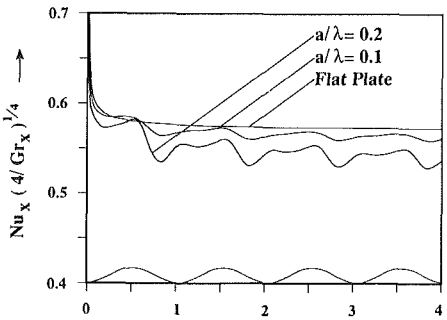

Fig. 5(*b*) Axial distribution of $Nu_x\ (4/Gr_x)^{1/4}$ for $Gr/Re^2 = 10$

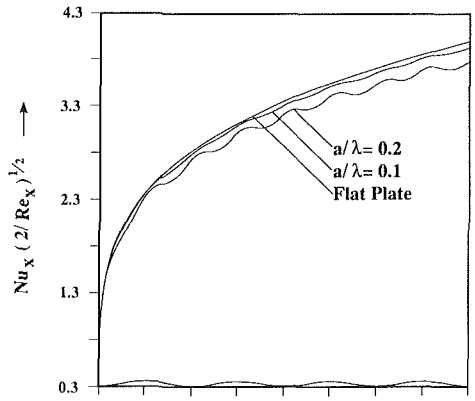

Fig. 6(*a*) Axial distribution of $Nu_x\ (2/Re_x)^{1/2}$ for $Gr/Re^2 = 100$

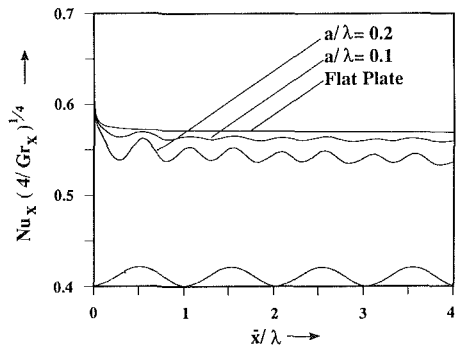

Fig. 6(*b*) Axial distribution of $Nu_x\ (4/Gr_x)^{1/4}$ for $Gr/Re^2 = 100$

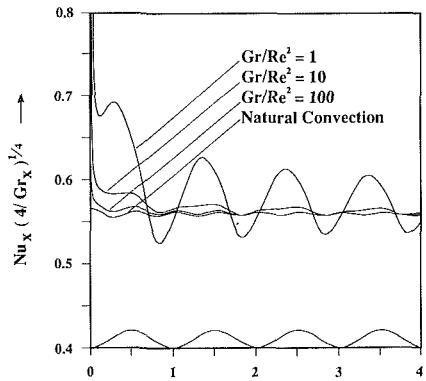

Fig. 7(*a*) Axial distribution of $Nu_x\ (4/Gr_x)^{1/4}$ for $a/\lambda = 0.1$

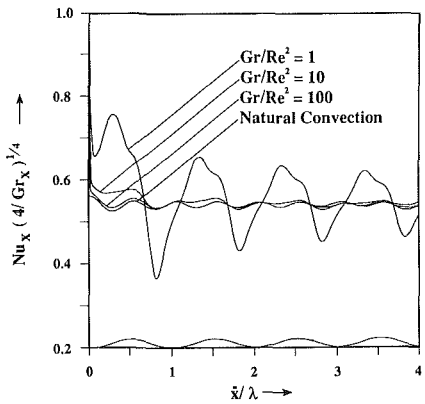

Fig. 7(*b*) Axial distribution of $Nu_x\ (4/Gr_x)^{1/4}$ for $a/\lambda = 0.2$

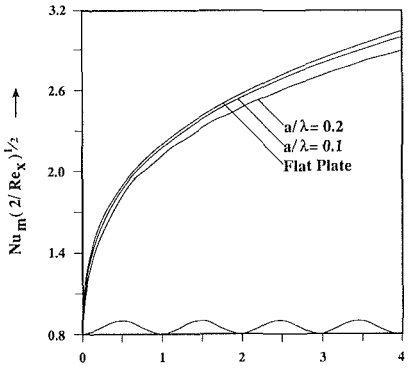

Fig. 8(*a*) Axial distribution of $Nu_m\ (2/Re_x)^{1/2}$ for $Gr/Re^2 = 10$

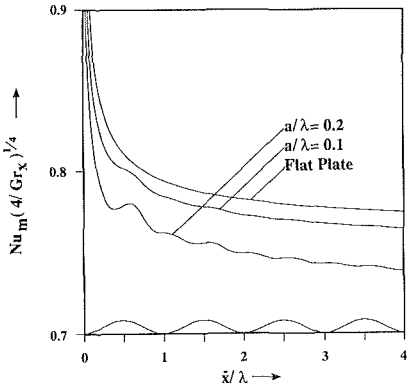

Fig. 8(*b*) Axial distribution of $Nu_m\ (4/Gr_x)^{1/4}$ for $Gr/Re^2 = 10$

order forced convection solution. The amplitude of the first harmonic decays as Gr/Re^2 increases. Thus, the first harmonic cannot be seen in the curve for $Gr/Re^2 = 100$, while the curve for $Gr/Re^2 = 1$ clearly shows the first harmonic. The curve for $Gr/Re^2 = 10$ shows a mixture of two harmonics. For $a/\lambda = 0.2$, the presence of the second harmonic can be seen in the curve for $Gr/Re^2 = 1$ (Fig. 7*b*).

In all cases, the amplitude of the oscillating Nusselt number gradually decreases downstream. This is due to an increase in the thermal boundary layer thickness. The local heat transfer coefficient is inversely proportional to the thickness of the thermal boundary layer. The latter varies periodically along the wavy surface. However, as the boundary layer thickness increases, the change in boundary layer thickness with x becomes a small fraction of the boundary layer thickness. Hence, the wavy surface effect gradually decreases downstream, as the boundary layer grows thicker.

The total Nusselt number is obtained by averaging the heat transfer over the surface from the leading edge ($x=0$) to $s(x)$. Thus,

$$\mathrm{Nu}_m = \frac{h_m \bar{x}}{\kappa} \tag{10a}$$

where

$$h_m = \frac{q_m}{T_w - T_\infty} \tag{10b}$$

$$q_m = \frac{1}{s}\int_0^s q\, ds \tag{10c}$$

$$s = \int_0^x (1+\sigma'^2)^{1/2} dx \tag{10d}$$

The variation of $\mathrm{Nu}_m(2/\mathrm{Re}_x)^{1/2}$ with x, given by

$$\mathrm{Nu}_m(2/\mathrm{Re}_x)^{1/2} = \frac{(2x)^{1/2}}{s}\int_0^x \left(\frac{u_w}{2x}\right)^{1/2} (1 + \sigma'^2)\left(\frac{\partial\theta}{\partial\eta}\right)_{\eta=0} dx \tag{10e}$$

is plotted in Fig. (8*a*) for $Gr/Re^2 = 10$ and $Pr = 1$. It is seen that the value of $Nu_m\ (2/Re_x)^{1/2}$ for the wavy surfaces is uniformly smaller than that of the corresponding flat plate (with equal projected area). This may be explained as follows. The important component of the buoyancy force at any x location is tangential to the wavy surface. Thus, this component depends on the slope of the wavy surface, and is equal to the total buoyancy force only at the crests and troughs of the surface. For the flat plate, on the other hand, the buoyancy force is always parallel to the surface. Hence, the total heat transfer rate for a wavy surface is less than the total heat transfer rate for a flat surface with equivalent projected area. The total Nusselt number shows the same periodic behavior as the local Nusselt number. The amplitude of oscillations of the total Nusselt number is, however, smaller than that of the local Nusselt number, and cannot be seen clearly in Fig. 8(*a*). The axial distribution of $Nu_m\ (4/Gr_x)^{1/4}$ brings out the periodicity of the total Nusselt number more clearly (Fig. 8*b*).

4 Conclusions

This investigation was conducted to find the influence of a forced flow on the natural-convection heat transfer characteristics of a vertical wavy surface. Numerical results for the wall heat transfer rate have been obtained for the wavy surface $\sigma_1 = (1/2)(1-\cos x)$. The wall heat transfer rate is found to vary according to the slope of the wavy surface. The axial distribution of the local Nusselt number shows a mixture of two harmonics. The first harmonic, which has a frequency equal to that of the wavy surface, is due to forced convection. The second harmonic, generated by the buoyancy, centrifugal, and viscous forces, is dominant at large values of Gr/Re^2 and a/λ. As the value of Gr/Re^2 increases, the mixed-convection heat transfer rate approaches the free-convection limit, which has a frequency equal to twice the frequency of the wavy surface. The values of the average Nusselt number for mixed convection along a wavy surface are found to be uniformly lower than the corresponding flat plate values.

References

Bhavnani, S. H., and Bergles, A. E., 1989, "Experimental Study of Laminar Natural Convection Heat Transfer From Wavy Surfaces," submitted to ASME Journal of Heat Transfer.

Ghosh Moulic, S., 1988, "Mixed Convection Along a Wavy Surface," M.S. Thesis, Arizona State University, Tempe, AZ.

Yao, L. S., 1983, "Natural Convection Along a Vertical Wavy Surface," ASME Journal of Heat Transfer, Vol. 105, pp. 465-467.

Yao, L. S., 1987, "Two-Dimensional Mixed Convection Along a Flat Plate," ASME Journal of Heat Transfer, Vol. 109, pp. 440-445.

Yao, L. S., 1988, "A Note on Prandtl's Transposition Theorem," ASME Journal of Heat Transfer, Vol. 110, pp. 507-508.

Combined Natural Convection and Forced Flow Through Small Openings in a Horizontal Partition, With Special Reference to Flows in Multicompartment Enclosures

M. Epstein

M. A. Kenton

Fauske & Associates, Inc.,
Burr Ridge, IL 60521

Estimates of the magnitude of buoyancy-driven exchange flows through openings in partitions that separate compartments are needed to assess the movement of toxic gases and smoke through buildings. An experiment using water and brine as a substitute for a light gas moving in a dense gas was designed to measure combined forced and buoyancy-driven exchange flow through a single opening in a horizontal partition. No theoretical treatment exists for this configuration. The same apparatus was used to determine the magnitude of the forced flow required to purge the opening of the oppositely directed buoyant component (i.e., the "flooding" limit). Finally, combined forced and buoyancy-driven flows in a multicompartment enclosure were measured. It has been demonstrated that the combined forced and buoyancy-generated flows in the multicompartment structure can be predicted by a direct application of the results of the study of exchange flow through a single opening.

Introduction

The present paper is a continuation of the work recently published by Epstein (1988). The previous paper dealt with buoyancy-driven exchange flow through an opening in a horizontal partition that separates two otherwise closed compartments. The fluid in the upper compartment is more dense than that in the lower compartment. The density difference induces a buoyancy-driven, countercurrent downflow of the heavier fluid and an upflow of the lighter fluid through the opening. A universal correlation between Froude number (dimensionless exchange flow rate) and opening aspect ratio was obtained. Epstein (1988) also investigated the buoyancy-driven flow with two openings in the horizontal partition. Two openings were observed to give rise to three different flow configurations involving both one-way and countercurrent flows within the openings. Indications were that a purging (or flooding) mechanism accounted for the observed transition between one-way and countercurrent flow in an opening, much as has been observed in vertical two-phase flows.

In the present paper we report an experimental study that provides an empirical formula for the one-way flooding flow rate that is necessary to prevent countercurrent exchange flow within a single opening in a horizontal partition. Also experimental results for forced fluid flow and corresponding reverse natural convection flow through a single opening in a horizontal partition are presented. An empirical correlation is developed that yields the magnitude of the buoyant component of this combined flow in terms of the pure countercurrent flow rate (Epstein, 1988) and the flooding flow rate for the opening. We shall see later in the paper, via an experimental study of natural and forced convection in a model three-compartment structure, that this correlation for combined flow in a single opening may represent the key to prediction of the convection patterns within complex building configurations.

Contributed by the Heat Transfer Division for publication in the JOURNAL OF HEAT TRANSFER. Manuscript received by the Heat Transfer Division June 20, 1988. Keywords: Building Heat Transfer, Enclosure Flows, Natural Convection.

As in the previous study (Epstein, 1988) and in the study of Steckler et al. (1986) on the movement of smoke fronts during fires in multiroom structures, brine and water were used to simulate buoyancy-driven gas movement between compartments. This so-called salt water modeling technique is known to be valid as long as molecular viscosity and thermal diffusivity are not important parameters. Steckler et al. (1986) examined the nondimensional (scaled) governing equations of mass, momentum, and energy transfer for free turbulent flow and concluded that the molecular transport terms are negligible in comparison with the other terms when the Reynolds number is larger than 10^4 and, therefore, that the equations are essentially identical for hot and cold gas and water–brine flows. It is noteworthy in this regard that Prahl and Emmons (1975) experimentally confirmed the applicability to gas exchange flows across vertical partitions of data obtained with liquid–liquid systems for Reynolds numbers as low as 10^3. One can arrive at the same conclusion for buoyancy-induced flows across horizontal partitions by comparing the brine–water data of Epstein (1988) with the hot gas flow data of Brown (1962).

There are two reasons for examining the exchange flow through a small opening in a horizontal partition in some detail. First, the rate of movement of radiological or toxic gases or smoke in tall industrial or commercial buildings under emergency conditions is mainly a function of leakage between floors as opposed to walls. Secondly, from a fundamental point of view, there is a big difference between horizontal and vertical openings (passages) with respect to the relative motion of the two fluids. The pattern of flow in the vertical passage (horizontal partition) is chaotic and may not be amenable to analysis, whereas the two fluids in a horizontal passage (vertical partition) are observed to be stably stratified. The application of simple momentum flux equations including an empirically determined flow coefficient to the superposed layers appears justified for the horizontal passages (Steckler et al., 1984; Prahl and Emmons, 1975; Brown and Solvason, 1962). A theoretical and experimental study of stratified, combined forced flow and natural convection across a rectangular

opening in a vertical partition has been reported by Shaw (1971). To the present authors' knowledge, the phenomenon of combined forced and natural exchange flow through a small opening in a horizontal partition has not been dealt with in the literature.

Combined Natural Convection and Forced Fluid Flow Through an Opening in a Vertical Partition

As a means of introducing our empirical approach to simultaneous forced flow and reverse natural convection flow thorugh an opening in a horizontal partition, let us first consider the simpler case of such a combined flow in an opening in a *vertical* partition. As mentioned in the Introduction, previous experimental studies for this case have shown that the lateral compartments exchange mass via a horizontal stratified flow, which can be treated semi-empirically by standard hydraulic practice. Shaw's theory (1971) of combined flow thorugh an opening in a vertical partition is expressed in terms of an excess supply pressure acting on the natural convection flow, which is not a convenient form for the purposes of the present study.

Consider the two-compartment configuration connected by a common opening in Fig. 1. For the sake of simplicity, we first focus our attention on a rectangular opening of width W and height H. Compartment 1 contains the heavier fluid of density ρ_H while compartment 2 is filled with the lighter fluid of density ρ_L. The contents of each compartment are assumed to be well mixed. Note that the compartments are not sealed. Fluid is supplied to compartment 1 and extracted from compartment 2 at a volumetric flow rate Q_u.[1] We are interested in determining the buoyancy-driven leakage back-flow Q_{BF} from compartment 2 to compartment 1 against the forced fluid flow Q within the opening.

The pressure P_1 in compartment 1 at a level z above the midplane is

$$P_1 = P_{01} - \rho_H g z \tag{1}$$

and the pressure P_2 in compartment 2 at this elevation is

$$P_2 = P_{02} - \rho_L g z \tag{2}$$

Note that the pressures P_{01} and P_{02} at the midplane are not equal owing to the excess pressure in compartment 1 due to the supply flow. The pressure difference between compartments at level z is

$$P_2 - P_1 = P_{02} - P_{01} + (\rho_H - \rho_L) g z \tag{3}$$

The flow velocity u within the opening at level z is obtained by using the Bernoulli equation. Thus

[1] The subscript u pertains to unidirectional or one-way flow.

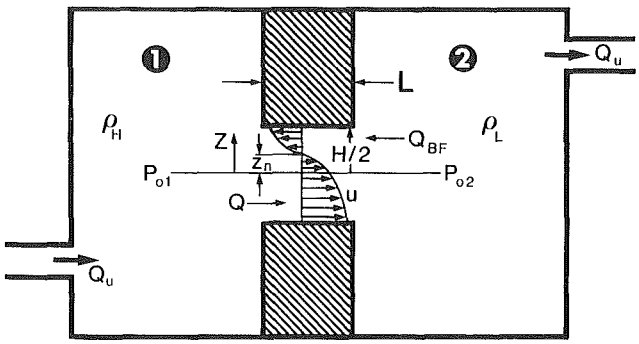

Fig. 1 Schematic representation of combined buoyantly driven and forced flow through a rectangular opening in a vertical partition

$$u = \sqrt{\frac{2(P_2 - P_1)}{\bar{\rho}}} = \sqrt{\frac{2\Delta\rho g z}{\bar{\rho}} - \frac{2(P_{01} - P_{02})}{\bar{\rho}}} \tag{4}$$

Strictly speaking, the use of an average density in equation (4) is only valid when $\Delta\rho/\bar{\rho} << 1$. However, this form of the Bernoulli equation permits a useful degree of simplicity in the analysis that follows and is sufficiently accurate for many situations of practical interest. The buoyant backflow through the opening, Q_{BF}, is obtained by integrating u over the vertical distance z from the "neutral plane." The neutral plane is defined by the condition that the velocity u is zero, namely [see Fig. 1 and equation (4)]

$$z_n = \frac{P_{01} - P_{02}}{g\Delta\rho} \tag{5}$$

Integrating from the neutral plane to the top of the opening at $z = H/2$ we obtain the total back flow

$$Q_{BF} = C_D W \int_{z_n}^{H/2} u\,dz = \frac{2C_D W}{3}\left(\frac{2\Delta\rho g}{\bar{\rho}}\right)^{1/2}\left(\frac{H}{2} - z_n\right)^{3/2} \tag{6}$$

where the pressure difference $P_{01} - P_{02}$ has been eliminated in favor of the neutral height via equation (5). The quantity C_D is the discharge (or orifice) coefficient of the opening, to be determined by experiment.

In the limit $Q_u = 0$, there is no net volume flow across the opening and fluid exchange between compartments takes place via purely buoyancy-driven countercurrent flow. Under this condition, the zero velocity plane coincides with the midplane of the opening. Thus the purely buoyancy-driven volumetric flow rate through half of the opening, Q_{cc}, is obtained by setting $z_n = 0$ in equation (6). The result is

Nomenclature

C_D = opening orifice coefficient
D = diameter of circular opening (aperture or tube)
g = acceleration due to gravity
H = height or length of rectangular opening
L = axial length of opening (partition thickness or tube length)
P = pressure
q = flooding or purging flow rate
Q = buoyancy-driven exchange flow rate
Q_{BF} = buoyancy-driven component of combined convection
Q_{cc} = purely buoyancy-driven exchange flow rate across a partition
Q_u = one-way buoyancy-driven or supply flow rate
R = $D/2$
S = length of a side for a square opening
u = velocity of fluid within opening
W = width of rectangular opening
z = vertical distance measured from center of opening in wall
z_n = vertical location of plane of zero velocity in opening in wall
$\Delta\rho$ = density difference $= \rho_H - \rho_L$
ρ_L = density of light fluid
ρ_H = density of heavy fluid
$\bar{\rho}$ = mean density $= (\rho_H + \rho_L)/2$

Subscripts

1, 2, 3 = compartment numbers in three-compartment apparatus

$$\frac{Q_{cc}}{\sqrt{W^2H^3g\Delta\rho/\bar{\rho}}}=\frac{C_D}{3} \tag{7}$$

Equation (6) can be transformed into a more compact form by normalizing it with respect to the purely countercurrent exchange rate to obtain

$$\frac{Q_{BF}}{Q_{cc}}=\left(1-\frac{2z_n}{H}\right)^{3/2} \tag{8}$$

Now the flow rate Q from compartment 1 to compartment 2 (see Fig. 1) is, after some simplification,

$$Q=C_DW\int_{-\frac{H}{2}}^{z_n} udz=\frac{2C_DW}{3}\left(\frac{2\Delta\rho g}{\bar{\rho}}\right)^{1/2}\left(\frac{H}{2}+z_n\right)^{3/2} \tag{9}$$

or, in dimensionless form,

$$\frac{Q}{Q_{cc}}=\left(1+\frac{2z_n}{H}\right)^{3/2} \tag{10}$$

A volumetric flow balance on, say, compartment 1 in Fig. 1 requires that

$$Q_u=Q-Q_{BF} \tag{11}$$

Combining equations (8), (10), and (11) gives the following expression for the location of the neutral plane within a rectangular opening in inverted form:

$$\frac{Q_u}{Q_{cc}}=\left(1+\frac{2z_n}{H}\right)^{3/2}-\left(1-\frac{2z_n}{H}\right)^{3/2} \tag{12}$$

The purging or flooding flow rate $Q_u=q$ necessary to render $Q_{BF}=0$ is achieved when the neutral height is positioned at the top of the opening, i.e., $z_n=H/2$. Thus, from equation (7) and (12),

$$q=2^{3/2}Q_{cc}=\frac{2C_D}{3}\sqrt{\frac{2W^2H^3g\Delta\rho}{\bar{\rho}}} \tag{13}$$

is the flooding condition for a rectangular opening in a wall.

When the quantity z_n/H lies somewhere between 0 and 1/2, which is the range of physical interest, the right-hand side of equation (12) can be approximated by the simple linear function

$$\frac{Q_u}{Q_{cc}}\simeq 2^{5/2}\frac{z_n}{H} \tag{14}$$

to within an accuracy of 5 percent. Using equations (13) and (14), equation (8) can be rewritten in terms of Q_{cc} and q as follows:

$$Q_{BF}=Q_{cc}(1-Q_u/q)^{3/2} \tag{15}$$

For combined flow through a *circular* opening in a wall, the theoretical results corresponding to equations (7), (8), and (10) are

$$\frac{Q_{cc}}{\sqrt{D^5g\Delta\rho/\bar{\rho}}}=\frac{C_D}{2}\int_0^1\sqrt{y(1-y^2)}dy=0.24C_D \tag{16}$$

$$\frac{Q_{BF}}{Q_{cc}}=2.083(1-z_n/R)^{3/2}\int_0^1 y^{1/2}\sqrt{1-[(1-z_n/R)y+z_n/R]^2}dy \tag{17}$$

and

$$\frac{Q}{Q_{cc}}=2.083(1+z_n/R)^{3/2}\int_0^1 y^{1/2}\sqrt{1-[z_n/R-(1+z_n/R)y]^2}dy \tag{18}$$

By setting $z_n/R=1$ in equation (17), integrating the result, and using equation (16), we get the flooding flow rate for circular openings in walls

$$q=3.143Q_{cc}=0.75C_D\sqrt{D^5g\Delta\rho/\bar{\rho}} \tag{19}$$

The integrals of equations (17) and (18) were evaluated numerically for the entire range of z_n/R values of interest. The resulting numerical data for Q_{BF}, Q, and Q_u, the latter quantity determined from equation (11), fit well the expression

$$Q_{BF}=Q_{cc}(1-Q_u/q)^{1.6} \tag{20}$$

Equations (15) and (20) express the buoyantly driven volumetric flow rates, Q_{BF}, through openings in vertical walls in the presence of oppositely directed forced flows Q_u. We note that the buoyant flow $Q_{BF}\to 0$ as the flooding limit $Q_u=q$ is approached, and that the condition of purely buoyantly driven countercurrent flow is reached when $Q_u=0$.

It is apparent from our previous work (Epstein, 1988) that it is not possible to derive from hydraulic theory alone similar functional relationships between Q_{BF} and Q_u that are applicable to openings in horizontal partitions, in view of the mingling of the heavy and light streams in the vertical orientation. For purposes of developing an empirical correlation for combined flow across a horizontal partition, it will be assumed here that the nature of the variation of Q_{BF} with Q_u is similar to that suggested by equations (15) and (20). Thus it is believed to be reasonable to proceed by first correlating measurements of the purely buoyantly driven countercurrent flow rate Q_{cc} and the flooding flow rate q and then determine whether the experimental results for Q_{BF} conform closely to the equation $Q_{BF}=Q_{cc}(1-Q_u/q)^m$, where m is some constant exponent. In this regard Epstein (1988) has already provided an empirical correlation for the buoyantly driven countercurrent exchange rate Q_{cc} in the form of the Froude number $Q_{cc}/(D^5g\Delta\rho/\bar{\rho})$ versus the length-to-diameter ratio of the opening. His result is

$$\frac{Q_{cc}}{(D^5g\Delta\rho/\bar{\rho})^{1/2}}=\frac{0.055[1+400(L/D)^3]^{1/6}}{\{1+0.00527[1+400(L/D)^3]^{1/2}[(L/D)^6+117(L/D)^2]^{3/4}\}^{1/3}} \tag{21}$$

This equation gives the volumetric flux of either fluid within a single opening connecting two closed compartments (i.e., pure countercurrent flow) for L/D's in the range 0.01–20 and $\Delta\rho/\bar{\rho}$'s in the range 0.025–0.17. While the above correlation is based mainly on data with round openings, the experimental evidence suggests that equation (21) can be applied with reasonable accuracy to square openings of characteristic dimension S (length of a side) by making the identification $D=1.1\,S$. Based on the theory presented in the foregoing for flow through openings in vertical partitions, we tentatively assume that the appropriate effective diameter for a rectangular opening of width W and length H is $D=1.1\,(H^3W^2)^{1/5}$ [see equation (7)].

In the following section, experimental results are presented for the volumetric flooding flow rate q, and q is correlated in terms of the dimensionless Froude number.

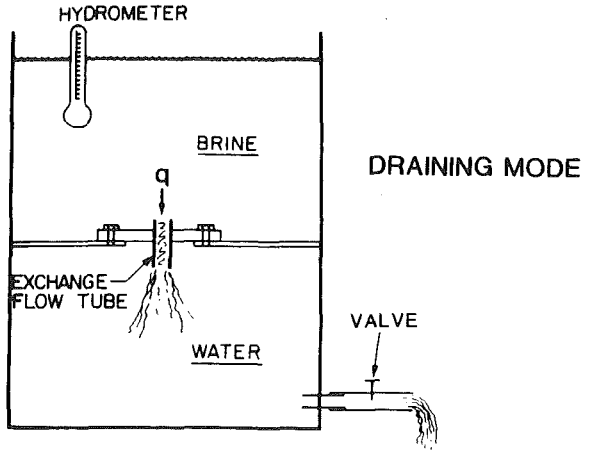

Fig. 2 Schematic diagram of the apparatus for the determination of the flooding flow rate via a quasi-steady draining technique

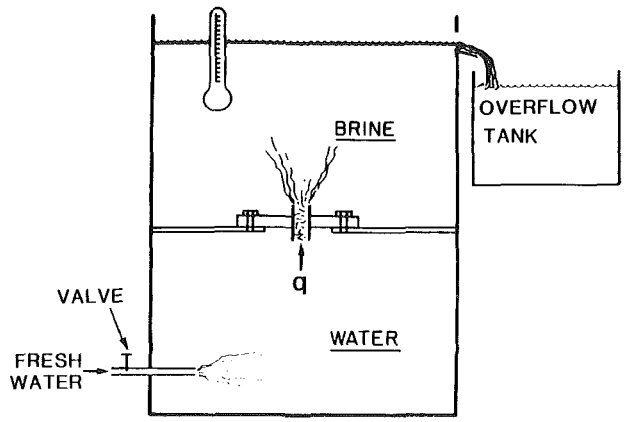

Fig. 3 Schematic diagram of the apparatus for the determination of the flooding flow rate at steady state by water injection

An Empirical Correlation for the Flooding (Purging) Condition

Separate experiments were performed on forced flow through a single opening to obtain a definitive relation between the flooding flow rate q, above which buoyancy-driven exchange flow is prevented, and the opening length-to-diameter ratio L/D. The same apparatus was employed in this study as in the pure exchange flow experiments described by Epstein (1988), except that fluid was supplied or extracted from the tank via a tube that penetrated one of the walls of the tank at the bottom of the lower compartment (see Figs. 2 and 3).

In the "extraction tests," the fresh water in the lower compartment was allowed to drain from the tank and enter the outlet tube under gravity. A valve was installed in the outlet tube to control the draining rate. In this manner a quasi-steady downward flow of brine was established in the opening connecting the two compartments (Fig. 2). At low draining rates the fresh water was observed to flow upward through the opening against the imposed downward brine flow. In this case the draining rate was not strong enough to overcome the buoyant force due to the density difference $\Delta\rho$ across the opening. At high draining rates the fresh water was prevented from entering the opening. This situation was evident by the absence of any signs of fresh water above the opening, either as a plume or in the form of individual packets (drops) of fluid. The flooding or purging condition was defined by an intermediate draining rate that represented a

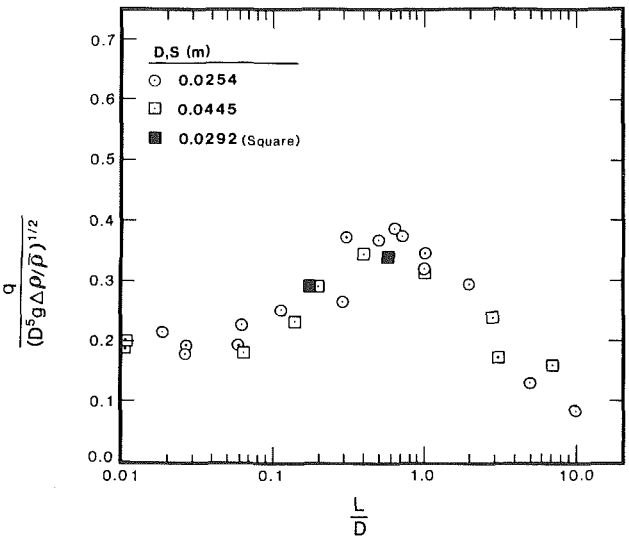

Fig. 4 Experimental results for the critical purging (or flooding) flow rate into a single opening in a horizontal partition

boundary between these countercurrent and cocurrent regimes of flow.

For openings of low L/D, the flooding condition was detected by adjusting the flow so that the rate of upflow of fresh water was reduced to a very slow rate of release of fluid packets into the upper compartment. With the tubelike openings (high L/D) it was found possible to adjust the draining rate so that the brine-water mixing zone filled the tube without any net upflow of water. The draining rate that produced this condition of incipient buoyant flow was defined and recorded as the flooding rate.

The aim of the second group of experiments on flooding was to determine the flooding condition in the presence of a steady-state forced-convection flow. This was accomplished by pumping fresh water through the control valve and into the lower compartment (see Fig. 3). An equivalent volumetric flow of brine was discharged from the tank at the free surface. In these experiments the observed flooding conditions were the same as those described above for the draining experiment, except that in this case it was the upward forced flow of water that prevented the countercurrent buoyant flow of brine through the opening.

The experimental results from the draining and steady-state experiments are brought together in Fig. 4 where, again, the results are plotted in the form of a Froude number versus L/D. The measured flooding flow rates and experiment parameters are presented in Table 1. The range of length scales and density differences investigated here may not appear to be wide enough to establish the generality of Fig. 4. However, previous comparisons with data on buoyantly driven flows in similar but much larger geometries indicate that the Froude number versus L/D relations for exchange flows show little dependence on density difference and can be developed with small scale simulations (Epstein, 1988; Prahl and Emmons, 1975). Results from experiments performed for the same conditions indicated that q was reproducible to within ± 8.0 percent. The two data points obtained with square openings were plotted using the notion of the effective diameter discussed previously and blend nicely with the round opening results. Aside from the moderate scatter, the dimensionless flow data can be regarded as lying on a single curve. Interestingly enough, the shape of the curve is similar to the Q_{cc} versus L/D trend reported by Epstein (1988) for exchange flow in a closed system. Presumably, the regimes of flow encountered in his study of pure countercurrent flow are also operative under

Table 1 Measured flooding rates q for flows through single openings in a horizontal partition

Opening	D(m) or S(m)	L(m)	ρ_H(kg m^{-3})(2)	q(m^3 s^{-1}) x 10^6
Square	0.0292	0.0180	1168.0	80.28
Square	0.0292	0.0060	1178.0	71.11
Round	0.0254	4.83 x 10^{-4}	1153.6	25.88
Round(1)	0.0254	6.86 x 10^{-4}	1151.7	23.56
Round(1)	0.0254	6.86 x 10^{-4}	1148.0	21.66
Round(1)	0.0254	1.57 x 10^{-3}	1160.7	28.37
Round(1)	0.0254	1.57 x 10^{-3}	1143.5	23.33
Round	0.0254	2.87 x 10^{-3}	1161.0	32.0
Tube	0.0254	7.94 x 10^{-4}	1150.5	31.46
Tube	0.0254	7.94 x 10^{-4}	1176.3	48.66
Tube	0.0254	0.0127	1140.8	42.95
Tube	0.0254	0.0152	1138.0	44.9
Tube	0.0254	0.0178	1136.0	43.06
Tube(1)	0.0254	0.0254	1137.6	37.45
Tube(1)	0.0254	0.0254	1172.4	46.0
Tube	0.0254	0.0508	1178.1	38.13
Tube	0.0254	0.127	1145.0	15.37
Tube	0.0254	0.254	1154.0	10.03
Round	0.0445	4.83 x 10^{-4}	1157.0	101.22
Round	0.0445	4.83 x 10^{-4}	1142.4	90.5
Round	0.0445	2.87 x 10^{-3}	1152.5	88.44
Round	0.0445	6.35 x 10^{-3}	1162.7	116.44
Round	0.0445	8.71 x 10^{-3}	1153.2	139.0
Tube	0.0445	0.0174	1149.8	159.8
Tube	0.0445	0.0436	1174.0	156.22
Tube(1)	0.0445	0.140	1160.2	115.55
Tube(1)	0.0445	0.131	1135.8	75.0
Tube	0.0445	0.31	1156.6	75.57

(1) Steady-state experiments with water injection. All other data obtained with draining technique.

(2) $\rho_L = 10^3$ kg m^{-3} in all experiments.

Table 2 Measured natural convection components Q_{BF} of combined flows through single openings in a horizontal partition

D(m)	L(m)	ρ_H(kg m^{-3})(1)	Q_u(m^3 s^{-1}) x 10^6	Q_{BF}(m^3 s^{-1}) x 10^6
0.0254	4.83 x 10^{-3}	1157.6	12.5	1.18
0.0254	4.83 x 10^{-3}	1152.6	10.0	1.82
0.0254	4.83 x 10^{-3}	1157.2	2.50	5.13
0.0254	2.87 x 10^{-3}	1145.0	8.33	3.69
0.0254	0.0127	1158.0	4.17	7.93
0.0254	0.0127	1161.5	13.33	3.60
0.0254	0.0254	1143.0	8.33	5.26
0.0254	0.0254	1150.5	24.67	1.26
0.0254	0.0254	1165.8	20.7	1.68
0.0254	0.0254	1162.8	9.55	5.25
0.0254	0.0508	1151.5	15.0	1.36
0.0254	0.0508	1157.1	16.66	1.09
0.0254	0.0508	1159.0	8.77	2.35
0.0254	0.127	1121.6	3.46	1.68
0.0254	0.127	1163.6	8.89	0.75
0.0254	0.127	1173.0	5.0	1.54
0.0445	0.0174	1149.0	16.7	30.2
0.0445	0.0174	1147.5	83.0	6.26
0.0445	0.0174	1142.7	50.0	15.52
0.0445	0.0174	1131.0	34.5	19.4

(1) $\rho_L \approx 10^3$ kg m^{-3} in all experiments.

flooding conditions when there is no net flow of one of the fluids within the opening.

For purposes of computer studies of natural convection in buildings, one is tempted to inquire whether a formula can be used to estimate q for cases of interest. The function

$$\frac{q}{(D^5 g\Delta\rho/\bar{\rho})^{1/2}} = \frac{0.19[1+4\times10^3(L/D)^3]^{1/9}}{(1+5.091\times10^{-2}(L/D)^{16/7}[1+4\times10^3(L/D)^3]^{4/9})^{1/4}} \quad (22)$$

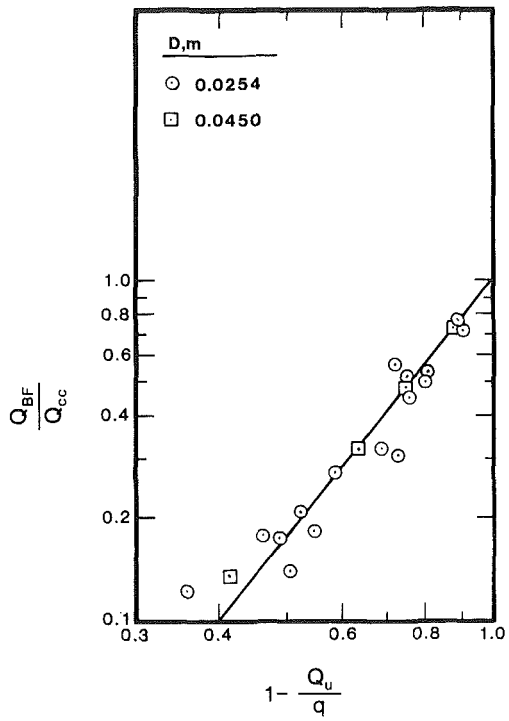

Fig. 5 The natural convection component Q_{BF} of combined natural convection and forced flow across circular openings in a horizontal partition; correlation of data in terms of Q_{cc}, Q_u, and q

was developed and found to pass through the data in Fig. 4 with a relative error of less than about 20 percent.

A Correlation for Combined Flow Through a Single Opening

The main intention of this portion of the study is to determine the effects of forced-fluid motion on natural convection across a single opening in a horizontal partition. In this section we will develop a correlation for combined forced flow and natural convection across a single opening. In the next section we will show how this correlation may be used to treat multiple openings and systems with more than two compartments.

The apparatus used for the combined convection experiments is the same as that already described and shown in Fig. 2 for measuring flooding rates by the draining technique. Combined convection conditions were obtained simply by adjusting the draining rate with the control valve to preselected values below the corresponding flooding rate for the experimental conditions chosen. The buoyancy-driven upflow of water Q_{BF} against the forced downflow of brine was obtained by measuring the rate of dilution of the brine in the upper compartment with a hydrometer (see Epstein, 1988). At high draining rates, but below the flooding rate, the countercurrent flow of water into the upper brine compartment was weak and it was difficult to detect density changes accurately during the course of a run without draining a significant fraction of the brine inventory. Errors resulting from this difficulty account for much of the scatter in the data. The scatter at forced flow rates Q_u greater than about 60 percent of the flooding rate q was so large that no meaningful data could be obtained. From a practical point of view this situation is not serious because the buoyant component of the flow is negligible compared to Q_u for $Q_u \gtrsim 0.6\ q$ (see below). The buoyancy-driven components Q_{BF} determined from the experiments are given in Table 2. The estimated experimental uncertainty in the reported values is between 10 and 30 percent, which again is mainly due to uncertainties in reading the hydrometer.

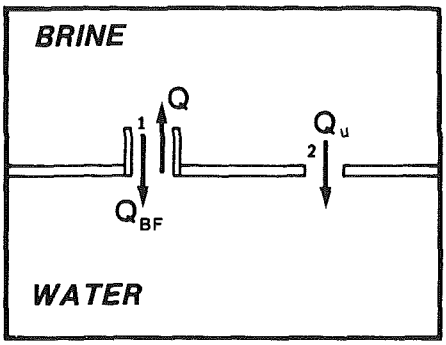

Fig. 6 Density-driven countercurrent and one-way flow between sealed compartments connected by two openings

The theory given previously for combined flow within an opening in a vertical partition suggests the correlation scheme shown in Fig. 5 where Q_{BF}/Q_{cc} is plotted against $1-Q_u/q$. We note from the figure that a power law interpolation equation does a reasonable job of correlating a wide variety of data obtained as part of this study for combined natural and forced convection flow. It can be seen from Fig. 5 that the externally supplied flow rate Q_u need only exceed a value equivalent to about 60 percent of the flooding rate q to essentially "wipe away" the natural convection component Q_{BF}. An expression for the solid, correlating line in the figure, which gives Q_{BF} to an accuracy of 25 percent, is

$$Q_{BF}=Q_{cc}(1-Q_u/q)^{2.3} \tag{23}$$

The only difference between this expression and equations (15) and (20) for the combined effect of natural and forced flow through openings in walls is in the value of the exponent. The increase in the exponent compared to the stratified case is not surprising considering that two fluids flowing in opposite directions through an opening in a vertical partition remain essentially unmixed while countercurrent flow in openings in horizontal partitions promotes vigorous mixing.

Combined Flow and Multiple Openings

It is interesting to inquire as to whether equation (23) for a single opening can be used to predict the measured exchange flow rates for the two-opening system reported in the previous paper (Epstein, 1988). The flow pattern of interest is shown schematically in Fig. 6. While in these experiments an externally supplied flow was not used, a natural unidirectional flow Q_u is present in the system owing to the difference in density between the light fluid that enters opening 1 and the heavier fluid above opening 2. We are particularly interested in the situation where the unidirectional flow is not strong enough to prevent the buoyant downflow of brine at opening 1, as illustrated in Fig. 6. The exchange flow rates for the flow configuration illustrated in this figure are more difficult to deal with than the exchange rates associated with a one-way loop flow, where Q_u is too strong for combined free and forced convection to develop in openings 1 and 2.

The quantity of major interest is the net exchange flow rate between compartments, namely Q. Clearly, the volumetric flows through the openings are related by the formula

$$Q=Q_u+Q_{BF} \tag{24}$$

It can be reasoned that the flow through opening 1 (short tube) behaves much like the combined flow through an isolated opening subject to an externally supplied flow. That is, the buoyancy-driven component of the flow can be replaced by equation (23). Consequently, equation (24) becomes

$$Q=Q_u+Q_{cc}(1-Q_u/q)^{2.3} \tag{25}$$

where we now identify Q_u with the one-way natural loop flow

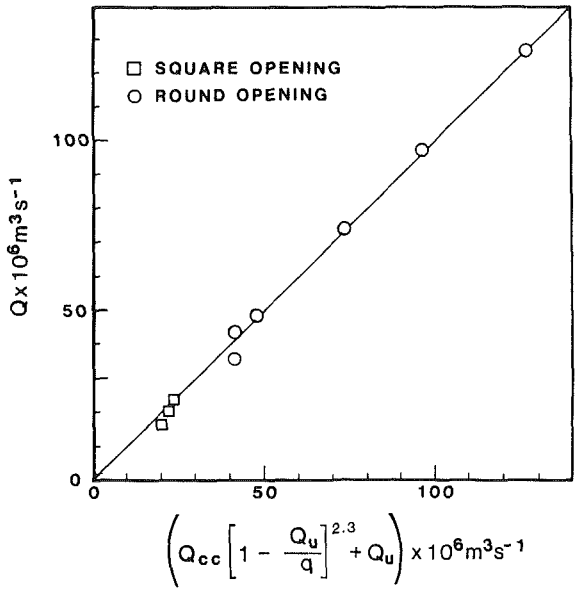

Fig. 7 Measured exchange rates across a horizontal partition with two openings, unidirectional flow in one opening and countercurrent in the other, plotted against equation (25)

in the system. A second and major assumption in the development is that the unidirectional loop flow Q_u that passes through both openings and appears in equation (25) can be evaluated by application of the Bernoulli equation, as if the unidirectional flow was the only flow in the system. The Bernoulli model for the determination of Q_u for the two-opening configuration shown in Fig. 6, for substitution into equation (25), is described by Epstein (1988).

The measured exchange rates Q for the experiments involving two openings and the flow pattern shown in Fig. 6 are plotted in Fig. 7 in the coordinate system suggested by equation (25). Five of the data points are taken from Table 3 of Epstein's (1988) paper, Experiments 1–4 and 9. Four additional experiments were performed with the two-opening configuration as part of the present study, including three runs in which opening 1 was a square of 0.0292 m side dimensions. The exchange rates fall consistently on a straight line and, aside from a small deviation for flow results obtained with square openings and with two holes cut in the partition (Experiment 9), can be regarded as lying on the theoretical curve.

In view of our success in applying equation (23) to two openings, we suggest that combined flow problems involving more than two openings and two compartments can be treated with this equation. The recommended procedure for solving such problems is as follows: The volumetric flow is calculated by first assuming one-way flow throughout the system. In this manner a Q_u is calculated for each opening using the Bernoulli equation and the appropriate orifice discharge coefficients. Then each opening is checked for countercurrent natural convection flow by calculating q and comparing it with Q_u. If openings are found such that $Q_u<q$ then the exchange flow rate in these openings are recomputed using equation (25). The Q_u's to be input in equation (25) are those already obtained from the initial, purely unidirectional analysis.

The experimental apparatus was modified to test this computational scheme, as shown in Fig. 8. As seen, a vertical wall with an opening at its center divides the upper compartment of the previous apparatus (see Fig. 3) into two rooms (compartments 2 and 3), resulting in a three-room configuration. The volume of the lower compartment is 0.0984 m^3 while the volume of each of the upper compartments is 0.0481 m^3. The cutting of two openings in the horizontal partition ensured fluid mechanical communication between all three compart-

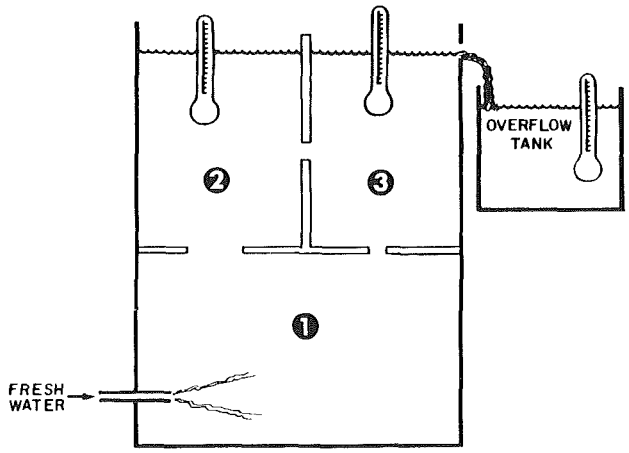

Fig. 8 Three-compartment test configuration; numbers identify compartments

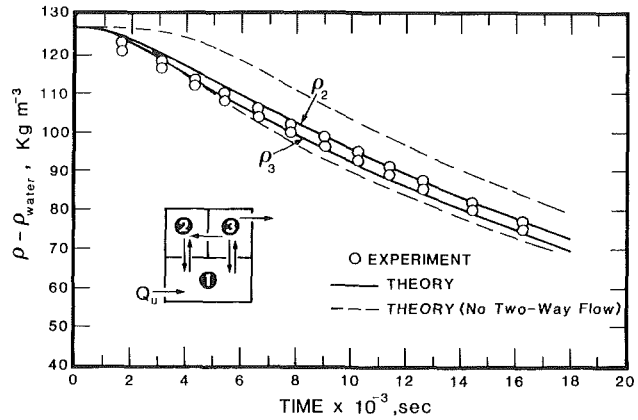

Fig. 10 Comparison between measured and predicted brine dilution histories in the three-compartment configuration with countercurrent flows between compartments

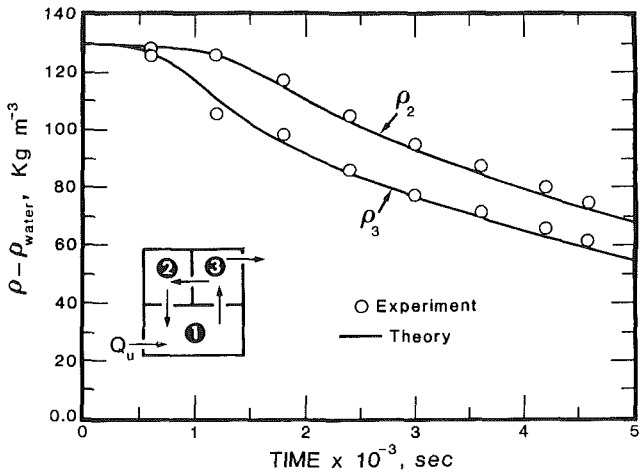

Fig. 9 Comparison between measured and predicted brine dilution histories in the three-compartment configuration under conditions where unidirectional flow prevails

ments and increased the number of openings to three. At the beginning of each experiment, the brine solution of known density was poured into the tank until all three compartments were filled. Flow of fresh water into the lower room (compartment 1) was then initiated by opening the valve on the supply tube. From then onward, the densities of the brine solutions in the upper compartments were carefully monitored. The fresh water flow was maintained constant throughout the data run at levels that ranged from 400 to 3000 ml min^{-1}. The brine solution flowed out of the tank via a weir arrangement at the free surface in compartment 3. In this manner the height of the liquid in the tank was maintained constant. The experimental volumetric flow rate was determined by measuring the volume of brine collected in the overflow tank as a function of time. Run times ranged from 1 to 5 hours, increasing with lower supply flow rates. Hydrometer data were collected at various intervals by temporarily turning off the supply flow and sealing the openings. During these "off periods" two density measurements were made of the mixtures in the upper compartments. The brine-water mixtures were mechanically stirred between hydrometer readings to obtain a "feeling" for the magnitude of brine-water stratification or, equivalently, the rapidity of mixing within the compartments. Density differences due to stratification (slow mixing) were found to be small on the scale of the density change measured over the course of an experiment. Some of the experiments were repeated with hydrometer readings taken at different intervals to ensure that the results are not sensitive to the density measurement technique nor to the effects of brine-water stratification. The apparatus shown in Fig. 8 can be regarded as a laboratory tool for simulating the fluid mechanical response of an actual building atmosphere, as represented by the brine, to an essentially point source release of hot gases, which can be identified with the injection of the less dense fresh water.

The measured dilution histories within the upper compartments are shown in Fig. 9 for a case in which all the compartments were connected by circular openings of 0.025 m in diameter and the flow rate was 2000 ml min^{-1}. During the first 8 minutes of the test, the flows from compartment 1 through the openings in the horizontal partition were unidirectional and upward. The flow through the vertical partition was unidirectional from compartment 2 to compartment 3. For the rest of the 1.28-hour experiment the flow through the opening connecting compartments 1 and 2 was unidirectional and downward. The flow through the vertical partition also changed direction and was unidirectional from compartments 3 to 2. The flow directions are indicated in Fig. 9. It is evident that the flow path of least resistance is from compartment 1 to compartment 3. Thus compartment 2 experiences the lowest rate of dilution by the incoming fresh water, resulting in a counterclockwise loop flow. The onset of this buoyancy-driven convective loop in the system at 8 minutes was predicted by the model. Also, good agreement is seen between predicted and experimental density versus time curves for compartments 2 and 3. Actually the calculational method was utilized in planning the experimental program as it was useful to know beforehand the flow patterns that would be observed for each set of experimental conditions. Thus, the theory was used to prepredict the experimental results.

It should be mentioned here that a discharge coefficient $C_D = 0.71$ was used in applying the Bernoulli flow model to predict the volumetric, unidirectional flows through all the openings. This value was deduced from separate experiments on pure buoyancy-driven exchange flow through the opening in the vertical partition; it agrees reasonably well with the value of approximately 0.68 measured by Prahl and Emmons (1975) and by Steckler et al. (1984) for flows through doors and windows.

The theory led us to believe that, if the 0.025-m-dia openings used in the experiment described above were changed so that the openings cut in the horizontal partition were substantially larger, say, 0.06 m in diameter, while the opening in the vertical partition was reduced in size to, say, 0.0095 m, countercurrent flow would occur in the openings in the horizontal partition. Indeed, this was observed in the experiments with openings of these sizes, beyond approximately 10 min. Figure 10 shows the results for a fresh water injection rate of 400 ml min^{-1}. The agreement between theory and ex-

periment is good and typical of the agreement obtained with all the tests peformed in the three-compartment configuration. The predicted density versus time results obtained with a purely unidirectional Bernoulli model are represented by the dashed lines in Fig. 10, These curves indicate the magnitude of the error incurred by ignoring the effects of countercurrent flow within the openings in the horizontal partition.

Conclusions

This paper presents the results of an experimental investigation of combined, countercurrent, forced and natural convection through an opening in a horizontal partition joining two compartments. The fluid above the partition in the upper compartment is heavier than the fluid below the partition in the lower compartment. The brine–water technique was used to simulate the key features of hot gas flows between compartments. Conclusions may be summarized in three main groups as follows:

(*a*) A flooding or purging mechanism accounts for the transition between one-way forced flow and countercurrent combined flow in an opening. The problem of flooding was investigated with a single opening, by allowing fresh water in the lower compartment to drain out from the bottom or by supplying a flow of fresh water into the lower compartment. By adjusting the drainage or supply rate until the buoyant flow was arrested, an empirical formula was obtained for calculating the flooding flow rate q that is necessary to prevent countercurrent flow within an opening in a horizontal partition.

(*b*) The combined flow regime of buoyancy-driven flow in opposition to the externally supplied flow within an opening lies between pure countercurrent buoyant flow Q_{cc} in a sealed system and the flooding condition. Measurements of combined exchange rates for flow through openings in horizontal partitions were made using the draining technique described above in (*a*). Correlation of the buoyancy component of the combined flow, Q_{BF}, was achieved with a function $Q_{BF}(Q_{cc}, q)$ suggested by the application of hydraulic theory to openings in walls that interpolates between the limits of pure countercurrent flow and the flooding condition.

(*c*) A methodology was developed for predicting the exchange flow rates within multicompartment buildings. Briefly, the Bernoulli equation is applied to flooded openings ($Q_u > q$) and the function $Q_{BF}(Q_{cc}, q)$ is used in the remaining openings for which $Q_u < q$. The natural and forced convection flow patterns and fluid densities within three compartments of the model-scale apparatus were measured experimentally and compared with calculations. The results indicate that the interpolation function $Q_{BF}(Q_{cc}, q)$ in combination with the Bernoulli model can be used to predict convection in multilevel/multicompartment buildings.

Whether or not the influence of stratification within compartments, an effect that was either eliminated by mixing or was found to be negligible in the absence of mixing in the present experiments, is sufficient to render invalid the extrapolation of present results to full-scale buildings may be a matter for further study. Our feeling is that the question as to what determines the magnitude of the stratification will be very difficult to deal with. In actual buildings the stratification is affected not only by the heat loads resulting from walls and internal structures, but also by the flow between compartments. It is believed, however, that the methodology developed in this paper for well-mixed compartments is applicable to actual buildings in that it will provide reasonable estimates of volume-averaged temperature and gas species concentrations.

Acknowledgments

The authors are grateful for Electric Power Research Institute (EPRI) funding and the support provided by Dr. Edward L. Fuller, EPRI Project Manager. The assistance of Mr. Alan S. La Croix and Mr. Verden R. Fletcher in conducting the experiments is also gratefully acknowledged.

References

Brown, W. G., 1962, "Natural Convection Through Rectangular Openings in Partitions—2. Horizontal Partitions," *Int. J. Heat Mass Transfer*, Vol. 5, pp. 869–878.

Brown, W. G., and Solvason, K. R., 1962, "Natural Convection Through Rectangular Openings in Partitions—Vertical Partitions," *Int. J. Heat Mass Transfer*, Vol. 5, pp. 859–867.

Epstein, M., 1988, "Buoyancy-Driven Exchange Flow Through Small Openings in Horizontal Partitions," ASME JOURNAL OF HEAT TRANSFER, Vol. 110, pp. 885–893.

Prahl, J., and Emmons, H. W., 1975, "Fire Induced Flow Through an Opening," *Combustion and Flame*, Vol. 25, pp. 369–385.

Shaw, B. H., 1971, "Heat and Mass Transfer by Natural Convection and Combined Natural Convection and Forced Air Flow Through Large Rectangular Openings in a Vertical Partition," Inst. Mech. Engrs. Symposium on *Heat and Mass Transfer by Combined Forced and Natural Convection*, Sept. 15, Paper No. C117/71.

Steckler, K. D., Baum, H. R., and Quintiere, J. G., 1984, "Fire Induced Flows Through Room Openings—Flow Coefficients," *20th Symposium (Int.) on Combustion*, The Combustion Institute, pp. 1591–1600.

Steckler, K. D., Baum, H. R., and Quintiere, J. G., 1985, "Salt Water Modeling of Fire Induced Flows in a Multiroom Enclosure," *21st Symposium (Int.) on Combustion*, The Combustion Institute, pp. 143–149.

The Energy Equation for Freezing of Biological Tissue

B. Rubinsky
Department of Mechanical Engineering,
University of California at Berkeley,
Berkeley, CA 94720

In the past, the process of freezing in biological tissue was modeled using the regular energy equation for a homogeneous compound. New experimental evidence shows that in tissue the water freezes separately in the vascular system and in the cells. The freezing process is affected by the water transport between the cells and the blood vessels. A new equation was developed to model the experimental results. In this work the general equation for freezing of biological tissue will be presented together with a linearized version of the new equation. A perturbation solution is obtained for the linearized equation to illustrate the effect of the water transport on the freezing process in tissue.

Introduction

Freezing of biological materials has important applications in food technology and in medicine. In food technology, freezing is used to retard the process of deterioration during storage and transportation (ASHRAE *Fundamentals*, 1986). In medicine, freezing is used for controlled destruction of malignant and other nondesirable types of tissue (cryosurgery) (Gage, 1982; Rubinsky, 1986). Freezing is also used, with the addition of appropriate chemicals, for preservation of the viability of biological materials (cryopreservation) (Mazur et al., 1970). Suspensions of different cells such as red blood cells, spermatoza, and embroys are commonly preserved by freezing (Mazur, 1970; Whittingham et al., 1972). Cryopreservation could also become an important method for storage of whole organs for transplantation and significant research has been done recently in this area (Pegg and Karow, 1988).

The study of freezing processes in biological tissue requires the ability to model freezing accurately. Previous analytical studies in this area have used equations and boundary conditions derived for solidification processes in homogeneous compounds. In some of these studies it was assumed that the phase transformation occurs at a constant temperature (ASHRAE *Fundamentals*, 1986; Cooper and Trezek, 1971), while in others it was assumed that the phase transformation occurs over a range of temperatures (Rubinsky and Cravalho, 1984; Comini and Del Guidice, 1976). However, recent experimental studies have shown that the freezing process in tissue is different from freezing in homogeneous compounds (Rubinsky et al., 1987). These experiments show that during freezing of tissue, ice forms first in the vascular system while the water in cells adjacent to the frozen blood vessels remains unfrozen. The ice propagates through the vascular system in the general direction of the temperature gradients but in the particular direction of the blood vessels. The freezing process is also affected by the water transport between the unfrozen cells and the frozen blood vessels and by the thermodynamics of intracellular nucleation and ice formation. This experimentally observed freezing process will serve as the basis for the derivation of a new energy equation for freezing of biological tissue. In this paper a brief presentation of the experimental results will be followed by the derivation of a mass and energy balance on a typical control volume in tissue. The resulting equations will be incorporated in a general equation for the heat transfer during freezing of tissue. A linearized version of the general equation will be used to perform a dimensionless analysis of the problem and to evaluate the effect of the different parameters on freezing in tissue. A perturbation solution of the linearized equation will illustrate the effect of the water transport between the unfrozen cells and the frozen vascular system, on the freezing process in tissue.

Experimental Observations

A brief description of the experimental results showing the process of freezing in tissue will be given next to provide the basis for the derivation of the new energy equation. Liver slices from Spraque–Dawley rats were frozen uniformly under controlled thermal conditions on a special directional solidification stage described in detail by Rubinsky and Ikeda (1985). The slices were frozen with constant cooling rates (i.e., constant rates of temperature drop per unit time) between 1°C/min and 4000°C/min. Cooling rate was chosen as the variable parameter in the experiments since it is established that this is a major factor affecting the viability of cells frozen in cellular suspensions (Mazur et al., 1970). After freezing, the samples were immersed in liquid nitrogen and transported to a low-temperature scanning electron microscope (AMRAY 1000). There the samples were fractured, gold-coated, and observed in a frozen hydrated state on a stage maintained at −180°C.

All the experiments show that continuous single ice crystals form along the blood vessels during the freezing of tissue. This observation is illustrated by Fig. 1, which shows single ice crystals in a large blood vessel and in the connecting smaller blood vessels (sinusoids). For freezing with low cooling rates,

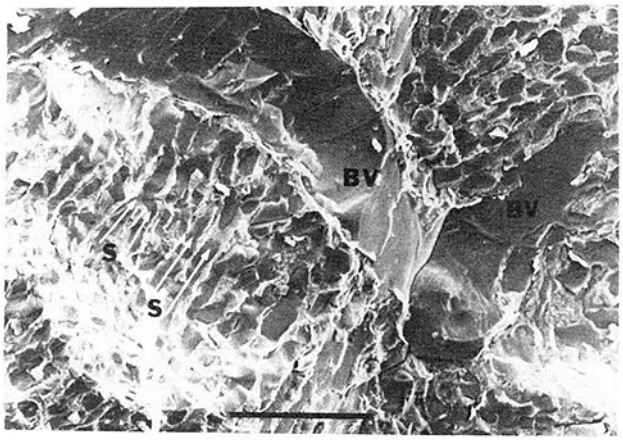

Fig. 1 Scanning electron micrograph of tissue frozen with a cooling rate of 4°C/min showing continuous ice formation in a large blood vessel B, and adjacent sinusoids, S (scale bar 10 μm)

Contributed by the Heat Transfer Division for publication in the JOURNAL OF HEAT TRANSFER. Manuscript received by the Heat Transfer Division August 22, 1980. Keywords: Biotechnology, Phase-Change Phenomena.

i.e., between 1°C/min and 10°C/min, it was observed that the sinusoids containing ice expand while the cells surrounding the frozen blood vessels (hepatocytes) shrink. The shrunken cells contain no ice. These observations are illustrated by Figs. 2(*a*), 2(*b*), and 3(*a*), 3(*b*). Figures 2(*a*) and 3(*a*) show a transverse and a longitudinal cross section, respectively, through sinusoids in the normal rat liver. Figures 2(*b*) and 3(*b*) show a transverse and a longitudinal cross section through a rat liver frozen with a cooling rate of 4°C/min. It is evident that the sinusoids contain single ice crystals. The distance between the centerlines in the frozen sinusoids is similar to the distance in the normal liver. However, the sinusoids have expanded and the cells surrounding the frozen sinusoids have dehydrated. The structure of tissue frozen at a high cooling rate of about 4000°C/min is shown in Fig. 4. Here, ice is observed in the vascular system but the blood vessels did not expand. Small intracellular ice crystals are seen in the frozen cells.

The following explanation was proposed for the process of freezing in tissue (Rubinsky et al., 1987). The explanation follows the approach taken by Mazur (1963) to explain the process of freezing of cells in cellular suspensions. In general, when a homogeneous compound is frozen, the freezing interface propagates in the direction of the temperature gradients by attachment of water molecules to the ice–water interface. However, in biological systems, the cell membrane presents a barrier to the attachment of water molecules to the ice structure and also to nucleation (Mazur, 1963; Chaw and Rubinsky, 1985). Therefore, when ice forms in the vascular system by random nucleation, the freezing interface, which cannot propagate through the cell membrane, is restricted to propagate along the blood vessels where there is no barrier to the attachment of new water molecules to the ice–water interface. This explains the continuous ice crystals observed in the vascular system of frozen biological tissue.

The water in cells surrounding the frozen blood vessels is compartmentalized in small volumes and therefore has a low probability for nucleation. It will remain in a supercooled state while ice forms in the vascular system. When ice forms in the blood vessels, the water is removed from the physiological solution and the solution remaining in the vascular space will become hypertonic. To equilibrate the difference in chemical potential between the supercooled water in cells and the solution in the vascular space, the water in the cells will leave through the cell membrane, which is permeable to water but impermeable to the electrolytes in the cell. Consequently the cells surrounding the frozen blood vessel will dehydrate and the water leaving the cell will freeze in the vascular space. This explains the expansion of the small blood vessels in tissue frozen with low cooling rates. Since the water transport across the cell membrane is a rate-dependent phenomenon, when the tissue is frozen with sufficiently high cooling rates the water in the cells can become sufficiently supercooled for random nucleation and intracellular freezing despite the small volume of the cell. This explains the intracellular ice formation observed following freezing with high cooling rates. This qualitative description of the freezing process in tissue will be used to derive the energy equation for freezing of biological tissue.

Derivative of the Mass Transfer Equations. The experimental results presented in the previous section show that the process of freezing in tissue is affected by the transport of water from cells surrounding the frozen blood vessels into the vascular space. Obviously, water transport must be considered when the energy equation for freezing of biological tissue is derived. This section deals with the derivation of an equation to describe the transport of water from cells (tissue) into the vascular system during freezing of tissue.

Extensive studies have been published on the mass transfer between cells in an organ and the fluid perfusing the tissue

Nomenclature

A = dimensionless number in equation (24)
c = heat capacity, J/kg K
C = molar concentration, M
H = cooling rate, K/s
j_v = volumetric flow rate of water per unit surface area, from tissue into vascular space, m^3/m^2s
k = thermal conductivity, W/m K
L = latent heat, J/kg
m = molal concentration, mol
n = direction normal to the unfrozen–partially frozen interface
o = osmotic coefficient
P = permeability of blood vessel–tissue interface to water, m/s M
q = heat flux, W
r = radius of blood vessel in Krogh cylinder, m
r_{max} = maximal radius of blood vessel in Krogh cylinder, m
R = dimensionless number defined in equation (19)
S = position of the completely unfrozen–frozen interface, m
Ste = dimensionless number defined in equation (19)
S_v = surface area of the blood vessel lumen in the Krogh cylinder, m
t = time, s
T = temperature, K
T_{ph} = phase transformation temperature for the physiological solution, K
ΔT = supercooling of solution in tissue, K
v = dissociation coefficient for electrolytes
v_n = normal velocity of unfrozen–frozen interface, m/s
V = volume of Krogh cylinder unit, m^3
V_{ns} = nonsolvent volume of the cells, m^3
V_t = volume occupied by cells in Krogh cylinder, m^3
x = Cartesian coordinate, m
Δx = typical dimension of Krogh cylinder, m
y = Cartesian coordinate, m
z = Cartesian coordinate, m
α = thermal diffusivity, m^2/s
ζ = dimensionless space variable defined in equation (18)
η = dimensionless space variable defined in equation (18)
θ = dimensionless temperature defined in equation (18)
ξ = dimensionless space variable defined in equation (18)
ρ = density, kg/m^3
τ = dimensionless time defined in equation (18)

Subscripts

i = ice
n = normal direction to the unfrozen–frozen interface
o = initial conditions
t = tissue
u = completely unfrozen tissue
v = vascular space
w = water

Superscript

— = dimensionless normalized with respect to x

Thermal properties without subscript are in the partially frozen region

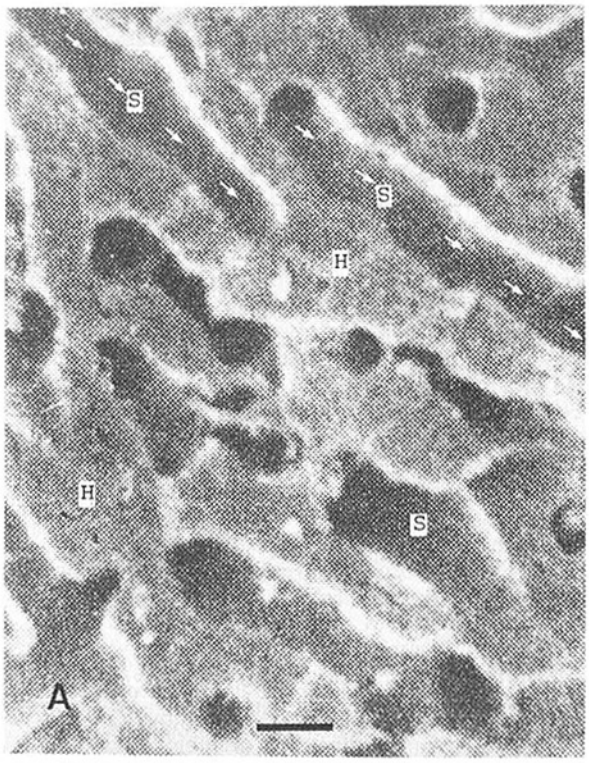

(a)

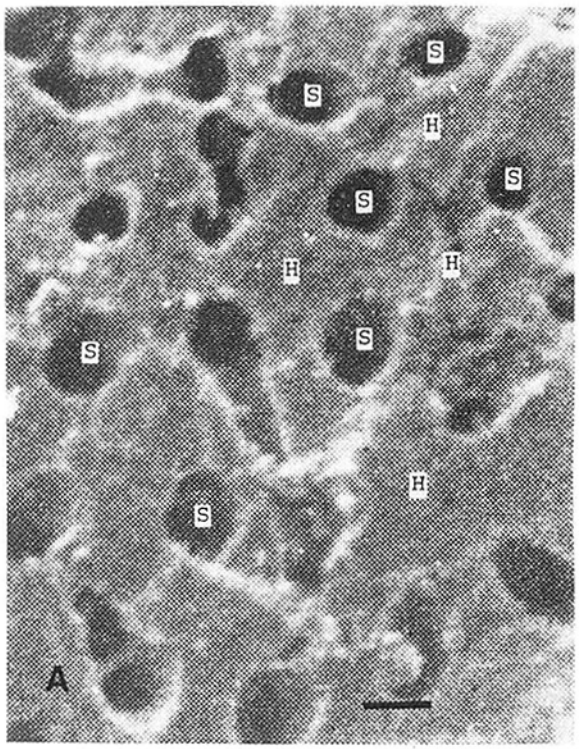

(a)

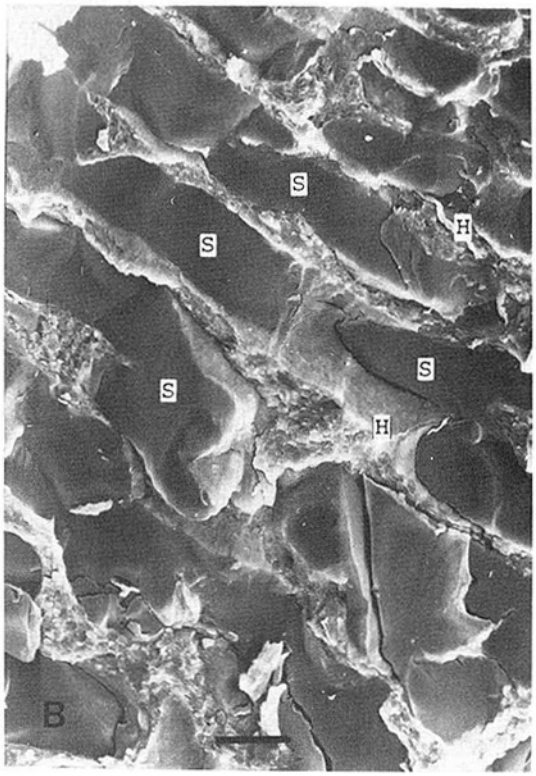

(b)

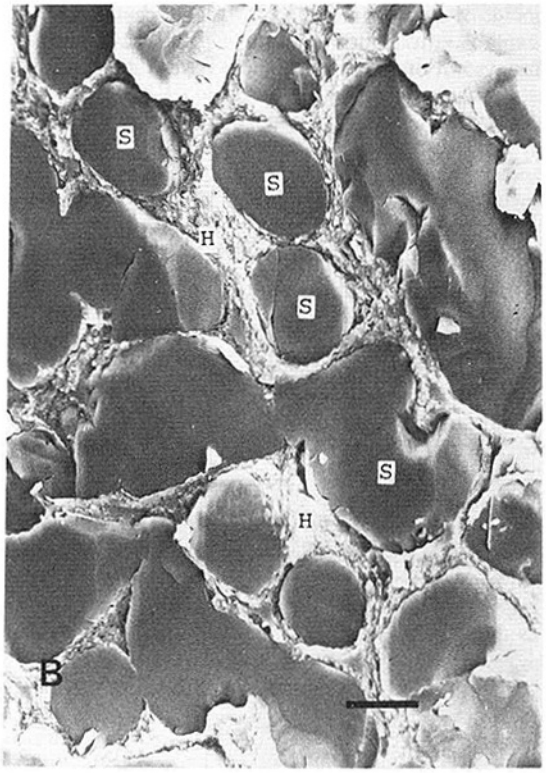

(b)

Fig. 2 Scanning electron microscope images of liver sinusoids (S), also showing adjacent hepatocytes (H). The structure of the normal liver (Fig. 2A, reprinted with permission from Motta et al., 1987) is compared with cross sections of tissue frozen at a cooling rate of 4°C/min (Fig. 2B) (scale bar 10 μm).

Fig. 3 Scanning electron microscope images of liver sinusoids (S), also showing adjacent hepatocytes (H). The structure of the normal liver (Fig. 3A, reprinted with permission from Motta et al., 1987) is compared with cross sections of tissue frozen at a cooling rate of 4°C/min (Fig. 3B) (scale bar 10 μm).

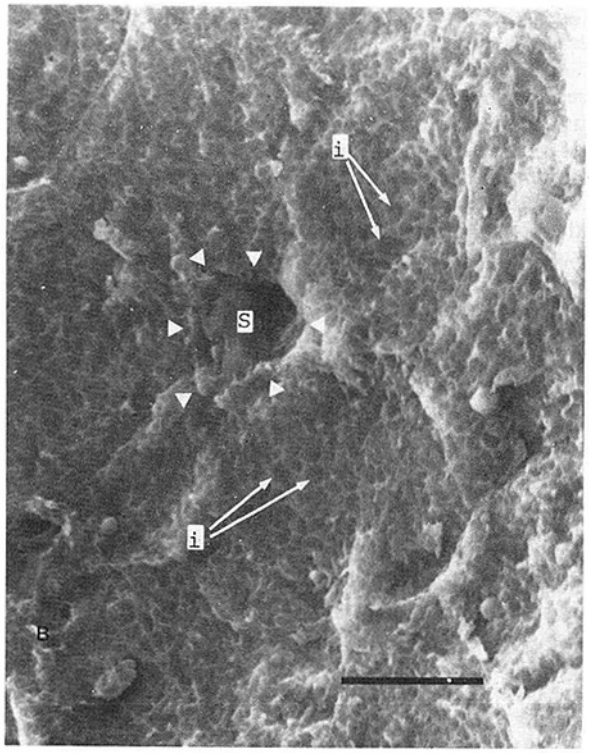

Fig. 4 Scanning electron micrograph of liver tissue frozen with cooling rates of approximately 4000°C/min showing ice in sinusoids, S, and intracellular ice, i, in hepatocytes, H (scale bar 10 μm)

through the vascular system. Several analytical models are available to describe these processes and reviews of literature in this area can be found in several texts and papers such as Crane and Larsen (1970), Middleman (1972), House (1974), and Hempling (1988). A basic assumption in most of the models is that the mass transport occurs in the smaller blood vessels (capillaries), where the ratio between the surface area of the blood vessel to the tissue volume is much larger than for the larger blood vessels. Because of the geometrically uniform distribution of the smaller blood vessels in tissue, the tissue is usually modeled by a large number of identical repetitive tissue-blood vessel units that together form the biological organ. The mass transfer process in such an individual unit is studied and the results assumed to be representative of the phenomena in the whole organ. The tissue-blood vessel unit is commonly referred to as a "Krogh cylinder" after the Danish physiologist, Krogh, who developed the concept (Krogh, 1919). Such a unit consists of a cylindrical blood vessel surrounded by tissue and is shown in schematic form in Fig. 5. The dimensions of the "Krogh cylinder" are obviously important since they must represent the physiological structure of the tissue. The correct choice of these dimensions will affect the analysis and will be different types of tissue. Usually the diameter of the cylindrical blood vessel is taken to be that of a capillary, while the typical dimension of the unit Δx in Fig. 5 is taken to be the distance between two adjacent capillaries. In classical applications the "Krogh cylinder" model is used to study the mass transport between a fluid perfusing the vascular system and the tissue. In these applications the length of the Krogh cylinder is important and is usually taken to be that of a typical capillary. In this work the "Krogh cylinder," tissue-blood vessel unit will be used to study the mass transfer process between the cells (tissue) and the blood vessel during freezing of tissue. Since in this problem there is no flow through the vascular system, the length of the unit has no physical significance for this study. Nevertheless, to define the model completely, it will be assumed that the tissue unit has a cubic shape.

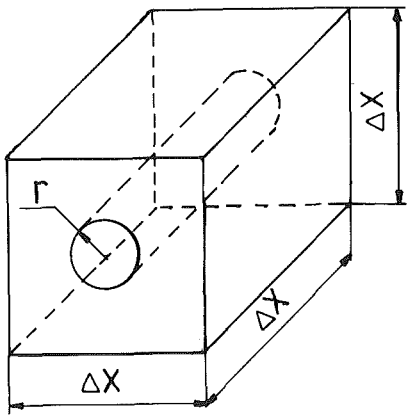

Fig. 5 Schematic drawing of the Krogh cylinder and the control volume

Several assumptions will be made in developing the mass transfer model. These assumptions are common and can also be found in the publications mentioned earlier. The tissue can be represented by one compartment containing a solution of electrolytes in water, initially in osmotic equilibrium with the solution in the blood vessel. The solute concentration in the tissue and in the blood vessel can each be represented by one lumped value. It is also assumed that the interface between the tissue and the blood vessel has one lumped set of mass transfer properties, is impermeable to the electrolytes in the tissue, and is permeable to water. It should be emphasized that more complex models are also available for the study of mass transfer processes in tissue. These models use multicompartmental division of tissue and variable permeabilities of the interface between the tissue and the blood vessel. However, since the goal of this paper is to derive for the first time an energy equation for the freezing of biological tissue, the simpler model should be sufficient to demonstrate the concepts. A special assumption will be introduced here for the thermal analysis. It will be assumed that the Krogh cylinder is small relative to the temperature gradients in the tissue and therefore can be considered to have a temperature that is spatially uniform.

In general, in a Krogh cylinder, the mass transfer process across the blood vessel–tissue interface can be modeled using the more complex Kedem-Katchalsky (1958) equations or the simpler Fick's law. Here the simpler Fick's law will be used to describe the flow of water from the cells (tissue) into the blood vessel

$$j_v = P(C_v - C_t) \tag{1}$$

where j_v is the volumetric flow rate of water from the tissue into the vascular space per unit surface area, while C_v and C_t are the molar concentration of the solution in the blood vessel and in the tissue, respectively. The permeability of the interface to water, P, represents the combined effect of the permeability of the cell membranes and of the blood vessel wall and includes the contributions of the different mass transfer mechanisms.

From considerations of continuity and conservation of mass in the tissue-blood vessel unit, the volumetric flow of water from the cells into the vascular system must equal the change in volume occupied by the cells, V_t.

$$j_v = \frac{1}{S_v}\frac{dV_t}{dt} \tag{2}$$

Since the cell membrane is impermeable to the electrolytes in the solution, the amount of solute, or electrolytes, in the cells will not change. The molar concentration of the solute in the cells, C_t, can therefore be evaluated at all times from the volume occupied by the cells, V_t, and from the initial concentration, C_{to},

$$C_t = C_{to}\frac{V_{to} - V_{ns}}{V_t - V_{ns}} \tag{3}$$

where V_{to} is the initial volume of the tissue and V_{ns} is the nonsolvent volume of the cells.

When ice forms in the blood vessels, water is removed from the solution as ice and the concentration of solute in the vascular system will increase. The ice forming in the vascular space must be in local thermodynamic equilibrium with the saline solution surrounding the ice. A unique thermodynamic relation exists between the temperature of an ice-saline mixture and the saline concentration. This relation, given by the thermodynamic phase diagram (Weast, 1986), can be used to correlate the local temperature in the frozen blood vessel with the local molal concentration m_v of the saline solution in the blood vessel

$$T = 273.15 - 1.86ovm_v \tag{4}$$

where o is the osmotic coefficient and v is the dissociation coefficient for the electrolyte.

When equations (4) and (3) are introduced into equation (1) and the resulting equation set equal to equation (2), a differential equation results for the transient change in the volume occupied by the cells, V_t, during the freezing of the tissue unit, as a function of the temperature of the tissue unit, $T(t)$

$$\frac{dV_t(t)}{dt} = PS_v\left[\frac{T(t) - 273.15}{1.86ov} + C_{to}\frac{V_{to} - V_{ns}}{V_t(t) - V_{ns}}\right] \tag{5}$$

where $V_t(0) = V_{to}$.

Equation (5) can be used to determine the mass transfer process during freezing if the local thermal history is known. It should be noticed that in deriving equation (5), molar concentration was used in equation (4) rather than the molal concentration required by that equation. This should lead to an error smaller than 10 percent in the estimate of concentration (Weast, 1986). Obviously, a more accurate solution could be obtained by solving equations (1) to (4) simultaneously.

Equations (1) to (5) are general and do not contain information on the geometry of the Krogh cylinder. The geometric relations are evident from Fig. 5, and are given by

$$\begin{aligned} V &= (\Delta x)^3 \\ V_t &= V - \pi r^2 \Delta x \\ S_v &= 2\pi r \Delta x \\ r(0) &= r_o \text{ and } r_{\max} = [(\Delta x^3 - V_{ns})/\Delta x]^{1/2} \end{aligned} \tag{6}$$

When the geometric relations are introduced in equation (5), an expression can be derived for the change in the radius of the blood vessel of the Krogh cylinder as a function of the thermal history during freezing

$$\frac{dr(t)}{dt} = -P\left[\frac{T(t) - 273.15}{1.86ov} + c_{to}\frac{(\Delta x)^3 - V_{ns} - \pi r_o^2 \Delta x}{(\Delta x)^3 - V_{ns} - \pi r(t)^2 \Delta x}\right] \tag{7}$$

and $r(0) = r_0$.

Derivation of the Energy Equations. As in all derivatives of the energy equation, a control volume must be specified and an energy balance established for that control volume. In the standard derivation of the energy equation, the control volume is taken as infinitesimally small, but large enough to ensure the continuity of the macroscopic thermodynamic properties of the material. The mathematical model developed in the previous section for the mass transfer process during freezing was based on the assumption that the biological tissue is composed of a large number of identical Krogh cylinder units. Therefore, the smallest control volume that satisfies the continuum behavior of the biological tissue is the Krogh cylinder. In this work, the energy equation for freezing of biological tissue will be derived for the Krogh cylinder shown in Fig. 5, taken as a control volume. To illustrate the typical dimensions of a Krogh cylinder, it should be mentioned that from scanning electron micrographs of the liver (Motta et al., 1978) it is possible to determine that the average diameter of a small blood vessel (sinusoid) is approximately 9 μm while the distance between capillaries is approximately 22 μm. Obviously, the spatial resolution of the solution obtained for such a control volume is restricted by the dimensions of the control volume and by the assumption made in the previous section that the temperature gradients in the tissue are small relative to the dimensions of the control volume.

In this derivation, similar to the standard derivation of the energy equation, the heat transferred by conduction into the control volume through its outer surface is given by Fourier's law

$$q_j = -k_j(\Delta x)^2\frac{\partial T}{\partial j} \text{ where } j = x, y, z \tag{8}$$

The heat leaving the control volume is determined through a series expansion of Fourier's law

$$q(j + \Delta j) = q_j + \frac{\partial q_j}{\partial j}\Delta x + \ldots 0(\Delta x^2) \tag{9}$$

where $j = x, y, z$.

Unique to the energy balance during freezing of tissue is the fact that there are two modes of energy storage in the control volume. More specifically, these models are sensible heat and latent heat during phase transformation. The contribution of the sensible heat to the energy storage process is similar to that in the regular energy equation and is given by

$$(\rho c)(\Delta x)^3\frac{\partial T}{\partial t} \tag{10}$$

The latent heat component is unique to the freezing process in biological tissue. The water leaving the cells freezes in the vascular system and the consequent change in enthalpy must be included by the energy balance. Since the concentration of the solution in the frozen blood vessel is determined through knowledge of the temperature of the control volume, the water leaving the tissue into the vascular system cannot contribute to the change in concentration and must therefore become chemically inert. In essence, all the water flowing from the cells into the frozen blood vessel must freeze. The change in enthalpy due to the freezing of water that flows from the cells into the blood vessel is given by

$$-\rho L j_v S_v \tag{11}$$

Using the standard procedure for deriving an energy equation, equations (9) to (11) can be combined in an energy balance for the control volume to obtain an energy equation for freezing of biological tissue

$$\nabla(k \nabla T) = \rho c\frac{\partial T}{\partial t} - \frac{\rho L j_v S_v}{(\Delta x)^3} \tag{12}$$

While the left-hand side terms and the first term on the right-hand side of equation (12) appear in the regular energy equation, the last term in equation (12) is special and dependent on the flow rate of water into the vascular space, j_v. This flow rate can also be expressed in terms of the change in the volume of the Krogh cylinder and in terms of the geometry of the control volume using equation (7). When this is done, equation (12) becomes

$$\nabla(k \nabla T) = \rho c\frac{\partial T}{\partial t} - \frac{2\pi r \rho L}{(\Delta x)^3}\frac{dr}{dt} \tag{13}$$

Equation (13) will describe the thermal history in a biological tissue when water leaves the cells to freeze in the

vascular space. This equation applies until the cells surrounding the blood vessel dehydrate completely, i.e., until the radius of the blood vessel has reached its maximal value r_{max} or until the supercooling of the intracellular water has reached a value at which the intracellular water freezes by random nucleation. Additional information can be obtained from the solution of equation (13). The intracellular concentration during freezing can be determined through the simultaneous solution of equations (13) and (1) to (5). The intracellular concentration can be used with an equation similar to equation (4) to determine the intracellular supercooling during the freezing of tissue. This is given by

$$\Delta T = 273.15 - T(t) - 1.86 o v m_t(t) \tag{14}$$

where $m_t(t)$ is the transient concentration of electrolytes in the cell. The intracellular supercooling ΔT can be used to evaluate the probability for intracellular freezing according to well-known nucleation theories such as Turnbull (1969). This is an interesting topic of research that will not be addressed in this work.

Several assumptions can be used to simplify equation (13). A basic assumption is that the change in density upon phase transformation can be neglected and that is does not contribute a convective heat transfer term. In a general formulation of equation (13), the thermal properties can be either isotropic or anisotropic depending on the structure of the tissue, and will also depend on the relative amounts of water and ice in the system, i.e., they will be temperature and time dependent. In the liver, which is the biological tissue that was studied experimentally, the orientation of the sinusoids is random and therefore the tissue can be assumed macroscopically isotropic. In addition, it can be assumed that the volume of the solution in the frozen vascular system is small relative to the volume of ice in the system. This assumption can be justified from the phase diagram by studying the fraction of ice as a function of temperature during the freezing of a saline solution. Details and a verification of this assumption can be found in the work of Rubinsky and Cravalho (1984). With the assumptions listed above, the thermal properties of the tissue can be determined as a function of the radius of the blood vessel through the expressions

$$k = ((\Delta x)^3 - \pi r^2 \Delta x) k_w + \pi r^2 k_i \Delta x)/(\Delta x)^3$$

$$\rho c = ((\Delta x)^3 - \pi r^2 \Delta x)(\rho c)_w + \pi r^2 (\rho c)_i \Delta x)/(\Delta x)^3 \tag{15}$$

Equations (7), (13), and (15) apply in the region in which ice has formed in the vascular system, while the water in cells surrounding the frozen blood vessels is still unfrozen. These equations must be solved simultaneously to determine the heat and mass transfer processes in the partially frozen region.

For a complete formulation of the problem, the energy equations for both the frozen and unfrozen regions are needed. These equations are the well-known energy equations in a homogeneous compound. The equation for the unfrozen region, which also applies, with the appropriate thermal properties, to the completely frozen region, is given by

$$\nabla (k_u \nabla T_u) = (\rho c)_u \frac{\partial T_u}{\partial t} \tag{16}$$

The boundary conditions between the completely unfrozen and the partially frozen region are given by

$$k \frac{\partial T}{\partial n} - k_u \frac{\partial T_u}{\partial n} = \rho L \frac{\pi r_o^2}{(\Delta x)^2} V_n \text{ on } S(x, y, z, t) \tag{17}$$

and

$$T(S(x, y, z, t)) = T_{ph}$$

Equations (17) represent the assumption that at the interface between the unfrozen and the partially frozen regions, the water in the vascular system freezes without supercooling while the water in the cells surrounding the frozen blood vessel is supercooled and does not freeze. The temperature at the interface T_{ph} is the phase transition temperature for physiological saline.

The conditions at the interface between the partially frozen tissue and the completely frozen tissue can be either geometric or thermodynamic. For freezing with low cooling rates the interface is the geometric location at which the cells become completely dehydrated and the radius of the blood vessel has reached its maximal value r_{max}. This location can be evaluated from the solution of equation (5). If the freezing is with a high cooling rate, the interface is determined at the location at which the supercooling given by equation (14) predicts a high probability for intracellular ice formation. This specific case requires additional concepts of nucleation theory, which will not be introduced in this first formulation of the energy equation for freezing of biological tissue.

In conclusion, equations (4) and (13) to (17), together with the appropriate initial and boundary conditions, can be used to determine the heat and mass transfer processes during freezing of biological tissue.

A Linearized Energy Equation for Freezing of Biological Tissue. Problems of heat transfer with phase transformation are nonlinear and difficult to solve. The nonlinearity is introduced through the boundary conditions at the interface between the solid and liquid phases. In this work, in addition to the nonlinear boundary conditions at the interface, the equations describing the heat and mass transfer process in the partially frozen region are nonlinear. Obviously, this makes any attempt to solve the problem of freezing biological tissue more difficult. To facilitate a better understanding of the importance of the new equations in studying solidification processes in tissue, a simplified dimensionless and linearized formulation of the equations for the heat and mass transfer in the partially frozen region was developed.

The main nonlinearity in the equations is associated with terms affected by the variation in the radius of the blood vessel. Consequently, these equations can be linearized for situations in which small changes occur in the radius of the blood vessel. Small changes in the radius will occur at short times after the onset of the freezing process and for small changes in temperature. For small changes in the radius of the blood vessel, it can be assumed that the radius of the blood vessel is fixed at its initial value r_o, which removes the nonlinearity from the equations and also allows the assumptions of constant thermal properties. The following dimensionless variables will be used in the linearized formulation:

$$\zeta = \frac{x}{\Delta x}; \quad \eta = \frac{y}{\Delta x}; \quad \xi = \frac{z}{\Delta x}; \quad \dot{r} = \frac{r}{\Delta x} \tag{18}$$

$$\tau = \frac{kt}{(\rho c)(\Delta x)^2} \text{ Ste}; \quad \theta = \frac{T - T_{ph}}{273.15 - T_{ph}}$$

Two dimensionless numbers emerge from this formulation

$$\text{Ste} = \frac{C(273.15 - T_{ph})}{L}; \quad R = \frac{P \Delta x c_{to}}{\alpha} \tag{19}$$

The dimensionless Stefan number Ste appears in all problems of heat transfer with phase transformation and represents the ratio between the energy stored in the system as sensible heat relative to the energy stored as latent heat. The dimensionless number R is unique to this problem and represents the ratio between the diffusion of mass (water) across the blood vessel–tissue interface relative to the diffusion of heat in the partially frozen region. When the dimensionless terms defined by equations (18) and (19) are introduced into equations (7) and (13), the change in the radius of the blood vessel in the Krogh cylinder during freezing becomes

$$\frac{d\bar{r}}{d\tau} = -\frac{R}{\text{Ste}}\theta; \quad \bar{r}(0) = \bar{r}_o \tag{20}$$

while the energy equation in the partially frozen region is given by

$$\nabla^2\theta = \text{Ste}\frac{\partial\theta}{\partial\tau} + \frac{2\pi\bar{r}_o R}{\text{Ste}}\theta(\tau) \tag{21}$$

The boundary conditions at the interface between the partially frozen and the unfrozen regions become

$$\frac{\partial\theta}{\partial n} - \frac{k_u}{k}\frac{\partial\theta_u}{\partial n} = \pi\bar{r}_o^2\bar{v}_n \tag{22}$$

and

$$\theta = \theta_u = 0 \text{ on } \bar{S}(\zeta, \eta, \xi, \tau)$$

Equations (20) and (21) provide insight into the effect of different parameters on the freezing process in tissue. It is obvious that both the rate of change in the radius of the capillaries (equation (20)) and the temperature history in the frozen tissue (equation (21)) will depend upon the dimensionless numbers R and Ste. Equation (20) shows that the rate of expansion of the blood vessel during freezing is directly proportional to the R number and inversely proportional to the Ste number. This implies that the expansion will be faster for larger R numbers, when the mass diffusivity is higher than the thermal diffusivity, and for smaller Ste numbers, when the amount of energy stored in the system as latent heat is larger than the amount of energy stored in the system as sensible heat. Equation (20) also shows that the rate of the change in radius is a function of temperature, which implies that a higher rate of change in temperature will result in a faster expansion of the vascular system.

In this work the results of the analysis will be discussed with respect to the freezing process in the liver. The physical and geometric data for the liver as listed in Table 1. From these data it is possible to evaluate the values for the R number and the Ste number, which are 3×10^{-3} and 2×10^{-3}, respectively. These two dimensionless numbers are much smaller than 1 but have the same order of magnitude. The fact that the Ste number is small is well known and is commonly used to obtain regular perturbation solutions for problems of heat transfer with phase transformation (Rubinsky and Cravalho, 1979). The Ste number multiplies the time-dependent term in equation (21) and is much smaller than 1. This implies that in a first-order expansion of the temperature distribution in terms of the Ste number, the contribution of the time-dependent term will disappear, leading to the so-called "quasi-steady" solution for the temperature distribution. On the other hand, the second term on the right-hand side of equation (21) is a ratio between the R number and the Ste number. In the particular situation discussed in this work, this ratio is on the order of 1. This demonstrates that the thermal history during freezing of biological tissue is strongly affected by the water transport process and therefore the water transport cannot be neglected.

A Solution to the Linearized Energy Equation. To illustrate the effect of water transport on the thermal history during freezing of biological tissue, a solution will be derived for a one-dimensional freezing process in liver tissue modeled as a semi-infinite domain. The analysis will deal only with the region of special interest to this work, the partially frozen region. The solution will be obtained for a situation in which the temperature of the tissue is initially at the phase transition value T_{ph}, and the tissue is frozen by imposing a constant cooling rate H on the outer surface of the domain. The governing equation and the relevant boundary and initial conditions are given below in a dimensional form.

$$\frac{\partial^2\theta}{\partial\eta^2} = \text{Ste}\frac{\partial\theta}{\partial\tau} + \frac{2\pi\bar{r}_o R}{\text{Ste}}\theta; \quad 0<\eta<\bar{S}(\tau) \tag{23}$$

$$\theta(\eta, 0) = 0; \quad \theta(S(\tau), \tau) = 0; \quad \theta(0, \tau) = -A\tau. \tag{24}$$

where

$$A = \frac{H(\Delta x)^2}{\text{Ste}(273.15 - T_{ph})\cdot\alpha}$$

and

$$\frac{\partial\theta}{\partial\eta} = \pi\bar{r}_o^2\frac{d\bar{S}}{d\tau} \text{ on } \bar{S}(\tau); \quad \bar{S}(0) = 0 \tag{25}$$

The solution to equations (23) and (25) will be obtained using a perturbation method and accordingly it will be assumed that the solution can be expanded in a regular perturbation series in terms of the Ste number, of the form

$$\theta = \theta_o + \text{Ste}\theta_1 + \ldots 0(\text{Ste}^2) \tag{26}$$

When equation (26) is introduced into equations (23) to (25) the following zeroth-order solution is obtained for the temperature distribution in the freezing region:

$$\theta = -A\tau\frac{\sinh((2\pi\bar{r}_o R/\text{Ste})^{1/2}(\bar{S}-\eta))}{\sinh((2\pi\bar{r}_o R/\text{Ste})^{1/2}\bar{S})}; \quad 0<\eta<\bar{S}(\tau) \tag{27}$$

An expression for the transient position of the partially frozen-unfrozen interface can be obtained by inserting equation (27) into equation (25)

$$\bar{S} = \frac{\text{arc cosh}(1 + A\tau^2/(\bar{r}_o\text{Ste}))}{(2\pi\bar{r}_o R/\text{Ste})^{1/2}} \tag{28}$$

Equations (27) and (28) can be introduced into equation (20) to obtain an expression for the expansion of the blood vessel $\bar{r}$ in tissue as a function of time and location. For example, equation (29) gives an expression for the transient expansion of the radius of blood vessels on the outer surface of the frozen tissue

$$\bar{r}(0, \tau) = \bar{r}_o + (RA\tau^2)/(2\,\text{Ste}) \tag{29}$$

For a better understanding of the effect of water transport on the thermal history during freezing, the solution given by equation (27) and (29) will be compared with the solution to a problem in which the freezing process in tissue is studied, assuming that the tissue freezes as a homogeneous compound. In this situation the governing equations become

$$\frac{\partial^2\theta}{\partial\eta^2} = \text{Ste}\frac{\partial\theta}{\partial\tau}; \quad 0<\eta<\bar{S}(\tau) \tag{30}$$

Table 1 Geometric and physical properties of the liver

Geometric data	$r_o = 4.5$ μm	$x = 22$ μm	$V_{ns} = 0.2$ V_{to}	
Thermal data	c (J/kg)	k (W/mK)	(kg/m^3)	L (kJ/kg)
Water	4.23×10^3	0.552	998	335
Ice	1.23×10^3	2.25	921	335
Partially frozen region	3.38×10^3	0.775	990	335
Mass transfer data	$c_o = 0.154$ M,	$P = 0.1$ m/s,	$O = 1$,	$v = 2$

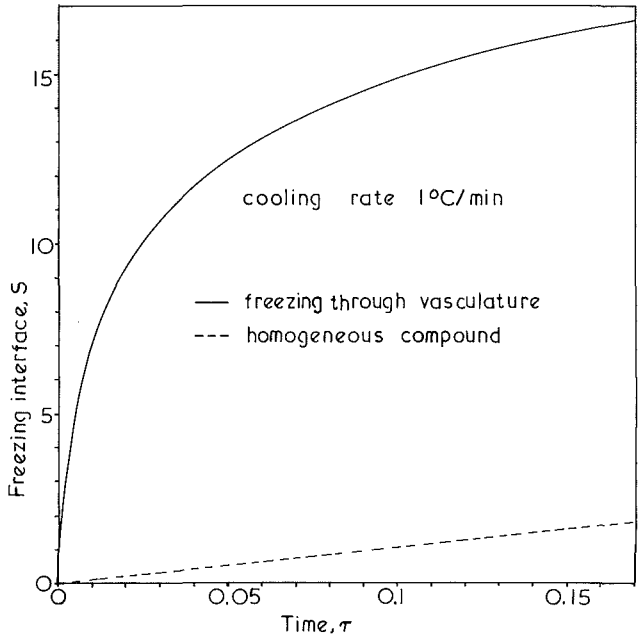

Fig. 6 Position of the unfrozen-frozen interface for freezing with a cooling rate of 1°C/min

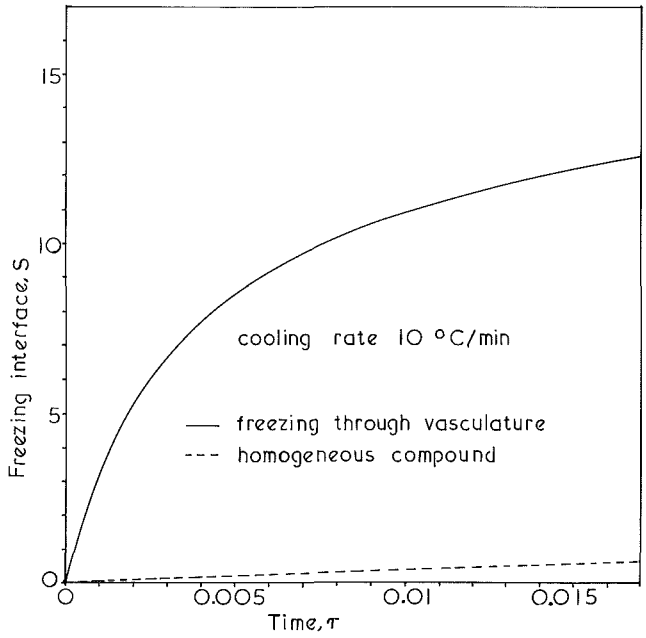

Fig. 7 Position of the unfrozen-frozen interface for freezing with a cooling rate of 10°C/min

$$\frac{\partial\theta}{\partial\eta}=\frac{d\bar{S}}{d\tau} \text{ on } \bar{S}(\tau); \quad \text{and } \bar{S}(0)=0 \tag{31}$$

The zeroth-order perturbation solution to these equations obtained using a method similar to that described by Rubinsky and Cravalho (1979) becomes

$$\theta=-A\tau(\eta-\bar{S})/\bar{S}; \quad 0<\eta<\bar{S}(\tau) \tag{32}$$

and

$$\bar{S}=A\tau^{1/2} \tag{33}$$

Results and Discussion

Equations (27), (28), (32), and (33) will be used to illustrate the effect of water transfer between cells and blood vessels on the thermal history during freezing. The study will be performed for liver tissue and the parameters given in Table 1 will be used in the analysis. The thermal history in the partially frozen region will be determined for a situation in which cooling rates H of 1°C/min and 10°C/min are applied at the outer surface of the freezing domain.

Figures 6 and 7 show the position of the completely unfrozen-partially frozen interface during freezing with cooling rates of 1°C/min and 10°C/min, respectively. The position was determined using equation (28). The figures compare the position of the interface when freezing is assumed to occur through the vasculature, to freezing in a homogeneous compound in which the position of the unfrozen-frozen interface is given by equation (33). The results show that the interface propagates much faster (by an order of magnitude) if the freezing is assumed to occur first through the vascular system. Although this result is obvious, the figures illustrate the magnitude of the effect and show that the freezing interface in tissue will propagate rapidly through the vascular system leaving behind a region of partially frozen tissue. In that region heat and mass transfer processes will occur that will affect the results of the freezing protocol with respect to the different applications discussed in the introduction to this work. A comparison of the two figures also shows that, as expected, the freezing interface propagates faster into the tissue when a higher cooling rate is imposed on the outer surface.

Figures 8 and 9 show typical temperature distributions in the frozen tissue during freezing with a cooling rate of 1°C/min and 10°C/min, respectively. The results compare the temperature profiles obtained with the model, which assumes that ice forms first and propagates through the vascular system (equation (27)) to temperature profiles obtained assuming a homogeneous compound behavior of the tissue (equation (32)). In the first case, which is the new model developed in this work, the temperature profile is much more shallow and the thermal effect penetrates deeper into the tissue. This is consistent with Figs. 6 and 7, showing the transient position of the interface. The shallow temperature profile can be explained by the fact that in the model developed in this work only the energy required to freeze the water in the vascular system has to be extracted at the interface between the unfrozen-partially frozen region. The temperature profile in the second case is very steep and almost linear. This is a well-known behavior during freezing processes in homogeneous compounds and is caused by the assumption that all the material undergoes phase transformation on the interface. It is interesting to notice that the temperature profile obtained with the model developed in this work is curved and therefore completely different from the linear profile obtained with the standard equations. The profile is curved because of the need to extract energy continuously through the frozen region as the water that leaves the tissue freezes in the blood vessel. The analytical results suggest that because of the curvature and the shallow temperature gradient in the vicinity of the freezing interface, the position of the interface and the process of intracellular freezing cannot be determined accurately by thermocouple measurements during experiments. This suggests a careful re-evaluation of the experimental temperature measurements in the different fields related to freezing of biological materials.

The results presented in these figures illustrate the important effect of the water transport process on the thermal history in the partially frozen region. The equations developed in this work can be used in systematic studies on the freezing process in biological tissue and can be used to determine the thermal history in the tissue as well as the mass transfer process. Studies with freezing of cells in suspension have shown (Mazur et al., 1970) that the viability and structural integrity

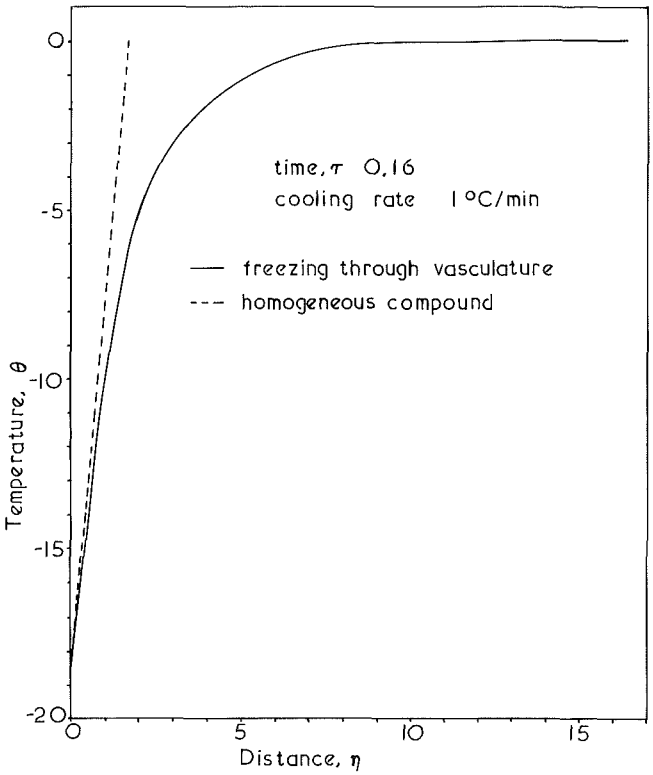

Fig. 8 Temperature distribution during freezing with a cooling rate of 1°C/min

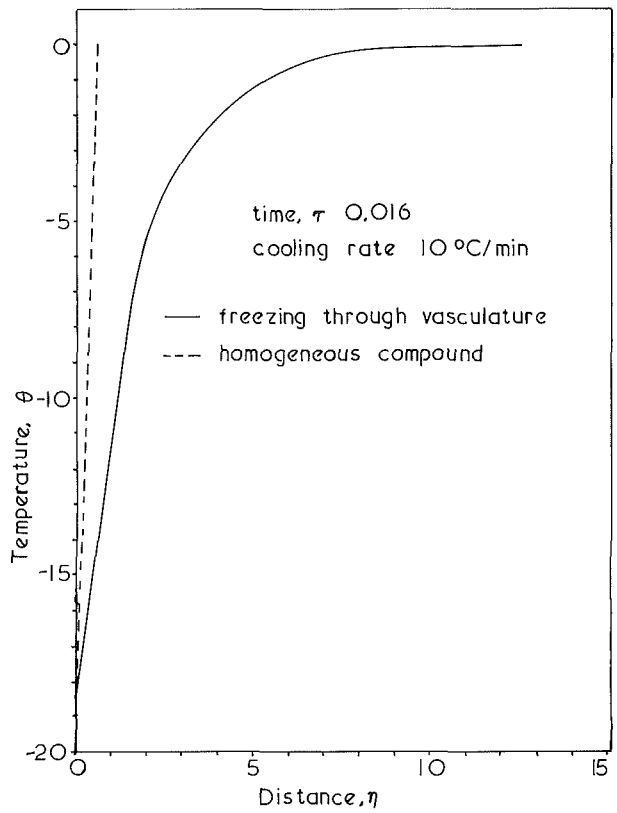

Fig. 9 Temperature distribution during freezing with a cooling rate of 10°C/min

of frozen cells are strongly affected by the water transfer process during freezing. Obviously, the equations developed in this work and the approach taken here can be used to determine the heat and mass transfer process during freezing of tissue and should be used in developing controlled freezing protocols for the different practical applications of freezing.

Conclusions

A new mathematical model was developed to describe the freezing process in biological tissue. The model is based on experimental evidence, which shows that during freezing of tissue, ice forms first and propagates through the vascular system, while the water in cells surrounding the blood vessels remains in a supercooled state. Driven by a difference in chemical potential, the water from the cells is transported into the blood vessels, where it freezes. A general set of equations, which include the effect of the water transport on the energy balance, were derived. A closed-form solution was obtained for a linearized version of these equations. The results demonstrate that the thermal behavior predicted by the new model is different from solutions obtained by modeling the tissue as a homogeneous compound without including the effect of water transport on the energy balance. Therefore, the water transport between the cells and the vascular system must be included in any realistic analysis of the freezing process in biological tissue. The work presented here is a first step in an effort to model accurately the freezing process in tissue and much more work remains to be done in this area, in particular the study of intracellular ice formation as well as complete solutions to the model proposed in this work.

Acknowledgments

The help of Dr. D. E. Pegg in the preparation of this paper is gratefully acknowledged. The author was supported by a Senior International Fellowship Award from the Fogarty International Center of the National Institutes of Health, USA, Grant No. 1 F06 TWO 1303-01.

References

ASHRAE, 1986, *Fundamentals*, ASHRAE Publications, Atlanta, GA.

Chaw, M. W., and Rubinsky, B., 1985, "Cryomicroscopic Observation on Directional Solidification in Onion Cells," *Cryobiology*, Vol. 22, pp. 392–399.

Cominì, G., and Del Guidice, S., 1976, "Thermal Aspects of Cryosurgery," ASME Journal of Heat Transfer, Vol. 43, pp. 543–549.

Cooper, T. E., and Trezek, G. J., 1971, "Rate of Lesion Growth Around Spherical and Cylindrical Cryoprobes," *Cryobiology*, Vol. 7, pp. 6–11.

Crane, G., and Larsen, N., eds., 1970, *Capillary Permeability*, Academic Press, New York.

Gage, A. A., 1982, "Current Issues in Cryobiology," *Cryobiology*, Vol. 19, pp. 219–222.

Hempling, H. H., 1988, "Mass Transfer of Liquids Across Biological Barriers," in: *The Biophysics of Organ Cryopreservation*, D. E. Pegg and A. M. Karow, eds., NATO ASI Series No. 147, Plenum Press, New York.

House, C. R., 1974, *Water Transport in Cells and Tissue*, Edward Arnold, London.

Kedem, O., and Katchalsky, A., 1958, "Thermodynamic Analysis of the Permeability of Biological Membranes to Non-electrolytes," *Biochim.-Biophys. Acta*, Vol. 27, pp. 229–246.

Krogh, A., 1919, "The Number and Distribution of Capillaries in Muscles With Calculation of Oxygen Pressure Head Necessary for Supplying the Tissue," *J. Physiol.*, Vol. 52, p. 409.

Middleman, S., 1972, *Transport Phenomena in the Cardiovascular System*, Wiley-Interscience, New York.

Mazur, P., 1963, "Kinetics of Water Loss From Cells at Subzero Temperatures and the Likelihood of Intracellular Freezing," *J. Gen. Physiology*, Vol. 47, pp. 347–369.

Mazur, P., 1970, "Cryobiology: The Freezing of Biological Systems," *Science*, Vol. 168, pp. 939–949.

Mazur, P., Leibo, S. P., Farrant, J., Chu, E. H. Y., Hanna, M. J., Jr., and Smith, L. H., 1970, "Interaction of Cooling Rates, Warming Rates and Protective Additives on the Survival of Frozen Mammalian Cells," in: *The Frozen Cell*, CIBA Symposium, G. E. W. Wolstenholm and M. O'Connor, eds., J. A. Churchill, London, pp. 69–85.

Motta, P., Muto, M., and Fugita, T., 1978, *The Liver: An Atlas of Scanning Electron Microscropy*, Igaku-Shoin, Tokyo.

Pegg, D. E. and Karrow, A. M., 1988, *The Biophysics of Organ Cryopreservation*, NATO ASI Series, No. 147, Plenum Press, New York.

Rubinsky, B., and Cravalho, E. G., 1979, "The Determination of the Thermal History in a One-Dimensional Freezing System by a Perturbation Method," ASME JOURNAL OF HEAT TRANSFER, Vol. 101, pp. 326–330.

Rubinsky, B., and Cravalho, E. G., 1984, "An Analytical Method to Evaluate Cooling Rates During Cryopreservation of Organs," *Cryobiology*, Vol. 21, pp. 303–320.

Rubinsky, B., 1986, "Cryosurgery, Imaging With Ultrasound," *Mechanical Engineering*, Vol. 108, pp. 48–52.

Rubinsky, B., Lee, C. Y., Bastacky, J., and Hayes, T. L., 1987, "The Mechanism of Freezing in Biological Tissue: The Liver," *Cryo-Letters*, Vol. 8, pp. 370–381.

Rubinsky, B., and Pegg, D. E., 1988, "A Mathematical Model for the Freezing Process in Biological Tissue," *Proceedings of the Royal Society B*, Vol. 234, pp. 343–358.

Turnbull, D. Y., 1989, "Under What Conditions Can a Glass be Formed?" *Contemp. Phys.*, Vol. 10, pp. 473–488.

Weast, R. C., ed., 1986, *CRC Handbook of Chemistry and Physics*, CRC Press, Boca Raton, FL.

M. S. Christenson

F. P. Incropera

Heat Transfer Laboratory,
School of Mechanical Engineering,
Purdue University,
West Lafayette, IN 47907

Experiments on Solidification of an Aqueous Sodium Carbonate Solution in a Horizontal Cylindrical Annulus

An experimental study of solidification has been performed for a binary Na_2CO_3–H_2O solution in a horizontal cylindrical annulus with varying initial concentration. Solutally driven flows and double-diffusive layering were found to influence solidification rates and macroscopic solute redistribution strongly.

Introduction

The important influence of natural convection flows on solidification processes involving both pure and multicomponent substances has been known for some time. In recent years experimental and theoretical treatments of the subject have been stimulated by engineering applications such as crystal growth (Ostrach, 1983), latent heat of fusion, thermal energy storage devices (Lane, 1983), and the casting of metals (Fisher, 1981).

The effect of natural convection on solidification in rectangular geometries has received most of the attention to date. Solidification of binary substances from above (Asai and Muchi, 1978), below (Webb and Viskanta, 1981), and the side (Szekely and Jassal, 1978; Christenson and Incropera, 1989) has been studied in detail. However, despite their importance, relatively little attention has been given to solidification in other geometries. Solidification around a cylinder or within a cylindrical annulus is of particular interest due to its application to phase change processes found in energy storage devices and casting processes.

Natural convection in single-phase systems contained within horizontal cylindrical annuli has been studied extensively, and the work of Kuehn and Goldstein (1976) provides a representative example of the available literature. Experimental and numerical results have been obtained for pure liquids and gases. Natural convection with phase change in a horizontal annulus has been studied by Herrmann et al. (1984) and White (1984), who experimentally considered the solidification of pure water around an isothermal cylinder. The studies revealed the important effects that the density inversion occurring at 4°C has on free convection in the liquid. Bathelt et al. (1979) considered solidification of a pure substance without a density inversion and obtained experimental and theoretical results for local heat transfer coefficents at the solid–liquid interface.

The present study has been motivated by the fact that, despite the importance of solidification in binary substances, the problem does not appear to have been previously considered for the horizontal annular geometry. Accordingly, the objective of this study has been to perform temperature and concentration measurements, as well as flow visualization, for solidification of the transparent Na_2CO_3–H_2O system in a cylindrical, horizontal, annular cavity. Solidification was induced at the center cylinder, while the outer cylinder and end walls were insulated. The results reveal many important features of the thermally and solutally driven flows, including the existence of double-diffusive convection during the solidification process.

Contributed by the Heat Transfer Division for publication in the JOURNAL OF HEAT TRANSFER. Manuscript received by the Heat Transfer Division May 9, 1988. Keywords: Mass Transfer, Materials Processing and Manufacturing Processes, Phase-Change Phenomena.

Experimental Procedures

A schematic of the test cell is shown in Fig. 1. The system consists of a central, cylindrical, copper heat exchanger from which solidification proceeds, a clear acrylic outer cylindrical shell, and clear, double-paned Lexan windows at both ends, which are sealed with silicone O-rings. The window provides visual access to the solidification process, and the double-pane construction significantly reduces heat gain from the ambient. The annular cavity dimensions were fixed at $r_o = 50.8$ mm, $r_i = 12.7$ mm, and $2L = 101.6$ mm, rendering end effects negligible.

To effect thermal control over the system, the central cylindrical heat exchanger was equipped with a single, four-pass channel through which a working fluid could circulate. Thermal conditions were set by a Neslab ULT-80DD constant temperature bath. While solidification was induced at the cold surface of the central cylinder ($r = r_i$), the outer surface ($r = r_o$) was insulated. The entire test cell was encased in 12.7-mm-thick foam insulation to minimize heat transfer from the ambient during experimentation.

Temperature distributions were obtained by means of four radial rakes, each of which was installed at the midplane of the test section ($z = 0$) and contained 12 copper-constantan thermocouple junctions. The rakes were positioned at circumferential locations corresponding to angles of $\theta = 0$, 45, 135, and 180 deg from the top of the cavity. The thermocouples were nonuniformly spaced along the rakes, with more junctions installed near the cold wall where large

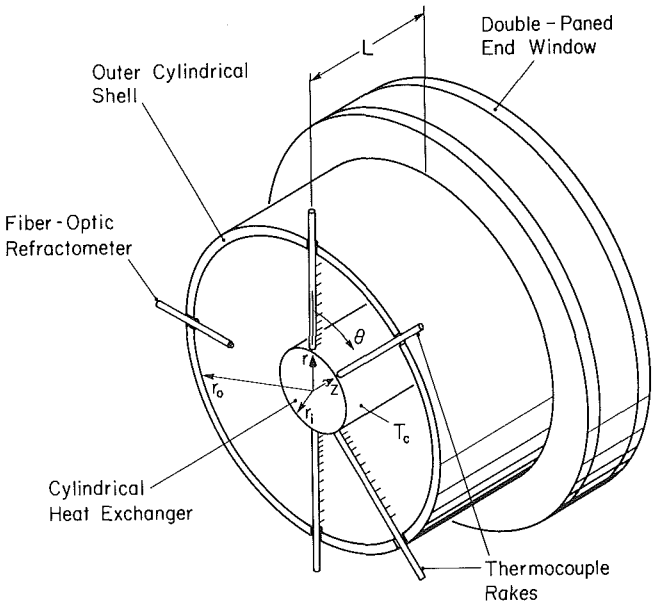

Fig. 1 *Schematic of test cell (sectioned at midplane)*

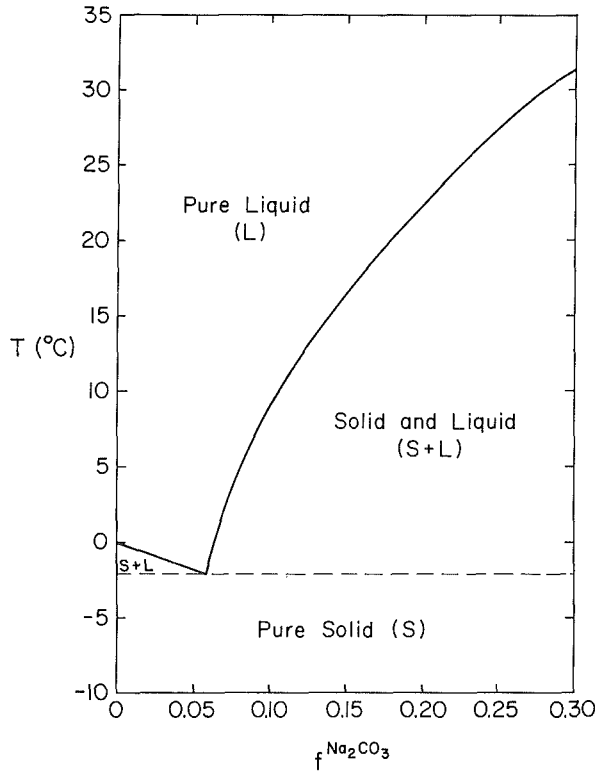

Fig. 2 Equilibrium phase diagram for Na_2CO_3-H_2O system (*International Critical Tables*, 1928)

temperature gradients were expected. As measured from the cold surface, rake thermocouple locations correspond to $(r-r_i)=1.6$, 3.2, 4.8, 6.4, 8.0, 9.5, 11.1, 12.7, 15.9, 19.1, 25.4, and 31.8 mm. Calibration of the thermocouples provided accuracy to within ± 0.05°C. The rakes were coated with an epoxy for protection from the Na_2CO_3-H_2O environment, and the time constant for an epoxy-coated thermocouple (70 ms) was much smaller than the time (~20 s) required for a 1°C temperature change within the system. Eight thermocouples installed in the cylindrical heat exchanger revealed temperature variations of less than ± 0.1°C.

The variation in concentration with time at a single location within the cavity was determined using a recently developed fiber-optic refractometer (Bergman et al., 1985). A 5-mW He-Ne laser beam was used as the input to the refractometer, and the output was detected with a photodiode. The electric current output of the photodiode was transformed to a voltage, which was measured using a digital voltmeter. Small random fluctuations inherent in the laser light source induced a measurement uncertainty of ± 2 mV. The probe was calibrated for the Na_2CO_3-H_2O system, and its sensitivity was determined to be 4.5 mV/percent change in concentration. Thus, in terms of the percent mass fraction of Na_2CO_3-H_2O in the solution, the accuracy of the device was ± 0.44 percent.

The uncladded portion of the refractometer (the probe tip) was placed at $r=40$ mm and $\theta=270$ deg. This choice was motivated by the expectation that the location would correspond to large changes in concentration and would be one of the last to solidify. Uncertainty in the placement of the probe was determined to be ± 1.0 mm in the r direction. The spatial resolution of the probe was approximately $0.5\times 0.5\times 1.0$ mm in the r, θ, and z directions, respectively.

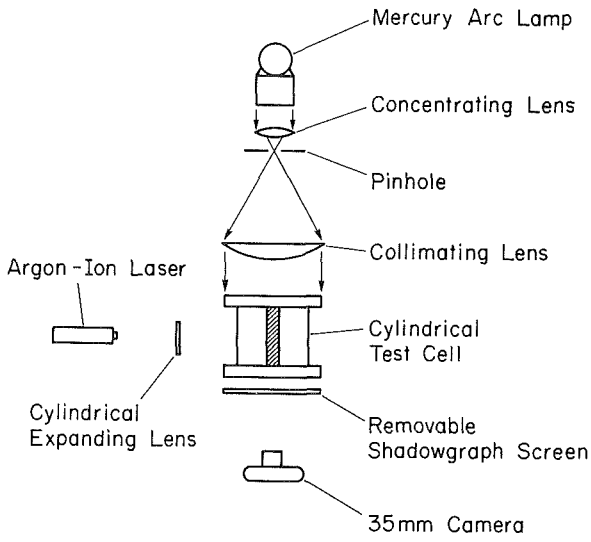

Fig. 3 Schematic (plan view) of test cell and flow visualization optics

The equilibrium phase diagram for aqueous sodium carbonate, which has a eutectic temperature and composition (Na_2CO_3 mass fraction) of $T_e=-2.1$°C and $f_e=0.059$, respectively, is shown in Fig. 2. This solution was selected for several reasons, including; (1) its transparency in the liquid phase, which facilitates flow visualization; (2) the availability of thermophysical property date (*International Critical Tables and Numerical Data*, 1928; *Thermophysical Properties Research Literature Retrieval Guide*, 1982), which facilitates simulation; and (3) the flexibility it provides for experimenting over a wide range of conditions corresponding to thermal and solutal buoyancy forces of varying magnitude and direction.

To begin an experiment, a solution of the desired composition was prepared by mixing the corresponding amounts of sodium carbonate and water. The solution was poured, while air was vented through the fill hole, and the system was allowed to equilibrate to room temperature ($T_o\approx 23$°C). At $t=0$, the cold wall was reduced to the desired temperature, while the outer wall was kept insulated. As solidification commenced, temperature and concentration data were read and stored by an HP3054A data acquisition system. Due to expansion of the solution during solidification, excess liquid was relieved through the fill hole of the cavity. At selected times during the process, the insulation was removed from the end windows and a photographic record was obtained. Two incandescent sources provided the necessary illumination from both the front and the back of the test cell. The experiment was terminated when complete solidification occurred.

Details of the flow occurring in the melt region were obtained by means of shadowgraphic and dye injection techniques (Fig. 3). Use of the shadowgraph allowed visualization of thermal and solutal flows and the tracking of interfaces associated with double-diffusive convection. In addition, solution of the original composition containing a fluorescent dye was injected with a hypodermic syringe, and illumination of the dye by a plane of light from a 40 mW argon-ion laser was

Nomenclature

f = mass fraction
L = cavity half-length
r, θ, z = cylindrical coordinates
t = time
T = temperature

Subscripts

c = cold boundary
e = eutectic
i = inner
liq = liquidus
o = outer, initial

Superscripts

α = constituent α (Na_2CO_3)

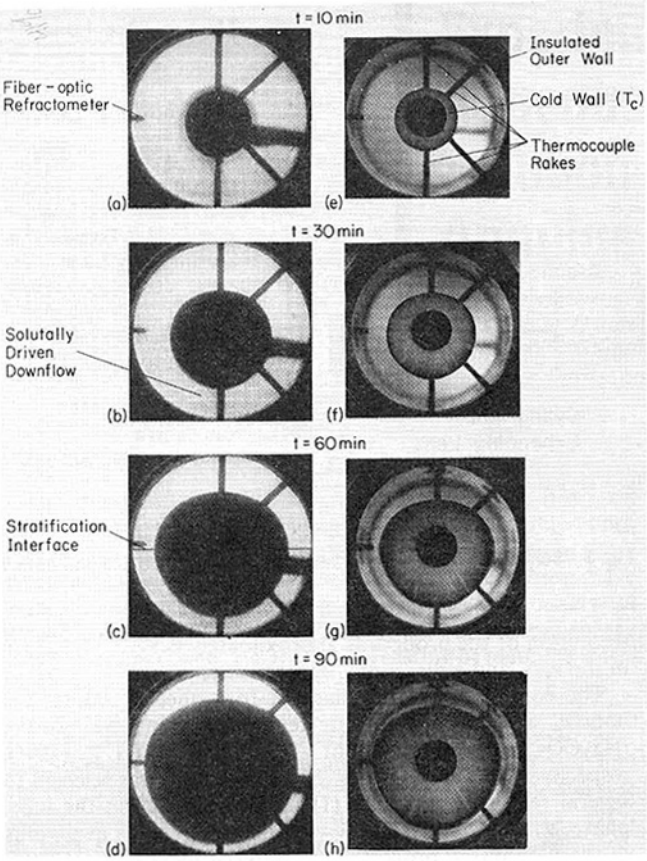

Fig. 4 Solidification morphology and flow patterns at selected times for $f_o^{\alpha} = 0.02$: shadowgraphs (*a*)-(*d*), photographs (*e*)-(*h*)

used to delineate double-diffusive convection effects and to provide information on detailed recirculation patterns.

Experimental Results

To study the effects of solution concentration on the solidification process, experiments were performed for initial Na_2CO_3 concentrations of $f_o^{\alpha} = 0.02$, 0.07, 0.10, and 0.17, thereby providing conditions both to the left and right of the eutectic point. For $f_o^{\alpha} < 0.059$, solidification is characterized by the preferential retention of water in the solid phase and by the rejection of water-deficient (Na_2CO_3-rich) interdendritic fluid from the mushy region. Hence, the thermal and solutal flows are mutually augmenting. For $f_o^{\alpha} > 0.059$, solidification is characterized by the rejection of water-rich fluid, which results in opposing thermal and solutal flows. The experiments were performed for a constant cold wall temperature ($T_c = -20°C$).

Although it is desirable to express results in terms of dimensionless parameters, this option is diminished by the existence of 13 parameters, the meaning and utility of which are clouded by the absence of true length, temperature, composition, and velocity scales (Bennon and Incropera, 1987). The existence of such scales is precluded by the irregular time-dependent geometry of the two-phase *mushy* and pure liquid regions.

The progression of solidification for $f_o^{\alpha} = 0.02$ is shown in Fig. 4, which presents both shadowgraphs and photographs. A shadowgraph, which is sensitive to changes in density gradient, is best suited for revealing features such as double-diffusive layering, while a photograph more clearly reveals phase change interfaces. The four thermocouple rakes, the fiber-optic refractometer, and the heat exchanger feed tubes are evident in the figure, as are the inner and outer walls of the annular cavity. The dark circular band appearing in some of the photographs is associated with the outer wall ($r = r_o$) at

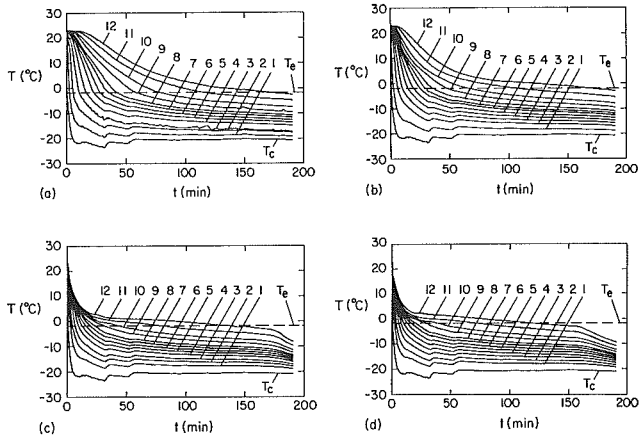

Fig. 5 Temperature histories at different r locations for $f_o^{\alpha} = 0.02$: (*a*) $\theta = 0$ deg, (*b*) $\theta = 45$ deg, (*c*) $\theta = 135$ deg, and (*d*) $\theta = 180$ deg

$z = L$. Temperature histories shown in Fig. 5 are numbered in sequence from the cold wall according to their respective r locations.

Although solidification is accompanied by mutually augmenting thermal and solutal flows in the melt, the simultaneous presence of these flows was not manifested until $t \approx 30$ min (Fig. 4(*b*)). Rather, the initial stages of solidification were marked solely by a strong thermal downflow along the phase front and an attendant thermal plume, which descended from the cylinder at $\theta = 180$ deg. The rapid cooling of the fluid below the cylinder (Figs. 5(*c*, *d*)) is indicative of the strength of the downflow, which induced counterrotating convection cells on both sides of the central cylinder. The convection cells extended to the top of the cylinder, where an interface formed due to thermal stratification in the melt. Two thermally driven, counterrotating convection cells also formed above this interface, as fluid ascended along the warm outer wall and descended due to cooling along $\theta = 0$ deg and the solidification front (Figs. 5(*a*, *b*)).

Due to the small difference in the liquidus and eutectic temperatures at this composition ($T_{liq} - T_e \approx 1°C$) and the initially large liquid superheat ($T_o - T_{liq} = 24°C$), the early stages of solidification ($t \lesssim 30$ min) corresponded approximately to solidification at the eutectic composition and the mushy region was extremely thin. This observation was supported by a nearly constant output of the refractometer. Thus, the rejection of water-deficient fluid and the attendant solutally driven flow were dominated by the strong thermal flow. Growth of the solid, which was initially uniform in the radial direction, became eccentric (Fig. 4(*e*)), as temperatures in the region of the melt below the cylinder decreased and thus became more conducive to solid formation (Figs. 5(*a*, *d*)).

As solidification progressed, the superheat of the melt decreased, reducing the strength of the thermal buoyancy forces and allowing solutal flows to become more pronounced (Fig. 4(*b*)). Water-deficient fluid was rejected from the growing mushy region, which appeared as a thin dark band at the solidification front in Fig. 4(*f*). With continued rejection of water-deficient fluid into the lower portion of the cavity, thermally and compositionally stratified conditions developed in the melt. A weak interface (indicating the existence of a weak vertical density variation) separated cool, water-deficient fluid in the lower region from warmer, fresher water in the upper unstratified region, and the interface ascended as solidification progressed. The interface was perceptible to the eye, but poor contrast precluded its appearance on the shadowgraphs. To note its location, the dark horizontal lines have therefore been added to Fig. 4(*c*). The effect of natural convection on the solidification process is clearly seen in Fig. 4(*g*) as a sharp change in liquidus front curvature at the stratification inter-

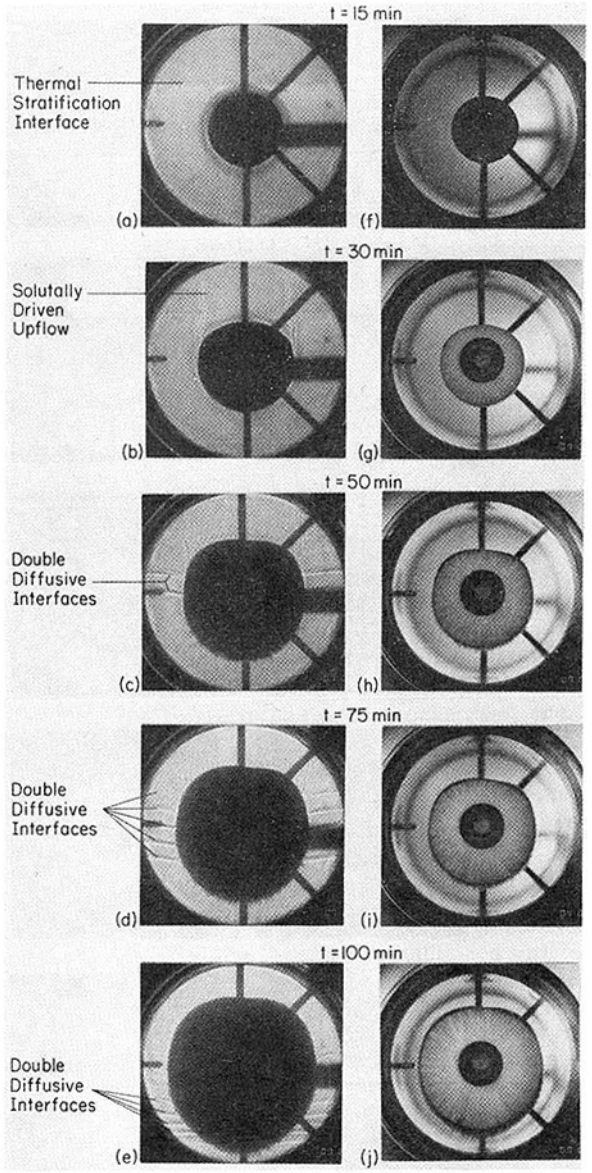

Fig. 6 Solidification morphology and flow patterns at selected times for $f_o^{\alpha} = 0.07$: shadowgraphs (a)-(d), photographs (e)-(h)

face. Solidification proceeded with nearly circumferential symmetry above the interface. Below the interface, however, solidification was retarded by the existence of a nearly eutectic composition in the melt and an attendant depression of the liquidus temperature. The growth rate increased and decreased in the upper and lower portions of the cavity, respectively, causing a slight reduction in the eccentricity of the solid. As solidification neared completion (Figs. 4(*d*, *h*)), water-deficient fluid continued to flow from the mush, but convection within the melt diminished and solidification became conduction dominated. Solidification was complete at $t \approx 200$ min.

For initial concentrations exceeding the eutectic, solutal and thermal flows are opposing.The progression of solidification for $f_o^{\alpha} = 0.07$ is shown in Fig. 6. Conditions are again thermally dominated at early times ($t \lesssim 20$ min), as evidenced by the highlighted thermal stratification interface at the top of the cylinder (Fig. 6(*a*)), the eccentricity of the solid phase (Fig. 6(*f*)), and the lack of a significant mushy region (Fig. 6(*f*)). Dominance of the thermal flow causes cool, water-rich fluid that is rejected during solidification to descend to the bottom of the cavity. Thus temperatures at $\theta = 135$ and 180 deg quickly approached the eutectic temperature, while those at $\theta = 0$ and 45 deg remained at much higher values (Fig. 7). The temperature histories again suggest the presence of thermally driven, counterrotating convection cells above and below the plane of stratification.

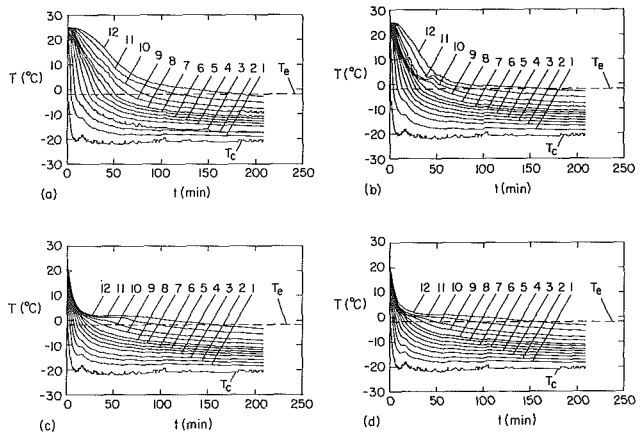

Fig. 7 Temperature histories at different r locations for $f_o^{\alpha} = 0.07$: (*a*) $\theta = 0$ deg, (*b*) $\theta = 45$ deg, (*c*) $\theta = 135$ deg, and (*d*) $\theta = 180$ deg

With increasing time, as the melt superheat is gradually reduced and thermal buoyancy forces weaken (Fig. 7), solutally induced flows become obvious as water-rich interdendritic fluid streams from the mush to the top of the cavity (Fig. 6(*b*)). Although fluid rejection occurred along the entire top surface of the solidification front, it was more concentrated at the sides of the solid mass due to the contribution of fluid ascending from lower regions of the solid. Thermally stratified conditions persisted outside of the central solutal flow zone. Growth of the mushy region was manifested at the bottom of the solidification front by the appearance of small, whiskerlike protrusions (Fig. 6(*g*)), while at the top, the phase interface flattened with time. Both of these effects were due to the accumulation of water-rich fluid of near eutectic composition in the upper portion of the cavity. In particular, solidification was enhanced at the bottom and retarded at the top of the cylinder due to changes in the liquidus temperature of the respective local liquid environments.

Conditions in the melt became double-diffusive as cold, water-rich fluid continued to ascend from the mush and several interfaces formed (Fig. 6(*c*)). The double-diffusive interfaces, which have not been highlighted, separated convection regions marked by distinct density differences, which were due to differences in temperature and composition within the melt. Globally, however, temperatures in upper regions of the melt (Figs. 7(*a*, *b*)) remained higher than those in lower regions (Figs. 7(*c*, *d*)). In fact, despite the flow of cool, water-rich fluid to the top of the cavity for $t \gtrsim 20$ min, stable thermal conditions persisted until $t \approx 100$ min. Thus, overall, a thermally and solutally stable condition (warm, water-rich fluid over cool, water-deficient fluid) persisted in the melt for much of the solidification process.

Neilson and Incropera (1987) provide detailed descriptions of the formation of double-diffusive interfaces for thermal destabilization of a salt-stratified solution by a cylindrical heat source. Although conditions differed from those of this study, physical mechanisms leading to double-diffusive layering are believed to be equivalent. Since the thermal diffusivity greatly exceeds the mass diffusivity, a small parcel of fluid exchanges heat much more efficiently than species with its local environment. Thus as cold, water-rich fluid rises from the mush, it retains its characteristic composition but equilibrates to the temperature of the local environment. Hence, as the solutal flows begin, the rejected fluid is heated rapidly by the warm environment above the cylinder, yet retains its slightly water-rich (Na_2CO_3-deficient) composition. With increasing time,

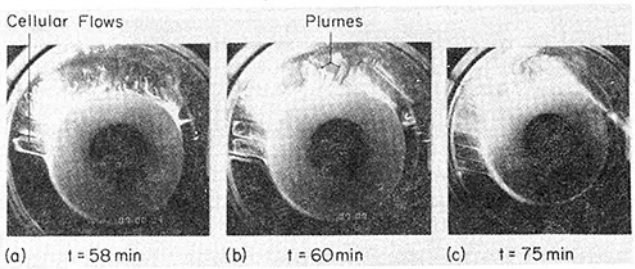

Fig. 8 Dye injection flow patterns at selected times for $f_o^\alpha = 0.07$

fluid of progressively smaller Na_2CO_3 composition is rejected and flows to the top of the cavity, displacing fluid of larger composition downward and outward. As indicated by the temperature histories 9–11 of Fig. 7(*b*), this relatively warm, water-deficient fluid collects at $\theta \approx 45$ deg, causing a slight increase in temperature at $t \approx 40$ min and the onset of double-diffusive layering. As solidification continues, cooler fluid of smaller Na_2CO_3 composition is displaced to the sides of the cavity, inducing the formation of double-diffusive interfaces and distinct convection layers.

Characteristics of flow within the convection layers were revealed by injecting fluorescent dye along the solidification front. As shown in Fig. 8, convection cells between double-diffusive interfaces were well formed, and each was characterized by a thermally induced, clockwise recirculation. Fluid within each cell was warmed as it flowed along the bottom interface toward the outer wall and cooled as it returned along the top interface. Hence, the layers were inclined slightly upward toward the outer wall. Rejection of water-rich fluid in the form of mushroom-capped plumes is also evident in Fig. 8(*a*, *b*).

Water enrichment of the melt continued to hinder growth of the solid at the top of the cylinder, as flattening of the interface became more pronounced (Fig. 6(*h*)), and by $t = 75$ min (Fig. 6(*d*)), five double-diffusive interfaces had formed. The structure of the convection layers is shown by the dye patterns of Fig. 8(*c*).

Interfaces continued to form and progress downward as the phase transformation neared completion (Fig. 6(*e*)). The interfaces became less well defined, as conditions in the melt approached those of the rejected fluid. The mushy region propagated further into the bottom of the cavity than at any other location (Fig. 6(*j*)). However, the eccentricity and the flatness at the top of the solid both diminished, indicating an increase in the growth rate at the top of the cavity. Temperatures at $\theta = 0$ and 45 deg were sufficiently reduced to enhance the growth of solid in this region (Figs. 7(*a*, *b*)).

For $t \gtrsim 100$ min, solid growth occurred at approximately the same rate around the circumference of the cylinder. The double-diffusive interfaces gradually eroded, as differences in temperature and composition between layers became insignificant due to heat and species diffusion across the interfaces. Fluid motion decreased, and complete solidification occurred at $t \approx 225$ min.

With increase of the initial solution concentration to $f_o^\alpha = 0.10$, magnitudes of the thermal and solutal buoyancy forces became approximately equal. The two flows again opposed one another, but by decreasing the initial superheat and increasing the difference in concentration between the original fluid and the rejected fluid, the solutal flow became prominent earlier in the process (Fig. 9).

In this case, solutally induced upflow was evident by $t \approx 5$ min (Fig. 9(*a*)). However, at this time both thermal and solutal buoyancy were significant, and as some of the solutal plumes rose from the mushy region, they were swept downward along the phase change interface by the thermally induced flow. Eventually, however, the thermal flow weakened so that all of the solutal plumes escaped to the top of the cavity. The flow of

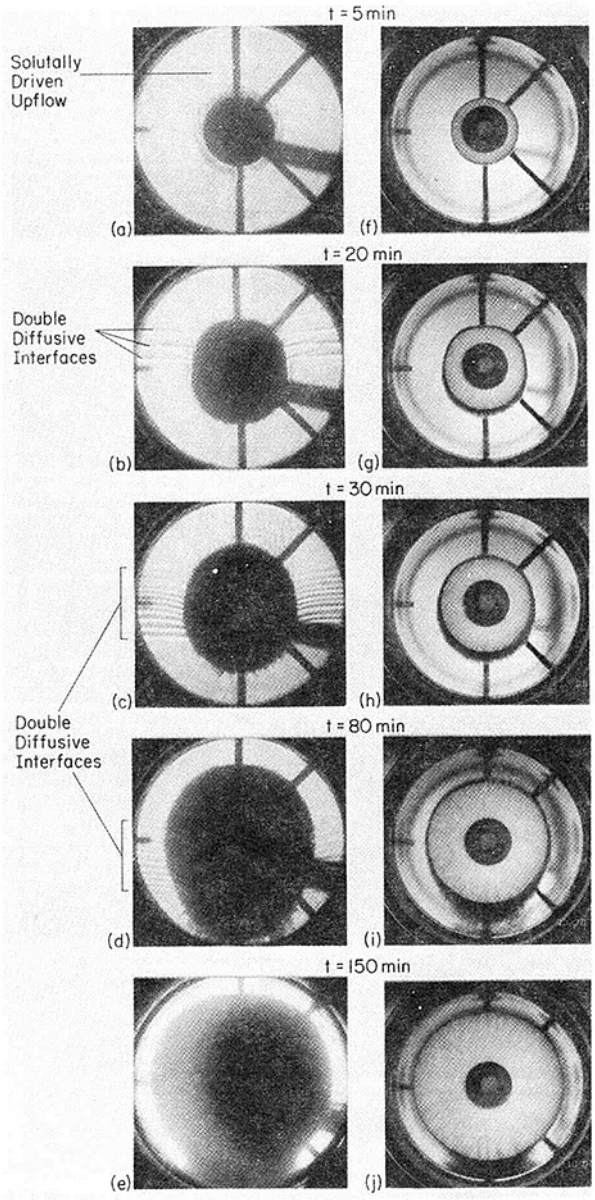

Fig. 9 Solidification morphology and flow patterns at selected times for $f_o^\alpha = 0.10$: shadowgraphs (*a*)-(*d*), photographs (*e*)-(*h*)

cold, but water-rich, interdendritic fluid to the bottom of the cavity was therefore discontinued much sooner than for the previous experiment and the attendant reduction in temperatures at $\theta = 135$ and 180 deg was smaller. The prominence of the solutal flow and the appearance of several double-diffusive interfaces became evident by $t = 20$ min (Fig. 9(*b*)). As suggested by temperature histories 6–9 of Fig. 10(*b*), progressively cooler fluid of reduced Na_2CO_3 composition was discharged into the top of the cavity and warmer fluid of larger composition was displaced to the sides of the cavity, producing double-diffusive layering. Again conditions were locally double-diffusive, while, overall, thermally and solutally stable conditions existed in the melt for $t \lesssim 25$ min (Fig. 10). Differences in the growth of solid and mush between the upper and lower regions of the cylinder were again observed (Fig. 9(*g*)), but the eccentricity and the flatness of the solidified material were not as great as for the previous experiment. These results confirm the prior conclusion that such effects are primarily due to thermally driven flows, which were more intense and existed for a longer period of time for $f_o^\alpha = 0.07$. Due to the larger difference between the liquidus and eutectic

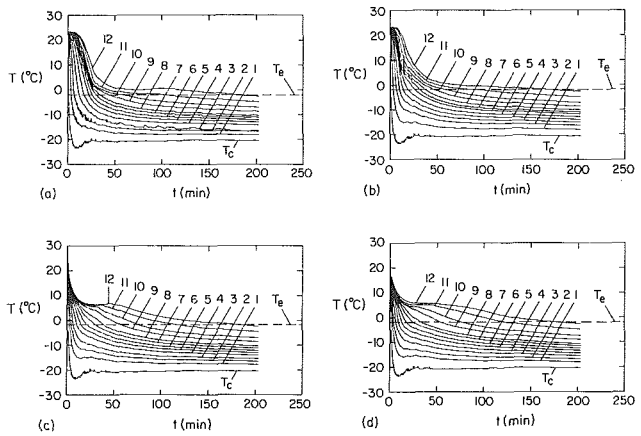

Fig. 10 Temperature histories at different r locations for $f_o^\alpha = 0.10$: (*a*) $\theta = 0$ deg, (*b*) $\theta = 45$ deg, (*c*) $\theta = 135$ deg, and (*d*) $\theta = 180$ deg

temperatures, the thickness of the mushy region increased with increasing concentration.

By $t = 30$ min (Fig. 9(*c*)), a large number of very thin convection layers had formed at both sides of the cylinder due to the continued rejection of cool, water-rich fluid. Conditions in the melt became globally double-diffusive, as temperatures in the upper half of the cavity became lower than those in the lower half (Fig. 10). This transition caused a convergence of double-diffusive interfaces in the central region of the cavity and the establishment of large convection zones at the top and bottom. The measured concentration of Na_2CO_3 gradually decreased by approximately 0.02 as the interfaces propagated downward from $t = 20$ to 50 min.

For $t \gtrsim 80$ min (Figs. 9(*d*, *e*, *i*, *j*)), conditions in the melt were similar to those for the latter stages of the previous experiment. The double-diffusive interfaces gradually weakened and eventually disappeared, as the layers equilibrated with respect to density due to diffusion across the interfaces. The solidified material was nearly concentric with the central heat exchanger, and except at $\theta \approx 180$ deg, where its thickness reached approximately 12 mm, the mushy region was extremely thin. Enhanced mushy region development in the lower portion of the cavity is attributed to the fact that the fluid remained at nearly the original composition. Solidification proceeded uniformly over the circumference for $t \gtrsim 150$ min, and the solution was completely solidified by $t \approx 225$ min. The overall change in the measured concentration was slightly less than 0.04, indicating that the melt was at approximately the eutectic composition when the solidification process was completed.

As the initial solution concentration is moved farther from the eutectic, solutal buoyancy forces exert a greater influence on the solidification process. With $f_o^\alpha = 0.17$, solutal forces dominated thermal convective transport from the outset. As early as 45 s, solutal plumes began rising to the top of the cavity, unimpeded by the thermal flow. The solutal upflow was clearly well established by $t = 2$ min (Fig. 11(*a*)), and a discernible mushy region had formed (Fig. 11(*f*)). The flow of cold, water-rich, interdendritic fluid to the lower regions of the cavity was weak so that temperatures at $\theta = 135$ and 180 deg (Figs. 12(*c*, *d*)) remained near the initial value, while those at $\theta = 0$ and 45 deg (Figs. 12(*a*, *b*)) decreased rapidly. The thermal downflow below the cylinder, as well as the structure of the solutal plumes above the cylinder, are clearly seen in Fig. 13(*a*), where fluorescent dye was injected along the solidification front. The solid mass grew concentrically with respect to the central cylinder, indicating absence of a strong thermal influence on the growth.

By $t = 8$ min (Fig. 11(*b*)), a single double-diffusive interface had formed. The interface separated two large convection zones in the upper and lower halves of the cavity. Global con-

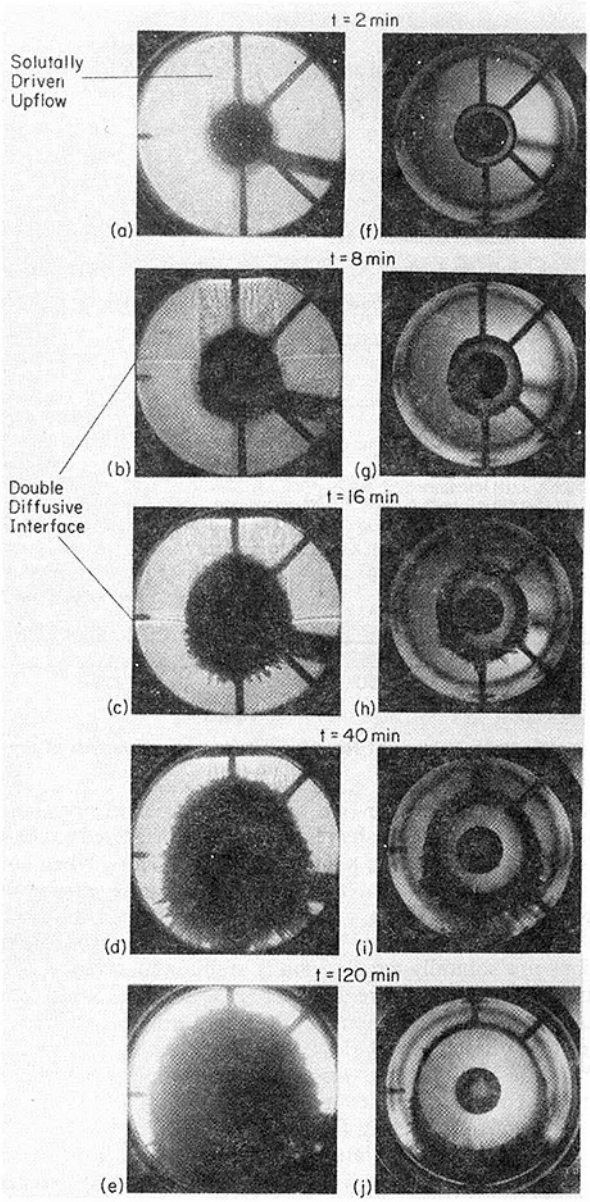

Fig. 11 Solidification morphology and flow patterns at selected times for $f_o^\alpha = 0.17$: shadowgraphs (a)-(*d*), photographs (*e*)-(*h*)

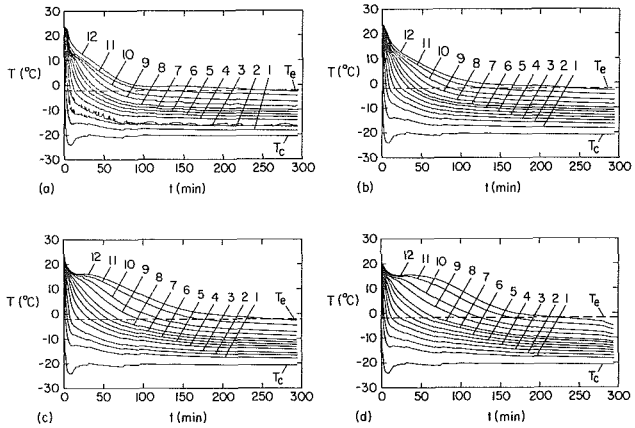

Fig. 12 Temperature histories at different r locations for $f_o^\alpha = 0.17$: (a) $\theta = 0$ deg, (*b*) $\theta = 45$ deg, (*c*) $\theta = 135$ deg, and (*d*) $\theta = 180$ deg

ditions in the melt immediately became double-diffusive as temperatures in the upper portion of the cavity decreased rapidly to values below those recorded in the lower portion

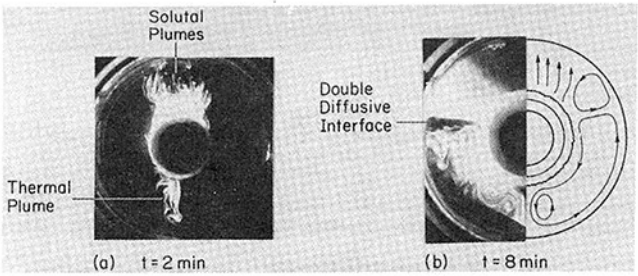

Fig. 13 Dye injection flow patterns at selected times for $f_o^{\alpha} = 0.17$

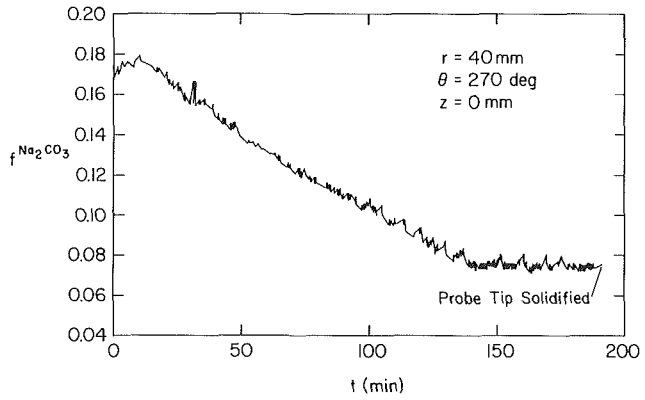

Fig. 14 Mass fraction of Na_2CO_3 solution as a function of time for $f_o^{\alpha} = 0.17$

(Fig. 12). Cool, water-rich, interdentritic fluid continuously ascended from the mushy region and was displaced to the sides of the cavity, forming a single interface. Thus, when solutal flows are dominant ($f_o^{\alpha} = 0.17$), conditions are globally double-diffusive and a single interface is formed. In contrast, when solutal and thermal flows are comparable, global conditions are solutally and thermally stable and many interfaces are produced. Apparently, for $f_o^{\alpha} = 0.17$, vigorous mixing associated with the unstable thermal conditions yielded large regions of well-mixed flow and thus a single interface. For $f_o^{\alpha} = 0.07$, such mixing was inhibited by the overall thermally stable conditions, allowing the formation of many small regions of recirculating flow.

Flow patterns associated with the two convection zones are shown schematically in Fig. 13(*b*). Flow in the bottom region consisted of a small cell at $\theta = 170$ deg contained within a larger thermally driven cell encompassing the entire bottom region. This flow was driven by the temperature difference between the liquidus interface and the outer wall. Flow in the top region consisted of thermally driven cells on both sides of a solutally driven upflow. In this case, the driving force for the cellular flow was the temperature difference between the cold ascending fluid and the warm outer wall.

The solid region continued to grow concentrically, while the mushy region extended slightly further in the radial direction at $\theta = 0$ and 180 deg (Fig. 11(*g*)). At $\theta = 180$ deg, the melt composition remained at the initial value, while at $\theta = 0$ deg, temperatures were low (Fig. 12(*a*)). Hence, the growth of mush was enhanced at both locations.

With increasing time the interface descended, as water-rich fluid continued to pour into the melt, and the circumferentially nonuniform growth of the mush became more pronounced (Figs. 11(*c*, *h*)). The measured concentration at $\theta = 270$ deg began to decrease gradually as the double-diffusive interface progressed downward past the tip of the refractometer (Fig. 14). Temperatures within the melt were much colder at $\theta = 0$ deg than at $\theta = 180$ deg (Figs. 12(*a*, *d*)). Also, temperatues at $\theta = 135$ and 180 deg were much warmer for this case than at corresponding times for $f_o^{\alpha} = 0.07$ and 0.10. This result confirms the dominance of the solutal flow, as cold fluid that had previously descended to the bottom of the cavity was now advected to the upper region by the strong solutal flow.

As solidification progressed, the double-diffusive interface was completely eroded, yielding single recirculation zones on both sides of the vertical midplane (Fig. 11(*d*)). Growth of mush at the bottom of the cylinder was marked by long protruding crystals, and the mushy region thickened at all circumferential locations (Fig. 11(*i*)). Several weak double-diffusive interfaces formed late in the process (Fig. 11(*e*)), and by $t = 120$ min (Fig. 11(*j*)), growth of the mushy region was retarded from $\theta = -90$ to $+90$ deg. In contrast, the mushy region extended to the outer wall at $\theta = 180$ deg. The concentration of the melt continued to decrease, and the overall change in concentration was approximately 0.11 (Fig. 14), indicating that the melt composition was nearly eutectic during the latter stages of solidification. Fluid motion diminished and conduction became the dominant mode of heat transfer throughout the system. The solution solidified completely at $t \approx 325$ min.

Summary

An experimental study of solidification for a binary mixture in an annular cavity has been conducted using aqueous sodium carbonate as the phase change material. By varying the initial solution concentration, the effects of thermal and solutal buoyancy driven flows on the solidification process were examined.

Initial Na_2CO_3 concentrations that were less than the eutectic produced solutal flows that aid thermally driven downflow along the liquidus interface. In contrast, concentrations greater than the eutectic produce an ascending solutal flow that opposes the thermal flow. In the opposing case, solute-deficient fluid is ejected from the mushy region and rises to create conditions conducive to double-diffusive convection at the top and sides of the cavity. In both cases, solute redistribution occurs as a result of the solutal flow, and the establishment of localized liquid regions of near-eutectic composition retards the solidification process.

The relative strengths of ascending solutal and counter-rotating thermal flows determine the extent of double-diffusive effects and solute redistribution. By increasing the initial solution concentration, solutal flow exert an increasingly more important effect on the solidification process. Solidification rates increase and the growth of the mushy region is much more pronounced. The liquidus interface appears smooth and regular for initial concentrations less than the eutectic, but irregular for concentrations greater than the eutectic.

Variation in the solidification rate around the circumference of the cylinder is the most tangible evidence of the influence of the solutal flows. Growth rates are retarded in regions of the melt characterized by near-eutectic composition and are enhanced at locations where the melt remains at nearly the original composition. The dominance of thermal flows in the initial stages of solidification for less concentrated solutions leads to an eccentric growth of the solid with respect to the central cylinder.

Melt conditions are double-diffusive when the initial Na_2CO_3 concentration exceeds the eutectic concentration. For concentrations that exceed the eutectic by small to moderate amounts, overall melt conditions remain stable, while numerous double-diffusive interfaces are formed. However, for larger initial concentrations, conditions become double-diffusive on a global basis and are characterized by a single interface.

The results of this study reveal the important effect of initial composition on the rate of solidification and liquidus front morphology, as well as on the extent of double-diffusive layering and solute redistribution, in a binary substance.

Acknowledgments

Support of this work by the U.S. Department of Energy under Award Number DE-FG02-87ER13759 is gratefully acknowledged.

References

Asai, S., and Muchi, I., 1978, "Theoretical Analysis and Model Experiments on the Formation Mechanism of Channel-Type Segregation," *Transactions ISIJ*, Vol. 18, pp. 90–98.

Bathelt, A. G., Van Buren, P. D., and Viskanta, R., 1979, "Heat Transfer During Solidification Around a Cooled Horizontal Cylinder," *AIChE Symposium Series*, Vol. 75, pp. 103–111.

Bennon, W. D., and Incropera, F. P., 1987, "A Continuum Model for Momentum, Heat and Species Transport in Binary, Solid-Liquid Phase Change Systems—II. Application to Solidification in a Rectangular Cavity," *International Journal of Heat and Mass Transfer*, Vol. 30, pp. 2171–2187.

Bergman, T. L., Incropera, F. P., and Stevenson, W. H., 1985, "Miniature Fiber-Optic Refractometer for Measurement of Salinity in Double-Diffusive Thermohaline Systems," *Review Scientific Instrumentation*, Vol. 56, pp. 291–296.

Christenson, M. S., and Incropera, F. P., 1989, "Solidification of an Aqueous Ammonium Chloride Solution in a Rectangular Cavity—I. Experimental Results," *International Journal of Heat and Mass Transfer*, Vol. 32, pp. 47–68.

Fisher, K. M., 1981, "The Effects of Fluid Flow on the Solidification of Industrial Castings and Ingots," *Physico Chemical Hydrodynamics*, Vol. 2, pp. 311–326.

Herrmann, J., Leidenfrost, W., and Viskanta, R., 1984, "Effect of Natural Convection on Freezing of Water Around an Isothermal, Horizontal Cylinder," *International Communications Heat Mass Transfer*, Vol. 11, pp. 301–310.

International Critical Tables and Numerical Data, 1928, *Physics, Chemistry and Technology*.

Kuehn, T. H., and Goldstein, R. J., 1976, "An Experimental and Theoretical Study of Natural Convection in the Annulus Between Horizontal Concentric Cylinders," *Journal of Fluid Mechanics*, Vol. 74, pp. 695–719.

Lane, G. A., 1983, *Solar Heat Storage: Latent Heat Material*, Vol. I, CRC Press, Boca Raton, FL.

Neilson, D. G., and Incropera, F. P., 1987, "Double-Diffusive Flow and Heat Transfer for a Cylindrical Source Submerged in a Salt-Stratified Solution," *International Journal Heat Mass Transfer*, Vol. 30, pp. 2559–2570.

Ostrach, S., 1983, "Fluid Mechanics in Crystal Growth—The 1982 Freeman Scholar Lecture," *Journal of Fluids Engineering*, Vol. 105, pp. 5–20.

Szekely, J., and Jassal, A. S., 1978, "An Experimental and Analytical Study of the Solidification of a Binary Dendritic System," *Metallurgical Transactions B*, Vol. 9B, pp. 389–398.

Thermophysical Properties Research Literature Guide, 1982, IFI/Plenum Data Series.

Webb, B. W., and Viskanta, R., 1986, "An Experimental and Analytical Study of Solidification of a Binary Mixture," *Proceedings of the 8th International Heat Transfer Conference*, Vol. 4, pp. 545–556.

White, D. A., 1984, "Melting of Ice and Freezing of Water Around a Horizontal, Isothermal Cylinder," M.S.M.E. Thesis, Purdue University, West Lafayette, IN.

Analysis of Volumetric Absorption of Solar Energy and Its Interaction With Convection

S. T. Thynell
Assistant Professor.
Mem. ASME

C. L. Merkle
Professor.
Mem. ASME

Department of Mechanical Engineering,
The Pennsylvania State University,
University Park, PA 16802

A theoretical analysis of the interaction of volumetric absorption of concentrated solar radiation and convection in a two-dimensional, axisymmetric absorption chamber is presented. Previous analytical works on the absorption of the radiant energy in such chambers have employed one-dimensional models to show that very high temperatures and therefore high thermodynamic efficiencies are achievable. In this work, the effects of using collimated as opposed to isotropic irradiation on the absorption efficiency are investigated for the one-dimensional case, and the effects of employing a more realistic two-dimensional model on the absorption efficiency are studied. The model is based on the assumptions that the velocity profile is uniform and that conduction within the fluid is negligible compared to convective and radiative transports of energy. Several parameter surveys are performed and compared with the results of previous one-dimensional models.

1 Introduction

The development of efficient methods for converting the sun's abundant radiant energy into electricity has received a considerable amount of attention. The research efforts related to space applications (Gilbreath and Billman, 1978), have yielded numerous new concepts, improved methods and more efficient devices for utilizing the sun's energy. Examples of such concepts and devices include, among others, photovoltaic devices, photochemical cells, photoemissive converters, thermionics, and heat engines.

Belonging to the class of heat engines, the solar thermal engine was conceived by Hertzberg et al. (1971) and subsequently improved (Hertzberg and Lau, 1978). The improved design concept has high achievable thermodynamic efficiencies despite the high rejection temperatures. The possibility of high rejection temperatures is important for space power reactors, whose size is often governed by the size of the radiator. In addition, the use of solar energy for propulsion purposes, in which the radiative energy is absorbed in a manner similar to that in the solar engine, has been proposed and conceptually evaluated (Shoji, 1984).

The previous theoretical analyses related to the solar thermal engine (Mattick et al., 1979; Mattick, 1980) have been focused on determining the absorption efficiency by using one-dimensional models. Although the considered working fluids in these models have been molecular gases, of which almost all are poor absorbers of radiant energy at low temperatures, it has been proposed that alkali vapors could be used to produce stable high-temperature plasmas (Mattick, 1978). The results of these studies have indicated that temperatures up to ~ 4000 K are achievable, thus leading to extremely high conversion efficiencies. Another conceivable approach for achieving efficient absorption in a transparent gas is to seed it with small particles (Hull and Hunt, 1984; Wang and Yuen, 1986). The maximum conversion efficiency for a power plant utilizing the solar thermal engine is estimated at ~ 75 percent for terrestrial applications and ~ 50 percent in space applications, which prohibit low rejection (outlet) temperatures (Hertzberg and Lau, 1978). Hence, the solar engine is attractive for energy conversion in both space-based and terrestrial power plants. In view of the predicted high conversion efficiencies of the present one-dimensional models, it is of particular interest to analyze the two-dimensional effects of a converging beam in the absorption chamber, which is a means for generating even higher temperatures of the working fluid.

The objectives of the study are to determine the volumetric efficiency of the absorption and the achievable exit temperatures of the working fluid for various optical dimensions, working fluid flow rates, radiative surface properties, and amount of beam focusing, and to compare these results based on a more realistic geometry with those considering a one-dimensional model. The outline of the study is as follows. In Section 2, models of the absorption chamber and beam convergence are illustrated. In Section 3, the equations governing conservation of energy and radiation heat transfer are presented. Finally, in Section 4, numerical results are presented for various representative situations, and comparisons to the one-dimensional formulation are discussed.

2 Description of Model

2.1 Model of Absorption Chamber. A model of the absorption chamber is shown in Fig. 1. The working fluid enters the cylindrical absorption chamber at the upstream position $x = 0$ having a one-dimensional velocity profile and a uniform temperature. The radiant energy is focused by means of either the lens located at the position ($x = 0$) or by an externally constructed system utilized for collecting the sun's energy. The working fluid absorbs the radiant energy during its flow toward the downstream exit ($x = L$), where the fluid is used in an appropriate thermodynamic cycle. The chamber walls are maintained externally at prescribed temperatures and their radiative properties are given.

2.2 Model of Collimated Beam. Due to constraints invoked by considerations of the second law of thermodynamics, tracking errors, effects of diffractions, and aberrations on the beam, there is a considerable spread of the rays near the focal point (Kreith and Kreider, 1978). It appears that simple analyses of the effects of tracking errors, diffraction, and aberration of such attenuating and converging beam are not available in the literature. However, to account for such effects in a very simplistic manner, the model shown in Fig. 2 is considered in the present analysis. As shown in this figure, the rays travel in straight paths toward the focal point, and the convergence of

Contributed by the Heat Transfer Division and presented at the National Heat Transfer Conference, Houston, Texas, July 24-27, 1988. Manuscript received by the Heat Transfer Division April 20, 1988. Keywords: Forced Convection, Radiation Interactions, Solar Energy.

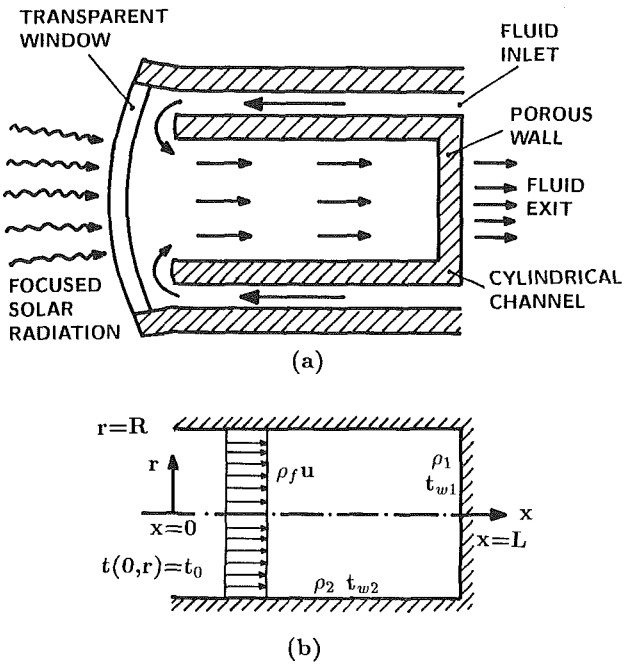

Fig. 1 *(a)* **Cross section of absorption chamber, and** *(b)* **physical model in two-dimensional cylindrical geometry and boundary conditions**

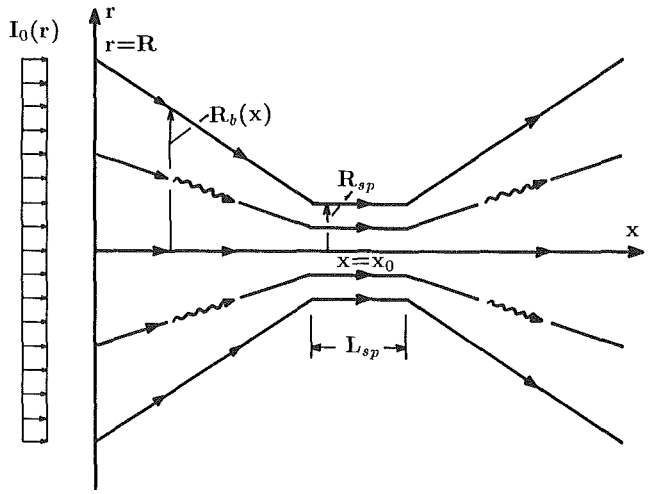

Fig.2 Model of converging focused beam. The location of the focal point is at $x = x_0$, the length of the spot is indicated by L_{sp}, and the radius of the spot is R_{sp}. The focal point may be located within the chamber or beyond the chamber backwall at $x = L$.

the rays follows the inverse square law. As the rays approach the focal point, however, they diverge abruptly into parallel rays. Immediately after the focal point, the rays diverge further according to the same inverse square law as before the focal point, i.e., the collimated beam is assumed symmetric. It should be noted that it is not necessary that the beam be symmetric with respect to a plane normal to the x axis located at the focal point, as several studies have indicated for laser beams propagating in nonabsorbing media (Holmes et al., 1972; Mahajan, 1983), but such an assumption is used in the present analysis.

3 Analysis

3.1 Assumptions. To develop a mathematical model for the interaction problem described previously, the following additional simplifying assumptions are introduced:

1 A steady state exists, and the medium is in local thermodynamic equilibrium (LTE).

2 Transport of energy takes place by convection and radiation only. Since the desired temperatures of the flowing gas are high, the mode of energy transfer by conduction is much less significant than that of radiation and convection.

3 The radial velocity component is negligible, and the axial velocity component is uniform.

4 All quantities remain invariant under translation around the x axis, i.e., the problem involves two-dimensional cylindrical geometry.

5 The specific heat c_p and absorption coefficient κ are independent of position. This assumption implies that the thermodynamic and radiative properties are temperature independent.

6 The scattering effects by the medium are negligible.This is a very good approximation for small particles ($\pi D_p/\lambda < 1$), which are considered in the present work as the absorption mechanism of the radiant energy. By using 0.1-μm-size carbon particles, which have been employed in experiments (Hunt and Hull, 1984), and by considering a characteristic wavelength of 0.707 μm, it is easily shown using the Mie theory (Özişik, 1973) that the single scattering albedo is about 0.05.

7 The absorption coefficient κ is independent of wavelength. Although the absorption coefficient for small particles is approximately inversely proportional to wavelength (Siegel and Howell, 1981), it is treated as gray.

Nomenclature

Bo = Boltzmann number, equation (3*a*)
c_p = specific heat
D_p = diameter of particles
$G(x, r)$ = incident radiation
$H_d(x, r)$ = defined by equation (A1)
$H_r(x, r)$ = defined by equations (A7), (A11), and (A15)
I_b = blackbody emission
I_{ref} = reference flux of collimated beam
$I(x, r, \theta, \phi)$ = radiation intensity
$I_0(r, \theta, \phi)$ = external irradiation from the sun at $x = 0$
L = axial optical depth
L_{sp} = $x_{usp} - x_{lsp}$ = axial optical length of spot (Fig. 2)
$q_r(x, r)$ = net radiant heat flux in radial direction
Q = dimensionless radiant heat loss along wall at $r = R$
r = optical radial coordinate
r_{wd} = specifies a radial location at $x = 0$ of the direct component of the incident beam, equation (A5)
r_{wr} = specifies a radial location at $x = 0$ of the reflected component of the incident beam, equations (A10), (A14), and (A18)
R = optical radius
$R_b(x)$ = optical radius of beam inside chamber, equation (A2)
R_{sp} = optical radius of spot (Fig. 2)
t = dimensionless fluid temperature, equation (3*b*)
t_0 = dimensionless fluid temperature at $x = 0$
t_{w1} = prescribed wall temperature at $x = L$
t_{w2} = prescribed wall temperature at $r = R$
T = fluid temperature
T_0 = fluid temperature at $x = 0$

8 The upstream boundary surface at $x = 0$ (the lens material) is completely transparent to radiation incident from within the medium.

9 The opaque bounding surfaces at $r = R$ and at $x = L$ are diffusely emitting and specularly reflecting. Unless the optical distances are quite large, so that most of the energy is absorbed before the beam reaches the back wall, the heat engine will not be effective. If this is true, the radiation intensity will become relatively weak near the bounding walls in the interior portion of the chamber, and consequently, treatment of the surface reflection as either diffuse or specular should yield nearly the same results.

10 Since the bounding surfaces at $x = L$ and $r = R$ are assumed opaque diffuse and gray, Kirchhoff's law is applicable.

11 The refractive index of the medium is unity, which for most gases is a very good approximation.

3.2 Energy Equation. Since steady-state conditions prevail and no radial velocity components exist, the use of the continuity equation yields the simple result that $\rho_f u = \text{const}$. Thus, the energy equation governing the temperature of the medium is decoupled from the momentum equations, and, in dimensionless form, it is given by (Özişik, 1973)

$$\text{Bo}\,\frac{\partial t(x, r)}{\partial x} = -4t^4(x, r) + \bar{G}(x, r), \qquad 0<x<L, \quad 0\le r<R \tag{1}$$

where the independent optical variables (x, r) are related to the physical variables by $x = \kappa x_p$ and $r = \kappa r_p$. Equation (1) is subject to the upstream boundary condition

$$t(0, r) = t_0, \qquad x=0, \quad 0\le r<R \tag{2}$$

The dimensionless variables are defined as

$$\text{Bo} = \frac{\rho_f u c_p T_{\text{ref}}}{\pi I_b(T_{\text{ref}})} \tag{3a}$$

$$t(x, r) = \frac{T(x, r)}{T_{\text{ref}}} \tag{3b}$$

$$\bar{G}(x, r) = \frac{\tilde{G}(x, r)}{I_{\text{ref}}}. \tag{3c}$$

Here ρ_f is the density, u the speed, c_p the specific heat, $T(x, r)$ the temperature of the fluid, $I_b(T)$ the Planck black-body function, $\tilde{G}(x, r)$ the incident radiation, and T_0 is the temperature of the fluid at the upstream location $x = 0$. Furthermore, T_{ref} and I_{ref} (W/m^2) are reference conditions of the temperature and the power in the collimated irradiation, respectively. It is assumed that these two reference quantities are related by

$$I_{\text{ref}} = \pi I_b(T_{\text{ref}}) = \sigma T_{\text{ref}}^4 \tag{4}$$

where σ is the Stefan–Boltzmann constant. For a good solar collector, the solar collection fraction is about 1/6 (Mattick, 1980), yielding $I_{\text{ref}} \simeq 1/6\ \pi\ I_b(T_{\text{sun}})$ and $T_{\text{ref}} \simeq (1/6)^{0.25}\ T_{\text{sun}} = 3700$ K, where we assume $T_{\text{sun}} \simeq 5800$ K. The incident radiation $\tilde{G}(x, r)$ is related to radiation intensity $\tilde{I}(x, r, \theta, \phi)$ by

$$\tilde{G}(x, r) = \int_{\phi=0}^{2\pi}\int_{\theta=0}^{\pi} \tilde{I}(x, r, \theta, \phi)\sin\theta\, d\theta\, d\phi \tag{5}$$

To obtain an expression for $\tilde{G}(x, r)$, it is necessary to solve the equation of radiative transfer governing the radiation intensity $\tilde{I}(x, r, \theta, \phi)$.

3.3 Equation of Radiative Transfer. The equation of radiative transfer in dimensionless form for an absorbing, emitting, gray, two-dimensional cylindrical medium in local thermodynamic equilibrium is given by (Chan, 1987)

$$\left[\cos\theta\,\frac{\partial}{\partial x} + \sin\theta\cos\phi\,\frac{\partial}{\partial r} - \sin\theta\,\frac{\sin\phi}{r}\,\frac{\partial}{\partial\phi} + 1\right]\bar{I}(x, r, \theta, \phi) = \frac{1}{\pi}\,t^4(x, r),$$

$$0<x<L, \quad 0<r<R, \quad 0\le\theta\le\pi, \quad 0\le\phi\le 2\pi \tag{6}$$

The corresponding boundary conditions are of the form

$$\bar{I}^+(0, r, \theta, \phi) = I_0(r, \theta, \phi), \qquad x=0, \quad 0\le r<R, \quad 0\le\theta<\frac{\pi}{2}, \quad 0\le\phi\le 2\pi \tag{7a}$$

$$\bar{I}^-(L, r, -\theta, \phi) = \frac{\epsilon_1}{\pi}\,t_{w1}^4(r) + \rho_1\bar{I}^+(L, r, \theta, \phi), \qquad x=L, \quad 0\le r<R, \quad 0\le\theta<\frac{\pi}{2}, \quad 0\le\phi\le 2\pi \tag{7b}$$

Nomenclature (cont.)

T_{ref} = reference temperature
T_{sun} = temperature of sun
u = axial fluid velocity
$U(y)$ = unit step function, equation (A6)
x = axial optical coordinate
x_0 = axial distance to focal point
x_{Bd} = defined by equation (A3)
x_{Br} = defined by equations (A8), (A12), and (A16)
x_{usp} = axial distance to upper surface of spot, equation (A19)
x_{lsp} = axial distance to lower surface of spot, equation (A20)
$\delta(y)$ = Dirac delta function
ϵ_i = emissivity, $i = 1, 2$
η = absorption efficiency
θ = polar angle
θ_d = defined by equation (A4)
θ_r = defined by equations (A9), (A13), and (A17)
κ = absorption coefficient
λ = wavelength
ρ_f = density of fluid
ρ_i = diffuse wall reflectivity, $i = 1, 2$
σ = Stefan–Boltzmann constant
ϕ = azimuth angle

Subscripts

d = direct component of external irradiation
f = fluid
r = reflected component of external irradiation (except on q_r)
ref = reference
0 = inlet condition
1 = wall at $x = L$
2 = wall at $r = R$

Superscripts

$\bar{}$ = dimensionless quantity
$\tilde{}$ = dimensional quantity
$\pm$ = forward and backward radiation intensities

$$\bar{I}^-(x, R, \theta, -\phi) = \frac{\epsilon_2}{\pi} t_{w2}^4(x) + \rho_2 \bar{I}^+(x, R, \theta, \phi),$$

$$0 < x < L, \quad r = R, \quad 0 \le \theta \le \pi, \quad -\frac{\pi}{2} \le \phi \le \frac{\pi}{2} \qquad (7c)$$

The dimensionless radiation intensity and collimated irradiation are defined, respectively, from

$$\bar{I}(x, r, \theta, \phi) = \frac{\tilde{I}(x, r, \theta, \phi)}{I_{\text{ref}}} \qquad (8a)$$

$$I_0(r, \theta, \phi) = \frac{\tilde{I}_0(r, \theta, \phi)}{I_{\text{ref}}} \qquad (8b)$$

Here $\tilde{I}(x, r, \theta, \phi)$ is the radiation intensity (W/m^2 sr), (θ, ϕ) the polar and azimuthal angles, respectively, $\tilde{I}_0(r, \theta, \phi)$ the distribution at $x = 0$ of the collimated irradiation from the sun (W/m^2 sr), t_{wi}, $i = 1, 2$, the temperatures of the walls at $x = L$ and $r = R$, respectively, and ϵ_i, $i = 1, 2$, are the emissivities of the wall surfaces at $x = L$ and $r = R$, respectively. Since Kirchhoff's law is applicable than $\epsilon_i = 1 - \rho_i$, $i = 1, 2$, where ρ_i, $i = 1, 2$, are the coefficients for specular reflection. The above equation (6) is a partial integro-differential equation, which contains significant singularities. As such it is difficult to solve numerically and also complicated to solve analytically due to the reflecting walls. The approach taken in this work is to identify via a ray tracing procedure the exact contribution from the collimated irradiation to the overall solution of the radiation as described next.

3.4 Construction of Solution. It is desirable to obtain an approximate yet accurate solution to equation (6) subject to boundary conditions given by equations (7). The approximation outlined next is based on the linearity of the equation of transfer and is split up into two parts: one that contains both a direct and a reflected component of the highly singular term due to the collimated irradiation, and the other that includes the (less singular) radiative contributions from the medium and the side walls. Such a splitting procedure requires one to use a ray tracing procedure due to the specularly reflecting surfaces. To employ the ray tracing procedure, it is necessary to specify the location of the focal point. It is obvious that there are numerous possibilities for its location; therefore, the solution given by equation (9) below is limited to cases where the focal point $x_0 > L$. Such a limitation implies that the reflected portion of the energy from the collimated irradiation is attenuated by the medium and finally escapes from the absorption chamber through the lens; therefore, the side wall at $r = R$ is subject to no direct heating by the beam. On the other hand, we note that the optical dimensions of the chamber must be much larger than unity in order to obtain efficient volumetric absorption. The requirement of such large optical dimensions indicates that the beam is attenuated considerably prior to a reflection by the wall at $x = L$ (or at $r = R$). Thus, if the involved optical dimensions are much larger than unity, then it is permissible to relax the previously given limitation of $x_0 > L$ and consider cases in which the focal point of the beam is located within the chamber. With this limitation in mind, the solution to the intensity $\bar{I}(x, r, \theta, \phi)$ for $r > 0$ is written as the sum of three components: (1) a direct component from the beam, (2) a specularly reflected component of the beam by the wall at $x = L$, and (3) reemission and reflection by the medium and bounding surfaces. Thus the expression for the intensity is

$$\bar{I}(x, r, \theta, \phi) = I_0(r_{wd}) H_d(x, r) \delta(\cos\theta - \cos\theta_d)\delta(\phi) e^{-x_{Bd}} + \rho_1 I_0(r_{wr}) H_r(2L - x, r)\delta(\cos\theta + \cos\theta_r)\delta(\phi) e^{-x_{Br}} + I(x, r, \theta, \phi), \qquad r > 0, \quad 0 \le \phi \le 2\pi, \quad 0 \le \theta \le \pi \qquad (9)$$

and, along the line $r = 0$, the solution is written as

$$\bar{I}(x, 0, \theta, \phi) = I_0(0)\delta(\phi)[\delta(\cos\theta - 1)e^{-x} + \rho_1 \delta(\cos\theta + 1)e^{-(2L-x)}] + I(x, 0, \theta, \phi), \qquad r = 0 \qquad (10)$$

Here $I_0(r_{wd})$ and $I_0(r_{wr})$ are the radial distributions of the collimated incident beam at the locations $(x = 0, r = r_{wd})$ and at $(x = 0, r = r_{wr})$, respectively. Expressions for the terms r_{wd} and r_{wr}, the cosines of the angles θ_r and θ_d, distances of photon propagations x_{Bd} and x_{Br}, the functions $H_d(x, r)$ and $H_r(x, r)$, which account for the effects of the direct and reflected converging beam, are given in the Appendix. In addition, $\delta(y)$ is the Dirac delta function.

Since the incident radiation $\bar{G}(x, r)$ is required in equation (1), equations (9) and (10) are substituted into equation (5). By performing the integrations, we obtain

$$\bar{G}(x, r) = I_0(r_{wd}) H_d(x, r) e^{-x_{Bd}} + \rho_1 I_0(r_{wr}) H_r(2L - x, r) e^{-x_{Br}} + G(x, r), \qquad r > 0 \qquad (11)$$

and, along the line $r = 0$, the expression for incident radiation is

$$\bar{G}(x, 0) = I_0(0)[e^{-x} + \rho_1 e^{-(2L-x)}] + G(x, 0), \qquad r = 0 \qquad (12)$$

Subtracting out the clearly dominating singular term in the solution to the intensity makes it permissible to use approximate methods for obtaining a solution to $I(x, r, \theta, \phi)$ in equations (9) and (10). The method chosen for such solution is the classical P_1 approximation. Since the P_1 approximation is well known, the reader is referred to Chan (1987) and Özişik (1973) for detailed information on this solution technique. Because the considered optical dimensions are much larger than unity, this should yield results that are quantitatively and qualitatively of sufficient accuracy.

3.5 Numerical Solution Procedure. The previously described problem is coupled in a highly nonlinear fashion. Consequently, a numerical scheme is employed iteratively to obtain an approximate solution. This scheme includes a fourth-order Runge–Kutta method for solving equation (1) subject to the initial condition given by equation (2), and a standard finite-difference scheme for solving the resulting problem of the P_1 approximation. The distributions of the temperature and incident radiation are initialized by utilizing the one-dimensional solution based on normally collimated irradiation. The iterative scheme is applied until convergence is established, which in the present work is assumed to be reached when the relative change in the temperature between two consecutive iterations is $< 10^{-4}$ for all locations within the medium.

3.6 One-Dimensional Solution. To obtain a one-dimensional formulation for which the temperature and radiation intensity are only functions of x, the previously described two-dimensional formulation must be restricted such that the following three conditions are satisfied: (1) The intensity of the incident beam must not vary in the radial direction; (2) the cylinder wall at $r = R$ must be purely reflecting, i.e., $\rho_2 = 1$; and (3) the temperature distribution of the wall t_{w1} at $x = L$ must be independent of the radial direction.

It is now recognized that the deposition of radiant energy by isotropic or by collimated irradiation is described mathematically by completely different expressions. As is well known, the isotropic irradiation effects lead to expressions for the incident radiation and net radiant heat flux involving the exponential integral functions $E_n(x)$ (Özişik, 1973), whereas the collimated irradiation effects are depicted by the exponential e^{-x} (see equations (9) and (10)). Consequently, different temperature distributions and absorption efficiencies are expected for these two types of irradiation.

Table 1 Comparison of results from "exact" solution and P_1 approximation of temperature distribution in a one-dimensional medium heated by either isotropic or normally collimated irradiation with $L = 3$ and $\rho_1 = 1$

t(x) FOR ISOTROPIC IRRADIATION						
x	Bo = 0.5		Bo = 1		Bo = 4	
	Exact	P_1	Exact	P_1	Exact	P_1
0.30	0.940	0.920	0.753	0.766	0.351	0.352
0.50	0.947	0.921	0.847	0.838	0.391	0.391
0.75	0.949	0.925	0.871	0.852	0.424	0.425
1.00	0.951	0.930	0.877	0.858	0.446	0.446
1.25	0.951	0.933	0.880	0.862	0.464	0.462
1.50	0.952	0.936	0.881	0.865	0.471	0.471
2.00	0.952	0.940	0.882	0.870	0.483	0.483
2.50	0.952	0.942	0.883	0.872	0.490	0.490
3.00	0.953	0.942	0.883	0.873	0.494	0.494
t(x) FOR NORMALLY COLLIMATED IRRADIATION						
x	Bo = 0.5		Bo = 1		Bo = 4	
	Exact	P_1	Exact	P_1	Exact	P_1
0.30	0.867	0.894	0.644	0.673	0.316	0.316
0.50	0.939	0.918	0.788	0.797	0.350	0.351
0.75	0.961	0.938	0.856	0.847	0.384	0.385
1.00	0.974	0.953	0.882	0.867	0.411	0.412
1.25	0.985	0.964	0.899	0.881	0.431	0.433
1.50	0.990	0.972	0.909	0.891	0.447	0.448
2.00	0.997	0.983	0.917	0.904	0.470	0.470
2.50	1.001	0.988	0.922	0.912	0.484	0.484
3.00	1.003	0.990	0.924	0.914	0.495	0.495

4 Discussion of Results

The previous analysis has revealed numerous important parameters in the problem formulation. To keep the volume of numerical results to a reasonable level, however, the following parameters will be kept constant: the optical radius $R = 1.5$, fluid temperature at the entrance $t_0 = 0.25$, wall temperatures $t_{w1} = 0.3$ and $t_{w2} = 0.3$, the spot radius $R_{sp} = 0.1R$, and the spot length $L_{sp} = 0.2L$. Thus the optical radius R is chosen larger than unity to assure that the results obtained from the P_1 approximation are of acceptable accuracy for small fluid flow rates (Bo $\simeq$ 1). For such low flow rates, the temperatures within the medium become large leading to significant re-emission. The values of the temperatures at the inlet (t_0) and at the wall (t_{w1}) are identical to the values assumed by Mattick (1980), thus permitting a comparison between the results of his one-dimensional analysis involving isotropic irradiation and ours involving normally collimated irradiation. The spot diameter is chosen so that the area ratio between the receiver entrance and the spot $(R/R_{sp})^2 = 100$, which is within both theoretical and practical considerations. Recent experiments have shown that achievable area ratios are, at least, about 7000 (Diver et al., 1983).

4.1 Accuracy of P_1 Approximation. To estimate the accuracy of the P_1 approximation, "exact" numerical results were generated by solving the one-dimensional problems involving isotropic and normally collimated irradiation. As shown by Mattick (1980), the coupled convective and radiative heat transfer problem in one-dimension is reducible to a Fredholm-type nonlinear integral equation of the second kind for the temperature distribution in the fluid. In the present work, the integral equation was solved numerically using a 40-point Gaussian quadrature for approximating the integral and Newton's method for solving the resulting nonlinear problem. In Table 1 we show both the exact results and those obtained from the P_1 approximation, as outlined in Section 3.6, of the temperature distribution in the one-dimensional case for both isotropic and normally incident radiation with $L = 3$, $\rho_1 = 1$, and Bo = 0.5, 1, and 4. To obtain the results in Table 1 at the equally spaced points, we employed a linear interpolation. Inspection of Table 1 reveals that for Bo > 1 the P_1 approximation is in excellent agreement with the exact solution. The error increases as the Boltzmann number decreases due to significant re-emission by the medium; for Bo = 0.5 the maximum error is approximately 5 percent. Hence the present approach, based on subtracting out the singularity due to isotropic or normally collimated irradiation and solving the remaining radiation problem by the P_1 approximation, yields results of sufficient accuracy.

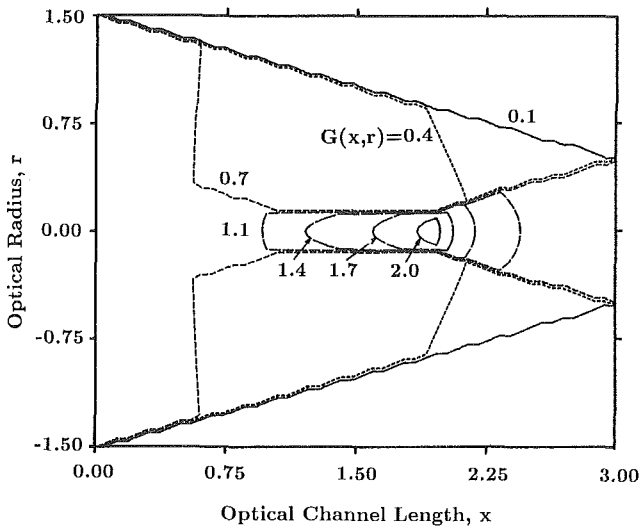

Fig. 3 Contour plot of incident radiation due to the forward and reflected components of collimated and converging beam in the attenuating medium

4.2 Isotropic Versus Normally Collimated Irradiation. Examination of the results in Table 1 also reveals that collimated irradiation establishes higher fluid exit temperatures, assuming that the analyses are based on the same reference temperature. In fact, higher exit temperatures than unity are achievable in the collimated case, which at first appears to be in violation of the second law of thermodynamics. However, the effect of a collimated source is that the radiative energy travels deeper into the fluid before being partly or completely absorbed, thereby establishing lower temperatures in the fluid near the receiver entrance. The lower temperatures near the entrance produce lower losses of energy by reradiation and more efficient volumetric absorption. Hence the directionality of the source of the radiative energy is an important aspect in the conversion of the radiant energy into sensible energy. A similar conclusion that collimated irradiation leads to higher maximum conversion efficiencies than the isotropic one has been reached by other workers (Parrott, 1978).

4.3 Attenuation of the Converging Beam. The results presented in this and subsequent sections include the effects of a converging beam on the temperature distributions and ab-

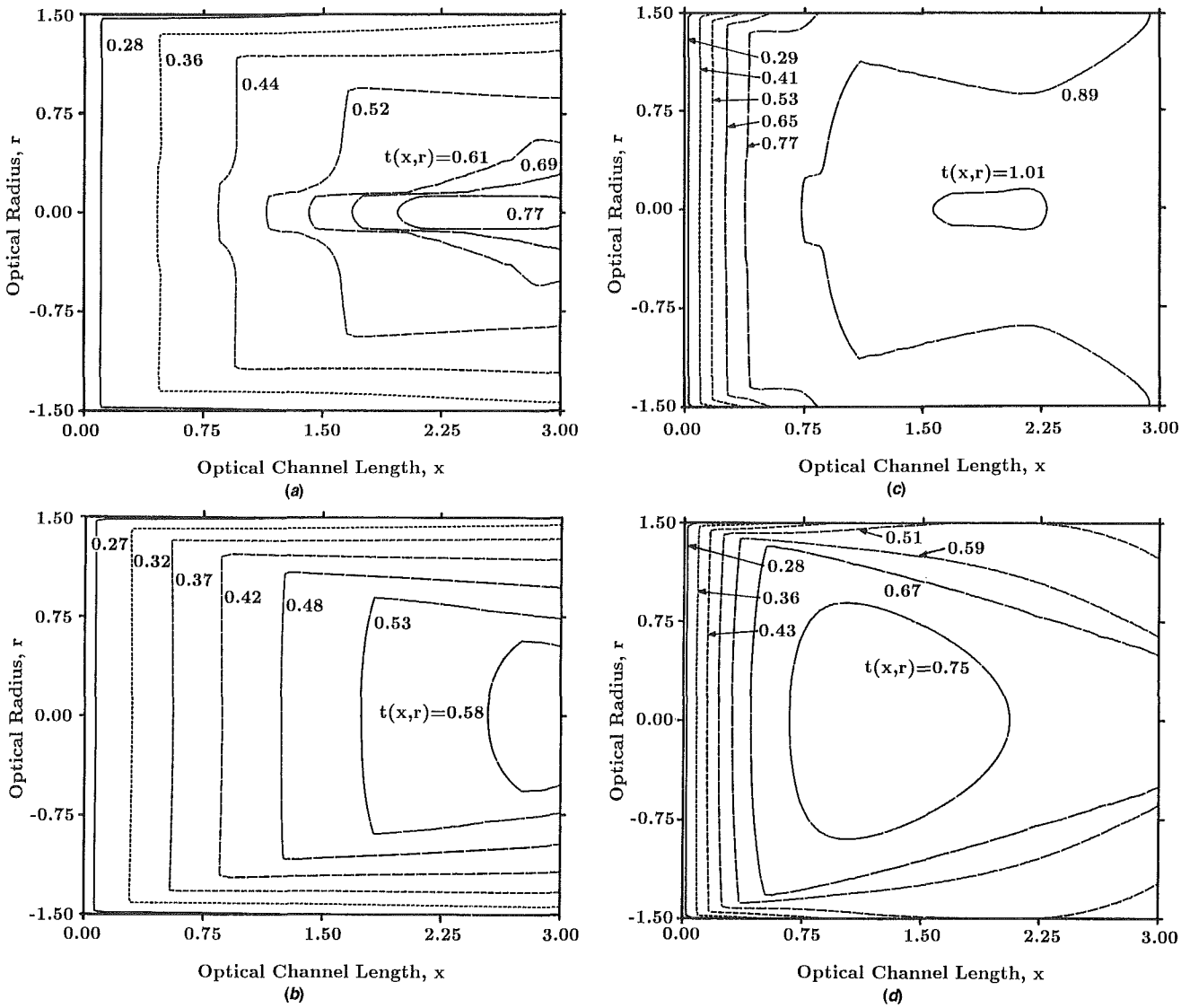

Fig. 4 Isotherms of a working fluid that is heated by collimated and converging irradiation of uniform radial strength at $x = 0$ with (*a*) Bo = 4 and $\rho_1 = \rho_2 = 1$, (*b*) Bo = 4 and $\rho_1 = \rho_2 = 0$, (*c*) Bo = 1 and $\rho_1 = \rho_2 = 1$, and (*d*) Bo = 1 and $\rho_1 = \rho_2 = 0$. The chamber radius $R = 1.5$ and distance to focal point $x_0 = 4.5$.

sorption efficiencies. In order to explain the predicted temperature profiles and absorption efficiencies better, we show in Fig. 3 the sum of the direct and specularly reflected components of the incident radiation of the converging beam. These two components are the first two terms on the right-hand side of equation (11). Based on a recent study by Jeter (1986), the distribution of the incident beam is taken to be uniform at $x = 0$; this assumption is also employed in the subsequent sections. Here, the channel length $L = 3$, the reflectivity $\rho_1 = 1$, and the geometric focal point is located at $x_0 = 4.5$. Inspection of this figure reveals that attenuation by the medium reduces the energy density from a theoretical limit of 100 ($= (R/R_{sp})^2$) down to approximately 2 units (just above the focal point), which is readily predicted from the exponential decay e^{-4}. The maximum energy density lies upstream of the focal point due to the specular reflection of the beam by the wall at $x = L$.

4.4 Distributions of Temperature $t(x, r)$. To illustrate representative results of the previously described interaction problem, we show in Figs. 4 the computed temperature distributions in the medium corresponding to Bo = 1 and 4, and specular reflectivities $\rho_1 = \rho_2 = 0$ and 1. In the case of a high fluid flow rate (Bo = 4), a comparison of Fig. 4(*a*) ($\rho_1 = \rho_2 = 1$) and Fig. 4(*b*) ($\rho_1 = \rho_2 = 0$) exposes the effect of the wall reflectivities on the temperature distribution. The use of perfectly reflecting walls rather than black walls leads to an approximately 25 percent larger core temperature ($r = 0$) near the exit wall. Similarly, a reduction in the fluid flow rate (Bo = 1) tends to equalize the temperature distribution within the absorption chamber, as shown in Figs. 4(*c*) and 4(*d*). Nevertheless, the effect of the wall reflectivities on the temperature distributions is still significant. Exit temperature increases of at least 35 percent are predicted in the case of perfectly reflecting bounding surfaces.

4.5 Distributions of Incident Radiation $G(x, r)$. To demonstrate the significance of the re-emission of radiation within the medium, we show in Figs. 5(*a*) and 5(*b*) the results of $G(x, r)$ in the case of perfectly reflecting walls and fluid flow rates corresponding to Bo = 1 and 4. These figures illustrate that the higher the temperatures within the medium, the more significant is the calculational procedure (P_1 approximation) and the role of $G(x, r)$ in the overall solution to the radiation problem. A comparison of Fig. 5(*a*) (Bo = 4) and Fig. 3 reveals that the re-emission by the medium is relatively insignificant,

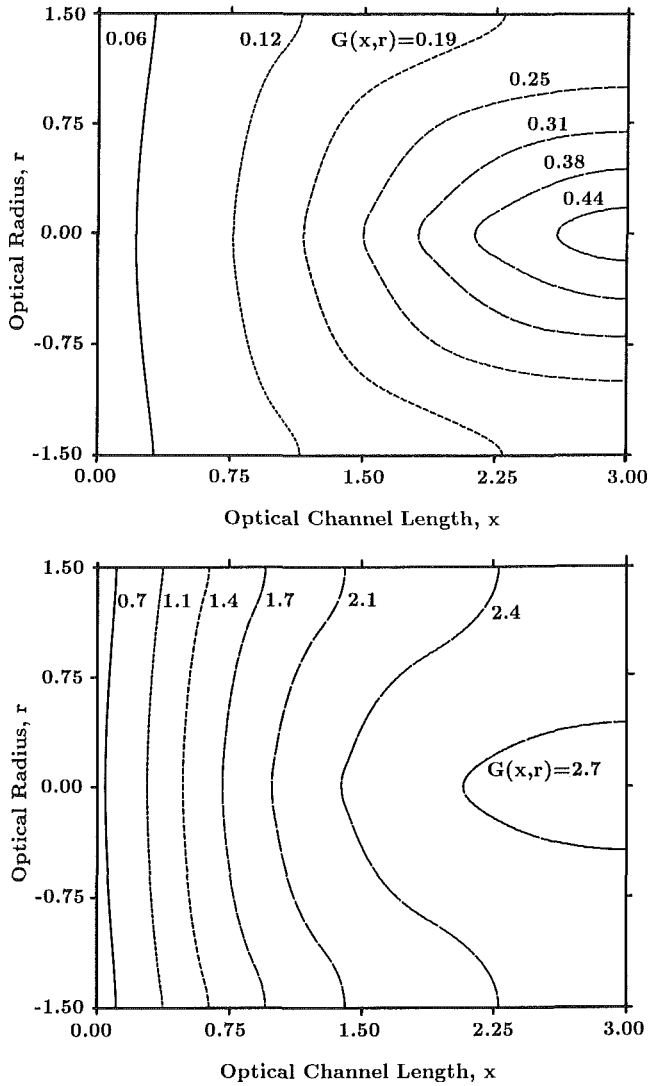

Fig. 5 Contour plot of incident radiation $G(x, r)$ in a working fluid that is heated by collimated and converging irradiation of uniform radial strength with (*a*) Bo = 4 and (*b*) Bo = 1. The chamber radius R = 1.5, distance to focal point x_0 = 4.5, and specular wall reflectivities $\rho_1 = \rho_2$ = 1.

because the medium temperatures are relatively low. However, as the flow rate is decreased to Bo = 1 in Fig. 5(*b*), the re-emission is much more significant and there result much smaller temperature gradients downstream of the receiver entrance. With such small temperature gradients within the working fluid, we deduce from equation (1) that $\tilde{G}(x, r) \rightarrow 4t^4(x, r)$.

4.6 Effects of Bo on Absorption Efficiency η and $t(L, 0)$. In Fig. 6, we illustrate the effects of Bo on the absorption efficiency η and temperature $t(L, 0)$ for the back wall reflectivities ρ_1 = 0, 0.5, and 1 with x_0 = 4.5, L = 3 and ρ_2 = 1. The absorption efficiency η is defined as one minus the ratio of losses by radiation at x = 0 to energy input by the beam; the radiative losses at x = 0 are composed of re-emission by the medium and reflection of the beam by the wall at $x = L$. Examination of Fig. 6 reveals that the efficiency decreases rapidly as the fluid flow rate decreases (Bo < 1). For larger fluid flow rates, with their ensuing lower temperatures, the efficiency becomes independent of the back wall reflectivity due to small reradiation and reflection losses; for Bo > ≃ 2, the efficiency is independent of the reflectivity ρ_1. This relatively weak dependence of the back wall reflectivity on the absorption efficiency is an important observation, since from

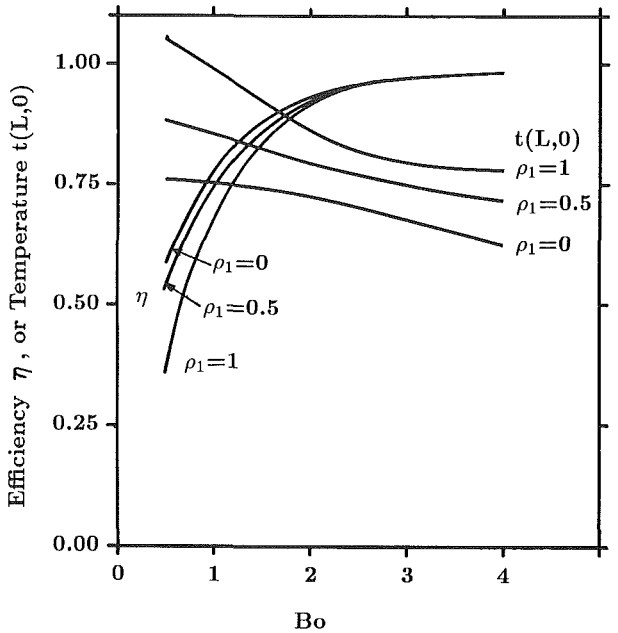

Fig. 6 Effects of Bo on the absorption efficiency η and exit centerline temperature $t(L, 0)$ of a working fluid that is heated by collimated and converging irradiation of uniform radial strength at x = 0 for the back wall reflectivities ρ_1 = 0, 0.5, and 1. For all cases, x_0 = 4.5, L = 3, R = 1.5, and ρ_2 = 1.

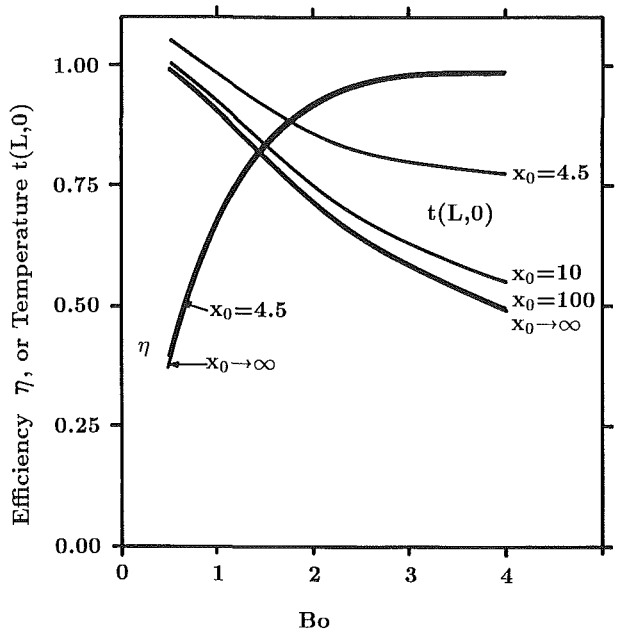

Fig. 7 Effects of Bo on the absorption efficiency η and exit centerline temperature $t(L, 0)$ of a working fluid that is heated by collimated and converging irradiation of uniform radial strength at x = 0 for the geometric focal point located at x_0 = 4.5, 10, 100, and $x_0 \rightarrow \infty$. For all cases, R = 1.5, $\rho_1 = \rho_2$ = 1, and L = 3.

a practical point of view, the back wall must be constructed of a porous material. The effects of Bo on the centerline temperature at the exit is also strong, but it is clearly also strongly dependent on the back wall reflectivity.

In Fig. 7, we show the effects of Bo on the absorption efficiency and exit centerline temperature for various locations of the geometric focal point x_0 = 4.5, 10, 100, and $x_0 \rightarrow \infty$, with L = 3, and $\rho_1 = \rho_2$ = 1. Inspection of Fig. 7 reveals that, in the special case of perfectly reflecting walls, the efficiency is almost independent of the location of the geometric focal point. The effect of Bo on the exit centerline temperature

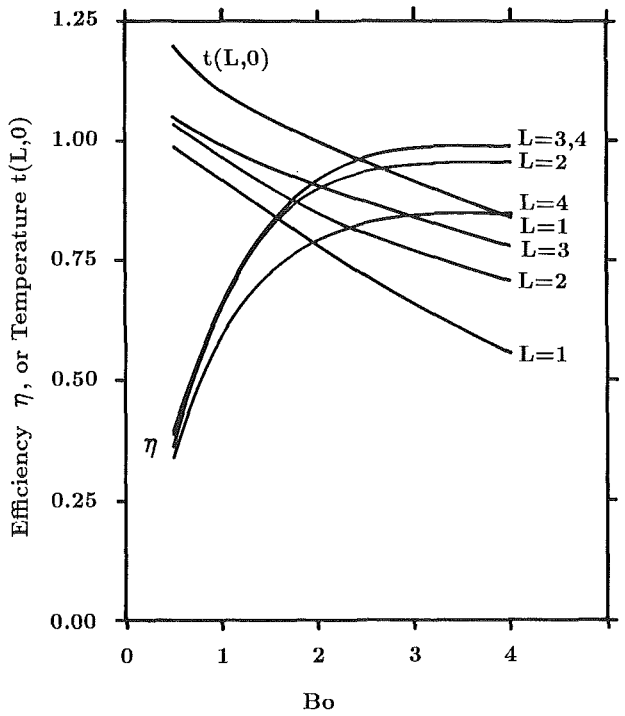

Fig. 8 Effects of Bo on the absorption efficiency η and exit centerline temperature $t(L, 0)$ of a working fluid that is heated by collimated and converging irradiation of uniform radial strength at $x = 0$ for optical channel lengths $L = 1, 2, 3$, and 4. For all cases, $R = 1.5$, $\rho_1 = \rho_2 = 1$, and $x_0 = 4.5$.

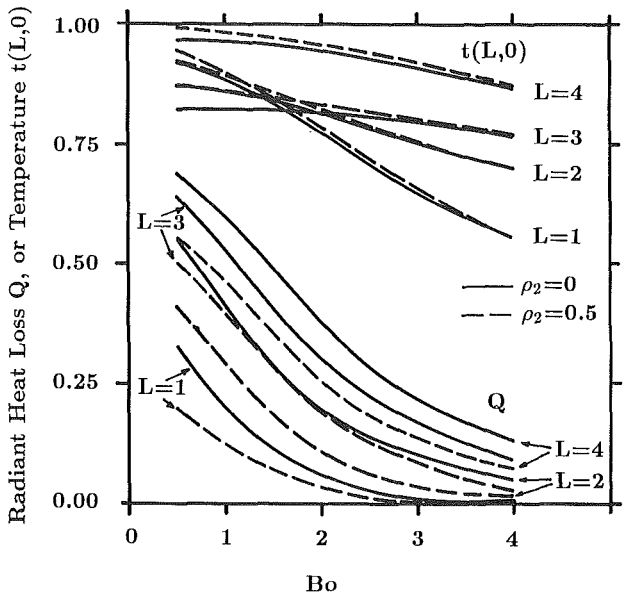

Fig. 9 Effects of Bo on the total net radiant heat loss at the side wall $r = R$ and exit centerline temperature $t(L, 0)$ of a working fluid that is heated by collimated and converging irradiation of uniform radial strength at $x = 0$ for the optical channel lengths $L = 1, 2, 3$, and 4 and wall reflectivity $\rho_2 = 0$ and 0.5. For all cases, $R = 1.5$, $\rho_1 = 1$, and $x_0 = 4.5$.

is strong, however. By utilizing a focused beam, it appears that approximately 50 percent larger exit centerline temperatures are achievable, which is important from thermodynamic considerations if any conversion device is attached to the absorption chamber.

In Fig. 8, we depict the effects of Bo on the absorption efficiency and exit centerline temperature for various channel lengths $L = 1, 2, 3$, and 4, with $x_0 = 4.5$, and $\rho_1 = \rho_2 = 1$. Examination of Fig. 8 reveals, as expected, that larger optical dimensions are required for obtaining an efficiency approaching unity. It is also clear that the efficiency becomes independent of the optical channel length, if $L > \simeq 3$. However, to obtain the maximum exit temperatures near the centerline, the geometric focus should be placed near the back wall, as shown by the case $L = 4$.

4.7 Effects of Bo on Net Total Dimensionless Radiation Loss at $r = R$. In Fig. 9, we show the effects of Bo on the net total dimensionless radiant heat loss through the side wall at $r = R$ for various channel lengths $L = 1, 2, 3$, and 4, wall reflectivities $\rho_2 = 0$ and 0.5, with $x_0 = 4.5$ and $\rho_1 = 1$. The total net dimensionless radiant heat loss on the side wall at $r = R$ is defined as the ratio of the total net radiation incident on the side wall from $x = 0$ to $x = L$ to the total energy input from the beam. This net radiative heat transfer is solely due to emission by the medium and emission/reflection by the side walls, since it is assumed that the beam neither directly nor by reflection is incident on the side wall. As shown by Chan (1987), the net radiative heat transfer in the radial direction at the wall $q_r(x, r)$ is related to the incident radiation by

$$q_r(x, R) = \frac{\epsilon_2}{2(2-\epsilon_2)} [G(x, R) - 4t_{w2}^4(x)] \qquad (13)$$

To obtain the net total radiative heat flux incident on the side wall, Simpson's numerical integration scheme is employed. As shown in Fig. 9, a significant heat load is applied on the side wall for the smaller fluid flow rates (Bo $\leq$ 1) and more than 50 percent of the energy incident from the converging beam must be removed by the external cooling fluid for specular reflectivities $\rho_2 \leq 0.5$ in order to maintain the wall at constant temperature. Thus, the efficiency is significantly altered by the radiative properties of the side wall, as well as the length of the channel. However, the centerline temperature at the exit remains almost unaffected by the wall reflectivity, which in part is attributable to the diffusion modeling of the radiative transfer according to the P_1 approximation.

5 Summary and Conclusions

An analytical investigation has been performed on the volumetric absorption efficiency of a collimated converging beam of focused solar energy in a flowing medium. Details of the assumptions and model development have been presented. A numerical solution scheme has been employed to investigate the effects of various parameters on the absorption efficiency. Based on the presented results, the following conclusions have been reached:

1 For optically thick media and purely reflecting bounding surfaces, the volumetric absorption efficiency is practically insensitive to whether the irradiation is isotropic, normally collimated, or the shape of a converging beam.

2 By utilizing a normally collimated beam rather than an isotropic one, it is possible to extract approximately 6 percent higher exit temperatures due to the smaller reradiation losses at the entrance of the receiver.

3 It is possible to extract a working fluid having a temperature at the centerline that is as much as 50 percent larger in the case of a converging beam than in the corresponding case of a collimated beam.

4 If the side wall reflectivity at $r = R$ is small ($\rho_2 \leq 0.5$), then the total net radiative heat transfer through the side wall contributes a significant portion of the heat loss from the absorption chamber.

5 The use of one-dimensional models in the description of the conservation of energy, rather than the two-dimensional model described in this paper, results in an overprediction of the peak temperatures.

Acknowledgment

The partial support received from the Air Force Office of Scientific Research through Grant No. AFOSR-84-0048 is gratefully acknowledged.

References

Chan, S. H., 1987, "Numerical Methods for Multidimensional Radiative Transfer Analysis in Participating Media," *Annual Review of Numerical Fluid Mechanics and Heat Transfer*, T.C. Chawla, ed., Vol. 1, pp. 305–350.

Diver, R. B., Carlson, D. E. E., Macdonald, F. J., and Fletcher, E. E., 1983, "A New High-Temperature Solar Research Furnace," ASME *Journal of Solar Energy Engineering*, Vol. 105, pp. 288–293.

Gilbreath, W. P., and Billman, K. W., 1978, "A Search for Space Energy Alternatives," *Radiation Energy Conversion in Space*, K.W. Billman, ed., Progress in Astronautics and Aeronautics, Academic Press, New York, Vol. 61, pp. 107–125.

Hertzberg, A., Christiansen, W. H., Johnston, E. W., and Ahlstrom, H. G., 1971, "Photon Machines," *Fundamental and Applied Laser Physics—Proceedings of the Esfahan Symposium*, Aug. 29–Sept. 5, M.S. Field, A. Javan, and N. A. Kurnit, eds., 1973, Wiley, New York, pp. 141–164.

Hertzberg, A., and Lau, C. V., 1978, "High Temperature Rankine Binary Cycle for Ground and Space Solar Engine Applications," *Radiation Energy Conversion in Space*, K. W. Billman, ed., Progress in Astronautics and Aeronautics, Academic Press, New York, Vol. 61, pp. 172–185.

Holmes, D. A., Korka, J.E., and Avizonis, X. X., 1972, "Parametric Study of Apertured Focused Gaussian Beams," *Appl. Optics*, Vol. 11, No. 3, pp. 565–574.

Hull, P. G., and Hunt, A. J., 1984, "A Reciprocating Solar-Heated Engine Utilizing Direct Absorption by Small Particles," ASME *Journal of Solar Energy Engineering*, Vol. 106, pp. 29–34.

Jeter, S. M., 1986, "The Distribution of Concentrated Solar Radiation in Paraboloidal Collectors," ASME *Journal of Solar Energy Engineering*, Vol. 108, pp. 219–225.

Kreith, F., and Kreider, J. F., 1978, *Principles of Solar Engineering*, Hemisphere Publishing Corporation, Washington, DC, pp. 244–250.

Mahajan, V. N., 1983, "Axial Irradiance and Optimum Focusing of Laser Beams," *Appl. Optics*, Vol. 22, No. 19, pp. 3042–3053.

Mattick, A. T., Hertzberg, A., Decher, R., and Lau, C. V., 1979, "High-Temperature Solar Photon Engines," *J. Energy*, Vol. 3, No. 1, pp. 30–39.

Mattick, A. T., 1978, "Absorption of Solar Radiation by Alkali Vapors," *Radiation Energy Conversion in Space*, K. W. Billman, ed., Progress in Astronautics and Aeronautics, Academic Press, New York, Vol. 61, pp. 159–171.

Mattick, A. T., 1980, "Coaxial Radiative and Convective Heat Transfer in Gray and Nongray Gases," *J. Quant. Spectrosc. Radiat. Transfer*, Vol. 24, pp. 323–334.

Özişik, M. N., 1973, *Radiative Transfer*, Wiley, New York.

Parrott, J. E., 1978, "Theoretical Upper Limit to the Conversion Efficiency of Solar Energy," *Solar Energy*, Vol. 21, pp. 227–229.

Shoji, J. M., 1984, "Potential of Advanced Solar Thermal Propulsion," *Orbit Raising and Maneuvering Propulsion: Research Status and Needs*, L. H. Caveny, ed., Progress in Astronautics and Aeronautics, Academic Press, New York, Vol. 89, pp. 30–47.

Siegel, R., and Howell, J. R., 1981, *Thermal Radiation Heat Transfer*, 2nd ed., McGraw-Hill, New York.

Wang, K. Y., and Yuen, W. W., 1986, "Rapid Heating of Gas/Small-Particle Mixture," *Radiation in Energy Systems*, Symp. Vol. HTD-55, The AIAA/ASME 4th Thermophysics and Heat Transfer Conference, Boston, MA, June 2–4, pp. 17–23.

APPENDIX

The functions describing the convergence of the collimated irradiation from the sun are given below. First contributions from the direct component are given by

$$H_d(x, r) = \frac{[r^2 + (x_0 - x)^2]^{1/2} x_0^2 U[R_b(x) - r]}{|x_0 - x|\,(x_0 - x)^2} \tag{A1}$$

$$R_b(x) = \frac{R}{x_0}\,|x_0 - x| \tag{A2}$$

$$x_{Bd} = x/\cos\theta_d \tag{A3}$$

$$\cos\theta_d = |x_0 - x|/[r^2 + (x_0 - x)^2]^{1/2} \tag{A4}$$

$$r_{wd} = r\,\frac{x_0}{|x_0 - x|} \tag{A5}$$

$U(y)$ is the unit step function, i.e.,

$$U(y) = \begin{cases} 1, & y > 0 \\ 0, & y < 0 \end{cases} \tag{A6}$$

Next the contributions from the reflected component of the converging beam are specified. First, the parameters describing the reflected converging beam as it propagates *toward* the focal point become

$$H_r(x, r) = H_d(2L - x, r) \qquad x > x_{usp}, \tag{A7}$$

$$x_{Br} = (2L - x)/\cos\theta_r \tag{A8}$$

$$\cos\theta_r = |x_0 - 2L + x|/[r^2 + (x_0 - 2L + x)^2]^{1/2} \tag{A9}$$

$$r_{wr} = r\,\frac{x_0}{|x_0 - 2L + x|} \tag{A10}$$

In the region where the reflected beams propagate in a parallel fashion, we find

$$H_r(x, r) = \frac{R^2}{R_{sp}^2}\,U(R_{sp} - r), \qquad x_{lsp} < x < x_{usp} \tag{A11}$$

$$x_{Br} = (x_0 - L_{sp}/2)/\cos\theta_r + x_{usp} - x \tag{A12}$$

$$\cos\theta_r = L_{sp}/[4r^2 + L_{sp}^2]^{1/2} \tag{A13}$$

$$r_{wr} = r\,\frac{2x_0}{L_{sp}} \tag{A14}$$

Finally, the reflected diverging component of the beam *after* the focal point is modeled as

$$H_r(x, r) = H_d(2L - x, r), \qquad x < x_{usp} \tag{A15}$$

$$x_{Br} = (2L - L_{sp} - x)/\cos\theta_r + L_{sp} \tag{A16}$$

$$\cos\theta_r = |x_0 - 2L + x|/[r^2 + (x_0 - 2L + x)^2]^{1/2} \tag{A17}$$

$$r_{wr} = r\,\frac{x_0}{|x_0 - 2L + x|} \tag{A18}$$

Here, we have defined

$$x_{usp} = 2L - x_0 + L_{sp}/2 \tag{A19}$$

$$x_{lsp} = 2L - x_0 + L_{sp}/2 \tag{A20}$$

Surface Exchange Model of Radiative Heat Transfer From Anisotropic Scattering Layers

Y. Ma
Graduate Research Assistant.

H. S. Lee
Assistant Professor.
Assoc. Mem. ASME

Department of Mechanical Engineering,
University of Minnesota,
Minneapolis, MN 55455

Scaling laws are developed that reduce the radiative heat transfer problem in an isothermal, absorbing-emitting, planar layer to a radiative exchange problem between gray surfaces through a nonparticipating medium. The wall reflectivity and the surface temperatures become the parameters to be scaled. The scaled parameters are obtained by matching the heat fluxes leaving the original layer. The resulting scaled nonparticipating reflectivity is found to be a function of the original medium reflectivity and the optical depth. The scaled nonparticipating surface temperatures include the influence of the medium temperature and the boundary source. Excellent agreement is shown for the layer reflectance, transmittance, and emittance of some anisotropic scattering media, which are scaled to a nonparticipating layer using this and the previously developed scaling laws.

1 Introduction

The radiative transfer in a one-dimensional, plane parallel medium is relatively easy to model, because of the simple geometry. Fortunately, many systems can be accurately described by such a model. Solutions for the one-dimensional planar layers are also important, because they shed some light on the nature of radiative transfer in participating media.

Obtaining solutions to the equation of transfer for an absorbing, emitting, and anisotropic scattering medium is not a trivial task, even for a one-dimensional planar geometry. The difficulty in solving this problem comes from the integro-differential nature of the equation of transfer, and a very complex kernel: the anisotropic scattering phase function.

An isotropic scattering medium is still modeled by an integro-differential equation of transfer, but the kernel is simply equal to unity. The transport equation for a nonscattering (absorbing-emitting) medium is reduced to an ordinary differential equation, for which exact analytic solutions are sometimes available. If there is no participating medium, the radiative heat transfer between the diffuse and gray surfaces is given by an algebraic expression, when the surfaces radiosities are assumed to be uniform. It is clear that if an anisotropic scattering layer can be modeled by a simpler type of layer, this automatically reduces the mathematical complexity of the governing equation.

Scaling is a method that allows one to model a system by using the solutions of another system. Strictly speaking, scaling is only applied to problems that are described by the same normalized governing equations. Scaling laws can then be formulated to describe the relationship between the various parameters of the systems. The radiative transfers in the various types of one-dimensional layer are very different from each other, and no amount of scaling in the strict sense can remove the differences. Approximate scaling laws have been introduced that reduce an anisotropic scattering layer to an isotropic scattering layer, and then further "scales" to an equivalent nonscattering layer (Lee and Buckius, 1982, 1983).

The two-step scaling process is shown schematically in Fig. 1 with the subscipts a to denote "anisotropic scattering," i to denote "isotropic scattering," and E to denote "equivalent nonscattering." A homogeneous and isothermal layer of anisotropic scattering medium is contained between black walls ($\rho = 0$). The wall at $\kappa_a = 0$ is hot at a uniform temperature T_1 and introduces a normalized radiation potential of $\phi_1 = 1$. The wall of κ_{oa} is considered to be cold and does not constitute a radiation source.

The first scaling step results in a layer of isotropic scattering medium between the same black walls. The second scaling step results in an equivalent nonscattering medium, contained between the scaled reflecting walls. The temperatures for the medium and the walls remain unchanged in both of these scaling steps. The wall reflectivity ρ_E is introduced in the second scaling step, to include the back-scattering effects of an isotropic scattering medium into a nonscattering medium simulation.

The scaling laws for modeling an anisotropic medium by an isotropic scattering medium have been developed by using the $P-1$ approximation (Lee and Buckius, 1982). These relationships are

$$\kappa_{oi} = (1 - \omega_a \langle \cos\theta \rangle)\kappa_{oa} \tag{1a}$$

and

$$\omega_i = \omega_a (1 - \langle \cos\theta \rangle)/(1 - \omega_a \langle \cos\theta \rangle), \tag{1b}$$

where the asymmetry factor, defined as

$$\langle \cos\theta \rangle = \frac{1}{2}\int_{-1}^{1} P(\cos\theta) d(\cos\theta) \tag{2}$$

is used as a single-parameter representation of the anisotropic scattering phase function. Excellent comparisons have been shown between the anisotropic scattering layer solutions and the corresponding $P-1$ scaled isotropic layer solutions.

The scaling relationships for modeling an isotropic scattering layer by an equivalent nonscattering layer are presented in terms of a linear or a square root scaling set (Lee and Buckius, 1983).

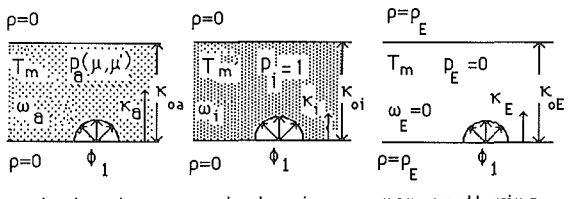

Fig. 1 Scaling from anisotropic to nonscattering medium

Contributed by the Heat Transfer Division and presented at the National Heat Transfer Conference, Houston, Texas, July 24-27, 1988. Manuscript received by the Heat Transfer Division January 6, 1988; revision received January 20, 1989. Keywords: Radiation.

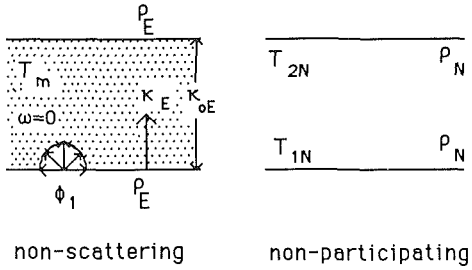

Fig. 2 Scaling from nonscattering to nonparticipating medium

Linear:

$$\kappa_{oE} = \kappa_{oi}(1-\omega_i) \text{ and } \rho_E = 1 - 2/(0.75\,\kappa_{oi}\omega_i + 2) \quad (3a)$$

Square root:

$$\kappa_{oE} = \kappa_{oi}\sqrt{(1-\omega_i)} \text{ and } \rho_E = \frac{2}{\omega_i}(1-\sqrt{(1-\omega_i)}) - 1 \quad (3b)$$

The square root scaling is shown to work well for the optically thick and the low albedo media, while the linear set is more accurate for the optically thin and the high albedo media (see Fig. 5 of Lee and Buckius, 1983).

Since the governing equations are so different, the approximate scaling process results in a loss of details in the radiation solution. When scaling from anisotropic to isotropic scattering, the angular details necessary for describing the intensity field are lost, and only the direction integrated quantities of the radiative heat flux and the average incident radiaton are scaled. In the scaling step from isotropic scattering to nonscattering, directional information is lost, and only the net radiative heat flux distribution is retained.

The goal of this work is to extend the scaling further, so the radiative transfer problem in a nonscattering (absorbing-emitting) layer is reduced to a surface exchange problem. In this final step of the scaling, the capability of predicting the heat flux distributions within a layer is lost, and only the net radiative fluxes exiting a layer can be modeled. This scaling model can be directly applied to engineering applications, where the evaluation of the radiative heat fluxes leaving a medium is of interest. The medium characteristics are then no longer of concern to the observer and can be replaced by an equivalent, scaled layer. The loss in solution details during the scaling can be justified, since the final scaled solution is simple, and it allows one to make reasonable estimates of the energy fluxes emerging from an anisotropic scattering layer.

2 Scaling

A simple scaling model can be developed by completely removing the participating medium and modifying the characteristics of the two boundary walls. This process is shown schematically in Fig. 2 with the subscripts E denoting "equivalent nonscattering," and N denoting "nonparticipating." The equivalent absorbing-emitting layer problem, with the isothermal medium temperature of T_m and the equivalent wall reflectivity of ρ_E, is scaled to a surface exchange model.

The nonparticipating reflectivities ρ_N, like the equivalent nonscattering reflectivities, are taken to be equal on both walls. This symmetry assures a correct response for the heat flux from an isothermal layer, when there is no boundary incidence. The wall source potentials are defined as $\phi_{1N} = \sigma T_{1N}^4/q_{ref}$ and $\phi_{2N} = \sigma T_{2N}^4/q_{ref}$. The spatial parameter κ must be dropped in the surface exchange model, since the net radiative heat flux in a nonparticipating medium is always a constant.

The scaling between the equivalent nonscattering and the surface exchange models cannot be achieved in a strict sense, because the heat transfer processes of the two problems are so different. The equation of transfer for an equivalent absorbing-emitting layer is

$$\mu\frac{dI_E}{d\kappa_E} + I_E = I_b(T_m) \quad (4a)$$

The equation of transfer for a nonparticipating layer is simply

$$dI_N/d\kappa_N = 0 \quad (4b)$$

There are no scaling groups that convert these equations into the same form, and considering the $P-1$ approximation again is not useful for this scaling step. The clue to making the surface exchange model work comes from the radiative heat flux solutions of the two problems.

To obtain the scaled parameters of the surface exchange model, the heat flux solutions are considered within the framework of the network analogy (Tong and Tien, 1980). This analogy interprets the radiative heat flux as the energy

Nomenclature

$\langle\cos\theta\rangle$ = scattering phase function asymmetry factor

$E_3(\kappa) = \int_0^1 \mu\exp(-\kappa/\mu)d\mu$ = exponential integral function of order 3

I = radiation intensity, W/m^2sr

L = layer thickness, m

T = temperature, K

$q = 2\pi\int_{-1}^{1} I(\kappa, \mu)\mu d\mu$ = radiant heat flux, W/m^2

$P(\cos\theta)$ = scattering phase function

PD = $\phi_1 - \phi_2$ = normalized surface potential difference

q_m = σT_m^4 = medium thermal emissive power, W/m^2

R = $q^-(0)/\sigma T_1^4$ = layer reflectance

y = coordinate, m

β = extinction coefficient, m^{-1}

E = $q^-(0)/q_m$ = layer emittance

θ = angle with the κ axis or the scattering angle

κ = βy = optical depth, optical coordinate

κ_o = βL = overall optical depth

μ = $\cos\theta$

ρ = wall reflectivity

σ = Stefan–Boltzmann constant = 5.6696×10^{-8} W/m^2K^4

σ_s = scattering coefficient, m^{-1}

T = $q^+(\kappa_o)/\sigma T_1^4$ = layer transmittance

ϕ = $\sigma T^4/q_{ref}$ = normalized surface potential

ω = σ_s/β = scattering albedo

Subscripts

a = anisotropic scattering

b = blackbody

E = equivalent nonscattering

i = isotropic scattering

m = medium quantity

N = nonparticipating

o = overall

ref = reference quantity

1 or 2 = wall values

Superscripts

* = dimensionless variable

\+ = positive κ direction

− = negative κ direction

flow due to a driving potential difference through a network resistance. The surface exchange problem fits neatly into this analogy. The net radiative heat flux, for the nonparticipating layer shown in Fig. 2, is given by

$$q_N^* = (\phi_{1N} - \phi_{2N}) / \left(\frac{2}{1-\rho_N} - 1 \right) \tag{5}$$

The numerator in equation (5) is the surface potential difference, and the denominator is the surface resistance. If the heat flux solution for the equivalent nonscattering layer problem can also be considered in the framework of this analogy, scaling can be established by setting the two heat fluxes equal to each other. This will result in expressions for the scaled potential difference $PD_N = \phi_{1N} - \phi_{2N}$, and the nonparticipating reflectivity ρ_N.

The net radiative heat flux for the equivalent nonscattering layer shown in Fig. 2 is given by

$$q_E^*(\kappa_E) = \frac{(1-\rho_E)}{(1-4\rho_E^2 E_3^2(\kappa_{oE}))}$$

$$* \{ 2[E_3(\kappa_E) - 2\rho_E E_3(\kappa_{oE}) E_3(\kappa_{oE} - \kappa_E)]\phi_1$$

$$+ 2(2\rho_E E_3(\kappa_{oE}) + 1)[E_3(\kappa_{oE} - \kappa_E) - E_3(\kappa_E)] q_m^* \} \tag{6}$$

It is not immediately clear whether equation (6) can be interpreted by the network analogy. Of obvious concern is the optical depth dependence of the heat flux when the medium is absorbing and emitting. This problem is partially overcome by interpreting the q_N^* as an overall response of the model to the external potential difference. The q_E^* of equation (6) is then only evaluated at the boundary points of the layer, $\kappa_E = 0$ or κ_{oE}.

Even with the questions of the optical depth dependence partially settled, there is still the issue of how to group the terms in equation (6) to define a potential difference and resistance. Some of the early attempts at scaling resulted in the nonparticipating reflectivity values becoming greater than one or the scaled wall temperatures being less than zero. While such combinations still result in the correct equivalent heat flux, it is much less confusing if the scaling results in physically realistic parameters.

The scaling presented here is obtained by setting the inverse of the surface resistance term of equation (5) equal to $(1-\rho_E)(1-4\rho_E E_3^2(\kappa_{oE}))/(1-4\rho_E^2 E_3^2(\kappa_{oE}))$. This group is obtained by multiplying the leading term in equation (6) with the coefficient for ϕ_1, evaluated at $\kappa_E = 0$. This particular grouping results in the scaled ρ_N with the desired trends. The main reason for the success of this grouping, rather than the many others that have been studied, is that it correctly includes the effects of the absorbing-emitting layer as the optical depth approaches zero. At the optically thin limit, emission from the medium becomes negligible, and the solution is dominated by the boundary incidence terms. The scaled surface reflectivity ρ_N is given by

$$\rho_N = \frac{\rho_E + 4\rho_E E_3^2(\kappa_{oE}) - 8\rho_E^2 E_3^2(\kappa_{oE})}{2 - \rho_E - 4\rho_E E_3^2(\kappa_{oE})} \tag{7}$$

This nonparticipating reflectivity is only a function of the medium properties: the overall optical depth, and the equivalent nonscattering reflectivity.

Figure 3 shows a graph of ρ_N versus ρ_E with the overall optical depth as a parameter. The nonparticipating reflectivity is shown to be always positive and never to exceed unity. At the two limiting values of $\rho_E = 0$ and $\rho_E = 1$, ρ_N equals ρ_E exactly. At other values of ρ_E, the reflectivity ρ_N tends to be slightly

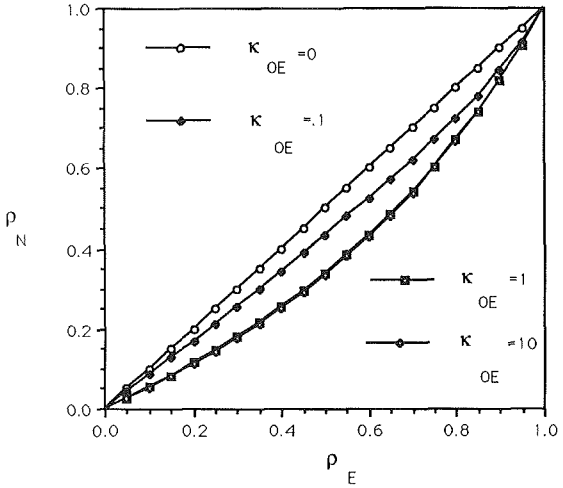

Fig. 3 Nonparticipating reflectivity

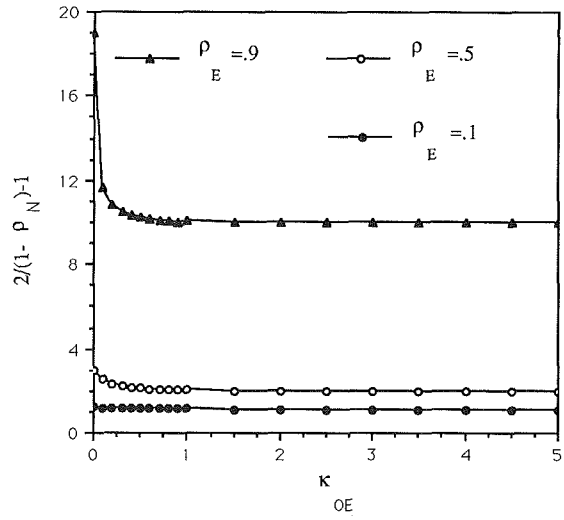

Fig. 4 Nonparticipating surface resistance

smaller than ρ_E for nonzero κ_{oE}. At a fixed ρ_E, ρ_N is seen to decrease with increasing κ_{oE}. This decrease can be understood to be the result of the stronger medium absorption, which makes the surface effects appear less significant. When κ_{oE} approaches infinity, $E_3(\kappa_{oE})$ approaches zero, and the reflectivity ρ_N is then a function only of ρ_E through

$$\rho_N = \frac{\rho_E}{2 - \rho_E} \tag{8}$$

When the optical depth goes to zero, the absorbing-emitting problem is exactly equal to the nonparticipating surface exchange model, and $\rho_N = \rho_E$.

The effect of the nonparticipating reflectivity on the heat flow can be seen in Fig. 4, where the resulting nonparticipating surface resistance is shown. Because the reflectivity decreases with increasing optical depth, this results in an overall decrease in the surface resistance. Therefore, as the optical depth is increased, the nonparticipating potential difference will have to be smaller than the original potential difference in order to match the same heat flux. The figure also shows the surface resistance increasing with increasing equivalent wall reflectivity. The nonparticipating potential difference will have to be larger than the original PD, in order to overcome this increased resistance to heat flow.

The scaling for the potential difference PD_N is determined by

$$PD_N(\kappa_E) = \phi_{1N} - \phi_{2N}$$

$$= \frac{2}{(1-4\rho_E E_3^2(\kappa_{oE}))}$$

$$*\{[E_3(\kappa_E) - 2\rho_E E_3(\kappa_{oE}) E_3(\kappa_{oE}-\kappa_E)]\phi_1$$

$$+ (2\rho_E E_3(\kappa_{oE}) + 1)[E_3(\kappa_{oE}-\kappa_E) - E_3(\kappa_E)]q_m^*\} \quad (9)$$

This potential difference acts as the driving force of the heat flux, and it influences the magnitude and the direction of heat flow. Since only the PD_N is meaningful to the calculation, one ϕ_N is always set equal to unity, while the other ϕ_N is obtained by evaluating equation (9) at either of the layer boundary points, depending upon the nature of the problem at hand. Determining the ϕ_{1N} and ϕ_{2N} thus ensures that the direction and the magnitude of q_N^* match that of q_E^*, while maintaining all positive wall temperatures.

For a properly normalized problem, this PD_N ranges in value between zero and one. The resulting normalized wall temperatures will also range in value between zero and one. A PD_N greater than one, which can happen with some of the scaling groups tested, results in normalized wall temperatures becoming greater than one. Although the actual value of the PD_N has no effect as far as the accuracy of the current scaling is concerned, the resulting wall temperatures are an important consideration for the calculations involving combined radiation and convection. The large wall temperatures raised to the fourth power can cause severe numerical problems.

For the particular case of a truly nonparticipating medium with $\kappa_{oE} = 0$, the above surface potential PD_N will also be equal to the original PD. Therefore, along with the fact that ρ_N is equal to ρ_E when $\kappa_{oE} = 0$, the current scaling group of ρ_N and PD_N reduces to the surface exchange result when the optical depth goes to zero.

The scaled potential ϕ_N can have various forms because PD_N depends on many variables: the κ_E evaluation point, the medium emissive power, and the original surface potential. The potential differences for calculating the reflectance, the emittance, and the transmittance of a layer are given below and summarized at the end of this discussion in a table.

When the medium reflection at its $\kappa_E = 0$ surface is to be considered, the backward flux $q^-(0)$ resulting from the incident radiation into a cold medium is needed. The reflectance of a layer is defined as

$$R = q^-(0)/\sigma T_1^4 \quad (10)$$

where $q^-(0) = q^+(0) - q(0)$. The $q^+(0)$ is taken to be the original scattering layer wall incidence σT_1^4, since the equivalent wall reflectivity is considered to be an imaginary quantity representing the medium scattering characteristics. Therefore, it will not directly reduce the radiation input to the layer. There is also no radiation input from the second wall ($T_2 = 0$).

The appropriate q_{ref} for this case is σT_1^4, and the potential ϕ_{1N} is set equal to unity. The other surface potential ϕ_{2N} is then set equal to $1 - PD_N(0)$, where $PD_N(0)$ is given by equation (9) evaluated at $\kappa_E = 0$ with $\phi_1 = 1$ and $q_m^* = 0$. The $PD_N(0)$ for this case is always equal to one for any optical depth and equivalent reflectivity, which means that the ϕ_{2N} is equal to zero. The corresponding nonparticipating wall temperatures are $T_{1N} = T_1$ and $T_{2N} = 0$. The nonparticipating potential difference is equal to the original PD, and the PD_N results in a net flux in the correct direction.

The PD_N can be shown to be directly related to the layer reflectance by

$$R = 1 - PD_N(1-\rho_N)/(1+\rho_N) \quad (11)$$

Since the PD_N is equal to one in this case, any effects of the participating media on the reflectance are incorporated into the formulation for the nonparticipating reflectivity. Figure 3 shows that ρ_N increases with increasing ρ_E, implying that the increased scattering in the medium (represented by a larger ρ_E) results in a larger amount of back-scattering from the medium. When the medium is only absorbing and emitting, there can be no reflectance from the layer.

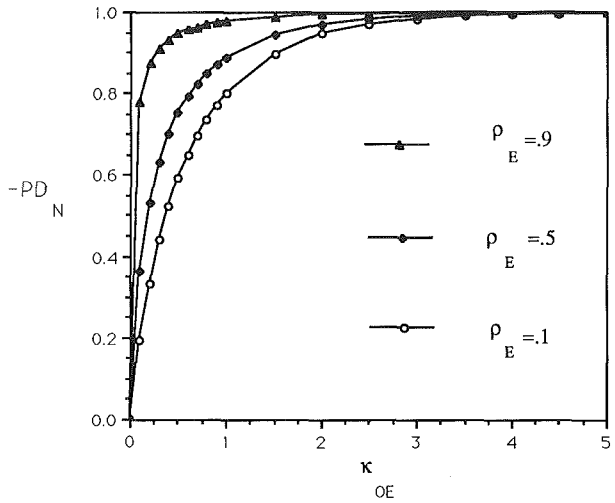

Fig. 5 Surface potential difference for emission

When the isothermal layer emission is under study, the flux emitted at the $\kappa_E = 0$ surface is the backward flux $q^-(0)$. Emittance is defined as the ratio of the heat flux leaving the $\kappa_E = 0$ surface to the medium emissive power q_m, when both the walls are cold ($T_1 = T_2 = 0$).

$$E = q^-(0)/q_m \quad (12)$$

The $q^-(0)$ is set equal to $-q(0)$, again treating the wall reflectivity as an imaginary quantity.

The $PD_N(0)$ in this case is negative, and this ensures a net flux in the negative κ_E direction. To be consistent, the high surface potential is chosen to be $\phi_{2N} = 1.0$. The lower surface potential is $\phi_{1N} = 1 + PD_N(0)$, with $\phi_1 = 0$ and $q_m^* = 1$ in equation (9). The appropriate q_{ref} for this case is σT_m^4, and the corresponding nonparticipating wall temperatures are $T_{1N} = T_m[1 + PD_N(0)]^{0.25}$ and $T_{2N} = T_m$.

The PD_N in this case can be shown to be directly related to the layer emittance by

$$E = -PD_N(1-\rho_N)/(1+\rho_N) \quad (13)$$

The trends of $-PD_N$ for the pure isothermal emission case, with respect to κ_{oE} and ρ_E, are presented in Fig. 5. The figure shows an increasing $|-PD_N|$ with larger κ_{oE}, which indicates a stronger medium emission from a thicker medium. Since the ρ_N also decreases with increasing optical depth, the effect is to augment the increased PD_N, and the layer emittance increases. For a fixed optical thickness, the absolute value of the potential difference increases with ρ_E. This increase in the PD_N partially overcomes the increased surface resistance shown in Fig. 4. However, the overall effect of an increased ρ_E is a decrease in the layer emittance, since the ρ_E can be understood to be a substitute for the screening effect of the scattering particles, as they block the medium emission from leaving the layer.

When the layer transmission is to be calculated for a boundary incidence case, the flux $q^+(\kappa_{oE})$ is needed. The definition of the transmittance for a layer is the ratio of the heat flux leaving the κ_{oE} surface to the incident radiation, when the medium temperature and T_2 are both zero

$$T = q^+(\kappa_{oE})/\sigma T_1^4 \quad (14)$$

Since the net $q(\kappa_{oE})$ is in the positive κ_E direction, PD_N is also

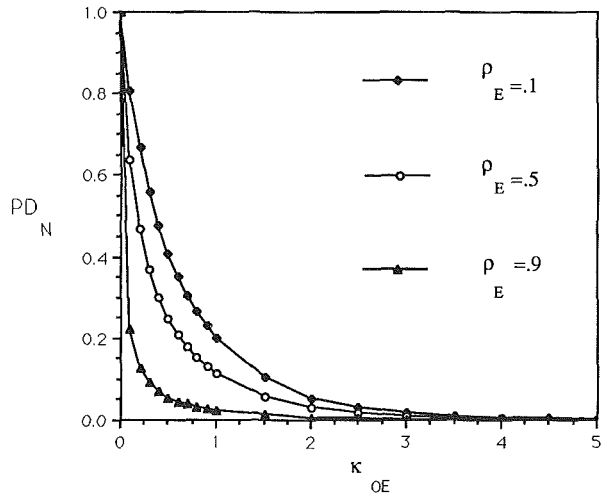

Fig. 6 Surface potential difference for transmission

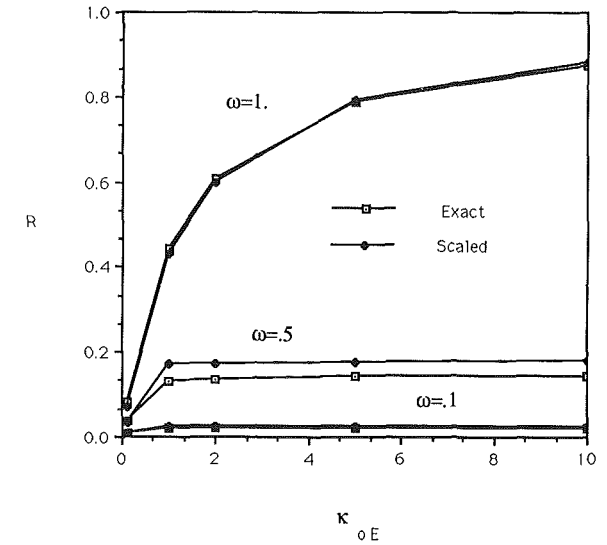

Fig. 7 Reflectance for a Rayleigh scattering medium

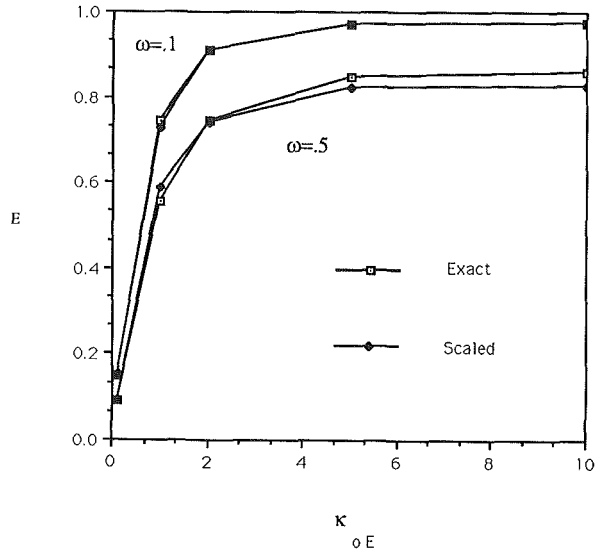

Fig. 8 Emittance for a backward scattering medium

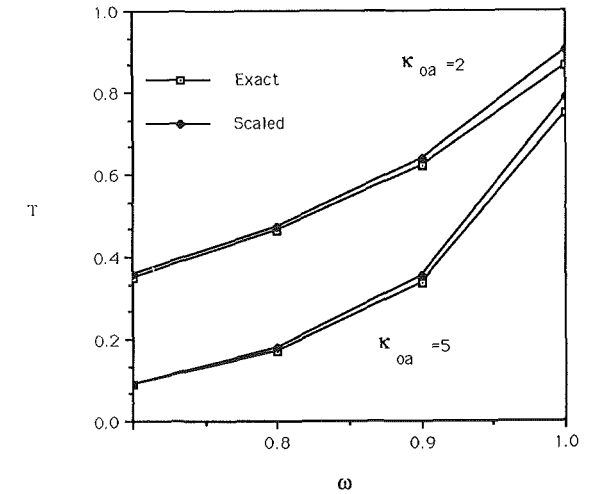

Fig. 9 Transmittance for a peaked forward scattering medium

positive. The q_{ref} is set equal to σT_1^4, and ϕ_{1N} is chosen to be equal to one. The remaining ϕ_{2N} is then equal to $1-PD_N(\kappa_{oE})$, where equation (9) is evaluated at $\kappa_E=\kappa_{oE}$ with $\phi_1=1$ and $q_m^*=0$. The corresponding wall temperatures are $T_{1N}=T_1$ and $T_{2N}=T_1[1-PD_N(\kappa_{oE})]^{0.25}$.

The layer transmittance can be shown to be

$$\mathrm{T}=PD_N(1-\rho_N)/(1+\rho_N) \tag{15}$$

The curves for PD_N with respect to ρ_E and κ_{oE} are shown in Fig. 6. The figure reveals that the potential difference decreases as ρ_E and κ_{oE} are increased. For a given ρ_E, the increasing optical depth results in a smaller ρ_N, but the effect of decreasing PD_N dominates, and the transmittance decrease due to the increasing attenuation effects of a thickening medium. At a fixed κ_{oE}, the PD_N decreases with increasing ρ_E, and ρ_N also increases, leading to a smaller transmittance, because the heat flux, which can penetrate into the medium, is reduced.

The table below presents a summary of the scaled surface potentials for calculating the reflectance, emittance, and transmittance of a layer. The nonparticipating wall reflectivity is given by equation (7) for all the cases.

	PD_N	ϕ_{1N}	ϕ_{2N}
R	1.0	1.0	0
E	$2[2\rho_E E_3(\kappa_{oE})+1][E_3(\kappa_{oE})-0.5]/(1-4\rho_E E_3^2(\kappa_{oE}))$	$1+PD_N$	1.0
T	$2E_3(\kappa_{oE})(1-\rho_E)/(1-4\rho_E E_3^2(\kappa_{oE}))$	1	$1-PD_N$

For the combined contributions from an external incidence ϕ_1 and an isothermal medium emission q_m, q_{ref} is set equal to the larger of q_m or ϕ_1. The potential difference of equation (9) is then evaluated at the exit location in question. If $PD_N<0$, the potential $\phi_{1N}=1.0$ is set as the high potential, and $\phi_{2N}=1-PD_N(0)$. If $PD_N<0$, $\phi_{2N}=1$ is the high potential, and $\phi_{1N}=1+PD_N(\kappa_{oE})$. In a similar fashion, simultaneous nonzero boundary conditions at both walls can also be included in the analysis.

3 Comparisons

The current scaling sequence, combined with the previous scaling steps presented in the introduction, allow for a simple calculation of the heat fluxes leaving an anisotropic scattering layer. Comparisons of the anisotropic scattering medium reflectance, transmittance, and emittance with the corresponding scaled results are shown in Figs. 7, 8, and 9. Figure 7

is the comparison for a Rayleigh scattering medium. Figure 8 is the comparison for a backward scattering medium, while Fig. 9 shows the comparison for a peaked forward scattering medium.

During the scaling from an isotropic scattering layer to an equivalent nonscattering layer, both the linear and the square root scaling rules are used, according to the criterion presented by Lee and Buckius (1983). The anisotropic scattering results are obtained either from the data published by Orchard (1967) or Sutton and Özişik (1979), or obtained from a one-dimensional *S-N* discrete ordinates code developed by Kim and Lee (1988). All figures show excellent agreements between the anisotropic and the scaled results.

The phase function used in Fig. 7 is given by the expression $P(\mu)=0.75\ (1+\mu^2)$, and the exact results are partially from Orchard (1967). The bottom two nearly overlapping curves in the figure are for a weak scattering case, where the albedo is 0.1. The top two nearly overlapping curves are for a pure scattering medium, where the albedo is one. Very small deviations from the exact solutions are observed for these two cases for all the layer optical depths considered. The pair of curves in the middle is for the case of albedo equal to 0.5, where a slightly larger error is found. Since the scaling from the nonscattering to a nonparticipating medium is exact for heat flux, this error is due to the approximations that are made in the previous scaling steps. In particular, a more accurate square root scaling rule for reducing an isotropic layer to a nonscattering layer is needed for better overall accuracy. Although not shown, even better agreements for the transmittance results are observed. The comparisons for the emittances are similar to those shown for the reflectance.

Figure 8 shows a comparison for a backward scattering phase function. The phase function expansion coefficients for the medium are presented by Lee and Buckius (1982), and the asymmetry factor is equal to -0.1884. The exact results for the figure are partially from Sutton and Özişik (1979), and good agreement is shown between the scaled and exact emittance. Similar accuracy can be shown for the reflectance and transmittance calculations, where the maximum error is found for the pure scattering cases, which have strong backscattering effects. Excellent agreement is found for all other cases considered, for this smooth backward scattering phase function.

A comparison of the transmittance between the anisotropic and the scaled results for a peaked forward phase function studied by Sutton and Özişik (1979) is shown in Fig. 9. Its expansion coefficients are given by Lee and Buckius (1982), the asymmetry factor is equal to 0.9273. Even for this highly forward scattering case good agreement is shown in the figure.

The results in Figs. 7, 8, and 9 suggest that for those applications, where only the estimate of the radiative heat flux leaving a layer is needed, the scaling from an anisotropic scattering layer all the way down to a nonparticipating layer does give very accurate results, without the need for large amounts of computing time. The discrepancies that do show up between the scaled and the exact anisotropic scattering results, are due to the compounding of the errors in each of the previous scaling steps. The current scaling step matches the heat fluxes of the nonscattering and the scaled nonparticipating media exactly.

4 Conclusions

Current investigation suggests the idea of scaling the radiative heat transfer problem in an absorbing-emitting medium to a two-surface exchange problem with a nonparticipating medium. The approach to accomplish the scaling is quite simple. The scaled nonparticipating reflectivity ρ_N carries the information of the original medium properties, and the scaled nonparticipating surface potential difference PD_N incorporates the influence of the boundary conditions and the medium temperature.

Estimates for the various heat fluxes leaving an anisotropic scattering medium can be obtained easily by utilizing this and the previously developed scaling laws. The scaled results for smooth backward scattering, sharply forward scattering, and Rayleigh scattering media are shown to be very accurate in comparison with the exact results. Application of this scaling procedure to more general situations of anisotropic scattering layers within gray walls or layers that are nonisothermal and inhomogeneous is also possible using the multilayer solution technique (Lee and Buckius, 1983, 1986). The ability to make estimates of the radiative flux emerging from an absorbing, emitting, and anisotropic scattering layer by a simple surface exchange calculation, has far-reaching implications to practical device design and complex conjugate heat transfer analysis.

Acknowledgments

This work was supported in part by the National Science Foundation Grant No. NSF/CBT-8451076. This PYI award was also partially supported by the Northern States Power Company. Partial support by the Academic Computing Services and Systems is also acknowledged. The help extended by T. K. Kim with the *S-N* method is appreciated.

References

Kim, T.-K., and Lee, H., 1988, "Effect of Anisotropic Scattering on Radiative Heat Transfer in Two-Dimensional Rectangular Enclosures," *Int. J. Heat Mass Transfer*, Vol. 31, pp. 1711–1721.

Lee, H., and Buckius, R. O., 1982, "Scaling Anisotropic Scattering in Radiation Heat Transfer for a Planar Medium," ASME JOURNAL OF HEAT TRANSFER, Vol. 104, pp. 68–75.

Lee, H., and Buckius, R. O., 1983, "Reducing Scattering to Nonscattering Problems in Radiation Heat Transfer," *Int. J. Heat Mass Transfer*, Vol. 26, pp. 1055–1062.

Lee, H., and Buckius, R. O., 1986, "Combined Mode Heat Transfer Analysis Using Radiation Scaling," ASME JOURNAL OF HEAT TRANSFER, Vol. 108, pp. 626–632.

Orchard, S. E., 1967, "Reflection and Transmission of Light by Thick Atmospheres of Pure Scatterers With a Phase Function: $1 + \tilde{\omega}_1 P_1(\cos\theta) + \tilde{\omega}_2 P_2(\cos\theta)$," *Astrophysical Journal*, Vol. 149, pp. 665–674.

Özişik, M. N., 1973, *Radiative Transfer and Interactions With Conduction and Convection*, Wiley, New York, pp. 334–339.

Sutton, W. H., and Özişik, M. N., 1979, "An Iterative Solution for Anisotropic Radiative Heat Transfer in a Slab," ASME JOURNAL OF HEAT TRANSFER, Vol. 101, pp. 695–698.

Tong, T. W., and Tien, C. L., 1980, "Resistance-Network Representation of Radiative Heat Transfer With Particulate Scattering," *J. Quant. Spectrosc. Radiat. Transfer*, Vol. 24, pp. 491–503.

Mean and Fluctuating Radiation Properties of Nonpremixed Turbulent Carbon Monoxide/Air Flames

M. E. Kounalakis
Research Assistant.

J. P. Gore[1]
Research Fellow.

G. M. Faeth
Professor.
Fellow ASME

Department of Aerospace Engineering
The University of Michigan,
Ann Arbor, MI 48109-2140

Mean and fluctuating spectral radiation intensities were measured for horizontal chordlike paths through turbulent nonpremixed carbon monoxide/air flames. Measurements in the 2700 nm radiation band of carbon dioxide revealed radiation fluctuations exceeding 50 percent in some locations even though mean radiation levels were not strongly influenced by turbulence/radiation interactions. Both time-independent and time-dependent stochastic simulations were developed to treat turbulence/radiation interactions as well as the temporal properties of flame radiation. The stochastic simulations were based on the laminar flamelet concept to relate scalar properties to mixture fracture, methods analogous to statistical time-series techniques to treat the probability density functions and spatial and temporal correlations of mixture fraction along the radiation path, and a narrow-band radiation model. The simulations yielded encouraging predictions of mean and fluctuating values, probability density functions, and temporal power spectra of spectral radiation intensities.

Introduction

Similar to other properties of a turbulent flame, radiation emitted from the flame varies with time even when the mean properties are stationary. This is widely recognized and is exploited so that fire and flame detectors can distinguish flames from background radiation (Porscht, 1975). Perhaps a more important effect, influencing many practical applications, is that turbulence/radiation interactions cause mean radiation properties of turbulent flames to differ considerably from estimates based on mean scalar properties in the flames. Flame radiation fluctuations are a direct manifestation of the nonlinearities that cause mean radiation levels to be biased in this manner; therefore, studying the temporal properties of radiation fluctuations (magnitudes, probability density functions, and temporal power spectral densities) provides information needed to understand turbulence/radiation interactions, similar to the information provided by the temporal properties of velocity and concentration fluctuations for understanding turbulent mixing. Motivated by these observations, the present investigation considered the temporal properties of radiation fluctuations from nonpremixed turbulent carbon monoxide/air flames.

Turbulence/radiation interactions in nonpremixed turbulent flames have attracted attention in the past. Cox (1977), Kabashnikov and Kmit (1979), and Grosshandler and Joulain (1986) used simplified models to show that turbulent fluctuations increase mean radiation levels from estimates based on mean scalar properties. Grosshandler and Vantelon (1985) developed an approximate model to compute effects of turbulent fluctuations on mean radiation properties, recently applied to ethanol pool fires by Fisher et al. (1987), who drew similar conclusions. Porscht (1975) reported earlier measurements of power spectral densities of the output of several flame radiation detectors that were viewing buoyant turbulent diffusion flames. He found large radiation fluctuations in comparison to mean radiation levels, experimentally demonstrating the importance of turbulence/radiation interactions. Later, Markstein (1981) used a scanning radiometer to measure radiance fluctuations in PMMA pool fires, reporting a number of turbulent radiation properties analogous to other turbulence properties, e.g., intermittency, fluctuation intensities, kurtosis, and spatial correlations.

The radiation properties of nonluminous and luminous turbulent diffusion flames have also been studied in this laboratory. The experiments involved buoyant jet diffusion flames burning in still air, considering the following fuels: hydrogen (Gore et al., 1987a; Kounalakis et al., 1988), carbon monoxide (Gore et al., 1987b), methane (Jeng et al., 1984; Jeng and Faeth, 1984a), natural gas (Gore et al., 1987c), ethylene (Gore and Faeth, 1986), and acetylene (Gore and Faeth, 1988). A time-independent stochastic method for treating turbulence/radiation interactions was developed that yielded encouraging agreement with measurements of mean spectral radiation intensities and radiative heat fluxes. It was found that turbulence/radiation interactions generally caused significant (more than 100 percent) increases of mean radiation levels above estimates based on mean scalar properties, although this effect was small for some nonluminous flame systems, e.g., carbon monoxide, methane, and natural gas/air flames.

The most recent work in this laboratory considered mean and fluctuating spectral radiation intensities in nonluminous nonpremixed turbulent hydrogen jet flames burning in still air (Kounalakis et al., 1988). Radiation fluctuations were analyzed using a narrow band radiation model combined with a time-dependent stochastic simulation of the scalar property variations of an array of statistically independent eddies along the radiation path. Encouraging agreement was found between predicted and measured mean and fluctuating values, probability density functions, and temporal power spectral densities of spectral radiation intensities for horizontal chordlike paths through the axis of the flames. Radiation fluctuation intensities of 20–110 percent were observed, providing additional direct evidence of effect of turbulence/radiation interactions in turbulent diffusion flames.

[1]Present address: Assistant Professor of Mechanical Engineering, The University of Maryland, College Park, MD.

Contributed by the Heat Transfer Division and presented at the ASME Winter Annual Meeting, Chicago, Illinois, December 1988. Manuscript received by the Heat Transfer Division July 20, 1988; revision received December 1988. Keywords: Fire/Flames, Radiation Interactions, Turbulence.

The objective of the present study was to extend the work of Kounalakis et al. (1988), as follows: to develop a more flexible stochastic simulation that removes the restriction of statistically independent eddies along the radiation path, and to evaluate effects of radiation fluctuations for turbulent nonpremixed carbon monoxide/air flames. Carbon monoxide/air flames are of interest for several reasons. First of all, reaction rates are reasonably fast, similar to hydrogen/air flames, so that local thermodynamic equilibrium is nearly maintained: this vastly simplifies analysis of scalar properties (Faeth and Samuelsen, 1986). Secondly, effects of turbulence/radiation interactions for carbon monoxide/air flames offer a contrast to hydrogen/air flames. In particular, turbulence/radiation interactions have little effect on mean spectral radiation intensities for carbon monoxide/air flames (Gore et al., 1987b), but have a significant effect for hydrogen/air flames (Gore et al., 1987a). Finally, carbon monoxide/air flames are nonluminous, so that the complications of soot properties in a turbulent environment can be avoided. Predictions and measurements were also extended from Kounalakis et al. (1988), to provide both streamwise and radial distributions of mean and fluctuating radiation properties in the flames.

The paper begins with a brief description of experimental and theoretical methods. Predicted and measured radiant emission properties are then examined, considering mean and fluctuating values, probability density functions, and temporal power spectral densities of spectral radiation intensities.

Experimental Methods

Apparatus. The experimental methods were similar to those of Kounalakis et al. (1988); therefore, the following discussion will be brief. Carbon monoxide was injected vertically upward from a water-cooled burner (exit diameter of 5 mm) and burned in still air. The flames were attached at the burner exit using a small coflow of hydrogen and burned within a screened enclosure to reduce effects of room disturbances. The burner could be traversed to accommodate rigidly mounted optical instrumentation, with positioning accuracies in the horizontal and vertical directions of 0.1 and 1 mm.

Instrumentation. The structure of the test flames was measured by Gore et al. (1987b), including: time-averaged mean and fluctuating streamwise velocities, mean concentrations of major gas species, mean temperatures, mean spectral radiation intensities, and mean radiative heat fluxes. Aside from preliminary measurements to insure that earlier flame conditions had been reproduced, present measurements were limited to mean and fluctuating spectral radiation intensities.

Spectral radiation intensities were measured for horizontal chordlike paths through the flames at various heights above the burner exit. Two fields of view were used, having diameters of 5 and 10 mm at the flame axis and field angles of 0.6 and 1.2 deg. The larger path diameter was somewhat smaller than the smallest integral scale lengths of the turbulence (estimated to be ca. 15 mm) in the region where measurements were made. A 125 mm low-resolution monochormator (Oriel Model 7240), and a PbS detector (New England Photomultiplier, Series E2) operating at room temperature, were used for the measurements. Signal-to-noise ratios were improved using a chopper operating at 900 Hz with a detector output bandwidth limited by a second-order low-pass filter having a break frequency of 400 Hz. A combination of order-sorting filters and gratings yielded observations in the 1200–4000 nm wavelength range. The monochromator/detector system was calibrated at several temperatures, to assure system linearity, using a blackbody source (Infrared Industries, Model 463). Wavelength readings were calibrated using lines generated by the harmonics of a mercury lamp and a HeNe laser. Experimental uncertainties (95 percent confidence) of these measurements were less than 20 percent, and were repeatable within this range. In addition, the earlier measurements of time-averaged spectral radiation intensities of the flames by Gore et al. (1987b) were repeated within 10 percent.

Measurements of spectral radiation intensity fluctuations were limited to a wavelength of 2700 nm (with a resolution of 40 nm at half-peak transmission). This wavelength corresponds to a region of strong emission in the 2700 nm band of carbon dioxide, yielding signal-to-noise ratios on the order of 10^3.

Nomenclature

a = random variable defined by equations (6) and (8)
$C(s)$ = lateral correlation coefficient of mixture fraction fluctuations, equation (1)
C_e = ratio of integral to dissipation length scales, equation (2)
C_μ = turbulence model constant
d = burner exit diameter
$E_\lambda(n)$ = temporal power spectral density function of i_λ
f = mixture fraction
g = mean-squared mixture fraction fluctuations
i_λ = spectral radiation intensity
k = turbulence kinetic energy
L_e = integral length scale
n = frequency
$\tilde{P}(\phi)$, $\tilde{P}(\phi)$ = time- and Favre-averaged probability density functions of variable ϕ
r = radial distance
$R(t)$ = temporal correlation coefficient of mixture fraction fluctuations, equation (3)
Re = burner Reynolds number
s = distance along radiation path
t = time
t_e = integral time scale
u = streamwise velocity
x = height above burner
z = random variable related to mixture fraction, equation (5)
Δs = spatial interval along radiation path
Δt = time interval
ϵ = rate of dissipation of turbulence kinetic energy
λ = wavelength
ρ = density
ϕ_{ij} = weighting factors in stochastic simulations

Subscripts

c = property along flame axis
i, j, k = value at positions i, j, and k

Superscripts

$( )'$ = fluctuation with respect to time average
$(\overline{\ })$, $(\overline{\ })'$ = time-averaged mean and root-mean-squared fluctuating quantities
$(\tilde{\ })$ = Favre-averaged mean quantity

Test Conditions. The test flames were identical to earlier work; a summary of their properties appears in Gore et al. (1987b). Two flames were considered, having Reynolds numbers at the burner exit of 7640 and 13,150 and chemical energy release rates of 5.3 and 8.9 kW. The flames were turbulent with turbulence intensities of ca. 6 percent at the burner exit. Initial Richardson numbers were relatively low, ca 10^{-5}; however, the effects of buoyancy were significant since the surroundings were still. Overall radiative heat losses were small, 8–12 percent of the chemical energy release rate. The initial conditions needed for structure predictions were estimated from measurements of mean and fluctuating streamwise and radial velocities at $x/d=2$, as described by Gore et al. (1987b).

Structure and Radiation Predictions

Structure Predictions. Analysis of radiation properties was based on predictions of the scalar structure. Scalar property predictions were similar to the earlier study of carbon monoxide/air flames (Gore et al., 1987b) and will only be described briefly. A Favre-averaged k–ϵ–g turbulence model was used, following Bilger (1976). The flow was taken to be a steady axisymmetric low Mach number turbulent jet in an infinite stagnant environment, under the boundary-layer approximations. The exchange coefficients of all species and heat were assumed to be the same, typical of most turbulence models of flames. Since the test flames only lost 8–12 percent of their energy release by radiation, combined flow and radiation analysis was not undertaken; instead, radiation was treated as a perturbation by correcting the energy release of reaction by a fixed fraction at each mixture fraction, to account for radiative heat losses. Turbulence/buoyancy interactions were also ignored to simplify the formulation. Jeng et al. (1982) have shown that this approximation has little effect on mean scalar structure predictions; however, scalar property fluctuations are influenced to a greater degree and this approximation deserves additional study. Finally, the chemistry of carbon monoxide oxidation is fast for present conditions, justifying the assumption of local thermodynamic equilibrium so that all scalar properties are only functions of mixture fraction which are called state relationships (Gore et al. 1987b; Faeth and Samuelsen, 1986). This approximation was shown to be satisfactory by comparing measurements in laminar and turbulent flames with predictions based on thermodynamic equilibrium using the Gordon and McBride (1971) algorithm. The corresponding state relationships used during present calculations can be found from Gore et al. (1987b).

The governing equations and empirical constants were established by matching measurements in round turbulent constant and variable density noncombusting jets and can be found in Jeng and Faeth (1984b). Time- and Favre-averaged scalar properties were found using a clipped Gaussian Favre-averaged probability density function (PDF) of mixture fraction. This approximation is supported by recent measurements in turbulent wall plumes (Lai and Faeth, 1987), as well as earlier studies showing only small effects of the functional form of the PDF(f) on the scalar structure of turbulent flames (Lockwood and Naguib, 1975). Computations were carried out using the GENMIX algorithm of Spalding (1977), with numerical accuracy similar to past work.

Narrow-Band Model. Spectral radiation intensities were found by solving the equation of radiative transfer for optical paths and spectral ranges viewed by the monochromator. A narrow-band model was used, ignoring scattering, following Ludwig et al. (1973). This involves the Goody statistical narrow-band model, with the Curtiss–Godson approximation to account for absorption effects along inhomogeneous gas paths. The 2700 and 4300 nm gas bands of carbon dioxide were considered using the RADCAL algorithm of Grosshandler (1980).

Simplified Radiation Models. Similar to Kounalakis et al. (1988), two methods were used to find mean scalar properties along the radiation path when turbulence/radiation interactions were ignored: the mean scalar property and the mean mixture fraction methods. The mean scalar property method is based on time-averaged scalar properties along the path, which is the most widely used method to predict mean radiation levels from turbulent flames (see Gore and Faeth, 1987b, and references cited therein). However, this approach implies that scalar properties are statistically independent at each point, which is not correct, due to their strong correlations through the state relationships. The mean mixture fraction method allows for these correlations by using scalar properties from the state relationships at time-averaged mixture fractions along the path.

Stochastic Simulations

Statistical Properties. Turbulence/radiation interactions were considered by extending the stochastic simulation approach of Kounalakis et al. (1988). Two types of stochastic simulation were considered: (1) time-independent, where statistically independent realizations of the spatial variation of mixture fractions along the radiation path were simulated; and (2) time-dependent, where both spatial and temporal variations of mixture fraction along the radiation path were simulated. In each case, given the mixture fraction distribution along the radiation path at any instant, the state relationships provide all scalar properties along the path and spectral radiation intensities can then be found from the narrow-band radiation model. For the time-independent simulation, sufficient realizations were obtained to yield statistically significant moments and probability-density functions of i_λ. The time-dependent simulation yields a time series, $i_\lambda(t)$, which can also be averaged to provide moments and probability-density functions of i_λ; however, the time series can be processed to yield temporal correlations and power spectra of i_λ as well.

The stochastic simulations were designed to satisfy the time-averaged probability-density functions, and spatial and temporal (time-dependent simulation only) correlations, of mixture fraction at each point along the radiation path. The present test conditions require that these statistical properties be simulated for horizontal chord like paths through the flames. Unfortunately, none of the statistical properties needed for the stochastic simulations have been measured for the test flames; therefore, it was necessary to estimate these properties from the present structure predictions, supplemented by additional information from the literature.

As noted earlier, it is reasonable to approximate the Favre-averaged PDF of the mixture fraction, $\tilde{P}(f)$, as a clipped-Gaussian function, which can be found from the structure predictions, e.g., $\tilde{P}(f)$ is only a function of $\tilde{f}$ and g. The time-averaged PDF of the mixture fraction, $\bar{P}(f)$, is then found immediately since $P(f)=\bar{\rho}\tilde{P}(f)/\rho(f)$ (Bilger, 1976). $\tilde{P}(f)$ is somewhat skewed, since $\rho(f)$ is not constant; nevertheless, $\tilde{P}(f)$ can be approximated as a clipped-Gaussian function similar to $\tilde{P}(f)$ but with different moments.

The one-time/two-point spatial correlation coefficient of mixture-fraction fluctuations for points along the radiation path is defined as follows:

$$C(s,\Delta s)=\overline{f'(s,t)f'(s+\Delta s,t)}/\left(\overline{f'(s)}\ \overline{f'(s+\Delta s)}\right) \qquad (1)$$

Corrsin and Uberoi (1951) and Becker et al. (1967) have measured the symmetric spatial correlation function in turbulent constant-density jets (where the two points are located along a horizontal path through the axis at equal radial distances on opposite sides of the axis). They find that C

reaches zero when the points are an integral scale, L_e apart; reaches maximum negative values in the range -0.1 to -0.2 for spacings in the range L_e to $2L_e$; and then gradually decays to zero at larger spacings. The present radiation paths are also horizontal and integral scales do not vary greatly over the cross section of jets (Becker et al., 1967); therefore, C was assumed to have the functional form measured by Corrsin and Uberoi (1951) and Becker et al. (1967), for lack of other information.

In order to complete the prescription of the spatial correlation function, an estimate of L_e must be made. Similarly to Kounalakis et al. (1988), L_e was estimated by assuming that it was proportional to the local dissipation length scale, found from the turbulence model, as follows:

$$L_e = C_e C_\mu^{3/4} k^{3/2}/\epsilon \tag{2}$$

C_μ in equation (2) is a standard turbulence model constant while C_e is a new empirical constant that was optimized by matching measurements and predictions.

The time-dependent stochastic simulation also requires temporal correlations of mixture fracture fluctuations. Becker et al. (1967) and Birch et al. (1978) have measured one-point/two-time concentration fluctuation correlation coefficients in constant-density turbulent jets. They find that these correlation coefficients have an exponential from over the bulk of the flow, as follows:

$$R(s,\Delta t) = \overline{f'(s,t)f'(s,t+\Delta t)}/\overline{f'(s)^2} = \exp(-\Delta t/t_e) \tag{3}$$

where t_e is the temporal integral scale. This form was adopted for the present time-dependent simulations. The temporal integral scale was estimated by applying Taylor's hypothesis, as follows:

$$t_e = L_e/\tilde{u} \tag{4}$$

The present structure predictions were used to calculate t_e, finding L_e from equation (2) and approximating $\tilde{u}$ by $\tilde{u}$. The time-dependent simulation also requires two-point/two-time mixture fracture fluctuation correlations; the method used to estimate these properties will be considered later.

A simulation to find radiation fluctuations should be based entirely on time-averaged properties. Unfortunately, while the present structure model can provide estimates of $\tilde{P}(f)$, it only yields Favre-averaged values of k and ϵ and mean streamwise velocities for use in equations (2) and (4). Stårner and Bilger (1980) show the time- and Favre-averaged mean velocities are nearly identical in jet flames but they found significant differences between time- and Favre-averaged turbulence properties. The present approximations were adopted for lack of an alternative but they clearly deserve further study.

Finally, since f has a clipped-Gaussian probability density function, it is convenient for the simulations to define a corresponding Gaussian random variable z, and its moments, so that

$$f=z, \quad 0\le z\le 1; \qquad f=0, \quad z<0; \qquad f=1, \quad z>1 \tag{5}$$

Time-Independent Simulation. The time-dependent simulation is a simple generalization of the time-independent simulation; therefore, the time-dependent formulation will be presented in some detail. The approach is based on the statistical time-series techniques of Box and Jenkins (1976).

A number of points, not necessarily equally spaced, are selected along the radiation path so that the equation of transfer can be numerically integrated using the narrow-band model. Numbering the points in ascending order along the path, the following autoregressive process is used to find the fluctuation of z at point i (Box and Jenkins, 1976):

$$z_1' = \sum_{j=p}^{i-1} \phi_{ij} z_j' + a_i, \qquad 1\le p\le i-1 \tag{6}$$

where p is selected to eliminate points having small correlation coefficients with respect to point i. The ϕ_{ij} are weighting factors that multiply fluctuations found for previous points so that the simulation satisfies spatial correlations along the path. The parameter a_i is an uncorrelated Gaussian random variable (random shock) having a mean value of zero and selected so that the simulation satisfies $\tilde{P}(z)$ at point i.

To find the ϕ_{ij}, equation (6) is multiplied by z_k', $k=p, \ldots, i-1$, and expected values are taken over many realizations. This yields

$$\overline{z_i' z_k'} = \sum_{j=p}^{i-1} \phi_{ij} \overline{z_j' z_k'}; \qquad k=p, \ldots, i-1 \tag{7}$$

The term $\overline{a_i z_k'}$ does not appear in equation (7) since a_i is uncorrelated with z_k' for $k<i$. The $\overline{z_i' z_k'}$ are spatial correlations that were found by assuming that the spatial correlation coefficients of f and z were the same, even though their probability density functions differ. With the $\overline{z_i' z_k'}$ known, equations (7) provide $i-p$ linear algebraic equations needed to find the ϕ_{ij}. This system of equations has a symmetric positive definite matrix and can be readily solved using Cholesky factorization (Strang, 1986).

The variance of a_i is found in a similar manner. First of all, equation (7) is multiplied by a_i and then expected values are taken over many realizations. Recalling that $\overline{a_i z_k'} = 0$ for $k<i$, this yields $\overline{a_i z'} = \overline{a_i^2}$, i.e., the only portion of z_i' correlated with a_i is a_i itself. Finally, multiplying equation (6) by z_i', and taking expected values again, yields

$$\overline{a_i^2} = \overline{z_i'^2} - \sum_{j=p}^{i-1} \phi_{ij} \overline{z_j' z_i'} \tag{8}$$

where $\overline{a_i^2}$ can be found since all quantities on the right-hand side of equation (8) are known.

The simulation is initiated by making a random selection for point 1, noting that $z_i' = a_1$ from equation (6) and that $\overline{a_1^2} = \overline{z_1'^2}$ from equation (8). The regression relationships are then successively applied to find the remaining z_i' along the path. Finally, the f_i are found from equation (5), noting that $z_i = \bar{z}_i + z_1'$, followed by computation of spectral radiation intensities for this realization as described earlier.

The stochastic simulation was evaluated for present test conditions. It was found that $\bar{f}$ and $\overline{f'^2}$ were satisfied with 1 percent everywhere for 10^4 realizations. Simiarly $\overline{f_i' f_j'}$ were satisfied within 5 percent for $\Delta s/L_e < 3$, except near the edge of the flow where they were only satisfied within 15 percent. Discrepancies at large Δs involve conditions where the correlations are small and can be improved by using a larger number of realizations. Errors near the edge of the flow are caused by use of a Gaussian random variable z to represent a clipped-Gaussian random variable f in a region where intermittency is significant. This is an intrinsic difficulty; however, the region involved does not have a large effect on i_λ.

In addition to the full simulations of spatial correlations, approximate simulations were also undertaken with points along the radiation path spaced a distance L_e apart, noting that $C(L_e) = 0$ and assuming that spatial correlations were zero at larger separations as well. This implies that points along the radiation path are statistically independent, which is the same as past work in this laboratory (e.g., Kounalakis et al., 1988).

Time-Dependent Simulation. The previously computed points used in the regression relationship of equation (6) only enter the calculation through their correlations and can represent various positions and times. Thus, the time-dependent simulation also uses equations (6)–(8) after appropriately numbering the points to keep track of them in space and time. The linear system of equations used to find the ϕ_{ij} is also solved in the same manner as before.

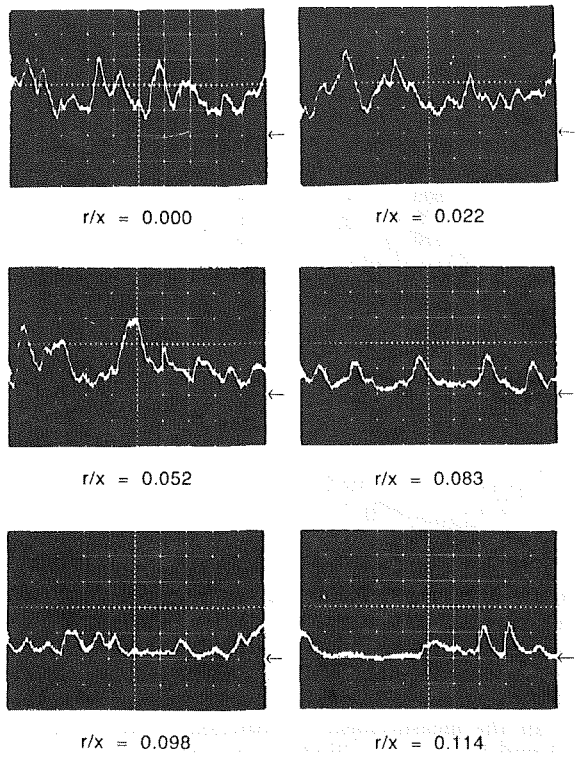

Fig. 1 Spectral radiation intensity signal at 2700 nm for horizontal chordlike paths through the flame (arrow denotes zero level; vertical scale, 1100 W/m^2 srμm per division; horizontal scale, 10 ms per division; Re = 13,150, $x/d = 65$)

The present simulations were designed to yield realizations of f along the radiation path at times Δt apart. The simulation was initiated by completing a realization along the path using the time-independent approach. The next realization, at Δt, was computed in the same manner but included all points in the first realization in the autoregressive process, equation (6). This process continued for subsequent times, including all previous points, until the temporal correlations were adequately represented. Subsequently, the points at the earliest time were dropped when calculations for the next time were begun.

The main new difficulty with the time-dependent simulation is that two-point/two-time correlations are required for the autoregressive process. Measurements of these properties for turbulent shear flows were not found in the literature; therefore, the following ad hoc expression was adopted for lack of an alternative:

$$\overline{f_i'(t) f_j'(t-k\Delta t)} = R_i(k\Delta t)\overline{f_i' f_j'} \tag{9}$$

Naturally, it would be just as plausible to use $R_j(k\Delta t)\overline{f_i' f_j'}$ on the right-hand side of equation (9) for a stationary turbulent flow. The difference between these two possibilities provides a crude measure of the potential errors resulting from use of equation (9). Referring to equations (3) and (4), and noting that L_e is relatively constant over a cross section of the flow (Becker et al., 1967), it is seen that potential errors are greatest in regions where $\bar{u}$ varies rapidly. Fortunately, spatial correlations become small within a separation distance L_e, and $\bar{u}$ doesn't vary greatly over such distances, which provides some justification for the present approach. In any event, this approximation had little effect on the computations, as discussed later.

Adopting equation (9) for two-point/two-time correlations yields a substantial simplification of the time-dependent simulation. Recalling that the temporal correlations of equation (3) are exponential in time, a derivation similar to Box and Jenkins (1976) for a pure time series with an exponential temporal correlation and stationary statistics can be carried out. The details are too lengthy to be shown here; however, the results are the same: $\phi_{ij} = 0$ for all points at times less than $t - \Delta t$. Thus, only the realization at $t - \Delta t$ must be retained while developing the realization at t, vastly reducing the storage and computational requirements of the simulation.

Analogous to the simplified time-independent simulation, simplified time-dependent calculations were undertaken using statistically independent points spaced a distance L_e apart along the radiation path. This reduces the simulation to a first-order (Markov) process in time at each point for an exponential temporal correlation yielding (Box and Jenkins, 1976):

$$z_i'(t) = R_i(\Delta t) z_i'(t-\Delta t) + a_i \tag{10}$$

where the variance of a_i is determined as follows:

$$\overline{a_i^2} = (1 - R_i(\Delta t)^2)\overline{z_i'^2} \tag{11}$$

This simulation is identical to the approach used by Kounalakis et al. (1988).

The accuracy of the time-dependent simulations was the same as the time-independent simulation with respect to $\bar{f}, \bar{f}'$, and the spatial correlations, and the properties were similar with respect to number of realizations and position in the flow. Discrepancies for temporal correlations were similar to the spatial correlations and the findings of Kounalakis et al. (1988). In order to satisfy the Nyquist sampling criterion when finding temporal power spectra of i_λ at the highest frequencies of interest, it was necessary to choose $\Delta t/t_e$ ca. 0.002 at the lowest velocity segment of the path.

Initial Observations and Calibrations

Observations. Measurements of spectral radiation intensities at 2700 nm were made in the two carbon monoxide/air flames studied by Gore et al. (1987b). Horizontal, chordlike paths through the flames were considered at $x/d = 35$, 50, and 65. The first two positions are near the flame tip (defined as the point where the mean mixture fraction along the axis is stoichiometric), and the last position is after the flame tip. Although the 2700 nm line is strong, transmittivities through the present laboratory flames were in the range 85–90 percent; therefore, the radiation process was essentially optically thin. The earlier results for hydrogen/air flames also involved optically thin conditions (Kounalakis et al., 1988).

Data traces of spectral radiation intensity as a function of time are illustrated in Fig. 1. These results are for a 10-mm-dia. radiation path at various radial distances from the flame axis for Re = 13,150 and $x/d = 65$; however, they are typical of other conditions. This position is beyond the flame tip so that maximum temperatures and carbon dioxide concentrations are at the axis. Spectral radiation intensities for paths crossing the flame near the axis ($r/x \leq 0.052$) generally have high values and never reach the baseline, indicating that there is always some radiating gas along these paths, i.e., radiation intermittencies are small. In this region, peak radiation levels remain about the same, while minimum and mean radiation levels decrease with increasing radial distance, tending to increase radiation fluctuation intensities ($\overline{i_\lambda'}/\bar{i}_\lambda$). Radiation fluctuation levels are still large for paths through the axis, however, reaching values on the order of 50 percent. When $r/x \geq 0.083$, spectral radiation intensities reach zero at times, indicating finite levels of radiation intermittency. Intermittency increases with increasing radial distance, which is qualitatively similar to intermittency for other scalar properties in turbulent jet flows (Becker et al., 1967).

Calibration of C_e. The integral length-scale parameter C_e in equation (2) was fitted by matching predictions and

Table 1 Mean and fluctuating Spectral Radiation Intensities[a]

x/d	$\bar{i}_\lambda$, W/m^{2}srμm				$\bar{i}'_\lambda/\bar{i}_\lambda$ (percent)	
	Measured[b]	Predicted[c] (stochastic)	Predicted[d] (mean prop)	Predicted[d] (mean f)	Measured[b]	Predicted[c] (stochastic)
Re = 7640:						
35	2400, 2600	3400	3000	3900	25, 24	26
50	2300, 2100	2600	1900	2100	33, 38	42
65	1400, 1300	1300	600	650	51, 50	69
Re = 13,150						
35	2500, 2700	3600	3200	4100	20, 19	25
50	2800, 2700	2900	2200	2500	26, 27	38
65	2000, 1600	1600	810	850	36, 39	62

[a]At a wavelength of 2700 nm with a resolution (half-peak transmission) of 40 nm.
[b]Results for 10 and 5 mm diameter radiation paths, respectively.
[c]Infinitely small path diameter and $C_e = 5.0$.
[d]Infinitely small path diameter.

measurements of radiation fluctuation intensities and temporal power spectra for radiation paths through the axis. The effect of varying C_e in the range 1–7 was similar to the findings of Kounalakis et al. (1988) for hydrogen/air flames: C_e had little influence on predictions of mean spectral radiation intensities, increasing C_e caused a proportional increase in predictions of radiation fluctuation intensities, and increasing C_e caused more signal energy of the temporal power spectral densities of spectral radiation intensity fluctuations to be concentrated at low frequencies. The best match between present predictions and measurements was achieved using $C_e = 5.0$, rather than $C_e = 6.6$ found earlier by Kounalakis et al. (1988). The difference between these values is small in comparison to the uncertainties of the analysis and no fundamental variation of C_e with experimental conditions should be inferred. Values of C_e in the range 5–7 imply 4–6 characteristic eddies along a horizontal radial path through the flame axis for both the carbon monoxide and hydrogen/air flames. This is plausible, since roughly the same number of integral concentration length scales are observed for similar paths in turbulent round jets (Becker et al., 1967; Birch et al., 1978).

Spatial Correlations. The effect of the fit of the spatial correlations was considered for both the time-independent and time-dependent simulations. Calculations were completed for conditions ranging from the simplified simulations (using statistically independent points along the path, which corresponds to two-point fits of the spatial correlations) up to densely spaced points along the path so that the spatial correlations were fitted by 20 points. The effect of carefully fitting the spatial correlations was remarkably small: the more exact fit caused negligible changes in mean values, fluctuations, and probability-density functions of spectral radiation intensities, while temporal power spectra at the highest frequencies considered were only reduced by about 5 percent. *Present results were for optically thin conditions; however,* Grosshandler and Joulain (1986) also found that radiation fluctuations were relatively insensitive to the wave form of scalar property variations along a radiation path for both optically thin and thick conditions.

Results and Discussion

Properties Along Axis. Measured and predicted mean and fluctuating spectral radiation intensities along the axis at $x/d = 35$, 50, and 65 are summarized in Table 1. Measurements include optical path diameters of 5 and 10 mm; however, differences between results for the two path diameters are comparable to experimental uncertainties and do not differ in any consistent pattern. This behavior was generally observed for other measured radiation properties, which is reasonable since both path diameters were somewhat smaller than the smallest integral scales (ca. 15 mm) for the range of the measurements. Predictions were obtained for $C_e = 5$ and represent the limit of an infinitely small diameter path.

Measured mean spectral radiation intensities in Table 1 are highest near the flame tip ($x/d = 35$ and 50) and then decrease beyond the flame tip ($x/d = 65$). The high values occur near the flame tip since a large fraction of the radiation path involves conditions near the stoichiometric mixture fraction where radiant emission levels are highest. Beyond the flame tip, however, radiant emission decreases with increasing distance from the burner due to reduced temperatures and carbon dioxide concentrations as the flow is diluted by mixing.

Measured radiation fluctuation intensities in Table 1 are never less than 20 percent and increase monotonically with increasing height above the burner, reaching values near 50 percent at $x/d = 65$. Kounalakis et al. (1988) observed the same trend for their hydrogen/air flames except that radiation fluctuation intensities were generally higher, reaching values near 100 percent just beyond the flame tip (which was at x/d ca. 90 for these flames). This is not unexpected since mean radiation levels are less influenced by turbulence for carbon monoxide flames than for hydrogen flames (Gore et al., 1987b). Specific reasons for this behavior are not known but may be related to the higher stoichiometric mixture fraction for carbon monoxide than hydrogen flames (0.29 in comparison to 0.028). This tends to reduce relative levels of mixture fraction fluctuations near strongly radiating stoichiometric conditions, tending to reduce radiation fluctuations as well.

The comparison between stochastic predictions and measurements in Table 1 is encouraging; trends with respect to position and flame Reynolds number are predicted quite well, and average differences between predictions and measurements are less than 30 percent, which is similar to the findings for hydrogen/air flames (Kounalakis et al., 1988). Errors between stochastic predictions and measured mean spectral radiation intensities are largest near the burner exit, $x/d = 35$, while errors for radiation fluctuation intensities are largest far from the burner, $x/d = 65$. In both instances, this reflects conditions where the predicted quantity is particularly sensitive to variations in streamwise position, and/or mixing predictions; therefore, the deficiences of the structure predictions are probably largely responsible for the difficulties. Another factor could be differences in spatial and temporal correlations from

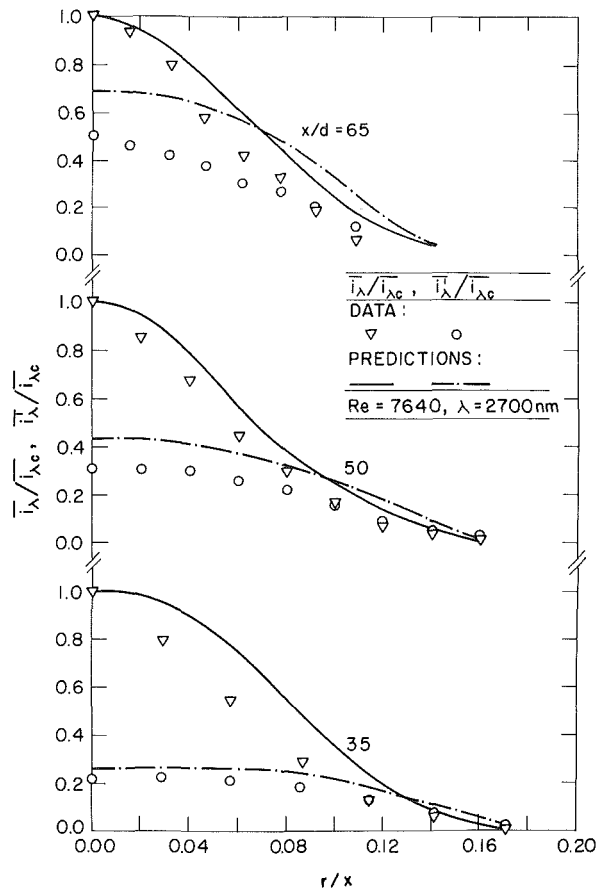

Fig. 2 Radial profiles of mean and fluctuating spectral radiation intensities at 2700 nm for chordlike paths; Re = 7640

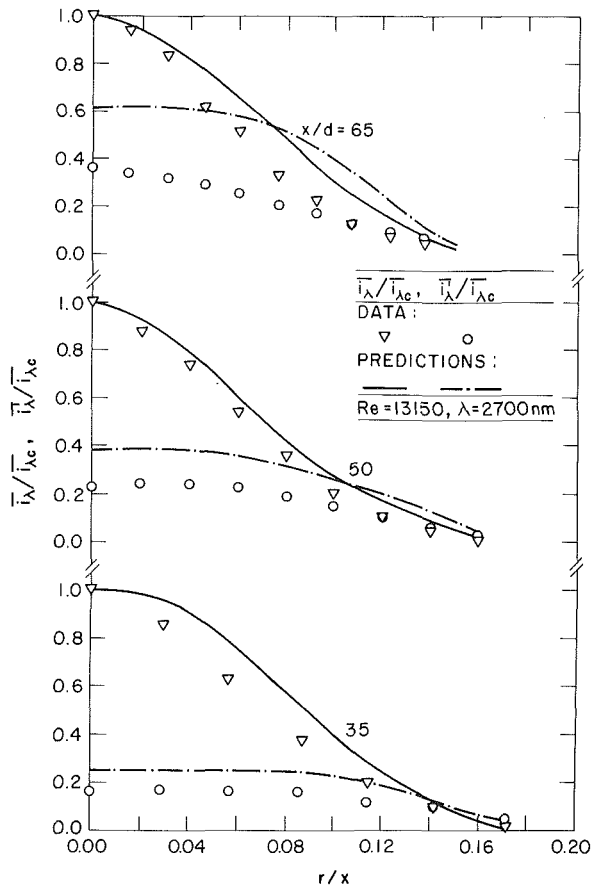

Fig. 3 Radial profiles of mean and fluctuating spectral radiation intensities at 2700 nm for chordlike paths; Re = 13,150

estimates used in the predictions. Measurements of these properties are needed to resolve this possibility.

The average errors of mean spectral radiation intensity predictions of the two mean property methods (see Table 1) are roughly twice as large as the stochastic method (31–38 percent as opposed to 19 percent). These differences are smaller than observed by Kounalakis et al. (1988) for hydrogen flames, which is expected based on past observations that effects of turbulence/radiation interactions are smaller for carbon monoxide than hydrogen flames due to differences in their turbulent scalar structure (Gore et al., 1987b). Predictions based on mean properties are generally less than stochastic predictions since mean property predictions are biased downward due to the nonlinear increase of radiant emission with temperature. The mean mixture fraction method gives a less consistent bias with respect to stochastic predictions showing that effects of correlations between scalar properties are important; however, this approach does not yield significant improvement of predictions in comparison to the mean property method for present test conditions. It appears that effects of turbulence/radiation interactions must be considered for accurate predictions of mean radiation levels from turbulent flames.

Radial Profiles. Predicted and measured radial variations of $\bar{i}_\lambda$ and $\bar{i}_\lambda'$, both normalized by $\bar{i}_{\lambda c}$, are illustrated in Figs. 2 and 3 for the two flames. Radial distances are plotted as r/x, the radial similarity variable for turbulent jet and plumes, to allow evaluation of estimates of flow widths. These measurements involve horizontal chordlike paths through the flames at various radial distances from the axis and heights above the burner exit. Finite levels of both radiation properties are observed out to r/x ca. 0.15, which corresponds to typical widths of scalar property variations in jet flames (Jeng and Faeth, 1984a, 1984b; Jeng et al., 1982; Lockwood and Naguib, 1975). Values of $\bar{i}_\lambda'/\bar{i}_{\lambda c}$ decrease with increasing radial distance, but much of the reduction near the edge of the flow is due to increasing radiation intermittancy, as can be seen from the results illustrated in Fig. 1. In general, the properties illustrated in Figs. 2 and 3 are qualitiatively similar to properties like velocity and mixture fraction in flames, when these properties are normalized in the same manner. The main exception is the progressive increase in $\bar{i}_\lambda'/\bar{i}_{\lambda c}$ with increasing height above the burner, which was discussed earlier. Another difference is the tendency for radiation fluctuations to have a much flatter profile near the axis before the flame tip ($x/d = 35$) than after the flame tip ($x/d = 65$). This behavior follows since the flame zone, which contributes most to the spectral radiation intensity, is located off-axis below the flame tip. The trends of the predictions are in good agreement with the measurements. The quantitative accuracy of the predictions is also encouraging, generally paralleling results along the axis discussed in connection with Table 1.

Probability Density Functions. Predicted and measured probability density functions of i_λ, for horizontal chord like paths through the axis, are illustrated in Figs. 4 and 5 for the two flames. Far from the burner, the PDFs are skewed, with the most probable value of i_λ being less than $\bar{i}_\lambda$. This is an effect of intermittency, since low mixture fractions yield conditions that contribute very little to $\bar{i}_\lambda$, similar to the results illustrated in Fig. 1. The predictions represent measured PDFs reasonably well, except at the highest position where the effect of skewness is overestimated. This discrepancy is also probably due to problems with the structure predictions, which

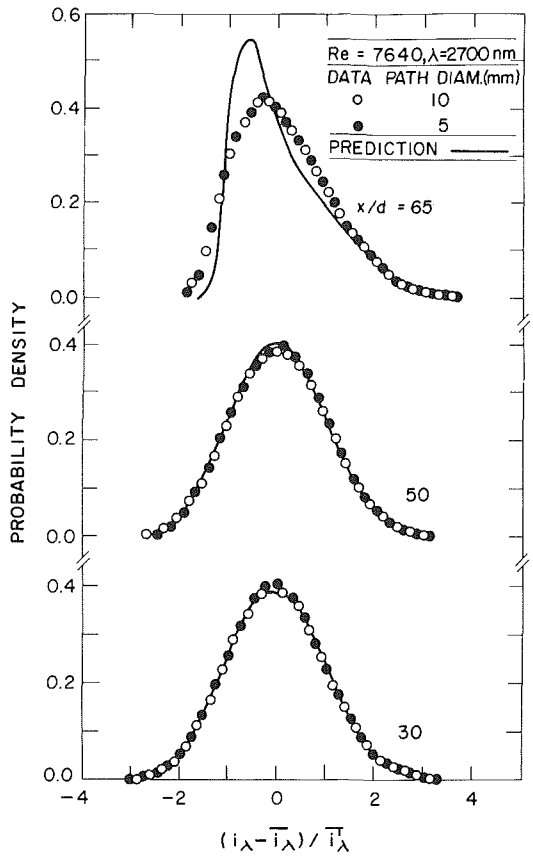

Fig. 4 Measured and predicted probability density functions of spectral radiation intensities at 2700 nm for chordlike paths through the axis; Re = 7640

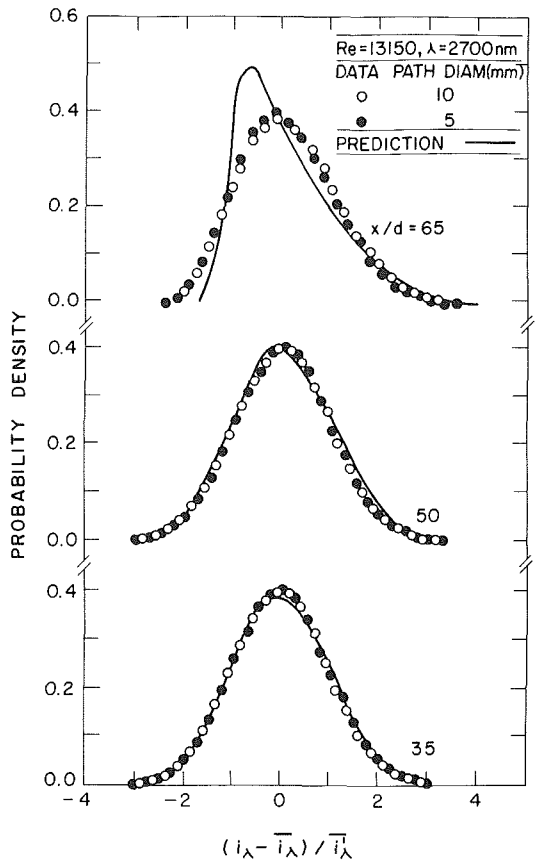

Fig. 5 Measured and predicted probability density functions of spectral radiation intensities at 2700 nm for chordlike paths through the axis; Re = 13,150

causes a similar overestimation of spectral intensity fluctuations at this position seen in Table 1 and in Figs. 2 and 3.

Power Spectra. Predicted and measured power spectra of radiation fluctuations are plotted as a function of frequency, both normalized by the characteristic frequency, $\bar{u}_c/x$, in Figs. 6 and 7. The power spectra are typical of other turbulence properties: exhibiting an energy-containing region with nearly constant $E_\lambda(n)$, at low frequencies; and an inertial-like region, where $E_\lambda(n)$ decays with increasing frequency, at high frequencies. At the highest frequencies, the rate of decay of the spectra becomes more rapid, suggesting approach to a high-frequency cutoff associated with a radiation microscale; however, present, signal-to-noise ratios were not high enough to define cutoff frequencies and scales accurately. Normalized break frequencies between the energy-containing and inertial regions tend to increase with increasing x/d, approaching values near unity at $x/d = 65$. It is probably fortuitous that the normalized break frequency approaches unity for the largest x/d considered during present measurements; however, the upward shift in the normalized break frequency near the burner can be explained by considering flame structure. In all regions, the highest-temperature portion of the flow provides the greatest contribution to spectral radiation intensities. Near the burner, these regions correspond to near-stoichiometric conditions near the flame sheet, which is located near the edge of the flow where local velocities are much smaller than at the axis. Integral length scales, however, are relatively constant across the width of the flow; thus, the most important contributions to radiation fluctuations are controlled by integral time scales, $t_e = L_e/\bar{u}$, that are longer than characteristic times related to the velocity at the axis. Near the flame tip and beyond, however, the maximum temperature region, which has the greatest contribuion to spectral radiation intensities, is along the axis where velocities are highest; therefore, the most important contributions to radiation fluctuations are controlled by shorter integral time scales and higher normalized break frequencies are expected for these conditions.

The rate of decay of the spectra in the inertial-like region is relatively large in comparison to the inertial range of the other turbulence properties, ca. $n^{-5/2}$ instead of $n^{-5/3}$, similar to observations for hydrogen/air flames (Kounalakis et al., 1988). This behavior is difficult to interpret since the radiation measurements involve the temporal variation of properties along a path across the entire width of the flow. The tendency for effects of scalar fluctuations on radiation properties to integrate out after ten or so spatial wavelengths may be a factor in the relatively fast truncation of high-frequency phenomena. Furthermore, the finite diameter of the optical path for the measurements is a contributing factor, since high-frequency effects require small spatial scales, which tend to be averaged out over the path crossection. The somewhat more rapid decay rate of the measurements for the larger diameter path provides experimental evidence for this effect.

The hydrogen flames exhibited a relatively prominent peak in the temporal power spectra, particularly in the region near the burner exit for the lowest Reynolds number flame (Kounalakis et al., 1988). This behavior was attributed to large-scale unsteady pulsations of the flow, which are often observed when effects of buoyancy are large in flames. Similar peaks are not observed in the spectra for the carbon monoxide flames illustrated in Figs. 6 and 7. This is supportive of the buoyancy hypothesis since the burner Reynolds numbers are roughly two times larger for carbon monoxide flames than for the hydrogen flames, tending to reduce effects of buoyancy at all locations in the high-temperature region of the flow. Fur-

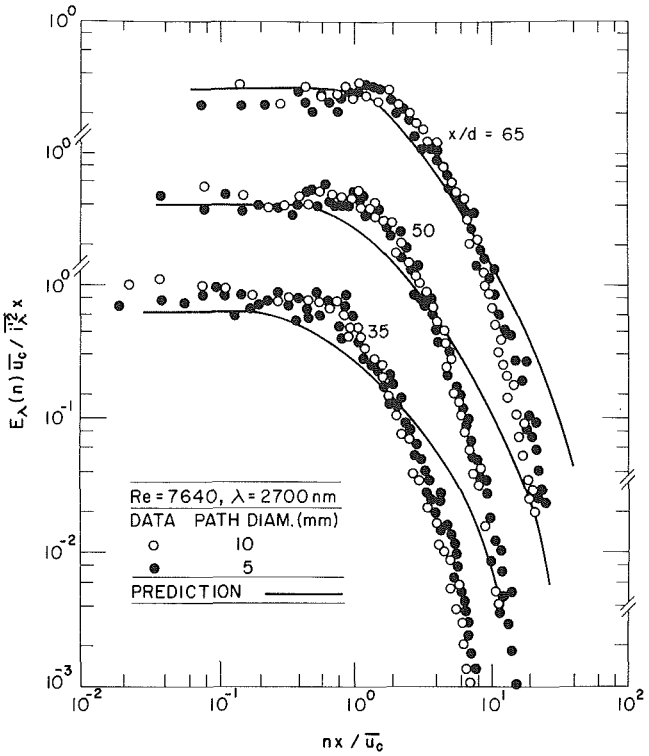

Fig. 6 Measured and predicted power spectral densities of spectral radiation intensities at 2700 nm for chordlike paths through the axis; Re = 7640

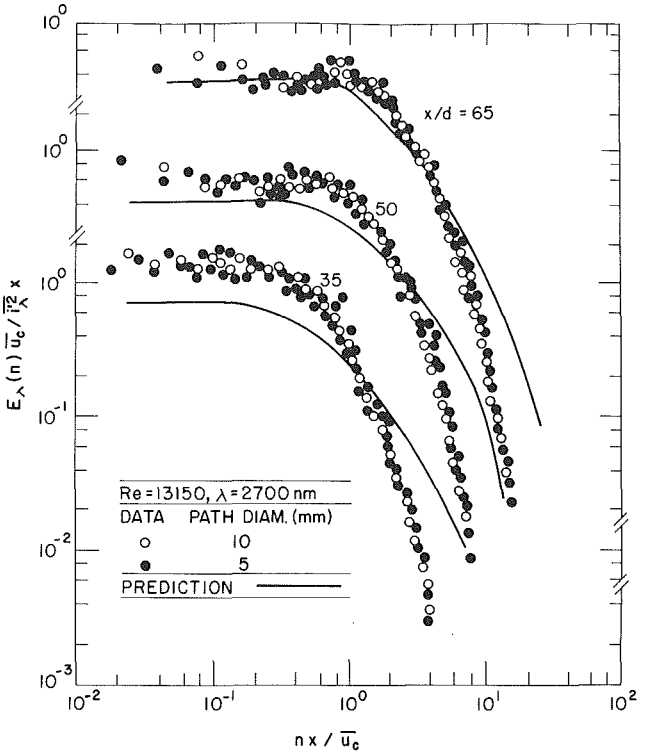

Fig. 7 Measured and predicted power spectral densities of spectral radiation intensities at 2700 nm for chordlike paths through the axis; Re = 13,150

thermore, the higher stoichiometric mixture fraction of carbon monoxide flames tends to keep the strongly radiating region near the flame sheet nearer to the axis, in comparison to hydrogen flames, similarly reducing the effects of buoyancy, which are largest near the edge of the flow.

The comparison between predicted and measured power spectra in Figs. 6 and 7 is encouraging, particularly since parameters in the simulation were based on structure predictions using a turbulence model. Break frequencies, and their shift toward higher values of $nx/\bar{u}_c$ with increasing x/d, are predicted reasonably well. The main deficiencies are underestimation of the slope of most of the decaying position of the spectra near the burner exit, and underestimation of rate decay of the measured spectra near the cutoff frequencies far from the burner exit. Notably, similar trends were observed for hydrogen/air flames, although these spectra also had additional complications due to pulsatile effects at low burner Reynolds numbers (Kounalakis et al., 1988). Difficulties with the measurements may explain part of the problem: The finite diameter of the radiation path tends to average higher frequency portions of the spectra spatially. This effect should influence a larger portion of the spectra near the burner where spatial scales are smallest, but to be confined to the high frequency end of the spectra far from the burner, generally as observed in Figs. 6 and 7. Another possibility involves present estimates of the statistical properties of mixture fraction fluctuations used in the stochastic simulations. More information on these properties is clearly needed in order to reduce uncertainties in estimates of effects of turbulence/radiation interactions.

Conclusions

Turbulence/radiation interactions in nonpremixed buoyant carbon monoxide/air jet flames were studied theoretically and experimentally. The main conclusions are as follows:

1 Turbulence/radiation interactions influence mean radiation levels of carbon monoxide flames but to a lesser extent than hydrogen flames, in agreement with the earlier observations of Gore et al. (1987b); nevertheless, radiation fluctuation intensities of 20–50 percent were observed for carbon monoxide flames, providing direct evidence of significant interactions between turbulence and radiation properties (turbulence/radiation interactions).

2 Power spectra of radiation fluctuations exhibit an energy-containing range for $nx/\bar{u}_c$ typically less than unity, with lower break frequencies observed before the flame tip; and an inertial-like range for frequencies greater than the break frequency, where spectra decay according to $n^{-5/2}$. Spatial averaging of radiation phenomena is probably responsible for the faster truncation of high-frequency, small spatial-scale phenomena than is generally observed for other scalar properties in turbulent flames.

3 Predictions of mean spectral radiation intensities were relatively independent of the integral length scales used in the stochastic simulation; however, predicted radiation fluctuations increase as integral length scales are increased. Length scales comparable to past measurements of integral length scales gave best agreement between predictions and measurements, suggesting that the largest turbulent structures in flames dominate effects of radiation fluctuations.

4 The present stochastic simulations were relatively independent of the actual shape of the spatial correlations of mixture fraction fluctuations with two-point fits (statistically independent points) giving nearly the same results as 20-point fits for the present optically thin flames. This agrees with Grosshandler and Joulain (1986), who found that radiation fluctuations were relatively insensitive to the wave form of scalar property variations for a range of optical depths.

5 Differences between predicted and measured mean and fluctuating spectral radiation intensities averaged less than 30 percent, with generally similar agreement for probability density functions and power spectra of radiation fluctuations. This agreement is similar to earlier findings for hydrogen

flames (Kounalakis et al., 1988), and is encouraging in view of the anticipated uncertainties of the structure predictions, the narrow-band radiation model, present estimates of the statistical properties of mixture-fraction fluctuations, and the measurements. Additional development of the stochastic simulation approach appears to be warranted, with particular emphasis on the statistical properties of mixture fraction fluctuations.

Acknowledgments

This research was supported by the Center for Fire Research of the National Bureau of Standards, Grant No. 60NANB5D0576, with B. J. McCaffrey and D. Evans serving as NBS Scientific Officers.

References

Becker, H. A., Hottel, H. C., and Williams, G. C., 1967, "The Nozzle-Fluid Concentration Field of the Round, Turbulent, Free Jet," *J. Fluid Mech.*, Vol. 30, pp. 285–303.

Bilger, R. W., 1976, "Turbulent Jet Diffusion Flames," *Prog. Energy Combust. Sci.*, Vol. 1, pp. 87–109.

Bilger, R. W., 1977, "Reaction Rates in Diffusion Flames," *Combust. Flame*, Vol. 30, pp. 277–284.

Birch, A. D., Brown, D. R., Dodson, M. G., and Thomas, J. R., 1978, "The Turbulent Concentration Field of a Methane Jet," *J. Fluid Mech.*, Vol. 88, pp. 431–449.

Box, G. E. P., and Jenkins, G. M., 1976, *Time Series Analysis*, Holden-Day, San Francisco, CA, pp. 51–66.

Corrsin, S., and Uberoi, M. S., 1951, "Spectra and Diffusion in a Round Turbulent Jet," NACA Report No. 1040.

Cox, G., 1977, "On Radiant Heat Transfer in Diffusion Flames," *Combust. Sci. Tech.*, Vol. 17, pp. 75–78.

Faeth, G. M., and Samuelsen, G. S., 1986, "Fast-Reaction Nonpremixed Combustion," *Prog. Energy Combust. Sci.*, Vol. 12, pp. 305–372.

Fischer, S. J., Hardouin-DuParc, B., and Grosshandler, W. L., 1987, "The Structure and Radiation of an Ethanol Pool Fire," *Combust. Flame*, Vol. 70, pp. 291–306.

Gordon, S., and McBride, B. J., 1971, "Computer Program for Calculation of Complex Chemical Equilibrium Compositions, Rocket Performance, Incident and Reflected Shocks and Chapman-Jouguet Detonations," NASA SP-273.

Gore, J. P., and Faeth, G. M., 1986, "Structure and Spectral Radiation Properties of Turbulent Ethylene/Air Diffusion Flames," *Twenty-First Symposium (International) on Combustion*, The Combustion Institute, Pittsburgh, pp. 1521–1531.

Gore, J. P., and Faeth, G. M., 1988, "Structure and Radiation Properties of Luminous Turbulent Acetylene/Air Diffusion Flames," ASME JOURNAL OF HEAT TRANSFER, Vol. 110, pp. 173–181.

Gore, J. P., Jeng, S.-M., and Faeth, G. M., 1987a, "Spectral and Total Radiation Properties of Turbulent Hydrogen/Air Diffusion Flames," ASME JOURNAL OF HEAT TRANSFER, Vol. 109, pp. 165–171.

Gore, J. P., Jeng, S. -M., and Faeth, G. M., 1987b, "Spectral and Total Radiation Properties of Turbulent Carbon Monoxide/Air Diffusion Flames," *AIAA J.*, Vol. 25, pp. 339–345.

Gore, J. P., Faeth, G. M., Evans, D., and Pfenning, C., 1987c, "Structure and Radiation Properties of Large-Scale Natural Gas/Air Diffusion Flames," *Fire and Materials*, Vol. 10, pp. 161–169.

Grosshandler, W. L., 1980, "Radiative Heat Transfer in Nonhomogeneous Gases: A Simplified Approach," *Int. J. Heat Mass Trans.*, Vol. 23, pp. 1447–1457.

Grosshandler, W. L., and Joulain, P., 1986, "The Effect of Large-Scale Fluctuations on Flame Radiation," *Prog. Astro. Aero*, Vol. 105, Part II, AIAA, Washington, pp. 123–152.

Grosshandler, W. L., and Vantelon, J. P., 1985, "Predicting Soot Radiation in Laminar Diffusion Flames," *Combust. Sci. Tech.*, Vol. 44, pp. 125–141.

Jeng, S.-M., and Faeth, G. M., 1984a, "Radiative Heat Fluxes Near Turbulent Buoyant Methane Diffusion Flames," ASME JOURNAL OF HEAT TRANSFER, Vol. 106, pp. 886–888.

Jeng, S.-M., and Faeth, G. M., 1984b, "Species Concentrations and Turbulence Properties in Buoyant Methane Diffusion Flames," ASME JOURNAL OF HEAT TRANSFER, Vol. 106, pp. 721–727.

Jeng, S.-M., and Faeth, G. M., 1984c, "Predictions of Mean Scalar Properties in Turbulent Propane Diffusion Flames," ASME JOURNAL OF HEAT TRANSFER, Vol. 106, pp. 891–893.

Jeng, S.-M., Chen, L.-D., and Faeth, G. M., 1982, "The Structure of Buoyant Methane and Propane Diffusion Flames," *Nineteenth Symposium (International) on Combustion*, The Combustion Institute, Pittsburgh, pp. 349–358.

Jeng, S.-M., Lai, M.-C., and Faeth, G. M., 1984, "Nonluminous Radiation in Turbulent Buoyant Axisymmetric Flames," *Combust. Sci. and Tech.*, Vol. 40, pp. 41–43.

Kabashnikov, V. P., and Kmit, G. I., 1979, "Influence of Turbulent Fluctuations on Thermal Radiation," *Appl. Spect.*, Vol. 31, pp. 963–967.

Kounalakis, M. E., Gore, J. P., and Faeth, G. M., 1988, "Turbulence/Radiation Interactions in Nonpremixed Hydrogen/Air Flames," *Twenty-Second Symposium (International) on Combustion*, The Combustion Institute, Pittsburgh, pp. 1281–1290.

Lai, M.-C., and Faeth, G. M., 1987, "Turbulence Structure of Vertical Adiabatic Wall Plumes," ASME JOURNAL OF HEAT TRANSFER, Vol. 109, pp. 663–670.

Lockwood, F. C., and Naguib, A. S., 1975, "The Predictions of the Fluctuations in the Properties of Free, Round-Jet, Turbulent Diffusion Flames," *Combust. Flame*, Vol. 24, pp. 109–124.

Ludwig, C. B., Malkmus, W., Reardon, J. E., and Thomson, J. A., 1973, *Handbook of Infrared Radiation From Combustion Gases*, NASA SP-3080.

Markstein, G. H., 1981, "Scanning-Radiometer Measurements of the Radiance Distribution in PMMA Pool Fires," *Eighteenth Symposium (International) on Combustion*, The Combustion Institute, Pittsburgh, pp. 537–547.

Porscht, R., 1975, "Studies on Characteristic Fluctuations of Flame Radiation Emitted by Fires," *Combust. Sci. and Tech.*, Vol. 10, pp. 73–84.

Spalding, D. B., 1977, *GENMIX: A General Computer Program for Two-Dimensional Parabolic Phenomena*, Pergamon Press, Oxford.

Ståarner, S. H., and Bilger, R. W., 1980, "Measurements of Scalar-Velocity Correlations in a Turbulent Diffusion Flame," *Eighteenth Symposium (International) on Combustion*, The Combustion Institute, Pittsburgh, pp. 921–930.

Strang, G., 1986, *Introduction to Applied Mathematics*, Wellesley-Cambridge Press, Wellesley, MA, pp. 15–31.

A Study of Heat Transfer and Particle Motion Relative to the Modified Chemical Vapor Deposition Process

M. Choi[1]

R. Greif

Department of Mechanical Engineering,
University of California at Berkeley,
Berkeley, CA 94720

H. R. Baum

Center for Fire Research,
National Institute of Standards and Technology,
Gaithersburg, MD 20899

Heat transfer and particle motion relative to the modified chemical vapor deposition process have been studied for general values of the torch speed. Three-dimensional temperature fields have been obtained over the entire cross section of the tube and the effects of tube rotation and localized torch heating in the axial and circumferential directions have been studied. The particle trajectories have been calculated from a formulation that includes the contributions from forced flow, i.e, Poiseuille flow in the axial direction, rigid body rotation about the tube axis, and thermophoretic contributions in the axial, radial, and angular directions. The particle trajectories are helices and are shown to be strongly dependent on the tube rotation.

Introduction

Much effort has been expended on the utilization of low-loss silica-based fibers as a transmission medium for light wave communication systems. The Modified Chemical Vapor Deposition (MCVD) process (MacChesney et al., 1974a, 1974b; Nagel et al., 1982) is widely used for the manufacture of high-quality optical fibers because of its relative simplicity, flexibility, and versatility. In the MCVD process, a controlled high-purity gas mixture of $SiCl_4$ with various dopants such as $GeCl_4$ and fluorinated hydrocarbons is passed into a rotating fused silica tube with pure oxygen (Li, 1985; Jablonowsky et al., 1987). The reagents are heated while flowing. When high temperatures are reached a homogeneous gas phase reaction takes place, which results in the formation of submicron particles. Some of the particles are deposited on the inner wall of the tube and subsequent heating from the moving torch fuses the deposited material, which forms a glassy film (Walker et al., 1980b). In MCVD, particle deposition is believed to result from thermophoresis (Simpkins et al., 1979; Walker et al., 1980a). After a number of layers are deposited, the temperature of the transversing burner is increased and the tube is collapsed to a rod, which is called a preform of the fiber. The preform is then drawn to, typically, a 125 μm diameter fiber (Paek, 1975). It is noted that laser enhancement of thermophoresis has been studied including the effects of buoyancy and variable properties (Wang et al., 1985; Morse et al., 1985, 1986; DiGiovanni et al., 1985).

Most studies of the MCVD process have neglected the effects of tube rotation and circumferential heating of the torch. Recent three-dimensional studies of heat transfer and particle motion for a fast-moving torch (Choi et al., 1987a, 1987b, 1989) have shown that the effects of tube rotation, circumferential heating of the torch, and variable properties are important for this limiting case. For completeness, it is noted that Yuen (1984) and Patula (1981) analyzed two-dimensional steady-state heat transfer in a rotating cylinder with a circumferential variation of the tube wall temperature with respect to the rolling process.

The speed of the torch is an important parameter with respect to the formation of particles and their subsequent trajectories and deposition. Previous studies by the authors (Choi et al., 1987a, 1989) have been limited to large values of the torch speed, which restricts the thermal effects to a boundary layer region near the rotating tube. However, for small and moderate values of the torch speed, which are the conditions of the greatest practical importance, the thermal effects extend to the center of the tube and the entire cross section must then be considered. The present study is valid for all values of the torch speed and the thermal effects now properly extend over the entire cross section of the tube. Of particular interest are the effects of tube rotation and localized heating on the heat transfer, particle trajectories, and deposition for general values of the torch speed.

Analysis

In the present study, the following assumptions are made:

1 The density and thermal conductivity of the gas are constant.

2 Axial conduction is negligible compared with axial convection (Walker et al., 1980a).

3 Natural convection is neglected (Simpkins et al., 1979; Metais et al., 1964).

4 The flow is fully developed with the Poiseuille velocity distribution in the axial direction and rigid body rotation, with an angular velocity Ω about the tube axis.

5 The torch speed U_o is constant and the study is limited to large times, i.e., quasi-steady-state conditions exist in a reference frame that moves with the torch.

Using the moving coordinate $\tilde{\xi}$ defined by $\tilde{\xi}=x/a-U_o t/a$ and $\tilde{r}=r/a$, the following three-dimensional energy equation is obtained:

$$\left(2\frac{U_{av}}{U_o}(1-\tilde{r}^2)-1\right)\frac{\partial H}{\partial\tilde{\xi}}+\Gamma\frac{\partial H}{\partial\theta}=\frac{1}{\mathrm{Pe}}\left\{\frac{1}{\tilde{r}}\frac{\partial}{\partial\tilde{r}}\left(\tilde{r}\frac{\partial H}{\partial\tilde{r}}\right)+\frac{1}{\tilde{r}^2}\frac{\partial^2 H}{\partial\theta^2}\right\} \quad (1)$$

The boundary conditions are given by

$$H(\tilde{\xi},0,\theta)=\text{finite} \quad (2a)$$

$$H_w=H_M f(\tilde{\xi},\theta) \quad \text{at} \quad \tilde{r}=1 \quad (2b)$$

H is the dimensionless temperature, $H=(T-T_\infty)/T_\infty$; Pe is the Peclet number, $U_o a/\alpha$; U_{av} is the average gas velocity; Γ is the rotation parameter, $\Omega a/U_o$; and $f(\tilde{\xi},\theta)$ respresents the variation of the wall temperature resulting from the torch

[1]Present address: Argonne National Laboratory, Argonne, IL.

Contributed by the Heat Transfer Division and presented at the National Heat Transfer Conference, Houston, Texas, July 1988. Manuscript received by the Heat Transfer Division April 6, 1988.

heating. In the present study $f(\tilde{\xi},\theta)$ is given by $\exp(-\lambda^2(\tilde{\xi}^2+1-\cos\theta))$, where λ is a parameter that characterizes the thickness of the torch (cf. Choi et al., 1987a, 1987b); large λ corresponds to concentrated torch heating and small λ refers to a broad heating distribution. Applying the Fourier transformation in the axial direction and the finite Fourier transformation in the angular direction to the energy equation (1) yields the following ordinary differential equation and boundary conditions:

$$\tilde{r}\frac{d}{d\tilde{r}}\left(\tilde{r}\frac{d\bar{\bar{H}}}{d\tilde{r}}\right)+A(\tilde{r})\bar{\bar{H}}=0 \tag{3}$$

$$\bar{\bar{H}}_W=\bar{\bar{H}}(\tilde{r}=1)=H_M 2\sqrt{\frac{\pi}{\lambda^2}}\exp\left(-\frac{z^2}{4\lambda^2}\right)e^{-\lambda^2}$$

$$\int_0^{\pi}\cos n\theta e^{\lambda^2\cos\theta}d\theta \tag{4a}$$

$$\bar{\bar{H}}(\tilde{r}=0)=\text{finite} \tag{4b}$$

where $\bar{\bar{H}}$ is the transformed temperature defined by

$$\bar{\bar{H}}=\int_{-\infty}^{\infty}e^{-iz\tilde{\xi}}\left\{\int_{-\pi}^{\pi}e^{-in\theta}H d\theta\right\}d\tilde{\xi} \tag{5}$$

$A(\tilde{r})$ is given by

$$A(\tilde{r})=\sum_{j=0}^{\infty}A_j\tilde{r}^j \tag{6}$$

where

$$A_0=-n^2,\quad A_1=0,$$

$$A_2=-\text{Pe}\left(2\frac{U_{av}}{U_o}-1\right)iz-\text{Pe}\Gamma in,\quad A_3=0,$$

$$A_4=\text{Pe}2\frac{U_{av}}{U_o}iz,\quad A_j=0,\quad j\geq 5$$

Equation (3) was solved by the method of Frobenius assuming that $\bar{\bar{H}}$ can be expressed as the sum of the series

$$\bar{\bar{H}}=\sum_{j=0}^{\infty}H_j\tilde{r}^{j+\beta} \tag{7}$$

The coefficients H_j are determined to be

$$H_{2j+1}=0\qquad j=0,1,2\ldots \tag{8}$$

$$\frac{H_2}{H_0}=-\frac{A_2}{(2+\beta)(1+\beta)+(2+\beta)+A_0}$$

$$\frac{H_{2j}}{H_0}=\frac{-\frac{H_{2j-4}}{H_0}A_4-\frac{H_{2j-2}}{H_0}A_2}{(2j+\beta)(2j-1+\beta)+(2j+\beta)+A_0}\qquad j=2,3,4\ldots$$

where β is equal to n. Note that the value of H_0 can be determined from the boundary condition at the wall; i.e.,

$$\bar{\bar{H}}(\tilde{r}=1)=\bar{\bar{H}}_W=H_0\sum_{j=0}^{\infty}\frac{H_j}{H_0} \tag{9}$$

where $\bar{\bar{H}}_W$ is given by equation (4*a*).

It is necessary to invert $\bar{\bar{H}}$ from the transformed coordinates (z, n) to the physical coordinates $(\tilde{\xi}, \theta)$. The inversion of $\bar{\bar{H}}$ from z to $\tilde{\xi}$ yields

$$\bar{H}(\tilde{\xi},\tilde{r},n)=\frac{1}{2\pi}\int_{-\infty}^{\infty}\bar{\bar{H}}e^{iz\tilde{\xi}}dz \tag{10}$$

The above integration was carried out numerically (the effects of the values of the upper and lower limits of integration and the size of the interval dz that were chosen were shown to have a negligible effect on the results, cf. Choi, 1987b). The inversion of the finite Fourier transformation from $\bar{H}(\tilde{\xi},\tilde{r},n)$ to $H(\tilde{\xi},\tilde{r},\theta)$ is obtained by utilizing the following relation:

$$H(\tilde{\xi},\tilde{r},\theta)=\frac{1}{\pi}\sum_{n=1}^{\infty}\{\bar{H}_{\text{real}}\cos n\theta-\bar{H}_{\text{imaginary}}\sin n\theta\}+\frac{1}{2\pi}\bar{H}_{\text{real},n=0} \tag{11}$$

where $\bar{H}_{\text{real}}$ and $\bar{H}_{\text{imaginary}}$ are the real and imaginary parts of $\bar{H}$, respectively.

Bulk Temperature and Temperature Gradients. The bulk temperature H_b is defined by

$$H_b(\tilde{\xi})=\frac{\int_0^1\int_{-\pi}^{\pi}2(1-\tilde{r}^2)\tilde{r}H d\theta d\tilde{r}}{\pi} \tag{12}$$

which can be rewritten as

Nomenclature

A_j = coefficients in equation (6)
a = tube radius
H = dimensionless temperature $=(T-T_\infty)/T_\infty$
H_j = coefficients in equation (7)
$\bar{\bar{H}}$ = transformed temperature in equation (5)
K = thermophoretic coefficient
n = Fourier mode
Pr = Prandtl number $=\nu/\alpha$
Pe = Peclet number $=U_o a/\alpha$
R = particle radius
r = radial coordinate
$\tilde{r}$ = dimensionless radial coordinate $=r/a$
t = time
$\tilde{t}$ = dimensionless time $=U_o t/a$
T = temperature
u = axial velocity
U_o = torch speed
U_{av} = average velocity of gas in the axial direction
V_T = thermophoretic velocity
w = circumferential velocity
x = axial coordinate
Y = stretched radial coordinate $=\dfrac{\left(1-\frac{r}{a}\right)}{\sqrt{\frac{\alpha}{U_o a}}}$
z = complex transformed coordinate
α = thermal diffusivity
Γ = rotation parameter $=a\Omega/U_o$
θ = angle
λ = parameter in torch heating distribution
λ_p = mean free path
ν = kinematic viscosity
ξ = moving coordinate $=x-U_o t$
$\tilde{\xi}$ = dimensionless moving coordinate $=\xi/a$
Ω = angular velocity of tube

Subscripts

b = bulk
M = maximum
rxn = reaction
w = wall
∞ = ambient

Superscript

~ = dimensionless

$$H_b(\tilde{\xi}) = \frac{2}{\pi}\int_0^1 (1-\tilde{r}^2)\tilde{r}\bar{\bar{H}}(\tilde{\xi}, \tilde{r}, n=0)d\tilde{r} \tag{13}$$

To calculate the thermophoretic contribution to the velocity, the gradients in temperature must be determined. In this study, the temperature gradients are not obtained by differentiating the calculated temperature fields but by directly inverting the transformed temperature gradients. The double integral transformation, i.e., the Fourier transformation with respect to $\tilde{\xi}$ and the finite Fourier transformation with respect to θ of the gradients, is given by

$$\left(\overline{\overline{\frac{\partial H}{\partial \tilde{\xi}}}}\right) = iz\bar{\bar{H}} \tag{14}$$

$$\left(\overline{\overline{\frac{\partial H}{\partial \tilde{r}}}}\right) = \frac{d\bar{\bar{H}}}{d\tilde{r}}$$

$$\left(\overline{\overline{\frac{\partial H}{\partial \theta}}}\right) = in\bar{\bar{H}}$$

Thermophoresis and Particle Motion. The thermophoretic velocity may be written in the following form (Talbot et al., 1980):

$$V_T = -K\frac{\nu}{T}\nabla T \tag{15}$$

where K is the thermophoretic coefficient. The value of K generally depends on the Knudsen number λ_p/R, where λ_p is the mean free path and R is the particle radius. In MCVD, Walker et al. (1980a) suggested that a value of 0.9 for K is appropriate and this value is used in the present work.

It is assumed that the motion of the particles is determined by thermophoresis in conjunction with forced flow; i.e., Poiseuille flow in the axial direction and rigid body rotation in the angular direction (for the fully developed flow condition). It is noted that the effect of the centrifugal force resulting from the rotation of the tube is negligible because of the small (submicron) size of the particles.

Using a Lagrangian description for the particle motion, the following differential equations are obtained for the velocity of the particle:

$$\frac{dx}{dt} = 2U_{av}\left(1-\left(\frac{r}{a}\right)^2\right) - K\frac{\nu}{T}\frac{\partial T}{\partial x} \tag{16}$$

$$\frac{dr}{dt} = -K\frac{\nu}{T}\frac{\partial T}{\partial r}$$

$$r\frac{d\theta}{dt} = r\Omega - K\frac{\nu}{T}\frac{\partial T}{\partial \theta}$$

dx/dt, dr/dt, and $r(d\theta)/dt$ are the axial, radial and angular velocities of the particles, respectively. It is noted that for the case of the fast-moving torch, the axial and angular components were neglected (Choi et al., 1989). The above equations are more general and may be rewritten, for constant properties, in the following dimensionless form:

$$\frac{d\tilde{\xi}}{d\tilde{t}} = 2\frac{U_{av}}{U_o}(1-\tilde{r}^2) - K\frac{\mathrm{Pr}}{\mathrm{Pe}}\frac{1}{(H+1)}\frac{\partial H}{\partial \tilde{\xi}} - 1 \tag{17}$$

$$\frac{d\tilde{r}}{d\tilde{t}} = -K\frac{\mathrm{Pr}}{\mathrm{Pe}}\frac{1}{(H+1)}\frac{\partial H}{\partial \tilde{r}}$$

$$\frac{d\theta}{d\tilde{t}} = \Gamma - K\frac{\mathrm{Pr}}{\mathrm{Pe}}\frac{1}{\tilde{r}^2}\frac{1}{(H+1)}\frac{\partial H}{\partial \theta}$$

The above coupled equations were solved by using the second-order Runge-Kutta method to determine the particle trajectories. Time sensitivity was tested and the results of particle trajectories for $\Delta\tilde{t}=0.005$ disagreed by less than 1 percent with the results for $\Delta\tilde{t}=0.01$. The value of $\Delta\tilde{t}=0.005$ was used in the present work.

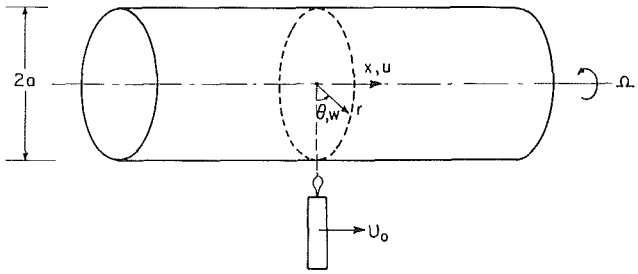

Fig. 1 Sketch of the system

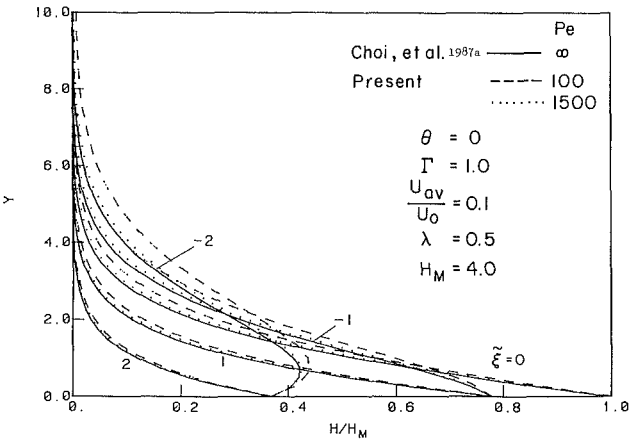

Fig. 2 Dimensionless temperature variation in the radial direction for large Pe numbers

Results and Discussion

It is first emphasized that the method of solution chosen, although ultimately numerical, is based on classical analytical techniques, namely, Fourier series and transformation and analytical series expansions. The series solution, equation (7), provides the exact radial variation of the transformed temperature. The only numerical approximations introduced in the calculations for temperature fields are those involved in the truncation of the Fourier series and the Frobenius series and the inversion of the Fourier integral to transform $\bar{\bar{H}}$ from the transformed coordinates to the physical coordinates. These approximations prove to result in a negligible error (Choi, 1987b). The same statements apply for the evaluation of the temperature gradients. To achieve comparable accuracy using conventional finite difference or finite element procedures would require a discretized domain with hundreds of thousands of cells or elements for the three-dimensional problem presented here.

Limiting Case for Large Torch Speeds (Pe>>1). The present analysis is valid for all values of the torch speed, i.e., all values of the Peclet number. In this section, results for the temperature fields for large Peclet numbers are presented and compared with previous results for the limiting case of $\mathrm{Pe}\to\infty$. Figures 2 and 3 show the temperature distribution in the radial direction, i.e., with respect to Y defined by $Y=\sqrt{\mathrm{Pe}}(1-\tilde{r})$ for different Peclet numbers. It is seen in Fig. 2 for $\theta=0$ and Fig. 3 for $\theta=\pi$ that the present results for Peclet numbers of 100 (dotted curves) and 1500 (dashed curves) approach the results from the previous study for $\mathrm{Pe}\to\infty$ (solid curves). This is another check on the results. The current work does not utilize the boundary layer approximations employed in the earlier work of Choi et al. (1987a) but the present results are even valid under these conditions, namely, large values of the

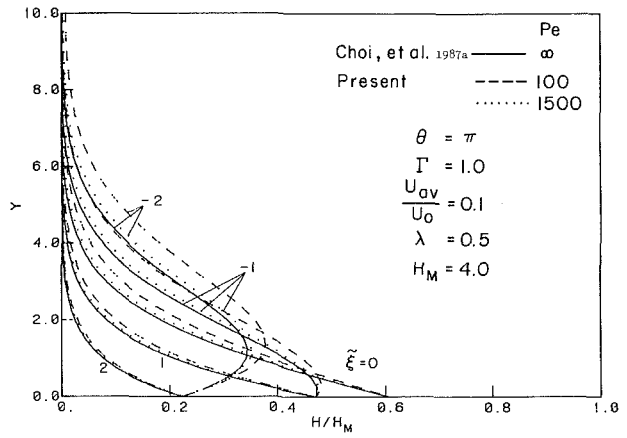

Fig. 3 Dimensionless temperature variation in the radial direction for large Pe numbers

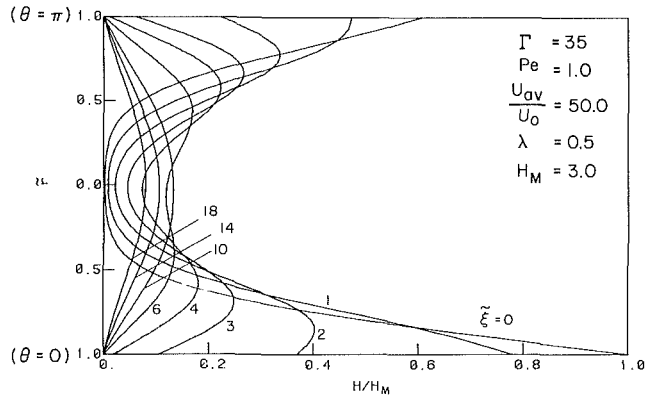

Fig. 5 Radial temperature distribution along the diameter containing $\theta = 0$ and π

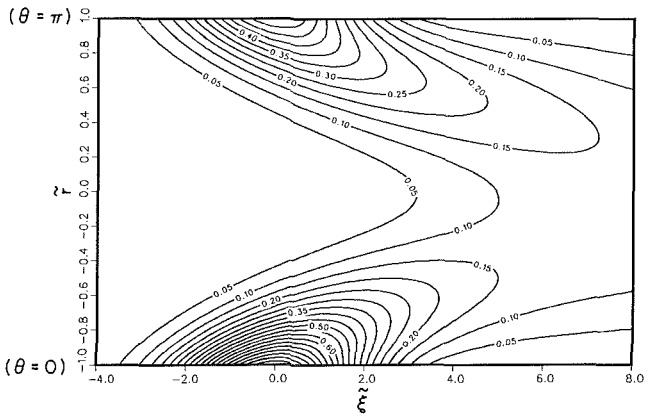

Fig. 4 Isotherm contours (H/H_M) in the plane going through center containing $\theta = 0$ and π; $\Gamma = 35$, Pe = 1.0, $U_{av}/U_o = 50$, $\lambda = 0.5$

Peclet number. Indeed, the very good agreement between the two results testifies to the power and generality of the present approach.

Temperature Fields. Figure 4 shows isothermal contours in the vertical $\tilde{r}$, $\tilde{\xi}$ plane containing $\theta = 0$ and π for a Peclet number of unity. It is seen in Fig. 4 that the effects of torch heating extend to the center of the tube while for large Peclet number the thermal effects are restricted to the region near the wall (Choi et al., 1987a).

For negative values of $\tilde{\xi}$, i.e., behind the torch, it is seen in Fig. 4 that the temperature decreases monotonically from the hot surface. This monotonically decreasing behavior also extends to a region ahead of the torch, i.e., up to positive values of $\tilde{\xi}$ approximately equal to two. However, beyond these locations, it is seen that the temperature of the gas may be greater than that of the surface. Figure 5 gives the radial temperature distributions at values of $\tilde{\xi}$ equal to 0, 1, 2, 3, 4, 6, 10, 14, and 18 along the diameter containing $\theta = 0$ and π, and shows that in the region ahead of the torch given by $\tilde{\xi} \geq 2$, the gas may be at a higher temperature than the wall. In previous studies of the fast-moving torch (Choi et al., 1987a), the gas ahead of the torch was always at a lower temperature than the surface. However, for the present slow-moving torch case, strong axial convection ($U_{av}/U_o = 50$) causes the gas ahead of the torch to have higher temperatures than those of the surface. Thus, hot particles will be carried downstream ahead of the torch and will then move toward the cool tube surface due to the thermophoretic force.

In Fig. 5, the effect of the rotation can also be seen; i.e., for $\tilde{\xi} = 0$, 1, and 2 the peak temperatures near the bottom half of the diameter (close to the surface at $\theta = 0$) are higher than those near the top half of the diameter (close to the surface at $\theta = \pi$). However, for $\tilde{\xi} = 4$ and 6, the situation is reversed, i.e., the peak temperatures are now larger on the top half of the diameter. This is due to the angular convection that helically carries the gas, which was strongly heated at the bottom half ($\theta = 0$) at $\tilde{\xi} = 0$ (directly above the highest surface temperature) into the top half ($\theta = \pi$) far ahead of the torch; e.g., at $\tilde{\xi} = 4$.

Wall Temperature Gradients. Figures 6, 7, and 8 are plots of the wall temperature gradient ($\partial H/\partial \tilde{r}_{\tilde{r}=1}$) for values of Γ equal to 1, 35, and 100. For small values of the rotation parameter Γ, the angular convection is small and, correspondingly, the variation of the wall temperature gradient in the angular direction is also small (cf. Fig. 7). This is in contrast to Fig. 9 for $\Gamma = 100$ where the large rotation results in a large variation of the wall temperature gradient in the angular direction. Note that the large variations of the radial temperature gradient for large Γ should cause large variations in the particle trajectories and deposition since the thermophoretic force is proportional to the temperature gradient.

Figure 9 shows the angular temperature distributions for two values of the rotation parameter Γ. For the slow-rotating case, i.e., $\Gamma = 1$, the temperature profiles in the gas (dashed curves) are similar to the wall temperature profile (solid curve). However, for the fast rotation case, i.e., $\Gamma = 100$, the variations of the gas temperatures (dotted curves) are markedly different and more uniform than the wall temperature profile (solid curve).

Bulk Temperature and the Effect of Torch Heating Profile. Figure 10 shows the wall temperature for three values of λ. The parameter λ is a measure of the torch heating profile; for small values of λ, the torch heating occurs over a broad range of the tube, while for large λ the torch heating is more concentrated. Here, different values of H_M have been chosen so that the integral of the wall temperature over the tube surface is the same for the three values of λ; i.e. $\int_{-\infty}^{\infty}\int_{-\pi}^{\pi} H_W d\theta d\tilde{\xi} =$ constant for different λ. The values of H_M are equal to 3, 2.2137, and 1.5548 for λ equal to 0.5, 0.4, and 0.3, respectively. Figure 11 is the plot of the bulk temperatures for the wall temperature variations shown in Fig. 10. It is seen in Fig. 11 that the bulk temperature for the broad heating case (small λ) is larger far behind the torch then for concentrated heating (large λ). However, in the region nearer the torch the situation is reversed. Far ahead of the torch, the bulk temperatures for the three different values of λ are nearly the same (recall that the integrals of the wall temperature over the surface are the same for the three curves).

Particle Trajectories. Figure 12(a) shows spiral particle

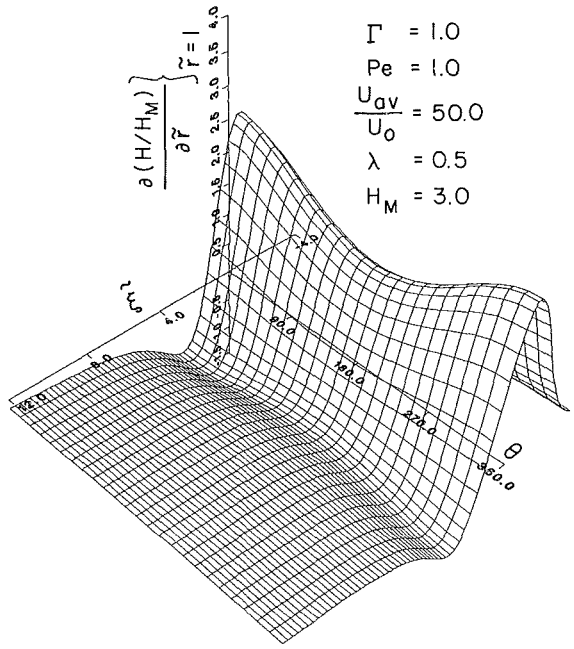

Fig. 6 Variation of the dimensionless temperature gradient at the wall for $\Gamma = 1$

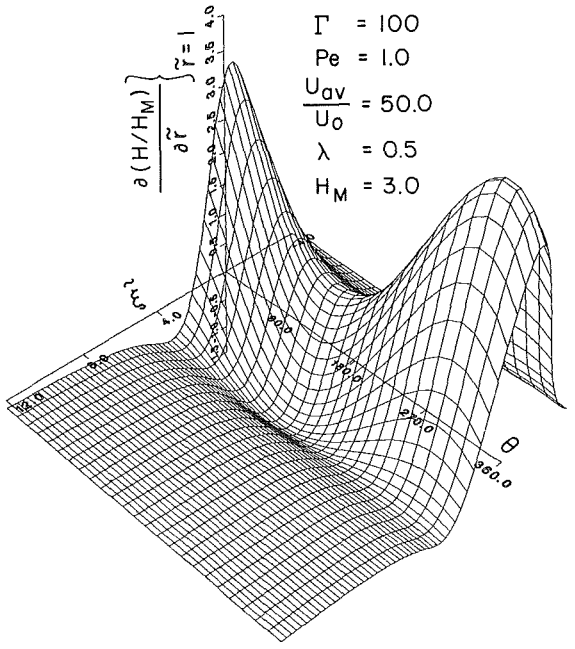

Fig. 8 Variation of the dimensionless temperature gradient at the wall for $\Gamma = 100$

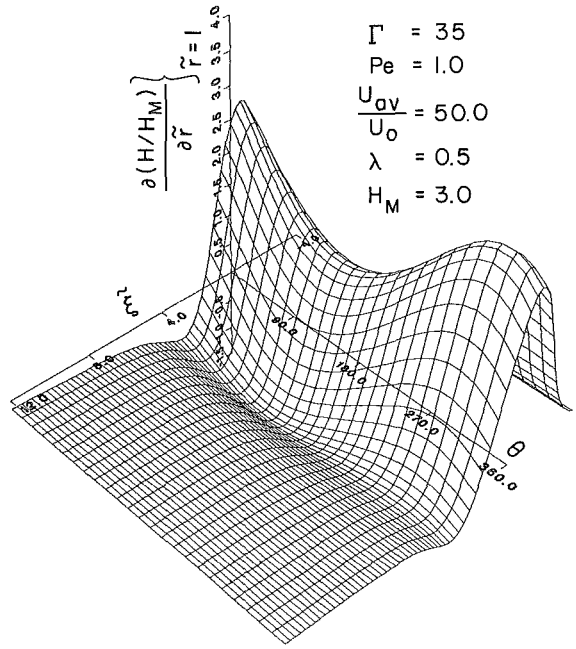

Fig. 7 Variation of the dimensionless temperature gradient at the wall for $\Gamma = 35$

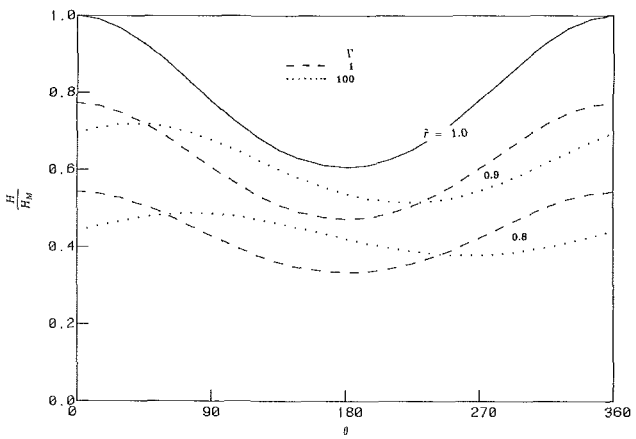

Fig. 9 Variation of the dimensionless temperature in the θ direction at $\xi = 0$; Pe = 1.0, $\lambda = 0.5$, $U_{av}/U_o = 50$

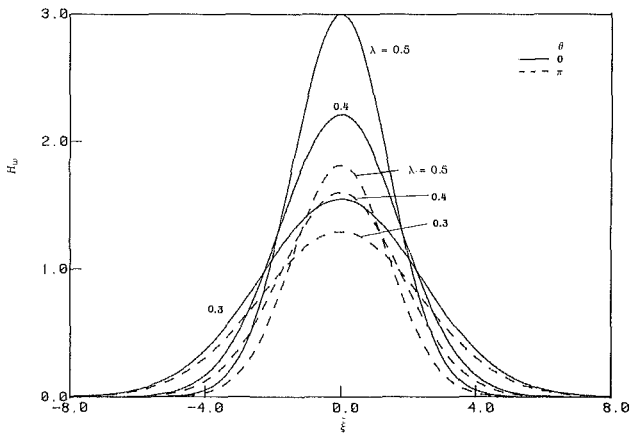

Fig. 10 Wall temperature (H_W) variation in the axial direction; Pe = 1.0, $\Gamma = 35$, $U_{av}/U_o = 50$

trajectories for a value of Γ equal to 35. Particles have been initiated at given locations ($\tilde{\xi}$, $\tilde{r}$, θ), e.g., in Fig. 12(*a*), initial sites at (0, 0.9, 0), (0, 0.8, 0) and (0, 0.7, 0) were assumed at the time $\tilde{t} = 0$. It is noted that the three-dimensional temperature fields could be used to determine where the particles are formed based on locations where the temperatures exceeded the reaction temperature T_{rxn}. This was not done in the present study.

As can be inferred from the radial temperature distribution in Fig. 5, thermophoresis first causes the particles to move toward the center, i.e., away from the hot wall toward the cold interior. Simultaneously, the axial and angular forced flow causes the particles to move downstream and also circumferentially, i.e., the particle trajectories are helices. In the

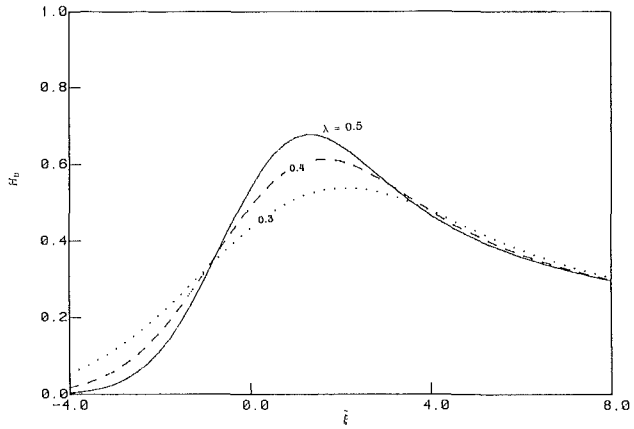

Fig. 11 Bulk temperature (H_b) variation in the axial direction; Pe = 1.0, Γ = 35, U_{av}/U_o = 50

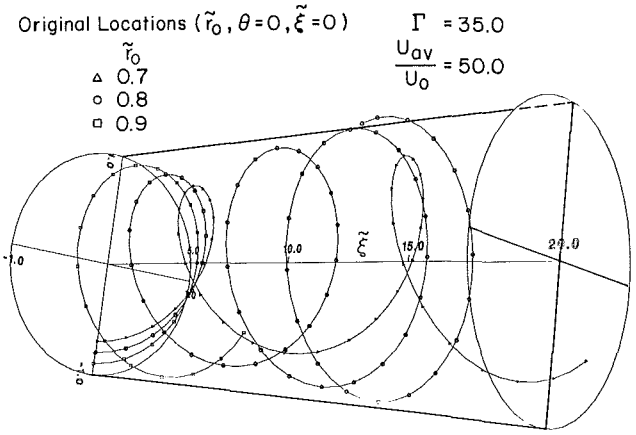

Fig. 12(*a*) Particle trajectories for Γ = 35; λ = 0.5, Pe = 1.0, H_M = 3.0

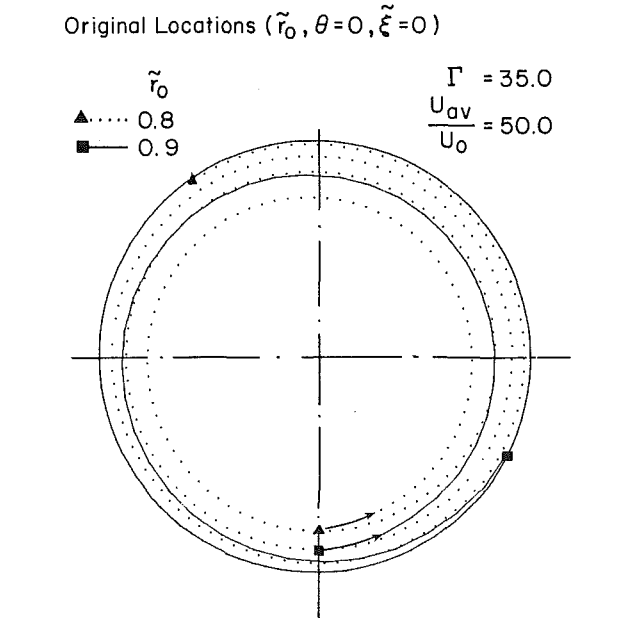

Fig. 12(*b*) Particle trajectories for Γ = 35 two-dimensional ($\tilde{r}$, θ) plot; λ = 0.5, Pe = 1.0, H_M = 3.0

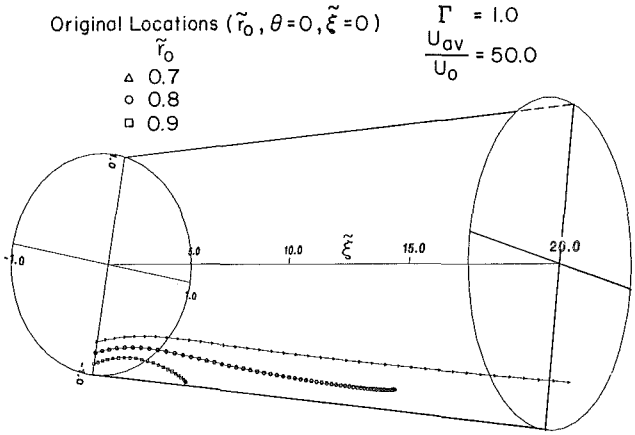

Fig. 13 Particle trajectories for Γ = 1.0; λ = 0.5, Pe = 1.0, H_M = 3.0

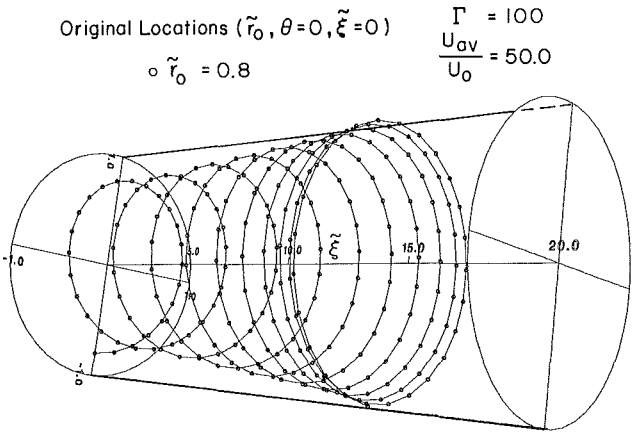

Fig. 14 Particle trajectories for Γ = 1.00; λ = 0.5, Pe = 1.0, H_M = 3.0

downstream region ahead of the torch ($\tilde{\xi} >> 0$), the radial temperature gradients may become negative corresponding to a hot gas and a cold wall (cf. Figs. 4 and 5). Thermophoresis now causes the particles to move toward the wall and finally results in deposition on the surface. The angular motion and deposition of two particles can be seen in Fig. 12(*b*), which is a plot of the particle trajectories viewed from the front of the tube.

Table 1 Locations of particle deposition; λ = 0.5, Pr = 1.0, K = 0.9, H_M = 3.0, U_{av}/U_o = 50.0

	Original location ($\tilde{\xi}=0$, $r/a=\tilde{r}_o$, $\vartheta=0$)			
Γ	$\tilde{r}_o=0.8$		$\tilde{r}_o=0.9$	
	$\tilde{\xi}_D$	ϑ_D	$\tilde{\xi}_D$	ϑ_D
1	13.2	0.177π	4.59	0.0655π
35	14.63	1.19π	4.3	0.343π
100	14.32	1.98π	4.48	0.767π

Figures 13 and 14 are plots of the particle trajectories for values of Γ = 1 and 100, respectively. For Γ = 1, tube rotation is small and there is little helical motion, while for Γ = 100, there is strong tube rotation and accordingly, the particle trajectories exhibit a marked helical pattern. Recall that rotation affects both the temperature gradients and the gas flow in the angular direction. Thus, for large values of Γ the variation of the temperature in the angular direction is significant and the resulting thermophoretic contribution as well as the forced rotation significantly influence the particle motion.

In Table 1, locations of deposition are shown for three values of Γ equal to 1, 35, and 100. For the cases studied, the dimensionless axial length that the particle travels before depositing, $\tilde{\xi}_D$, is not strongly dependent on the tube rotation

(approximately 10 percent variation with respect to Γ for the particle originating from (0, 0.8, 0) and approximately 5 percent variation for the particle originating from (0, 0.9, 0)). However, for both particles, the angular locations of the deposition, θ_D, are shown to be strongly dependent on the tube rotation.

Summary and Conclusions

Results have been obtained for the heat transfer and particle trajectories relative to the modified chemical vapor deposition process for general values of the torch speed. Tube rotation and circumferential and axial variations of the torch heating were included for the case of constant properties under quasi-steady-state conditions. The following conclusions have been made.

1 Thermal effects penetrate to the center of the tube for moderate values of the torch speed.

2 As the torch speed increases the results for the temperature distribution approach those for the limiting case of a fast moving torch, i.e., for the infinite Peclet number case (Choi et al., 1987a).

3 For a slow-moving torch and large gas velocity ($U_{av}/U_o = 50$), the gas may be at a higher temperature than the wall in the region ahead of the torch.

4 For large values for the rotation parameter $\Gamma = \Omega a/U_o$, the radial temperature gradients vary significantly in the angular direction.

5 The motion of the particles is assumed to be governed by thermophoresis and the gas flow. The particles initially move toward the center of the tube and then move toward the wall as they progress downstream and deposit on the wall. For moderate and large values of Γ, the particle trajectories are helices while for small values of Γ, there is little helical motion.

6 The particle trajectories and the locations of deposition are strongly dependent on the rotation parameter Γ.

Acknowledgments

The authors are deeply indebted to Dr. U. C. Paek, AT&T Engineering Research Center, for providing valuable comments and discussion. Support from the National Science Foundation and the Computing Center of the University of California at Berkeley is gratefully acknowledged.

References

Choi, M., Baum, H. R., and Greif, R., 1987a, "The Heat Transfer Problem During the Modified Chemical Vapor Deposition Process," ASME JOURNAL OF HEAT TRANSFER, Vol. 109, pp. 642–646.

Choi, M., 1987b, "Studies of Heat and Mass Transfer During Chemical Vapor Deposition," Ph.D. dissertation, University of California at Berkeley.

Choi, M., Greif, and Baum, H. R., 1989, "Three Dimensional Analysis of Unsteady Heat Transfer and Thermophoretic Deposition for Variable Property Flow," in preparation.

DiGiovanni, D., Wang, C. Y., Morse, T. F., and Cipolla, J. W., Jr., 1985, "Laser Induced Buoyancy and Forced Convection in Vertical Tubes," in: *Natural Convection: Fundamentals and Applications*, S. Kakac, W. Aung, and R. Viskanta, eds., Hemisphere, New York, pp. 1118–1139.

Jablonowski, D. P., Paek, U. C., and Watkins, L. S., 1987, "Optical Fiber Manufacturing Techniques," *AT&T Technical J.*, Vol. 66, pp. 33–44.

Li, T., 1985, *Optical Fiber Communications*, Academic Press, Inc., Vol. 1, Fiber Fabrication, pp. 1–30.

MacChesney, J. B., O'Connor, P. B., DiMarcello, F. V., Simpson, J. R., and Lazay, P. D., 1974a, "Preparational Low-Loss Optical Fibers Using Simultaneous Vapor Phase Deposition and Fusion," in: *Proc. 10th Int. Congr. Glass.*, Kyoto, Japan, pp. 6-40–6-44.

MacChesney, J. B., O'Connor, P. B., and Presby, H. M., 1974b, "A New Technique for Preparation of Low-Loss and Graded Index Optical Fibers," *Proc. IEEE 62*, pp. 1278–1279.

Metais, B., and Eckert, E. R. G., 1964, "Forced, Mixed and Free Convection Regimes," ASME JOURNAL OF HEAT TRANSFER, Vol. 86, pp. 295–297.

Morse, T. F., Wang, C. Y., and Cipolla, J. W., Jr., 1985, "Laser Induced Thermophoresis and Particulate Deposition Efficiency," ASME JOURNAL OF HEAT TRANSFER, Vol. 107, No. 1, pp. 155–160.

Morse, T. F., DiGiovanni, D., Wang, C. Y., and Cipolla, J. W., Jr., 1986, "Laser Enhancement of Thermophoretic Deposition Processes," *J. of Lightwave Technology*, Vol. LT-4, No. 2, pp. 151–155.

Nagel, S. R., MacChesney, J. B., and Walker, K. L., 1982, "An Overview of the Modified Chemical Vapor Deposition (MCVD) Process and Performance," *IEEE Journal of Quantum Electronics*, Vol. QE-18, No. 4, pp. 459–476.

Paek, U. C., 1975, "Calculation of Cooling Rate and Induced Stresses in Drawing of Optical Fibers," *J. of American Ceramic Society*, Vol, 58, pp. 330–335.

Patula, E. J., 1981, "Steady-State Temperature Distribution in a Rotating Roll Subject to Surface Heat Fluxes and Convective Cooling," ASME JOURNAL OF HEAT TRANSFER, Vol. 103, pp. 36–41.

Simpkins, P. G., Kosinski, S. G., and MacChesney, J. B., 1979, "Thermophoresis: The Mass Transfer Mechanism in Modified Chemical Vapor Deposition," *J. Appl. Physics*, Vol. 50, pp. 5676–5681.

Talbot, L., Cheng, R. K., Schefer, R. W., and Willis, D. R., 1980, "Thermophoresis of Particles in a Heated Boundary Layer," *J. Fluid Mech.*, Vol. 101, part 4, pp. 737–758.

Walker, K. L., Geyling, F. T., and Nagel, S. R., 1980a, "Thermophoretic Deposition of Small Particles in the Modified Chemical Vapor Deposition (MCVD) Process," *J. Am. Ceram. Soc.*, Vol. 63, pp. 552–558.

Walker, K. L., Harvey, J. W., Geyling, F. T., and Nagel, S. R., 1980b, "Consolidation of Particulate Layers in the Fabrication of Optical Fiber Preforms," *J. Am. Ceram. Soc.*, Vol. 63, pp. 96–102.

Wang, C. Y., Morse, T. F., and Cipolla, J. W., Jr., 1985, "Laser Induced Natural Convection and Thermophoresis," ASME JOURNAL OF HEAT TRANSFER, Vol. 107, pp. 161–167.

Yuen, W. Y. D., 1984, "On the Steady-State Temperature Distribution in a Rotating Cylinder Subject to Heating and Cooling Over Its Surface," ASME JOURNAL OF HEAT TRANSFER, Vol. 106, pp. 578–585.

Transient Mass Transfer in Parallel Passage Dehumidifiers With and Without Solid Side Resistance

Y. K. Chuah[1]

P. Norton

F. Kreith

Solar Energy Research Institute, Golden, CO 80401

Desiccant dehumidifiers have been used in industrial and commercial processes to provide air of lower relative humidity than can be achieved readily with vapor compression equipment. Parallel passage rotary wheel regenerators with silica gel on the passage walls are used as dehumidifiers for air-conditioning applications. This study presents an investigation of transient mass transfer in a parallel passage dehumidifier with a thin layer of silica gel on the passage walls. A two-film resistance model was used to approximate the overall transfer resistance between the process air and the solid desiccant. Isothermal transient mass transfer experiments using parallel passages with silica gel coated walls were conducted and analyzed. It was found that the two-film model agrees with the experimental results within the experimental accuracy. Although only silica gel was used in this study, the results may be extended to other solid desiccants.

Introduction

Desiccants have been used for many years to provide dry air for a variety of industrial and commercial processes, and several desiccant air-conditioning systems have been marketed for situations requiring such low relative humidities that they cannot be readily achieved with vapor compression equipment. But thermal efficiencies of currently available drying equipment tend to be low and parasitic power requirements high. Recently, however, a significant research effort has been initiated to develop desiccant air-conditioning systems that can compete with conventional vapor compression cooling. To achieve this goal, the COP must be high and parasitic requirements low. Barlow (1983) proposed the following requirements for high-performance dehumidifiers:

1 High heat and mass transfer Ntu's
2 High ratio of Sherwood number to friction factor
3 Small solid side resistance to mass transfer
4 Large transfer surface area per unit volume
5 Suitable desiccant properties

Several geometries have been investigated with regard to these requirements. Barlow concluded that those having parallel passages with a solid desiccant on the walls give the best performance. Mei and Lavan (1983) tested and analyzed a parallel passage crossflow dehumidifier, but the rotary dehumidifier/regenerator wheel shown in Fig. 1 appears to be the front runner in the current desiccant system development effort. In a typical desiccant cooling system, process air is dehumidified by passing it through the dehumidifier passages of the wheel. The low-humidity air is then evaporatively cooled as described in detail by Barlow (1983). The desiccant material that has been saturated with moisture is continually regenerated with hot air in the other half of the rotary wheel.

There have been many theoretical and experimental studies of the performance of various types of parallel passage dehumidifiers (Schlepp and Barlow, 1984; Bharathan et al., 1987; Biwas et al., 1984; Kim et al., 1985; Ghezelayagh and Gidaspow, 1982; Raghavan and Gidaspow, 1985; Maclaine-cross and Banks, 1972; Banks, 1985). Schlepp and Barlow (1984) and Bharathan et al. (1987) present the design of a rotary wheel dehumidifier and also some experimental results on its performance. Biwas et al. (1984) and Kim et al. (1985) investigated transient heat and mass transfer in a parallel adiabatic passage dehumidifier and found that using an average-lumped resistance for the mass transfer may be sufficient to model the transfer process. Mei and Levan (1983), Ghezelayagh and Gidaspow (1982), and Raghavan and Gidaspow (1985) considered the use of desiccant sheets on the passage walls with silica gel crystals embedded in a matrix. In this configuration, the diffusion in the solid can be controlled by both the macropore diffusion into the matrix sheet and the micropore diffusion into the silica gel. Maclaine-cross and Banks (1972) and Banks (1985) used presently available data for heat transfer rotary regenerators to predict heat and mass transfer in a rotary wheel dehumidifier. They transformed the describing equations with the aid of combined potentials and thus decoupled and simplified the equations for heat and mass transfer to resemble those for heat transfer alone.

According to heat and mass transfer analogy, the mass transfer Sherwood number for a given geometry will be equal to the heat transfer Nusselt number if there is no other potential than the concentration gradient and the Lewis number is

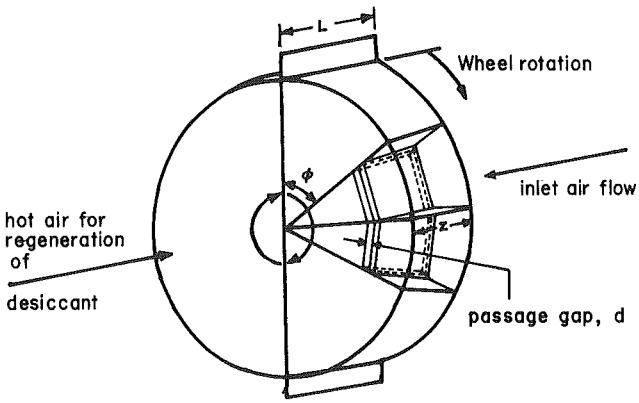

Fig. 1 Rotary desiccant wheel with parallel passages

[1]Present address: Energy and Mining Research/Service, Industrial Technology Research Institute, Chu Tung, Taiwan.

Contributed by the Heat Transfer Division and presented at the ASME-JSME Thermal Engineering Joint Conference, Honolulu, Hawaii, March 1987. Manuscript received by the Heat Transfer Division March 2, 1988. Keywords: Mass Transfer, Modeling and Scaling, Transient and Unsteady Heat Transfer.

unity. For developed laminar flow in ducts, the Nusselt number is not a function of Prandtl number and thus exactly equal to the Sherwood number. For simultaneous heat and mass transfer in a gaseous mixture, the coupling of heat and mass transfer is usually small and has been found (Tewfik, 1964) to have more effect on the temperature gradient than on the concentration gradient. When the concentration of the diffusive species is low, the coupling effects have been found (Tewfik, 1964) to be negligible. Therefore, for the heat and mass transfer in a desiccant dehumidifier wheel, the coupling in the gas phase may be neglected, as demonstrated by Hougen and Marshall (1947) in their correlation of Ahlberg's (1939) experimental data for adsorption in a silica gel granular bed.

Using a mass transfer Sherwood number equal to the heat transfer Nusselt number implies that the solid side resistance to mass transfer is negligibly small. The assumption underlying this simplification has been questioned in the past, but heretofore no quantitative information on the relative significance of the solid side resistance in parallel passage desiccant systems has been available. The goal of this study was first analytically and experimentally to determine the transient mass transfer in air flow through a parallel passage with silica gel coating on the surface; then, to compare the analytic and experimental results and develop a model to predict the relative importance of gas phase and solid side resistance in the process. Although only silica gel was used in this work, the information developed here should also be applicable to other materials.

In this study, transient mass transfer in three parallel passages of different gaps were measured under isothermal conditions. The variation of outlet condition with time for a step change in humidity at the inlet (the breakthrough curve) was monitored during these experiments, and the breakthrough curves were then analyzed to obtain the overall mass transfer coefficient. As the gas phase transfer resistance can be calculated from available analytic solutions (Shaw and London, 1978), the component of the total resistance in the solid side can be inferred. A correlation for estimating the resistance in the solid is proposed and tested. This method of determining a transfer coefficient is described by Eckert and Goldstein (1976).

Analysis

The describing equations for isothermal laminar mass transfer in a constant cross-sectional area passage are:

Gas phase

$$\rho_a V_a \frac{\partial C}{\partial Z} = hA''_{tr}(C_s - C) \tag{1}$$

Solid phase

$$h(C - C_s) = \rho_s t_s \frac{\partial X}{\partial \tau} \tag{2}$$

Equations (1) and (2) are based on the following assumption:

1 Axial dispersion in both the gas and solid phases is negligible.
2 Storage in gas phase can be neglected.
3 A two-film model is postulated so that an overall transfer coefficient can be used. Also, bulk concentration can be used in both the gas the solid phases.

Equations (1) and (2) can be normalized as

$$(1)\quad \frac{\partial C}{\partial Z^*} = \text{Ntu}\,(C_s - C) \tag{3}$$

$$(2)\quad \frac{\partial X}{\partial \tau^*} = \frac{\text{Ntu}}{R}(C - C_s) \tag{4}$$

where

$$\tau^* = \frac{\tau}{L/V_a}$$

$$Z^* = Z/L$$

The boundary and initial conditions are

$$\text{at } Z^* = 0,\ C = C_{\text{in}};\ \text{at } \tau^* = 0,\ C_s = C_{\text{init}} \tag{5}$$

The left-hand side of equation (4) can be written in the form

$$\frac{\partial X}{\partial \tau^*} = \frac{\partial C_s}{\partial \tau^*}\frac{dX}{dC_s} \tag{6}$$

where dX/dC_s is determined from the equilibrium isotherm of the desiccant, which is usually presented in the form

$$X = X(RH, T) \tag{7}$$

where RH = relative humidity and T = temperature.

Equations (3)–(6) show that in the passage the concentration C of water vapor in air and also the equilibrium concentration C_s of the solute at the gas–solid interface depend on Ntu, R, and (dX/dC_s).

Silica Gel Isotherms

In this study, Davison's grade 40 silica gel was used as the desiccant. Since there can be variations between different batches of silica gel of the same grade, the equilibrium

Nomenclature

A_{tr} = transfer area, m^2
A''_{tr} = transfer area per unit volume, m^2/m^3
C = moisture concentration in air, kg H_2O/kg air
C_s = equilibrium air moisture concentration at the interface of solid and air, kg H_2O/kg air
Diff = molecular diffusivity of water vapor in air, m^2/s
d = passage gap, m
D_s = diffusivity of water in solid, m^2/s
d_h = hydraulic diameter, m
E = adsorption potential
h = overall mass transfer coefficient, kg/m^2s
H = equilibrium constant in equation (13)
K = (m^3H_2O/m^3 desiccant)/(m^3 H_2O/m^3 air) in equation (20)
L = length of test passage, m
$\dot{m}$ = mass flow rate of air, kg/s
$\dot{m}''$ = mass flux of moisture, kg/m^2s
Ntu = number of transfer units = $hA_{tr}/\dot{m}$
P_v = vapor pressure, Pa
P_s = saturation pressure, Pa
R = mass of gel/mass of air in passage
Re = Reynolds number = $V_a d/\nu_a$
RH = relative humidity
Sh = Sherwood number = hd_n/ρ_aDiff
slp = slope of breakthrough curve
T = temperature, °C
t_s = thickness of gel on wall, m
V_a = velocity of air, m/s
W = humidity ratio
X = moisture uptake, kg H_2O/kg desiccant
X' = local moisture uptake, kg H_2O/kg desiccant
Z = axial coordinate in the passage, m
ν = kinematic viscosity, m^2/s
ρ_a = density of air, kg/m^3
ρ_s = density of silica gel, kg/m^3
τ = time, s

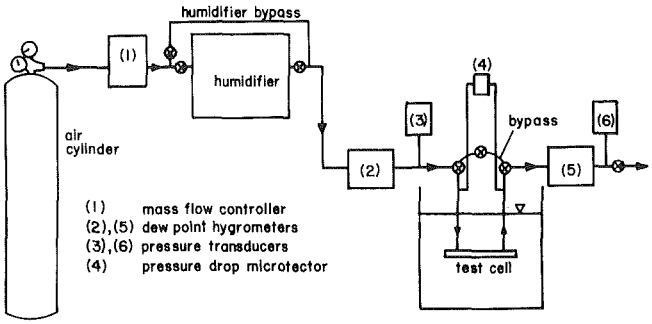

Fig. 2 Experimental setup

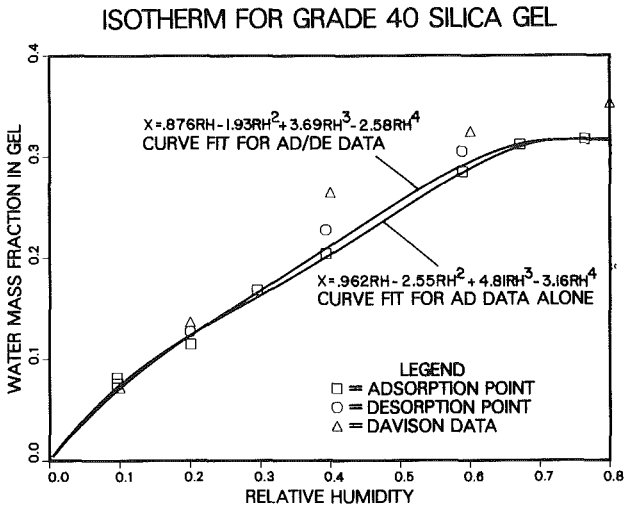

Fig. 3 Isotherms for Davison's grade 40 silica gel

isotherm for the silica gel used in this study was measured experimentally. The isotherm points were measured in the experimental setup shown in Fig. 2, but a steel column (i.d. = 2.7 mm, length = 10.8 cm) packed with silica gel was used in place of the parallel plate test cell. First dry air was passed through the column until the outlet dew point indicated a dry condition in the column for at least 20 min. Then, air of known moisture level was passed through the column until the outlet dew point indicated that the silica gel in the packed column was saturated. To determine the total moisture adsorbed, the difference in weight of the packed column before and after the adsorption of moisture was measured. Desorption points were measured similarly, but starting with air of high humidity level. Then, an equilibrium point at a lower humidity was established by desorption of moisture from the silica gel.

Altogether eight adsorption and three desorption points were measured and the isotherm points are shown in Fig. 3. It appears that the desorption points at a certain relative humidity level are usually slightly above the adsorption points. A polynomial fit for the adsorption points and an averaged fit for both adsorption and desorption isotherm points are also presented in Fig. 3. The first of the two polynominals is designated AD (adsorption) and the second AD/DE (adsorption/desorption).

The isotherm points were measured at 21.1°C (70°F), but extrapolation of the data to other temperatures is possible. Jury and Edwards (1971) found that when the fractional moisture uptake X (kg of H_2O/kg of desiccant) is plotted against adsorption potential (Dubinin-Polanyi Theorem), data for silica gel collected between 27.8°C and 93.3°C (82°F and 200°F) falls approximately on one line. According to the Dubinin-Polanyi Theorem, the adsorption potential of a desiccant, E, can be written as

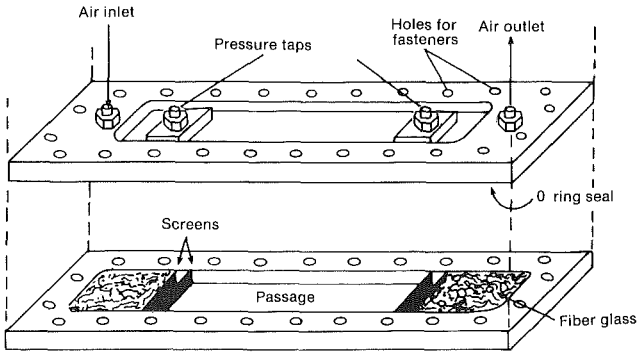

Fig. 4 Schematic diagram showing construction of a test cell

Table 1 Physical characteristics of the test cells

Lexan test cells (3 different gap sizes)
Overall dimensions: 1.91 cm × 27.0 cm × 7.2 cm
Passage gaps = 1 mm, 3 mm, 5 mm
(passage gaps were adjusted by applying layers of tape on the passage walls)
Passage width = 4.0 cm
Passage length = 12.0 cm

$$E = -RT \ln \left(\frac{P_v}{P_s}\right) = -RT \ln \text{(relative humidity)} \tag{8}$$

Since the moisture uptake X is a function of E, for a given moisture uptake, the change in relative humidity (RH) from temperature T_1 to T_2 can be represented by the equation

$$RH_2 = RH_1^{(T_1/T_2)} \tag{9}$$

For $X = 0.30$, a change of temperature from 20°C to 25°C will change the equilibrium value of relative humidity from 0.600 to 0.605. This scheme was used to account for minor temperature variations.

For a given moisture uptake X in the desiccant an equilibrium relative humidity can be determined if the temperature is known. Then the equilibrium concentration C_s on the surface of the desiccant can be determined from the equation

$$\frac{C_s}{1-C_s} = 0.6219 \frac{RH \times P_{\text{sat}}}{P - RH \times P_{\text{sat}}} \tag{10}$$

where P is the operating pressure.

Experimental Procedure

A schematic diagram of the test cell, which was made of Lexan, is shown in Fig. 4. The bottom side of the top piece is flat, except for a groove to accommodate an O-ring pressure seal. In the bottom piece a rectangular cutout was milled to serve as the air passage. The pressure taps were installed at the inlet and outlet between a pair of screens as shown. They were connected to absolute pressure gages and a pressure difference gage. Fiberglass wool was used to straighten the flow ahead of the entrance. Relevant data for the three test cells used are presented in Table 1.

Tapes with glue on both sides were placed on the upper and lower walls of the air passage. The tape was Mystic 6466 polyester film with a total thickness of 0.076 mm and thermosetting adhesive on both sides. The outside of each tape was coated with silica gel particles. Three test cells with gaps of about 1, 3, and 5 mm were constructed. The size of the gap was controlled by using a different number of layers of tape on the walls.

The experimental setup for the mass transfer experiments is shown schematically in Fig. 2. Before an experiment dry air from the air cylinder with less than 4 ppm of water vapor was

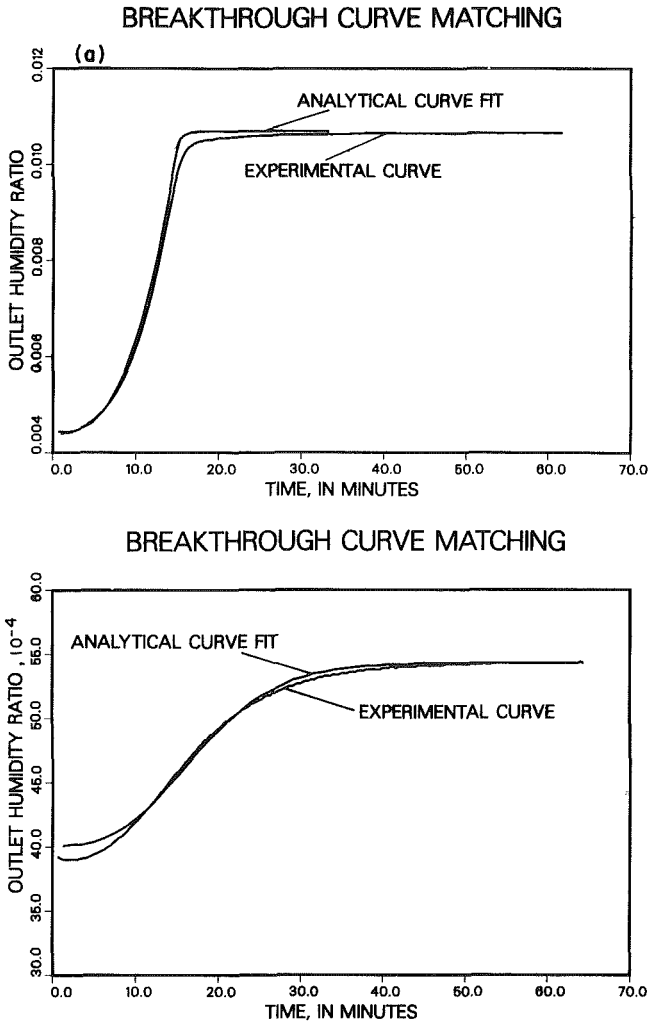

Fig. 5 Examples of matching experimental breakthrough curves with predicted ones: (*a*) second column and (*b*) last column under 3 mm group in Table 2

passed through the humidifier bypass to dry the silica gel in the test cell. The desired humidity level in the air to be used in a sorption test was obtained by cooling the water bath in the humidifier to a predetermined temperature level. The initial conditions for a test were established by passing this conditioned air through the cell until the outlet dew point reading remained unchanged at the desired level for at least half an hour. Then the test cell was sealed off and the test cell bypass opened.

The temperature level in the humidifier was then changed to initiate the step change in the inlet air humidity. The air moisture concentration was allowed to stabilize and then the test cell bypass valves were switched to the test cell to begin the experiment. The stabilization process after changing the temperature level in the humidifier typically took about one hour.

The volumetric flow at standard temperature and pressure was controlled by a Tylan mass flow controller. The dew points of the air before entering and after leaving the test cell were determined with two General Eastern dew point hygrometers. The pressures upstream and downstream of the test section were measured with two MKS diaphragm-type pressure transducers.

During an experiment the moisture concentration at the outlet initially remained the same as the initial concentration in the test cell for a finite period because it takes some time for the concentration wave to emerge from the test cell. The experiment was terminated after the breakthrough curve was completed, i.e., after the outlet hygrometer reading had stabilized for a period of time. The pressure and the dew point were monitored throughout the experiment. The concentration change at the outlet due to a step change at the inlet, called the "breakthrough curve," was thus determined as a function of time. The condition during a test was maintained isothermally by submerging the test cell in a constant temperature water bath, as shown in Fig. 2. The assumption of isothermal condition has been validated as shown by Chuah et al. (1986).

Transfer Coefficient

In the transient measurement of a transfer coefficient, the dependent variable is measured as a function of time at the outlet and compared to the predicted values for a range of values of the transfer coefficient. The transfer coefficient is then obtained by matching the experimentally measure curve to the predicted one. Examples of matching the breakthrough curves are shown in Fig. 5 (*a*, *b*).

In this study, equations (3)–(7) were solved numerically to obtain the value of C at the outlet and a convergence scheme was added to the computer program to determine that value of the transfer coefficient, which gives a breakthrough curve that matches the experimental curve within a given tolerance.

One can also see in Fig. 5(*a*, *b*) that the slope of a breakthrough curve stays rather constant in the middle range of the breakthrough step. When other parameters are the same, the slope of the curve, slp, in this range (e.g., from 40 to 60 percent of breakthrough step) depends on transfer coefficient alone, or

$$\text{slp} = \text{slp}(h) \tag{11}$$

Then the transfer coefficient h can be corrected using the equation

$$h_{\text{new}} = h + \frac{dh}{d\text{slp}} (\text{slp(exp)} - \text{slp(pred)}) \tag{12}$$

The computer run was started by solving the governing equations twice for two initial guesses of the transfer coefficient h_1 and h_2 to estimate the differential $dh/d\text{slp}$. The computation was stopped when both $(h_{\text{new}} - h)$ and [slp(exp) − slp(pred)] fell within a preset tolerance level.

To estimate the magnitude of the solid side resistance, the gas side transfer coefficient must be known. For isothermal mass transfer, only a single transfer potential exists and the analogy between heat and mass transfer is valid for the gas side resistance. The analytically calculated Sherwood numbers for flow between parallel plates with constant boundary concentration and constant flux are 7.54 and 8.235, respectively (Shah and London, 1978). However, in a transient experiment the boundary condition is complex and an accurate analysis of the effective gas side Sherwood number is difficult. We believe that the test conditions in this study fall between the two extremes, but constant flux conditions were assumed in our comparisons. When the gas phase transfer coefficient is known, the solid side mass transfer resistance can be estimated as shown below.

Two-Film Model

To estimate the relative values of solid and gas-side resistance a two-film model will be used. The mass flux in the solid is given by

$$\dot{m}'' = -\rho_a D_s \frac{\partial(HX)}{\partial y} \tag{13}$$

where

H = equilibrium constant (kg H_2O/kg air)/(kg H_2O/kg desiccant), and is determined from the equilibrium isotherm.

The diffusivity of moisture in the solid is typically on the order of 10^{-10} m^2/s. To solve the diffusion equation in the solid requires not only an accurate knowledge of the diffusivity of vapor in the desiccant, but also its dependence on variables such as the concentration of moisture. In our experiments, silica gel particles were attached to an adhesive tape substrate, and the exact geometry for the pore diffusion process in the solid in this case is thus quite complex. However, it has been shown (Shaw and London, 1978) that for packed columns of spherical particles it is satisfactory to model the diffusion in the solid by assuming a uniform, lumped resistance for the solid phase and using an average water vapor concentration in the solid if the isotherm is nearly linear, as for regular density silica gel. As shown in Fig. 3 the isotherm of the silica gel used in this study is nearly linear. Hence, by assuming also a constant resistance in the gas phase, we have a simple two-film model with h in equation (1) as the total mass transfer coefficient.

If the silica gel layer on the walls is thin, the system can be modeled as a thin slab of desiccant of thickness t_s on the walls of a passage as shown in Fig. 6. Since for this study the thickness of the slab is only about 0.1 mm, a linear moisture distribution in the solid can be assumed and equation (13) becomes

$$m'' = \left(\frac{\rho_a D_s H}{t_s}\right)\Delta X' \tag{14}$$

The total transfer resistance is given by

$$\frac{1}{h} = \frac{1}{h_g} + \frac{H}{h_s} \tag{15}$$

where h_g and h_s are the transfer coefficients in the gas and the solid phase, respectively. From equation (14)

$$h_s = \frac{\rho_a D_s H}{t_s} \tag{16}$$

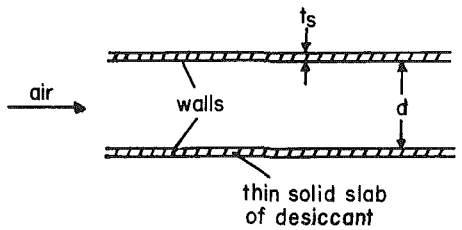

Fig. 6 Two-film model with thin solid slabs of desiccant on the walls

and therefore

$$\frac{1}{h} = \frac{1}{h_g} + \frac{t_s}{\rho_a D_s} \tag{17}$$

and

$$\frac{1}{\mathrm{Sh}} = \frac{1}{\mathrm{Sh}_g} + \left(\frac{\mathrm{Diff}}{D_s}\right)\left(\frac{t_s}{d_h}\right) \tag{18}$$

where d_h is the hydraulic diameter. For a parallel passage of gap d

$$\frac{1}{\mathrm{Sh}} = \frac{1}{\mathrm{Sh}_g} + \frac{1}{2}\left(\frac{\mathrm{Diff}}{D_s}\right)\left(\frac{t_s}{d}\right) \tag{19}$$

Based on the analysis of Aris (1959) for a parallel passage with a layer of adsorbing liquid on one wall only, Ruthven (1986) derived the equation below for estimating an effective Sherwood number Sh for a parallel passage silica gel-air system with transfer occurring at one wall only:

$$\frac{1}{\mathrm{Sh}} = \frac{1}{\mathrm{Sh}_{\mathrm{gas}}} + \frac{1}{6}\left(\frac{\mathrm{Diff}}{KD_s'}\right)\left(\frac{t_s}{d}\right) \tag{20}$$

where the value of K in (m^3 H_2O/m^3 desiccant)/(m^3 H_2O/m^3 air) is obtained from the adsorption isotherm and $\mathrm{Sh}_{\mathrm{gas}}$ is the value of the Sherwood number if only gas phase resistance exists. KD_s' in equation (20) is equivalent to D_s in equation (19). One can see that equations (19) and (20) have the same parametric dependence for the second term. Equation (18) is a closed-form equation for estimating a Sherwood number that is valid when the equilibrium isotherm is essentially linear and the average diffusivity in the solid is known. It is used here for predicting the Sherwood number.

Results and Discussion

In this study, a majority of the tests were adsorption tests using Davison's grade 40 silica gel, which was ground to 100–140 mesh (0.114–0.149 mm). The adsorption test results for this silica gel size are presented in Table 2 for different passage gaps.

Although extreme care was taken in the measurement of the total mass of dry silica gel in the passage, there still remained an uncertainty in the total gel mass in the passage as silica gel could readsorb during the coating. Also, there is a question regarding the "effective" gel mass in the method of gel application because some surface area of the gel may be rendered inactive by the glue on the wall. Therefore, for every test, the effective gel mass was measured dynamically from the breakthrough curve. In this measurement, the total amount of water adsorbed by the gel was first computed from

$$\text{total water adsorbed} = \dot{m}_{\mathrm{air}} \int_0^{\tau_{\mathrm{exp}}} (C_{\mathrm{in}} - C_{\mathrm{out}})\, d\tau \tag{21}$$

Table 2 Summary of the adsorption test results analyzed with both adsorption data and adsorption-desorption data isotherms; gel size was 100–140 mesh (0.114–0.149 mm)

Flow rate, sccm	1335	1335	1335	1335	1000	1000	1000	1038
Gel on wall, g	0.847	0.847	0.847	0.847	0.788	0.702	0.702	0.706
Actual passage gap, mm	1.02	1.02	1.02	1.02	3.38	3.28	3.28	5.23
Temperature, °C	24.6	21.4	21.5	20.9	20.3	20.5	20.6	20.9
Pressure, kPa	101	102	102	101	102	102	102	101
Initial C_s, C_{init}, 10^{-2}	0.421	0.444	0.442	0.446	0.442	0.442	0.378	0.446
Inlet C, C_{in}, 10^{-2}	1.02	1.05	1.06	1.06	1.07	1.07	0.54	1.09
Re $= Vd_h/\nu$	76.1	76.9	76.9	77.0	54.5	54.6	54.6	54.2
Effective total gel mass, g	0.702	0.681	0.692	0.663	0.442	0.650	0.807	0.704
Sh[1]	1.18	2.96	4.62	2.64	3.93	7.47	4.87	9.87
Sh[2]	1.05	2.18	3.14	1.97	3.12	5.55	5.08	7.72

[1]Obtained using adsorbtion data isotherm.
[2]Obtained using adsorption-desorption isotherm.

Table 3 Comparison of the measured average and the predicted Sherwood numbers for an empty passage

Gap size	AD isotherm Sh	AD/DE isotherm Sh	Predicted Sh
1 mm	3.41	2.43	3.60
3 mm	5.44	4.58	5.76
5 mm	9.87	7.72	6.55

Table 4 Sherwood number with different particle sizes; passage gap = 3.24 mm; Reynolds number is 49

Gel size	Effective thickness	Sh from equation (18)	Measured Sh
100–140 mesh	0.074 mm	5.82	5.08
60–80 mesh	0.091 mm	5.43	4.73
40–45 mesh	0.180 mm	4.07	3.49

where C_{in} and C_{out} are the concentration at the inlet and outlet, respectively. The final moisture uptake (= total water content/total gel mass in the passage) in the gel was calculated from the final relative humidity in the passage using the isotherm. The effective gel mass was then determined from the total water adsorbed and the initial moisture uptake in the gel. For most of the test, the effective gel mass was typically 20 percent less than the value measured from weight differences. Using the effective gel mass as the input, a good match between the experimental breakthrough curve and the analytically predicted curve was obtained, as shown in Fig. 5(*a*, *b*).

In the determination of the Sherwood number, the largest source of uncertainty is the uncertainty in the equilibrium isotherm. As shown in Table 2, using a slightly different isotherm can produce a substantially different Sherwood number. Norton (1986) estimated the uncertainty in the calculated Sherwood number resulting from uncertainty in the isotherm. His analysis showed that the uncertainty in the Sherwood number due to the uncertainty in the isotherm was ± 35 percent. Other possible sources of uncertainty include uncertainties in the initial condition, water bath temperature, slope matching, and effective gel mass in the passage. The total uncertainty in the experimental Sherwood number was estimated by Norton (1986) to be ± 43 percent for any single experiment.

The average Sherwood numbers ($Sh = hd_h/\rho_a Diff$), based on the hydraulic diameter of the empty passage as the characteristic length, for a range of Reynolds number from 50 to 70 are summarized in Table 3. As explained later on, Column 1 of Table 2 was not used in the calculation of the average Sherwood number.

Equation (18) can be used to estimate an overall Sherwood number for an empty passage with the solid side resistance taken into consideration. To use equation (18), a gas side Sherwood has to be estimated first. For the largest gap passage, a correction for entrance and side wall effects is needed for the Sherwood number. Using the data and formulas presented by Shah and London (1978), we first obtained a Sherwood number for a constant-flux boundary and also included entrance effects. Then the Sherwood number was corrected for side wall effects. For the range of flow conditions in this study, the corrected gas-phase Sherwood number is about 7.10 for the 5 mm passage and 7.50 for the 3 mm passage. A Sherwood number of 8.235 was used for the 1 mm passage as the side wall and entrance effects are both small.

Using an effective gel thickness of 0.07 mm, the predicted Sherwood numbers including solid-side resistance for 1 mm, 3 mm, and 5 mm passages are, respectively, 3.60, 5.76, and 6.55 as shown in Table 3. There values were computed using a solid side diffusivity of 1.0×10^{-10} m^2/s, which was estimated from data of Dengler and Kruckels (1970) However, for comparison

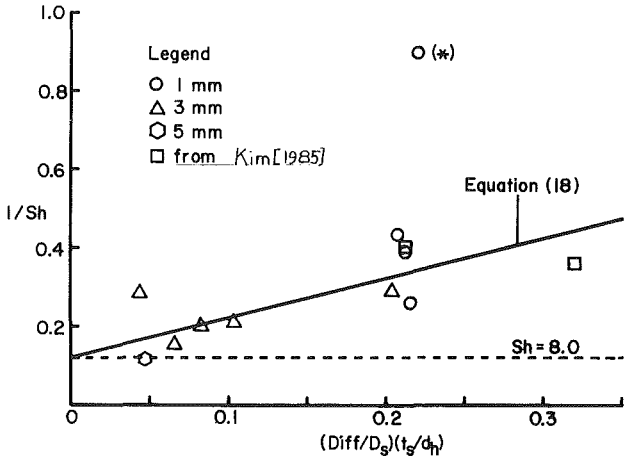

Fig. 7 Overall resistance 1/Sh versus the ratio of gas side resistance to resistance in solid (Diff/D_s) (t_s/d_h)

with the measured value of Sh, the analytic estimate has to be made using gel thickness and moisture content of each individual case. Table 3 shows a comparison of the predicted values with the experimental values. They have the same trends and the values for each gap size are similar.

The Sherwood number is seen to depend on the passage gap, an indication of the importance of solid side resistance. The gas side transfer coefficient is inversely proportional to the passage gap ($Sh = hd_h/p_a Diff$), but the solid side resistance is independent of the passage gap. As the gas side transfer resistance decreases proportionately with the passage gap, solid side resistance becomes dominant. This is confirmed by the experimental results, which show that the overall Sherwood number decreases with decreasing passage gap.

Adsorption tests were also made for an empty 3.24 mm passage using 60–80 mesh (0.177–0.250 mm) and 40–45 mesh (0.326–0.373 mm) gel particles. The results from these tests are shown in Table 4. Equation (18) was used to predict the effect of particle size. Again, we see the same trends and magnitudes of the predicted and experimental values.

From the above results, one can see the importance of solid side resistance in small gap (~ 1 mm) passages and when the gel size is large. Accurate determination of an overall Sh using equation (18) is quite difficult due to the lack of data on solid side diffusivity for the type of gel application used in this study. However, equation (18) does illustrate the parametric dependence of the solid side resistance.

Figure 7 shows a plot of 1/Sh versus (Diff/D_s) (t_s/d_h). The abscissa is physically the ratio of gas phase resistance to the resistance in the solid. The point indicated by an asterisk is seven standard deviations from the best fit and was therefore discarded. All other points fall close to the prediction of equation (18). Also shown in Fig. 7 are two measured values from experiments by Kim et al. (1985). These Sherwood numbers were not derived by curve matching, but a transfer coefficient was estimated that will predict a breakthrough curve close to the experimental one. For the two points shown, the predicted breakthrough curves were reasonably close to the experimental ones. One can see that these two points are also close to the prediction of equation (18).

Pressure drop data were taken by Norton (1986) over a range of Reynolds numbers between 50 and 200, which brackets the range of conditions in the mass transfer tests. The experimental results are compared in Fig. 8 with an analysis by Curr et al. (1972) for rectangular ducts. The uncertainty in the experimental results was shown by Norton (1986) to be ± 12 percent for the friction factor and ±6 percent for the Reynolds number. The agreement between analysis and experiment is within these uncertainty limits.

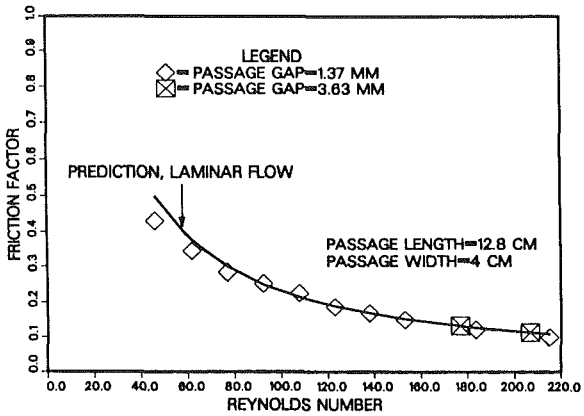

Fig. 8 Friction factor versus Reynolds number for flow through rectangular passages; comparison of experimental data by Norton (1986) with analysis by Curr et al. (1972)

Summary and Conclusions

Transient mass transfer in a flow of moist air through a parallel passage dehumidifier with silica gel coated walls was investigated under isothermal conditions. An analysis is presented using a simple two-film model in which the gas film resistance can be obtained from available analytic solutions by means of the analogy between heat and mass transfer and the resistance in the solid film estimated by assuming a linear moisture distribution in the thin silica gel slab. This analytic approach was used to derive a relation for the overall transfer resistance between the gas and the solid in the form

$$\frac{1}{\mathrm{Sh}}=\frac{1}{\mathrm{Sh}_{\mathrm{gas}}}+\left(\frac{\mathrm{Diff}}{D_s}\right)\left(\frac{t_s}{d_h}\right) \tag{18}$$

The analytical predicitons were verified by experiments in passages with 1 to 5 mm gaps in which the overall Sherwood number could be measured by matching predicted and experimental breakthrough curves. The analysis is applicable to other desiccant materials and can be used to predict the performance characteristics of dehumidifiers, including the ribbon wound dehumidifier/regenerator wheel proposed for future desiccant air-conditioning systems. It should be noted, however, that the validity of the two-film model has so far only been verified over a limited range of parameters; when the solid side resistance overwhelmingly dominates, the distribution of resistance will have to be modeled in more detail. It is suggested that in future work the limits of the parameters over which the simple theory proposed here is valid should be investigated.

Acknowledgments

We thank Dr. A. Pesaran and Dr. A. Czanderna for permission to use the isothermal test loop that they designed and built at SERI. We also thank Prof. R. E. West of the University of Colorado and Prof. Douglas Ruthven of the University of New Brunswick for constructive suggestions. Financial support for the experimental work was provided by the Gas Research Institute.

References

Ahlberg, J. E., 1939, "Rates of Water Vapor Adsorption From Air by Silica Gel," *Industrial Engineering Chemistry*, Vol. 31, pp. 988–992.

Aris, R., 1959, "On the Dispersion of a Solute by Diffusion, Convection, and Exchange Between Phases," *Proceedings of the Royal Society*, Ser. A, Vol. 252.

Banks, J. P., 1985, "Prediction of Heat and Mass Regenerator Performance Using Nonlinear Analogy Method: Part 1—Basis; Part 2—Comparison of Methods," ASME JOURNAL OF HEAT TRANSFER, Vol. 107, pp. 222–238.

Barlow, R. S., 1983, "An Assessment of Dehumidifier Geometries of Desiccant Cooling Systems," SERI/TR-252-1529, Solar Energy Research Institute, Golden, CO.

Bharathan, D., Parsons, J. M., and Maclaine-cross, I., 1987, "Experimental Studies of Heat and Mass Exchange in Parallel-Passage Rotary Desiccant Dehumidifiers for Solar Cooling Applications," Report No. SERI/TR-252-2897, Solar Energy Research Institute, Golden, CO.

Biswas, P., Kim, S., and Mills, A. F., 1984, "A Compact Low-Pressure Drop Desiccant Bed for Solar Air Conditioning Applications: Analysis and Design," ASME *Journal of Solar Energy Engineering*, Vol. 106, pp. 153–158.

Chuah, Y. K., Kreith, F., and Norton, P., 1986, "Innovative Dehumidifier Development — Final Report," GRI-86/0228, Gas Research Institute, Chicago, IL.

Curr, R. M., Sharma, D., and Tatchell, D. G., 1972, "Numerical Predictions of Some Three Dimensional Boundary Layers in Ducts," *Compt. Meth. Appl. Mech. Eng.*, Vol. 1, pp. 143–158.

Dengler, W., and Kruckels, W., 1970, "Diffusion von Wasserdampf in Einzelkörern technischer Adsorbentien," *Chemie-Ing.-Techn.*, Vol. 42.

Eckert, E. R. G., and Goldstein, R. J., 1976, *Measurements in Heat Transfer*, 2nd ed., Hemisphere Publishing Company, Washington, DC, Chap. 8.

Edwards, D. K., Denny, V. E., and Mills, A. F., 1979, *Transfer Processes*, Hemisphere/McGraw-Hill, New York.

Ghezelayagh, H., and Gidaspow, D., 1982, "Micro-Macropore Model for Sorption of Water on Silica Gel in a Dehumidifier," *Chemical Engineering Science*, Vol. 8, pp. 1181-1197.

Hougen, O. A., and Marshall, W. R., 1947, "Adsorption From a Fluid Stream Flowing Through a Stationary Granular Bed," Chemical Engineering Progress, Vol. 43, pp. 197–208.

Jury, S. H., and Edwards, H. R., 1971, "The Silica Gel-Water Vapor Sorption Term," *Canadian Journal of Chemical Engineering*, Vol. 49, pp. 663.

Kim, S., Biswas, P., and Mills, A. F., 1985, "A Compact Low-Pressure Drop Desiccant Bed for Solar Air Conditioning Applications: Bench Scale Tests," ASME *Journal of Solar Energy Engineering*, Vol. 107, pp. 120–127.

Maclaine-cross, I. L., and Banks, P. J., 1972, "Coupled Heat and Mass Transfer in Regenerators—Prediction Using an Analogy with Heat Transfer," *International Journal of Heat and Mass Transfer*, Vol. 15, pp. 1225–1242.

Mei, V. C., and Lavan, Z., 1983, "Performance of Cross-Cooled Desiccant Dehumidifiers," ASME *Journal of Solar Energy Engineering*, Vol. 105, pp. 300–304.

Norton, P., 1986, "Mass Transfer in Sphere Packed Parallel Passages," Masters Thesis, University of Colorado, Boulder, CO.

Raghavam, V., and Gidaspow, D., 1985, "Diffusion and Adsorption of Moisture in Desiccant Sheets," *AIChE Journal*, Vol. 31, pp. 1791–1800.

Ruthven, D. M., 1984, *Principles of Adsorption and Adsorption Processes*, New York, Chaps. 8-9.

Ruthven, D. M., 1986, private communication.

Schlepp, D., and Barlow, R., 1984, "Performance of the SERI Parallel-Passage Dehumidifier," SERI/TR-252-1951, Solar Energy Research Institute, Golden, CO.

Shah, R. K., and London, A. L., 1978, "Laminar Flow Forced Convection in Ducts," *Advances in Heat Transfer*, Supplement I, Academic Press, New York.

Tewfik, O. E., 1964, "One Dimensional Mass and Heat Transfer and Their Coupling," *International Journal of Heat and Mass Transfer*, Vol. 7, pp. 409–421.

APPENDIX

The diffusivity of water vapor in air, Diff, is calculated using the following empirical correlation (Edwards et al., 1979):

$$D=1.735\times10^{-9}\frac{(T+273.15)^{1.685}}{P}\ \mathrm{m^2/s}$$

where T is in °C and P in atm.

The saturation pressure for water was taken from the 1977 ASHRAE fundamentals. A curve was fitted for the saturation pressures from a temperature range of −20°C to 100°C. In this range the equation presented below is accurate to three significant figures (or about 1 percent accuracy compared to ASHRAE data):

For $100°\mathrm{C}\geq T>0°\mathrm{C}$

$$\log_{10}P_s=10.1946-\frac{1730.63}{T+2.33.426}-1.22066\times10^{-4}T+6.85300\times10^{-3}\log_{10}T$$

and for $0°\mathrm{C}\geq T\geq-20°\mathrm{C}$

$$\log_{10}P_s=34.470-\frac{3457.7}{T+273.15}-7.8790\log_{10}(T+273.15)+2.2610\times10^{-6}(T+273.15)^2$$

Single- and Two-Phase Convective Heat Transfer From Smooth and Enhanced Microelectronic Heat Sources in a Rectangular Channel

D. E. Maddox

I. Mudawar

Boiling and Two-Phase Flow Laboratory,
School of Mechanical Engineering,
Purdue University,
West Lafayette, IN 47907

Experiments have been performed to assess the feasibility of cooling microelectronic components by means of single-phase and two-phase forced convection. Tests were conducted using a single heat source flush mounted to one wall of a vertical rectangular channel. An inert fluorocarbon liquid (FC-72) was circulated upward through the channel at velocities up to 4.1 m/s and with subcooling up to 46°C. The simulated microelectronic heat sources tested in this study include a smooth surface and three low-profile microstud surfaces of varying stud height, each having a base area of 12.7×12.7 mm^2. Correlations were developed for the single-phase convective heat transfer coefficient over the Reynolds number range from 2800 to 1.5×10^5, where Reynolds number is based on the length of the heater. The results demonstrate that the low thermal resistances required for cooling of microelectronic heat sources may be achieved with single-phase forced convection by using high fluid velocity coupled with surface enhancement. Experiments were also performed to understand better the parametric trends of boiling heat transfer from the simulated microelectronic heat source. It was found that increased velocity and subcooling and the use of microstud surfaces enhance nucleate boiling, increase the critical heat flux, and reduce the magnitude of temperature overshoot upon the inception of nucleation.

Introduction

In recent years continued miniaturization of semiconductor electronics has led to significant increases in the heat dissipation of microelectronic chips. The power density for a single chip is already up to 40 W/cm^2 and is expected to exceed 100 W/cm^2 in the next decade. As this trend continues, new technologies must be developed to meet chip cooling demands. One area of interest is cooling by direct immersion in dielectric fluids such as the 3M Fluorinerts. Although the thermal transport properties of these fluids are poor, their effectiveness can be improved considerably by such factors as forced convection, structural enhancement, and boiling.

Single-phase forced convection presents a reliable form of direct immersion cooling, which has been proven capable of meeting requirements in microelectronic cooling. Tuckerman and Pease (1981), for example, attained a heat flux of 790 W/cm^2 using an enhanced surface consisting of microscopic channels 50 μm wide and 300 μm deep through which water was forced at a rate of about 8.6 ml/s. Based on heat transfer correlations developed for water, they estimated the thermal resistance for the FC-77 Fluorinert to be about 2.3 times greater than that for water. Although these values are above the expected requirements for electronic cooling, a pressure drop of over 214 kPa is required for a single 1 cm^2 heat source. This problem is a serious drawback when considering a system with a large number of computer chips.

In a more basic study, Incropera et al. (1986) obtained correlations for a single 12.7×12.7 mm^2 smooth heat source, flush mounted in a rectangular flow channel. The fluids tested were water and FC-77, and experimental data covered the Reynolds number range $1000 < \mathrm{Re}_D < 14000$. Their data were correlated by the equation

$$\overline{\mathrm{Nu}}_L = 0.13\ \mathrm{Re}_D^{0.64}\ \mathrm{Pr}^{0.38} \left(\frac{\mu_m}{\mu_w}\right)^{0.25} \tag{1}$$

Samant and Simon (1986) also considered single-phase cooling of a heater in a rectangular channel, but in their case the heater was very small, with a length of only 0.25 mm and a width of 2.0 mm. Because of the short length, the thermal boundary layer was very thin, causing the heat transfer coefficient to be considerably higher than for a typical computer chip. Their data were fitted by the equation

$$\overline{\mathrm{Nu}}_H = 0.47\ \mathrm{Re}_H^{0.58}\ \mathrm{Pr}^{0.50} \tag{2}$$

where both Nusselt number and Reynolds number were based on the height of the flow channel perpendicular to the heater surface.

Additional experiments were performed by Ramadhyani and Incropera (1987) to increase the heat transfer coefficient by means of surface enhancement. Their work included two types of fins: a basic cylindrical pin, 11.2 mm in height and 2.03 mm in diameter; and a finned pin consisting of the basic fin with a series of square fins protruding along its length. These fins increased the area of the heated surface by factors of 8 and 12.8, respectively. The results of the experiments for FC-77 showed that the thermal resistance could be reduced by a factor as high as 20 for the basic pinned surface. Additional reductions in thermal resistance achieved through the use of finned pins were small ($\approx$20 percent).

The results of Ramadhyani and Incropera were attained with moderate levels of pressure drop across the heater surfaces (up to 0.68 kPa). Other methods, such as the microchannel of Tuckerman and Pease, have reached considerably higher cooling rates but with a penalty of very high pressure drop. For

Contributed by the Heat Transfer Division and presented at the National Heat Transfer Conference, Houston, Texas, August 1988. Manuscript received by the Heat Transfer Division March 16, 1988. Keywords: Augmentation and Enhancement, Boiling, Electronic Equipment.

such high heat fluxes it may be more appropriate to consider cooling by two-phase forced convection.

Although considerable work has been done in the area of pool boiling, there have been few flow boiling studies applicable to electronic cooling. One relevant study was performed by Katto and Kurata (1980). Their experiments involved a submerged jet flowing parallel to a small rectangular heater. Experiments were conducted for water and R-113, and all tests were made using saturated fluid at atmospheric pressure. Three heater surfaces, having the dimensions 10×10 mm^2, 15×10 mm^2, and 20×10 mm^2, were tested. The results were restricted to data and correlations for critical heat flux (CHF). The maximum values of CHF were obtained with the 15×10 mm^2 surface. Typical values for R-113 were 45.4 W/cm^2 at 2.1 m/s and 78.2 W/cm^2 at 6.02 m/s.

One drawback of two-phase systems is the thermal shock associated with a sudden drop in surface temperature that sometimes occurs upon the incipience of boiling. This phenomenon, called hysteresis, was encountered by Samant and Simon (1986) in experiments with flow boiling of FC-72 over the same small heater used in their single-phase experiments. However, the large degree of temperature overshoot in their data may be attributed to two aspects of the small size of their heater. First, the total number of surface cavities with vapor embryos would be small for such a small heater so incipience is more likely to be delayed. Second, the region of nucleation at the point of incipience is likely to be a large fraction of the total surface. Thus the effect of initial nucleation on the overall heat transfer coefficient is considerable. These effects are not likely to be as significant with heat sources as large as a typical computer chip, yet Samant and Simon's results may still be useful in understanding parametric influences on hysteresis. A study by Mudawwar et al. (1987) involving heat transfer to falling films of FC-72 from heat sources similar in size to those used in the present study showed little or no hysteresis for the full range of their operating conditions. Little hysteresis was also found in jet impingement R-113 boiling experiments by Ma and Bergles (1983). The large magnitude of hysteresis associated with pool boiling of low contact angle fluids such as R-113 and FC-72 (Bergles and Chyu, 1982; Marto and Lepere, 1982) suggests that fluid motion tends to reduce hysteresis for larger heat sources.

The present study includes results of experiments involving both single-phase and two-phase flow of FC-72 over heat sources with smooth and microstud surfaces. The objectives of the single-phase experiments were to expand the data base of Incropera et al. to a much higher Reynolds number range and to enhance heat transfer using a low-flow blockage microstud surface attachment. The two-phase experiments were performed to develop an understanding of the effects of forced convection, subcooling, and surface enhancement on the boiling curve in an effort to improve heat transfer performance for typical electronic cooling applications. Particular emphasis was placed on reducing hysteresis and increasing CHF. More specifically, it was desired to increase the heat transfer rate in the fully developed nucleate boiling range, especially at a surface temperature of 85°C, which is considered the maximum allowable chip junction temperature for reliable computer operation.

In selecting an appropriate enhanced surface for this study, a low-profile fin enhancement was chosen because of its limited flow blockage and low pressure drop characteristics. Furthermore, for the case where a series of heat sources are mounted in a flow channel, low-profile fins serve to minimize the thickening of the bubble boundary layer formed by nucleate boiling on the upstream heat source. The microstud surface was chosen because of its proven effectiveness in increasing the heat transfer rate in the fully developed nucleate boiling region (Grimley et al., 1987). Choice of spacing and width of the fins was based on the work of Nakayama (1984), and three fin heights were tested to determine the effect of fin height on boiling performance. The maximum fin height of 1.02 mm was limited by machinability and fin strength.

Experimental Apparatus

The flow loop of the experimental system is shown schematically in Fig. 1. The test heater was mounted in one side of a vertically oriented rectangular flow channel with an entrance length of 76 cm. The entrance reservoir upstream from the flow channel contained a nozzle that smoothly converged the flow to the channel dimensions. Also contained in the entrance reservoir was an immersion heater to control fluid temperature at the entrance to the test section. Any vapor formed by this heater was bypassed directly into the upper reservoir. The upper reservoir contained both an immersion heater and a coil-type condenser to aid in control of operating conditions.

Fluid was circulated through the flow loop by means of a magnetically coupled centrifugal pump. At the pump outlet a bypass line branched off from the main line to provide low fluid velocities in the test section while maintaining adequate flow through the pump. The fluid in the main line passed through a flat-plate heat exchanger, a filter, and a turbine flow meter on its way to the test section.

A cross-sectional view of the test heater assembly is shown

Nomenclature

a = microstud height
D = hydraulic diameter of flow channel
G = mass velocity = $\rho_f U$
H = height of flow channel perpendicular to heater surface
k = thermal conductivity of liquid based on channel entrance temperature
L = heater length in the flow direction
$\overline{\mathrm{Nu}}_H$ = average Nusselt number based on channel height perpendicular to heater surface = $qH/(T_w - T_m)k$
$\overline{\mathrm{Nu}}_L$ = average Nusselt number based on heater length = $qL/(T_w - T_m)k$
Pr = Prandtl number of liquid based on channel entrance temperature
q = heat flux
q_m = critical heat flux (CHF)
q_m^* = dimensionless CHF = $(q_m/Gh_{fg})/(\rho_g/\rho_f)^{0.582}$
Re_D = Reynolds number based on channel hydraulic diameter
Re_H = Reynolds number based on channel height perpendicular to heater surface
Re_L = Reynolds number based on heater length
$\mathrm{T_{CHF}}$ = mean heater surface temperature at critical heat flux
T_m = liquid temperature at channel entrance
T_{sat} = saturation temperature
T_w = mean temperature of heater surface
$\Delta T_{\mathrm{sat}} = T_w - T_{\mathrm{sat}}$
$\Delta T_{\mathrm{sub}} = T_{\mathrm{sat}} - T_m$
U = mean fluid velocity
We = Weber number = $G^2 L/(\sigma \rho_f)$
μ_m = dynamic viscosity based on liquid temperature at channel entrance
μ_w = dynamic viscosity of liquid based on heater surface temperature
ρ_f = density of saturated liquid
ρ_g = density of saturated vapor
σ = surface tension

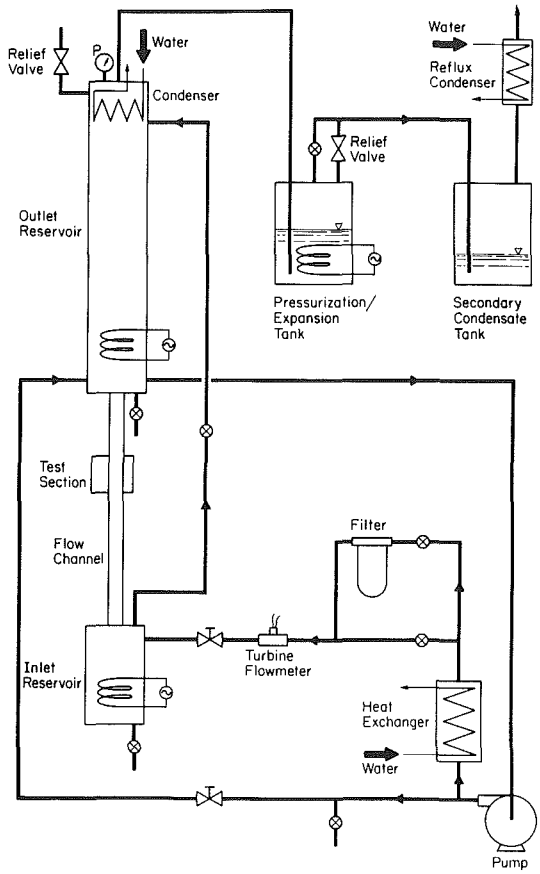

Fig. 1 Schematic diagram of the experimental facility

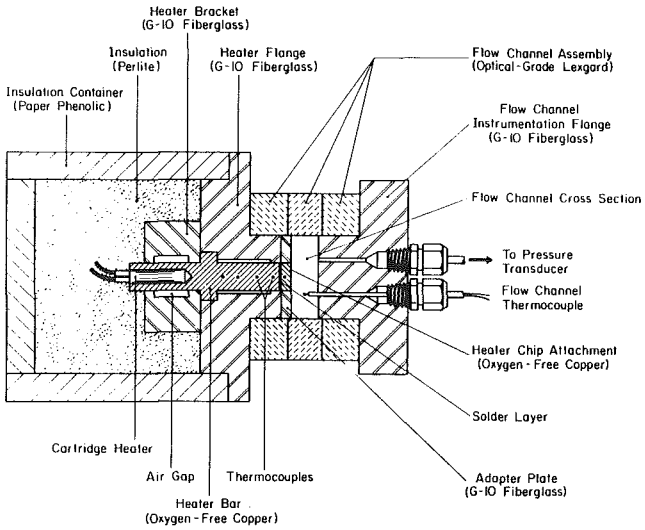

Fig. 2 Cross-sectional diagram of the heater assembly

in Fig. 2. The heater element consisted of a cylindrical cartridge heater embedded in an oxygen-free copper bar, which was mounted in a G-10 fiberglass flange. The 12.7×12.7 mm^2 simulated chip was soldered to the bar and surrounded by an adapter plate, which was flush mounted to the wall of the flow channel. The heat flux was measured by a series of four thermocouples located along the length of a section of the copper bar having the same 12.7×12.7 mm^2 cross section as the surface attachment. The square-shaped section was insulated from the surrounding fiberglass flange with an air gap partially filled with silicone rubber having a thermal conductivity 0.06 percent

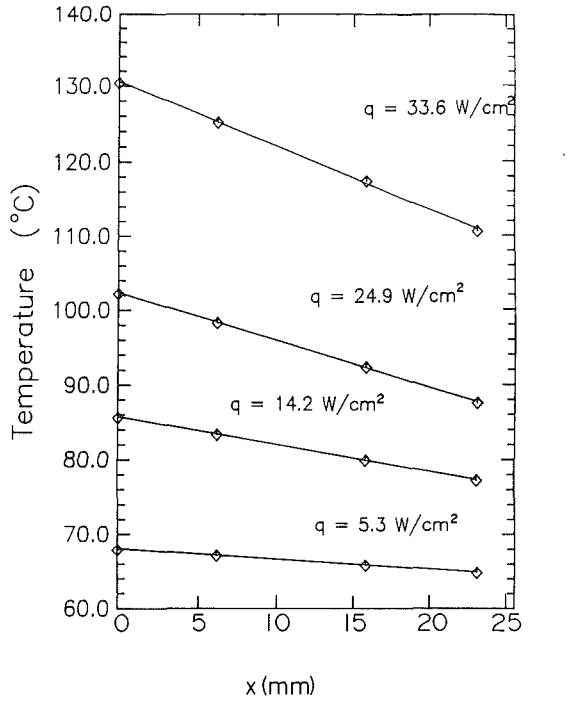

Fig. 3 Sample of measured temperature profiles along the calorimeter bar

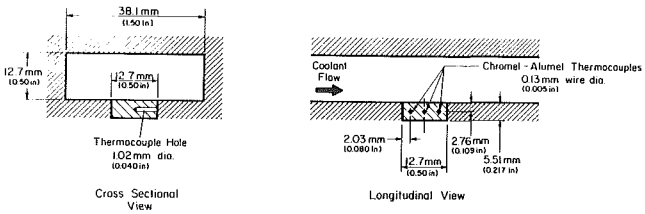

Fig. 4 Location of heat source in the flow channel wall

that of copper. This ensured one-dimensional heat flow along the instrumented portion of the heater. The thermocouples were made from 0.13-mm wires, and were set in the center of the bar. The temperature gradient used for evaluating the heat flux was calculated from a linear least-squares fit to the four temperature measurements. The sample temperature profiles shown in Fig. 3 illustrate the linearity associated with these measurements. A fifth thermocouple embedded in the simulated chip provided a temperature, which was then extrapolated based on conduction resistance between the thermocouple and the boiling surface to obtain the surface temperature. In one variation of the smooth surface chip three thermocouples were embedded in the chip along its length to measure the temperature variation of the heater surface in the flow direction. The total axial temperature differential was limited to 0.1°C except for fluxes close to CHF where the differential was as high as 1.2°C. The thermocouple arrangement is illustrated in Fig. 4, which also shows the location of the surface chip with respect to the flow channel. Voltage signals from the thermocouples and heater were processed and controlled by means of a Compaq 286 microcomputer used with a Keithley System 500 data acquisition and control system.

The heater surface tested in this study included a smooth surface and microstud surfaces of three different fin heights. The construction of the microstud surfaces is illustrated in Fig. 5. The square studs were oriented diagonally with respect to the direction of fluid flow to provide a more streamlined fin arrangement. The finned surfaces were machined by cutting two series of perpendicular grooves diagonally across the sur-

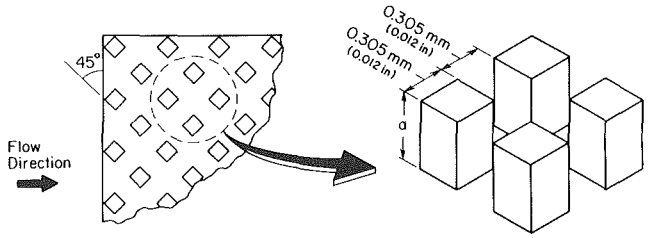

Fig. 5 Schematic of the microstud-enhanced surfaces

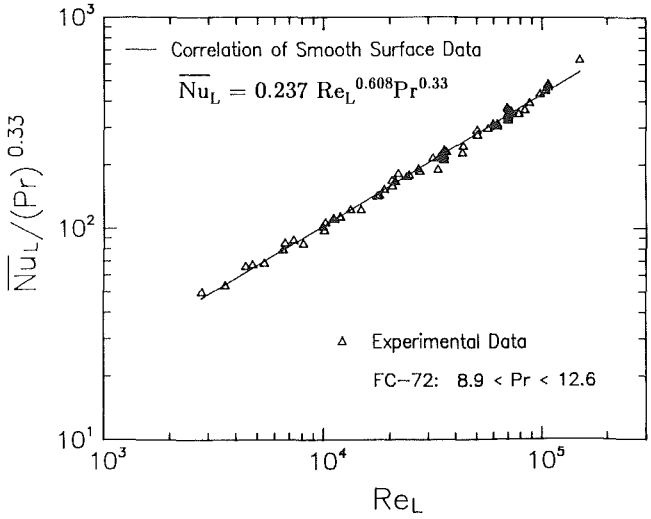

Fig. 6 Single-phase data and correlation for the smooth surface

face. The heights of these fins were 0.25, 0.51, and 1.02 mm. All surfaces were prepared before each experimental run by a vapor blast treatment consisting of a high-pressure stream of air, water, and abrasive particles to ensure uniform surface microstructure.

At the beginning of each experimental run the system was deaerated by operating the immersion heaters and the test heater and circulating the fluid through the flow loop. Vapor and air were allowed to exit from the top of the upper reservoir, passing through the pressurization tank and into the secondary condensate tank. The reflux condenser on the condensate tank allowed the air to escape from the system while recondensing the test fluid. When the system was completely deaerated, the outlet of the pressurization tank was closed off. If fluid subcooling was desired, the power to the immersion heaters and the water flow through the heat exchangers were adjusted to decrease the fluid temperature. The system pressure was maintained by adjusting the power to the immersion heater in the pressurization tank.

The procedure for obtaining data in the single-phase experiments was to start at one limit of the velocity range and to adjust the heat flux such that the heater surface temperature was about 10°C below the expected boiling incipience point. When the system reached steady state, the data were recorded, and a new velocity was then chosen. This procedure was repeated until the other limit of the velocity range was reached. In the boiling experiments, the procedure varied depending on the objective of the individual run. In general, the test heater was turned off after dearation for a given nonboiling period, and the power was then increased in small increments. In most cases the period without boiling was less than 2 h. In a few cases, however, it was increased in order to determine its effect on hysteresis. Following each power increment, steady-state conditions were reached after a waiting period of 15 to 30 min. Smaller power increments were added near boiling incipience

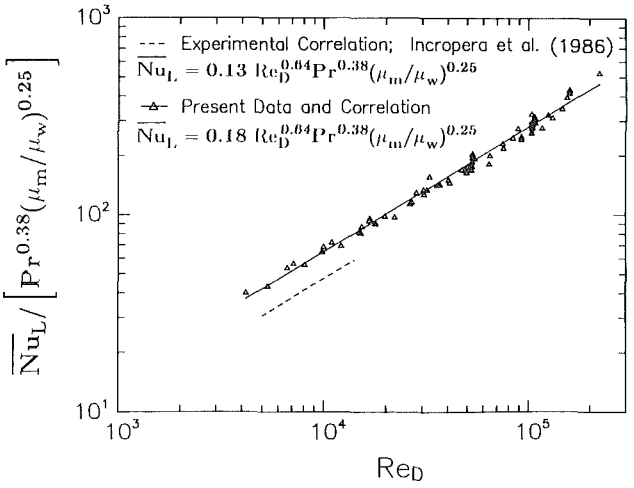

Fig. 7 Comparison of single-phase smooth surface data with the correlation of Incropera et al. (1986)

and CHF in order to obtain accurate measurements at these points.

Results

Single-Phase Studies. Figure 6 shows the single-phase atmospheric pressure FC-72 data for the smooth surface. The data are correlated in the Reynolds number range $2800 < Re_L < 1.5 \times 10^5$ by the equation

$$\overline{Nu}_L = 0.237\ Re_L^{0.608}\ Pr^{0.33} \quad (3)$$

where all properties are based on the mean fluid temperature at the entrance to the flow channel. The Prandtl number exponent was chosen as 1/3, which is typical for turbulent channel flow since the exponent could not be directly deduced from the limited Pr range of the present study. The maximum and mean deviations of data from equation (3) are 13.9 and 3.5 percent, respectively.

The present data were also correlated with respect to Re_D, the Reynolds number based on the channel hydraulic diameter. This parameter is more important than Re_L in electronic cooling applications involving a large array of microelectronic heat sources lined up along the flow channel. A comparison of the smooth surface single-phase results with the correlation of Incropera et al. (1986) is shown in Fig. 7. The viscosity ratio multiplier and Prandtl number exponent given in Fig. 7 are not necessarily recommended for design purposes since they were utilized solely for the purpose of comparison with the correlation of Incropera et al. The slopes of the two correlations are almost identical but the data of the present study lie approximately 37 percent higher than the correlation of Incropera et al. One possible explanation for this difference is channel orientation. Incropera et al. used a horizontal flow configuration with the heater facing upward while, in the present study, a vertical upward flow configuration was used. Density gradients in the vertical configuration may cause the thermal boundary layer to accelerate, thus enhancing heat transfer. Another reason for the difference may be the different treatment of heat losses in the two studies. In the present study, heat flux was calculated from the temperature gradient in the copper bar of the base heater. The temperature profile in this bar was very linear, suggesting that heat loss was very small. A very small heat loss, however, may occur beyond this bar near the chip surface. Nevertheless, the dimensions of this region are similar to those of the heater used by Incropera et al., so the loss should not be greater than the 8 percent predicted for their heater. It should also be noted that their data were corrected for the numerically predicted heat loss, which rep-

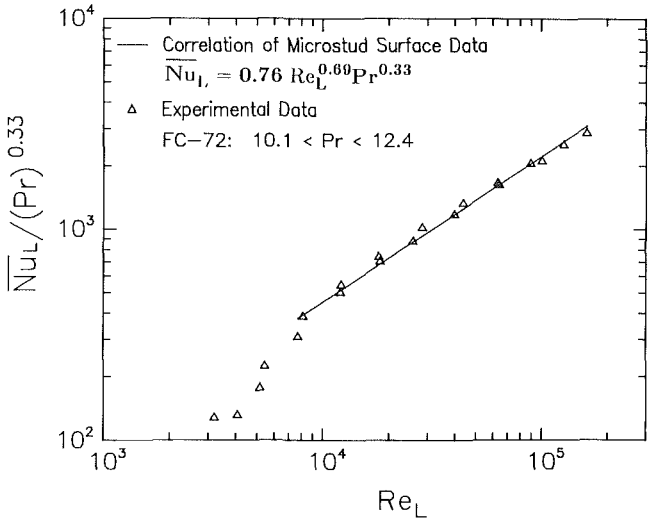

Fig. 8 Single-phase data and correlation for the microstud surface

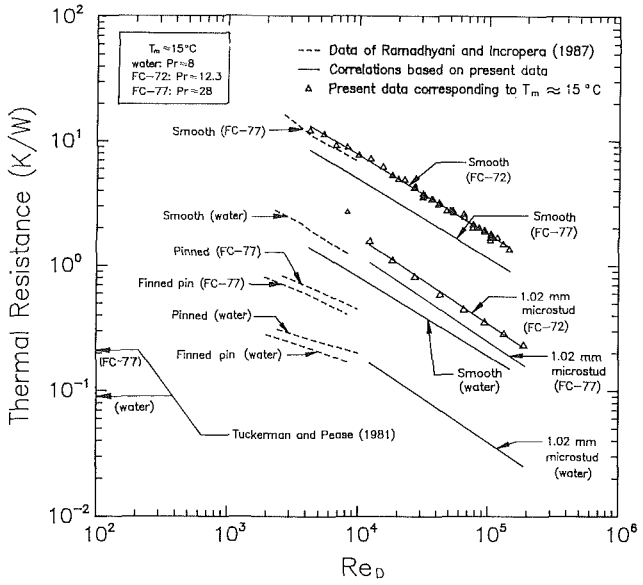

Fig. 9 Single-phase thermal resistance versus Reynolds number for smooth and microstud surfaces of the present study along with the data of Ramadhyani and Incropera (1987)

resents an upper limit, rather than the actual value, of heat loss. Another argument against the influence of heat loss in the present study is the fact that, although the data were taken over a wide range of heat flux (1.4 to 29.7 W/cm^2), they followed a well-established correlation as shown in Fig. 7. On a percentage basis, heat loss should decrease with increasing heat transfer coefficient. The fact that the slope of the present correlations was almost equal to the slope of the correlation by Incropera et al. suggests that heat loss in the present study does not account for the differences between the two correlations. Thus it can be concluded that the heat flux calculations of the present study satisfactorily accounted for heat loss.

Experimental data were also obtained in the present study using a compact heater of shallower construction (see details of heater design in Mudawwar et al., 1987), which consisted of a resistive wire sandwiched between two thin plates of a thermally conducting ceramic material and clamped against a copper plate, which supplied the heat to the chip attachment. This heater was designed to reduce heat loss by bringing the heating element closer to the wetted surface. The heat loss was numerically estimated to be less than 6 percent of the supplied electrical energy for the conditions of the present study. The compact heater was utilized primarily in high critical heat flux experiments where the calorimeter bar overheated beyond the maximum allowable temperature of the fiberglass flange. It was found that the electrical flux measured with the compact heater was about 4 percent lower than the heat flux measured by the calorimeter bar via linear curve fits of thermocouple readings. This fact is further evidence of the accuracy of the flux measurements using the calorimeter bar.

Figure 8 shows the single-phase data and correlation for the 1.02-mm microstud surface. At the lower end of the Reynolds number range the Nusselt number falls off rapidly, suggesting a change in the flow regime. Figure 9 shows a comparison of thermal resistances for the smooth and microstud surfaces of the present study along with the water and FC-77 data of Ramadhyani and Incropera. At the low end of the Reynolds number range, the thermal resistance for the microstud surface is reduced by a factor of 3.1 compared to the smooth surface. The reduction is much larger at higher velocities, with values of 4.3 at $Re_D = 12{,}000$, 5.4 at $Re_D = 1.5\times10^5$, and 6.2 at $Re_L = 1.5\times10^5$. Although this reduction is not as great as that obtained by the pin fins of Ramadhyani and Incropera, the use of higher velocity can offset the difference. For example, at $Re_D = 1.9\times10^5$ the thermal resistance of the microstud surface was 0.23 K/W, whereas for the most enhanced surface of Ramadhyani and Incropera, the minimum thermal

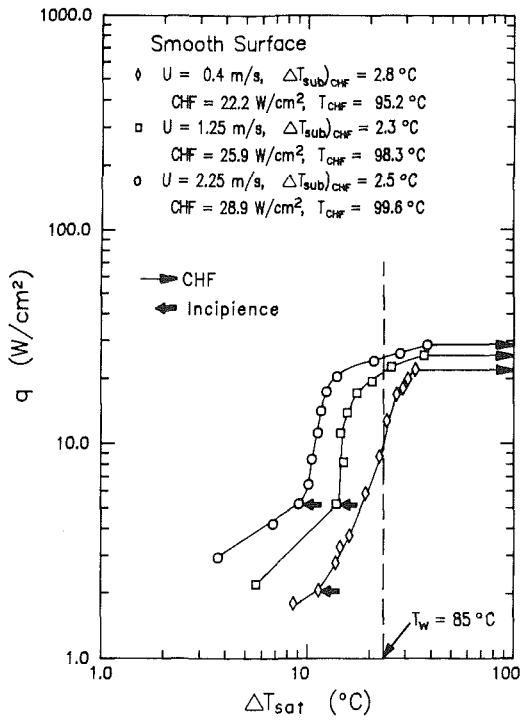

Fig. 10 Effect of velocity on the boiling curve for the smooth surface

resistance for FC-77 was about 0.42 K/W at $Re_D = 8100$. This conclusion may sound trivial, yet its practical implications are very important. Although microfin surfaces require higher coolant flow rates compared to the heavily finned surfaces of Ramadhyani and Incropera, they offer the advantages of minimal flow blockage and potentially lower pressure drop, allowing a large number of microelectronic heat sources to be mounted in series along the same flow channel.

The thermal resistance values can also be used to calculate the maximum values of heat dissipation for each surface, based on a typical surface-to-fluid temperature difference of 40°C (for FC-72) and a surface area of 12.7×12.7 mm^2. At $Re_D = 1.9\times10^5$, a thermal resistance of 1.3 K/W for the smooth

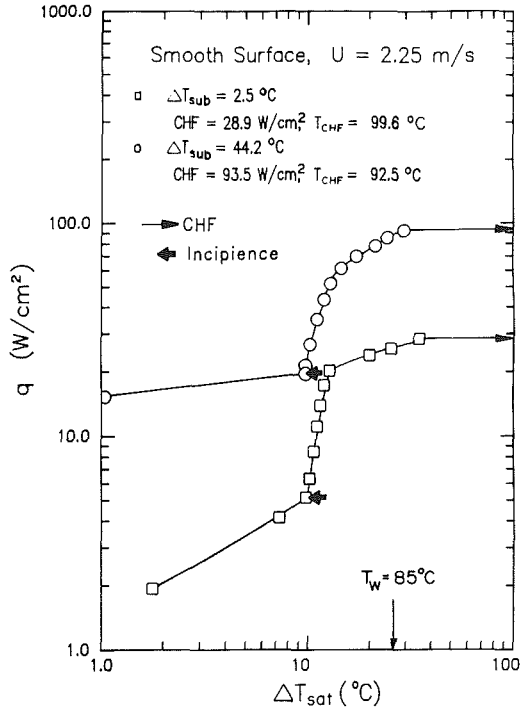

Fig. 11 Effect of subcooling on the boiling curve for the smooth surface

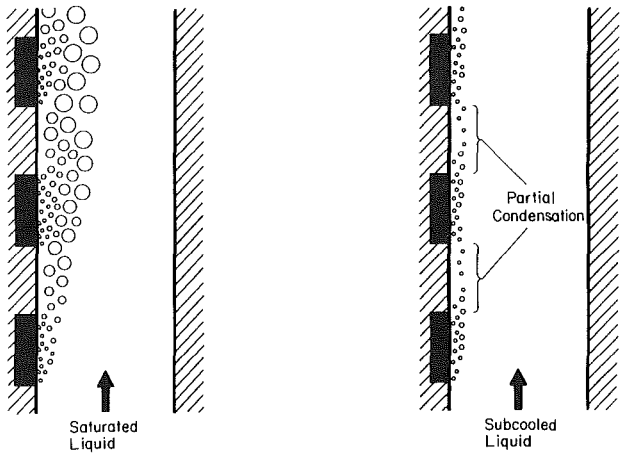

Fig. 12 Development of bubble boundary layers for the cases of high and zero subcooling

surface under these conditions corresponds to a heat flux of 19 W/cm². At the same Reynolds number for the microstud surface, a thermal resistance of 0.23 K/W corresponds to a heat flux of 108 W/cm². However, single-phase heat transfer rates calculated directly from equation (3) or Fig. 9 should be limited to heat flux levels below those required to trigger nucleation of bubbles on the surface. This limitation is of paramount importance in some applications where operation in the two-phase mode may be undesirable.

Two-Phase Studies. Figure 10 shows the effect of velocity on the cooling performance of the smooth surface. The higher velocities resulted in significant enhancement in the single-phase and nucleate boiling regions. At a surface temperature of 85°C, for example, an increase in velocity from 0.4 m/s to 2.25 m/s increased the heat flux by a factor of 2.6. At fluxes near CHF, however, the higher velocities showed significant reduction in the heat transfer coefficient, and the curves began to converge. The enhancement of CHF due to an increase in velocity from 0.4 m/s to 2.25 m/s was 28 percent.

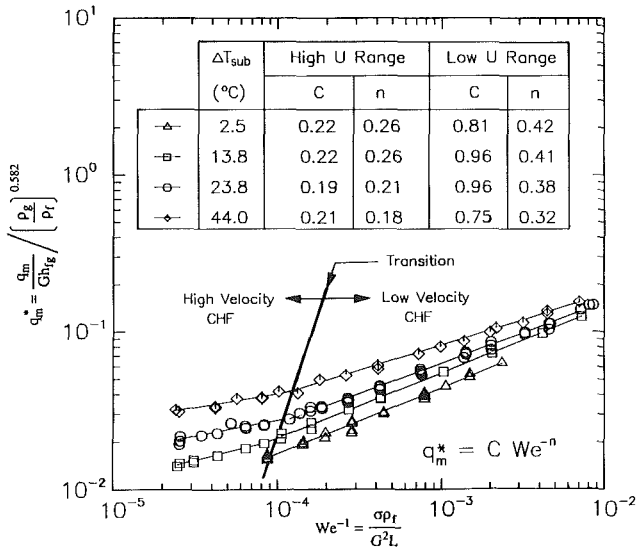

Fig. 13 Correlations of the critical heat flux for the smooth surface with velocity and subcooling

With fluid subcooling, the enhancement of the heat transfer coefficient was considerably higher at fluxes close to CHF. This is shown in Fig. 11, which includes boiling curves for the smooth surface with 2.5°C and 44.2°C subcooling. The heat flux for the case with 44.2°C subcooling was increased above that for saturated boiling by a factor of 3 throughout the higher heat flux region. The value of CHF with 44.2°C subcooling was 93.5 W/cm² and the heat flux at a surface temperature of 85°C was 75 W/cm². This enhanced heat transfer performance can be explained by the lower temperature of liquid leaving the bulk region toward the heater surface during boiling.

Another advantage of subcooling is the fact that the low bulk fluid temperature causes vapor bubbles to recondense both as the bubbles are formed and after they leave the surface. Flow visualization has revealed that subcooling significantly reduces both bubble departure diameter and the thickness of the bubble boundary layer. This is illustrated schematically in Fig. 12, which shows the development of bubble boundary layers for cases of high and low subcooling. With high subcooling the bubbles are so small and recondense so quickly, they are barely visible. These facts have important implications for electronic cooling since highly subcooled flow would allow an array of heat sources to be mounted along the length of a flow channel without the danger of compromising the cooling performance of downstream heat sources.

CHF data were taken over a velocity range of 0.2 to 4.1 m/s and subcooling up to 46°C. Figure 13 shows CHF increasing with both velocity and subcooling. The data reveal a transition from a lower slope at lower velocity to a steeper slope at high velocity. This trend indicates a marked change in the CHF mechanism with increased velocity. Flow visualization revealed that for the lower velocity range, CHF was caused by dryout following the formation of a single continuous blanket, which covered the entire heated surface. On the other hand, CHF in the high velocity range was accompanied by dryout over several smaller discrete portions of the surface. Figure 13 also shows CHF correlations with the inverse Weber number for each of the four levels of subcooling. The exponent of the vapor-to-liquid density ratio term was chosen as the average of the values from the studies by Katto and Kurata (1980) and Yagov and Puzin (1984) for channel flow because the range of density ratio in the present study was fairly constant.

The results for the microstud surfaces, shown in Fig. 14, revealed more complicated nucleate boiling characteristics. This was probably due to the existence of different boiling regimes

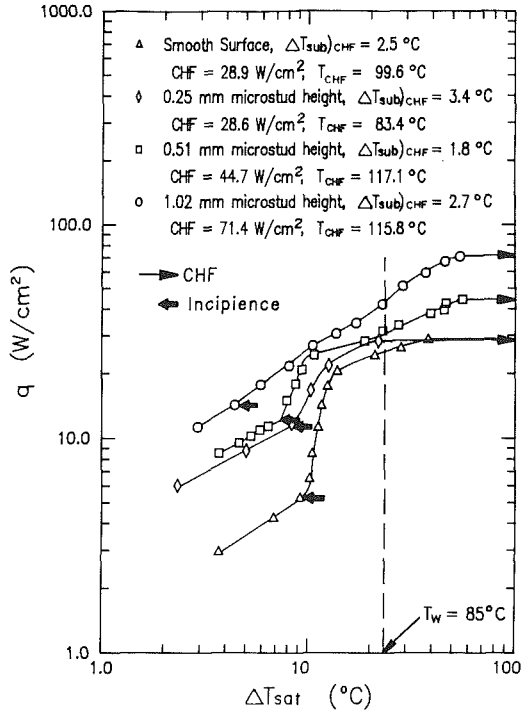

Fig. 14 Effect of fin height on the boiling curve for microstud surfaces

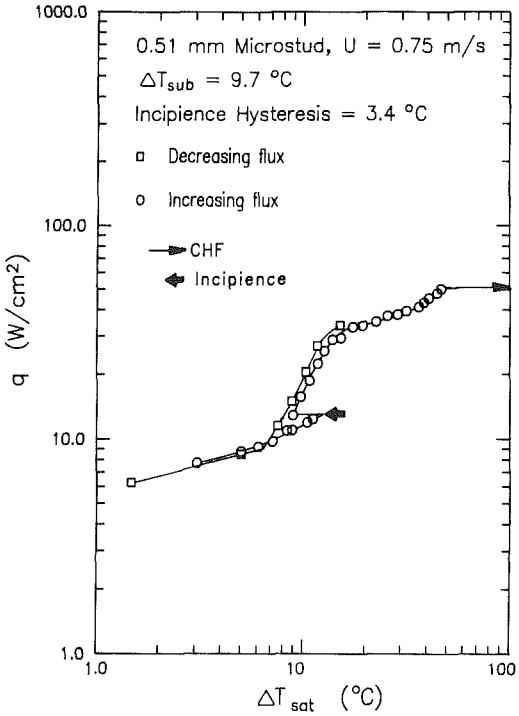

Fig. 15 Hysteresis in the boiling curve of the 0.51-mm microstud surface

between the base surface and the tips of the fins. All fin heights provided substantial enhancement in the single-phase region. The degree of enhancement then decreased in the nucleate boiling region. As the curves progressed toward the point of departure from nucleate boiling, the curves for the smooth surface and the surface with the shortest microstud height both broke abruptly to CHF, while surfaces with longer microstuds extended the boiling region to higher fluxes. The explanation for this behavior is that the tips of the longer fins remained in the nucleate boiling regime even after the base surface had departed from nucleate boiling. The 0.51 and 1.02-mm microstud heights showed enhancement of CHF over the smooth surface by factors of 1.5 and 2.5, respectively. The highest CHF value of 262 W/cm² was obtained with the 1.02-mm microstud surface at a velocity of 4.1 m/s and 46°C subcooling.

Hysteresis. It is very difficult to correlate the phenomenon of hysteresis because of the large number of variables that influence the onset of nucleation from wall cavities. Small deviations in such factors as size and distribution of surface cavities, fluid purity, and the history of vapor embryos at the boiling surface all have substantial influences on the amount of temperature overshoot associated with the onset of nucleation. Therefore efforts were made to determine qualitatively the effects of certain parameters on hysteresis and to obtain worst case values for overshoot.

One factor that has been found to have a substantial influence on hysteresis is the period of time during which the chip remains in the nonboiling state both before and during the increase of heat flux toward incipience. It is hypothesized that during this waiting period vapor embryos within the surface cavities shrink in size, requiring higher heat flux for nucleation. For every case in which hysteresis exceeded 2°C, the nonboiling period was greater than one hour. Aside from this fact there was no apparent correlation between the waiting period and the magnitude of hysteresis.

Another factor that has been considered is the presence of dissolved air in the fluid. If air makes its way into a surface cavity, it would create artificial embryos, resulting in premature boiling and reduced temperature overshoot. Two experimental runs with large amounts of air in the system yielded hysteresis values of 2°C. Thus, while the presence of air may reduce hysteresis, it does not eliminate it entirely.

The worst case of hysteresis obtained in the present study suggests some trends of hysteresis associated with the effects of enhancement. A temperature overshoot of 7.5°C occurred in an experiment with the smooth surface at a low velocity of 0.75 m/s and almost zero subcooling. However, extensive testing with the microstud surface at similar conditions resulted in a maximum temperature overshoot of 4°C. Thus, it can be concluded that the presence of microstuds generally reduces hysteresis. One explanation for this behavior is that the studs enhance single-phase heat transfer considerably compared to the lower nucleate boiling range. Thus the percentage increase in the heat transfer coefficient at incipience is less, and the resulting temperature drop is smaller than for an unenhanced surface. Another possible explanation is related to the hydrodynamics of fluid flow around a stud. Higher velocities tend to increase cavitation downstream of the studs, which may trigger boiling at a relatively lower wall superheat as Fig. 14 clearly indicates.

Another explanation for the relatively high degree of overshoot at low velocity and zero subcooling is the effect of fluid flow on the propagation of the nucleation front with increased heat flux. Boiling tends to start at the downstream edge of the heater because the fluid superheat is greatest at this point. Fluid drag forces at high velocities tend to push the bubbles downstream away from nonboiling portions of the heater, inhibiting the spread of nucleation. Since only a small portion of the heater experiences boiling at incipience, the overall heat transfer coefficient for the surface increases only slightly, resulting in a small surface temperature drop. Higher fluid velocities also increase the single-phase heat transfer coefficient prior to boiling. Thus, the nucleate boiling contribution to the overall heat transfer coefficient following the onset of nucleation becomes less significant with increased velocity. Fluid subcooling produces a similar effect by decreasing the bubble size. The smaller bubbles are less likely to spread boiling to neighboring nucleation sites, and propagation of the boiling front is inhibited.

These velocity and subcooling effects are in general agreement with the results of Samant and Simon as reported by Bar-Cohen and Simon (1986). Their data showed a very strong relation between velocity and temperature overshoot, and a weaker but still distinct relationship for subcooling.

The data for an experimental run in which hysteresis occurred are shown in Fig. 15. This run was made for the 0.51-mm microstud surface with a fluid velocity of 0.75 m/s and 9.7°C subcooling. The procedure for the run was to start at a high rate of boiling and progress down the boiling curve into the single-phase region. Next, the system was run for two hours without boiling before progressing up the curve first toward incipience and finally to CHF. The intention of this procedure was to measure both the incipience hysteresis and an overall hysteresis in the boiling curve. The incipience hysteresis in this case was 3.4°C, while the curve hysteresis was much smaller.

Summary

Studies have been performed based on experiments in single-phase and two-phase forced convection cooling of a simulated microelectronic heat source. Key results are as follows:

1 New single-phase correlations were developed over the Reynolds number range $2800 < \mathrm{Re}_L < 1.5\times10^5$ ($4200 < \mathrm{Re}_D < 2.25\times10^5$) for a smooth surface, and $7700 < \mathrm{Re}_L < 1.6\times10^5$ ($1.16\times10^4 < \mathrm{Re}_D < 2.4\times10^5$) for a microstud surface. For a heater-to-fluid temperature difference of 40°C and a Reynolds number $\mathrm{Re}_D = 1.9\times10^5$, it was determined that the smooth surface could dissipate 19 W/cm^2, and the microstud surface 108 W/cm^2. The authors postulate that use of the low pressure drop microstud surface with high fluid velocity may be preferred over the use of higher pressure drop heavily finned surfaces at lower velocities.

2 Increasing fluid velocity resulted in significant enhancement in the single-phase and nucleate boiling regions of the boiling curve, but severe degradation in the nucleate boiling performance occurred prior to CHF with higher velocities and CHF enhancement was considerably smaller.

3 Fluid subcooling substantially increased cooling performance near CHF. At 44.2°C subcooling, the value of CHF was 93.5 W/cm^2, showing an increase by a factor of 3.2 over the case of near-saturated boiling.

4 For multichip cooling applications, subcooling offers the advantage of reduced bubble boundary layer thickness, thus making it more feasible to line heat sources up along the flow direction in a channel.

5 Increasing stud height showed significant enhancement throughout the boiling curve. The 1.02 mm microstud showed CHF values as high as 260 W/cm^2, presumably because nucleate boiling continued at the tips of the fins even after a departure from normal nucleate boiling had occurred near the base surface. Although trends in the data suggest that longer studs should improve performance further, such a surface would be difficult to manufacture. However, it is possible that for a different stud width and spacing, a longer stud may still improve performance.

6 It was found that the degree of hysteresis at boiling incipience was influenced by a number of factors. First, significant hysteresis occurred only after the heater surface remained in a nonboiling state prior to incipience for at least one hour. Also, increases in the single-phase heat transfer coefficient due to increased velocity and surface enhancement tend to reduce hysteresis because the sudden increase in heat transfer rate at boiling incipience is less. The microstuds may further reduce hysteresis as a result of cavitation downstream individual studs. Furthermore, flow visualization indicated that velocity reduces temperature drop at the incipience by inhibiting propagation of the bubble front in the upstream direction. These points agree with the fact that the worst case of temperature overshoot in the present study, which was 7.5°C, occurred with the smooth surface at a low velocity and low subcooling.

Acknowledgments

Support of this work by a grant from the Data Systems Division of IBM is gratefully acknowledged. The assistance of Mr. Richard C. Chu, Mr. Robert E. Simons, and Dr. Dereje Agonafer of IBM is appreciated. The authors also thank Mr. R. D. Danielson of the Industrial Chemical Products Division of 3M for providing fluid samples and technical information on the test fluid.

References

Bar-Cohen, A., and Simon, T. W., 1986, "Wall Superheat Excursions in the Boiling Incipience of Dielectric Fluids," *Heat Transfer in Electronic Equipment*, ASME HTD-Vol. 57, pp. 83–94.

Bergles, A. E., and Chyu, M. C., 1982, "Characteristics of Nucleate Pool Boiling From Porous Metallic Coatings," ASME JOURNAL OF HEAT TRANSFER, Vol. 104, pp. 279–285.

Grimley, T. A., Mudawwar, I., and Incropera, F. P., 1987, "Enhancement of Boiling Heat Transfer in Falling Films," *Proceedings of the 1987 ASME/JSME Thermal Engineering Joint Conference*, Vol. 3, pp. 411–418.

Incropera, F. P., Kerby, J. S., Moffatt, D. F., and Ramadhyani, S., 1986, "Convection Heat Transfer From Discrete Heat Sources in a Rectangular Channel," *Int. J. of Heat and Mass Transfer*, Vol. 29, pp. 1051–1058.

Katto, Y., and Kurata, C., 1980, "Critical Heat Flux of Saturated Convective Boiling on Uniformly Heated Plates," *Int. J. of Multiphase Flow*, Vol. 6, pp. 575–582.

Ma, C. F., and Bergles, A. E., 1983, "Boiling Jet Impingement Cooling of Simulated Microelectronic Chips," in: *Heat Transfer in Electronic Equipment*, ASME HTD-Vol. 28, pp. 5–12.

Marto, P. J., and Lepere, V. J., 1982, "Pool Boiling Heat Transfer From Enhanced Surfaces to Dielectric Fluids," ASME JOURNAL OF HEAT TRANSFER, Vol. 104, pp. 292–299.

Mudawwar, I., Incropera, T. A., and Incropera, F. P., 1987, "Boiling Heat Transfer and Critical Heat Flux in Liquid Films Falling on Vertically-Mounted Heat Sources," *Int. J. of Heat and Mass Transfer*, Vol. 30, pp. 2083–2095.

Nakayama, N., Nakajima, T., and Hirasawa, S., 1984, "Heat Sink Studs Having Enhanced Boiling Surfaces for Cooling of Microelectronic Components," ASME Paper No. 84-WA/HT-89.

Ramadhyani, S., and Incropera, F. P., 1987, "Forced Convection Cooling of Discrete Heat Sources With and Without Surface Enhancement," *Proceedings of the International Symposium on Cooling Technology for Electronic Equipment*, Honolulu, HI, pp. 249–264.

Samant, K. R., and Simon, T. W., 1986, "Heat Transfer From a Small, High-Heat-Flux Patch to a Subcooled Turbulent Flow," *Proceedings of the AIAA/ASME Heat Transfer and Thermophysics Conf.*, Boston, MA.

Tuckerman, D. B., and Pease, R. F., 1981, "Ultrahigh Thermal Conductance Microstructures for Cooling Integrated Circuits," *Proceedings of the 32nd Electronics Components Conference*, pp. 145–149.

Yagov, V. V., and Puzin, V. A., 1984, "Critical Heat Fluxes in Forced-Convection Boiling of Refrigerant-12 Under Conditions of Local Heat Sources," *Heat Transfer—Soviet Research*, Vol. 16, pp. 47–55.

Heat Transfer From a Small Heated Region to R-113 and FC-72

K. R. Samant
Senior Engineer,
E. I. du Pont de Nemours and Co., Inc.,
Seaford, DE 19973
Assoc. Mem. ASME

T. W. Simon
Associate Professor,
Mechanical Engineering Department,
University of Minnesota,
Minneapolis, MN 55455
Mem. ASME

An experimental investigation of heat transfer from a small heated patch to a subcooled, fully developed turbulent flow is conducted. The test patch, approximately 0.25 mm long and 2.0 mm wide, is located on the floor of a small rectangular channel through which a coolant (R-113 or FC-72) is circulated. A thin film of Nichrome deposited on a quartz substrate serves as an integrated heater element and resistance thermometer. The maximum achievable heat flux with R-113, limited by the thermal decomposition temperature of the fluid, is 2.04 MW/m² at a bulk velocity of 1.8 m/s and a high wall superheat of 80°C. The results obtained with FC-72 show large temperature excursions at the onset of nucleate boiling and a boiling hysteresis near the onset of nucleate boiling. These effects decrease with increasing velocity and/or subcooling. The heat flux at departure from nucleate boiling increases with increasing velocity and/or subcooling. A maximum heat flux of 4.26 MW/m² at departure from nucleate boiling is observed.

Introduction

Heat transfer from a small, high-heat-flux region is encountered in such applications as x-ray sources for lithography and medical applications, gas turbines, and superconductors. For example, heat fluxes as high as 250 MW/m², with a heated length of about 2.8 mm, were achieved in a prototype x-ray source built by Leslie et al. (1983). Presently, very little experimental data on boiling heat transfer from such a short heated length exist and prototypes, e.g., that of Leslie et al. (1983), are designed using empirical correlations valid for larger heated areas with lower heat fluxes.

The present study seeks to provide a data base for the applications mentioned above and to extend the domain of boiling heat transfer research to a very small heated length. The situation in the present investigation is shown in Fig. 1. A small heated patch, 0.25 mm long in the streamwise direction and 2.0 mm wide in the cross-stream direction, is located on the floor of a rectangular channel, which carries coolant circulating at high velocity. At the patch, the flow is isothermal and the velocity profile is fully developed. Refrigerant-113 (trichlorotrifluorethane) or Fluorinert FC-72 (manufactured by the 3M Company) is used as a coolant. The characteristics of heat transfer from the heated patch to the subcooled flow are investigated.

Previous Work

Baker (1972) investigated the heated length effect for single-phase forced convection showing heat transfer coefficients 15 time higher for small heaters (of nearly the same size as that of the present study) than for larger heaters. The effect of heater size on pool boiling characteristics was also presented by Baker (1973). To the authors' knowledge, the smallest heated length in any forced convection boiling study is ~1.5 mm (Ma and Bergles, 1986). A submerged jet of R-113, impinging at the center or at the edge of a 5×5 mm or a 3×3 mm heater surface, was used to achieve wall heat fluxes in excess of 1 MW/m². Ma and Bergles (1983), in a similar experiment, used a submerged jet of R-113, impinging either at the center or at the edge of a 5×5 mm vertical heater surface, to achieve wall heat fluxes as high as 1 MW/m². The burnout heat flux was proportional to the one-third power of jet velocity and showed a weak dependence on subcooling. At a given jet velocity, the burnout heat flux was about 25 percent higher for the shorter heated length (jet directed at the center) than it was for the other cases (jet centerline to one side of the heated region). The heater surfaces failed at the burnout heat flux; burnout occurred at the edge of the heated region farthest from the jet center. Pool boiling data showed large temperature excursions; the wall temperature decreased by 10–15°C at the onset of nucleate boiling. In the nucleate boiling regime, wall superheats were higher for increasing heat flux than for decreasing heat flux, a phenomenon known as boiling hysteresis. The events of both temperature excursion and boiling hysteresis were reduced by jet impingement.

In another study with a circular jet impinging at the center of heated circular disks (diameters ranging from 11 mm to 21 mm), Monde and Katto (1978) observed heat fluxes up to ~20 MW/m² with water and ~0.9 MW/m² with R-113. Based on a dimensional analysis, a generalized correlation for the burnout heat flux was presented. Katto and Shimizu (1979) in a similar experiment examined the variation of critical heat flux with jet velocity at different saturation pressures (6.0 to 27.9 bars) and proposed four characteristic regimes for the dependence of critical heat flux on jet velocity. Lienhard and Hasan (1979) presented a single correlation for the data of Monde and Katto (1978), Katto and Shimizu (1979), and Katto and Monde (1974) for the entire range of variables.

Katto (1981) correlated available critical heat flux data for forced convection boiling of water and R-113 in rectangular channels with a heated lower surface and with heated upper and lower surfaces in the range of $0.417 \le L/D \le 6.02$ with a

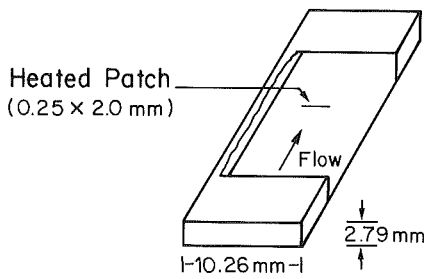

Fig. 1 Schematic of the heat transfer situations

Contributed by the Heat Transfer Division and presented at the AIAA/ASME 4th Thermophysics and Heat Transfer Conference, Boston, Massachusetts, June 2–4, 1986. Manuscript received by the Heat Transfer Division March 20, 1987. Keywords: Boiling, Forced Convection.

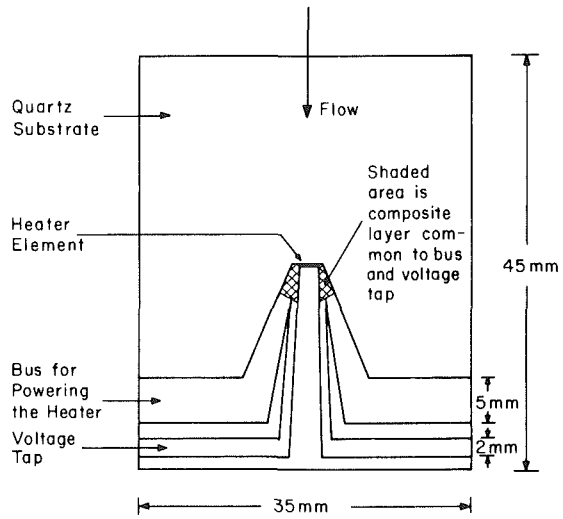

Fig. 2 Heater wafer with sputtered Nichrome surface and copper buses

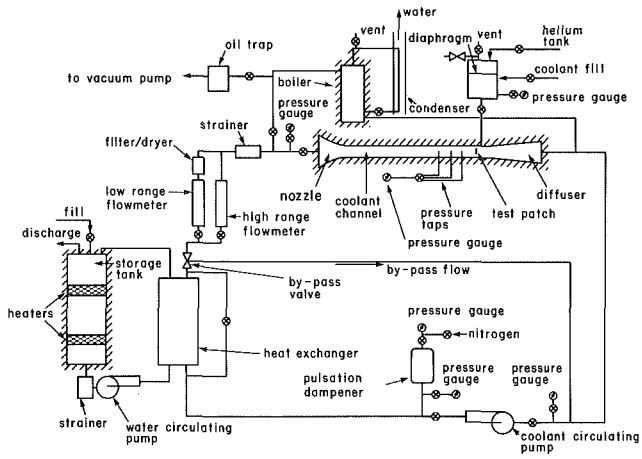

Fig. 3 Schematic of the test loop

smallest heated length of 1 cm. In general, the correlations show an increase in critical heat flux with increasing bulk velocity, increasing subcooling, and decreasing heated length. Tolubinskiy and Matorin (1983), in a study involving flow boiling of binary mixtures inside a 4-mm-i.d. heated pipe, observed that the critical heat flux was independent of the heated length for L/D values above ~10. It was also found that the influence of subcooling on critical heat flux was more pronounced at higher velocities. The data of Merilo (1977) for forced convection boiling of R-12 and water in a heated tube showed no influence of heated length in the L/D range of ~200–400. Bergles (1977, 1963) found that for subcooled flow in small diameter tubes, there was no influence of heated length on critical heat flux for L/D greater than 20, while Groenveld (1981) found that, for simple geometries, this limit was 30 for subcooled inlet conditions and 200 for two-phase inlet conditions. Maulbetsch and Griffith (1966) indicated that this limit for subcooled entrance conditions may be near 100.

Experimental Facility

The test patch is a thin film of Nichrome (0.25 mm long in the streamwise direction, 2.0 mm wide in the cross-stream direction, and 2 μm thick) sputtered on a quartz substrate (Fig. 2). Heating is achieved by channeling direct current into the test patch via a 25-μm-thick bus constructed as a composite layer of Nichrome, copper, and gold. Separate voltage taps are provided for measuring the voltage drop across only the test patch. A small correction to the heater calibration is applied to account for the voltage drop across the shaded area in Fig. 2. A shadowgraph was used to measure the area of the test patch with an estimated uncertainty of 2 percent. Thickness was calculated from the knowledge of coating time and coating rate and therefore could not be directly measured. Thickness variation may lead to temperature and heat flux variation. However, it should be recognized that the variation of a sputtered surface of this size is expected to be only a few percent and that the results presented here are average values. The details of the heater design and fabrication are given by Samant et al. (1984).

The test section consists of the nozzle, channel, and diffuser arrangement shown in Fig. 3. The heater wafer is placed inside a rectangular cavity on the floor of the channel in such a way that the surface of the heater wafer remains flush with the floor of the channel. Two pairs of copper bars embedded into either side of the channel make contact with the bus bars and voltage taps on the heater wafer upon assembly.

Working fluid is circulated through the test section by a high-pressure, low-volume pump (Fig. 3). A heat exchanger is provided for thermal control of the working fluid by exchange with a secondary-side circulation of water. Flow rate through the test section is measured by flow meters installed upstream of the nozzle. A boiler/condenser system is incorporated to degas the working fluid. It was found experimentally that run-

Nomenclature

a = coefficient in equation (4)
A^+ = Van Driest constant
b = exponent in equation (4)
c = coefficient in equation (4)
c_0 = coefficient in equation (2)
C_p = specific heat, kJ/kg K
d = exponent in equation (4)
dR/dT = slope of the calibration curve, Ohm/°C
D = heated equivalent diameter, m
h = heat transfer coefficient, W/m^{2}K
H = channel height, m
I = current, A
k = thermal conductivity, W/mK
l = mixing length, m
L = heated length, m
Nu = Nusselt number = hH/k
P = pressure at test patch, kPa
Pr = Prandtl number = $\mu C_p/k$
q_w = wall heat flux, MW/m^2, W/m^2
r_b = bubble radius, m
R = resistance, Ohm
Re = Reynolds number = $u_b H/\nu$
T = temperature, °C
u_b = bulk velocity, m/s
y = distance from the wall, m
y^+ = nondimensional distance from wall
α = temperature coefficient of resistance, 1/°C
$(\Delta T)_{sub}$ = subcooling, °C
κ = Von Karman constant
μ = dynamic viscosity, Pa•s
ν = kinematic viscosity, m^2/s
σ = surface tension, N/m
τ_w = wall shear stress, N/m^2

Subscripts

b = bubble, bulk
B = bus
eff = effective
SAT = saturated
SUB = subcooled
Tb = at temperature T_b
Tw = at temperature T_w
w = at the wall

ning the degassing facility for about 6–8 h was sufficient to degas the test loop. To minimize moisture content, the entire test loop is evacuated using a reciprocating vacuum pump to pressures as low as 200 μm of mercury for as long as 48 h.

The bulk temperature of the flow is measured with chromel-constantan thermocouples installed in the flow upstream of the nozzle. The entire test section is insulated to prevent thermocouple conduction errors and heat transfer between the working fluid and the environment. The pressure at the test patch location is measured by three pressure taps located on the top of the channel. The hydrodynamics of the flow are fully developed at the location of these pressure taps. The development length, calculated by a numerical solution of the governing continuity and momentum equations for developing turbulent flow between two parallel plates, was found to be much shorter than the distance of the farthest upstream tap from the channel inlet. The taps are upstream of the test patch; therefore, a small pressure drop correction between the taps and the test patch is applied. The absolute pressure at the test patch is governed by the pressure in the working fluid reservoir, which is in communication with a section of the channel 35 mm (1.373 in.) downstream of the test patch.

Experimental Procedure

A typical experiment involves in-situ calibration of the test patch, a test run, followed by another in-situ calibration. A programmable d-c power supply is used to power the test patch and a series resistor, which is immersed in a thermally insulated oil container for stability. A laboratory computer controls the output of the power supply via a power supply programmer. Voltage drops across the test patch and the series resistor and thermocouple emfs are measured by a multichannel data acquisition/control unit.

During the pretest calibration, working fluid is circulated through the test section at low velocity and small current is used to measure the resistance of the test patch. Under these conditions, the viscous dissipation and self-heating (due to applied current) effects are negligible and the measured resistance is the test patch resistance at the bulk temperature of the fluid as indicated by the thermocouples. The procedure is then repeated at several increasing bulk temperature values to obtain a pretest calibration curve. The test run involves powering the test patch to increasing/decreasing heat flux levels to generate a boiling curve. The post-test calibration is obtained by following a procedure similar to the one used for the pretest calibration except that the bulk temperature of the fluid is reduced from the test run value to a low value to obtain the calibration curve. A typical set of calibration curves is shown in Fig. 4. For each data point on the calibration curve (and boiling curve) an average of, typically, 20 data points is taken to obtain average values.

Data Reduction

Wall-to-Bulk Temperature Difference. Measurements of heater resistance in the unpowered state (R_{Tb}) and in the energized state (R_{Tw}), in conjunction with the slope of the heater calibration curve, give the wall-to-bulk temperature difference

$$T_w - T_b = \frac{R_{Tw} - R_{Tb}}{dR/dT\text{-}\alpha_B R_B} \tag{1}$$

The parameter $\alpha_B R_B$ is a small correction applied to the slope of the calibration curve as a result of the shaded area of Fig. 2 being common to both the voltage tap and the current carrying bus. Uncertainties of less than 3 percent in the measurement of wall-to-bulk temperature difference are estimated.

Wall Heat Flux. The total energy supplied to the heater element is I^2R_{Tw}. However, due to substrate conduction, heat

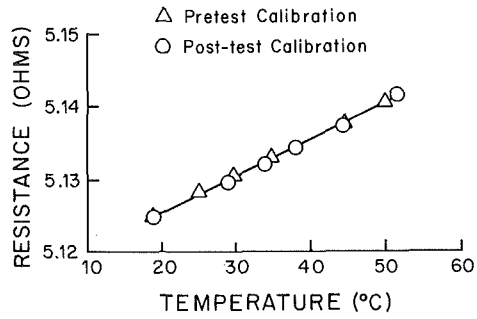

Fig. 4 In-situ calibration

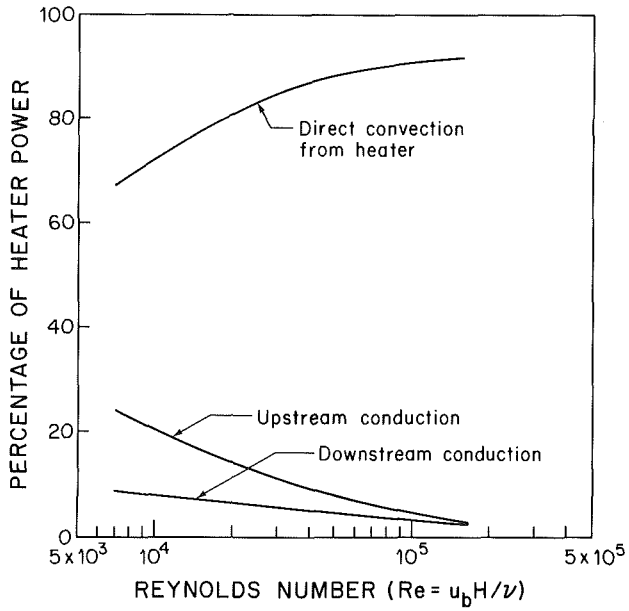

Fig. 5 Substrate conduction effect (FC-72)

transfer from the test patch directly to the flow by convection is lower than this value; heat is conducted upstream and downstream before being convected to the flow. The wall heat fluxes presented herein are based on the energy flow directly from the heater surface to the fluid. Details of the substrate conduction are given by Samant (1984). The results are summarized below.

A numerical analysis of the governing momentum and energy equations for the conjugate conduction/convection problem of heat transfer above and below the heater/quartz surface is performed using the computational procedure of Patankar and Spalding (1970). For single-phase situations, the standard Prandtl mixing length turbulence closure model is used. Results of such a computation for FC-72 are presented in Fig. 5. At low Reynolds numbers, the conduction effect is significant due to a relatively lower heat transfer coefficient from the test patch to the flow. As the flow velocity increases, however, an increasingly higher fraction of the heater power is directly convected to the flow and the correction due to conduction becomes less significant. Similar results are obtained with R-113.

For two-phase situations, a modification to the standard Prandtl mixing length model was developed. As shown in Fig. 5, substrate conduction becomes significant only at low velocities. During a boiling situation, the substrate conduction is further reduced due to increased heat transfer coefficient on the test patch relative to the single-phase heat transfer coefficient on the substrate. Therefore, for the present purpose, an approximate analysis will suffice. The two-phase system is treated as a continuous medium governed by the conservation equations for the liquid phase: The effect of increased heat

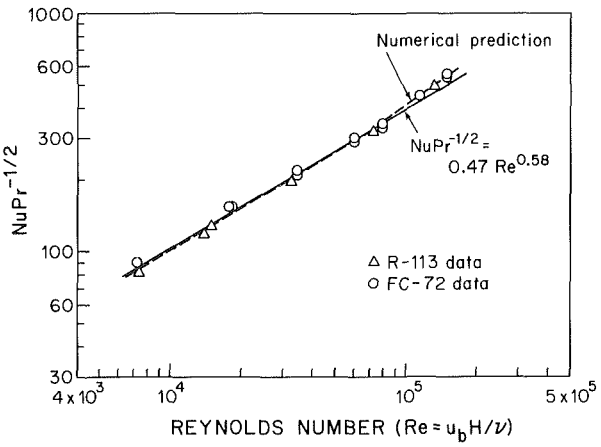

Fig. 6 Single-phase Nusselt number values for R-113 and FC-72

transfer due to boiling is incorporated by augmenting Prandtl mixing length. The agitation of the thermal boundary layer due to nucleation, growth, and collapse of bubbles is believed to be an important contributor to the enhanced heat transfer during nucleate boiling. Because of the short heated length involved, the bubble layer is expected to be very thin; a bubble may be growing and collapsing on or near the heater surface. Therefore, it is only necessary to augment the Prandtl mixing length on the wall. It is hypothesized that bubbles act as roughness elements in increasing the mixing in the near wall region. Therefore, at the wall

$$l \sim r_b$$

where the bubble radius, r_b, is obtained from a force balance

$$r_b \sim \left[\frac{\sigma H}{\tau_{w,\text{eff}}}\right]^{1/2}$$

A modified mixing length is proposed as follows:

$$l = C_0\left[\frac{\sigma H}{\tau_{w,\text{eff}}}\right]^{1/2} + Ky(1 - e^{-y^+/A^+}) \tag{2}$$

The governing equations were solved for each data point in the two-phase region of a boiling curve using the modified mixing length. The proportionality constant C_0 was adjusted to make the computed average wall temperature equal the measured value. Results indicated that the substrate conduction with nucleate boiling was much less important than with the single-phase situation and was found to decrease further with increasing heat flux and/or velocity. The uncertainty in the wall heat flux measurement is estimated to be less than 8 percent.

Results and Discussion

Single-Phase Heat Transfer. Experiments with R-113 were terminated at a wall temperature of 120°C to prevent corrosion of the heater surface by hydrogen chloride gas formed upon thermal decomposition of R-113. The maximum heat flux achieved, limited by decomposition, was 2.04 MW/m^2 at a bulk velocity of 16.5 m/s. Even at a low velocity of 1.8 m/s and a wall superheat of ~80°C, there was no evidence of boiling.

Nusselt number values with R-113 and FC-72 are shown in Fig. 6. The following correlation was developed from the combined data:

$$\text{Nu} = 0.47\ \text{Re}^{0.58}\text{Pr}^{0.50} \tag{3}$$

The fluid properties were evaluated at the bulk temperature. Equation (3) correlates the data with a maximum deviation of 7.6 percent and a standard deviation of 5.6 percent. The experimental data compare very well with the results of the numerical solution. The governing set of equations with applicable boundary conditions was solved using the solution procedure described in Patankar and Spalding (1970). The Prandtl mixing length model with a turbulent Prandtl number of 0.9 was used for turbulence closure and fluid property dependence on temperature was incorporated. The effect of substrate conduction was incorporated by defining a preheating length, expressed as a fraction of the actual heater length, to equal the ratio of upstream conduction to the direct convection from the heater. Computations were performed for several Reynolds numbers with various values of heat flux, which was assigned to be uniform over the entire heated length (preheating plus heater).

Two-Phase Heat Transfer. This section discusses the boiling curves (Fig. 7–10) obtained with FC-72 over a range of velocity and subcooling values. Test conditions and key boiling characteristics are given in Table 1.

The various regimes of a typical boiling curve are first discussed with reference to Fig. 7. As the wall heat flux is increased (open symbols), the heat transfer is, initially, by single-phase forced convection (A-B). A wall superheat of ~50°C is required to initiate boiling (B). At the onset of nucleate boiling, there is a sudden drop of ~10°C in the wall temperature due to the increased heat transfer coefficient on the heater surface as a result of boiling; region B-C is the temperature excursion. Further increases in heat flux, in the nucleate boiling regime (C-D), cause little change in the wall temperature and the heat transfer coefficient increases as more nucleation sites become active at higher heat fluxes. Several theories have been proposed in the literature (Hsu and Graham, 1976) for the increased heat transfer in the nucleate boiling regime. Agitation of the thermal boundary layer by the growth and collapse of vapor bubbles on the wall and within the bubble layer is believed to be a major contributor. The bubble layer is expected to be very thin due to the small heated length in the present investigation and the agitation of the thermal boundary layer is believed to be mostly due to the bubble dynamics. The maximum heat flux achieved in the nucleate boiling regime is called the departure from nucleate boiling (DNB) and is denoted by D in Fig. 7. As the heat flux is increased beyond the DNB value, the rate of formation of vapor bubbles exceeds the rate of collapse and removal from the heated surface. Under these conditions, boiling becomes unstable as an intermittent vapor film develops on the surface and the convective heat transfer coefficient drops. This process is called transition boiling. The surface is alternately covered with a vapor blanket and a liquid layer, resulting in an oscillating surface temperature. The data presented here are time- and space-averaged (over the patch area) values obtained over long time periods. These long-time averages were stable.

Data obtained with decreasing heat flux are indentified with closed symbols. The wall superheat corresponding to decreasing heat flux values within the transition boiling regime is essentially the same as that for increasing heat flux; hence, no hysteresis in the transition boiling regime is observed. Many of the nucleate boiling data are repeated upon decreasing heat flux as well. However, as the heat flux is further decreased, there appears to be a clear hysteresis in the data in the lower heat flux portion of the nucleate boiling regime; nucleate boiling persists to relatively low wall heat flux (low wall superheat) values. The boiling curve obtained with decreasing heat flux is EDCFA as opposed to AFBCDE obtained with increasing heat flux.

Hysteresis in the boiling curve, near the onset of the nucleate boiling, is a familiar characteristic of fluorocarbons and has been reported by others (Ma and Bergles, 1983; Hwang and Moran, 1981). These fluids have a small bubble-to-surface contact angle; hence larger cavities are easily flooded. Since a vapor embryo is needed for nucleation, a cavity

that is completely filled with liquid cannot act as a nucleation site. A higher superheat is needed to initiate boiling from the small cavities that retain vapor (Hwang and Moran, 1981). Once boiling has begun, however, a lower superheat is needed to maintain boiling. This results in lower superheats for established boiling (decreasing heat flux) than those for the nonboiling situation (increasing heat flux).

Temperature Excursion and Boiling Hysteresis. Temperature excursion and boiling hysteresis appeared to decrease with increasing subcooling and/or velocity (Table 1). The effect of subcooling at 4.11 m/s is shown in Fig. 8 (*b*, *c*). The boiling curve at the maximum test velocity of 16.86 m/s and 45.7°C subcooling is also shown (Fig. 8(*a*)). At 4.11 m/s, the temperature excursion at the onset of nucleate boiling is completely eliminated as subcooling is increased from 12.6°C to 54.4°C. However, there still remains a perceptible boiling hysteresis near the onset of nucleate boiling. The effect of velocity is shown in Fig. 9. The large temperature excursion of about 27°C in the 2.05 m/s run is reduced to ~10°C at 4.11 m/s. At a higher velocity of 7.25 m/s and an increased subcooling of 56.2°C, only a small hysteresis remains (Fig. 10) and there is no evidence of boiling hysteresis at the maximum velocity of 16.86 m/s (Fig. 8(*a*)).

The maximum temperature excursion in this investigation was ~27°C at a bulk velocity of 2.05 m/s and a subcooling of 13.4°C. This value is much higher than previously observed. Ma and Bergles (1983) reported temperature excursions of 10–15°C in pool boiling of R-113 and a 5×5 mm Constantan foil; temperature excursions of as small as ~3°C were observed by Hwang and Moran (1981) in pool boiling of FC-86 on a 0.279 cm² silicon chip. The large temperature excursions observed here are presumed to be due to the very small heat transfer surface; there are fewer cavities with vapor embryo to initiate boiling. As shown by Bar-Cohen and Simon (1986) both homogeneous and heterogeneous nucleation may be present in these data.

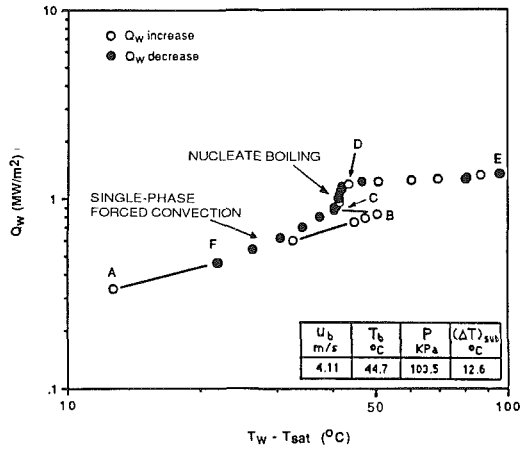

Fig. 7 Boiling curve for $u_b = 4.11$ m/s and $(\Delta T)_{sub} = 12.6$°C

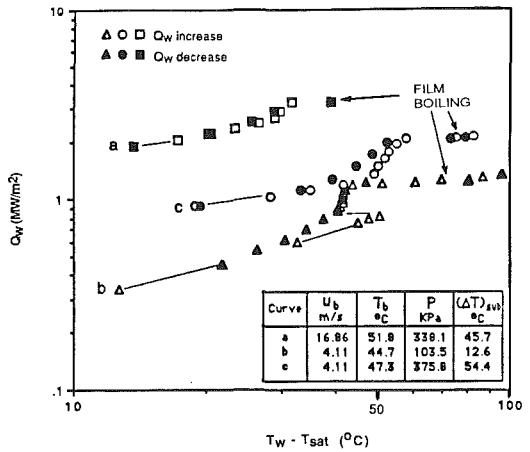

Fig. 8 Boiling curves at several bulk velocity and subcooling values

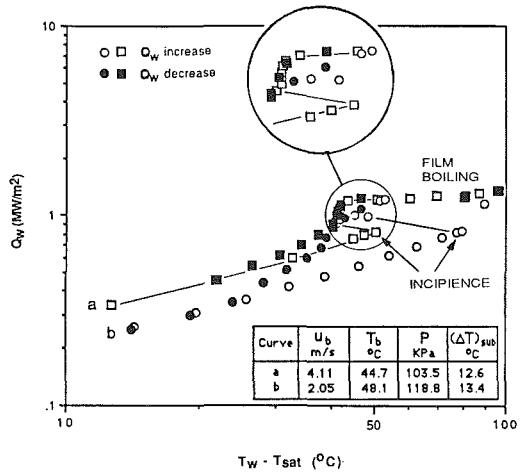

Fig. 9 Effect of velocity on temperature excursion and boiling hysteresis

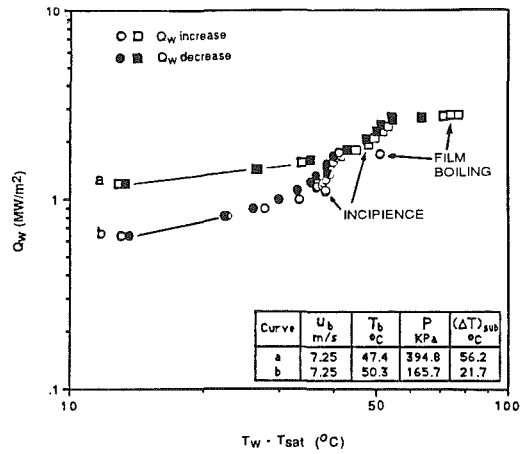

Fig. 10 Effect of subcooling on temperature excursion and the boiling hysteresis at 7.25 m/s

Table 1 Test conditions and key boiling characteristics

Bulk velocity, u_b (m/s)	Bulk temperature, T_b (°C)	Pressure at test patch, P (kPa)	Subcooling, $(\Delta T)_{SUB}$ (°C)	Temperature excursion at incipience (°C)	Critical heat flux (MW/m²)	Boiling curve figure
2.05	48.1	118.8	13.4	26.7	1.22	9(*b*)
4.11	44.7	103.5	12.6	10.1	1.19	7, 8(*b*), 9(*a*)
4.11	47.3	375.8	54.4	0	2.10	8(*c*)
7.25	47.4	394.8	56.2	0	2.69	10(*a*)
7.25	50.3	165.7	21.7	1.7	1.71	10(*b*)
16.86	51.8	338.1	45.7	0	3.28	8(*a*)

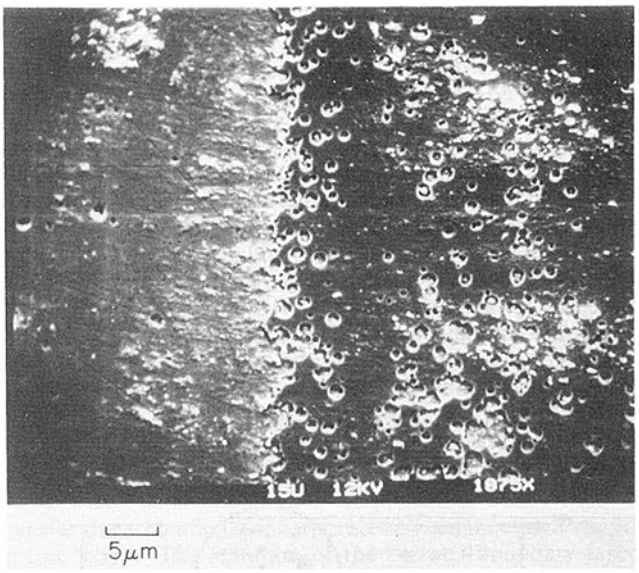

Fig. 11 Surface cavities as seen under SEM (1875 ×)

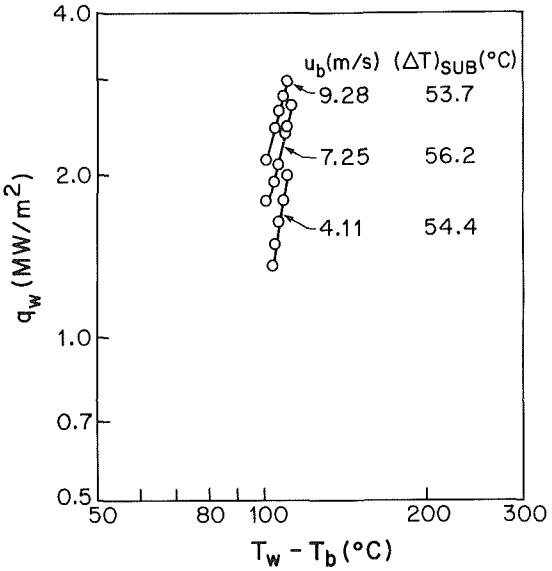

Fig. 12 Effect of velocity on nucleate boiling

Microscopic Observations of the Heater Surface. After the experiment was completed, a scanning electron microscope (SEM) was used to examine the structure of the heater surface while an X-ray Energy Spectrometry (XES) system was used to characterize the composition of the surface material. In Fig. 11, an etched line can be seen along the heater span. This separation is due to the photoetching process, which over-etched the chromium layer and thus undercut a strip of chromium from the heater patch. From the XES analysis, the right layer contains higher chromium composition than the left. This undercutting phenomenon is normal in a photolithography process.

Many pits can be observed on the right side of the surface (flow direction is from left to right). The shapes of these pits are irregular but most are circular cavities. An estimation of the circular cavity size is 0.20–0.25 μm (the diameter of the circular pit). A critical bubble size of 0.07 μm at the onset of nucleate boiling was shown by Bar-Cohen and Simon (1986) to be consistent with heterogeneous nucleation. The critical size would correspond to a cavity size of slightly over 0.1 μm. Apparently most of the cavities in the 0.20–0.25 μm range were flooded and inactive.

Nucleate Boiling Regime. The nucleate boiling regime is characterized by high convective heat transfer coefficients; high heat fluxes are achieved with only small increases in wall temperature. These regions are rather short at low velocity and low subcooling due to the high wall superheat at the onset of nucleate boiling (see Fig. 9(*b*)). They are also rather short for high velocities due to the high single-phase heat flux (see Fig. 8(*a*)). The effect of velocity on nucleate boiling is shown in Fig. 12. As shown, the slope of the boiling curves in the nucleate boiling regime increases with velocity although the log–log nature of the plot is deceiving. The nucleate boiling range is expanded as DNB is delayed with increasing subcooling; the increased rate of bubble collapse in the subcooled flow retards the development of a vapor film. For example, at a bulk velocity of 4.11 m/s, the DNB is increased from 1.19 MW/m^2 to 2.10 MW/m^2 as the subcooling is increased from 12.6°C to 54.4°C (Table 1). The effect of subcooling is more pronounced at higher velocities. At 7.25 m/s, the DNB heat flux is increased from 1.71 MW/m^2 to 2.69 MW/m^2, as the subcooling is increased from 21.7°C to 56.2°C.

Departure From Nucleate Boiling (DNB). The heat flux at DNB increases with increasing subcooling or velocity. A maximum of 4.26 MW/m^2 was observed at a bulk velocity of 16.86 m/s and a subcooling of 68.1°C.

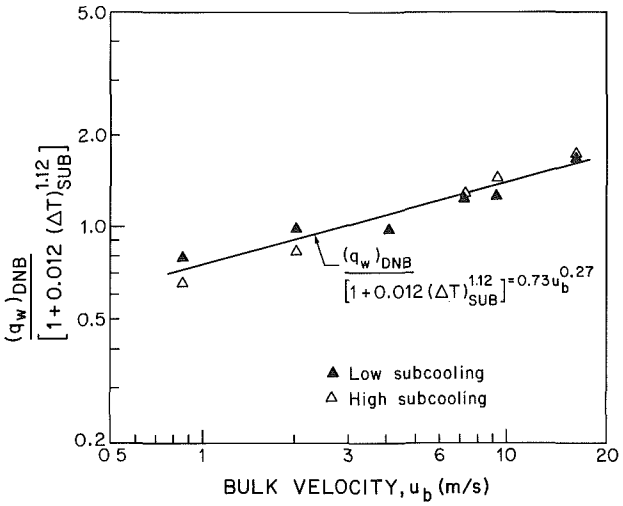

Fig. 13 Wall heat flux at the departure from nucleate boiling

From the correlations presented by Katto (1981) for critical heat flux in forced convection boiling in channels with heated surfaces, there is an indication that the present data may depend on bulk velocity and subcooling in the following manner:

$$(q_w)_{DNB} = a(u_b)^b[1 + c(\Delta T)^d_{SUB}] \quad (4)$$

The following combination of a, b, c, and d was found to best fit the data:

$$(q_w)_{DNB} = 0.73(u_b)^{0.27}[1 + 0.012(\Delta T)^{1.12}_{SUB}] \quad (5)$$

The measured data along with equation (5) are shown in Fig. 13. It should be noted that equation (5) has no heated length effect, which is known to be important. The influence of heated length is the topic of a continuation study. The validity of equation (5) is claimed only within the range of a subcooling and bulk velocity studied here. Equation (5) represents the data with a maximum deviation of 11.5 percent and a standard deviation of 8.8 percent. As the figure shows, the influence of subcooling is slightly velocity dependent.

Several existing correlations were reviewed to test the suitability of standard boiling correlation for the present high-velocity, short heating length situation. Most of these (Zenkevich, 1960; Zenkevich et al., 1958) are for fluids other

than FC-72 and do not include the effect of short heating length. The correlation of Katto (1981) gives critical heat flux values for saturated boiling when the heated length, normalized by the heated diameter, lies between 1 and 5. Therefore, it cannot be used to represent the subcooled boiling situation considered here ($L/D = 0.0036$ for this study). The correlation of Bernath (1961) was chosen for comparison mainly due to its wide use (e.g., Leslie et al., 1983). It is recognized that no heated length effect is included in this correlation. Bernath's correlation was found to grossly underpredict the burnout heat flux. The predicted values of heat flux for DNB are, in fact, lower than even the measured onset of nucleate boiling heat flux.

Lee et al. (1988) compared the critical heat flux data of the present study with data on impinging jets and cylinders in crossflow. The data from the present study were shown to be in good agreement with jet impingement data of Ma and Bergles (1983) and Monde and Katto (1978) involving heated lengths of 2.5 mm and 5 mm, respectively. The submerged jet data were correlated better than the free jet data due to the apparent similarity of the submerged jet to the channel flow of the present study.

Burnout. No damage to the heater surface due to overheating (the so-called burnout phenomenon) was observed in the present investigation even at a low velocity and low subcooling. This is presumed to be due to the short heating length. On surfaces with longer heated lengths, burnout due to a high local temperature was observed at the farthest downstream edge (e.g., Ma and Bergles, 1983). The absence of burnout greatly increases the utility of this short-heating-length heat transfer surface: All measurements were taken with the same test patch.

Conclusions

An experimental investigation of heat transfer from a small region to a fully developed turbulent channel flow of R-113 and FC-72 was conducted. The following conclusions were drawn:

1 For test runs with R-113, the maximum heat flux, limited by the thermal decomposition temperature of R-113, was 2.04 MW/m^2 at a bulk velocity of 16.5 m/s. No boiling was observed with R-113 even at a low velocity of 1.8 m/s and a high wall superheat of 80°C.

2 The results obtained with FC-72 showed a large temperature excursion at the onset of nucleate boiling (ONB) and a boiling hysteresis near the ONB. A maximum temperature excursion of ~27°C was observed at a low velocity of 2.05 m/s and a subcooling of 13.4°C. The large temperature excursion is presumed to be due to the very short heated length; there are fewer cavities with vapor embryo to initiate boiling. The temperature excursion and boiling hysteresis appeared to decrease with increasing velocity and/or subcooling. No temperature excursion or boiling hysteresis was observed at the maximum velocity of 16.86 m/s.

3 The departure from nucleate boiling (DNB) heat flux is delayed as the subcooling is increased due to an increased rate of bubble collapse in the subcooled flow. It also increases with increasing velocity because of an increased bubble removal rate by larger shear stresses. The slope of the boiling curve in the nucleate boiling regime increases with velocity. The effect of subcooling in delaying DNB is more pronounced at higher velocities. A maximum heat flux of 4.26 MW/m^2 at departure from nucleate boiling is observed at the maximum velocity of 16.86 m/s and a subcooling of 68.1°C.

4 The correlation of Bernath (1961) grossly underpredicts the DNB heat flux; the predicted value is even lower than the heat flux at the onset of nucleate boiling (ONB). The correlation of Lee et al. (1988) is recommended for boiling on small heated areas.

Acknowledgments

This research was mainly supported by the National Science Foundation under grant No. NSF/MEA-8302411. Dr. Win Aung was the grant monitor. Additional support was provided by the Graduate School of the University of Minnesota, the AMOCO Foundation, and the 3M Company.

References

Baker, E., 1972, "Liquid Cooling of Microelectronic Devices by Free and Forced Convection," *Microelectronics and Reliability*, Vol. 11, pp. 213–222.

Baker, E., 1973, "Liquid Immersion Cooling of Small Electronic Devices," *Microelectronics and Reliability*, Vol. 12, pp. 163–173.

Bar-Cohen, A., and Simon, T. W., 1986, "Wall Superheat Excursions in the Boiling Incipience of Dielectric Fluids," *1986 AIAA/ASME Heat Transfer and Thermophysics Conference*, ASME HTD-Vol. 57, pp. 83–94.

Bergles, A. E., 1963, "Subcooled Burnout in Tubes of Small Diameter," ASME Paper No. 63-WA-182.

Bergles, A. E., 1977, "Burnout in Boiling Heat Transfer, Part II: Subcooled and Low-Quality Forced Convection Systems," *Nuclear Safety*, Vol. 18, pp. 154–167.

Bernath, L., 1961, "A Theory of Local Boiling Burnout and Its Application to Existing Data," *Chemical Engineering Program Symposium Series*, Vol. 56, No. 30, pp. 95–116.

Groenveld, D. C., 1981, "Heat Transfer Phenomena Related to the Boiling Crisis," Chalk River Nuclear Labs (Ontario) AECL-7239.

Hsu, Y. Y., and Graham, R. W., 1976, *Transport Processes in Boiling and Two-Phase Systems*, McGraw-Hill, New York.

Hwang, K. P., and Moran, K. P., 1981, "Boiling Heat Transfer of Silicon Integrated Circuits Chip Mounted on a Substrate," *Heat Transfer in Electronic Equipment*, Kelleher and Yovanovich, eds., HTD-Vol. 20, pp. 53–59.

Katto, Y., and Monde, M., 1974, "Study of Mechanisms of Burnout With an Impinging Jet," *Proceedings of the 5th Int. Heat Transfer Conference*, Tokyo, Japan, Vol. IV, B 6.2, pp. 245–249.

Katto, Y., and Shimizu, J., 1979, "Upper Limit of CHF in the Saturated Forced Convection Boiling on a Heated Disk With a Small Impinging Jet," ASME JOURNAL OF HEAT TRANSFER, Vol. 101, pp. 265–269.

Katto, Y., 1981, "General Features of CHF of Forced Convection Boiling in Uniformly Heated Rectangular Channels," *International Journal of Heat and Mass Transfer*, Vol. 24, pp. 1413–1419.

Lee, T. Y., Simon, T. W., and Bar-Cohen, A., 1988, "An Investigation of Short Heating Length Effect on Flow Boiling Critical Heat Flux in a Subcooled Turbulent Flow," *Cooling Technology for Electronic Equipment*, W. Aung, ed., Hemisphere, Washington, DC, pp. 435–450.

Leslie, B., Neukermans, A., Simon, T., and Foster, J., 1983, "Enhanced Brightness of X-Ray Source," *Journal of the Vacuum Society*, Technol. B., Vol. 1, No. 4, pp. 1251–1256.

Lienhard, J. H., and Hasan, M. Z., 1979, "Correlation of Burnout Data for Disk Heaters Cooled by Liquid Jets," ASME JOURNAL OF HEAT TRANSFER, Vol. 101 pp. 383–384.

Ma, C.-F., and Bergles, A. E., 1983, "Boiling Jet Impingement Cooling of Simulated Microelectronic Chips," *Heat Transfer in Electronic Equipment—1983*, S. Oktay and A. Bar-Cohen, eds., ASME HTD-Vol. 28, pp. 5–12.

Ma, C.-F., and Bergles, A. E., 1986, "Jet Impingement Nucleate Boiling," *International Journal of Heat and Mass Transfer*, Vol. 29, pp. 1095–1101.

Maulbetsch, J. S., and Griffith, P., 1966, "Systems Induced Flow Instabilities in Forced Convection Flows With Subcooled Boiling," *3rd Int. Heat Transfer Conference*, Vol. 4, pp. 247–257.

Merilo, M., 1977, "Critical Heat Flux Experiments in a Vertical and Horizontal Tube With Both Freon-12 and Water as Coolant," *Nuclear Engineering and Design*, Vol. 44, pp. 1–16.

Monde, M., and Katto, Y., 1978, "Burnout in a High Heat-Flux Boiling System With an Impinging Jet," *International Journal of Heat and Mass Transfer*, Vol. 21, pp. 295–305.

Patankar, S. V., and Spalding, D. B., 1970, *Heat and Mass Transfer in Boundary Layers—A General Calculation Procedure*, Intertext Books, London.

Samant, K. R., Simon, T. W., and Stuart, R. V., 1984, "Using Thin-Film Technology to Fabricate a Small Patch Boiling and Heat Transfer Test Section," *New Experimental Techniques in Heat Transfer*, ASME HTD-Vol. 31, pp. 33–38.

Samant, K. R., 1984, "Heat Transfer From a Small High-Heat-Flux Patch to a Subcooled Turbulent Flow," Ph.D. Thesis, Mechanical Engineering Department, University of Minnesota, Minneapolis, MN.

Tolubinskiy, V. I., and Matorin, A. S.,1973, "Forced Convection Boiling Heat Transfer," *Soviet Research*, Vol. 5, pp. 98–101.

Zenkevich, B. A., Subbotin, V. I., and Troianov, M. F., 1958, "Critical Heat Load for Longitudinal Wetting of a Tube Bundle for Heated to Saturated Temperature," *Soviet J. Atomic Energy*, Vol. 4, p. 485.

Zenkevich, B. A., 1960, "Critical Heat Fluxes for a Bundle of Tubes Cooled in Pressurized Water," *J. Nucl. Energy*, Pt. B, Reactor Technol., Vol. 1, p. 197.

Effect of Noncondensibles on Condensation and Evaporation of Bubbles

A. Ullmann

R. Letan

Mechanical Engineering Department,
Ben-Gurion University of the Negev,
Beer-Sheva, Israel

The fraction of noncondensibles in a bubble controls the temperature driving force in the process of condensation and evaporation. It affects the vapor partial pressure, and consequently the apparent temperature of saturation. The present work deals with a bubble condensing in immiscible and miscible liquids, and with the evaporation of a bubble in an immiscible liquid. The complete, exact expression of the dimensionless apparent saturation temperature is formulated, and all its terms are examined, including the variation of physical properties. The analysis is extended over systems of R-113, pentane, and hexane. The exact relation is compared with previous approximate solutions and the limits of application are illustrated. At small temperature differences the approximate models are adequate. The discrepancy increases at high temperature differences. The rate of collapse is examined in a system of R-113 in water. Experimental rates of videotaped collapsing bubbles were obtained up to a temperature difference of 20°C. The effect of noncondensibles is most pronounced at the higher temperature difference. Comparison of theoretical curves at a temperature difference of 30°C shows the exact termination of the process to be faster than the approximate prediction. The deviation increases with the concentration of the noncondensibles. Relations formulated for evaporation of liquid in presence of noncondensibles were tested experimentally. Vapor of R-113 was experimentally obtained in a bubble of air down to 20°C below the satuaration temperature. The measurements showed good agreement with the predictions.

Introduction

In this work, attention is directed to the effect of noncondensibles on condensation of vapor and on evaporation of liquid in a bubble. In the presence of noncondensibles, the partial pressure of the vapor is smaller than the total pressure in the bubble. The corresponding saturation temperature is lowered with the vapor pressure.

In a collapsing bubble the fraction of noncondensibles increases as the process progresses. Obviously, the fraction of vapor decreases, and with it the apparent saturation temperature. The temperature difference between the bubble and the cooling liquid decreases, and the rate of collapse follows accordingly. In an evaporation process these effects are reversed.

The effects of noncondensibles were studied by many researchers both theoretically and experimentally. Votta (1964) derived a relation that accounts for the rate of diffusion of noncondensibles. Chao and co-workers (Florschuetz and Chao, 1965; Wittke and Chao, 1967) investigated the effects of noncondensibles on collapse of steam bubbles in subcooled water. In these works the Dalton Law was used to obtain the partial pressure of the vapor and noncondensibles. A linear relationship was assumed between the saturation temperature and pressure at small differences of temperature.

Isenberg and Sideman (1969) considered in a similar way the effect of noncondensibles on the saturation temperature. The work was conducted with pentane bubbles in water.

Many of the works found in the literature deal with the effects on rates of condensation. Webb et al. (1981) analyzed the effect of noncondensibles on multicomponent diffusional interactions. Corradini (1984) considered the heat transfer coefficient in condensation on a cold wall. Kotake (1985) studied mixtures of two and three components, analyzing the rate of condensation. The vapor and the noncondensibles were assumed to obey the Dalton Law of partial pressures. Hijikata et al. (1984) analyzed the rate of condensation in a mixture or air and water vapor in a thermosyphon. The noncondensibles were treated as ideal gases. The Dalton Law was applied for partial pressures and the Clausius–Clapeyron relation for pressure and saturation temperature.

Lerner (1983) investigated the collapse of freon-113 bubbles in water. He calculated the saturation temperature without neglecting the term of temperature driving force. Most of his other assumptions were applied as in the previous works.

The purpose of the present work is to formulate general exact relations operable at any conditions, and to examine the validity of the approximations. The effect of noncondensibles is experimentally tested in collapsing and evaporating bubbles.

Generalized Relations in Condensation

The purpose of the work is to analyze the effect of noncondensibles in bubbles condensing in immiscible and miscible liquids.

A Bubble in an Immiscible Liquid. The effect of noncondensibles on condensation of vapor in a bubble will be analyzed in several stages. The aim is to reach an exact solution without any approximations, and then to examine the acceptability of the approximations.

The system to be analyzed contains a bubble of vapor and gas, which collapses in a liquid of a lower temperature. The liquid is immiscible with the fluid of the bubble, and the condensate accumulates in the bubble. The vapor and the noncondensible gas are assumed to be uniformly distributed in the vapor–gas phase.

To formulate the exact model we have to define the basic terms, and then proceed to the more complex relations.

The noncondensible gas in the vapor is considered an ideal gas. By the Dalton Law the properties of each component are considered as though each component existed separately at the

Contributed by the Heat Transfer Division and presented at the 25th National Heat Transfer Conference, Houston, Texas, July 24–27, 1988. Manuscript received by the Heat Transfer Division March 8, 1988. Keywords: Condensation, Evaporation, Phase-Change Phenomena.

volume and temperature of the mixture. If the mixture in the bubble is considered to obey the Dalton Law then the total pressure is the sum of the partial pressures

$$P = P_v + P_g \tag{1}$$

As the condensation process proceeds, the fraction of noncondensibles increases, the vapor partial pressure decreases, and so does the corresponding apparent saturation temperature T_s^*. With it, the temperature driving force $(T_s^* - T_\infty)$ falls down, and the rate of condensation is reduced. The process stops altogether by the time the apparent saturation temperature T_s^* approaches the temperature of the surrounding cooling liquid T_∞.

The total volume of the bubble is

$$V_{T,o} = V_{vg} = \frac{4}{3}\pi R_o^3 \tag{2}$$

At the final stage of collapse, the bubble holds both the condensate and the vapor–gas. The final volume is

$$V_{T,f} = \frac{4}{3}\pi R_f^3 \tag{3}$$

The temperature of the vapor decreases with its partial pressure. As the vapor temperature reaches the temperature of the cooling liquid the condensation process terminates

$$T_{v,f} = T_\infty \tag{4}$$

Mass balance on the condensible component yields

$$V_{T,o} \cdot \rho_{v,o} = V_{l,f} \cdot \rho_{l,f} + V_{vg,f} \cdot \rho_{vf} \tag{5}$$

The vapor density relates to the vapor mass being uniformly distributed in the whole volume of the gas phase, at the apparent saturation temperature, and the partial pressure pertaining to the vapor.

The condensate volume is therefore

$$V_{l,f} = V_{T,f} - V_{vg,f} \tag{6}$$

Combining equation (5) with equations (3) and (6) yields

$$\rho_{v,o} = \bar{R}_f^3 \cdot \rho_{l,f} + \frac{V_{vg,f}}{V_{T,o}}(\rho_{vf} - \rho_{l,f}) \tag{7}$$

The ideal gas equation of state is applied to the noncondensibles

$$\frac{P_{g,o} \cdot V_{vg,o}}{T_{s,o}} = \frac{P_{g,f} \cdot V_{vg,f}}{T_\infty} \tag{8}$$

We assume that pressure changes in the bubble due to interfacial tension or hydrostatic head are negligible, and the pressure of the cooling liquid P_∞ is the pressure imposed on the bubble. Then equation (1) is utilized for the partial pressure of noncondensibles

$$\frac{V_{vg,f}}{V_{vg,o}} = \frac{T_\infty}{T_{s,o}} \cdot \frac{(P_\infty - P_{v,o})}{(P_\infty - P_{v,f})} \tag{9}$$

By equation (2) $v_{vg,o} = V_{T,o}$. Equation (9) substituted in equation (7) yields the normalized final radius

$$\bar{R}_f^3 = \frac{\rho_{v,o}}{\rho_{l,f}} + \frac{T_\infty}{T_{s,o}} \cdot \frac{(P_\infty - P_{v,o})}{(P_\infty - P_{v,f})}\left[1 - \frac{\rho_{vf}}{\rho_{l,f}}\right] \tag{10}$$

The final apparent saturation temperature is known to be T_∞. Therefore, the corresponding vapor pressure $p_{v,f}$ of the condensible vapor is also known, as well as all the other properties at that state, including the density of the vapor $\rho_{v,f}$ and that of the condensate, $\rho_{l,f}$.

If the initial and final radii of the colllapsing bubble are known, then equation (10) is implicit in $T_{s,o}$, the initial apparent saturation temperature, and the corresponding properties at this state. The vapor pressure $P_{v,o}$ and density $\rho_{v,o}$ are related to the temperature $T_{s,o}$ and are available.

The normalized instantaneous radius R can be obtained by the same steps as those applied to the derivation of equation (10). Thus,

$$\bar{R}^3 = \frac{\rho_{v,o}}{\rho_1} + \frac{(P_\infty - P_{v,o})}{(P_\infty - P_v)} \cdot \frac{T_s^*}{T_{s,o}}\left[1 - \frac{\rho_v}{\rho_1}\right] \tag{11}$$

Equation (11) presents us with the apparent saturation temperature T_S^*, and the corresponding properties, at any instantaneous size of the bubble R, provided the initial conditions are specified.

The presently derived relations have to be compared with relations of similar character utilized in previous works in the literature. To conduct a comparison, some terms have to be redefined.

The normalized apparent saturation temperature is used in the form

$$\phi_s = \frac{T_s^* - T_\infty}{T_s - T_\infty} \tag{12}$$

Nomenclature

h_{fg} = latent heat, J/kg
m = mass, kg
M = molecular weight, kg/kg mole
n = moles of vapor and gas, kg mole
n_g = moles of gas, kg mole
P = total pressure in a bubble, Pa or MPa
P_g = partial pressure of gas, Pa or MPa
P_v = partial pressure of vapor, Pa or MPa
P_∞ = total pressure outside a bubble, Pa or MPa
R = instantaneous radius, m
R_f = final radius, m
R_o = initial radius, m
$\bar{R}$ = R/R_o = normalized radius
$\tilde{R}$ = specific gas constant, N•m/kg•K
T = temperature, °C
T_s = saturation temperature at total pressure, °C
T_s^* = apparent saturation temperature
$T_{s,o}$ = $(T_s^*)_{t=0}$ = initial temperature at vapor partial pressure, °C
T_∞ = temperature of continuous liquid, °C
t = time, s
t_f = final time = time at termination of collapse, s
V = volume, m³
ΔT = temperature difference $(T_s - T_\infty)$, °C
α = (m_g/m_{vo}) = mass fraction of noncondensibles
Γ = (n_g/n) = mole fraction of noncondensibles
ρ = density, kg/m³
$\bar{\rho}$ = average density, kg/m³
ϕ_s = $(T_s^* - T_\infty)/(T_s - T_\infty)$ = normalized apparent saturation temperature
ϕ_{sL} = defined by equation (38)
ϕ_{sU} = defined by equation (15)

Subscripts

f = final, at $t = t_f$
g = gas
l = liquid
o = initial, at $t = 0$
s = at saturation temperature at the total pressure
so = at saturation temperature, at the initial vapor partial pressure, at $t = 0$
T = total
v = vapor
vg = vapor-gas

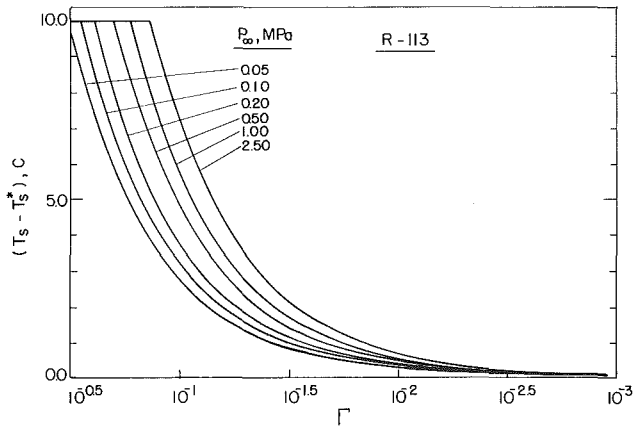

Fig. 1 Effects of pressure P_∞ and mole fraction of noncondensibles Γ on subcooling $(T_S - T_S^*)$, of a condensing R-113 bubble

where T_s is the saturation temperature at the total pressure in the bubble.

The ratio between the maximum temperature driving force in the system and the largest difference in pressure is defined as

$$b = \frac{T_s - T_\infty}{P_\infty - P_{v,f}} \tag{13}$$

Another ratio of importance is the one related to the instantaneous temperature driving force and to the respective difference in pressure

$$x = \frac{T_s^* - T_\infty}{P_v - P_{v,f}} \tag{14}$$

By combination of equations (10)–(14) and rearrangement of terms we obtain the generalized relation of the normalized apparent saturation temperature in an immiscible bubble

$$\phi_s = \frac{\left(\bar{R}^3 - \frac{\rho_{v,o}}{\rho_1}\right)\left(1 - \frac{\rho_{v,f}}{\rho_{l,f}}\right) - \left(\bar{R}_f^3 - \frac{\rho_{v,o}}{\rho_{l,f}}\right)\left(1 - \frac{\rho_v}{\rho_1}\right)}{\left(\frac{b}{x}\right)\left(\bar{R}^3 - \frac{\rho_{v,o}}{\rho_1}\right)\left(1 - \frac{\rho_{v,f}}{\rho_{l,f}}\right) + \left(\bar{R}_f^3 - \frac{\rho_{v,o}}{\rho_{l,f}}\right)\left(1 - \frac{\rho_v}{\rho_l}\right)\left(\frac{T_s - T_\infty}{T_\infty}\right)} \tag{15}$$

The normalized final radius of an immiscible bubble expressed in equation (10) can also be obtained as

$$\bar{R}_f^3 = \frac{\rho_{v,o}}{\rho_{l,f}} + \frac{P_\infty \cdot \Gamma_o \cdot b}{(T_s - T_\infty)}\left(\frac{T_\infty}{T_{s,o}}\right)\left(1 - \frac{\rho_{v,f}}{\rho_{l,f}}\right) \tag{16}$$

where Γ is the mole fraction of the noncondensible gas

$$\Gamma = \frac{P_g}{P} \tag{17}$$

in a mixture that obeys the Dalton Law. Γ_o expresses the initial fraction at $t = 0$.

Equations (15)–(17) are employed to illustrate in Fig. 1 the effect of noncondensible on the saturation temperature deviation. The system pressure is shown to accentuate the effect of noncondensibles.

The properties employed in the previous equations can be further used to formulate another useful relation, which relates the ratio of the residual noncondensed mass of vapor and the total mass of condensibles in the initial bubble

$$\frac{m_{v,f}}{m_{v,o}} = \frac{V_{vg,f} \cdot \rho_{v,f}}{V_{vg,o} \cdot \rho_{v,o}} = \frac{(P_\infty - P_{v,o})}{(P_\infty - P_{v,f})} \cdot \left(\frac{T_\infty}{T_{s,o}}\right) \cdot \left(\frac{\rho_{v,f}}{\rho_{v,0}}\right) \tag{18}$$

Equation (18) outlines the effect of noncondensibles on the residual vapor in the bubble. These effects have far-reaching practical implications upon the design of condensers.

The relations presented in equations (15) and (16) for a bubble condensing in an immiscible liquid are full and exact solutions. Comparison of this generalized model with approximate solutions available in the literature would show the range of applicability of the aproximations.

A Bubble in a Miscible Liquid. Let us consider also the process of bubble collapse in a subcooled miscible liquid. In such systems the bubble is identifiable only in its gas phase, namely,

$$V_{vg} = \frac{4}{3}\pi R^3 \tag{19}$$

By using equation (8) for the noncondensibles that are preserved in the bubble we obtain the final radius

$$\frac{P_{g,o}}{P_{g,f}} = \frac{V_{vg,f}}{V_{vg,o}} \cdot \frac{T_{s,o}}{T_\infty} = \bar{R}_f^3 \left(\frac{T_{s,o}}{T_\infty}\right) \tag{20}$$

and the instantaneous radius

$$\frac{P_{g,o}}{P_g} = \bar{R}^3 \cdot \left(\frac{T_{s,o}}{T_s^*}\right) \tag{21}$$

The ratio of the radii is

$$\left(\frac{\bar{R}_f}{\bar{R}}\right)^3 = \left(\frac{T_\infty}{T_s^*}\right) \cdot \frac{(P_\infty - P_v)}{(P_\infty - P_{v,f})} \tag{22}$$

Equation (22) provides the apparent saturation temperature as a function of the bubble size in a miscible liquid.

The normalized apparent saturation temperature for miscible fluids is obtained through the same steps that lead to equation (15). The relation is derived as

$$\phi_s = \frac{\bar{R}^3 - \bar{R}_f^3}{\left(\frac{b}{x}\right)\bar{R}^3 + \bar{R}_f^3\left(\frac{T_s - T_\infty}{T_\infty}\right)} \tag{23}$$

for the miscible fluids.

All the formulations obtained herein are applicable at any operating conditions.

Approximate Relations in Condensation

The approximate solutions used in the literature are compared with the exact solution of equation (15) to examine the applicability of the approximations. The comparison is conducted with the model used by Chao and co-workers (1965 and 1967) in a miscible fluid and with the models of Lerner (1985) and Sideman (1965) in immiscible fluids.

Chao and co-workers used for the normalized apparent saturation temperature,

$$\phi_s = \frac{\bar{R}^3 - \bar{R}_f^3}{\bar{R}^3} \tag{24}$$

This relation for a miscible fluid can be obtained from equation (23) by approximating

$$b = x \tag{25}$$

and assuming a small temperature difference

$$(T_s - T_\infty) \cong 0 \tag{26}$$

Isenberg and Sideman (1969) used for the collapse of an immiscible bubble

$$\phi_s = \frac{\bar{R}^3 - \bar{R}_f^3}{\bar{R}^3 - \dfrac{\rho_{v,s}}{\rho_{l,s}}} \tag{27}$$

and

$$\bar{R}_f = \frac{\tilde{R}_v \cdot T_s^2 \cdot \Gamma_o}{h_{fg} \cdot (T_s - T_\infty)} + \frac{\rho_{v,s}}{\rho_{l,s}} \tag{28}$$

where $\rho_{v,s} = \rho_v(T_s)$.

These equations (27) and (28) can be obtained from equations (15) and (16), respectively, by introducing the following approximations, in addition to equations (25) and (26):

$$b = \frac{T_s - T_\infty}{P_\infty - P_{v,\,f}} = \frac{\tilde{R}_v \cdot T_s^2}{(h_{fg})_s \cdot P_\infty} \tag{29}$$

This is the Clapeyron equation applicable at low pressure ($\rho_v << \rho_l$).

That approximation was also employed by Isenberg and Sideman explicitly in the form

$$1 - \frac{\rho_v}{\rho_1} \cong 1 \tag{30}$$

It says that in organic fluids the density of vapor is much lower than that of the condensate.

Also

$$\rho_{v,o} \cong \rho_{v,s} \tag{31}$$

is approximated. Here the vapor density at initiation of collapse is assumed to be the same as the one at total pressure.

The condensate density was considered constant during the process

$$\rho_1 = \rho_{l,s} = \text{const} \tag{32}$$

The above-cited approximations of equations (29)–(32), if introduced into the generalized equations (15) and (16), lead to the approximate equations (27) and (28), respectively.

Lerner (1983) derived the relation of the apparent saturation temperature for an immiscible bubble in the following form:

$$T_s^* = \frac{T_s}{1 + \dfrac{\tilde{R}_g \cdot \alpha \cdot (\rho_{v,s}) \cdot b}{\bar{R}^3(1+\alpha) - \dfrac{\rho_{v,s}}{\rho_{l,s}}}} \tag{33}$$

where $\rho_{v,s}$ and $\rho_{l,s}$ are the respective densities of vapor and liquid at the total pressure.

Lerner assumed the initial average density of the gas phase to be approximately equal to the vapor density at total pressure

$$\bar{\rho}_o \cong \rho_{v,s} \tag{34}$$

Defining the mass fraction of noncondensibles

$$\alpha = \frac{m_g}{m_{v,o}} \tag{35}$$

and by equation (34),

$$\rho_{v,s} = \rho_{v,o}(1+\alpha) \tag{36}$$

This is substituted into equation (33) to yield

$$T_s^* = \frac{T_s}{1 + \dfrac{\tilde{R}_g \cdot \alpha \cdot (\rho_{v,o}) \cdot b}{\bar{R}^3 - \dfrac{\rho_{v,o}}{\rho_{l,s}}}} \tag{37}$$

and then normalized to

$$\phi_s = \frac{\bar{R}^3 - \bar{R}_f^3}{\left(\bar{R}^3 - \dfrac{\rho_{v,o}}{\rho_{l,s}}\right) + \left(\bar{R}_f^3 - \dfrac{\rho_{v,o}}{\rho_{l,s}}\right)\left(\dfrac{T_s - T_\infty}{T_\infty}\right)} \tag{38}$$

This relation was utilized by Lerner (1983). It can be obtained by introducing the approximations of equations (25), (30), and (32) into equation (15).

When the approximation of $(T_s - T_\infty) \approx 0$ (equation (26)) is introduced into Lerner's relation, it would have resulted in Sideman's equation (27).

The relations formulated in equations (15) and (16) for immiscible fluids, and in equation (23) for a miscible fluid, apply to any conditions. No approximations of any kind have been introduced into those formulations. The equations previously used in the literature were simplified by some approximations, and are therefore restricted to specified conditions.

The exact and approximate relations, as well as the effect of the fluid properties, are experimentally tested in a process of collapse up to $\Delta T = 20°C$ in R-113 bubbles collapsing in water. Above that ΔT, the collapse process is tested theoretically in the same system.

Exaporation of a Bubble in an Immiscible Liquid

In a bubble at thermodynamic equilibrium, the vapor, the gas (noncondensible), and the liquid are at the same temperature. The partial pressure of the vapor is the saturation pressure, or vapor pressure at the bubble temperature. Assuming the noncondensibles are an ideal gas, then equations (17) applies. Equations (1) and (17) yield

$$\Gamma = \frac{P - P_v}{P} \tag{39}$$

The vapor pressure P_v depends on temperature. Therefore, the mole fraction of noncondensibles can be obtained at any pressure as a function of temperature.

For an ideal gas by Amagat's rule the partial volumes of the components are detemined by the respective mole fractions. Thus, the total volume of gaseous phase is obtained by

$$\frac{V_{vg}}{V_g} = \frac{1}{\Gamma(T, P)} \tag{40}$$

and the vapor volume by

$$\frac{V_v}{V_g} = \frac{1}{\Gamma} - 1 \tag{41}$$

If an air bubble is introduced into a liquid, the liquid evaporates into the bubble until the partial pressure of the vapor reaches the vapor pressure value at the respective temperature. Equation (40) yields the bubble volume, and equation (41) the partial volume of the vapor. The same effect would be achieved were the air introduced into a liquid droplet.

In an experimental study the amount of air introduced into a bubble has to be measured, or the bubble volume has to be recorded. That can be done by letting the bubble rise in a column from a zone of lower temperature to a zone of higher temperature and to come to thermodynamic equilibrium in each zone.

By equation (40) we obtain

$$\frac{V_{vg,2}}{V_{vg,1}} = \frac{V_{g,2}}{V_{g,1}} \cdot \frac{\Gamma_1(T, P)_1}{\Gamma_2(T, P)_2} \tag{42}$$

If $T_2 > T_1$ the bubble would increase in volume on its way up the column. The volume of the noncondensibles in the bubble varies with the temperature and the hydrostatic pressure. Assuming the noncondensibles behave as an ideal gas, and

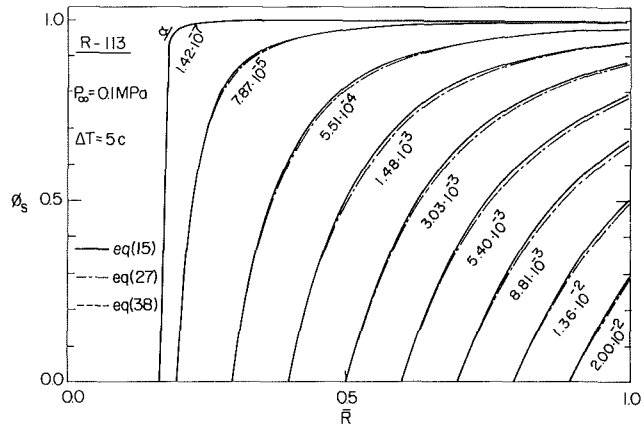

Fig. 2 Variation of normalized apparent saturation temperature ϕ_s, with mass fraction of noncondensibles α, in a bubble of R-113 collapsing ($\bar{R}$ = normalized radius) at temperature difference $\Delta T = 5°C$

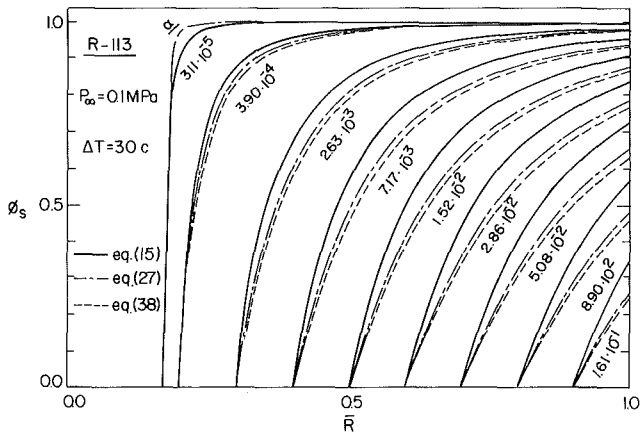

Fig. 3 Variation of normalized apparent saturation temperature ϕ_s, with mass fraction of noncondensibles α, in a bubble of R-113 collapsing ($\bar{R}$ = normalized radius) at temperature difference $\Delta T = 30°C$

also do not diffuse into the immiscible surrounding liquid, then

$$\frac{V_{g,2}}{V_{g,1}} = \frac{T_2}{T_1} \cdot \frac{P_1}{P_2} \tag{43}$$

Measurements of temperatures at two locations and the respective heights yield the volumetric ratio of the gas (air). Recording the size of the vapor-gas bubble at the same two points provides the V_{vg} ratios. Then the ratio of Γ, the mole fraction, can be obtained by equation (42).

Experimentally the mole fraction of noncondensibles can be obtained by equation (39) and by measuring P and T for $P_v(T)$; specifically: $\Gamma_1(P_1, P_v(T_1))$ and $\Gamma_2(P_2, P_v(T_2))$.

Equations (39)–(43) are formulated in a way that makes the presentation of experimental results explicit. Thus, the bubble volume V_{vg} can be videotaped at two locations to yield the volumetric ratio. The measured respective temperatures and pressures provide the ratio of gas volume, equation (43).The mole fractions are obtained by equation (39) using again the measured pressures, P_1 and P_2, and the temperatures T_1 and T_2, for the vapor pressures $P_v(T_1)$ and $P_v(T_2)$.

The validity of equation (42) could be tested by plotting the two sides of equation (42), and comparing the experimental results. The mole fraction Γ obtained in this way can also be presented against ΔT, to illustrate the effect of noncondensibles on evaporation below the saturation temperature.

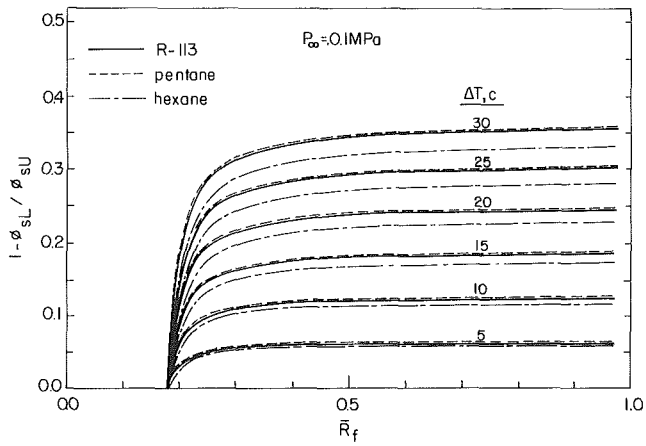

Fig. 4 Variation of normalized difference between exact and approximate apparent saturation temperature ($1-\phi_{sL}/\phi_{sU}$), against the temperature difference ΔT, and the final normalized radius $\bar{R}_f$ of a bubble of R-113, pentane, and hexane

Results and Discussion

Condensation. The generalized formulations are numerically compared with the approximate models for a bubble collapsing in an immiscible liquid.

A computer program of thermodynamic properties of R-113, pentane, and hexane was set to solve numerically the equations derived herein.

Figure 1 illustrates the decrease in saturation temperature due to the presence of noncondensibles. The decrease is expressed as the difference between the saturation temperature at the total pressure and the apparent saturation temperature at the vapor partial pressure. The difference $(T_s - T_s^*)$ increases with the fraction of noncondensibles and with pressure. A numerical example could be most illustrative: At $\Gamma = 0.1$ and $P_\infty = 0.05$ MPa the temperature is lowered by 2.8°C. At the same fraction $\Gamma = 0.1$ and $P_\infty = 2.5$ MPa the temperature is lowered by 7.8°C. Practically the curves indicate the minimum temperature difference necessary to initiate condensation in the presence of noncondensibles. In an evaporation process, on the other hand, the effect is reversed.

In Figs. 2 and 3 the normalized apparent saturation temperature ϕ_s is examined in R-113 at $\Delta T = 5$, 30°C. The generalized equation (15) is compared with the approximate relations (27) and (38). In Fig. 2 at $\Delta T = 5°C$ the approximate curves deviate slightly from the exact solution at the higher fractions of noncondensibles. At $\Delta T = 30°C$ the discrepancy is most apparent.

The discrepancy between the exact solution, equation (15), and Lerner's approximated relation, equation (38), is examined by the ratio of the respective ϕ_s functions. Figure 4 presents the ratio as $\{1-[\phi_{sL}/\phi_{sU}]\}$ against $\bar{R}_f$, and ΔT, as a parameter $\bar{R}_f$ was selected as the independent variable because the maximum error is obtained at the termination of the collapse process. Figure 4 shows that each curve of $y(\bar{R}_f)$ reaches an asymptotic value steeply and remains unchangeable with $\bar{R}_f$, namely with the fraction of noncondensibles. It can be observed that actually, ΔT determines the deviation. At $\Delta T = 5°C$ the deviation is about 5 percent, but increases to 35 percent at $\Delta T = 30°C$. The curves are plotted for R-113, pentane, and hexane. There is very little difference between freon-113 and pentane, because of their very close ratios of vapor to liquid densities, and similar variation of $x(T_s^*)$.

The final size of the bubble $\bar{R}_f$ is presented in Fig. 5, versus ΔT and α. The size decreases with ΔT and inversely with α. These results directly affect the design of condensers.

The presence of noncondensibles in vapor prevents some of

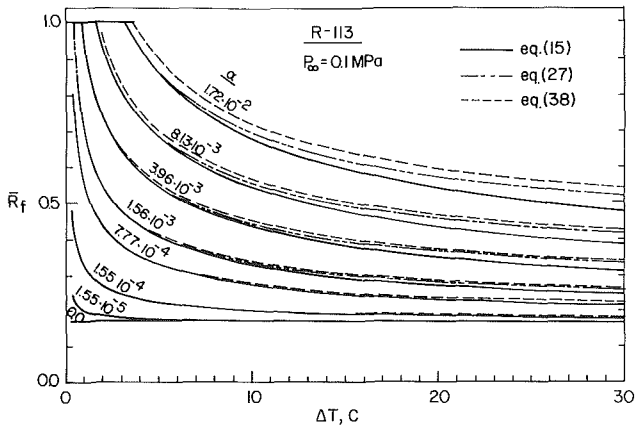

Fig. 5 Variation of normalized final radius of an R-113 bubble with the temperature difference ΔT and the mass fraction of noncondensibles α

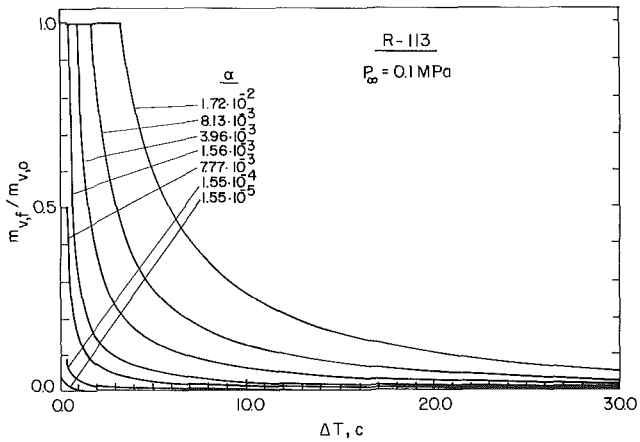

Fig. 6 Variation of the ratio of final noncondensed to initial vapor mass, $(m_{v,f}/m_{v,o})$, against the temperature difference ΔT and the mass fraction of noncondensibles α in a bubble of R-113

the vapor to be condensed. The mass ratio of the finally noncondensed vapor, $m_{v,f}$, and the initial mass of vapor, $m_{v,o}$ is examined in Fig. 6 for R-113 bubbles (equation (18)). In the lower range of $\Delta T < 10°C$ the noncondensed fraction reaches the limit of 1.0 steeply. Thus, the condensation is halted completely. We have seen the same effect in Fig. 1, which related to the minimum temperature difference needed to initiate condensation. These results show the mass losses to be anticipated in a condensation process and practically determine the feasibility of the process.

An actual collapse process was experimentally conducted, and the rates videotaped (Fig. 7). The rates were measured up to a temperature difference of 20°C.

The exact and approximate solutions were also examined in an actual collapse process. Figures 8 and 9 show the collapse rate $\bar{R}(t)$ of an R-113 bubble in water. The process shown in Fig. 8 was conducted at $\Delta T = 8.2°C$. The experimental points are also plotted. The collapse illustrated in Fig. 9 relates to $\Delta T = 30°C$. The rate of collapse was predicted by using Kalman's model (Kalman et al., 1986).

At the temperature difference $\Delta T = 8.2°C$ (Fig. 8) the exact and approximate functions are very close. The deviation between the curves appears smaller than the experimental error. The discrepancy becomes apparent at higher temperature differences.

The theoretical exact and approximate rates of collapse are compared in Fig. 9 at a temperature difference of 30°C.

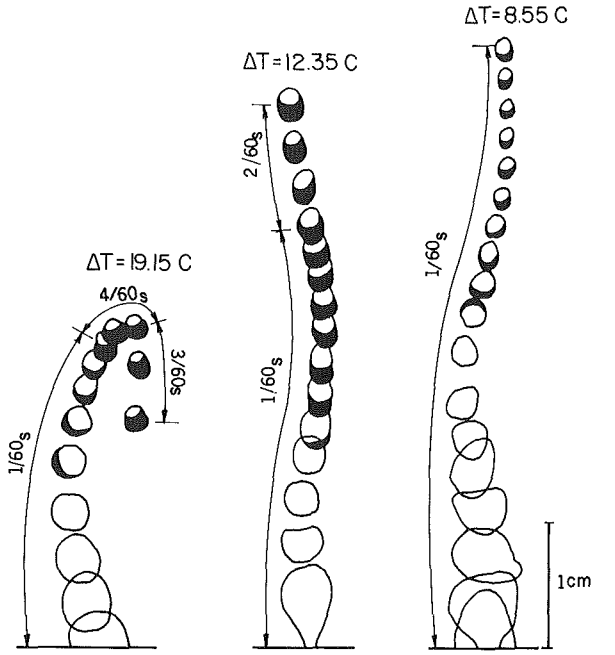

Fig. 7 Videotaped collapse of an R-113 bubble in water at three temperatures

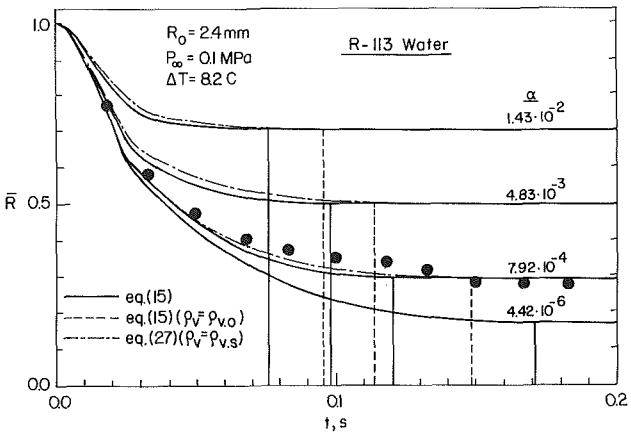

Fig. 8 Variation of the collapse rate of an R-113 bubble in water with the mass fraction of noncondensibles α, at a temperature difference $\Delta T = 8.2°C$

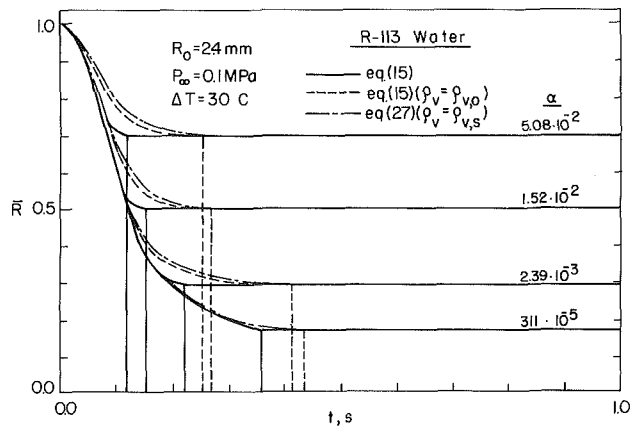

Fig. 9 Variation of the collapse rate of an R-113 bubble in water with the mass fraction of noncondensibles α at a temperature difference $\Delta T = 30°C$

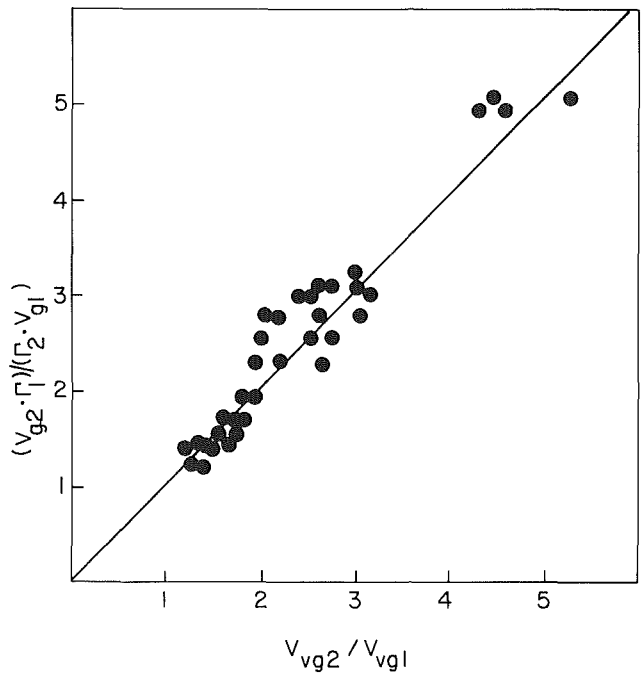

Fig. 10 Evaporation of R-113 in a bubble of air rising in water: comparison of measured and calculated bubble volumetric ratio, (V_{vg2}/V_{vg1}), in two temperature zones

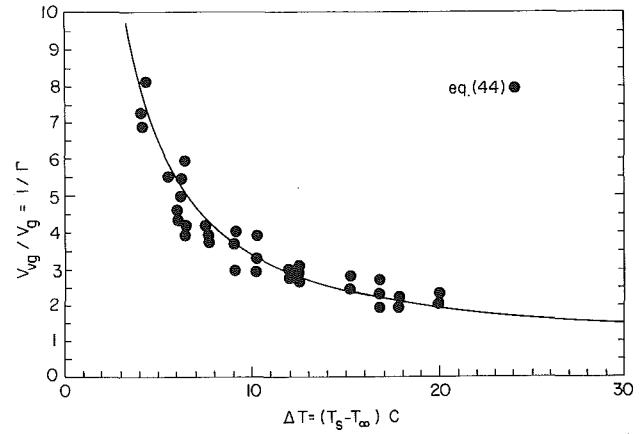

Fig. 11 Evaporation of R-113 in a bubble of air rising in water: variation of the vapor-gas bubble volume with subcooling of water (Γ = mole fraction of air, T_∞ = temperature of water, T_s = saturation temperature of R-113)

Curves of dimensionless bubble radius against time are presented at four mass fraction α of noncondensibles. For each mass fraction of noncondensibles two approximate curves are compared against the exact solid curve. One of the approximate solutions is obtained by equation (27). The other approximate curve is obtained by the exact equation (15) using an approximate density $\rho_v(T_{s,o})$. The solid curve is the exact solution by equation (15) with the vapor real density calculated at the apparent saturation temperature $\rho_v(T_s^*)$. Figure 9 shows that the adjustment of vapor density in $R(t)$, the collapse rate, has a much more pronounced effect on the predicted curve than the other factors in the equation, provided the noncondensibles are uniformly distributed.

The exact curve at the real values of density predicts faster rates of collapse and shorter times of termination. The discrepancy of the approximate curve becomes obvious at higher concentrations of noncondensibles. At the low mass fraction, $\alpha = 3\times10^{-5}$, the predicted approximate and exact collapse rates are practically the same. At the higher mass fraction, $\alpha = 5\times10^{-2}$, the predicted exact termination of condensation is $t_f = 0.12$ s, while the approximate value is $t_f = 0.25$ s, which is more than twice the real time duration.

The real rates of collapse are thus faster than the approximate predictions. The practical implication of those results would be the design of shorter condensers.

Evaporation. Experiments in evaporation were conducted by injecting an air bubble into a layer of liquid R-113. The bubble of air and liquid R-113 rose in a column of water in which the lower zone was maintained at a low temperature T_1, and the upper zone at $T_2 > T_1$. The assumptions involved in equation (39)–(43) were tested experimentally and the results are presented in Figs. 10 and 11. Equation (42) is verified in Fig. 10 by experimentally testing all the terms of the equation and comparing both sides of the equation. The bubble volumes V_{vg} at two locations were videotaped. The gas (air) ratio of volumes V_g was obtained by equation (43) using the measured temperatures and pressures. The mole fractions Γ were obtained by equation (39) using the measured pressure P and the measured temperature by which the vapor pressure $P_v(T)$ is calculated. The graphic comparison of the experimental terms appears adequate within the experimental error of 15 percent.

In Fig. 11 the mole fraction Γ of the gas (air) is computed using a program of thermodynamic properties and applying equation (39). The chosen parameters used in the computation were: P, the total pressure, and T_∞, the water temperature. $P_v(T_\infty)$ and $T_s(P)$ were calculated to yield ΔT and Γ. The experimental measurements related P_1, P_2 to T_1, T_2 and to the videotaped $(V_{vg,2}/V_{vg,1})$.

The independent variable ΔT was comprised of $T_s(P_2)$ and $T_\infty = T_2$. The mole fraction $1/\Gamma_2(T_2, P_2)$ was then obtained by equation (42) rearranged as

$$\frac{1}{\Gamma_2(T_2,P_2)} = \frac{V_{vg,2}}{V_{g,2}} = \left(\frac{V_{vg,2}}{V_{vg,1}}\right)\cdot\left(\frac{V_{g,1}}{V_{g,2}}\right)\cdot\frac{1}{\Gamma_1(T_1,P_1)} \tag{44}$$

where $\Gamma_1(T_1, P_1)$ is calculated by equation (39), and the gas volumetric ratio by equation (43) using the measured respective temperature and pressure.

The theoretical curve in Fig. 11 compares well with the experimental results. These results clearly illustrate that in the presence of noncondensibles evaporation takes place much below the saturation temperature. For $(T_s - T_\infty)\to\infty$ evaporation stops altogether. At $(T_s - T_\infty)\cong 10°C$ the evaporated R-113 vapor occupied in the bubble a volume two times larger than the gas ($V_{vg}/V_g \cong 3$), and at $\Delta T \cong 3°C$ the vapor volume V_v increased to 9 V_g ($V_{vg}/V_g \cong 10$). Thus, the role of noncondensibles in evaporation is reversed to the one encountered in condensation.

Conclusions

A generalized exact relation of the apparent saturation temperature was derived. The exact relation was compared with previous approximate solutions. The discrepancy between the exact and approximate functions increased with the temperature driving force, and with the fraction of noncondensibles.

The minimum temperature difference necessary to conduct a condensation process increased with the fraction of noncondensibles, and with the total pressure in the bubble.

The mass of the residual noncondensed vapor trapped in the gaseous phase of the bubble increases with the fraction of noncondensibles and with the temperature of the cooling medium.

The rate and termination of collapse predicted by the exact relations are faster than the approximate values. In the approximations the term of vapor density has the most pronounced effect on the curve of collapse. The deviation of the approximate collapse curves grows with the fraction of noncondensibles and with the temperature difference.

Assumptions of noncondensibles as an ideal gas, partial pressures, and partial volumes in the mixture of vapor–gas in evaporation were validated experimentally.

Evaporation of liquid in a bubble containing noncondensibles was shown to take place much below the saturation temperature. R-113 vapor was experimentally obtained in the bubble down to 20°C below the saturation temperature. The theoretical curve fitted the experimental data well.

References

Corradini, M. L., 1984, "Turbulent Condensation on a Cold Wall in the Presence of a Noncondensible Gas," *Nuclear Technology*, Vol. 64, pp. 186–195.

Florschuetz, L. W., and Chao, B. T., 1965, "On the Mechanics of Vapor Bubble Collapse," ASME JOURNAL OF HEAT TRANSFER, Vol. 87, pp. 209–220.

Hijikata, K., Chen, S. J., and Tien, C. L., 1984, "Noncondensible Gas Effect on Condensation in a Two-Phase Closed Thermosyphon," *International Journal of Heat and Mass Transfer*, Vol. 27, No. 8, pp. 1319–1325.

Isenberg, J., and Sideman, S., 1970, "Direct Contact Heat Transfer With Change of Phase: Bubble Condensation in Immiscible Liquids," *International Journal of Heat and Mass Transfer*, Vol. 13, pp. 997–1011.

Kalman, H., Ullmann, A., and Letan, R., 1986a, "Dynamics of a Condensing Bubble in Zones of Time-Dependent Velocity," *Proceedings, 8th International Heat Transfer Conference*, Hemisphere, NY, Vol. 4, pp. 1925–1930.

Kalman, H., Ullmann, A., and Letan, R., 1986b, "Visualization Studies of a Freon-113 Bubble Condensing in Water," ASME JOURNAL OF HEAT TRANSFER, Vol. 108, pp. 543–545.

Kotake, S., 1985, "Effects of a Small Amount of Noncondensable Gas on Film Condensation of Multicomponent Mixtures," *International Journal of Heat and Mass Transfer*, Vol. 28, No. 2, pp. 407–414.

Lerner, Y., 1983, "Condensation of Bubbles," M.Sc. Thesis, Ben-Gurion University, Beer-Sheva, Israel.

Votta, F., 1964, "Condensing From Vapor-Gas Mixtures," *Chemical Engineering*, Vol. 70, pp. 223–228.

Webb, D. R., Panchal, C. B., and Coward, I., 1981, "The Significance of Multicomponent Diffusional Internations in the Process of Condensation Gas," *Chem. Eng. Science*, Vol. 36, pp. 85–95.

Wittke, D. D., and Chao, B. T., 1967, "Collapse of Vapor Bubbles With Translatory Motion," ASME JOURNAL OF HEAT TRANSFER, Vol. 89, pp. 17–24.

S. Kim
Associate Professor,
Department of Mechanical Engineering,
Kukmin University,
Sungbukku, Seoul, Korea 132

A. F. Mills
Professor,
Department of Mechanical, Aerospace, and Nuclear Engineering,
University of California,
Los Angeles, CA 90024
Assoc. Mem. ASME

Condensation on Coherent Turbulent Liquid Jets: Part I—Experimental Study

Condensation on coherent turbulent liquid jets was investigated experimentally in order to obtain a data base for the liquid side heat transfer coefficient. Jet breakup was identified by means of high-speed photography. Nozzles were formed from smooth and roughened glass tubes to define the initial turbulence level in the jets. Jet diameters of 3–7 mm and lengths of 2–12 cm were tested at jet velocities of 1.4–12 m/s giving Reynolds numbers of 6000–40,000. Viscosity and surface tension were varied by using ethanol, and water from 277–300 K, as test liquids. The Stanton number was found to be essentially independent of jet diameter, but to decrease with length to the power of −0.57, velocity to the power of −0.20, surface tension to the power of −0.30, and viscosity to the power of −0.1.

1 Introduction

Condensation on a round or planar turbulent jet is of engineering significance. Turbulent jet direct contact condensers have been used in conjunction with dry cooling towers for fossil fuel power plants in the so-called Heller system. Turbulent jet condensers have also been proposed for open-cycle ocean thermal energy conversion based on the Claude cycle. Recently we reviewed previous experimental studies of both condensation on, and evaporation from, turbulent liquid jets (Mills et al., 1982). Most of these studies involved condensation of steam on water jets for practical application to direct contact condensers. When the data were plotted in terms of jet parameters, namely, $\mathrm{St}=h_L/\rho cU$, $\mathrm{Re}=Ud/\nu$, Pr, and L/d, there was no correlation whatsoever. We concluded that phenomena other than turbulent transport in a coherent liquid jet were playing a key role in much of the data, for example, jet breakup into a dispersed phase and entrainment into a collection pool. Thus there are many features of the problem that require further investigation; the present study concerns the liquid side heat transfer coefficient in coherent turbulent liquid jets. Using both experiment and theoretical analysis we have attempted to determine the dependence of this coefficient on geometric parameters, hydrodynamic parameters, and thermophysical properties. We do not claim to present design data for jet condensers.

This paper reports the results of an experimental study of condensation of saturated vapor on a coherent round turbulent liquid jet. The parameters varied include jet diameter, velocity, and length, the viscosity and surface tension of the liquid, and the initial turbulence level in the jet. A companion paper (Kim and Mills, 1989) reports the solution of the conservation equations governing mass, momentum, and energy in laminar and turbulent jets using finite difference numerical methods. Both eddy diffusivity and two equation models of turbulence were tested against the experimental data.

Two previous experimental studies have provided relevant and useful data. Ofer (Mills et al., 1982; Ofer, 1982) obtained data for evaporation from round water jets at 290–300 K. He found that the Stanton number was independent of jet diameter, and varied with jet velocity and length as

$$\mathrm{St} \propto U^{-0.244} L^{-0.416} \tag{1}$$

for $3<U<12$ m/s, $1.6<L<17.1$ cm, $1.8<d<5.6$ mm ($8000<\mathrm{Re}<28{,}000$, $6<L/d<43$). The effects of liquid viscosity and surface tension were not explored. Iciek (1983) obtained data for condensation on round water jets at 300–340 K, $4\le L\le 90$ cm, $2.01\le d\le 7.30$ mm. The jet velocity range was not specified, but the data presented include $0.815<U<1.72$ m/s and $4100<\mathrm{Re}<6900$. Continuous (coherent) jets were defined as jets for which $L<11.5\ \mathrm{We}^{0.31}$, and their recommended correlation for such jets was

$$\mathrm{St}=0.00375\,(L/d)^{-0.28}\mathrm{Fr}^{-0.10} \tag{2a}$$

In terms of the primitive variables the Stanton number varies as

$$\mathrm{St} \propto U^{-0.2}\, L^{-0.28}\, d^{\,0.38} \tag{2b}$$

Iciek examined the effect of nozzle shape and length. When a tapered inlet was used it was found that a long nozzle was required to ensure turbulent flow at the nozzle exit; however, when a sharp-edged inlet was used the nozzle length did not appear to affect heat transfer, provided it was long enough to produce an axisymmetric jet. Our study was made prior to the publication of Iciek's work, and we chose to use a long nozzle with an inlet turbulence trip to ensure that turbulence parameters were defined at the nozzle exit. In addition the effect of turbulence intensity could be ascertained by varying the roughness of the nozzle. Iciek's results indicate that the performance of our long smooth nozzles is not substantially different from the short-edged nozzles he recommends for practical application.

2 Experimental Apparatus

A detailed description of the experimental apparatus is given by Kim (1983). Figure 1 shows a schematic of the system. The liquid loop is comprised of the jet test chamber, nozzle and receiver assemblies, cooler, reservoir, pumps, and flowmeter. The test chamber is a 60-cm-long, 12-cm-dia flanged thick wall glass tube closed at each end by stainless steel plates held in place by bolted flanges and sealed with Viton O-rings. Vapor is admitted at the top of the chamber to obtain cocurrent flow of vapor and jet. Two type-K thermocouples are located in the chamber to measure the wet bulb (saturation) temperature of the vapor. The nozzle assembly, shown in Fig. 2(*a*), consists of a short calming section, pressure regulator, and a three-junction thermopile. The nozzle section is made of standard glass tubing in sizes from 2.4–7.0 mm I.D., and is smoothly connected to a 12.7 mm O.D. glass tube that slides to adjust the jet length. To ensure fully developed turbulent flow at the nozzle exit, nozzle lengths of greater than 30 diameters are used, and a turbulence trip is located in the contraction. Two roughened nozzles were

Contributed by the Heat Transfer Division for publication in the JOURNAL OF HEAT TRANSFER. Manuscript received by the Heat Transfer Division January 26, 1987. Keywords: Condensation, Jets, Turbulence.

prepared from 5.5 mm I.D. tube to give values of k_s/d of 0.026 and 0.035 (fully rough friction factors of 0.054 and 0.060, respectively). The receiver assembly, shown in Fig. 2(b), is designed to collect the jet with minimal vapor entrainment. The collectors are glass tubes with conically ground tips of diameter approximately 1 mm larger than the corresponding nozzle diameter. Vapor entrainment is minimized by regulating the back pressure in the receiver using a glass regulator. A magnifying glass and side lighting are provided to observe the collection process. Two-dimensional nozzle and collector manipulators are used to align the nozzle with the collector. The reservoir is a 25-cm-dia glass flask located 0.7 m above the pumps, which are magnetically coupled units with liquid compartments of glass-filled Teflon and stainless steel. The cooler is a copper tubing counter-flow heat exchanger, with water–Prestone II coolant supplied from a refrigeration plant, via a reservoir containing a variable transformer controlled immersion heater for load balancing.

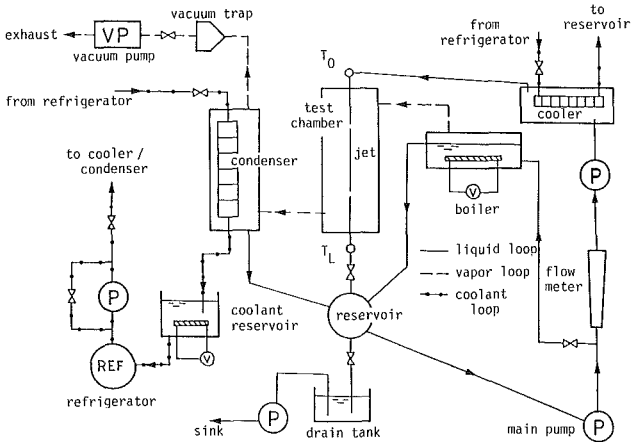

Fig. 1 Schematic of experimental system

Vapor is generated in a 3.7 kW maximum rated unit controlled by a variable transformer. Makeup liquid is supplied from the liquid loop through a connecting glass tube and regulating valve, and excess liquid overflows into the reservoir in the liquid loop. An auxiliary condenser is connected to the test chamber and serves to control the vapor velocity in the chamber, so as to eliminate noncondensable gas effects. The condensate is refluxed down to the reservoir by gravity. A Welch Duo-Seal vacuum pump exhausts end gases from the auxiliary condenser through an electrically heated suction line.

The pressure in the test chamber is measured by a mercury manometer. In order to prevent vapor condensation in the manometer, it is installed in a temperature-controlled enclosure, with appropriate corrections made for temperature-dependent mercury properties. The reference pressure is maintained at less than 50 μm Hg absolute, and monitored by a

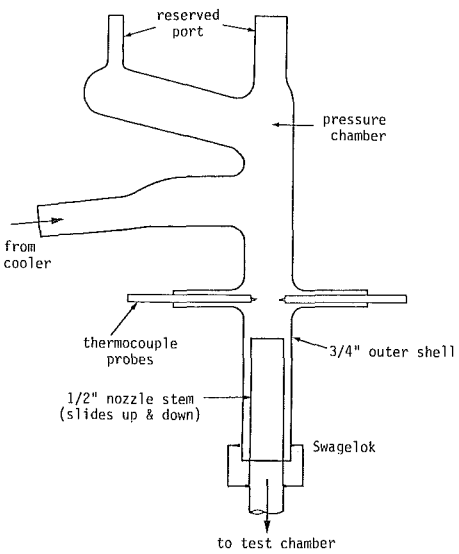

Fig. 2(a) Nozzle assembly

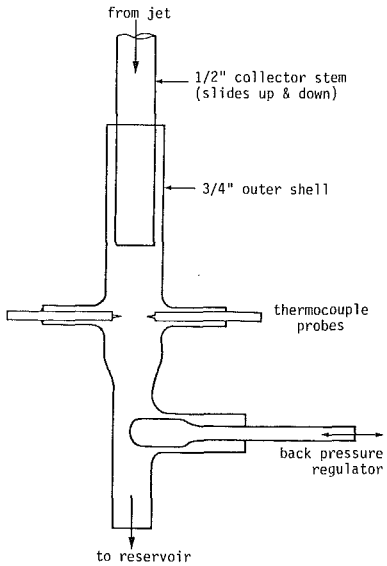

Fig. 2(b) Receiver assembly

Nomenclature

c = specific heat
d = jet diameter, m
F = ratio of rough nozzle to smooth nozzle friction factors
Fr = Froude number $= U^2/dg$
f = condensation coefficient; friction factor
g = acceleration due to gravity
h_L = liquid side heat transfer coefficient
h_{fg} = latent heat of vaporization
Ja = Jakob number $= c(T_s - T_0)/h_{fg}$
k = slenderness ratio $= L/d$
k_s = equivalent sand grain roughness
L = jet length, m
N_{tu} = number of transfer units $= 4h_L(L/d)/\rho cU$
Pr = Prandtl number $= \nu/\alpha$
q = surface heat flux
R = universal gas constant
Re = Reynolds number $= Ud/\nu$
St = Stanton number $= h_L/\rho cU$
Su = Suratman number $= \sigma d/\rho\nu^2$
T = temperature
U = bulk jet velocity, m/s
V = turbulence intensity
v_g = vapor specific volume
We = Weber number $= \rho U^2 d/\sigma$
α = thermal diffusivity
ϵ = heat transfer effectiveness
μ = dynamic viscosity
ν = kinematic viscosity, m^2/s
ρ = liquid density, kg/m^3
σ = surface tension, N/m

Subscripts

b = bulk
c = centerline
L = outlet
R = rough
S = smooth
s = surface
sat = saturation
O = inlet

Superscripts

* = normalized

thermocouple vacuum gage. The heights of the columns are determined by sighting with a cathetometer having a least count of 0.05 mm. All thermocouples are type K, manufactured by Omega Eng. Inc. A Fluke Data Logger with a built-in cold junction compensator and least count of 0.1°F (0.06°C) is used to measure the thermocouple outputs. A rotameter is used to measure liquid flow rate and was carefully recalibrated with tap water at 22°C before installation. For other liquids the standard density correction formula was used.

3 Test Procedures

A special effort was required to maintain the system free of contamination and leakage. All components were thoroughly cleaned before assembly. Distilled water was used for the water tests and was periodically checked for both organic and inorganic contamination using the Crits ring test (Crits, 1961), and an electronic conductivity probe and bridge. Organic contaminants were always less than 20 ppm, while salt content was less than 10 ppm. The extensive use of glass components allowed the absence of air leaks to be monitored by filling the system with water and applying a vacuum: Leaks produce easily seen air bubbles.

Prior to a set of tests an appropriate nozzle and collector pair are installed and the system filled with the test liquid. Also the Data Logger is programmed and checked out. System startup involves three major steps:

1 Deaeration and system cooldown. The refrigeration system is started and coolant flow rate adjusted. The vacuum line heater is turned on with the valve on the vacuum line closed; after a few minutes the vacuum pump is started and the valve opened slightly. Next the circulation pump is started and adjusted to give a low flow rate so there is no splashing in the test chamber, and the desired reservoir water level obtained.

2 Jet establishment. The circulation pump is briefly turned off to check if there is vapor entrapped in the rotor shell, and then the flow rate is increased to obtain the required flow rate. The jet is aligned by using the nozzle and collector manipulators. The receiver pressure regulator is used to maintain the water level and pressure in the collector so as to minimize vapor entrainment.

3 Thermal equalizing. The vapor generator and mixing chamber heaters are turned on and adjusted to give an energy balance; the amount of coolant bypass of the cooler and condenser are also adjusted if necessary. The vapor saturation temperature is monitored to determine when steady state is attained.

Test data are taken over the shortest time interval consistent with obtaining precise measurements, rather than taking data over a long period of time and averaging the measurements. Any errors so introduced are offset by the large number of tests accomplished. The essential measurements are simply liquid flow rate, inlet and outlet liquid temperatures, vapor saturation temperature, and manometer heights.

4 Data Reduction

The jet condenser is a single stream heat exchanger, with effectiveness ϵ given by

$$\epsilon = \frac{T_L - T_0}{T_s - T_0} \tag{3}$$

where T_0, T_L, and T_s are the liquid inlet, outlet, and surface temperatures, respectively, and T_s is assumed constant. The number of transfer units is then

$$N_{tu} = -\ln(1-\epsilon) \tag{4}$$

Assuming a constant jet diameter, an average Stanton number is calculated from

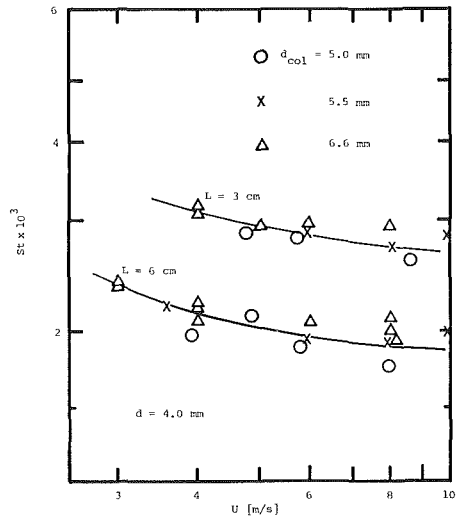

Fig. 3 Effect of collector size on measurement of T_L

$$\mathrm{St} = \frac{h_L}{\rho c U} = \frac{N_{tu}}{4(L/d)} \tag{5}$$

It was found necessary to correct the measured temperature in the nozzle assembly for condensation on the outside of the nozzle to obtain the true bulk liquid temperature of the liquid ejected by the nozzle (T_0). The correction was made by modeling the nozzle as a single-stream exchanger, with heat transfer across three thermal resistences in series, namely a condensate film resistance given by a uniform heat flux Nusselt type analysis, a tube wall conduction resistance, and an internal convective resistance given by the Dittus-Boelter correlation. The relative error in the effectiveness ranged up to 20 percent in the parameter range tested, and thus correction was made in all the data. The correction was further evaluated by performing some experiments with insulated nozzles, as will be discussed in connection with the measurement of the jet core temperature. The condensate formed on the outside of the nozzle runs down to the tip and is entrained on the cold jet. The resulting increase in the bulk temperature was calculated from an energy balance and found to be negligible (<0.01 K) in the parameter range of concern. As a further check for other unwanted effects some experiments were performed with a condensate deflector on the nozzle tip to prevent entrainment, and no significant effect on the effectiveness was found.

Figure 3 shows some systematic effects of collector size on the measurement of temperature T_L, possibly due to vapor entrainment, splashing, or skimming of the jet. The effects of vapor entrainment were established using a correlation of Van de Sande and Smith (1976) for entrainment by a jet impinging on an open pool. Details are given by Kim (1983) showing an upper limit of the possible error less than 0.1 K. Thus in the experimental work care was taken not to skim liquid from the jet, while minimizing vapor entrainment, and no correction was made to the measured value of T_L.

Potential application of the results of this study to open cycle ocean thermal energy conversion dictated the use of water as the primary test fluid and saturation temperatures as low as 277 K. The high liquid side heat transfer coefficients obtained, particularly for short jets, result in the interfacial resistance not being completely negligible. The interfacial resistance is conveniently given in terms of an interfacial heat transfer coefficient (Nabavian and Bromley, 1963) as

$$h_i = \frac{f}{1-0.5f}\left[\frac{1}{2\pi RT}\right]^{1/2}\frac{h_{fg}^2}{T_s v_g}; \qquad h_i = \frac{q_s}{T_{\mathrm{sat}} - T_s} \tag{6}$$

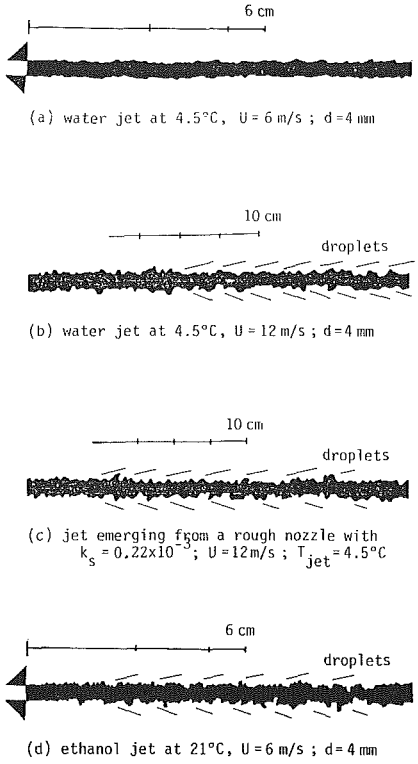

Fig. 4 High-speed photographs showing effects of velocity, test liquid, and nozzle roughness on surface stability

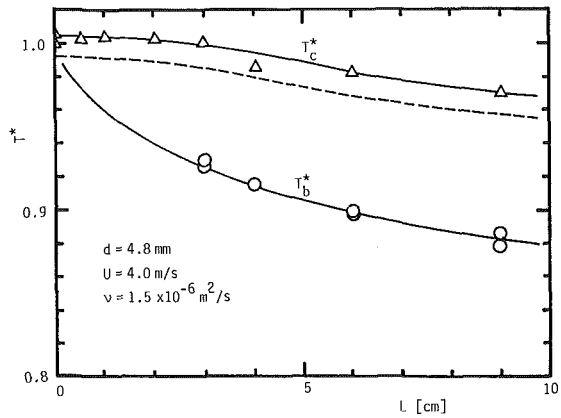

Fig. 5 Thermal entrance region: jet centerline temperature versus distance from nozzle

where f is the condensation coefficient and is the fraction of molecules striking the surface that actually condense, T_s is the liquid surface temperature, T_{sat} is the saturation temperature corresponding to the vapor pressure, and v_g is the vapor specific volume evaluated at $T = (T_{sat} + T_s)/2$. Mills and Seban (1968) showed that there was no justification for using a value of f less than unity for condensation of steam on water. Owing to the variation of T_s and h_L along the jet an exact correction for the effect of interfacial resistance is very difficult. However, based on average values of h_i and h_L, the maximum error incurred in h_L by ignoring the interfacial resistance is 12 percent, which is of a similar magnitude to the scatter in the data. Thus the interfacial resistance was ignored, except that in the statistical analysis and correlation of the Stanton number, which is the primary result of this study, data points for which the interfacial resistance was greater than 5 percent of the liquid side resistance were excluded.

5 Results and Discussion

5.1 Droplet Formation and Jet Breakup. High-speed photography was used to identify the onset of droplet formation. A 16 mm high-speed camera (Redlake 41-0004) was used to take photographs on Kodak 4-X reversal film, with three 1 kW quartz lamps for lighting. To obtain reasonable resolution the shutter speed was limited to 3000 frames per second. Some typical frames are shown in Fig. 4, where the effects of jet velocity, nozzle roughness, and test liquid are clearly seen. It was found that the onset of droplet formation was at a jet length of 6 to 9 cm, depending primarily on diameter and liquid. Although the quality of the photographs was not entirely satisfactory, this result was adequate for the present purpose. Further study of droplet formation would require better lighting and a shutter speed of perhaps 10,000 frames per second. The criterion used by Iciek (1983) to define a coherent jet gave a "breakup length" of 15 cm in his experiments. In our work a coherent jet was defined in terms of onset of droplet formation, and thus restricted the data of concern to somewhat shorter jet lengths.

5.2 Core Temperature and Thermal Entrance Length. In a previous study (Mills et al., 1982) we demonstrated that mass transport in turbulent jets was an entrance region problem. In order to obtain direct experimental indication of the extent of the entrance region for heat transport, measurements of the developing temperature profile are required. Thus an attempt was made to measure the variation of temperature along the centerline of the jet, T_c, using a streamlined reinforced thermocouple probe. Accurate centering was difficult because of the jet momentum; about 20-30 data points were recorded, and T_c was taken to be the lowest value that appeared at least three times. Typical results for the normalized centerline temperature $T_c^* = (T_c - T_s)/(T_0 - T_s)$ are shown in Fig. 5, together with a lower limit curve assuming a random error of ± 0.1 K in the thermocouple reading. Also shown is the corresponding variation of the normalized bulk temperature $T_b^* = (T_b - T_s)/(T_0 - T_s)$ where T_b was taken as T_L for the corresponding jet length. If an entrance length L_e is defined as the location where the centerline temperature commences to change, then a value of $L_e/d = 6$–8 is indicated in the parameter range under consideration. A few more diameters would be required for the thermal entrance effect to be negligible. Notice that these lengths are about 10 percent of the corresponding values for laminar jets.

5.3 Stanton Number Behavior. The measured Stanton numbers are plotted to display the effects of the parameters varied in the experiments.

Effect of Jet Velocity U. Figure 6 shows that the slope of ln St versus ln U plots varies slightly, depending on the value of U itself. The average slope is -0.2, which agrees with other typical turbulent flows, e.g., flow in a pipe.

Effect of Jet Length L. Figure 7 shows a marked L dependence ($St \propto L^{-0.57}$ is obtained from statistical analysis). This dependence is larger than for a laminar jet, and implies an effect of axial decay of turbulence in addition to an entrance region effect. It is not expected that this dependence will extrapolate to larger values of L because of jet breakup.

Effect of Jet Diameter d. Figure 8 shows only a weak dependence of St on d. The scatter in the data is thought to be mostly due to collector effects, as discussed in Section 4. Laminar jets also show only a slight geometric effect. For a turbulent jet it might be though that there could be an additional effect through the bulk value of eddy diffusivity ($\epsilon_b \propto \nu Re^{0.9}$, Hinze, 1975), or through the bulk value of turbulence intensity ($V_b \propto U Re^{-1/8}$, Blasius and Schlichting, 1979). The observed weak diameter dependence therefore suggests that the transport process is better described by the level of V_b, rather than of ϵ_b.

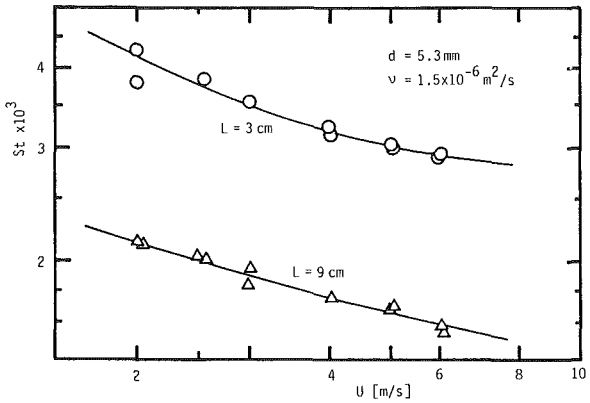

Fig. 6 Effect of jet velocity on Stanton number

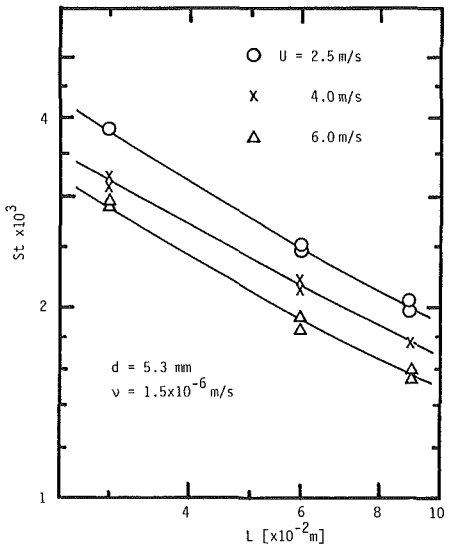

Fig. 7 Effect of jet length on Stanton number

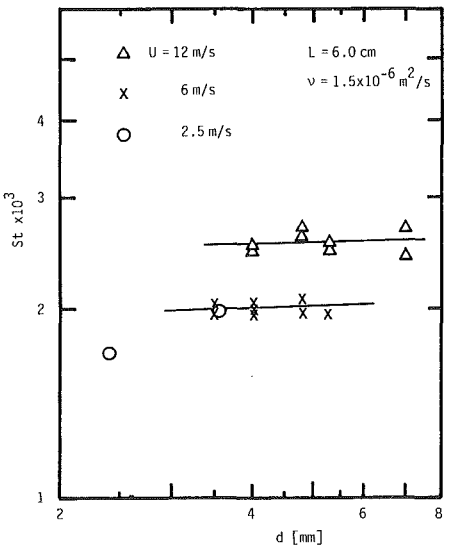

Fig. 8 Effect of jet diameter on Stanton number

Effect of Viscosity ν and Thermal Diffusivity α. Figure 9 shows St versus U for various test liquids, i.e., various combinations of ν and α. It proved infeasible to vary ν and α independently by an appropriate choice of liquids. Rather, by increasing the water temperature from 277 K to 300 K, ν was decreased by 40 percent, while α increased by 14 percent; there

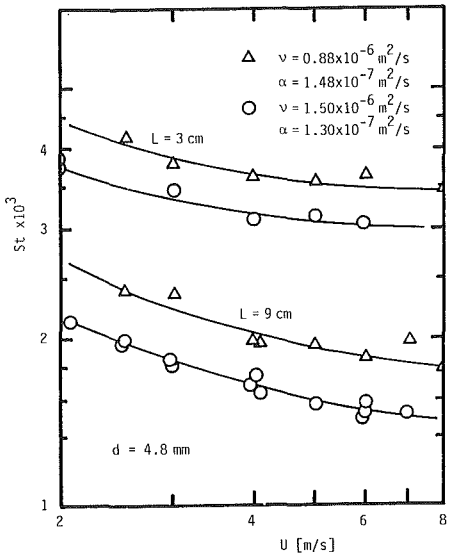

Fig. 9 Effects of viscosity and thermal diffusivity on Stanton number

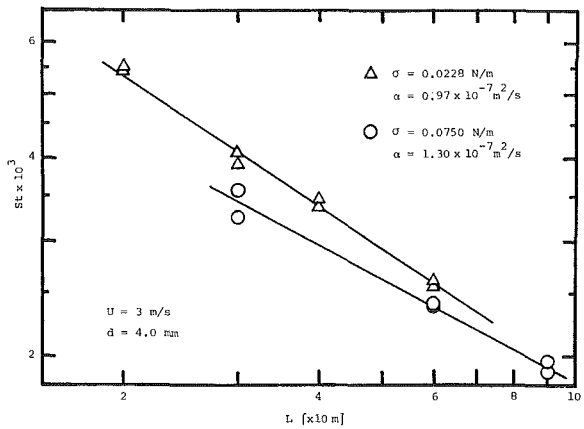

Fig. 10 Effect of surface tension on Stanton number

was a corresponding increase in St of about 15 to 20 percent. To see what portion of this increase is attributable to the decrease in viscosity, a dependence of St on α must be assumed. Based on known behavior of other turbulent transport problems, St can be expected to depend on α raised to an exponent between 1/2 and 2/3. As will be shown in the statistical analysis that follows, the resulting ν dependence is St $\propto \nu^{-0.1}$, which includes both effects via the initial condition of the jet, and via axial and radial damping of turbulence subsequently.

Effect of Surface Tension σ. The low surface tension of ethanol allows jet breakup to occur at much lower velocities than for water. Thus the ethanol data were very carefully screened before inclusion in the statistical analysis. Notwithstanding the lower thermal diffusivity for ethanol, the Stanton numbers are larger than for water. Using the same range of α dependence as discussed above, the net effect of surface tension is St $\propto \sigma^{-(0.2-0.3)}$. This result suggests that surface tension does damp turbulence near the interface, in line with the model proposed by Levich (1962).

Effect of Nozzle Roughness. Figure 11 shows St versus U for the two roughened nozzles. The initial bulk turbulence intensity V_b is proportional to the square root of the nozzle friction factor, and was increased by 30 to 60 percent by roughness; the statistical analysis shows a corresponding increase St $\propto V_b^{0.4}$. This result is consistent with the diameter effect noted earlier, i.e., the most important turbulence property controlling the transport process is V_b. Further, using the

Blasius formula for V_b (Schlichting, 1979) we have St $\propto \nu^{-0.05}$, which is the viscosity effect due to the initial condition of the jet; the remaining dependence St $\propto \nu^{-0.05}$ must be due to subsequent turbulence damping. Figure 11 also confirms an earlier jet breakup due to roughness.

5.4 Statistical Analysis and Correlation. Examination of the governing conservation equations, boundary conditions, and possible turbulence models suggested the following Stanton number dependence:

$$\mathrm{St} = \mathrm{St}\ (U, L, d, \nu, \alpha, \sigma/\rho, F) \tag{7}$$

where σ/ρ has been included rather than σ and ρ separately, since only this combination is expected. There are many possible choices for a parameter to characterize the roughened nozzles; instead of using a fundamental parameter such as equivalent sand grain roughness, we choose to use the ratio of the friction factor f to the corresponding value for a smooth nozzle, denoted F. Although scaling of the energy conservation equation and its boundary conditions indicates that $\Delta T = T_s - T_0$ is an expected parameter, it was not included in the statistical analysis. The relevant dimensionless group is the Jakob number $\mathrm{Ja} = c_p \Delta T / h_{fg}$, which characterizes the effect of a moving interface on the temperature profiles, i.e., a "blowing" effect. Simple Couette flow analysis indicates that the expected reduction in the liquid side heat transfer coefficient is less than 2 percent for the water jets, and less than 5 percent for the alcohol jets. Practical considerations did not allow a significant variation of Jakob number, and also led to a somewhat systematic variation of ΔT with temperature level. Thus inclusion of ΔT in the statistical analysis would lead to an inability to discern effects of temperature-dependent liquid properties, in particular, viscosity.

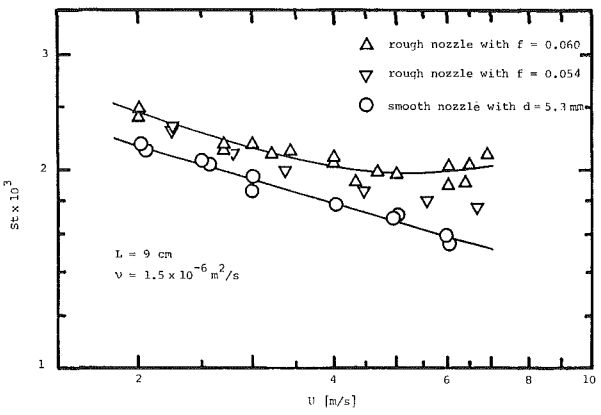

Fig. 11 Effect of nozzle roughness on Stanton number

A functional relationship of the form

$$\mathrm{St} = a_o U^{a1} L^{a2} d^{a3} \nu^{a4} \alpha^{a5} (\sigma/\rho)^{a6} F^{a7} \tag{8}$$

is postulated, where, for simplicity, constant exponents were assumed for a least-squares regression analysis. Owing to the lack of a broad data base for the effect of thermal diffusivity α, the exponent a_7 was varied parametrically, initially with values of 1/3, 1/2 and 2/3, to span the expected range. Also, since the diameter dependence proved to be very weak, the data were recorrelated with exponent $a_3 = 0$. Table 1 shows the results for correlations of all the data, and for short jets ($L = 6$ cm) only. An increased length dependence is seen for shorter jets, suggesting entrance region effects. Also it is seen that the viscosity dependence is less for shorter jets, perhaps indicating less viscous damping of turbulence.

Assuming that the assumption of constant exponents is adequate, the correlation equation (8) can be recast in the dimensionless form

$$\mathrm{St} = b_0\ \mathrm{Re}^{b1}\ \mathrm{Su}^{b2}\ k^{b3}\ \mathrm{Pr}^{b4}\ F^{b5} \tag{9}$$

Comparison of equations (8) and (9) gives

$$b_1 = a_1;\quad b_2 = a_6;\quad b_3 = a_2;\quad b_4 = -a_5;\quad b_5 = a_7 \tag{10a}$$

$$a_3 = a_1 + a_6 - a_2 \tag{10b}$$

$$a_4 = a_1 - a_5 - 2a_6 \tag{10c}$$

Table 1 shows that the correlations with a higher α exponent a_5 are in better accord with equations (10*b*) and (10*c*); thus a correlation of all the data was also made with $a_5 = 0.7$, which gave a low relative error of only 6.2 percent. The correlations are also in better accord with equations (10*b*) and (10*c*) for short jets. The discrepancies seen in equations (10*b*) and (10*c*) may be due to exponents that are not true constants, but weak functions of the parameters themselves, and due to systematic errors in the data. Indeed, if the dependence on σ and ν were weaker, the discrepancies would be smaller. For low σ or low ν jets, undetected droplet formation might have occurred; also the virtually negligible interfacial resistance for the alcohol jet increases the σ exponent somewhat.

Our preferred correlation of Stanton number is thus

$$\mathrm{St} = 0.57 U^{-0.20} L^{-0.57} \nu^{-0.1} \alpha^{0.7} (\sigma/\rho)^{-0.3} F^{0.18} \tag{11}$$

with a relative error of 6.2 percent. If the main source of dimensional discrepancy is attributed to error in determining the surface tension and diameter dependences (the former due to sparsity of data, the latter due to difficulty in collecting the jet) then a possible dimensionless correlation is

Table 1 Selected results of the least-squares regression analysis (the relative error is the standard deviation divided by the average value of the Stanton number; an asterisk denotes a prescribed quantity)

Correlation Number	a_o	a_1(U)	a_2(L)	a_3(d)	a_4(ν)	a_5(α)	a_6($\frac{\sigma}{\rho}$)	a_7(f)	Relative Error Percent
	ALL DATA								
1.	0.00035	-0.21	-0.57	-0.03	-0.13	0.33*	-0.15	-	0.10
2.	0.0043	-0.21	-0.57	-0.03	-0.10	0.50*	-0.21	-	0.10
3.	0.51	-0.21	-0.57	-0.03	-0.08	0.67*	-0.25	-	0.10
4.	0.00039	-0.20	-0.57	0*	-0.13	0.33*	-0.15	-	0.10
5.	0.0047	-0.20	-0.57	0*	-0.10	0.50*	-0.20	-	0.10
6.	0.52	-0.20	-0.57	0*	-0.08	0.67*	-0.27	-	0.10
7.	0.57	-0.20*	-0.57*	0*	-0.10*	0.70*	-0.3*	0.18	0.062
	SHORT JETS ONLY (L ≤ 6 cm)								
8.	0.013	-0.23	-0.71	0.015	-0.03	0.33*	-0.15	-	0.10
9.	0.12	-0.23	-0.71	0.015	-0.01	0.50*	-0.20	-	0.10
10.	1.8	-0.23	-0.71	0.015	0.03	0.67*	-0.26	-	0.10
11.	0.010	-0.23	-0.71	0*	-0.03	0.33*	-0.15	-	0.10
12.	0.12	-0.23	-0.71	0*	-0.01	0.50*	-0.20	-	0.10
13.	1.7	-0.23	-0.71	0*	0.03	0.67*	-0.26	-	0.10

$$\mathrm{St} = 3.2\ \mathrm{Re}^{-0.20}\mathrm{Su}^{-0.19}k^{-0.57}\mathrm{Pr}^{-0.7}F^{0.18} \quad (12)$$

with a relative error of 12 percent. Equation (12) gives $\mathrm{St} \propto \sigma^{-0.19}\, d^{0.18}$ in contrast to the $\mathrm{St} \propto \sigma^{-0.3} d^{0}$ of equation (11). Equation (12) is, of course, a biased representation of the experimental data, but is preferred for extrapolation to other liquids, and to jet diameters outside the range tested. It also may be superior to equation (11) as a guide to developing an appropriate theory. We note also that further experimental data, particularly for the effects of σ and α, would assist in reducing the ambiguities apparent in our results.

5.5 Comparisons With Previous Studies. Using equation (11), two important observations can be made regarding the previous studies mentioned in the Introduction.

1 In the parameter range of Ofer's experiments with evaporating water jets at about 295 K, equation (11) reduces to

$$\mathrm{St} = 5.7 \times 10^{-4} U^{-0.20} L^{-0.57} \quad (14)$$

while Ofer (1982) obtained

$$\mathrm{St} = 8.47 \times 10^{-4} U^{-0.244} L^{-0.416} \quad (15)$$

Equation (14) gives values about 30–60 percent higher than equation (15). This discrepancy is partially attributable to a larger interfacial resistance included in Ofer's data, but is probably primarily due to the greater difficulty in collecting the more unstable evaporating jets. However, the higher Stanton numbers obtained in our study for condensation do confirm an absence of noncondensable gas effects on the condensation process.

2 Iciek's correlation equation (2*b*) has an identical U dependence, while the smaller negative exponent on L is expected due to the longer jet studied. There is of course a significant discrepancy in the d exponent, 0.38 versus 0.0. This discrepancy could be mostly due to the fact that the correlation was made in terms of dimensionless groups rather than the primitive variables. Since d is combined with L in L/d and with U^2 in Fr, it was not correlated in an unbiased manner.

6 Conclusions and Recommendations

1 The average Stanton number for vapor condensing on a coherent round turbulent jet is given by

$$\mathrm{St} = 0.57\ U^{-0.20} L^{-0.57} \nu^{-0.1} \alpha^{0.7} (\sigma/\rho)^{-0.3} F^{0.18} \quad \text{(SI units)}$$

with a relative error (standard deviation/average St) of 6.2 percent, in the parameter range $\mathrm{Re} = 6000$–$40{,}000$, jet diameter 3–7 mm, jet length 2–12 cm, saturation temperatures 10–30°C for water and ethanol, and nozzle equivalent sand grain roughness of 0–0.17 mm.

2 The recommended dimensionless form of the correlation is

$$\mathrm{St} = 3.2\mathrm{Re}^{-0.20}\mathrm{Su}^{-0.19}k^{-0.57}\mathrm{Pr}^{-0.7}F^{0.18}$$

with a relative error of 12 percent.

3 Turbulence damping is caused by both viscosity and surface tension.

4 The initial value of bulk turbulence intensity has a much larger effect on heat transfer than does the initial value of the bulk eddy diffusivity.

5 The thermal boundary layer grows quite quickly, with a thermal entrance length at the order of 10 diameters, but the Stanton number continues to decay thereafter.

6 Recommendations for future experimental work include a more sophisticated photographic study to identify the onset of droplet formation, and use of liquids that will allow the effects of thermal diffusivity and surface tension to be further defined.

Acknowledgments

This study was supported by the U.S. Department of Energy, Grant No. DE-FG02-80CS89501, through the Solar Energy Research Institute, Golden, CO. The grant monitor was Dr. T. Penney. Computer time was supplied by the Campus Computing Network of the University of California, Los Angeles.

References

Crits, G. J., 1961, "The Crits Organic Ring Test," presented at the Symposium on Analytical Methods With Emphasis on Minor Elements, ACS Division of Water and Waste Chemistry, Chicago, IL.

Hinze, O., 1975, *Turbulence*, 2nd ed., McGraw-Hill, New York.

Iciek, J., 1983, "The Hydrodynamics of a Free Liquid Jet and Their Influence on Direct Contact Heat Transfer—III. Direct Contact Heating of a Cylindrical Free Falling Liquid Jet," *Int. J. Multiphase Flow*, Vol. 9, pp. 167–179.

Kim, S., 1983, "An Investigation of Heat and Mass Transport in Turbulent Liquid Jets," Ph.D. Dissertation, School of Engineering and Applied Science, University of California, Los Angeles, CA.

Kim, S., and Mills, A. F., 1989, "Condensation on Coherent Turbulent Jets: Part II—A Theoretical Study," ASME JOURNAL OF HEAT TRANSFER, Vol. 111, this issue.

Levich, V. G., 1962, *Physicochemical Hydrodynamics*, Prentice Hall, Inc., New Jersey.

Mills, A. F., and Seban, R. A., 1967, "The Condensation Coefficient of Water," *Int. J. Heat Mass Transfer*, Vol. 10, pp. 1815–1827.

Mills, A. F., Kim, S., Leininger, T., Ofer, S., and Pesaran, A. A., 1982, "Heat and Mass Transport in Turbulent Liquid Jets," *Int. J. Heat Mass Transfer*, Vol. 25, pp. 889–897.

Ofer, S., 1982, "An Experimental Study of Evaporation From Round Turbulent Water Jets," M.S. Thesis, School of Engineering and Applied Science, University of California, Los Angeles, CA.

Nabavian, K., and Bromley, L. A., 1963, "Condensation Coefficient of Water," *Chem. Engr. Sci.*, Vol. 18, pp. 651–660.

Schlichting, H., 1979, *Boundary Layer Theory*, 7th ed., McGraw-Hill, New York.

Van De Sande, E., and Smith, J. M., 1976, "Jet Break-up and Air Entrainment by Low Velocity Turbulent Jets," *Chem. Eng. Sci.*, Vol. 31, pp. 219–224.

Condensation on Coherent Turbulent Jets: Part II—A Theoretical Study

S. Kim
Associate Professor,
Department of Mechanical Engineering,
Kukmin University,
Sungbukku, Seoul, Korea 132

A. F. Mills
Professor,
Department of Mechanical, Aerospace, and Nuclear Engineering,
University of California,
Los Angeles, CA 90024
Assoc. Mem. ASME

Condensation on coherent turbulent liquid jets was investigated theoretically. The governing conservation equations were obtained using an order of magnitude analysis, and were solved numerically using a finite difference method. The Boussinesq hypothesis was invoked to model turbulent transport. Various eddy diffusivity models, of varying degrees of complexity, were evaluated through comparison with experimental data, and shortcomings noted. An ad hoc model, which allows for axial decay of turbulence by viscosity, and radial decay by both surface tension and viscosity, is shown to be in reasonable agreement with experiment. Numerical solutions were also obtained for laminar jets, and are essentially exact; these solutions are used to give some insight into the nature of the jet heat transfer problem.

1 Introduction

An experimental study of condensation on round coherent turbulent liquid jets is reported in a companion paper (Kim and Mills, 1989). A data base was obtained for the liquid side heat transfer coefficent as a function of jet diameter, length, and velocity, and liquid viscosity and surface tension. The effect of initial turbulence level was also obtained by using both smooth and roughened wall nozzles. We now report the results of an analytical study, in which the applicability of existing turbulence models to liquid jets was explored.

It is usually possible to calculate heat transfer coefficients for turbulent flows by solving model conservation equations for mass, momentum, and energy, with appropriate boundary conditions. A common procedure used to develop the model equations is to time average the fluctuating components of the dependent variables, and to model the resulting Reynolds fluxes following Boussinesq, hence introducing the turbulent eddy diffusivity ϵ and the turbulent Prandtl number Pr_t. Then the remaining problem is to provide a satisfactory specification for these quantities, particularly for ϵ. In the case of turbulent liquid jets, a major difficulty is that the turbulence is expected to decay both in the axial direction by the action of viscosity (Batchelor, 1953; Brumfield and Theofanous, 1976) and in a radial direction possibly due to the action of surface tension (Levich, 1962), or due to the action of viscosity (Henstock and Hanratty, 1979).

The major focus of this work was to evaluate the suitability of simple algebraic models for the eddy diffusivity, which incorporate both axial and radial decay. However, the more sophisticated approach of solving one or more differential equations to obtain the eddy diffusivity was also evaluated, and will be reported. In addition, in order to establish the validity of our numerical procedures, and to gain some insight into the nature of the jet heat transfer problem, the governing conservation equations were also solved for laminar jets, and some pertinent results are presented here.

2 Analysis

Figure 1 shows the jet and a cylindrical coordinate system. Using an eddy diffusivity model, the mean conservation equations for a steady, constant property, axisymmetric turbulent jet are

Mass:

$$\frac{\partial u}{\partial z}+\frac{1}{r}\frac{\partial (rv)}{\partial r}=0 \tag{1}$$

Axial Momentum:

$$u\frac{\partial u}{\partial z}+v\frac{\partial u}{\partial r}=\frac{1}{r}\frac{\partial}{\partial r}\left\{r\nu\left(1+\frac{\epsilon}{\nu}\right)\frac{\partial u}{\partial r}\right\}+g \tag{2}$$

Energy:

$$u\frac{\partial T}{\partial z}+v\frac{\partial T}{\partial r}=\frac{1}{r}\frac{\partial}{\partial r}\left\{r\nu\left(\frac{1}{\mathrm{Pr}}+\frac{\epsilon}{\nu}\frac{1}{\mathrm{Pr}_t}\right)\frac{\partial T}{\partial r}\right\} \tag{3}$$

Scaling of the complete conservation equations showed that the above equations are valid for the slenderness ratio, and Reynolds, Peclet, and Weber numbers, all much greater than unity. The gravity term is retained since the Froude number proves to be order of magnitude unity in some cases (Kim, 1983).

The initial conditions for these parabolic partial differential equations were taken as

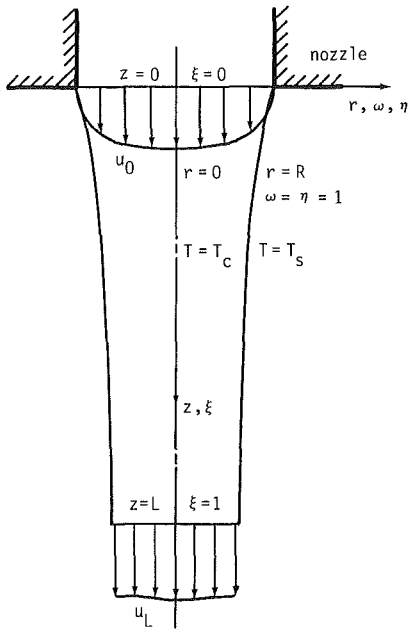

Fig. 1 Schematic of the jet and the coordinate system

Contributed by the Heat Transfer Division for publication in the JOURNAL OF HEAT TRANSFER. Manuscript received by the Heat Transfer Division January 26, 1987. Keywords: Condensation, Jets, Turbulence.

$$z=0:\ \frac{u}{U}=1.224\left(1-\frac{r}{R}\right)^{1/7} \tag{4a}$$

$$T=T_{\text{in}} \tag{4b}$$

The initial velocity profile is the 1/7 power law for fully developed turbulent pipe flow, to simulate the nozzles used in the experimental study, while the uniform temperature profile is appropriate for a perfectly insulated nozzle wall. The boundary conditions are, by symmetry,

$$r=0:\ \frac{\partial u}{\partial r}=\frac{\partial T}{\partial r}=0 \tag{5}$$

while at the jet surface a negligible shear stress and condensation from a saturated vapor with a negligible interfacial resistance are assumed

$$r=R:\ v=-k\frac{\partial T}{\partial r}\Big/\rho h_{fg};\ \frac{\partial u}{\partial r}=0;\ T=T_s=T_{\text{sat}}(P) \tag{6}$$

Mass and momentum conservation dictates that the free surface of the jet is not a coordinate surface of the cylindrical coordinate system. Thus a von Mises type transformation z, $r\rightarrow z$, ω is made, where ω is a normalized stream function

$$\omega=\frac{\psi-\psi_c}{\psi_s-\psi_c} \tag{7}$$

This transformation was introduced by Patankar and Spalding (1967) for boundary layer problems, and applied to condensation on laminar falling films by Denny and Mills (1969). The advantages of using the ω coordinate here are that both the contraction of the jet radius and the increase in local flow rate are easily accommodated. For convenience, $\psi_c=0$ is used. Use of a stream function automatically satisfies the mass conservation equation (1). A further transformation z, $\omega\rightarrow\xi(z/L)$, $\eta(\omega)$ is made to facilitate node stacking in the finite difference numerical procedure. Then with nondimensionalization, equations (2) and (3) reduce to

$$\frac{\partial\phi^*}{\partial\xi}=E^*\frac{\partial\phi^*}{\partial\eta}+F^*\frac{\partial^2\phi^*}{\partial\eta^2}+S^* \tag{8}$$

where the superscript * denotes dimensionless quantities, and the parameters involved are listed in Table 1. The initial conditions and Dirichlet-type boundary conditions transform simply; the Neumann-type conditions require careful transformation to yield

Table 1 Variables and parameters in the general equation (8)

Equation	Dependent Variable ϕ^*	Total Diffusivity D^*	Source Term S^*
momentum	$\frac{u}{U}=u^*$	$\epsilon^+=(1+\frac{\epsilon}{\nu})$	$\frac{gL}{u^*U_0^2\xi'}$
energy	$\frac{T-T_s}{T_0-T_s}=T^*$	$Pr^{-1}+(\epsilon^+-1)Pr_t^{-1}$	0
k equation	$k/k_{0,c}$	$1+(\epsilon^+-1)\sigma_k^{-1}$	$\frac{L}{u^*U_0\xi'k_{0,c}}\{P_k-D_k\}$
e equation	$e/e_{0,c}$	$1+(\epsilon^+-1)\sigma_e^{-1}$	$\frac{L}{u^*U_0\xi'e_{0,c}}\{P_e-D_e\}$

$$E^*=(G^*\eta'+\frac{2\nu L\psi_{s,0}}{\psi_s^2}D^*u^*r^*\eta'')/\xi'$$

$$F^*=\frac{2\nu L\ \psi_{s,0}}{\psi_s^2}(D^*u^*r^*)\eta'^2/\xi'$$

$$S^*=\frac{LS}{U_0\phi_{0,b}\ u^*\xi'}$$

$$G^*=\frac{\psi}{\psi_s}\psi_{s,z}+\frac{2\nu L}{\psi_s}D^*+\frac{2\nu L\psi_{s,0}}{\psi_s^2}r^{*2}\eta'\frac{\partial}{\partial\eta}(u^*D^*)$$

$$P_k=\epsilon(\frac{\partial u}{\partial r})^2 \qquad D_k=e+2\nu(\frac{\partial k^{1/2}}{\partial r})^2$$

$$P_e=c_1f_1\frac{e}{k}\epsilon(\frac{\partial u}{\partial r})^2 \qquad D_e=c_2f_2\frac{e^2}{k}-2\nu\epsilon(\frac{\partial^2u}{\partial r^2})^2$$

$$\eta=0:\ \frac{\partial\phi^*}{\partial\eta}=\frac{1}{E^*}\left(\frac{\partial\phi^*}{\partial\xi}-S^*\right) \tag{9a}$$

$$\eta=\eta_R:\ \frac{\partial\phi^*}{\partial\eta}=0,\ \text{provided } u\neq 0 \tag{9b}$$

3 Turbulence Models

Models for the eddy diffusivity were developed using Prandtl's mixing length hypothesis

$$\epsilon\sim Vl \tag{10}$$

where V and l are the turbulence intensity and mixing length,

Nomenclature

C_f = friction coefficient
C_p = specific heat, J/kg K
d = initial jet diameter, m
e = turbulence dissipation rate
F = friction coefficient ratio $=C_{f,R}/C_{f,S}$
g = graviational acceleration, m/s^2
h_L = liquid side heat transfer coefficient, W/m^{2}K
h_{fg} = latent heat of vaporization, J/kg
k = turbulent kinetic energy, m^2/s^2; thermal conductivity, W/mK
l = mixing length, m
L = jet length, m
Pr = Prandtl number
q_s = heat flux, W/m^2
R = jet radius, m
Re = Reynolds number
St, St° = Stanton numbers
t = time, s
T = temperature, K
u = streamwise velocity component, m/s
U = jet bulk velocity (initial value unless otherwise stated), m/s
v = radial velocity component, m/s
V = turbulence intensity, m/s
We = Weber number
y = distance from a free surface, m
z = axial coordinate, m
α = thermal diffusivity, m^2/s
ϵ = eddy diffusivity, m^2/s
η, ψ = dimensionless cross-stream coordinates
λ = damping zone parameter, m
ν = kinematic viscosity, m^2/s
ξ = dimensionless axial coordinate
ρ = density, kg/m^3
σ = surface tension, N/m

Subscripts

b = bulk
c = centerline
e = turbulence dissipation
k = kinetic energy of turbulence
s = interface
t = turbulent
0 = initial value

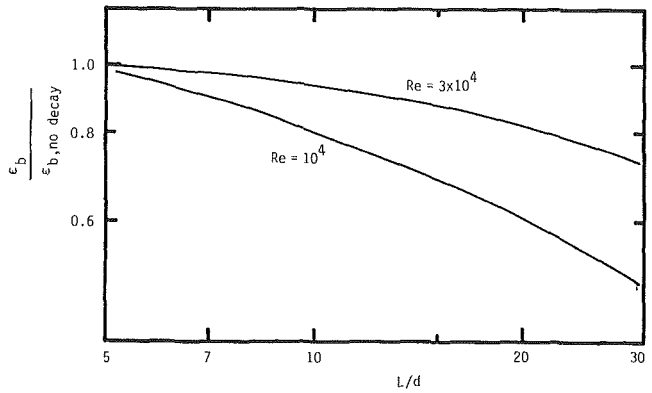

Fig. 2 Homogeneous turbulence decay due to viscosity

respectively. In this section we only consider algebraic specifications of these quantities. Use of additional differential equations to determine V and l is discussed in the Appendix.

3.1 Axial Decay. Since shear stresses in the jet are small, the turbulence decays in the axial direction by viscous damping. The bulk turbulence is assumed to be isotropic, and following Brumfield and Theofanous (1976), data for decay of homogeneous turbulence downstream of a grid given by Batchelor (1953) are used

$$V_b = V_0\{1 + t/T^*\}^{-1/2} \tag{11a}$$

$$l_b = l_0\{1 + t/T^*\}^{1/2} \tag{11b}$$

for the initital decay period $0 < t < t^*$, where $t = \int_0^z dz/U_{\text{local}}$, $T^* = l_0/V_0$, $t^* \simeq 10T^*$, and the subscript 0 denotes values at the nozzle exit. For the final decay period $t > t^*$

$$V_b = V^* l^{*5/2}\{l^{*2} + 2\pi\nu(t - t^*)\}^{-5/4} \tag{12a}$$

$$l_b = \{l^{*2} + 2\pi\nu(t - t^*)\}^{1/2} \tag{12b}$$

where the superscript * denotes values at t^*. Using the Blasius formula, and data of Martin and Johanson (1965),

$$V_0 = 0.2U\text{Re}^{-1/8} \tag{13a}$$

$$l_0 = 2.5 \times 10^{-4} d\text{Re}^{0.509} \tag{13b}$$

Then using equation (10) we have in the jet core,

$$\epsilon_b = V_b l_b \tag{14}$$

Figure 2 shows the ratio of ϵ_b to its initial value and the signficance of the axial decay.

3.2 Radial Decay. Very little is presently known about the decay of turbulence in a liquid near a liquid–gas interface. Two models have been proposed in the literature, one postulating a surface tension damping, the other a viscous damping.

Surface Tension Damped Turbulence Model. Levich (1962) postulated that the dynamic thrust of an eddy approaching the interface must be balanced by a surface tension force. He also assumed a linear decrease of V and l, and used Prandtl's mixing length hypothesis to give

$$\epsilon \sim (\rho V_b^3/\sigma)y^2 \tag{15}$$

for $0 < y < \lambda$, where y is measured from the interface.

Viscosity Damped Turbulence Model. Henstock and Hanratty (1979) assumed that both the turbulence intensity and the mixing length are damped from their bulk values to zero at the interface by viscosity. Then from dimensional considerations

$$\epsilon \sim (V_b^3 l_b/\nu^2)y^2 \tag{16}$$

Table 2 Comparison of eddy diffusivity models (radial decay)

Basic form	Assumption	Resulting Form	Parametric Dependence**	Reference
$\epsilon = cV\ell$	$\ell = \frac{\ell_b}{\lambda}y \quad \lambda = \frac{\sigma}{\rho V_b^2}$	$\epsilon = c\frac{\rho^2 V_b^5 \ell_b}{\sigma^2}y^2$	$\sim U^{4.9} d^{0.9} \nu^{0.1} \sigma^{-2.0} \rho^{2.0}$	
$\epsilon = cV\ell$	$\ell = \frac{\ell_b}{\lambda}y \quad \lambda = \frac{\nu}{V_b}$	$\epsilon = c\frac{V_b^3 \ell_b}{\nu^2}y^2$	$\sim U^{3.1} d^{1.1} \nu^{-2.1}$	Henstock and Hanratty (1979)
$\epsilon = cV\ell$	$\ell = y \quad \lambda = \frac{\sigma}{\rho V_b^2}$	$\epsilon = c\frac{\rho V_b^3}{\sigma}y^2$	$\sim U^{2.6} d^{-0.4} \nu^{0.4} \sigma^{-1.0} \rho^{1.0}$	Levich (1962)
$\epsilon = cV\ell$	$\ell = y \quad \lambda = \frac{\nu}{V_b}$	$\epsilon = c\frac{V_b^2}{\nu}y^2$	$\sim U^{1.8} d^{-0.3} \nu^{-0.8}$	
$\epsilon = ay^n$	$a = \alpha\,\text{Re}^{\beta}$		$\sim U^{\beta} d^{\beta} \nu^{-\beta}$	Lamourelle and Sandall (1972)†

* for the first four models, $V = \frac{V_b}{\lambda}y$ is assumed

** based on the expressions $V_b = V_{b,0} \sim U\,\text{Re}^{-0.125}$, $\ell_b = \ell_{b,0} \sim d\,\text{Re}^{0.509}$

† Lamourelle and Sandall give $\beta = 1.68$ from their falling film experiment

Generalized Eddy Diffusivity Model. In order to allow for the possibility of either, or both, surface tension and viscosity effects on radial decay of turbulence, a generalized eddy diffusivity model is proposed. For a Prandtl number that is at least somewhat greater than unity, a one-term approximation may be suitable. Thus we write

$$\epsilon = ay^n, \quad 0 < y < \lambda \tag{17}$$

The coefficient a is postulated to depend on local bulk values of the intensity and mixing length, and on fluid properties, that is,

$$a = a(V_b, l_b, \nu, \sigma, \rho) \tag{18}$$

The form of equation (18), and the value of the exponent n, are to be determined by comparison with experiment.

The above models for radial decay of turbulence are compared in Table 2.

4 Numerical Procedures

Discretization of equation (8) follows Patankar and Spalding (1967) in using an integral averaged implicit finite difference scheme. The convective term $\partial\phi^*/\partial\xi$ is evaluated as an integral average over a computational cell bounded by $(\xi - \Delta\xi)$, ξ and $(\eta - \Delta\eta/2)$, $(\eta + \Delta\eta/2)$. Second-order correct central differences are used for the cross-stream derivatives. The result is a set of nonlinear algebraic equations to be solved at each axial step. Forward marching without iteration was used by evaluating nonlinear coefficients and the source term in terms of known upstream values. The linearized tridiagonal matrix system was efficiently solved using the Thomas algorithm (Ames, 1977). The system was found to be well conditioned and round-off error difficulties were not encountered. However, special care was required near $\xi = 0$ due to singularities imposed by the initial boundary conditions at R_0. No attempt was made to obtain a correct solution near $\xi = 0$; instead, downstream errors were made negligible by node stacking near $\xi = 0$, and by imposing an intermediate value of shear stress, or small nonzero surface velocity at $\xi = 0$. These simple remedies proved quite adequate from a computational viewpoint.

Node points in the radial direction are distributed in a logarithmic fashion as suggested by Wassel (1973)

$$1 - \eta = \ln[1 + \gamma(1 - \omega)]/\gamma_0; \quad \gamma_0 = \ln(1 + \gamma) \tag{19}$$

Node points in the axial direction are distributed as

$$\xi = z^{\beta} \tag{20}$$

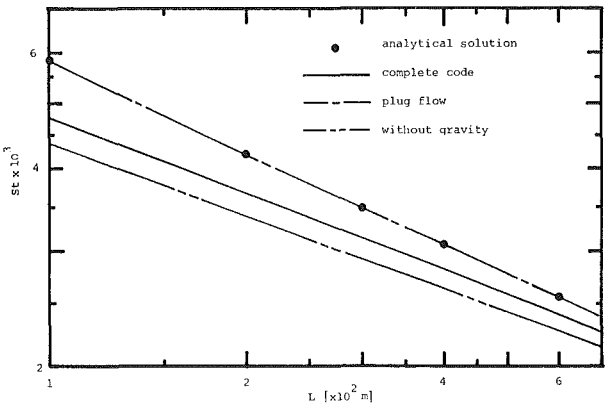

Fig. 3 Effect of simplifying assumptions on laminar jet heat transfer

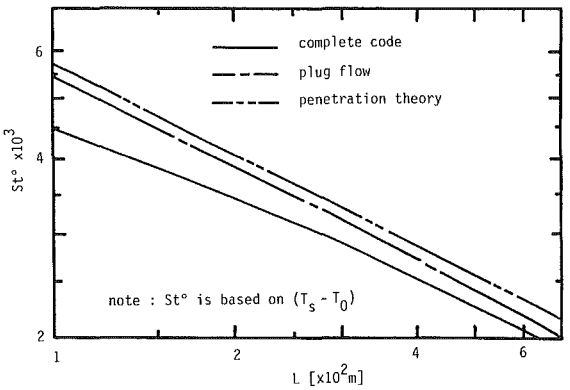

Fig. 4 Evaluation of the applicability of penetration theory to laminar jets

The stacking parameters γ and β are in the ranges 0–20 and 1–2, respectively.

A preliminary study was made to investigate the effect of the numerical method on accuracy of the results. The parameters included the method of discretization, node density, node stacking, smoothing of the initial singularities, etc. It was found that grid sizes as small as 41×61 could be used with insignificant numerical error. The criteria used to check accuracy included overall mass, momentum, and energy balances, and exact asymptotic solutions for both laminar and turbulent jets (Kim, 1983).

5 Laminar Jets

Results were obtained for laminar jets as an accuracy check, and also to provide some insight into the jet heat transfer problem. To calculate laminar jets the eddy diffusivity ϵ was set equal to zero, and equation (4*a*) replaced by a parabolic initial velocity profile

$$z=0: \frac{u}{U}=2\left[1-\left(\frac{r}{R}\right)^2\right] \tag{21}$$

To illustrate the effects of assuming plug flow and ignoring gravity, the following parameters for a water jet are considered: $d=2$ mm, $L=100$ mm, $U=0.553$ m/s, $T_0=15°C$, $T_s=25°C$, which corresponds to a jet Reynolds number Ud/ν of 1000. Figure 3 shows the average Stanton number $\mathrm{St}=\int_0^L h_L dz/\rho C_p UL$ as a function of length. It is seen that the effect of gravity is to increase the Stanton number, while the assumption of a plug velocity profile overestimates the Stanton number. Also shown in Fig. 3 is the analytical solution for the limit case of plug flow, zero gravity, and no mass entrainment: The problem then reduces to the familiar one of transient conduction in a cylinder, and the solution is in the form of a Bessel's function series. There is essentially no discrepancy between the series and finite difference solutions. The effect of the developing velocity profile on the temperature profile is complicated. Calculated temperature profiles show a blowing effect for the parabolic initial profile, which may explain the corresponding 8.5 percent higher Stanton number for a plug flow. Recall from the mass conservation equation, equation (1), $\partial u/\partial z=(-1/r)(\partial vr/\partial r)$, and thus v is always negative near the surface as the velocity profile develops.

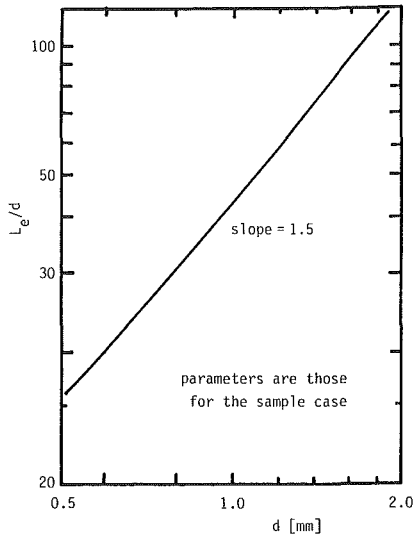

Fig. 5 Thermal entrance length L_e for laminar jets

Note that if the jet is viewed as a direct contact condenser, then it is a single-stream heat exchanger. With Stanton number defined in terms of initial diameter and bulk velocity, the exchanger effectiveness is

$$\epsilon=\frac{T_{b,L}-T_0}{T_s-T_0}=1-\exp(-4\mathrm{St}L/d) \tag{22}$$

Thus for a given jet diameter and length, Stanton number results can equivalently be interpreted in terms of heat exchanger effectiveness.

It is also of some interest to compare the plug flow solution with penetration theory, which gives an average Stanton number based on temperature dependence (T_s-T_0) of

$$\mathrm{St}°=\frac{2}{\sqrt{\pi}}(\mathrm{RePr}L/d)^{-1/2}; \qquad \mathrm{St}°=\frac{\int_0^L q_s dz}{\rho C_p U(T_s-T_0)L} \tag{23}$$

Figure 4 shows the comparison, and the higher Stanton numbers given by penetration theory, as expected.

To give an indication of the thermal entrance length, the jet entrance length L_e at which the growing thermal boundary layer meets the centerline (defined as when $T_c^*=(T_s-T_c)/(T_s-T_0)$ changes by 1 percent) is shown in Fig. 5. These values are somewhat larger than the entrance region estimated from the plug flow series solution, which gave $L_e/d\simeq 0.01$ Pe. For the parameter range under consideration $\mathrm{RePr}=(1000)(8)=8000$, indicating $L_e\sim 80d$. Thus the jet heat transfer problem for coherent laminar jets is usually of the entrance region type.

A brief numerical study of the effects of various parameters was made, in particular to determine the effect of jet diameter, since the diameter effect proved troublesome in the correlation of experimental data for turbulent jets. An approximate correlation of the Stanton number is

$$\mathrm{St}\propto U^{-0.6}L^{-0.4}d^{-0.2}\alpha^{0.55}\nu^{-0.05}g^{0.02} \tag{24}$$

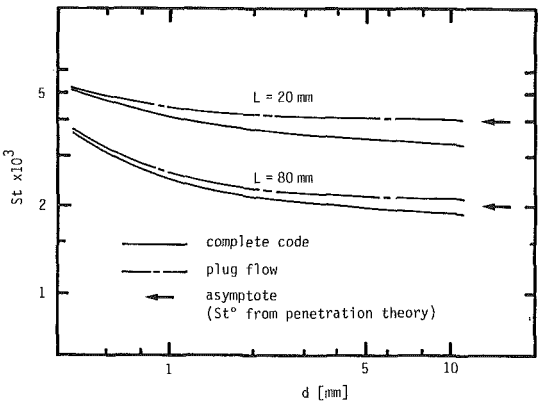

Fig. 6 Effect of jet diameter on Stanton number for laminar jets

in the parameter range characterized by the sample case. For short jets, $L/d \leq 50$, there is a negligible diameter effect and a zero exponent on d is appropriate. For longer jets the diameter effect increases: The negative exponent on diameter results from the driving force $(T_s - T_b)$ decreasing faster than the surface heat flux. This behavior is illustrated in Fig. 6. Notice that penetration theory gives

$$\mathrm{St}^\circ \propto U^{-0.5} L^{-0.5} d^0 \alpha^{0.5} \tag{25}$$

which is shown as an asymptote in Fig. 6.

6 Results: Turbulent Jets

The one-term approximation for the eddy diffusivity ϵ near the interface, equation (17), can be regarded as a general form since it can represent most of the algebraic models listed in Table 2. The required values of the exponent n and coefficient a were systematically developed based on the essential features of the experimental results reported in Part I of this study.

Model 1 ($n = 0$, $a = \text{const}$). The simplest ϵ model is one in which ϵ is constant throughout the flow field, and has been used by Bharathan and Penney (1984) and Wassel and Ghiaasiaan (1985). The transport phenomena then correspond to the laminar case discussed above, but with a high effective thermal diffusivity, $\alpha_{\text{eff}} = \epsilon_{b,0} = \text{const}$. Equation (24) applies, and if the small viscosity and gravity effects are ignored, the Stanton number is given approximately as

$$\mathrm{St} \propto U^{-0.6} L^{-0.4} d^{-0.2} \epsilon_{b,0}^{0.55} \tag{26}$$

Two possible approaches to specify the turbulent eddy diffusivity will be considered: (*a*) Following Hinze (1975) we can take $(\epsilon/\nu) = 0.035(C_f/2)^{1/2}\mathrm{Re}$, and with $C_f/2 \simeq 0.023\mathrm{Re}^{-0.2}$, we obtain

$$\epsilon_{b,0} = 0.0053 \mathrm{Re}^{0.9} \nu F^{0.5} \tag{27}$$

where F is the ratio of rough nozzle friction coefficient to the smooth nozzle value. Then substituting into equation (26) gives

$$\mathrm{St} \propto U^{-0.1} L^{-0.4} d^{0.3} \nu^{0.06} \alpha^0 (\sigma/\rho)^0 F^{0.28} \tag{28}$$

which is compared to the experimental result

$$\mathrm{St} \propto U^{-0.20} L^{-0.57} d^0 \nu^{-0.1} \alpha^{0.7} (\sigma/\rho)^{-0.3} F^{0.18} \tag{29}$$

A large incompatibility in the thermal diffusivity exponent is noticed, while, of course, equation (28) does not contain a surface tension dependence. Lesser discrepancies in the other exponents are apparent.

(*b*) Alternatively, equations (13*a*) and (13*b*) give

$$\epsilon_{b,0} = 5 \times 10^{-5} \mathrm{Re}^{1.384} \nu \tag{30}$$

and substituting into equation (28) gives

$$\mathrm{St} \propto U^{0.16} L^{-0.4} d^{0.56} \nu^{-0.21} \alpha^0 (\sigma/\rho)^0 \tag{31}$$

Similar comments to those made for equation (28) apply. However, more significantly, numerical solutions of the governing equations using equations (27) or (30) gives Stanton numbers that are one or two orders of magnitude higher than the experimental values. Thus Model 1 is quite unsatisfactory, and the need to incorporate turbulence decay is clear.

Model 2 ($n = 0$, $a = a(z)$). This model allows for axial decay of turbulence, but not for radial decay. The decay law developed by Batchelor, equations (11) and (12), can be combined with equation (14) to give

$$\epsilon_b = V_0 l_0 \text{ for } 0 \leq t \leq t^* \tag{32}$$

$$\epsilon_b = V_0 l_0 [1 + 2\pi\nu(t - t^*)/l^{*2}]^{-3/4} \text{ for } t > t^* \tag{33}$$

Using equations (13) the initial decay period is

$$t^* \simeq 0.125 \mathrm{Re}^{0.634} (d/U) \tag{34}$$

In the pertinent parameter range the initial decay length $L^* (= t^*/U)$ is about five diameters. For short jets, say $L/d < 10$, the law of the initial period, equation (32), is expected to prevail, giving no explicit viscous damping of ϵ. However, the experimental results do show evidence of viscous damping, even for shorter jets (of course the observed viscosity effects are partly due to the initial condition of the jet). Thus there is indicated a possible radial damping of turbulence by viscosity. For larger jets the axial decay of ϵ due to viscosity would be expected to prevail, as shown in Fig. 2. But numerical solutions using this model gave Stanton number values almost one order of magnitude too high, and so we conclude that it is essential to include radial decay of turbulence in the model.

Model 3 ($n \neq 0$, $a = \text{const}$). In this model radial decay of ϵ is allowed from its bulk value to zero at the interface, but axial decay is assumed negligible. Numerical solutions using this model showed that the experimental values of Stanton number could be matched with an exponent n in equation (17) in the range 2–3, if the thickness of the damped turbulence zone

$$\lambda = \frac{c\sigma}{\rho V_b^2} \tag{35}$$

was taken from Levich's model with $c = 1$. However it was not possible to obtain good agreement with the parameter dependence indicated by equation (29).

Model 4 ($n \neq 0$, $a \neq \text{const}$). The preceding discussion indicates that ϵ must depend on both axial and radial position, as well as other flow parameters. A fairly general model will be developed with the following features:

(*i*) For radial decay of ϵ, two zones are assumed, the bulk (core) zone, and the decay zone, as shown in Fig. 7. The discontinuity in slope at $y = \lambda$ is not realistic, but is a result of using equation (17).

(*ii*) In the radial decay zone a normalized form of equation (17) will be used, namely

$$\frac{\epsilon}{\epsilon_b} = \left(\frac{y}{\lambda}\right)^n \tag{36}$$

where $\epsilon_b = V_b l_b$ is the bulk value of the local eddy diffusivity, and λ is the thickness of the zone. Further, it is postulated that radial decay is a local phenomenon, and that the effect of interface curvature is negligible. Then we may write λ as a function of local parameters

$$\lambda = \lambda(V_b, l_b, \sigma/\rho, \nu) \tag{37}$$

Local values of jet velocity U and diameter d are not included in equation (37), because they are not very different from their initial values, which are already accounted for in V_b and l_b. Also, the Weber number is large enough to exclude a large-

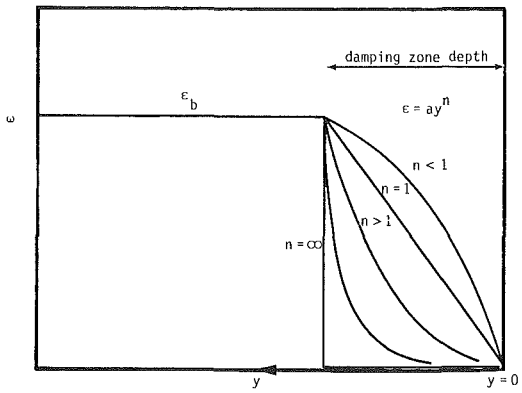

Fig. 7 Two-zone model for radial decay of turbulence

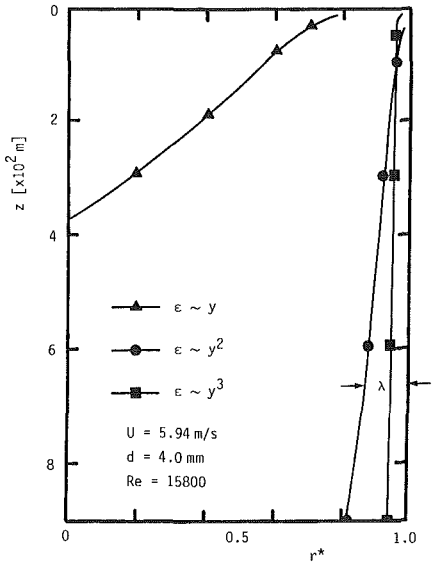

Fig. 8 Axial growth of damping zone thickness

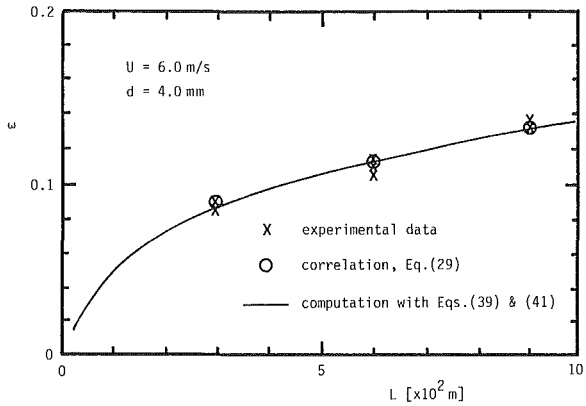

Fig. 9 Effectiveness of a turbulent water jet at $T_0 = 277.3$ K

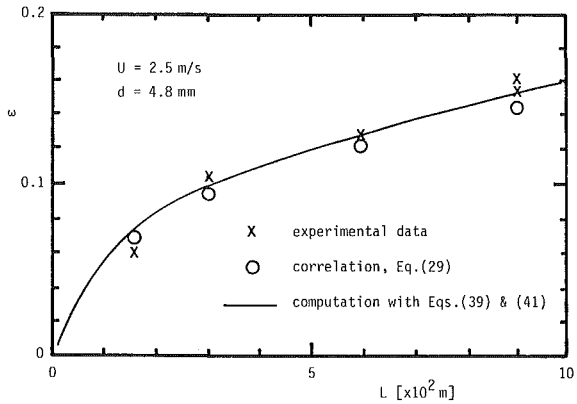

Fig. 10 Effectiveness of an ethanol jet at $T_0 = 292.2$ K

scale curvature (diameter) effect. Assuming a power law form with constant coefficients for simplicity, equation (37) becomes

$$\lambda = a_0 V_b^{a_1} l_b^{a_2} (\sigma/\rho)^{a_3} \nu^{a_4} \tag{38}$$

(*iii*) In the bulk zone, isotropic turbulence is assumed, which will be reasonable provided the thickness of the zone is at least larger than the scale of the turbulence. Some caution is required to ensure that this condition is met.

The remaining task is to detemine the exponent n in equation (36) and the constants a in equation (38). As a first step a set n, a_0, a_1, a_2 was obtained with the properties σ/ρ and ν held constant. The exponent n was assumed to be an integer, and an iterative process used to match calculated and measured Stanton numbers. Figure 8 shows the resulting growth of the damping zone depth for values of $n = 1, 2, 3$. If λ should be of the order of the surface protuberance curvature, as suggested by Davies (1972), our experimental observations indicate $\lambda << R$ for the first 20 mm of jet, and that λ might grow to be $\lambda \sim R$ toward the end of the jet. Thus Fig. 8 indicates that $n = 2$ is the most reasonable choice, giving

$$\frac{\epsilon}{\epsilon_b} = \left(\frac{y}{\lambda}\right)^2 \tag{39}$$

The remaining constants were determined by a simple iteration process; with a slight adjustment of constants to have an approximate dimensional consistency, the final form becomes

$$\lambda = 0.68 V_b^{-0.8} l_b^{0.6} (\sigma/\rho)^{0.3} \nu^{0.2} \qquad \text{(SI units)} \tag{40}$$

or, in dimensionless form, with an additional adjustment of the exponent on V_b,

$$\frac{\lambda}{l_b} = 0.68 \mathrm{Re}_t^{-0.1} \mathrm{We}_t^{-0.3} \tag{41}$$

where Re_t and We_t are the Reynolds and Weber numbers based on bulk turbulence parameters V_b and l_b. Equation (41) predicts the experimental data for Stanton number with a relative error (standard deviation/average value) of within 20 percent. The error could be due to the one-term approximation, omitted parameters, or experimental error. The model gives

$$\epsilon \propto \frac{V_b^{2.6} \rho^{0.6}}{l_b^{0.2} \sigma^{0.6} \nu^{0.4}} y^2 \tag{42}$$

indicating both a surface tension and viscous damping of turbulence. Also, V_b is seen to play a dominant role in the transport process, as was indicated by the experimental results in Part I of this study. Comparison with Table 2 shows that this model can be viewed as an ad hoc combination of previous models. Sample comparisons of the experimental data, the correlation of experimental data, equation (29), and numerical calculations using equations (39) and (41), are shown in Figs. 9 and 10 for a water jet and an ethanol jet, respectively. Satisfactory agreement can be seen.

Calculations of the axial variation of core temperature using this model indicate that the thermal boundary layer grows to equal the jet radius in a length $L_e \simeq 8d$, which is in agreement with experimental measurements. Although this entrance length is relatively short (compared to the laminar case), entrance region effects are always significant for coherent turbulent jets. In this connection, and for the sake of com-

pleteness, it is appropriate to mention the surface renewal model of Higbie (1935) and Danckwerts (1951). In this model it is postulated that eddies from the bulk flow are brought to the interface as a consequence of turbulence, and unsteady diffusion takes place for a short period of time before the eddy is replaced by another. To be physically reasonable such eddies must be assumed to be relatively large, and in fact, recent work on open channel flows of Komori and Ueda (1982) concluded that the large energy-containing eddies, with a size close to the integral scale of turbulence, control transport near the interface. But if the eddies are large then there cannot be an entrance effect, in direct contradiction to our experimental data for turbulent jets. Thus we conclude that a surface renewal type model is inappropriate in this situation.

7 Conclusions

1 A satisfactory eddy diffusivity model for the prediction of heat transfer in a coherent turbulent liquid jet must account for both axial and radial decay of turbulence.

2 An ad-hoc algebraic eddy diffusivity model that accounts for axial decay of turbulence due to viscosity, and radial decay of turbulence due to both viscosity and surface tension, has been developed. The model gives Stanton numbers that agree with our experimental results to within 20 percent accuracy.

3 The same model gives an approximate thermal entrance length of about eight diameters, which agrees with our experimental measurements. However, the Stanton number continues to decrease thereafter due to axial decay of turbulence.

As discussed by Mills et al. (1982), and in Part I of this contribution, the above conclusions apply only to coherent turbulent jets from nozzles that produce an initial velocity profile and turbulence characteristic of fully developed pipe flow. The conclusions are less applicable to coherent jets formed by very short nozzles, and are quite invalid for jets that exhibit droplet formation.

Acknowledgments

This study was supported by the U.S. Department of Energy, Grant No. DE-FG02-80CS89501, through the Solar Energy Research Institute, Golden, CO. The grant monitor was Dr. T. Penney. Computer time was supplied by the Campus Computing Network of the University of California, Los Angeles.

References

Ames, W. F., 1977, *Numerical Methods for Partial Differential Equations*, Academic Press, New York.

Batchelor, G. K., 1953, *The Theory of Homogeneous Turbulence*, Univ. Press, Cambridge, MA.

Bharathan, D., and Penney, T., 1984, "Flash Evaporation From Turbulent Water Jets," ASME JOURNAL OF HEAT TRANSFER, Vol. 106, pp. 407-416.

Brumfield, L. K., and Theofanous, T. G., 1976, "Turbulent Mass Transfer in Jet Flow and Bubble Flow: A Reappraisal of Levich's Theory," *AIChE J.*, Vol. 22, No. 3, pp. 607-610.

Danckwerts, P. V., 1951, "Significance of Liquid Film Coefficients in Gas Absorption," *Ind. Engr. Chem.*, Vol. 43, No. 6, pp. 1460-1467.

Davies, J. T., 1972, *Turbulence Phenomena*, Academic Press, New York.

Denny, V. E., and Mills, A. F., 1969, "Nonsimilar Solutions for Laminar Film Condensation on a Vertical Surface," *Int. J. Heat and Mass Transfer*, Vol. 12, pp. 965-979.

Henstock, W. H., and Hanratty, T. J., 1979, "Gas Absorption by a Liquid Layer Flowing on the Wall of a Pipe," *AIChE J.*, Vol. 25, No. 1, pp. 122-132.

Higbie, R., 1935, "The Rate of Absorption of a Pure Gas Into a Still Liquid During Short Periods of Exposure," *Trans. AIChE*, Vol. 31, pp. 365-388.

Hinze, O., 1975, *Turbulence*, 2nd ed., McGraw-Hill, New York.

Jones, W. P., and Launder, B. E., 1972, "The Prediction of Laminarization With a Two Equation Model of Turbulence," *Int. J. Heat and Mass Transfer*, Vol. 15, pp. 301-314.

Kim, S., 1983, "An Investigation of Heat and Mass Transport in Turbulent Liquid Jets," Ph.D. Dissertation, School of Engineering and Applied Science, University of California, Los Angeles, CA.

Kim, S., and Mills, A. F., 1989, "Condensation on Coherent Turbulent Liquid Jets. I. Experimental Study," ASME JOURNAL OF HEAT TRANSFER, Vol. 111, this issue.

Komori, S., and Ueda, H., 1982, "Turbulence Structure and Transport Mechanisms at the Free Surface in an Open Channel Flow," *Int. J. Heat and Mass Transfer*, Vol. 25, pp. 513-521.

Lamourelle, A. P., and Sandall, O. C., 1972, "Gas Absorption Into a Turbulent Liquid," *Chem. Engr. Sci.*, Vol. 27, pp. 1035-1043.

Launder, B. E., and Spalding, D. B., 1972, *Mathematical Models of Turbulence*, Academic Press, London.

Levich, V. G., 1962, *Physicochemical Hydrodynamics*, Prentice Hall, New Jersey.

Martin, G. Q., and Johanson, L. N., 1965, "Turbulence Characteristics of Liquids in Pipe Flow," *AIChE J.*, Vol. 11, pp. 29-33.

Mills, A. F., Kim, S., Leininger, T., Ofer, S., and Pesaran, A. A., 1982, "Heat and Mass Transport in Turbulent Liquid Jets," *Int. J. Heat Mass Transfer*, Vol. 25, pp. 889-897.

Patankar, S. V., and Spalding, D. B., 1967, "A Finite Difference Procedure for Solving the Equations of the Two Dimensional Boundary Layer," *Int. J. Heat and Mass Transfer*, Vol. 10, pp. 1389-1411.

van Driest, E. R., 1956, "On Turbulent Flow Near a Wall," *J. Aero. Sci.*, Vol. 23, pp. 1007-1011.

Wassel, A. T., 1973, "Nongrey Radiative Transfer in a Turbulent Cylindrical Medium," Ph.D. Dissertation, University of California, Los Angeles, CA.

Wassel, A. T., and Ghiaasiaan, S. M., 1985, "Falling Jet Flash Evaporators for Open Cycle Ocean Thermal Energy Conversion," *Int. Comm. Heat and Mass Transfer*, Vol. 12, pp. 113-125.

APPENDIX

Two-Equation Model of Turbulence

Launder and Spalding (1972) have reviewed in detail possible two-equation models of turbulence, which allow the turbulence intensity and mixing length to be determined through solution of two auxiliary differential equations. A popular approach is to use differential equations for the turbulent kinetic energy k, and the turbulence dissipation rate e (the notation e is used instead of the conventional ϵ to avoid confusion with the eddy diffusivity). Usual applications have involved situations where the turbulent Reynolds number $\mathrm{Re}_t = k^2/\nu e$ is large. Jones and Launder (1972) proposed an extended form of the k-e model so as to include the effects of molecular viscosity near a wall. This model is more appropriate for turbulent jets and was chosen for the present study. The two differential equations are

$$u\frac{\partial k}{\partial z} + v\frac{\partial k}{\partial r} = \frac{1}{r}\frac{\partial}{\partial r}\left\{r\epsilon_k \frac{\partial k}{\partial r}\right\} + \epsilon\left(\frac{\partial u}{\partial r}\right)^2 - \left\{e + 2\nu\left(\frac{\partial k^{1/2}}{\partial r}\right)^2\right\} \tag{A1}$$

$$u\frac{\partial e}{\partial z} + v\frac{\partial e}{\partial r} = \frac{1}{r}\frac{\partial}{\partial r}\left\{r\epsilon_e \frac{\partial e}{\partial r}\right\} + c_1 f_1 \frac{e}{k}\epsilon\left(\frac{\partial u}{\partial r}\right)^2 - \left\{c_2 f_2 \frac{e^2}{k} - 2\nu\epsilon\left(\frac{\partial^2 u}{\partial r^2}\right)^2\right\} \tag{A2}$$

and using the Prandtl-Kolmogorov and Boussinesq hypotheses, the eddy diffusivity is given as

$$\epsilon = c_\mu f_\mu k^2/e \tag{A3}$$

The constants and coefficients are expected to vary somewhat with flow situation and are to be determined from experimental data. Equations (A1) and (A2) can be easily transformed into the ξ-η plane and written in the general form, equation (8). The variables and parameters are explained in Table 1.

Initial conditions were obtained from fully developed turbulent pipe flow data. van Driest's (1956) mixing length expression gives in the inner region

$$l = 0.4y\{1 - \exp(-y^+/26)\} \tag{A4}$$

Then with a constant shear assumption

$$\frac{\epsilon}{\nu} = -\frac{1}{2} + \frac{1}{2}\{1 + 0.64y^{+2}[1 - \exp(-y^+/26)]^2\}^{1/2} \quad \text{(A5)}$$

where $y^+ = (R-r)v^*/\nu$; $v^* = (C_f/2)^{1/2}U$, $C_f/2 = 0.023\mathrm{Re}^{-0.2}$. In the core region Hinze (1975) gives

$$\frac{\epsilon}{\nu} = 0.035\ (C_f/2)^{1/2}\mathrm{Re}$$

The boundary conditions for the equations are as before.

Calculations were made using this model. It was hoped that some success would be obtained by making minor changes in the values of the adjustable parameters developed by previous workers for flows past solid walls. However, it was found that more fundamental changes were necessary to predict jet behavior adequately. Such modifications include:

(*i*) f_μ should have higher values in the interface region.

(*ii*) There should be appropriate nonisotropic correction terms, possibly involving surface tension.

(*iii*) Initial conditions for k and e should be more carefully specified.

The lack of experimental data for the structure of turbulence in a liquid jet makes the development of such modifications very difficult at the present time.

Journal of Heat Transfer

Technical Notes

This section contains shorter technical papers. These shorter papers will be subjected to the same review process as that for full papers.

Flow and Heat Transfer in Microchannels Using a Microcontinuum Approach

A. M. Jacobi[1]

Nomenclature

c_p = specific heat
D = inside diameter of tube
I_n = modified Bessel function of the first kind, of order n
k = thermal conductivity
κ_v, μ_v, γ_v = viscosity coefficients for a micropolar fluid
Nu_D = Nusselt number $= hD/k$
P = pressure
q_s = heat flux imposed at tube wall
R = radial distance
R^* = dimensionless radius $= R/D$
T = temperature
w = axial velocity of micropolar fluid
w^* = dimensionless velocity $= w/w_m$, equation (4)
z = axial distance
θ^* = dimensionless temperature $= (T_w - T)/q_s D/k$
ν = gyration of micropolar fluid
ρ = density
χ = viscosity ratio $= \kappa_v/\mu_v$

Introduction

Heat and mass transfer in small channels has many important applications. Recent advances in electronic cooling technology have suggested the use of microchannels for cooling electronic components (Tuckerman, 1984; Koh and Colony, 1986). Such small channels make use of the constant Nu_D, which is well established for classical fully developed laminar flow and heat transfer (Incropera and DeWitt, 1985), and a small diameter, e.g., 50 μm, to provide very large transfer coefficients. Thus, with a large number of microchannels to provide heat transfer area, very large cooling requirements can be accommodated by circulating a liquid through the channels. Application is also found in modeling blood flow in arterioles, where the arterial diameter approaches the scale of the substructure of blood (Ariman, 1971). In this respect, a microcontinuum approach has been widely employed.

As the characteristic diameter approaches the molecular or substructure level, an analysis based on classical continuum mechanics is justifiably subject to scrutiny. Application of the classical results is examined in this work by use of the micro-elastic theory advanced by Eringen and Suhubi (1964). Eringen (1964) extended the theory of micro-elastic solids to liquids, referred to as simple microfluids. However, even when the constitutive equations of Eringen are linearized, the simple microfluid would possess 22 viscosity coefficients. A subclass of simple microfluids was introduced by Eringen (1966) and was given the name micropolar.

An extension to heat-conducting micropolar fluids was first presented by Kazakia and Ariman (1971). In this work energy conservation equations were given, as were the necessary constitutive relations. With the introduction of these equations, the velocity, gyration, and temperature fields may be found for a prescribed flow.

The theory of micropolar flow has received a great deal of attention in the literature, and thorough reviews of microcontinuum fluids have been given by Ariman et al. (1973, 1974). Many interesting micropolar hydrodynamic problems have been recently solved by Sastry and Rao (1982), Agarwal and Dhanapal (1987a, 1987b), Kamel (1987), Rao and Kasiviswanathan (1987), Ramkissoon (1986), and Rao et al. (1987). The theory has been applied to heat transfer problems by Balaram and Sastry (1973), Bhargava and Rani (1985), Lien and Chen (1987), Gorla and Reddy (1987), and Gorla and Takhar (1987). However, the theory has not yet been applied to the constant area circular duct with a uniform heat flux imposed at the wall. The purpose of this note is to employ Eringen's theory to predict how heat transfer may be affected as the classical fluid model breaks down. Such predictions hold not only theoretical importance, but may serve useful in modeling heat transfer in microchannels, or arterioles where the theory has been widely applied.

Fluid Flow and Heat Transfer

The following assumptions are made in the analysis: (1) steady laminar, fully developed flow, (2) constant thermophysical properties, (3) prescribed uniform heat flux on the tube wall, and (4) the classical concept of thermal conductivity is valid. As a result of the assumptions, the flow is decoupled from the temperature field. For such a model, the solutions for velocity and gyration are given by Eringen (1966)

$$\frac{w}{w_o} = 1 - R^{*2} + \frac{\kappa_v}{\mu_v + \kappa_v} \frac{I_o(\lambda)}{\lambda I_1(\lambda)} \left[\frac{I_o(\lambda R^*)}{I_o(\lambda)} - 1 \right] \quad (1)$$

[1]The Johns Hopkins University, School of Mechanical Engineering, Baltimore, MD 21218.

Contributed by the Heat Transfer Division for publication in the JOURNAL OF HEAT TRANSFER. Manuscript received by the Heat Transfer Division August 17, 1987. Keywords: Biotechnology, Forced Convection.

$$\frac{\nu D}{w_o} = R^* - \frac{I_1(\lambda R^*)}{I_1(\lambda)} \tag{2}$$

where

$$w_o = \frac{-D^2}{2(2\mu_v + \kappa_v)} \frac{dP}{dz} \text{ and } \lambda = D\left[\frac{2\mu_v + \kappa_v}{\mu_v + \kappa_v} \frac{\kappa_v}{\gamma_v}\right]^{1/2} \tag{3}$$

Here, w_o is the centerline velocity is classical Poiseuille flow. Equation (1) reduces to the classical result for $\kappa_v = 0$, and equation (2) gives $\nu = 0$. Also, note that

$$w^* = w/w_m = \frac{w/w_o}{w_m/w_o} \tag{4}$$

where w_m is the mean velocity.

By making use of equation (4), equation (1) may be integrated over R^* from 0 to 1, to give

$$w^* = \frac{1 - R^{*2} + \frac{\chi}{1+\chi} \frac{1}{\lambda} \frac{I_o(\lambda)}{I_1(\lambda)} \left[\frac{I_o(\lambda R^*)}{I_o(\lambda)} - 1\right]}{\frac{1}{2} + \frac{\chi}{1+\chi} \frac{2}{\lambda} \left[\frac{1}{\lambda} - \frac{I_o(\lambda)}{2I_1(\lambda)}\right]} \tag{5}$$

The energy equation for negligible heat conduction in the axial direction, in comparison to the radial one, and negligible viscous dissipation is

$$\rho\, c_p\, w \frac{\partial T}{\partial w} = \frac{1}{R} \frac{1}{\partial R}\left(k\, R \frac{\partial T}{\partial R}\right) \tag{6}$$

For the case of a constant heat flux, by considering an infinitesimal control volume, one can easily show that

$$2q_s = \rho c_p w_m D \frac{dT_m}{dz} = \rho c_p w_m D \frac{\partial T}{\partial z} \tag{7}$$

The energy equation may be cast in dimensionless form as

$$-2\, w^* = \frac{1}{R^*} \frac{d}{dR^*}\left(R^* \frac{d\theta^*}{dR^*}\right) \tag{8}$$

By substituting equation (5) into (8), integrating and applying the boundary conditions that θ^* be bounded for $R^* = 0$, and $\theta^* = 0$ for $R^* = 1$, it can be shown that

$$\theta^* = \left\{ \frac{\frac{3}{8} - \frac{R^{*2}}{2} + \frac{R^{*4}}{8} + \frac{\chi}{1+\chi} \frac{2}{\lambda} \frac{I_o(\lambda)}{I_1(\lambda)} \left[\frac{R^{*2}}{4} - \frac{1}{4} + \frac{1}{\lambda^2}\left(1 - \frac{I_o(\lambda R^*)}{I_o(\lambda)}\right)\right]}{\frac{1}{2} + \frac{\chi}{1+\chi} \frac{2}{\lambda} \left[\frac{1}{\lambda} - \frac{I_o(\lambda)}{2I_1(\lambda)}\right]} \right\} \tag{9}$$

Manipulating the definition of θ^* yields the definition of the mean, or *mixing cup* temperature

$$\theta_m^* = 2\int_0^1 w^* R^* \theta^* dR^* \tag{10}$$

Finally, from Newton's Law of cooling we can show that

$$\text{Nu} = \frac{2}{\theta_m^*} \tag{11}$$

Integration of equation (10) was accomplished by subdividing the interval and using a 21-point Gauss-Kronrod rule to estimate the intergral of each of these subintervals. The error for each subinterval was estimated by comparing to a 10-point Gauss quadrature rule. The estimated relative error was always less than $3.4(10^{-4})$ percent for $0 < \lambda < 50$, and $0 < \chi < 100$.

Results and Discussion

The deviation from the classical solution is determined by χ and λ. The model reduces to the classical one for $\chi \to 0$ or $\lambda \to 0$. However, the velocity and temperature fields deviate from the classical profiles as χ and λ are included. The velocity and temperature fields for slug flow, Newtonian flow, and micropolar flow are given in Fig. 1 where they may be compared.

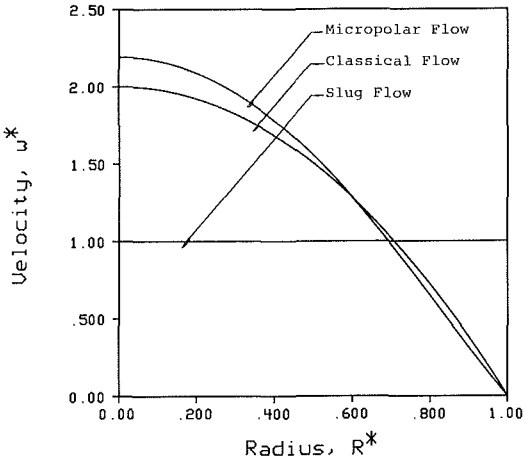

Fig. 1(*a*) Dimensionless velocity distribution ($\chi = 25$ and $\lambda = 5$)

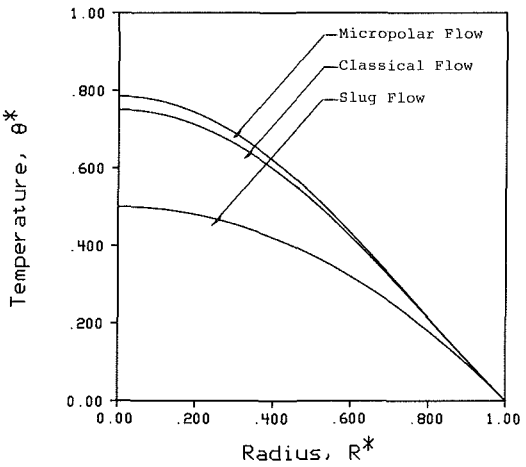

Fig. 1(*b*) Dimensionless temperature distribution ($\chi = 25$ and $\lambda = 5$)

The velocity distribution was given by Eringen (1966), and was discussed there. The temperature distribution, given in Fig. 1(*b*), shows that the deviation from the classical flow manifests itself in a "taller" temperature profile. This is in sharp contrast to the slug flow case, where the temperature profile is flattened.

The variation of the Nu_D is given in Fig. 2. From the illustrations it is apparent that the behavior differs significantly from the classical result of $\text{Nu}_D = 4.3636$ (Incropera and DeWitt, 1985). The dependence on χ is simple, and is shown in Fig. 2(*a*). As $\chi \to \infty$ the Nu_D asymptotically approaches some lower value that depends upon λ, and differs from the classical Nu_D. The dependence of Nu_D on λ is given in Fig. 2(*b*). This interesting behavior shows that the heat transfer is minimized for $\lambda \approx 6.2$. For the case of $\chi = 100$ and $\lambda = 6.2$, $\text{Nu}_D = 4.0757$.

The figures clearly indicate that as $\lambda \to 0$ or as $\chi \to 0$ the results collapse to the classical result for Nu_D.

Conclusions

The micropolar fluid theory of Eringen (1966) has been ap-

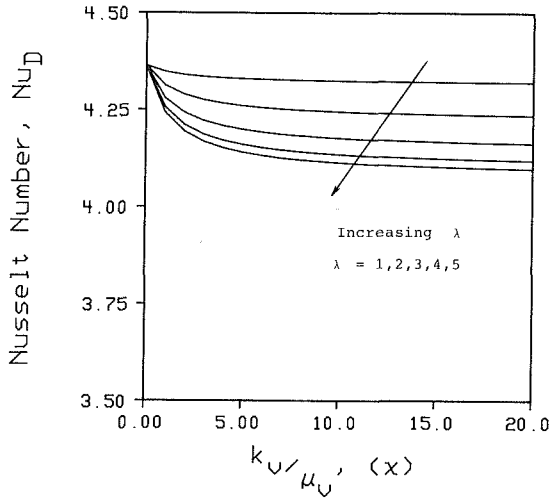

Fig. 2(*a*) Variation of the Nusselt number with χ and λ

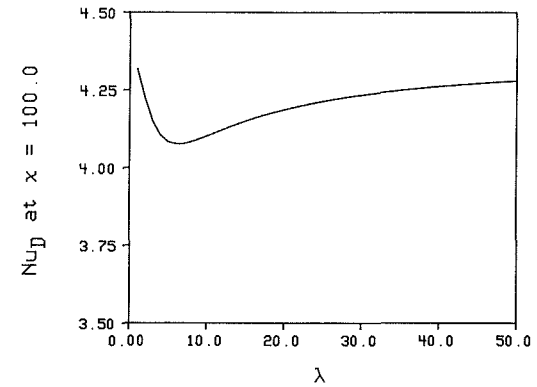

Fig. 2(*b*) Nusselt number deviation from the classical results with λ ($\chi = 100$)

plied to the case of fully developed heat transfer in a constant area circular duct with a prescribed constant heat flux at the wall. The Nu_D was found to differ from the classical value of $Nu_D = 4.3636$. Apparently, the Nu_D is reduced by as much as 7 percent for this micropolar flow. This result has significant implications in the modeling of heat transfer in microchannels, arterioles, and other applications involving polar fluids.

Although the micropolar fluid theory has been applied to many situations, now including this one, the primary drawback to these analyses is the unknown viscosity coefficients. Some recent empirical work has been conducted in this area (Prokhorenko et al., 1987), but before the theory can be fully utilized, further work must be done in quantifying the microstructural parameters.

Acknowledgments

This work was undertaken and pursued with the encouragement of Professors Raymond Viskanta and Victor Goldschmidt of Purdue University; their help in preparing this note is gratefully acknowledged.

The author is also indebted to the anonymous reviewers for thorough, constructive reviews, which significantly improved this note.

References

Agarwal, R. S., and Dhanapal, C., 1987a, "Numerical Solution of Micropolar Fluid Flow Between a Rotating and a Porous Stationary Disc," *International Journal of Engineering Science*, Vol. 25, pp. 1403–1417.

Agarwal, R. S., and Dhanapal, C., 1987b, "Numerical Solution to the Flow of a Micropolar Fluid Between Porous Walls of Different Permeability," *International Journal of Engineering Science*, Vol. 25, pp. 325–336.

Ariman, T., 1971, "On the Analysis of Blood Flow," *Journal of Biomechanics*, Vol. 4, pp. 185–192.

Ariman, T., Turk, M. A., and Sylvester, N. D., 1973, "Microcontinuum Fluid Mechanics—A Review," *International Journal of Engineering Science*, Vol. 11, pp. 905–930.

Ariman, T., Turk, M. A., and Sylvester, N. D., 1974, "Applications of Microcontinuum Fluid Mechanics," *International Journal of Engineering Science*, Vol. 12, pp. 273–293.

Balaram, M., and Sastry, V., 1973, "Micropolar Free Convection Flow," *International Journal of Heat and Mass Transfer*, Vol. 16, pp. 437–441.

Bhargava, R., and Rani, M., 1985, "Numerical Solution of Heat Transfer in Micropolar Fluid Flow in a Channel With Porous Walls," *International Journal of Engineering Science*, Vol. 23, pp. 409–413.

Eringen, A., 1964, "Simple Microfluids," *International Journal of Engineering Science*, Vol. 2, pp. 205–217.

Eringen, A., 1966, "Theory of Micropolar Fluids," *Journal of Mathematics and Mechanics*, Vol. 16, pp. 1–18.

Eringen, A., and Suhubi, E., 1964, "Nonlinear Theory of Simple Micro-Elastic Solids I," *International Journal of Engineering Science*, Vol. 2, pp. 189–203.

Gorla, R. S. R., and Takhar, H. S., 1987, "Free Convection Boundary Layer Flow of a Micropolar Fluid Past Slender Bodies," *International Journal of Engineering Science*, Vol. 25, pp. 949–962.

Gorla, R. S. R., and Reddy, P. V., 1987, "Flow and Heat Transfer From a Continuous Surface in a Parallel Free Stream of Micropolar Fluid," *International Journal of Engineering Science*, Vol. 25, pp. 1243–1249.

Incropera, F. P., and D. P. DeWitt, 1985, *Fundamentals of Heat Transfer*, 2nd ed., Wiley, New York.

Kamel, M. T., 1987, "Flow of a Micropolar Fluid in a Diverging Channel," *International Journal of Engineering Science*, Vol. 25, pp. 759–768.

Kazakia, Y., and Ariman, T., 1971, "Heat-Conducting Micropolar Fluids," *Rheological Acta*, Vol. 10, pp. 319–325.

Koh, J. C. Y., and Colony, R., 1986, "Heat Transfer of Microstructures for Integrated Circuits," *International Communications in Heat and Mass Transfer*, Vol. 13, pp. 89–98.

Lien, F. S., and Chen, C. K., 1987, "Mixed Convection of Micropolar Fluid About a Sphere With Blowing and Suction," *International Journal of Engineering Science*, Vol. 25, pp. 775–784.

Prokhorenko, P. P., Migun, N. P., and Grebenshchikov, S. V., 1987, "Experimental Studies of Polar Indicator Liquids Used in Capillary Penetrant Testing," *International Journal of Engineering Science*, Vol. 25, pp. 769–773.

Ramkissoon, H., 1986, "The Effect of a Boundary on the Motion of a Sphere in Polar Fluids," *International Journal of Engineering Science*, Vol. 24, pp. 227–234.

Rao, A. R., and Kasiviswanathan, S. R., 1987, "A Class of Exact Solutions for the Flow of a Micropolar Fluid," *International Journal of Engineering Science*, Vol. 25, pp. 443–453.

Rao, S. K. L., Iyengar, T. K. V., and Raju, K. V., 1987, "The Rectilinear Oscillations of an Elliptic Cylinder in Incompressible Micropolar Fluid," *International Journal of Engineering Science*, Vol. 25, pp. 531–548.

Sastry, V., and Rao, V. R., 1982, "Numerical Solution of Micropolar Fluid Flow in a Channel With Porous Walls," *International Journal of Engineering Science*, Vol. 20, pp. 631–642.

Tuckerman, D. B., 1984, "Heat Transfer Microstructures for Integrated Circuits," Ph.D. Dissertation, Stanford University, CA.

Maximum Velocity Location and Pressure Drop of Fully Developed Laminar Flow in Circular Sector Ducts

Q. M. Lei[1] and A. C. Trupp[1]

Nomenclature

A = cross-sectional area of circular sector duct $= \phi R_0^2$

C = dimensionless constant $= (dP/dx)R_0^2/(U_m\mu)$

D_h = equivalent hydraulic diameter $= 2\phi R_0/(1+\phi)$

f = Fanning friction factor $= D_h(-dP/dx)/(2\rho U_m^2)$

$K(\infty)$ = incremental pressure drop number for fully developed flow when $x = \infty$

[1]Department of Mechanical Engineering, University of Manitoba, Winnipeg, Manitoba, Canada R3T 2N2.

Contributed by the Heat Transfer Division for publication in the JOURNAL OF HEAT TRANSFER. Manuscript received by the Heat Transfer Division July 18, 1988. Keywords: Augmentation and Enhancement, Finned Surfaces, Heat Exchangers.

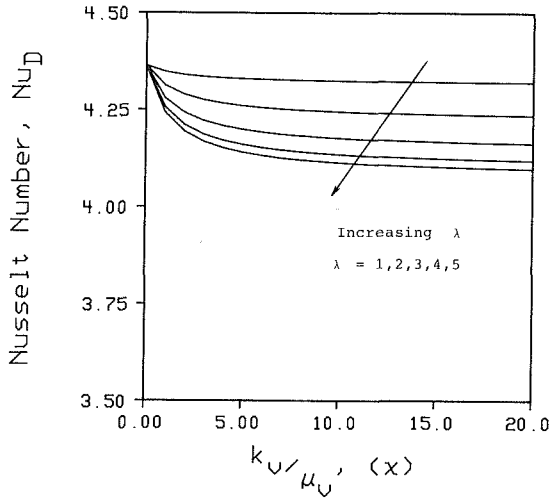

Fig. 2(*a*) Variation of the Nusselt number with χ and λ

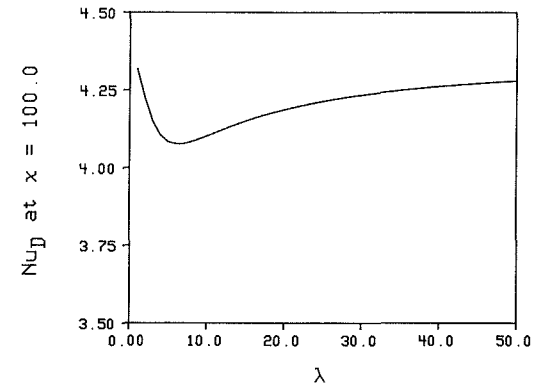

Fig. 2(*b*) Nusselt number deviation from the classical results with λ ($\chi = 100$)

plied to the case of fully developed heat transfer in a constant area circular duct with a prescribed constant heat flux at the wall. The Nu_D was found to differ from the classical value of $Nu_D = 4.3636$. Apparently, the Nu_D is reduced by as much as 7 percent for this micropolar flow. This result has significant implications in the modeling of heat transfer in microchannels, arterioles, and other applications involving polar fluids.

Although the micropolar fluid theory has been applied to many situations, now including this one, the primary drawback to these analyses is the unknown viscosity coefficients. Some recent empirical work has been conducted in this area (Prokhorenko et al., 1987), but before the theory can be fully utilized, further work must be done in quantifying the microstructural parameters.

Acknowledgments

This work was undertaken and pursued with the encouragement of Professors Raymond Viskanta and Victor Goldschmidt of Purdue University; their help in preparing this note is gratefully acknowledged.

The author is also indebted to the anonymous reviewers for thorough, constructive reviews, which significantly improved this note.

References

Agarwal, R. S., and Dhanapal, C., 1987a, "Numerical Solution of Micropolar Fluid Flow Between a Rotating and a Porous Stationary Disc," *International Journal of Engineering Science*, Vol. 25, pp. 1403–1417.

Agarwal, R. S., and Dhanapal, C., 1987b, "Numerical Solution to the Flow of a Micropolar Fluid Between Porous Walls of Different Permeability," *International Journal of Engineering Science*, Vol. 25, pp. 325–336.

Ariman, T., 1971, "On the Analysis of Blood Flow," *Journal of Biomechanics*, Vol. 4, pp. 185–192.

Ariman, T., Turk, M. A., and Sylvester, N. D., 1973, "Microcontinuum Fluid Mechanics—A Review," *International Journal of Engineering Science*, Vol. 11, pp. 905–930.

Ariman, T., Turk, M. A., and Sylvester, N. D., 1974, "Applications of Microcontinuum Fluid Mechanics," *International Journal of Engineering Science*, Vol. 12, pp. 273–293.

Balaram, M., and Sastry, V., 1973, "Micropolar Free Convection Flow," *International Journal of Heat and Mass Transfer*, Vol. 16, pp. 437–441.

Bhargava, R., and Rani, M., 1985, "Numerical Solution of Heat Transfer in Micropolar Fluid Flow in a Channel With Porous Walls," *International Journal of Engineering Science*, Vol. 23, pp. 409–413.

Eringen, A., 1964, "Simple Microfluids," *International Journal of Engineering Science*, Vol. 2, pp. 205–217.

Eringen, A., 1966, "Theory of Micropolar Fluids," *Journal of Mathematics and Mechanics*, Vol. 16, pp. 1–18.

Eringen, A., and Suhubi, E., 1964, "Nonlinear Theory of Simple Micro-Elastic Solids I," *International Journal of Engineering Science*, Vol. 2, pp. 189–203.

Gorla, R. S. R., and Takhar, H. S., 1987, "Free Convection Boundary Layer Flow of a Micropolar Fluid Past Slender Bodies," *International Journal of Engineering Science*, Vol. 25, pp. 949–962.

Gorla, R. S. R., and Reddy, P. V., 1987, "Flow and Heat Transfer From a Continuous Surface in a Parallel Free Stream of Micropolar Fluid," *International Journal of Engineering Science*, Vol. 25, pp. 1243–1249.

Incropera, F. P., and D. P. DeWitt, 1985, *Fundamentals of Heat Transfer*, 2nd ed., Wiley, New York.

Kamel, M. T., 1987, "Flow of a Micropolar Fluid in a Diverging Channel," *International Journal of Engineering Science*, Vol. 25, pp. 759–768.

Kazakia, Y., and Ariman, T., 1971, "Heat-Conducting Micropolar Fluids," *Rheological Acta*, Vol. 10, pp. 319–325.

Koh, J. C. Y., and Colony, R., 1986, "Heat Transfer of Microstructures for Integrated Circuits," *International Communications in Heat and Mass Transfer*, Vol. 13, pp. 89–98.

Lien, F. S., and Chen, C. K., 1987, "Mixed Convection of Micropolar Fluid About a Sphere With Blowing and Suction," *International Journal of Engineering Science*, Vol. 25, pp. 775–784.

Prokhorenko, P. P., Migun, N. P., and Grebenshchikov, S. V., 1987, "Experimental Studies of Polar Indicator Liquids Used in Capillary Penetrant Testing," *International Journal of Engineering Science*, Vol. 25, pp. 769–773.

Ramkissoon, H., 1986, "The Effect of a Boundary on the Motion of a Sphere in Polar Fluids," *International Journal of Engineering Science*, Vol. 24, pp. 227–234.

Rao, A. R., and Kasiviswanathan, S. R., 1987, "A Class of Exact Solutions for the Flow of a Micropolar Fluid," *International Journal of Engineering Science*, Vol. 25, pp. 443–453.

Rao, S. K. L., Iyengar, T. K. V., and Raju, K. V., 1987, "The Rectilinear Oscillations of an Elliptic Cylinder in Incompressible Micropolar Fluid," *International Journal of Engineering Science*, Vol. 25, pp. 531–548.

Sastry, V., and Rao, V. R., 1982, "Numerical Solution of Micropolar Fluid Flow in a Channel With Porous Walls," *International Journal of Engineering Science*, Vol. 20, pp. 631–642.

Tuckerman, D. B., 1984, "Heat Transfer Microstructures for Integrated Circuits," Ph.D. Dissertation, Stanford University, CA.

Maximum Velocity Location and Pressure Drop of Fully Developed Laminar Flow in Circular Sector Ducts

Q. M. Lei[1] and A. C. Trupp[1]

Nomenclature

A = cross-sectional area of circular sector duct $= \phi R_0^2$

C = dimensionless constant $= (dP/dx)R_0^2/(U_m\mu)$

D_h = equivalent hydraulic diameter $= 2\phi R_0/(1+\phi)$

f = Fanning friction factor $= D_h(-dP/dx)/(2\rho U_m^2)$

$K(\infty)$ = incremental pressure drop number for fully developed flow when $x = \infty$

[1]Department of Mechanical Engineering, University of Manitoba, Winnipeg, Manitoba, Canada R3T 2N2.

Contributed by the Heat Transfer Division for publication in the JOURNAL OF HEAT TRANSFER. Manuscript received by the Heat Transfer Division July 18, 1988. Keywords: Augmentation and Enhancement, Finned Surfaces, Heat Exchangers.

P = pressure
P_0 = pressure at entrance
R = radial coordinate
R_0 = radius of tube
r = dimensionless radial coordinate $= R/R_0$
r^* = radial distance, normalized by R_0, where the axial velocity has its maximum value
Re = Reynolds number $= \rho U_m D_h/\mu$
U = axial velocity
U_m = mean axial velocity
u = dimensionless axial velocity $= U/U_m$
u_{max} = dimensionless maximum velocity at $r = r^*$ and $\theta = \phi$
x = axial coordinate
θ = angular coordinate
μ = dynamic viscosity
ρ = density
ϕ = half the apex angle of a circular sector duct

Introduction

Circular sector ducts have become increasingly important as they continue to appear as flow passages in multipassage tubes. They also represent the limiting cases of internally finned tubes having equispaced, full tapered fins. For circular sector ducts in fully developed laminar flow, Eckert et al. (1958) were the first to derive an analytical expression for the velocity profile from the analogous torsion solution. Sparrow and Haji-Sheikh (1965) extended their work and plotted f Re and $K(\infty)$ for apex angles up to π. They computed the incremental pressure drop $K(\infty)$ using the method developed by Lundgren et al. (1964) based on a linearized momentum technique. All of these results have been compiled by Shah and London (1978). However, there are no published data for the maximum velocity u_{max} and its location r^*. For developing laminar flow, this information is very useful in determining hydrodynamic entrance length based on the velocity at r^* attaining a particular percentage of the fully developed value. Unlike that of symmetric ducts such as the circular tube and rectangular ducts, the maximum velocity of the circular sector duct occurs away from the centroid on the axis of symmetry. The purpose of this note is to present the results of u_{max} and r^* and to extend the value for f Re and $K(\infty)$ for apex angles up to 2π.

Analysis

The analysis employs the cylindrical polar coordinate system (r, θ) in the duct cross section shown in Fig. 1 (see inset). The flow is assumed to be laminar, fully developed, and with constant fluid properties. Using quantities defined in the Nomenclature and taking advantage of symmetric flow about the line of $\theta = \phi$, the nondimensional momentum equation and boundary conditions are

$$\frac{1}{r}\frac{\partial}{\partial r}\left(r\frac{\partial u}{\partial r}\right)+\frac{1}{r^2}\frac{\partial u}{\partial \theta^2}=C \tag{1}$$

$$u(r, 0)=u(1, \theta)=0, \text{ and } \frac{\partial u}{\partial \theta}(r, \phi)=0 \tag{2}$$

It is first noted that special care is required to find the limit of $u(r, \theta)$ from the series solution of Eckert et al. (1958) as $\phi \to \pi/4$ or $\phi \to 3\pi/4$. In the other analytical solutions (Soliman and Feingold, 1977; Hu and Chang, 1973) the limits are easier, but for the limiting case of full finned tubes, there is no physical meaning when the number of fins is assigned to be a nonintegral value. Therefore, a complete, well-behaved solution of equation (1) with equation (2) was developed by the finite Fourier transform method as follows:

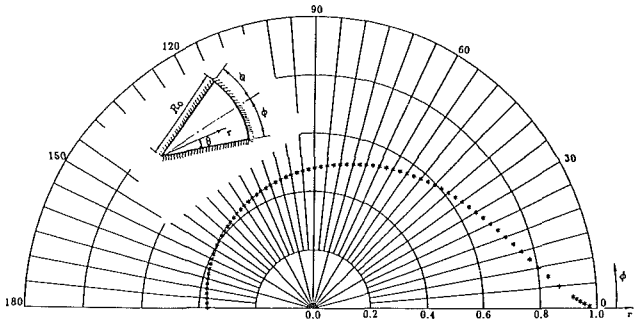

Fig. 1 Location of u_{max} for circular sector ducts

$$u(r, \theta)=\frac{16C}{\pi}\sum_{\substack{n=1\\ n\neq m}}^{\infty}\frac{r^2-r^{\frac{(2n-1)\pi}{2\phi}}}{(2n-1)(16-(2n-1)^2(\pi/\phi)^2)}\sin\left(\frac{(2n-1)\pi\theta}{2\phi}\right)+G_m \tag{3}$$

The last term G_m gives the limiting value as $\phi \to \pi/4$ or $\phi \to 3\pi/4$, which corresponds to $m=1$ and $m=2$, respectively, and takes the form

$$G_1=G_2=\frac{C}{4\phi}r^2 \ln r \sin 2\theta \tag{4}$$

For any other ϕ, $m=0$ and $G_0=0$. The constant C is obtained by mass conservation and is given by

$$C=-\frac{f\,\mathrm{Re}}{2}\left(\frac{\phi+1}{\phi}\right)^2 \tag{5}$$

where

$$f\,\mathrm{Re}=\frac{\pi^2}{8(\phi+1)^2}\frac{1}{\Sigma_{n=1}^{\infty}(4\pi n^2+(8\phi-4\pi)n+\pi-4\phi)^{-2}} \tag{6}$$

In the special case $\phi=\pi/2$, f Re can be expressed in closed form as

$$f\,\mathrm{Re}=\frac{8\pi^4}{(\pi^2-8)(\pi+2)^2}\approx 15.7668$$

Equation (6) is well behaved for all ϕ, unlike equation (390) in the book by Shah and London (1978), which requires special efforts to obtain the limit of U_m as $\phi \to \pi/4$ or $\phi \to 3\pi/4$.

Turning now to the shape of the velocity field and the maximum velocity, due to symmetry, the maximum velocity occurs on the symmetry line defined by $\theta=\phi$. Hence by setting the first derivative of $u(r, \theta=\phi)$ to zero, the location of the maximum velocity is found by

$$\sum_{\substack{n=1\\ n\neq m}}^{\infty}\frac{(-1)^n\left(2r-\frac{(2n-1)\pi}{2\phi}r^{\frac{(2n-1)\pi}{2\phi}-1}\right)}{\frac{(2n-1)\pi}{2\phi}\left(\left(\frac{(2n-1)\pi}{2\phi}\right)^2-4\right)}+(-1)^{m+1}B_m=0 \tag{7}$$

where $B_0=0$, $B_1=B_2=\frac{1}{8}(2r \ln r+r)$. Equation (7) has a unique nonzero root at $r=r^*$ for each given ϕ. Substituting r^* with ϕ into equation (3) thus gives u_{max}.

In engineering applications dealing with ducts that are not too short, the total pressure drop between the duct inlet and a far downstream station x can be approximated by

Table 1 Flow characteristics of circular sector ducts

2ϕ (Deg)	r^*	u_{max}	fRe	$K(\infty)$ Present	$K(\infty)$ Shah & London (1978)
0	-	3.00000	12.0000	2.9710	2.971
2	0.95734	2.80928	12.1074	2.8189	-
8	0.88730	2.56777	12.4096	2.4957	2.480
10	0.87003	2.51826	12.5042	2.4110	-
15	0.83350	2.42489	12.7284	2.2375	2.235
20	0.80342	2.35858	12.9364	2.1048	-
25	0.77767	2.30883	13.1298	2.0008	-
30	0.75510	2.27013	13.3099	1.9177	1.855
36	0.73121	2.23384	13.5103	1.8385	-
40	0.71682	2.21417	13.6351	1.7952	-
45	0.70026	2.19344	13.7822	1.7494	1.657
50	0.68504	2.17612	13.9200	1.7109	-
55	0.67096	2.16149	14.0495	1.6784	-
60	0.65787	2.14902	14.1711	1.6508	1.580
65	0.64563	2.13831	14.2857	1.6271	-
70	0.63415	2.12905	14.3936	1.6067	-
72	0.62975	2.12570	14.4351	1.5993	-
75	0.62334	2.12101	14.4955	1.5890	-
80	0.61313	2.11397	14.5917	1.5736	1.530
90	0.59427	2.10234	14.7688	1.5484	-
100	0.57720	2.09323	14.9277	1.5288	1.504
110	0.56162	2.08597	15.0709	1.5134	-
120	0.54731	2.08013	15.2004	1.5012	1.488
130	0.53409	2.07538	15.3177	1.4914	-
140	0.52183	2.07148	15.4245	1.4834	-
150	0.51039	2.06824	15.5218	1.4769	-
160	0.49970	2.06553	15.6107	1.4715	1.468
170	0.48967	2.06324	15.6921	1.4670	-
180	0.48022	2.06130	15.7668	1.4632	1.463
190	0.47131	2.05964	15.8356	1.4600	-
200	0.46287	2.05820	15.8989	1.4573	-
210	0.45488	2.05696	15.9573	1.4549	-
220	0.44729	2.05587	16.0114	1.4528	-
230	0.44006	2.05491	16.0614	1.4510	-
240	0.43317	2.05406	16.1078	1.4494	-
260	0.42030	2.05263	16.1908	1.4466	-
270	0.41428	2.05201	16.2281	1.4454	-
290	0.40296	2.05094	16.2951	1.4432	-
300	0.39764	2.05047	16.3253	1.4423	-
320	0.38758	2.04963	16.3799	1.4404	-
340	0.37824	2.04889	16.4276	1.4388	-
360	0.36952	2.04823	16.4696	1.4372	-

$$\frac{P_0 - P(x)}{\frac{1}{2}\rho U_m^2} = f\frac{x}{D_h} + K(\infty) \tag{8}$$

where $K(\infty)$ can be computed via the method of Lundgren et al. (1964) as

$$K(\infty) = \frac{2}{A}\int (u^3 - u^2)dA \tag{9}$$

Results and Discussion

The present computed results for r^*, u_{max}, f Re, and $K(\infty)$ are listed in Table 1 and shown in Figs. 1 and 2. To minimize truncation error, all computations involving a series form were continued until the absolute value of the last term of the series was smaller than 10^{-12}. For r^*, equation (7) was solved by Newton's method. Each r^* value listed in Table 1 corresponds to making the absolute value of the left-hand side equation (7) smaller than 10^{-8}. In addition, the occurrence of u_{max} at r^* was confirmed by comparing the numerical value of $u(r^*, \phi)$ with the values of $u(1.0001r^*, \phi)$ and $u(0.9999r^*, \phi)$.

As shown in Table 1, with increasing ϕ, the location of the maximum velocity moves from near the curved surface toward the apex. This behavior is illustrated in Fig. 1. It is noted that u_{max} occurs at the radius center (i.e., $r^* = 0.5$) for ϕ about 80 deg. Figure 2 shows that the normalized maximum velocity u_{max} increases sharply as 2ϕ becomes smaller than about 60 deg. This is probably because U_m is progressively reduced (relative to U_{max}) by increasing corner effects associated with reducing ϕ at small apex angles. Also note that as $\phi \to 0$, u_{max} approaches the correct limiting value of 3.00 (Shah and London, 1978).

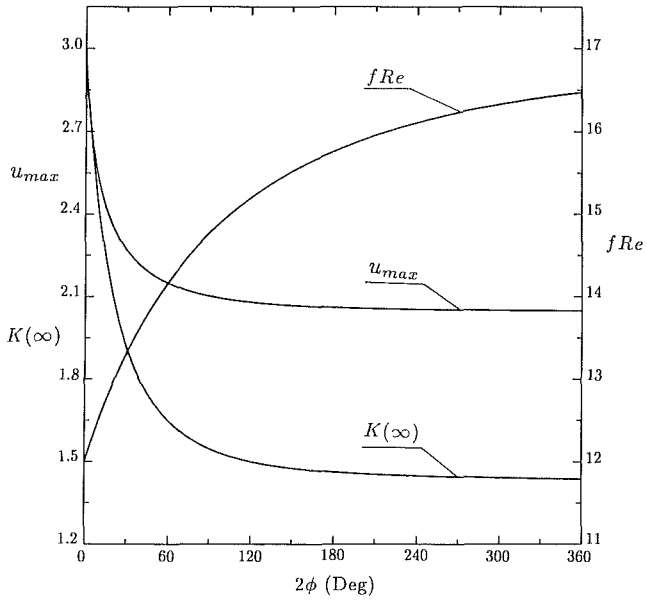

Fig. 2 u_{max}, $K(\infty)$, and f Re versus the apex angle of circular sector ducts

For f Re, as was shown in equation (6), as $\phi \to 0$, f Re $\to 12.000$, which is one-half the corresponding value for the parallel plate channel. In general, the f Re values presented in Table 1 are in excellent agreement with those tabulated in Shah and London (1978) for $0 \le \phi \le \pi/2$. The f Re values for the extended range, $\pi/2 \le \phi \le \pi$, are also believed to be of high accuracy. For $\phi = \pi$, the present f Re value agreed well (as did r^* and u_{max} also) with values calculated from the equations of Soliman and Feingold (1977) for one internally full finned tube.

For $K(\infty)$, the numerical integration in equation (9) was performed by employing the trapezoidal rule. Different fine grid sizes were used so as to make the fifth digit after the decimal of each $K(\infty)$ independent of grid size. For example, for $\phi = \pi$, a fine (r, ϕ) grid of 70×214 was used. The present computed values of $K(\infty)$ are listed in Table 1 together with the available values from Shah and London (1978). Comparison shows that the present results are slightly higher than the existing values (maximum difference of about 5 percent), although the agreement is excellent for $\phi = \pi$. In the limit as $\phi \to 0$, $K(\infty) \to 2.971$. Figure 2 shows that $K(\infty)$ has a trend versus ϕ that is similar to u_{max}.

Acknowledgments

This research was supported by the Natural Sciences and Engineering Research Council of Canada.

References

Eckert, E. R. G., Irvine, T. F., Jr., and Yen, J. T., 1958, "Local Laminar Heat Transfer in Wedge-Shaped Passages," *Trans. ASME*, Vol. 80, pp. 1433-1438.

Hu, M. H., and Chang, Y. P., 1973, "Optimization of Finned Tubes for Heat Transfer in Laminar Flow," ASME JOURNAL OF HEAT TRANSFER, Vol. 95, pp. 332-338.

Lundgren, T. S., Sparrow, E. M., and Starr, J. B., 1964, "Pressure Drop Due to the Entrance Region in Ducts of Arbitrary Cross Section," ASME *Journal of Basic Engineering*, Vol. 86, pp. 620-626.

Shah, R. K., and London, A. L., 1978, "Laminar Flow Forced Convection in Ducts," *Advances in Heat Transfer*, Supplement, Academic Press, New York.

Soliman, H. M., and Feingold, A., 1977, "Analysis of Fully Developed Laminar Flow in Longitudinal Internally Finned Tubes," *The Chemical Engineering Journal*, Vol. 14, pp. 119-128.

Sparrow, E. M., and Haji-Sheikh, A., 1965, "Laminar Heat Transfer and Pressure Drop in Isosceles Triangular, Right Triangular, and Circular Sector Ducts," ASME JOURNAL OF HEAT TRANSFER, Vol. 87, pp. 426-427.

Further Analyses of Laminar Flow Heat Transfer in Circular Sector Ducts

Q. M. Lei[1] and A. C. Trupp[1]

Nomenclature

C = constant = $(dP/dx)R_0^2/(U_m\mu)$
c_p = specific heat at constant pressure
dP/dx = axial pressure gradient
D_h = hydraulic diameter = $2\phi R_0/(1+\phi)$
h = average heat transfer coefficient
k = thermal conductivity of fluid
Nu = average Nusselt number
q'' = constant heat flux
R, r = radial coordinate, $r = R/R_0$
R_0 = radius of tube
t, T = temperature, $T = (t-t_c)/(q''R_0/k)$
U, u = axial velocity, $u = U/U_m$
x = axial coordinate
θ = angular coordinate
μ = dynamic viscosity
ρ = density
ϕ = half the apex angle of a circular sector duct

Subscripts

c = curved surface
$H1$ = uniform axial heat flux with uniform peripheral temperature for all surfaces
$H1_{ad}$ = uniform axial heat flux and uniform peripheral temperature for the curved surface; adiabatic flat surfaces
m = bulk mean
$\bar{w}$ = average over all walls

Introduction

Heat transfer in circular sector ducts is often encountered in multipassage tubes. Certain flow characteristics of circular sector ducts for apex angles up to π have been determined as documented by Shah and London (1978). Recently, Lei and Trupp (1989) have more completely analyzed the flow characteristics of fully developed laminar flow for apex angles up to 2π, including the location of the maximum velocity. Heat transfer results of fully developed laminar flow in circular sector ducts are also available for certain boundary conditions. Trupp and Lau (1984) numerically determined the average Nusselt number (Nu_T) for isothermal walls. Eckert et al. (1958) initially derived an analytical expression for the temperature profile for the case of $H1$. Sparrow and Haji-Sheikh (1965) extended their work and plotted Nu_{H1} for apex angles up to π. However, the above work required numerical integration (or equivalent) to obtain a value for Nu_{H1}. Regarding the $H1_{ad}$ boundary condition, Date (1974) numerically obtained a limiting value of $Nu_{H1_{ad}}$ for the semicircular duct from his prediction of circular tubes containing a twisted tape (straight and nonconducting tape). Hong and Bergles (1976) also reported an asymptotic value of $Nu_{H1_{ad}}$ for the semicircular duct from their entrance region solution. Otherwise it appears that there are no published analytical results of $Nu_{H1_{ad}}$ for circular sector ducts. The purpose of this technical note is to communicate these results. In addition, a novel series expression for Nu_{H1} is presented together with results for apex angles up to 2π.

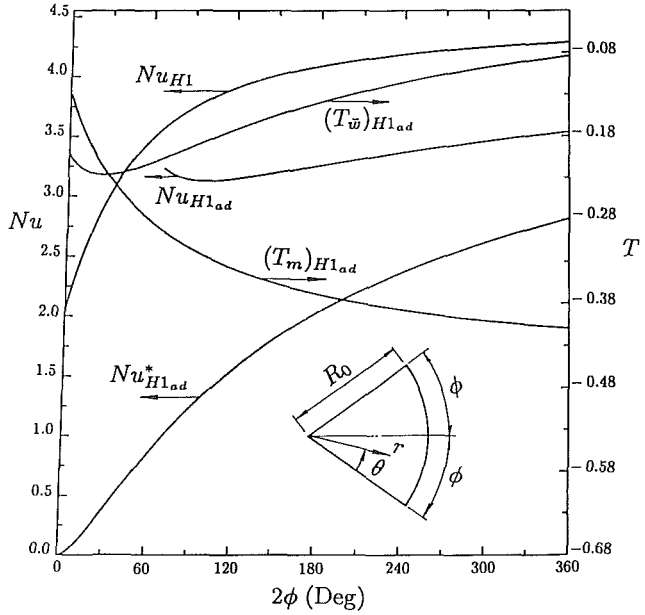

Fig. 1 Fully developed laminar heat transfer for circular sector ducts

Analysis

The duct cross section, together with the cylindrical coordinate system used in the analysis, is shown in Fig. 1 (see inset). The analysis is limited to laminar, hydrodynamically and thermally fully developed flow of a constant properties fluid. Body forces, axial conduction, and viscous dissipation within the fluid are assumed negligible. Due to symmetry, solutions are necessary only within half of the geometry. Using quantities defined in the Nomenclature, the nondimensional energy equation is

$$\frac{1}{r}\frac{\partial}{\partial r}\left(r\frac{\partial T}{\partial r}\right)+\frac{1}{r^2}\frac{\partial^2 T}{\partial \theta^2}=C_1 u(r,\theta) \tag{1a}$$

where from Lei and Trupp (1989)

$$u(r,\theta)=\frac{2C}{\phi}\sum_{n=1}^{\infty}\frac{r^2-r^{\lambda n}}{\lambda_n(4-\lambda_n^2)}\sin(\lambda_n\theta) \text{ with } \lambda_n=\frac{(2n-1)\pi}{2\phi} \tag{1b}$$

$$C=\frac{-\phi^2}{\Sigma_{n=1}^{\infty}(\lambda_n(\lambda_n+2))^{-2}} \tag{1c}$$

For the $H1_{ad}$ condition

$$\frac{\partial T}{\partial \theta}(r,0)=\frac{\partial T}{\partial \theta}(r,\phi)=T(1,\theta)=0 \text{ and } C_1=2 \tag{2}$$

For the $H1$ condition

$$T(r,0)=\frac{\partial T}{\partial \theta}(r,\phi)=T(1,\theta)=0 \text{ and } C_1=\frac{2(\phi+1)}{\phi} \tag{3}$$

The solution of equation (1) with equation (2) can be obtained by using the finite Fourier transform method, which results in

[1]Department of Mechanical Engineering, University of Manitoba, Winnipeg, Manitoba, Canada R3T 2N2.

Contributed by the Heat Transfer Division for publication in the JOURNAL OF HEAT TRANSFER. Manuscript received by the Heat Transfer Division August 29, 1988. Keywords: Augmentation and Enhancement, Forced Convection, Heat Exchangers.

$$T(r,\theta)=\frac{C}{4\phi^2}\sum_{n=1}^{\infty}G(\lambda_n,r)+\frac{8C}{\phi^2}\sum_{m=1}^{\infty}S(\beta_m,\lambda_n,r)\cos(\beta_m\theta)\ \text{with}\ \beta_m=\frac{m\pi}{\phi} \tag{4}$$

where

$$G(\lambda_n,r)=\frac{(\lambda_n+6)(2-\lambda_n)+(\lambda_n+2)^2r^4-16r^{\lambda_n+2}}{\lambda_n^2(\lambda_n+2)^2(4-\lambda_n^2)} \tag{5}$$

$$S(\beta_m,\lambda_n,r)=\sum_{n=1}^{\infty}\frac{(\lambda_n+6)(2-\lambda_n)r^{\beta_m}+((\lambda_n+2)^2-\beta_m^2)r^4-(16-\beta_m^2)r^{\lambda_n+2}}{(16-\beta_m^2)((\lambda_n+2)^2-\beta_m^2)(\lambda_n^2-\beta_m^2)(4-\lambda_n^2)} \tag{6}$$

Like most series solutions (e.g., Eckert et al., 1958), the denominators of equations (5) and (6) may become zero for some special apex angles. But, fortunately, limits do exist for these special cases and these are given as follows:

$$G(\lambda_n\to 2,r)=\frac{1}{32}(1-r^4+2r^4\ln r) \tag{7a}$$

$$S(\beta_m\to 4,\lambda_n\neq 2,r)=\sum_{n=1}^{\infty}\frac{(\lambda_n+6)(2-\lambda_n)r^4\ln r-8r^4+8r^{\lambda_n+2}}{8(\lambda_n^2-16)(4-\lambda_n^2)(2-\lambda_n)(\lambda_n+6)} \tag{7b}$$

$$S(\beta_m\to 4,\lambda_n=2,r)=\frac{r^4\ln r}{3072}(1-4\ln r) \tag{7c}$$

$$S(\beta_m\neq 4,\lambda_n\to(\beta_m-2),r)=\frac{2\beta_m r^4-2\beta_m r^{\beta_m}-(16-\beta_m^2)r^{\beta_m}\ln r}{8\beta_m^2(16-\beta_m^2)(1-\beta_m)(4-\beta_m)} \tag{7d}$$

$$S(\beta_m\neq 4,\lambda_n\to 2,r)=\frac{8r^{\beta_m}-8r^4+(16-\beta_m^2)r^4\ln r}{4(16-\beta_m^2)^2(4-\beta_m^2)} \tag{7e}$$

Since heat input is imposed on only the curved surface, an average heat transfer coefficient may be defined by $2\phi R_0 q''=h_{\bar{w}}(2\phi R_0+2R_0)(t_{\bar{w}}-t_m)$. Hence

$$h_{\bar{w}}=\left(\frac{\phi}{1+\phi}\right)\frac{q''}{t_{\bar{w}}-t_m}\ \text{and}\ \mathrm{Nu}_{H1_{ad}}=\frac{h_{\bar{w}}D_h}{k}=2\left(\frac{\phi}{1+\phi}\right)^2\frac{1}{T_{\bar{w}}-T_m} \tag{8}$$

As discussed later, this definition, based on overall average wall temperature, is improper for small apex angles. Thus, another average heat transfer coefficient, based on t_c-t_m, may be defined by

$$h=\left(\frac{\phi}{1+\phi}\right)\frac{q''}{t_c-t_m}\ \text{and}\ \mathrm{Nu}^*_{H1_{ad}}=\frac{hD_h}{k}=-2\left(\frac{\phi}{1+\phi}\right)^2\frac{1}{T_m} \tag{9}$$

The relationship between these two Nusselt numbers is given by $\mathrm{Nu}^*_{H1_{ad}}/\mathrm{Nu}_{H1_{ad}}=1-T_{\bar{w}}/T_m$, where

$$T_m=\frac{2}{\phi}\int_0^1\int_0^{\phi}Turdrd\theta \tag{10}$$

and it may be shown that

$$T_{\bar{w}}=\frac{C}{5\phi^2(1+\phi)}\sum_{n=1}^{\infty}\frac{\lambda_n+7}{\lambda_n^2(\lambda_n+3)(\lambda_n+2)^2}+\frac{8C}{5\phi^2(1+\phi)}\sum_{m=1}^{\infty}Q(\beta_m,\lambda_n) \tag{11a}$$

where

$$Q(\beta_m,\lambda_n)=\sum_{n=1}^{\infty}\frac{5(\lambda_n+6)(\lambda_n+3)+(1+\beta_m)(\beta_m^2-\lambda_n^2-9\lambda_n-34)}{(1+\beta_m)(\lambda_n+3)(\lambda_n+2)(16-\beta_m^2)((\lambda_n+2)^2-\beta_m^2)(\lambda_n^2-\beta_m^2)} \tag{11b}$$

Again, the singularity of equation (11*b*) for some special apex angles can readily be eliminated by taking its limiting values. Similarly, the solution of equation (1) that satisfied equation (3) is

$$T(r,\theta)=-C\frac{\phi+1}{\phi^2}\sum_{i=1}^{\infty}H(\chi_i,r)\sin(\chi_i\theta)\ \text{with}\ \chi_i=\frac{(2i-1)\pi}{2\phi} \tag{12a}$$

where

$$H(\chi_i,r)=\frac{(\chi_i-2)(\chi_i+6)r^{\chi_i}-4(\chi_i+1)r^4-(\chi_i^2-16)r^{\chi_i+2}}{\chi_i(\chi_i^2-4)(\chi_i^2-16)(\chi_i+1)} \tag{12b}$$

$$H(\chi_i\to 2,r)=\frac{2r^4-3r^4\ln r-2r^2}{72}\ \text{and}\ H(\chi_i\to 4,r)=\frac{2r^4-2r^6+5r^4\ln r}{480} \tag{12c}$$

The average heat transfer coefficient for the $H1$ condition is defined in the customary manner by $q''=h_w(t_w-t_m)$ and $\mathrm{Nu}_{H1}=h_wD_h/k$, where T_m is given by equation (10). Unlike the solution of Eckert et al. (1958), equation (12) with equations (1*b*) and (1*c*) offers a very easy way to obtain T_m through an orthogonality feature. As a result, Nu_{H1} can be written in closed form, without any numerical integration, as

$$\mathrm{Nu}_{H1}=\frac{2\phi^4}{(1+\phi)^2C^2}\left(\sum_{i=1}^{\infty}\frac{\chi_i^2+7\chi_i+11}{(\chi_i+2)^3(\chi_i+6)(\chi_i(\chi_i+4)(\chi_i+1))^2}\right)^{-1} \tag{13}$$

In the limit as $\phi\to 0$, equation (13) yields the well-known result of 105/51, i.e., 2.0588.

Results and Discussion

The present computed results for $\mathrm{Nu}^*_{H1_{ad}}$, $\mathrm{Nu}_{H1_{ad}}$, and Nu_{H1} are listed in Table 1. Figure 1 graphically shows these results and includes the average wall and bulk mean temperatures for the $H1_{ad}$ condition. To minimize truncation error, all calculations involving a series form were continued until the absolute value of the last term of the series was smaller than 10^{-10}. Computation tests showed that reducing this control factor to 10^{-15} produced no significant improvement of accuracy. The numerical integration of equation (10) for T_m was performed by employing the trapezoidal rule. Different fine grid sizes were used so as to make the fifth digit after the decimal of each T_m independent of grid size. For example, for $\phi=\pi$, a fine (r,ϕ) grid of 50×151 was used.

From Table 1, for the semicircular duct ($\phi=\pi/2$), the present $\mathrm{Nu}_{H1_{ad}}$ value of 3.256 agrees well with the numerical values of 3.170 from Shah and London (1978) (Date, 1974) and 3.160 from Hong and Bergles (1976) after they are converted to a similar basis. But although the differences are within 3 percent, in order to confirm the accuracy of the

Table 1 Heat transfer characteristics of circular sector ducts

2ϕ (Deg)	$Nu_{H1_{ad}}$	$Nu'_{H1_{ad}}$	Nu_{H1} Present	Nu_{H1} Shah & London (1978)
0	-	0.000	2.0588	2.059
2	-	0.004	2.1469	-
8	-	0.052	2.3841	2.384
10	-	0.075	2.4554	-
15	-	0.142	2.6189	2.619
18	-	0.186	2.7077	-
20	-	0.217	2.7633	-
24	-	0.279	2.8670	-
30	-	0.376	3.0052	3.005
36	-	0.472	3.1257	-
40	-	0.536	3.1976	-
45	-	0.615	3.2792	3.27
50	-	0.691	3.3527	-
60	-	0.839	3.4792	3.479
65	-	0.910	3.5338	-
72	-	1.005	3.6023	-
80	-	1.108	3.6707	3.671
90	-	1.230	3.7440	-
100	3.128	1.343	3.8064	3.806
110	3.134	1.450	3.8600	-
120	3.146	1.549	3.9062	3.906
130	3.161	1.642	3.9466	-
140	3.179	1.729	3.9819	-
150	3.198	1.811	4.0132	-
160	3.217	1.887	4.0409	4.04
170	3.236	1.959	4.0657	-
180	3.256	2.027	4.0880	4.089
190	3.275	2.091	4.1081	-
200	3.294	2.152	4.1263	-
210	3.313	2.209	4.1429	-
220	3.332	2.264	4.1581	-
240	3.367	2.365	4.1848	-
260	3.399	2.456	4.2076	-
270	3.414	2.498	4.2178	-
290	3.444	2.578	4.2362	-
300	3.458	2.615	4.2445	-
320	3.486	2.685	4.2597	-
340	3.512	2.749	4.2732	-
360	3.536	2.809	4.2852	-

present result, equation (1) with equation (2) was also solved by a finite difference method using a band storage linear equation solver. The numerical value of 3.255 was obtained for $Nu_{H1_{ad}}$ with the $(r, \pi/2)$ grid of 30×44. It is believed that similar high accuracy was also obtained for the other ducts.

For the $H1_{ad}$ condition, the surface temperature for the curved surface is constant (at t_c or $T_c=0$) whereas for the flat surfaces, the temperature is maximum at $r=1$ and decreases monotonically with decreasing r to reach a minimum at $r=0$. The overall average wall temperature (t_w) is consequently less than t_c, hence $T_{\bar{w}}$ is negative. Figure 1 shows how $T_{\bar{w}}$ varies with ϕ. As ϕ decreases (from large ϕ), the size of the heated curved surface decreases; hence, $T_{\bar{w}}$ decreases. In the meantime, T_m, which is also shown in Fig. 1, varies with the opposite trend with ϕ. Consequently $T_{\bar{w}}<T_m$ for $2\phi<\sim30$ deg. This, in turn, causes a discontinuity in $Nu_{H1_{ad}}$ whereby $Nu_{H1_{ad}}\to\infty$ as $T_{\bar{w}}\to T_m$, followed by negative $Nu_{H1_{ad}}$ numbers. The behaviors of $T_{\bar{w}}$ and T_m at small ϕ are therefore such that the computation of $Nu_{H1_{ad}}$ through equation (8) leads to improper results. Otherwise, as shown in Fig. 1, $Nu_{H1_{ad}}$ is fairly constant for $2\phi>\sim100$ deg, rising only slightly with increasing ϕ. In Table 1, the unrealistic values of $Nu_{H1_{ad}}$ are not presented for $2\phi<100$ deg. On the other hand, $Nu^*_{H1_{ad}}$, defined by equation (9), is well behaved for all apex angles and varies smoothly with ϕ (see Fig. 1). As $\phi\to0$, $Nu^*_{H1_{ad}}\to0$ due to the vanishing heat input. At $\phi=\pi$, which represents a tube with one internal full fin (nonconducting), $Nu^*_{H1_{ad}}$ becomes 2.809.

As shown in Table 1, values for Nu_{H1} calculated from the series expression of equation (13) are in excellent agreement with those in Shah and London (1978) for $0\le\phi\le\pi/2$. The Nu_{H1} values for the extended range, $\pi/2<\phi\le\pi$, are also believed to be of high accuracy. For $\phi=\pi$, which represents a tube with one internal full fin (perfectly conducting), the present Nu_{H1} is 4.2852.

The Nu_{H1} and $Nu^*_{H1_{ad}}$ values listed in Table 1 may be compared directly (for a given ϕ) since they are defined on the same surface area and temperature difference bases. Naturally, values for Nu_{H1} are always higher than those for $Nu^*_{H1_{ad}}$ because of the larger heat input area of the $H1$ condition (Fig. 1). In the engineering applications such as internal full-fin tubes, the two thermal conditions considered in this analysis may represent the limiting cases between which a real situation resides. Accordingly, where applicable, the data in Table 1 will bracket the probable thermal performance.

Acknowledgments

This research was supported by the Natural Sciences and Engineering Research Council of Canada.

References

Date, A. W., 1974, "Prediction of Fully-Developed Flow in a Tube Containing a Twisted-Tape," *Int. J. Heat Mass Transfer*, Vol. 17, pp. 845–859.

Eckert, E. R. G., Irvine, T. F., Jr., and Yen, J. T., 1958, "Local Laminar Heat Transfer in Wedge-Shaped Passages," *Trans. ASME*, Vol. 80, pp. 1433–1438.

Hong, S. W., and Bergles, A. E., 1976, "Laminar Flow Heat Transfer in the Entrance Region of Semi-circular Tubes With Uniform Heat Flux," *Int. J. Heat Mass Transfer*, Vol. 19, pp. 123–124.

Lei, Q. M., and Trupp, A. C., 1989, "Maximum Velocity Location and Pressure Drop of Fully Developed Laminar Flow in Circular Sector Ducts," ASME JOURNAL OF HEAT TRANSFER, Vol. 111, this issue.

Shah, R. K., and London, A. L., 1978, "Laminar Flow Forced Convection in Ducts," *Advances in Heat Transfer*, Supplement, Academic Press, New York.

Sparrow, E. M., and Haji-Sheikh, A., 1965, "Laminar Heat Transfer and Pressure Drop in Isosceles Triangular, Right Triangular, and Circular Sector Ducts," ASME JOURNAL OF HEAT TRANSFER, Vol. 87, pp. 426–427.

Trupp, A. C., and Lau, A. C. Y., 1984, "Fully Developed Laminar Heat Transfer in Circular Sector Ducts With Isothermal Walls," ASME JOURNAL OF HEAT TRANSFER, Vol. 106, pp. 467–469.

Further Results for Laminar Heat Transfer in Annular Sector and Circular Sector Ducts

T. M. Ben-Ali,[1] H. M. Soliman,[2] and E. K. Zariffeh[3]

Nomenclature

A_c = cross-sectional area $=\phi(r_2^2-r_1^2)$, m^2
c_p = specific heat, J/kg•K
d_h = hydraulic diameter $=4A_c/P$, m
dp/dx = axial pressure gradient, Pa/m
dt_b/dx = axial gradient of bulk temperature, °C/m
D_h = dimensionless hydraulic diameter $=d_h/(2r_2)$
f = friction factor $=(d_h/4)(-dp/dx)/(\rho u_m^2/2)$
$\bar{h}$ = cross-sectional average heat transfer coefficient $=q/[P(t_w-t_b)]$, W/m²•K

[1]Graduate Student, Department of Mechanical Engineering, University of Manitoba, Winnipeg, Manitoba, Canada R3T 2N2.

[2]Professor, Department of Mechanical Engineering, University of Manitoba, Winnipeg, Manitoba, Canada R3T 2N2; Mem. ASME.

[3]Engineer, Wardrop Engineering, Inc., Winnipeg, Manitoba, Canada R3C 3H1; currently, Heat Transfer Engineer, Atomic Energy of Canada Limited, Pinawa, Manitoba, Canada R0E 1L0.

Contributed by the Heat Transfer Division for publication in the JOURNAL OF HEAT TRANSFER. Manuscript received by the Heat Transfer Division August 2, 1988. Keywords: Forced Convection, Numerical Methods.

Table 1 Heat transfer characteristics of circular sector ducts

2ϕ (Deg)	$Nu_{H1_{ad}}$	$Nu'_{H1_{ad}}$	Nu_{H1} Present	Nu_{H1} Shah & London (1978)
0	-	0.000	2.0588	2.059
2	-	0.004	2.1469	-
8	-	0.052	2.3841	2.384
10	-	0.075	2.4554	-
15	-	0.142	2.6189	2.619
18	-	0.186	2.7077	-
20	-	0.217	2.7633	-
24	-	0.279	2.8670	-
30	-	0.376	3.0052	3.005
36	-	0.472	3.1257	-
40	-	0.536	3.1976	-
45	-	0.615	3.2792	3.27
50	-	0.691	3.3527	-
60	-	0.839	3.4792	3.479
65	-	0.910	3.5338	-
72	-	1.005	3.6023	-
80	-	1.108	3.6707	3.671
90	-	1.230	3.7440	-
100	3.128	1.343	3.8064	3.806
110	3.134	1.450	3.8600	-
120	3.146	1.549	3.9062	3.906
130	3.161	1.642	3.9466	-
140	3.179	1.729	3.9819	-
150	3.198	1.811	4.0132	-
160	3.217	1.887	4.0409	4.04
170	3.236	1.959	4.0657	-
180	3.256	2.027	4.0880	4.089
190	3.275	2.091	4.1081	-
200	3.294	2.152	4.1263	-
210	3.313	2.209	4.1429	-
220	3.332	2.264	4.1581	-
240	3.367	2.365	4.1848	-
260	3.399	2.456	4.2076	-
270	3.414	2.498	4.2178	-
290	3.444	2.578	4.2362	-
300	3.458	2.615	4.2445	-
320	3.486	2.685	4.2597	-
340	3.512	2.749	4.2732	-
360	3.536	2.809	4.2852	-

present result, equation (1) with equation (2) was also solved by a finite difference method using a band storage linear equation solver. The numerical value of 3.255 was obtained for $Nu_{H1_{ad}}$ with the $(r, \pi/2)$ grid of 30×44. It is believed that similar high accuracy was also obtained for the other ducts.

For the $H1_{ad}$ condition, the surface temperature for the curved surface is constant (at t_c or $T_c=0$) whereas for the flat surfaces, the temperature is maximum at $r=1$ and decreases monotonically with decreasing r to reach a minimum at $r=0$. The overall average wall temperature (t_w) is consequently less than t_c, hence $T_{\bar{w}}$ is negative. Figure 1 shows how $T_{\bar{w}}$ varies with ϕ. As ϕ decreases (from large ϕ), the size of the heated curved surface decreases; hence, $T_{\bar{w}}$ decreases. In the meantime, T_m, which is also shown in Fig. 1, varies with the opposite trend with ϕ. Consequently $T_{\bar{w}}<T_m$ for $2\phi<\sim30$ deg. This, in turn, causes a discontinuity in $Nu_{H1_{ad}}$ whereby $Nu_{H1_{ad}}\to\infty$ as $T_{\bar{w}}\to T_m$, followed by negative $Nu_{H1_{ad}}$ numbers. The behaviors of $T_{\bar{w}}$ and T_m at small ϕ are therefore such that the computation of $Nu_{H1_{ad}}$ through equation (8) leads to improper results. Otherwise, as shown in Fig. 1, $Nu_{H1_{ad}}$ is fairly constant for $2\phi>\sim100$ deg, rising only slightly with increasing ϕ. In Table 1, the unrealistic values of $Nu_{H1_{ad}}$ are not presented for $2\phi<100$ deg. On the other hand, $Nu^*_{H1_{ad}}$, defined by equation (9), is well behaved for all apex angles and varies smoothly with ϕ (see Fig. 1). As $\phi\to0$, $Nu^*_{H1_{ad}}\to0$ due to the vanishing heat input. At $\phi=\pi$, which represents a tube with one internal full fin (nonconducting), $Nu^*_{H1_{ad}}$ becomes 2.809.

As shown in Table 1, values for Nu_{H1} calculated from the series expression of equation (13) are in excellent agreement with those in Shah and London (1978) for $0\le\phi\le\pi/2$. The Nu_{H1} values for the extended range, $\pi/2<\phi\le\pi$, are also believed to be of high accuracy. For $\phi=\pi$, which represents a tube with one internal full fin (perfectly conducting), the present Nu_{H1} is 4.2852.

The Nu_{H1} and $Nu^*_{H1_{ad}}$ values listed in Table 1 may be compared directly (for a given ϕ) since they are defined on the same surface area and temperature difference bases. Naturally, values for Nu_{H1} are always higher than those for $Nu^*_{H1_{ad}}$ because of the larger heat input area of the $H1$ condition (Fig. 1). In the engineering applications such as internal full-fin tubes, the two thermal conditions considered in this analysis may represent the limiting cases between which a real situation resides. Accordingly, where applicable, the data in Table 1 will bracket the probable thermal performance.

Acknowledgments

This research was supported by the Natural Sciences and Engineering Research Council of Canada.

References

Date, A. W., 1974, "Prediction of Fully-Developed Flow in a Tube Containing a Twisted-Tape," *Int. J. Heat Mass Transfer*, Vol. 17, pp. 845–859.

Eckert, E. R. G., Irvine, T. F., Jr., and Yen, J. T., 1958, "Local Laminar Heat Transfer in Wedge-Shaped Passages," *Trans. ASME*, Vol. 80, pp. 1433–1438.

Hong, S. W., and Bergles, A. E., 1976, "Laminar Flow Heat Transfer in the Entrance Region of Semi-circular Tubes With Uniform Heat Flux," *Int. J. Heat Mass Transfer*, Vol. 19, pp. 123–124.

Lei, Q. M., and Trupp, A. C., 1989, "Maximum Velocity Location and Pressure Drop of Fully Developed Laminar Flow in Circular Sector Ducts," ASME JOURNAL OF HEAT TRANSFER, Vol. 111, this issue.

Shah, R. K., and London, A. L., 1978, "Laminar Flow Forced Convection in Ducts," *Advances in Heat Transfer*, Supplement, Academic Press, New York.

Sparrow, E. M., and Haji-Sheikh, A., 1965, "Laminar Heat Transfer and Pressure Drop in Isosceles Triangular, Right Triangular, and Circular Sector Ducts," ASME JOURNAL OF HEAT TRANSFER, Vol. 87, pp. 426–427.

Trupp, A. C., and Lau, A. C. Y., 1984, "Fully Developed Laminar Heat Transfer in Circular Sector Ducts With Isothermal Walls," ASME JOURNAL OF HEAT TRANSFER, Vol. 106, pp. 467–469.

Further Results for Laminar Heat Transfer in Annular Sector and Circular Sector Ducts

T. M. Ben-Ali,[1] H. M. Soliman,[2] and E. K. Zariffeh[3]

Nomenclature

A_c = cross-sectional area $=\phi(r_2^2-r_1^2)$, m^2
c_p = specific heat, J/kg•K
d_h = hydraulic diameter $=4A_c/P$, m
dp/dx = axial pressure gradient, Pa/m
dt_b/dx = axial gradient of bulk temperature, °C/m
D_h = dimensionless hydraulic diameter $=d_h/(2r_2)$
f = friction factor $=(d_h/4)(-dp/dx)/(\rho u_m^2/2)$
$\bar{h}$ = cross-sectional average heat transfer coefficient $=q/[P(t_w-t_b)]$, W/m²•K

[1]Graduate Student, Department of Mechanical Engineering, University of Manitoba, Winnipeg, Manitoba, Canada R3T 2N2.

[2]Professor, Department of Mechanical Engineering, University of Manitoba, Winnipeg, Manitoba, Canada R3T 2N2; Mem. ASME.

[3]Engineer, Wardrop Engineering, Inc., Winnipeg, Manitoba, Canada R3C 3H1; currently, Heat Transfer Engineer, Atomic Energy of Canada Limited, Pinawa, Manitoba, Canada R0E 1L0.

Contributed by the Heat Transfer Division for publication in the JOURNAL OF HEAT TRANSFER. Manuscript received by the Heat Transfer Division August 2, 1988. Keywords: Forced Convection, Numerical Methods.

k = thermal conductivity, W/m•K
Nu = Nusselt number $= \bar{h} d_h/k$
P = wetted perimeter $= 2\phi(r_1 + r_2) + 2(r_2 - r_1)$, m
q = rate of heat input per unit length, W/m
r = radial coordinate, m
r_1 = inner radius of duct, m
r_2 = outer radius of duct, m
r_h = hydraulic radius $= A_c/P$, m
R = dimensionless radial coordinate $= r/r_2$
R_1 = radius ratio of duct $= r_1/r_2$
R_h = dimensionless hydraulic radius $= r_h/r_2$
Re = Reynolds number $= \rho u_m d_h/\mu$
t = fluid temperature, °C
t_b = fluid bulk temperature, °C
t_w = wall temperature for the (H1) and (T) cases and average wall temperature for the (H2) case, °C
T = dimensionless temperature $= (t - t_w)/[(\rho c_p u_m r_2^2/k)(dt_b/dx)]$
T_b = dimensionless bulk temperature
u = local velocity, m/s
u_m = mean velocity, m/s
U = dimensionless velocity $= u/[(r_2^2/\mu)(-dp/dx)]$
U_m = dimensionless mean velocity
θ = angular coordinate
μ = dynamic viscosity, N•s/m²
ρ = density, kg/m³
ϕ = half opening angle of duct
∇^2 = Laplacian operator $= \partial^2/\partial R^2 + (1/R)\partial/\partial R + (1/R^2)\partial^2/\partial\theta^2$

1 Introduction

In a previous publication (Soliman, 1987), the laminar, fully developed, forced-convection flow in annular sector ducts was investigated theoretically assuming incompressible Newtonian fluids with constant properties and negligible axial conduction and viscous dissipation. Analytical (series) solutions were developed for the velocity distribution and the temperature distribution for the condition of uniform heat input axially and uniform wall temperature circumferentially (the (H1) conditions). From these solutions, it was possible to evaluate fRe and Nu_{H1} for the whole geometric range, $0.05 \le R_1 \le 0.95$ and 2.5 deg $\le \phi \le$ 175 deg. For the thermal boundary condition of uniform heat input axially and circumferentially, known as the (H2) condition, a least-squares matching technique was used, which was successful in producing results for Nu_{H2} only for a portion of the geometric range ($\phi \le 120$ deg).

The purpose of this note is to extend the results of Nu_{H2} to the whole geometric range and to produce new results for the thermal condition of uniform wall temperature both axially and circumferentially (the (T) condition). A numerical (finite difference) approach was used in generating the present results, confirmed with a finite element code. Free convective effects are neglected in this analysis. These effects can be significant, particularly on heat transfer, at very low Reynolds numbers or very high Grashof numbers. Therefore, the present results may not be accurate for such conditions. Also, due to the assumption of constant properties, the present results may not be applicable to cases with very high temperature differences between the inlet and outlet of the ducts.

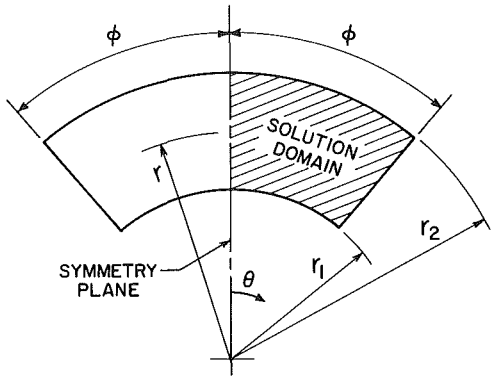

Fig. 1 Geometry and coordinate system

2 Analysis

Figure 1 shows the geometry under consideration together with the coordinate system. Solutions are necessary only within the hatched area of Fig. 1 due to symmetry. Using the definitions given in the Nomenclature, the governing equations can be written in the following nondimensional form:

Momentum Equation

$$\nabla^2 U = -1 \tag{1}$$

Energy Equation of the (H1) and (H2) Conditions

$$\nabla^2 T = U/U_m \tag{2}$$

Energy Equation for the (T) Condition

$$\nabla^2 T = (U/U_m)(T/T_b) \tag{3}$$

The applicable boundary conditions for the momentum equation and the (H1) and (T) energy equations are: $U = T = 0$ along the solid boundaries and $\partial U/\partial\theta = \partial T/\partial\theta = 0$ along the symmetry plane. For the (H2) energy equation, the boundary conditions are

$$\partial T/\partial R = R_h \quad \text{at } R = 1, \quad 0 \le \theta < \phi \tag{4a}$$
$$\partial T/\partial R = -R_h \quad \text{at } R = R_1, \quad 0 \le \theta < \phi \tag{4b}$$
$$\partial T/\partial\theta = R_h R \quad \text{at } \theta = \phi, \quad R_1 < R < 1 \tag{4c}$$

and

$$\partial T/\partial\theta = 0 \quad \text{at } \theta = 0, \quad R_1 < R < 1 \tag{4d}$$

Our main objective in this note is to produce friction factor and Nusselt number results, which are quite useful in the design of compact heat exchangers where annular sector passages may be used. These design parameters were calculated using the definitions given in the Nomenclature, which may be reduced to the following dimensionless forms:

$$f\mathrm{Re} = 2D_h^2/U_m \tag{5}$$

where

$$U_m = \left[\int_0^{\phi}\int_{R_1}^{1} URdRd\theta\right]/[\phi(1 - R_1^2)/2] \tag{6}$$

and, for all thermal boundary conditions,

$$\mathrm{Nu} = -D_h^2/T_b \tag{7}$$

where

$$T_b = \left[\int_0^{\phi}\int_{R_1}^{1} UTRdRd\theta\right]/[\phi U_m(1 - R_1^2)/2] \tag{8}$$

The governing equations (1)–(3), subject to the appropriate boundary conditions, were solved numerically using the method of finite difference with second-order central-difference expressions for the derivatives. Backward and for-

Table 1 Values of Nu_{H2} for annular sector ducts

R_1	2ϕ=5°	10°	15°	20°	30°	40°	50°	60°	90°
0.05	0.0242	0.1055	0.2543	0.4730	1.070	1.732	2.276	2.643	3.035
0.10	0.0326	0.1427	0.3415	0.6253	1.348	2.041	2.531	2.821	3.060
0.15	0.0445	0.1950	0.4610	0.8253	1.661	2.340	2.745	2.948	3.065
0.20	0.0618	0.2746	0.6250	1.083	2.000	2.603	2.901	3.025	3.060
0.25	0.0872	0.3760	0.8460	1.398	2.325	2.806	3.000	3.064	3.049
0.30	0.1253	0.5298	1.135	1.760	2.602	2.942	3.053	3.079	3.037
0.35	0.1842	0.7479	1.488	2.129	2.810	3.023	3.077	3.079	3.024
0.40	0.2756	1.045	1.881	2.456	2.946	3.065	3.085	3.072	3.009
0.45	0.4190	1.423	2.258	2.713	3.024	3.083	3.080	3.061	2.994
0.50	0.6420	1.849	2.575	2.887	3.065	3.086	3.070	3.046	2.979
0.55	0.9751	2.266	2.802	2.992	3.084	3.080	3.055	3.028	2.962
0.60	1.426	2.603	2.946	3.051	3.088	3.066	3.035	3.005	2.945
0.65	1.945	2.826	3.025	3.079	3.081	3.046	3.011	2.982	2.931
0.70	2.419	3.015	3.111	3.129	3.062	3.069	3.040	2.957	2.916
0.75	2.742	3.036	3.088	3.082	3.033	2.986	2.955	2.934	2.906
0.80	2.922	3.077	3.085	3.056	2.993	2.953	2.930	2.916	2.896
0.85	3.024	3.089	3.052	3.008	2.950	2.922	2.908	2.899	2.884
0.90	3.083	3.049	2.987	2.947	2.912	2.898	2.889	2.883	2.868
0.95	3.046	2.944	2.910	2.897	2.882	2.867	2.867	2.869	2.881

R_1	120°	150°	180°	210°	240°	270°	300°	330°	350°
0.05	3.040	2.978	2.918	2.869	2.832	2.803	2.780	2.763	2.753
0.10	3.028	2.967	2.915	2.876	2.847	2.825	2.808	2.794	2.787
0.15	3.015	2.959	2.915	2.883	2.859	2.841	2.828	2.816	2.810
0.20	3.003	2.953	2.916	2.888	2.868	2.853	2.842	2.833	2.827
0.25	2.992	2.947	2.914	2.891	2.874	2.862	2.852	2.845	2.840
0.30	2.982	2.941	2.912	2.892	2.878	2.867	2.860	2.853	2.849
0.35	2.971	2.934	2.909	2.892	2.880	2.872	2.865	2.860	2.856
0.40	2.960	2.927	2.905	2.891	2.882	2.875	2.870	2.865	2.861
0.45	2.948	2.919	2.902	2.891	2.883	2.878	2.873	2.869	2.868
0.50	2.937	2.913	2.899	2.890	2.882	2.879	2.875	2.871	2.870
0.55	2.926	2.906	2.895	2.887	2.882	2.880	2.876	2.871	2.871
0.60	2.916	2.901	2.891	2.886	2.881	2.879	2.875	2.869	2.869
0.65	2.908	2.897	2.888	2.883	2.878	2.878	2.872	2.865	2.865
0.70	2.900	2.892	2.885	2.880	2.874	2.867	2.866	2.866	2.867
0.75	2.893	2.887	2.882	2.875	2.868	2.868	2.869	2.870	2.871
0.80	2.887	2.876	2.868	2.868	2.869	2.871	2.874	2.877	2.878
0.85	2.876	2.868	2.870	2.872	2.876	2.880	2.884	2.889	2.890
0.90	2.869	2.874	2.881	2.887	2.894	2.900	2.905	2.909	2.911
0.95	2.894	2.906	2.913	2.920	2.922	2.905	2.929	2.882	2.870

Table 2 Values of Nu_T for annular sector ducts

R_1	2ϕ=5°	10°	15°	20°	30°	40°	50°	60°	90°
0.05	1.559	1.839	2.051	2.221	2.478	2.665	2.803	2.906	3.089
0.10	1.707	1.996	2.208	2.374	2.615	2.780	2.893	2.973	3.097
0.15	1.869	2.164	2.372	2.529	2.746	2.882	2.967	3.019	3.091
0.20	2.045	2.341	2.541	2.684	2.868	2.966	3.015	3.038	3.086
0.25	2.235	2.526	2.711	2.833	2.971	3.023	3.035	3.038	3.049
0.30	2.440	2.717	2.876	2.971	3.045	3.046	3.032	3.029	3.128
0.35	2.657	2.909	3.013	3.087	3.087	3.045	3.019	3.026	3.189
0.40	2.886	3.096	3.166	3.163	3.090	3.025	3.010	3.041	3.280
0.45	3.121	3.264	3.265	3.203	3.067	3.004	3.018	3.083	3.402
0.50	3.355	3.405	3.316	3.194	3.029	2.997	3.053	3.157	3.562
0.55	3.578	3.498	3.310	3.146	2.997	3.019	3.125	3.270	3.754
0.60	3.773	3.523	3.249	3.077	2.988	3.079	3.241	3.426	3.987
0.65	3.911	3.462	3.153	3.012	3.021	3.191	3.408	3.640	4.262
0.70	3.962	3.337	3.051	2.980	3.113	3.366	3.642	3.910	4.576
0.75	3.876	3.173	2.984	3.013	3.289	3.629	3.960	4.256	4.939
0.80	3.634	3.026	3.000	3.153	3.582	4.008	4.377	4.686	5.342
0.85	3.295	2.980	3.174	3.467	4.054	4.536	4.913	5.205	5.775
0.90	3.005	3.197	3.662	4.009	4.782	5.250	5.573	5.812	6.238
0.95	3.220	4.145	4.827	5.298	5.860	6.168	6.389	6.544	6.814

R_1	120°	150°	180°	210°	240°	270°	300°	330°	350°
0.05	3.175	3.231	3.278	3.330	3.388	3.451	3.519	3.589	3.638
0.10	3.157	3.222	3.301	3.392	3.491	3.594	3.699	3.798	3.864
0.15	3.155	3.254	3.372	3.502	3.632	3.768	3.896	4.020	4.095
0.20	3.180	3.322	3.480	3.641	3.807	3.961	4.107	4.241	4.327
0.25	3.236	3.423	3.619	3.812	3.996	4.166	4.323	4.466	4.553
0.30	3.326	3.553	3.782	3.999	4.198	4.379	4.542	4.688	4.776
0.35	3.440	3.711	3.967	4.201	4.411	4.597	4.762	4.908	4.995
0.40	3.590	3.892	4.169	4.415	4.631	4.818	4.982	5.124	5.208
0.45	3.763	4.096	4.388	4.641	4.856	5.041	5.200	5.335	5.420
0.50	3.966	4.322	4.621	4.874	5.080	5.263	5.413	5.540	5.620
0.55	4.198	4.565	4.867	5.109	5.310	5.483	5.622	5.737	5.811
0.60	4.457	4.828	5.118	5.352	5.539	5.700	5.825	5.926	5.993
0.65	4.747	5.108	5.382	5.597	5.766	5.912	6.020	6.103	6.164
0.70	5.055	5.396	5.651	5.843	5.989	6.099	6.205	6.295	6.347
0.75	5.386	5.699	5.923	6.085	6.204	6.315	6.406	6.482	6.526
0.80	5.744	5.997	6.175	6.323	6.437	6.528	6.601	6.664	6.699
0.85	6.105	6.308	6.463	6.579	6.666	6.735	6.792	6.839	6.865
0.90	6.488	6.646	6.755	6.834	6.894	6.941	6.979	7.010	7.075
0.95	6.952	7.035	7.093	7.131	7.161	7.185	7.202	7.218	7.226

ward differences were used in expressing equations (4*a*)-(4*c*). A comparison between the results of three and five points backward and foward differences showed less than 0.8 percent deviation in the values of Nu_{H2}; therefore, three points were used. The resulting systems of linear algebraic equations were solved using the Gauss-Seidel method with overrelaxation factors ranging from 1.9 to 1.99. Iterations continued until values of U and T at all mesh points had converged to within $\pm 10^{-3}$ percent. In the case of the (T)boundary condition, an initial distribution of temperature and the corresponding bulk temperature were substituted in the right-hand side of equation (3). Iterations were continued until a new converged solution for T was obtained and a new T_b was calculated from equation (8). The procedure was repeated until T_b converged to within $\pm 10^{-2}$ percent.

The solution domain in the R and θ directions was discretized by an even two-dimensional mesh. Solutions were obtained for a number of extreme geometries using different mesh sizes. Based on these results, it was found that good accuracy (as demonstrated quantitatively later by the fRe and Nu values) could be achieved using a total of 800 nodal points. The number of subdivisions in the R and θ directions was selected so that their ratio was approximately equal to $2(1-R_1)/[\phi(1+R_1)]$ with the constraint that neither number be less than 10.

3 Results and Discussion

The geometric range covered in this investigation is given by

$$R_1 = 0 \text{ (circular sector duct) to } 0.95$$

$$\phi = 2.5 \text{ to } 175 \text{ deg}$$

Values of fRe and Nu_{H1} were developed mainly for assessment of numerical accuracy through comparison with similar results reported by Shah and London (1978) and Soliman (1987). The present results of fRe for the vast majority of gemoetries were within ± 0.5 percent of those reported by Shah and London (1978). Slightly higher deviations were noted for large R_1 and ϕ; however, the maximum deviation was 1.02 percent at $R_1 = 0.85$ and $\phi = 175$ deg. Also, the present values of Nu_{H1} were generally within ± 0.4 percent of those reported by Soliman (1987) with a maximum deviation of 3.18 percent at $R_1 = 0.95$ and $\phi = 175$ deg. These comparisons confirm the adequacy of the selected mesh and due to the close agreement demonstrated above, the present values of fRe and Nu_{H1} will not be reported.

Values of Nu_{H2} for the whole geometric range are listed in Table 1. Comparing these values with the ones reported earlier (Soliman, 1987) for a portion of the geometry range, we find the agreement is generally within ± 0.8 percent for the vast majority of the geometries. An interesting observation from the complete set of results given in Table 1 is that for $\phi \geq 90$ deg, the geometry has very little effect on Nu_{H2}, which can be seen to range from 2.75 to 3.07. Another important observation is that as R_1 and ϕ increase, the value of Nu_{H2} does not seem to be approaching the corresponding value for parallel plates as is the case with fRe, Nu_{H1}, and Nu_T. This is because the areas near the short sides of the duct, where the local heat transfer coefficients are low, are still receiving the same average heat flux. These trends are similar to the ones reported recently by Shah and Bhatti (1987) for rectangular ducts.

Values of Nu_T for the whole geometric range are listed in Table 2. In order to enhance our confidence in these results, an independent check was made using a two-dimensional finite element code based on the method described by Zienkiewicz (1977). The code divides the solution domain into a set of isoparametric, Lagrangian, quadrilateral elements and uses a variational technique to minimize the integral of weighted residual over the entire domain. A nonuniform grid was used with a higher concentration of nodes near the duct walls (particularly the corners) in order to allow for a finer analysis of the critical zones. The deviation between the set of values in Table 2 and the predictions of the finite element code was less than 1 percent for most geometries and never exceeded 3 percent.

In terms of trends, we note that values of Nu_{H1} are the

Table 3 Values of fRe, Nu_{H1}, Nu_{H2}, and Nu_T for circular sector ducts: ( ) from Shah and London (1978); [ ] from Trupp and Lau (1984)

2ϕ, Degrees	fRe	Nu_{H1}	Nu_{H2}	Nu_T
5	12.33	2.245	0.018	1.423
10	12.56 (12.50)	2.433	0.078 (0.081)	1.692 [1.686]
15	12.78 (12.73)	2.597 (2.619)	0.189 (0.195)	1.901 [1.898]
20	12.98 (12.94)	2.742	0.354 (0.362)	2.073 [2.072]
30	13.35 (13.31)	2.983 (3.005)	0.833 (0.838)	2.341 [2.342]
40	13.67 (13.64)	3.178	1.426 (1.400)	2.543 [2.543]
50	13.95	3.337	1.990	2.700
60	14.20 (14.17)	3.464 (3.479)	2.421	2.822 [2.819]
90	14.79	3.730	2.984	3.060
120	15.22 (15.20)	3.893 (3.906)	3.046 (2.898)	3.191 [3.188]
150	15.54	3.999	2.995	3.268
180	15.79 (15.77)	4.072 (4.089)	2.930 (2.923)	3.316 [3.316]
210	15.98	4.127	2.871	3.347
240	16.15	4.171	2.821	3.370
270	16.29	4.208	2.781	3.389
300	16.42	4.244	2.749	3.407
330	16.54	4.280	2.723	3.427
350	16.62	4.304	2.708	3.443

highest for all geometries. Nu_T always exceeds Nu_{H2} for $\phi \geq 45$ deg, while for $\phi < 45$ deg, Nu_T is generally higher than Nu_{H2} except for a small number of geometries surrounding the location $\phi(1+R_1)=(1-R_1)$. In other words, Nu_{H2} exceeds Nu_T only when the geometry approaches a square-duct geometry. For such cases, the present results become close to the square-duct results of $Nu_{H2}=3.091$ and $Nu_T=2.976$. The local maxima and minima exhibited in Tables 1 and 2 as R_1 and/or ϕ vary are attributed to both the heat transfer performance of the duct and the use of the hydraulic diameter as the characteristic length in Nusselt number.

Results for the special case of circular sector ducts were generated by setting $R_1 = 1 \times 10^{-5}$ in the present computer program. These results are given in Table 3 in which comparisons are made with Shah and London (1978) and Trupp and Lau (1984) for $\phi \leq 90$ deg. Very good agreement can be seen from the tabulated values, thus further enhancing our confidence in the present numerical accuracy. In Table 3, values of fRe, Nu_{H1}, and Nu_T increase continuously with ϕ, while Nu_{H2} reaches a maximum near $\phi = 60$ deg, beyond which it decreases with further increase in ϕ.

Acknowledgments

Financial assistance provided by the Natural Sciences and Engineering Research Council of Canada is gratefully acknowledged.

References

Shah, R. K., and Bhatti, M. S., 1987, "Laminar Convective Heat Transfer in Ducts," *Handbook of Single-Phase Convective Heat Transfer*, S. Kakac et al., eds., Wiley, New York, Chap. 3.

Shah, R. K., and London, A. L., 1978, *Laminar Flow Forced Convection in Ducts*, Academic Press, New York.

Soliman, H. M., 1987, "Laminar Heat Transfer in Annular Sector Ducts," ASME JOURNAL OF HEAT TRANSFER, Vol. 109, pp. 247-249.

Trupp, A. C., and Lau, A. C. Y., 1984, "Fully Developed Laminar Heat Transfer in Circular Sector Ducts With Isothermal Walls," ASME JOURNAL OF HEAT TRANSFER, Vol. 106, pp. 467-469.

Zienkiewicz, O. C., 1977, *The Finite Element Method*, 3rd ed., McGraw-Hill, New York.

Turbulent Heat Transfer in Parallel Flow Boundary Layers With Streamwise Step Changes in Surface Conditions

W. R. Lindberg,[1] R. C. Lee,[2] and L. B. Smathers[3]

Nomenclature

A^+ = constant used in Van Driest mixing length formulation $\simeq 25$

A_n = constants used in series solution for Stanton numbers with flux boundary condition $= C_n Y_{n,0}$

C = constant used in evaluation of St_k given in equation (10) $\simeq 1$

C_n = constants in series solution of equation (3)

C_P = specific heat

G_n = constants used in series solution for Stanton numbers with temperature boundary condition $= C_n Y'_{n,0}$

k = thermal conductivity

k_s = equivalent sand grain roughness

l^+ = dimensionless mixing length $= lu_*/\nu$

L^+ = dimensionless downstream length $= Lu_*/\nu$

$P(y^+)$ = nondimensional parameter $= 1/\mathrm{Pr} + \epsilon_H/\nu$

Pr = Prandtl number $= \nu/\alpha$

Pr_t = turbulent Prandtl number

q_0 = heat flux prescribed at the wall for cases (b) and (d)

Re_k = roughness Reynolds number $= k_s u_*/\nu$

St_k = roughness Stanton number defined by equations (9) and (10)

St_x^* = local Stanton number based on friction velocity $= q_0/(T_0 - T_\infty)\rho C_p u_*$

T^+ = dimensionless temperature (as defined by equations (2a) and (2b))

T_0 = temperature prescribed at the wall for cases (a) and (c)

u_* = friction velocity

U = average velocity $= U(y)$

U^+ = dimensionless velocity $= U/u_*$

V, W = auxiliary homogeneous functions defined by equation (8)

x = coordinate in stream direction

x^+ = Reynolds number based on friction velocity $= xu_*/\nu$

y = coordinate normal to stream direction

y^+ = dimensionless wall coordinate $= yu_*/\nu$

[1] Professor, Department of Mechanical Engineering, University of Wyoming, Laramie, WY 82071; Mem. ASME.

[2] Department of Mechanical Engineering, University of Wyoming, Laramie, WY 82071; present address: Department of Mechanical Engineering, Utah State University, Logan, UT 84322; Assoc. Mem. ASME.

[3] Research Associate, Department of Mechanical Engineering, University of Wyoming, Laramie, WY 82071.

Contributed by the Heat Transfer Division for publication in the JOURNAL OF HEAT TRANSFER. Manuscript received by the Heat Transfer Division February 4, 1987. Keywords: Forced Convection, Turbulence.

Table 3 Values of fRe, Nu_{H1}, Nu_{H2}, and Nu_T for circular sector ducts: ( ) from Shah and London (1978); [ ] from Trupp and Lau (1984)

2ϕ, Degrees	fRe	Nu_{H1}	Nu_{H2}	Nu_T
5	12.33	2.245	0.018	1.423
10	12.56 (12.50)	2.433	0.078 (0.081)	1.692 [1.686]
15	12.78 (12.73)	2.597 (2.619)	0.189 (0.195)	1.901 [1.898]
20	12.98 (12.94)	2.742	0.354 (0.362)	2.073 [2.072]
30	13.35 (13.31)	2.983 (3.005)	0.833 (0.838)	2.341 [2.342]
40	13.67 (13.64)	3.178	1.426 (1.400)	2.543 [2.543]
50	13.95	3.337	1.990	2.700
60	14.20 (14.17)	3.464 (3.479)	2.421	2.822 [2.819]
90	14.79	3.730	2.984	3.060
120	15.22 (15.20)	3.893 (3.906)	3.046 (2.898)	3.191 [3.188]
150	15.54	3.999	2.995	3.268
180	15.79 (15.77)	4.072 (4.089)	2.930 (2.923)	3.316 [3.316]
210	15.98	4.127	2.871	3.347
240	16.15	4.171	2.821	3.370
270	16.29	4.208	2.781	3.389
300	16.42	4.244	2.749	3.407
330	16.54	4.280	2.723	3.427
350	16.62	4.304	2.708	3.443

highest for all geometries. Nu_T always exceeds Nu_{H2} for $\phi \geq 45$ deg, while for $\phi < 45$ deg, Nu_T is generally higher than Nu_{H2} except for a small number of geometries surrounding the location $\phi(1+R_1)=(1-R_1)$. In other words, Nu_{H2} exceeds Nu_T only when the geometry approaches a square-duct geometry. For such cases, the present results become close to the square-duct results of $Nu_{H2}=3.091$ and $Nu_T=2.976$. The local maxima and minima exhibited in Tables 1 and 2 as R_1 and/or ϕ vary are attributed to both the heat transfer performance of the duct and the use of the hydraulic diameter as the characteristic length in Nusselt number.

Results for the special case of circular sector ducts were generated by setting $R_1 = 1 \times 10^{-5}$ in the present computer program. These results are given in Table 3 in which comparisons are made with Shah and London (1978) and Trupp and Lau (1984) for $\phi \leq 90$ deg. Very good agreement can be seen from the tabulated values, thus further enhancing our confidence in the present numerical accuracy. In Table 3, values of fRe, Nu_{H1}, and Nu_T increase continuously with ϕ, while Nu_{H2} reaches a maximum near $\phi = 60$ deg, beyond which it decreases with further increase in ϕ.

Acknowledgments

Financial assistance provided by the Natural Sciences and Engineering Research Council of Canada is gratefully acknowledged.

References

Shah, R. K., and Bhatti, M. S., 1987, "Laminar Convective Heat Transfer in Ducts," *Handbook of Single-Phase Convective Heat Transfer*, S. Kakac et al., eds., Wiley, New York, Chap. 3.

Shah, R. K., and London, A. L., 1978, *Laminar Flow Forced Convection in Ducts*, Academic Press, New York.

Soliman, H. M., 1987, "Laminar Heat Transfer in Annular Sector Ducts," ASME JOURNAL OF HEAT TRANSFER, Vol. 109, pp. 247-249.

Trupp, A. C., and Lau, A. C. Y., 1984, "Fully Developed Laminar Heat Transfer in Circular Sector Ducts With Isothermal Walls," ASME JOURNAL OF HEAT TRANSFER, Vol. 106, pp. 467-469.

Zienkiewicz, O. C., 1977, *The Finite Element Method*, 3rd ed., McGraw-Hill, New York.

Turbulent Heat Transfer in Parallel Flow Boundary Layers With Streamwise Step Changes in Surface Conditions

W. R. Lindberg,[1] R. C. Lee,[2] and L. B. Smathers[3]

Nomenclature

- A^+ = constant used in Van Driest mixing length formulation $\simeq 25$
- A_n = constants used in series solution for Stanton numbers with flux boundary condition $= C_n Y_{n,0}$
- C = constant used in evaluation of St_k given in equation (10) $\simeq 1$
- C_n = constants in series solution of equation (3)
- C_P = specific heat
- G_n = constants used in series solution for Stanton numbers with temperature boundary condition $= C_n Y'_{n,0}$
- k = thermal conductivity
- k_s = equivalent sand grain roughness
- l^+ = dimensionless mixing length $= lu_*/\nu$
- L^+ = dimensionless downstream length $= Lu_*/\nu$
- $P(y^+)$ = nondimensional parameter $= 1/\mathrm{Pr} + \epsilon_H/\nu$
- Pr = Prandtl number $= \nu/\alpha$
- Pr_t = turbulent Prandtl number
- q_0 = heat flux prescribed at the wall for cases (b) and (d)
- Re_k = roughness Reynolds number $= k_s u_*/\nu$
- St_k = roughness Stanton number defined by equations (9) and (10)
- St_x^* = local Stanton number based on friction velocity $= q_0/(T_0 - T_\infty)\rho C_p u_*$
- T^+ = dimensionless temperature (as defined by equations (2a) and (2b))
- T_0 = temperature prescribed at the wall for cases (a) and (c)
- u_* = friction velocity
- U = average velocity $= U(y)$
- U^+ = dimensionless velocity $= U/u_*$
- V, W = auxiliary homogeneous functions defined by equation (8)
- x = coordinate in stream direction
- x^+ = Reynolds number based on friction velocity $= xu_*/\nu$
- y = coordinate normal to stream direction
- y^+ = dimensionless wall coordinate $= yu_*/\nu$

[1] Professor, Department of Mechanical Engineering, University of Wyoming, Laramie, WY 82071; Mem. ASME.

[2] Department of Mechanical Engineering, University of Wyoming, Laramie, WY 82071; present address: Department of Mechanical Engineering, Utah State University, Logan, UT 84322; Assoc. Mem. ASME.

[3] Research Associate, Department of Mechanical Engineering, University of Wyoming, Laramie, WY 82071.

Contributed by the Heat Transfer Division for publication in the JOURNAL OF HEAT TRANSFER. Manuscript received by the Heat Transfer Division February 4, 1987. Keywords: Forced Convection, Turbulence.

Y_n = eigenvector solution defined by equation (4)
$Y_{n,0}$ = eigenvector solution at the wall
$Y'_{n,0}$ = derivative of the eigenvector solution at the wall $= dY_n/dy^+ \mid y^+ = 0$
α = thermal diffusivity $= K/\rho c$
δT_0 = roughness film temperature drop
δT_0^+ = dimensionless roughness film temperature drop $= \delta T_0 \rho C_p u_* / q_0$ St_k^{-1}
δy_0^+ = modification of mixing length for fully rough surfaces $= 0.031\ \mathrm{Re}_k$
Δ^+ = dimensionless thermal boundary layer thickness
ϵ_H = turbulent thermal eddy diffusivity
κ = von Karman constant $\simeq 0.41$
λ_n = eigenvalue
μ = dynamic viscosity
ν = kinematic viscosity
ρ = density

Superscripts

$+$ = denotes a dimensionless variable
$*$ = value referenced to the friction velocity
$\bar{}$ = averaged value

Subscripts

k = referenced to roughness height k_s
n = summation index
0 = referenced to a value at the wall
∞ = referenced to a free-stream value

Introduction

This paper examines the convective heat/mass transfer behavior of a turbulent boundary layer with parallel streamlines. The most notable example of such a flow is an atmospheric boundary layer with a stready mean wind in the absence of topography. The classic, two-dimensional problem involves the surface boundary condition of a finite-length step change in temperature/concentration in the streamwise direction of an atmospheric flow. In the literature on geophysical evapotranspiration, this problem is known as Sutton's problem (cf. Sutton, 1934, and Brutsaert, 1984). This flow situation is equally applicable to heat/mass transfer in solar ponds, ground solar collectors, and heated roadways, as examples.

The most commonly used predictor of the average convective transfer coefficient for these applications is the empirical form, which seems to have originated with Nusselt and Jurges (1922)

$$h_c = C_1 U_s + C_2$$

where h_c is the heat/mass transfer convective coefficient, U_s is the wind speed at some fixed elevation, and C_1 and C_2 are constants (for example: Jaluria and Cha, 1985; Kind et al., 1983; Williams, 1976; Bailey et al., 1975; and Garg, 1982). The constant C_2 is included to account for free convection effects. The incorporation of local convective behavior is only infrequently done, although some analyses have included this variation (Brutsaert, 1984).

The present note revisits the Sutton problem, with the van Driest eddy diffusivity model, and expands the types of boundary conditions that are examined to include surface changes in temperature/concentration and fluxes. The parallel streamline condition allows for Graetz-type solutions, with boundary conditions at the surface and in the far flow field. The predicted results are presented as a series of power law correlations of the relevant nondimensional parameters.

Theory

For steady, parallel flow, negligible viscous dissipation, constant properties, and a turbulent eddy diffusivity parameterization, the energy equation may be written

$$U\frac{\partial T}{\partial x} = \frac{\partial}{\partial y}\left[(\alpha+\epsilon_H)\frac{\partial T}{\partial y}\right] \tag{1}$$

In the absence of buoyancy effects, we shall take ϵ_H to be a function of y alone.

The boundary conditions and nondimensionalization of temperature will depend on the type of flow being examined. Due to the homogeneity in temperature, we may proceed to assume a nondimensional temperature T^+ as either

$$T^+ = \frac{T - T_0}{T_\infty - T_0} \tag{2a}$$

or

$$T^+ = \frac{(T_\infty - T)\cdot u_* k}{\nu q_0} \tag{2b}$$

which will be defined for each type of flow.

In terms of nondimensional variables equation (1) becomes

$$\frac{\partial T^+}{\partial x^+} = \frac{1}{U^+}\frac{\partial}{\partial y^+}\left[\left(\frac{1}{\mathrm{Pr}}+\frac{\epsilon_H}{\nu}\right)\frac{\partial T^+}{\partial y^+}\right]$$

$$= \frac{1}{U^+}\frac{\partial}{\partial y^+}\left[P(y)\frac{\partial T^+}{\partial y^+}\right] \tag{3}$$

This linear equation in T^+ is solved by the usual separation of variables

$$T^+(x^+, y^+) = \sum_{n=1}^{\infty} C_n Y_n(Y^+)\exp(-\lambda_n^2 x^+)$$

The eigenfunctions $Y_n(y^+)$ are solutions to the Sturm–Liouville equation

$$\frac{d}{dy^+}\left[P(y^+)\frac{dY}{dy^+}\right] + U^+\lambda^2 Y = 0 \tag{4}$$

We shall consider four distinct sets of boundary conditions:
(a) Smooth surface, step change in surface temperature;
(b) Smooth surface, step change in surface heat flux;
(c) Fully rough surface, step change in surface temperature; and
(d) Fully rough surface, step change in surface heat flux.

Case (a): Smooth Surface, Step Change in Surface Temperature. The dimensionless boundary conditions for T^+ defined by equation (2a) are

(i) $T^+(x^+, 0) = 0,\ x^+ > 0$

(ii) $\partial T^+/\partial y^+ = 0,\ y^+ \to \infty$

(iii) $T^+(0, y^+) = 1$

An integral heat balance over a differential element δx wide and extending to large y^+ yields

$$\mathrm{St}_x^* = -\frac{d}{dx^+}\int_0^\infty T^+ U^+ dy^+$$

$$= \sum_{n=1}^{\infty} C_n \lambda_n^2 \exp(-\lambda_n^2 x^+)\cdot\int_0^\infty Y_n U^+ dy^+ \tag{5}$$

The first integral of equation (4) may be evaluated for $y^+ = 0$ to ∞; equation (5) then becomes

$$\mathrm{St}_x^* = \frac{1}{\mathrm{Pr}}\sum_{n=1}^{\infty} G_n \exp(-\lambda_n^2 x^+) \tag{6}$$

The corresponding average Stanton number over a heated section up to $x = L$ may then be easily determined.

Case (b): Smooth Surface, Step Change in Surface Heat Flux. The dimensionless boundary conditions for T^+ defined by equation (2*b*) are

$$\left.\frac{dV}{\partial y^+}\right|_{y^+=0}=1 \qquad \left.\frac{\partial W}{\partial y^+}\right|_{y^+=0}=0$$

$$V(\infty)=0 \qquad W(x,\infty)=0$$

$$W(0,y^+)=-V(y^+)$$

where use has been made of auxiliary function $V(y^+)$

$$T^+(x^+,y^+)=V(y^+)+W(x^+,y^+) \tag{7}$$

in order to accommodate the nonhomogeneous wall boundary condition.

The auxiliary equation has an exact solution of the form

$$V(y^+)=-\frac{1}{\mathrm{Pr}}\int_{y^+}^{\infty}\frac{dy^+}{P(y^+)} \tag{8}$$

The local Stanton number may then be written

$$\mathrm{St}_x^* = -[\mathrm{Pr}T^+(x^+,0)]^{-1}$$

$$= -\left\{\mathrm{Pr}\left[\sum_{n=1}^{\infty}A_n\exp(-\lambda_n^2x^+)+V(0)\right]\right\}^{-1}$$

where $A_n=C_nY_{n,0}$.

Case (c): Fully Rough Surface, Step Change in Surface Temperature. A fully rough surface will be assumed to exist when the roughness Reynolds number, defined as

$$\mathrm{Re}_k=\frac{u_*k_s}{\nu}$$

exceeds a value of 70. The parameter k_s in the roughness Reynolds number is the "equivalent sand grain roughness" (Schlichting, 1968). This roughness is assumed to exist for a sufficient distance upstream for an equilibrium velocity profile to exist at the beginning of the surface temperature change.

The wall temperature boundary condition for this case may be written as

$$T(x,0)=T_0-\delta T_0$$

The introduction of δT_0 as a measure of the temperature change through a quiescent film adjacent to the roughness depressions is discussed by Kays and Crawford (1980). A roughness Stanton number may be defined as

$$\mathrm{St}_k=\frac{q_0}{\delta T_0\rho C_pu_*} \tag{9}$$

and experiments by Dipprey and Sabersky (1968) have indicated that

$$\mathrm{St}_k=C\mathrm{Re}_k^{-0.2}\mathrm{Pr}^{-0.44} \tag{10}$$

where C is a number whose value is close to unity (Pimenta et al., 1975). The heat flux at the wall may be written as

$$q_0=-C_p\mu\left\{P(y)\frac{\partial T}{\partial y}\right\}_{y=0} \tag{11}$$

An expression for δT_0 may then be determined by combining equations (9), (10), and (11)

$$\delta T_0=-\frac{\nu}{Cu_*}(\mathrm{Re}_k^{0.2}\mathrm{Pr}^{0.44})\left\{P(y)\frac{\partial T}{\partial y}\right\}_{y=0}$$

If we define the nondimensional temperature as in case (*a*), the boundary conditions become

(*i*) $T^+(x^+,0)=\mathrm{St}_k^{-1}\left\{P(y)\dfrac{\partial T}{\partial y}\right\}_{y=0}$

(*ii*) $T^+(x^+,\infty)=1$

or $\partial T^+/\partial y^+|_{y^+\to\infty}=0$

(*iii*) $T^+(0,y^+)=1$

The formulation for the Stanton number is very similar to case (*a*), with the exception that ϵ_H does not vanish for $y^+=0$, and the first integral of equation (4) must be modified to account for this. With this modification, the local Stanton number may be written as

$$\mathrm{St}_x^*=\left[P(y^+)\Big|_{y^+=0}\right]\sum_{n=1}^{\infty}G_n\exp(-\lambda_n^2x^+)$$

An average Stanton number may then be determined as well.

Case (d): Fully Rough Surface, Step Change in Surface Heat Flux. In comparison to case (*b*) ϵ_H does not vanish at the wall ($y^+=0$), so the wall boundary condition (*i*) becomes

$$\left[\left(1+\frac{\epsilon_H}{\alpha}\right)\frac{\partial T^+}{\partial y^+}\right]_{y^+=0}=1$$

This nonhomogeneous boundary condition has the same form as the corresponding condition in case (*b*), necessitating the use of an auxiliary function, $V(y^+)$, as given in equation (7), where $P(y^+)$ is modified due to the rough surface model for ϵ_H.

The evaluation of the Stanton number requires the use of the concept of the roughness film temperature drop δT_0. The eigenvalue analysis will yield the temperature $T^+(x^+,0)$, which is outside of the roughness film, so

$$T^+(x^+,0)=T_0^+-\delta T_0^+=W(x^+,0)+V(0)$$

where T_0^+ is the nondimensional wall temperature. The local Stanton number is then evaluated as

$$\mathrm{St}^* = -[\mathrm{Pr}(T^+(x^+,0)+\delta T_0^+)]^{-1}$$

$$= -\left\{\mathrm{Pr}\left[\sum_{n=1}^{\infty}A_n\exp(-\lambda_n^2x^+)+V(0)+\delta T_0^+\right]\right\}^{-1} \tag{12}$$

where $\delta T_0{}^+=\mathrm{St}_k^{-1}$ as before.

Eddy Diffusivity Model

Consistent with the level of the formulation, we have employed the van Driest (1956) mixing length model and the concept of turbulent Prandtl number in the evaluation of the eddy diffusivity. In nondimensional variables, this model is

$$\frac{\epsilon_H}{\nu}=(l^+)^2\mathrm{Pr}_t\frac{dU^+}{dy^+}$$

where $l^+=\kappa y^+[1-\exp(-y^+/A^+)]$.

The mixing-length formulation is modified for the case of fully rough surfaces by using

$$l^+=\kappa(y^++\delta y_0^+)$$

where $\delta y_0^+=0.031\ \mathrm{Re}_k$ (Kays and Crawford, 1980).

Rather than complicate the presentation of the results with two or more independent parameters, which would result from an outer region mode, the van Driest model was extended beyond its admitted range of validity. Various other more realistic outer models were then used and compared to the overextended van Driest model. It was concluded that the calculated results were very insensitive to the outer region flow model within the limits of the range of x^+ calculated (up to $x^+=10^7$). Essentially, the results are insensitive to the following outer region models:

(*a*) van Driest's model, over extended to $y^+\geq 10^5$;

(*b*) mixing length $l^+=\text{const}$ for $y^+\geq 10^3$, 10^4, 10^5 (it should be noted that $l^+\sim\text{const}$ implies $\epsilon_H\sim\text{const}$). These conclusions are consistent with many other models of heat transfer in turbulent flows and reflect the strong dependence

of heat transport behavior on the wall region. The convenience of not having to introduce another parameter into the formulation is quite attractive.

Numerical Procedure

The solution of equation (4) with the appropriate boundary conditions was done numerically. In order to extend the range of y^+ to the order of 10^5, a variable step size was used. This step size was tailored to be a constant over each (approximate) decade in y^+ and the same number of steps were used for each decade in y^+. The eigenvalues for the resulting nonsymmetric matrices were numerically determined and an orthogonal set was constructed through the use of transposed matrix operations (Carnahan et al. 1969).

With approximately 20 steps per decade, integrations out to y^+ of 5×10^5 are possible. This corresponds to x^+ values of up to 10^7 (with the outer boundary conditions still being satisfied).

Four Prandtl (or Schmidt) numbers were chosen for the numerical calculations: 0.5, 0.7, 2.0, 7.0. A turbulent Prandtl number of 0.9 was used for all of the numerical calculations. A roughness Reynolds number Re_k was chosen to be 70 for cases (c) and (d).

Results

Values of St_x^* for the four cases were calculated as functions of x^+ and Pr. For cases (a) and (c), values of $\overline{\mathrm{St}}^*$ were also evaluated. The rough surface cases were examined for $\mathrm{Re}_k = 70$ only.

Adequate curve fits to these results are

$$\text{Case } (a): \quad \mathrm{St}_x^* = 0.155\ \mathrm{Pr}^{-0.79}(x^+)^{-0.111\mathrm{Pr}^{-0.36}} \tag{13}$$

$$\text{Case } (b): \quad \mathrm{St}_x^* = 0.124\ \mathrm{Pr}^{-0.77}(x^+)^{-0.081\mathrm{Pr}^{-0.42}} \tag{14}$$

$$\text{Case } (c): \quad \mathrm{St}_x^* = 0.227\ \mathrm{Pr}^{-0.40}(x^+)^{-0.144\mathrm{Pr}^{-0.093}} \tag{15}$$

$$\text{Case } (d): \quad \mathrm{St}_x^* = \frac{(x^+)^{-0.122\exp(-0.193\ \mathrm{Pr})}}{(1.627+0.647\ \mathrm{Pr})^2} \tag{16}$$

These suggested curve fits are within ± 7 percent for the limits $0.5 \le \mathrm{Pr} \le 7.0$ and $10^4 < x^+ < 10^7$. The average Stanton numbers for cases (a) and (c) may be estimated from

$$\text{Case } (a): \quad \overline{\mathrm{St}}^*/\mathrm{St}_x^* = 1.13\ \mathrm{Pr}^{0.040}$$

$$\text{Case } (c): \quad \overline{\mathrm{St}}^*/\mathrm{St}_x^* = 1.17\ \mathrm{Pr}^{-0.013}$$

within ± 5 percent for $0.5 \le \mathrm{Pr} \le 7.0$ and $10^5 < x^+ < 10^7$, where the value of St_x^* is found using equation (13) or equation (15), respectively.

The thermal boundary layer growth was also examined. An initial slow development was observed for $x^+ \lesssim 10^3$, after which the boundary layer grew as

$$\Delta^+ \sim 0.3(x^+)^{0.84}$$

for case (a) and $\mathrm{Pr} = 0.7$. The other cases were similar. This development length increases with increasing Prandtl number, while the thermal boundary layer thickness decreases slightly with increasing Pr. An exponent of 0.8 has been reported for most experiments on the growth of this "internal boundary layer" (Brutsaert, 1984).

References

Bailey, R. T., Mitchell, J. W., and Beckman, W. A., 1975, "Convective Heat Transfer From a Desert Surface," ASME JOURNAL OF HEAT TRANSFER, Vol. 97, pp. 104–109.

Brutsaert, W., 1984, *Evaporation Into the Atmosphere*, D. Reidel Publishing Co., Boston, corrected ed.

Carnahan, B., Luther, H. A., and Wilkes, J. O., 1969, *Applied Numerical Methods*, Wiley, New York.

Dipprey, D. F., and Sabersky, R. H., 1963, "Heat and Momentum Transfer in Smooth and Rough Tubes at Various Prandtl Numbers," *Int. J. Heat Mass Transfer*, Vol. 6, pp. 329–353.

Garg, H. P., 1982, *Treatise on Solar Energy, Vol. 1 Fundamentals of Solar Energy*, Wiley, New York.

Jaluria, Y., and Cha, C. K., 1985, "Heat Rejection to the Surface Layer of a Solar Pond," ASME JOURNAL OF HEAT TRANSFER, Vol. 107, pp. 99–106.

Kays, W. M., and M. E. Crawford, 1980, *Convective Heat and Mass Transfer*, 2nd ed., McGraw-Hill, New York.

Kind, R. J., Gladstone, D. H., and Moizer, A. D., 1983, "Convective Heat Losses From Flat-Plate Solar Collectors in Turbulent Winds," ASME *J. Solar Energy Engineering*, Vol. 105, pp. 80–85.

Nusselt, W., and Jurges, W., 1922, "Die Kuhlung Einer Ebenen Wand Durch Einen Luftstrom," *Gesundheits Ingenieur*, Vol. 52, No. 45, pp. 641–642.

Pimenta, M. M., Moffat, R. J., and Kays, W. M., 1975, Report No. HMT-21, Dept. of Mechanical Engineering, Stanford University, Stanford, CA.

Schlichting, H., 1968, *Boundary-Layer Theory*, 6th ed., McGraw-Hill, New York, pp. 578–580.

Sutton, O. G., 1934, "Wind Structure and Evaporation in a Turbulent Atmosphere," *Proc. Roy. Soc. London, A*, Vol. 146, pp. 701–722.

Van Driest, E. R., 1956, "On Turbulent Flow Near a Wall," *J. Aeronautical Sciences*, Vol. 23, pp. 1007–1011.

Williams, G. P., 1976, "Design Heat Requirements for Embedded Snow-Melting Systems in Cold Climates," *Transportation Research Record*, Vol. 576, Transportation Research Board, National Research Council, Washington, DC, pp. 20–32.

Heat Transfer Measurements From a Surface With Uniform Heat Flux and an Impinging Jet

J. W. Baughn[1] and S. Shimizu[2]

Introduction

There are numerous studies, mostly experimental, on the flow characteristics and heat transfer associated with jet impingement on surfaces. These studies have considered both single jets and multiple jets (i.e., arrays) and many different aspects of impinging jets including the effects of crossflow, jet orientation (oblique jets), jet temperature, rotating surfaces, and different surface shapes. The present study is concerned with the case of a single circular turbulent air jet at the ambient air temperature impinging on a flat stationary surface. For even this simplest case, there is a very large body of literature and a full review is not possible in this note. Gauntner et al. (1970) present an early survey of the literature on flow characteristics of such a jet, Donaldson et al. (1971) review heat transfer characteristics, and Martin (1977) reviews heat and mass transfer. Some of the earliest measurements of heat transfer were done by Gardon and Cobonpue (1962) and by Gardon and Akfirat (1965, 1966). More recent measurements have been made by Goldstein and Behbahani (1982), and Hrycak (1983). The effects of a jet temperature different from the ambient temperature have recently been studied by Hollworth and Gero (1985) and Striegl and Diller (1984).

There are also some recent attempts to do numerical studies of the heat transfer for an impinging jet on a surface. Amano and Brandt (1984) did a numerical study of the flow

[1]Professor, Department of Mechanical Engineering, University of California, Davis, CA 95616; Mem. ASME.

[2]Research Engineer, Canon Corporation, Yokohama, Japan.

Contributed by the Heat Transfer Division for publication in the JOURNAL OF HEAT TRANSFER. Manuscript received by the Heat Transfer Division June 9, 1988. Keywords: Augmentation and Enhancement, Measurement Techniques, Turbulence.

of heat transport behavior on the wall region. The convenience of not having to introduce another parameter into the formulation is quite attractive.

Numerical Procedure

The solution of equation (4) with the appropriate boundary conditions was done numerically. In order to extend the range of y^+ to the order of 10^5, a variable step size was used. This step size was tailored to be a constant over each (approximate) decade in y^+ and the same number of steps were used for each decade in y^+. The eigenvalues for the resulting nonsymmetric matrices were numerically determined and an orthogonal set was constructed through the use of transposed matrix operations (Carnahan et al. 1969).

With approximately 20 steps per decade, integrations out to y^+ of 5×10^5 are possible. This corresponds to x^+ values of up to 10^7 (with the outer boundary conditions still being satisfied).

Four Prandtl (or Schmidt) numbers were chosen for the numerical calculations: 0.5, 0.7, 2.0, 7.0. A turbulent Prandtl number of 0.9 was used for all of the numerical calculations. A roughness Reynolds number Re_k was chosen to be 70 for cases (c) and (d).

Results

Values of St_x^* for the four cases were calculated as functions of x^+ and Pr. For cases (a) and (c), values of $\overline{\mathrm{St}}^*$ were also evaluated. The rough surface cases were examined for $\mathrm{Re}_k = 70$ only.

Adequate curve fits to these results are

$$\text{Case } (a): \quad \mathrm{St}_x^* = 0.155\ \mathrm{Pr}^{-0.79}(x^+)^{-0.111\mathrm{Pr}^{-0.36}} \tag{13}$$

$$\text{Case } (b): \quad \mathrm{St}_x^* = 0.124\ \mathrm{Pr}^{-0.77}(x^+)^{-0.081\mathrm{Pr}^{-0.42}} \tag{14}$$

$$\text{Case } (c): \quad \mathrm{St}_x^* = 0.227\ \mathrm{Pr}^{-0.40}(x^+)^{-0.144\mathrm{Pr}^{-0.093}} \tag{15}$$

$$\text{Case } (d): \quad \mathrm{St}_x^* = \frac{(x^+)^{-0.122\exp(-0.193\ \mathrm{Pr})}}{(1.627+0.647\ \mathrm{Pr})^2} \tag{16}$$

These suggested curve fits are within ± 7 percent for the limits $0.5 \le \mathrm{Pr} \le 7.0$ and $10^4 < x^+ < 10^7$. The average Stanton numbers for cases (a) and (c) may be estimated from

$$\text{Case } (a): \quad \overline{\mathrm{St}}^*/\mathrm{St}_x^* = 1.13\ \mathrm{Pr}^{0.040}$$

$$\text{Case } (c): \quad \overline{\mathrm{St}}^*/\mathrm{St}_x^* = 1.17\ \mathrm{Pr}^{-0.013}$$

within ± 5 percent for $0.5 \le \mathrm{Pr} \le 7.0$ and $10^5 < x^+ < 10^7$, where the value of St_x^* is found using equation (13) or equation (15), respectively.

The thermal boundary layer growth was also examined. An initial slow development was observed for $x^+ \lesssim 10^3$, after which the boundary layer grew as

$$\Delta^+ \sim 0.3(x^+)^{0.84}$$

for case (a) and $\mathrm{Pr} = 0.7$. The other cases were similar. This development length increases with increasing Prandtl number, while the thermal boundary layer thickness decreases slightly with increasing Pr. An exponent of 0.8 has been reported for most experiments on the growth of this "internal boundary layer" (Brutsaert, 1984).

References

Bailey, R. T., Mitchell, J. W., and Beckman, W. A., 1975, "Convective Heat Transfer From a Desert Surface," ASME JOURNAL OF HEAT TRANSFER, Vol. 97, pp. 104–109.

Brutsaert, W., 1984, *Evaporation Into the Atmosphere*, D. Reidel Publishing Co., Boston, corrected ed.

Carnahan, B., Luther, H. A., and Wilkes, J. O., 1969, *Applied Numerical Methods*, Wiley, New York.

Dipprey, D. F., and Sabersky, R. H., 1963, "Heat and Momentum Transfer in Smooth and Rough Tubes at Various Prandtl Numbers," *Int. J. Heat Mass Transfer*, Vol. 6, pp. 329–353.

Garg, H. P., 1982, *Treatise on Solar Energy, Vol. 1 Fundamentals of Solar Energy*, Wiley, New York.

Jaluria, Y., and Cha, C. K., 1985, "Heat Rejection to the Surface Layer of a Solar Pond," ASME JOURNAL OF HEAT TRANSFER, Vol. 107, pp. 99–106.

Kays, W. M., and M. E. Crawford, 1980, *Convective Heat and Mass Transfer*, 2nd ed., McGraw-Hill, New York.

Kind, R. J., Gladstone, D. H., and Moizer, A. D., 1983, "Convective Heat Losses From Flat-Plate Solar Collectors in Turbulent Winds," ASME *J. Solar Energy Engineering*, Vol. 105, pp. 80–85.

Nusselt, W., and Jurges, W., 1922, "Die Kuhlung Einer Ebenen Wand Durch Einen Luftstrom," *Gesundheits Ingenieur*, Vol. 52, No. 45, pp. 641–642.

Pimenta, M. M., Moffat, R. J., and Kays, W. M., 1975, Report No. HMT-21, Dept. of Mechanical Engineering, Stanford University, Stanford, CA.

Schlichting, H., 1968, *Boundary-Layer Theory*, 6th ed., McGraw-Hill, New York, pp. 578–580.

Sutton, O. G., 1934, "Wind Structure and Evaporation in a Turbulent Atmosphere," *Proc. Roy. Soc. London, A*, Vol. 146, pp. 701–722.

Van Driest, E. R., 1956, "On Turbulent Flow Near a Wall," *J. Aeronautical Sciences*, Vol. 23, pp. 1007–1011.

Williams, G. P., 1976, "Design Heat Requirements for Embedded Snow-Melting Systems in Cold Climates," *Transportation Research Record*, Vol. 576, Transportation Research Board, National Research Council, Washington, DC, pp. 20–32.

Heat Transfer Measurements From a Surface With Uniform Heat Flux and an Impinging Jet

J. W. Baughn[1] and S. Shimizu[2]

Introduction

There are numerous studies, mostly experimental, on the flow characteristics and heat transfer associated with jet impingement on surfaces. These studies have considered both single jets and multiple jets (i.e., arrays) and many different aspects of impinging jets including the effects of crossflow, jet orientation (oblique jets), jet temperature, rotating surfaces, and different surface shapes. The present study is concerned with the case of a single circular turbulent air jet at the ambient air temperature impinging on a flat stationary surface. For even this simplest case, there is a very large body of literature and a full review is not possible in this note. Gauntner et al. (1970) present an early survey of the literature on flow characteristics of such a jet, Donaldson et al. (1971) review heat transfer characteristics, and Martin (1977) reviews heat and mass transfer. Some of the earliest measurements of heat transfer were done by Gardon and Cobonpue (1962) and by Gardon and Akfirat (1965, 1966). More recent measurements have been made by Goldstein and Behbahani (1982), and Hrycak (1983). The effects of a jet temperature different from the ambient temperature have recently been studied by Hollworth and Gero (1985) and Striegl and Diller (1984).

There are also some recent attempts to do numerical studies of the heat transfer for an impinging jet on a surface. Amano and Brandt (1984) did a numerical study of the flow

[1]Professor, Department of Mechanical Engineering, University of California, Davis, CA 95616; Mem. ASME.

[2]Research Engineer, Canon Corporation, Yokohama, Japan.

Contributed by the Heat Transfer Division for publication in the JOURNAL OF HEAT TRANSFER. Manuscript received by the Heat Transfer Division June 9, 1988. Keywords: Augmentation and Enhancement, Measurement Techniques, Turbulence.

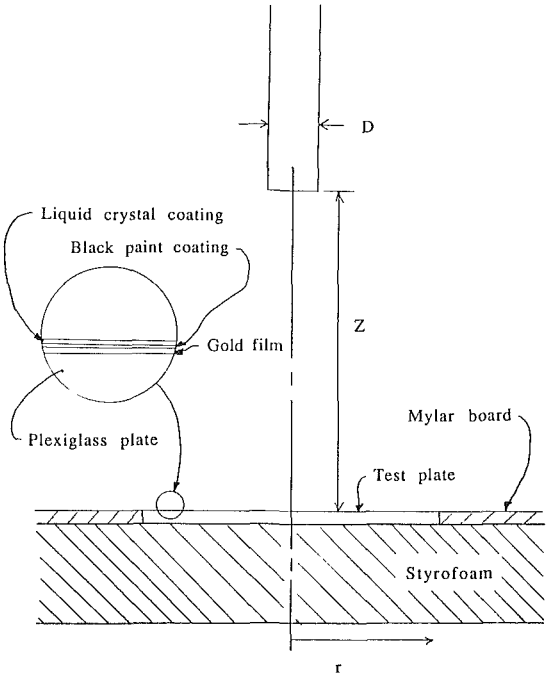

Fig. 1 Diagram of impingement test section

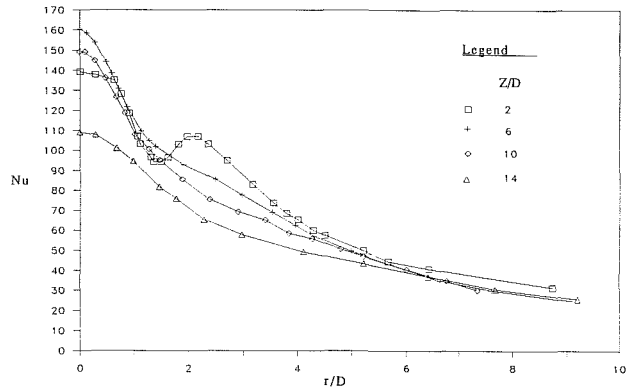

Fig. 2 Nusselt number distribution along the surface (Re = 23,750)

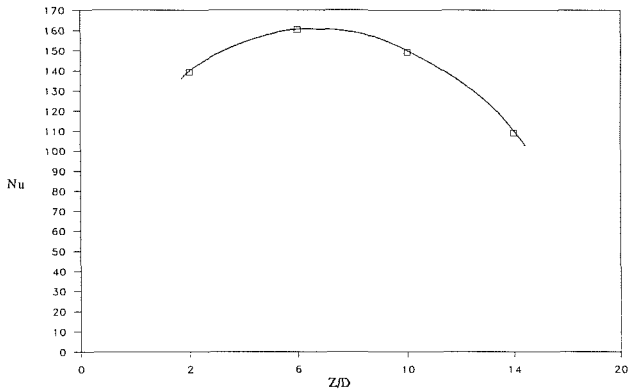

Fig. 3 Effect of jet distance on the heat transfer at the stagnation point (Re = 23,750)

characteristics of a turbulent jet and Polat et al. (1985) have done a numerical study of heat transfer.

One of the difficulties in comparing recent numerical work with previous experimental results is the lack of data on the jet characteristics and in some cases the mixed thermal boundary conditions at the surface (Launder, 1987). The present work provides some new experimental results that attempt to overcome this difficulty by using a fully developed jet and a well-controlled thermal boundary condition (i.e., a uniform heat flux). No other similar measurements were found in the literature.

Experimental Technique and Apparatus

The experimental technique used is described by Simonich and Moffat (1982) and Baughn et al. (1986). In this technique, a uniform heat flux is established by electrically heating a very thin gold coating on a plastic substrate. The surface temperature distribution is measured using liquid crystals. An isotherm on the surface represents a contour of constant heat transfer coefficient and is a line of a particular color (a light green was used for most of the data here). The liquid crystal used here had a narrow range of approximately 1°C over which the full color spectrum occurs. Temperature resolution of the green color was better than 0.1°C. The position of the green line is shifted by changing the electrical heating of the gold coating and thus the surface heat flux. This allows a complete mapping of the heat transfer coefficient over the entire surface. Since the temperature differences are small (on the order of 10°C), the resulting heat transfer coefficients are independent of the level of heat flux used.

The apparatus consisted essentially of a blower, a long pipe for development of the flow (2.5 cm i.d. and 72 diameters long), and a test section. The upstream development length of 72 diameters provides nearly fully developed flow at the jet exit. The turbulence level at the center of the jet at the exit was measured with a hot wire and was 4.1 percent at a Reynolds number of 21,000. This is consistent with the measurements of Hisida and Nagamo (1979). The velocity profile for a fully developed flow is available in Schlicting (1968) and the turbulence distribution is discussed by Hinze (1959). The test section, shown in Fig. 1, had a thin (0.64 cm thick) Plexiglas plate on the front of which the plastic sheet containing the gold coating was glued and on the back of which there was Styrofoam for insulation. The liquid crystal was air brushed on the surface of the gold coating. A Mylar board surrounded the Plexiglas surface to ensure a flat smooth surface.

The data reduction was straightforward and consisted of computing the surface heat flux from the gold coating voltage, current (determined from a shunt resistor), and the area. A radiation correction, using a measured emissivity of 0.5, was made to determine the convective component of the surface heat flux. The radiation correction was usually less than 5 percent. Conduction losses with this technique have previously been shown to be less than 1 percent due to the low thermal conductivity of the plastic substrate and are neglected. Using the ambient temperature and liquid crystal temperature, the heat transfer coefficient and corresponding Nusselt number based on the jet diameter were then calculated.

A standard uncertainty analysis was performed using the method of Kline and McClintock. The uncertainty in the Nusselt number (based on 20:1 odds) was estimated at 2.4 percent. The uncertainty in the Reynolds number was estimated at 2.3 percent. The uncertainty in position r/D and Z/D was less than 1 percent. Details of the uncertainty analysis are given in Hechanova (1988).

Results

The distribution of the Nusselt number along the surface (for Re = 23,750) is shown in Fig. 2. The symmetry around the jet was quite good as evidenced by the fact that the color band was very close to a perfect circle. One of the most interesting

distributions occurs when the jet is quite close to the surface ($Z/D=2$). In this case, the maximum heat transfer is at the stagnation point; the heat transfer then has a minimum at r/D of approximately 1.3, and another maximum at approximately 1.8. For certain runs this results in three concentric circles of color on the test section. The effect of jet distance from the surface on the stagnation point heat transfer is shown in Fig. 3. As found by other investigators, the maximum stagnation point heat transfer occurs at a Z/D of approximately 6. It is hoped that these results will be generally useful to those attempting to model turbulent jets impinging on a surface.

Acknowledgments

The authors gratefully acknowledge the support of the University of California UERG program. Professor Brian Launder made the original suggestion that these data were needed and made valuable suggestions during the course of work. The assistance of Anthony Hechanova, who has continued this research, is also appreciated.

References

Abuaf, N., Urbaetis, S. P., and Palmer, O. F., 1985, "Convection Thermography," General Electric Corporation Research and Development Report No. 85CRD168.

Amano, R. S., and Brandt, H., 1984, "Numerical Study of Turbulent Axisymmetric Jets Impinging on a Flat Plate and Flowing Into an Axisymmetric Cavity," ASME *Journal of Fluids Engineering*, Vol. 106, pp. 410-417.

Baughn, J. W., Hoffman, M. A., and Makel, D. B., 1986, "Improvements in a New Technique for Measuring and Mapping Heat Transfer Coefficients," *Review of Scientific Instruments*, Vol. 57, pp. 650-654.

Donaldson, C. duP., Snedeker, R. S., and Margolis, D. P., 1971, "A Study of Free Jet Impingement. Part 2. Free Jet Turbulent Structure and Impingement Heat Transfer," *Journal of Fluid Mechanics*, Vol. 45, Part 3, pp. 477-512.

Gardon, R., and Cobonpue, J., 1962, "Heat Transfer Between a Flat Plate and Jets of Air Impinging on It," *International Developments in Heat Transfer*, ASME, pp. 454-460.

Gardon, R., and Akfirat, C. J., 1965, "The Role of Turbulence in Determining the Heat-Transfer Characteristics of Impinging Jets," *International Journal of Heat and Mass Transfer*, Vol. 8, pp. 1261-1272.

Gardon, R., and Akfirat, C. J., 1966, "Heat Transfer Characteristics of Impinging Two-Dimensional Air Jets," ASME JOURNAL OF HEAT TRANSFER, Vol. 88, pp. 101-108.

Gauntner, J. W., Livingwood, J. N. B., and Hrycak, P., 1970, "Survey of Literature on Flow Characteristics of a Single Turbulent Jet Impinging on a Flat Plate," NASA TN D-5652.

Goldstein, R. J., and Behbahani, A. I., 1982, "Impingement of a Circular Jet With and Without Cross Flow," *International Journal of Heat and Mass Transfer*, Vol. 25, pp. 1377-1382.

Hechanova, T. E., 1988, "An Experimental Study of Entrainment Effects on Heat Transfer From a Surface With a Fully Developed Impinging Jet," M. S. Thesis, University of California, Davis.

Hinze, J. O., 1975, *Turbulence*, 2nd ed., McGraw-Hill, New York.

Hippensteele, S. A., Russell, L. M., and Stepka, P. S., 1983, "Evaluation of a Method for Heat Transfer Measurements and Thermal Visualization Using a Composite of a Heater Element and Liquid Crystals," ASME JOURNAL OF HEAT TRANSFER, Vol. 105, pp. 184-189.

Hishida, M., and Nagamo, Y., "Structure of Turbulent Velocity and Temperature Fluctuations in Fully Developed Pipe Flow," ASME JOURNAL OF HEAT TRANSFER, Vol. 101, pp. 15-22.

Hollworth, B. R., and Gero, L. R., 1985, "Entrainment Effects on Impingement Heat Transfer: Part II—Local Heat Transfer Measurements," ASME JOURNAL OF HEAT TRANSFER, Vol. 107, pp. 910-915.

Hrycak, P., 1983, "Heat Transfer for Round Impinging Jets to a Flat Plate," *International Journal of Heat and Mass Transfer*, Vol. 26, pp. 1857-1865.

Launder, B. E., 1987, personal communication.

Martin, H., 1977, "Heat and Mass Transfer Between Impinging Gas Jets and Solid Surfaces," *Advances in Heat Transfer*, Vol. 13, pp. 1-60.

Polat, S., Mujumdar, A. S., and Douglas, W. J. M., 1985, "Heat Transfer Distribution Under a Turbulent Impinging Jet—A Numerical Study," *Drying Technology*, Vol. 3, pp. 15-37.

Schlicting, H., 1968, *Boundary Layer Theory*, 6th ed., McGraw-Hill, New York.

Simonich, J. C., and Moffat, R. J., 1982, "A New Technique for Mapping Heat-Transfer Coefficient Contours," *Review of Scientific Instruments*, Vol. 53, pp. 678-683.

Striegl, S. A., and Diller, T. E., 1984, "The Effect of Entrainment Temperature on Jet Impingement Heat Transfer," ASME JOURNAL OF HEAT TRANSFER, Vol. 106, pp. 27-33.

Convective Heat Transfer Measurement Involving Flow Past Stationary Circular Disks

G. L. Wedekind[1]

Introduction

Considerable empirical data exist in the literature for forced convection heat transfer involving external flow over a variety of geometries, and for various ranges of Reynolds number. In fact, many current heat transfer textbooks (Kreith and Bohn, 1986; Incropera and Dewitt, 1981; Holman, 1986) present empirical correlations for flow over a flat plate, a sphere, a spheroid, and tubes in cross flow, and for tubes of cylindrical, square, hexagonal, and other assorted cross sections. A geometry that appears to be missing from this list is that of a thin circular disk. Although there has been considerable theoretical and experimental research devoted to natural convection for stationary and rotating circular disks and disk systems, such as that reported by Zakerullah and Ackroyd (1979), Mochizuki and Yeng (1986), and Owens (1984), this author is not aware of any published empirical data for forced convection heat transfer involving flow past a simple stationary circular disk, whose axis is perpendicular to the flow. Such is the purpose of this paper.

The disk geometry and its orientation to the external flow is schematically represented in Fig. 1. The disk has a diameter d, thickness t, is at a uniform temperature T, and is oriented as shown in a fluid having a uniform approach velocity v_f and a free-stream temperature T_f. The symbol $\dot{Q}$ represents the rate of convective heat transfer from the disk to the moving fluid.

Experimental Apparatus and Measurement Techniques

The circular disks that were used as heat transfer models for the experimental data presented in this paper were commercially available disk-type thermistors.[2] Five different models were tested. Thermistors were chosen as the heat transfer models because they provided a unique combination for indirectly measuring the surface temperature T, and the convective heat transfer rate $\dot{Q}$ (Wedekind, 1977). The thermistor was self-heated by means of Joule heating. Losses through the thermistor lead wires (0.22 mm dia) were minimized (less than 3 percent) by using an alloyed steel (such as 20 percent nickel steel), which had a poor enough thermal conductivity to minimize any "fin effect," yet a sufficient electrical conductivity that a negligible amount of Joule heating would exist in the lead wires themselves.

Therefore, by setting up an electrical circuit such as that shown in Fig. 2, the thermistor current and resistance could be accurately and simultaneously measured during self-heating, thus making it possible indirectly to measure not only the convective heat transfer rate, but also the average temperature of the thermistor as well; the latter by having precalibrated the resistance/temperature characteristics of each thermistor heat transfer model. Thermistors have a high resistance coefficient; therefore, the heat transfer surface temperature T could be in-

[1]Professor of Engineering, Oakland University, Rochester, MI 48309; Mem. ASME.

[2]Thermistors are semiconductors of ceramic material made by sintering mixtures of metalic oxides such as manganese, nickel, cobalt, copper, iron, and uranium. Disks are made by pressing thermistor material under high pressure in a round die to produce flat coinlike pieces. These pieces are sintered and then coated with silver on the two flat surfaces. Reference: Thermistor Manual; Fenwal Electronics, Framingham, MA 01701.

Contributed by the Heat Transfer Division for publication in the JOURNAL OF HEAT TRANSFER. Manuscript received by the Heat Transfer Division June 1, 1987. Keywords: Forced Convection, Measurement Techniques.

distributions occurs when the jet is quite close to the surface ($Z/D = 2$). In this case, the maximum heat transfer is at the stagnation point; the heat transfer then has a minimum at r/D of approximately 1.3, and another maximum at approximately 1.8. For certain runs this results in three concentric circles of color on the test section. The effect of jet distance from the surface on the stagnation point heat transfer is shown in Fig. 3. As found by other investigators, the maximum stagnation point heat transfer occurs at a Z/D of approximately 6. It is hoped that these results will be generally useful to those attempting to model turbulent jets impinging on a surface.

Acknowledgments

The authors gratefully acknowledge the support of the University of California UERG program. Professor Brian Launder made the original suggestion that these data were needed and made valuable suggestions during the course of work. The assistance of Anthony Hechanova, who has continued this research, is also appreciated.

References

Abuaf, N., Urbaetis, S. P., and Palmer, O. F., 1985, "Convection Thermography," General Electric Corporation Research and Development Report No. 85CRD168.

Amano, R. S., and Brandt, H., 1984, "Numerical Study of Turbulent Axisymmetric Jets Impinging on a Flat Plate and Flowing Into an Axisymmetric Cavity," ASME *Journal of Fluids Engineering*, Vol. 106, pp. 410-417.

Baughn, J. W., Hoffman, M. A., and Makel, D. B., 1986, "Improvements in a New Technique for Measuring and Mapping Heat Transfer Coefficients," *Review of Scientific Instruments*, Vol. 57, pp. 650-654.

Donaldson, C. duP., Snedeker, R. S., and Margolis, D. P., 1971, "A Study of Free Jet Impingement. Part 2. Free Jet Turbulent Structure and Impingement Heat Transfer," *Journal of Fluid Mechanics*, Vol. 45, Part 3, pp. 477-512.

Gardon, R., and Cobonpue, J., 1962, "Heat Transfer Between a Flat Plate and Jets of Air Impinging on It," *International Developments in Heat Transfer*, ASME, pp. 454-460.

Gardon, R., and Akfirat, C. J., 1965, "The Role of Turbulence in Determining the Heat-Transfer Characteristics of Impinging Jets," *International Journal of Heat and Mass Transfer*, Vol. 8, pp. 1261-1272.

Gardon, R., and Akfirat, C. J., 1966, "Heat Transfer Characteristics of Impinging Two-Dimensional Air Jets," ASME JOURNAL OF HEAT TRANSFER, Vol. 88, pp. 101-108.

Gauntner, J. W., Livingwood, J. N. B., and Hrycak, P., 1970, "Survey of Literature on Flow Characteristics of a Single Turbulent Jet Impinging on a Flat Plate," NASA TN D-5652.

Goldstein, R. J., and Behbahani, A. I., 1982, "Impingement of a Circular Jet With and Without Cross Flow," *International Journal of Heat and Mass Transfer*, Vol. 25, pp. 1377-1382.

Hechanova, T. E., 1988, "An Experimental Study of Entrainment Effects on Heat Transfer From a Surface With a Fully Developed Impinging Jet," M. S. Thesis, University of California, Davis.

Hinze, J. O., 1975, *Turbulence*, 2nd ed., McGraw-Hill, New York.

Hippensteele, S. A., Russell, L. M., and Stepka, P. S., 1983, "Evaluation of a Method for Heat Transfer Measurements and Thermal Visualization Using a Composite of a Heater Element and Liquid Crystals," ASME JOURNAL OF HEAT TRANSFER, Vol. 105, pp. 184-189.

Hishida, M., and Nagamo, Y., "Structure of Turbulent Velocity and Temperature Fluctuations in Fully Developed Pipe Flow," ASME JOURNAL OF HEAT TRANSFER, Vol. 101, pp. 15-22.

Hollworth, B. R., and Gero, L. R., 1985, "Entrainment Effects on Impingement Heat Transfer: Part II—Local Heat Transfer Measurements," ASME JOURNAL OF HEAT TRANSFER, Vol. 107, pp. 910-915.

Hrycak, P., 1983, "Heat Transfer for Round Impinging Jets to a Flat Plate," *International Journal of Heat and Mass Transfer*, Vol. 26, pp. 1857-1865.

Launder, B. E., 1987, personal communication.

Martin, H., 1977, "Heat and Mass Transfer Between Impinging Gas Jets and Solid Surfaces," *Advances in Heat Transfer*, Vol. 13, pp. 1-60.

Polat, S., Mujumdar, A. S., and Douglas, W. J. M., 1985, "Heat Transfer Distribution Under a Turbulent Impinging Jet—A Numerical Study," *Drying Technology*, Vol. 3, pp. 15-37.

Schlicting, H., 1968, *Boundary Layer Theory*, 6th ed., McGraw-Hill, New York.

Simonich, J. C., and Moffat, R. J., 1982, "A New Technique for Mapping Heat-Transfer Coefficient Contours," *Review of Scientific Instruments*, Vol. 53, pp. 678-683.

Striegl, S. A., and Diller, T. E., 1984, "The Effect of Entrainment Temperature on Jet Impingement Heat Transfer," ASME JOURNAL OF HEAT TRANSFER, Vol. 106, pp. 27-33.

Convective Heat Transfer Measurement Involving Flow Past Stationary Circular Disks

G. L. Wedekind[1]

Introduction

Considerable empirical data exist in the literature for forced convection heat transfer involving external flow over a variety of geometries, and for various ranges of Reynolds number. In fact, many current heat transfer textbooks (Kreith and Bohn, 1986; Incropera and Dewitt, 1981; Holman, 1986) present empirical correlations for flow over a flat plate, a sphere, a spheroid, and tubes in cross flow, and for tubes of cylindrical, square, hexagonal, and other assorted cross sections. A geometry that appears to be missing from this list is that of a thin circular disk. Although there has been considerable theoretical and experimental research devoted to natural convection for stationary and rotating circular disks and disk systems, such as that reported by Zakerullah and Ackroyd (1979), Mochizuki and Yeng (1986), and Owens (1984), this author is not aware of any published empirical data for forced convection heat transfer involving flow past a simple stationary circular disk, whose axis is perpendicular to the flow. Such is the purpose of this paper.

The disk geometry and its orientation to the external flow is schematically represented in Fig. 1. The disk has a diameter d, thickness t, is at a uniform temperature T, and is oriented as shown in a fluid having a uniform approach velocity v_f and a free-stream temperature T_f. The symbol $\dot{Q}$ represents the rate of convective heat transfer from the disk to the moving fluid.

Experimental Apparatus and Measurement Techniques

The circular disks that were used as heat transfer models for the experimental data presented in this paper were commercially available disk-type thermistors.[2] Five different models were tested. Thermistors were chosen as the heat transfer models because they provided a unique combination for indirectly measuring the surface temperature T, and the convective heat transfer rate $\dot{Q}$ (Wedekind, 1977). The thermistor was self-heated by means of Joule heating. Losses through the thermistor lead wires (0.22 mm dia) were minimized (less than 3 percent) by using an alloyed steel (such as 20 percent nickel steel), which had a poor enough thermal conductivity to minimize any "fin effect," yet a sufficient electrical conductivity that a negligible amount of Joule heating would exist in the lead wires themselves.

Therefore, by setting up an electrical circuit such as that shown in Fig. 2, the thermistor current and resistance could be accurately and simultaneously measured during self-heating, thus making it possible indirectly to measure not only the convective heat transfer rate, but also the average temperature of the thermistor as well; the latter by having precalibrated the resistance/temperature characteristics of each thermistor heat transfer model. Thermistors have a high resistance coefficient; therefore, the heat transfer surface temperature T could be in-

[1]Professor of Engineering, Oakland University, Rochester, MI 48309; Mem. ASME.

[2]Thermistors are semiconductors of ceramic material made by sintering mixtures of metalic oxides such as manganese, nickel, cobalt, copper, iron, and uranium. Disks are made by pressing thermistor material under high pressure in a round die to produce flat coinlike pieces. These pieces are sintered and then coated with silver on the two flat surfaces. Reference: Thermistor Manual; Fenwal Electronics, Framingham, MA 01701.

Contributed by the Heat Transfer Division for publication in the JOURNAL OF HEAT TRANSFER. Manuscript received by the Heat Transfer Division June 1, 1987. Keywords: Forced Convection, Measurement Techniques.

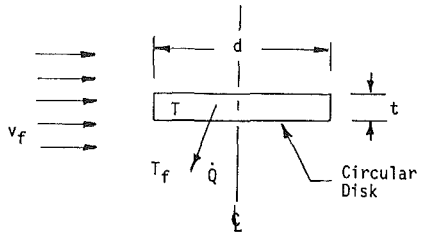

Fig. 1 Schematic of disk and orientation to flow

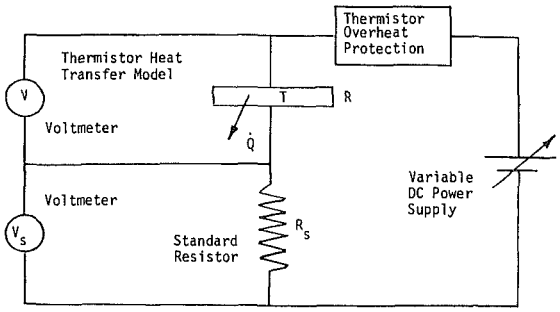

Fig. 2 Electrical circuit; measurement of thermistor temperature and heat transfer rate

directly measured quite accurately,[3] without the many difficulties encountered in attempting to measure surface temperatures (especially on small heat transfer models) by conventional means.[4]

The average convective heat transfer coefficient h can be expressed in terms of the heat transfer rate $\dot{Q}$, the heat transfer area A (the total surface area of the disk), and the temperature difference $(T-T_f)$ between the surface and the fluid; thus

$$h=\dot{Q}/A(T-T_f) \tag{1}$$

Since care was given to make the "fin effect" of the lead (support) wires negligible, the heat transfer rate $\dot{Q}$ from the disk thermistor is equal to the Joule heating of the thermistor, thus

$$\dot{Q}=V^2/R \tag{2}$$

However, since the thermistor is in series with a standard resistor of known value, R_s, then the thermistor resistance R can be expressed as

$$R=R_s(V/V_s) \tag{3}$$

Substituting equation (3) into equation (2) provides a means of indirectly measuring the convective heat transfer rate from the disk in terms of the standard resistance R_s, and the voltage drop across the thermistor and the standard resistor, V and V_s, respectively; thus

$$\dot{Q}=(VV_s)/R_s \tag{4}$$

The disk surface temperature T is indirectly measured by utilizing the exponential relationship that exists between the thermistor resistance R and its absolute temperature T, which is of the form

$$R=R(T)=\alpha e^{\beta/T} \tag{5}$$

where the parameters α and β are unique for a given thermistor, and can be determined by calibration measurements. Once these parameters are known for a given thermistor heat transfer model, the thermistor temperature T can be readily determined in terms of its resistance R by rearranging equation (5); thus

$$T=\beta/\ln(R/\alpha) \tag{6}$$

where R is given by equation (3).

A sketch of the experimental apparatus,[5] which amounts to a miniature wind tunnel made possible by the smallness of the thermistor heat transfer models, is shown in Fig. 3. The inside diameter of the test section where the thermistor disks were mounted was 3.25 cm. The length of the velocity development or approach section was 26.5 cm. Uniformity of velocity upstream of the heat transfer model was within 8 percent as measured by a pitot-tube traverse. The air velocity was varied by controlling the inlet air flow rate. The free-stream air temperature was measured with a thermocouple probe, and a d-c power supply was used as the current source to self-heat the thermistor. Multimeters were used simultaneously to measure the voltage drop across the thermistor and a standard resistor of known resistance, which, as shown in Fig. 2, was connected in series with the thermistor.[6]

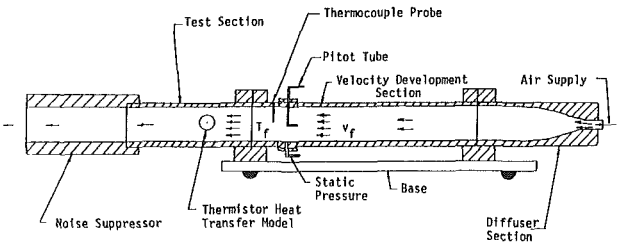

Fig. 3 Sketch of experimental apparatus

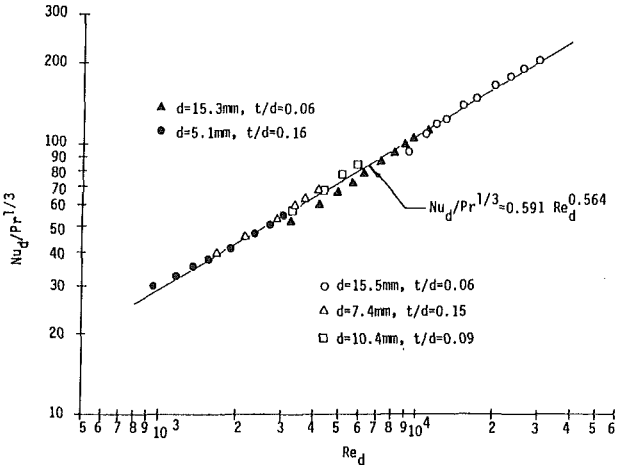

Fig. 4 Convective heat transfer for flow past a stationary circular disk whose axis is perpendicular to the flow

Experimental Data and Results

As was mentioned earlier, five different sized disk heat transfer models were tested. Their diameters d ranged from 5.1-15.5 mm, and the thickness to diameter ratio, t/d, from

[3] This assumes the temperature to be uniform within the thermistor. Since the thermistor is thin, with a uniform voltage difference between its flat surfaces, the current flux will be uniform, resulting in a uniform Joule heating within the disk. Therefore, a simple one-dimensional thermal analysis indicates a worst case temperature difference between the center plane and the flat surfaces of the disk to be less than 1°C for the range of experimental data presented. Radial temperature variation, due to local variation in the convective boundary flux, will also be small because the thermal conductivity of the thermistor material is sufficiently high.

[4] The experimental measurement difficulties alluded to here are those associated with attempting to measure surface temperatures by mounting a temperature sensor such as a thermocouple on the surface. The presence of the thermocouple distorts the true surface temperature to varying degrees, depending upon the relative size of heat transfer surface. The major mechanism for this distortion is the conduction fin effects within the thermocouple wires, which would tend to lower the temperature of a heated surface at the point of measurement.

[5] A Convective Heat Transfer Measurement System, Model #9056, which utilizes a variety of thermistor geometries as convective heat transfer models, is manufactured by TECHNOVATE, Inc., Pompano Beach, FL 33069.

[6] Care had to be taken in such a circuit to guard against the possibility of thermistor overheat, due to the negative resistance coefficient characteristic of most thermistors.

0.06–0.16. The edges of the disks were relatively sharp (edge radius $\cong 0.04$ mm). Air velocities v_f, ranged from approximately 2–35 m/s (7–114 ft/s), temperature differences $(T - T_f)$ from 39–56°C (70–100°F), and convective heat transfer coefficients h from 81–307 $W/m^2 - °C$ (14–54 $Btu/hr - ft^2 - °F$). Property values for the air, which was at atmospheric pressure, were evaluated at a film temperature, $(T + T_f)/2$. This yielded Reynolds numbers, $Re_d = \rho v_f d/\mu$, ranging from 9.6×10^2 to 3.0×10^4.

The experimental results are depicted in dimensionless form in Fig. 4, where $Nu_d/Pr^{1/3}$ is plotted as a function of Re_d. Experiments yielding these data have been repeated many times over a number of years, with excellent repeatability. A single empirical correlation, which best fits all of the data, is given by

$$Nu_d = 0.591\ Pr^{1/3}\ Re_d^{0.564}; \quad 9 \times 10^2 \le Re_d \le 3 \times 10^4 \qquad (7)$$

with a correlation coefficient of 0.997, and a maximum deviation of less than 12 percent. Interestingly, an analysis of the experimental uncertainty in the indirect measurement of the convective heat transfer coefficient, due to uncertainties in the various direct measurements, indicates a maximum error of approximately 12 percent. From a statistical perspective, however, the measurement errors would normally be expected to be less than the maximum. This seems to be borne out in the relatively small level of scatter in the experimental data. One of the reasons for this relatively high level of accuracy is due to the technique of using thermistor disks as the heat transfer models, and utilizing their associated resistance/temperature characteristics for measuring surface temperature and Joule heating for measuring heat transfer rate. It should be noted that the range of Reynolds numbers obtained for the above data represented the limits of the existing experimental apparatus and heat transfer models, not necessarily the limit of the correlation.

Experimental uncertainty in the Prandtl number is assumed negligible since it is primarily a function of air temperature, which was accurate to within ±0.6°C. Maximum experimental uncertainty in Reynolds number was ±7 percent, due primarily to uncertainty in the velocity measurement. Maximum experimental uncertainty in the Nusselt number was ±12 percent, due primarily to uncertainty in the measured convective heat transfer coefficient. Uncertainty in geometry measurements were relatively small, and thus their only significant influence was in the measurement uncertainty of the convective heat transfer coefficient.

Although only thin disks were tested (the thickness-to-diameter ratio t/d varied from 0.06–0.16), an attempt was made to discern any influence of the thickness-to-diameter ratio. If any influence existed, it must have been less than that of the experimental uncertainty in the measurements, since no discernible pattern of influence was observed. Referring to Fig. 4, there appears to be some systematic difference between the experimental data for the 15.3-mm-dia disk represented by the solid triangles and the rest of the data. The possibility that this systematic difference is caused by blockage effects seems to be ruled out by the fact that this disk, even though it was the largest of the heat transfer models, occupied only 1.8 percent of the cross-sectional area of the test section duct. Furthermore, the data for a different disk model but with the same 15.3-mm diameter (represented by open circles) agrees with the rest of the data.

One possible explanation for the apparent systematic difference in the data for the one model could be that the axis of the disk was not perfectly perpendicular to the flow stream when the data were taken. However, it is important not to lose sight of the relatively small amount of scatter that exists in the overall data, especially when consideration is given to the complexity of the physical mechanisms involved, and the normal level of experimental scatter found in most empirical correlations for convective heat transfer.

Acknowledgments

The author would like to thank the many students who have participated over the years in developing the experimental capability, and in the acquisition of the data pertinent to this paper.

References

Holman, J. P., 1986, *Heat Transfer*, McGraw-Hill, New York, pp. 291–293, 308–309.

Incropera, F. P., and DeWitt, D. P., 1981, *Fundamentals of Heat Transfer*, Wiley, New York, pp. 344–345, 363–364.

Kreith, F., and Bohn, M. S., 1986, *Principles of Heat Transfer*, Harper and Row, New York, pp. 236, 356, 361.

Mochizuki, S., and Yeng, Wen-Jei, 1986, "Three Mechanisms of Convective Enhancement in Stationary Disk Systems," ASME JOURNAL OF HEAT TRANSFER, Vol. 108, pp. 978–980.

Owens, J. M., 1984, "Fluid Flow and Heat Transfer in Rotating Disk Systems," in: *Heat and Mass Transfer in Rotating Machinery*, D. E. Metzger and N. H. Afgan, eds., Hemisphere, Washington, DC, pp. 81–102.

Wedekind, G. L., 1977, "Convective Heat Transfer Measurement System," Compendium, CLOSE Workshop, ASEE Annual Meeting, University of North Dakota, p. 67.

Zakerullah, M., and Ackroyd, J. A. D., 1979, "Laminar Natural Convection Boundary Layers on Horizontal Circular Disk," *Journal of Applied Mathematics and Physics*, Vol. 30, pp. 427–435.

Variable Property Effects on Convection in a Heat Generating Porous Medium

C. L. G. Dona[1] and W. E. Stewart, Jr.[1]

Nomenclature

- a = coefficient in momentum equation
- b = coefficient in momentum equation
- c_p = specific heat
- d = diameter
- DH = hydraulic diameter
- g = gravitational acceleration
- H = height of cylinder
- k_m = bulk thermal conductivity
- k_E = Ergun product constant
- P = pressure
- $\dot{q}'''$ = uniform heat generation rate per unit volume
- r = radial direction
- R = radius of cylinder
- Ra = modified Rayleigh number $= \dfrac{gR^2H\dot{q}'''\kappa(\rho c_p)_f}{\nu_f k_m^2 T_\infty k_E}$
- Ra_∞ = reference Rayleigh number = Ra T/T_∞
- t = time
- T = temperature
- T_∞ = isothermal boundary temperature
- v_r = radial velocity
- v_z = axial velocity
- v = total velocity $= (v_r^2 + v_z^2)^{1/2}$
- z = axial direction
- α = $k_m/(\rho c_p)_f$
- ϵ = porosity

[1]Energy Research Laboratory, Department of Mechanical and Aerospace Engineering, University of Missouri—Columbia/Kansas City, Truman Campus, Independence, MO 64050.

Contributed by the Heat Transfer Division for publication in the JOURNAL OF HEAT TRANSFER. Manuscript received by the Heat Transfer Division September 7, 1988. Keywords: Enclosure Flows, Natural Convection, Porous Media.

0.06–0.16. The edges of the disks were relatively sharp (edge radius $\cong 0.04$ mm). Air velocities v_f, ranged from approximately 2–35 m/s (7–114 ft/s), temperature differences $(T - T_f)$ from 39–56°C (70–100°F), and convective heat transfer coefficients h from 81–307 $W/m^2 - °C$ (14–54 $Btu/hr - ft^2 - °F$). Property values for the air, which was at atmospheric pressure, were evaluated at a film temperature, $(T + T_f)/2$. This yielded Reynolds numbers, $Re_d = \rho v_f d/\mu$, ranging from 9.6×10^2 to 3.0×10^4.

The experimental results are depicted in dimensionless form in Fig. 4, where $Nu_d/Pr^{1/3}$ is plotted as a function of Re_d. Experiments yielding these data have been repeated many times over a number of years, with excellent repeatability. A single empirical correlation, which best fits all of the data, is given by

$$Nu_d = 0.591\ Pr^{1/3}\ Re_d^{0.564}; \quad 9 \times 10^2 \le Re_d \le 3 \times 10^4 \qquad (7)$$

with a correlation coefficient of 0.997, and a maximum deviation of less than 12 percent. Interestingly, an analysis of the experimental uncertainty in the indirect measurement of the convective heat transfer coefficient, due to uncertainties in the various direct measurements, indicates a maximum error of approximately 12 percent. From a statistical perspective, however, the measurement errors would normally be expected to be less than the maximum. This seems to be borne out in the relatively small level of scatter in the experimental data. One of the reasons for this relatively high level of accuracy is due to the technique of using thermistor disks as the heat transfer models, and utilizing their associated resistance/temperature characteristics for measuring surface temperature and Joule heating for measuring heat transfer rate. It should be noted that the range of Reynolds numbers obtained for the above data represented the limits of the existing experimental apparatus and heat transfer models, not necessarily the limit of the correlation.

Experimental uncertainty in the Prandtl number is assumed negligible since it is primarily a function of air temperature, which was accurate to within ±0.6°C. Maximum experimental uncertainty in Reynolds number was ±7 percent, due primarily to uncertainty in the velocity measurement. Maximum experimental uncertainty in the Nusselt number was ±12 percent, due primarily to uncertainty in the measured convective heat transfer coefficient. Uncertainty in geometry measurements were relatively small, and thus their only significant influence was in the measurement uncertainty of the convective heat transfer coefficient.

Although only thin disks were tested (the thickness-to-diameter ratio t/d varied from 0.06–0.16), an attempt was made to discern any influence of the thickness-to-diameter ratio. If any influence existed, it must have been less than that of the experimental uncertainty in the measurements, since no discernible pattern of influence was observed. Referring to Fig. 4, there appears to be some systematic difference between the experimental data for the 15.3-mm-dia disk represented by the solid triangles and the rest of the data. The possibility that this systematic difference is caused by blockage effects seems to be ruled out by the fact that this disk, even though it was the largest of the heat transfer models, occupied only 1.8 percent of the cross-sectional area of the test section duct. Furthermore, the data for a different disk model but with the same 15.3-mm diameter (represented by open circles) agrees with the rest of the data.

One possible explanation for the apparent systematic difference in the data for the one model could be that the axis of the disk was not perfectly perpendicular to the flow stream when the data were taken. However, it is important not to lose sight of the relatively small amount of scatter that exists in the overall data, especially when consideration is given to the complexity of the physical mechanisms involved, and the normal level of experimental scatter found in most empirical correlations for convective heat transfer.

Acknowledgments

The author would like to thank the many students who have participated over the years in developing the experimental capability, and in the acquisition of the data pertinent to this paper.

References

Holman, J. P., 1986, *Heat Transfer*, McGraw-Hill, New York, pp. 291–293, 308–309.

Incropera, F. P., and DeWitt, D. P., 1981, *Fundamentals of Heat Transfer*, Wiley, New York, pp. 344–345, 363–364.

Kreith, F., and Bohn, M. S., 1986, *Principles of Heat Transfer*, Harper and Row, New York, pp. 236, 356, 361.

Mochizuki, S., and Yeng, Wen-Jei, 1986, "Three Mechanisms of Convective Enhancement in Stationary Disk Systems," ASME JOURNAL OF HEAT TRANSFER, Vol. 108, pp. 978–980.

Owens, J. M., 1984, "Fluid Flow and Heat Transfer in Rotating Disk Systems," in: *Heat and Mass Transfer in Rotating Machinery*, D. E. Metzger and N. H. Afgan, eds., Hemisphere, Washington, DC, pp. 81–102.

Wedekind, G. L., 1977, "Convective Heat Transfer Measurement System," Compendium, CLOSE Workshop, ASEE Annual Meeting, University of North Dakota, p. 67.

Zakerullah, M., and Ackroyd, J. A. D., 1979, "Laminar Natural Convection Boundary Layers on Horizontal Circular Disk," *Journal of Applied Mathematics and Physics*, Vol. 30, pp. 427–435.

Variable Property Effects on Convection in a Heat Generating Porous Medium

C. L. G. Dona[1] and W. E. Stewart, Jr.[1]

Nomenclature

- a = coefficient in momentum equation
- b = coefficient in momentum equation
- c_p = specific heat
- d = diameter
- DH = hydraulic diameter
- g = gravitational acceleration
- H = height of cylinder
- k_m = bulk thermal conductivity
- k_E = Ergun product constant
- P = pressure
- $\dot{q}'''$ = uniform heat generation rate per unit volume
- r = radial direction
- R = radius of cylinder
- Ra = modified Rayleigh number $= \dfrac{gR^2H\dot{q}'''\kappa(\rho c_p)_f}{\nu_f k_m^2 T_\infty k_E}$
- Ra_∞ = reference Rayleigh number = Ra T/T_∞
- t = time
- T = temperature
- T_∞ = isothermal boundary temperature
- v_r = radial velocity
- v_z = axial velocity
- v = total velocity $= (v_r^2 + v_z^2)^{1/2}$
- z = axial direction
- α = $k_m/(\rho c_p)_f$
- ϵ = porosity

[1]Energy Research Laboratory, Department of Mechanical and Aerospace Engineering, University of Missouri—Columbia/Kansas City, Truman Campus, Independence, MO 64050.

Contributed by the Heat Transfer Division for publication in the JOURNAL OF HEAT TRANSFER. Manuscript received by the Heat Transfer Division September 7, 1988. Keywords: Enclosure Flows, Natural Convection, Porous Media.

θ = dimensionless temperature = $(T - T_\infty)/(\dot{q}''' RH/k_m)$
κ = bulk permeability $= \dfrac{\epsilon^3 d^2}{150(1-\epsilon)^2 k_E}$
μ = dynamic viscosity
ν_f = kinematic viscosity of air $= \mu/\rho$
$\nu_{f\infty}$ = kinematic viscosity of air at $T_\infty = \mu_\infty/\rho_\infty$
ρ = density of air
ρ_∞ = density of air at T_∞
σ = $(\rho c_p)_m/(\rho c_p)_f$
ψ = stream function

Superscript

— = dimensional value

Introduction

Convection heat transfer in a fluid-saturated porous medium has many applications, such as in oil and gas production, grain storage, and geothermal energy. A number of numerical studies have been carried out using Darcy's law to formulate the natural convection heat transfer mathematically in enclosures of internally heat-generating porous media (e.g., Tveitereid, 1967; Beukema et al. 1983; Stewart and Dona, 1988).

Kwok and Chen (1987) considered temperature-dependent density and kinematic viscosity in the stability of convection in a vertical porous layer. Inclusion of variable viscosity produced stable flows over greater temperature differences in the porous layer. Zhong et al. (1985) found that variable viscosity tended to delay the onset of convection in a square cavity, due to higher temperatures and the resultant higher viscosities. Blythe and Simpkins (1981) showed the variation in dimensionless temperature in a differentially heated porous layer to be as much as 30 percent.

Generally, Darcy's law remains valid as long as the Reynolds number, vD_H/γ_f, remains less than 1, where v is defined as

$$v = = \frac{\kappa}{\mu}(-\nabla P + \rho g) \tag{1}$$

When Re increases above 1, inertia effects, which are ignored in equation (1), may become significant. Irmay (1958) started with the Navier-Stokes equations to derive a momentum equation of the form

$$\nabla (dP + z) = a\mathbf{v} + bv\mathbf{v} \tag{2}$$

to be used for apparent Reynolds numbers greater than one. Different modifications of equation (1) have been suggested to take into account inertia forces (after Forchheimer).

Experimental verification of equation (2) was found by Ward (1964) for both laminar and turbulent flow in porous media, by Beavers and Sparrow (1969) for non-Darcy flow through fibrous porous media, by Masha et al. (1974) for non-Darcy flow of compressible gases in porous media, and by Koh et al. (1977) for isothermal and nonisothermal gaseous flow through a porous medium. Patterson et al. (1971) extended equation (2), calculating values of a and b specifically for packed beds of cereal grain of different densities, porosities, and temperatures.

This paper uses Irmay's momentum equation, equation (2), for radial and axial equations that include inertia terms. With the corresponding energy equation, equation (2) was used to model an internally heat-generating porous medium in a short, vertical circular cylinder ($R = 2$ m, $H = 4$ m). The cylinder side and top are isothermal and at the same temperature (T_∞). The bottom surface of the cylinder is adiabatic.

The variations in density and viscosity with temperature and inertia are investigated. For slow flows, the effect of inertia would be expected to be small. For large temperature variations, the effects of variable dynamic viscosity and density are expected to be large. The density and the dynamic viscosity of air were represented by the relationships $\rho = \rho_\infty(1 - (T - T_\infty)/T)$ and $\nu = \nu_\infty(1 + 2(T - T_\infty)/T_\infty)$. These relationships for ρ and ν are accurate for air between 20 and 200°C.

Numerical Model

An incompressible fluid is assumed for the fluid (thermophysical properties of air) except in the buoyancy term, ρg_z, using the Boussinesq approximation. The resulting axial and radial equations, respectively, from equation (2), are, using the coefficients of Patterson et al. (1971) for a' and b'

$$\frac{\partial P}{\partial \bar{z}} = -(a + b(\bar{v}_z^2 + \bar{v}_r^2)^{1/2})\bar{v}_z - \rho g_z \tag{3}$$

$$\frac{\partial P}{\partial \bar{r}} = -(a + b(\bar{v}_z^2 + \bar{v}_r^2)^{1/2})\bar{v}_r \tag{4}$$

where

$$a = k_E\left(150\frac{(1-\epsilon)^2}{\epsilon^3}\frac{\mu}{d^2}\right)$$

$$b = k_E\left(1.75\frac{(1-\epsilon)}{\epsilon^3}\frac{\rho}{d}\right)$$

Nondimensionalizing the equations with

$$r = \bar{r}/R, \quad \bar{z}/R, \quad \psi = \bar{\psi}/(\alpha R),$$

$$\theta = (T - T_\infty)/(\dot{q}''' RH/k_m), \text{ and } t = \alpha \bar{t}/R^2$$

the nondimensional energy equation becomes (Stewart and Dona, 1988)

$$\sigma\frac{\partial\theta}{\partial t} + \frac{1}{r}\frac{\partial\psi}{\partial z}\frac{\partial\theta}{\partial r} - \frac{1}{r}\frac{\partial\psi}{\partial r}\frac{\partial\theta}{\partial z} = \frac{1}{r}\frac{\partial}{\partial r}\left(r\frac{\partial\theta}{\partial r}\right) + \frac{\partial^2\theta}{\partial z^2} + \frac{R}{H} \tag{5}$$

where the solid and fluid are assumed to be in thermal equilibrium.

By taking the cross derivatives of equations (3) and (4) to eliminate the pressure terms, and using the approximation $\rho = \rho_\infty(1 - (T - T_\infty)/T)$ in the buoyancy term, the nondimensional momentum equation becomes

$$\left(1 + \frac{b}{a}\frac{\alpha}{R}v_T\right)\left(\frac{1}{r^2}\frac{\partial\psi}{\partial r} - \frac{1}{r}\frac{\partial^2\psi}{\partial r^2} - \frac{1}{r}\frac{\partial^2\psi}{\partial r^2}\right)$$
$$+ \frac{b}{a}\frac{\alpha}{R}\frac{1}{v_T}\left(\frac{1}{r}\frac{\partial\psi}{\partial r}\left(\frac{1}{r}\frac{\partial\psi}{\partial z}\left(\frac{1}{r}\frac{\partial^2\psi}{\partial z\partial r} - \frac{1}{r^2}\frac{\partial\psi}{\partial z}\right)\right.\right.$$
$$\left.\left. - \frac{1}{r}\frac{\partial\psi}{\partial r}\left(\frac{1}{r^2}\frac{\partial\psi}{\partial r} - \frac{1}{r}\frac{\partial^2\psi}{\partial r^2}\right)\right)\right) + \frac{b}{a}\frac{\alpha}{R}\frac{1}{v_T}$$
$$\frac{1}{r}\frac{\partial\psi}{\partial z}\left(\frac{1}{r}\frac{\partial\psi}{\partial z}\frac{1}{r}\frac{\partial^2\psi}{\partial z^2} + \frac{1}{r}\frac{\partial\psi}{\partial r}\frac{1}{r}\frac{\partial^2\psi}{\partial z\partial r}\right)$$
$$= -\mathrm{Ra}\frac{\partial\theta}{\partial r} \tag{6}$$

where

$$v_T = \left(\left(\frac{1}{r}\frac{\partial\psi}{\partial r}\right)^2 + \left(\frac{1}{r}\frac{\partial\psi}{\partial z}\right)^2\right)^{1/2}$$

The Rayleigh number, which varies with temperature, as defined by equation (6), is

$$\mathrm{Ra} = \frac{gR^2H\dot{q}'''\kappa(\rho c_p)_f}{\nu_f k_m^2 T} \tag{7}$$

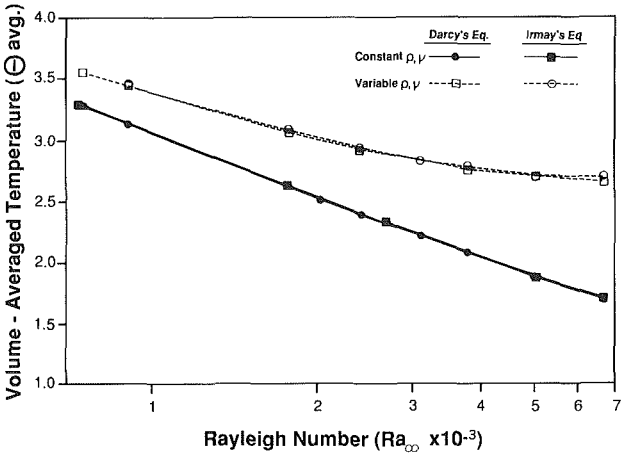

Fig. 1 Comparison of volume-averaged temperatures with Rayleigh number, with and without inertia effects, variable density, and viscosity

Also, a Rayleigh number can be defined that normalizes the temperature variations as

$$\mathrm{Ra}_\infty = T/T_\infty \mathrm{Ra} \tag{8}$$

Stream function values at the cylinder surfaces and axial centerline were set equal to zero to allow for slip flow to occur at all surfaces. The boundary conditions and initial condition for equations (5) and (6) are $\theta(1, z, t)=0$, $\theta(r, H/R, t)=0$, $\partial\theta(r, 0, t)/\partial z=0$, $\partial\theta(0, z, t)/\partial r=0$, $\theta(r, z, 0)=0$, $\psi(r, 0, t)=0$, $\psi(r, H/R, t)=0$, $\psi(1, z, t)=0$, and $\psi(0, z, t)=0$. The solution technique, using explicit finite differences for equations (5) and (6), was previously described by Stewart and Dona (1988).

Results and Discussion

Dimensionless temperature results obtained from varying heat generation rate (Ra_∞) for constant and variable density and viscosity with and without inertia effects are shown in Fig. 1. Using Darcy's law (equation (1)) without inertia terms for the range of relatively low Rayleigh numbers shows the change in volume-averaged dimensionless temperature, θ_{avg}, to be relatively insignificant.

The differences due to the addition of the temperature-dependent density and dynamic viscosity values in the value of θ_{avg} are also shown in Fig. 1. At low Rayleigh numbers, the average dimensional temperatures are small, where conduction dominates and θ_{avg} is large. For constant and variable density and viscosity, the difference in θ_{avg} is on the order of 10 percent. As the heat generation rate and resultant dimensional temperatures increased, convection increases and θ_{avg} decreases. The difference between θ_{avg} for constant and variable density and viscosity also increases. This increase in θ_{avg} occurs because the Rayleigh number is proportional to ρ_f, which decreases with temperature, and inversely proportional to ν_f, which increases with temperature. The relative reduction in Rayleigh number decreases the convective flow with a resultant increase in temperature and θ_{avg}.

At a Rayleigh number of 7000, the difference between θ_{avg} for constant and variable density and viscosity is approximately 57 percent as compared to the 30 percent maximum difference found by Blythe and Simpkins. The larger variation in θ_{avg} found in this study is largely explained by (1) the use of both variable density and viscosity as opposed to use by Blythe and Simpkins of variable viscosity only, and (2) the significant difference in boundary conditions between the two studies. Blythe and Simpkins modeled the temperature variation in a rectangular cavity with the two vertical surfaces at different but steady temperatures. In this study, the maximum temperature increases with heat generation rate and occurs at the middle of the cylinder where the symmetric, reflective boundary condition effectively creates an insulatory boundary. Both of these differences would be expected to produce the larger temperature variation found here.

Oscillatory behavior, though not considered here, may potentially develop at large Rayleigh numbers. Oscillatory behavior is not expected to develop for the cylinder modeled here. The maximum temperature does not exist near the bottom of the cylinder, but rather near $Z=0.83$, almost at the top of the cylinder. This also results in a positive temperature gradient, from the bottom to the top, for 83 percent of the height of the cylinder.

The accuracy of the numerical simulation can be determined from the difference between the heat generated and the heat removed at the boundary of the cylinder at steady state. The heat removed at the boundary of the cylinder is determined by a heat balance on each boundary node in the finite difference model. The results of these calculations reveal differences between 5 to 10 percent, over the Rayleigh number range, in heat generated/heat lost for the constant density and viscosity case, with or without inertia terms. The maximum difference for variable density and viscosity was approximately 1.4 percent between the inertia/no inertia cases, and for constant density and viscosity the difference was approximately 0.4 percent between the inertia/no inertia cases over the whole Rayleigh number range.

Conclusions

Natural convection heat transfer in a short vertical cylinder has been investigated numerically for a volumetrically heated porous medium. The inclusion of inertia in the momentum equations results in small differences in the maximum temperatures that occur in the cylinder for Rayleigh numbers up to 7000. The effects of variable density and viscosity, at the highest Rayleigh number, result in a significant change in volume-averaged dimensionless temperatures, approximately 57 percent. The use of temperature variable properties has revealed the requirement for inclusion of this refinement in numerical models and especially for the physical situation modeled in this study.

References

Beavers, G. S., and Sparrow, E. M., 1969, "Non-Darcy Flow Through Fibrous Porous Media," ASME *Journal of Applied Mechanics*, Vol. 36, pp. 711-714.

Beukema, K. J., Bruin, S., and Schenk, J., 1983, "Three-Dimensional Natural Convection in a Confined Porous Medium With Internal Heat Generation," *International Journal of Heat and Mass Transfer*, Vol. 26, pp. 451-458.

Blythe, P. A., and Simpkins, P. G., 1981, "Convection in a Porous Layer for a Temperature Dependent Viscosity," *International Journal of Heat and Mass Transfer*, Vol. 24, pp. 497-506.

Irmay, S., 1958, "On the Theoretical Derivation of Darcy and Forchheimer Formulae," *Trans. Am. Geophys. Un.*, Vol. 39, pp. 702-706.

Kowk, L. P., and Chen, C. F., 1987, "Stability of Thermal Convection in a Vertical Porous Layer," *Proc. ASME/JSME Thermal Engineering Joint Conference*, Honolulu, HI, Vol. II, pp. 343-348.

Koh, J. C., Dutton, J. L., and Benson, B. A., 1977, "Friction Factor for Isothermal and Nonisothermal Flow Through Porous Media," ASME JOURNAL OF HEAT TRANSFER, Vol. 99, pp. 367-373.

Masha, B. A., Beavers, G. S., and Sparrow, E. M., 1974, "Experiments on the Resistance Law for Non-Darcy Compressible Gas Flows in Porous Media," ASME *Journal of Fluids Engineering*, pp. 353-357.

Patterson, R. J., Bakkar-Arkema, F. W., and Bickert, W. G., 1971, "Static Pressure Airflow Relationships in Packed Beds of Granular Biological Materials Such as Grain—II," *Trans. Am. Soc. Agric. Engrs.*, Vol. 14, pp. 172-174, 178.

Stewart, W. E., Jr., and Dona, C. L. G., 1988, "Free Convection in a Heat-Generating Porous Medium in a Finite Vertical Cylinder," ASME JOURNAL OF HEAT TRANSFER, Vol. 110, pp. 517-520.

Tveitereid, M., 1967, "Thermal Convection in a Horizontal Porous Layer With Internal Heat Sources," *International Journal of Heat and Mass Transfer*, Vol. 20, pp. 1045-1050.

Ward, J. C., 1964, "Turbulent Flow in Porous Media," *J. of the Hydraulics Division*, Hy. 5, pp. 1-11.

Zhong, Z. Y., Yang, K. T., and Lloyd, J. R., 1985, "Variable Property Effects in Laminar Natural Convection in a Square Enclosure," ASME JOURNAL OF HEAT TRANSFER, Vol. 107, pp. 133-138.

Forced Convection in a Channel Filled With a Porous Medium: An Exact Solution

K. Vafai[1] and S. J. Kim[1]

Nomenclature

C_p = specific heat, $Jkg^{-1}K^{-1}$
Da = Darcy number, defined by equation (7*a*)
h = convective heat transfer coefficient, $Wm^{-2}K^{-1}$
H = one half of channel height
F = a function that depends on the Reynolds number and the microstructure of the porous medium
k_e = effective thermal conductivity, $Wm^{-1}K^{-1}$
K = permeability of the porous medium, m^2
Nu = Nusselt number, defined by equation (12)
p = pressure
T = temperature, K
u = dimensionless x-component velocity $= \langle u \rangle / u_\infty$
u_∞ = x-component velocity outside the momentum boundary layer
x = horizontal coordinate
y = vertical coordinate
α_e = effective thermal diffusivity $= k_e/\rho_f C_p$, m^2s^{-1}
δ = porosity of the porous medium
Λ_I = inertia parameter, defined by equation (7*b*)
μ_f = fluid viscosity, $kg\ m^{-1}s^{-1}$
ν_f = kinematic viscosity, m^2s^{-1}
ρ_f = fluid density, $kg\ m^{-3}$
$\langle\ \rangle$ = "local volume average" of a quantity

Introduction

Utilizing porous media in such contemporary technology as thermal insulation, direct contact heat exchangers, and nuclear waste repositories has provided strong impetus for the analyses of fluid flow and heat transfer through porous media. In most applications the Reynolds number based on the pore size is greater than unity and there is an impermeable boundary, which make Darcy's law inapplicable. For these reasons the inertia and boundary effects have been included in a number of recent studies on convective heat transfer in porous media. These effects are incorporated by using the general flow model known as the Brinkman-Forschheimer-extended Darcy model. In general, these effects on convective flow and heat transfer through porous media have been studied by a number of different investigators. For example, Vafai and Tien (1981) studied forced convection over a horizontal flat plate, Hong et al. (1985) investigated natural convection over a vertical flat plate, and Parang and Keyhani (1987) analyzed mixed convection through an annulus region.

The problem of forced convection in a porous channel was studied by Koh and his co-workers (1974, 1975) to investigate the performance of a heat exchanger containing a high-conductivity porous medium. Their analysis was based on a slug flow model. They have shown that for a constant heat flux boundary condition the wall temperature is significantly decreased by the insertion of a porous material in the channel. To account for the effect of a solid boundary, Kaviany (1985) used a numerical solution of laminar flow in a porous channel bounded by isothermal parallel plates based on the Brinkman-extended Darcy model. Recently Poulikakos and Renken (1987) performed a numerical investigation on the effects of flow inertia, variable porosity, and a solid boundary on fluid flow and heat transfer through porous media bounded by parallel plates or circular pipe. They found that boundary and inertia effects decrease the Nusselt number, whereas variable porosity effects increase the Nusselt number.

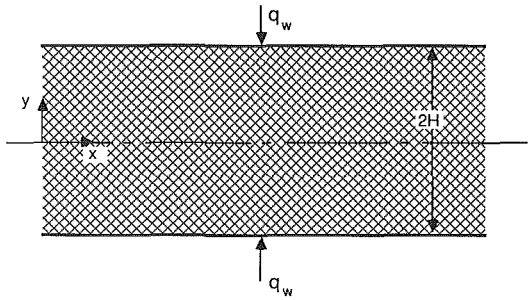

Fig. 1 Schematic of the problem and the corresponding coordinate system

In this paper fully developed forced convection in a porous channel bounded by parallel plates is considered based on the general flow model. Exact solutions are obtained and presented for both the velocity and the temperature fields. From these results the Nusselt number can be expressed in terms of the Darcy number and the inertia parameter. Finally, comparisons are made with the limiting case of no inertia and/or boundary effects. These results provide an in-depth insight into the underlying relationships between all of the pertinent variables. Furthermore, they can be used as strong candidates for bench marking of many numerical schemes.

Analysis

The geometry of the problem under consideration is shown in Fig. 1. A channel bounded by two parallel plates is filled with a granular porous medium. The heat transfer to (or from) the channel takes place at the solid walls. We concentrate on the portion of the channel that comes after the thermal entry length. It is also assumed that the properties of the porous medium and the fluid are isotropic and homogeneous, and that the porous medium is in local thermodynamic equilibrium with the fluid. Then for a constant porosity the governing equations, which account for the inertia and boundary effect, are (Vafai and Tien, 1981)

$$\frac{\mu_f}{\delta}\frac{d^2\langle u\rangle}{dy^2} - \frac{\mu_f}{K}\langle u\rangle - \rho_f\frac{F\delta}{K^{1/2}}\langle u\rangle^2 - \frac{d\langle p\rangle^f}{dx} = 0 \tag{1}$$

$$\langle u\rangle\frac{\partial\langle T\rangle}{\partial x} = \frac{\alpha_e}{\delta}\frac{\partial^2\langle T\rangle}{\partial y^2} \tag{2}$$

It should be noted that in the energy equation the transverse thermal dispersion has been embedded in the effective thermal conductivity term. In other words the effective thermal conductivity in the energy equation is a combination of stagnant and dispersion transport mechanisms. Hence the effective thermal conductivity can be decomposed into two parts; one stands for the stagnant thermal conductivity of the fluid-saturated porous medium and the other incorporates the additional thermal transport due to the transverse mixing (Cheng, 1987). Essentially this approach corresponds to just changing the value of the effective thermal conductivity, which was

[1]Department of Mechanical Engineering, Ohio State University, Columbus, OH 43210.

Contributed by the Heat Transfer Division for publication in the JOURNAL OF HEAT TRANSFER. Manuscript received by the Heat Transfer Division June 15, 1988. Keywords: Forced Convection, Geophysical Heat Transfer, Porous Media.

pointed out by Beckermann and Viskanta (1987). Also note that the axial conduction term has been neglected in equation (2). The axial conduction is usually negligible for most applications; however, it can become important under certain circumstances (Prasad and Tuntomo, 1987).

The appropriate boundary conditions are

$$\frac{d\langle u\rangle}{dy}=0,\quad \frac{\partial\langle T\rangle}{\partial y}=0 \text{ at } y=0 \tag{3a}$$

$$\langle u\rangle=0,\quad \frac{\partial\langle T\rangle}{\partial y}=\frac{q_w}{k_e} \text{ at } y=H \tag{3b}$$

Momentum Boundary Layer. Introduction of the following dimensionless variables

$$u^*=\frac{\langle u\rangle}{u_\infty},\quad x^*=\frac{x}{H},\quad y^*=\frac{y}{H}$$

transforms equations (1) and (3) into

$$\frac{d^2u}{dy^2}-\frac{\delta H^2}{K}u-\frac{u_\infty F\delta^2H^2}{\nu_f K^{1/2}}u^2-\frac{\delta H}{\mu_f u_\infty}\frac{d\langle p\rangle^f}{dx}=0 \tag{4}$$

$$\frac{du(0)}{dy}=0 \tag{5a}$$

$$u(1)=0 \tag{5b}$$

where * is dropped for convenience and u_∞ denotes the velocity outside the momentum boundary layer, which is of the order of $\sqrt{K/\delta}/H$ (Vafai and Tien, 1981).

Outside the momentum boundary layer, the momentum equation reduces to

$$-\frac{\delta H}{\mu_f u_\infty}\frac{d\langle p\rangle^f}{dx}=\frac{\delta H^2}{K}+\frac{u_\infty F\delta^2H^2}{\nu_f K^{1/2}} \tag{5}$$

Combining equations (4) and (5) yields

$$\frac{d^2u}{dy^2}=\mathrm{Da}^{-1}(u-1)+\Lambda_I\mathrm{Da}^{-1/2}(u^2-1) \tag{6}$$

where the Darcy number and the inertia parameter are defined as

$$\mathrm{Da}=\frac{1}{H^2}\frac{K}{\delta} \tag{7a}$$

$$\Lambda_I=\delta^{3/2}F\frac{u_\infty H}{\nu_f} \tag{7b}$$

It should be noted the inertia parameter is directly related to the Reynolds number, so it can also be considered as a modified Reynolds number. After some algebraic manipulations, the final integration of equation (6) yields

$$u=1-\frac{A+B}{A}\operatorname{sech}^2[D(y+C_1)] \tag{8}$$

where

$$A=\frac{2}{3}\Lambda_I\mathrm{Da}^{-1/2},\quad B=\mathrm{Da}^{-1}+\frac{4}{3}\Lambda_I\mathrm{Da}^{-1/2},\quad D=\frac{\sqrt{A+B}}{2}.$$

Equation (8) is of the same form as those that have been obtained by Vafai and Thiyagaraja (1987), Cheng (1987), and Beckermann and Viskanta (1987) for the flow over a flat plate embedded in a porous medium. The similarity in the velocity profiles is a consequence of the fact that the thickness of the viscous boundary layer does not grow as the streamwise coordinate increases. This was proven by Vafai and Tien (1981), and also substantiated by Kaviany (1985). Hence it is noted that there is no interaction between the two viscous boundary layers at the upper and the lower walls.

Applying the no-slip condition at the wall gives

$$C_1=-\frac{1}{D}\operatorname{sech}^{-1}\sqrt{\frac{A}{A+B}}-1$$

For the case where the inertial effects are neglected the velocity profile expressed by equation (8) approaches the following expression asymptotically:

$$u=1-\frac{\cosh[\mathrm{Da}^{-1/2}y]}{\cosh\mathrm{Da}^{-1/2}} \tag{9}$$

which is the solution of equation (6) when the inertial effects are neglected. For this case (without the inertial effects) the solution given by equation (6) matches that given by Poulikakos and Kazmierczak (1987).

We also note that the mean velocity needed in the thermal boundary layer calculations is obtained by direct integration of equation (8). This results in

$$u_m=1-\frac{A+B}{A}\frac{\tanh[D(1+C_1)]-\tanh[DC_1]}{D} \tag{10}$$

Thermal Boundary Layer. The procedure for obtaining the fully developed temperature profile in the channel subjected to the constant wall heat flux is very lengthy. The procedure used here has some similarities to that used for regular fluid flow. Hence, for the sake of brevity, details are omitted here. After considerable algebraic manipulations the solution of equation (2), satisfying equation (3), is expressed in nondimensional form as

$$\frac{T_w-\langle T\rangle}{q_w/h}=\left\{\frac{1}{2}(1-y^2)+\frac{A+B}{A}\left(\frac{\tanh[DC_1]}{D}(1-y)+\frac{1}{D^2}\ln\frac{\cosh[D(y+C_1)]}{\cosh[DC_1]}\right)\right\}u_m/\Gamma \tag{11}$$

where

$$\Gamma=\left(\frac{1}{3}+\frac{A+B}{A}\left[\frac{S(-e^{2DC_1})-S(-e^{2D(1+C_1)})}{D^3}-\frac{1}{D^3}\left\{2D+\frac{A+B}{A}\left(\tanh[DC_1]+\frac{\Delta_1}{\Delta}\right)\right\}\log(e^{2D(1+C_1)}+1)-\frac{1}{D^3}\frac{A+B}{A}\left(\tanh[DC_1]+\frac{\Delta_1}{\Delta}\right)\log(e^{2DC_1}+1)+\frac{1}{2D}\left(\tanh[DC_1]+\frac{3\Delta_2+\Delta_3}{\Delta}\right)+\frac{A+B}{A}\frac{2}{D^3}\frac{1}{\Delta}(D\tanh[DC_1]\Delta_4+D\Delta_4+\Delta_5)\right]\right)$$

and $S(x)$ is the Spence Dilogarithm and

$$\Delta=e^{2D(1+2C_1)}+(e^{2D}+1)e^{2DC_1}+1$$

$$\Delta_1=e^{2D(1+2C_1)}-(e^{2D}-1)e^{2DC_1}-1$$

$$\Delta_2=e^{2D(1+2C_1)}+e^{2DC_1}$$

$$\Delta_3=e^{2D(1+C_1)}+1$$

$$\Delta_4=-(e^{2D}-1)e^{2DC_1}$$

The Nusselt number is defined as

$$\mathrm{Nu}=\frac{h\,D_h}{k_e} \tag{12}$$

where D_h is the hydraulic diameter of the channel. Using equation (11) we find that the Nusselt number can be represented as

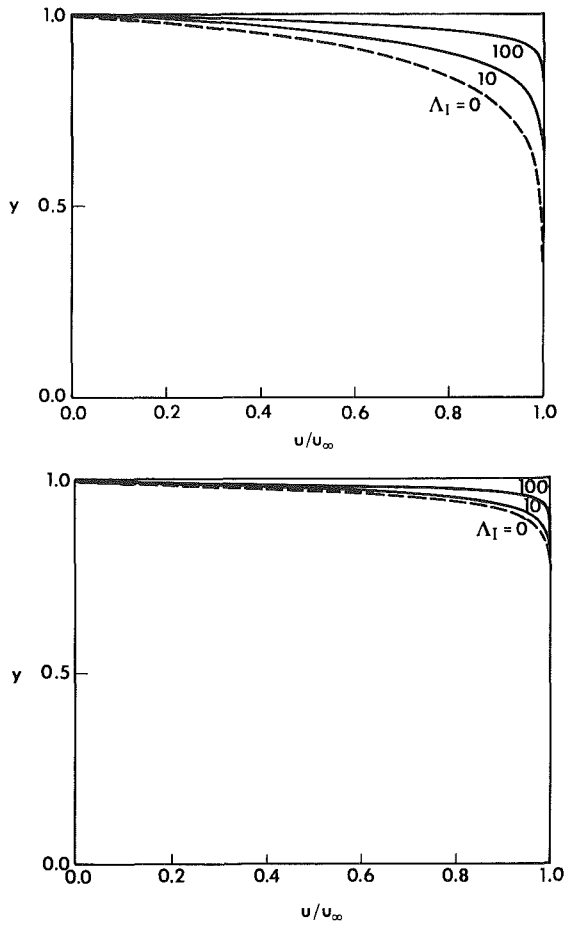

Fig. 2 Fully developed dimensionless velocity profiles: (*a*) $Da^{-1/2} = 10$, (*b*) $Da^{-1/2} = 30$

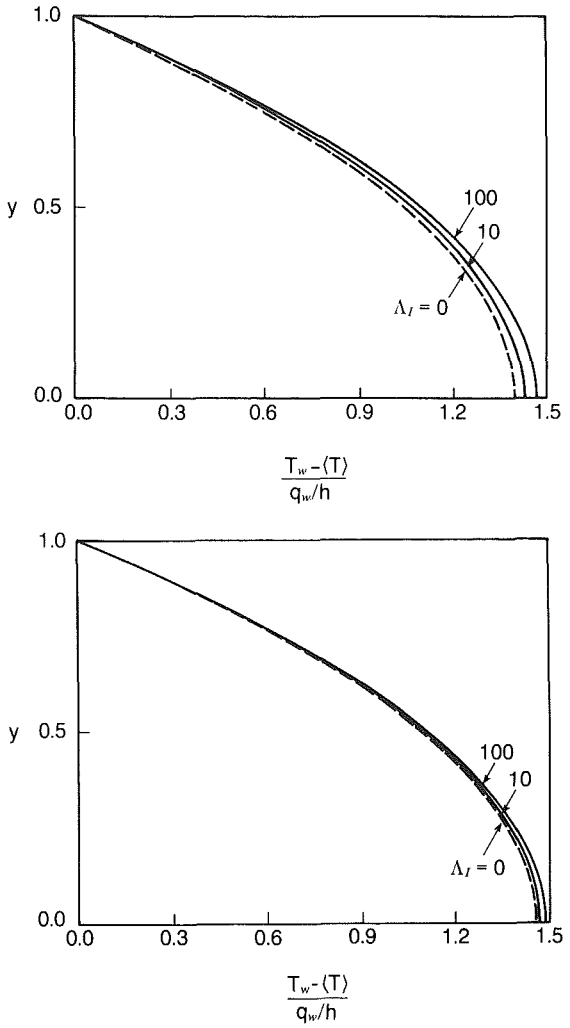

Fig. 3 Fully developed dimensionless temperature profiles: (*a*) $Da^{-1/2} = 10$, (*b*) $Da^{-1/2} = 30$

$$\mathrm{Nu} = \frac{4\,u_m{}^2}{\Gamma} \tag{13}$$

For a limiting case of $\Lambda_I = 0$, solutions for the temperature profile and the Nusselt number become

$$\frac{T_w - \langle T \rangle}{q_w/h} = \left[\frac{1}{2}(1-y^2) - \mathrm{Da}\left(1 - \frac{\cosh[\mathrm{Da}^{-1/2}y]}{\cosh \mathrm{Da}^{-1/2}}\right)\right]$$

$$\times (1 - \mathrm{Da}^{1/2}\tanh\,\mathrm{Da}^{-1/2}) \Big/ \left[\frac{1}{3} - \mathrm{Da}\left(2 + \frac{1}{2\cosh^2 \mathrm{Da}^{-1/2}}\right)\right.$$

$$\left. + \frac{5}{2}\,\mathrm{Da}^{3/2}\tanh\,\mathrm{Da}^{-1/2}\right] \tag{14}$$

$$\mathrm{Nu} = \frac{4(1 - \mathrm{Da}^{1/2}\tanh\,\mathrm{Da}^{-1/2})^2}{\frac{1}{3} - \mathrm{Da}\left(2 + \frac{1}{2\cosh^2 \mathrm{Da}^{-1/2}}\right) + \frac{5}{2}\,\mathrm{Da}^{3/2}\tanh\,\mathrm{Da}^{-1/2}} \tag{15}$$

Results and Discussion

The results for the fully developed velocity profile are shown in Figs. 2(*a*) and 2(*b*) for the two values of the Darcy number. These are $Da^{-1/2} = 10$ and 30. Also shown in these figures are the results for when the inertial effects are neglected. As shown in Fig. 2(*a*) the thickness of the momentum boundary layer decreases as the inertia effect becomes significant. This can be explained by the fact that the thickness of the momentum boundary layer is $O(Da^{1/2})$ when $\Lambda_I \ll 1$, while the thickness is $O(Da^{1/4}/\Lambda_I{}^{1/2})$ when $\Lambda_I \gg 1$. Hence it can be concluded that the thickness of the velocity boundary layer for a high-permeability porous medium depends not only on the Darcy number but also on the inertia parameter. This trend, however, becomes weak for a low-permeability porous medium, i.e., the thickness of the momentum boundary layer becomes independent of the inertia parameter as the permeability of the porous medium decreases, as shown in Fig. 2(*b*).

The invariant dimensionless temperature profiles for the two values $Da^{-1/2} = 10$ and 30 are shown in Figs. 3(*a*) and 3(*b*). It can be seen that the inertia effects will have less of an effect on the temperature profile as the permeability of the porous medium decreases. Finally, the variation of the Nusselt number for the fully developed temperature and velocity fields as a function of the Darcy number is shown in Fig. 4. The magnitude of the Nusselt number reaches its asymptotic maximum value as the permeability decreases. This, as expected, corresponds to the slug flow through the channel. Also the magnitude of Nu for $\Lambda_I = 0$ approaches 8.24 as $K \to \infty$, which corresponds to the fully developed Newtonian flow through the channel. This is because the momentum equation used in the previous section reduces to the Navier-Stokes equation as $K \to \infty$. Hence the Nusselt number for the fully developed flow field varies between 8.24 (for $K \to \infty$) and 12.0 (for $K \to 0$) depending on the value of the Darcy number. Furthermore, the variation of the Nusselt number when $\Lambda_I = 0$ (for constant heat flux) is qualitatively the same as that for forced convec-

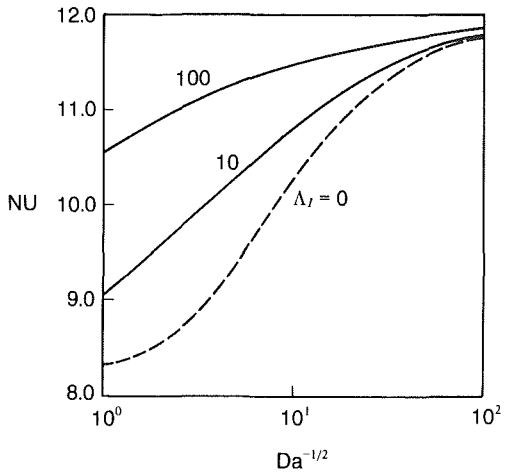

Fig. 4 Variation of the Nusselt number

tion in a porous channel bounded by isothermal parallel plates (Kaviany, 1985).

It should be noted that the Nusselt number increases with an increase in the inertia parameter. This is because an increase in the inertia parameter, due to more vigorous mixing of the fluid, causes a more uniform velocity profile (as can be seen in Fig. 2). This in turn causes a more uniform temperature distribution across the channel, which gives rise to a lower value of the temperature difference, $T_w - T_m$. Therefore, there is a significant increase in the Nusselt number for a relatively high permeability medium as the inertia parameter increases since the Nusselt number is inversely proportional to the temperature difference, $T_w - T_m$.

Conclusion

The problem of forced convection in a channel filled with a porous medium and bounded by two parallel plates is analyzed. Exact solutions are obtained for the velocity and temperature fields. It is shown that for a high-permeability porous medium the thickness of the momentum boundary layer depends on both the Darcy number and the inertia parameter, while that for a low-permeability porous medium depends only on the Darcy number. Also, it is shown that neglecting the inertia effect can lead to serious errors for the Nusselt number calculations. It should be noted that there is a significant increase in the rate of heat transfer as the inertia parameter increases especially for high to medium permeability porous media.

References

Beckermann, C., and Viskanta, R., 1987, "Forced Convection Boundary Layer Flow and Heat Transfer Along a Flat Plate Embedded in a Porous Medium," *Int. J. Heat Mass Transfer*, Vol. 30, pp. 1547–1551.

Cheng, P., 1987, "Wall Effects on Fluid Flow and Heat Transfer in Porous Media," *Proceedings of the 1987 ASME-JSME Thermal Engineering Joint Conference*, Vol. 2, Honolulu, HI.

Hong, J. T., Tien, C. L., and Kaviany, M., 1985, "Non-Darcian Effects on Vertical-Plate Natural Convection in Porous Media With High Porosities," *Int. J. Heat Mass Transfer*, Vol. 28, pp. 2149–2157.

Kaviany, M., 1985, "Laminar Flow Through a Porous Channel Bounded by Isothermal Parallel Plates," *Int. J. Heat Mass Transfer*, Vol. 28, pp. 851–858.

Koh, J. C. Y., and Colony, R., 1974, "Analysis of Cooling Effectiveness for Porous Material in a Coolant Passage," ASME JOURNAL OF HEAT TRANSFER, Vol. 96, pp. 324–330.

Koh, J. C. Y., and Stevens, R. L., 1975, "Enhancement of Cooling Effectiveness by Porous Materials in Coolant Passages," ASME JOURNAL OF HEAT TRANSFER, Vol. 97, pp. 309–311.

Parang, M., and Keyhany, M., 1987, "Boundary and Inertia Effects on Flow and Heat Transfer in Porous Media," *Int. J. Heat Mass Transfer*, Vol. 24, pp. 195–203.

Prasad, V., and Tuntomo, A., 1987, "Inertia Effects on Natural Convection in a Vertical Porous Cavity," *Num. Heat Transfer*, Vol. 11, pp. 295–320.

Poulikakos, D., and Kazmierczak, M., 1987, "Forced Convection in a Duct Partially Filled With a Porous Material," ASME JOURNAL OF HEAT TRANSFER, Vol. 109, pp. 653–662.

Poulikakos, D., and Renken, K., 1987, "Forced Convection in a Channel Filled With Porous Medium, Including the Effects of Flow Inertia, Variable Porosity, and Brinkman Friction," ASME JOURNAL OF HEAT TRANSFER, Vol. 109, pp. 880–888.

Vafai, K., and Thiyagaraja, R., 1987, "Analysis of Flow and Heat Transfer at the Interface Region of a Porous Medium," *Int. J. Heat Mass Transfer*, Vol. 30, pp. 1391–1405.

Vafai, K., and Tien, C. L., 1981, "Boundary and Inertia Effects on Flow and Heat Transfer in Porous Media," *Int. J. Heat Mass Transfer*, Vol. 24, pp. 195–203.

Natural Convection Along a Vertical Wavy Surface With Uniform Heat Flux

S. Ghosh Moulic[1] and L. S. Yao[1]

Nomenclature

- a = amplitude
- g = gravitational acceleration
- Gr = modified Grashof number, equation (2*e*)
- k = wave number = $2\Pi/\ell$
- ℓ = wavelength
- Nu = Nusselt number, equations (5) and (6)
- Pr = Prandtl number
- q = surface heat flux, normal to the surface
- s = distance measured along the surface from the leading edge
- T = temperature
- u, v = velocity components
- $\bar{u}, \bar{v}$ = dimensional velocity components
- x, y = coordinates
- $\bar{x}, \bar{y}$ = dimensional coordinates
- α = dimensionless amplitude = a/ℓ
- β = thermal expansion coefficient
- θ = dimensionless temperature
- κ = thermal conductivity
- ν = kinematic viscosity
- σ = surface geometry function

Superscripts

- $\bar{}$ = dimensional quantity
- $'$ = derivative with respect to x

Subscripts

- m = mean value
- w = surface
- x = local value
- ∞ = free stream

Introduction

Laminar free convection along a semi-infinite vertical wavy surface has been studied by Yao (1983) for the case of uniform surface temperature. This is a model problem for the investigation of heat transfer from roughened surfaces in order to understand heat transfer enhancement. In many applications of practical importance, however, the surface temperature is nonuniform. In this note, the case of uniform surface heat flux rate, which is often approximated in practical applications and is easier to measure in a laboratory, has been investigated. Numerical results have been obtained for a sinusoidal wavy surface. The results show that the Nusselt number varies periodically along the wavy surface. The wavelength of the Nus-

[1]Department of Mechanical and Aerospace Engineering, Arizona State University, Tempe, AZ 85287-6106.

Contributed by the Heat Transfer Division for publication in the JOURNAL OF HEAT TRANSFER. Manuscript received by the Heat Transfer Division August 7, 1987. Keywords: Natural Convection.

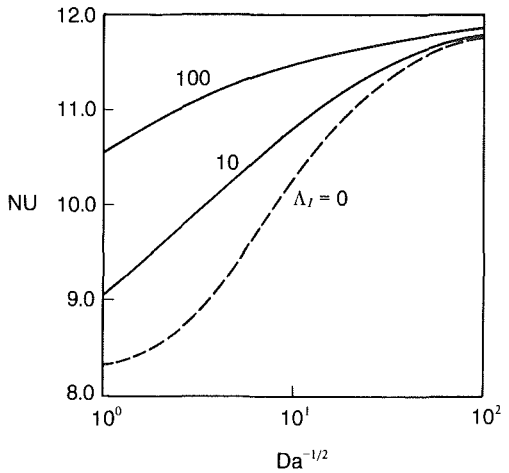

Fig. 4 Variation of the Nusselt number

tion in a porous channel bounded by isothermal parallel plates (Kaviany, 1985).

It should be noted that the Nusselt number increases with an increase in the inertia parameter. This is because an increase in the inertia parameter, due to more vigorous mixing of the fluid, causes a more uniform velocity profile (as can be seen in Fig. 2). This in turn causes a more uniform temperature distribution across the channel, which gives rise to a lower value of the temperature difference, $T_w - T_m$. Therefore, there is a significant increase in the Nusselt number for a relatively high permeability medium as the inertia parameter increases since the Nusselt number is inversely proportional to the temperature difference, $T_w - T_m$.

Conclusion

The problem of forced convection in a channel filled with a porous medium and bounded by two parallel plates is analyzed. Exact solutions are obtained for the velocity and temperature fields. It is shown that for a high-permeability porous medium the thickness of the momentum boundary layer depends on both the Darcy number and the inertia parameter, while that for a low-permeability porous medium depends only on the Darcy number. Also, it is shown that neglecting the inertia effect can lead to serious errors for the Nusselt number calculations. It should be noted that there is a significant increase in the rate of heat transfer as the inertia parameter increases especially for high to medium permeability porous media.

References

Beckermann, C., and Viskanta, R., 1987, "Forced Convection Boundary Layer Flow and Heat Transfer Along a Flat Plate Embedded in a Porous Medium," *Int. J. Heat Mass Transfer*, Vol. 30, pp. 1547–1551.

Cheng, P., 1987, "Wall Effects on Fluid Flow and Heat Transfer in Porous Media," *Proceedings of the 1987 ASME-JSME Thermal Engineering Joint Conference*, Vol. 2, Honolulu, HI.

Hong, J. T., Tien, C. L., and Kaviany, M., 1985, "Non-Darcian Effects on Vertical-Plate Natural Convection in Porous Media With High Porosities," *Int. J. Heat Mass Transfer*, Vol. 28, pp. 2149–2157.

Kaviany, M., 1985, "Laminar Flow Through a Porous Channel Bounded by Isothermal Parallel Plates," *Int. J. Heat Mass Transfer*, Vol. 28, pp. 851–858.

Koh, J. C. Y., and Colony, R., 1974, "Analysis of Cooling Effectiveness for Porous Material in a Coolant Passage," ASME JOURNAL OF HEAT TRANSFER, Vol. 96, pp. 324–330.

Koh, J. C. Y., and Stevens, R. L., 1975, "Enhancement of Cooling Effectiveness by Porous Materials in Coolant Passages," ASME JOURNAL OF HEAT TRANSFER, Vol. 97, pp. 309–311.

Parang, M., and Keyhany, M., 1987, "Boundary and Inertia Effects on Flow and Heat Transfer in Porous Media," *Int. J. Heat Mass Transfer*, Vol. 24, pp. 195–203.

Prasad, V., and Tuntomo, A., 1987, "Inertia Effects on Natural Convection in a Vertical Porous Cavity," *Num. Heat Transfer*, Vol. 11, pp. 295–320.

Poulikakos, D., and Kazmierczak, M., 1987, "Forced Convection in a Duct Partially Filled With a Porous Material," ASME JOURNAL OF HEAT TRANSFER, Vol. 109, pp. 653–662.

Poulikakos, D., and Renken, K., 1987, "Forced Convection in a Channel Filled With Porous Medium, Including the Effects of Flow Inertia, Variable Porosity, and Brinkman Friction," ASME JOURNAL OF HEAT TRANSFER, Vol. 109, pp. 880–888.

Vafai, K., and Thiyagaraja, R., 1987, "Analysis of Flow and Heat Transfer at the Interface Region of a Porous Medium," *Int. J. Heat Mass Transfer*, Vol. 30, pp. 1391–1405.

Vafai, K., and Tien, C. L., 1981, "Boundary and Inertia Effects on Flow and Heat Transfer in Porous Media," *Int. J. Heat Mass Transfer*, Vol. 24, pp. 195–203.

Natural Convection Along a Vertical Wavy Surface With Uniform Heat Flux

S. Ghosh Moulic[1] and L. S. Yao[1]

Nomenclature

- a = amplitude
- g = gravitational acceleration
- Gr = modified Grashof number, equation (2*e*)
- k = wave number = $2\Pi/\ell$
- ℓ = wavelength
- Nu = Nusselt number, equations (5) and (6)
- Pr = Prandtl number
- q = surface heat flux, normal to the surface
- s = distance measured along the surface from the leading edge
- T = temperature
- u, v = velocity components
- $\bar{u}, \bar{v}$ = dimensional velocity components
- x, y = coordinates
- $\bar{x}, \bar{y}$ = dimensional coordinates
- α = dimensionless amplitude = a/ℓ
- β = thermal expansion coefficient
- θ = dimensionless temperature
- κ = thermal conductivity
- ν = kinematic viscosity
- σ = surface geometry function

Superscripts

- $\bar{}$ = dimensional quantity
- $'$ = derivative with respect to x

Subscripts

- m = mean value
- w = surface
- x = local value
- ∞ = free stream

Introduction

Laminar free convection along a semi-infinite vertical wavy surface has been studied by Yao (1983) for the case of uniform surface temperature. This is a model problem for the investigation of heat transfer from roughened surfaces in order to understand heat transfer enhancement. In many applications of practical importance, however, the surface temperature is nonuniform. In this note, the case of uniform surface heat flux rate, which is often approximated in practical applications and is easier to measure in a laboratory, has been investigated. Numerical results have been obtained for a sinusoidal wavy surface. The results show that the Nusselt number varies periodically along the wavy surface. The wavelength of the Nus-

[1]Department of Mechanical and Aerospace Engineering, Arizona State University, Tempe, AZ 85287-6106.

Contributed by the Heat Transfer Division for publication in the JOURNAL OF HEAT TRANSFER. Manuscript received by the Heat Transfer Division August 7, 1987. Keywords: Natural Convection.

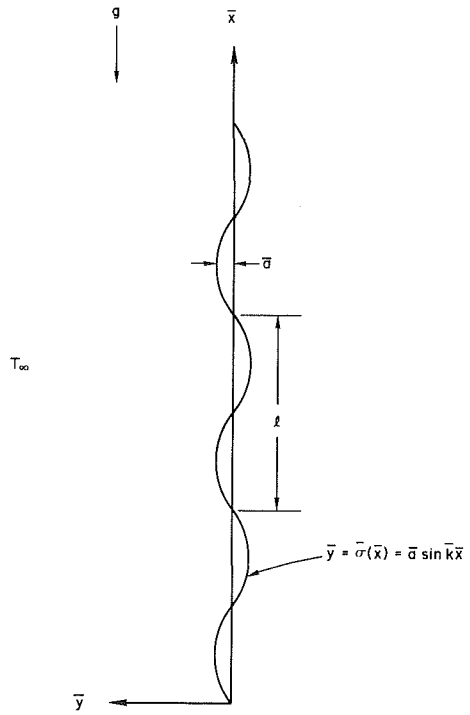

Fig. 1 Physical model and coordinates

selt number variation is half of that of the wavy surface, while the amplitude gradually decreases downstream where the boundary layer grows thick. It is hoped that experimental results will become available in the near future to verify the results of this investigation.

Analysis

The physical geometry and coordinate system are illustrated in Fig. 1. The wavy surface is described by $\bar{y} = \bar{\sigma}(\bar{x})$. The selected characteristic length is the wavelength ℓ of the surface. The local heat-flux rate normal to the surface is maintained at a constant value q. The flow is considered to be steady and the Boussinesq approximation has been employed.

The dimensionless forms of the governing equations in the transformed boundary-layer coordinates (x, y) (Yao, 1988) after ignoring terms of smaller order of magnitude in Gr are

$$(5x)\frac{\partial u}{\partial x} + 3u - y\frac{\partial u}{\partial y} + \frac{\partial v}{\partial y} = 0 \tag{1a}$$

$$(5x)\,u\frac{\partial u}{\partial x} + (v - yu)\frac{\partial u}{\partial y} + \left(3 + \frac{5x\sigma'\sigma''}{1+\sigma'^2}\right)u^2 = \frac{\theta}{1+\sigma'^2} + (1+\sigma'^2)\frac{\partial^2 u}{\partial y^2} \tag{1b}$$

$$(5x)\,u\frac{\partial \theta}{\partial x} + (v - yu)\frac{\partial \theta}{\partial y} + u\theta = \frac{1+\sigma'^2}{\mathrm{Pr}}\frac{\partial^2 \theta}{\partial y^2} \tag{1c}$$

where

$$x = \frac{\bar{x}}{l}, \quad y = \frac{\bar{y} - \bar{\sigma}}{l}\left(\frac{\mathrm{Gr}}{5x}\right)^{1/5} \tag{2a}$$

$$u = \frac{\bar{u}l}{5x\nu}\left(\frac{5x}{\mathrm{Gr}}\right)^{2/5}, \quad v = \frac{(\bar{v} - \sigma'\bar{u})l}{\nu}\left(\frac{5x}{\mathrm{Gr}}\right)^{1/5} \tag{2b}$$

$$\theta = \frac{T - T_\infty}{\left(\frac{ql}{\kappa}\right)}\left(\frac{\mathrm{Gr}}{5x}\right)^{1/5} \tag{2c}$$

$$\sigma' = \frac{d\bar{\sigma}}{d\bar{x}} = \frac{d\sigma}{dx} \tag{2d}$$

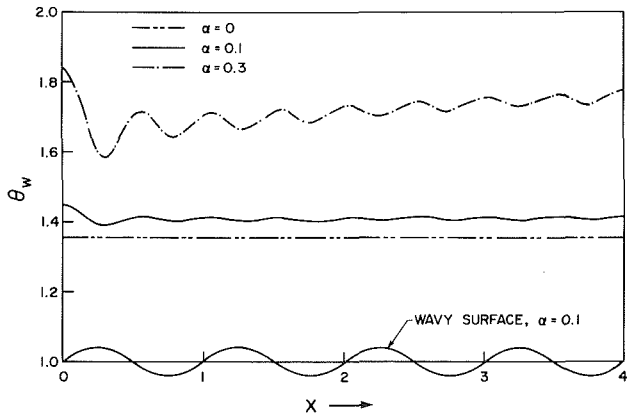

Fig. 2 Surface temperatures for Pr = 1

and

$$\mathrm{Gr} = \frac{g\beta q l^4}{\kappa\nu^2}, \quad \mathrm{Gr}_x = \frac{g\beta q \bar{x}^4}{\kappa\nu^2} \tag{2e}$$

The boundary conditions are

$$(i)\quad \text{At } y = 0, \quad u = v = 0, \quad \frac{\partial \theta}{\partial y} = -\frac{1}{(1+\sigma'^2)^{1/2}} \tag{3a}$$

$$(ii)\quad \text{As } y \to \infty, \quad u \to 0, \quad \theta \to 0 \tag{3b}$$

The numerical method used is identical to that used by Yao (1983). Derivatives with respect to x are approximated by backward differences, while derivatives with respect to y are approximated by central differences. At every x station, the computations are iterated until the difference of two successive iterations becomes less than 10^{-4}. After several trials, the grid size in the y direction was fixed at 0.02, and the step size in the x direction at 0.025. The numerical results are believed to be accurate to the third decimal point, and are much better than 1 percent. The time required for the computations is negligible, as this is a boundary layer computation.

The analysis presented in this section is valid for any surface $y = \sigma(x)$. In the next section, results are presented for the periodic surface $\sigma = \alpha \sin(2\pi x)$.

Results and Discussion

The surface temperature distribution

$$\frac{T_w - T_\infty}{\left(\frac{q\bar{x}}{\kappa}\right)}\left(\frac{\mathrm{Gr}_x}{5}\right)^{1/5} = \theta(x, 0) \tag{4}$$

is plotted in Fig. 2 for $\alpha = 0$, 0.1, and 0.3 and Pr = 1. The surface temperature varies according to the slope of the wavy surface. The wavelength of the surface temperature variation is half of that of the wavy surface. This is due to (*i*) the effect of centrifugal forces, the third term of (1*b*), whose frequency is twice that of the wavy surface, and (*ii*) the alignment of the buoyancy force with respect to the solid surface, as indicated by the fourth term of (1*b*). Consequently, the peaks of the surface temperature occur near the nodes of the sinusoidal surface, where heat is convected away from the surface at a slower rate, and are shifted slightly downstream of the nodes due to the *nonlinear* convection effect. The component of the buoyancy force driving the flow is that tangential to the wavy surface. This is equal to the total buoyancy force only at the crests and troughs of the wavy surface. Thus, the component of the buoyancy force driving the flow has local maxima near the crests and troughs of the wavy surface, and heat is convected away from the surface at a faster rate near the crests and troughs of the surface as the buoyancy forces accelerate the fluid near the wall and thin boundary layer, thereby increasing the local heat transfer coefficient. Since the wall heat

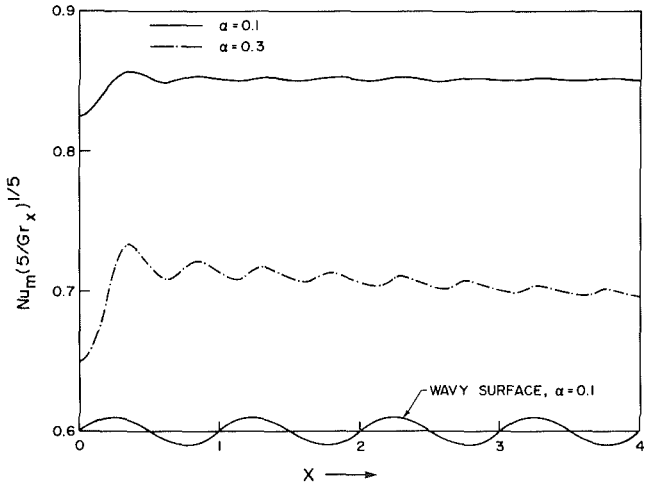

Fig. 3 Averaged Nusselt number for Pr = 1

flux is kept constant, the wall temperature distribution has local minima near the crests and troughs of the wavy surface. The peaks of the wall temperature distribution occur near the nodes of the wavy surface, where the boundary layer is thicker compared to the crests and troughs (Yao, 1983).

The local Nusselt number can be calculated in terms of the surface temperature as

$$\mathrm{Nu}_x = \frac{h_x \bar{x}}{\kappa} = \frac{q\bar{x}}{\kappa(T_w - T_\infty)} = \frac{1}{\theta(x, 0)} \left(\frac{\mathrm{Gr}_x}{5}\right)^{1/5} \tag{5}$$

The average Nusselt number is obtained, based on the average plate minus ambient temperature. Thus

$$\mathrm{Nu}_m = \frac{h_m \bar{x}}{\kappa} = \frac{q\bar{x}}{\kappa(T_w - T_\infty)_m} \tag{6a}$$

where

$$(T_w - T_\infty)_m = \frac{1}{s} \int_0^s (T_w - T_\infty)\, ds \tag{6b}$$

and

$$s = \int_0^x (1 + \sigma'^2)^{1/2}\, dx \tag{6c}$$

This yields

$$\mathrm{Nu}_m(5/\mathrm{Gr}_x)^{1/5} = \frac{x^{1/5} \int_0^x (1 + \sigma'^2)^{1/2}\, dx}{\int_0^x (1 + \sigma'^2)^{1/2} x^{1/5} \theta(x, 0)\, dx} \tag{6d}$$

Equation (6*d*) is plotted in Fig. 3 for $\alpha = 0.1$ and 0.3 and Pr = 1. The total Nusselt number for a sinusoidal wavy surface is uniformly smaller than that of the corresponding flat plate. This may be explained as follows. For the flat plate, the buoyancy force is everywhere parallel to the surface. For the wavy surface, on the other hand, the important component of the buoyancy force (that component tangential to the wavy surface) is less than the total buoyancy force, except at the crests and troughs of the wavy surface. Consequently, at any x location, the thermal boundary layer for the flat plate is thinner than that for the wavy surface, as the buoyancy force that accelerates the fluid near the wall is larger. Thus, the local heat transfer coefficient for the wavy surface is smaller than that of the corresponding flat plate at the same location. Since the wall heat flux is maintained constant, the wall temperature at any x location for the wavy surface is larger than that of the corresponding flat plate, and so is $(T_w - T_\infty)_m$. It follows that the total Nusselt number, defined by equation (6*a*), for the wavy surface is smaller than that for the corresponding flat plate at all x locations. This is a consequence of the fact that the component of the buoyancy force parallel to the wavy surface varies. The wavelength of the variation of the total Nusselt number is half of that of the wavy surface, while the amplitude decays downstream. For $\alpha = 0.1$, the curve approaches a constant value that is lower than the value (0.8840) for a flat plate.

As a check, the natural-convection boundary-layer equations in curvilinear orthogonal coordinates, normal and tangential to the wavy surface (Goldstein, 1965), were solved. The results of this independent computation agree to the third decimal place with those presented above.

References

Goldstein, S., 1965, *Modern Developments in Fluid Dynamics*, Vol. 1, Dover Publications, Inc., New York, pp. 119-122.

Yao, L. S., 1983, "Natural Convection Along a Vertical Wavy Surface," ASME JOURNAL OF HEAT TRANSFER, Vol. 105, pp. 465-468.

Yao, L. S., 1988, "A Note on Prandtl's Transposition Theorem," ASME JOURNAL OF HEAT TRANSFER, Vol. 110, pp. 507-508.

Natural Convection Along Slender Vertical Cylinders With Variable Surface Heat Flux

J. J. Heckel,[1,2] T. S. Chen,[1] and B. F. Armaly[1]

Introduction

Heat transfer by natural convection along a vertical cylinder has been analyzed rather extensively by many investigators using different solution methods. The surface heating conditions that have been considered include uniform wall temperature, UWT (see, for example, Elenbaas, 1948; Sparrow and Gregg, 1956; Minkowycz and Sparrow, 1974; Kuiken, 1974; Lee et al., 1986a), variable wall temperature (Kuiken, 1968; Fujii and Uehara, 1970; Lee et al., 1988), and uniform surface heat flux, UHF (Kuiken, 1968; Lee et al., 1987). The major restriction to most of these studies is that the solutions are valid only for cylinders with small surface curvature, that is, for cylinders whose diameters are not small. The exceptions to this are the treatments of Kuiken (1974) and Lee et al. (1986a, 1987, 1988).

As part of their study on mixed convection along slender vertical cylinders, Lee et al. (1986a, 1987) also analyzed the limiting case of natural convection for the UWT and UHF cases. They employed a weighted finite-difference method that can overcome the numerical difficulties associated with the large surface curvatures to solve the transformed system of equations and presented Nusselt number results for $0.1 \leq \mathrm{Pr} \leq 100$. Very recently, this solution method was applied successfully to slender vertical cylinders with power-law variation in the wall temperature, $T_w(x) = T_\infty + ax^n$. In this latter study (Lee et al., 1988), Nusselt numbers are presented for $0.1 \leq \mathrm{Pr} \leq 100$, covering $-0.4 \leq n \leq 0.5$ and $0 \leq \Lambda_1 \leq 50$, where $\Lambda_1 = (2x/r_o)\mathrm{Gr}_x^{-1/4}$ is the surface curvature parameter. To date no analysis seems to have been presented for natural convection along slender vertical cylinders under the variable surface heat flux condition, $q_w(x)$, and this has motivated the present study as a supplement to the solution of the problem with variable wall temperature.

[1]Department of Mechanical and Aerospace Engineering, University of Missouri—Rolla, Rolla, MO 65401.

[2]Present address: Department of Mechanical Engineering, U.S. Military Academy, West Point, NY 10996.

Contributed by the Heat Transfer Division for publication in the JOURNAL OF HEAT TRANSFER. Manuscript received by the Heat Transfer Division May 26, 1988. Keywords: Natural Convection, Numerical Methods.

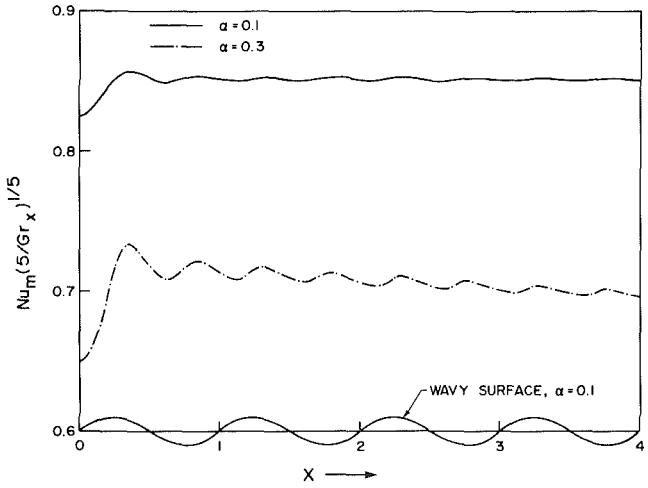

Fig. 3 Averaged Nusselt number for Pr = 1

flux is kept constant, the wall temperature distribution has local minima near the crests and troughs of the wavy surface. The peaks of the wall temperature distribution occur near the nodes of the wavy surface, where the boundary layer is thicker compared to the crests and troughs (Yao, 1983).

The local Nusselt number can be calculated in terms of the surface temperature as

$$\mathrm{Nu}_x = \frac{h_x\bar{x}}{\kappa} = \frac{q\bar{x}}{\kappa(T_w - T_\infty)} = \frac{1}{\theta(x,\,0)}\left(\frac{\mathrm{Gr}_x}{5}\right)^{1/5} \tag{5}$$

The average Nusselt number is obtained, based on the average plate minus ambient temperature. Thus

$$\mathrm{Nu}_m = \frac{h_m\bar{x}}{\kappa} = \frac{q\bar{x}}{\kappa(T_w - T_\infty)_m} \tag{6a}$$

where

$$(T_w - T_\infty)_m = \frac{1}{s}\int_0^s (T_w - T_\infty)\,ds \tag{6b}$$

and

$$s = \int_0^x (1+\sigma'^2)^{1/2}\,dx \tag{6c}$$

This yields

$$\mathrm{Nu}_m(5/\mathrm{Gr}_x)^{1/5} = \frac{x^{1/5}\int_0^x (1+\sigma'^2)^{1/2}\,dx}{\int_0^x (1+\sigma'^2)^{1/2}x^{1/5}\theta(x,\,0)\,dx} \tag{6d}$$

Equation (6*d*) is plotted in Fig. 3 for $\alpha = 0.1$ and 0.3 and Pr = 1. The total Nusselt number for a sinusoidal wavy surface is uniformly smaller than that of the corresponding flat plate. This may be explained as follows. For the flat plate, the buoyancy force is everywhere parallel to the surface. For the wavy surface, on the other hand, the important component of the buoyancy force (that component tangential to the wavy surface) is less than the total buoyancy force, except at the crests and troughs of the wavy surface. Consequently, at any x location, the thermal boundary layer for the flat plate is thinner than that for the wavy surface, as the buoyancy force that accelerates the fluid near the wall is larger. Thus, the local heat transfer coefficient for the wavy surface is smaller than that of the corresponding flat plate at the same location. Since the wall heat flux is maintained constant, the wall temperature at any x location for the wavy surface is larger than that of the corresponding flat plate, and so is $(T_w - T_\infty)_m$. It follows that the total Nusselt number, defined by equation (6*a*), for the wavy surface is smaller than that for the corresponding flat plate at all x locations. This is a consequence of the fact that the component of the buoyancy force parallel to the wavy surface varies. The wavelength of the variation of the total Nusselt number is half of that of the wavy surface, while the amplitude decays downstream. For $\alpha = 0.1$, the curve approaches a constant value that is lower than the value (0.8840) for a flat plate.

As a check, the natural-convection boundary-layer equations in curvilinear orthogonal coordinates, normal and tangential to the wavy surface (Goldstein, 1965), were solved. The results of this independent computation agree to the third decimal place with those presented above.

References

Goldstein, S., 1965, *Modern Developments in Fluid Dynamics*, Vol. 1, Dover Publications, Inc., New York, pp. 119-122.

Yao, L. S., 1983, "Natural Convection Along a Vertical Wavy Surface," ASME JOURNAL OF HEAT TRANSFER, Vol. 105, pp. 465-468.

Yao, L. S., 1988, "A Note on Prandtl's Transposition Theorem," ASME JOURNAL OF HEAT TRANSFER, Vol. 110, pp. 507-508.

Natural Convection Along Slender Vertical Cylinders With Variable Surface Heat Flux

J. J. Heckel,[1,2] T. S. Chen,[1] and B. F. Armaly[1]

Introduction

Heat transfer by natural convection along a vertical cylinder has been analyzed rather extensively by many investigators using different solution methods. The surface heating conditions that have been considered include uniform wall temperature, UWT (see, for example, Elenbaas, 1948; Sparrow and Gregg, 1956; Minkowycz and Sparrow, 1974; Kuiken, 1974; Lee et al., 1986a), variable wall temperature (Kuiken, 1968; Fujii and Uehara, 1970; Lee et al., 1988), and uniform surface heat flux, UHF (Kuiken, 1968; Lee et al., 1987). The major restriction to most of these studies is that the solutions are valid only for cylinders with small surface curvature, that is, for cylinders whose diameters are not small. The exceptions to this are the treatments of Kuiken (1974) and Lee et al. (1986a, 1987, 1988).

As part of their study on mixed convection along slender vertical cylinders, Lee et al. (1986a, 1987) also analyzed the limiting case of natural convection for the UWT and UHF cases. They employed a weighted finite-difference method that can overcome the numerical difficulties associated with the large surface curvatures to solve the transformed system of equations and presented Nusselt number results for $0.1 \le \mathrm{Pr} \le 100$. Very recently, this solution method was applied successfully to slender vertical cylinders with power-law variation in the wall temperature, $T_w(x) = T_\infty + ax^n$. In this latter study (Lee et al., 1988), Nusselt numbers are presented for $0.1 \le \mathrm{Pr} \le 100$, covering $-0.4 \le n \le 0.5$ and $0 \le \Lambda_1 \le 50$, where $\Lambda_1 = (2x/r_o)\mathrm{Gr}_x^{-1/4}$ is the surface curvature parameter. To date no analysis seems to have been presented for natural convection along slender vertical cylinders under the variable surface heat flux condition, $q_w(x)$, and this has motivated the present study as a supplement to the solution of the problem with variable wall temperature.

[1]Department of Mechanical and Aerospace Engineering, University of Missouri—Rolla, Rolla, MO 65401.

[2]Present address: Department of Mechanical Engineering, U.S. Military Academy, West Point, NY 10996.

Contributed by the Heat Transfer Division for publication in the JOURNAL OF HEAT TRANSFER. Manuscript received by the Heat Transfer Division May 26, 1988. Keywords: Natural Convection, Numerical Methods.

Analysis

Consider a semi-infinite, vertical cylinder with radius r_o that is aligned in a quiescent ambient fluid at temperature T_∞. The axial coordinate x is measured upward for $q_w > 0$ and downward for $q_w < 0$, while the radial coordinate r is measured from the axis of the cylinder. The surface of the cylinder is subjected to an arbitrary heat flux $q_w(x)$, and the gravitational acceleration g is acting downward. The fluid properties are assumed to be constant except for variations in density, which induce the buoyancy force. Under laminar boundary layer assumptions and the Boussinesq approximation, the governing conservation equations for the problem under study are the same as equations (1)–(3) given by Lee et al. (1988). The boundary conditions are

$$u = v = 0, \quad \frac{\partial T}{\partial r} = \frac{-q_w(x)}{k} \text{ at } r = r_o \tag{1a}$$

$$u \to 0, \quad T \to T_\infty \text{ as } r \to \infty \tag{1b}$$

$$u = 0, \quad T = T_\infty \quad \text{at } x = 0, \; r \geq r_o \tag{1c}$$

where u and v are the velocity components in the x and r directions, respectively, and T is the fluid temperature. All other notations that appear in this note are the standard ones, and there is no need to define them individually.

To proceed with the analysis, the conservation equations, along with the boundary conditions, are transformed into a dimensionless form by introducing the following dimensionless variables:

$$\eta = \frac{(r^2 - r_o^2)}{2r_o x} (\mathrm{Gr}_x^*/5)^{1/5}, \quad \lambda = \frac{2x}{r_o} (\mathrm{Gr}_x^*/5)^{-1/5} \tag{2}$$

$$f(\lambda, \eta) = \psi(x, r)/[5\nu r_o (\mathrm{Gr}_x^*/5)^{1/5}],$$

$$\theta(\lambda, \eta) = \frac{(T - T_\infty)(\mathrm{Gr}_x^*/5)^{1/5}}{q_w(x)x/k} \tag{3}$$

where $\mathrm{Gr}_x^* = g\beta q_w (x)x^4/k\nu^2$ is the modified Grashof number, η is the pseudosimilarity variable, $f(\lambda, \eta)$ is the reduced stream function, $\theta(\lambda, \eta)$ is the dimensionless temperature, λ is the curvature parameter, and $\psi(x, r)$ is the stream function that satisfies the continuity equation, with $u = (\partial\psi/\partial r)/r$ and $v = -(\partial\psi/\partial x)/r$.

The transformation yields

$$(1 + \eta\lambda)f''' + \lambda f'' + (\gamma + 4)ff'' - (2\gamma + 3)f'^2 + \theta = \lambda(\gamma - 1)\left(f'' \frac{\partial f}{\partial \lambda} - f' \frac{\partial f'}{\partial \lambda}\right) \tag{4}$$

$$(1 + \eta\lambda)\theta'' + \lambda\theta' + \mathrm{Pr}(\gamma + 4)f\theta' - \mathrm{Pr}(4\gamma + 1)f'\theta = \mathrm{Pr}\lambda(\gamma - 1)\left(\theta' \frac{\partial f}{\partial \lambda} - f' \frac{\partial \theta}{\partial \lambda}\right) \tag{5}$$

$$f(\lambda, 0) = f'(\lambda, 0) = 0, \quad \theta'(\lambda, 0) = -1$$
$$f'(\lambda, \infty) = 0, \quad \theta(\lambda, \infty) = 0 \tag{6}$$

where

$$\gamma = \frac{x}{q_w} \frac{dq_w}{dx} \tag{7}$$

and the primes denote partial differentiation with respect to η. For the case of power law variation $q_w(x) = ax^n$, one finds from equation (7) that $\gamma = n$.

For slender cylinders, the curvature parameter $\lambda = 2(x/r_o)(\mathrm{Gr}_x^*/5)^{-1/5}$ can be large. To lower the maximum value of calculations in the x or λ coordinate, one introduces a new $\xi(x)$ variable defined by

$$\xi = [x/r_o)\mathrm{Gr}_x^{*-1/5}]^{1/2} \tag{8}$$

such that $\lambda = C\xi^2$, with $C = 2 \cdot 5^{1/5}$, and $\xi = (\Lambda/2)^{1/2}$, with $\Lambda = (2x/r_o)(\mathrm{Gr}_x^{*-1/5})$.

Substituting equation (8) and $\gamma = n$ into equations (4)–(6) results in

$$(1 + a_1\eta)f''' + a_1 f'' + a_2 ff'' + a_3 f'^2 + a_4\theta = a_5\left(f'' \frac{\partial f}{\partial \xi} - f' \frac{\partial f'}{\partial \xi}\right) \tag{9}$$

$$(1 + a_1\eta)\theta'' + a_1\theta' + \mathrm{Pr}\, a_2 f\theta' + \mathrm{Pr}\, a_6 f'\theta = \mathrm{Pr}\, a_5\left(\theta' \frac{\partial f}{\partial \xi} - f' \frac{\partial \theta}{\partial \xi}\right) \tag{10}$$

$$f(\xi, 0) = f'(\xi, 0) = 0, \quad \theta'(\xi, 0) = -1$$
$$f'(\xi, \infty) = \theta(\xi, \infty) = 0 \tag{11}$$

where

$$a_1 = C\xi^2, \quad a_2 = n + 4, \quad a_3 = -(2n + 3)$$
$$a_4 = 1, \quad a_5 = \xi(n - 1)/2, \quad a_6 = -(4n + 1) \tag{12}$$

The physical quantities of interest include the local Nusselt number Nu_x, the average Nusselt number $\overline{\mathrm{Nu}}_L$, the local wall shear stress τ_w, the axial velocity distribution u, and the temperature profile $\phi(\xi, \eta) = \theta(\xi, \eta)/\theta(\xi, 0)$. The local Nusselt number $\mathrm{Nu}_x = hx/k$, with $h = q_w/(T_w - T_\infty)$, can be expressed as

$$\mathrm{Nu}_x(\mathrm{Gr}_x^*/5)^{-1/5} = -\phi'(\xi, 0) \tag{13}$$

and the average Nusselt number $\overline{\mathrm{Nu}}_L = \bar{h}L/k$ as

$$\overline{\mathrm{Nu}}_L\, (\mathrm{Gr}_L^*/5)^{-1/5} = -\frac{10}{1 - n} \xi_L^N \int_0^{\xi_L} \xi^M \phi'(\xi, 0) d\xi \tag{14}$$

where $\xi_L = \xi$ at $x = L$, $M = (7 + 3n)/(1 - n)$, and $N = (8 + 2n)/(n - 1)$. The local wall shear stress, defined by $\tau_w = \mu(\partial u/\partial r)_{r=r_o}$, has the expression

$$\tau_w = 5 \frac{\mu\nu}{x^2} (\mathrm{Gr}_x^*/5)^{3/5} f''(\xi, 0) \tag{15}$$

The axial velocity distribution can be written as

$$\frac{ux}{\nu} = 5(\mathrm{Gr}_x^*/5)^{2/5} f'(\xi, \eta) \tag{16}$$

Results and Discussion

Equations (9)–(11) constitute a system of nonlinear partial differential equations in the (ξ, η) coordinates with parameters Pr and n. The method described by Lee et al. (1986a, 1986b) was employed to solve this system of equations. The details of the solution procedure parallel those described previously (Lee et al., 1986a, 1987, 1988), and to conserve space they are omitted here. It suffices to point out that a proper choice of the step size $\Delta\eta$ and the dimensionless boundary-layer thickness η_∞ is important in obtaining accurate numerical results. For $\Lambda = 50$ and $\mathrm{Pr} = 0.7$, for example, the calculations yielded $\mathrm{Nu}_x\mathrm{Gr}_x^{*-1/5} = 16.6$ with $\Delta\eta = 0.036$ and $\eta_\infty = 7.24$, and 6.43 with $\Delta\eta = 0.01$ and $\eta_\infty = 45$. In general, the value of η_∞ needs to be increased as the surface curvature becomes larger. In the present study, all calculations were performed with $\Delta\eta = 0.01$ and η_∞ was varied from 10 to 45 as ξ was increased from 0 to 5 (corresponding to Λ from 0 to 50). A solution was considered to be convergent when the calculated values of $f(\xi, \eta)$, $f'(\xi, \eta)$, and $\phi(\xi, \eta) = \theta(\xi, \eta)/\theta(\xi, 0)$ between two successive iterations differed by less than 10^{-4} at all nodes (i.e., at all η values for a given ξ). The solution was not sensitive to the step size in ξ and $\Delta\xi = 0.1$ was used.

Typical numerical results for the case of power law variation of surface heat flux $q_w(x)$ were obtained for values of the exponent n of -0.5, -0.25, 0, 0.25, and 0.5 for Prandtl numbers of 0.1, 0.7, 7, and 100 over the range of $0 \leq \xi \leq 5$ (i.e., $0 \leq \Lambda \leq 50$). Representative values of n fall within the physical limits of realism, $-1 \leq n < 1$, for power law variation of the surface heat flux (see, for example, Gebhart, 1971).

Table 1 The $Nu_x\ Gr_x^{*-1/5}$ results for power law variation of the surface heat flux

ξ	Pr = 0.1			Pr = 0.7			Pr = 7			Pr = 100		
	n			n			n			n		
	−0.5	0	0.5	−0.5	0	0.5	−0.5	0	0.5	−0.5	0	0.5
0	0.1937	0.2634	0.3052	0.3673	0.4834	0.5517	0.6791	0.8699	0.9817	1.2264	1.5560	1.7489
0.5	0.2579	0.3416	0.3881	0.4338	0.5640	0.6375	0.7497	0.9533	1.0701	1.2967	1.6385	1.8361
1.0	0.4370	0.5448	0.5992	0.6228	0.7820	0.8669	0.9472	1.1809	1.3094	1.4994	1.8736	2.0844
1.5	0.7520	0.8691	0.9233	0.9108	1.1013	1.1997	1.2504	1.5135	1.6482	1.8158	2.2352	2.4639
2.0	1.2436	1.3243	1.3661	1.2859	1.5052	1.6143	1.6306	1.9828	2.1434	2.2212	2.6904	2.9403
2.5	1.8517	1.8971	1.9252	1.7690	2.0068	2.1158	2.1091	2.4967	2.6805	2.6882	3.2133	3.4882
3.0	2.5546	2.5789	2.5966	2.4354	2.6321	2.7241	2.6564	3.0592	3.2664	3.3141	3.8831	4.1922
3.5	3.3546	3.3666	3.3769	3.2846	3.3915	3.4561	3.2483	3.6970	3.9225	3.9592	4.6065	4.9329
4.0	4.2554	4.2626	4.2691	4.2249	4.2757	4.3173	3.9665	4.4554	4.6793	4.7318	5.4551	5.7807
4.5	5.2719	5.2756	5.2791	5.2532	5.2828	5.3094	4.9552	5.3785	5.5723	5.5524	6.3389	6.7196
5.0	6.4191	6.4224	6.4252	6.4093	6.4271	6.4447	6.2231	6.4791	6.6276	6.4725	7.3556	7.7619

Table 2 The $Nu_x/Nu_{x,UHF}$ results for power law variation of the surface heat flux

ξ	Pr = 0.1			Pr = 0.7			Pr = 7			Pr = 100		
	n			n			n			n		
	−0.5	0.25	0.5	−0.5	0.25	0.5	−0.5	0.25	0.5	−0.5	0.25	0.5
0	0.7353	1.0872	1.1584	0.7597	1.0778	1.1412	0.7806	1.0707	1.1285	0.7882	1.0682	1.1240
0.5	0.7551	1.0758	1.1361	0.7692	1.0923	1.1303	0.7864	1.0678	1.1226	0.7914	1.0664	1.1206
1.0	0.8021	1.0562	1.0998	0.7964	1.0607	1.1085	0.8021	1.0604	1.1088	0.8003	1.0622	1.1125
1.5	0.8652	1.0352	1.0623	0.8270	1.0504	1.0893	0.8262	1.0471	1.0890	0.8124	1.0568	1.1023
2.0	0.9391	1.0174	1.0316	0.8543	1.0411	1.0725	0.8224	1.0443	1.0810	0.8256	1.0519	1.0929
2.5	0.9761	1.0080	1.0148	0.8815	1.0307	1.0543	0.8448	1.0414	1.0736	0.8535	1.0479	1.0856
3.0	0.9905	1.0036	1.0069	0.9253	1.0195	1.0350	0.8683	1.0383	1.0677	0.8535	1.0432	1.0796
3.5	0.9964	1.0016	1.0031	0.9685	1.0102	1.0190	0.8786	1.0345	1.0610	0.8595	1.0405	1.0709
4.0	0.9983	1.0008	1.0015	0.9881	1.0051	1.0097	0.8903	1.0285	1.0503	0.8674	1.0341	1.0597
4.5	0.9993	1.0003	1.0007	0.9944	1.0026	1.0050	0.9213	1.0200	1.0360	0.8759	1.0292	1.0601
5.0	0.9995	1.0002	1.0004	0.9972	1.0014	1.0027	0.9605	1.0124	1.0229	0.8799	1.0320	1.0552

Attention is first turned to the local Nusselt number. For given values of Pr and n, as the surface curvature Λ or $\xi = (\Lambda/2)^{1/2}$ is increased the value of $Nu_x\ Gr_x^{*-1/5}$ is found to increase. This can be seen from Table 1. It can also be noted from the table that as the curvature increases the effect of the Prandtl number on the Nusselt number diminishes. This can be explained by noting that as the curvature increases the first two terms of the energy equation (10) become dominant and the problem becomes essentially independent of Pr. Another trend revealed in the table is that the Nusselt number becomes almost independent of n as the curvature increases. This is particularly true for fluids with low Prandtl numbers. Figure 1 shows a plot of $Nu_x/Nu_{x,p}$ versus Λ for the UHF case ($n=0$), where $Nu_{x,p}$ is the local Nusselt number for a vertical flat plate. It demonstrates that the $Nu_x/Nu_{x,p}$ ratio for the UHF case increases from 1 as Λ increases from 0 and that the relative effect of surface curvature on the Nusselt number is stronger for fluids with a smaller Prandtl number. Figure 2 is a plot of $Nu_x/Nu_{x,\,UHF}$ versus n for flat plates, demonstrating the effect of n on the local Nusselt number. It shows that the value of $Nu_x Gr_x^{*-1/5}$ increases with increasing value of n (see also Table 1).

In Table 2 are listed the $Nu_x/Nu_{x,UHF}$ ratios for various values of $\xi = (\Lambda/2)^{1/2}$. It can be seen from the table that as the curvature increases the effect of n on Nu_x decreases and the Nusselt number ratio approaches 1.0. This can be explained again by the dominance of the first two terms in equations (9) and (10) for large values of the curvature, which essentially makes them independent of n. Table 3 lists the average Nusselt number results $\overline{Nu}_L\ Gr_L^{*-1/5}$. For given values of Pr and n, the average Nusselt number is seen to increase as the surface curvature ξ_L increases.

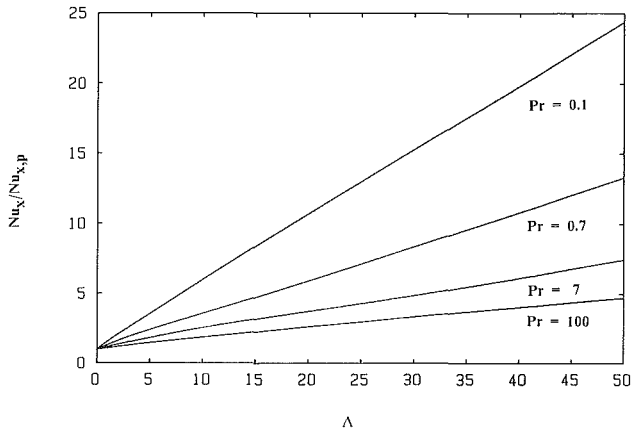

Fig. 1 $Nu_x/Nu_{x,p}$ versus Λ for uniform surface heat flux (UHF, $n = 0$)

For practical applications, the local Nusselt number results from the present calculations in the ranges of $0 \le \Lambda \le 50$, $-0.5 \le n \le 0.5$, and $0.1 \le Pr \le 100$ can be correlated in the following form:

Table 3 The $\overline{Nu}_L Gr_L^{*-1/5}$ results for power law variation of the surface heat flux

ξ_L	Pr = 0.1			Pr = 0.7			Pr = 7			Pr = 100		
	n			n			n			n		
	−0.5	0	0.5	−0.5	0	0.5	−0.5	0	0.5	−0.5	0	0.5
0	0.3818	0.4543	0.4678	0.7239	0.8338	0.8457	1.339	1.500	1.505	2.417	2.6814	2.6810
0.5	0.4710	0.5637	0.6039	0.8162	0.9466	0.9983	1.436	1.617	1.683	2.515	2.801	2.896
1.0	0.7218	0.8494	0.8805	1.081	1.252	1.288	1.714	1.936	1.966	2.797	3.125	3.154
1.5	1.141	1.297	1.328	1.490	1.706	1.753	2.140	2.403	2.439	3.244	3.634	3.678
2.0	1.794	1.926	1.940	2.026	2.279	2.334	2.691	3.063	3.123	3.828	4.286	4.347
2.5	2.649	2.724	2.715	2.688	2.979	3.032	3.366	3.816	3.890	4.516	5.042	5.120
3.0	3.654	3.677	3.645	3.544	3.833	3.870	4.157	4.634	4.718	5.335	5.961	6.054
3.5	4.796	4.778	4.727	4.646	4.868	4.874	5.035	5.538	5.635	6.305	7.011	7.137
4.0	6.075	6.027	5.961	5.953	6.077	6.054	6.008	6.569	6.677	7.373	8.163	8.293
4.5	7.499	7.430	7.355	7.409	7.459	7.414	7.198	7.786	7.887	8.562	9.431	9.609
5.0	9.080	9.000	8.924	9.015	9.018	8.963	8.696	9.226	9.308	9.859	10.850	11.046

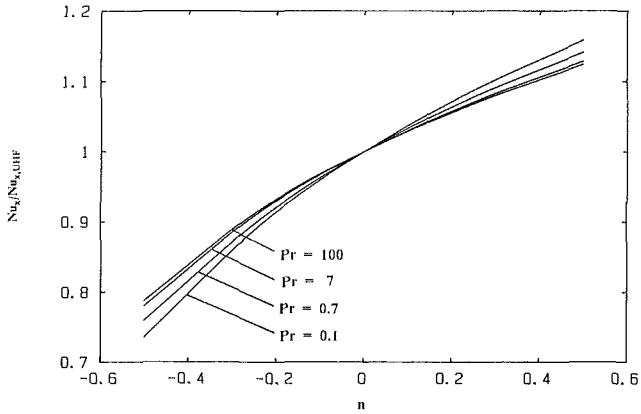

Fig. 2 $Nu_x/Nu_{x,UHF}$ versus n for flat plates ($\Lambda = 0$)

$$Nu_x Gr_x^{*-1/5} = \alpha(Pr)[A(\Lambda) + f_1(Pr)\Lambda](1 + VW) \quad (17)$$

where

$$\alpha(Pr) = Pr^{2/5}(4 + 9Pr^{1/2} + 10Pr)^{-1/5} \quad (18a)$$

$$A(\Lambda) = 1 + 0.09\Lambda^{1/2} \quad (18b)$$

$$f_1(Pr) = (0.032 + 0.176Pr^{-0.384}) \quad (18c)$$

$$V = \{[0.328 + 0.343 \exp(-2.12Pr^{1/5})] - 0.195n\}n \quad (18d)$$

$$W = \exp[-(0.0265 + 0.0907Pr^{-0.444})\Lambda^{0.8}] \quad (18e)$$

The average Nusselt number for the same ranges of parametric values can be correlated by

$$\overline{Nu}_L Gr_L^{*-1/5} = \frac{5}{4}\alpha(Pr)\,[B(\Lambda) + f_2(Pr)\Lambda](1 + \bar{V}) \quad (19)$$

where

$$B(\Lambda) = 1 + 0.08\Lambda^{1/2} \quad (20a)$$

$$f_2(Pr) = (0.026 + 0.14Pr^{-0.39}) \quad (20b)$$

$$\bar{V} = (4VW - n\bar{W})/(4 + n\bar{W}) \quad (20c)$$

$$\bar{W} = \exp(-0.5\Lambda^{0.6}) \quad (20d)$$

with Λ in equations (19) and (20) now standing for Λ_L or Λ at $x = L$.

It is interesting to note that for the UHF case ($n = 0$) V and $\bar{V}$ in equations (17) and (19) become zero. It is also interesting to note that for the flat plate (i.e., $\Lambda = 0$) the terms $[A(\Lambda) + f_1(Pr)\Lambda]$ and $[B(\Lambda) + f_2(Pr)\Lambda]$ both become one. Therefore, for the flat plate solution under UHF, $Nu_x\, Gr_x^{*-1/5} = \alpha(Pr)$, where $\alpha(Pr)$ is taken from Fujii and Fujii (1976). The maximum error in the correlations for the local and average Nusselt numbers is less than 5 percent for the UHF case and less than 8.3 percent for the variable heat flux condition.

References

Elenbaas, W., 1948, "The Dissipation of Heat by Free Convection From Vertical and Horizontal Cylinders," *Journal of Applied Physics*, Vol. 19, pp. 1148-1154.

Fujii, T., and Fujii, M., 1976, "The Dependence of Local Nusselt Number in the Case of Free Convection Along a Vertical Surface With Uniform Heat Flux," *International Journal of Heat and Mass Transfer*, Vol. 19, pp. 121-122.

Fujii, T., and Uehara, H., 1970, "Laminar Natural Convective Heat Transfer From the Outer Surface of a Vertical Cylinder," *International Journal of Heat and Mass Transfer*, Vol. 13, pp. 607-615.

Gebhart, B., 1971, *Heat Transfer*, 2nd ed., McGraw-Hill, New York, p. 340.

Kuiken, H. K., 1968, "Axisymmetric Free Convection Boundary Layer Flow Past Slender Bodies," *International Journal of Heat and Mass Transfer*, Vol. 11, pp. 1141-1153.

Kuiken, H. K., 1974, "The Thick Free-Convective Boundary-Layer Along a Semi-infinite Isothermal Vertical Cylinder," *Journal of Applied Mathematics and Physics* (ZAMP), Vol. 25, pp. 497-514.

Lee, H. R., Chen, T. S., and Armaly, B. F., 1988, "Natural Convection Along Vertical Cylinders With Variable Surface Temperature," ASME JOURNAL OF HEAT TRANSFER, Vol. 110, pp. 103-108.

Lee, S. L., Chen, T. S., and Armaly, B. F., 1986a, "Mixed Convection Along Isothermal Vertical Cylinders and Needles," *Proceedings of the Eighth International Heat Transfer Conference*, Vol. 3, pp. 1425-1432.

Lee, S. L., Chen, T. S., and Armaly, B. F., 1986b, "New Finite Difference Solution Methods for Wave Instability Problems," *Numerical Heat Transfer*, Vol. 10, pp. 1-8.

Lee, S. L., Chen, T. S., and Armaly, B. F., 1987, "Mixed Convection Along Vertical Cylinders and Needles With Uniform Surface Heat Flux," ASME JOURNAL OF HEAT TRANSFER, Vol. 109, pp. 711-716.

Minkowycz, W. J., and Sparrow, E. M., 1974, "Local Nonsimilar Solutions for Natural Convection on a Vertical Cylinder," ASME JOURNAL OF HEAT TRANSFER, Vol. 96, pp. 178-183.

Sparrow, E. M., and Gregg, J. L., 1956, "Laminar-Free-Convection Heat Transfer From the Outer Surface of a Vertical Circular Cylinder," *Transactions ASME*, Vol. 78, pp. 1823-1829.

A General Correlation for Melting in Rectangular Enclosures

C. Beckermann[1]

Introduction

The problem of melting of ordinary (nonmetallic) and metallic solids in enclosures has received considerable research attention due to its importance, for example, in materials pro-

[1]Department of Mechanical Engineering, The University of Iowa, Iowa City, IA 52242.

Contributed by the Heat Transfer Division for publication in the JOURNAL OF HEAT TRANSFER. Manuscript received by the Heat Transfer Division September 13, 1988. Keywords: Modeling and Scaling, Natural Convection, Phase-Change Phenomena.

Table 3 The $\overline{Nu}_L Gr_L^{*-1/5}$ results for power law variation of the surface heat flux

ξ_L	Pr = 0.1			Pr = 0.7			Pr = 7			Pr = 100		
	n			n			n			n		
	−0.5	0	0.5	−0.5	0	0.5	−0.5	0	0.5	−0.5	0	0.5
0	0.3818	0.4543	0.4678	0.7239	0.8338	0.8457	1.339	1.500	1.505	2.417	2.6814	2.6810
0.5	0.4710	0.5637	0.6039	0.8162	0.9466	0.9983	1.436	1.617	1.683	2.515	2.801	2.896
1.0	0.7218	0.8494	0.8805	1.081	1.252	1.288	1.714	1.936	1.966	2.797	3.125	3.154
1.5	1.141	1.297	1.328	1.490	1.706	1.753	2.140	2.403	2.439	3.244	3.634	3.678
2.0	1.794	1.926	1.940	2.026	2.279	2.334	2.691	3.063	3.123	3.828	4.286	4.347
2.5	2.649	2.724	2.715	2.688	2.979	3.032	3.366	3.816	3.890	4.516	5.042	5.120
3.0	3.654	3.677	3.645	3.544	3.833	3.870	4.157	4.634	4.718	5.335	5.961	6.054
3.5	4.796	4.778	4.727	4.646	4.868	4.874	5.035	5.538	5.635	6.305	7.011	7.137
4.0	6.075	6.027	5.961	5.953	6.077	6.054	6.008	6.569	6.677	7.373	8.163	8.293
4.5	7.499	7.430	7.355	7.409	7.459	7.414	7.198	7.786	7.887	8.562	9.431	9.609
5.0	9.080	9.000	8.924	9.015	9.018	8.963	8.696	9.226	9.308	9.859	10.850	11.046

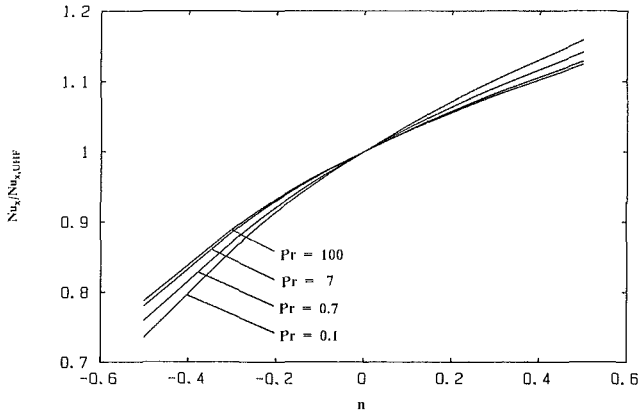

Fig. 2 $Nu_x/Nu_{x,UHF}$ versus n for flat plates ($\Lambda = 0$)

$$Nu_x Gr_x^{*-1/5} = \alpha(Pr)[A(\Lambda) + f_1(Pr)\Lambda](1 + VW) \quad (17)$$

where

$$\alpha(Pr) = Pr^{2/5}(4 + 9Pr^{1/2} + 10Pr)^{-1/5} \quad (18a)$$

$$A(\Lambda) = 1 + 0.09\Lambda^{1/2} \quad (18b)$$

$$f_1(Pr) = (0.032 + 0.176Pr^{-0.384}) \quad (18c)$$

$$V = \{[0.328 + 0.343 \exp(-2.12Pr^{1/5})] - 0.195n\}n \quad (18d)$$

$$W = \exp[-(0.0265 + 0.0907Pr^{-0.444})\Lambda^{0.8}] \quad (18e)$$

The average Nusselt number for the same ranges of parametric values can be correlated by

$$\overline{Nu}_L Gr_L^{*-1/5} = \frac{5}{4}\alpha(Pr)\,[B(\Lambda) + f_2(Pr)\Lambda](1 + \bar{V}) \quad (19)$$

where

$$B(\Lambda) = 1 + 0.08\Lambda^{1/2} \quad (20a)$$

$$f_2(Pr) = (0.026 + 0.14Pr^{-0.39}) \quad (20b)$$

$$\bar{V} = (4VW - n\bar{W})/(4 + n\bar{W}) \quad (20c)$$

$$\bar{W} = \exp(-0.5\Lambda^{0.6}) \quad (20d)$$

with Λ in equations (19) and (20) now standing for Λ_L or Λ at $x = L$.

It is interesting to note that for the UHF case ($n = 0$) V and $\bar{V}$ in equations (17) and (19) become zero. It is also interesting to note that for the flat plate (i.e., $\Lambda = 0$) the terms $[A(\Lambda) + f_1(Pr)\Lambda]$ and $[B(\Lambda) + f_2(Pr)\Lambda]$ both become one. Therefore, for the flat plate solution under UHF, $Nu_x\, Gr_x^{*-1/5} = \alpha(Pr)$, where $\alpha(Pr)$ is taken from Fujii and Fujii (1976). The maximum error in the correlations for the local and average Nusselt numbers is less than 5 percent for the UHF case and less than 8.3 percent for the variable heat flux condition.

References

Elenbaas, W., 1948, "The Dissipation of Heat by Free Convection From Vertical and Horizontal Cylinders," *Journal of Applied Physics*, Vol. 19, pp. 1148-1154.

Fujii, T., and Fujii, M., 1976, "The Dependence of Local Nusselt Number in the Case of Free Convection Along a Vertical Surface With Uniform Heat Flux," *International Journal of Heat and Mass Transfer*, Vol. 19, pp. 121-122.

Fujii, T., and Uehara, H., 1970, "Laminar Natural Convective Heat Transfer From the Outer Surface of a Vertical Cylinder," *International Journal of Heat and Mass Transfer*, Vol. 13, pp. 607-615.

Gebhart, B., 1971, *Heat Transfer*, 2nd ed., McGraw-Hill, New York, p. 340.

Kuiken, H. K., 1968, "Axisymmetric Free Convection Boundary Layer Flow Past Slender Bodies," *International Journal of Heat and Mass Transfer*, Vol. 11, pp. 1141-1153.

Kuiken, H. K., 1974, "The Thick Free-Convective Boundary-Layer Along a Semi-infinite Isothermal Vertical Cylinder," *Journal of Applied Mathematics and Physics* (ZAMP), Vol. 25, pp. 497-514.

Lee, H. R., Chen, T. S., and Armaly, B. F., 1988, "Natural Convection Along Vertical Cylinders With Variable Surface Temperature," ASME JOURNAL OF HEAT TRANSFER, Vol. 110, pp. 103-108.

Lee, S. L., Chen, T. S., and Armaly, B. F., 1986a, "Mixed Convection Along Isothermal Vertical Cylinders and Needles," *Proceedings of the Eighth International Heat Transfer Conference*, Vol. 3, pp. 1425-1432.

Lee, S. L., Chen, T. S., and Armaly, B. F., 1986b, "New Finite Difference Solution Methods for Wave Instability Problems," *Numerical Heat Transfer*, Vol. 10, pp. 1-8.

Lee, S. L., Chen, T. S., and Armaly, B. F., 1987, "Mixed Convection Along Vertical Cylinders and Needles With Uniform Surface Heat Flux," ASME JOURNAL OF HEAT TRANSFER, Vol. 109, pp. 711-716.

Minkowycz, W. J., and Sparrow, E. M., 1974, "Local Nonsimilar Solutions for Natural Convection on a Vertical Cylinder," ASME JOURNAL OF HEAT TRANSFER, Vol. 96, pp. 178-183.

Sparrow, E. M., and Gregg, J. L., 1956, "Laminar-Free-Convection Heat Transfer From the Outer Surface of a Vertical Circular Cylinder," *Transactions ASME*, Vol. 78, pp. 1823-1829.

A General Correlation for Melting in Rectangular Enclosures

C. Beckermann[1]

Introduction

The problem of melting of ordinary (nonmetallic) and metallic solids in enclosures has received considerable research attention due to its importance, for example, in materials pro-

[1]Department of Mechanical Engineering, The University of Iowa, Iowa City, IA 52242.

Contributed by the Heat Transfer Division for publication in the JOURNAL OF HEAT TRANSFER. Manuscript received by the Heat Transfer Division September 13, 1988. Keywords: Modeling and Scaling, Natural Convection, Phase-Change Phenomena.

cessing and latent heat energy storage. It is well known that natural convection in the melt, as well as heat conduction in the solid, considerably influence the solid/liquid interface shape and motion. However, attempts to correlate the average heat transfer and melting rates have been relatively unsuccessful, except for a few special cases (Viskanta, 1985).

Many experimental and numerical studies of melting with natural convection have shown that three distinctive heat transfer regimes can be identified (Viskanta, 1985): (1) an initial regime during which the heat transfer in the small melt layer is by pure conduction, (2) a transition regime characterized by developing natural convection in the melt, and (3) a quasi-steady natural convection regime during which the heat transfer rate across the melt region is approximately constant. The above scenario of the heat transfer processes across the melt holds for a large range of Rayleigh (Ra), Stefan (Ste), and Prandtl (Pr) numbers, as well as for a variety of geometries. Recently, it has been shown that the above regimes also exist during melting with heat conduction in the solid (Benard et al., 1986; Beckermann and Viskanta, 1989).

Despite a good understanding of the physical phenomena occurring during melting in enclosures, it has not been possible to correlate the melting rates and heat transfer data of various independent investigators accurately (Viskanta, 1985). For the case of melting from a vertical wall of a solid that is at the fusion temperature, Webb and Viskanta (1985) concluded that conventional correlation techniques fail to collapse the data, because the length scale in the governing dimensionless parameters changes with time as the size of the melt region increases. Through a careful scaling analysis, Jany and Bejan (1988) were able to construct heat transfer and melt fraction correlations that cover the entire time domain. Their investigation is, however, limited to melting from a heated vertical wall inside cavities with the solid at the fusion temperature and laminar natural convection in the melt. No attempt is made to generalize these results for other initial and boundary conditions. For example, they conclude "if one is to consider the additional effect of [heat] conduction in the solid, one must construct a new scenario . . . It is not a question of merely introducing a new dimensionless group . . .".

Consequently, the objective of this study is to demonstrate that a more general melt fraction correlation can be obtained covering the entire time domain as well as the additional effect of heat conduction in the solid. The present analysis is based on the assumptions that (1) the melting proceeds through the three heat transfer regimes described above and (2) the liquid and solid Stefan numbers are small so that the heat transfer is quasi-steady (i.e., negligible thermal inertia of the liquid and solid). The latter assumption is supported by the fact that in virtually all previous numerical and experimental studies the Stefan numbers were less than about 0.3 (Webb and Viskanta, 1985; Viskanta, 1985; Benard et al., 1986). For conciseness, this study concentrates on melting in rectangular enclosures. However, the methods presented can easily be applied to other geometries (e.g., cylinders, etc.). The melt fraction correlation derived in this study is validated using the example of melting of metals in vertical cavities.

Analysis

The physical system considered in the present study consists of a rectangular enclosure with two vertical side walls of height H held at uniform temperatures and the connecting walls of length L well insulated. Initially, the enclosure is filled with a solid of fusion temperature T_f. Melting is initiated by raising the left ("hot") wall temperature to $T_H > T_f$, while maintaining the right ("cold") wall at $T_C \leq T_f$. The assumption of quasi-steady heat transfer in the liquid and solid regions (see the Introduction) implies that the difference between the heat transfer rates supplied through the hot wall and extracted through the cold wall is exclusively used to advance the melting front. In other words, the thermal inertia of the system is assumed to be negligibly small, so that the mean temperatures of the liquid and solid are constant. Again, this assumption is good in the limit of small Stefan numbers. An overall energy balance on the enclosure can now be written, in dimensionless form, as

$$\overline{\mathrm{Nu}}_H - \overline{\mathrm{Nu}}_C = \frac{d\bar{s}}{d\tau} \tag{1}$$

The use of the average melt region width $\bar{s}$ is preferable over the melt fraction f, because it eliminates the aspect ratio A as a parameter in equation (1). The two quantities $\bar{s}$ and f are related by

$$f = \frac{1}{HL}\int_0^H S\,dy = \bar{s}A \tag{2}$$

where $A = H/L$, S is the local melt region width, and y is the vertical coordinate. The other dimensionless quantities in equation (1) are defined as

$$\tau = \frac{c_l(T_H - T_f)}{\Delta h_f}\,\frac{t\alpha_l}{H^2}\,\frac{\rho_l}{\rho_s} = \mathrm{Ste}\ \mathrm{Fo}/\rho^*$$

dimensionless time

$$\overline{\mathrm{Nu}}_H = \frac{\overline{q''_H}H}{(T_H - T_f)k_l}$$

average Nusselt number at the hot wall (3)

$$\overline{\mathrm{Nu}}_C = \frac{\overline{q''_C}H}{(T_H - T_f)k_l}$$

average Nusselt number at the cold wall

where k, c, ρ, α, $\overline{q''}$, t, and Δh_f are the thermal conductivity, specific heat, density, thermal diffusivity, average heat flux, time, and latent heat of fusion, respectively, while the subscripts l and s denote the liquid and solid phases, respectively. According to the above definitions, the average Nusselt numbers at the hot and cold walls will be equal at steady state. Furthermore, it is evident that equation (1) can also be derived by integrating a local interfacial energy balance over the height of the enclosure and relating the heat transfer rates on both sides of the solid/liquid interface to the heat transfer rates at the hot and cold walls.

The fact that equation (1) is valid regardless of the particular physical situation considered (i.e., Ra, Pr, orientation of the enclosure, etc.), together with the fact that virtually all melting processes are characterized by the three heat transfer regimes outlined in the Introduction, holds the key for obtaining a general correlation for the melt fraction (i.e., $\bar{s}$). Because the Nusselt numbers are not constant, equation (1) cannot be integrated over the entire time domain. For the case of $\overline{\mathrm{Nu}}_C = 0$ (no heat conduction in the solid), a number of investigators have integrated equation (1) by using separate $\overline{\mathrm{Nu}}_H$ relations for the various heat transfer regimes (Webb and Viskanta, 1985; Benard et al., 1985; Jany and Bejan, 1988; and others). Through comparisons with experiments and numerical simulations, these studies have shown that accurate melt fraction correlations can be obtained by simply matching the solutions for the first conduction regime and the third quasi-steady natural convection regime. This approach is followed in the present study.

Conduction Regime. In the initial conduction regime, the solid/liquid interface is planar and parallel to the hot wall, so that the heat transfer through the liquid and solid regions is one dimensional. Consequently, the Nusselt numbers for regime 1 can be expressed as

$$\overline{\mathrm{Nu}}_{H,1}=\frac{1}{\bar{s}} \qquad \overline{\mathrm{Nu}}_{C,1}=\frac{\Phi}{1-\bar{s}} \tag{4}$$

where the subcooling parameter Φ is defined as $\Phi=(T_f-T_C)k_s/(T_H-T_f)k_l$. Equation (1) can now be written as

$$\frac{1}{\bar{s}}-\frac{\Phi}{1-\bar{s}}=\frac{d\bar{s}}{d\tau} \tag{5}$$

With $\bar{s}(\tau=0)=0$, the solution to equation (5) is given by

$$\tau=\bar{s}\bar{s}_c-\bar{s}_c^2\ln(1-\bar{s}/\bar{s}_c)+\bar{s}_c^3[1.5+0.5(1-\bar{s}/\bar{s}_c)^2$$
$$-2(1-\bar{s}/\bar{s}_c)+\ln(1-\bar{s}/\bar{s}_c)] \tag{6}$$

where $\bar{s}_c$ is the average melt region width at steady state, if the entire melting process were conduction dominated, and is given by

$$\bar{s}_c=\frac{1}{1+\Phi} \tag{7}$$

It can immediately be seen that for the case of $\Phi=0$ (i.e., no heat conduction in the solid, equation (6) reduces to $\bar{s}=(2\tau)^{1/2}$, which is nothing else but Neumann's solution in the limit of Ste$\to$0. It is interesting to note that for Ste$=0.1$, the constant $2^{1/2}$ is only 1.6 percent higher than for Ste$\to$0. For Ste$=0.3$, the difference increases to 4.6 percent. Virtually all previous studies of melting in enclosures have been performed for Ste<0.3 (Webb and Viskanta, 1985).

Following the procedure proposed by Benard et al. (1985), the conduction regime ends at the time τ_o when $\overline{\mathrm{Nu}}_{H,1}$ is equal to $\overline{\mathrm{Nu}}_{H,3}$, the average Nusselt number at the hot wall during the third quasi-steady convection regime. Consequently, the time τ_o can be calculated by substituting $\bar{s}_o=1/\overline{\mathrm{Nu}}_{H,3}$ into equation (6).

Convection Regime. In the third quasi-steady natural convection regime, the solid/liquid interface is no longer planar, so that the heat transfer by conduction through the solid region is two (or three) dimensional. In the present study, the average Nusselt number at the cold wall during the third regime is approximated by

$$\overline{\mathrm{Nu}}_{C,3}=\frac{c\Phi}{1-\bar{s}} \tag{8}$$

where c is not necessarily constant since the shape of the solid region can vary continuously. It will be shown, however, that for a reasonably wide range of the governing parameters, c can be taken as constant, if c is determined through appropriate comparisons with experiments or numerical simulations.

For the convection regime, equation (1) can now be rewritten as

$$\overline{\mathrm{Nu}}_{H,3}-\frac{c\Phi}{1-\bar{s}}=\frac{d\bar{s}}{d\tau} \tag{9}$$

Note that $\overline{\mathrm{Nu}}_{H,3}$ is constant throughout the quasi-steady natural convection regime, as has been established by many researchers for a large variety of physical situations (Viskanta, 1985). With the initial condition $\bar{s}(\tau_o)=\bar{s}_o=1/\overline{\mathrm{Nu}}_{H,3}$, equation (9) can be integrated to yield

$$(\bar{s}-\bar{s}_o)-(1-\bar{s}_f)\ln\left(\frac{\bar{s}-\bar{s}_f}{\bar{s}_o-\bar{s}_f}\right)=\overline{\mathrm{Nu}}_{H,3}(\tau-\tau_o) \tag{10}$$

where $\bar{s}_f$ is the (final) average melt region width when melting ends, and is given by

$$\bar{s}_f=1-\frac{c\Phi}{\overline{\mathrm{Nu}}_{H,3}} \tag{11}$$

Note that according to equation (11) and with the knowledge of $\overline{\mathrm{Nu}}_{H,3}$ (see below), the constant c can be directly determined from final melt fraction data. Again, in the case of $\Phi=0$ (i.e., no heat conduction in the solid), equation (10) reduces to $\bar{s}-\bar{s}_o=\overline{\mathrm{Nu}}_{H,3}\,(\tau-\tau_o)$. This linear variation of the melt fraction (i.e., $\bar{s}$) with time is well known for melting of a solid at its fusion temperature during the quasi-steady convection regime (Webb and Viskanta, 1985; Benard et al., 1985; Jany and Bejan, 1988). For the case of $\Phi=0$, an additional regime can be identified after part of the solid/liquid interface reaches the right ("cold") wall. This fourth "shrinking solid" (Jany and Bejan, 1988) regime has been considered in detail in other studies (Benard et al., 1985). Also, note that $\Phi=0$ not only implies that $T_C=T_f$, but that the entire solid is isothermally at the fusion temperature and, according to equations (4) and (8), that the Nusselt number at the cold wall is equal to zero. Consequently, the case of $\Phi=0$ applies to both, enclosures with $T_C=T_f$ and enclosures with an adiabatic right ("cold") wall.

For the case of $\Phi=0$, Jany and Bejan (1988) proposed to match the melt fraction (i.e., $\bar{s}$) correlations for the conduction and convection regimes by combining them in a canonical relationship. The results of Benard et al. (1985), as well as the present comparisons (see below) indicate, however, that this is not necessary, because at τ_o equations (6) and (10) match relatively smoothly.

Nusselt Number Correlations. By specifying $\overline{\mathrm{Nu}}_{H,3}$, the general melt fraction (i.e., $\bar{s}$) correlation, equations (6) and (10), can be adapted to a particular physical situation. Theoretically, $\overline{\mathrm{Nu}}_{H,3}$ is a function of the size and shape of the melt region, the orientation of the enclosure, and the Rayleigh and Prandtl numbers. It is known, however, that most correlations for natural convection in rectangular enclosures also work if the enclosure has curved surfaces (Lienhard, 1973). This has prompted many researchers to calculate $\overline{\mathrm{Nu}}_{H,3}$ from standard correlations for steady natural convection in rectangular enclosures without phase change. The validity of the above approach has been demonstrated for a large variety of physical systems, including melting of paraffins and metals from the side without heat conduction in the solid (Benard et al., 1985; Viskanta, 1985; Webb and Viskanta, 1986a; Jany and Bejan, 1988), with heat conduction in the solid (Benard et al., 1986; Beckermann and Viskanta, 1989), as well as melting from below (Gau and Viskanta, 1986). Some investigators (Hale and Viskanta, 1980; Webb and Viskanta, 1986b) have calculated the Rayleigh number in such standard Nusselt number correlations by choosing the instantaneous average melt region width $\bar{s}$ as the characteristic length scale, instead of H. This results, however, in a continuously varying Nusselt number and contradicts the observed quasi-steady heat transfer behavior during the third regime. Furthermore, it is known that for vertical enclosures, the aspect ratio has only a minor effect on the Nusselt number, if the vertical dimension (i.e., H) is used as the characteristic length scale (Jany and Bejan, 1988).

A number of investigators have measured quasi-steady Nusselt numbers directly, under melting conditions (Viskanta, 1985). Interestingly, it has been found that a single $\overline{\mathrm{Nu}}_{H,3}$ correlation can be used for melting of a paraffin (Pr$\approx$50) inside a vertical cavity, regardless of whether there is heat conduction in the solid or not (Benard et al., 1985, 1986). Unfortunately, Benard et al. (1986) do not provide any melt fraction data for their experiment with $\Phi=5.952$, so that the present melt fraction correlation cannot be tested for Pr>1 and $\Phi\neq0$. Furthermore, the $\overline{\mathrm{Nu}}_{H,3}$ correlation by Benard et al. (1985, 1986) is in close agreement with standard Nusselt number correlations for steady natural convection in vertical cavities without phase change, indicating that such standard correlations can generally be used to calculate $\overline{\mathrm{Nu}}_H$ during the third regime.

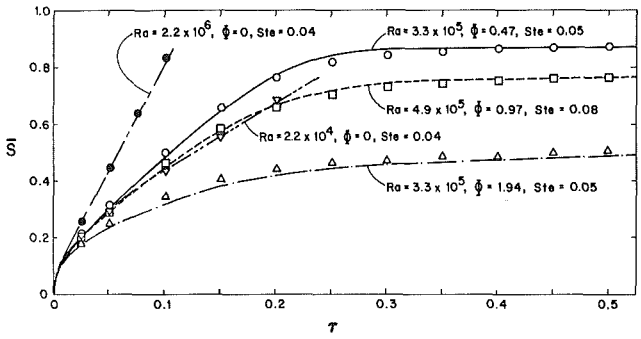

Fig. 1 Comparison of the melt fraction correlation (lines) with previous numerical data (● and ▽: Webb and Viskanta, 1986a; ○, □, and △: Beckermann and Viskanta, 1988) for melting of gallium (Pr = 0.021) inside a vertical cavity

Example: Melting of Metals in Vertical Cavities

For the case of melting of metals with heat conduction in the solid inside a vertical rectangular enclosure, Beckermann and Viskanta (1989) obtained the following $\overline{Nu}_{H,3}$ correlation:

$$\overline{Nu}_{H,3} = 0.5(\mathrm{RaPr})^{0.25} \tag{12}$$

The validity of the above correlation was tested for $10^4 < \mathrm{Ra} < 10^6$, $\mathrm{Pr} < 1$, $0.01 < \mathrm{Ste} < 0.09$, and $\Phi < 2.5$. Equation (12) is in good agreement with a similar correlation obtained by Webb and Viskanta (1986a) for melting of gallium without heat conduction in the solid, as well as with Nusselt number data for steady natural convection (i.e., without melting) of tin and gallium in a vertical square enclosure (Wolff et al., 1988). These observations further support the simple treatment of the third regime proposed in the present study (see also the section Nusselt Number Correlations).

Figure 1 shows a comparison of the present melt fraction (i.e., $\bar{s}$) correlation with numerical data obtained by Webb and Viskanta (1989) (● and ▽) and Beckermann and Viskanta (1989) (○, □, and △) for melting of gallium (Pr = 0.021) inside vertical rectangular enclosures. It should be noted that the numerical results of the above two investigations were verified experimentally. The constant c in equation (11) was determined by Beckermann and Viskanta (1989), who found that with $c = 1.19$, equation (11) correlates the final melt fraction data (i.e., at steady state) to within 3 percent. It can be seen from Fig. 1 that the present melt fraction (i.e., $\bar{s}$) correlation (lines) fits the numerical results (symbols) very well. Slightly better agreement could have been obtained by using the numerically determined Nusselt numbers in the melt fraction correlation, instead of calculating them from equation (12). For the three cases with heat conduction in the solid, some disagreement is due to inaccuracies in the constant c (= 1.19). As discussed earlier, c varies slightly during the third regime, because of variations in the shape of the solid region. It should also be noted that the numerical simulations for the case of no heat conduction in the solid ($\Phi = 0$) were terminated before the solid/liquid interface reaches the right ("cold") wall (Webb and Viskanta, 1986a). This time instant also marks the end of the validity of the present melt fraction correlation. For $\Phi \neq 0$, the interface does not come into contact with the cold wall, so that the present correlation works throughout the entire time domain.

Conclusions

A model has been presented for melting in rectangular enclosures with natural convection in the melt and heat conduction in the solid. By assuming negligible thermal inertia in the liquid and solid regions, and dividing the time domain into three heat transfer regimes, the model equation has been integrated to yield simple algebraic expressions for the time variation of the melt fraction. The expressions are independent of the dimensionless parameters of the problem and can, therefore, be applied to any situation involving melting in differentially heated rectangular enclosures. The present melt fraction correlation can be adapted to a particular physical system by specifying the average Nusselt number at the hot wall during the third, quasi-steady convection regime. Such Nusselt numbers can generally be obtained from standard correlations for pure natural convection (i.e., without melting). As opposed to previous correlations, the present melt fraction correlation is equally valid for melting with and without heat conduction in the solid region.

The usefulness and accuracy of the proposed melt fraction correlation have been demonstrated for melting of metals in vertical cavities. The correlation is found to agree to within a few percent with melt fraction data from previous two-dimensional numerical simulations. Therefore, this correlation represents the first one to predict the time variation of the melt fraction realistically during melting with natural convection in the melt and heat conduction in the solid.

It is expected that the general melt fraction correlation derived in this study can equally well be applied to other configurations. Correlations, similar to the present one in the limiting case of *no* heat conduction in the solid, have been found to work well, for example, for melting of paraffins at their fusion temperature inside vertical (Benard et al., 1985) inclined (Webb and Viskanta, 1986b), and horizontal (Hale and Viskanta, 1980) rectangular enclosures. Since Nusselt number correlations are available for these configurations, extension to melting *with* heat conduction in the solid would require determination of the constant c only (from final melt fraction data). However, the lack of melt fraction data for the case of melting with heat conduction in the solid makes a definite test of the present melt fraction correlation for other configurations impossible.

It is possible to extend the present analysis to large Stefan numbers (i.e., large thermal inertia of the liquid and solid regions). For the case of $\Phi = 0$, Jany and Bejan (1988) proposed a simple procedure for correlating the melting rate for large liquid thermal inertia [i.e., the Nusselt numbers are reduced by a factor of the order of $1/(1 + \mathrm{Ste})$]. This procedure could easily be adapted to the present case of melting with heat conduction in the solid (i.e., $\Phi \neq 0$).

Finally, it should be mentioned that the present correlation is not directly applicable to solidification, because the heat transfer across the liquid does not proceed through the same three regimes as in melting and, in addition, may not be quasi-steady. While some of the basic methods presented in this study may be utilized, correlation of solid fraction data for solidification represents a major challenge for future research.

Acknowledgments

The work reported in this paper was supported, in part, by the National Science Foundation under Grant No. CBT8808888 and through The University of Iowa Old Gold Summer Fellowship.

References

Beckermann, C., and Viskanta, R., 1989, "Effect of Solid Subcooling on Natural Convection Melting of a Pure Metal," ASME JOURNAL OF HEAT TRANSFER, Vol. 111, pp. 416–424.

Benard, C., Gobin, D., and Martinez, F., 1985, "Melting in Rectangular Enclosures: Experiments and Numerical Simulations," ASME JOURNAL OF HEAT TRANSFER, Vol. 107, pp. 794–803.

Benard, C., Gobin, D., and Zanoli, A., 1986, "Moving Boundary Problem: Heat Conduction in the Solid Phase of a Phase-Change Material During Melting Driven by Natural Convection in the Liquid," *International Journal of Heat and Mass Transfer*, Vol. 29, pp. 1669–1681.

Gau, C., and Viskanta, R., 1986, "Melting and Solidification of a Pure Metal on a Vertical Wall," ASME JOURNAL OF HEAT TRANSFER, Vol. 108, pp. 174–181.

Hale, N. W., and Viskanta, R., 1980, "Solid-Liquid Phase-Change Heat Transfer and Interface Motion in Materials Cooled or Heated From Above or Below," *International Journal of Heat and Mass Transfer*, Vol. 23, pp. 283–292.

Jany, P., and Bejan, A., 1988, "Scaling Theory of Melting With Natural Convection in an Enclosure," *International Journal of Heat and Mass Transfer*, Vol. 31, pp. 1221–1235.

Lienhard, J. H., 1973, "On the Commonality of Equations for Natural Convection From Immersed Bodies," *International Journal of Heat and Mass Transfer*, Vol. 16, pp. 2121–2123.

Viskanta, R., 1985, "Natural Convection in Melting and Solidification," in: *Natural Convection: Fundamentals and Applications*, S. Kakac et al., eds., Hemisphere, Washington, DC, pp. 845–877.

Webb, B. W., and Viskanta, R., 1985, "On the Characteristic Length Scale for Correlating Melting Heat Transfer Data," *Int. Comm. Heat Mass Transfer*, Vol. 12, pp. 637–646.

Webb, B. W., and Viskanta, R., 1986a, "Analysis of Heat Transfer During Melting of a Pure Metal From an Isothermal Vertical Wall," *Numerical Heat Transfer*, Vol. 5, pp. 539–558.

Webb, B. W., and Viskanta, R., 1986b, "Natural-Convection-Dominated Melting Heat Transfer in an Inclined Rectangular Enclosure," *International Journal of Heat and Mass Transfer*, Vol. 29, pp. 183–192.

Wolff, F., Beckermann, C., and Viskanta, R., 1988, "Natural Convection of Liquid Metals in Vertical Cavities," *Experimental Thermal and Fluid Science*, Vol. 1, pp. 83–91.

Radiation View Factors From a Finite Rectangular Plate

B. T. F. Chung[1] and M. M. Kermani[2]

Introduction

The determination of radiation view factors from a differential strip to a rectangular plate, or in more general cases, radiation from a rectangular plate to other finite geometries, has practical importance in many engineering applications. Examples are radiation exchange within the internal engine cavities of gas turbines, furnaces, kilns, reactors, and other devices that normally operate at high temperatures. Hamilton and Morgan (1952) determined view factors analytically for several cases regarding a differential element and a differential strip to a plate. Their formulations are restricted to special conditions in that the elements under consideration are in a particular orientation and location with respect to the plate. Other formulations reported by Hottel and Sarofim (1967), Sparrow and Cess (1978), and Siegel and Howell (1981) also apply to special cases in that either the surface under consideration (plate, differential strip, or cylinder) is infinitely long, or there are two planar surfaces that share a common edge. To date, the general analytical expression for view factor from a rectangular plate with an arbitrary orientation and dimensions has not been available.

This study attempts to develop an exact and general formula for shape factors: (1) from a differential element to an arbitrary nonintersecting finite rectangular plate, and (2) from a differential strip to a rectangular plate with the former being in a plane that has parallel generating lines to the latter. This formula is then used to generate the view factors from a rectangular plate to some finite geometries via single integration.

[1]Professor, Department of Mechanical Engineering, The University of Akron, Akron, OH; Mem. ASME.

[2]Research Associate, Department of Mechanical Engineering, The University of Akron, Akron, OH 44325; Student Mem. ASME.

Contributed by the Heat Transfer Division for publication in the JOURNAL OF HEAT TRANSFER. Manuscript received by the Heat Transfer Division May 26, 1988. Keywords: Furnaces and Combustors, Radiation.

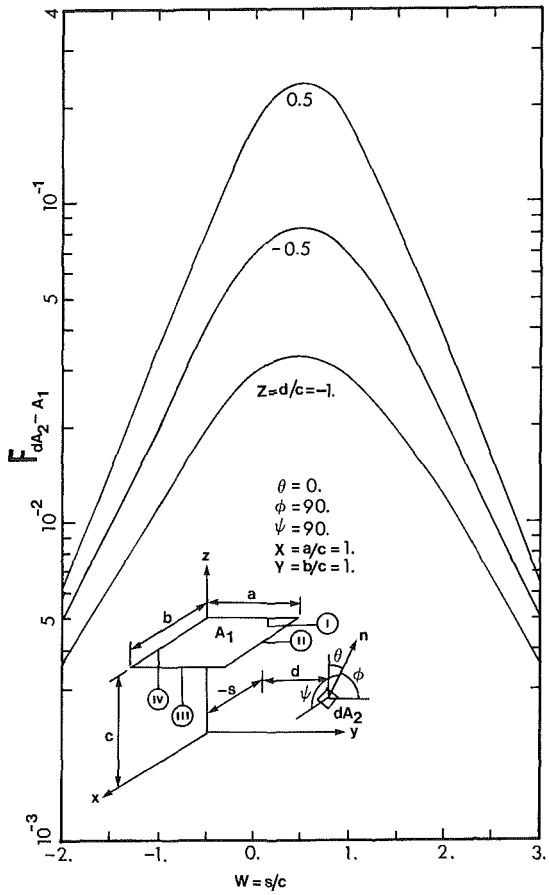

Fig. 1 Shape factor from a differential element to a rectangular plate

Mathematical Analysis and General Formulation

***(a)* Shape Factor From a Differential Element to a Nonintersecting Rectangle.** Consider an element with the coordinates and orientation shown in the sketch of Fig. 1, such that the plane of the differential element dA_2 does not intersect the plate. The view factor given by Sparrow and Cess (1978) has the form

$$F_{dA_2-A_1} = l_2/2\pi \oint [(z-z_2)dy-(y-y_2)dz)]/Le^2$$

$$+ m_2/2\pi \oint [(x-x_2)dz-(z-z_2)dx]/Le^2$$

$$+ n_2/2\pi \oint [((y-y_2)dx-(x-x_2)dy)]/Le^2$$

where the contour of integration consists of lines I to IV shown in the sketch; L_e is the distance from the element to the appropriate contour, $l_2 = \cos\Psi$, $m_2 = \cos\Phi$, and $n_2 = \cos\theta$. Performing the integration and nondimensionalizing the result yields

$$F_{dA_2-A_1} = \frac{l_2}{2\pi}\left\{\frac{1}{\sqrt{W^2+1}}\left(\tan^{-1}\frac{X-Z}{\sqrt{W^2+1}}+\tan^{-1}\frac{Z}{\sqrt{W^2+1}}\right)\right.$$

$$\left.-\frac{1}{\sqrt{1+(W-Y)^2}}\left(\tan^{-1}\frac{X-Z}{\sqrt{1+(W-Y)^2}}+\tan^{-1}\frac{Z}{\sqrt{1+(W-Y)^2}}\right)\right\}$$

$$+\frac{m_2}{2\pi}\left\{\frac{1}{\sqrt{1+Z^2}}\left(\tan^{-1}\frac{Y-W}{\sqrt{1+Z^2}}+\tan^{-1}\frac{W}{\sqrt{1+Z^2}}\right)\right.$$

$$\left.-\frac{1}{\sqrt{1+(Z-X)^2}}\left(\tan^{-1}\frac{Y-W}{\sqrt{1+(Z-X)^2}}\right)+\tan^{-1}\frac{W}{\sqrt{1+(Z-X)^2}}\right)\right\}$$

$$+\frac{n_2}{2\pi}\left\{\frac{W}{\sqrt{1+W^2}}\left(\tan^{-1}\frac{X-Z}{\sqrt{1+W^2}}+\tan^{-1}\frac{Z}{\sqrt{1+W^2}}\right)\right.$$

Hale, N. W., and Viskanta, R., 1980, "Solid-Liquid Phase-Change Heat Transfer and Interface Motion in Materials Cooled or Heated From Above or Below," *International Journal of Heat and Mass Transfer*, Vol. 23, pp. 283–292.

Jany, P., and Bejan, A., 1988, "Scaling Theory of Melting With Natural Convection in an Enclosure," *International Journal of Heat and Mass Transfer*, Vol. 31, pp. 1221–1235.

Lienhard, J. H., 1973, "On the Commonality of Equations for Natural Convection From Immersed Bodies," *International Journal of Heat and Mass Transfer*, Vol. 16, pp. 2121–2123.

Viskanta, R., 1985, "Natural Convection in Melting and Solidification," in: *Natural Convection: Fundamentals and Applications*, S. Kakac et al., eds., Hemisphere, Washington, DC, pp. 845–877.

Webb, B. W., and Viskanta, R., 1985, "On the Characteristic Length Scale for Correlating Melting Heat Transfer Data," *Int. Comm. Heat Mass Transfer*, Vol. 12, pp. 637–646.

Webb, B. W., and Viskanta, R., 1986a, "Analysis of Heat Transfer During Melting of a Pure Metal From an Isothermal Vertical Wall," *Numerical Heat Transfer*, Vol. 5, pp. 539–558.

Webb, B. W., and Viskanta, R., 1986b, "Natural-Convection-Dominated Melting Heat Transfer in an Inclined Rectangular Enclosure," *International Journal of Heat and Mass Transfer*, Vol. 29, pp. 183–192.

Wolff, F., Beckermann, C., and Viskanta, R., 1988, "Natural Convection of Liquid Metals in Vertical Cavities," *Experimental Thermal and Fluid Science*, Vol. 1, pp. 83–91.

Radiation View Factors From a Finite Rectangular Plate

B. T. F. Chung[1] and M. M. Kermani[2]

Introduction

The determination of radiation view factors from a differential strip to a rectangular plate, or in more general cases, radiation from a rectangular plate to other finite geometries, has practical importance in many engineering applications. Examples are radiation exchange within the internal engine cavities of gas turbines, furnaces, kilns, reactors, and other devices that normally operate at high temperatures. Hamilton and Morgan (1952) determined view factors analytically for several cases regarding a differential element and a differential strip to a plate. Their formulations are restricted to special conditions in that the elements under consideration are in a particular orientation and location with respect to the plate. Other formulations reported by Hottel and Sarofim (1967), Sparrow and Cess (1978), and Siegel and Howell (1981) also apply to special cases in that either the surface under consideration (plate, differential strip, or cylinder) is infinitely long, or there are two planar surfaces that share a common edge. To date, the general analytical expression for view factor from a rectangular plate with an arbitrary orientation and dimensions has not been available.

This study attempts to develop an exact and general formula for shape factors: (1) from a differential element to an arbitrary nonintersecting finite rectangular plate, and (2) from a differential strip to a rectangular plate with the former being in a plane that has parallel generating lines to the latter. This formula is then used to generate the view factors from a rectangular plate to some finite geometries via single integration.

[1]Professor, Department of Mechanical Engineering, The University of Akron, Akron, OH; Mem. ASME.

[2]Research Associate, Department of Mechanical Engineering, The University of Akron, Akron, OH 44325; Student Mem. ASME.

Contributed by the Heat Transfer Division for publication in the JOURNAL OF HEAT TRANSFER. Manuscript received by the Heat Transfer Division May 26, 1988. Keywords: Furnaces and Combustors, Radiation.

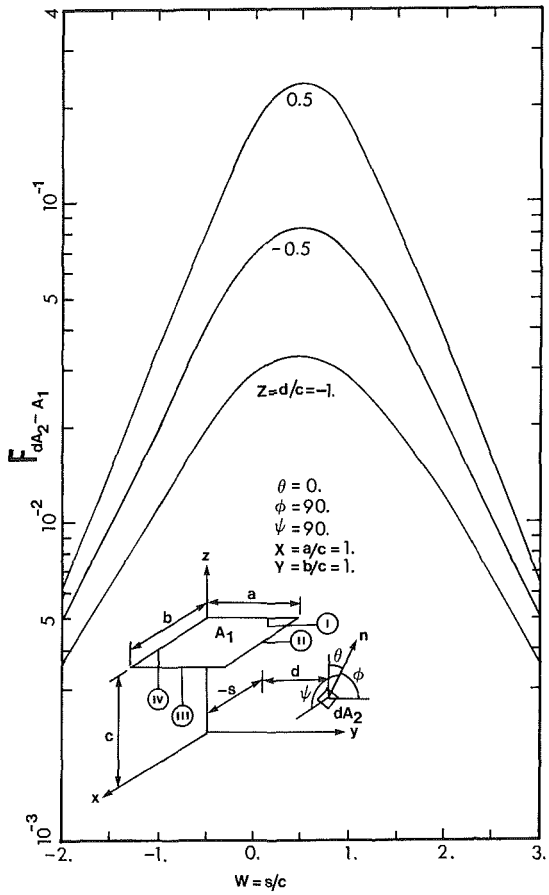

Fig. 1 Shape factor from a differential element to a rectangular plate

Mathematical Analysis and General Formulation

***(a)* Shape Factor From a Differential Element to a Nonintersecting Rectangle.** Consider an element with the coordinates and orientation shown in the sketch of Fig. 1, such that the plane of the differential element dA_2 does not intersect the plate. The view factor given by Sparrow and Cess (1978) has the form

$$F_{dA_2-A_1} = l_2/2\pi \oint [(z-z_2)dy-(y-y_2)dz)]/Le^2$$

$$+ m_2/2\pi \oint [(x-x_2)dz-(z-z_2)dx]/Le^2$$

$$+ n_2/2\pi \oint [((y-y_2)dx-(x-x_2)dy)]/Le^2$$

where the contour of integration consists of lines I to IV shown in the sketch; L_e is the distance from the element to the appropriate contour, $l_2 = \cos\Psi$, $m_2 = \cos\Phi$, and $n_2 = \cos\theta$. Performing the integration and nondimensionalizing the result yields

$$F_{dA_2-A_1} = \frac{l_2}{2\pi}\left\{\frac{1}{\sqrt{W^2+1}}\left(\tan^{-1}\frac{X-Z}{\sqrt{W^2+1}}+\tan^{-1}\frac{Z}{\sqrt{W^2+1}}\right)\right.$$

$$\left.-\frac{1}{\sqrt{1+(W-Y)^2}}\left(\tan^{-1}\frac{X-Z}{\sqrt{1+(W-Y)^2}}+\tan^{-1}\frac{Z}{\sqrt{1+(W-Y)^2}}\right)\right\}$$

$$+\frac{m_2}{2\pi}\left\{\frac{1}{\sqrt{1+Z^2}}\left(\tan^{-1}\frac{Y-W}{\sqrt{1+Z^2}}+\tan^{-1}\frac{W}{\sqrt{1+Z^2}}\right)\right.$$

$$\left.-\frac{1}{\sqrt{1+(Z-X)^2}}\left(\tan^{-1}\frac{Y-W}{\sqrt{1+(Z-X)^2}}\right)+\tan^{-1}\frac{W}{\sqrt{1+(Z-X)^2}}\right)\right\}$$

$$+\frac{n_2}{2\pi}\left\{\frac{W}{\sqrt{1+W^2}}\left(\tan^{-1}\frac{X-Z}{\sqrt{1+W^2}}+\tan^{-1}\frac{Z}{\sqrt{1+W^2}}\right)\right.$$

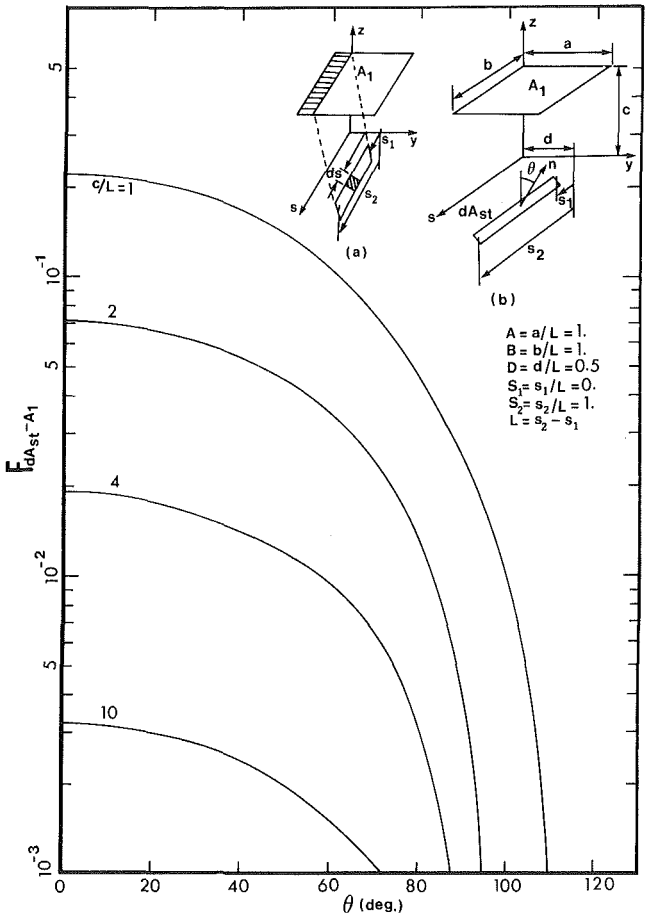

Fig. 2 Shape factor from a differential strip to a rectangular plate

$$-\frac{W-Y}{\sqrt{1+(W-Y)^2}}\left(\tan^{-1}\frac{X-Z}{\sqrt{1+(W-Y)^2}}+\tan^{-1}\frac{Z}{\sqrt{1+(W-Y)^2}}\right)$$
$$+\frac{X-Z}{\sqrt{1+(X-Z)^2}}\left(\tan^{-1}\frac{Y-W}{\sqrt{1+(Z-X)^2}}+\tan^{-1}\frac{W}{\sqrt{1+(Z-X)^2}}\right)$$
$$+\frac{Z}{\sqrt{1+Z^2}}\left(\tan^{-1}\frac{Y-W}{\sqrt{1+Z^2}}+\tan^{-1}\frac{W}{\sqrt{1+Z^2}}\right)\Bigg\} \quad (1)$$

where $X=a/c$, $Y=b/c$, $Z=d/c$, and $W=s/c$.

Figure 1 illustrates some numerical results of equation (1) when the element is parallel to the plate.

(b) **Shape Factor From a Differential Strip to a Parallel Plate.** Applying the reciprocal rule and knowing that a finite strip consists of many similar infinitesimal elements and that the view factor from this plate to the strip is the sum of view factors from the plate to each differential element forming the strip (see the sketches in Fig. 2), one can write

$$F_{st.-A_1}=(1/L)\int_{S_1}^{S_2} F_{dA_2-A_1}\,dS \quad (2)$$

where L is the length of the strip. After carrying out the integration and nondimensionalizing the resulting expression one obtains the following closed-form solution for the view factor from a differential strip to a parallel plate:

$$F_{st.-A_1}=[f_1(S_2)+f_2(S_2)]-[f_1(S_1)+f_2(S_1)] \quad (3)$$

$$f_1(S)=\frac{m}{2\pi}C\Bigg\{\frac{1}{2}\ln\left[\frac{((B-S)^2+C^2+D^2)(S^2+C^2+(D-A)^2}{((B-S)^2+C^2+(D-A)^2)(S^2+C^2+D^2)}\right]$$
$$+\frac{S}{\sqrt{C^2+D^2}}\tan^{-1}\frac{S}{\sqrt{C^2+D^2}}-\frac{B-S}{\sqrt{C^2+D^2}}\tan^{-1}\frac{B-S}{\sqrt{C^2+D^2}}$$
$$-\frac{S}{\sqrt{C^2+(D-A)^2}}\tan^{-1}\frac{S}{\sqrt{C^2+(D-A)^2}}$$
$$+\frac{B-S}{\sqrt{C^2+(D-A)^2}}\tan^{-1}\frac{B-S}{\sqrt{C^2+(D-A)^2}}\Bigg\}$$

$$f_2(S)=\frac{n}{2\pi}\Bigg\{\sqrt{S^2+C^2}\left(\tan^{-1}\frac{A-D}{\sqrt{S^2+C^2}}+\tan^{-1}\frac{D}{\sqrt{S^2+C^2}}\right)$$
$$-\sqrt{(S-B)^2+C^2}\left(\tan^{-1}\frac{A-D}{\sqrt{C^2+(S-B)^2}}+\tan^{-1}\frac{D}{\sqrt{C^2+(S-B)^2}}\right)$$
$$-\frac{(B-S)(A-D)}{\sqrt{C^2+(D-A)^2}}\tan^{-1}\frac{B-S}{\sqrt{C^2+(D-A)^2}}$$
$$+\frac{S(A-D)}{\sqrt{C^2+(D-A)^2}}\tan^{-1}\frac{S}{\sqrt{C^2+(D-A)^2}}$$
$$-\frac{D(B-S)}{\sqrt{C^2+D^2}}\tan^{-1}\frac{B-S}{\sqrt{C^2+D^2}}+\frac{DS}{\sqrt{C^2+D^2}}\tan^{-1}\frac{S}{\sqrt{C^2+D^2}}\Bigg\}$$

where $S_2=1+S_1$, $A=a/L$, $B=b/L$, $C=c/L$, $D=d/L$, $S_1=s_1/L$, $n=\cos\theta$, and $m=\sin\theta$. If the plane of the strip element intersects the plate, only the portion of the plate that can be seen by the strip element is considered to be the actual plate. Sketch (a) in Fig. 2 demonstrates this point. Figure 2 depicts the view factors from a differential strip to a parallel square that lies directly above the strip and has the same length as the differential strip.

(c) **View Factors From a Rectangular Plate to Other Finite Geometries.** The expression dF_{A_1-st} mentioned above can be further integrated to yield the view factor from a plate to other finite geometries. Note that planar geometries can be parametrically expressed by $y=y_o+a_1t$, $z=z_o+a_2t$, $x_1=x_{01}+a_{31}t$, and $x_2=x_{02}+a_{32}t$, where $0\le t\le 1$. Thus the view factor from a plate to another flat surface can be obtained by integrating the following expression from zero to unity:

$$dF_{A_1-st.}=\frac{1}{A_1}[(f_1(x_2)+f_2(x_2))-(f_1(x_1)$$
$$+f_2(x_1))](x_2-x_1)\sqrt{a_1^2+a_2^2}\,dt$$

Figure 3(a) illustrates this situation. If the finite geometry under consideration is a solid cylinder, then, as illustrated in Fig. 3(b), one obtains

$$F_{A_1-cyl.}=\sum_{i=1}^{3}F_{A_1-i}$$

where

$$F_{A_1-i}=\int_{\phi_i}^{\phi_{i+1}}\frac{1}{A_1}F_{st.-A_1}Lrd\phi$$

As demonstrated in Fig. 3(b), there are three regions of interest when evaluating $F_{st.-A_1}$. For $\phi_1\le\phi\le\phi_2$, and $\phi_3\le\phi\le\phi_4$, all the points on the cylindrical element "see" only a portion of the flat plate, but for $\phi_2\le\phi\le\phi_3$, all the points of the cylindrical element "see" the whole plate. For further details of mathematical analysis and derivation, the interested reader may refer to the report by Chung and Kermani (1988).

Results and Discussion

The present formulation, namely, equations (1) and (2), was first examined by considering a few simplified cases for which

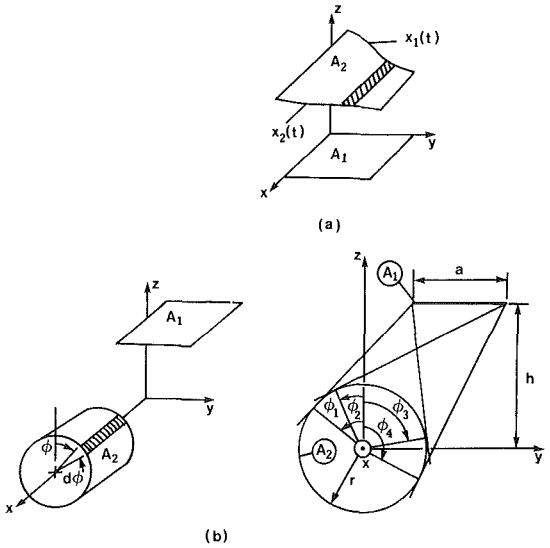

Fig. 3 *(a)* Radiation from a differential strip on a flat surface to a rectangle; *(b)* radiation from a differential strip on a cylindrical surface to a rectangle

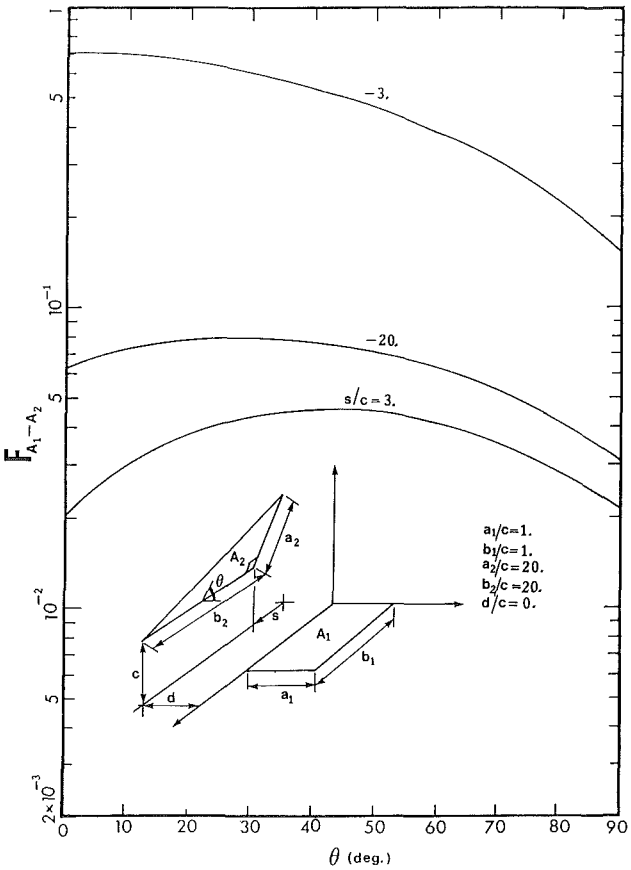

Fig. 4 View factor from a rectangular plate to a right triangular plate as a function of θ

the solutions are available in the literature. They are found to reduce to the analytical solutions of Hamilton and Morgan (1952) under various limiting conditions.

A general computer program was developed that employs a 32-point Gauss quadrature technique (with a double precision) to evaluate the shape factors numerically. The program generated results that are in agreement, up to six significant digits, with the existing cases listed by Howell (1982). This program has the capability of handling both cylindrical and planar geometries, and was used to generate the view factor from a rectangular plate to a triangular plate. The results are shown in Fig. 4. Additional view factors from rectangular to parallel plate and a parallel cylinder have been reported by Chung and Kermani (1988).

References

Chung, B. T. F., and Kermani, M. M., 1988, Technical Report, The University of Akron, Akron, OH.

Hamilton, D. C., and Morgan, W. R., 1952, "Radiant-Interchange Configuration Factors," NASA TN 2836.

Hottel, H. C., and Sarofim, A. F., 1967, *Radiation Transfer*, McGraw-Hill, New York.

Howell, J. R., 1982, *A Catalogue of Radiation Configuration Factors*, McGraw-Hill, New York.

Siegel, R., and Howell, J. R., 1981, *Thermal Radiation Heat Transfer*, 2nd ed., McGraw-Hill, New York.

Sparrow, E. M., and Cess, R. D., 1978, *Radiation Heat Transfer*, augmented ed., Hemisphere Publishing Corp., Washington, DC.

Analysis of Radiative Transfer in Rectangular Enclosures Using a Discrete Exchange Factor Method

M. H. N. Naraghi[1] and M. Kassemi[2]

Introduction

The objective of the present work is to apply the discrete exchange factor (DEF) method to a gray rectangular enclosure containing an absorbing-emitting and isotropically scattering medium. The results of this method are compared to those of the zonal (Larsen and Howell, 1985) and discrete-ordinate (Fiveland, 1984) methods and exact solutions (Shah, 1979; Crosbie and Schrenker, 1984). The accuracy of the method is demonstrated for different gas and surface conditions and the effect of the number of nodes on the computational time is also examined.

Analysis

Consider the two-dimensional rectangular gray enclosure shown in Fig. 1. The four boundaries (surfaces 1, 2, 3, and 4) are assumed diffuse opaque surfaces and the medium consists of an absorbing-emitting and isotropically scattering gas. The optical thicknesses of the medium in the x and y directions are ζ and η, respectively. The discrete exchange factor (DEF) formulation is obtained by discretizing the continuous exchange factor (CEF) equations using a Gaussian quadrature integration technique (Naraghi et al., 1988). The position of nodal points for a 5×5 nodal Gaussian quadrature method applied to a rectangular enclosure is shown in Fig. 1. In this method the direct exchange factors are between differential surface and gas strips located at nodal points for a two-dimensional system are given by the following equations (Hottel and Sarofim, 1967):

$$\overline{dss}(\mathbf{r}_i, \mathbf{r}_j) = \frac{2}{\pi |\mathbf{r}_i - \mathbf{r}_j|} \cos\theta_i \cos\theta_j f_3(K_t |\mathbf{r}_i - \mathbf{r}_j|) \frac{dA_j}{L} \tag{1}$$

$$\overline{dsg}(\mathbf{r}_i, \mathbf{r}_j) = \frac{2K_t}{\pi |\mathbf{r}_i - \mathbf{r}_j|} \cos\theta_i f_2(K_t |\mathbf{r}_i - \mathbf{r}_j|) \frac{dV_j}{L} \tag{2}$$

[1]Assistant Professor, Department of Mechanical Engineering, Manhattan College, Riverdale, NY 10471; Assoc. Mem. ASME.

[2]NRC Research Resident, NASA Lewis Research Center, Cleveland, OH 44135.

Contributed by the Heat Transfer Division for publication in the JOURNAL OF HEAT TRANSFER. Manuscript received by the Heat Transfer Division August 19, 1988. Keywords: Radiation.

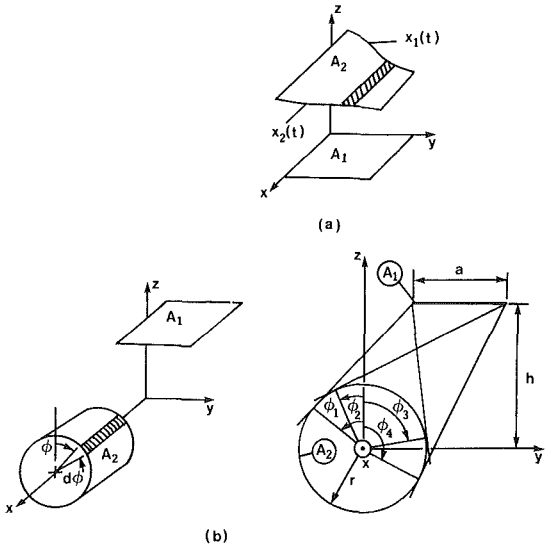

Fig. 3 *(a)* Radiation from a differential strip on a flat surface to a rectangle; *(b)* radiation from a differential strip on a cylindrical surface to a rectangle

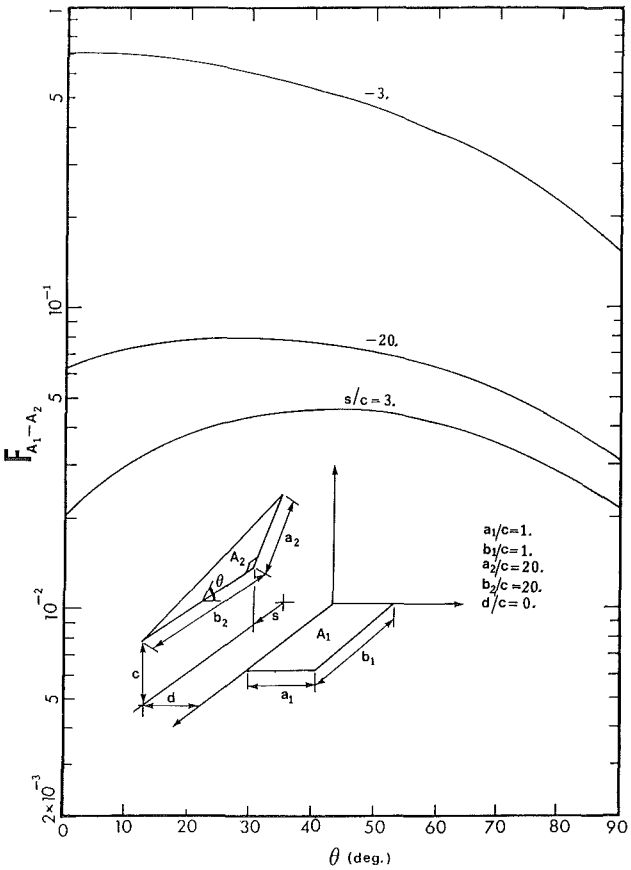

Fig. 4 View factor from a rectangular plate to a right triangular plate as a function of θ

the solutions are available in the literature. They are found to reduce to the analytical solutions of Hamilton and Morgan (1952) under various limiting conditions.

A general computer program was developed that employs a 32-point Gauss quadrature technique (with a double precision) to evaluate the shape factors numerically. The program generated results that are in agreement, up to six significant digits, with the existing cases listed by Howell (1982). This program has the capability of handling both cylindrical and planar geometries, and was used to generate the view factor from a rectangular plate to a triangular plate. The results are shown in Fig. 4. Additional view factors from rectangular to parallel plate and a parallel cylinder have been reported by Chung and Kermani (1988).

References

Chung, B. T. F., and Kermani, M. M., 1988, Technical Report, The University of Akron, Akron, OH.

Hamilton, D. C., and Morgan, W. R., 1952, "Radiant-Interchange Configuration Factors," NASA TN 2836.

Hottel, H. C., and Sarofim, A. F., 1967, *Radiation Transfer*, McGraw-Hill, New York.

Howell, J. R., 1982, *A Catalogue of Radiation Configuration Factors*, McGraw-Hill, New York.

Siegel, R., and Howell, J. R., 1981, *Thermal Radiation Heat Transfer*, 2nd ed., McGraw-Hill, New York.

Sparrow, E. M., and Cess, R. D., 1978, *Radiation Heat Transfer*, augmented ed., Hemisphere Publishing Corp., Washington, DC.

Analysis of Radiative Transfer in Rectangular Enclosures Using a Discrete Exchange Factor Method

M. H. N. Naraghi[1] and M. Kassemi[2]

Introduction

The objective of the present work is to apply the discrete exchange factor (DEF) method to a gray rectangular enclosure containing an absorbing-emitting and isotropically scattering medium. The results of this method are compared to those of the zonal (Larsen and Howell, 1985) and discrete-ordinate (Fiveland, 1984) methods and exact solutions (Shah, 1979; Crosbie and Schrenker, 1984). The accuracy of the method is demonstrated for different gas and surface conditions and the effect of the number of nodes on the computational time is also examined.

Analysis

Consider the two-dimensional rectangular gray enclosure shown in Fig. 1. The four boundaries (surfaces 1, 2, 3, and 4) are assumed diffuse opaque surfaces and the medium consists of an absorbing-emitting and isotropically scattering gas. The optical thicknesses of the medium in the x and y directions are ζ and η, respectively. The discrete exchange factor (DEF) formulation is obtained by discretizing the continuous exchange factor (CEF) equations using a Gaussian quadrature integration technique (Naraghi et al., 1988). The position of nodal points for a 5×5 nodal Gaussian quadrature method applied to a rectangular enclosure is shown in Fig. 1. In this method the direct exchange factors are between differential surface and gas strips located at nodal points for a two-dimensional system are given by the following equations (Hottel and Sarofim, 1967):

$$\overline{dss}(\mathbf{r}_i, \mathbf{r}_j) = \frac{2}{\pi |\mathbf{r}_i - \mathbf{r}_j|} \cos\theta_i \cos\theta_j f_3(K_t |\mathbf{r}_i - \mathbf{r}_j|) \frac{dA_j}{L} \tag{1}$$

$$\overline{dsg}(\mathbf{r}_i, \mathbf{r}_j) = \frac{2K_t}{\pi |\mathbf{r}_i - \mathbf{r}_j|} \cos\theta_i f_2(K_t |\mathbf{r}_i - \mathbf{r}_j|) \frac{dV_j}{L} \tag{2}$$

[1]Assistant Professor, Department of Mechanical Engineering, Manhattan College, Riverdale, NY 10471; Assoc. Mem. ASME.

[2]NRC Research Resident, NASA Lewis Research Center, Cleveland, OH 44135.

Contributed by the Heat Transfer Division for publication in the JOURNAL OF HEAT TRANSFER. Manuscript received by the Heat Transfer Division August 19, 1988. Keywords: Radiation.

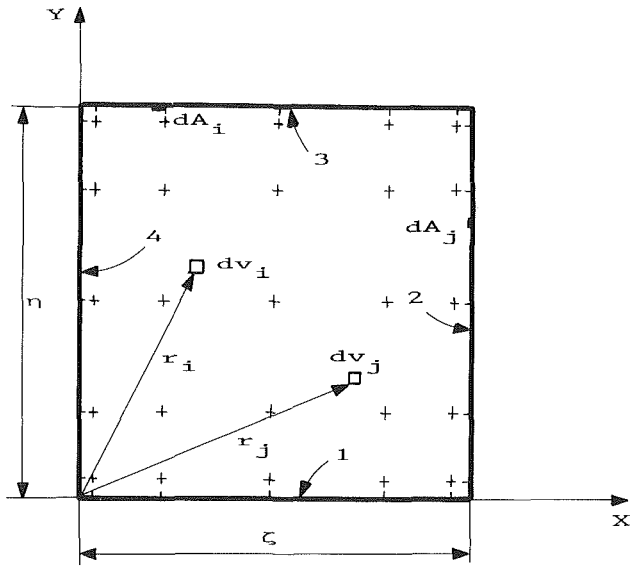

Fig. 1 Schematic of a rectangular enclosure and positions of nodal points in a rectangular enclosure for a five-point Gaussian quadrature method

$$\overline{dgs}(\mathbf{r}_i, \mathbf{r}_j) = \frac{1}{2\pi |\mathbf{r}_i - \mathbf{r}_j|} \cos\theta_j f_2(K_t |\mathbf{r}_i - \mathbf{r}_j|) \frac{dA_j}{L} \tag{3}$$

and

$$\overline{dgg}(\mathbf{r}_i, \mathbf{r}_j) = \frac{K_t}{2\pi |\mathbf{r}_i - \mathbf{r}_j|} f_1(K_t |\mathbf{r}_i - \mathbf{r}_j|) \frac{dV_j}{L} \tag{4}$$

where $f_n(x) = \int_0^{\pi/2} e^{-x/\cos\theta} \cos^{n-1}\theta \, d\theta$ and $K_t = K_a + K_s$.

The direct exchange factors between nodes form matrices: $\mathbf{dss} = [\overline{ds_i s_j}]$, $\mathbf{dsg} = [\overline{ds_i g_j}]$, $\mathbf{dgs} = [\overline{dg_i s_j}]$ and $\mathbf{dgg} = [\overline{dg_i g_j}]$. The total exchange factor represents the differential fraction of energy that is emitted from a differential surface or gas at node i and reaches another differential surface or gas at node j, directly or after multiple reflection and scattering from the surfaces and gas, respectively. Similar to the direct exchange factors, the total exchange factors form four matrices: $\mathbf{DSS} = [\overline{DS_i S_j}]$, $\mathbf{DSG} = [\overline{DS_i G_j}]$, $\mathbf{DGS} = [\overline{DG_i S_j}]$, and $\mathbf{DGG} = [\overline{DG_i G_j}]$. Explicit matrix relations given by Naraghi et al. (1988) can be used to determine matrices of total exchange factors in terms of matrices of direct exchange factors. Once the discrete total exchange factors are determined then nodal heat and emissive powers can be related through

$$q_{s_i} = E_{s_i} - \sum_{j=1}^{N_s} w_{s_j} E_{s_j} \overline{DS_j S_i} - \sum_{j=1}^{N_g} w_{g_j} E_{g_j} \overline{DG_j S_i} \tag{5}$$

and

$$q_{g_i} = E_{g_i} - \sum_{j=1}^{N_s} w_{s_j} E_{s_j} \overline{DS_j G_i} - \sum_{j=1}^{N_g} w_{g_j} E_{g_j} \overline{DG_j G_i} \tag{6}$$

Note that $E_{sj} = \epsilon_j \sigma T_j^4$ and $E_{gj} = 4K_t(1-\omega_0)\sigma T_j^4$ are surface and gas nodal emissive powers, respectively.

In calculating the direct exchange factor from a gas node to itself the distance between two nodes is zero and equation (4) becomes singular. The direct exchange factors from gas nodes must satisfy the conservation equation, which in discretized form is given by

$$\sum_{j=1}^{N_s} w_{s_j} \overline{dg_i s_j} + \sum_{j=1}^{N_g} w_{g_j} \overline{dg_i g_j} = 1 \tag{7}$$

All exchange factors in equation (7) are calculated using equations (3) and (4) except the exchange from a gas node to itself. Thus, equation (7) may be used to evaluate this direct exchange factor. When a higher order Gaussian quadrature method is used, the distance between gas and surface nodes close to the wall becomes small. Consequently, equations (2) and (3) give inaccurate values for the direct exchange factors between the surface and the nearest gas node. To obtain an accurate prediction of these exchange factors the discretized form of the conservation of energy equation from surface nodes, i.e.,

$$\sum_{j=1}^{N_s} w_{s_j} \overline{ds_i s_j} + \sum_{j=1}^{N_g} w_{g_j} \overline{ds_i g_j} = 1 \tag{8}$$

is used to evaluate the exchange factor from a surface node to the closest gas node in terms of other exchange factors, which are evaluated from equations (1) and (2). It should be noted that the discrete exchange factors satisfy the reciprocity rule and this can be used to evaluate the exchange factor from a gas node to the closest surface node.

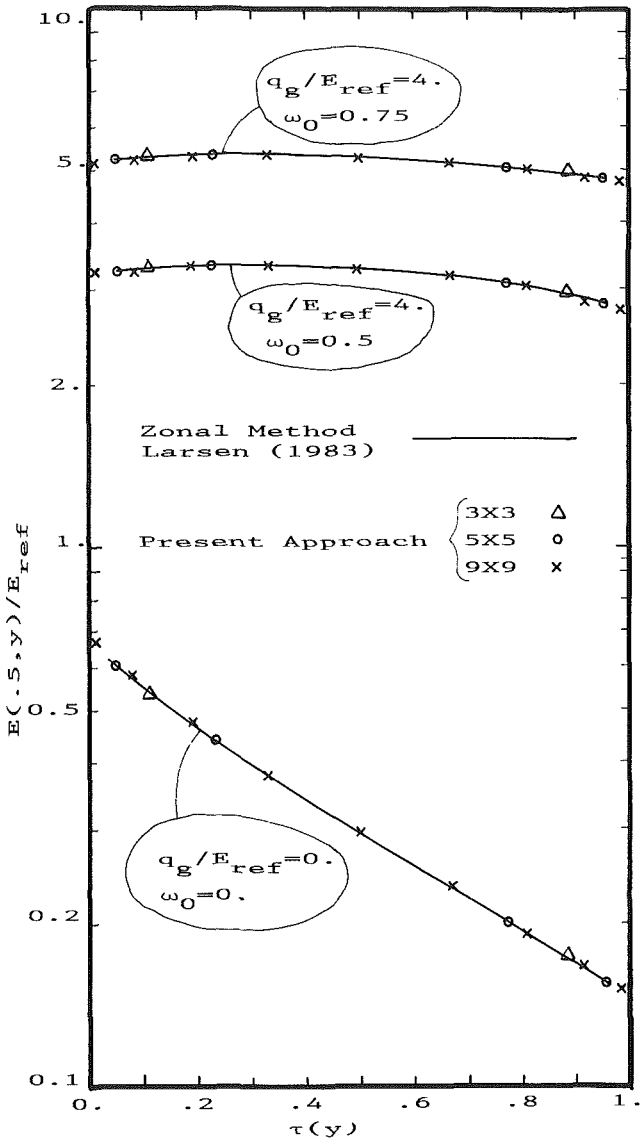

Fig. 2 Centerline (x = 0.5) dimensionless emissive power for a rectangular enclosure with black walls when $\zeta = \eta = 1$, $E_1/E_{ref} = 1$, and $E_2 = E_3 = E_4 = 0.0625E_{ref}$

Results and Discussion

The discrete exchange factor (DEF) method is used to study radiative transfer in rectangular enclosures. First a rectangular enclosure with four black surfaces where $\zeta = \eta = 1$, $E_1/E_{ref} = 1$

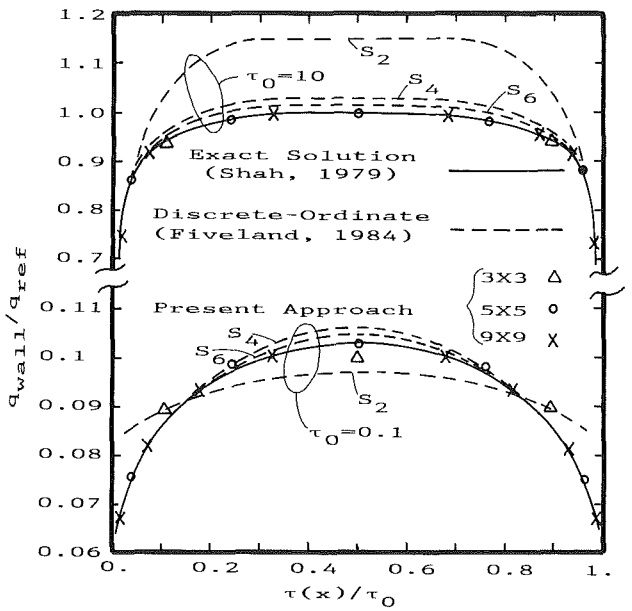

Fig. 3 Dimensionless wall heat flux for a rectangular enclosure with black cold walls $E_g = 4$ and $\zeta = \eta = 10$ and 0.1

Table 1 A comparison of VAX 11/780 CPU times for different nodal sizes

Nodal size	CPU time, s
3×3	37
5×5	76
9×9	362

and $E_2 = E_3 = E_4 = 0.0625E_{ref}$ is considered. Figure 2 shows centerline dimensionless emissive power versus position. This same problem was also analyzed by Larsen (1983) using an 11×11 zonal method for different scattering albedos. As is shown in this figure the agreement is excellent even when a small number of nodes (3×3 nodes) is used in the present approach. For a higher order Gaussian quadrature method, the distance between surface and gas nodes next to each others becomes very small (see Fig. 1) and equations (2) and (3) become singular. Consequently, the exchange factors between surface and the closest gas nodes become slightly inaccurate. This problem can be avoided in two ways:

1 The conservation equation (8) can be used for evaluation of these exchange factors as described in the previous section.

2 A lower order Gaussian quadrature method (5×5) can be used.

Furthermore, a smaller number of nodes reduces the computational time substantially. Table 1 shows the CPU times for three nodal sizes. As is shown in this table, for a 3×3 nodal size the computational time is substantially lower than that of a 9×9, while the accuracy of the results is not much different for the problem considered.

To establish the accuracy of the present approach for optical thicknesses other than unity, comparison is made to the results of the discrete-ordinate method (Fiveland, 1984) and exact solution (Shah, 1979). The rectangular enclosure considered by these authors consists of four black cold walls with $E_g = 4$ and $\omega_0 = 0$. The resulting dimensionless wall heat fluxes versus dimensionless optical depth are presented in Fig. 3. The results shown in this figure for $\tau_0 = \zeta = \eta = 10$ (optically thick medium) indicate that for all the grid sizes considered, the present approach agrees well with the exact solution of Shah (1979). Note, however, that there is a noticeable discrepancy in the predictions of the discrete-ordinate method. For an optically thin medium, $\tau_0 = \zeta = \eta = 0.1$, the results based on a 9×9 grid compare excellently with the exact solution. The agreement is also excellent for the 5×5 case. The 3×3 results are slightly off, but they still provide a better prediction than those of the S_2 discrete-ordinate method. It should be noted that the results of the discrete-ordinate model S_n presented by Fiveland (1984) are based on 20×20 nodes and $n(n+2)$ fluxes.

More comparisons between the results of the present approach and those of the finite element method (Razzaque, 1981), zonal method (Larsen, 1983; Larsen and Howell, 1985), and exact solution (Crosbie and Schrenker, 1984) are presented by Naraghi and Kassemi (1988).

Concluding Remarks

The discrete exchange factor method was used to analyze the radiative heat transfer in rectangular enclosures. The numerical results obtained are in excellent agreement with existing methods. It has been shown that the present approach with a nodal size of 3×3 provides results close to those of an 11×11 zonal method. In the zonal method the surface and gas zones are finite areas and volumes, respectively. Hence, evaluation of direct exchange factors (areas) requires multiple integrations of equations (1)–(4) (up to five integrations). In the present approach, radiative exchange between differential surface areas and gas volumes located at nodal points are evaluated. Consequently, only one integration (integration in $f_n(x)$) is needed for evaluation of the direct exchange factors.

The DEF method yields results very close to the exact solution for both optically thin and thick media. The results based on the present approach, in spite of using a smaller number of nodes, is more accurate than those of the discrete ordinate method. In this work only gray enclosures were considered. For nongray problems, a band model in which the range of active wavelengths is subdivided into finite bands can be employed. At each band nongray band properties are assumed and by integrating over all bands the nongray solution can be obtained.

Acknowledgments

This work was partially supported by NASA grant NAG 3-892.

References

Crosbie, A. L., and Schrenker, R. G., 1984, "Radiative Transfer in a Two-Dimensional Rectangular Medium Exposed to Diffuse Radiation," *J. Quant. Spectrosc. and Radiat. Transfer*, Vol. 31, No. 4, pp. 339–372.

Fiveland, W. A., 1984, "Discrete-Ordinate Solution of the Radiative Transport Equation for Rectangular Enclosures, ASME JOURNAL OF HEAT TRANSFER, Vol. 4, No. 1, pp. 3–14.

Hottel, H. C., and Sarofim, A. F., 1967, *Radiative Transfer*, McGraw-Hill, New York.

Larsen, M. E.,, 1983, "The Exchange Factor Method: an Alternative Zonal Formulation for Analysis of Radiating Enclosures Containing Participating Media," Ph.D. dissertation, The University of Texas at Austin.

Larsen, M. E., and Howell, J. R., 1985, "The Exchange Factor Method: An Alternative Basis for Zonal Analysis of Radiating Enclosures," ASME JOURNAL OF HEAT TRANSFER, Vol. 107, No. 4, pp. 936–942.

Naraghi, M. H. N., Chung, B. T. F., and Litkouhi, B., 1988, "A Continuous Exchange Factor Method for Radiative Exchange in Enclosures With Participating Media," ASME JOURNAL OF HEAT TRANSFER, Vol. 110, No. 2, pp. 456–462.

Naraghi, M. H. N., and Kassemi, M., 1988, "Radiative Transfer in Rectangular Enclosures: A Discretized Exchange Factor Solution," *Proceedings of the 1988 National Heat Transfer Conference*, Houston, TX, July 24–27, H. R. Jacobs, ed., ASME Vol. 1, pp. 259–267.

Razzaque, M. M., 1981, "Finite Element Analysis of Combined Heat Transfer Including Radiation in Gray Radiating Media," Ph.D. dissertation, The University of Texas at Austin.

Shah, N., 1979, "New Method of Computation of Radiation Heat Transfer in Combustion Chambers," Ph.D. dissertation, Department of Mechanical Engineering, Imperial College of Science and Technology, University of London, United Kingdom.

Heat and Mass Transfer From a Row of Tubes in a Vertical Plane of an Evaporative Heat Dissipator

R. S. Rana,[1] V. Charan,[2] and H. K. Varma[2]

Nomenclature

A = surface area, m^2
EP = dimensionless enthalpy potential $= \Delta i / i_{fg}$
i_a = enthalpy of air, J kg^{-1}
i_{s,t_c} = enthalpy of saturated air at average wall temperature, J kg^{-1}
i_{fg} = latent heat of vaporization of water at inlet temperature, J kg^{-1}
K = mass transfer coefficient during simultaneous air and water flow, kg m^{-2} s^{-1}
Nu = Nusselt number
Q = heat flow rate, W
Re = Reynolds number $= 4\Gamma/\mu$ for film flow over a horizontal tube
T = temperature, K
μ = dynamic viscosity, N s m^{-2}
Γ = mass flow rate of cooling water per side per unit axial length of the tube, kg m^{-1} s^{-1}
Δi = enthalpy potential defined by equation (4), J kg^{-1}

Subscripts

a = air
c = test unit surface
exp = experimental
o = outside
p = process fluid (hot water)
w = cooling water
1 = inlet
2 = outlet

Introduction

Evaporative cooling is used in the chemical industry and in refrigeration systems. In an evaporative tubular heat exchanger, the water is made to fall over horizontal tubes inside which hot fluid passes. Water flowing over the tubes is cooled evaporatively by the air blown from bottom to top. Simultaneous heat and mass transfer takes place in the equipment. The investigation of heat and mass transfer of a row of tubes is considered here as the first step in addressing the problem of evaporative cooling in a bank of tubes.

The theoretical mass transfer coefficient with simultaneous water and air flow, for a row of tubes, can be calculated from its convective heat transfer coefficient with air alone, h_a, by using the Lewis relation for an air–water mixture (Rana et al., 1986). For humid air, the Lewis number Le is taken as 0.92 (Charan and Wasekar, 1979) and h_a is given by the following equation, developed by Rana et al. (1985):

$$\mathrm{Nu} = 0.242(\mathrm{Re}_a)^{0.628} \tag{1}$$

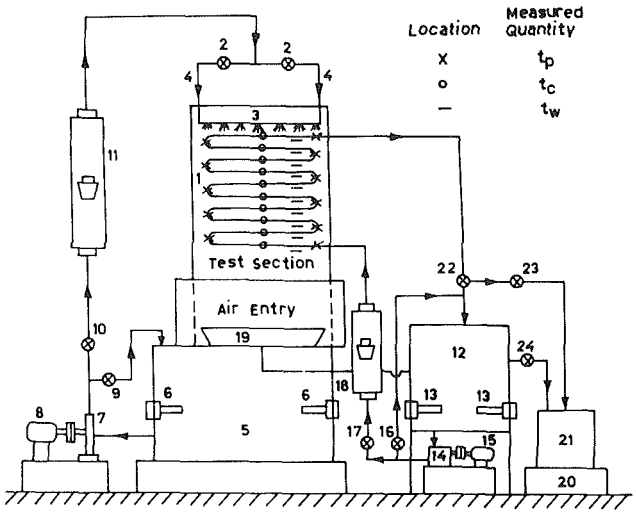

Fig. 1 Schematic of the experimental setup

The Reynolds number of air Re_a is calculated as follows:

$$\mathrm{Re}_a = D_o \, v_{a,\max} \rho_a / \mu_a \tag{2}$$

where the velocity of air $v_{a,\max}$ is based on the minimum free area of flow, obtained by subtracting the projected area of tubes from the cross-sectional area of the test section, ρ_a and μ_a are density and dynamic viscosity, respectively, evaluated at the mean air film temperature, and D_o is the outer diameter of tubes of the test unit.

The experimental mass transfer coefficient with simultaneous air and water flow, $K_{\exp}$, is normally calculated on the basis of the log mean enthalpy difference Δi between enthalpy of saturated air at the test unit average surface temperature and that of air flowing in the test unit as given by

$$Q_{wa} = K_{\exp} \, A_o \, \Delta i \tag{3}$$

where

$$\Delta i = \frac{(i_{s,t_{c_1}} - i_{a_1}) - (i_{s,t_{c_2}} - i_{a_2})}{\log[(i_{s,t_{c_1}} - i_{a_1})/(i_{s,t_{c_2}} - i_{a_2})]} \tag{4}$$

and Q_{wa} is the energy dissipated in evaporative cooling given by the product of flow rate of hot water and its temperature difference at the inlet and exit of the test unit.

Evaporative effectiveness EE is the ratio of energies dissipated in evaporative cooling to that for water cooling (Rana and Charan, 1983). The procedure for experimental determination of energies dissipated in evaporative cooling and simple water cooling processes is given by Rana et al. (1986).

Test Facility

The test facility used in this investigation is shown schematically in Fig. 1. A detailed description of the test facility is given by Rana et al. (1986). The main differences in the present setup and that of Rana et al. (1986) are: (*i*) The test unit, 1, consists of ten tubes in a vertical plane joined by U-bends at the ends, (*ii*) the horizontal projection of the top tube of the test unit on which water falls is 638 mm, (*iii*) the

[1]Mechanical Engineering Department, Punjab Engineering College, Chandigarh—160 012, India.
[2]Mechanical and Industrial Engineering Department, Roorkee University, Roorkee—247 667, India.
Contributed by the Heat Transfer Division for publication in the JOURNAL OF HEAT TRANSFER. Manuscript received by the Heat Transfer Division June 8, 1987. Keywords: Forced Convection, Mass Transfer.

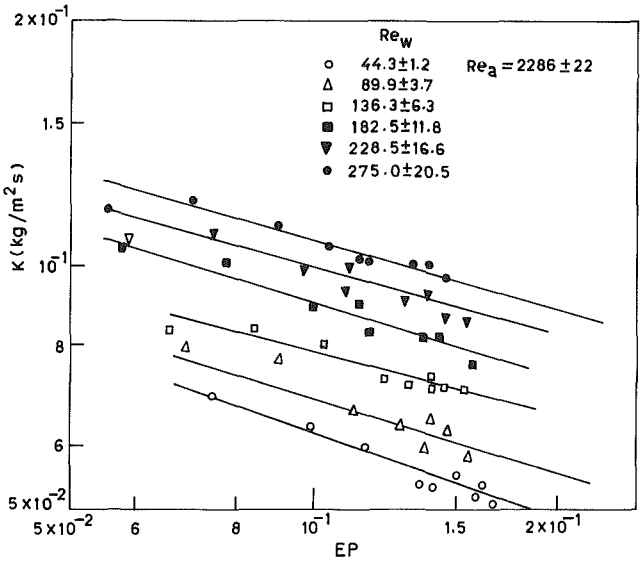

Fig. 2 Effect of *EP* on *K* of a row of tubes

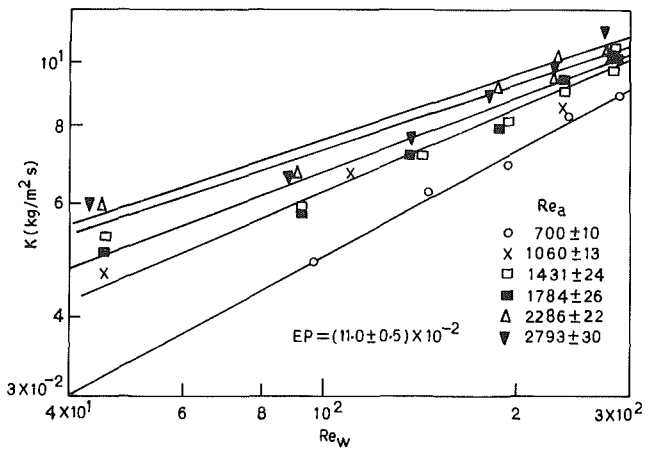

Fig. 3 Effect of Re_w on *K* of a row of tubes

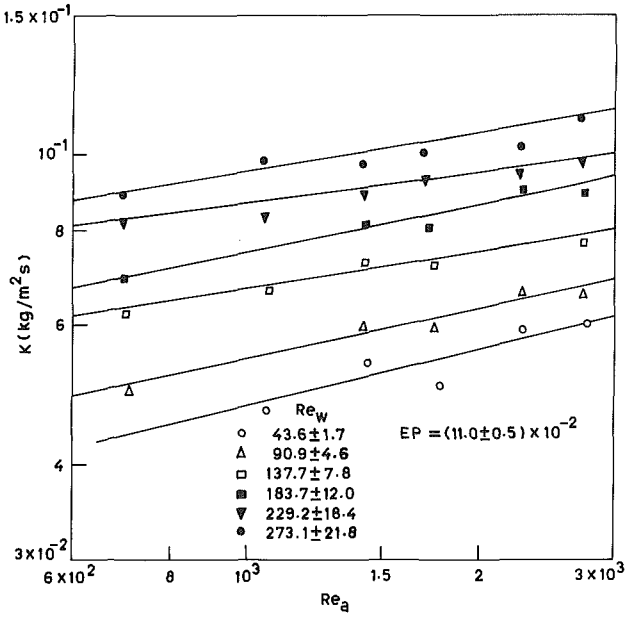

Fig. 4 Effect of Re_a on *K* of a row of tubes

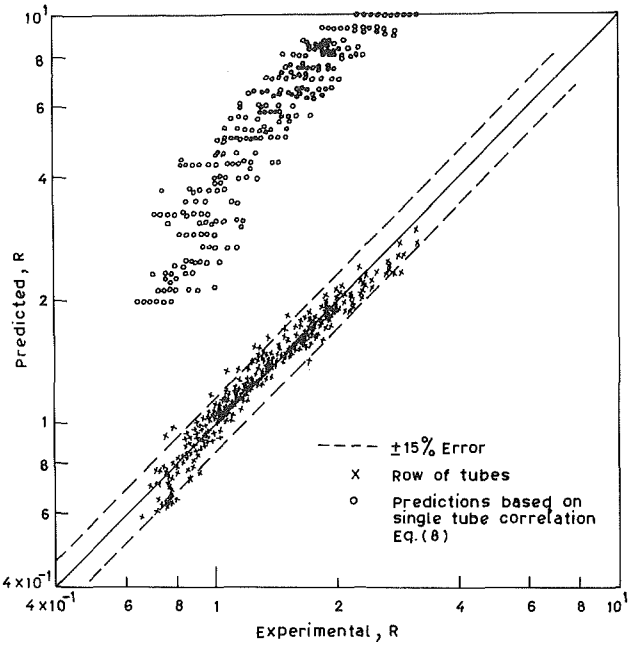

Fig. 5 Comparison between experimental *K* of a row of tubes and predicted *K* of a single tube/row of tubes

total length of the test unit including bend lengths is 6703 mm, (*iv*) an additional nine thermocouples, marked with an "X", are provided in the bends to measure the cooling of process fluid affected by each tube, (*v*) ten thermocouples marked with an "O" are provided at the center of each tube, to get the average temperature of the tube wall, and (*vi*) the temperature of cooling water falling from each tube is recorded by thermocouples placed at the "-" signs.

Test Procedure

The test procedure is reported by Rana et al. (1986). Minor changes in the flow rates of fluids are affected to adjust the range of Reynolds number of fluids to the present test unit.

Results and Discussion

1 Mass Transfer Coefficient. The mass transfer coefficient with simultaneous water and air flow was calculated by equation (3) for dimensionless enthalpy potential varying from 5.44×10^2 to 0.1971, the Reynolds number of cooling water varying from 41.9 to 294.3, and the Reynolds number of air varying from 692 to 2764. Its value lies between 2.58×10^{-2} and 0.1275 kg m^{-2} s^{-1} for the range of variables stated above. Typical graphic representations of *K* versus *EP*, Re_w, and Re_a while keeping the other two parameters constant are shown in Figs. 2-4.

The experimental values of *K* were compared with the following correlation (equation (5)) for the mass transfer coefficient of a single tube developed by Rana et al. (1986) to investigate the effect of the number of tubes on this coefficient, as shown in Fig. 5:

$$K_{exp} = 1.8433 \times 10^{-3} (EP)^{-0.0652} (Re_w)^{0.6707} (Re_a)^{0.2506} \quad (5)$$

The values of *K* calculated by equation (5) were found to be 200 to 700 percent higher than the experimental values for a single row of tubes. This is because the heat transfer rate is impaired due to the loss of cooling water in case of row of tubes. This loss is caused by: (*i*) air flow, which deflects the water from its vertical path as it falls from tube to tube, and (*ii*) splashing from the tube surface.

The following correlation is obtained for the heat and mass transfer coefficient of a row of tubes by using a regression analysis:

Table 1

Measurement	Uncertainty interval	Measurement	Uncertainty interval
Tube diameter	±0.1 mm	Water temperature	±0.025°C
Tube length	±0.5 mm	Wall temperature	±0.025°C
Water flow rate	±1 percent	Air temperature	±0.1°C

$$K_{\exp} = 9.843 \times 10^{-4}(EP)^{-0.3837}(\mathrm{Re}_w)^{0.3787}(\mathrm{Re}_a)^{0.2149} \quad (6)$$

The experimental values are compared with the above correlation and are shown in Fig. 5 itself. It is observed that for 95 percent of the test runs, the predicted values lie within ±15 percent of the experimental values and for all tests, they lie within ±25 percent of the experimental values. The mean and standard deviations are 0.2894 and 7.63 percent, respectively.

The experimental value of K was calculated by equation (3). The uncertainty intervals for individual measurements are summarized in Table 1. The uncertainty errors were calculated for all the test runs using the method suggested by Schultz and Cole (1979). The expected experimental error in K was about ±5 percent.

2 Ratio of Experimental and Theoretical Mass Transfer Coefficient. The ratio of experimental and theoretical mass transfer coefficients R was calculated for 324 test runs conducted in the range of variables mentioned in the case of mass transfer coefficient. It is found to lie between 0.653 and 3.157 and is correlated by the following equation:

$$R = 1.7838(EP)^{-0.3985}(\mathrm{Re}_w)^{0.3765}(\mathrm{Re}_a)^{-0.4114} \quad (7)$$

The predicted values are compared with the experimental values as shown in Fig. 6. The deviations are the same as in the case of the mass transfer coefficient discussed earlier. The mean and standard deviations are 0.2934 and 7.68 percent, respectively.

The experimental values of the ratio R of a row of tubes have been compared with equation (8), developed by Rana et al. (1986), for a single tube

$$R = 1.1578(EP)^{-0.0654}(\mathrm{Re}_w)^{0.6706}(\mathrm{Re}_a)^{-0.2691} \quad (8)$$

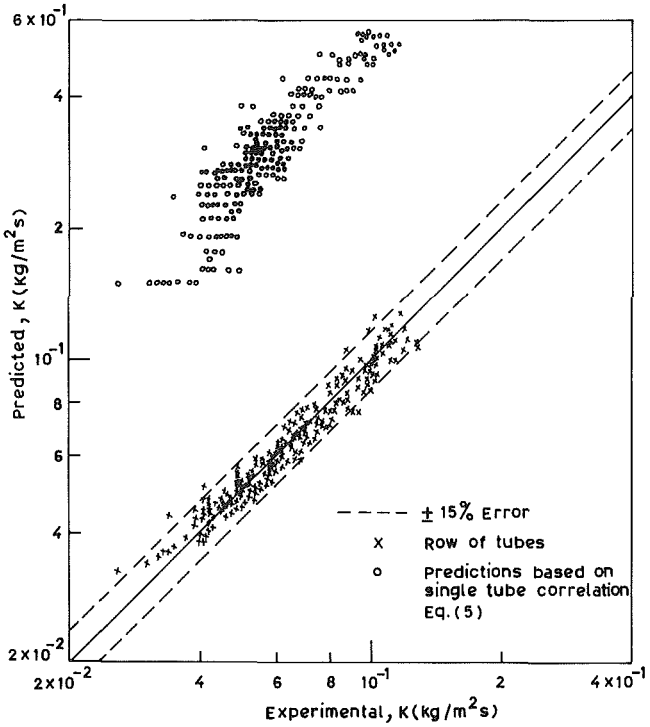

Fig. 6 Comparison between experimental R of a row of tubes and predicted R of a single tube/row of tubes

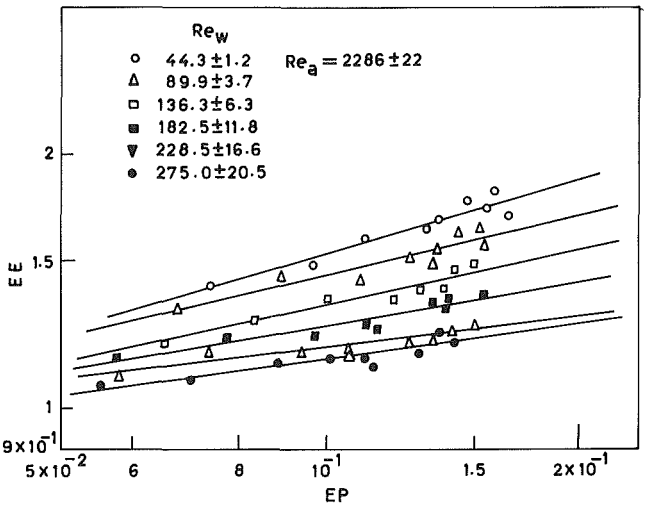

Fig. 7 Effect of *EP* on *EE* of a row of tubes

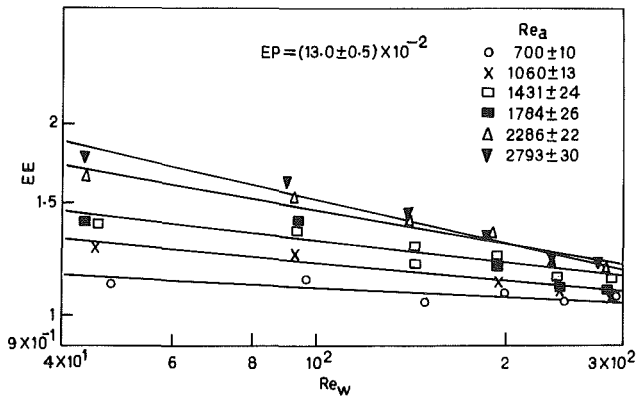

Fig. 8 Effect of Re_w on *EE* of a row of tubes

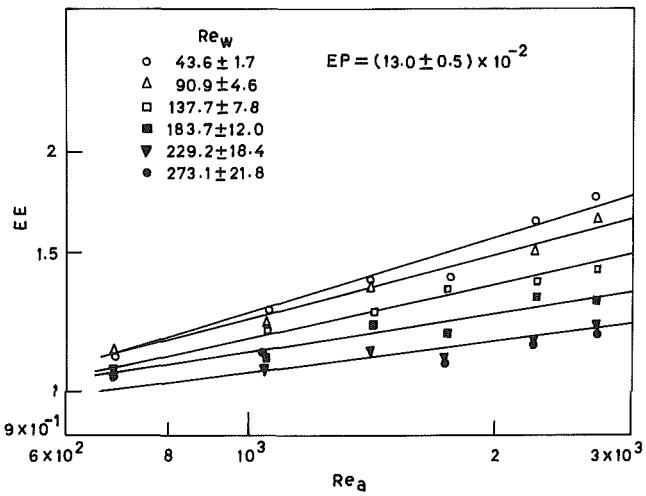

Fig. 9 Effect of Re_a on *EE* of a row of tubes

This comparison is made to observe the effect of the number of tubes on the ratio R and is shown in Fig. 6. The predicted values for a single tube are 117 to 487 percent higher than the experimental values of the ratio R for a row of tubes. The reasons for this difference are the same as discussed for the case of the mass transfer coefficient of a row of tubes.

3 Evaporative Effectiveness. The evaporative effectiveness *EE* is found to lie between 1 and 1.824 for all but four of the 324 test runs. For these four, the value is less than 1. The effect of *EP*, Re_w, and Re_a on *EE* is graphically depicted in Figs. 7–9. With the help of a regression technique, the

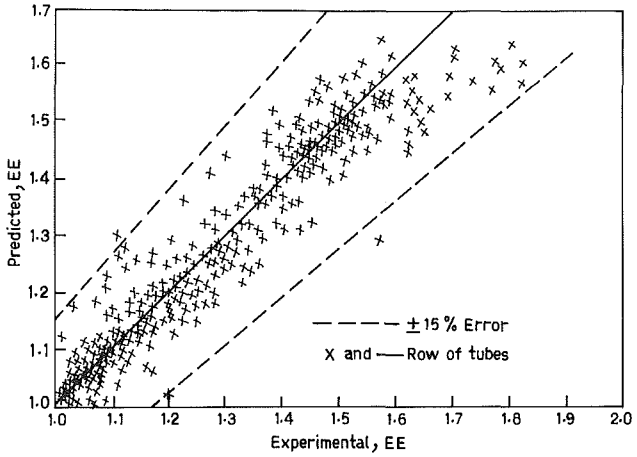

Fig. 10 Comparison between experimental and predicted *EE* of a row of tubes

following correlation was obtained for evaporative effectiveness:

$$EE = 0.8565\,(EP)^{0.1198}(\mathrm{Re}_w)^{-0.1252}(\mathrm{Re}_a)^{0.1688} \tag{9}$$

The predicted values are compared with experimental values as shown in Fig. 10. It can be seen that for all but two of the 324 test runs, the predicted values lie within ±15 percent of the experimental values. The mean and standard deviations are 0.1688 and 5.78 percent, respectively.

Conclusions

1 The mass transfer coefficient for simultaneous water and air flow over a row of tubes cannot be predicted by the correlation for a single tube developed by Rana et al. (1986). The following correlation is proposed for this coefficient in the range of $5.44\times10^{-2} < EP < 0.1971$, $41.9 < \mathrm{Re}_w < 294.3$, and $692 < \mathrm{Re}_a < 2764$:

$$K = 9.843\times10^{-4}(EP)^{-0.3837}(\mathrm{Re}_w)^{0.3787}(\mathrm{Re}_a)^{0.2194}$$

2 The ratio of experimental and theoretical mass transfer coefficients could be estimated, in the above-mentioned range of parameters, by the following correlation:

$$R = 1.7838(EP)^{-0.3985}(\mathrm{Re}_w)^{0.3765}(\mathrm{Re}_a)^{-0.4114}$$

The ratio cannot be estimated from a similar relation for a single tube given by Rana et al. (1986).

3 The evaporative effectiveness for the range of operating parameters given above could be correlated by the following dimensionless equation:

$$EE = 0.8565\,(EP)^{0.1198}(\mathrm{Re}_w)^{-0.1252}(\mathrm{Re}_a)^{0.1688}$$

Acknowledgments

This work has been carried out with partial financial assistance from the Council of Scientific and Industrial Research, New Delhi, India.

References

Charan, V., and Wasekar, R. E., 1979, "Heat and Mass Transfer in an Evaporative Heat Dissipator," *XV International Congress of Refrigeration*, Venezia, Italy, Paper No. B1-58.

Rana, R. S., and Charan, V., 1983, "Heat and Mass Transfer From a Single Horizontal Tube of an Evaporative Tubular Heat Exchanger," *International Communication in Heat and Mass Transfer*, Vol. 10, pp. 403–412.

Rana, R. S., Charan, V., and Varma, H. K., 1985, "Heat Transfer to Air From a Row of Tubes in Vertical Plane," *VIII National Heat and Mass Transfer Conference, Vishakhapatnam (India)*, Paper No. HMT-H12-85, pp. 617–621.

Rana, R. S., Charan, V., and Varma, H. K., 1986, "Heat and Mass Transfer From a Horizontal Tube of an Evaporative Heat Dissipator," *International Journal of Heat and Mass Transfer*, Vol. 29, pp. 555–562.

Schultz, R. R., and Cole, R., 1979, "Uncertainty Analysis in Boiling Nucleation," *AIChE Symposium Series*, No. 189, Vol. 75, pp. 32–39.

The Influence of End Conditions on Minimum Film Boiling From a Cylinder

K.-H. Chang,[1] L. C. Witte,[2] and S. Sankaran[3]

Nomenclature

D = heater diameter
g = gravitational acceleration
h_{fg} = latent heat of vaporization
L = heater length
q = heat flux density
$q_{\min}$ = minimum heat flux density
$q^*_{\min}$ = dimensionless minimum heat flux density

$$= \frac{q_{\min}}{\rho_v h_{fg}}\left[\frac{(\rho_l-\rho_v)\sigma g}{(\rho_l+\rho_v)^2}\right]^{1/4}$$

R = heater radius
R^* = dimensionless radius of heater $= R[(\rho_l-\rho_v)g/\sigma]^{1/2}$
T = temperature
T_w = wall temperature
ΔT_w = wall superheat $= T_w - T_{\mathrm{sat}}$
ρ_l, ρ_v = liquid, vapor densities
σ = surface tension

Introduction

Upon preparing for an experiment in which liquid–solid contacts were to be measured near the minimum film boiling point in flow boiling, it became clear that the thermal condition of the heater ends could exercise undue restrictions on the achievable minimum heat flux and wall superheat. For the experiment in question, the heater was to be heated electrically while suspended horizontally across a flow of Freon-11 (R-11). The heater surface was mounted flush with the inside wall of the test section, bringing into play the interaction with the wall as well as potential axial heat loss from the heater during film boiling. Thus we set out to investigate the influence of end conditions using a simpler pool boiling apparatus very similar to the flow boiling apparatus.

End effects, depth of immersion, and size are known to affect $q_{\min}$ data (see Shoji et al., 1987), as well as $q_{\max}$ data for horizontal cylinders (see Elkassabgi and Lienhard, 1987). Theoretical equations developed to describe $q_{\min}$ and $q_{\max}$ data are generally based on an infinite-cylinder model rather than one with finite length. Until recently little systematic work had been done to clarify these effects.

This paper details how modifications of the end conditions for an electrically heated cylinder influence the minimum film boiling point that is achievable in R-11. The modifications consisted of providing guard heating of the ends along with properly designed heater supports so that the heater temperature does not fall off precipitously near the ends. If the end temperature is not maintained high enough, transition boiling begins at the ends while the majority of the heater is immersed in a vapor film. Once the film begins to collapse, it becomes unstable and nucleate boiling ensues.

[1]Design Engineer, IMO Delaval, Inc., Los Angeles, CA.

[2]Professor, Department of Mechanical Engineering, University of Houston, Houston, TX 77204-4792; Fellow ASME.

[3]Research Assistant, Department of Mechanical Engineering, University of Houston, Houston, TX 77204-4792.

Contributed by the Heat Transfer Division for publication in the JOURNAL OF HEAT TRANSFER. Manuscript received by the Heat Transfer Division August 26, 1988; revision received December 15, 1988. Keywords: Boiling, Measurement Techniques, Natural Convection.

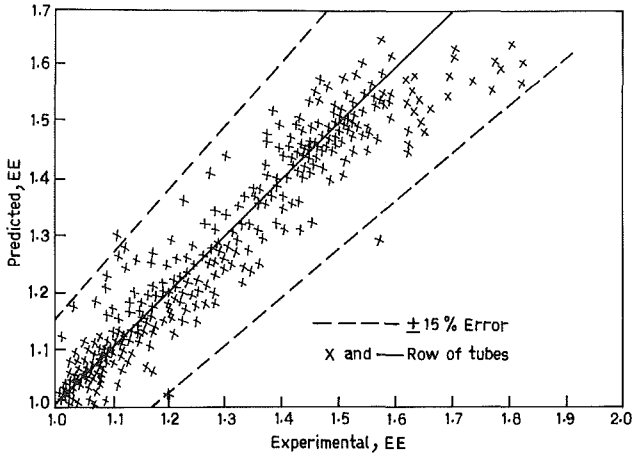

Fig. 10 Comparison between experimental and predicted *EE* of a row of tubes

following correlation was obtained for evaporative effectiveness:

$$EE = 0.8565\,(EP)^{0.1198}(\mathrm{Re}_w)^{-0.1252}(\mathrm{Re}_a)^{0.1688} \tag{9}$$

The predicted values are compared with experimental values as shown in Fig. 10. It can be seen that for all but two of the 324 test runs, the predicted values lie within ±15 percent of the experimental values. The mean and standard deviations are 0.1688 and 5.78 percent, respectively.

Conclusions

1 The mass transfer coefficient for simultaneous water and air flow over a row of tubes cannot be predicted by the correlation for a single tube developed by Rana et al. (1986). The following correlation is proposed for this coefficient in the range of $5.44\times10^{-2} < EP < 0.1971$, $41.9 < \mathrm{Re}_w < 294.3$, and $692 < \mathrm{Re}_a < 2764$:

$$K = 9.843\times10^{-4}(EP)^{-0.3837}(\mathrm{Re}_w)^{0.3787}(\mathrm{Re}_a)^{0.2194}$$

2 The ratio of experimental and theoretical mass transfer coefficients could be estimated, in the above-mentioned range of parameters, by the following correlation:

$$R = 1.7838(EP)^{-0.3985}(\mathrm{Re}_w)^{0.3765}(\mathrm{Re}_a)^{-0.4114}$$

The ratio cannot be estimated from a similar relation for a single tube given by Rana et al. (1986).

3 The evaporative effectiveness for the range of operating parameters given above could be correlated by the following dimensionless equation:

$$EE = 0.8565\,(EP)^{0.1198}(\mathrm{Re}_w)^{-0.1252}(\mathrm{Re}_a)^{0.1688}$$

Acknowledgments

This work has been carried out with partial financial assistance from the Council of Scientific and Industrial Research, New Delhi, India.

References

Charan, V., and Wasekar, R. E., 1979, "Heat and Mass Transfer in an Evaporative Heat Dissipator," *XV International Congress of Refrigeration*, Venezia, Italy, Paper No. B1-58.

Rana, R. S., and Charan, V., 1983, "Heat and Mass Transfer From a Single Horizontal Tube of an Evaporative Tubular Heat Exchanger," *International Communication in Heat and Mass Transfer*, Vol. 10, pp. 403–412.

Rana, R. S., Charan, V., and Varma, H. K., 1985, "Heat Transfer to Air From a Row of Tubes in Vertical Plane," *VIII National Heat and Mass Transfer Conference, Vishakhapatnam (India)*, Paper No. HMT-H12-85, pp. 617–621.

Rana, R. S., Charan, V., and Varma, H. K., 1986, "Heat and Mass Transfer From a Horizontal Tube of an Evaporative Heat Dissipator," *International Journal of Heat and Mass Transfer*, Vol. 29, pp. 555–562.

Schultz, R. R., and Cole, R., 1979, "Uncertainty Analysis in Boiling Nucleation," *AIChE Symposium Series*, No. 189, Vol. 75, pp. 32–39.

The Influence of End Conditions on Minimum Film Boiling From a Cylinder

K.-H. Chang,[1] L. C. Witte,[2] and S. Sankaran[3]

Nomenclature

D = heater diameter
g = gravitational acceleration
h_{fg} = latent heat of vaporization
L = heater length
q = heat flux density
$q_{\min}$ = minimum heat flux density
$q^*_{\min}$ = dimensionless minimum heat flux density

$$= \frac{q_{\min}}{\rho_v h_{fg}}\left[\frac{(\rho_l-\rho_v)\sigma g}{(\rho_l+\rho_v)^2}\right]^{1/4}$$

R = heater radius
R^* = dimensionless radius of heater $= R[(\rho_l-\rho_v)g/\sigma]^{1/2}$
T = temperature
T_w = wall temperature
ΔT_w = wall superheat $= T_w - T_{\mathrm{sat}}$
ρ_l, ρ_v = liquid, vapor densities
σ = surface tension

Introduction

Upon preparing for an experiment in which liquid–solid contacts were to be measured near the minimum film boiling point in flow boiling, it became clear that the thermal condition of the heater ends could exercise undue restrictions on the achievable minimum heat flux and wall superheat. For the experiment in question, the heater was to be heated electrically while suspended horizontally across a flow of Freon-11 (R-11). The heater surface was mounted flush with the inside wall of the test section, bringing into play the interaction with the wall as well as potential axial heat loss from the heater during film boiling. Thus we set out to investigate the influence of end conditions using a simpler pool boiling apparatus very similar to the flow boiling apparatus.

End effects, depth of immersion, and size are known to affect $q_{\min}$ data (see Shoji et al., 1987), as well as $q_{\max}$ data for horizontal cylinders (see Elkassabgi and Lienhard, 1987). Theoretical equations developed to describe $q_{\min}$ and $q_{\max}$ data are generally based on an infinite-cylinder model rather than one with finite length. Until recently little systematic work had been done to clarify these effects.

This paper details how modifications of the end conditions for an electrically heated cylinder influence the minimum film boiling point that is achievable in R-11. The modifications consisted of providing guard heating of the ends along with properly designed heater supports so that the heater temperature does not fall off precipitously near the ends. If the end temperature is not maintained high enough, transition boiling begins at the ends while the majority of the heater is immersed in a vapor film. Once the film begins to collapse, it becomes unstable and nucleate boiling ensues.

[1]Design Engineer, IMO Delaval, Inc., Los Angeles, CA.

[2]Professor, Department of Mechanical Engineering, University of Houston, Houston, TX 77204-4792; Fellow ASME.

[3]Research Assistant, Department of Mechanical Engineering, University of Houston, Houston, TX 77204-4792.

Contributed by the Heat Transfer Division for publication in the JOURNAL OF HEAT TRANSFER. Manuscript received by the Heat Transfer Division August 26, 1988; revision received December 15, 1988. Keywords: Boiling, Measurement Techniques, Natural Convection.

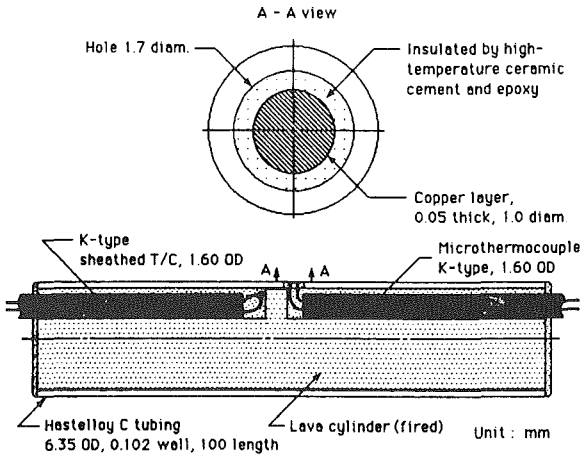

Fig. 1 K-type microthermocouple installed in the cylindrical heater

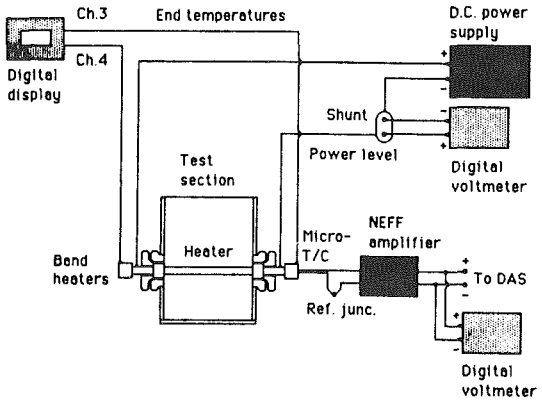

Fig. 2 Schematic diagram of the experimental measurement system

Experimental Apparatus

Experiments were performed with a thin-walled Hastelloy C heater of 0.635-cm o.d., 0.102-mm wall thickness, 10 cm long, with a lava insert for structural rigidity. Figure 1 shows the heater in transverse section. Installed in the heater surface wall is a microthermocouple probe designed to detect liquid–solid contact. A groove was machined in the lava insert and a 1.60-mm o.d. Inconel sheathed chromel-alumel thermocouple with 0.4-mm wires was laid into it. The wires were brought out to the surface through a 1.7-mm hole drilled into the Hastelloy heater. The wires were surrounded with high-temperature ceramic cement. This electrically insulated the probe from the heating surface.

A 0.05-mm-thick copper layer was electrochemically plated over the thermocouple wires to form a rapid response thermojunction. We estimate the response time for the probe to be 0.9 ms. Prior to plating the thermocouple probe, the entire assembly was heated for several hours in a furnace; this caused the lava to expand so that a good thermal fit for all of the components was created. The heater/microthermocouple probe is discussed in much greater detail by Chang (1987) and Chang and Witte (1988). The other thermocouple shown in the sketch was used to monitor the average temperature of the heater rather than the surface fluctuations. It was found that the behavior of this thermocouple agreed well with the temporal average of the surface microthermocouple.

Figure 2 shows how the heating element was situated inside a plexiglass container that could be filled with R-11. The container was 80×80 mm with a height of 125 mm. Brass buses and teflon bushings were used to support the heater. The front faces of the buses and bushings were flush with the inside wall of the plexiglass container.

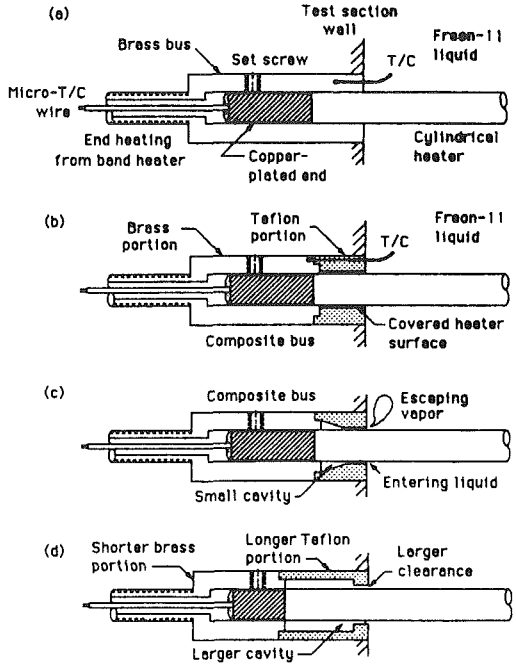

Fig. 3 Modifications of the buses connected to the cylindrical heater

Experiments were carried out by first heating the element in air to a temperature higher than what was thought to be the minimum wall superheat condition and then filling the container with R-11 so that the heater was immersed. This procedure involved partial quenching as the liquid contacted and immersed the heater. However, heat was being generated continuously in the thin-walled tubing so that a stable film boiling point could be achieved if the temperature before immersion was high enough. This procedure circumvented the need to drive the heater past the q_{max} point prior to entry into film boiling. The R-11 was introduced very gently into the container so as not to produce any significant convection currents.

The voltage output of the microthermocouple probe was recorded by a DEC Micro-11 computer equipped with a variable gain A/D board. A Neff preamplifier fed the signal to the data acquisition system. The system proved capable of temperature resolution of ± 0.25°C. An uncertainty analysis (see Chang, 1987) showed that the uncertainty in the heat flux was about ± 3 percent. The heat flux was calculated using the entire heated length of the heater apparatus.

Guard heaters were installed on the ends of the buses to counteract axial heat loss along the heater surface. They were 2.54-cm-dia band heaters rated at 150 W. Thermocouples were installed under these heaters on the bus surfaces. In some tests, thermocouples were also installed on the brass buses near the point where the buses were connected to the heater. Figures 3(a) and 3(b) show this arrangement. These thermocouples measured what we will subsequently call "end temperatures."

To improve the performance of the heater various modifications were undertaken. The next section describes the actions taken and the resulting effects on heater performance.

Improvement of End Conditions

Point 1 on Fig. 4 shows the lowest achievable q_{min} point for the heater without guard heating and when the buses were totally immersed in R-11.

The first modification was to remove the buses from the liquid by placing them outside the container as shown

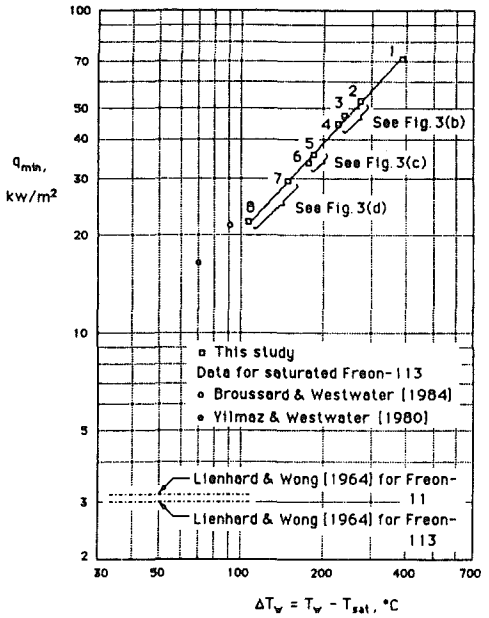

Fig. 4 Minimum film boiling points of saturated pool Freon-11 from a 6.35-mm cylindrical heater

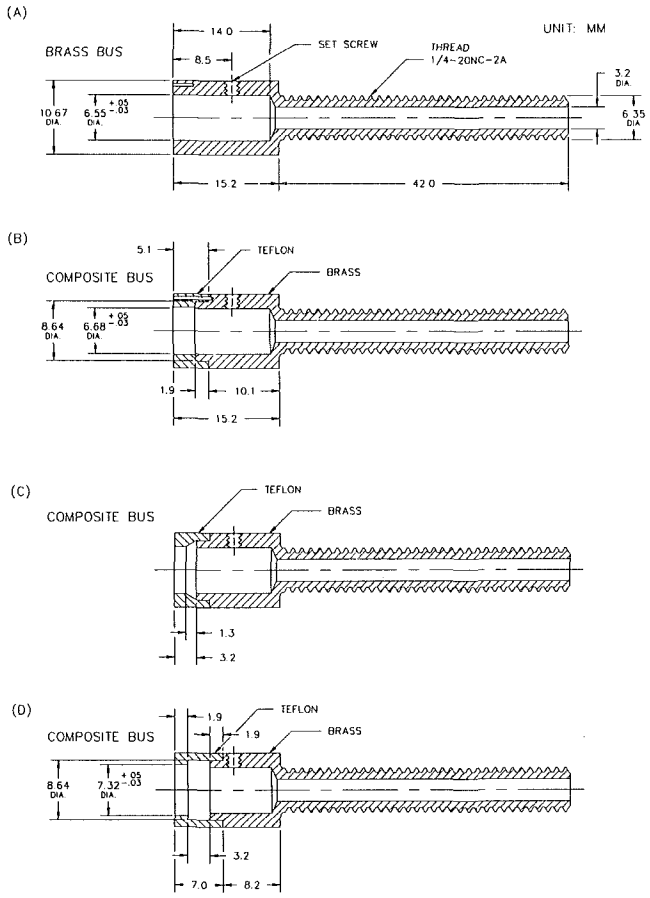

Fig. 5 Details of the heater end conditions shown schematically in Fig. 3

schematically in Fig. 2. Although this allowed lower q_{min} values, a further modification of installing a teflon bushing between the brass bus and the R-11 improved the performance even more. Figure 3(b) shows the configuration, while points 2, 3, and 4 of Fig. 4 show the resulting improvements. Improvement from point 2 to point 4 was achieved by controlling the end temperatures by proper levels of guard heating. Point 2 was achieved with the guard heaters maintaining nonuniform end temperatures of 170°C and 155°C. Point 3 resulted when guard heating was increased to maintain end temperatures at 211°C and 192°C. Point 4 also involved nonuniform end temperatures of 199°C and 182°C. The comparison of point 3 with point 4 showed that raising the end temperatures does not necessarily insure lower minimum heat flux.

A further modification was made, based on the work of Shoji et al. (1987). The teflon bushing was machined so that a small 0.2-mm clearance between the heater surface and the bushing was created; this led to a small re-entrant cavity as shown in Fig. 3(c). This modification gave significant improvement as evidenced by points 5 and 6 on Fig. 4. A small amount of liquid seeps into the cavity and is boiled, and is forced back out. This insulates the heater ends quite well. Point 5 involved uniform end temperatures of 208°C. Point 6 also resulted from uniform end temperatures of 211°C. However, the end temperatures used were thought to be too high, so further modifications were made.

Points 7 and 8 in Fig. 4 show the results of a final modification of the heater assembly. A longer teflon bushing with a larger internal cavity was installed along with a shorter brass bus. This is shown in Fig. 3(d). The clearance between the teflon bushing and the heater surface was increased to 0.5 mm. This allowed a little more liquid to enter and a little more vapor to remain in contact with the heater. This was intended to prevent overheating of the portion of the heater covered by the teflon. Careful adjustment of the level of guard heating led from point 7 to point 8 (end temperature: 182°C).

Figure 5 shows detailed, dimensional drawings of the heater end connections corresponding to Figs. 3(a–d) for the convenience of the reader.

These modifications lowered the achievable q_{min} point from 71 kW/m², $\Delta T_w = 390$°C, down to 22 kW/m², $\Delta T_w = 106$°C. Furthermore, when vapor film collapse occurred at point 8, it began near the center of the heater rather than the end, indicating that a true minimum point was being achieved.

Comparisons to Other Measurements

Figure 4 shows the prediction of Lienhard and Wong for saturated R-11 boiling from an electrically heated 6.35-mm cylinder ($L/D > 500$). While the modification of the heater assembly moved the q_{min} much closer to the prediction, it is far higher than the prediction of Lienhard and Wong. The data of Westwater and co-workers using steam-heated cylinders ($L/D = 20$) in R-113 are also shown for comparison. Their data also fall considerably above the prediction of Lienhard and Wong. Hesse's datum was produced with combined electrical and fluid heating for an L/D of 25. His datum falls considerably above Berenson's (1961) prediction for a flat plate.

Shoji et al. (1987) have performed extensive testing of various end conditions for electrically heated horizontal cylinders of various diameters (L/D from 22 to 2000) in R-113 and water. They found that for "small" heaters, characterized by R^*, where $R^* = R\,[(\rho_l - \rho_v)g/\sigma]^{1/2}$, they could achieve good agreement between achievable q_{min} and the Lienhard–Wong prediction. Figure 6 presents Shoji's data for R-113, along with the data of other investigators, including our datum for R-11. All these data deviate from the cylinder prediction of Lienhard and Wong at higher R^*, tending to agree better with Berenson's prediction for a flat plate. However, all the data exceed Berenson's prediction, indicating that none of the heaters involved are capable of theoretical minima as predicted by either Lienhard and Wong or Berenson.

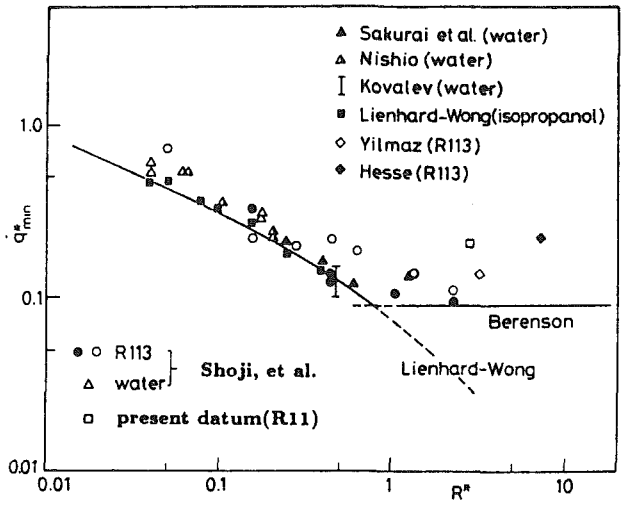

Fig. 6 Comparison of experimental q_{min} data to the predictions of Lienhard and Wong, and Berenson

It is clear that our datum representing the least achievable q_{min} for our apparatus is in reasonable agreement with the results of other researchers.

Conclusions

We have shown that the end conditions for a horizontal cylindrical heater can have a dramatic influence on the achievable q_{min}. This result emphasizes that great care must be exercised in carrying out experiments designed to measure q_{min}. Inappropriately designed apparatus can yield results that do not represent true q_{min} behavior. Through guard heating and careful design of end supports and electrical buses, q_{min} can be brought down to a value that is in reasonable agreement with predictions and data of other investigators.

Acknowledgments

The authors are grateful for the financial support of NSF Grant No. MEA-8411894 during this study. We also express our appreciation to Dr. Masahiro Shoji, University of Tokyo, for his suggestions for heater modifications.

References

Berenson, P. J., 1961, "Film-Boiling Heat Transfer From a Horizontal Surface," ASME JOURNAL OF HEAT TRANSFER, Vol. 83, pp. 351-358.

Broussard, R. A., and Westwater, J. W., 1984, "Boiling Heat Transfer of Freon-113 Flowing Normal to a Cylinder," AIAA Paper No. AIAA-84-1708.

Chang, K.-H., 1987, "The Instability of Vapor Films in Flow Boiling From Cylinders," Ph.D. Dissertation, University of Houston, Houston, TX.

Chang, K.-H., and Witte, L. C., 1988, "Liquid-Solid Contact During Flow Boiling of Freon-11," *Proc. 1988 National Heat Transfer Conference*, ASME HTD-Vol. 96, pp. 659-665.

Elkassabgi, Y., and Lienhard, J. H., 1987, "Sidewall and Immersion Depth Effects on Pool Boiling Burnout for Horizontal Cylindrical Heaters," ASME JOURNAL OF HEAT TRANSFER, Vol. 109, No. 4, pp. 1055-1057.

Hesse, G., 1973, "Heat Transfer in Nucleate Boiling, Maximum Heat Flux and Transition Boiling," *Int. J. Heat Mass Trans.*, Vol. 16, pp. 1611-1627.

Kovalev, K. A., 1966, "An Investigation of Minimum Heat Fluxes in Pool Boiling of Water," *Int. J. Heat Mass Trans.*, Vol. 9, No. 11, pp. 1219-1226.

Lienhard, J. H., and Wong, P. T. Y., 1964, "The Dominant Unstable Wavelength and Minimum Heat Flux During Film Boiling on a Horizontal Cylinder," ASME JOURNAL OF HEAT TRANSFER, Vol. 86, No. 2, pp. 220-226.

Nishio, S., 1985, *Trans. Jap. Soc. Mech. Engr., B.*, Vol. 51, No. 470, p. 340 (in Japanese) (data reported by Shoji et al., 1987).

Sakurai, A., and Shiotsu, X., 1986, *The 18th Japanese National Heat Transfer Symposium* (in Japanese) (data reported by Shoji et al., 1987).

Shoji, M., Okamoto, A., Kaneko, Y., and Kawada, M., 1987, "Effects of Size and End Conditions of a Heated Surface Upon Minimum Film Boiling," *JSME Int. Journal*, Vol. 30, No. 268, pp. 1587-1594.

Yilmaz, S., and Westwater, J. W., 1980, "Effect of Velocity on Heat Transfer to Boiling Freon-113," ASME JOURNAL OF HEAT TRANSFER, Vol. 102, No. 1, pp. 26-31.

Uniqueness of System Response Time for Transient Condensing Flows

G. L. Wedekind,[1] B. T. Beck,[2] B. L. Bhatt,[3] and G. L. Roslund[4]

Nomenclature

A_t = total cross-sectional area of flow channel, m^2
$\bar{f}_q$ = peripherally averaged applied heat flux, W/m^2
h = enthalpy of saturated liquid, J/kg
L = length of evaporating flow system, m
$m'_{a,i}$ = initial vapor accumulation rate for a step increase in inlet flow rate, kg/s
$m'_{r,i}$ = initial vapor removal rate for a step decrease in inlet flow rate, kg/s
m_t = local total mass flow rate of fluid (liquid and vapor), kg/s
M'_e = excess mass of vapor, kg
M'_s = vapor shortage, kg
p = local pressure of fluid, N/m^2
P = inside perimeter of flow channel, m
t = time, s
V'_e = volume of excess vapor, m^3
V'_s = volume of temporary vapor shortage, m^3
x = local instantaneous flow quality
x_i = flow quality at inlet
x_o = flow quality at effective position η of representative propagating void α_o
z = axial position in flow system measured from inlet, m
α = instantaneous area mean void fraction
α_i = void fraction at inlet
α_o = representative propagating void
$\bar{\alpha}$ = system mean void fraction, see equation (3)
η = instantaneous effective position of representative propagating void, m
ρ = density of saturated liquid, kg/m^3
τ = time constant characterizing response of effective position of representative propagating void, s
τ^* = time constant for system involving complete condensation or vaporization, s

Subscripts and Superscripts

Barred ($\bar{}$) quantities are generally considered to be spatially averaged, where the averaging is presumed to take place within the appropriate region under consideration. Primed (′) symbols of quantities refer to saturated vapor.

[1]Professor of Engineering, Oakland University, Rochester, MI 48309-4401; Mem. ASME.

[2]Associate Professor of Mechanical Engineering, Kansas State University, Manhattan, KS; Mem. ASME.

[3]Professor of Engineering, Oakland University, Rochester, MI 48309-4401; Mem. ASME.

[4]Administrator of Statistical Programs, General Motors Corporation, Detroit, MI.

Contributed by the Heat Transfer Division for publication in the JOURNAL OF HEAT TRANSFER. Manuscript received by the Heat Transfer Division August 13, 1987. Keywords: Condensation, Transient and Unsteady Heat Transfer.

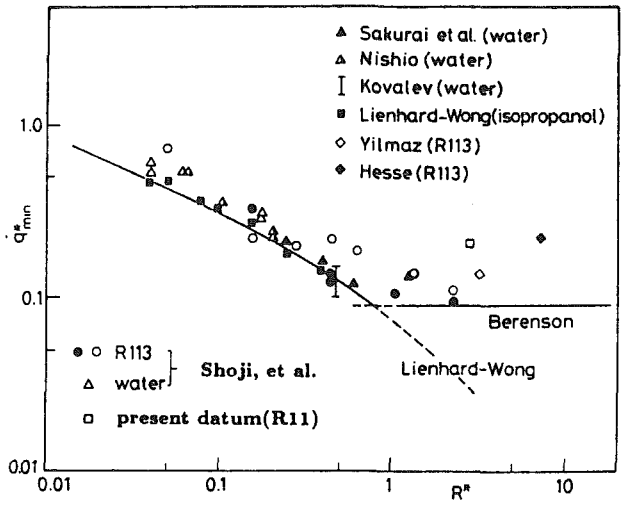

Fig. 6 Comparison of experimental q_{min} data to the predictions of Lienhard and Wong, and Berenson

It is clear that our datum representing the least achievable q_{min} for our apparatus is in reasonable agreement with the results of other researchers.

Conclusions

We have shown that the end conditions for a horizontal cylindrical heater can have a dramatic influence on the achievable q_{min}. This result emphasizes that great care must be exercised in carrying out experiments designed to measure q_{min}. Inappropriately designed apparatus can yield results that do not represent true q_{min} behavior. Through guard heating and careful design of end supports and electrical buses, q_{min} can be brought down to a value that is in reasonable agreement with predictions and data of other investigators.

Acknowledgments

The authors are grateful for the financial support of NSF Grant No. MEA-8411894 during this study. We also express our appreciation to Dr. Masahiro Shoji, University of Tokyo, for his suggestions for heater modifications.

References

Berenson, P. J., 1961, "Film-Boiling Heat Transfer From a Horizontal Surface," ASME JOURNAL OF HEAT TRANSFER, Vol. 83, pp. 351–358.

Broussard, R. A., and Westwater, J. W., 1984, "Boiling Heat Transfer of Freon-113 Flowing Normal to a Cylinder," AIAA Paper No. AIAA-84-1708.

Chang, K.-H., 1987, "The Instability of Vapor Films in Flow Boiling From Cylinders," Ph.D. Dissertation, University of Houston, Houston, TX.

Chang, K.-H., and Witte, L. C., 1988, "Liquid–Solid Contact During Flow Boiling of Freon-11," *Proc. 1988 National Heat Transfer Conference*, ASME HTD-Vol. 96, pp. 659–665.

Elkassabgi, Y., and Lienhard, J. H., 1987, "Sidewall and Immersion Depth Effects on Pool Boiling Burnout for Horizontal Cylindrical Heaters," ASME JOURNAL OF HEAT TRANSFER, Vol. 109, No. 4, pp. 1055–1057.

Hesse, G., 1973, "Heat Transfer in Nucleate Boiling, Maximum Heat Flux and Transition Boiling," *Int. J. Heat Mass Trans.*, Vol. 16, pp. 1611–1627.

Kovalev, K. A., 1966, "An Investigation of Minimum Heat Fluxes in Pool Boiling of Water," *Int. J. Heat Mass Trans.*, Vol. 9, No. 11, pp. 1219–1226.

Lienhard, J. H., and Wong, P. T. Y., 1964, "The Dominant Unstable Wavelength and Minimum Heat Flux During Film Boiling on a Horizontal Cylinder," ASME JOURNAL OF HEAT TRANSFER, Vol. 86, No. 2, pp. 220–226.

Nishio, S., 1985, *Trans. Jap. Soc. Mech. Engr., B.*, Vol. 51, No. 470, p. 340 (in Japanese) (data reported by Shoji et al., 1987).

Sakurai, A., and Shiotsu, X., 1986, *The 18th Japanese National Heat Transfer Symposium* (in Japanese) (data reported by Shoji et al., 1987).

Shoji, M., Okamoto, A., Kaneko, Y., and Kawada, M., 1987, "Effects of Size and End Conditions of a Heated Surface Upon Minimum Film Boiling," *JSME Int. Journal*, Vol. 30, No. 268, pp. 1587–1594.

Yilmaz, S., and Westwater, J. W., 1980, "Effect of Velocity on Heat Transfer to Boiling Freon-113," ASME JOURNAL OF HEAT TRANSFER, Vol. 102, No. 1, pp. 26–31.

Uniqueness of System Response Time for Transient Condensing Flows

G. L. Wedekind,[1] B. T. Beck,[2] B. L. Bhatt,[3] and G. L. Roslund[4]

Nomenclature

A_t = total cross-sectional area of flow channel, m^2
$\bar{f}_q$ = peripherally averaged applied heat flux, W/m^2
h = enthalpy of saturated liquid, J/kg
L = length of evaporating flow system, m
$m'_{a,i}$ = initial vapor accumulation rate for a step increase in inlet flow rate, kg/s
$m'_{r,i}$ = initial vapor removal rate for a step decrease in inlet flow rate, kg/s
m_t = local total mass flow rate of fluid (liquid and vapor), kg/s
M'_e = excess mass of vapor, kg
M'_s = vapor shortage, kg
p = local pressure of fluid, N/m^2
P = inside perimeter of flow channel, m
t = time, s
V'_e = volume of excess vapor, m^3
V'_s = volume of temporary vapor shortage, m^3
x = local instantaneous flow quality
x_i = flow quality at inlet
x_o = flow quality at effective position η of representative propagating void α_o
z = axial position in flow system measured from inlet, m
α = instantaneous area mean void fraction
α_i = void fraction at inlet
α_o = representative propagating void
$\bar{\alpha}$ = system mean void fraction, see equation (3)
η = instantaneous effective position of representative propagating void, m
ρ = density of saturated liquid, kg/m^3
τ = time constant characterizing response of effective position of representative propagating void, s
τ^* = time constant for system involving complete condensation or vaporization, s

Subscripts and Superscripts

Barred ($\bar{}$) quantities are generally considered to be spatially averaged, where the averaging is presumed to take place within the appropriate region under consideration. Primed ($'$) symbols of quantities refer to saturated vapor.

[1]Professor of Engineering, Oakland University, Rochester, MI 48309-4401; Mem. ASME.

[2]Associate Professor of Mechanical Engineering, Kansas State University, Manhattan, KS; Mem. ASME.

[3]Professor of Engineering, Oakland University, Rochester, MI 48309-4401; Mem. ASME.

[4]Administrator of Statistical Programs, General Motors Corporation, Detroit, MI.

Contributed by the Heat Transfer Division for publication in the JOURNAL OF HEAT TRANSFER. Manuscript received by the Heat Transfer Division August 13, 1987. Keywords: Condensation, Transient and Unsteady Heat Transfer.

Introduction

The unique characteristics under consideration in this paper are encountered in condensing flows, and have to do with a system's response time for various degrees of outlet flow quality. Specifically, the system response time for condensing flows appears to increase monotonically with decreasing outlet flow quality, reaching a maximum for systems having an outlet flow quality of between 10 and 20 percent. The system response time then decreases for outlet flow qualities that are less than that value.

These unique characteristics are predicted theoretically by the system mean void fraction model. The purpose of this paper is to develop analytically the characteristics, explain the physics of the phenomena responsible, and discuss the experimental verification efforts that have thus far been carried out.

Analytical Development of Unique Characteristics

Unified System Mean Void Fraction Model. The system mean void fraction model has been developed for two-phase transient evaporating and condensing flow systems. It allows for separated flows, and for an axial distribution of local void fraction. Thus it is a distributed model. The principal governing equations are written in integral form, encompassing a finite region upstream of a particular representative propagating void (Fig. 1). Incorporating the concept of a system mean void fraction, the governing equations can be formulated such that they are identical for complete or incomplete evaporating and condensing flows (Wedekind et al., 1984).

Combined Conservation Equations. The conservation of mass and energy equations can be combined as was done by Beck and Wedekind (1981) to yield the following equation governing the response of the effective position, $\eta(t)$, of the representative propagating void, α_o, for a constant heat flux $\bar{f}_q$:

$$\{\rho-(\rho-\rho')(1-x_o)\}(\alpha_o-\bar{\alpha})\frac{(h'-h)}{\bar{f}_q P}A_t\frac{d\eta(t)}{dt}$$

$$+\eta(t)=\frac{(h'-h)}{\bar{f}_q P}(x_o-x_i)m_t(z,\,t)_{z=0} \tag{1}$$

This differential equation is valid for either evaporating or condensing flows, recognizing that $\bar{f}_q>0$ for vaporization and $\bar{f}_q<0$ for condensation.

System Time Constant. Being first order, equation (1) has a time constant τ, which is given by the following expression, which incorporates various geometric, thermodynamic, transport, and two-phase flow parameters:

$$\tau=\frac{\{\rho-(\rho-\rho')(1-x_o)\}(h'-h)(\alpha_0-\bar{\alpha})A_t}{\bar{f}_q P} \tag{2}$$

The system mean void fraction[5] $\bar{\alpha}$ is defined in general, and calculated specifically, for a uniform heat flux as follows:

$$\bar{\alpha}\equiv\frac{1}{\eta(t)}\int_{z=0}^{\eta(t)}\alpha(z,\,t)dz=\frac{1}{(x_o-x_i)}\int_{x=x_i}^{x_o}\alpha(x)dx \tag{3}$$

where the expression

$$\alpha(z,\,t)_{z=\eta(t)}=\alpha_0 \tag{4}$$

implicitly defines $\eta(t)$, the effective position within the two-phase region associated with the particular value of an area mean void fraction α_0, which is the representative propagating void.

[5] Defined in this manner, the system mean void fraction is assumed to be time invariant, an assumption that has been shown to be reasonable in many previous applications (Wedekind and Stoecker, 1968; Wedekind et al., 1978; Wedekind and Bhatt, 1977; Beck and Wedekind, 1981).

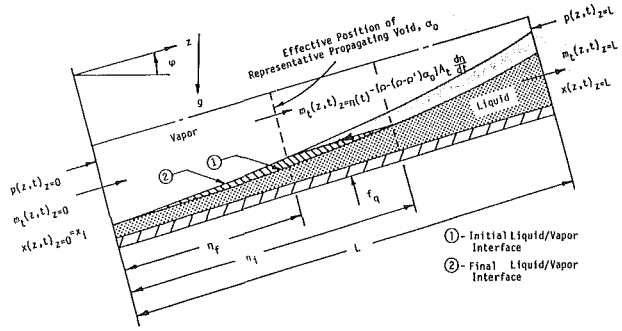

Fig. 1 Schematic of condensing flow system; explanation of system time constant for step decrease in inlet flow rate

Physical Significance of System Time Constant. It is important to consider the physical significance of the system time constant τ. Consider the schematic shown in Fig. 1. The two-phase system under consideration extends from the condenser inlet to the effective position $\eta(t)$ of the representative propagating void α_o. Therefore, for a step decrease in inlet vapor flow rate, this position will undergo a transient shift from η_i to η_f. In order for the shift to take place, there is a temporary excess mass of vapor M'_e, which must be removed, where $M'_e=\rho' V'_e$. The temporary excess volume of vapor V'_e can be visualized from the schematic as the triangular-shaped, cross-hatched area bounded by the initial and final liquid/vapor interface, and the horizontal line representing the top of the area swept out by the propagating void α_o. A careful examination indicates that this volume can be expressed as

$$V'_e=\bar{\alpha}A_t(\eta_i-\eta_f)-\alpha_o A_t(\eta_i-\eta_f)=(\bar{\alpha}-\alpha_o)A_t(\eta_i-\eta_f) \tag{5}$$

The initial vapor removal rate $m'_{r,i}$ is expressed as the difference between the initial outlet and inlet vapor flow rate plus the initial condensation rate; thus

$$m'_{r,i}=x_o m_t(z,\,t)_{\substack{z=\eta(t)\\t=0}}-x_i m_t(z,\,t)_{\substack{z=0\\t=0}}-\frac{\bar{f}_q P}{(h'-h)}\eta(t)_{t=0} \tag{6}$$

Using equation (18) of Beck and Wedekind (1981) for the local mass flow rate, and the steady-state form of equation (1), equation (6) can be simplified after considerable rearrangement to yield

$$m'_{r,i}=\frac{\bar{f}_q P(\eta_f-\eta_i)}{(h'-h)\left\{1+\left[\left(\frac{\rho}{\rho'}\right)-1\right]x_o\right\}} \tag{7}$$

Dividing the temporary excess mass of vapor M'_e by the initial vapor removal rate $m'_{r,i}$, using equations (6) and (7), yields

$$\frac{M'_e}{m'_{r,i}}$$

$$=\frac{\rho' V'_e}{m'_{r,i}}=\frac{\{\rho-(\rho-\rho')(1-x_o)\}(h'-h)(\alpha_o-\bar{\alpha})A_t}{\bar{f}_q P}=\tau \tag{8}$$

which is seen to be the same as equation (2). Therefore, the system time constant τ can be expressed as the ratio of the temporary excess mass of vapor M'_e to the initial vapor removal rate $m'_{r,i}$. Physically then, for a step decrease in the condenser inlet flow rate, the system time constant is the amount of time necessary to remove the temporary excess vapor, at the initial vapor removal rate.

For a step increase in inlet flow rate, a similar formulation can be carried out, but with a few minor changes in physical interpretation. Instead of a temporary *excess* mass of vapor

$\rho' V'_e$, there would be a temporary vapor *shortage* $\rho' V'_s$. In addition, instead of an initial vapor *removal* rate $m'_{r,i}$, there would be an initial vapor *accumulation* rate $m'_{a,i}$.

The interesting result is that the ratio $(\rho' V's)/m'_{a,i}$ for a step increase can be shown to be identical to the ratio $(\rho' V'_e)/m'_{r,i}$ for a step decrease, as given by equation (8). Physically then, for a step increase in the condenser inlet flow rate, the system time constant becomes the amount of time necessary to accumulate the temporary vapor shortage, at the initial vapor accumulation rate.

It is important to note that the identical expression can be shown to exist for evaporating flow systems as well, thus affirming the generality of the system time constant τ, as well as clarifying its physical significance.

Characteristics of System Time Constant Ratio

Variation With Outlet Quality. In order to examine the system time constant variation with outlet quality, it is convenient to develop a time constant ratio τ/τ^*, which is the ratio of the system time constant τ, with an arbitrary propagation flow quality x_o, to the time constant τ^*, for a similar system but with total vaporization or condensation.

Evaporating Flow. $\bar{f}_q > 0$, $\alpha_o > \bar{\alpha}$, $0 < x_o \leq 1$. For complete vaporization, $x_o = 1$ and $\alpha_o = 1$; thus equation (2) becomes

$$\tau_e^* = \rho A_t \frac{(h' - h)}{\bar{f}_q P} (1 - \bar{\alpha})_{x_o = 1} \tag{9}$$

Therefore, the time constant ratio for evaporating flow can be expressed as

$$\tau_e/\tau_e^* = \left\{1 - \left[1 - \left(\frac{\rho}{\rho'}\right)\right](1 - x_o)\right\} \frac{(\alpha_o - \bar{\alpha})}{(1 - \bar{\alpha})_{x_o = 1}} \tag{10}$$

Condensing Flow. $\bar{f}_q < 0$, $\alpha_o < \bar{\alpha}$, $0 \leq x_o < 1$. For complete condensation, $x_o = 0$, and $\alpha_o = 0$; thus equation (2) becomes

$$\tau_c^* = \rho' A_t \frac{(h' - h)}{\bar{f}_q P} \bar{\alpha}_{x_o = 0} \tag{11}$$

Therefore, the time constant ratio for condensing flow can then be expressed as

$$\tau_c/\tau_c^* = \left\{1 + \left[\left(\frac{\rho}{\rho'}\right) - 1\right] x_o\right\} \frac{(\bar{\alpha} - \alpha_o)}{\bar{\alpha}_{x_o = 0}} \tag{12}$$

Variation With Density Ratio. Using equation (3) and an appropriate relationship between void fraction and flow quality,[6] equations (10) and (12) can be evaluated as a function of various propagating flow qualities x_o. The results are depicted in Fig. 2 for three different liquid to vapor density ratios (ρ/ρ'), and an inlet quality $x_i = 0$, for evaporating flow; and $x_i = 1$, for condensing flow. For reference purposes, a liquid-to-vapor density ratio of 30 corresponds to a saturation pressure of about 5170 kN/m^2 for water, or 690 kN/m^2 for Refrigerant-12. Density ratios of 60 and 120 correspond to saturation pressures for water at about 2760 and 1380 kN/m^2, respectively.

Physical Explanation. A physical mechanism for the characteristic can be extracted from the physical interpretation of the system time constant τ as expressed in equation (8). For a step decrease in inlet flow rate, the system time constant τ has been shown to be the ratio of the temporary excess vapor $\rho' V'_e$ to the initial vapor removal rate $m'_{r,i}$. A careful study of the two terms indicates that as the propagating flow quality x_o approaches that of complete condensation, $0.1 > x_o \geq 0$, the initial vapor removal rate $m'_{r,i}$ increases much faster than the magnitude of the temporary excess vapor $\rho' V'_e$. This characteristic is depicted in Fig. 3, and would be the same for a step increase in the inlet vapor flow rate.

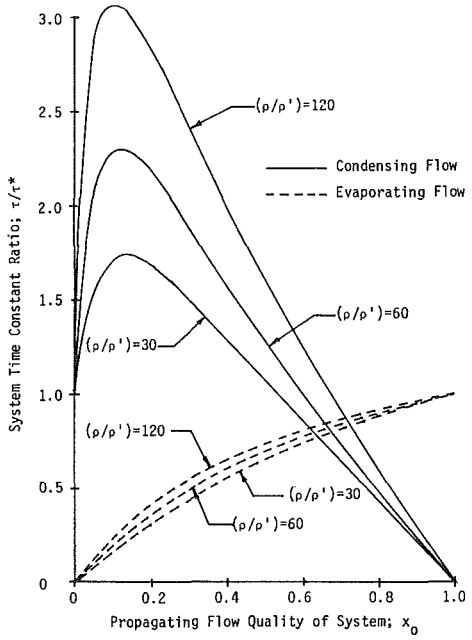

Fig. 2 Characteristics of system time constant ratio; transient condensing and evaporating flow systems

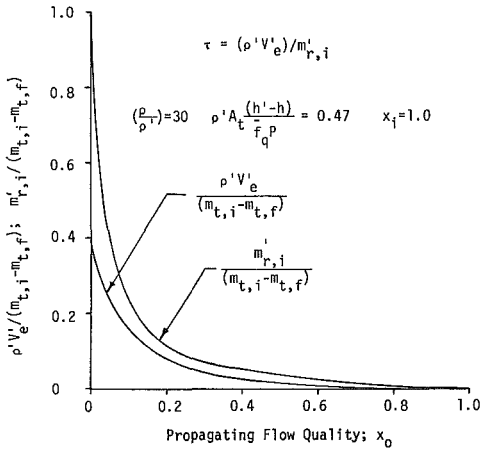

Fig. 3 Influence of propagating flow quality on excess vapor, and initial vapor removal rate, for a step decrease in inlet vapor flow rate to condenser

Experimental Verification. Direct experimental verification of the characteristics is very difficult due to the inherent fluctuations that are always present in two-phase flows, and due to the limitations of existing two-phase flow instrumentation. Another difficulty encountered is that the system response times under consideration here are very short, ranging from 0.3–1.0 s for the experimental apparatus currently available to the authors. Therefore, it is very difficult to obtain experimentally a relative step change in the inlet flow rate.

The authors have tried to verify this unique response characteristic by simultaneously measuring the transient two-phase pressure drop between the condenser inlet and various positions along the condenser tube. However, when an attempt was made experimentally to achieve a relative step change, using a very fast-acting solenoid valve, the "water-

[6] A number of void fraction/flow quality relationships have been proposed for steady-state conditions. The particular one used should be carefully chosen as a result of proven accuracy for the particular flow situation under consideration. For computational simplicity, the model presented by Zivi (1964) is used here. However, it seems reasonable that the results shown in Figs. 2 and 3 would essentially be the same for any of the relationships.

hammer'' type of pressure noise virtually masked the desired pressure measurement. When a slower change in the inlet flow rate was made to eliminate the ''water-hammer'' noise, then the results were such that with the inherent fluctuations, clear verification of the characteristics was inconclusive. It is hoped that other researchers will be able to contribute to the experimental evidence related to these unique characteristics.

Acknowledgments

The authors would like to acknowledge the National Science Foundation, Division of Chemical, Biochemical and Thermal Engineering, Thermal Systems and Engineering Program, for its part in the support of this research under Grant No. MEA-8314966.

References

Beck, B. T., and Wedekind, G. L., 1981, ''A Generalization of the System Mean Void Fraction Model for Transient Two-Phase Evaporating Flows,'' ASME JOURNAL OF HEAT TRANSFER, Vol. 103, pp. 81–85.

Wedekind, G. L., and Bhatt, B. L., and Beck, B. T., 1978, ''A System Mean Void Fraction Model for Predicting Various Transient Phenomena Associated With Two-Phase Evaporating and Condensing Flows,'' *International Journal of Multiphase Flow*, Vol. 4, pp. 97–114.

Wedekind, G. L., and Bhatt, B. L., 1977, ''An Experimental and Theoretical Investigation Into Thermally Governed Transient Flow Surges in Two-Phase Condensing Flow,'' ASME JOURNAL OF HEAT TRANSFER, Vol. 99, pp. 561–567.

Wedekind, G. L., Beck, B. T., Bhatt, B. L., and Roslund, G. L., 1984, ''A Unified System Mean Void Fraction Model for Predicting Transient Characteristics of Flow Quality, Void Fraction, Flowrate and Pressure Drop in Evaporating and Condensing Flows,'' *Two-Phase Flow and Heat Transfer; China–U.S. Progress*, Xue-jun Chen and T. N. Veziroglu, eds., Hemisphere Publishing Co., Washington, DC, pp. 633–646.

Wedekind, G. L., and Stoecker, W. F., 1968, ''Theoretical Model for Predicting the Transient Response of the Mixture-Vapor Transition Point in Horizontal Evaporating Flow,'' ASME JOURNAL OF HEAT TRANSFER, Vol. 90, pp. 165–174.

Zivi, S. M., 1964, ''Estimation of Steady-State Steam Void Fraction by Means of the Principle of Minimum Entropy Production,'' ASME JOURNAL OF HEAT TRANSFER, Vol. 86, pp. 247–252.

Journal of Heat Transfer

Discussion

Predicting the Performance of an Evaporative Condenser[1]

W. Leidenfrost.[2] In their introduction, Peterson et al. refer to the article "Evaporative Cooling and Heat Transfer Augmentation Related to Reduced Condenser Temperature," by W. Leidenfrost and B. Korenic, published in *Heat Transfer Engineering*, Vol. 3, Nos. 3-4, pp. 38-59 (1982). The four authors criticize this article and declare it as unnecessarily overcomplicated by comparing it with their simpler approach, which can yield satisfactory results (within 30 percent). They fail to recognize that at present high-speed computers allow more complete and more complex analysis, which yields better results. These authors state further that in the referred article errors were made by assuming that the air heat transfer coefficient for dry tubes is equal to that of wet tubes and by assuming that wetted and dry tubes have identical surface areas for heat transfer with the surrounding air. Those statements miss the fact that in the criticized article two coefficients were introduced relating wet and dry heat transfer coefficients and wet and dry surface areas. Those coefficients can be approximated to be equal to unity but can easily be varied especially in the more complicated program.

All these statements made by the four authors do not do any harm and could remain unchallenged. However, they made another statement that cannot be left unanswered. They state that the Re number of a falling film defined by Leidenfrost and Korenic as the film velocity times its thickness and divided by the kinematic viscosity of the liquid in the film is not dimensionless. It is very surprising that the four authors did not recognize a widely accepted and century-old combination of the above parameters.

Such statements cannot go unchallenged, especially not when made in the JOURNAL OF HEAT TRANSFER.

Authors' Closure

While not disagreeing that the more accurate model can be solved on a computer, in our experience with testing large evaporative condensers (those with duties of 250 kW to 2 MW), the experimental data are usually rather inaccurate. Wet bulb temperatures are notoriously difficult to measure, and the measured duty of the condenser is very sensitive to changes in this value. Thus, in these situations, the types of errors introduced in the modeling, for example assuming Lewis numbers of 1, etc., are far less than those inherent in typical experimental data.

It is also very useful when testing a working condenser to have a very simple model so that data measured on site can be checked immediately for consistency, as it has been the exception to find a refrigeration plant where all the instruments are actually working correctly. Usually the experimental procedure has to be modified on site as one decides which instruments are probably accurate.

With regard to the dimensions in the paper by Leidenfrost and Korenic (1982); we have the following problems:

- Equations (35) and (36) are not dimensionally consistent if the Reynolds number is dimensionless.
- Using the definition given in equation (37), $\dot{m}_{Wvc}$ is defined as a volumetric flow rate per unit length. The subsequent equations and the Reynolds number (equation (40)) are dimensionally inconsistent when this definition is used. The symbol $\dot{m}_{Wvc}$ is not defined in the nomenclature, but is referred to equation (37) as a volumetric flow rate.

Presumably $\dot{m}$, the mass flow rate, should have been used in equation (37), but there is no obvious or simple way in which equations (35) and (36) can be made dimensionally correct.

An Extension to the Irreversibility Minimization Analysis Applied to Heat Exchangers[1]

D. P. Sekulic.[2] The authors have presented an interesting extension to the irreversibility minimization analysis applied to heat exchangers. The objective of this communication is to call attention to some limitations of the proposed methodology.

1 The objective function [equation (12)] cannot be used to optimize a cocurrent flow heat exchanger. The objective function for this arrangement (the curve Ns versus N_{tu}) does not have an extremum for an arbitrary finite thermal size (N_{tu}) (Sekulic, 1986; Bejan, 1988). In fact, from the relation

$$\frac{\partial}{\partial N_{tu}}(Ns_{\Delta T}) = \frac{\partial}{\partial \epsilon}(Ns_{\Delta T})\frac{\partial \epsilon}{\partial N_{tu}}$$

it is clear that for cocurrent flow the maximum of $Ns_{\Delta T}$ occurs only when $N_{tu} \to \infty$; in other words

$$\frac{\partial}{\partial \epsilon}(Ns_{\Delta T}) \neq 0 \text{ for } N_{tu} > 0, \text{ and } \frac{\partial}{\partial N_{tu}}(\epsilon) = 0 \text{ for } N_{tu} \to \infty$$

In conclusion, the cocurrent flow arrangement does not enjoy the objective function optimum mentioned in the paper (for any choice of ω, N_{tu}, τ, or γ parameters). In addition, the above conclusion holds for several other flow arrangements, but for different reasons.

[1] By D. Peterson, D. Glasser, D. Williams, and R. Ramsden, published in the August 1988 issue of the ASME JOURNAL OF HEAT TRANSFER, Vol. 110, No. 3, pp. 748-753.

[2] Purdue University, West Lafayette, IN.

[1] By S. Aceves-Saborio, J. Ranasinghe, and G. M. Reistad, published in the February 1989 issue of the ASME JOURNAL OF HEAT TRANSFER, Vol. 111, No. 1, pp. 29-36.

[2] Senior Fulbright Scholar, Department of Mechanical Engineering and Materials Sciences, School of Engineering, Duke University, Durham, NC 27706; also Assoc. Professor, Department of Mechanical Engineering, University of Novi Sad, 21000 Novi Sad, Yugoslavia.